



*polymers*

# Advanced Polymer Simulation and Processing Volume II

---

Edited by

Célio Bruno Pinto Fernandes, Salah Aldin Faroughi,  
Luís L. Ferrás and Alexandre M. Afonso

Printed Edition of the Special Issue Published in *Polymers*

# **Advanced Polymer Simulation and Processing- Volume II**



# Advanced Polymer Simulation and Processing- Volume II

Editors

**Célio Bruno Pinto Fernandes**

**Salah Aldin Faroughi**

**Luís L. Ferrás**

**Alexandre M. Afonso**

MDPI • Basel • Beijing • Wuhan • Barcelona • Belgrade • Manchester • Tokyo • Cluj • Tianjin



*Editors*

Célio Bruno Pinto Fernandes  
University of Minho  
Portugal

Salah Aldin Faroughi  
Texas State University  
USA

Luís L. Ferrás  
University of Porto  
Portugal

Alexandre M. Afonso  
University of Porto  
Portugal

*Editorial Office*

MDPI  
St. Alban-Anlage 66  
4052 Basel, Switzerland

This is a reprint of articles from the Special Issue published online in the open access journal *Polymers* (ISSN 2073-4360) (available at: [https://www.mdpi.com/journal/polymers/special\\_issues/Polym\\_Simul\\_Process](https://www.mdpi.com/journal/polymers/special_issues/Polym_Simul_Process)).

For citation purposes, cite each article independently as indicated on the article page online and as indicated below:

LastName, A.A.; LastName, B.B.; LastName, C.C. Article Title. <i>Journal Name</i> <b>Year</b> , <i>Volume Number</i> , Page Range.
--

**Volume 2**

ISBN 978-3-0365-6666-5 (Hbk)

ISBN 978-3-0365-6667-2 (PDF)

**Volume 1-2**

ISBN 978-3-0365-6662-7 (Hbk)

ISBN 978-3-0365-6663-4 (PDF)

© 2023 by the authors. Articles in this book are Open Access and distributed under the Creative Commons Attribution (CC BY) license, which allows users to download, copy and build upon published articles, as long as the author and publisher are properly credited, which ensures maximum dissemination and a wider impact of our publications.

The book as a whole is distributed by MDPI under the terms and conditions of the Creative Commons license CC BY-NC-ND.

# Contents

<b>About the Editors</b> . . . . .	<b>ix</b>
<b>Preface to “Advanced Polymer Simulation and Processing- Volume II”</b> . . . . .	<b>xi</b>
<b>Jiquan Li, Jie Bei, Wenyong Liu, Xinxin Xia, Bida Zhou, Xiang Peng and Shaofei Jiang</b> Warpage Prediction of RHCM Crystalline Parts Based on Multi-Layers Reprinted from: <i>Polymers</i> <b>2021</b> , <i>13</i> , 1814, doi:10.3390/polym13111814 . . . . .	<b>1</b>
<b>Khagendra Baral, Puja Adhikari, Bahaa Jawad, Rudolf Podgornik and Wai-Yim Ching</b> Solvent Effect on the Structure and Properties of RGD Peptide (1FUUV) at Body Temperature (310 K) Using Ab Initio Molecular Dynamics Reprinted from: <i>Polymers</i> <b>2021</b> , <i>13</i> , 3434, doi:10.3390/polym13193434 . . . . .	<b>15</b>
<b>Lihua Ye, Muhammad Muzamal Ashfaq, Aiping Shi, Syyed Adnan Raheel Shah and Yefan Shi</b> Performance Analysis of Indentation Punch on High Energy Lithium Pouch Cells and Simulated Model Improvement Reprinted from: <i>Polymers</i> <b>2021</b> , <i>13</i> , 1971, doi:10.3390/polym13121971 . . . . .	<b>29</b>
<b>Lin Deng, Suo Fan, Yun Zhang, Zhigao Huang, Huamin Zhou, Shaofei Jiang and Jiquan Li</b> Multiscale Modeling and Simulation of Polymer Blends in Injection Molding: A Review Reprinted from: <i>Polymers</i> <b>2021</b> , <i>13</i> , 3783, doi:10.3390/polym13213783 . . . . .	<b>51</b>
<b>Matheus Tozo de Araujo, Laison Furlan, Analice Brandi and Leandro Souza</b> A Semi-Analytical Method for Channel and Pipe Flows for the Linear Phan-Thien-Tanner Fluid Model with a Solvent Contribution Reprinted from: <i>Polymers</i> <b>2022</b> , <i>14</i> , 4675, doi:10.3390/polym14214675 . . . . .	<b>77</b>
<b>Matthias Schmid, Dominik Altmann and Georg Steinbichler</b> A Simulation-Data- Based Machine Learning Model for Predicting Basic Parameter Settings of the Plasticizing Process in Injection Molding Reprinted from: <i>Polymers</i> <b>2021</b> , <i>13</i> , 2652, doi:10.3390/polym13162652 . . . . .	<b>95</b>
<b>Michelle Spanjaards, Gerrit Peters, Martien Hulsen and Patrick Anderson</b> Numerical Study of the Effect of Thixotropy on Extrudate Swell Reprinted from: <i>Polymers</i> <b>2021</b> , <i>13</i> , 4383, doi:10.3390/polym13244383 . . . . .	<b>109</b>
<b>M. M. A. Spanjaards , G. W. M. Peters, M. A. Hulsen and P. D. Anderson</b> Towards the Development of a Strategy to Characterize and Model the Rheological Behavior of Filled, Uncured Rubber Compounds Reprinted from: <i>Polymers</i> <b>2021</b> , <i>13</i> , 4068, doi:10.3390/polym13234068 . . . . .	<b>133</b>
<b>Mujtahid Kaavessina, Sperisa Distantina and Esa Nur Shohih</b> A Slow-Release Fertilizer of Urea Prepared via Melt Blending with Degradable Poly(lactic acid): Formulation and Release Mechanisms Reprinted from: <i>Polymers</i> <b>2021</b> , <i>13</i> , 1856, doi:10.3390/polym13111856 . . . . .	<b>157</b>
<b>N’dri Arthur Konan, Eilis Rosenbaum and Mehrdad Massoudi</b> On the Response of a Herschel–Bulkley Fluid Due to a Moving Plate Reprinted from: <i>Polymers</i> <b>2022</b> , <i>14</i> , 3890, doi:10.3390/polym14183890 . . . . .	<b>171</b>

<b>Patrick Hirsch, Marianne John, Daniel Leipold, André Henkel, Sylvia Gipser, Ralf Schlimper and Matthias Zscheuye</b> Numerical Simulation and Experimental Validation of Hybrid Injection Molded Short and Continuous Fiber-Reinforced Thermoplastic Composites Reprinted from: <i>Polymers</i> <b>2021</b> , <i>13</i> , 3846, doi:10.3390/polym13213846 . . . . .	<b>193</b>
<b>Quang Truong Pham, Gia Long Ngo, Xuan An Nguyen, Chi Thanh Nguyen, Isabelle Ledoux-Rak and Ngoc Diep Lai</b> Direct Synthesis of Gold Nanoparticles in Polymer Matrix Reprinted from: <i>Polymers</i> <b>2023</b> , <i>15</i> , 16, doi:10.3390/polym15010016 . . . . .	<b>211</b>
<b>Rabie A. Abu Saleem, Nisrin Abdelal, Ahmad Alsabbagh, Maram Al-Jarrah and Fatima Al-Jawarneh</b> Radiation Shielding of Fiber Reinforced Polymer Composites Incorporating Lead Nanoparticles—An Empirical Approach Reprinted from: <i>Polymers</i> <b>2021</b> , <i>13</i> , 3699, doi:10.3390/polym13213699 . . . . .	<b>223</b>
<b>Salah A. Faroughi, Ana I. Roriz and Célio Fernandes</b> A Meta-Model to Predict the Drag Coefficient of a Particle Translating in Viscoelastic Fluids: A Machine Learning Approach Reprinted from: <i>Polymers</i> <b>2022</b> , <i>14</i> , 430, doi:10.3390/polym14030430 . . . . .	<b>239</b>
<b>Salah A. Faroughi and Francesco Del Giudice</b> Microfluidic Rheometry and Particle Settling: Characterizing the Effect of Polymer Solution Elasticity Reprinted from: <i>Polymers</i> <b>2022</b> , <i>14</i> , 657, doi:10.3390/polym14040657 . . . . .	<b>263</b>
<b>Shuxin Huang</b> Viscoelastic Property of an LDPE Melt in Triangular- and Trapezoidal-Loop Shear Experiment Reprinted from: <i>Polymers</i> <b>2021</b> , <i>13</i> , 3997, doi:10.3390/polym13223997 . . . . .	<b>283</b>
<b>Thanh Trung Do, Tran Minh The Uyen and Pham Son Minh</b> The Feasibility of an Internal Gas-Assisted Heating Method for Improving the Melt Filling Ability of Polyamide 6 Thermoplastic Composites in a Thin Wall Injection Molding Process Reprinted from: <i>Polymers</i> <b>2021</b> , <i>13</i> , 1004, doi:10.3390/polym13071004 . . . . .	<b>305</b>
<b>Vladimir Shelukhin</b> Flows of Linear Polymer Solutions and Other Suspensions of Rod-like Particles: Anisotropic Micropolar-Fluid Theory Approach Reprinted from: <i>Polymers</i> <b>2021</b> , <i>13</i> , 3679, doi:10.3390/polym13213679 . . . . .	<b>323</b>
<b>Zhongke Yuan, Xiaochuan Chen and Dingshan Yu</b> Recent Advances in Elongational Flow Dominated Polymer Processing Technologies Reprinted from: <i>Polymers</i> <b>2021</b> , <i>13</i> , 1792, doi:10.3390/polym13111792 . . . . .	<b>339</b>
<b>Wiesław Frącz, Grzegorz Janowski and Łukasz Bąk</b> Influence of the Alkali Treatment of Flax and Hemp Fibers on the Properties of PHBV Based Biocomposites Reprinted from: <i>Polymers</i> <b>2021</b> , <i>13</i> , 1965, doi:10.3390/polym13121965 . . . . .	<b>355</b>
<b>Xiaodong Li, Meishuai Zou, Lisha Lei and Longhao Xi</b> Non-Isothermal Crystallization Kinetics of Poly(ethylene glycol) and Poly(ethylene glycol)-B-Poly( $\epsilon$ -caprolactone) by Flash DSC Analysis Reprinted from: <i>Polymers</i> <b>2021</b> , <i>13</i> , 3713, doi:10.3390/polym13213713 . . . . .	<b>381</b>

<b>Yan-Mao Huang, Wen-Ren Jong and Shia-Chung Chen</b> Transfer Learning Applied to Characteristic Prediction of Injection Molded Products Reprinted from: <i>Polymers</i> <b>2021</b> , <i>13</i> , 3874, doi:10.3390/polym13223874 . . . . .	<b>391</b>
<b>Yong-Jie Zeng, Sheng-Jye Hwang, Yu-Da Liu and Chien-Sheng Huang</b> Mold Flow Analysis of Motor Core Gluing with Viscous Flow Channels and Dipping Module Reprinted from: <i>Polymers</i> <b>2021</b> , <i>13</i> , 2186, doi:10.3390/polym13132186 . . . . .	<b>423</b>
<b>You Wu, Dandan Ju, Hao Wang, Chengyue Sun, Yiyong Wu, Zhengli Cao and Oleg V Tolochko</b> Simulation of the Particle Transport Behaviors in Nanoporous Matter Reprinted from: <i>Polymers</i> <b>2022</b> , <i>14</i> , 3563, doi:10.3390/polym14173563 . . . . .	<b>441</b>
<b>Vladimir Shelukhin</b> Rotational Particle Separation in Solutions: Micropolar Fluid Theory Approach Reprinted from: <i>Polymers</i> <b>2021</b> , <i>13</i> , 1072, doi:10.3390/polym13071072 . . . . .	<b>451</b>





# About the Editors

## **Célio Bruno Pinto Fernandes**

Dr. Célio Fernandes obtained his Education of Mathematics degree from the University of Minho (Portugal) in 2005. After graduating, C. Fernandes obtained his Applied Mathematics MSc degree at the University of Porto (Portugal) in 2007. During this period, C. Fernandes employed spectral methods to describe the melt flow that occurs in the polymer extrusion process. Afterwards, C. Fernandes joined the Department of Polymer Engineering at the University of Minho (Portugal) where he completed his Ph.D. degree in Science and Engineering of Polymers and Composites in 2012. During this period, C. Fernandes made important contributions to the field of the Injection Molding Process by applying multi-objective evolutionary algorithms to solve the inverse problem of finding the best injection molding parameters to achieve predefined criteria. C. Fernandes was a visiting Post-Doctoral researcher at MIT, USA in 2017. C. Fernandes has been working with the open-source computational fluid dynamics library OpenFOAM. He has established new numerical methods for the solution of viscoelastic matrix-based fluids using the finite volume method, such as an immersed boundary method able to fully-resolve particle-laden viscoelastic flows and developed a fully implicit log-conformation tensor coupled algorithm for the solution of incompressible non-isothermal viscoelastic flows.

## **Salah Aldin Faroughi**

Dr. Salah A. Faroughi is an Assistant Professor in the Ingram School of Engineering at Texas State University. He holds a B.Sc. and M.Sc. in Mechanical Engineering. He obtained his Ph.D. in Civil and Environmental Engineering at Georgia Institute of Technology, where he investigated the effect of microstructures (e.g., particle shape, size, type, orientation, and rearrangement) on the rheophysics and thermophysics of complex particulate matter (e.g., fluids and composites). He did his postdoctoral study at the Massachusetts Institute of Technology in the department of Mechanical Engineering. His postdoc research focused on the development of high-performance computing algorithms augmented using physics-based deep learning models to explore the dynamics of particle-laden viscoelastic materials. His studies provided answers to multiple long-lived fundamental questions and resulted in several well-cited papers published in prestigious journals such as *Nature*, *Journal of Applied Physics*, *Physical Review E*, and *JNNFM*, among many others.

## **Luís L. Ferrás**

L. L. Ferrás is an Assistant Professor at the Department of Mechanical Engineering, Faculty of Engineering, University of Porto (FEUP) and a researcher at the Centre for Mathematics, University of Minho, Portugal. He received his Ph.D. in Science and Engineering of Polymers and Composites from the University of Minho in 2012, a Ph.D. in Mathematics from the University of Chester in 2019, and was a visiting researcher at MIT in 2016. His current research interests are numerical analysis, applied mathematics, partial and fractional differential equations, mathematical modeling, computational mechanics, computational fluid dynamics, complex viscoelastic flows, rheology, anomalous diffusion, and machine learning.

**Alexandre M. Afonso**

Afonso graduated in Chemical Engineering from Faculty of Engineering of the University of Porto (FEUP) in 2000, with a final-year Research Project at the Universidad Politecnica de Catalunya graded with an Honor Grade (10/10). In 2005, Afonso completed an MSc in Heat and Fluid mechanics and, in 2010, completed a PhD degree in Biological and Chemical Engineering from FEUP. Currently, Afonso is an Assistant Professor at the Department of Mechanical Engineering at FEUP.

# Preface to “Advanced Polymer Simulation and Processing- Volume II”

Polymer-processing techniques are of the utmost importance for producing polymeric parts. They must produce parts with the desired qualities, which are usually related to mechanical performance, dimensional conformity, and appearance. Aiming to maximize the overall efficiency of the polymer-processing techniques, advanced modeling codes along with experimental measurements are needed to simulate and optimize the processes. Our objective with this reprint is to provide a text that exploits the digital transformation of the plastics industry, both through the creation of more robust and accurate modeling tools and the development of cutting-edge experimental techniques.

We would like to thank all those who have supported us in completing this work.

**Célio Bruno Pinto Fernandes, Salah Aldin Faroughi, Luís L. Ferrás, and Alexandre M. Afonso**  
*Editors*



## Article

# Warpage Prediction of RHCM Crystalline Parts Based on Multi-Layers

Jiquan Li <sup>1,2</sup>, Jie Bei <sup>1</sup>, Wenyong Liu <sup>1</sup>, Xinxin Xia <sup>1</sup>, Bida Zhou <sup>1</sup>, Xiang Peng <sup>1,2</sup> and Shaofei Jiang <sup>1,2,\*</sup>

<sup>1</sup> College of Mechanical Engineering, Zhejiang University of Technology, Hangzhou 310014, China; Lijq@zjut.edu.cn (J.L.); nbbeijie@163.com (J.B.); liuwenyonglwy@163.com (W.L.); sherlockingxia@163.com (X.X.); zhoubidazbd@163.com (B.Z.); pengxiang@zjut.edu.cn (X.P.)

<sup>2</sup> National International Joint Research Center of Special Purpose Equipment and Advanced Processing Technology, Zhejiang University of Technology, Hangzhou 310014, China

\* Correspondence: jsf75@zjut.edu.cn

**Abstract:** Warpage is a typical defect for injection-molded parts, especially for crystalline parts molded by rapid heat cycle molding (RHCM). In this paper, a prediction method is proposed for predicting the warpage of crystalline parts molded by the RHCM process. Multi-layer models were established to predict warpage with the same thicknesses as the skin-core structures in the molded parts. Warpages were defined as the deformations calculated by the multi-layer models. The deformations were solved using the classical laminated plate theory by Abaqus. A model was introduced to describe the elastic modulus with the influence of temperature and crystallinity. The simulation process was divided into two procedures, before ejection and after ejection. Thermal stresses and thermal strains were simulated, respectively, in the procedure before ejection and after ejection. The prediction results were compared with the experimental results, which showed that the average errors between predicted warpage and average experimental warpage are, respectively, 7.0%, 3.5%, and 4.4% in conventional injection molding (CIM), in RHCM under a 60 °C heating mold (RHCM60), and in RHCM under a 90 °C heating mold (RHCM90).

**Keywords:** warpage; prediction; crystallinity; multi-layer structure; simulation

**Citation:** Li, J.; Bei, J.; Liu, W.; Xia, X.; Zhou, B.; Peng, X.; Jiang, S. Warpage Prediction of RHCM Crystalline Parts Based on Multi-Layers. *Polymers* **2021**, *13*, 1814. <https://doi.org/10.3390/polym13111814>

Academic Editors: Célio Bruno Pinto Fernandes, Salah Aldin Faroughi, Luís L. Ferrás, Alexandre M. Afonso

Received: 1 May 2021  
Accepted: 27 May 2021  
Published: 31 May 2021

**Publisher's Note:** MDPI stays neutral with regard to jurisdictional claims in published maps and institutional affiliations.



**Copyright:** © 2021 by the authors. Licensee MDPI, Basel, Switzerland. This article is an open access article distributed under the terms and conditions of the Creative Commons Attribution (CC BY) license (<https://creativecommons.org/licenses/by/4.0/>).

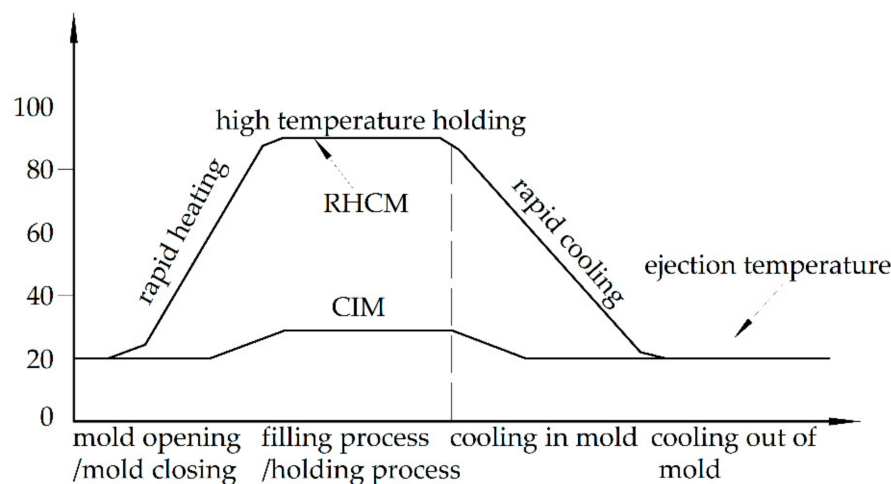
## 1. Introduction

Rapid heat cycle molding (RHCM) is a special injection molding technology used to mold parts with a high surface quality without extending the cycle time [1]. Some defects in the plastic parts produced by conventional injection molding (CIM) can be solved by RHCM, such as flow mark, silver mark, jetting mark, weld mark, exposed fibers, short shot, etc. [2]. However, RHCM is not a nostrum for all the defects in injection-molded parts. Warpage is one of the defects that cannot be solved by RHCM [3].

Warpage is a distortion where the shape or dimension of a molded part deviates from that of the intended design [4]. It is caused by the residual stresses in the molded part after ejection, which mainly result from the non-uniform shrinkage of the polymer in different positions of the molded part [3]. Unfortunately, non-uniform shrinkage is inevitable due to the inhomogeneous temperature history of polymer in different positions, inhomogeneous pressure distribution, etc. [5]. In particular, in injection-molded crystalline parts, the inhomogeneous condition of polymer will introduce more complex crystallization than in static crystallized parts. The complex crystallization will introduce more complicated shrinkage and greater warpage [6,7].

Some researchers have discussed the influences of the processing parameters on the warpage of CIM parts through experiments [8–12], and the warpage has been optimized based on experimental results [13–17]. These works have provided guidance to reduce the warpage of injection-molded parts. However, the guidance is usually not universal to all parts. The prediction of warpage by computer will solve the issue of universality. Some

methods have been introduced and developed to predict the warpage of CIM parts [18–20], and some of them have been introduced into commercial software, such as Moldflow and Moldex 3D. The large warpage is considered as the main defect of RHCM parts [21]. Unlike the conventional injection molding (CIM) process, the RHCM process employs a dynamic mold temperature control strategy based on rapid mold heating and cooling [22]. In RHCM, the mold temperature is heated to a relatively high preset value before melt injection and remains constant during the filling and packing phases. On gate solidification, the mold is rapidly cooled to allow the solidification and the demolding of the polymer part [23], as shown in Figure 1. The different temperature histories in the mold introduce various thermal and shear histories to the polymer. Stratification is the most distinguishable feature in the inhomogeneous distribution of process parameters in molten polymer during molding and the microstructure in the molded parts after molding. The different crystal morphology of each layer introduces different mechanical properties. The layers with different mechanical properties will complicate the warpage of RHCM parts. The warpage prediction of RHCM parts is difficult because Moldflow cannot set multi-layer material and crystallinity. Therefore, it will be very meaningful to propose a prediction method to accurately predict the warpage of crystalline parts molded using the RHCM process.



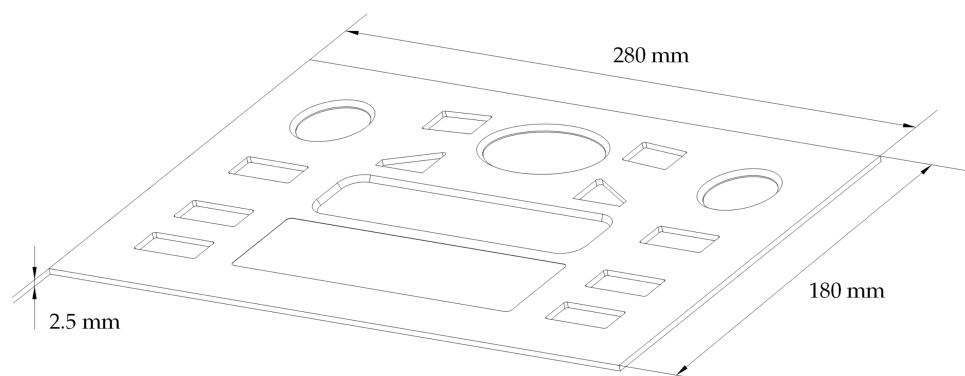
**Figure 1.** The RHCM process.

In this paper, a prediction method is proposed to calculate the warpage of RHCM parts based on multi-layers, according to the common skin-core structure in the molded parts [3] and the layer distribution of pressure and temperature along the thickness during the molding process. The thicknesses of the multi-layers were determined as the thicknesses of the skin-core structure in the molded parts, measured using a polarizing microscope (PLM). A model was introduced to describe the elastic modulus with the influence of temperature and crystallinity [24]. Finally, the predicted results were compared with the warpage information of the parts obtained using a 3D laser scanner.

## 2. Experimental

### 2.1. Part Preparation

A semi-crystalline iPP (T30S, Zhenhai branch of Sinopec Corp, Ningbo, China) was used to mold parts. The parameters of the polymer were as follows: melt flow index (MFR) of 2.5 g/10 min, melting point of 167 °C, density of 0.91 g/cm<sup>3</sup>, and an isotactic index greater than 94%. An injection molding machine (MA3800/2250, Haitian International Holdings Ltd., Ningbo, China) was employed to produce CIM and RHCM parts with a size of 280 × 180 × 2.5 mm, as shown in Figure 2.



**Figure 2.** Shape and dimensions of the experimental part.

The same RHCM mold was used in this study as in an earlier study [25]. Electrical heating rods and cooling tunnels were deployed in the stationary mold, which could be rapidly heated by electric heating before filling and cooled by circulating water after filling. Meanwhile, the moving mold only had regular cooling tunnels. The heating of the electrical heating rods was controlled by an MTS-32II mold heating temperature controller (Beijing CHN-TOP Machinery Group Co Ltd., Beijing, China), the heating rods and heating temperature controller were all turned off. Parts were molded under the following process conditions: melt temperature of 220 °C, injection pressure of 90 MPa, packing pressure of 50 MPa, cooling time of 30 s, and coolant temperature at room temperature (20 °C). CIM was conducted at room temperature. Room temperature is usually 20 or 25 °C according to the literature [22,25–27]. Combined with the actual room temperature, the mold temperature was 20 °C in this study. The iPP used in this experiment was a fast crystallizing polymer, and its crystallization temperature ranged from 20 to 120 °C [28,29]. The mold temperature was determined by the microscopic morphological structure, which had a significant difference between 60 and 90 °C [25,27]. The stratification in the microstructure of parts can be better observed and analyzed. Combined with the room temperature at the time of the experiments, the mold temperatures containing large differences were determined to be 20, 60, and 90 °C; the parts molded under 60 and 90 °C were marked as RHCM60 and RHCM90, respectively.

### 2.2. Polarizing Microscope Experiment

Samples with dimensions of 8 × 8 × 2.5 mm were taken from the center of the molded parts, as shown in Figure 3. The location was determined mainly by avoiding the weld mark. Thin slices of specimens were cut along the thickness direction of samples and observed using a polarizing microscope (U-FMP, Olympus Corporation, Tokyo, Japan). The thickness of each layer was investigated on the PLM results along the thickness direction.

### 2.3. WAXD Experiment

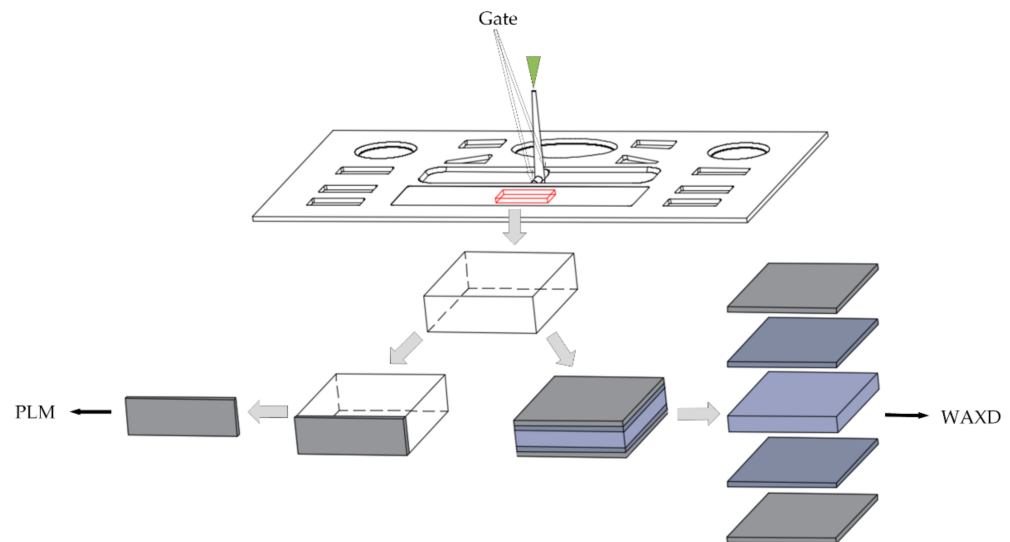
Wide-angle X-ray diffraction (WAXD) was employed to determine the crystallinity of each layer. The samples were polished with coarse and fine sandpaper to the location range of each layer. WAXD was conducted on an X-Pert PRO X-ray diffraction instrument (PANalytical B. V., Almelo, The Netherlands) with an X-ray source of  $K\alpha$  radiation from a Cu target ( $\lambda = 0.154056$  nm), a voltage of 40 kV, and a current of 40 mA. Its diffraction angle  $2\theta$  ranged from 10° to 40°. The crystallinities were calculated using X'Pert HighScore Plus.

### 2.4. 3D Scanning

The warpages of the molded parts were measured using a 3D laser scanner (Faroarm, Faro, FL, USA). The surface of the part was set as the reference plane and the thickness direction of the part was set as the z direction. The warpage was defined as the difference between the maximum value in the z direction of the molded part and the reference plane.



Five parts molded under the same molding conditions were chosen to be scanned, and the average of the warpages was taken as the measured warpage for discussion. The measured warpage was compared with the prediction results to verify the accuracy of the prediction method.



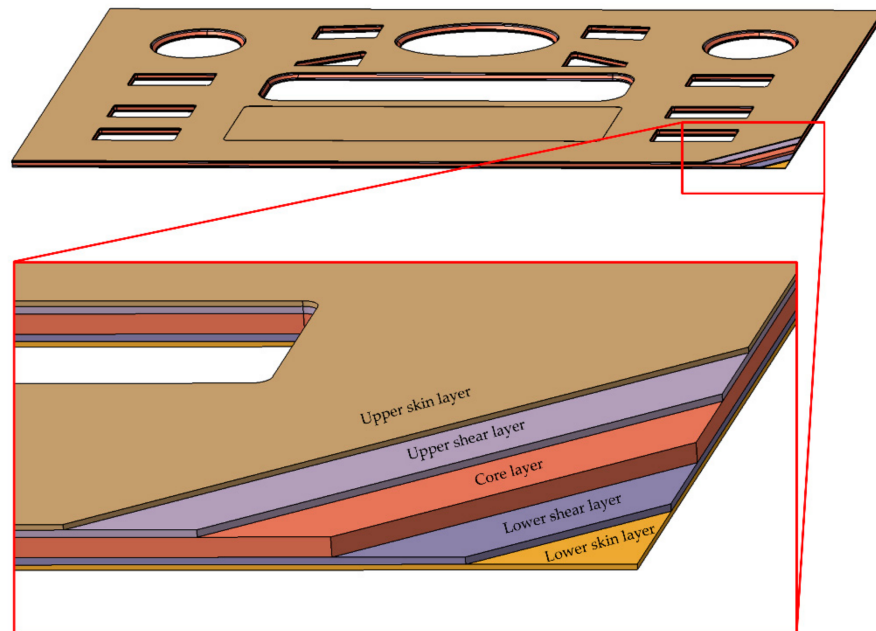
**Figure 3.** Experimental sample.

### 3. Methodology

Shear stratification and temperature stratification usually appear in a polymer during injection molding [30], and multi-layer structures always appear in the molded parts along the thickness direction [31]. A multi-layer structure is always introduced by the fountain flow due to the thin-walled, large-plane part characteristics. In the fountain flow, the temperature and shear of the polymer usually show stratification distribution. The solid area, liquid melt area, and two-phase area of the polymer will appear in the cavity during the filling process [30]. The whole polymer presents five areas along the thickness direction, namely the upper solid area, upper two-phase area, liquid melt area, lower two-phase solid area, and lower solid area. Additionally, skin-core structures will appear in the parts molded by CIM and RHCM [30–32].

Polypropylene can be considered an intercalated homogeneous material based on the Eshelby equivalence principle [33] and the Mori–Tanaka method [34]. The crystals produced during crystallization are considered to be inclusions, and the amorphous phase is considered to be the matrix. Furthermore, the multi-layers of the parts are divided according to the crystal morphology of the parts along the thickness direction. The different crystal morphology of each layer introduces different mechanical properties, e.g., modulus and strength [35–37]. The inhomogeneous distribution of mechanical properties and temperature will introduce non-uniform shrinkage and result in warpage of the parts.

A multi-layer model was established to predict the warpage of injection-molded parts, because the stratification is the most distinguishable feature in the inhomogeneous distribution of process parameters in a molten polymer during molding and the microstructure in the molded parts after molding. In the model, the overall shape and dimensions were the same as those of the part. However, the model was divided into five layers along the thickness direction, namely the upper skin layer, upper shear layer, core layer, lower shear layer, and lower skin layer, as shown in Figure 4. The thicknesses of the layers in the model were the same as those of the parts.



**Figure 4.** The multi-layer model with five layers.

Warpages were defined as deformations of the molded parts. The deformations in the multi-layer model were solved using the classical Laminated Plate Theory [38] by Abaqus. The layers with different mechanical properties were treated as layers with different angles during the solving simulation. The crystallinities of each layer in the model were obtained by measuring the corresponding positions of molded parts with WAXD. The mechanical properties of each layer necessary for prediction were calculated using the following model describing the elastic modulus with the influence of temperature and crystallinity [24].

$$\begin{cases} E(\theta) = E_0 \cdot \exp[-b(\theta - \theta_0)] \\ E_0 = a \cdot \exp\left(\frac{cw}{1-w}\right) \end{cases} \quad (1)$$

where  $\theta_0$  is the reference temperature (room temperature);  $E_0$  is the elastic modulus at the reference temperature;  $a$ ,  $b$ , and  $c$  are material parameters;  $w$  and  $\theta$  are the crystallinity and service temperature, respectively. The same material was used to mold the part as in our past study, and the parameters were introduced [39].

The complex crystallization is inevitable due to the inhomogeneous temperature history, which will introduce more complicated shrinkage and greater warpage. The internal thermal stress of the part cannot be released by the mold constraint before ejection. The part produces warpage due to internal thermal stress release after ejection. The simulation process was divided into two stages: before ejection and after ejection. In the simulation before ejection, temperature histories were summarized from the simulation results of heat transmission between the polymer and mold. Additionally, the thermal stresses were simulated under shape restriction, where the shape was same as the cavity. In the simulation after ejection, temperature histories were summarized from the simulation results of heat transmission between the polymer and atmosphere, and the deformation was calculated from the thermal strains simulated without deformation restriction.

The simulations before ejection were conducted under the initial conditions with the temperature of the moving mold at 20 °C; the temperature of the stationary mold at 20, 60, and 90 °C; a melt temperature of 220 °C. Thermal load was introduced by the density variations because of the temperature dropping during the molding process,

and the density variations were described by a modified two-domain Tait equation of state [20,40–42] in this paper.

$$V(T, P) = V_0(T) \left\{ 1 - C \ln \left[ 1 + \frac{P}{B(T)} \right] \right\} + V_1(T, P) \quad (2)$$

where  $V(T, P)$  is the specific volume at temperature  $T$  and pressure  $P$ ;  $V_0$  is the specific volume at atmospheric pressure;  $C$  is a constant, whose value is 0.0894;  $B$  is the pressure sensitivity of the material.

In the simulation after ejection, the simulation results of the parts in the first stage were introduced as the initial conditions. The thicknesses of each layer were determined by the data measured in PLM, and different mechanical properties were introduced in each layer. The mold restriction was removed, and the parts were cooled at room temperature. Additionally, the centers of the parts were fixed. Thus, the simulation results of warpage were obtained.

#### 4. Results and Discussion

##### 4.1. Multi-Layer Structure of Injection-Molded Parts

##### 4.1.1. Skin-Core Structures Investigated by PLM

The typical skin-core structures of the molded parts were obtained by morphology investigation with PLM along the thickness direction under different process conditions, as shown in Figure 5. The thicknesses of the layers changed with each different molding process, as shown in Table 1. The upper skin layer of each injection-molded part was near to the stationary side with heating rods.

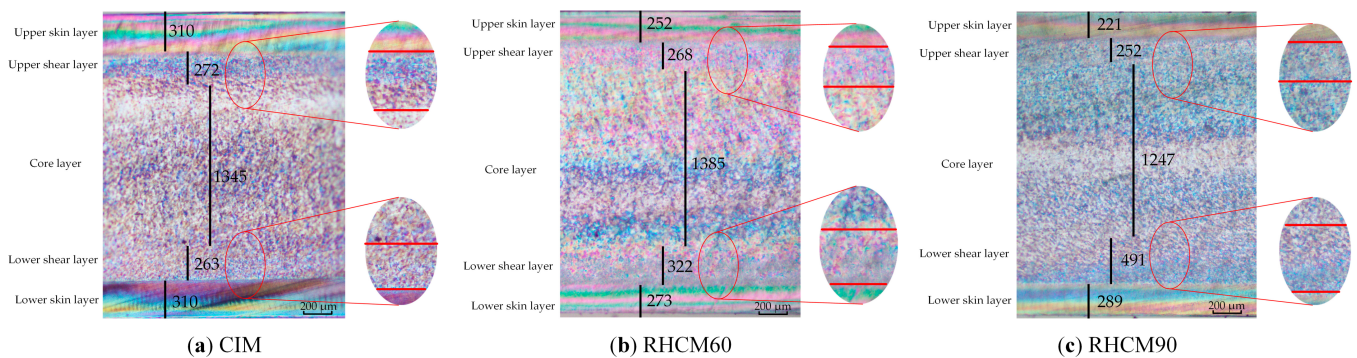


Figure 5. Polarized micrographs of parts under different processes.

Table 1. The thickness of each layer under different processes.

Layer	CIM (μm)	RHCM60 (μm)	RHCM90 (μm)
Upper skin layer	310	252	221
Upper shear layer	272	268	252
Core layer	1345	1385	1247
Lower shear layer	263	322	491
Lower skin layer	310	273	289

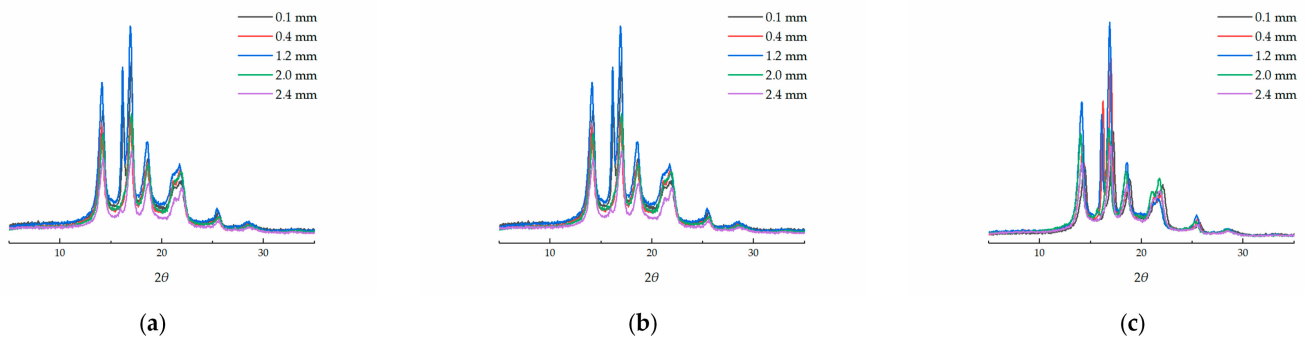
The thicknesses of the layers were almost symmetrical along the thickness direction in the skin-core structures of the CIM parts. The mold temperature of the stationary side was the same as that of the moving side. Therefore, the temperature distribution of polymer in the cavity was symmetrical and introduced symmetrical skin-core structures.

The thicknesses of the layers were obviously asymmetrical in the skin-core structures of the RHCM parts, introduced by the different temperatures between the stationary side and the moving side of the mold. Since the upper skin layer of the part was near the

stationary side with heating rods, the thicknesses of the upper layers were smaller than those of the lower layers. The thicknesses of the upper skin layer and the lower skin layer in RHCM90 were 221 and 289  $\mu\text{m}$ , respectively, a change by 30.8%. The thicknesses of the upper shear layer and the lower shear layer in RHCM90 were 252 and 491  $\mu\text{m}$ , respectively, a change by 94.8%. The thickness variation in the upper and lower shear layers was three times greater than that in the upper and lower skin layers. The asymmetrical distribution of the layer thicknesses will introduce greater warpage.

#### 4.1.2. Crystallinity of Each Layer

The position range of each layer in the molded parts was divided according to the crystal morphology observed in PLM. The distances  $x$  from the upper surface of the sample were set as the positions of certain layers to conduct the WAXD investigation, and 0.1, 0.4, 1.2, 2.0, and 2.4 mm were considered to be the positions of the upper skin layer, upper shear layer, core layer, lower shear layer, and lower skin layer, respectively. The crystallinity diffraction pattern of each layer obtained by WAXD is shown in Figure 6. The crystallinity of each layer could be calculated from the crystallinity diffraction pattern using X'Pert HighScore Plus. The calculated results of the crystallinities are shown in Table 2.



**Figure 6.** Crystallinity diffraction pattern of parts with different molding conditions by WAXD: (a) CIM, (b) RHCM60, (c) RHCM90.

**Table 2.** Crystallinity of each layer under different processes.

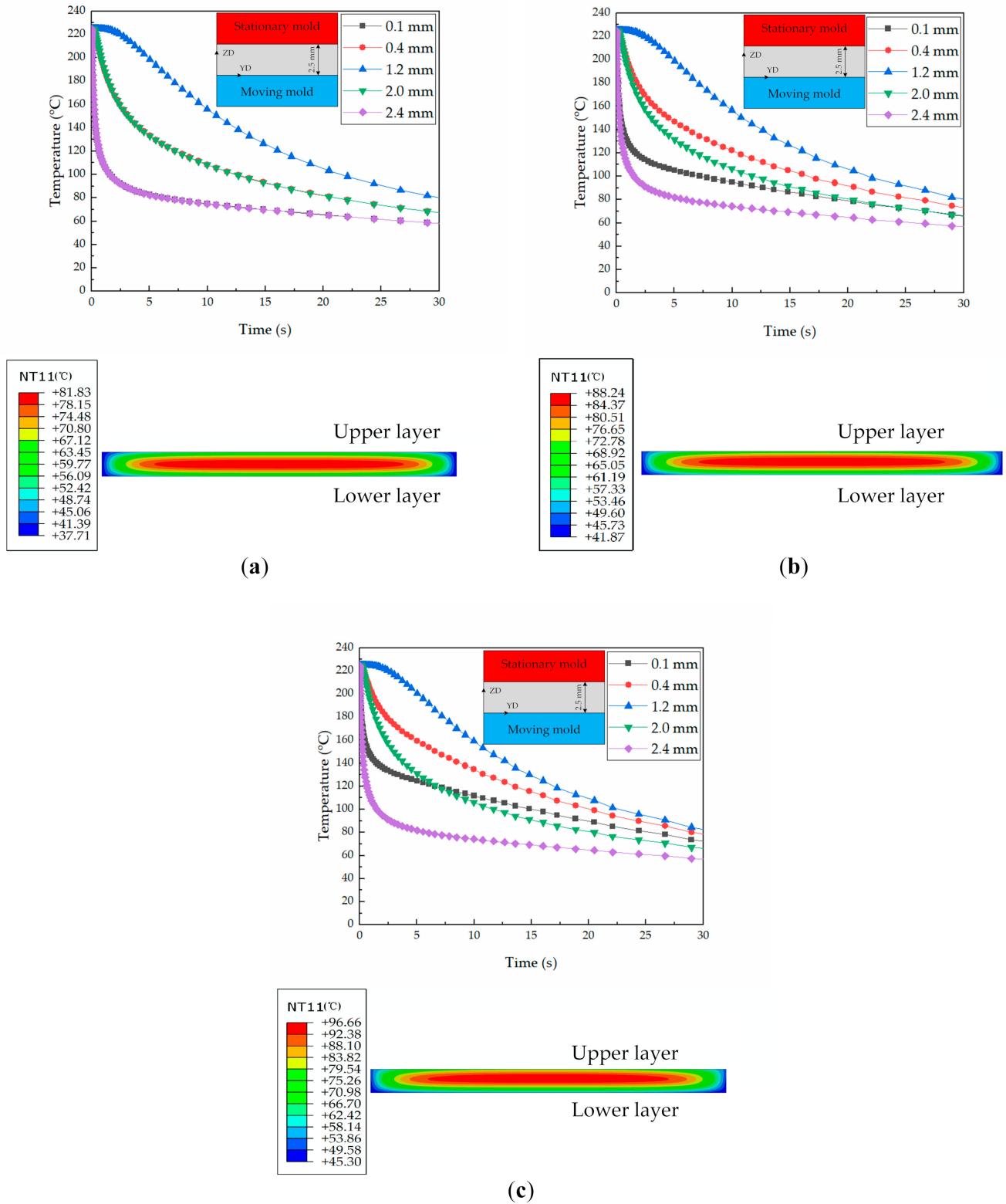
Thickness Position $x$ (mm)	CIM	RHCM60	RHCM90
0.1	35.24%	40.28%	42.41%
0.4	37.34%	42.43%	44.83%
1.2	43.50%	45.56%	47.51%
2.0	36.96%	40.82%	42.93%
2.4	35.10%	37.60%	38.15%

The crystallinities of the layers were almost symmetrical along the thickness direction in the skin-core structures of the CIM parts, with the same pattern as the thicknesses of the layers. The crystallinity increased from 35.10% in the lower skin layer to 43.50% in the core layer, a change by 23.9%.

The crystallinities of the layers were asymmetrical in the skin-core structures of the RHCM parts, also with the same pattern as the thicknesses of the layers. The crystallinity in RHCM90 increased from 38.15% to 47.51% in the lower skin layer vs. in core layer, a change by 24.5%. The crystallinity difference of the RHCM parts was smaller than that of the CIM parts. However, the crystallinity in the lower skin layer was much smaller than that in the upper skin layer. The crystallinity changed by 12.0% from that in the upper skin layer to that in the core layer, which is only half of the value from in the lower skin layer to that in core layer. The asymmetrical distribution of crystallinities would also introduce greater warpage.

#### 4.2. Temperature Histories of Polymer

The temperature histories of polymer in the layers were obtained by conducting a heat transmission simulation on the representative position, and the results are shown in Figure 7.



**Figure 7.** Simulated temperature histories in the thickness direction under different processing conditions: (a) CIM, (b) RHCM60, and (c) RHCM90.

Figure 7a shows that the temperature histories are symmetrical along the thickness direction of the parts in CIM due to the temperature of the stationary side being the same as that of the moving side. Meanwhile, in RHCM, the temperature histories of polymer in the layers are asymmetrical along the thickness direction. The asymmetry increases with the increase in mold temperature, and the difference in the temperature histories between different layers will also increase. In RHCM60, the temperature difference at the ejecting time (the specific time is 30 s) between the upper and lower skin layers is 10 °C. In RHCM90, the temperature difference at the ejecting time between the upper and lower skin layers increases to 20 °C. The core layer temperature will also increase with the increase in heating temperature. The temperature of the core layer at the ejecting time in CIM is about 80 °C, but those in RHCM60 and RHCM90 increase to 90 and 95 °C, respectively. The higher temperatures will introduce higher crystallinities, as shown in Section 4.1.

#### 4.3. Warpage Prediction

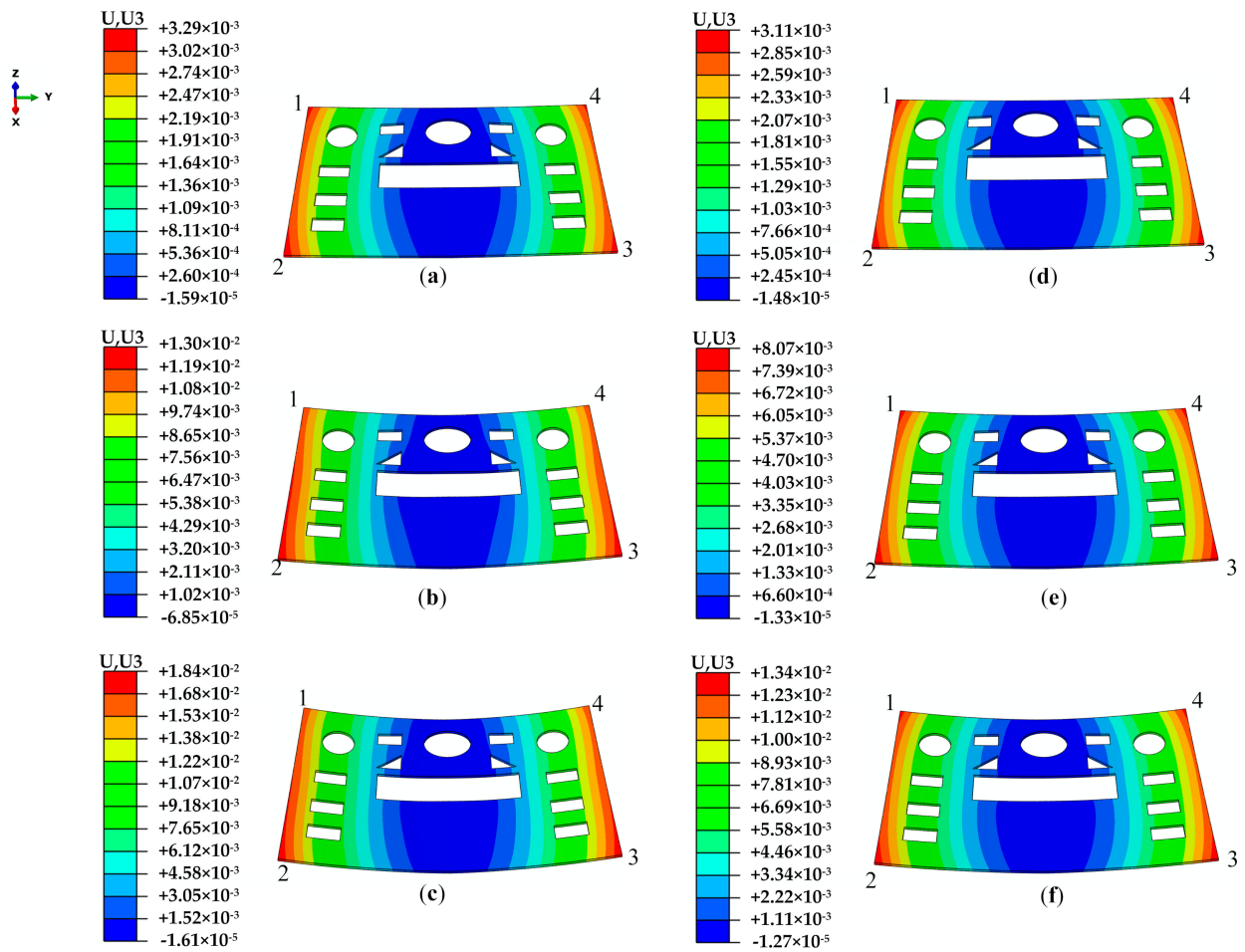
The multi-layer structures always appear in the molded parts along the thickness direction due to the inhomogeneous temperature history. The different crystal morphology of each layer introduces different mechanical properties. The layers with different mechanical properties will complicate the warpage of the part. Stratification is the most distinguishable feature in the inhomogeneous distribution of process parameters in molten polymer during molding and the microstructure in the molded parts after molding. However, the effect of stratification is ignored in the usual warpage simulation. The warpage prediction was conducted with and without the influence of crystallinity to verify the significance of the introduction of the model describing the elastic modulus with the influence of temperature and crystallinity. In the prediction without the influence of crystallinity, the elastic modulus was a function of temperature. The predicted results with different molding conditions are shown in Figure 8, where results with crystallinity are shown in Figure 8a–c and results without crystallinity are shown in Figure 8d–f. The maximum value of warpage appears very near to one of the corners of the parts. Numbers 1, 2, 3, and 4 are used to mark the different corners for further discussion.

From Figure 8a–f, it can be seen that the total predicted warpage ranges of the parts under different conditions are  $-0.02\sim 3.29$ ,  $-0.07\sim 13.00$ ,  $-0.02\sim 18.40$ ,  $-0.01\sim 3.11$ ,  $-0.01\sim 8.07$ , and  $-0.01\sim 13.40$  mm, respectively. The results show that the warpage is influenced by the crystallinity, and the predicted warpage with crystallinity is larger than that without crystallinity, especially in the parts molded using the RHCM process. The maximum values of warpage in the CIM parts are 3.29 and 3.11 mm with and without crystallinity, respectively, a change by 5.8%. The maximum values of warpage of the RHCM60 parts are 13.00 and 8.07 mm, a change by 61.1%. The maximum values of warpage of the RHCM90 parts are 18.40 and 13.40 mm, a change by 37.3%. Therefore, bigger errors will occur if crystallinity is not considered in warpage prediction of the crystalline parts molded by the RHCM process.

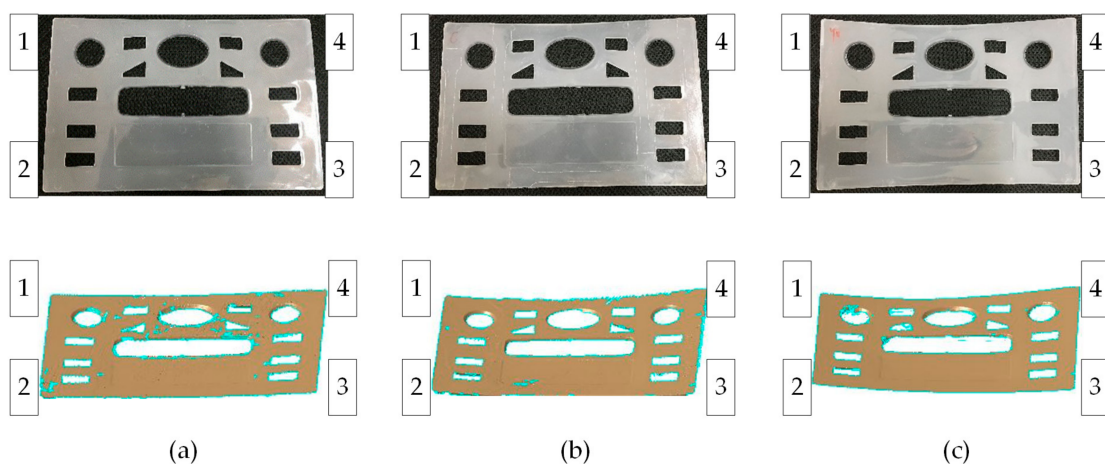
The predicted warpage increases as the heating temperature increases, and the warpage with crystallinity is more sensitive to heating temperature than that without crystallinity. The maximum value of warpage with crystallinity gradually increased from 3.29 mm for the CIM to 18.40 mm for the RHCM90, an increase of 459.3%. The maximum value of warpage without crystallinity gradually increased from 3.11 mm for the CIM to 13.40 mm for the RHCM90, an increase of 330.9%.

#### 4.4. Comparison of Warpages of Experiment and Prediction

The parts were molded under the aforementioned conditions, and warpages were measured by a 3D laser scanner. The parts and the scanned results are shown in Figure 9. The maximum warpage also appears at one of the corners of the parts. Numbers 1, 2, 3, and 4 are used to mark the different corners for further discussion, with the same marking method as in the prediction.



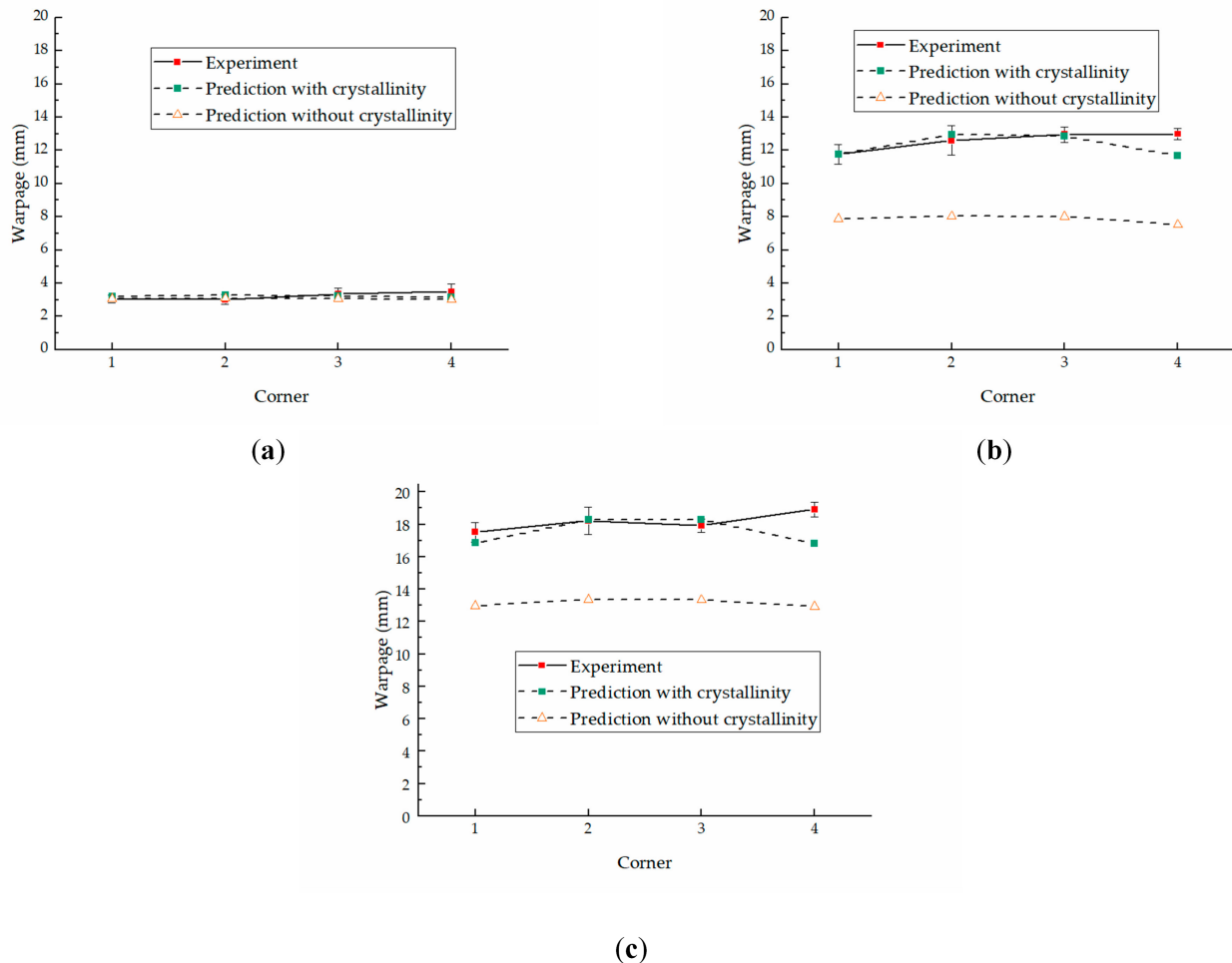
**Figure 8.** The total predicted warpage results of the parts (unit: m): (a–c) prediction with crystallinity; (d–f) prediction without crystallinity. (a,d) CIM; (b,e) RHCM60; (c,f) RHCM90.



**Figure 9.** Warpage information of real parts measured by a 3D laser scanner under different molding conditions: (a) CIM, (b) RHCM60, (c) RHCM90.

The maximum values of warpage are shown in Figure 10, including the data of experiments and predictions with crystallinity and without crystallinity. The predicted warpage with crystallinity is much closer to the experimental warpage. The average errors of the four corners between the predicted warpage and average experimental warpage

are 0.23, 0.44, and 0.81 mm, respectively, in CIM, RHCM60, and RHCM90, with respective deviations of 7.0%, 3.5%, and 4.4%. The maximum errors are 0.35, 1.30, and 2.12 mm, respectively, with deviations of 10.1%, 10.0%, and 11.2%. The difference is mainly due to the crystallinity of each layer in the simulation. The crystallinities of each layer in the model were obtained by measuring the corresponding positions of molded parts with WAXD. However, the crystallinity measured with WAXD cannot accurately represent the actual crystallinity of the layer. In addition, experimental errors, characterization errors, etc., which have an impact on the distribution of the model's multiple layers and the mechanical properties of each layer during warpage prediction.



**Figure 10.** The maximum values of warpages of experiment and prediction: (a) CIM, (b) RHCM60, (c) RHCM90.

The predicted warpage without crystallinity deviates more from the experimental warpage in the parts molded by the RHCM process than that with crystallinity. The average errors of warpage prediction of CIM are 0.23 and 0.22 mm with and without crystallinity, respectively, with a difference of 4.5%. The small difference is mainly due to the symmetrical distribution of thickness and crystallinity. However, the difference is much greater between the warpage prediction with and without crystallinity for parts molded by the RHCM process. The average errors of the warpage prediction of RHCM60 are 0.44 and 4.71 mm with and without crystallinity, respectively, with a difference of 970.5%. Additionally, the average errors of warpage prediction of RHCM90 are 0.81 and 5.00 mm, with a difference of 517.3%. They are mainly introduced by the asymmetrical distribution of thickness and crystallinity, as discussed previously.



## 5. Conclusions

This paper presented a novel method for predicting the warpage of crystalline parts molded using the RHCM process. A multi-layer model was established based on the stratification in the polymer temperature during molding and in the microstructure of parts after molding. A model was introduced to describe the mechanical properties with the influence of temperature and crystallinity. Finally, experimental warpage was measured using a 3D scanner to verify the predicted warpage. According to the results obtained in this study, the following conclusions can be drawn: (1) The microstructure and temperature are symmetrical along the thickness direction in CIM and are asymmetrical in RHCM. (2) The predicted warpage is influenced by the crystallinity, and the warpage predicted with crystallinity is larger than that predicted without crystallinity, especially in the parts molded by RHCM. (3) The predicted warpage increases as the heating temperature increases, and the warpage with crystallinity is more sensitive to heating temperature than that without crystallinity. (4) The predicted warpage with crystallinity is much closer to the experimental warpage than that without crystallinity, which shows that it is very important to consider crystallization in warpage prediction. (5) The proposed method can predict the warpage of crystalline parts molded by RHCM, and its predicted results agree well with the warpage measured on molded parts using a 3D scanner. In general, the proposed method is accurate and effective. It is a potential candidate technology for the quantitative prediction of the warpage of plate parts and for optimizing the molding process for manufacturing.

**Author Contributions:** J.L. and S.J. proposed the method of warpage prediction; S.J. conceived and designed the experiments; X.X. and B.Z. were responsible for injection molding experiments; J.B. and W.L. were responsible for the PLM and WAXD testing of molded parts; J.B. and X.P. were responsible for the simulation analysis; S.J. analyzed the results; J.L. wrote the paper. All authors have read and agreed to the published version of the manuscript.

**Funding:** This research was funded by the National Natural Science Foundation (grant no.51875525) and by the Natural Science Foundation of Zhejiang Province (grant nos. LY20E050100, LY19E050004, and LY19E050009).

**Acknowledgments:** The authors would like to acknowledge the financial support from the National Natural Science Foundation (grant no.51875525) and by the Natural Science Foundation of Zhejiang Province (grant nos. LY20E050100, LY19E050004, and LY19E050009).

**Conflicts of Interest:** The authors declare no conflict of interest.

## References

1. Nian, S.-C.; Huang, M.-S.; Tsai, T.-H. Enhancement of induction heating efficiency on injection mold surface using a novel magnetic shielding method. *Int. Commun. Heat Mass Transf.* **2014**, *50*, 52–60. [[CrossRef](#)]
2. Huang, M.-S.; Tai, N.-S. Experimental rapid surface heating by induction for micro-injection molding of light-guided plates. *J. Appl. Polym. Sci.* **2009**, *113*, 1345–1354. [[CrossRef](#)]
3. Wang, X.; Zhao, G.; Wang, G. Research on the reduction of sink mark and warpage of the molded part in rapid heat cycle molding process. *Mater. Des.* **2013**, *47*, 779–792. [[CrossRef](#)]
4. Fitzharris, E.R.; Watanabe, N.; Rosen, D.W.; Shofner, M.L. Effects of material properties on warpage in fused deposition modeling parts. *Int. J. Adv. Manuf. Technol.* **2018**, *95*, 2059–2070. [[CrossRef](#)]
5. Nian, S.-C.; Wu, C.-Y.; Huang, M.-S. Warpage control of thin-walled injection molding using local mold temperatures. *Int. Commun. Heat Mass Transf.* **2015**, *61*, 102–110. [[CrossRef](#)]
6. Chang, R.Y.; Tsaur, B.D. Experimental and theoretical studies of shrinkage, warpage, and sink marks of crystalline polymer injection molded parts. *Polym. Eng. Sci.* **1995**, *35*, 1222–1230. [[CrossRef](#)]
7. Hakimian, E.; Sulong, A.B. Analysis of warpage and shrinkage properties of injection-molded micro gears polymer composites using numerical simulations assisted by the Taguchi method. *Mater. Des.* **2012**, *42*, 62–71. [[CrossRef](#)]
8. Guo, K.-Q.; Huang, H.-X. Cellular Structure and Warpage of Microcellular Injection Molded Electrical Boxes Fabricated at Higher Injection Speeds. *Acta Polym. Sin.* **2019**, *50*, 850–856.
9. Izadi, O.; Silani, M.; Mosaddegh, P.; Farzin, M. Warpage and bending behavior of polymer–metal hybrids: Experimental and numerical simulations. *Int. J. Adv. Manuf. Technol.* **2018**, *98*, 873–885. [[CrossRef](#)]

10. Sánchez, R.; Aisa, J.; Martinez, A.; Mercado, D. On the relationship between cooling setup and warpage in injection molding. *Measurement* **2012**, *45*, 1051–1056. [[CrossRef](#)]
11. Sun, X.; Zeng, D.; Tibbenham, P.; Su, X.; Kang, H.-T. A new characterizing method for warpage measurement of injection-molded thermoplastics. *Polym. Test.* **2019**, *76*, 320–325. [[CrossRef](#)]
12. Xie, Z.; Wu, X.; Giacomini, A.J.; Zhao, G.; Wang, W. Suppressing shrinkage/warpage of PBT injection molded parts with fillers. *Polym. Compos.* **2018**, *39*, 2377–2384. [[CrossRef](#)]
13. Fernandes, C.; Pontes, A.J.; Viana, J.C.; Gaspar-Cunha, A. Modeling and Optimization of the Injection-Molding Process: A Review. *Adv. Polym. Technol.* **2018**, *37*, 429–449. [[CrossRef](#)]
14. Kitayama, S.; Onuki, R.; Yamazaki, K. Warpage reduction with variable pressure profile in plastic injection molding via sequential approximate optimization. *Int. J. Adv. Manuf. Technol.* **2014**, *72*, 827–838. [[CrossRef](#)]
15. Sudsawat, S.; Sriseubsai, W. Warpage reduction through optimized process parameters and annealed process of injection-molded plastic parts. *J. Mech. Sci. Technol.* **2018**, *32*, 4787–4799. [[CrossRef](#)]
16. Wang, X.; Li, H.; Gu, J.; Li, Z.; Ruan, S.; Shen, C.; Wang, M. Pressure analysis of dynamic injection molding and process parameter optimization for reducing warpage of injection molded products. *Polymers* **2017**, *9*, 85. [[CrossRef](#)]
17. Yasin, S.B.M.; Mohd, N.F.; Mahmud, J.; Whashilah, N.S.; Razak, Z. A reduction of protector cover warpage via topology optimization. *Int. J. Adv. Manuf. Technol.* **2018**, *98*, 2531–2537. [[CrossRef](#)]
18. Li, X.; Wei, Q.; Li, J.; Yang, J.; Guan, J.; Qiu, B.; Xu, J.; Wang, X. Numerical simulation on crystallization-induced warpage of injection-molded PP/EPDM part. *J. Polym. Res.* **2019**, *26*, 1–11. [[CrossRef](#)]
19. Nguyen, T.K.; Hwang, C.J.; Lee, B.-K. Numerical investigation of warpage in insert injection-molded lightweight hybrid products. *Int. J. Precis. Eng. Manuf.* **2017**, *18*, 187–195. [[CrossRef](#)]
20. Sun, X.; Su, X.; Tibbenham, P.; Mao, J.; Tao, J. The application of modified PVT data on the warpage prediction of injection molded part. *J. Polym. Res.* **2016**, *23*, 86. [[CrossRef](#)]
21. Li, X.P.; Zhao, G.Q.; Guan, Y.J. Characteristic of rapid heating cycle moulding and warpage analysis of products. *Plast. Rubber Compos.* **2011**, *40*, 425–432. [[CrossRef](#)]
22. Wang, G.; Zhao, G.; Guan, Y. Thermal response of an electric heating rapid heat cycle molding mold and its effect on surface appearance and tensile strength of the molded part. *J. Appl. Polym. Sci.* **2012**, *101*, 1339–1352. [[CrossRef](#)]
23. Crema, L.; Sorgato, M.; Zanini, F.; Carmignato, S.; Lucchetta, G. Experimental analysis of mechanical properties and microstructure of long glass fiber reinforced polypropylene processed by rapid heat cycle injection molding. *Compos. Part A Appl. Sci. Manuf.* **2018**, *107*, 366–373. [[CrossRef](#)]
24. Li, J.; Zhu, Z.; Li, T.; Peng, X.; Jiang, S.; Turng, L.-S. Quantification of the Young's modulus for polypropylene: Influence of initial crystallinity and service temperature. *J. Appl. Polym. Sci.* **2020**, *137*, 48581. [[CrossRef](#)]
25. Li, J.; Zheng, W.; Jiang, S.; Chai, G. An experimental study of skin layer in rapid heat cycle molding. *Polym. Plast. Technol. Eng.* **2014**, *53*, 488–496. [[CrossRef](#)]
26. Guilong, W.; Guoqun, Z.; Huiping, L.; Yanjin, G. Analysis of thermal cycling efficiency and optimal design of heating/cooling systems for rapid heat cycle injection molding process. *Mater. Des.* **2010**, *31*, 3426–3441. [[CrossRef](#)]
27. Li, J.; Zhou, H.; Xu, F.; Jiang, S.; Zheng, W.  $\beta$ -Crystal formation in isotactic polypropylene due to rapid heat cycle molding. *Polym. Adv. Technol.* **2015**, *26*, 1312–1319. [[CrossRef](#)]
28. Zhao, P.; Yang, W.; Wang, X.; Li, J.; Yan, B.; Fu, J. A novel method for predicting degrees of crystallinity in injection molding during packing stage. *Proc. Inst. Mech. Eng. Part B J. Eng. Manuf.* **2019**, *233*, 204–214. [[CrossRef](#)]
29. Guo, J.; Narh, K.A. Computer simulation of stress-induced crystallization in injection molded thermoplastics. *Polym. Eng. Sci.* **2001**, *41*, 1996–2012. [[CrossRef](#)]
30. Zhou, Y.; Deng, H.; Yu, F.; Bai, H.; Zhang, Q.; Chen, F.; Wang, K.; Fu, Q. Processing condition induced structural evolution in the alternating multi-layer structure during high speed thin-wall injection molding. *Polymer* **2016**, *99*, 49–58. [[CrossRef](#)]
31. Maeda, K.; Yamada, K.; Yamada, K.; Kotaki, M.; Nishimura, H. Structure and fracture toughness of thin-wall polypropylene moulded at different injection speeds. *Thin Walled Struct.* **2018**, *125*, 12–20. [[CrossRef](#)]
32. Li, J.; Yang, S.; Turng, L.-S.; Zheng, W.; Jiang, S. Comparative study of crystallization and lamellae orientation of isotactic polypropylene by rapid heat cycle molding and conventional injection molding. *e-Polymers* **2017**, *17*, 71–81.
33. Ogden, R. Proceedings of the Royal Society A: Mathematical. *Phys. Eng. Sci.* **1972**, *326*, 565.
34. Mori, T.; Tanaka, K. Average stress in matrix and average elastic energy of materials with misfitting inclusions. *Acta Metall.* **1973**, *21*, 571–574. [[CrossRef](#)]
35. Liparoti, S.; Speranza, V.; Sorrentino, A.; Titomanlio, G. Mechanical properties distribution within polypropylene injection molded samples: Effect of mold temperature under uneven thermal conditions. *Polymers* **2017**, *9*, 585. [[CrossRef](#)]
36. Ponçot, M.; Addiego, F.; Dahoun, A. True intrinsic mechanical behaviour of semi-crystalline and amorphous polymers: Influences of volume deformation and cavities shape. *Int. J. Plast.* **2013**, *40*, 126–139. [[CrossRef](#)]
37. Van Drongelen, M.; van Erp, T.B.; Peters, G.W.M. Quantification of non-isothermal, multi-phase crystallization of isotactic polypropylene: The influence of cooling rate and pressure. *Polymer* **2012**, *53*, 4758–4769. [[CrossRef](#)]
38. Jones, R.M. *Mechanics of Composite Materials*; CRC Press: Boca Raton, FL, USA, 1998; ISBN 156032712X.
39. Li, J.; Li, T.; Jia, Y.; Yang, S.; Jiang, S.; Turng, L.-S. Modeling and characterization of crystallization during rapid heat cycle molding. *Polym. Test.* **2018**, *71*, 182–191. [[CrossRef](#)]

40. Bondarenko, E.V.; Motavkin, A.V.; Skorodumov, V.F. PVT Properties of crystalline polymers. Comparison of Theoretical Predictions and Experimental Data. *Fibre Chem.* **2014**, *46*, 228–230. [[CrossRef](#)]
41. Pignon, B.; Tardif, X.; Lefèvre, N.; Sobotka, V.; Boyard, N.; Delaunay, D. A new PVT device for high performance thermoplastics: Heat transfer analysis and crystallization kinetics identification. *Polym. Test.* **2015**, *45*, 152–160. [[CrossRef](#)]
42. Rodgers, P.A. Pressure–volume–temperature relationships for polymeric liquids: A review of equations of state and their characteristic parameters for 56 polymers. *J. Appl. Polym. Sci.* **1993**, *48*, 1061–1080. [[CrossRef](#)]

## Article

# Solvent Effect on the Structure and Properties of RGD Peptide (1FUV) at Body Temperature (310 K) Using Ab Initio Molecular Dynamics

Khagendra Baral<sup>1</sup>, Puja Adhikari<sup>1</sup>, Bahaa Jawad<sup>1</sup>, Rudolf Podgornik<sup>2,3,4,5</sup> and Wai-Yim Ching<sup>1,\*</sup>

- <sup>1</sup> Department of Physics and Astronomy, University of Missouri-Kansas City, Kansas City, MO 64110, USA; kbx67@mail.umkc.edu (K.B.); paz67@umkc.edu (P.A.); bajrmd@mail.umkc.edu (B.J.)
- <sup>2</sup> School of Physical Sciences, Kavli Institute of Theoretical Science, University of Chinese Academy of Sciences, Beijing 100049, China; rudipod@gmail.com
- <sup>3</sup> CAS Key Laboratory of Soft Matter Physics, Institute of Physics, Chinese Academy of Sciences, Beijing 100090, China
- <sup>4</sup> Wenzhou Institute of the University of Chinese Academy of Sciences, Wenzhou 325000, China
- <sup>5</sup> Department of Physics, Faculty of Mathematics and Physics, University of Ljubljana, SI-1000 Ljubljana, Slovenia
- \* Correspondence: chingw@umkc.edu

**Abstract:** The structure and properties of the arginine-glycine-aspartate (RGD) sequence of the 1FUV peptide at 0 K and body temperature (310 K) are systematically investigated in a dry and aqueous environment using more accurate ab initio molecular dynamics and density functional theory calculations. The fundamental properties, such as electronic structure, interatomic bonding, partial charge distribution, and dielectric response function at 0 and 310 K are analyzed, comparing them in dry and solvated models. These accurate microscopic parameters determined from highly reliable quantum mechanical calculations are useful to define the range and strength of complex molecular interactions occurring between the RGD peptide and the integrin receptor. The in-depth bonding picture analyzed using a novel quantum mechanical metric, the total bond order (TBO), quantifies the role played by hydrogen bonds in the internal cohesion of the simulated structures. The TBO at 310 K decreases in the dry model but increases in the solvated model. These differences are small but extremely important in the context of conditions prevalent in the human body and relevant for health issues. Our results provide a new level of understanding of the structure and properties of the 1FUV peptide and help in advancing the study of RGD containing other peptides.

**Keywords:** RGD peptide (1FUV); ab initio molecular dynamics; total bond order; partial charge; dielectric function

**Citation:** Baral, K.; Adhikari, P.; Jawad, B.; Podgornik, R.; Ching, W.-Y. Solvent Effect on the Structure and Properties of RGD Peptide (1FUV) at Body Temperature (310 K) Using Ab Initio Molecular Dynamics. *Polymers* **2021**, *13*, 3434. <https://doi.org/10.3390/polym13193434>

Academic Editor: Célio Bruno Pinto Fernandes

Received: 17 September 2021

Accepted: 29 September 2021

Published: 7 October 2021

**Publisher's Note:** MDPI stays neutral with regard to jurisdictional claims in published maps and institutional affiliations.



**Copyright:** © 2021 by the authors. Licensee MDPI, Basel, Switzerland. This article is an open access article distributed under the terms and conditions of the Creative Commons Attribution (CC BY) license (<https://creativecommons.org/licenses/by/4.0/>).

## 1. Introduction

Biomolecular materials containing the arginine-glycine-aspartate (RGD) sequence are always at the center of biophysics research in their application such as in the bone scaffold, synthesis, and regeneration of tissue and cartilage [1,2], in imaging as radiotracers [3–6], for cancer therapy [7–9], and in targeted drug delivery [10–15]. The RGD motif peptide serves as a primary integrin recognition site in extracellular matrix proteins since it has a strong binding affinity to integrins, which are heterodimeric cell surface receptors and mediate cell-extracellular matrix adhesion [16–19]. Out of 24 known integrins, one third of them bind to the RGD motif as the primary recognition sequence in their ligands, which makes RGD an attractive target in numerous drug delivery systems [20–24]. The increased application of integrins in drug development and their functions in the physiological processes requires a complete understanding of the structure and properties of the RGD peptides at body temperature (310K), crucial in the design of selective inhibitors. Therefore, a detailed study of the structure and properties of 1FUV in RGD peptides at 310 K is of particular

interest in delineating the modifications that occur with a rise or fall of body temperature. Moreover, the short- and long-range interactions are crucial for the molecular recognition and self-assembly of biological macromolecules, and consequently determining the microscopic parameters such as partial charge and frequency-dependent dielectric functions based on more accurate quantum mechanical calculation will facilitate the fundamental understanding of electrostatic, polar, and van der Waals-London dispersion interaction in biological (macro)molecules.

The peptide-water interfacial reactions are of paramount importance in biological systems as solvation is ubiquitous in biological interaction with water as an inevitable component in blood and multicomponent body fluids. Understanding the peptide-water interaction is also essential regarding the RGD-targeted drug delivery mechanisms. It is, therefore, crucial to investigate the consequences of peptide-water interaction and aqueous solvation and its effects on internal bonding, charge distribution, and dielectric response. The solubility of 1FUV in water is generally attributed to the hydrogen bonding between water molecules and oxygen from the peptide backbone. To explore the details of peptide solvation properties, molecular dynamics (MD), molecular mechanics, and Monte Carlo methods, all based on specific force field parameters, are widely used. Nevertheless, the information on the role played by the hydrogen bond (HB) within RGD and at the RGD-water interface is in general still missing, as are the relevant *ab initio* MD (AIMD) studies [12,25–27]. Classical MD studies cannot provide a quantitative description of essentially quantum HBs (O–H and N–H) since they depend on the details of the force field parameterization. Consequently, the need for AIMD simulation in the study of dry and aqueous solvated peptide/protein over classical MD has been repeatedly recognized [28–31] and a more accurate AIMD calculation with a sufficiently large number of water molecules is highly desirable for a complete understanding of 1FUV aqueous solvation.

Although experimental techniques such as nuclear magnetic resonance (NMR), surface-enhanced Raman spectroscopy, X-ray photoelectron spectroscopy, etc., are used to investigate the structure and properties of RGD containing peptides [16,32–35], the experimental studies specifically involving 1FUV are scant. Moreover, although experimental studies can probe the consequent changes of the peptide structure due to water contact, they cannot provide critical information and details of microscopic properties and interfacial reaction mechanisms at the atomistic scale. Computer-assisted atomistic simulation thus seems the best alternative to investigate the molecular behavior and provide new insights to complement the meager experimental data [36,37], in many cases guiding the experiments as well. Nevertheless, only a few computational studies have so far been reported on the 1FUV peptide [38].

To answer the issues raised above and provide new insights into the study of the 1FUV peptide, this study is designed to simulate four models of dry and solvated 1FUV at 0 K and body temperature, namely 1FUV0, 1FUV310, 1FUVS0, and 1FUVS310, respectively. Our study provides a deeper understanding of the temperature-dependent structure, fundamental properties, peptide-water interfacial reaction mechanism, and solvation effect. To the best of our knowledge, our effort is the first example of a study dedicated to the 1FUV peptide using AIMD that ensures the reliability of the simulated structures and calculated properties. The rest of the paper is structured as follows. In the next section, a brief description of the modeling technique followed by the simulation workflow is described. The main part is the result and discussion section, in which we discuss our findings and articulate the future prospects for applying AIMD to other complex biomolecular systems.

## 2. Materials and Methods

### 2.1. Modeling 1FUV Peptide

The RGD peptides that specifically bind to  $\alpha_v\beta_3$  and  $\alpha_v\beta_5$  integrins have medical significance in designing the inhibitors of tumor and retinal angiogenesis [39,40], in osteoporosis [41], and in targeted drugs for tumor vasculature [42]. Considering the importance

of  $\alpha_v\beta_3$  and  $\alpha_v\beta_5$  integrins [16] and as 1FUV binds only to these integrins, we choose to focus on 1FUV in this work.

The initial structure of 1FUV was taken from the Research Collaboratory for Structural Bioinformatics protein data bank (PDB) generated from the NMR measurements [43]. The stored PDB file contains about 19 such models with the same composition, the number of atoms, molecular weight, and the chemical formula, but slightly different molecular volumes. In this study, we chose the first model out of 19, which has 135 atoms comprised of 11 amino acids. The initial atomic positions of 1FUV were enclosed in a sufficiently large supercell of size  $37.12 \text{ \AA} \times 34.41 \text{ \AA} \times 28.95 \text{ \AA}$  to avoid any unintended interaction due to periodic boundary conditions. This structure was then fully relaxed by applying a density functional theory (DFT)-based Vienna ab initio simulation package (VASP) [44,45] known for its efficiency in structure optimization and energy minimization to obtain 1FUV0, the structure at 0 K. We used a projector-augmented wave method [46,47] with Perdew-Burke-Ernzerhof potential for the exchange correlation functional within the generalized gradient approximation [48]. We employed a relatively high cutoff energy of 500 eV and set the electronic convergence criterion at  $10^{-5}$  eV. The force convergence criterion for ionic relaxation was set at  $10^{-3}$  eV/Å. A single K-point calculation was used as the simulated models are sufficiently large supercells.

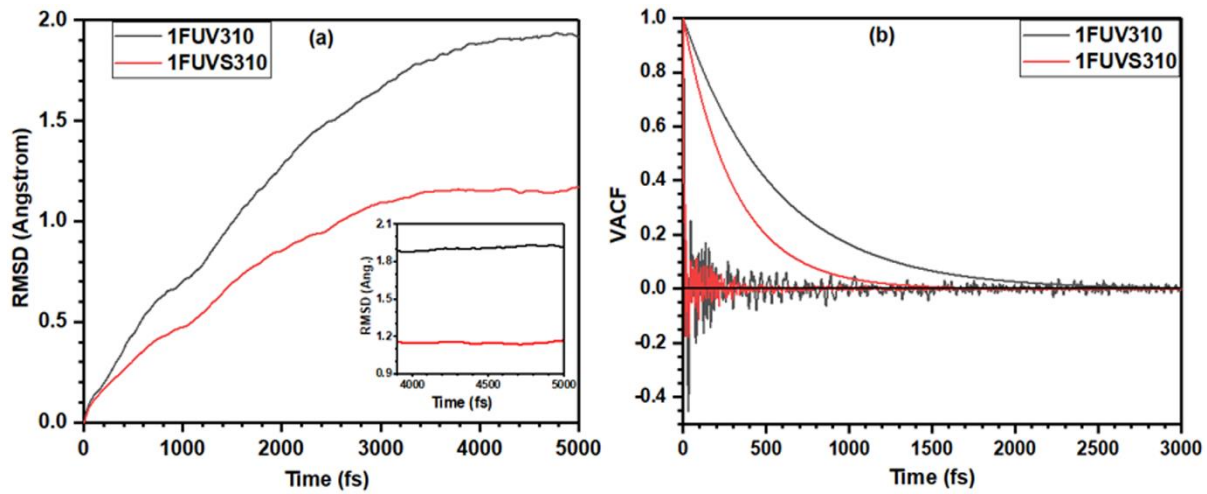
The fully relaxed structure at 0 K was then heated slowly to 310 K, equivalent to human body temperature, using NVT ensemble within 4 ps. A Nose thermostat was used to control the temperature of the heat bath [49,50]. A time step of 0.5 fs was used for the ionic motion during the simulation to ensure accuracy for integration of the equation of motion, especially for the light atoms such as hydrogen. The peptide model at this elevated temperature was then equilibrated for 5 ps to obtain the equilibrium structure at 310 K, viz. 1FUV310. Out of 5 ps run, the fluctuations of temperature and pressure were minimized by the initial 4 ps run, and the averaged output structure is taken from the last 1 ps run, thus used as a production run. The solvated model at 0 K (1FUVS0) was constructed based on 1FUV0 by surrounding the peptide structure with 80 water molecules. The 1FUVS0 was then again fully relaxed by using VASP. Similar to the dry model, this solvated structure was then heated to 310 K to obtain the 1FUVS310 model using NVT ensemble within 4 ps. The same protocol as used in the dry model was adopted to obtain the equilibrated structure of the solvated model at 310 K.

To reveal the structural stability of simulated models, we present the root-mean-square deviation (RMSD) of atomic positions of the peptide structure during equilibration at 310 K in Figure 1a. The time-RMSD profile of global structure shows a smooth increase followed by a leveling off at  $\sim 1.90 \text{ \AA}$  in the dry model and  $\sim 1.15 \text{ \AA}$  in the solvated model, respectively, indicating that the equilibrium has been reached. The constant RMSD shown in the inset for the last 1 ps run, used as a production run, ensures the sufficient equilibration of simulated structures. Figure 1b shows the velocity autocorrelation function (VACF), including exponential fitting, during the equilibration of dry and solvated structures at 310 K which confirms the loss of initial velocity from the previous configuration and attest to sufficient equilibration of the systems. It also implies that the amplitude of VACF is smaller in the solvated model and dies out quicker than that in the dry model. In addition, the exponential fitting shows the solvated model reaches equilibrium faster than the dry model.

## 2.2. Calculation of Properties

The AIMD simulated and VASP relaxed structures discussed above are then used as input for the electronic structures and dielectric response calculations using the in-house developed package of the orthogonalized linear combination of atomic orbitals (OLCAO) methodology [51]. The combination of these two DFT methods, VASP and OLCAO, is found to be robust and highly effective in studying the electronic structure and bonding properties, especially for complex biomolecules [52–55]. In recent years, we have further demonstrated that the combination of these two methods is extremely effective

in dealing with new and emerging problems for complex protein structures related to SARS-CoV-2 [56–60].



**Figure 1.** Calculated (a) RMSD and (b) VACF including exponential fitting, of simulated dry and solvated 1FUUV peptide at 310 K.

The OLCAO is an all-electron method using local density approximation of DFT in which the Gaussian-type orbitals are employed for the expansion of the atomic basis set. There are many advantages of using OLCAO for electronic structure calculation, such as the flexibility of the basis sets choice, lower computational cost, and ease of bonding and charge transfer analysis using the Mulliken scheme [51]. The implementation of localized atomic orbitals in the basis expansion enables us to quantify the charge transfer and interatomic bonding via effective charge ( $Q^*$ ) on each atom and bond order (BO) value between pairs of atoms ( $\rho_{\alpha\beta}$ ) using the Mulliken scheme [61,62] as

$$Q_{\alpha}^* = \sum_i \sum_{n,occ} \sum_{j,\beta} C_{i\alpha}^{*n} C_{j\beta}^n S_{i\alpha,j\beta} \quad (1)$$

$$\rho_{\alpha\beta} = \sum_{n,occ} \sum_{i,j} C_{i\alpha}^{*n} C_{j\beta}^n S_{i\alpha,j\beta} \quad (2)$$

where  $S_{i\alpha,j\beta}$  is the overlap matrix between the basis Bloch sums of the orbital index ( $i, j$ ) and atomic specification ( $\alpha, \beta$ ).  $N$  is the band index,  $i, j$  are the orbital quantum numbers, and  $C_{j\beta}^n$  is the eigenvector coefficient.

From the calculated value of  $Q^*$  the charge transfer between the ions due to atomic interaction can be quantified in terms of the partial charge (PC). It is defined as the deviation of  $Q^*$  from the charge of neutral atom  $Q^0$  and is given by  $\Delta Q = Q^0 - Q^*$ . The BO value calculated from the above equation gives the direct quantitative measure of bond strength between a pair of bonded atoms. The sum of all BO values in the system is the total bond order (TBO), which is a quantum mechanically calculated parameter. It is a single quantum mechanical metric helpful in assessing the internal cohesion and strength in a material [63]. The use of TBO to characterize the internal strength of a material and correlate it with the calculated physical properties is a novel and highly appealing concept.

OLCAO is equally suitable to calculate the imaginary part,  $\epsilon_2(\hbar\omega)$ , of the frequency-dependent complex dielectric function within the random phase approximation of inter-band optical transition theory according to the following equation:

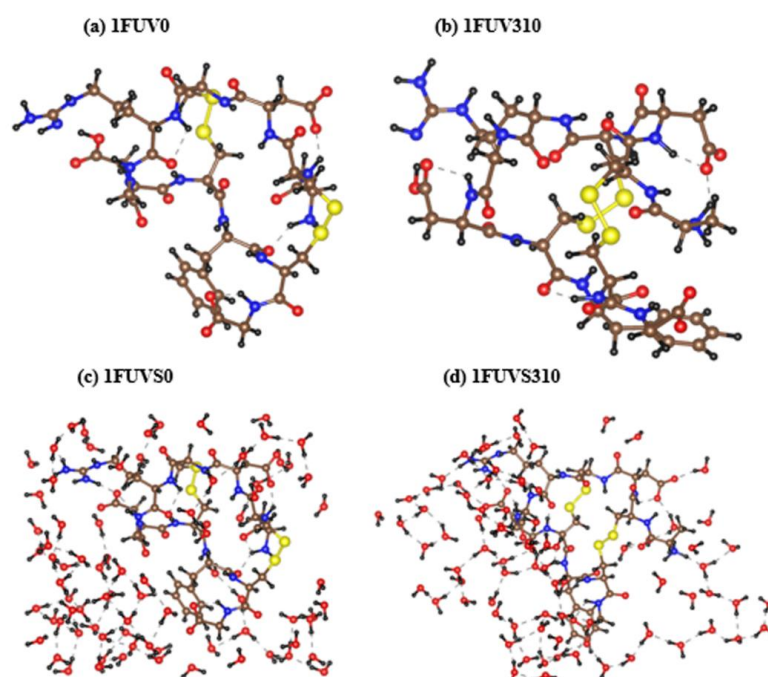
$$\epsilon_2(\hbar\omega) = \frac{e^2}{\pi m \omega^2} \int_{BZ} dk^3 \sum_{n,l} \left| \left\langle \psi_n(\vec{k}, \vec{r}) \left| -i\hbar \vec{\nabla} \right| \psi_l(\vec{k}, \vec{r}) \right\rangle \right|^2 \times f_l(\vec{k}) \left[ 1 - f_n(\vec{k}) \right] \delta \left[ E_n(\vec{k}) - E_l(\vec{k}) - \hbar\omega \right] \quad (3)$$

### 3. Results

#### 3.1. Analysis of 1FUV Structures

The RGD peptide, 1FUV, studied in this work contains 11 amino acid sequence ACDCRGDCFCG, namely alanine (Ala, A), cysteine (Cys, C), asparagine (Asp, D), arginine (Arg, R), glycine (Gly, G), and phenylalanine (Phe, F). As this amino acid sequence contains four C, this peptide is also known as RGD-4C, in which the cysteine position is at 2, 4, 8, and 10th place of the sequence, named as Cys1, Cys2, Cys3, and Cys4, respectively. Each Cys amino acid contains the S atom and the arrangement of two Cys, and hence the S–S bond plays an important role in the configuration and dipole moment of this peptide [64]. Although the presence of four Cys groups in RGD-4C allows three possible combinations of S–S bonds, only two natural configurations of this peptide exist based on the S–S bonding arrangement [16]. The peptide with Cys1–Cys4 and Cys2–Cys3 disulfide bonding arrangement is known as RGD-A isomer, while the one with Cys1–Cys3, Cys2–Cys4 bonding arrangement is known as RGD-B isomer [16]. As RGD-A is a far stronger binder to integrin  $\alpha_v\beta_3$  than RGD-B [16], it is reasonable to explore details of the structure and properties of RGD-A.

The relaxed structures for RGD-A peptide (1FUV) at 0 K and 310 K in the dry and aqueous environment are shown in Figure 2. 1FUV0 shows only a minor change in its structure due to VASP relaxation compared with the original NMR structure [16] taken from the PDB. However, there are noticeable changes in its conformation after AIMD simulation at 310 K. It shows a rotation of amino acid groups and changes in the bond length (BL) and BO value, which will be discussed in detail later. In the case of the solvated model, there again appear notable changes in the peptide structure. More water molecules interact with the peptide and there is a rotation of amino acid groups at 310 K as compared with 0 K. In both dry and solvated models, the S–S bond containing amino acids come closer at 310 K as compared with those at 0 K. However, the average S–S BL increases and hence its strength decreases at 310 K. It is noticed that the configurations of HBs, O–H, change at 310 K as compared with 0 K, resulting in the overall decrease in its strength in the dry model. However, in the solvated model, a large contribution of O–H bonding strength comes from peptide–water interaction due to which its value increases at 310 K. These differences are, although small, important on issues related to human health.

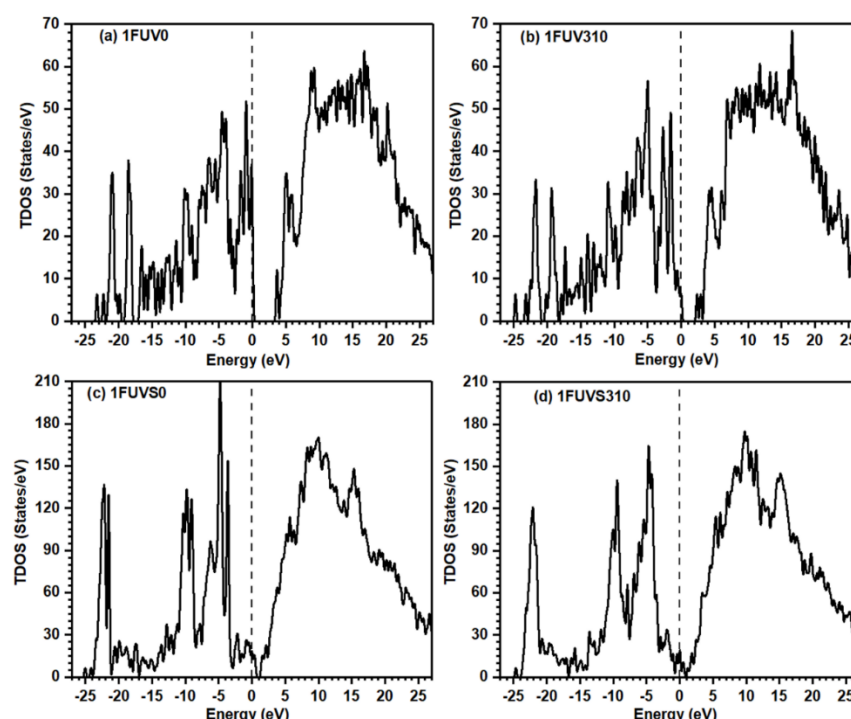


**Figure 2.** Structures of dry (a,b) and solvated (c,d) 1FUV peptide at 0 K and 310 K, respectively. (N = Blue, C = Brown, O = Red, H = Black, and S = Yellow).



### 3.2. Electronic Structure and Interatomic Bonding

Electronic structures are the fundamental properties of a material that help to understand many other physical properties. The calculated total density of states (TDOS) for the simulated models is shown in Figure 3. The top of the valence band is set at 0 eV. The overall features of TDOS at 0 K and 310 K in dry and solvated models look similar as they contain the same amino acid groups; however, there is a decrease in the highest occupied molecular orbital (HOMO)-lowest unoccupied molecular orbital (LUMO) gap with the increase in temperature. The position of the energy difference between HOMO and LUMO plays the main role in various chemical reactions. The number of peaks decreases in solvated models as compared with the dry model, but the overall intensity increases. The HOMO-LUMO gap for 1FUUV0 is  $\sim 3.40$  eV, while its value in 1FUUV310 decreases to  $\sim 2.10$  eV due to a temperature rise, indicating that the molecule is chemically more reactive at a higher temperature. The HOMO-LUMO gap decreases largely in solvated models as compared with dry models. In 1FUUVS0, this gap is  $\sim 0.3$  eV, but it disappears in 1FUUVS310.



**Figure 3.** Calculated TDOS for dry and solvated 1FUUV peptide at 0 K and 310 K.

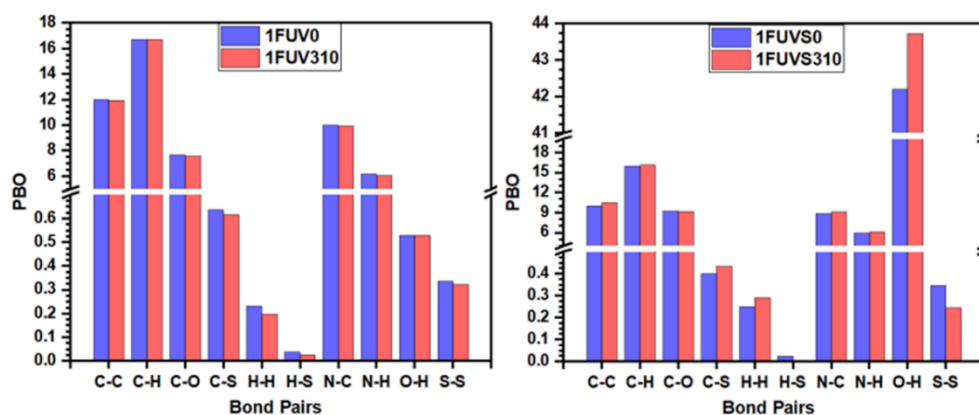
The nature of bonding and its quantitative assessment is important in the electronic structure study of the material. While most of the MD studies interpret the bonding analysis based exclusively on the geometric distance configuration, OLCAO can quantify the strength of each bonded pair by providing the BO value. We calculate the TBO values in all 4 models and resolve them into partial pair-resolved BO (PBO) components. This is an unorthodox approach that generalizes the bonding between individual bonded pairs simply and effectively to reveal the hidden details which cannot be extricated by other methods, either experimental or computational.

In general, the BO value scales inversely with BL; however, the actual BO value of a bonded pair depends on its bonding environment and the atoms surrounding it. The calculated values of TBO and PBO are listed in Table 1, showing that at 310 K the TBO value decreases in the dry model, resulting from the elongation of some bonds. The TBO value of the solvated model increases at 310 K, opposite to the case of the dry model, which is due to the formation of more bonds between the peptide backbone and water at this elevated temperature. Figure 4 shows the comparison of PBO values for each bonded pair in simulated models at 0 K and 310 K in the form of a vertical bar diagram. The scale breaks

are used along the vertical axis to delineate the minor differences between PBO values and show their magnified image. Figure 4 shows that there is a minor change in the PBO values due to the rise of temperature, except in the case of the O–H pair in the solvated model. The PBO for the O–H pair increases sharply in the solvated model at 310 K as compared with the model at 0 K, which arises due to the interaction of more water molecules with the peptide, and an increase in the HBs population at 310 K. It should be emphasized again that the small changes in these numbers at different temperature can be significant in the context of the human body.

**Table 1.** Calculated TBO and PBO values for each bonded pair in simulated models.

Models	TBO	PBO										
		C-C	C-H	C-O	C-S	H-H	H-S	H-O	N-C	N-H	N-O	S-S
1FUV0	54.272	11.991	16.680	7.669	0.637	0.232	0.037	0.529	9.979	6.181	0.001	0.336
1FUV310	53.887	11.944	16.705	7.581	0.617	0.198	0.027	0.530	9.926	6.034	0.000	0.323
1FUVS0	93.166	9.990	15.947	9.234	0.400	0.251	0.025	42.207	8.859	5.905	0.003	0.346
1FUVS310	95.663	10.479	16.119	9.125	0.434	0.292	0.005	43.724	9.111	6.119	0.000	0.246

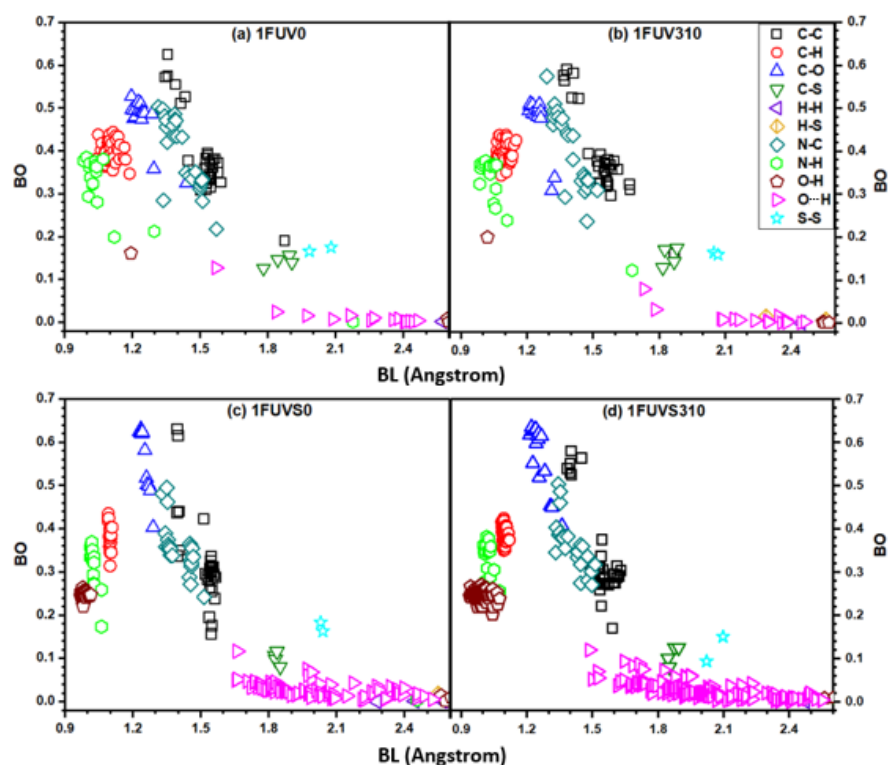


**Figure 4.** Comparison of PBO values for each bonded pair in dry and solvated 1FUV at 0 K and 310 K.

We provide further information on the strength of individual bonded pairs presenting a complex distribution of BO versus BL in Figure 5. It clearly shows a wide variety of bonding pairs ranging from a strong covalent bond originating from N–H, N–C, C–H, C–C, C–O, and O–H pairs to weaker covalent bonds at longer BL. HBs are extremely weak but not entirely negligible because of their sheer numbers. The first group of strong covalent bonds arises from N–H, C–H, and O–H pairs with BL less than 1.2 Å. The next group of covalent BO pairs arises from C–C, C–O, and N–C bonds, whose BL lies in the range 1.2–1.7 Å. The C–C bonds show two clusterings, one having a high BO greater than 0.5 e from C–C double bonds, whereas the other group has a BO value less than 0.4 e from single C–C bonds. The BO values for N–C pairs also exhibit a group separation, having BO values greater than 0.4 e and less than 0.4 e.

The HBs are distributed in the range of 1.5–2.5 Å, with some O–H pairs having relatively higher BO values up to 0.1 e. In solvated models, the covalent O–H bonds within the water molecule have BO values higher than 0.2 e, while those bonds originating from the next neighbor or weak HBs beyond 2.5 Å have almost zero BO values. The bonding distributions due to C–S and S–S pairs have BO values comparable or slightly higher than those of strong HBs. The S–S bonding configurations are important in peptide structure, and they show significant changes in BO values due to the rise of temperature and solvation. Especially in the solvated model at 310 K, the BO of S–S bonds has a large difference. Wang et al. studied the influence of disulfide bond on properties of RGD peptide using MD and found that this bond causes the restriction on peptide mobility and affects its dipole

moment [64]. The bonded pairs H–H and H–S with BL larger than 2.5 Å have BO values close to zero.



**Figure 5.** BO versus BL plot for dry and solvated 1FUV at 0 K and 310 K.

### 3.3. Hydrogen Bonding Analysis

Hydrogen bonding is especially important in a biomolecular system since it provides the key information to understand many intriguing phenomena, making the detailed analysis of HBs in the solvated models crucial. Unfortunately, in most MD studies, the analysis of HBs is carried out based exclusively on structural data, such as the BL and the location of HBs, failing to provide a quantitative assessment of HB strength and their local bonding arrangements. On the contrary, we bring forth quantitative information and deeper analysis of HBs using ab initio calculation in terms of BO–BL plot, as shown in Figure 5. It shows there exists some strong HB with BO value  $\sim 0.1$  e, while most of the HBs have BO less than 0.1 e. At the body temperature, the overall strength of HB from the O–H bonding pair slightly decreases in the dry model while it increases in the solvated model.

In the case of solvated models, the change in the HB pattern is more complicated due to the presence of H<sub>2</sub>O molecules which increase the population and strength of O–H bonds at 310 K. The more HBs imply the stronger binding force of biomolecule with solvent. There is one HB originating from the N–H pair within the peptide backbone whose BO value at 310 K increases in the dry model and decreases in the solvated model because of the rotation and changes in the configuration of the peptide structure. The results on HB analysis in solvated models indicate a significant difference in the human body as compared with the vicinal environment of a dry peptide at zero temperature.

### 3.4. Partial Charge Distribution

The PC distribution of biomolecules is important for determining the long-range electrostatic and polar interaction involving the molecule. It entails a deep qualitative understanding of the structure and reactivity of a molecule. Rather than just making a rudimentary judgment by dividing PC into positive, negative, and neutral as adopted in many simplified calculations, we provide a quantitative assessment of PC of every atom in

the simulated models. As the PC gives the quantity of charge transfer in atomic interaction, a positive value implies a loss, and a negative value means the gain of electronic charge.

The distribution of calculated PC for each atom in dry and solvated models is shown in Figures 6 and 7, respectively, which provide a wealth of information that corroborates the electronic structure results discussed above. The solid symbols represent PC of ions at 0 K, while the hollow symbols represent PC at the body temperature. O (P) and H (P) denote O and H atoms from the peptide backbone while O (W) and H (W) denote those from the water molecule. In both dry and solvated models at 310 K, small changes appear in the PC of ions compared with their values in corresponding models at 0 K. Figures 6 and 7 show that H and S lose charges, N gains charge, while C is both losing or gaining charges. In the dry model, O gains charge, while in the solvated model (Figure 7), few O atoms from the peptide backbone lose charge, and the remaining gain charge. The calculated PC values for each atom are scattered in a certain range rather than clustering and overlapping to each other, which implies the PC value is not the same even for the same atom in the same model, as their values depend on the local bonding environment. The PC of O and H in water and peptide backbone is not the same, implying that their local bonding characteristics are completely different (Figure 7). The dispersed distribution of calculated PC for each atom implies that the quantum mechanical calculation is essential to deal with such type of problem rather than using MD studies in which the PC values are predefined and kept constant in the simulation where the local environment changes.

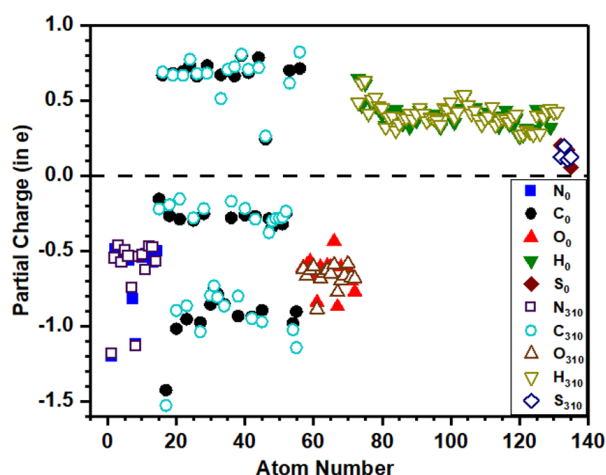


Figure 6. Calculated partial charge for each atom in dry 1FUV at 0 K and 310 K. (The subscripts 0 and 310 denote the temperature 0 K and 310 K, respectively).

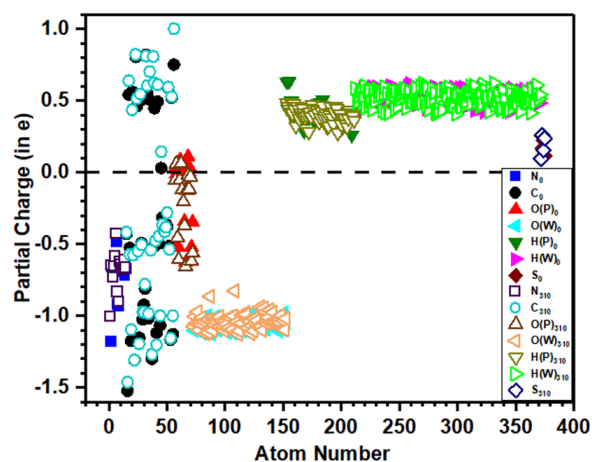


Figure 7. Calculated partial charge for each atom in solvated models of 1FUV at 0 K and 310 K. (The subscripts 0 and 310 denote the temperature 0 K and 310 K, respectively).

### 3.5. Dielectric Response

The dielectric response of biomolecules in an aqueous solution has been studied for decades [65–67] and remains a subject of active research. The static dielectric constant of peptide/protein plays a crucial role in the calculation of the electrostatic field obtained by solving the Poisson–Boltzmann equation [68]. However, it is interesting to note that the dielectric properties of the 1FUV are seldom reported. We present a detailed analysis of the imaginary part,  $\varepsilon_2(\hbar\omega)$ , of the frequency-dependent dielectric function, based on the ab initio calculation under random phase approximation such as those used in inorganic crystals and glasses [69–72].

Figure 8a shows the spectrum for  $\varepsilon_2(\hbar\omega)$  in 1FUV0 calculated using OLCAO, displaying a sharp peak at  $\sim 5.70$  eV and one broad peak at  $\sim 14.30$  eV. A similar spectrum is observed in the dry model at 310 K; however, the broad peak position shifts slightly to the lower energy side. In solvated models, in addition to the two peaks observed in dry models, there appears another sharp peak at  $\sim 0.1$  eV, but with slightly less intensity (Figure 8b). One of the striking features observed is that at the body temperature, the absorption end of  $\varepsilon_2(\hbar\omega)$  shifts to lower energy which is consistent with the decrease in the HOMO–LUMO gap at 310 K. We want to make it clear that our aim in this work is to compare the full dielectric spectra at 0 K and body temperature in case of a dry and solvated environment and the actual calculation of the dielectric constant is out of the scope of this work.

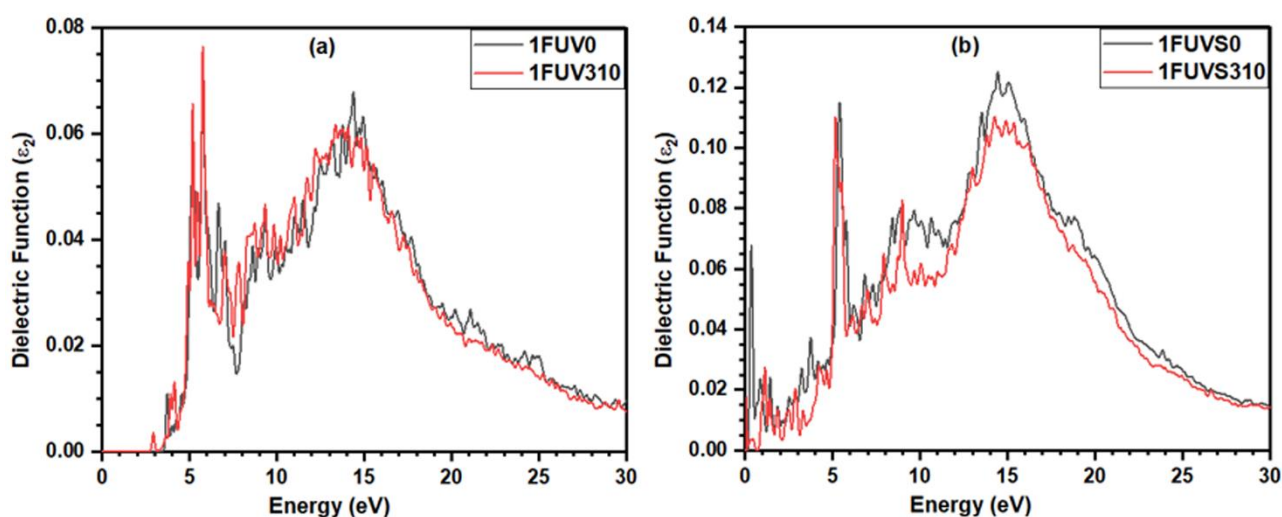


Figure 8. Calculated imaginary part of the complex dielectric function for (a) dry and (b) solvated 1FUV at 0 K and 310 K.

## 4. Discussions and Summary

In this section, we discuss the results presented above and summarize the main findings to answer the queries raised in the introduction. More accurate AIMD and DFT calculations adopted in this work provide us a wealth of quantitative information on the fundamental properties of 1FUV, which are not yet available or cannot be attained by an experimental protocol. Our findings provide a comparative analysis of the structure and properties of 1FUV and a better understanding of its solvation properties at 0 K and body temperature, 310 K. The key message is that there are discernible changes in the peptide structure and properties at 310 K, which could point to the potential implications for human health issues if such calculations can eventually be applied to large biomolecular systems.

Our results show noticeable changes in the conformation of amino acids at body temperature than at 0 K. The major structural differences observed in dry and solvated peptides at body temperature help in designing the specificity of integrins. The disulfide bridge connectivity greatly determines the orientation of the RGD motif and peptide structure which may dictate selectivity towards different integrins. The HOMO–LUMO gap

of 1FUV decreases due to the rise of temperature and solvation effect. Such information is quite helpful to understand the chemical reactions involving biomolecules.

The bonding analysis is a significant result that helps to understand the interatomic interaction within 1FUV and other biomolecules. The TBO value decreases in the dry model while it increases in the solvated model at 310 K. The dry model at 0 K is more cohesive than that at 310 K, characterized by a higher TBO value, while it is just the opposite in the solvated models. The BO-BL plot analysis provides a detailed picture of interatomic bonding within the peptide structure and its explicit solvent environment. The solvated model shows a considerable peptide-water interactions occur at 310 K, increasing the HBs population than at 0 K. The detailed analysis of HBs and quantification of their strength is crucial in understanding the biological interactions inside the human body and for the design and delivery of RGD peptide-targeted drugs. The partial charge analysis provides another set of significant parameters to define the reactivity of biomolecules and their interactions with the integrins. It shows that the PC value strongly depends on the temperature as well as the solvated environment. Furthermore, the calculated PC values scatter in a certain range, even for the same atom in the same model. Quantum mechanical calculation is, therefore, absolutely necessary to capture all these crucial differences and to provide more accurate results inaccessible to classical MD studies.

Another important result is the calculation of the dielectric response function and its relation to the dielectric constant. Although this topic has attracted researchers from various backgrounds for a long time, unified and reliable *ab initio* calculations are still out of reach. As an initial assessment, we analyze the imaginary part of the dielectric function of the 1FUV peptide and study the differences in the dielectric spectra due to the rise in temperature and the solvation effect. Such optical spectra are helpful to estimate the long-range van der Waals–London interaction in biomolecules, as shown in the study of carbon nanotubes [73]. Overall, our results show apparent differences in bonding, PC, and dielectric function between the 1FUV at 0 K and the body temperature in a dry and solvated environment. These results can be quite helpful to develop and refine the force field parameters used in MD simulation. Unfortunately, as there is a lack of theoretical studies in 1FUV and the focus of the existing experimental study [16] is different, we are unable to compare our results with the previous results. However, we anticipate that our results will inspire future experimental and/or theoretical works to investigate further the 1FUV and related peptides, including the effect of salts and different numbers of water molecules, which significantly influence peptide structure and properties.

In the past, we have successfully demonstrated the applicability of AIMD in the study of oxide glassy materials and fluoride salts [74–77]. Our accomplishment in the present work is applying AIMD to a relatively small peptide structure that looks quite promising. It ensures the feasibility and encourages a further study of other possibly more complex biomolecules by using AIMD, of course assuming sufficient computing resources to be available.

**Author Contributions:** W.-Y.C., K.B. and P.A. conceived the project. K.B. and W.-Y.C. performed the calculations and made figures. K.B. and W.-Y.C. drafted the paper with inputs from P.A., R.P. and B.J. All authors participated in the discussion and interpretation of the results. All authors edited and proofread the final manuscript. All authors have read and agreed to the published version of the manuscript.

**Funding:** This project is funded by the National Science Foundation of USA: RAPID DMR/CMMT-2028803.

**Institutional Review Board Statement:** Not applicable.

**Informed Consent Statement:** Not applicable.

**Data Availability Statement:** Data that supports the results in this study are available from the corresponding author upon reasonable request.

**Acknowledgments:** This research used the resources of the National Energy Research Scientific Computing Center supported by DOE under Contract No. DE-AC03-76SF00098 and the Research Computing Support Services (RCSS) of the University of Missouri System. R.P. would like to acknowledge the support from the 1000-Talents Program of the Chinese Foreign Experts Bureau, the School of Physics, the University of the Chinese Academy of Sciences, Beijing, and the Institute of Physics of the Chinese Academy of Sciences, Beijing.

**Conflicts of Interest:** The authors declare no conflict of interest.

## References

- Alipour, M.; Baneshi, M.; Hosseinkhani, S.; Mahmoudi, R.; Jabari Arabzadeh, A.; Akrami, M.; Mehrzad, J.; Bardania, H. Recent progress in biomedical applications of RGD-based ligand: From precise cancer theranostics to biomaterial engineering: A systematic review. *J. Biomed. Mater. Res. A* **2020**, *108*, 839–850. [[CrossRef](#)] [[PubMed](#)]
- Jeschke, B.; Meyer, J.; Jonczyk, A.; Kessler, H.; Adamietz, P.; Meenen, N.M.; Kantlehner, M.; Goepfert, C.; Nies, B. RGD-peptides for tissue engineering of articular cartilage. *Biomaterials* **2002**, *23*, 3455–3463. [[CrossRef](#)]
- Dijkgraaf, I.; Beer, A.J.; Wester, H.-J. Application of RGD-containing peptides as imaging probes for alphavbeta3 expression. *Front. Biosci.* **2009**, *14*, 887–899. [[CrossRef](#)] [[PubMed](#)]
- Ko, H.Y.; Choi, K.-J.; Lee, C.H.; Kim, S. A multimodal nanoparticle-based cancer imaging probe simultaneously targeting nucleolin, integrin  $\alpha_v\beta_3$  and tenascin-C proteins. *Biomaterials* **2011**, *32*, 1130–1138. [[CrossRef](#)] [[PubMed](#)]
- Liu, S. Radiolabeled multimeric cyclic RGD peptides as integrin  $\alpha_v\beta_3$  targeted radiotracers for tumor imaging. *Mol. Pharm.* **2006**, *3*, 472–487. [[CrossRef](#)] [[PubMed](#)]
- Liu, S. Radiolabeled cyclic RGD peptide bioconjugates as radiotracers targeting multiple integrins. *Biocon. Chem.* **2015**, *26*, 1413–1438. [[CrossRef](#)]
- Danhier, F.; Le Breton, A.; Pr at, V. RGD-based strategies to target Alpha(v) Beta (3) integrin in cancer therapy and diagnosis. *Mol. Pharm.* **2012**, *9*, 2961–2973. [[CrossRef](#)]
- Yin, H.-Q.; Bi, F.-L.; Gan, F. Rapid synthesis of cyclic RGD conjugated gold nanoclusters for targeting and fluorescence imaging of Melanoma A375 Cells. *Biocon. Chem.* **2015**, *26*, 243–249. [[CrossRef](#)]
- Fu, S.; Xu, X.; Ma, Y.; Zhang, S.; Zhang, S. RGD peptide-based non-viral gene delivery vectors targeting integrin  $\alpha_v\beta_3$  for cancer therapy. *J. Drug Target.* **2019**, *27*, 1–11. [[CrossRef](#)]
- Sun, Y.; Kang, C.; Liu, F.; Zhou, Y.; Luo, L.; Qiao, H. RGD peptide-based target drug delivery of doxorubicin nanomedicine. *Drug Dev. Res.* **2017**, *78*, 283–291. [[CrossRef](#)]
- Nikfar, Z.; Shariatinia, Z. Tripeptide arginyl-glycyl-aspartic acid (RGD) for delivery of cyclophosphamide anticancer drug: A computational approach. *Int. J. Nano Dimen.* **2020**, *11*, 312–336.
- Nikfar, Z.; Shariatinia, Z. The RGD tripeptide anticancer drug carrier: DFT computations and molecular dynamics simulations. *J. Mol. Liq.* **2019**, *281*, 565–583. [[CrossRef](#)]
- Jin, H.; Varner, J. Integrins: Roles in cancer development and as treatment targets. *Br. J. Cancer* **2004**, *90*, 561–565. [[CrossRef](#)]
- Sun, Y.-X.; Zeng, X.; Meng, Q.-F.; Zhang, X.-Z.; Cheng, S.-X.; Zhuo, R.-X. The influence of RGD addition on the gene transfer characteristics of disulfide-containing polyethyleneimine/DNA complexes. *Biomaterials* **2008**, *29*, 4356–4365. [[CrossRef](#)] [[PubMed](#)]
- Temming, K.; Schiffelers, R.; Molema, G.; Kok, R.J. RGD-based strategies for selective delivery of therapeutics and imaging agents to the tumour vasculature. *Drug Resist. Updates* **2005**, *8*, 381–402. [[CrossRef](#)]
- Assa-Munt, N.; Jia, X.; Laakkonen, P.; Ruoslahti, E. Solution structures and integrin binding activities of an RGD peptide with two isomers. *Biochemistry* **2001**, *40*, 2373–2378. [[CrossRef](#)]
- Ruoslahti, E.; Pierschbacher, M.D. New perspectives in cell adhesion: RGD and integrins. *Science* **1987**, *238*, 491–497. [[CrossRef](#)]
- Paradise, R.K.; Lauffenburger, D.A.; Van Vliet, K.J. Acidic extracellular pH promotes activation of integrin  $\alpha_v\beta_3$ . *PLoS ONE* **2011**, *6*, e15746. [[CrossRef](#)]
- Craig, D.; Gao, M.; Schulten, K.; Vogel, V. Structural insights into how the MIDAS ion stabilizes integrin binding to an RGD peptide under force. *Structure* **2004**, *12*, 2049–2058. [[CrossRef](#)]
- Ruoslahti, E. Integrins. *J. Clin. Investig.* **1991**, *87*, 1–5. [[CrossRef](#)]
- Barczyk, M.; Carracedo, S.; Gullberg, D. Integrins. *Cell Tiss. Res.* **2010**, *339*, 269–280. [[CrossRef](#)]
- Takada, Y.; Ye, X.; Simon, S. The integrins. *Genome Biol.* **2007**, *8*, 1–9. [[CrossRef](#)]
- Li, J.; Wang, Y.; Liang, R.; An, X.; Wang, K.; Shen, G.; Tu, Y.; Zhu, J.; Tao, J. Recent advances in targeted nanoparticles drug delivery to melanoma. *Nanomed. Nanotechnol. Biol. Med.* **2015**, *11*, 769–794. [[CrossRef](#)]
- Marinelli, L.; Lavecchia, A.; Gottschalk, K.-E.; Novellino, E.; Kessler, H. Docking studies on  $\alpha_v\beta_3$  integrin ligands: Pharmacophore refinement and implications for drug design. *J. Med. Chem.* **2003**, *46*, 4393–4404. [[CrossRef](#)]
- Li, N.; Qiu, S.; Fang, Y.; Wu, J.; Li, Q. Comparison of Linear vs. Cyclic RGD Pentapeptide Interactions with Integrin  $\alpha_v\beta_3$  by molecular dynamics simulations. *Biology* **2021**, *10*, 688. [[CrossRef](#)]
- Damjanovic, J.; Miao, J.; Huang, H.; Lin, Y.-S. Elucidating solution structures of cyclic peptides using molecular dynamics simulations. *Chem. Rev.* **2021**, *121*, 2292–2324. [[CrossRef](#)] [[PubMed](#)]
- Muir, J.; Costa, D.; Idriss, H. DFT computational study of the RGD peptide interaction with the rutile TiO<sub>2</sub> (110) surface. *Surf. Sci.* **2014**, *624*, 8–14. [[CrossRef](#)]

28. Xu, M.; Zhu, T.; Zhang, J.Z.H. A force balanced fragmentation method for ab initio molecular dynamic simulation of protein. *Front. Chem.* **2018**, *6*, 189. [[CrossRef](#)] [[PubMed](#)]
29. Isborn, C.M.; Mar, B.D.; Curchod, B.F.E.; Tavernelli, I.; Martínez, T.J. The charge transfer problem in density functional theory calculations of aqueously solvated molecules. *J. Phys. Chem. B* **2013**, *117*, 12189–12201. [[CrossRef](#)]
30. Ufimtsev, I.S.; Luehr, N.; Martínez, T.J. Charge transfer and polarization in solvated proteins from ab initio molecular dynamics. *J. Phys. Chem. Lett.* **2011**, *2*, 1789–1793. [[CrossRef](#)]
31. Wei, D.; Guo, H.; Salahub, D. Conformational dynamics of an alanine dipeptide analog: An ab initio molecular dynamics study. *Phys. Rev. E* **2001**, *64*, 011907. [[CrossRef](#)]
32. Jois, S.D.; Tambunan, U.S.; Chakrabarti, S.; Siahaan, T.J. Solution structure of a cyclic RGD peptide that inhibits platelet aggregation. *J. Biomol. Struct. Dyn.* **1996**, *14*, 1–11. [[CrossRef](#)]
33. Portela, A.; Yano, T.-A.; Santschi, C.; Martin, O.J.F.; Tabata, H.; Hara, M. Highly sensitive SERS analysis of the cyclic Arg-Gly-Asp peptide ligands of cells using nanogap antennas. *J. Biophotonics* **2016**, *10*, 294–302. [[CrossRef](#)]
34. Stevens, J.S.; de Luca, A.C.; Pelendritis, M.; Terenghi, G.; Downes, S.; Schroeder, S.L.M. Quantitative analysis of complex amino acids and RGD peptides by X-ray photoelectron spectroscopy (XPS). *Surf. Interf. Anal.* **2013**, *45*, 1238–1246. [[CrossRef](#)]
35. Zhang, R.; Huang, G.; Chen, L.; Wu, W. Studies on the conformations and Hydrogen-bonding interactions of RGD tri-peptide in aqueous solutions by molecular dynamics simulations and 2D-NOESY spectroscopy. *J. Solut. Chem.* **2015**, *44*, 1281–1291. [[CrossRef](#)]
36. Karplus, M.; McCammon, J.A. Molecular dynamics simulations of biomolecules. *Nat. Struct. Biol.* **2002**, *9*, 646–652. [[CrossRef](#)] [[PubMed](#)]
37. Wakefield, A.E.; Wuest, W.M.; Voelz, V.A. Molecular simulation of conformational pre-organization in cyclic RGD peptides. *J. Chem. Inf. Model.* **2015**, *55*, 806–813. [[CrossRef](#)]
38. Adhikari, P.; Wen, A.M.; French, R.H.; Parsegian, V.A.; Steinmetz, N.F.; Podgornik, R.; Ching, W.-Y. Electronic structure, dielectric response and surface charge distribution of RGD (1FUUV) peptide. *Sci. Rep.* **2014**, *4*, 5605. [[CrossRef](#)] [[PubMed](#)]
39. Brooks, P.C.; Strömblad, S.; Klemke, R.; Visscher, D.; Sarkar, F.H.; Cheresch, D.A. Antiintegrin alpha v beta 3 blocks human breast cancer growth and angiogenesis in human skin. *J. Clin. Investig.* **1995**, *96*, 1815–1822. [[CrossRef](#)]
40. Hammes, H.-P.; Brownlee, M.; Jonczyk, A.; Sutter, A.; Preissner, K.T. Subcutaneous injection of a cyclic peptide antagonist of vitronectin receptor-type integrins inhibits retinal neovascularization. *Nat. Med.* **1996**, *2*, 529–533. [[CrossRef](#)]
41. Yamamoto, M.; Fisher, J.E.; Gentile, M.; Sedor, J.G.; Leu, C.-T.; Rodan, S.B.; Rodan, G.A. The integrin ligand echistatin prevents bone loss in ovariectomized mice and rats. *Endocrinology* **1998**, *139*, 1411–1419. [[CrossRef](#)]
42. Arap, W.; Pasqualini, R.; Ruoslahti, E. Cancer treatment by targeted drug delivery to tumor vasculature in a mouse model. *Sciences* **1998**, *279*, 377–380. [[CrossRef](#)]
43. Solution Structure of an RGD Peptide Isomer-A. Available online: <https://www.rcsb.org/structure/1FUUV> (accessed on 7 June 2021).
44. Kresse, G.; Furthmüller, J. Efficient iterative schemes for ab initio total-energy calculations using a plane-wave basis set. *Phys. Rev. B* **1996**, *54*, 169–186. [[CrossRef](#)]
45. Kresse, G.; Furthmüller, J. *Vienna Ab-Initio Simulation Package (VASP)*; University of Vienna: Vienna, Austria, 2001.
46. Blöchl, P.E. Projector augmented-wave method. *Phys. Rev. B* **1994**, *50*, 17953. [[CrossRef](#)]
47. Kresse, G.; Joubert, D. From ultrasoft pseudopotentials to the projector augmented-wave method. *Phys. Rev. B* **1999**, *59*, 1758. [[CrossRef](#)]
48. Perdew, J.P.; Burke, K.; Ernzerhof, M. Generalized gradient approximation made simple. *Phys. Rev. Lett.* **1996**, *77*, 3865. [[CrossRef](#)]
49. Nosé, S. A unified formulation of the constant temperature molecular dynamics methods. *J. Chem. Phys.* **1984**, *81*, 511–519. [[CrossRef](#)]
50. Nosé, S. A molecular dynamics method for simulations in the canonical ensemble. *Mol. Phys.* **1984**, *52*, 255–268. [[CrossRef](#)]
51. Ching, W.-Y.; Rulis, P. *Electronic Structure Methods for Complex Materials: The Orthogonalized Linear Combination of Atomic Orbitals*; Oxford University Press: Oxford, UK, 2012.
52. Eifler, J.; Podgornik, R.; Steinmetz, N.F.; French, R.H.; Parsegian, V.A.; Ching, W. Charge distribution and hydrogen bonding of a collagen  $\alpha_2$ -chain in vacuum, hydrated, neutral, and charged structural models. *Int. J. Quantum Chem.* **2016**, *116*, 681–691. [[CrossRef](#)]
53. Poudel, L.; Steinmetz, N.F.; French, R.; Parsegian, V.A.; Podgornik, R.; Ching, W.-Y. Implication of the solvent effect, metal ions and topology in the electronic structure and hydrogen bonding of human telomeric G-quadruplex DNA. *Phys. Chem. Chem. Phys.* **2016**, *18*, 21573–21585. [[CrossRef](#)] [[PubMed](#)]
54. Poudel, L.; Tamerler, C.; Misra, A.; Ching, W.-Y. Atomic-scale quantification of interfacial binding between peptides and in-organic crystals: The case of calcium carbonate binding peptide on aragonite. *J. Phys. Chem. C* **2017**, *121*, 28354–28363. [[CrossRef](#)]
55. Jawad, B.; Poudel, L.; Podgornik, R.; Steinmetz, N.F.; Ching, W.-Y. Molecular mechanism and binding free energy of doxorubicin intercalation in DNA. *Phys. Chem. Chem. Phys.* **2019**, *21*, 3877–3893. [[CrossRef](#)]
56. Adhikari, P.; Ching, W.-Y. Amino acid interacting network in the receptor-binding domain of SARS-CoV-2 spike protein. *RSC Adv.* **2020**, *10*, 39831–39841. [[CrossRef](#)]



57. Adhikari, P.; Li, N.; Shin, M.; Steinmetz, N.F.; Twarock, R.; Podgornik, R.; Ching, W.-Y. Intra- and intermolecular atomic-scale interactions in the receptor binding domain of SARS-CoV-2 spike protein: Implication for ACE2 receptor binding. *Phys. Chem. Chem. Phys.* **2020**, *22*, 18272–18283. [[CrossRef](#)]
58. Ching, W.-Y.; Adhikari, P.; Jawad, B.; Podgornik, R. Ultra-large-scale ab initio quantum chemical computation of bio-molecular systems: The case of spike protein of SARS-CoV-2 virus. *Comput. Struct. Biotech. J.* **2021**, *19*, 1288–1301. [[CrossRef](#)] [[PubMed](#)]
59. Jawad, B.; Adhikari, P.; Podgornik, R.; Ching, W.-Y. Key interacting residues between RBD of SARS-CoV-2 and ACE2 receptor: Combination of molecular dynamic simulation and density functional calculation. *J. Chem. Inf. Model.* **2021**, *61*, 4425–4441. [[CrossRef](#)] [[PubMed](#)]
60. Jawad, B.; Poudel, L.; Podgornik, R.; Ching, W.-Y. Thermodynamic dissection of the intercalation binding process of doxorubicin to dsDNA with implications of ionic and solvent effects. *J. Phys. Chem. B* **2020**, *124*, 7803–7818. [[CrossRef](#)] [[PubMed](#)]
61. Mulliken, R.S. Electronic population analysis on LCAO–MO molecular wave functions. I. *J. Chem. Phys.* **1955**, *23*, 1833–1840. [[CrossRef](#)]
62. Mulliken, R.S. Electronic population analysis on LCAO–MO molecular wave functions. II. overlap populations, bond orders, and covalent bond energies. *J. Chem. Phys.* **1955**, *23*, 1841–1846. [[CrossRef](#)]
63. Dharmawardhana, C.C.; Misra, A.; Ching, W.-Y. Quantum mechanical metric for internal cohesion in cement crystals. *Sci. Rep.* **2014**, *4*, 7332. [[CrossRef](#)]
64. Wang, Y.; Goh, S.-Y.; Kuczera, K. Molecular dynamics study of disulfide bond influence on properties of an RGD peptide. *J. Pept. Res.* **1999**, *53*, 188–200. [[CrossRef](#)]
65. Löffler, G.; Schreiber, H.; Steinhauser, O. Calculation of the dielectric properties of a protein and its solvent: Theory and a case study. *J. Mol. Biol.* **1997**, *270*, 520–534. [[CrossRef](#)]
66. Schutz, C.N.; Warshel, A. What are the dielectric constants of proteins and how to validate electrostatic models? *Proteins Struct. Funct. Bioinform.* **2001**, *44*, 400–417. [[CrossRef](#)]
67. King, G.; Lee, F.S.; Warshel, A. Microscopic simulations of macroscopic dielectric constants of solvated proteins. *J. Chem. Phys.* **1991**, *95*, 4366–4377. [[CrossRef](#)]
68. Gilson, M.K.; Honig, B.H. Calculation of electrostatic potentials in an enzyme active site. *Nature* **1987**, *330*, 84–86. [[CrossRef](#)] [[PubMed](#)]
69. Aryal, S.; Rulis, P.; Ouyang, L.; Ching, W.Y. Structure and properties of the low-density phase  $\epsilon$ -Al<sub>2</sub>O<sub>3</sub> from first principles. *Phys. Rev. B* **2011**, *84*, 174123. [[CrossRef](#)]
70. Baral, K.; Adhikari, P.; Ching, W.Y. Ab initio modeling of the electronic structures and physical properties of a-Si<sub>1-x</sub>GexO<sub>2</sub> Glass (x = 0 to 1). *J. Am. Ceram. Soc.* **2016**, *99*, 3677–3684. [[CrossRef](#)]
71. Hasan, S.; Baral, K.; Li, N.; Ching, W.-Y. Structural and physical properties of 99 complex bulk chalcogenides crystals using first-principles calculations. *Sci. Rep.* **2021**, *11*, 1–18. [[CrossRef](#)]
72. Hussain, A.; Mehmood, S.; Rasool, M.; Aryal, S.; Rulis, P.; Ching, W. Electronic structure, mechanical, and optical properties of CaO Al<sub>2</sub>O<sub>3</sub> system: A first principles approach. *Ind. J. Phys.* **2016**, *90*, 917–929. [[CrossRef](#)]
73. Rajter, R.F.; French, R.; Ching, W.Y.; Carter, W.C.; Chiang, Y.M. Calculating van der Waals–London dispersion spectra and Hamaker coefficients of carbon nanotubes in water from ab initio optical properties. *J. Appl. Phys.* **2007**, *101*, 054303. [[CrossRef](#)]
74. Baral, K.; Li, A.; Ching, W.-Y. Ab initio modeling of structure and properties of single and mixed alkali silicate glasses. *J. Phys. Chem. A* **2017**, *121*, 7697–7708. [[CrossRef](#)] [[PubMed](#)]
75. Baral, K.; Li, A.; Ching, W.-Y. Ab initio molecular dynamics simulation of Na-doped aluminosilicate glasses and glass-water interaction. *AIP Adv.* **2019**, *9*, 075218. [[CrossRef](#)]
76. Baral, K.; Li, A.; Ching, W.-Y. Ab initio study of hydrolysis effects in single and ion-exchanged alkali aluminosilicate glasses. *J. Phys. Chem. B* **2020**, *124*, 8418–8433. [[CrossRef](#)] [[PubMed](#)]
77. Baral, K.; San, S.; Sakidja, R.; Couet, A.; Sridharan, K.; Ching, W.-Y. Temperature-dependent properties of molten Li<sub>2</sub>BeF<sub>4</sub> Salt using Ab initio molecular dynamics. *ACS Omega* **2021**, *6*, 19822–19835. [[CrossRef](#)] [[PubMed](#)]

## Article

# Performance Analysis of Indentation Punch on High Energy Lithium Pouch Cells and Simulated Model Improvement

Lihua Ye <sup>1,\*</sup>, Muhammad Muzamal Ashfaq <sup>1,\*</sup>, Aiping Shi <sup>2</sup>, Syeed Adnan Raheel Shah <sup>3</sup> and Yefan Shi <sup>4</sup><sup>1</sup> School of Automotive and Traffic Engineering, Jiangsu University, Zhenjiang 212013, China<sup>2</sup> School of Agricultural Equipment Engineering, Jiangsu University, Zhenjiang 212013, China; shap@ujs.edu.cn<sup>3</sup> Department of Civil Engineering, Pakistan Institute of Engineering and Technology, Multan 66000, Pakistan; syeed.adnanraheelshah@uhasselt.be<sup>4</sup> Department of Electrical and Computer Engineering, Binghamton University, Binghamton, NY 13902, USA; yshi37@binghamton.edu

\* Correspondence: yelihua@ujs.edu.cn (L.Y.); muhammadmuzamal598@gmail.com (M.M.A.)

† Equally contributor in the study.

**Abstract:** In this research, the aim relates to the material characterization of high-energy lithium-ion pouch cells. The development of appropriate model cell behavior is intended to simulate two scenarios: the first is mechanical deformation during a crash and the second is an internal short circuit in lithium-ion cells during the actual effect scenarios. The punch test has been used as a benchmark to analyze the effects of different state of charge conditions on high-energy lithium-ion battery cells. This article explores the impact of three separate factors on the outcomes of mechanical punch indentation experiments. The first parameter analyzed was the degree of prediction brought about by experiments on high-energy cells with two different states of charge (greater and lesser), with four different sizes of indentation punch, from the cell's reaction during the indentation effects on electrolyte. Second, the results of the loading position, middle versus side, are measured at quasi-static speeds. The third parameter was the effect on an electrolyte with a different state of charge. The repeatability of the experiments on punch loading was the last test function analyzed. The test results of a greater than 10% state of charge and less than 10% state of charge were compared to further refine and validate this modeling method. The different loading scenarios analyzed in this study also showed great predictability in the load-displacement reaction and the onset short circuit. A theoretical model of the cell was modified for use in comprehensive mechanical deformation. The overall conclusion found that the loading initiating the cell's electrical short circuit is not instantaneously instigated and it is subsequently used to process the development of a precise and practical computational model that will reduce the chances of the internal short course during the crash.

**Keywords:** lithium-ion; high energy pouch cell; state of charge; electrolyte; load position; modeling

**Citation:** Ye, L.; Ashfaq, M.M.; Shi, A.; Shah, S.A.R.; Shi, Y. Performance Analysis of Indentation Punch on High Energy Lithium Pouch Cells and Simulated Model Improvement. *Polymers* **2021**, *13*, 1971. <https://doi.org/10.3390/polym13121971>

Academic Editors: Célio Bruno Pinto Fernandes, Salah Aldin Faroughi, Luís L. Ferrás and Alexandre M. Afonso

Received: 2 May 2021

Accepted: 5 June 2021

Published: 15 June 2021

**Publisher's Note:** MDPI stays neutral with regard to jurisdictional claims in published maps and institutional affiliations.



**Copyright:** © 2021 by the authors. Licensee MDPI, Basel, Switzerland. This article is an open access article distributed under the terms and conditions of the Creative Commons Attribution (CC BY) license (<https://creativecommons.org/licenses/by/4.0/>).

## 1. Introduction

In recent decades, energy derived from fossil fuels has become harmful to the climate and its sources are decreasing with time [1]; that is why electric vehicles are expected to replace vehicles in which gasoline is used as an energy source. To overcome that deprivation of this energy in the future, batteries are considered to be one of the significant methods of storing energy that is being produced by different sources. Lithium-ion batteries have proven to be very profitable, and they are used in many electronic gadgets [2]. Moreover, they are also not used in various electric sources, such as mobile phones, laptops, and cameras, but are widely used as energy storage systems in electric vehicles due to their high capacity, low self-discharge, long life, high energy density, and low climatic effect characteristics. In some conditions, lithium batteries have also proven to be the cause of thermal runaway, mechanical abuse, and release of toxic gases [2–5]. Thus, interest in lithium-ion batteries from researchers has increased in recent years [6–11]. Electrochemical

technologies are particularly significant in present society, and it is an exciting time for researchers that are active in this sector [12]. This is a vital topic for research for electric vehicles, specifically when considering the massive operational range that electric vehicles would be subjected to [13–15].

Sony Ericson established the first battery in 1991, and a lithium-ion battery was later commercially introduced [16,17]. Since then, millions of cells are in the market with their different specifications [18–20]. For many years, customer's demand and best purposes have persisted in maintaining more extended battery running time. To meet customer's needs, producers have appropriately responded to increase battery performance by changing the cell's chemistry, which directly affects its memory loss and high electric density. Different li-ion cells include various types of materials, and the material containing titanium [21–23], silicon, and graphite oxide for the negative electrode, LiMO<sub>y</sub>, in which oxides, manganese oxide (MO<sub>y</sub>), cobalt oxide, and ferrous phosphate, etc. can be used as a metal oxide [24]. Direct contact between electrodes can cause a short circuit. A separator is used for this type of short circuit to make a cell safe [25–27]. A separator is made of different materials, such as polypropylene, for a lithium polymer cell. Still, in the lithium-ion cell, SEI (Solid Electrolyte Interphase) usually consists of Li<sub>2</sub>O (Lithium Oxide) [28,29], LiF (Lithium Fluoride) [30], Li<sub>2</sub>CO<sub>3</sub> (Lithium Carbonate) [31], and polyolefin [32–34]. The electrolyte depicted in this study consists of a conductive salt, e.g., lithium hexafluorophosphate (LiPF<sub>6</sub>), and a solvent dimethyl carbonate (DMC), and ethylene carbonate (EC), diethyl carbonate (EC), or ethyl methyl carbonate (EMC) [35]. The use of metallic lithium leads to safety hazards [36] and low cycle efficiency due to lithium's reactivity with ordinary liquid electrolytes [37]. The energy density of a lithium-ion battery is higher than other battery sources. In the pouch/prismatic cells, one thing that is more common is that the electrodes/separator assembly is not wrapped in its mount. The length to thickness ratio, rather than the actual dimensions, is the thing that matters; the prismatic battery is regarded as an-isotropic multi-layered thick plate [38–40].

There is a need to overcome these internal short circuits due to mechanical failure which is due to accidents, according to the International Energy Agency [40–43]. Unfortunately, manufacturers could not provide the reasons and mechanisms of internal structural failure. Detailed computational modeling of the battery can explain the origins of failure, mechanisms of failure, and their implications to the battery pack design; thus, it can provide suitable enhancements in format [44]. Some previous studies are improving their mechanical and electrical performance by changing their material structures [45]. As a result, this led to battery-pack designs in EV (Electric Vehicle). Battery protection was examined [46]. Researchers observed changes by applying different loading conditions on lithium-ion battery cells, and they investigated the effects on cells while using the load in various conditions [47–49]. Suppose that an accident or mishap occurs in an electric vehicle. In that case, it can also harm the battery pack by intruding on external objects, which can lead to the mechanical deformation of lithium-ion cells. These external objects can occur from various directions, e.g., in-plane loading, which can compress the cell's narrow border, and out-of-plane indentation, which can punch a vast surface of pouch cell perpendicularly [50–52]. Electricity, thermal, and mechanical integrities are the three main factors that are mutually related to battery protection [53,54]. Crash experiments of an EV provide a lesson from where it was once found that, instead of minor intrusion into a battery pack, a disastrous result was produced [55–57]. However, its overcharging also includes one of the most severe safety issues for applications of lithium-ion batteries [30,58]. Analysis of outcomes from quasi-static loading states on the reaction of the cell and most of the primary research and modeling work were done [58–60].

Several quasi-static indentation tests were carried out on lithium-ion pouch cells. These indentation tests were prompted at the onset of the internal short circuit. The location of fracture occurs before catastrophic failure of the entire pouch cell with unusual local damage, and accretion appears precisely on the layers. The transient breach occurs in the higher portion of the covered layers, the main force drops, and the synchronous

strike of an inner short circuit occurs within the sac cell, while the down part of the pouch cell comprehensively stays. During the indentation tests process, for lithium pouch cells, the common structural unyielding increases at first before its final drop, and it then enters a stagnant condition. After the curvature point, a load of indentation makes the viscid forces stronger. It aggravates the separator into constituent layers and the particles of graphite de-coat from the anode [61]. The overall performance of the lithium-ion battery can be understood when researchers also investigated the status of mechanical stress on a lithium-ion battery, which is mainly caused by external stress. A variety of different mechanical models have been established to investigate the effects on lithium-ion battery packs by applying mechanical loads, which is one of the prominent reasons for the internal short circuit [62,63]. A collective numerical, analytical, and experimental approach was performed to develop a new cell failure model and to understand the primary mechanism of failure. As soon as the large format pouch cells were subjected to indentation leading to failure, an examination of failure regions demonstrated a fracture surface angle to the battery plane [64,65]. The research combined both experimental and computational studies [66,67]. Dynamic finite element simulations were performed to study pouch cells' mechanical behavior, such as internal interfacial behavior, loading, and boundary conditions, which shows a direct interaction between cell boundaries and impactor leading to the significant change in the residual velocity [68,69].

This research will focus on complete cell indentation tests on a specific model of high-energy pouch lithium-ion cells to facilitate the exploration of buckling response under various confinement levels. It also focuses on determining the effects on electrolytes while applying a different type of load by changing the punch size and punch position with the other soc. It will help to identify a model for battery cells when different mechanical loads are applied to it. Taking some measures can improve the application of lithium-ion batteries in different technologies. These measures can include strengthening the batteries' walls, the storage chambers, material strength, compartment ventilation for fire suppression, and ingress and egress points. This indicates that cell battery model will help to build blocks for developing a battery pack model, as shown in Figure 1. It is a homogenized form of the battery cell where all five distinctive materials are smudged into one homogenized medium in the battery pack. Theoretically, even though provisional imperfections or modal patterns may be added, such a homogenized model will not simulate realistic buckling patterns because the battery's actual configuration is anisotropic.

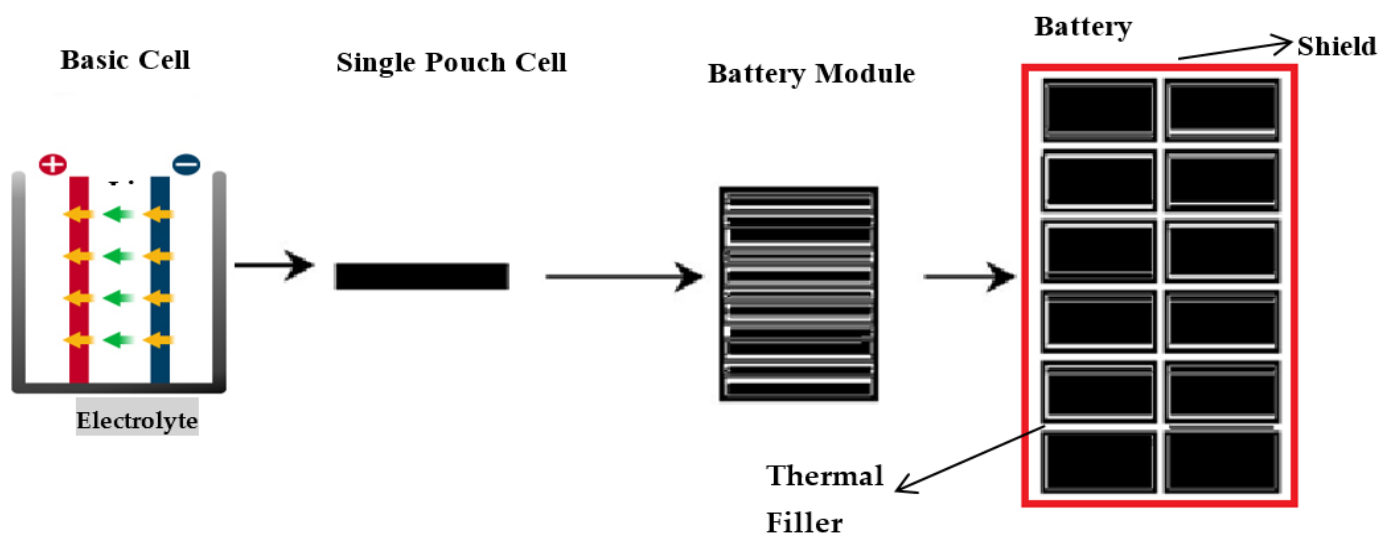


Figure 1. Preferable sketch of lithium-ion battery pack design and outer shield.

The comprehensive computational modeling will offer valuable information in the allocation to close the design feedback loop, leading to a robust design overall and providing the best solution.

## 2. Materials and Methods

### 2.1. Mechanical Indentation

The mechanical indentation test has been used in this study, including information regarding the physical and mechanical properties, the electrochemical characteristics, and the operating properties of the cells. Manufacturers are requested to discharge the cell of no more than 10% state of charge to avoid extreme reactions at the point of indentation tests. The other two cells have more than 10% state of charge with preventive measures to maintain the environment from severe reactions.

These types of cells are typical of those that can be found in electric vehicle applications or an energy storage system due to their incredible efficiency and high capacity [38,39]. These cells also have a stackable geometry and packaging. Lithium-ion cells provide compelling advantages to manufacturers. Any desired shape can be produced according to the requirement of the customer. Space and weight requirements can be met for mobile devices and notebook computers [70,71]. Testing on four pouch-type cells of li-ion is conducted in this work. The following sections describe the equipment, preparation, and results from those tests. Firstly, the Punch Indentation testing results are described after the battery component descriptions.

In this study, High-energy lithium-ion pouch cells GPLFP (Gee Power LiFe Polymer Battery (Cell Manufacturing Company Guangdong, China) 11192320ES-50 Ah have been used, as depicted in Figure 2. Lithium-ion accumulators have 95% high discharge efficiency, which also shows low self-emit when compared to rechargeable cells, such nickel-cadmium and nickel manganese accumulators. There is an energy density of more than 200 W-h/kg for the commercially available lithium-ion battery.

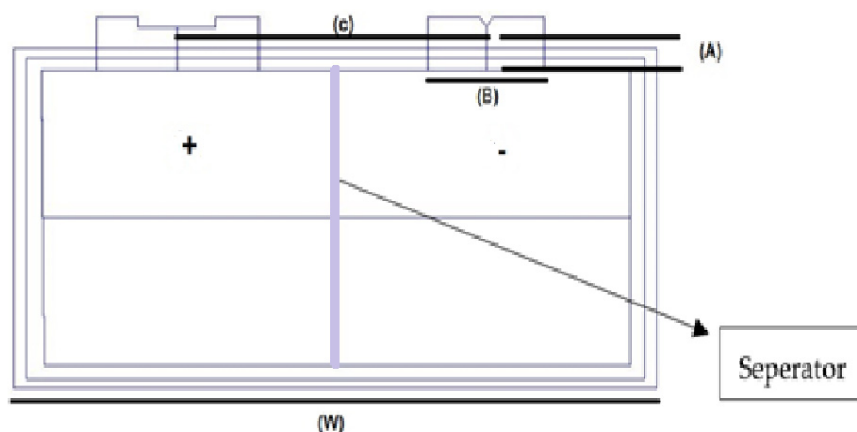


Figure 2. High-energy lithium pouch cell diagram.

Lithium presents advantageous properties, such as greater battery life, being present in many weights, reliability, foolproof safety, more energy repository, balance, and compatibility [18]. Figure 2 shows the major specifications of this cell. The online information sheet for this cell is provided in [72] to the interested reader and it is also shown in Table 1. Lithium pouch cells consist of stacked layers of anodes, separators, and cathodes that are sandwiched between the laminated film layers. These pouch cells can be created in customized sizes and shapes. Pouch cells are then linked in sequence and parallel to accumulate the preferred voltage and capacity. In a pouch cell configuration, “S” in the number specifies how many are in the series, and the “P” specifies the number of pack assemblies. For example, if you have a 4s4p pack, this would be a total of sixteen cells—four packs of four batteries each.

**Table 1.** Model: GPLFP 11192320ES-50 Ah.

Cell Specifications	Values
Nominal Capacity	50 Ah
Nominal Voltage	3.2 V
Width	193 mm max
Length	320 mm max
Thickness	11.3 mm max
Weight	1300 g
Tab width	50 ± 0.5 mm
Electrolyte	lithium hexafluorophosphate (LiPF <sub>6</sub> )
Center	100 ± 2.0 mm

Test cell specifications [72].

## 2.2. Indentation Test

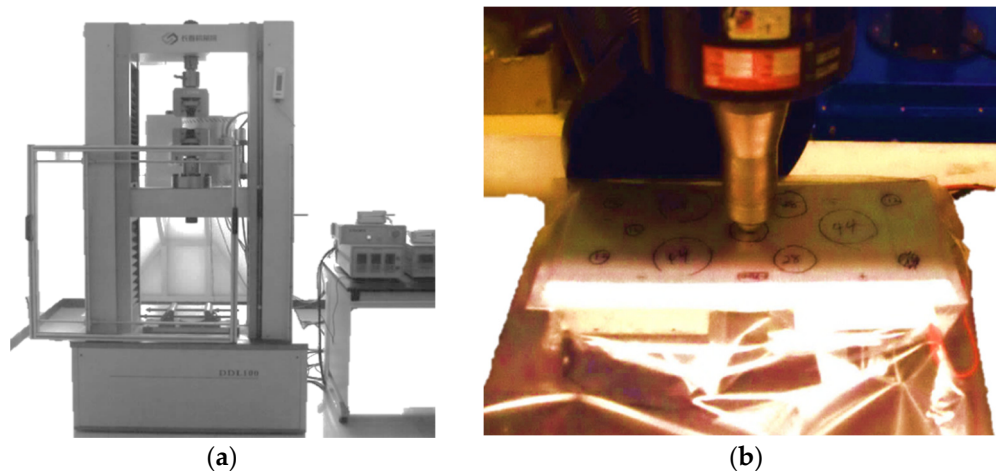
Before testing, the cells have been discharged to the preferred discharge cut-off voltage of 2.5 V [72] to stop intense reactions all through the testing scenarios. Two cells have been on more than 10% soc and two cells have been kept on less than 10% soc. A complete test application has been performed to complete the calibration process and validate the corresponding models. Figure 3 presents four types of punch used in experiments that were carried out on the lithium-ion battery. Table 2 represents total number of punch tests applied on each cell. The cells were tested using the universal testing machine (UTM) loading frame that was equipped with a 200 kN load cell in the whole experiment, as shown in Figure 4. The first test of each cell included voltage monitoring in determining the onset of the internal electric short circuit. The punches have been placed in the center and on edges of the cell lengthwise and widthwise. All of these punches are used for all four cells. No punch is specified for any specified cell. Each cell used to be subjected to 10 consecutive indentation tests using three sizes of hemispherical punches—small (12 mm diameter), medium (28 mm diameter), and massive (44 mm diameter), and a flat cylindrical punch (25 mm diameter) [9,72], as can be seen in Figure 3.



**Figure 3.** Indentation, different sizes of punch are used, which are hemispherical punches of diameters 12 mm, 28 mm, and 44 mm, and a flat cylindrical punch of 25 mm.

**Table 2.** Number of tests on each cell.

Cell No.	Order & Number in Experiments Performed
1	With >10% soc Medium (2) Large (2) Small (4) one voltage Cylindrical (2)
2	With >10% soc Small (4), one voltage Medium (2) Large (2) Cylindrical (2)
3	With <10% soc Large (2), Medium (2) Small (4) one voltage Cylindrical (2)
4	With <10% soc Cylindrical (2) Large (2) Medium (2) Small (4) one voltage



**Figure 4.** (a) Punching on the cell during the test (number of punches with different size were used) (b) Universal testing machine >50 kN.

### 2.3. Testing Procedure of Punch Indentation

A complete test application has been performed to complete the calibration process and validate the corresponding model. In preparation for testing, the cells have been separately placed in two-gallon Ziploc bags with SOLUSORB<sup>®</sup> solvent adsorbent to include any electrolyte leakage that can also occur throughout the testing procedure. The bags have been then marked to determine appropriately spaced punch locations, such that the preceding tests would no longer influence the subsequent identical cell indentation test results. The prepared cell was then positioned on a stable, flat metallic surface under the loading frame with the suitable test location being found below the hemispherical punch to be used. For the first test of every cell, voltmeter leads have been linked to positive and negative cell terminals inside the bag using alligator clips, and the container used to be semi-sealed around the edges. The punch used is lowered to a point entirely above the cell's surface. A fume extractor was placed inside six inches of the setup to remove the

poisonous fumes released during and post-test. Figure 4 presents a standard, first-run test setup. The voltmeter was removed in subsequent identical cell test runs.

The following parameters are measured at 1-s intervals using meter view c software:

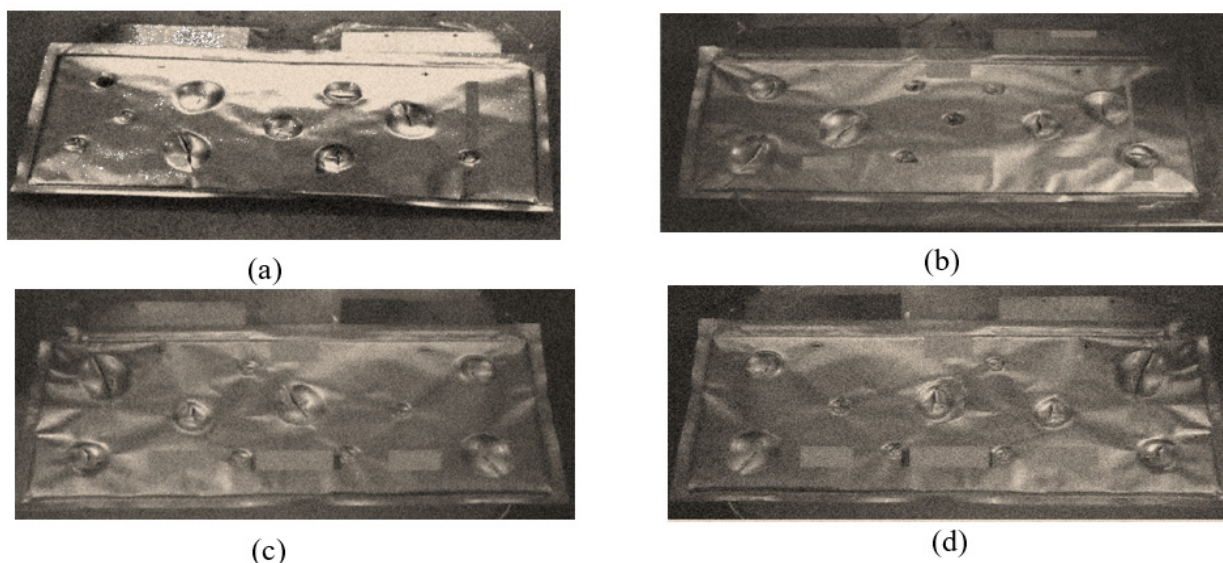
- The test computing device and displacement over time. In all of these tests, displacement is constant with a fixed rate of 1 mm/min., while related testworks04 software measured and recorded test machine load and crosshead displacement in 1-s intervals.
- Over time, cell voltage has been determined with a standard voltmeter at the end of the cell positive and negative electrodes. Voltage measurements have been measured simultaneously on the first test of each cell using a general voltmeter that is connected to the cell terminals and have been recorded at 1-s intervals using meter view c software.
- The outside temperature of a cell over time, as determined by thermo-couple.
- It is also mentioned that all of these tests are carried out at room temperature because, under intense cold or warm temperatures, the material properties can appreciably change, and the min-max range of temperature for batteries ( $-20\text{ }^{\circ}\text{C}$  to  $60\text{ }^{\circ}\text{C}$ ) is essential at a variety of variable temperatures above the characterization and evaluation be carried out.
- Photographs during tests are captured at a rate of average 5 min.
- When one short circuit is achieved, all of these monitoring devices work until these parameters again come back to their constant state.

Many tests are conducted to achieve fast reduction in force to locate punch on cells and the voltage readings indicating short circuit of cell. Between identical cell test scenarios, the loading frame used to be lifted and reset for cell repositioning and punches change-out when necessary.

### 3. Results

#### 3.1. Testing Results of Punch Indentation

Observing previous cells' tests revealed no leakage or pretension of the pouch cells due to short circuit chemical reactions, and there will be no gas formation because it can cause an explosion. Nevertheless, a, b, c, d reveal the observational test results following the completion of all testing, as shown in Figure 5.



**Figure 5.** Cell-1 post test (a), cell-2 post test (b), cell-3 post test (c), and cell-4 post test (d).

For the initial tests of cells 1, 2, and 3, 4, as shown in Figure 5, both load and voltage are graphs of a displacement function. The voltage drops when a short circuit occurs in any of the indentation tests. Figures 6–9 show each cell with greater than 10% soc. It is



understood that the onset of a short circuit is directly connected with the cell’s mechanical failure. Test data also revealed, with an increase in punch radius, the beginning of electric short circuit successively occurred later, starting at time = 180 s, time = 260 s, time = 289 s, and time = 304 s or small, medium, large, and a flat cylindrical punch sizes, respectively. A hemispherical punch with 44 mm size did not produce any short circuit or drop in voltage until 5 kN, as shown in Figure 9.

Figures 6–13 shows that the voltage drop is at the point of a short circuit in all tests. It can be determined that the cut-off voltage of all punches starts from 2.5, but the drops in voltage displacement and peak loads are different for both cells for all punch types in both soc conditions. However, a drop-in voltage of small punch with size 12 mm, medium punch with size 28 mm, 44 mm, and flat cylindrical punch with size 25 mm goes on an ending of 1.90, 0.65, −0.42, and 0.75. Nevertheless, a large punch with a size of 44 mm shows −0.42 voltages at 50 kN load when the load is removed back from the cell, as shown in Figure 9 for greater than 10% soc.

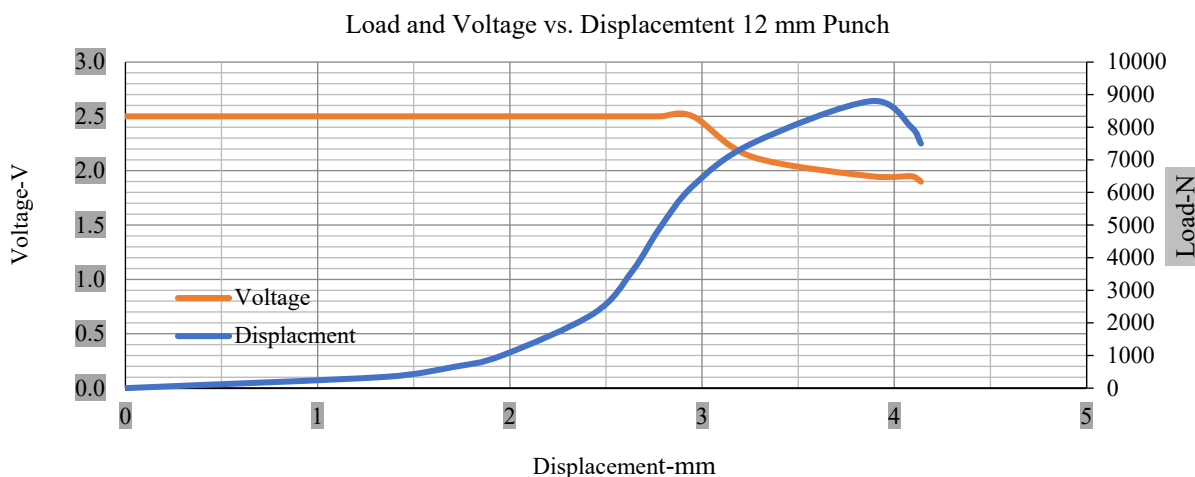


Figure 6. Load and voltage vs. displacement 12 mm punch greater than 10% soc.

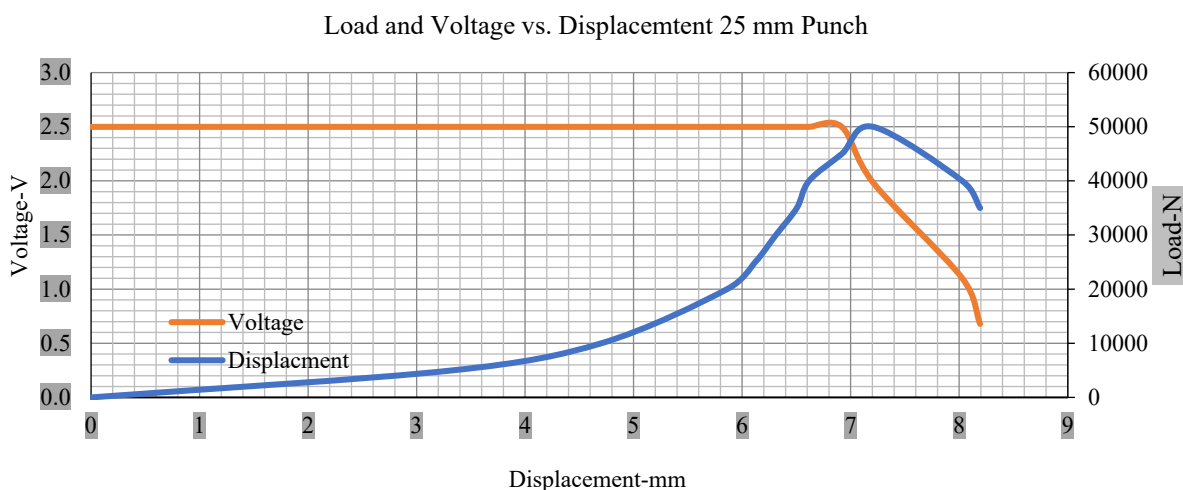


Figure 7. Load and voltage vs. displacement 25 mm punch greater than 10% soc.

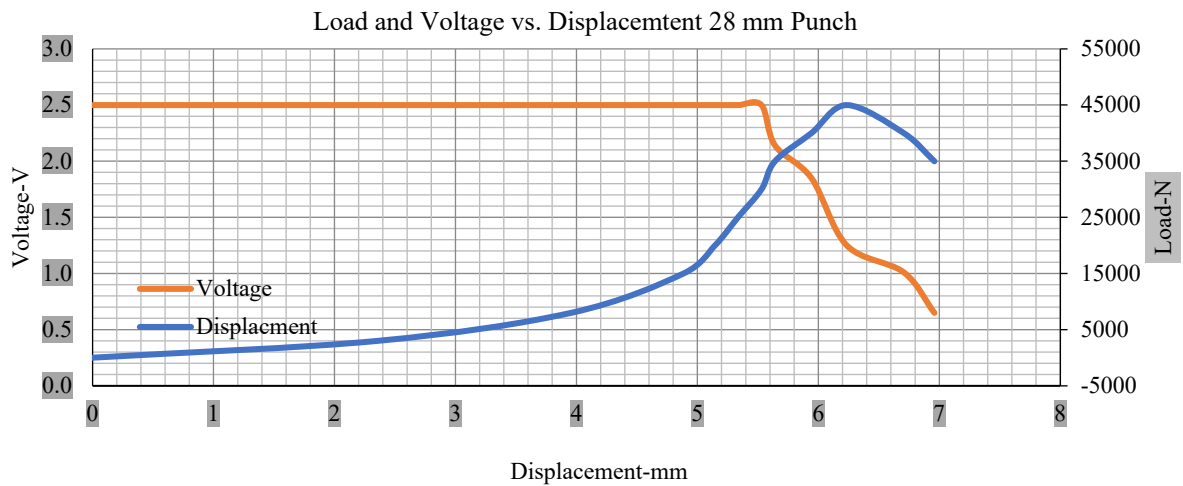


Figure 8. Load and voltage vs. displacement 28 mm punch greater than 10% soc.

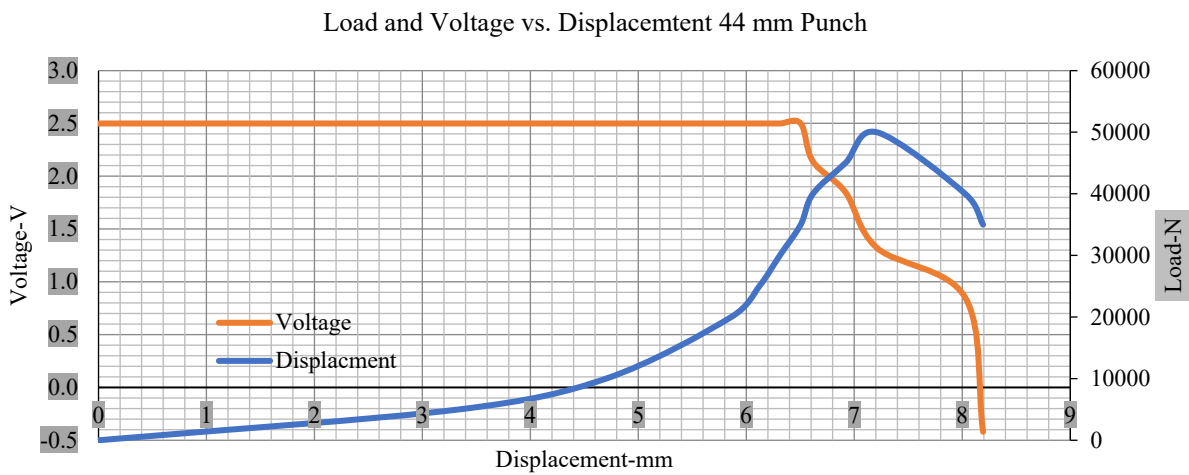


Figure 9. Load and voltage vs. displacement 44 mm punch greater than 10% soc.

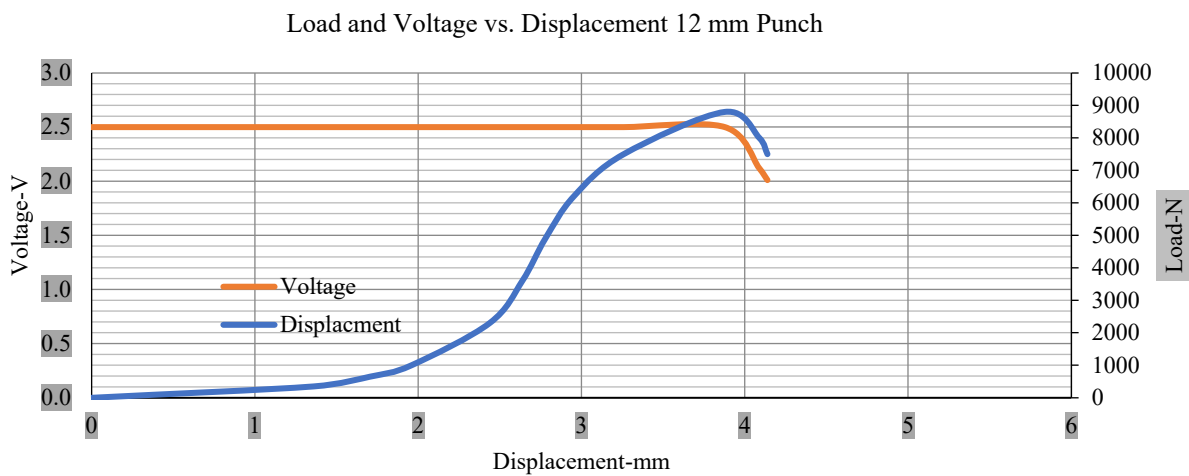


Figure 10. Load and voltage vs. displacement 12 mm punch less than 10% soc.

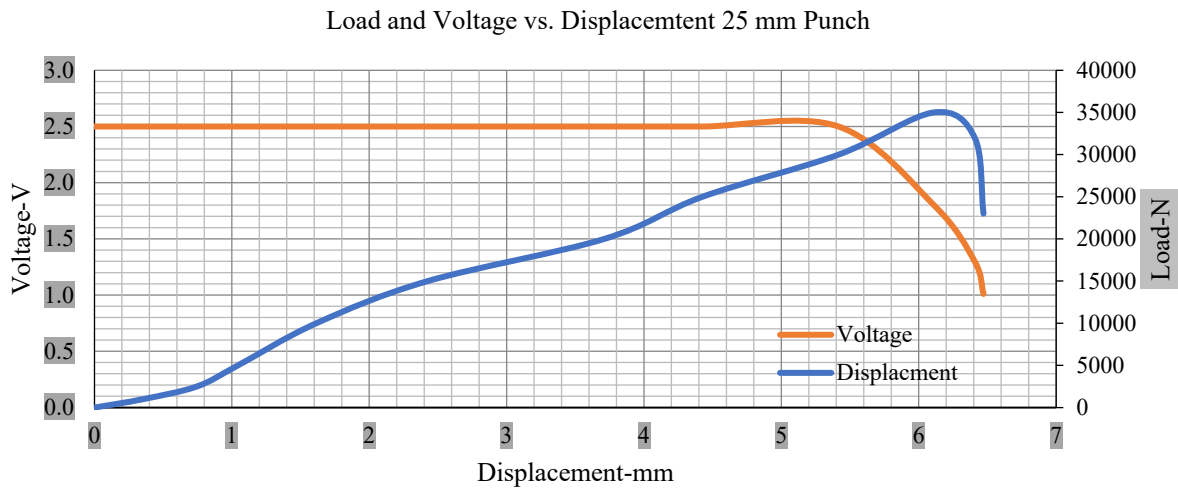


Figure 11. Load and voltage vs. displacement 25 mm punch less than 10% soc.

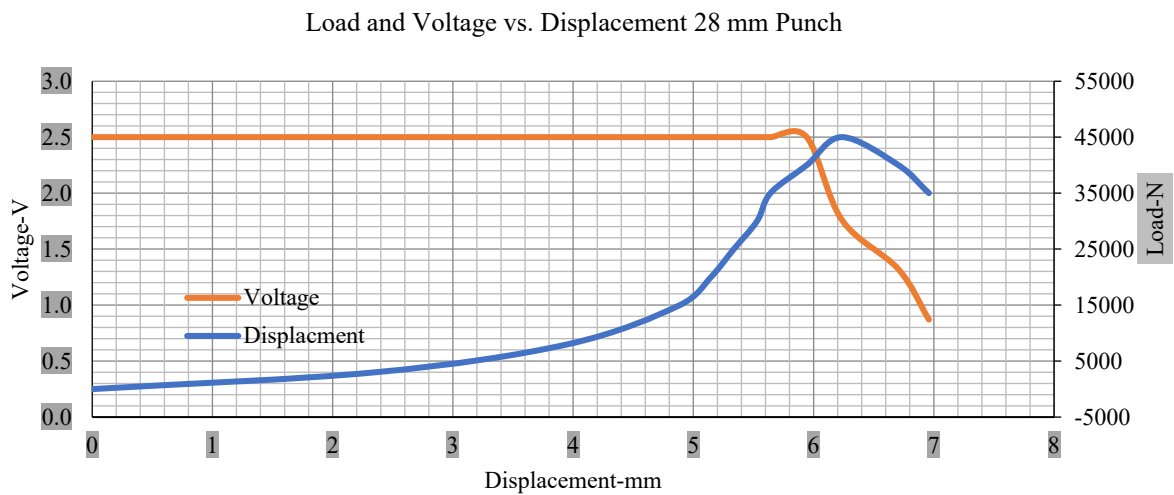


Figure 12. Load and voltage vs. displacement 28 mm punch less than 10% soc.

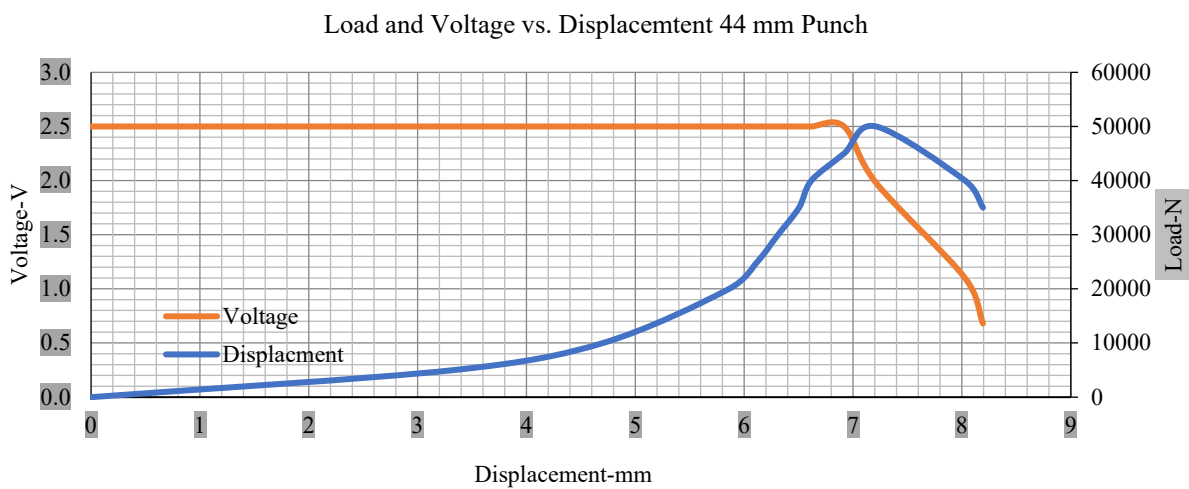


Figure 13. Load and voltage vs. displacement 44 mm punch less than 10% soc.

Thus, the values for less than 10% soc drop in the voltage of small, medium punch, large punch, and flat cylindrical punch are 1.98, 1.01, 0.81, and 0.68. A drop in voltage

rebound is found after a preliminary drop for punch indentation for all cells, and then the voltage progressively lowered to 0 to  $-0.30$  over 15 s.

With the exception of the small and medium punch studies, local deformation that can be securely tolerated from 6 mm (small cell) to 10 mm (medium cell) through the cell levels and even 12 mm punch also did not produce much deformation, as shown in Figures 6–13.

As predicted, the cells trigger a voltage drop just under the large punch of 44 mm, as shown in Figure 9 and the displacement graph, and it is considerably deeper and quicker than other punch indentations. The hassle is pushed through the basic geometry of a massive punch that is defined in terms of the tip’s central angle and radius. These findings measure the pattern that is expected in every other situation; those batteries can safely handle extra blunt object intrusion. For 44 mm punch with less than 10% soc, the displacements are 6.474 and 6.324, and, for the other two cells with greater than 10%, the soc displacements are 6.493 and 6.503, respectively, as shown in Figure 17.

This analysis measures the point between two of these similarities and variations. Moreover, an investigation has been performed in relation to how these materials’ properties can be changed when indentation moves from the middle to the corners of the cell. However, in these experiments, the indentation punch position has also been changed from the mid to corner, and the readings are shown for less and greater than 10% soc.

### 3.2. Effect of Electrolyte with the State of Charge

Different indentation tests have been performed on less than 10% state of charge cell to evaluate the electrolyte impact on lithium cells’ loading response. Tests were performed with more than 10% state of charge cell; all of the experiments have been conducted with 12 mm, 25 mm, 28 mm, and 44 mm diameter punch, and all the experiments have been completed at a rate of 1 mm/min. loading. All of the punch tests are performed twice, except for the punch with a 12 mm diameter. These tests have been performed on both soc cells. The cells with less than 10% soc have a much more rigid reaction and a high force level, being significantly more than 10% soc. In contrast, for the estimated force for the last two cells with less than 10% soc, with 28 mm punch, the displacements are 5.466 and 5.316, and, for the first two cells with greater than 10%, the soc displacements are 5.529 and 5.506, as shown in Figures 14–17.

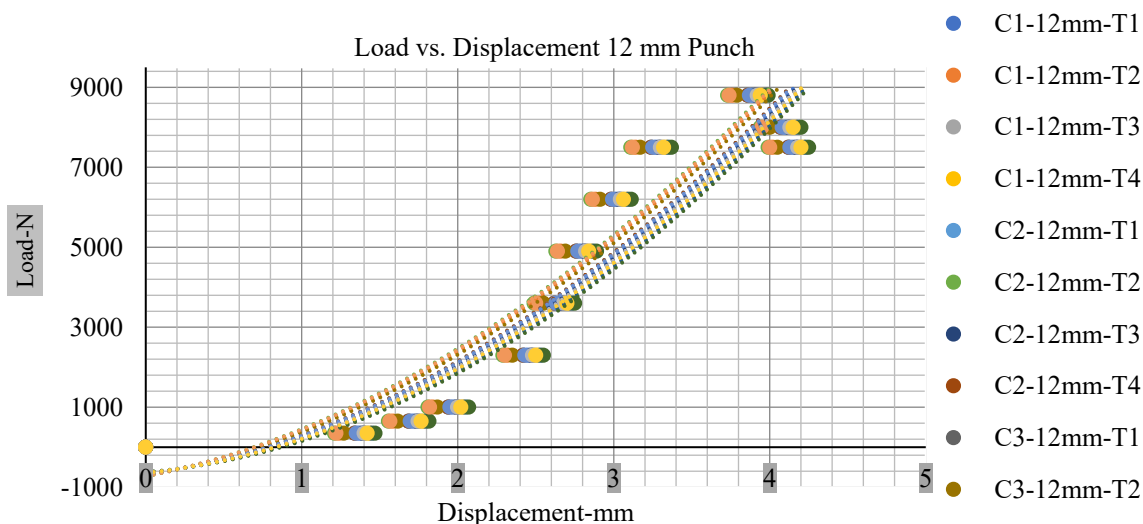


Figure 14. Load vs. displacement 12 mm low to peak loads.

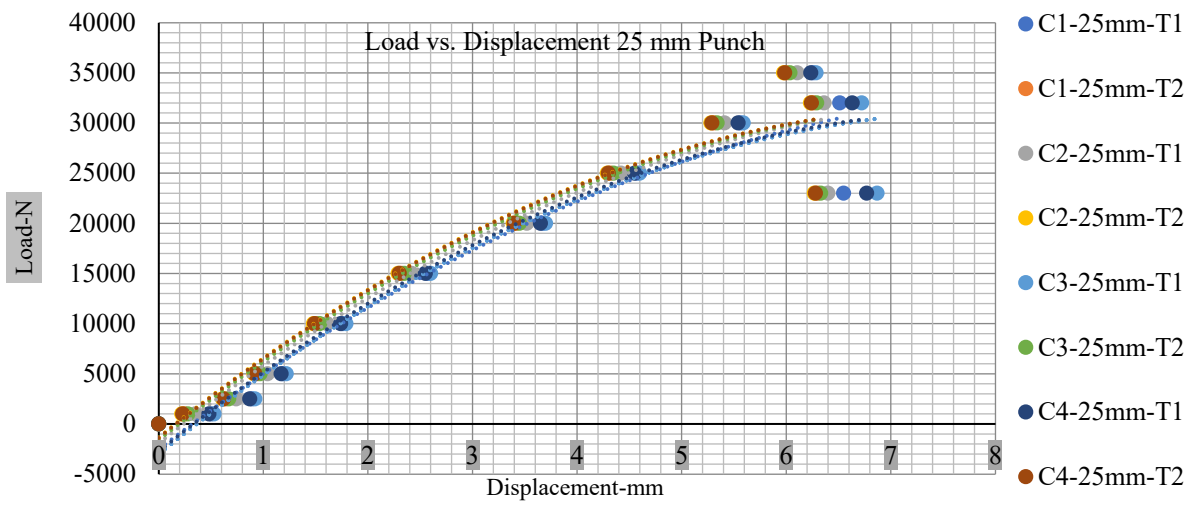


Figure 15. Load vs. displacement 25 mm low to peak loads.

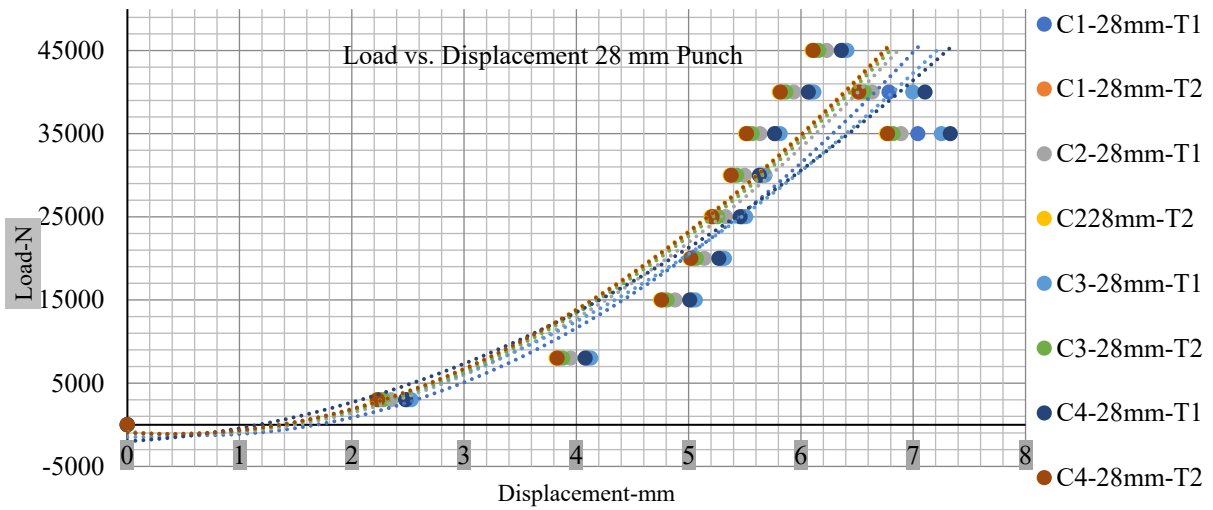


Figure 16. Load vs. displacement 28 mm low to peak loads.

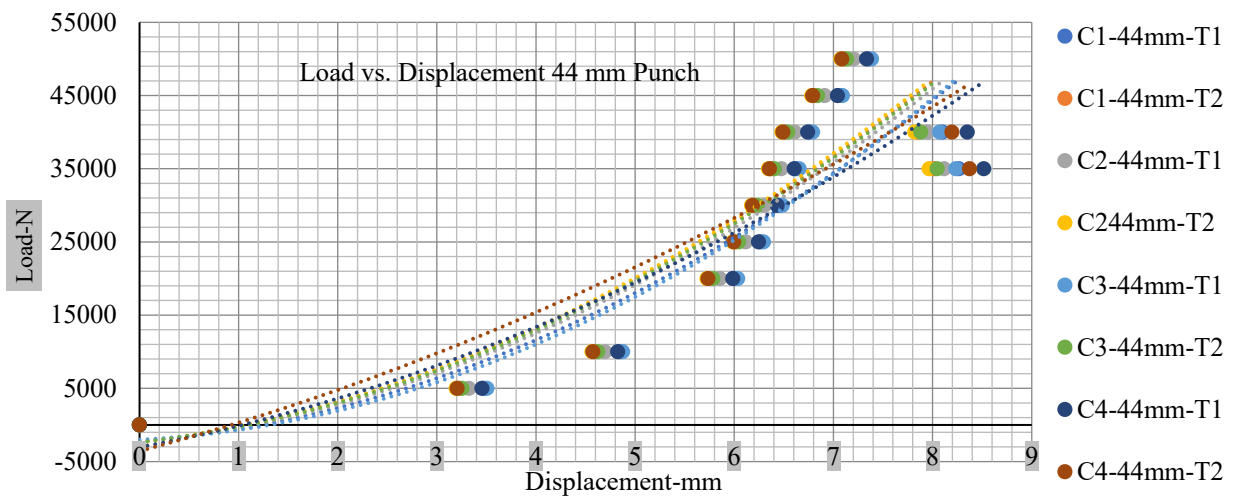


Figure 17. Load vs. displacement 44 mm low to peak loads.

The short circuit onset is observed from the voltage decrease in the cell, which has greater than 10% soc; the punch with a 44 mm diameter starts from 2.14 and ends at  $-0.42$ , which clearly shows a high short circuit.

Thus, short circuit, punch displacements with greater than 10% SOC at onset are 2.952 mm, 3.712 mm, 5.529 mm, and 6.503 mm, and, similarly for less than 10% soc, 3.88 mm, 5.42 mm, 5.94 mm, and 6.92 mm for a small, medium, large, and a flat cylindrical punch. In less than 10% soc, the flat cylindrical punch has a diameter of 28 mm, in which the short circuit force initiates no drop in.

However, for a hemispherical punch with 44 mm diameter, the onset of the short circuit coincides with a load drop, and the resistance is measured, compression is reported, and a drop in resistance is shown from 900 to 0.

No calculation of the voltage drop is found for the cells with less than 10% soc, which causes a short circuit. However, the same patterns follow the cell's homogenized reaction and become softer in the wet state. Comparing the onset contrast to a cell with less than 10% soc and loss is earlier when a cell with greater than 10% soc is tested.

### 3.3. Loading Positions with Different State of Charge

This experiment has been conducted to explore the impact of changing load positions on cells. For this purpose, two cells are manufactured with a soc less than 10%, and two cells are more than 10% soc to check the effects of a short circuit; on the other hand, during experiments, all of the cells are kept in two-gallon zip-lock bags [70]. All of these cells are subjected to the punch indentation loads, and variations in the cells' response have been examined. Tests are performed on lithium-ion cells with pouch cover. However, previous researches have demonstrated that not applying thin foil fused aluminum/polyester of pouch cover, under these loading conditions and not adding power or strength to the cell and calculated data of the cell explicitly represent the electrode/separator stack properties [69].

The hemispherical punch loading has been extended to a pointed matrix, starting from the cell center and moving towards the corners, and then the findings are compared. The quasi-static is tested at a 1 mm/min. rate loading time, checking. Apart from this, the results are consistent with the experiments. For this purpose, indentation testing with four different types of diameters punches has been carried out. Several hemispherical and flat cylindrical punch experiments have been conducted equally on greater than 10% and less than 10% soc cells at different locations. Several punches have been made on four cells. The measurement is placed in the middle of the cell between 30 mm–55 mm from the long edge of the cell. These are punches with a different punch diameter, and the distance is different on all cells, between 50 mm–60 mm from the long edge in the second test, and 10–15 mm from the long edge in the third. A fourth is conducted on the corner of the cell. All of the tests are conducted in this measurement, but the sizes of punch are different, and variability has been established from the multiple experiments.

Figure 5a–d presents the coordinates of the punch. Some tests are in the middle, some are on the corner, and some are between the hub and center to check the maximal measurement of force with greater than 10% soc (with 44 mm punch diameter) regarding a crosshead of 7.21 mm, 50 kN. Some of the tests are performed with a hemispherical punch with a 44 mm diameter on the corner of the cell, and some are performed in the middle of the cell. The center of cell tests has a great deal of lower maximum power, which is predicted from the cell's edge containing less substance than the middle of the cell.

Figures 18–21 show the peak load and deformation depth at short circuit versus all four cells and different punch diameters. It is fascinating to observe that the short circuit's peak load should almost linearly grow high with an extended punch diameter. In this experiment, a punch diameter of 44 mm creates a large voltage drop with greater than 10% soc, as shown in the graph presented in Figure 9. Nevertheless, the load increases with the increase in the punch's diameter, as shown in Figures 18–21, and high displacements are shown in Figures 14–17. The peak loads and displacements differential between

less than 10% soc and greater than 10% soc with hemispherical punches are applied. The hemispherical punch with 28 mm diameter shows maximum force measurements of 40–45 kN with lesser and greater than 10% soc. The 44 mm diameter punch shows 50 kN with lesser and greater than 10% soc. Tables A1–A4 (Appendix A) show force-displacement readings.

This allows researchers to use a single cell for running several tests without the fear that the punch’s position would impact the results and only the punch diameter can change it. This study discusses which variables in similar experiments can be carefully regulated and left accessible for operator convenience. Tables A1–A4 (Appendix A) the test readings on each cell.

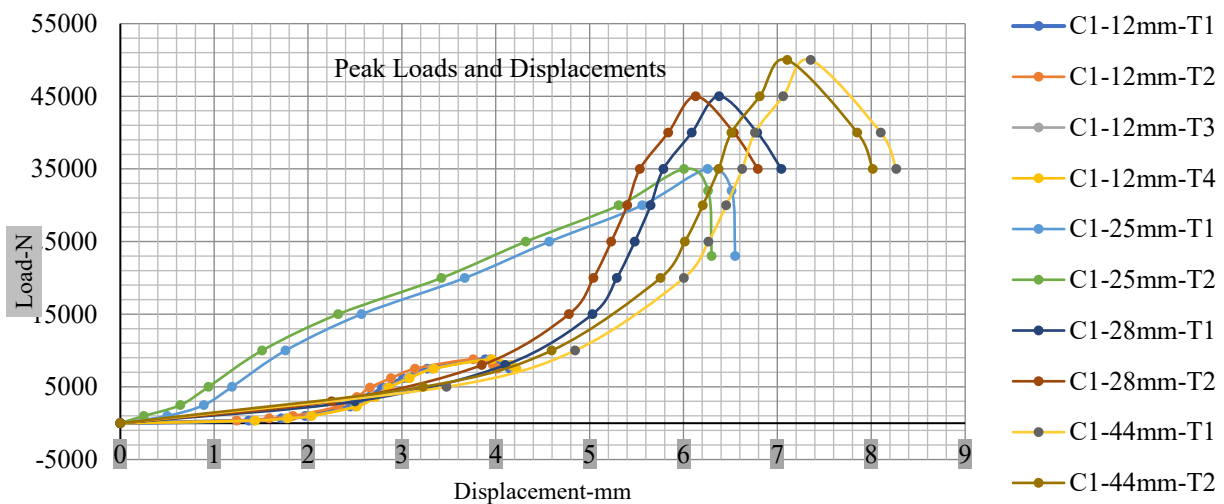


Figure 18. Cell 1 peak loads and displacements.

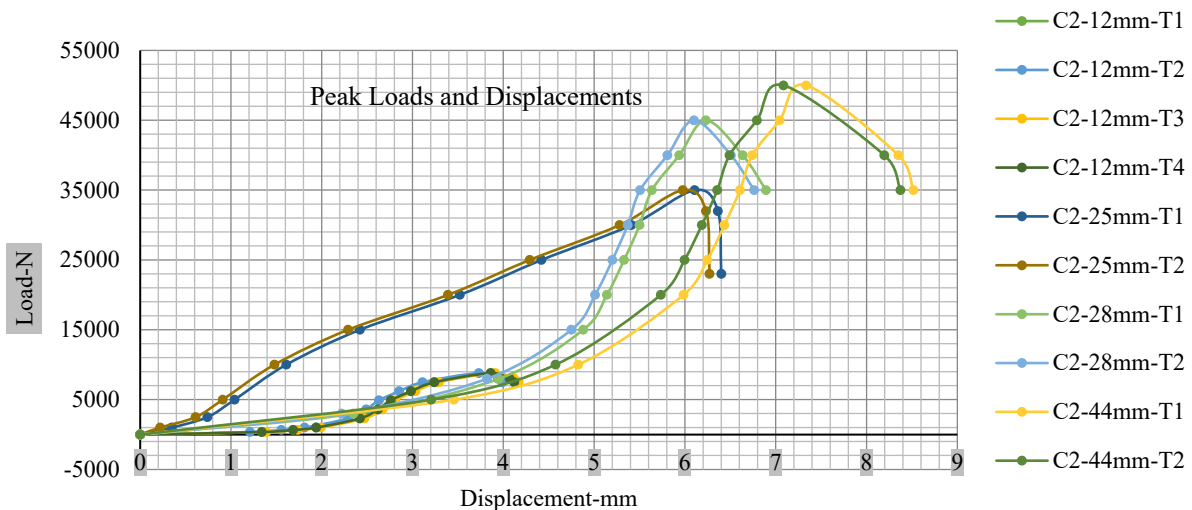


Figure 19. Cell 2 peak loads and displacements.

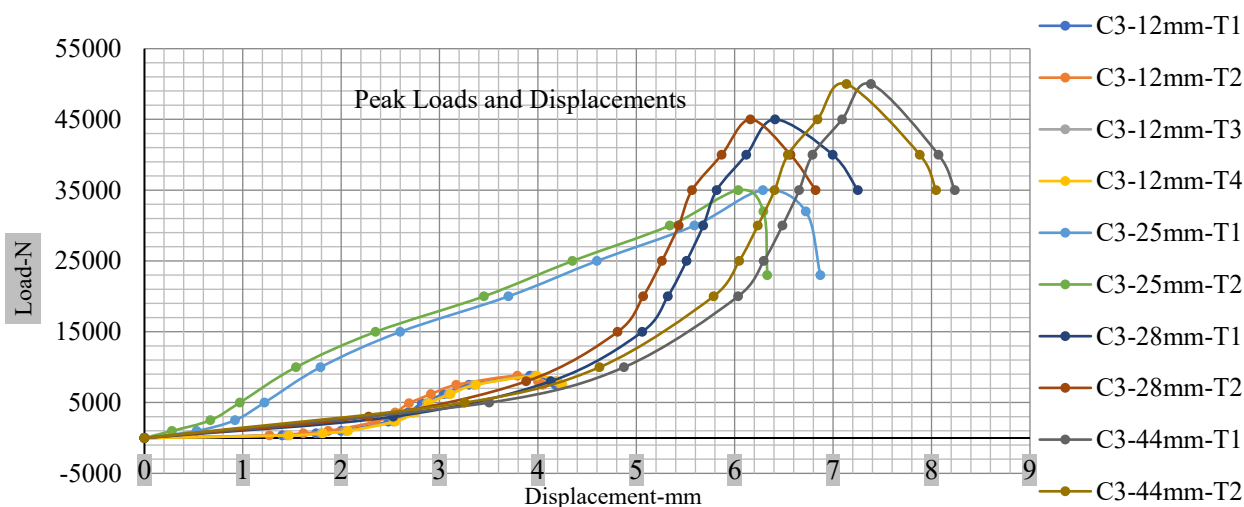


Figure 20. Cell 3 peak loads and displacements.

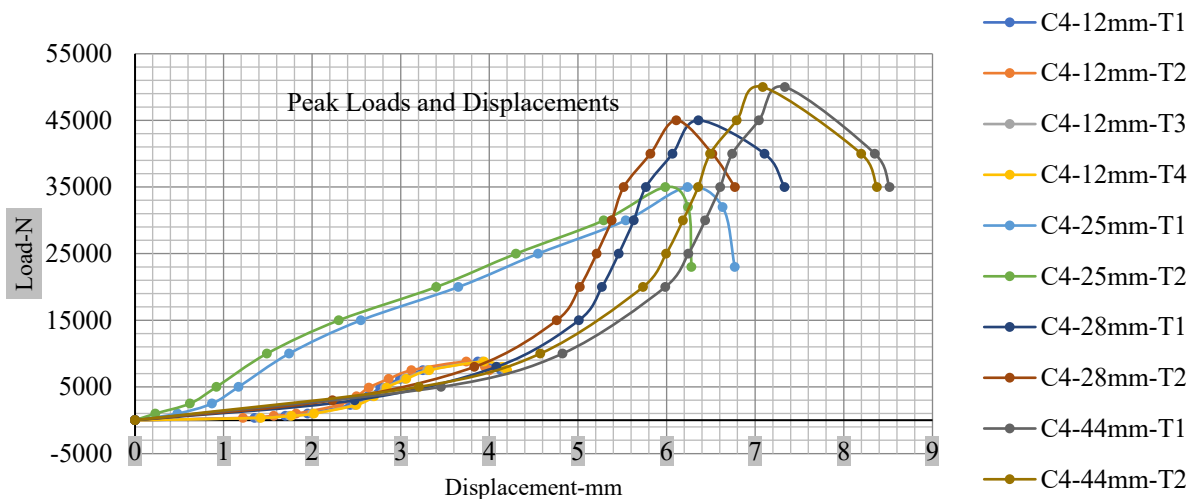


Figure 21. Cell 4 peak loads and displacements.

The involvement of electrolytes has been shown to have a direct effect on the cell’s reaction. When a load is applied to the cell, with an increasing load, electrolyte structure also changes because of this internal short circuit that changes the cell’s condition. In all indentation punch filling cases, the pouch cells with an electrolyte with less than 10% soc have soc in all types of diameters. Therefore, researchers should pay particular attention while testing a cell’s mechanical reaction. During the indentation process, the local deformation of each separator before the commencement of the short circuit is another indirect evidence of the fracture sequence. For this reason, separators between each of the four electrode pairs from the pouch cell subjected to 45 kN indentation were investigated using SEM, as shown in Figure 22. The depletion of the thickness separator in the area just below the indenter (center) was compared to the area further out from the indenter (the margin area) as shown in Figure 23.



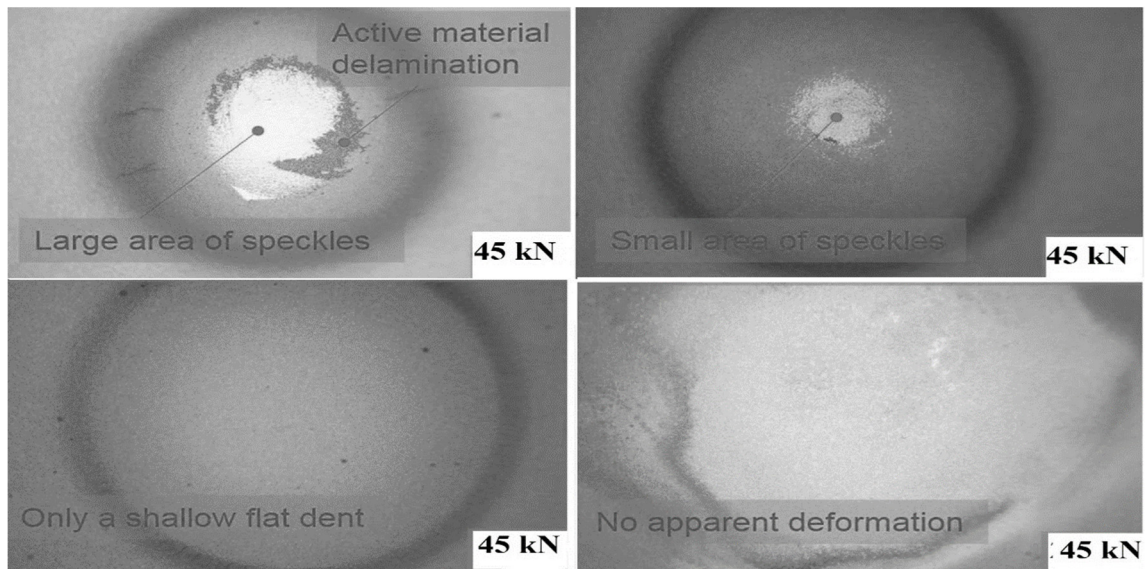


Figure 22. Post-mortem examination of the loaded area.

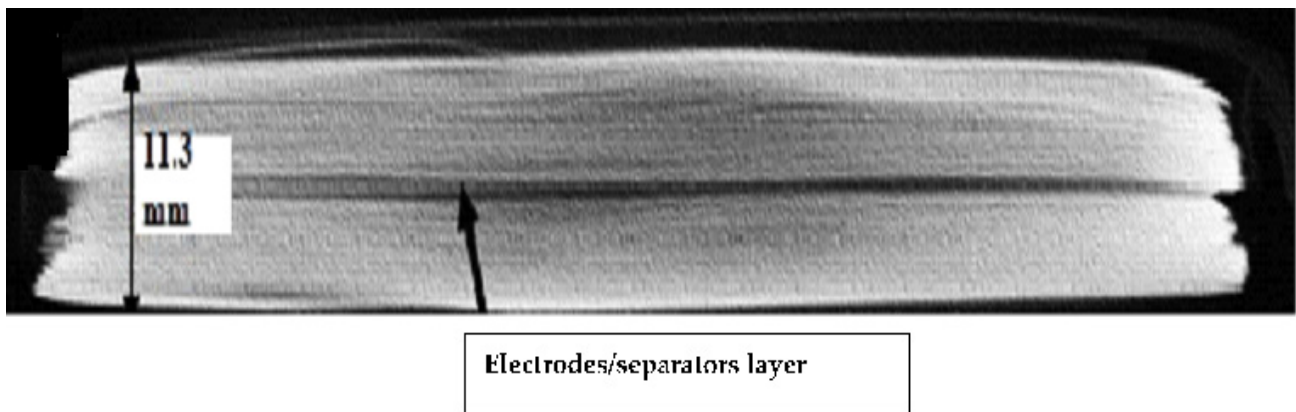


Figure 23. Interior of battery cells after opening the cover of a pouch cell, the first layer seen is a separator layer.

#### 4. Conclusions

This research investigates findings from three related major study areas: material description of Lithium cells used in experiments, the inner short circuit in lithium-ion battery cell starting point when the load is being applied, and the maximum reaction of cell load-carrying capacity. Performance characteristics for the lithium-ion pouch battery are calculated in different conditions.

Four types of hemispherical punch indentation tests have been used to obtain better results to build a computational model pouch-type lithium-ion battery cells. The force-displacement curves and the internal short circuits for these experiments operating at a rate of 1 mm/min. have been very compatible with the results found in this analysis, and they have validated these results.

The overall conclusion is that the cell's electrical short circuit is not instigated instantaneously when loading begins. These data can feed into numerical models and help to determine nominal battery pack loading conditions for improved staff protection under an optimal cell with optimization conditions. These results will further define the initial requirements in a previously developed successful modeling tool and enable the model to more accurately predict individual cell behavior in crash scenarios.

**Author Contributions:** For this research, Conceptualization M.M.A. & L.Y.; S.A.R.S.; Methodology, M.M.A.; Software, M.M.A.; data curation and writing—original draft preparation, M.M.A.; writing—review and editing, visualization, Y.S.; supervision, A.S.; funding acquisition, L.Y. All authors have read and agreed to the published version of the manuscript.

**Funding:** This work was supported by the Priority Academic Program Development of Jiangsu University Higher Institutions [PAPD]; State Key Laboratory of Engines, Tianjin University (GKF2015-004); the National Key Technology R&D Program [2016YFD0702003].

**Institutional Review Board Statement:** Not applicable.

**Informed Consent Statement:** Not applicable.

**Data Availability Statement:** Data will be available on suitable demand.

**Acknowledgments:** This research was sponsored by the National Key Technology R&D Program (2016YFD0701002); Graduate Student Innovation Fund Project of Jiangsu Province (KYCX18\_2247); National Spark Program (2015GA690172); Jiangsu Province Key Technology R&D Program (BE2016341); State Key Laboratory of Engines, Tianjin University (GKF2015-004); Priority Academic Program Development of Jiangsu Higher Education Institutions (PAPD).

**Conflicts of Interest:** The authors declare no conflict of interest.

## Appendix A

**Table A1.** Peak force and associated displacement for punch test cell 1 (C1).

12 mm Load (N)	25 mm Load (N)	28 mm Load (N)	44 mm Load (N)	C1-12 mm-T1	C1-12 mm-T2	C1-12 mm-T3	C1-12 mm-T4	C1-25 mm-T1	C1-25 mm-T2	C1-28 mm-T1	C1-28 mm-T2	C1-44 mm-T1	C1-44 mm-T2
0	0	0	0	0.0	0	0	0	0	0	0	0	0	0
350	1000	3000	5000	1.37	1.24	1.42	1.44	0.5	0.25	2.5	2.25	3.475	3.225
650	2500	8000	10,000	1.716	1.586	1.766	1.786	0.89	0.64	4.1	3.85	4.845	4.595
1000	5000	15,000	20,000	1.97	1.84	2.02	2.04	1.19	0.94	5.03	4.78	6.005	5.755
2300	10,000	20,000	25,000	2.45	2.32	2.5	2.52	1.76	1.51	5.29	5.04	6.265	6.015
3600	15,000	25,000	30,000	2.65	2.52	2.7	2.72	2.57	2.32	5.48	5.23	6.455	6.205
4900	20,000	30,000	35,000	2.79	2.66	2.84	2.86	3.67	3.42	5.65	5.4	6.625	6.375
6200	25,000	35,000	40,000	3.013	2.883	3.063	3.083	4.57	4.32	5.786	5.536	6.761	6.511
7500	30,000	40,000	45,000	3.27	3.14	3.32	3.34	5.56	5.31	6.087	5.837	7.062	6.812
8800	35,000	45,000	50,000	3.89	3.76	3.94	3.96	6.256	6.006	6.38	6.13	7.355	7.105
8000	32,000	40,000	40,000	4.1	3.97	4.15	4.17	6.512	6.262	6.786	6.536	8.101	7.851
7500	23,000	35,000	35,000	4.15	4.02	4.2	4.22	6.55	6.3	7.042	6.792	8.267	8.017

**Table A2.** Peak force and associated displacement for punch test cell 2 (C2).

12 mm Load (N)	25 mm Load (N)	28 mm Load (N)	44 mm Load (N)	C2-12 mm-T1	C2-12 mm-T2	C2-12 mm-T3	C2-12 mm-T4	C2-25 mm-T1	C2-25 mm-T2	C2-28 mm-T1	C2-28 mm-T2	C2-44 mm-T1	C2-44 mm-T2
0	0	0	0	0.0	0	0	0	0	0	0	0	0	0
350	1000	3000	5000	1.34	1.21	1.39	1.34	0.35	0.22	2.35	2.22	3.455	3.205
650	2500	8000	10,000	1.686	1.556	1.736	1.686	0.74	0.61	3.95	3.82	4.825	4.575
1000	5000	15,000	20,000	1.94	1.81	1.99	1.94	1.04	0.91	4.88	4.75	5.985	5.735
2300	10,000	20,000	25,000	2.42	2.29	2.47	2.42	1.61	1.48	5.14	5.01	6.245	5.995
3600	15,000	25,000	30,000	2.62	2.49	2.67	2.62	2.42	2.29	5.33	5.2	6.435	6.185
4900	20,000	30,000	35,000	2.76	2.63	2.81	2.76	3.52	3.39	5.5	5.37	6.605	6.355
6200	25,000	35,000	40,000	2.983	2.853	3.033	2.983	4.42	4.29	5.636	5.506	6.741	6.491
7500	30,000	40,000	45,000	3.24	3.11	3.29	3.24	5.41	5.28	5.937	5.807	7.042	6.792
8800	35,000	45,000	50,000	3.86	3.73	3.91	3.86	6.106	5.976	6.23	6.1	7.335	7.085
8000	32,000	40,000	40,000	4.07	3.94	4.12	4.07	6.362	6.232	6.636	6.506	8.351	8.196
7500	23,000	35,000	35,000	4.12	3.99	4.17	4.12	6.4	6.27	6.892	6.762	8.517	8.373

**Table A3.** Peak force and associated displacement for punch test cell 3 (C3).

12 mm Load (N)	25 mm Load (N)	28 mm Load (N)	44 mm Load (N)	C3-12 mm-T1	C3-12 mm-T2	C3-12 mm-T3	C3-12 mm-T4	C3-25 mm-T1	C3-25 mm-T2	C3-28 mm-T1	C3-28 mm-T2	C3-44 mm-T1	C3-44 mm-T2
0	0	0	0	0.0	0	0	0	0	0	0	0	0	0
350	1000	3000	5000	1.4	1.27	1.45	1.47	0.53	0.28	2.53	2.28	3.505	3.255
650	2500	8000	10,000	1.746	1.616	1.796	1.816	0.92	0.67	4.13	3.88	4.875	4.625
1000	5000	15,000	20,000	2	1.87	2.05	2.07	1.22	0.97	5.06	4.81	6.035	5.785
2300	10,000	20,000	25,000	2.48	2.35	2.53	2.55	1.79	1.54	5.32	5.07	6.295	6.045
3600	15,000	25,000	30,000	2.68	2.55	2.73	2.75	2.6	2.35	5.51	5.26	6.485	6.235
4900	20,000	30,000	35,000	2.82	2.69	2.87	2.89	3.7	3.45	5.68	5.43	6.655	6.405
6200	25,000	35,000	40,000	3.043	2.913	3.093	3.113	4.6	4.35	5.816	5.566	6.791	6.541
7500	30,000	40,000	45,000	3.3	3.17	3.35	3.37	5.59	5.34	6.117	5.867	7.092	6.842
8800	35,000	45,000	50,000	3.92	3.79	3.97	3.99	6.286	6.036	6.41	6.16	7.385	7.135
8000	32,000	40,000	40,000	4.13	4	4.18	4.2	6.722	6.292	6.996	6.566	8.071	7.881
7500	23,000	35,000	35,000	4.18	4.05	4.23	4.25	6.87	6.33	7.252	6.822	8.237	8.047

**Table A4.** Peak force and associated displacement for punch test cell 4 (C4).

12 mm Load (N)	25 mm Load (N)	28 mm Load (N)	44 mm Load (N)	C4-12 mm-T1	C4-12 mm-T2	C4-12 mm-T3	C4-12 mm-T4	C4-25 mm-T1	C4-25 mm-T2	C4-28 mm-T1	C4-28 mm-T2	C4-44 mm-T1	C4-44 mm-T2
0	0	0	0	0.0	0	0	0	0	0	0	0	0	0
350	1000	3000	5000	1.35	1.22	1.4	1.42	0.48	0.23	2.48	2.23	3.455	3.205
650	2500	8000	10,000	1.696	1.566	1.746	1.766	0.87	0.62	4.08	3.83	4.825	4.575
1000	5000	15,000	20,000	1.95	1.82	2	2.02	1.17	0.92	5.01	4.76	5.985	5.735
2300	10,000	20,000	25,000	2.43	2.3	2.48	2.5	1.74	1.49	5.27	5.02	6.245	5.995
3600	15,000	25,000	30,000	2.63	2.5	2.68	2.7	2.55	2.3	5.46	5.21	6.435	6.185
4900	20,000	30,000	35,000	2.77	2.64	2.82	2.84	3.65	3.4	5.63	5.38	6.605	6.355
6200	25,000	35,000	40,000	2.993	2.863	3.043	3.063	4.55	4.3	5.766	5.516	6.741	6.491
7500	30,000	40,000	45,000	3.25	3.12	3.3	3.32	5.54	5.29	6.067	5.817	7.042	6.792
8800	35,000	45,000	50,000	3.87	3.74	3.92	3.94	6.236	5.986	6.36	6.11	7.335	7.085
8000	32,000	40,000	40,000	4.08	3.95	4.13	4.15	6.632	6.242	7.106	6.516	8.351	8.196
7500	23,000	35,000	35,000	4.13	4	4.18	4.2	6.77	6.28	7.332	6.772	8.517	8.373

## References

- Wang, Q.; Mao, B.; Stoliarov, S.I.; Sun, J. A review of lithium ion battery failure mechanisms and fire prevention strategies. *Prog. Energy Combust. Sci.* **2019**, *73*, 95–131. [\[CrossRef\]](#)
- Feng, X.; Fang, M.; He, X.; Ouyang, M.; Lu, L.; Wang, H.; Zhang, M. Thermal runaway features of large format prismatic lithium ion battery using extended volume accelerating rate calorimetry. *J. Power Sources* **2014**, *255*, 294–301. [\[CrossRef\]](#)
- Ali, M.Y.; Lai, W.J.; Pan, J. Computational models for simulation of a lithium-ion battery module specimen under punch indentation. *J. Power Sources* **2015**, *273*, 448–459. [\[CrossRef\]](#)
- Ren, F.; Cox, T.; Wang, H. Thermal runaway risk evaluation of Li-ion cells using a pinch-torsion test. *J. Power Sources* **2014**, *249*, 156–162. [\[CrossRef\]](#)
- Zhao, C.; Sun, J.; Wang, Q. Thermal runaway hazards investigation on 18650 lithium-ion battery using extended volume accelerating rate calorimeter. *J. Energy Storage* **2020**, *28*, 101232. [\[CrossRef\]](#)
- Zhang, X.; Wierzbicki, T. Characterization of plasticity and fracture of shell casing of lithium-ion cylindrical battery. *J. Power Sources* **2015**, *280*, 47–56. [\[CrossRef\]](#)
- Zhu, J.; Wierzbicki, T.; Li, W. A review of safety-focused mechanical modeling of commercial lithium-ion batteries. *J. Power Sources* **2018**, *378*, 153–168. [\[CrossRef\]](#)
- Dubaniewicz, T.H.; Ducarme, J.P. Are Lithium Ion Cells Intrinsically Safe? *IEEE Trans. Ind. Appl.* **2013**, *49*, 2451–2460. [\[CrossRef\]](#)
- Luo, H.; Xia, Y.; Zhou, Q. Mechanical damage in a lithium-ion pouch cell under indentation loads. *J. Power Sources* **2017**, *357*, 61–70. [\[CrossRef\]](#)
- Chen, Y.; Santhanagopalan, S.; Babu, V.; Ding, Y. Dynamic mechanical behavior of lithium-ion pouch cells subjected to high-velocity impact. *Compos. Struct.* **2019**, *218*, 50–59. [\[CrossRef\]](#)
- Sarkar, A.; Shrotriya, P.; Chandra, A. Modeling of separator failure in lithium-ion pouch cells under compression. *J. Power Sources* **2019**, *435*, 226756. [\[CrossRef\]](#)
- Bélander, D. Editorial Overview: Materials and characterization tools for electrochemical energy storage in batteries and electrochemical capacitors. *Mater. Sci.* **2018**, 9–10. [\[CrossRef\]](#)
- Zagal, J.H.; Zagal, J.H. Editorial Overview: Tuning chemistry for better electrocatalysis. *Curr. Opin. Electrochem.* **2018**, *9*, A3–A4. [\[CrossRef\]](#)

14. Ali, L.; Nawaz, A.; Iqbal, S.; Basheer, M.A.; Hameed, J.; Albasher, G.; Adnan, S.; Shah, R.; Bai, Y. Dynamics of Transit Oriented Development, Role of Greenhouse Gases and Urban Environment: A Study for Management and Policy. *Sustainability* **2021**, *13*, 2536. [[CrossRef](#)]
15. An, H.; Razzaq, A.; Nawaz, A.; Noman, S.M.; Khan, S.A.R. Nexus between green logistic operations and triple bottom line: Evidence from infrastructure-led Chinese outward foreign direct investment in Belt and Road host countries. *Environ. Sci. Pollut. Res.* **2021**. [[CrossRef](#)]
16. Goodenough, J.B.; Kim, Y. Challenges for rechargeable Li batteries. *Chem. Mater.* **2010**, *22*, 587–603. [[CrossRef](#)]
17. Trevey, J.E. Advances and Development of All-Solid-State Lithium-Ion Batteries. *Appl. Sci.* **2011**, *10*, 38–45.
18. Sarkar, A. Thermo-Mechanical Modeling and Parametric Analysis of Lithium-Ion Battery. Master's Thesis, Iowa State University, Ames, IA, USA, 2017.
19. Nawaz, A.; Su, X.; Nasir, I.M. BIM Adoption and Its Impact on Planning and Scheduling Influencing Mega Plan Projects-(CPEC-) Quantitative Approach. *Complexity* **2021**. [[CrossRef](#)]
20. Nawaz, A.; Waqar, A.; Shah, S.A.R.; Sajid, M.; Khalid, M.I. An innovative framework for risk management in construction projects in developing countries: Evidence from Pakistan. *Risks* **2019**, *7*, 24. [[CrossRef](#)]
21. Yang, Y.; Chen, H.; Zou, X.; Shi, X.-L.; Liu, W.-D.; Feng, L.; Suo, G.; Hou, X.; Ye, X.; Zhang, L. Flexible carbon-fiber/semimetal Bi nanosheet arrays as separable and recyclable plasmonic photocatalysts and photoelectrocatalysts. *ACS Appl. Mater. Interfaces* **2020**, *12*, 24845–24854. [[CrossRef](#)]
22. Lu, H.; Zhu, Y.; Yuan, Y.; He, L.; Zheng, B.; Zheng, X.; Liu, C.; Du, H. LiFSI as a functional additive of the fluorinated electrolyte for rechargeable Li-S batteries. *J. Mater. Sci. Mater. Electron.* **2021**, *32*, 5898–5906. [[CrossRef](#)]
23. Zhang, H.; Sun, M.; Song, L.; Guo, J.; Zhang, L. Fate of NaClO and membrane foulants during in-situ cleaning of membrane bioreactors: Combined effect on thermodynamic properties of sludge. *Biochem. Eng. J.* **2019**, *147*, 146–152. [[CrossRef](#)]
24. Heimes, H.H.; Kampker, A.; Lienemann, C.; Locke, M.; Offermanns, C.; Michaelis, S.; Rahimzei, E. *Manufacturing of Lithium-Ion Battery Cell Components*; PEM der RWTH Aachen University & VDMA: Aachen, Germany, 2019; ISBN 978-3-947920-07-5.
25. Zhang, L.; Wang, H.; Zhang, X.; Tang, Y. A Review of Emerging Dual-Ion Batteries: Fundamentals and Recent Advances. *Adv. Funct. Mater.* **2021**, 2010958. [[CrossRef](#)]
26. Tan, L.; Sun, Y.; Wei, C.; Tao, Y.; Tian, Y.; An, Y.; Zhang, Y.; Xiong, S.; Feng, J. Design of Robust, Lithiophilic, and Flexible Inorganic-Polymer Protective Layer by Separator Engineering Enables Dendrite-Free Lithium Metal Batteries with LiNi<sub>0.8</sub>Mn<sub>0.1</sub>Co<sub>0.1</sub>O<sub>2</sub> Cathode. *Small* **2021**, *17*, 2007717. [[CrossRef](#)] [[PubMed](#)]
27. Tong, X.; Ou, X.; Wu, N.; Wang, H.; Li, J.; Tang, Y. High Oxidation Potential ≈ 6.0 V of Concentrated Electrolyte toward High-Performance Dual-Ion Battery. *Adv. Energy Mater.* **2021**. [[CrossRef](#)]
28. Pan, Q.; Zheng, Y.; Tong, Z.; Shi, L.; Tang, Y. Novel Lamellar Tetrapotassium Pyromellitic Organic for Robust High-Capacity Potassium Storage. *Angew. Chemie Int. Ed.* **2021**. [[CrossRef](#)]
29. Zhang, Y.; Liu, G.; Zhang, C.; Chi, Q.; Zhang, T.; Feng, Y.; Zhu, K.; Zhang, Y.; Chen, Q.; Cao, D. Low-cost Mg<sub>0.5</sub>FexMn<sub>2-x</sub>O<sub>4</sub> cathode materials for high-performance aqueous rechargeable magnesium-ion batteries. *Chem. Eng. J.* **2020**, *392*, 123652. [[CrossRef](#)]
30. Liu, Y.; Wei, Z.; Zhong, B.; Wang, H.; Xia, L.; Zhang, T.; Duan, X.; Jia, D.; Zhou, Y.; Huang, X. O-, N-Coordinated single Mn atoms accelerating polysulfides transformation in lithium-sulfur batteries. *Energy Storage Mater.* **2021**, *35*, 12–18. [[CrossRef](#)]
31. Minakshi, M. Design, Development and Thermal Analysis of and Stationary Applications. *Energies* **2020**, *13*, 1477.
32. Yu, D.; Mao, Y.; Gu, B.; Nojavan, S.; Jermisittiparsert, K.; Nasser, M. A new LQG optimal control strategy applied on a hybrid wind turbine/solid oxide fuel cell/in the presence of the interval uncertainties. *Sustain. Energy Grids Netw.* **2020**, *21*, 100296. [[CrossRef](#)]
33. Gong, C.; Hu, Y.; Gao, J.; Wang, Y.; Yan, L. An improved delay-suppressed sliding-mode observer for sensorless vector-controlled PMSM. *IEEE Trans. Ind. Electron.* **2019**, *67*, 5913–5923. [[CrossRef](#)]
34. Kang, Y.; Zhang, Y.-H.; Shi, Q.; Shi, H.; Xue, D.; Shi, F.-N. Highly efficient Co<sub>3</sub>O<sub>4</sub>/CeO<sub>2</sub> heterostructure as anode for lithium-ion batteries. *J. Colloid Interface Sci.* **2021**, *585*, 705–715. [[CrossRef](#)]
35. Nawaz, A.; Su, X.; Din, Q.M.U.; Khalid, M.I.; Bilal, M.; Shah, S.A.R. Identification of the h&s (Health and safety factors) involved in infrastructure projects in developing countries—a sequential mixed method approach of OLMT-project. *Int. J. Environ. Res. Public Health* **2020**, *17*, 635. [[CrossRef](#)]
36. Commarieu, B.; Paoletta, A.; Daigle, J.; Zaghbi, K. Toward high lithium conduction in solid polymer and polymer–ceramic batteries. *Curr. Opin. Electrochem.* **2018**, *9*, 56–63. [[CrossRef](#)]
37. Dai, Z.; Xie, J.; Fan, X.; Ding, X.; Liu, W.; Zhou, S.; Ren, X. Enhanced energy storage properties and stability of Sr (Sc<sub>0.5</sub>Nb<sub>0.5</sub>) O<sub>3</sub> modified 0.65 BaTiO<sub>3</sub>-0.35 Bi<sub>0.5</sub>Na<sub>0.5</sub>TiO<sub>3</sub> ceramics. *Chem. Eng. J.* **2020**, *397*, 125520. [[CrossRef](#)]
38. Ni, T.; Chang, H.; Song, T.; Xu, Q.; Huang, Z.; Liang, H.; Yan, A.; Wen, X. Non-intrusive online distributed pulse shrinking-based interconnect testing in 2.5 D IC. *IEEE Trans. Circuits Syst. II Express Briefs* **2019**, *67*, 2657–2661. [[CrossRef](#)]
39. Chen, C.; Wang, X.; Wang, Y.; Yang, D.; Yao, F.; Zhang, W.; Wang, B.; Sewvandi, G.A.; Yang, D.; Hu, D. Additive Manufacturing of Piezoelectric Materials. *Adv. Funct. Mater.* **2020**, *30*, 2005141. [[CrossRef](#)]
40. *Global EV Outlook 2017: Two Million and Counting* | en | OECD; OECD: Paris, France, 2017.
41. Hao, W.; Shah, S.M.A.; Nawaz, A.; Asad, A.; Iqbal, S.; Zahoor, H.; Maqsoom, A. The Impact of Energy Cooperation and the Role of the One Belt and Road Initiative in Revolutionizing the Geopolitics of Energy among Regional Economic Powers: An Analysis of Infrastructure Development and Project Management. *Complexity* **2020**, *2020*, 8820021. [[CrossRef](#)]

42. Huo, C.; Hameed, J.; Nawaz, A.; Shah, S.A.R.; Alqahtani, W.; Maqsoom, A.; Anwar, M.K. Scientific Risk Performance Analysis and Development of Disaster Management Framework influencing COVID-19: A Case Study of Developing Asian Countries. *J. King Saud Univ.* **2021**, *33*, 101348. [CrossRef]
43. Ruiz, V.; Pfrang, A.; Kriston, A.; Omar, N.; Van den Bossche, P.; Boon-Brett, L. A review of international abuse testing standards and regulations for lithium ion batteries in electric and hybrid electric vehicles. *Renew. Sustain. Energy Rev.* **2018**, *81*, 1427–1452. [CrossRef]
44. Ouyang, L.; Cao, Z.; Wang, H.; Hu, R.; Zhu, M. Application of dielectric barrier discharge plasma-assisted milling in energy storage materials e A review. *J. Alloys Compd.* **2017**, *691*, 422–435. [CrossRef]
45. Chen, Y.X. Simulation-Based Design of Integrated Public Transit and Shared Autonomous Mobility-on-Demand Systems. 2016. Available online: <https://dspace.mit.edu/bitstream/handle/1721.1/117945/1051237118-MIT.pdf?sequence=1&isAllowed=y> (accessed on 11 May 2018).
46. Greve, L.; Fehrenbach, C. Mechanical testing and macro-mechanical finite element simulation of the deformation, fracture, and short circuit initiation of cylindrical Lithium ion battery cells. *J. Power Sources* **2012**, *214*, 377–385. [CrossRef]
47. Liu, B.; Yin, S.; Xu, J. Integrated computation model of lithium-ion battery subject to nail penetration. *Appl. Energy* **2016**, *183*, 278–289. [CrossRef]
48. Goodman, J.K.S.; Miller, J.T.; Kreuzer, S.; Forman, J.; Wi, S.; Choi, J.; Oh, B.; White, K. Lithium-ion cell response to mechanical abuse: Three-point bend. *J. Energy Storage* **2020**, *28*, 101244. [CrossRef]
49. Ni, T.; Yao, Y.; Chang, H.; Lu, L.; Liang, H.; Yan, A.; Huang, Z.; Wen, X. LCHR-TSV: Novel low cost and highly repairable honeycomb-based TSV redundancy architecture for clustered faults. *IEEE Trans. Comput. Des. Integr. Circuits Syst.* **2019**, *39*, 2938–2951. [CrossRef]
50. Liu, X.; Rao, R.; Shi, J.; He, J.; Zhao, Y.; Liu, J.; Du, H. Effect of oxygen vacancy and A-site-deficiency on the dielectric performance of BNT-BT-BST relaxors. *J. Alloys Compd.* **2021**, *875*, 159999. [CrossRef]
51. Zhang, H.; Guan, W.; Zhang, L.; Guan, X.; Wang, S. Degradation of an Organic Dye by Bisulfite Catalytically Activated with Iron Manganese Oxides: The Role of Superoxide Radicals. *ACS Omega* **2020**, *5*, 18007–18012. [CrossRef]
52. Yan, X.; Huang, X.; Chen, Y.; Liu, Y.; Xia, L.; Zhang, T.; Lin, H.; Jia, D.; Zhong, B.; Wen, G. A theoretical strategy of pure carbon materials for lightweight and excellent absorption performance. *Carbon N. Y.* **2021**, *174*, 662–672. [CrossRef]
53. Sahraei, E.; Campbell, J.; Wierzbicki, T. Modeling and short circuit detection of 18650 Li-ion cells under mechanical abuse conditions. *J. Power Sources* **2012**, *220*, 360–372. [CrossRef]
54. Wang, H.; Kumar, A.; Simunovic, S.; Allu, S.; Kalnaus, S.; Turner, J.A.; Helmers, J.C.; Rules, E.T.; Winchester, C.S.; Gorney, P. Progressive mechanical indentation of large-format Li-ion cells. *J. Power Sources* **2017**, *341*, 156–164. [CrossRef]
55. Kurzweil, P.; Brandt, K. Electrochemical Power Sources: Fundamentals, Systems, and Applications. In *Chapter-7: Lithium-Secondary Cell: Sources of Risks and Their Effects*; Elsevier: Amsterdam, The Netherlands, 2019.
56. Sun, M.; Yan, L.; Zhang, L.; Song, L.; Guo, J.; Zhang, H. New insights into the rapid formation of initial membrane fouling after in-situ cleaning in a membrane bioreactor. *Process Biochem.* **2019**, *78*, 108–113. [CrossRef]
57. Lai, W.; Yusuf, M.; Pan, J. Mechanical behavior of representative volume elements of lithium-ion battery cells under compressive loading conditions. *J. Power Sources* **2014**, *245*, 609–623. [CrossRef]
58. Wierzbicki, T.; Sahraei, E. Homogenized mechanical properties for the jellyroll of cylindrical. *J. Power Sources* **2013**, *241*, 467–476. [CrossRef]
59. Spielbauer, M.; Berg, P.; Ringat, M.; Bohlen, O.; Jossen, A. Experimental study of the impedance behavior of 18650 lithium-ion battery cells under deforming mechanical abuse. *J. Energy Storage* **2019**, *26*, 101039. [CrossRef]
60. Dixon, B.; Mason, A.; Sahraei, E. Effects of electrolyte, loading rate and location of indentation on mechanical integrity of li-ion pouch cells. *J. Power Sources* **2018**, *396*, 412–420. [CrossRef]
61. Berg, P.; Soellner, J.; Jossen, A. Structural dynamics of lithium-ion cells—Part I: Method, test bench validation and investigation of lithium-ion pouch cells. *J. Energy Storage* **2019**, *26*, 100916. [CrossRef]
62. Zhu, X.; Wang, H.; Wang, X.; Gao, Y.; Allu, S.; Cakmak, E.; Wang, Z. Internal short circuit and failure mechanisms of lithium-ion pouch cells under mechanical indentation abuse conditions: An experimental study. *J. Power Sources* **2020**, *455*, 227939. [CrossRef]
63. Chung, S.H.; Tancogne-Dejean, T.; Zhu, J.; Luo, H.; Wierzbicki, T. Failure in lithium-ion batteries under transverse indentation loading. *J. Power Sources* **2018**, *389*, 148–159. [CrossRef]
64. Maqsoom, A.; Babar, Z.; Shaheen, I.; Abid, M.; Kakar, M.R.; Mandokhail, S.J.; Nawaz, A. Influence of Construction Risks on Cost Escalation of Highway-Related Projects: Exploring the Moderating Role of Social Sustainability Requirements. *Iran. J. Sci. Technol.-Trans. Civ. Eng.* **2021**. [CrossRef]
65. Nawaz, A.; Su, X.; Iqbal, S.; Zahoor, H.; Asad, A.; Asghar, S.; Basit, F.; Barkat, M.Q.; Souhail, A.; Raheel Shah, S.A. Validating a Phenomenological Mathematical Model for Public Health and Safety Interventions Influencing the Evolutionary Stages of Recent Outbreak for Long-Term and Short-Term Domains in Pakistan. *Complexity* **2020**, *2020*, 8866071. [CrossRef]
66. Ratner, A. Dynamic Mechanical Compression Impulse of Lithium-Ion Pouch Cells. *Energies* **2020**, *13*, 2105. [CrossRef]
67. Zhu, J.; Koch, M.M.; Lian, J.; Li, W.; Wierzbicki, T. Mechanical Deformation of Lithium-Ion Pouch Cells under In-Plane Loads—Part I: Experimental Investigation. *J. Electrochem. Soc.* **2020**, *167*, 090533. [CrossRef]
68. Yoshio, M.; Brodd, R.J.; Kozawa, A. *Lithium-Ion Batteries: Science and Technologies*; Springer: New York, NY, USA, 2009; ISBN 9780387344447.

69. Murata, K.; Izuchi, S.; Yoshihisa, Y. Overview of the research and development of solid polymer electrolyte batteries. *Electrochim. Acta* **2000**, *45*, 1501–1508. [[CrossRef](#)]
70. Yong, G. GeePower Energy Technology Co., Limited.: Guangdong, China. 2015. Available online: <https://geebattery.com/about-us> (accessed on 11 May 2018).
71. Sahraei, E.; Meier, J.; Wierzbicki, T. Characterizing and modeling mechanical properties and onset of short circuit for three types of lithium-ion pouch cells. *J. Power Sources* **2014**, *247*, 503–516. [[CrossRef](#)]
72. Sahraei, E.; Hill, R.; Wierzbicki, T. Calibration and finite element simulation of pouch lithium-ion batteries for mechanical integrity. *J. Power Sources* **2012**, *201*, 307–321. [[CrossRef](#)]



Review

# Multiscale Modeling and Simulation of Polymer Blends in Injection Molding: A Review

Lin Deng <sup>1</sup>, Suo Fan <sup>1</sup>, Yun Zhang <sup>2</sup>, Zhigao Huang <sup>2,\*</sup>, Huamin Zhou <sup>2</sup>, Shaofei Jiang <sup>3</sup> and Jiquan Li <sup>3</sup>

<sup>1</sup> School of Mechanical and Electrical Engineering, Wuhan Institute of Technology, Wuhan 430205, China; dengl@wit.edu.cn (L.D.); fan\_suo@wit.edu.cn (S.F.)

<sup>2</sup> State Key Laboratory of Material Processing and Die & Mold Technology, Huazhong University of Science and Technology, Wuhan 430074, China; marblezy@hust.edu.cn (Y.Z.); hmzhou@hust.edu.cn (H.Z.)

<sup>3</sup> College of Mechanical Engineering, Zhejiang University of Technology, Hangzhou 310014, China; jsf75@zjut.edu.cn (S.J.); Lijq@zjut.edu.cn (J.L.)

\* Correspondence: huangzhigao@hust.edu.cn

**Abstract:** Modeling and simulation of the morphology evolution of immiscible polymer blends during injection molding is crucial for predicting and tailoring the products' performance. This paper reviews the state-of-the-art progress in the multiscale modeling and simulation of injection molding of polymer blends. Technological development of the injection molding simulation on a macroscale was surveyed in detail. The aspects of various models for morphology evolution on a mesoscale during injection molding were discussed. The current scale-bridging strategies between macroscopic mold-filling flow and mesoscopic morphology evolution, as well as the pros and cons of the solutions, were analyzed and compared. Finally, a comprehensive summary of the above models is presented, along with the outlook for future research in this field.

**Keywords:** polymer blends; injection molding; microstructure; multiscale simulation

**Citation:** Deng, L.; Fan, S.; Zhang, Y.; Huang, Z.; Zhou, H.; Jiang, S.; Li, J. Multiscale Modeling and Simulation of Polymer Blends in Injection Molding: A Review. *Polymers* **2021**, *13*, 3783. <https://doi.org/10.3390/polym13213783>

Academic Editors: Célio Bruno Pinto Fernandes, Salah Aldin Faroughi, Luís L. Ferrás and Alexandre M. Afonso

Received: 27 August 2021

Accepted: 25 October 2021

Published: 31 October 2021

**Publisher's Note:** MDPI stays neutral with regard to jurisdictional claims in published maps and institutional affiliations.



**Copyright:** © 2021 by the authors. Licensee MDPI, Basel, Switzerland. This article is an open access article distributed under the terms and conditions of the Creative Commons Attribution (CC BY) license (<https://creativecommons.org/licenses/by/4.0/>).

## 1. Introduction

The product performance of immiscible polymer blends is significantly affected by their microstructure, which is formed during mixing and processing. Most polymer blend products are made by injection molding. Therefore, an accurate description of the morphology evolution in polymer blends during the injection molding process is the necessary condition for predicting and tailoring their final properties [1]. However, the simulation of the injection molding of polymer blends is a challenging task. The mold-filling flow of polymer blend melt spans macro- and mesoscales, and no single model is capable of simulating these complex processes on both scales at the same time [2]. Therefore, a multiscale modeling and simulation approach is necessary for the injection molding process of polymer blends. In this paper, recent advances in the development of macroscopic and mesoscopic models are reviewed for the injection molding of polymer blends as well as scale-bridging methodologies. Here, this review restricts its attention to papers that connect microstructure with flow and rheology; the flow field is well defined. A review of all the publications pertaining to polymer blends with surfactants or compatibilizers would go beyond our scope limitations, though they are technologically important.

The rest of the paper is organized as follows. In Section 2, the process of mold-filling of polymer blends is described on both macro- and mesoscales, and the framework of multiscale modeling is thoroughly described. In Section 3, the historical development of the mold-filling flow simulation of polymer melt is overviewed. In Section 4, mesoscopic models for droplet morphology evolution during processing are compared. Different scale-bridging methodologies between microstructure evolution and mold-filling flow are discussed in Section 5. In Section 6, a summary is made, and an outlook for the future is suggested.



## 2. Framework of Multiscale Modeling

Multiscale modeling and simulation of polymer processing has been a hot research area, but it should be recognized that it is not a burgeoning field formed only during the past decade. Its development goes back to the computational fluid dynamics of polymer melt flow and the exploration of the molecular structure of polymers, both of which have laid the foundation of multiscale research. Therefore, the multiscale modeling and simulation of polymer processing ought to cover the consensus of available research, i.e., increasingly sophisticated injection molding simulation, and focus on the spawned problems when coupled with different models.

As shown in Figure 1, polymeric materials have a unique hierarchical structure, from atom to monomer, chain, and conformation with corresponding simulation methods on each scale. For the injection molding of polymers, the orientation, stretching, and crystallization of the polymer molecules occurs on the microscale, while on the macroscale, the polymer melt fills the mold cavity as continuum fluid.

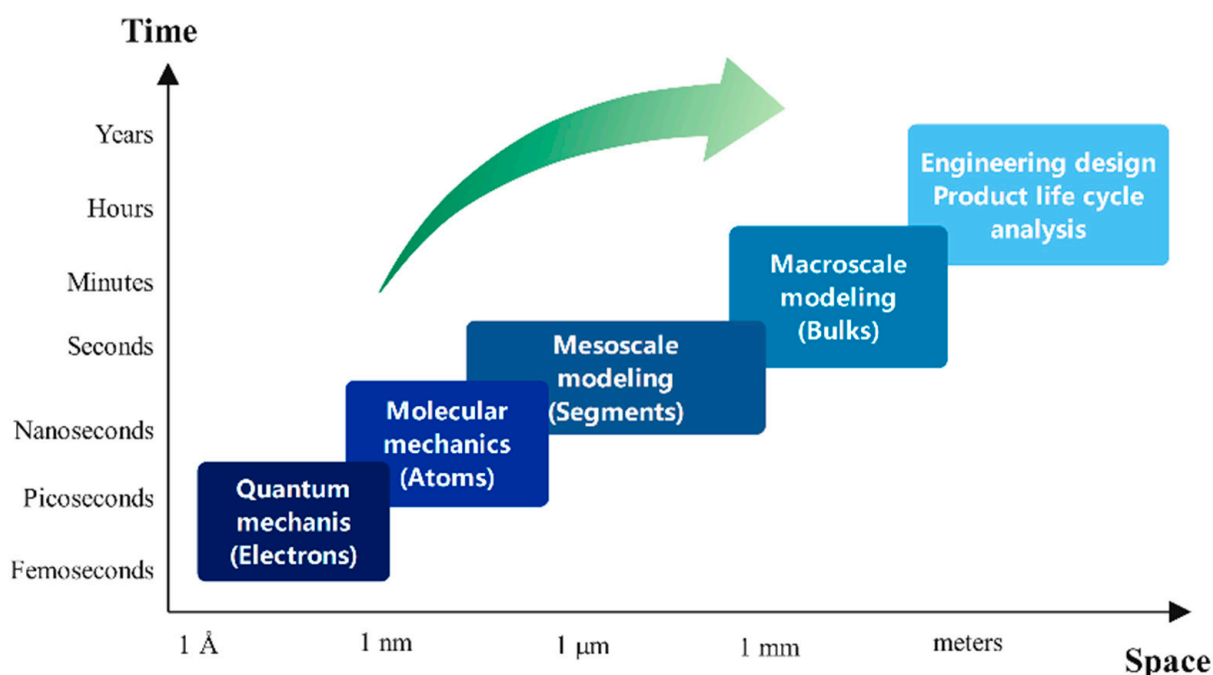


Figure 1. Spatial and temporal multiscale of polymer.

For polymer blends, it is mesoscopic morphology that has the most direct influence on the mold-filling flow of polymer blend melt and the final performance of the products. The interest in the multiscale modeling and simulation of injection molding of polymer blends is focused primarily on the macroscopic mold-filing of polymer blend melt and the simultaneous mesoscopic morphology evolution.

**Macroscale** ( $\sim 10^{-3}$  m,  $\sim 1$  s): The solid plastic pellets melt at a certain temperature above the melting point and are injected into the mold at a certain speed under the pressure of the injection machine. The polymer melt expels the air from the cavity until it fills the entire mold cavity and finally cools and solidifies to get the product as the designed mold cavity. The polymer blend melt is considered to be a continuous fluid, with the inside microstructure neglected. Injection molding of polymer melt is a non-Newtonian, non-isothermal, and unsteady process of mass, momentum, and heat transfer with the moving polymer–air front.

**Mesoscale** ( $\sim 10^{-6}$  m,  $\sim 10^{-6}$ – $10^{-3}$  s): Mesoscale morphology is formed in the compounding and granulation stages prior to injection molding. In the equipment, such as roll mills, mixing machines or screw extruders, a sea-island-like multiphase structure emerges [3,4] when the micron-sized droplets are dispersed throughout the matrix. During

the injection molding stage, the dispersed droplets inside the blend melt undergo complex morphology evolution under the combined action of shear, pressure and heat, and interfacial tension [5]. Finally, the blend morphology is frozen inside the product as the polymers cool and solidify after the flow ceases.

The macroscopic and mesoscopic physics of the injection molding of polymer blends are described using separate models. The mold-filling flow of the polymer melt is a free surface flow and can be described using the fields of velocity, pressure, temperature, and phase fraction. Using an appropriate constitutive equation and a PVT state equation of polymer melt, the conservation equations for the mold filling flow can be closed, and, thus, the mold filling flow can be modeled on a macroscopic scale. Using different discretization methods, such as the finite difference (FD), finite element (FE), or finite volume (FV) methods, the above equations can be solved numerically and the mold-filling flow process of the polymer melt can be accurately simulated.

In contrast, there is no unified approach for the description of the polymer blends morphology, and, accordingly, there are different modeling approaches for the morphology evolution of polymer blends. One type of method makes certain assumptions about and parameterizes the shape of the dispersed phase droplets and then establishes the evolution equations for the morphological parameters of the polymer blends. This class of methods is relatively simple, easy to implement, and computationally low but is only applicable under limited conditions. A different class of models uses the polymer molecular structure, coarse-grained particles, and component concentrations to describe the polymer blend morphology, thus modeling the evolution of the morphology of the blend separately. These methods are free of the assumption of polymer blend morphology and are more applicable to various cases; however, the computational overhead is usually expensive.

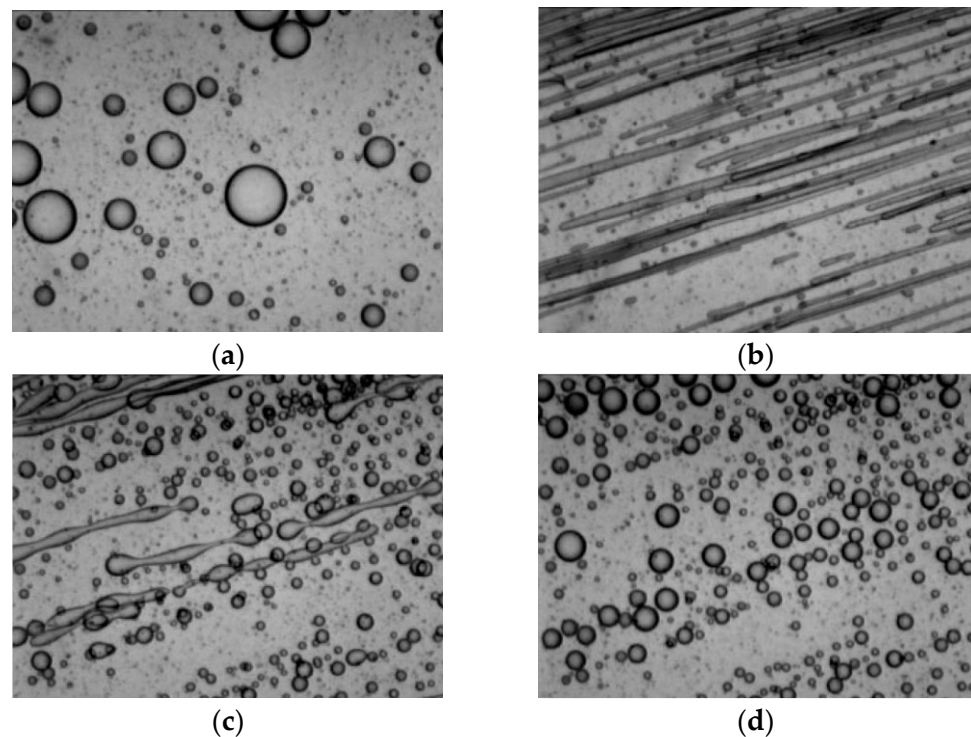
Given the macroscopic models of the mold-filling flow of polymer melt and the mesoscopic models of the polymer blend morphology evolution established, the key to the success of multiscale modeling and the simulation of injection molding of polymer blends is revealing the interactions between the physics of different scales and developing corresponding scale-bridging strategies. As discussed above, the multiple fields of velocity and pressure, as well as the temperature of the mold-filling flow, are the driving force of the morphology evolution of polymer blends. In turn, the morphology makes the stress–strain response characteristics of the polymer blend markedly different from a simple linear combination of the components. Therefore, various scale-coupling methods are used in different ways to represent the factors of mesoscopic morphology in the macroscopic model of the mold-filling flow.

According to the analysis of injection molding on macro- and mesoscales, the modeling and simulation of injection molding of polymer blends can be decomposed into three ingredients: macroscopic mold-filling flow modeling, mathematical characterization of polymer blend morphology and the modeling of its evolution, and, more importantly, the coupling of the models on macro- and mesoscales. This paper is dedicated to reviewing the multiscale modeling and simulation of injection molding of polymer blends from three aspects: macroscopic mold-filling flow simulation, mesoscopic morphology evolution simulation, and scale-bridging methods, corresponding to the following sections.

### 3. Mesoscopic Modeling of Droplet Morphology Evolution

Before articulating the mesoscopic modeling methods of droplet morphology evolution, it is better to revisit the typical experiment of droplet morphology evolution in a typical flow field of injection molding. From the SEM observation of Figure 2, it can be seen that in the initial stationary state, the droplets appear as spheres with a relatively large volume mean radius and radius distribution range. When the shearing flow starts, the droplets are subjected to strong shear, and the droplet morphology gradually changes from spherical to ellipsoidal, and then, finally, to elongated fibrous, at a certain angle to the shear direction, while some droplets break up and produce two or more sub-droplets. When the shear flow field is weakened and stopped, the droplet deformation degree decreases and

the shape starts to return to a spherical shape with a smaller average radius and a more uniform-sized distribution than in the initial state.



**Figure 2.** Morphology of the dispersed phase in PDMS/PB blends. (a) Before shearing; (b) during shearing; (c) 25 s after shearing stop; (d) 89 s after shearing stop (experimental results from the literature [6]).

Many researchers have contributed to the numerical and experimental work of the morphology evolution of single droplets. In general, both the phenomenological and theoretical models can be roughly divided into three categories: droplet models based on ellipsoid approximation, phase field methods based on the Cahn-Hilliard equation, and the pseudo-potential model based on the lattice Boltzmann method.

### 3.1. Ellipsoid Droplet Models

Doi and Ohta proposed a theoretical model using the interfacial area per unit volume  $Q$  and interface tensor  $q$  to characterize the microstructure.

$$Q \equiv \frac{1}{V} \int_A dA \text{ and } q = \frac{1}{V} \int_A \left( nn - \frac{1}{3}I \right) dA \quad (1)$$

where  $A$  represents the interfacial surface contained in  $V$ , with each surface increment  $dA$  having a unit normal vector  $n$ , and  $I$  is the unit tensor.

They wrote the time derivative of each variable as the sum of two terms: one for external flow (deformation) and one for relaxation due to interfacial tension:

$$\dot{Q} = \dot{Q}_{flow} + \dot{Q}_{relax} \text{ and } \dot{q} = \dot{q}_{flow} + \dot{q}_{relax} \quad (2)$$

The Doi and Ohta model is applicable to arbitrary polymer blend morphology; however, due to the underlying closure problem, different expressions for the convective terms have been proposed, leading to convective nonlinearities.

For a droplet in simple shear field, when the viscosity ratio  $p$  is much larger than 1 and the volume fraction is below 1, the droplet will maintain an ellipsoidal shape for a wide range of capillary numbers and viscosity ratios. When the critical breakup scenario is approached, the droplet shape will deviate from the ellipsoidal assumption and the model itself will fail.

### 3.1.1. Basic Quantities

As shown in Figure 3 below, three quantities are usually defined to characterize a deformed droplet in a planar flow field: the equivalent radius  $R$ , the deformation degree  $Df$ , and the orientation angle  $\theta$ , where  $Df = (a - b)/(a + b)$ , and  $a$  and  $b$  are the length and width of the droplet in the  $x - y$  plane of the flow, respectively.  $R$ ,  $a$  and  $b$  have the relation of  $R^3 = ab^2$ . It is apparent that a larger  $Df$  indicates a more deformed droplet.  $\theta$  is the angle between the principal axis of the droplet and the reference direction, usually the flow direction surrounding the droplet.

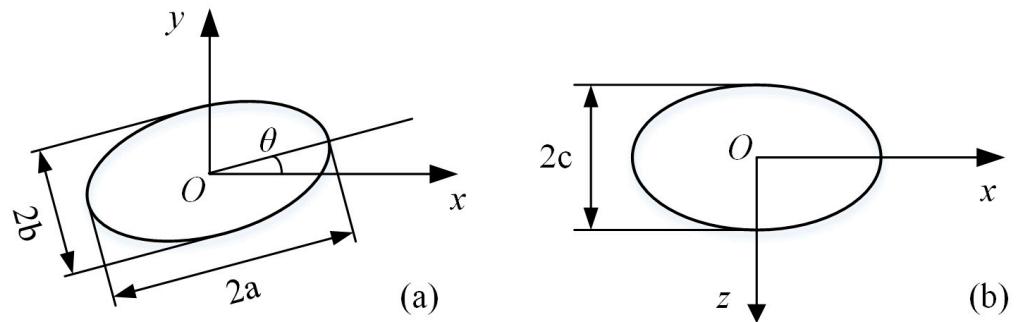


Figure 3. Schematic diagram of droplet geometry model parameters in the (a) flow plane and (b) rotational plane.

The study of the fundamentals of droplet deformation began with Taylor [7], who studied the basics of the deformation and breakup of a single Newtonian droplet in a viscous matrix. It was found that the deformation and breakup of the sheared droplet depended on two dimensionless quantities, namely, the droplet–matrix viscosity ration  $p = \eta_d/\eta_m$  and the capillary number  $Ca = \eta_m \gamma R/\Gamma$ , where  $\eta_d$  and  $\eta_m$  are the viscosities of the droplet and the matrix,  $\gamma$  is the shear rate, and  $\Gamma$  is the interfacial tension between the phases of the droplet and matrix. The capillary number characterizes the competition of the viscous stress that drives the droplet deformation against the interfacial tension that maintains the original shape. Droplets exhibit different orientations when different forces dominate, as described in detail below.

### 3.1.2. Deformation

Based on the ellipsoid description, the droplet shape can be described by a second-order tensor  $G$ , whose eigenvalues are equal to the reciprocal of the ellipsoidal semi-axis length squared, and the corresponding eigenvector defines the orientation angle of the droplet. The evolution of  $G$  can be expressed by the following equation [8]:

$$\frac{DG_{ij}}{Dt} + L_{ki}G_{kj} + G_{ik}L_{kj} = 0 \tag{3}$$

where  $\frac{D}{Dt}$  represents the material derivative,  $L$  is the velocity gradient tensor inside the droplet, and  $i$  and  $j$  denote the space index and can be  $x$ ,  $y$ , and  $z$ .

Once the velocity gradient tensor  $L$  is known, Equation (3) can be solved, and then the shape evolution of the ellipsoidal droplet will be uniquely determined with a proper initial condition. In fact, the most significant difference among the ellipsoid droplet models lies in how to calculate the velocity gradient tensor  $L$ .

Maffettone-Minale (MM) model [9]: Velocity gradient tensor  $L$  is expressed as:

$$L_{ij} = w_{ij}^A + f_2 e_{ij}^A + \frac{f_1}{2\tau_r} \left( \frac{3G_{ij}}{G_{kk}} - \delta_{ij} \right) \tag{4}$$

where  $\tau_r = \eta_m R/\Gamma$  is the surface-tension relaxation time,  $e_{ij}$  and  $w_{ij}$  are the deformation rate tensor and the vorticity tensor, respectively, both of which can be obtained from the velocity gradient tensor  $L_{ij}$ :  $e_{ij} = (L_{ij} + L_{ji})/2$ ,  $w_{ij} = (L_{ij} - L_{ji})/2$ .  $e_{ij}$  with superscript A denotes the externally applied deformation rate, while  $e_{ij}$  without superscript is related to the deformation of the droplet itself.

The parameters  $f_1$  and  $f_2$  are phenomenological model parameters for which certain choices have been proposed:

$$f_1 = \frac{40(p+1)}{(2p+3)(19p+16)}, f_2 = \frac{5}{2p+3} + \frac{3Ca^2}{2+6Ca^2} \tag{5}$$

The above model is referred to as the MM2 model. When  $f_2$  is simplified to  $f_2 = 5/(2p+3)$  the model is referred to as the MM1 model.

Jackson-Tucker (JT) model [10]: In a coordinate system coinciding with the main axes of the droplet, the velocity gradient tensor  $L$  can be expressed as:

$$L' = fL'_{Eshelby} + (1-f)L'_{slender}, p < 0.1 \tag{6}$$

$$L' = L'_{Eshelby}, p \geq 0.1 \tag{7}$$

where  $f$  is a composite parameter depending on the dimensionless length of the droplet's semi-major axis and equivalent radius  $a/R$ .  $L'_{Eshelby}$  and  $L'_{slender}$  represent the velocity gradient components obtained from the solution of Eshelby's theory [11] for elastic ellipsoidal particles in elastic media and Khakhar and Ottino's proposed filamentary theory [12], respectively.

Yu model [13]. The velocity gradient tensor  $L$  was expressed as:

$$L_{ij} = w_{ij}^A + (B_{mnkl} + C_{mnkl})r_{im}r_{uk}e_{uv}^A r_{vl}r_{jn} + r_{im}(\bar{L}_{mn}^\alpha + L_{mn}^\beta)r_{jn} \tag{8}$$

where  $r_{ij}$  is the transformation matrix that rotates the droplet axis in alignment with the coordinate system.

The velocity gradient tensor  $L$  in the Yu model consists of two major components: the components due to the external flow and the other one due to interface dynamics. The former of these can be referred to as the corresponding part of the JT model, for example. The meanings of the symbols in the equations and the detailed solutions can be found in the corresponding literature [13].

In addition to the above theoretical models, several traditional empirical models have found a wide application in simulations for simplicity and ease of use [14], such as the affine deformation model and Cox's theoretical formulation [15].

The affine deformation model [16] assumes that the lengths of the two minor axes,  $B$  and  $W$ , always keep equal when the droplet is deformed. The major axis  $L$ , minor axes  $W$  and  $B$ , and the angle between the major axis and flow direction  $\theta$  are calculated as:

$$L/R = 0.5\gamma + 0.5\sqrt{4 + \gamma^2} \tag{9}$$

$$B/R = \left(0.5\gamma + 0.5\sqrt{4 + \gamma^2}\right)^{-0.5} \tag{10}$$

$$\tan \theta = \left(0.5\gamma + 0.5\sqrt{4 + \gamma^2}\right)^{-1} \tag{11}$$

where shear rate  $\gamma$  represents the flow field that the droplet experienced.

The Cox theoretical formulation [15] is applicable to systems in all ranges of viscosity ratios when interfacial tension and viscous forces act simultaneously, and the predictions of deformation degree and orientation angle are given by:

$$Df = Ca \frac{19p+16}{16p+16} \frac{1}{\sqrt{(19pCa/20)^2 + 1}} \tag{12}$$

$$\theta = \frac{1}{4}\pi + \frac{1}{2} \tan^{-1}\left(\frac{19pCa}{20}\right) \tag{13}$$

### 3.1.3. Breakup

When the capillary number  $Ca$  is slightly larger than the critical value  $Ca_{crit}$ , the pattern of droplet breakup depends on the viscosity ratio [2]: when  $p$  is much smaller than 1, the droplet is extremely stretched into an S-shape and small droplets are released at both ends; when  $p \approx 1$ , the droplet gradually necks out from the middle part until it breaks up into

two sub-droplets, with some smaller satellite droplets in between. When  $Ca$  far exceeds  $Ca_{crit}$ , the droplet stretches into an elongated fiber.

Based on the results of experimental studies on the droplet deformation and breakup mechanism under simple flow conditions, a simplified capillary number  $k^* = Ca/Ca_{crit}$  (i.e., the ratio of the local capillary number to the critical value) can be defined. Depending on the cases, most researchers [14,17,18] have adopted the following general rule to describe droplet behavior.

- (1)  $k^* < 0.1$ , droplets do not deform;
- (2)  $0.1 < k^* < 1$ , droplets deform, but do not break up;
- (3)  $1 < k^* < 4$ , droplets deform and split into two major sub-droplets;
- (4)  $k^* > 4$ , droplets form fibers with the affine deformation of the medium.

$Ca_{crit}$  decides whether the deformed droplets reach equilibrium shapes or breakup into sub-droplets.  $Ca_{crit}$  of a specific droplet depends on the viscosity ratio and the ambient flow field type. The following empirical de Bruijn formula [19] is commonly used to write  $Ca_{crit}$  as a function of  $p$  for simple shear fields [20].

$$\lg Ca_{crit} = -0.506 - 0.0995 \lg p + 0.124 (\lg p)^2 - \frac{0.115}{\lg p - \lg 4.08} \quad (14)$$

The breakup of a droplet into two major sub-droplets by necking can be calculated using the direct method. Assuming that a droplet of equivalent diameter  $D_0$  splits completely into two sub-droplets of the same diameter without considering the effect of surrounding droplets, the diameter of the split sub-droplet,  $d \approx 0.794D_0$ , can be obtained according to the principle of volume conservation.

Based on the definition of the actual time required for breakup,  $t_b$ , a statistically significant average of the breakup process, can also be calculated. The rate of change of the total number of droplets  $N_d$  is first obtained as:

$$\frac{dN_d}{dt} = \frac{\dot{\gamma} N_d}{Ca_{crit} t_b^*} \quad (15)$$

where  $N_d = \frac{6\phi V}{\pi D_0^3}$ ,  $V$  is the total volume of the solution and  $D_0$  is the droplet diameter. This leads to the rate equation for droplet breakup [18].

$$\left( \frac{dD_0}{dt} \right)_{break} = \frac{-\dot{\gamma} D_0}{3Ca_{crit} t_b^*} \quad (16)$$

By comparing the above two models, it is easy to find that the direct method is simple and fast to calculate but cannot reflect the change trend in the breakup process. The physical meaning of the statistical method is clearer and scalable and the rate of change formula is easy to couple with others; however, the calculation cost is relatively high.

There are limited studies on droplet models for filament breakup processes, and most of them use empirical formulas or fluid-dynamics-related theories for approximate calculations. For example, based on the Rayleigh theory of capillary number instability [21] and the principle of volume conservation, the following equation can be used to calculate the final size of the fiber after the breakup [14]:

$$R_{drops} = R_0 \sqrt[3]{\frac{3\pi}{2X_m}} \quad (17)$$

where  $R_0$  is the fiber diameter before the breakup, which can be approximated as the critical diameter  $d^*$  at the moment of fiber breakup, and  $X_m$  represents the main wave number. When  $p = 1$ ,  $X_m \approx 0.56$ , the diameter of the droplet after breakup  $d \approx 2d^*$  is obtained using the above equation.

### 3.1.4. Coalescence

For the coalescence process of two spherical particles of the same size in a shear flow field, the coalescence rate can be expressed as a function of collision probability and the kinetics of the collision process. Collision probability  $p_{coll}$  can be expressed as (see [14]):

$$p_{coll} = \exp\left(\frac{-\pi}{8\dot{\gamma}\phi t_{loc}}\right) \quad (18)$$

where  $t_{loc}$  is the local residence time.

The liquid film discharge probability  $p_{exp}$  depends on the activity of the interface, which depends on the viscosity ratio  $p$ : the larger the value of  $p$ , the less active the interface is. For inactive interfaces with  $p$  much larger than 1, the liquid film discharge probability can be calculated using the following equation [14]:

$$p_{exp} = \exp\left[-\frac{9}{8}\left(\frac{R}{h_c}\right)^2 k^{*2}\right] \quad (19)$$

In the above equation,  $h_c$  is the critical thickness of the liquid film at the time of the breakup, which can be obtained by experiment, and  $k^*$  is defined as before.

Thus, the coalescence chance of droplets  $p_{coal}$  can be expressed as the product of  $p_{coll}$  and  $p_{exp}$ .

Considering the role of various factors in the coalescence process, the following equation for the evolution of the diameter of the dispersed phase in the coalescence process can be obtained [18].

$$\left(\frac{dD_0}{dt}\right)_{coal} = CD_0^{-1}\phi^{8/3}\dot{\gamma} \quad (20)$$

where  $C$  is the coalescence constant.

Take the assumption that the shape change of droplets during breakup and coalescence can be linearly superimposed; the resultant droplet diameter change rate can be calculated from Equations (15) and (19) as [18].

$$\left(\frac{dD_0}{dt}\right) = \left(\frac{dD_0}{dt}\right)_{break} + \left(\frac{dD_0}{dt}\right)_{coal} \quad (21)$$

The above equation can be integrated in time by various numerical methods, such as the finite difference method, to obtain the change in droplet diameter under the combined effect of breakup and coalescence.

Since the rate of change of droplet size at equilibrium is 0, according to the above Equations (15), (19), and (20), then we have [18]:

$$D_{eq} = D_{eq}^0 + \left(6CCa_{crit}t_b^*\phi^{8/3}\right)^{1/2} \quad (22)$$

where  $D_{eq}$  is the diameter at equilibrium and  $D_{eq}^0$  is the diameter at zero component (i.e., without any dispersed phase), obtained by extrapolation. Using the above equation, the coalescence constant  $C$  of a certain blend can be obtained by preparing a series of materials with different components, i.e., calculated by the slope of the curve of  $D_{eq}$  versus  $\phi^{4/3}$ . Using the coalescence probability formula obtained earlier, an approximate formula for the radius of the new particle after coalescence can also be obtained. Assuming the interaction of two droplets of the same size, the volume conservation principle yields (see [22]):

$$R^* = R\left(\frac{2}{2-p_{coal}}\right)^{1/3} \quad (23)$$

where  $R$  and  $R^*$  represent the radii of droplets before and after coalescence. Obviously,  $R = R^*$  when coalescence is not considered, i.e.,  $p_{coal} = 0$ ;  $R = 2^{1/3}R^*$  when coalescence is complete, i.e.,  $p_{coal} = 1$ .

Although the above experimental and probabilistic models cannot track the interfacial changes during droplet coalescence in real-time, they can reflect the changes of dispersed phase size in each part of the system due to the coalescence process and are simple and easy to implement.

### 3.1.5. Size Distribution

For a discrete model of a system (droplet volume is a product of an integer and the elementary volume  $V_1$ ), the following equation describes the change in the number of droplets of volume  $kV_1$ ,  $n_k$  with time  $t$  [23]:

$$\frac{dn_k}{dt} = \frac{1}{2} \sum_{i+j=k} C(i, j)n_i n_j - F(k)n_k - \sum_{j=1} C(k, j)n_k n_j + \sum_{j=k+1} \omega(k, j)n_f(j)F(j)n_j \tag{24}$$

where  $C(i, j)$  is the coagulation kernel,  $F(i)$  is the overall breakup frequency,  $n_f(i)$  is the number of fragments formed at the breakup of a droplet of volume  $iV_1$ , and  $\omega(i, j)$  is the probability that a fragment formed by the breakup of a droplet of volume  $jV_1$  will have volume  $iV_1$ .

Tokita [24] considered the average droplet size in steady shear flow. He assumed that the droplets were still monodisperse in size and derived the following dependence of steady radius of droplet  $R$  on system parameters:

$$R = \frac{12\sigma P_c \phi}{\pi \eta_{ap} \dot{\gamma} - 4P_c \phi E_{DK}} \tag{25}$$

where  $\eta_{ap}$  is the apparent viscosity of the blend and  $E_{DK}$  is the volume energy.

Fortelný and Kovár [24] expanded the function of  $F(k)$  as the Taylor series of  $Ca$  on the right of  $Ca_c$ :

$$F(k; Ca) = \left( \frac{\partial F}{\partial Ca} \right)_{Ca_c} (Ca - Ca_c) + \frac{1}{2} \left( \frac{\partial^2 F}{\partial Ca^2} \right)_{Ca_c} (Ca - Ca_c)^2 + \dots \tag{26}$$

Substitution of Equation (26) into Equation (24) leads to the linear dependence of  $R$  on the volume fraction of droplets  $\phi$ :

$$R = R_c + \frac{4\sigma P_c}{\pi \eta_m f_F} \phi \tag{27}$$

Huneault et al. [18] developed a computational model for droplet size evolution during mixing in a screw extruder. They considered that the blend components showed power-law relations between shear stress and shear rate. They assumed that the droplet deformation took place only within the pressurized screw zones. The authors proposed the following equation for  $R$ :

$$R = R^0 + \left( 1.5C_H Ca_c t_B^* \phi^{8/3} \right)^{1/2} \tag{28}$$

where  $R^0$  is the droplet radius for  $\phi = 0$ , and  $t_B^*$  is the dimensionless breakup time, which is a function of  $p$  and is independent of  $Ca$ .

Fortelny and Juza [25] recently formulated equations for the calculations of steady drop size in flowing immiscible polymer blends based on the monodisperse-drop-size assumption.

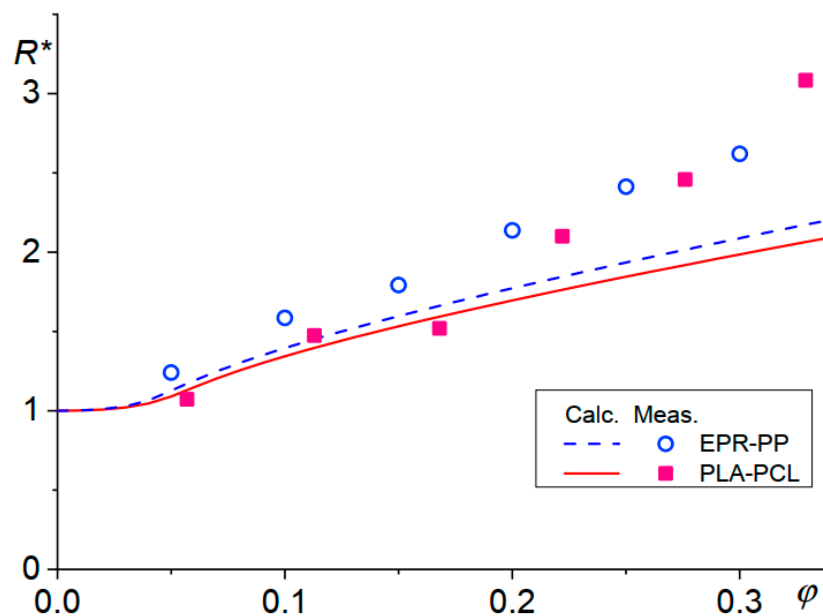
$$a_m (R^* - 1)^{a_c + 1/2} + (R^* - 1)^{1/2} - \frac{4(1+p)}{\pi} k_1 P_c(R) \phi (R^* - 1) - \frac{4(1+p)}{\pi} k_0 P_c(R) \phi = 0 \tag{29}$$

where  $R^*$  is the ratio of  $R$  and its critical value for breakup,  $R_c$ , and  $a_m = 8.759$  and  $a_c = 1.748$ ,  $k_0 = 4.3$  and  $k_1 = 27.7$  are the numerical constants determined from the experimental data of Cristini et al. [26]. The prediction of this model agreed well with the experimental data when the component ratio was low, as can be seen in Figure 4.

For  $Ca \gg Ca_c$ , the approach led to the following equation:

$$R^{*1/3} = \frac{4}{\pi} \frac{\phi}{g(p) Ca_c^{1/3}} P_c(R) \tag{30}$$





**Figure 4.** Reduced droplet sizes calculated using Equation (24) and the experimental sizes for blends ethylene-propylene rubber (EPR)-polypropylene (PP) [27] (dashed line and empty circles) and poly(lactic acid) (PLA)-poly(caprolactone) (PCL) [28] (solid line, full squares).

Janssen and Meijer [14] studied the evolution of droplet size in an extruder using a two-zone model. The model of a cascade of ideal mixers was used for residence time distribution in the weak zone.

Patlazhan and Lindt [29] solved Equation (24) using an expression for droplet breakup constructed by a combination of the results of Tomotika's theory [30]. Droplet size distribution function, as a function of the initial droplet size distribution,  $p$ , and the average number of daughter droplets, was calculated numerically.

Delamare and Vergnes [31] studied the evolution of droplet size distribution in a twin-screw extruder. Average droplet diameters and local distribution of the droplet sizes were calculated numerically as functions of the parameters of blends and the extrusion process.

Potente and Bastian [32] derived an algorithm for the calculation of droplet size evolution during extrusion using the finite and boundary element methods for the determination of stress acts on the droplets during their trajectories.

Peters et al. [33] derived a constitutive equation for liquid mixture based on the Lee and Park model of immiscible polymer blends [34]. A scheme for the calculation of morphology evolution, considering the above events, was proposed. Results of the theory were compared with experimentally determined time dependence of rheological functions in various flow regimes and not with droplet size distribution.

More recently, Wong W.-H. B. et al. [35] extended the constitutive modeling of dispersive mixtures proposed by Peters G.W.M. [33] to study the polydisperse droplet size distribution numerically. The simulation procedure contained an additional morphology state and behaved better in complex flows, i.e., eccentric cylinder flow.

### 3.2. Phase Field Models

It is straightforward to model the polymer blends at continuum length scales in the Cahn–Hilliard–Cook framework [36]. The Cahn–Hilliard equation has multiple complexities from both mathematical and physical viewpoints. Mathematically, as a partial differential equation, it has strong nonlinearity. Physically, the Cahn–Hilliard equation is fundamentally related to the thermodynamics of the polymer blends, and this relationship is reflected in the Gibbs free energy of the mixing function.

In the case of polymer blends, the most common choice is the Cahn–Hilliard model, which is a remarkably simple and powerful equation, so that a wealth of supporting data can be found from the literature.

$$\frac{\partial c}{\partial t} + \mathbf{u} \cdot \nabla c = D \nabla^2 \mu \quad (31)$$

where  $c$  is the composition of the fluid,  $\mathbf{u}$  is the velocity of the flow field,  $D$  is a diffusion coefficient of the  $\text{m}^2/\text{s}$  unit,  $\mu = c^3 - c - \gamma \nabla^2 c$  is the chemical potential at that location, and  $\sqrt{\gamma}$  is the thickness of the two-phase transition region (interface).

Later, Cook et al. [37] further modified the Cahn–Hilliard equation by adding a thermal noise term,  $\xi$ , thus making the equation thermodynamically more complete and presenting the well-known Cahn–Hilliard–Cook equation, namely:

$$\frac{\partial c}{\partial t} + \nabla \cdot (\mathbf{u}c) = D \nabla^2 \mu + \xi \quad (32)$$

where  $\xi$  satisfies the fluctuation dissipation theorem.

$$\langle \xi(\mathbf{r}, t) \rangle = 0 \quad (33)$$

$$\langle \xi(\mathbf{r}, t) \xi(\mathbf{r}', t') \rangle = 2k_B T D \nabla^2 \delta(\mathbf{r} - \mathbf{r}') \delta(t' - t) \quad (34)$$

Although a thermal noise term is added to the equation, the thermal noise only plays an important role in the initial stage of phase separation and has a negligible role in the evolution of the dispersed phase morphology after complete phase separation.

The flux  $j_i$  of species  $i$  can be written as

$$\mathbf{j}_i = - \sum_j M_{ij} \nabla \mu_j \quad (35)$$

To obtain the transport equation for species  $i$ , the continuity equation is applied:

$$\frac{\partial \phi_i}{\partial t} + \nabla \cdot \mathbf{j}_i = 0 \quad (36)$$

where  $t$  denotes time. For an  $N$  component system, typically,  $N - 1$  transport equations are defined, and  $\phi_N$  for the last component is inferred from a material balance equation  $\sum_i \phi_i = 1$ , where  $\phi_i$  is the volume fraction of species  $i$ . For a binary system with components 1 and 2, the transport equation for species  $i$  can then be written as:

$$\frac{\partial \phi_1}{\partial t} = \nabla \cdot (M_{12} \nabla \mu_{12}) \quad (37)$$

An expression for the chemical-potential difference,  $\mu_{ij}$ , can be obtained by considering the generalized  $N$ -component Landau–Ginzburg free-energy functional equation for inhomogeneous systems enclosed within a dimensionless volume.

$$\mu_{12} = \frac{\partial g_m}{\partial \phi_1} - \kappa \nabla^2 \phi_1 \quad (38)$$

Prusty and Keestra et al. [38] used a diffusion interface model based on Cahn–Hilliard theory to study the internal structural evolution of poly(methyl methacrylate) (PMMA)/poly(styrene-co-acrylonitrile) (SAN)28 blends and compared it with small-angle scattering (SALS) experiments. The simulation results showed that the coarsening kinetics are mainly dominated by the flow when the capillary number exceeds 10.

Kohler and Krekhov et al. [39], on the other hand, discussed the dynamic critical properties of PDMS/PEMS blends in the framework of the generalized Cahn–Hilliard model and examined the formation process of internal structures in the presence of an inhomogeneous spatial distribution of temperature and found that when the temperature of the spatially periodic temperature field changes by more than a critical value, the process of coarsening will be blocked.

Keestra and Goossens et al. [40] used a diffusion interface model based on Cahn–Hilliard theory to simulate and study the phase morphology of the PMMA/SAN blends under a flat plate shear flow field with increasing shear intensity, and the results ob-

tained were consistent with those of optical microscopy and small-angle light scattering (SALS) experiments.

Parsa and Ghiass et al. [41] developed a kinetic model for the phase separation process of polystyrene/polyvinyl methyl ether blends based on the nonlinear Cahn–Hilliard theory, identified a variety of dispersed phase morphologies such as droplets and rods, and revealed that the initial component concentration of the polymer blends and temperature distribution were the main controlling factors of phase separation and morphology evolution.

Carolan and Chong et al. [42] implemented the Cahn–Hilliard model in the open-source computational fluid dynamics software library OpenFOAM and investigated the “sea-island” droplets structure and co-continuous structure during processing, revealing that the initial concentration of the two phases has a decisive role in the final phase morphology.

Tabatabaieyazdi and Chan et al. [43] coupled the nonlinear Cahn–Hilliard model with Flory–Huggins–de-Gennes to simulate surface-oriented phase separation phenomena in binary polymer blends and investigated, for the first time, the different temperature gradients on the surface enrichment rate.

In recent years, the development of the Cahn–Hilliard model in immiscible polymer blends showed a trend in integration with the Doi–Ohta model [44,45]. By extracting new coarse-grained variables, microstructural models on different levels were coupled. Through this coarse-grained method, the morphology evolution of polymer blends could be studied from the thermodynamic perspective.

### 3.3. Lattice Boltzmann Method

A major advantage of the Lattice Boltzmann method is its ability to serve as a solver for conservation equations, such as the Navier–Stokes equation describing holonomic flow; at the same time, its mesoscopic nature provides a viable way to incorporate the microscopic dynamics of forming liquid–liquid interfaces and liquid–solid interfaces. In the last two decades, several multiphase models have been developed in the LBM research community. The first is the Rothman–Keller (RK) LB model, proposed by Gunstensen et al. in 1991, based on Rothman and Keller’s lattice gas (cellular-automaton) model [46], which uses a color gradient to achieve phase separation and model the interaction forces at the multiphase interface [47]. The second one is the pseudo-potential model proposed by Shan and Chen [48], which considers nonlocal inter-particle interactions by introducing a pseudo-potential. Another is the free energy model proposed by Swift [49], which proposes a generalized equilibrium state distribution function for a non-ideal pressure tensor, thus introducing multiphase interactions directly into the collision process of the distribution function. Another one is the mean field LB model proposed by He et al. [50] for incompressible multiphases, with suitable external force terms near the interface.

Among the above-mentioned models, the Shan–Chen pseudo-potential multiphase flow model is, to the best of the authors’ knowledge, the most widely used multiphase flow lattice Boltzmann model because it has the advantages of simplicity of approach and generality. Its basic idea is to use the pseudo-potential (also often called effective mass) to reflect the microscopic intermolecular forces on a mesoscopic scale. This automatic phase separation mechanism is an attractive feature of the pseudo-potential model because the two-phase interface is no longer a mathematical boundary and no longer requires any explicit interface tracing or interface capture techniques. Because of its remarkable computational efficiency and clear picture of the underlying microphysics, the Shan–Chen pseudo-potential multiphase model has become a promising technique for simulating and studying polymer blends.

Taking the most widely used single relaxation time LBM-BGK as an example, its distribution function evolution equation is

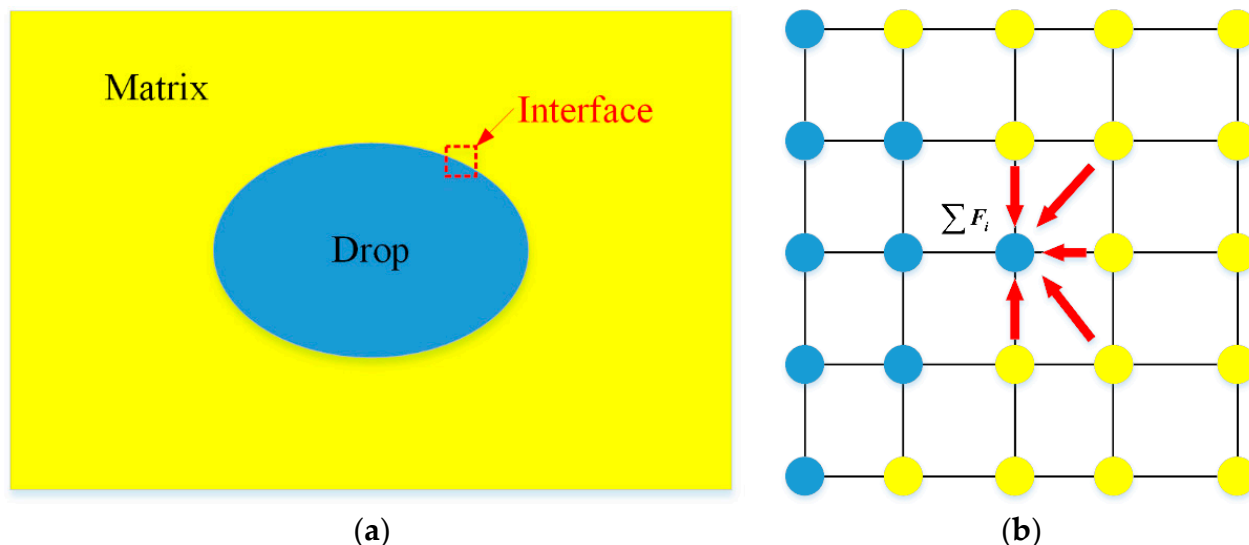
$$\begin{aligned} f_{\sigma,\alpha}(\mathbf{x} + c\mathbf{e}_\alpha\Delta t, t + \Delta t) - f_{\sigma,\alpha}(\mathbf{x}, t) \\ = -\frac{1}{\tau_{\sigma,\alpha}}\left(f_{\sigma,\alpha}(\mathbf{x}, t) - f_{\sigma,\alpha}^{eq}(\mathbf{x}, t)\right) + F_{\sigma,\alpha}(\mathbf{x}, t) \end{aligned} \quad (39)$$

where  $f_{\sigma,\alpha}(x,t)$  is the probability of finding a fluid particle of component  $\sigma$  at position  $x$  and time  $t$  with the discrete velocity  $e_\alpha$ .

To introduce nonlocal interactions between particles, Shan and Chen defined the force on a particle with component  $\sigma$  at spatial position  $x$  from a particle of component  $\bar{\sigma}$  at spatial position  $x'$  as

$$F(x, x') = -G(|x - x'|) \psi_\sigma(x) \psi_{\bar{\sigma}}(x') (x' - x) \tag{40}$$

where  $G$  is a symmetric Green's function, and  $\psi$  is an effective mass that depends on the local density of the components. The inter-particle force separates the different phases automatically, as illustrated in Figure 5.



**Figure 5.** The principle of the pseudo-potential model: (a) the schematic of the drop–interface–matrix structure; (b) the pseudo-potential force between particles at the interface.

The force defined in Equation (40), along the vector between the two lattice positions, satisfies Newton's third law while the global conservation of momentum is maintained [51].

As shown in Figure 5 above, the combined force on the particle at position  $x$  is the sum of the forces acting on it by all neighboring particles.

$$F(x) = -\psi(x) \sum G(|x - x'|) \psi(x') (x' - x) \tag{41}$$

In the lattice space system, if we consider  $N$  neighboring particles interacting with the particle at the current position  $x$  and let  $G(|e_\alpha|)$  be just a function of  $|e_\alpha|$ , i.e., the interaction between the particles is isotropic, then the interaction force  $F(x)$  can be further expressed as:

$$F_{\sigma\bar{\sigma}}(x) = -g_{\sigma\bar{\sigma}} \psi_\sigma(x) c_s^2 \sum_{\alpha=1}^N w(|e_\alpha|^2) \psi(x+e_\alpha) e_\alpha \tag{42}$$

where  $g_{\sigma\bar{\sigma}}$  is the interaction strength between component  $\sigma$  and  $\bar{\sigma}$  and is linked to the thickness of the interface, and  $w(|e_\alpha|^2)$  is the weight that is used to calculate the isotropic interaction force.

Macroscopic density  $\rho_\sigma$  and momentum  $\rho_\sigma u_\sigma$  are defined as the zeroth and first-order moment of the distribution function:

$$\begin{aligned} \rho_\sigma &= \sum_i f_{\sigma,i} \\ \rho_\sigma u_\sigma &= \sum_i e_i f_{\sigma,i} \end{aligned} \tag{43}$$

In addition, in the Shan–Chen pseudo-potential model, the macroscopic velocity of the flow field as a whole is redefined as the average of the velocities before and after the collision, i.e.:

$$\rho u = \sum_\sigma \rho_\sigma u_\sigma + \delta t \sum_\sigma F_\sigma / 2 \tag{44}$$

By performing the Taylor expansion of Equation (39) to the second-order by Chapman–Enskog analysis, the continuity equation for each component can be obtained as follows:

$$\frac{\partial \rho_\sigma}{\partial t} + \nabla \cdot (\rho_\sigma \mathbf{u}) = -\nabla \cdot \mathbf{j}_\sigma \tag{45}$$

Additionally, the continuity equation within the entire flow field is as follows:

$$\frac{\partial \rho}{\partial t} + \nabla \cdot (\rho \mathbf{u}) = 0 \tag{46}$$

where  $\mathbf{j}_\sigma = \rho_\sigma(\mathbf{u}_\sigma - \mathbf{u})$  is the diffusive mass flux of component  $\sigma$ . By the same analysis method, the momentum equation for the entire flow field can also be obtained from Equation (39), when the macroscopic viscosity of the fluid can be written as:

$$v_\sigma = \frac{1}{\text{dim} + 2} \left( \sum_\sigma \frac{\rho_\sigma}{\rho} \tau_\sigma - \frac{1}{2} \right) \tag{47}$$

The above analysis demonstrates that the pseudo-potential mode of LBM is equivalent to the Navier–Stokes equations of multiphase flow with second-order accuracy.

The comparison of the mesoscale methods for droplet morphology evolution is arranged in Table 1 for the future choice of the reader according to different fitness.

**Table 1.** Comparison of three droplet morphology evolution models.

	Ellipsoid Models	Phase Field Models	LBM
Morphology	ellipsoid	arbitrary	arbitrary
Interface tracking	√	×	×
Interface type	sharp	diffuse	diffuse
Flow filed inside drops	×	√	√
Physical domain size	large	medium	small
Source of model parameters	physical properties	first-principles calculations	physical properties
Solving method	implicit	implicit	explicit
Computation cost	low	medium	high
External field incorporation	×	√	√
Phase transition incorporation	×	√	√

#### 4. Macroscopic Mold-Filling Flow Simulation

The mold-filing flow of the polymer melt is a non-Newtonian, non-isothermal, and unsteady process with moving free-surface. This complex process is governed by conservation laws and the constitutive equation, and the simulation of mold-filling flow is, in essence, to solve the governing equations numerically.

Mass:

$$\frac{\partial \rho}{\partial t} + \rho \nabla \cdot \mathbf{u} + \mathbf{u} \cdot \nabla \rho = 0 \tag{48}$$

Momentum:

$$\frac{\partial(\rho \mathbf{u})}{\partial t} + \nabla \cdot (\rho \mathbf{u} \mathbf{u}) = -\nabla P + \nabla \cdot (\eta \nabla \mathbf{u}) + \rho \mathbf{f} \tag{49}$$

Energy:

$$\rho c_p \frac{\partial T}{\partial t} + \nabla \cdot (\rho T \mathbf{u}) = \nabla \cdot (\lambda \nabla T) + \Phi \tag{50}$$

where  $\mathbf{u}$ ,  $P$ , and  $T$  are the velocity, pressure, and temperature of the mold-filling flow;  $\mathbf{f}$  is the external force field;  $\rho$ ,  $\eta$ ,  $c_p$ , and  $\lambda$  are the density, viscosity, specific heat, and heat conductivity of the polymer melt;  $\Phi$  is the heat dissipation.

The simulation of the mold-filling flow of polymer melt during injection molding has undergone a tortuous development process from 1D, 2D, 2.5D to 3D. Among them,

the research on one-dimensional flow simulation started in the 1960s, and the simulation objects were mainly round tubes with simple geometry or rectangular or centrally cast discs [11–16]. Williams et al. [2,17] conducted an exhaustive study of the circular tube flow of plastic melts. 1D flow analysis can obtain the pressure and temperature distribution of the melt. The calculation is fast, and the location of the flow front is easy to determine, but it is limited to simple and regular geometry, which is difficult to adapt to the actual needs of production.

Since plastic injection molded products are generally thin-walled structures, the dimensions in the thickness direction are much smaller than the overall dimensions of the product, and the longer molecular chain structure of the plastic melt leads to strong viscosity, with inertia forces much smaller than the viscous shear stress. Hieber et al. [19–22] extended the flow model of the Hele–Shaw assumption [52,53] to the two-dimensional flow of polymer melt. The Hele–Shaw model neglects the inertia and gapwise velocity components for polymer melt flow in thin cavities. The flow-governing equations are simplified into a single Poisson equation based on these assumptions.

Simplified Momentum Equation:

$$\frac{\partial P}{\partial x} = \frac{\partial}{\partial z} \left( \eta \frac{\partial v_x}{\partial z} \right) \quad (51)$$

$$\frac{\partial P}{\partial y} = \frac{\partial}{\partial z} \left( \eta \frac{\partial v_y}{\partial z} \right) \quad (52)$$

$$\frac{\partial P}{\partial z} = 0 \quad (53)$$

Simplified Energy Equation:

$$\rho C_p \left( \frac{\partial T}{\partial t} + v_x \frac{\partial T}{\partial x} + v_y \frac{\partial T}{\partial y} \right) = \eta \dot{\gamma}^2 + k \frac{\partial^2 T}{\partial z^2} \quad (54)$$

The mathematical model proposed by Hieber et al. is more in line with the actual situation of plastic injection molding and takes into account the possibility of implementing numerical calculations, so it is followed by many researchers [18,23–25].

The 2.5D flow simulation is an approximate 3D simulation method that goes through two stages: a mid-plane model and a surface model. Although both theoretical and application examples have demonstrated that the mid-plane model can accurately simulate the filling flow of polymer melt, it is often difficult to extract the mid-plane from the product, which, in turn, leads to secondary modeling problems in CAE software.

In order to solve the problem of secondary modeling of the mid-surface model, the surface model based on solid technology (surface technology), which preserves all the advantages of the mid-surface model, the two-sided analysis model comes out. The first integrated mathematical model of the surface model was presented by Zhou et al. [14,32,33]. At present, the surface model has already become the mainstream model of injection molding simulation and is widely used in commercial CAE systems [34–41].

With the development of industrial technology, the shape of plastic parts is becoming more and more complex, and wall thickness inhomogeneity is becoming more and more prominent. The limitations of the mid-plane model and the surface model are becoming increasingly obvious. In recent years, the accelerating speed of computers and the continuous progress of numerical analysis technology have laid a solid foundation for the application of three-dimensional modeling and simulation.

Chang [27] et al. presented an implicit finite volume approach to simulate three-dimensional mold filling. This method can more accurately predict the critical three-dimensional phenomena encountered during mold filling than the existing Hele–Shaw analysis model. It has been proven to be a highly effective and flexible tool for simulating mold-filling problems.

Kim [28] et al. used mixed interpolation cells of velocity and pressure and simultaneous interpolation cells to simulate velocity and pressure fields during the mold-filling

process, respectively, and concluded that the numerical efficiency of simultaneous interpolation is higher.

Hetu [14] et al. used mini cells to solve the instability problem of velocity and pressure and the Lesaint-Raviart method to eliminate the numerical oscillations caused by convective terms.

Pichelin et al. [29,30] used hybrid cells and the explicit Taylor–Galerkin intermittent finite element method to simulate the mold-filling process, and a fountain effect at the flow front was observed.

Li, Q. et al. simulated melt filling and primary gas penetration in a gas-assisted injection molding (GAIM) process using finite volume and domain extension methods with SIMPLEC technology, and the CLSVOF (coupled level set and volume of fluid) method was employed to capture the moving interfaces [54].

Vietri, U. et al. improved the predictions of the description of pressure profiles by introducing the effect of pressure on viscosity and the effect of cavity deformation during molding [55].

He, L. et al. investigated the three-dimensional (3D) injection molding flow of short fiber-reinforced polymer composites using a smoothed particle hydrodynamics (SPH) simulation method [56].

Liang, J. et al. improved the numerical stability of 3D FVM simulation in plastic injection molding by proposing a novel and robust interpolation scheme for face pressure [57].

Xu, X.Y. et al. enhanced the accuracy, stability, and boundary treatment of the smoothed particle hydrodynamics (SPH) method and investigated the injection molding process of polymer melt based on a generalized Newtonian fluid model [58].

Liu, Q.S. et al. integrated the Rolie–Poly constitutive equation with the continuity, momentum, and level set equations to investigate the role of viscoelasticity of polymer melt during injection mold filling [59].

In summary, the main differences among the three mainstream models of mold-filing flow of polymer melt were compared in several areas, as shown in Table 2.

**Table 2.** Differences among three models.

	Mid-Plane Model	Surface Model	Solid Model
Thin-wall laminar flow assumptions	√	√	×
Incompressibility assumption	√	√	√
Inertia and volume forces	×	×	×
Heat transfer in direction of flow	√	√	×
Internal heat source items	×	×	×
Constant physical parameters	√	√	√
Planar-shaped flow front	√	√	×
Grid size	small	medium	large
Algorithm complexity	simple	complex	more complex
Calculation time	short	ordinary	long

## 5. Scale-Bridging Strategies

Since there are two ways to describe fluid flows, namely, the Lagrangian description and the Eulerian description, accordingly, the scale-bridging strategies of multiscale simulation of injection molding of polymer blends can be roughly divided into the particle-based scale-bridging method and parameter-based method, which are used with the macroscale mold-filling flow simulation of the two descriptions separately.

### 5.1. Parameter-Based Methods

For the Eulerian description of fluid dynamics, the physical parameters in the governing equations of the mold-filling flow consist of single-valued conditions. Other than measurements from experiments in conventional ways, these macroscopic physical parameters can be determined from the microscale molecule conformation or mesoscale blend morphology of polymers. With the physical parameters as a bridge, the simulations are coupled on macroscopic and mesoscopic or mesoscopic scales.

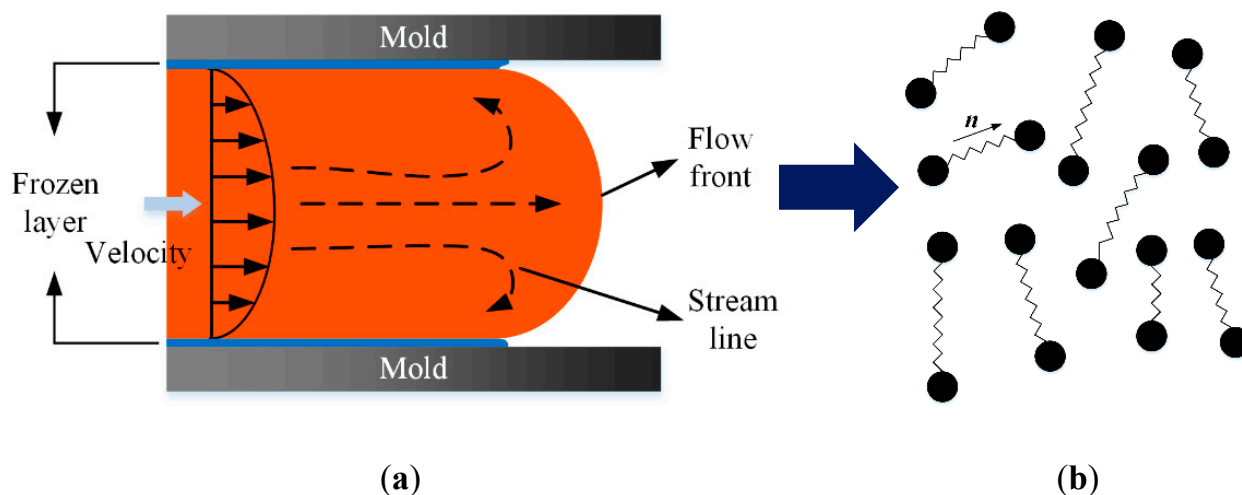
Based on the ellipsoidal description of droplets, Yu, W. and C. Zhou [60] proposed a rheological constitutive equation for an immiscible polymer blend by adding the contribution of the interfacial stresses to the Newtonian stresses resulting from components.

$$\tau = 2\eta_m e^A + 2(\eta_d - \eta_m)\phi e - \frac{\Gamma\phi}{L_c} \left( \frac{A}{\text{tr}A} - \frac{1}{3}\delta \right) \quad (55)$$

where  $A$  is the area tensor, converted from the ellipsoid morphology tensor  $G$ .

The explicit expression of Equation (55) is very simple, and it is straightforward to bridge the mesoscale blend morphology and macroscale mold-filling process. However, its drawbacks are just as obvious and have been figured out in the literature [61,62]. First of all, the effect of droplet breakup or coalescence on stress is not included in this model, let alone in the case where the ellipsoidal description fails. What is worse, integrating the viscoelasticity of the polymers into the constitutive model of polymer blends based on the ellipsoid description is tough work. Therefore, it is reasonable to develop the rheological model of polymer blends from the molecular physics of polymers.

The simplest physics model for polymeric fluids is the bead-spring model [63], where a polymer molecule is highly coarse-grained into a pair of beads connected by a spring, as depicted in Figure 6. In spite of its extreme simplicity, the bead-spring model is able to reproduce some complex rheological phenomenon of polymers, such as shearing-thinning [64,65], shear-thickening [66,67], and viscoelasticity [68,69].



**Figure 6.** Procedure of the parameter-based scale-bridging methods: (a) macroscopic mold-filling simulation; (b) polymer chains conformation.

However, due to some missing structure details of polymer molecules, it is almost impossible for the bead-spring model to deal with the entanglement of polymer melts, which is inevitable in the processing of polymers.

Molecular models of the dynamics of polymer melts and, more generally, dense polymer solutions began with the famed reptation theory by Gennes [70] and the tube model by Doi and Edwards [71]. Unlike the molecular simulations of small molecule fluids, such as water, the most difficult aspect of the molecular simulations of polymers is the handling of the entanglement problem between molecular chains. Inspired by the notion



of reptation and tubes, proposed by Gennes and Doi and Edwards, subsequent research has developed a series of rheological models for polymer melts.

Likhtman, A.E. and R.S. Graham have demonstrated that the molecular tube theory can also provide a route to constructing a family of very simple differential constitutive equations for linear polymers [72], just like the widely-used Giesekus, PTT, Larson, or pom–pom equations.

Hua, C.C. and J.D. Schieber extended the original (mean-field) tube model to realistic two or three-dimensional (3D) multichain situations and proposed the so-called slip-link model [73], where the polymer entanglement was considered as a pair of slip links, together with the repetitive movement of the probe chain along the primitive path. This idea was followed by many succeeding scholars.

For instance, considering that the polymer melt always undergoes entanglement and crystallization, Andreev, M. and G.C. Rutledge recently introduced two new parameters, which are functions of the degree of crystallinity, to modify the slip-link model [74]. The model was validated using experimental datasets for isotactic polypropylene.

Taletskiy implemented the discretization of the slip-link model through a rigorous mathematical derivation and gave its computational algorithm, optimized especially for coarse-grained simulations, clearing the way for future industrial applications [75].

Becerra, D. et al. constructed a hierarchy of strongly connected models for discrete slip-link theory and presented the method of determining the values of the four parameters of the discrete slip-link model, especially the friction parameter from the first principles of simulation [76].

During the past two decades, the slip-link model has achieved noticeable success and progress; however, its limitations cannot be ignored. The slip-link model is largely applicable to linear polymers but fails to capture the complex rheology of star, branched, or crosslinked polymers.

To overcome this drawback, Masubuchi, Y. et al. developed the PCN model [77]. Polymer chains were coarse-grained at a level of entanglement molecular weight, and the entangled network of polymers was represented in a (3D) real space. Using the PCN model, the viscosity of bidisperse polystyrene melts [78], block copolymers [79], star polymers [80], branched polymers [79], and uncrosslinked and crosslinked polymers [81] was studied for both shear and elongational flow fields, in agreement with both the experimental data and the conventional phenomenological constitutive model [82].

After years of development and maintenance, the PCN model was incorporated into the commercial simulator NAPLES and then as a package of the software J-OCTA for multiscale simulation of polymer processing [83].

More recently, Huang, L.H. et al. proposed a multiscale computer simulation scheme to investigate the stress-morphology coupling of a Nylon 6/ACM blend under processing conditions in a real extruder [84]. The composition–stress–morphology relationship of the polymer blends was crucial for processing and was revealed by a large-scale rheological simulator (NAPLES) without recruiting any freely adjustable parameters. Although this research was aimed at the extrusion of polymers, the proposed strategy was universal and is a promising tool for the analysis of injection molding of polymer blends.

On the other hand, deep learning technology is developing rapidly and has brought revolutionary advances in the engineering and science of polymers [85]. Unlike the phenomenological approach, which obtains the parameters of the constitutive model from experiments, or the numerical approach, which obtains the stress response of polymers through simulation, deep learning techniques provide fuzzy prediction on the rheology of polymers through ever-richer datasets and more rational deep learning algorithms.

Tran, H.D. et al. [86] succeeded in predicting dozens of polymer properties, appropriate for a range of applications, using the web-based machine-learning capability of Polymer Genome.

Alqahtani, A.S. [87] developed a novel model to predict the viscosity of HPAM polymers by combining fundamental, physical models and machine learning methods, with a great agreement with the measurement of the ARES G2 rheometer.

To the authors' knowledge, currently, there is a lack of studies on the rheology of polymer blends using deep learning techniques; the authors suggest that the application of image analysis methods to establish the correlation between the morphology and rheology of polymer blends is a feasible direction.

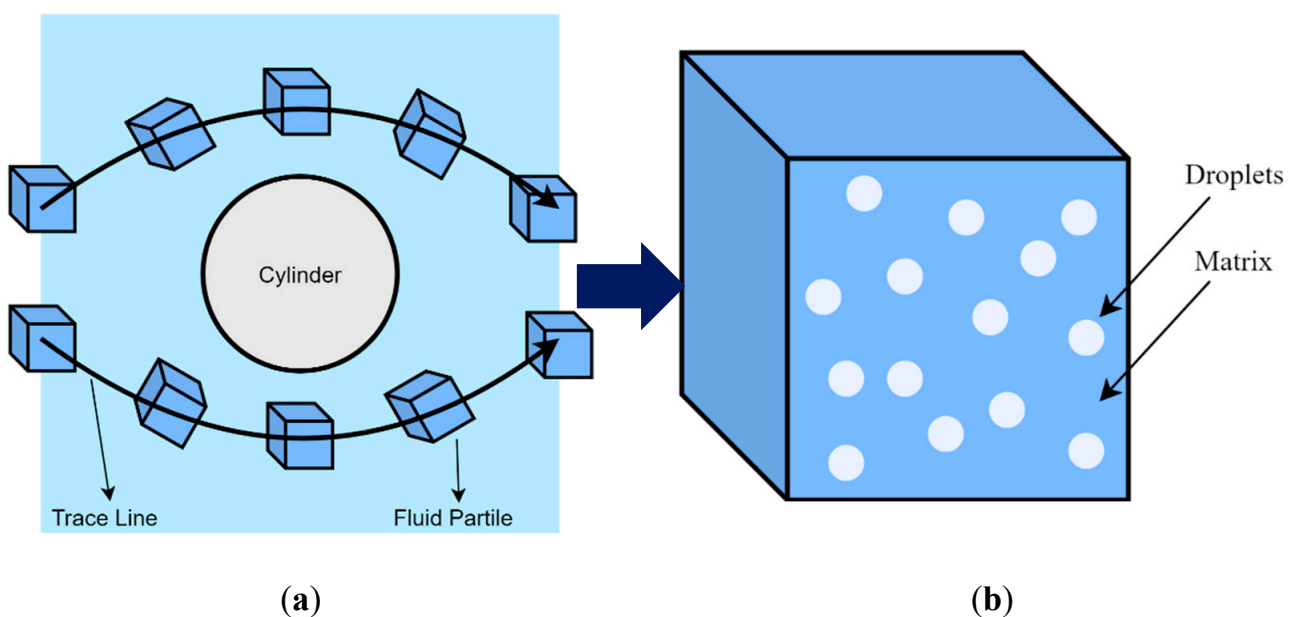
Although deep learning techniques have recently made many valuable explorations in polymer research, they still face several problems and challenges, such as the need for more datasets to train the models; the underlying algorithms of deep learning still need further optimization, and there is the need to get rid of reliance on existing constitutive models. However, it is undeniable that the use of deep learning techniques for the processing of polymers will be a future trend [88].

### 5.2. Particle-Based Methods

In the mold-filling flow of polymer blends, the immersed droplets also drift with the flow rather than being fixed at certain points. The droplet shape is not only decided by the local flow field but also depends on the history of the flow force exerted on it [2]. The Lagrangian description is more direct and has an inherent advantage over the Eulerian description in coupling macroscopic flow field simulation with the mesoscopic polymer blend morphology simulation.

Since the SPH method was established in 1977 by Lucy [89], Gingold, and Monaghan [90], it has become an alternative to the conventional FDM, FEM, and FVM methods in simulating the injection molding of polymers [3,58,91].

In the SPH method, the polymer blend melt is made of a large number of virtual fluid particles, the motion of which is obtained by integrating Newton's second law. Take the flow around a column as an example. As shown in Figure 7, each fluid particle contains a given number of droplets that move inside the particles. While the motion of the fluid particles is simulated using the SPH method, the history of the flow field force on the droplets inside the fluid particles is determined, and then the morphology evolution of the polymer blends during the flow is obtained. In turn, the morphology of the fluid particles contributes to the SPH simulation of the particles' motion.



**Figure 7.** Particle-based scale-bridging method: (a) a fluid particle trace in the flow around circular cylinder; (b) a fluid particle containing droplets.

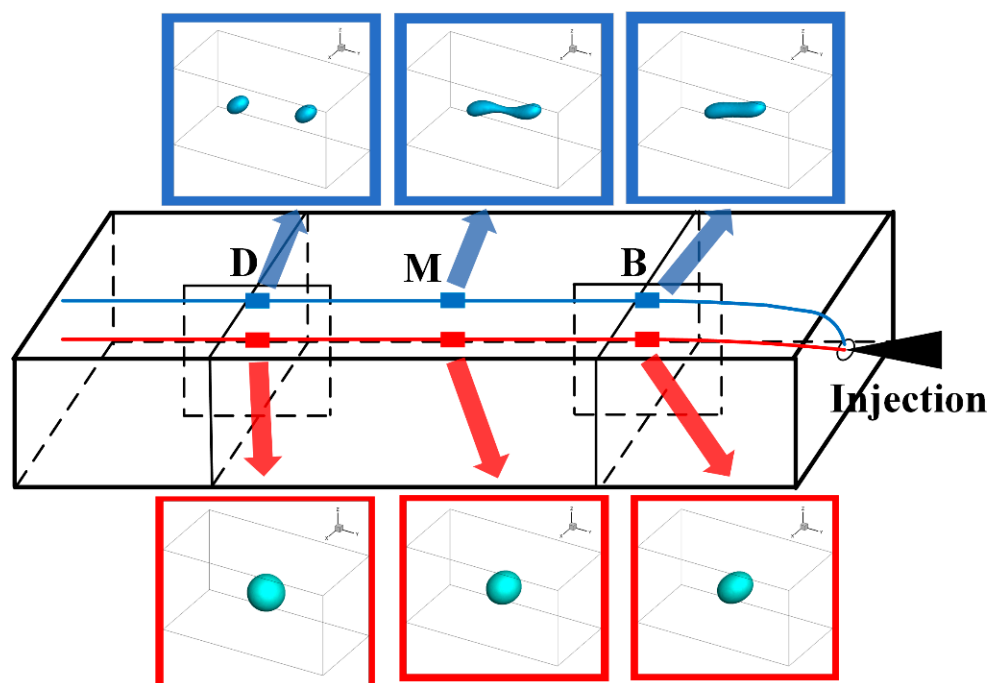
Because of the mesh-free discreteness characteristics of the SPH method, the SPH method can be coupled with whatever micro- or mesoscopic models of the polymers inside the fluid particles.

Murashima, T. et al. integrated molecular dynamics [92] and the coarse-grained dumbbell model [93] with the SPH method to investigate polymeric flow, taking into account the memory effect of polymers.

Likewise, Sato, T. et al. employed the well-known slip-link model inside fluid particles to study entanglement dynamics at the microscopic level [94].

Lee, J. et al. [95] exploited the fact that both SPH and LBM have good parallel computing properties and utilized the LBM inside the fluid particles to simulate the turbulent flow of polymers, the computational cost of which is usually very high.

Recently, Deng et al. [5] integrated the Eulerian model of mold-filling flow and the Lagrangian droplet trajectory tracking method for injection molding of immiscible polymer blends. As shown in Figure 8, different patterns of morphology evolution of the droplets, along their trajectories, were successfully simulated.



**Figure 8.** Droplet morphology evolution along their trajectories during mold-filling.

In theory, the particle-based scale-bridging method is more suitable for the simulation of polymeric flow for the unique memory effect of polymers. However, the Lagrangian macroscopic simulation of the mold-filling flow of polymer melt has many drawbacks and is not as mature as the conventional Eulerian methods. Firstly, it is more difficult to prescribe boundary conditions in SPH than other mesh-based methods; secondly, the computational overhead of the SPH method is remarkably larger, reducing the overall efficiency of the multiscale simulation; furthermore, as the mold-filling flow is a convection-dominant process and the SPH method is explicit, the problem of numerical stability must be observed.

## 6. Outlook and Summary

The development of polymer blend products necessitates an in-depth understanding of the processes at different time and length scales during injection molding. This need has greatly promoted the advance in theoretical and numerical methods to model and simulate the inherent hierarchical phenomena in polymer blends. The present review attempts

to survey the state-of-the-art of various multiscale simulation approaches as applied to polymer blends.

On the macroscopic scale, simulation of the plastic injection molding filling process is a comprehensive technology based on theories and techniques related to many disciplines, and this involves a wide range of research topics. Although fruitful achievements and progress have been made in academia, there are still some areas needing improvement and refinement:

- Polymer melts are mostly viscoelastic fluids. Although the generalized Newtonian fluid model has been able to accurately simulate the filling flow process in most cases, for some products with high requirements on mechanical properties, optical properties, or geometric accuracy, the residual stress caused by viscoelasticity during the filling and packing process is often not negligible. Therefore, how to establish a stable and efficient method for solving the viscoelastic flow solution for the actual product forming process is also an important topic worth studying.
- The energy equation of the filling flow process is significantly convection-dominant, and the boundedness of the discrete scheme of the convection term in the equation has an important impact on the accuracy and stability of the whole filling flow simulation. Therefore, it is necessary to study the discrete scheme of the convection diffusion equation with high accuracy under an unstructured grid to satisfy the boundedness.
- In the simulation of the mold-filling flow process, the solution of the algebraic equation system occupies most of the computational time, among which the solution of the velocity-pressure coupled algebraic equation system takes the most time. Therefore, for the research and development of efficient solution methods for the velocity-pressure-coupled algebraic equation system, shortening the process is also an important part of the next work.

On the mesoscopic scale, some preliminary work has been done for the morphology evolution of individual droplets in simple shear or tensile flow fields, but much remains to be explored and studied with respect to the microstructure evolution inside the blends in more complex injection molding processes:

- When the fraction of the blends exceeds a certain range (greater than about 40%), the dispersed phase no longer exists in the form of isolated droplets, and the simulation algorithm based on the ellipsoidal assumption becomes invalid and other morphology models could be considered, such as the interfacial tensor model.
- Most current models of droplet morphology evolution are limited to Newtonian fluids due to the non-uniformity and strong nonlinearity of the viscoelastic constitutive equations. However, the elasticity of the polymer melt has a significant effect on the evolution of droplet morphology, so the role of component elasticity on phase morphology should be considered, for example, by introducing empirical parameters into the models.
- The evolution equation of droplet size distribution is an important way to parameterize the microstructure of the blend. However, the current evolution models are still based on the ellipsoidal droplet assumption, which cannot characterize the complex morphology of the dispersed phase, so there is a need to establish the evolution equations of the dispersed phase distribution based on the tensor form or the component concentration form in the future.

In terms of macroscopic and mesoscopic scale bridging, particle-based scale coupling methods have been increasingly focused on and applied due to the unsteady flow of the injection molding process and the complex molecular structure of polymers, but there are still some key issues to be studied and solved:

- Compared with traditional Eulerian methods, such as the finite volume method and the finite element method, the SPH method, based on the Lagrangian description, has the natural advantage of automatically recording polymer history in simulating polymer melt flow; however, poor numerical stability, high computational cost, and

difficulty in boundary handling confine its further application in simulating polymer processing, which needs to be addressed in the future.

- The rheological constitutive relationship of polymers is the key to realizing the coupling between macroscopic and mesoscopic scales; however, it is not easy to establish the constitutive relationship of polymer blends in traditional equation form. It is a promising alternative to use the current data-driven modeling method based on deep learning to propose the constitutive relationship of polymer blends.
- Since the size of the dispersed phase droplets in the blend is very small and their number is very large, simulating the morphological evolution of the entire dispersed phase during the mold-filling flow is still unaffordable under current computing power, so it is necessary to investigate the use of parallel computing and GPU accelerometers to increase the efficiency of the simulation and the use of multidimensional fractal theory for the parametric description of dispersed phase morphology.

For injection molding of polymer blends, developing multiscale modeling and simulation methods could lead to the design of products simultaneously, on many scales, instead of trial-and-error experimentations. Although it will not be easy in the forthcoming years, it undeniably represents the remarkable value of the future of polymer science.

**Author Contributions:** Conceptualization, L.D. and Y.Z.; methodology, L.D.; software, S.F.; validation, J.L.; formal analysis, Z.H.; investigation, L.D.; resources, L.D.; data curation, S.F.; writing—original draft preparation, L.D.; writing—review and editing, S.J.; visualization, S.F.; supervision, H.Z.; project administration, Y.Z.; funding acquisition, L.D. All authors have read and agreed to the published version of the manuscript.

**Funding:** This research was funded by National Natural Science Foundation of China grant number 51805379.

**Institutional Review Board Statement:** The study was conducted according to the guidelines of the Declaration of Helsinki, and approved by the Institutional Review Board (or Ethics Committee) of NAME OF INSTITUTE (protocol code XXX and date of approval).

**Informed Consent Statement:** Informed consent was obtained from all subjects involved in the study.

**Data Availability Statement:** The data presented in this study are openly available in corresponding references.

**Acknowledgments:** This work was financially supported by the National Natural Science Foundation of China (no. 51805379).

**Conflicts of Interest:** The authors declare no conflict of interest.

## Abbreviations

$\eta_m$	polymer viscosity of matrix
$\eta_d$	polymer viscosity of droplet
$\gamma$	shear rate
$\Gamma$	interfacial tension
$R$	droplet radius
$D_0$	droplet diameter
$Ca$	capillary number
$Ca_{crit}$	critical capillary number
$p$	viscosity ratio
$G$	ellipsoid droplet tensor
$L$	velocity gradient tensor
$Df$	droplet deformability
$L$	major axis of droplet
$B$	minor axis of droplet
$W$	width of droplet
$\theta$	orientation angle of droplet
$\tau_r$	surface-tension relaxation time

$e_{ij}$	deformation rate tensor
$w_{ij}$	vorticity tensor
$f_1$	MM model parameter
$f_2$	MM model parameter
$k^*$	simplified capillary number
$d$	diameter of the split sub-droplet
$d^*$	critical diameter of fiber breakup
$t_b$	time required for droplet breakup
$N_d$	total number of droplets of volume $V$
$X_m$	main wave number
$p_{coll}$	collision probability
$t_{loc}$	local residence time
$p_{exp}$	liquid film discharge probability
$h_c$	critical thickness of the liquid film for breakup
$D_{eq}$	diameter at equilibrium
$D_{eq}^0$	diameter at zero component
$R^*$	radii of droplets after coalescence
$nk$	number of droplets of volume $kV_1$
$C(i, j)$	coalescence coagulation kernel
$F(i)$	overall breakup frequency
$n_f(i)$	number of fragments formed at breakup of a droplet of volume $iV_1$
$\omega(i, j)$	probability that a fragment formed by the breakup of a droplet of volume $jV_1$ will have volume $iV_1$
$\eta_{app}$	apparent viscosity of the blend
$EDK$	volume energy
$R_0$	droplet radius for $\phi = 0$
$t_B^*$	dimensionless breakup time
$R_c$	critical value for breakup
$R^*$	ratio of $R$ and $R_c$
$D$	diffusion coefficient
$\mu$	chemical potential
$c$	concentration of the fluid
$\xi$	thermal noise
$f_{\sigma,\alpha}(x,t)$	particle probability distribution function
$e\alpha$	discrete particle velocity
$G( e\alpha )$	interaction function of pseudo-potential lattice Boltzmann method
$g_{\sigma\bar{\sigma}}$	interaction constant
$w( e\alpha _2)$	weight function of LBM
$\rho$	density
$u$	velocity
$P$	pressure
$T$	temperature
$c_p$	specific heat
$\lambda$	heat conductivity
$\eta$	viscosity
$A$	area tensor
$\dim$	dimension
$\nu_\sigma$	kinematic viscosity of component $\sigma$
$\rho_\sigma$	density of component $\sigma$
$\tau_\sigma$	relaxation time of component $\sigma$
$j_\sigma$	momentum flux of component $\sigma$

## References

1. Zhou, H. *Computer Modeling for Injection Molding: Simulation, Optimization, and Control*; Wiley: Hoboken, NJ, USA, 2013. [[CrossRef](#)]
2. Tucker, C.L., III; Moldenaers, P. Microstructural evolution in polymer blends. *Ann. Rev. Fluid Mech.* **2002**, *34*, 177–210. [[CrossRef](#)]
3. Ren, M.K.; Gu, J.F.; Li, Z.; Ruan, S.L.; Shen, C.Y. Simulation of polymer melt injection molding filling Flow based on an improved SPH method with modified low-dissipation riemann solver. In *Macromol. Theory Simulations*; Wiley Online Library: Hoboken, NJ, USA, 2021. [[CrossRef](#)]

4. Ying, J.; Xie, X.; Peng, S.; Zhou, H.; Li, D. Morphology and rheology of PP/POE blends in high shear stress field. *J. Thermoplast. Compos. Mater.* **2018**, *31*, 1263–1280. [[CrossRef](#)]
5. Deng, L.; Fan, S.; Zhang, Y.; Huang, Z.G.; Jiang, S.F.; Li, J.Q.; Zhou, H.M. A novel multiscale methodology for simulating droplet morphology evolution during injection molding of polymer blends. *Polymers* **2021**, *13*, 133. [[CrossRef](#)]
6. Iza, M.; Bousmina, M. Nonlinear rheology of immiscible polymer blends: Step strain experiments. *J. Rheol.* **2000**, *44*, 1363–1384. [[CrossRef](#)]
7. Taylor, G.I. The viscosity of a fluid containing small drops of another fluid. *Proc. R. Soc. Lond. Ser. A* **1932**, *138*, 41–48.
8. Doi, M.; Ohta, T. Dynamics and rheology of complex interfaces. I. *J. Chem. Phys.* **1991**, *95*, 1242–1248. [[CrossRef](#)]
9. Maffettone, P.L.; Minale, M. Equation of change for ellipsoidal drops in viscous flow. *J. Non-Newton. Fluid Mech.* **1998**, *78*, 227–241. [[CrossRef](#)]
10. Jackson, N.E.; Tucker, C.L. A model for large deformation of an ellipsoidal droplet with interfacial tension. *J. Rheol.* **2003**, *47*, 659–682. [[CrossRef](#)]
11. Eshelby, J.D. The Determination of the elastic field of an ellipsoidal inclusion, and related problems. *Proc. R. Soc. Math. Phys. Eng. Sci.* **1957**, *241*, 376–396. [[CrossRef](#)]
12. Khakhar, D.V.; Ottino, J.M. Deformation and breakup of slender drops in linear flows. *J. Fluid Mech.* **1986**, *166*, 265–285. [[CrossRef](#)]
13. Yu, W.; Bousmina, M. Ellipsoidal model for droplet deformation in emulsions. *J. Rheol.* **2003**, *47*, 1011–1039. [[CrossRef](#)]
14. Janssen, J.M.H. Dynamics of liquid-liquid mixing. *Polym. Eng. Sci.* **1995**, *35*, 1766–1780. [[CrossRef](#)]
15. Cox, R. The deformation of a drop in a general time-dependent fluid flow. *J. Fluid Mech.* **1969**, *37*, 601–623. [[CrossRef](#)]
16. Delaby, I.; Ernst, B.; Froelich, D.; Muller, R. Droplet deformation in immiscible polymer blends during transient uniaxial elongational flow. *Polym. Eng. Sci.* **1996**, *36*, 1627–1635. [[CrossRef](#)]
17. Elemans, P. Modelling of Processing of Incompatible Polymer Blends. Ph.D. Thesis, Technische Universiteit Eindhoven, Eindhoven, The Netherlands, 1989.
18. Huneault, Z.; Shi, H.; Utracki, L.A. Development of polymer blend morphology during compounding in a twin-screw extruder. Part IV: A new computational model with coalescence. *Polym. Eng. Sci.* **1995**, *35*, 115–127. [[CrossRef](#)]
19. Debruijn, R.A. Deformation and Breakup of Drops in Simple Shear Flows. Ph.D. Thesis, Technische Universiteit Eindhoven, Eindhoven, The Netherlands, 1991.
20. Grace, H.P. Dispersion phenomena in high viscosity immiscible fluid systems and application of static mixers as dispersion devices in such systems. *Chem. Eng. Commun.* **1982**, *14*, 225–277. [[CrossRef](#)]
21. Rayleigh, L. On the instability of jets. *Proc. Lond. Math. Soc.* **1878**, *1*, 4–13. [[CrossRef](#)]
22. Loor, A.D.; Cassagnau, P.; Michel, A.; Vergnes, B. Morphological changes of a polymer blend into a twin-screw extruder. *Int. Polym. Process. J. Polym. Process. Soc.* **1994**, *9*, 211–218. [[CrossRef](#)]
23. Fortelný, I. Theoretical aspects of phase morphology development. In *Micro- and Nanostructured Multiphase Polymer Blend Systems*; CRC Press: Boca Raton, FL, USA, 2005.
24. Tokita, N. Analysis of morphology formation in elastomer blends. *Rubber Chem. Technol.* **1977**, *50*, 292–300. [[CrossRef](#)]
25. Fortelný, I.; Jůza, J. Prediction of average droplet size in flowing immiscible polymer blends. *J. Appl. Polym. Sci.* **2017**, *134*, 45250. [[CrossRef](#)]
26. Cristini, V.; Guido, S.; Alfani, A.; Blawdziewicz, J.; Loewenberg, M. Drop breakup and fragment size distribution in shear flow. *J. Rheol.* **2003**, *47*, 1283–1298. [[CrossRef](#)]
27. Fortelný, I.; Dimzoski, B.; Michálková, D.; Mikešová, J.; Kaprálková, L. Dependence of the average size of particles formed during steady mixing on their concentration in immiscible polymer blends. *J. Macromol. Sci. Part B* **2013**, *52*, 662–673. [[CrossRef](#)]
28. Fortelný, I.; Ostafińska, A.; Michálková, D.; Jůza, J.; Mikešová, J.; Šlouf, M. Phase structure evolution during mixing and processing of poly(lactic acid)/polycaprolactone (PLA/PCL) blends. *Polym. Bull.* **2015**, *72*, 2931–2947. [[CrossRef](#)]
29. Patlazhan, S.A.; Lindt, J.T. Kinetics of structure development in liquid-liquid dispersions under simple shear flow—Theory. *J. Rheol.* **1996**, *40*, 1095–1113. [[CrossRef](#)]
30. Janssen, J. Emulsions: The dynamics of liquid-liquid mixing. In *Materials Science and Technology*; Wiley: Hoboken, NJ, USA, 2006.
31. Delamare, L.; Vergnes, B. Computation of the morphological changes of a polymer blend along a twin-screw extruder. *Polym. Eng. Sci.* **1996**, *36*, 1685–1693. [[CrossRef](#)]
32. Potente, H.; Bastian, M. Calculating morphology development of polymer blends in extruders on the basis of results of boundary and finite element simulations using the sigma simulation software. *Polym. Eng. Sci.* **2000**, *40*, 727–737. [[CrossRef](#)]
33. Peters, G.W.M.; Hansen, S.; Meijer, H.E.H. Constitutive modeling of dispersive mixtures. *J. Rheol.* **2001**, *45*, 659–689. [[CrossRef](#)]
34. Lee, H.M.; Park, O.O. Rheology and dynamics of immiscible polymer blends. *J. Rheol.* **1994**, *38*, 1405–1425. [[CrossRef](#)]
35. Wong, W.-H.B.; Janssen, P.J.A.; Hulsen, M.A.; Anderson, P.D. Numerical simulations of the polydisperse droplet size distribution of disperse blends in complex flow. *Rheol. Acta* **2021**, *60*, 187–207. [[CrossRef](#)]
36. Spencer, R.; Gilmore, G. Some flow phenomena in the injection molding of polystyrene. *J. Colloid Sci.* **1951**, *6*, 118–132. [[CrossRef](#)]
37. Kovács, M.; Larsson, S.; Mesforush, A. Finite element approximation of the Cahn–Hilliard–Cook equation. *SIAM J. Numer. Anal.* **2011**, *49*, 2407–2429. [[CrossRef](#)]
38. Prusty, M.; Keestra, B.; Goossens, J.; Anderson, P. Experimental and computational study on structure development of PMMA/SAN blends. *Chem. Eng. Sci.* **2007**, *62*, 1825–1837. [[CrossRef](#)]

39. Koehler, W.; Krekhov, A.; Zimmermann, W. Thermal diffusion in polymer blends: Criticality and pattern formation. In *Complex Macromolecular Systems I*; Muller, A.H.E., Schmidt, H.W., Eds.; Springer: Berlin/Heidelberg, Germany, 2010; Volume 227, pp. 145–198.
40. Keestra, B.J.; Goossens, J.G.P.; Anderson, P.D. Structure development of PMMA/SAN blends in shear flow. *Chem. Eng. Sci.* **2011**, *66*, 4960–4971. [[CrossRef](#)]
41. Parsa, M.A.; Ghiass, M.; Moghbeli, M.R. Mathematical modelling and phase separation kinetics of polystyrene/polyvinylmethylether blend. *Iran. Polym. J.* **2011**, *20*, 689–696.
42. Carolan, D.; Chong, H.M.; Ivankovic, A.; Kinloch, A.J.; Taylor, A.C. Co-continuous polymer systems: A numerical investigation. *Comput. Mater. Sci.* **2015**, *98*, 24–33. [[CrossRef](#)]
43. Tabatabaieyazdi, M.; Chan, P.K.; Wu, J. A computational study of long range surface-directed phase separation in polymer blends under a temperature gradient. *Comput. Mater. Sci.* **2016**, *111*, 387–394. [[CrossRef](#)]
44. Jelic, A.; Ilg, P.; Ottinger, H.C. Bridging length and time scales in sheared demixing systems: From the Cahn-Hilliard to the Doi-Ohta model. *Phys. Rev. E* **2010**, *81*, 011131. [[CrossRef](#)]
45. Zander, C.; Hopp-Hirschler, M.; Nieken, U. Mesoscopic simulation and characterization of the morphological evolution in phase separating fluid mixtures. *Comput. Mater. Sci.* **2018**, *149*, 267–281. [[CrossRef](#)]
46. Rothman, D.H.; Keller, J.M. Immiscible cellular-automaton fluids. *J. Stat. Phys.* **1988**, *52*, 1119–1127. [[CrossRef](#)]
47. Gunstensen, A.K.; Rothman, D.H.; Zaleski, S.; Zanetti, G. Lattice Boltzmann model of immiscible fluids. *Phys. Rev. A* **1991**, *43*, 4320. [[CrossRef](#)]
48. Shan, X.; Chen, H. Simulation of nonideal gases and liquid-gas phase transitions by the lattice Boltzmann equation. *Phys. Rev. E* **1994**, *49*, 2941–2948. [[CrossRef](#)]
49. Swift, M.R.; Orlandini, E.; Osborn, W.R.; Yeomans, J.M. Lattice Boltzmann simulations of liquid-gas and binary fluid systems. *Phys. Rev. E* **1996**, *54*, 5041. [[CrossRef](#)] [[PubMed](#)]
50. He, X.Y.; Chen, S.Y.; Zhang, R.Y. A lattice Boltzmann scheme for incompressible multiphase flow and its application in simulation of Rayleigh-Taylor instability. *J. Comput. Phys.* **1999**, *152*, 642–663. [[CrossRef](#)]
51. Shan, X.; Doolen, G. Multicomponent lattice-Boltzmann model with interparticle interaction. *J. Stat. Phys.* **1995**, *81*, 379–393. [[CrossRef](#)]
52. Pantani, R.; Speranza, V.; Titomanlio, G. Thirty years of modeling of injection molding. A brief review of the contribution of UNISA code to the Field. *Int. Polym. Proc.* **2016**, *31*, 655–663. [[CrossRef](#)]
53. Liparoti, S.; Speranza, V.; Pantani, R.; Titomanlio, G. Modeling of the injection molding process coupled with the fast mold temperature evolution. *J. Electrochem. Soc.* **2019**, *166*, B3148–B3155. [[CrossRef](#)]
54. Li, Q.; Ouyang, J.; Wu, G.; Xu, X. Numerical simulation of melt filling and gas penetration in gas assisted injection molding. *Comput. Model. Eng. Sci.* **2011**, *82*, 215–232. [[CrossRef](#)]
55. Vietri, U.; Sorrentino, A.; Speranza, V.; Pantani, R. Improving the predictions of injection molding simulation software. *Polym. Eng. Sci.* **2011**, *51*, 2542–2551. [[CrossRef](#)]
56. He, L.; Lu, G.; Chen, D.; Li, W.; Lu, C. Three-dimensional smoothed particle hydrodynamics simulation for injection molding flow of short fiber-reinforced polymer composites. *Model. Simul. Mater. Sci. Eng.* **2017**, *25*, aa6dc9. [[CrossRef](#)]
57. Liang, J.; Luo, W.; Huang, Z.; Zhou, H.; Zhang, Y.; Zhang, Y.; Fu, Y. A robust finite volume method for three-dimensional filling simulation of plastic injection molding. *Eng. Comput.* **2017**, *34*, 814–831. [[CrossRef](#)]
58. Xu, X.Y.; Yu, P. Modeling and simulation of injection molding process of polymer melt by a robust SPH method. *Appl. Math. Model.* **2017**, *48*, 384–409. [[CrossRef](#)]
59. Liu, Q.S.; Liu, Y.Q.; Jiang, C.T.; Wang, X.H. Numerical simulation of viscoelastic flows during injection mold filling based on Rolie-Poly model. *J. Non-Newton. Fluid Mech.* **2019**, *263*, 140–153. [[CrossRef](#)]
60. Yu, W.; Zhou, C. A simple constitutive equation for immiscible blends. *J. Rheol.* **2007**, *51*, 179–194. [[CrossRef](#)]
61. Zou, F.S.; Dong, X.; Lin, D.M.; Liu, W.; Wang, D.J.; Han, C.C. Morphological and rheological responses to the transient and steady shear flow for a phase-separated polybutadiene/polyisoprene blend. *Polymer* **2012**, *53*, 4818–4826. [[CrossRef](#)]
62. Mwasame, P.M.; Wagner, N.J.; Beris, A.N. On the macroscopic modelling of dilute emulsions under flow. *J. Fluid Mech.* **2017**, *831*, 433–473. [[CrossRef](#)]
63. Liu, B.; Wang, J.; Fan, X.; Kong, Y.; Gao, H. An effective bead-spring model for polymer simulation. *J. Comput. Phys.* **2008**, *227*, 2794–2807. [[CrossRef](#)]
64. Datta, R.; Yelash, L.; Schmid, F.; Kummer, F.; Oberlack, M.; Lukáčová-Medvid'ová, M.; Virnau, P. Shear-thinning in oligomer melts—Molecular origins and applications. *Polymers* **2021**, *13*, 2806. [[CrossRef](#)]
65. Ryder, J.F.; Yeomans, J.M. Shear thinning in dilute polymer solutions. *J. Chem. Phys.* **2006**, *125*, 194906. [[CrossRef](#)] [[PubMed](#)]
66. Cruz, C.; Chinesta, F.; Regnier, G. Review on the brownian dynamics simulation of bead-rod-spring models encountered in computational rheology. *Arch. Comput. Methods Eng.* **2012**, *19*, 227–259. [[CrossRef](#)]
67. Fetisko, S.W.; Cummings, P.T. Brownian dynamics simulation of bead-spring chain models for dilute polymer solutions in elongational flow. *J. Rheol.* **1995**, *39*, 285–299. [[CrossRef](#)]
68. Townsend, A.K.; Wilson, H.J. Small-and large-amplitude oscillatory rheometry with bead-spring dumbbells in Stokesian Dynamics to mimic viscoelasticity. *J. Non-Newton. Fluid Mech.* **2018**, *261*, 136–152. [[CrossRef](#)]



69. Vladkov, M.; Barrat, J.-L. Linear and nonlinear viscoelasticity of a model unentangled polymer melt: Molecular dynamics and rouse modes analysis. *Macromol. Theory Simul.* **2006**, *15*, 252–262. [[CrossRef](#)]
70. Gennes, P.G.D. Reptation of a polymer chain in the presence of fixed obstacles. *J. Chem. Phys.* **1971**, *55*, 572–579. [[CrossRef](#)]
71. Doi, M.; Edwards, S.F. Dynamics of concentrated polymer systems. Part 3—The constitutive equation. *J. Chem. Soc. Faraday Trans. 2 Mol. Chem. Phys.* **1978**, *74*, 1818–1832. [[CrossRef](#)]
72. Likhtman, A.E.; Graham, R.S. Simple constitutive equation for linear polymer melts derived from molecular theory: Rolie-Poly equation. *J. Non-Newton. Fluid Mech.* **2003**, *114*, 1–12. [[CrossRef](#)]
73. Hua, C.C.; Schieber, J.D. Segment connectivity, chain-length breathing, segmental stretch, and constraint release in reptation models. I. Theory and single-step strain predictions. *J. Chem. Phys.* **1998**, *109*, 10018–10027. [[CrossRef](#)]
74. Andreev, M.; Rutledge, G.C. A slip-link model for rheology of entangled polymer melts with crystallization. *J. Rheol.* **2020**, *64*, 213–222. [[CrossRef](#)]
75. Taletskiy, K. *Entangled Polymer Rheology: Efficient Algorithms and Coarse-Graining of Slip-Link Model*; Illinois Institute of Technology: Chicago, IL, USA, 2018.
76. Becerra, D.; Cordoba, A.; Katarova, M.; Andreev, M.; Venerus, D.C.; Schieber, J.D. Polymer rheology predictions from first principles using the slip-link model. *J. Rheol.* **2020**, *64*, 1035–1043. [[CrossRef](#)]
77. Masubuchi, Y.; Takimoto, J.-I.; Koyama, K.; Ianniruberto, G.; Marrucci, G.; Greco, F. Brownian simulations of a network of reptating primitive chains. *J. Chem. Phys.* **2001**, *115*, 4387–4394. [[CrossRef](#)]
78. Takeda, K.; Sukumaran, S.K.; Sugimoto, M.; Koyama, K.; Masubuchi, Y. Primitive chain network simulations for elongational viscosity of bidisperse polystyrene melts. *Adv. Model. Simul. Eng. Sci.* **2015**, *2*, 11. [[CrossRef](#)]
79. Masubuchi, Y.; Ianniruberto, G.; Greco, F.; Marrucci, G. Primitive chain network model for block copolymers. *J. Non-Crystalline Solids* **2006**, *352*, 5001–5007. [[CrossRef](#)]
80. Masubuchi, Y.; Ianniruberto, G.; Marrucci, G. Primitive chain network simulations of entangled melts of symmetric and asymmetric star polymers in uniaxial elongational flows. *arXiv* **2021**, arXiv:2101.06819.
81. Li, Y.; Kröger, M.; Liu, W.K. Primitive chain network study on uncrosslinked and crosslinked cis-polyisoprene polymers. *Polymer* **2011**, *52*, 5867–5878. [[CrossRef](#)]
82. Masubuchi, Y.; Matsumiya, Y.; Watanabe, H.; Marrucci, G.; Ianniruberto, G. Primitive chain network simulations for pom-pom polymers in uniaxial elongational flows. *Macromolecules* **2014**, *47*, 3511–3519. [[CrossRef](#)]
83. Masubuchi, Y. PASTA and NAPLES: Rheology simulator. In *Computer Simulation of Polymeric Materials: Applications of the OCTA System*; Springer: Singapore, 2016; pp. 101–127. [[CrossRef](#)]
84. Huang, L.H.; Wu, C.H.; Hua, C.C.; Huang, T.J. Multiscale simulations of coupled composition-stress-morphology of binary polymer blend. *Polymer* **2020**, *193*, 122366. [[CrossRef](#)]
85. Sha, W.; Li, Y.; Tang, S.; Tian, J.; Zhao, Y.; Guo, Y.; Zhang, W.; Zhang, X.; Lu, S.; Cao, Y.-C.; et al. Machine learning in polymer informatics. *InfoMat* **2021**, *3*, 353–361. [[CrossRef](#)]
86. Tran, H.D.; Kim, C.; Chen, L.H.; Chandrasekaran, A.; Batra, R.; Venkatram, S.; Kamal, D.; Lightstone, J.P.; Gurnani, R.; Shetty, P.; et al. Machine-learning predictions of polymer properties with Polymer Genome. *J. Appl. Phys.* **2020**, *128*, 171104. [[CrossRef](#)]
87. Alqahtani, A.S. New Polymer Rheology Models Based on Machine Learning. Ph.D. Thesis, The University of Texas at Austin, Austin, TX, USA, 2019.
88. Larson, R.G.; Desai, P.S. Modeling the rheology of polymer melts and solutions. *Annu. Rev. Fluid Mech.* **2015**, *47*, 47–65. [[CrossRef](#)]
89. Lucy, L.B. A numerical approach to the testing of the fission hypothesis. *Astron. J.* **1977**, *82*, 1013–1024. [[CrossRef](#)]
90. Gingold, R.A.; Monaghan, J.J. Smoothed particle hydrodynamics: Theory and application to non-spherical stars. *Mon. Not. R. Astron. Soc.* **1977**, *181*, 375–389. [[CrossRef](#)]
91. de Campos Galuppo, W.; Magalhães, A.; Ferrás, L.L.; Nóbrega, J.M.; Fernandes, C. New boundary conditions for simulating the filling stage of the injection molding process. *Eng. Comput.* **2021**, *38*, 762–778. [[CrossRef](#)]
92. Murashima, T.; Yasuda, S.; Taniguchi, T.; Yamamoto, R. Multiscale modeling for polymeric flow: Particle-fluid bridging scale methods. *J. Phys. Soc. Jpn.* **2013**, *82*, 012001. [[CrossRef](#)]
93. Murashima, T.; Taniguchi, T. Multiscale lagrangian fluid dynamics simulation for polymeric fluid. *J. Polym. Sci. Pol. Phys.* **2010**, *48*, 886–893. [[CrossRef](#)]
94. Sato, T.; Taniguchi, T. Multiscale simulations for entangled polymer melt spinning process. *J. Non-Newton. Fluid Mech.* **2017**, *241*, 34–42. [[CrossRef](#)]
95. Lee, J.; Dunweg, B.; Schumacher, J. Multiscale modelling strategy using the lattice Boltzmann method for polymer dynamics in a turbulent flow. *Comput. Math. Appl.* **2010**, *59*, 2374–2379. [[CrossRef](#)]

## Article

# A Semi-Analytical Method for Channel and Pipe Flows for the Linear Phan-Thien-Tanner Fluid Model with a Solvent Contribution

Matheus Tozo de Araujo <sup>1,†</sup>, Laison Furlan <sup>1,†</sup>, Analice Brandi <sup>2,†</sup> and Leandro Souza <sup>1,\*,†</sup><sup>1</sup> Department of Applied Mathematics and Statistics, University of Sao Paulo, Sao Carlos 13566-590, Brazil<sup>2</sup> Department of Mathematics and Computer Science, Sao Paulo State University, Presidente Prudente 19060-900, Brazil

\* Correspondence: lefraso@icmc.usp.br

† These authors contributed equally to this work.

**Abstract:** This work presents a semi-analytical method for laminar steady-state channel and pipe flows of viscoelastic fluids using the Linear Phan-Thien-Tanner (LPTT) constitutive equation, with solvent viscosity contribution. For the semi-analytical method validation, it compares its results and two analytical solutions: the Oldroyd-B model and the simplified LPTT model (without solvent viscosity contribution). The results adopted different values of the dimensionless parameters, showing their influence on the viscoelastic fluid flow. The results include the distribution of the streamwise velocity component and the extra-stress tensor components in the wall-normal direction. In order to investigate the proposed semi-analytical method, different solutions were obtained, both for channel and pipe flows, considering different values of Reynolds number, solvent viscosity contribution in the homogeneous mixture, elongational parameter, shear parameter, and Weissenberg number. The results show that the proposed semi-analytical method can find a laminar solution using the non-Newtonian LPTT model with solvent viscosity contribution and verify the effect of the parameters in the resulting flow field.

**Keywords:** Phan-Thien-Tanner constitutive equation; semi-analytical method; solvent viscosity contribution; pipe flow; channel flow

**Citation:** de Araujo, M.T.; Furlan, L.; Brandi, A.; Souza, L.

A Semi-Analytical Method for Channel and Pipe Flows for the Linear Phan-Thien-Tanner Fluid Model with a Solvent Contribution'. *Polymers* **2022**, *14*, 4675. <https://doi.org/10.3390/polym14214675>

Academic Editor: Célio Bruno Pinto Fernandes

Received: 17 October 2022

Accepted: 29 October 2022

Published: 2 November 2022

**Publisher's Note:** MDPI stays neutral with regard to jurisdictional claims in published maps and institutional affiliations.



**Copyright:** © 2022 by the authors. Licensee MDPI, Basel, Switzerland. This article is an open access article distributed under the terms and conditions of the Creative Commons Attribution (CC BY) license (<https://creativecommons.org/licenses/by/4.0/>).

## 1. Introduction

Due to the use of viscoelastic fluids in some industries, there is interest in obtaining an analytical solution of constitutive models that describe the behaviour of this type of fluid flow. Several researchers have investigated the analytical solutions of many constitutive models, such as the Oldroyd-B, Giesekus, FENE, and PTT models. Investigations of non-Newtonian fluid flow with heat transfer is also an interesting phenomena [1,2]. Hulsen [3] presented the analytical solution of the Leonov and Giesekus models and some properties such as tensor restrictions and the possibility of arising instabilities due to numerical approximation errors.

An exact solution for tube and slit flows of a FENE-P fluid was found by [4]. Yoo and Choi [5] and Schleiniger and Weinacht [6] present solutions for pipe and channel flows of the Giesekus model for Poiseuille flow. With the same model, Raisi et al. [7] obtained the solution for the Couette-Poiseuille flow. Hayat et al. [8] derived the exact solution for the Oldroyd-B model applied to five different flow problems, and Hayat et al. [9] presented the exact solution of this same model to six different problems of unsteady flow.

More recently, Tomé et al. [10] presented a way to obtain the analytical solution for the Giesekus model (based on [6]), with the pressure gradient being calculated numerically and considering  $\beta = 0$ . Furlan et al. [11] studied an analytical solution of the Giesekus model without restrictions on the model parameters.

There are several studies in the literature in which the analytical solution for the LPTT model is obtained. For the simplified LPTT model, the solutions are presented in [12–15] and the solution for the LPTT model for purely polymeric fluid flow without simplifications is presented in Alves et al. [16]. There is a simplification of the LPTT model equations in the solutions referenced above: the parameter  $\zeta = 0$  in the LPTT model or the solvent contribution is considered zero in the homogeneous mixture.

The present work shows a semi-analytical method to obtain the flow variables when using the LPTT viscoelastic fluid model for channel and pipe flow without simplifications and considering a solvent contribution in the homogeneous mixture. Channel flow is referred to as the two-dimensional flow between two parallel plates. The proposed method is valid for laminar flow.

The paper is organized as follows. Section 2 presents the governing equations and the mathematical manipulations needed to obtain the semi-analytical method for the LPTT fluid flow with a solvent contribution in the homogeneous mixture; the results obtained using the method proposed are presented in Section 3. The main conclusions are presented in Section 4.

## 2. Mathematical Formulation

The Phan-Thien-Tanner (PTT) constitutive equation was derived from Phan-Thien and Tanner [17] work. The viscoelastic fluid model considered in this analysis is governed by its dimensional form given by:

$$f(\text{tr}(\mathbf{T}))\mathbf{T} + \lambda \left( \frac{\partial \mathbf{T}}{\partial t} + \nabla \cdot (\mathbf{u}\mathbf{T}) - (\nabla \mathbf{u} - \zeta \mathbf{D}) \cdot \mathbf{T} - \mathbf{T} \cdot (\nabla \mathbf{u} - \zeta \mathbf{D})^T \right) = 2\eta_p \mathbf{D}, \quad (1)$$

where  $\mathbf{u}$  denotes the velocity field,  $t$  is the time,  $\mathbf{T}$  and  $\mathbf{D}$  are the extra-stress and deformation-rate tensors, respectively,  $\lambda$  is the fluid relaxation time,  $\eta_p$  is the polymer viscosity, and  $\zeta$  is a positive parameter of the PTT model connected with the shear stress behaviour of the fluid.

The function  $f(\text{tr}(\mathbf{T}))$  depends on the trace of extra-stress tensor  $\mathbf{T}$  and determines the form of the PTT model [18]:

- (i) Linear:  $f(\text{tr}(\mathbf{T})) = 1 + \frac{\lambda \epsilon}{\eta_p} \text{tr}(\mathbf{T})$ ,
- (ii) Quadratic:  $f(\text{tr}(\mathbf{T})) = 1 + \frac{\lambda \epsilon}{\eta_p} \text{tr}(\mathbf{T}) + \frac{1}{2} \left( \frac{\lambda \epsilon}{\eta_p} \text{tr}(\mathbf{T}) \right)^2$ ,
- (iii) Exponential:  $f(\text{tr}(\mathbf{T})) = \exp \left( \frac{\lambda \epsilon}{\eta_p} \text{tr}(\mathbf{T}) \right)$ .

The linear form was the original form proposed by Phan-Thien and Tanner [17], and it was used for the PTT model in this work, also called the LPTT model. The parameter  $\epsilon$  in the function  $f(\text{tr}(\mathbf{T}))$  is related to the elongational behaviour of the fluid, precluding an infinite elongational viscosity in a simple stretching flow as it would occur for an upper-convected Maxwell model (UCM), in which  $\epsilon = 0$  [13].

It is considered a fully developed flow for two-dimensional channel and axisymmetric pipe flow (Figure 1). The flow is considered incompressible and isothermal, without the influences of external forces. Furthermore, it is used a compact notation [16,19] with index  $j = 0$  for channel flow or  $j = 1$  for pipe flow.

In the fully developed flows analyzed here (parallel flow), the velocity and extra-stress tensor components are function of the cross-stream coordinate ( $y$  or  $r$ ), the pressure gradient in the streamwise direction  $P_x$  is constant and the continuity equation implies a zero transverse velocity component ( $v = 0$ ).

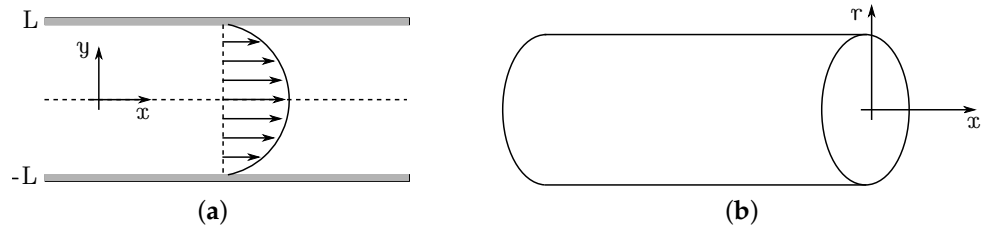


Figure 1. Poiseuille planar channel (a), and Poiseuille pipe (b) flows.

With the adopted formulation, the  $x$ -momentum equation does not change with the non-Newtonian constitutive model and can be integrated to give

$$-P_x \frac{y}{2^j} + \frac{\beta}{Re} \frac{du(y)}{dy} + T_{xy}(y) = 0. \tag{2}$$

The constitutive equation for each extra-stress tensor component, giving the assumption of parallel flow, can be simplified to the following set of expressions

$$\left(1 + \frac{\epsilon Re Wi}{(1-\beta)} (T_{xx}(y) + T_{yy}(y))\right) T_{xx}(y) = 2Wi \left(1 - \frac{\xi}{2}\right) T_{xy}(y) \frac{du(y)}{dy}, \tag{3}$$

$$\begin{aligned} \left(1 + \frac{\epsilon Re Wi}{(1-\beta)} (T_{xx}(y) + T_{yy}(y))\right) T_{xy}(y) &= \frac{(1-\beta)}{Re} \frac{du(y)}{dy} + \\ &- Wi \left(\frac{\xi}{2} T_{xx}(y) \frac{du(y)}{dy} - \left(1 - \frac{\xi}{2}\right) T_{yy}(y) \frac{du(y)}{dy}\right), \end{aligned} \tag{4}$$

$$\left(1 + \frac{\epsilon Re Wi}{(1-\beta)} (T_{xx}(y) + T_{yy}(y))\right) T_{yy}(y) = -Wi \xi T_{xy}(y) \frac{du(y)}{dy}. \tag{5}$$

The system of Equations (2)–(5) is in dimensionless form where the dimensionless parameters  $Re = \frac{\rho UL}{\eta_0}$  and  $Wi = \frac{\lambda U}{L}$  denote the Reynolds and Weissenberg numbers, respectively. The Reynolds number is based in total shear viscosity  $\eta_0$ , and  $\eta_0 = \eta_s + \eta_p$  where  $\eta_s$  and  $\eta_p$  represent the Newtonian solvent and polymeric viscosities, respectively, and  $\rho$  is the fluid density,  $U$  is the velocity scale and  $L$  is the channel (or pipe) half-width. The amount of Newtonian solvent is controlled by the dimensionless solvent viscosity coefficient, parameter  $\beta = \frac{\eta_s}{\eta_0}$ . In Weissenberg number the  $\lambda$  parameter is the relaxation-time of the fluid.

Dividing Equation (3) by Equation (5), the relation between the extra-stress tensor components  $T_{xx}(y)$  and  $T_{yy}(y)$ , can be obtained:

$$T_{yy}(y) = \frac{\xi T_{xx}(y)}{-2 + \xi}. \tag{6}$$

From Equation (2) it can be obtained:

$$\frac{du(y)}{dy} = -\frac{Re(T_{xy}(y) - 2^{-j} P_x y)}{\beta}. \tag{7}$$

Substituting Equations (6) and (7) in Equation (3) and solving the resulting equation for the tensor component  $T_{xx}(y)$ , it can be obtained:

$$\begin{aligned} T_{xx}(y) = & -\left(\frac{(-1 + \beta)(-2 + \xi)}{4\epsilon Re Wi(-1 + \xi)}\right) \left(-1 \pm \left(1 - 2^{3-j} \epsilon Re^2 T_{xy}(y) Wi^2 \times \right. \right. \\ & \left. \left. \times \frac{(2^j T_{xy}(y) - P_x y)(-1 + \xi)}{(-1 + \beta)\beta}\right)^{\frac{1}{2}}\right). \end{aligned}$$

Using the hypothesis that the extra-stress tensor is zero at the channel (or pipe) centre, one solution can be discarded, resulting thus in a single solution for the tensor  $T_{xx}(y)$ :

$$T_{xx}(y) = - \left( \frac{(-1 + \beta)(-2 + \xi)}{4\epsilon Re Wi (-1 + \xi)} \right) \left( -1 + \left( 1 - 2^{3-j} \epsilon Re^2 T_{xy}(y) Wi^2 \times \right. \right. \tag{8}$$

$$\left. \left. \times \frac{(2^j T_{xy}(y) - P_x y)(-1 + \xi)}{(-1 + \beta)\beta} \right)^{\frac{1}{2}} \right).$$

All solutions obtained for the flow components are functions of the tensor component  $T_{xy}(y)$ . Therefore, it is necessary to obtain an analytical solution for  $T_{xy}(y)$  to obtain analytical solutions for these components.

Substituting all the equations obtained for the fluid flow variables (Equations (6)–(8)) in Equation (4); and solving the resulting equation for the tensor component  $T_{xy}(y)$ , a solution for this component can be obtained for a given set of parameters  $Re$ ,  $Wi$ ,  $\beta$ ,  $\epsilon$ ,  $\xi$  and the pressure gradient  $P_x$ .

$$T_{xy}(y) = \left( 2^{-2j-\frac{1}{3}} \left( 8^j P_x Re^4 y (\beta - 1)^3 (2\epsilon\beta(\xi - 1) + (\beta - 1)(\xi - 2)\xi)^3 \right. \right. \tag{9}$$

$$\times \left( 27 \times 4^{j+1} \epsilon^2 \beta^2 (\xi - 1)^2 + 9 \times 2^{2j+1} \epsilon \beta (6\beta - 1) (\xi - 2) \xi (\xi - 1) \right. \\ \left. + (\xi - 2)^2 \xi^2 \left( 9 \times 4^j \beta (3\beta - 1) - 2P_x^2 Re^2 Wi^2 y^2 (\xi - 2) \xi \right) \right) Wi^4 \\ \left. + (64^j P_x^2 Re^8 Wi^8 y^2 (\beta - 1)^6 (2\epsilon\beta(\xi - 1) + (\beta - 1)(\xi - 2)\xi)^6 \right. \\ \left. \times \left( 27 \times 4^{j+1} \epsilon^2 \beta^2 (\xi - 1)^2 + 9 \times 2^{2j+1} \epsilon \beta (6\beta - 1) (\xi - 2) \xi (\xi - 1) \right. \right. \\ \left. \left. + (\xi - 2)^2 \xi^2 \left( 9 \times 4^j \beta (3\beta - 1) - 2P_x^2 Re^2 Wi^2 y^2 (\xi - 2) \xi \right) \right)^2 \right. \\ \left. - 4^{3j+1} Re^6 Wi^6 (\beta - 1)^6 (2\epsilon\beta(\xi - 1) + (\beta - 1)(\xi - 2)\xi)^6 \right. \\ \left. \times \left( 3 \times 2^{2j+1} \epsilon \beta (\xi - 1) + (\xi - 2) \xi \left( P_x^2 Re^2 Wi^2 (\xi - 2) \xi y^2 + 3 \times 4^j \beta \right) \right)^3 \right)^{\frac{1}{2}} \right)^{\frac{1}{3}} \\ \times \frac{1}{3 Re^2 Wi^2 (2\epsilon\beta(\xi - 1) + (\beta - 1)(\xi - 2)\xi)^2} + \frac{2^{1-j} P_x y (\beta - 1) (\xi - 2) \xi}{6\epsilon\beta(\xi - 1) + 3(\beta - 1)(\xi - 2)\xi} \\ + \left( \sqrt[3]{2} (\beta - 1)^2 \left( 3 \times 2^{2j+1} \epsilon \beta (\xi - 1) + (\xi - 2) \xi \left( P_x^2 Re^2 Wi^2 (\xi - 2) \xi y^2 + 3 \times 4^j \beta \right) \right) \right) \\ \left/ \left( 3 \left( 8^j P_x Re^4 y (\beta - 1)^3 (2\epsilon\beta(\xi - 1) + (\beta - 1)(\xi - 2)\xi)^3 \right. \right. \right. \\ \times \left( 27 \times 4^{j+1} \epsilon^2 \beta^2 (\xi - 1)^2 + 9 \times 2^{2j+1} \epsilon \beta (6\beta - 1) (\xi - 2) \xi (\xi - 1) \right. \\ \left. + (\xi - 2)^2 \xi^2 \left( 9 \times 4^j \beta (3\beta - 1) - 2P_x^2 Re^2 Wi^2 y^2 (\xi - 2) \xi \right) \right) Wi^4 \\ \left. + (64^j P_x^2 Re^8 Wi^8 y^2 (\beta - 1)^6 (2\epsilon\beta(\xi - 1) + (\beta - 1)(\xi - 2)\xi)^6 \right. \\ \left. \times \left( 27 \times 4^{j+1} \epsilon^2 \beta^2 (\xi - 1)^2 + 9 \times 2^{2j+1} \epsilon \beta (6\beta - 1) (\xi - 2) \xi (\xi - 1) \right. \right. \\ \left. \left. + (\xi - 2)^2 \xi^2 \left( 9 \times 4^j \beta (3\beta - 1) - 2P_x^2 Re^2 Wi^2 y^2 (\xi - 2) \xi \right) \right)^2 \right. \\ \left. - 4^{3j+1} Re^6 Wi^6 (\beta - 1)^6 (2\epsilon\beta(\xi - 1) + (\beta - 1)(\xi - 2)\xi)^6 \right. \\ \left. \times \left( 3 \times 2^{2j+1} \epsilon \beta (\xi - 1) + (\xi - 2) \xi \left( P_x^2 Re^2 Wi^2 (\xi - 2) \xi y^2 + 3 \times 4^j \beta \right) \right)^3 \right)^{\frac{1}{2}} \right)^{\frac{1}{3}} \right).$$

From Equation (9), it is possible to obtain the distribution of the values of the  $T_{xy}$  component analytically. After obtaining this solution, using Equations (6)–(8) one obtains the distributions for the other components of the flow, but the streamwise velocity component. This velocity component is obtained using numerical schemes by integrating Equation (7). The above variables were written as a function of  $y$ . For axisymmetric pipe flow, it is

necessary to replace  $y$  with  $r$ . It should be emphasised that the proposed method does not require any iteration to obtain a solution for a given pressure gradient.

### 2.1. LPTT Flow Versus Newtonian Flow

To compare the results obtained with the semi-analytical method for the LPTT model with the Newtonian solution, one must find the pressure gradient that gives the same flow rate for both fluid flows. The flow rate is obtained by the integral of the streamwise velocity component with respect to the wall-normal direction. The resulting flow rate should be  $4/3$  for channel flow and  $\pi/2$  for pipe flow.

Initially, for a given initial pressure gradient in the streamwise direction ( $P_x < 0$ ), it is calculated the components of the fluid flow  $T_{xy}(y)$ ,  $\frac{du(y)}{dy}$ ,  $T_{xx}(y)$ ,  $T_{yy}(y)$  using Equations (6)–(9) analytically; and the velocity profile  $u(y)$  is calculated by integrating Equation (7) numerically. And, with the  $u(y)$  distribution it is possible to calculate the flow rate.

An iterative Newton-Raphson's method is adopted to find the pressure gradient ( $P_x$ ) that gives the flow rate of  $4/3$  for channel flow and  $\pi/2$  for pipe flow. The following subsection presents the verification of the semi-analytical method.

The semi-analytical method works in the following way:

1. Set values to the parameters ( $\beta, Wi, Re, \zeta, \epsilon$ );
2. Give an initial pressure gradient ( $P_x$ );
3. Solve Equation (9) to find  $T_{xy}$ ;
4. Integrate Equation (7) to find  $u$ ;
5. Calculate the flow rate by solving  $\int_{-1}^1 u(y)dy$ ;
6. If the flow rate is not  $4/3$  for channel flow or  $\pi/2$  for pipe flow, an iterative Newton-Raphson's method is adopted to give another value of pressure gradient ( $P_x$ ), and we go back to step 3; otherwise, continue;
7. Solve Equation (8) to find  $T_{xx}$ ;
8. Solve Equation (6) to find  $T_{yy}$ .

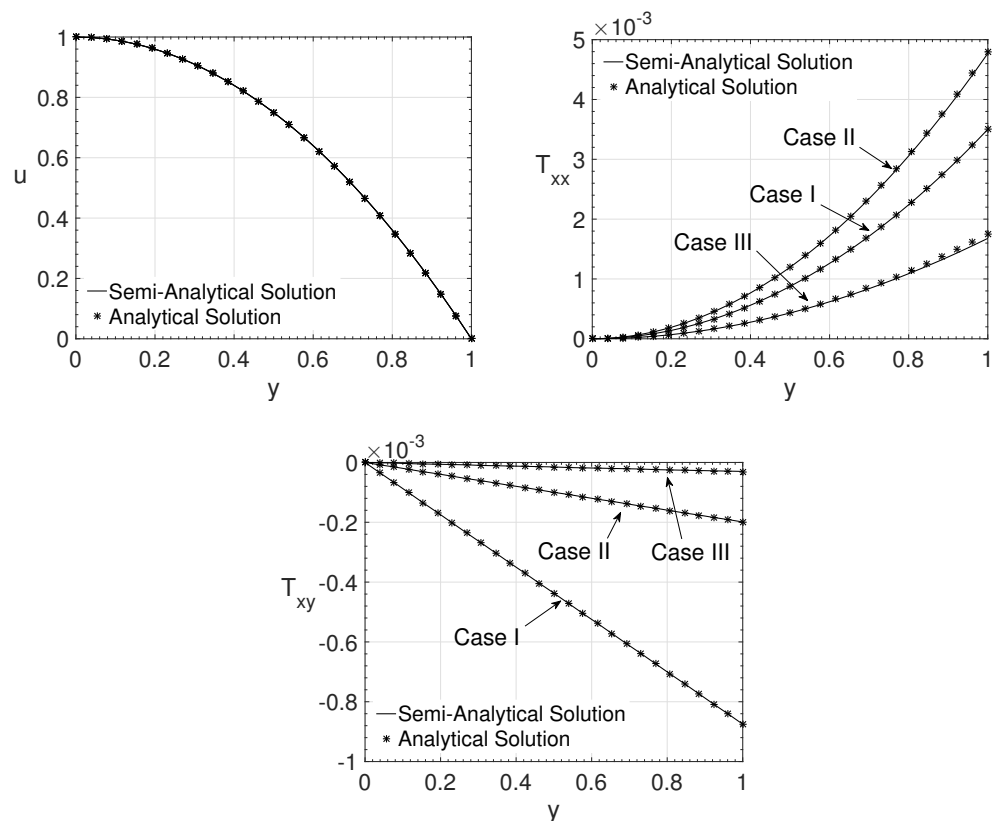
### 2.2. Verification

Here the verification of the proposed method is carried out by comparing the results obtained with the semi-analytical proposed method with two analytical solutions: the Oldroyd-B (channel flow) and the LPTT (pipe flow) models considering a purely polymeric fluid ( $\beta = 0$ ) [16]. Half of the domain was adopted in the graphics since all results are symmetric about the channel (or pipe) centre.

For the first comparison, with the analytical solution of the Oldroyd-B model, the values of the LPTT model parameters adopted were  $\epsilon = 0.0001$  and  $\zeta = 0.0001$ . Three cases were considered for the channel flow ( $j = 0$ ):

- Case I:  $Re = 2000$ ,  $\beta = 0.125$  and  $Wi = 1$ ;
- Case II:  $Re = 5000$ ,  $\beta = 0.5$  and  $Wi = 6$ ;
- Case III:  $Re = 8000$ ,  $\beta = 0.875$  and  $Wi = 14$ .

Figure 2 shows the streamwise velocity component  $u$  and the components of the non-Newtonian extra-stress tensor  $T_{xx}$  and  $T_{xy}$  distribution in the wall-normal direction  $y$ . It is possible to observe an excellent agreement between the results. The analytical value of the extra-stress tensor component  $T_{yy}$ , in this case, is zero. The results for this component obtained by the method proposed have values below  $10^{-9}$ , which was considered a roundoff error.



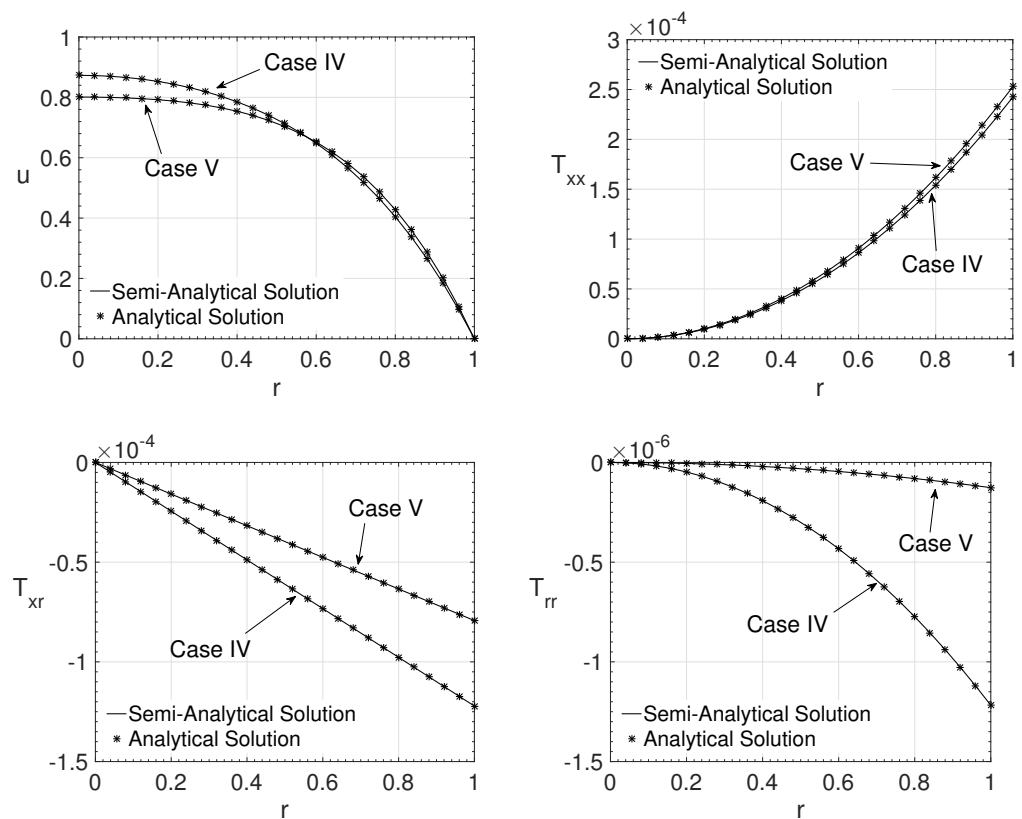
**Figure 2.** Wall-normal variation  $y$  of the streamwise velocity component  $u$  and the extra-stress tensor components  $T_{xx}$  and  $T_{xy}$  for the cases I, II and III.

For the verification using the analytical solution of the LPTT model for purely polymeric fluid flow, as proposed in Alves et al. [16], the value of the parameter  $\beta = 0.0001$  was adopted in the semi-analytical method. Two cases were investigated for pipe flow ( $j = 1$ ):

- Case IV:  $Re = 8000, \epsilon = 0.8, \xi = 0.01$  and  $Wi = 1$ ;
- Case V:  $Re = 5000, \epsilon = 1.2, \xi = 0.001$  and  $Wi = 4$ .

Figure 3 shows the streamwise velocity component  $u$  and the components of the extra-stress tensor  $T_{xx}$ ,  $T_{xy}$  and  $T_{yy}$  variation in the radial direction  $r$ . The comparison is carried out between the semi-analytical method results and the analytical solution proposed by Alves et al. [16]. It is also possible to observe a good agreement between the results obtained using the semi-analytical method for the LPTT model and the analytical solution for the purely polymeric LPTT model [16] in a pipe flow.

The results obtained in this section show that the proposed method could give reliable results if the fluid is modelled by Oldroyd-B (channel flow) or by a purely polymeric LPTT model (pipe flow). All the parameters had different values; therefore, this gives confidence that the proposed semi-analytical method provides the right results in channel or pipe flows. In the next section, the effects of the variation of the LPTT model parameters outside these boundaries are investigated.



**Figure 3.** Radial variation  $r$  of the streamwise velocity component  $u$  and the extra-stress tensor components  $T_{xx}$ ,  $T_{xr}$  and  $T_{rr}$  for the cases IV and V.

### 3. Results

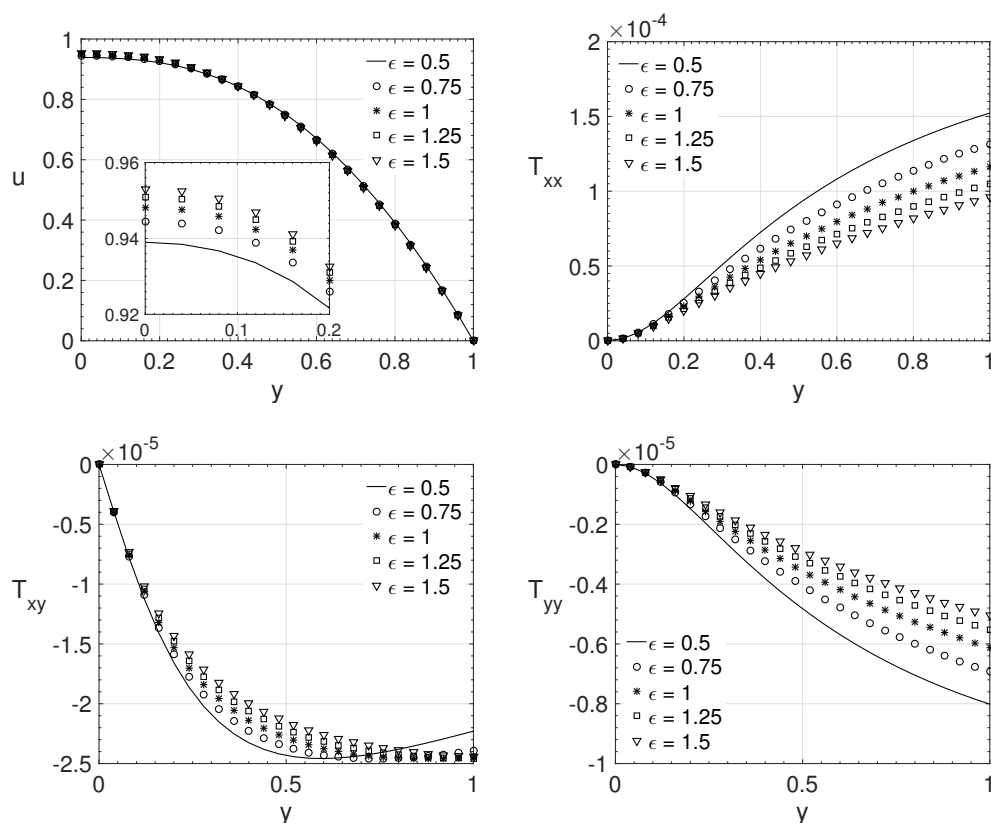
The present section presents the results obtained using the semi-analytical method. To explore the range and efficiency of the proposed method in this work, some values of the dimensionless parameters ( $Re$ ,  $Wi$ ,  $\beta$ ,  $\epsilon$ , and  $\zeta$ ) were investigated for channel and pipe flows.

The section was divided into four subsections. The first one is dedicated to verifying the influence of the  $\epsilon$  parameter. The second one shows some results to verify the influence of the  $\zeta$  parameter in the fluid flow. The third subsection explores the behaviour of the extra-stress tensor  $T_{xy}$  component under certain parameter combinations; and the last subsection shows where the Valid Solution Regions for the proposed method.

#### 3.1. Parameter $\epsilon$

The influence of the  $\epsilon$  parameter on the fluid flow components is analyzed here. This parameter is related to the elongational behaviour of the fluid. In the first results, presented in Figure 4, the parameters adopted for a channel flow were:  $Re = 5000$ ,  $\beta = 0.25$ ,  $\zeta = 0.1$  and  $Wi = 7$ . Five values for the  $\epsilon$  parameter were used:  $\epsilon = 0.5, 0.75, 1.0, 1.25$  and  $1.5$ . It is presented the wall-normal variation ( $0 \leq y \leq 1$ ) of the streamwise velocity component  $u$  and the components of the extra-stress tensor  $T_{xx}$ ,  $T_{xy}$  and  $T_{yy}$ . The value of the maximum streamwise velocity component at the middle of the channel increases with  $\epsilon$ . The opposite occurs for the extra-stress tensor components; the maximum absolute values of the tensors decrease as the  $\epsilon$  value increases, except for the values of the extra-stress tensor component  $T_{xy}$  when the coordinate approaches the wall. For this tensor component, it is possible to observe an interesting behaviour for the fluid flow with  $\epsilon = 0.5$  and  $0.75$ ; its maximum value is not at the wall as expected.

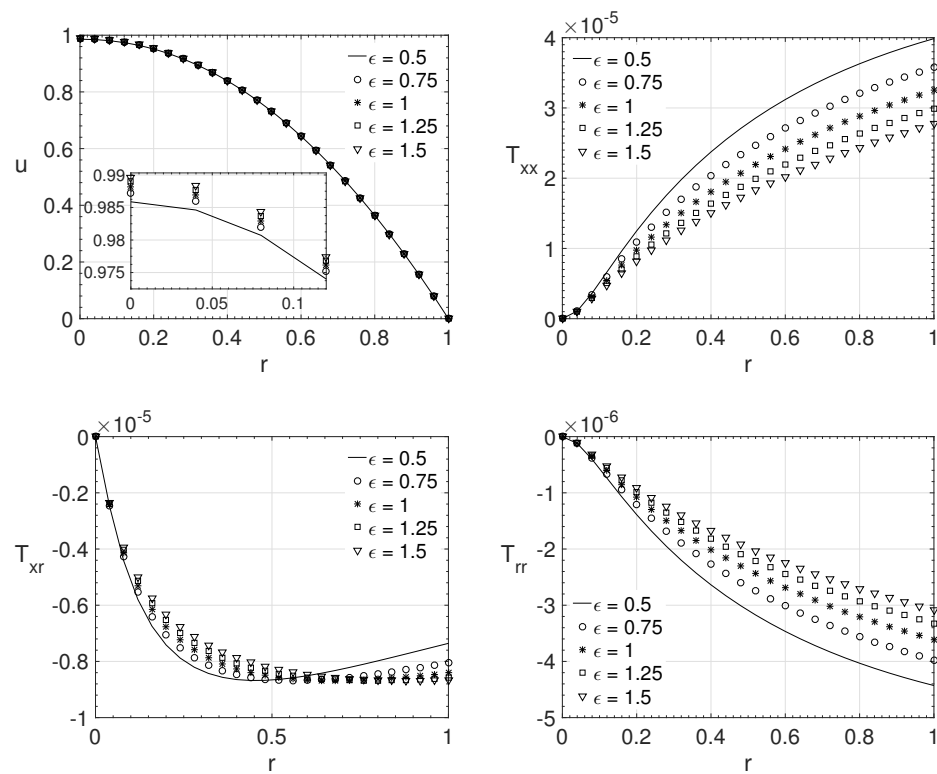




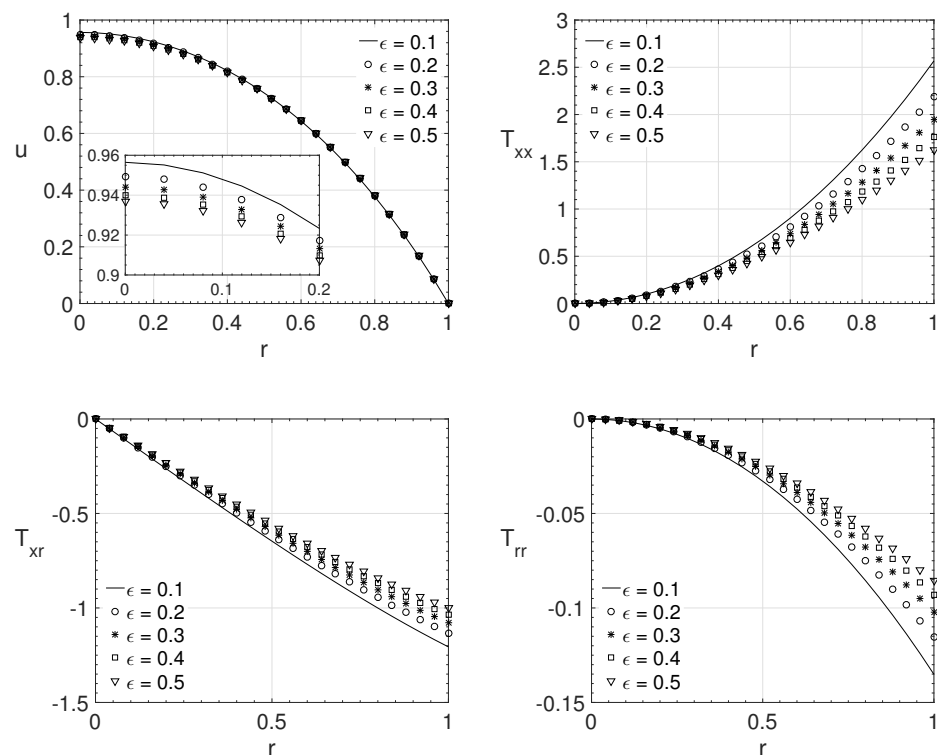
**Figure 4.**  $\epsilon$  influence on the wall-normal variation  $y$  of the streamwise velocity component  $u$  and the extra-stress tensor components  $T_{xx}$ ,  $T_{xy}$  and  $T_{yy}$ . Dimensionless parameters:  $Re = 5000$ ,  $\beta = 0.25$ ,  $\xi = 0.1$  and  $Wi = 7$ .

Figure 5 shows the influence of the  $\epsilon$  parameter for pipe flow ( $j = 1$ ), adopting the following parameters:  $Re = 6000$ ,  $\beta = 0.75$ ,  $\xi = 0.2$  and  $Wi = 4$ . The same variation adopted in the last comparisons, on the  $\epsilon$  parameter, was adopted here ( $\epsilon = 0.5, 0.75, 1.0, 1.25$  and  $1.5$ ). It can be observed that the maximum streamwise velocity component  $u$  at the pipe center is less pronounced when the Newtonian contribution is higher ( $\beta = 0.75$ ). The maximum streamwise velocity component  $u$  value also increases with the value of  $\epsilon$ . The same behavior of the previous comparison for the extra-stress tensor was observed here, as the value of  $\epsilon$  increases, the value of the extra-stress tensor components decreases (in absolute value). For the extra-stress tensor component  $T_{xy}$ , the maximum value is not at the wall, and it can be noted for  $\epsilon = 0.5, 0.75, 1.0$  and  $1.25$ . It also can be noticed that as the Newtonian contribution (solvent contribution- $\beta \rightarrow 1$ ) increases, the magnitude of the non-Newtonian tensor components value decreases, thus making the influence of these components on the velocity profile less important.

The influence of the  $\epsilon$  parameter, for pipe flow ( $j = 1$ ), adopting low values for the Reynolds ( $Re$ ) and the Weissenberg numbers ( $Wi$ ) is shown in Figure 6. The results show radial variation  $r$  of the streamwise velocity component  $u$  and the components of the extra-stress tensor  $T_{xx}$ ,  $T_{xr}$  and  $T_{rr}$ . The adopted parameters were:  $Re = 1$ ,  $\beta = 0.2$ ,  $\xi = 0.1$ , and  $Wi = 0.6$ . The values for the  $\epsilon$  parameter were ( $\epsilon = 0.1, 0.2, 0.3, 0.4$  and  $0.5$ ). It can be observed that the maximum streamwise velocity decreases as the parameter  $\epsilon$  increases. This behavior is also observed on maximum values of the extra-stress tensor components (in absolute values). Figure 6 shows an opposite behavior for the maximum streamwise velocity component that the ones observed in the last two cases (Figures 4 and 5).



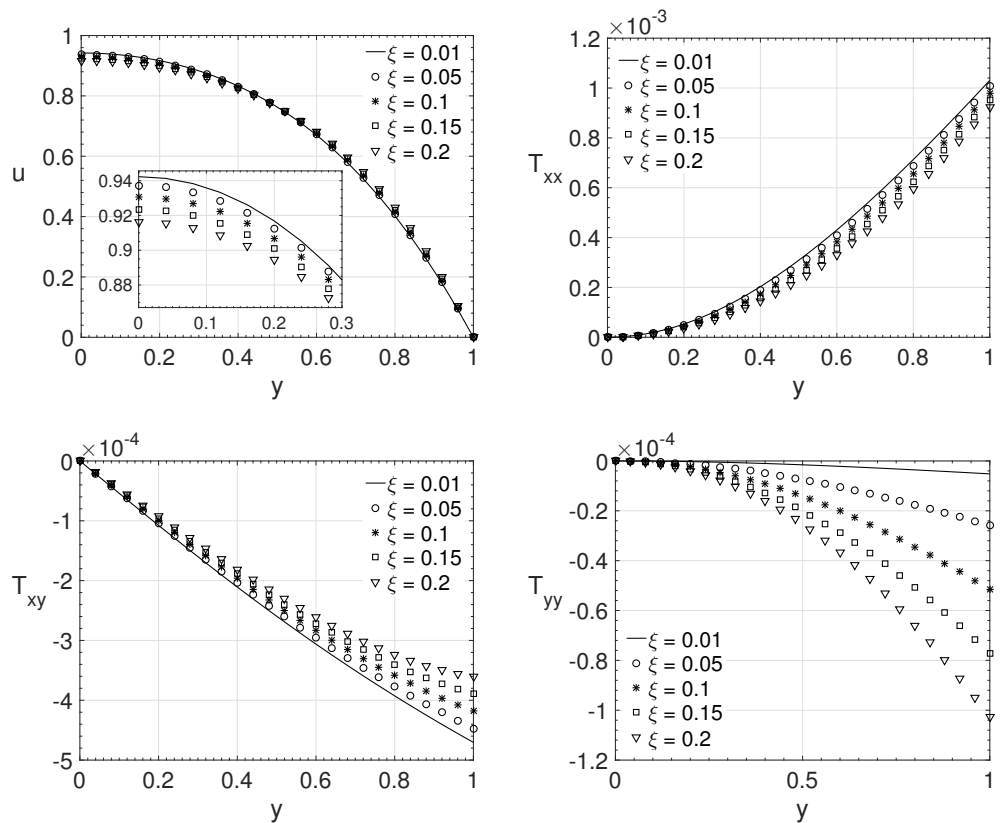
**Figure 5.**  $\epsilon$  influence on the radial variation  $r$  of the streamwise velocity component  $u$  and the extra-stress tensor components  $T_{xx}$ ,  $T_{xr}$  and  $T_{rr}$ . Dimensionless parameters:  $Re = 6000$ ,  $\beta = 0.75$ ,  $\xi = 0.2$  and  $Wi = 4$ .



**Figure 6.**  $\epsilon$  influence on the radial variation  $r$  of the streamwise velocity component  $u$  and the extra-stress tensor components  $T_{xx}$ ,  $T_{xr}$  and  $T_{rr}$ . Dimensionless parameters:  $Re = 1$ ,  $\beta = 0.2$ ,  $\xi = 0.1$  and  $Wi = 0.6$ .

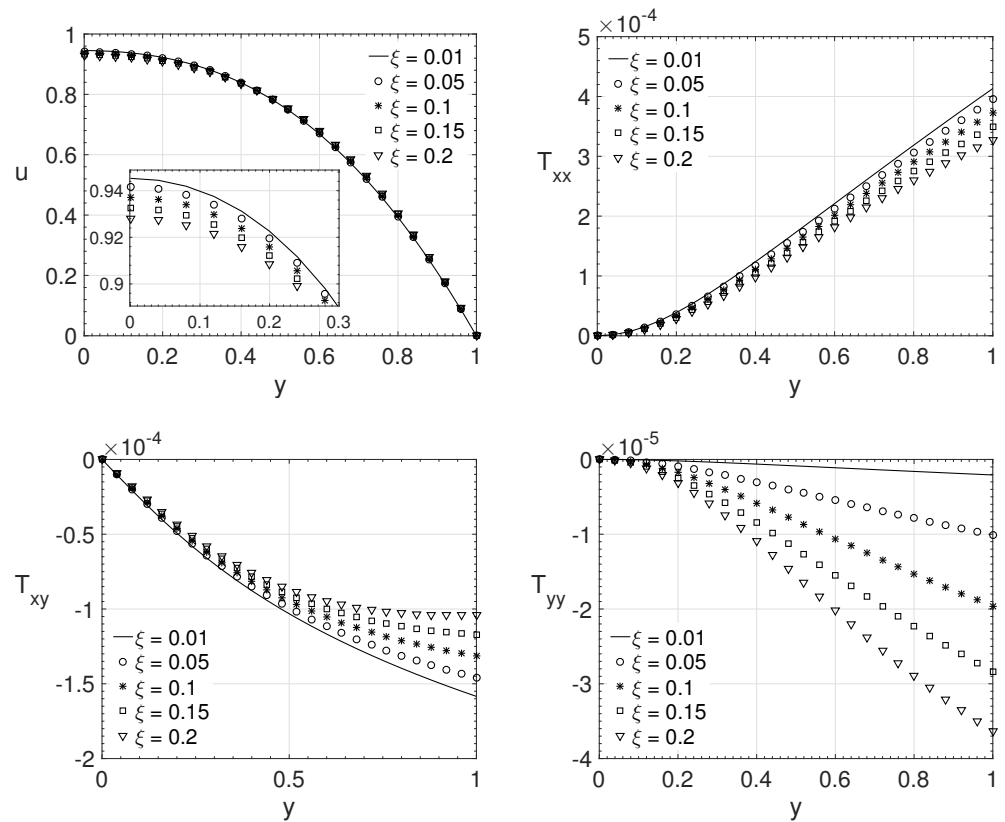
### 3.2. Parameter $\zeta$

To verify the influence of the  $\zeta$  parameter on the LPTT model, it was generated different fluid flows by varying its value. This parameter is connected with the shear stress behavior of the non-Newtonian fluid. Figure 7 shows the wall-normal variation  $y$  of the streamwise velocity component  $u$  and the components of the extra-stress tensor  $T_{xx}$ ,  $T_{xy}$  and  $T_{yy}$  for a channel flow ( $j = 0$ ). The dimensionless parameters adopted were:  $Re = 2000$ ,  $\beta = 0.125$ ,  $\epsilon = 0.5$  and  $Wi = 1$ . Five different values for  $\zeta$  were investigated: 0.01, 0.05, 0.1, 0.15 and 0.2. It can be observed that the maximum absolute values of  $u$ ,  $T_{xx}$  and  $T_{xy}$  decrease as the parameter  $\zeta$  increases. The opposite occurs with the maximum absolute value of extra-stress tensor component  $T_{yy}$ , it increases with  $\zeta$  parameter.



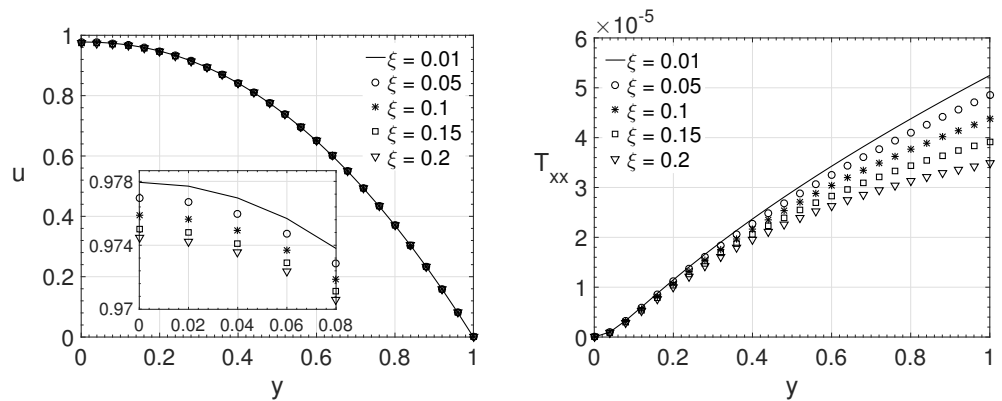
**Figure 7.**  $\zeta$  influence on the wall-normal variation  $y$  of the streamwise velocity component  $u$  and the extra-stress tensor components  $T_{xx}$ ,  $T_{xy}$  and  $T_{yy}$ . Dimensionless parameters:  $Re = 2000$ ,  $\beta = 0.125$ ,  $\epsilon = 0.5$  and  $Wi = 1$ .

Figure 8 shows the wall-normal variation  $y$  of the streamwise velocity component  $u$  and the components of the extra-stress tensor  $T_{xx}$ ,  $T_{xy}$  and  $T_{yy}$ , for a channel flow ( $j = 0$ ). The dimensionless numbers adopted were:  $Re = 3000$ ,  $\beta = 0.25$ ,  $\epsilon = 0.75$  and  $Wi = 2$ . The same variation adopted in the last comparisons, on the  $\zeta$  parameter, was adopted here ( $\zeta = 0.01, 0.05, 0.1, 0.15$  and  $0.2$ ). The streamwise velocity component  $u$  and the extra-stress tensors components  $T_{xx}$ ,  $T_{xy}$  and  $T_{yy}$  shows the same behavior observed in the last case, for  $u$ ,  $T_{xx}$  and  $T_{xy}$  their maximum absolute values decreases as the parameter  $\zeta$  increase and the opposite occurs for  $T_{yy}$  component as the parameter  $\zeta$  increase.

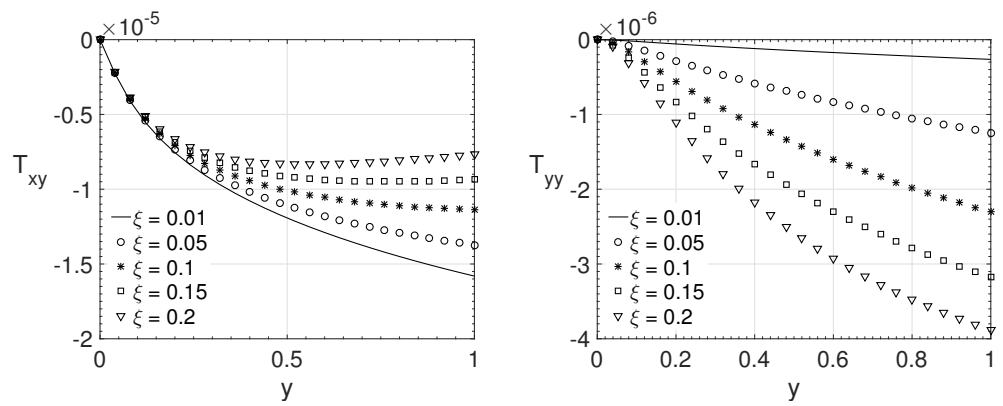


**Figure 8.**  $\zeta$  influence on the wall-normal variation  $y$  of the streamwise velocity component  $u$  and the extra-stress tensor components  $T_{xx}$ ,  $T_{xy}$  and  $T_{yy}$ . Dimensionless parameters:  $Re = 3000$ ,  $\beta = 0.25$ ,  $\epsilon = 0.75$  and  $Wi = 2$ .

Using the dimensionless parameters:  $Re = 10,000$ ,  $\beta = 0.5$ ,  $\epsilon = 1.0$ ,  $Wi = 5$  and  $j = 0$  (channel flow), the wall-normal variation  $y$  of the streamwise velocity component  $u$  and the components of the extra-stress tensor  $T_{xx}$ ,  $T_{xy}$  and  $T_{yy}$  are shown in Figure 9. The same variation adopted in the last comparisons, on the  $\zeta$  parameter, was adopted here ( $\zeta = 0.01, 0.05, 0.1, 0.15$  and  $0.2$ ). In these results the same behavior of the one observed for the last two case was achieved, the absolute maximum value of the extra-stress tensor component  $T_{yy}$  increases with the parameter  $\zeta$ . The opposite occurs with the other variables.

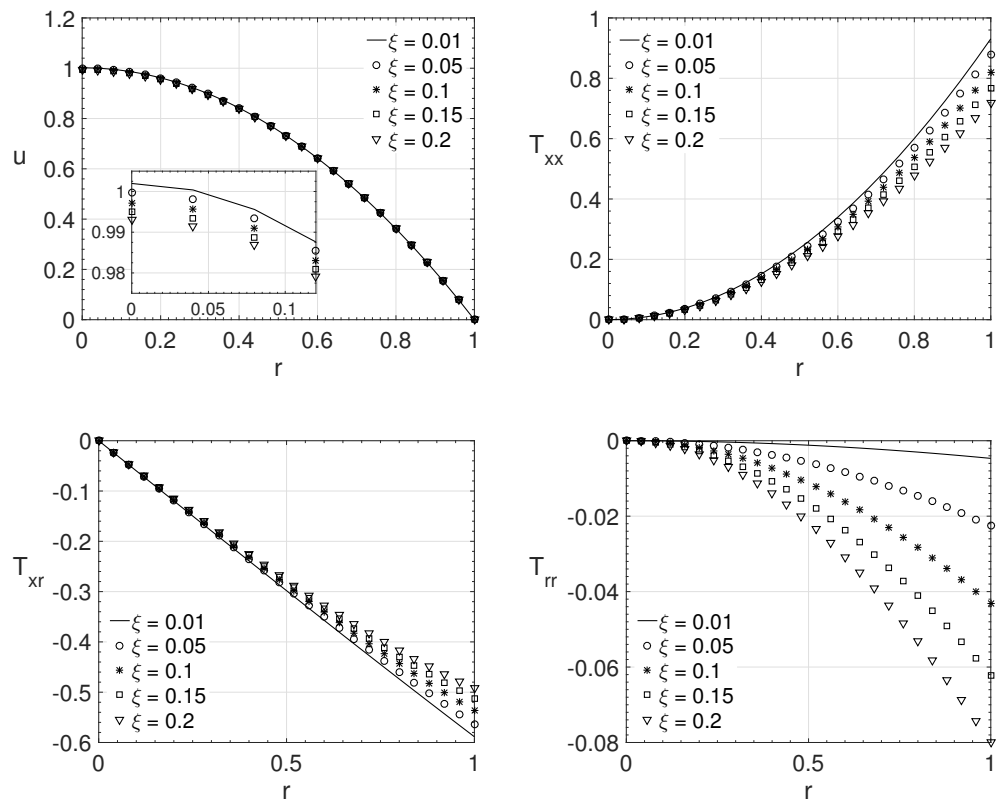


**Figure 9.** Cont.



**Figure 9.**  $\zeta$  influence on the wall-normal variation  $y$  of the streamwise velocity component  $u$  and the extra-stress tensor components  $T_{xx}$ ,  $T_{xy}$  and  $T_{yy}$ . Dimensionless parameters:  $Re = 10,000$ ,  $\beta = 0.5$ ,  $\epsilon = 1$  and  $Wi = 5$ .

Figure 10 shows the influence of the  $\zeta$  parameter, for pipe flow ( $j = 1$ ), as low values of Reynolds number ( $Re$ ) and the Weissenberg number ( $Wi$ ) are adopted. The considered parameters are:  $Re = 1$ ,  $\beta = 0.7$ ,  $\epsilon = 0.01$  and  $Wi = 0.4$ . The  $\zeta$  parameter values used here are ( $\zeta = 0.01, 0.05, 0.1, 0.15$  and  $0.2$ ). The observed behavior of the variables are the same of the last case. However, in the present case one can observe that the magnitude of the extra-stress tensor components increases substantially when low Reynolds number is adopted.



**Figure 10.**  $\zeta$  influence on the radial variation  $r$  of the streamwise velocity component  $u$  and the extra-stress tensor components  $T_{xx}$ ,  $T_{xr}$  and  $T_{rr}$ . Dimensionless parameters:  $Re = 1$ ,  $\beta = 0.7$ ,  $\epsilon = 0.01$  and  $Wi = 0.4$ .

From Figures 7–10, it is possible to observe the behavior of the variables when the  $\zeta$  parameter change its value. As the parameter  $\zeta$  increases, it is possible to observe that the maximum streamwise velocity component value decreases. The same behaviour can be noted on the maximum absolute value of the extra-stress tensor components  $T_{xx}$  and  $T_{xy}$  (or  $T_{xr}$  for pipe flows) close/or at the wall. For the extra-stress tensor component  $T_{yy}$  (or  $T_{rr}$ ), the opposite behavior is observed, its maximum value increases with the dimensionless parameter  $\zeta$ . This behaviour can be noted even for low values of Reynolds number, as Figure 10 shows.

It is worth mentioning that to obtain the fluid flow solution is necessary to check if the Equation (9) has a real solution. The solution for this variable needs the calculation of a square root, a cubic root, and a quotient's product. The extra-stress tensor component  $T_{xy}$  value is a function of the fluid flow parameters, and, for some combinations of them, the resulting value can be complex. When this happens, all the fluid flow variables are complex; therefore, this result is not the sought one.

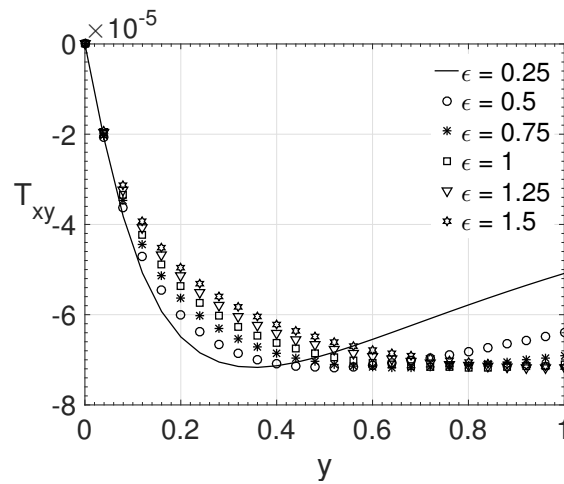
The semi-analytical results presented here agree with the boundary conditions and solution intervals presented by Alves et al. [16]. In terms of solution ranges, the parameter  $\epsilon$  can admit values within the open range  $(0, 2)$ . For the  $\zeta$  parameter, its values can be varied within the open range  $(0, \frac{1}{2})$ . It is worth mentioning that, even if there is a solution for some values of these parameters beyond the above limits, many of these values do not present physical properties [20] and, therefore, they are not within the scope of this study.

### 3.3. $T_{xy}$ Behaviour

From the results presented in Section 3.1, we observe an unusual behaviour for the extra-stress tensor component  $T_{xy}$ , as seen in Figures 4 and 5. It was observed that the maximum value of the extra-stress tensor component  $T_{xy}$  does not occur at the wall with some parameter combinations. Before the semi-analytical solution was obtained, the research group used a high-order numerical simulation to obtain the laminar solution for the LPTT model in a straight channel. The solutions with both methods were compared and agreed with each other. Therefore, the behaviour of the extra-stress tensor  $T_{xy}$  was double-checked. The behaviour observed here is really from the viscoelastic model and therefore is necessary to investigate which parameters influence it.

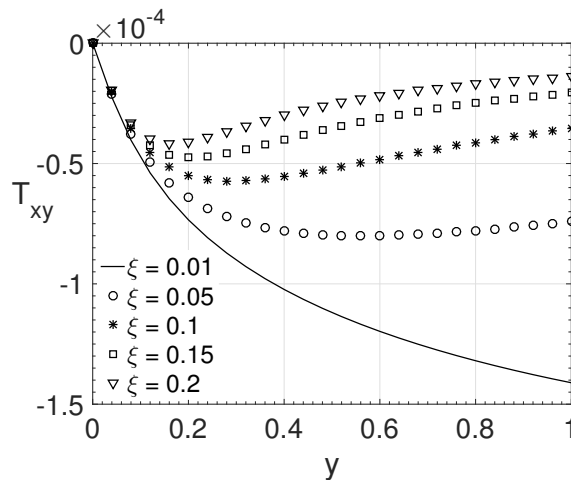
It was observed that the Reynolds number and total viscosity (either with more solvent or polymer viscosity in the mixture) do not affect the behaviour of this extra-stress component. The  $T_{xy}$  component was affected by the parameters  $\epsilon$ ,  $\zeta$ , and the Weissenberg number. An investigation was carried out using different values for these parameters and observing how the  $T_{xy}$  component is affected.

For the simulations performed, the Reynolds number ( $Re = 1000$ ) and  $\beta$  ( $\beta = 0.5$ ) were kept. Figure 11 shows the variation of the  $\epsilon$  parameter considering  $\zeta = 0.1$  and  $Wi = 8$ . The values for the parameter  $\epsilon$  considered were: 0.25, 0.50, 0.75, 1.0, 1.25 and 1.5. Figure 11 shows that as the value of  $\epsilon$  decreases, the maximum value of the tensor  $T_{xy}$  moves towards the channel centre. This shows that a greater opposition to stretching (higher elongational viscosity) influences the maximum value for the component  $T_{xy}$  to move away from the wall.



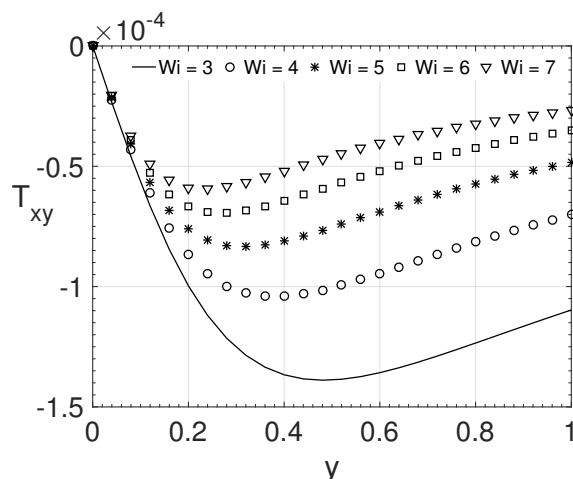
**Figure 11.**  $\epsilon$  influence on the wall-normal variation  $y$  of the extra-stress tensor component  $T_{xy}$ . Dimensionless parameters:  $Re = 1000$ ,  $\beta = 0.5$ ,  $\zeta = 0.1$  and  $Wi = 8$ .

Figure 12 presents the variation in the  $\zeta$  parameter values considering  $\epsilon = 0.25$  and  $Wi = 10$ . The values for the parameter  $\zeta$  considered were: 0.01, 0.05, 0.1, 0.15, and 0.2. From Figure 12 it is possible to observe that as the value of  $\zeta$  increases, the value of the tensor component  $T_{xy}$  at the wall decreases. As the value of  $\zeta$  increases, the maximum value of the tensor  $T_{xy}$  moves towards the channel centre. This shows that the normal stress differences combined with high elongational viscosity exhibit a strong influence on this behaviour.



**Figure 12.**  $\zeta$  influence on the wall-normal variation  $y$  of the extra-stress tensor component  $T_{xy}$ . Dimensionless parameters:  $Re = 1000$ ,  $\beta = 0.5$ ,  $\epsilon = 0.25$  and  $Wi = 10$ .

For our last investigation, presented in Figure 13, we performed the variation for the Weissenberg number, considering  $\epsilon = 0.25$  and  $\zeta = 0.2$ . The values for the parameter  $Wi$  considered were: 3.0, 4.0, 5.0, 6.0, and 7.0. It is possible to observe, from Figure 13, that as the Weissenberg number increases, the maximum value of the tensor component  $T_{xy}$  moves towards the channel centre.



**Figure 13.** *Wi* influence on the wall-normal variation *y* of the extra-stress tensor component  $T_{xy}$ . Dimensionless parameters:  $Re = 1000$ ,  $\beta = 0.5$ ,  $\epsilon = 0.25$  and  $\zeta = 0.2$ .

From the analysis carried out, it was possible to verify the influence of these parameters on the behaviour of the extra-stress tensor  $T_{xy}$  component. Parameter values that emphasize this behaviour were chosen for the simulations. These values comprehend low values for  $\epsilon$ ,  $\zeta$  close to 0.2, and Weissenberg numbers higher than 1. This behaviour arises from the combination of high elongational viscosity and a high relationship between normal stress differences and high elasticity. The physical combination of these properties causes the maximum value of the extra-stress tensor  $T_{xy}$  component to move towards the channel centre. The strong interaction between fluid molecules allied with high elongational viscosity and high elasticity can explain this physical behaviour.

It is worth mentioning that this behaviour happens both for the channel and the pipe, although the simulations showed here were performed only for channels.

### 3.4. Semi-Analytical Method Limits

Numerical simulations with different parameter values were performed to observe which ones allow the existence of the solution. It was verified that the Reynolds number does not influence the existence of a solution as long as  $Re > 0$ . However, the other non-dimensional parameters showed an influence. To understand which type of influence and which combinations of values are necessary to obtain a valid solution, different simulations were performed, varying the parameters  $\epsilon$ ,  $\zeta$  and  $\beta$  (Figure 14), and  $\epsilon$ ,  $\zeta$  and the Weissenberg number (*Wi*) (Figure 15).

Adopting fixed values for *Re* and *Wi* and varying the values of the other parameters was obtained the Figure 14. The parameters interval adopted was  $0 \leq \epsilon \leq 2$ ,  $0 \leq \zeta \leq 0.5$  and  $0.1 \leq \beta \leq 0.9$ . Figure 14 presents the Valid Solution Region (VSR) where it is possible to obtain the solution of the flow for different values of  $\beta$ . The line pointed out as  $\beta = 0.1$  shows the limits of a combination ( $\epsilon, \zeta$ ) values where the solution is valid (VSR). The VSR increases with  $\beta$ . For smaller values of  $\beta$  (higher polymer viscosity in the mixture), the values of  $\epsilon$  and  $\zeta$  cannot be as large as, for example, the value of  $\beta$  being 0.9.



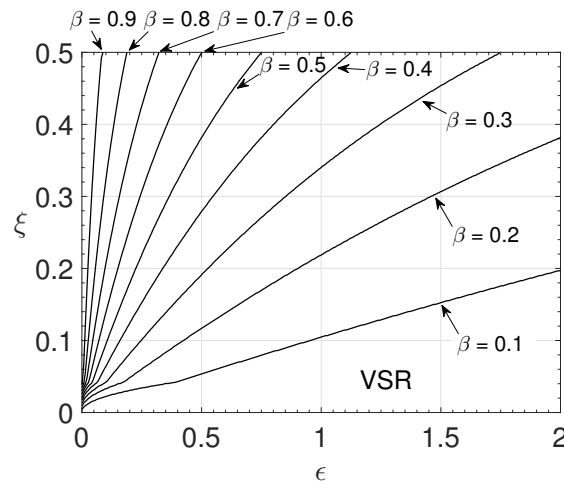


Figure 14. Valid solution region for different  $\beta$  values with  $\epsilon$  and  $\zeta - Re = 1000$  and  $Wi = 3.0$ .

To obtain Figure 15, values for  $Re$  and  $\beta$  were kept constant. For the parameter  $\epsilon$ , it was considered the interval  $(0, 0.75)$ . For the  $\zeta$  variation, it was maintained the same variation performed for the Figure 14, and for the Weissenberg number, the values: 1, 2, 3, 5 and 10 were considered. Figure 15 presents the regions for the limitation of obtaining the solutions. It can be observed that, for  $Wi = 1$ , it is possible to obtain solutions for small values of the parameter  $\epsilon$ , even for values of  $\zeta$  greater than 0.2. On the other hand, as the value of  $Wi$  increases, it is possible to observe that the solution becomes more sensitive for smaller values of both  $\epsilon$  and  $\zeta$ . All solutions exist for parameter  $\epsilon > 0.75$ .

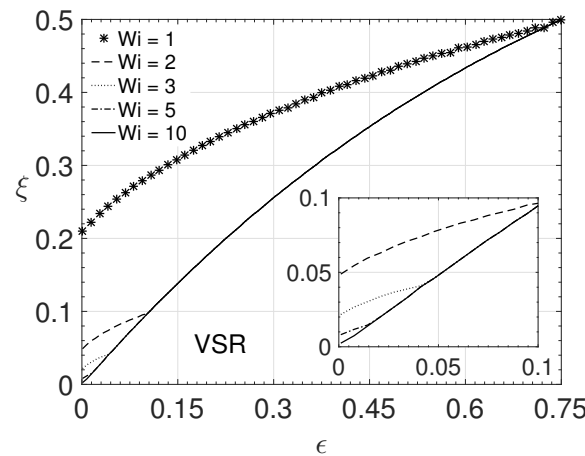


Figure 15. Valid solution region for different  $Wi$  values with  $\epsilon$  and  $\zeta - Re = 2000$  and  $\beta = 0.5$ .

In general, the solution presented in this paper has limitations when considering low values for  $\beta$ . This limitation is due to the impossibility, in these cases, of considering a higher elongational viscosity for the LPTT model (low values of  $\epsilon$ ) and also a more significant influence of the differences in normal stresses (higher values for the parameter  $\zeta$ ). Therefore, in order to obtain solutions considering high elongational viscosity and also a more significant influence of normal stress differences, it is necessary that the values for the parameter  $\beta$  are higher than 0.3, as can be observed in Figure 14.

It is worth mentioning that the valid solution region considering channel flow was also verified for pipe flow, and the results remain the same.

#### 4. Conclusions

This paper presents a semi-analytical method for the laminar steady channel and pipe flows of the LPTT fluid, with elongational and shear parameter variations. For the verification of the proposed semi-analytical method, its results were compared with the

Oldroyd-B model analytical solution, and the solution presented by Alves et al. [16] for the LPTT model without solvent viscosity ( $\beta \rightarrow 0$ ). The verification results obtained by the semi-analytical method proposed in this work showed a good agreement compared to both analytical solutions used as references.

The results presented explored the effect of the parameters  $\epsilon$  and  $\zeta$  on the velocity profile and the non-Newtonian extra-stress tensor components. From the analysis, it was possible to verify that the parameter  $\epsilon$  reduces the impact of the tensor components on the velocity profile when it is increased for a high Reynolds number.

The parameter  $\zeta$  has the opposite effect on the maximum value of the streamwise velocity component. As the value of this parameter increases, the velocity profile in the middle of the channel (or pipe) decreases. On the other hand, the extra-stress tensor components  $T_{xx}$  and  $T_{xy}$  (or  $T_{xr}$  for pipe flows) decrease (in absolute value) as parameter  $\zeta$  increases. For the extra-stress tensor component  $T_{yy}$  (or  $T_{rr}$ ), its absolute value increases with the parameter  $\zeta$ . The solution for the simplified LPTT model, with  $\zeta = 0$ , for this tensor component is zero.

Another interesting behaviour was observed for the extra-stress tensor component  $T_{xy}$  (or  $T_{xr}$  for pipe flows). Its maximum value moves towards the channel centre with a specific combination of the parameters  $\epsilon$ ,  $\zeta$ , and the Weissenberg number. It was observed that the combination of high elongational viscosity, the high relationship between normal stress differences, and high elasticity could be responsible for this behaviour.

It was explored for which values of the parameters are present in the flow, it is possible to obtain the solution. In other words, the limitations of the presented solution were explored.

**Author Contributions:** methodology, M.T.d.A., L.F., A.B. and L.S.; investigation, M.T.d.A., L.F., A.B. and L.S.; writing—original draft preparation, M.T.d.A., L.F., A.B. and L.S.; writing—review and editing, M.T.d.A., L.F., A.B. and L.S. All authors have read and agreed to the published version of the manuscript.

**Funding:** Research was carried out using the computational resources of the Center for Mathematical Sciences Applied to Industry (CeMEAI), funded by FAPESP grant 2013/07375-0.

**Institutional Review Board Statement:** Not applicable.

**Data Availability Statement:** Not applicable.

**Acknowledgments:** M.T.d.A., L.F. and L.S. acknowledge the Department of Applied Mathematics and Statistics—University of Sao Paulo, Sao Carlos. A.B. acknowledges the Department of Mathematics and Computer Science—Sao Paulo State University, Presidente Prudente.

**Conflicts of Interest:** The authors declare no conflict of interest.

## References

1. Khan, N.S.; Humphries, U.W.; Kumam, W.; Kumam, P.; Muhammad, T. Assessment of irreversibility optimization in Casson nanofluid flow with leading edge accretion or ablation. *ZAMM-J. Appl. Math. Mech./Z. Für Angew. Math. Mech.* **2022**, *102*, e202000207. [[CrossRef](#)]
2. Khan, N.S.; Humphries, U.W.; Kumam, W.; Kumam, P.; Muhammad, T. Dynamic pathways for the bioconvection in thermally activated rotating system. *Biomass Convers. Biorefinery* **2022**. [[CrossRef](#)]
3. Hulsen, M.A. Some properties and analytical expressions for plane flow of Leonov and Giesekus models. *J. Non-Newton. Fluid Mech.* **1988**, *30*, 85–92. [[CrossRef](#)]
4. Oliveira, P.J. An exact solution for tube and slit flow of a FENE-P fluid. *Acta Mech.* **2002**, *158*, 157–167. [[CrossRef](#)]
5. Yoo, J.Y.; Choi, H.C. On the steady simple shear flows of the one-mode Giesekus fluid. *Rheol. Acta* **1989**, *28*, 13–24. [[CrossRef](#)]
6. Schleiniger, G.; Weinacht, R.J. Steady Poiseuille flows for a Giesekus fluid. *J. Non-Newton. Fluid Mech.* **1991**, *40*, 79–102. [[CrossRef](#)]
7. Raisi, A.; Mirzazadeh, M.; Dehnavi, A.; Rashidi, F. An approximate solution for the Couette–Poiseuille flow of the Giesekus model between parallel plates. *Rheol. Acta* **2008**, *47*, 75–80. [[CrossRef](#)]
8. Hayat, T.; Khan, M.; Ayub, M. Some simple flows of an Oldroyd-B fluid. *Int. J. Eng. Sci.* **2001**, *39*, 135–147. [[CrossRef](#)]
9. Hayat, T.; Khan, M.; Ayub, M. Exact solutions of flow problems of an Oldroyd-B fluid. *Appl. Math. Comput.* **2004**, *151*, 105–119. [[CrossRef](#)]

10. Tomé, M.F.; Araujo, M.T.; Evans, J.D.; McKee, S. Numerical solution of the Giesekus model for incompressible free surface flows without solvent viscosity. *J. Non-Newton. Fluid Mech.* **2019**, *263*, 104–119. [[CrossRef](#)]
11. Furlan, L.J.S.; Araujo, M.T.; Brandi, A.C.; Cruz, D.O.A.; de Souza, L.F. Different Formulations to Solve the Giesekus Model for Flow between Two Parallel Plates. *Appl. Sci.* **2021**, *11*, 10115. [[CrossRef](#)]
12. Pinho, F.T.; Oliveira, P.J. Analysis of forced convection in pipes and channels with the simplified Phan-Thien-Tanner fluid. *Int. J. Heat Mass Transf.* **2000**, *43*, 2273–2287. [[CrossRef](#)]
13. Pinho, F.T.; Oliveira, P.J. Axial annular flow of a nonlinear viscoelastic fluid—An analytical solution. *J. Non-Newton. Fluid Mech.* **2000**, *93*, 325–337. [[CrossRef](#)]
14. Cruz, D.O.A.; Pinho, F.T.; Oliveira, P.J. Analytical solutions for fully developed laminar flow of some viscoelastic liquids with a Newtonian solvent contribution. *J. Non-Newton. Fluid Mech.* **2005**, *132*, 28–35. [[CrossRef](#)]
15. Ferrás, L.L.; Nóbrega, J.M.; Pinho, F.T. Analytical solutions for channel flows of Phan-Thien-Tanner and Giesekus fluids under slip. *J. Non-Newton. Fluid Mech.* **2012**, *171–172*, 97–105. [[CrossRef](#)]
16. Alves, M.A.; Pinho, F.T.; Oliveira, P.J. Study of steady pipe and channel flows of a single-mode Phan-Thien-Tanner fluid. *J. Non-Newton. Fluid Mech.* **2001**, *101*, 55–76. [[CrossRef](#)]
17. Phan-Thien, N.; Tanner, R.I. A new constitutive equation derived from network theory. *J. Non-Newton. Fluid Mech.* **1977**, *2*, 353–365. [[CrossRef](#)]
18. Paulo, G.S. Solução Numérica do Modelo PTT Para Escoamentos Viscoelásticos com Superfícies Livres. Ph.D. Thesis, Universidade de São Paulo, São Paulo, Brazil, 2006.
19. Oliveira, P.J.; Pinho, F.T. Analytical solution for fully developed channel and pipe flow of Phan-Thien–Tanner fluids. *J. Fluid Mech.* **1999**, *387*, 271–280. [[CrossRef](#)]
20. Bird, R.B.; Curtiss, C.F.; Armstrong, R.C.; Hassager, O. *Dynamics of Polymeric Liquids. Vol. 1: Fluid Mechanics*; John Wiley and Sons Inc.: New York, NY, USA, 1987.

## Article

# A Simulation-Data-Based Machine Learning Model for Predicting Basic Parameter Settings of the Plasticizing Process in Injection Molding

Matthias Schmid <sup>1,\*</sup>, Dominik Altmann <sup>1,2</sup> and Georg Steinbichler <sup>1</sup>

<sup>1</sup> Institute of Polymer Injection Moulding and Process Automation, Johannes Kepler University Linz, Altenberger Straße 69, 4040 Linz, Austria; dominik.altmann@jku.at (D.A.); georg.steinbichler@jku.at (G.S.)

<sup>2</sup> Kompetenzzentrum Holz GmbH (Wood K Plus)—Biobased Composites and Processes, Altenberger Strasse 69, 4040 Linz, Austria

\* Correspondence: matthias.schmid@jku.at; Tel.: +43-732-2468-6732

**Abstract:** The optimal machine settings in polymer processing are usually the result of time-consuming and expensive trials. We present a workflow that allows the basic machine settings for the plasticizing process in injection molding to be determined with the help of a simulation-driven machine learning model. Given the material, screw geometry, shot weight, and desired plasticizing time, the model is able to predict the back pressure and screw rotational speed required to achieve good melt quality. We show how data sets can be pre-processed in order to obtain a generalized model that performs well. Various supervised machine learning algorithms were compared, and the best approach was evaluated in experiments on a real machine using the predicted basic machine settings and three different materials. The neural network model that we trained generalized well with an overall absolute mean error of 0.27% and a standard deviation of 0.37% on unseen data (the test set). The experiments showed that the mean absolute errors between the real and desired plasticizing times were sufficiently small, and all predicted operating points achieved good melt quality. Our approach can provide the operators of injection molding machines with predictions of suitable initial operating points and, thus, reduce costs in the planning phase. Further, this approach gives insights into the factors that influence melt quality and can, therefore, increase our understanding of complex plasticizing processes.

**Citation:** Schmid, M.; Altmann, D.; Steinbichler, G. A Simulation-Data-Based Machine Learning Model for Predicting Basic Parameter Settings of the Plasticizing Process in Injection Molding. *Polymers* **2021**, *13*, 2652. <https://doi.org/10.3390/polym13162652>

Academic Editors: Célio Bruno Pinto Fernandes, Salah Aldin Faroughi, Luís L. Ferrás and Alexandre M. Afonso

**Keywords:** machine learning; multilayer perceptron; neural network; regression; plasticizing; polymers; basic settings; prediction; simulation; data-based; model; quality

Received: 6 July 2021

Accepted: 6 August 2021

Published: 10 August 2021

**Publisher's Note:** MDPI stays neutral with regard to jurisdictional claims in published maps and institutional affiliations.



**Copyright:** © 2021 by the authors. Licensee MDPI, Basel, Switzerland. This article is an open access article distributed under the terms and conditions of the Creative Commons Attribution (CC BY) license (<https://creativecommons.org/licenses/by/4.0/>).

## 1. Introduction

Finding optimal parameter settings for the plasticizing process (see Section 2.1—“The Plasticizing Process and S3 Simulation Software”) is one of the most important tasks in operating polymer processing machines. In injection molding and extrusion, the goal is to determine an operating point that satisfies all melt quality and machine lifetime requirements. The most relevant parameters with the highest impact on melting behavior are the pressure, screw rotational speed, and cylinder temperatures [1].

Especially in injection molding, much information is available about the early product cycle stages of the process. In this paper, we wanted to push the approach of a simulation-driven data-based model as we found that simulations have become increasingly used for the screw layout and process optimization. This valuable information could also be employed to determine basic machine settings. From personal experience and collaborating work, we observed that many operators adjust the plasticizing parameters for process stability but without additional knowledge about the current process. Due to the complex melting behavior—depending on the molecular weight, molecular weight distribution, chain branching, shear rate, and shear stress—of polymers, we found that it is not known exactly whether a selected operating point is efficient [2].

A data-based digital twin (virtual representation) of the plasticizing process (physical object) that “knows” the correlations between the melt quality and plasticizing parameters (predicting the performance of a physical twin) could, therefore, be beneficial [3]. A simulation-data-based model could already be built in the screw-selection phase. Given the boundary conditions of the main process, such as the material, screw geometry, and maximum cycle time, a digital twin could assist the operator by predicting relevant basic parameter settings that require little optimization.

Research has focused intensively on machine-learning models of the injection process to predict quality parameters, such as the weight or dimensions of parts [4–6]. However, one of many problems that influence the final part quality can already occur one step earlier, that is, in the plasticizing process, often due to insufficient melt quality.

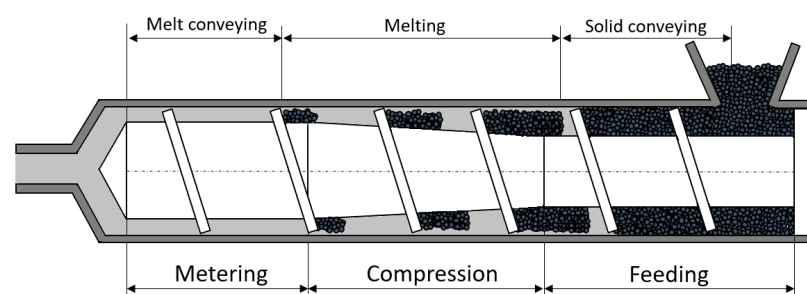
This paper describes the development of a supervised regression model that—given minimal input information—is able to predict the basic settings for the plasticizing process. The generation and preprocessing of a simulation-based data set are explained in detail. We further describe the process of building an artificial neural network (multilayer perceptron), discuss its accuracy, and compare the results of experiments with those using the predicted basic settings.

## 2. Basics

This paper describes the workflow to construct a regression model that can predict the basic machine setup for the process parameters of the back pressure and screw rotational speed. Additionally, the approach for the experimental evaluation will be explained in detail. All distributions and parameter values shown in this section are based on the material “PP-HE125MO” and a three-zone screw with LD 20 and a 30 mm diameter.

### 2.1. The Plasticizing Process and S3 Simulation Software

As already mentioned, the plasticizing unit is one of the most important functional components of an injection molding machine with the task to feed in solid material and melt it along the screw length. The unit usually includes a barrel combined with a specific reciprocating single screw, a drive, and heating bands. A typical setup is shown in Figure 1.



**Figure 1.** Schematic representation of the functional zones of a plasticizing unit [7].

Three main functional zones can be identified that are responsible for solid conveying, melting, and melt conveying. To gain better insights into these processes, a software tool called S3 (screw simulation software) [8] was developed with the aims of (i) predicting the screw geometries and process parameters that are optimal in terms of part quality and the machine lifetime for a given application and (ii) finding a good compromise between the computational power required and model accuracy. The simulation times achieved with this software can be as short as one minute.

The input parameters include the barrel and screw geometries, materials, and process and simulation parameters. The output parameters include the plasticizing rate and time, power consumption, pressure build-up, temperature distribution, and melting behavior. The latter parameter is defined in the simulations by a melting curve (percentage of molten material) along the length of the screw and measured visually during the experiments.

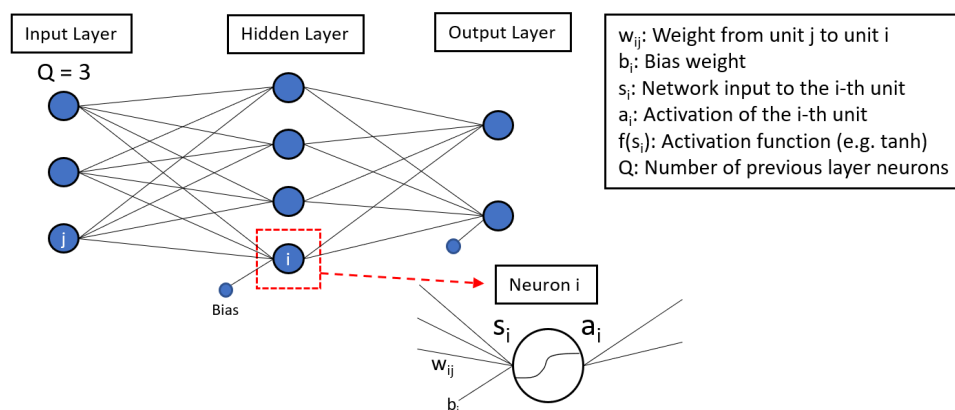
Commercial software solutions are often based on analytical models or are not developed for the discontinuous plasticizing process as in injection molding. The main advantage of the S3 software is the flexibility regarding its easy implementation of new material and calculation models or various new approaches. A detailed description of the S3 software and its comparison with other software can be found in [8].

## 2.2. Artificial Neural Networks

Artificial neural networks are currently one of the most important supervised machine learning methods, characterized by the presence of labels (i.e., target values) that can be either numerical data (task: regression) or categorical data (task: classification) [9].

The simplest form of a neural network consists of only two layers—an input layer and an output layer. This specific case is called a linear perceptron, since it can distinguish only linearly separable data. However, in real life, many problems can only be modeled non-linearly, and neural networks with at least one hidden layer, and non-linear activation functions (called multilayer perceptrons) were, therefore, introduced [10].

More complex models with many hidden layers are called deep neural networks (there is no consensus on the number of hidden layers required to use this term). The network built in this work consists of three hidden layers and is defined as a multilayer perceptron. There are two phases in training a neural network: the forward pass and the backward pass. Figure 2 shows a schematic representation of the forward pass of a multilayer perceptron with one hidden layer. The sizes (i.e., the numbers of neurons) of the input and output layers are defined by the data to be processed.



**Figure 2.** Forward pass of a multilayer perceptron. The red box shows the determination of the pre-activation and activation in one neuron of the hidden layer. The pre-activation is calculated by the linear sum of the product of all previous neurons  $x_j$  (input layer) with their corresponding weights  $w_{ij}$  plus a bias term  $b_i$ . The pre-activation  $s_i$ , then, serves as input to the non-linear activation function, which gives  $a_i$ .

In the first phase, the inputs are moved forward in the output layer direction. Every neuron in the hidden layer has one pre-activation  $s_i$  and one activation  $a_i$ . The forward pass, which can be interpreted as the prediction of the output, is illustrated in more detail for the neuron in the red box in Figure 2. The pre-activations are calculated by:

$$s_i = \sum_{j=1}^Q w_{ji} x_j + b_i. \quad (1)$$

This gives the linear sum of three products of the input neurons  $x_j$  with their corresponding weights  $w_{ij}$  plus a bias term  $b_i$ . Depending on the non-linear activation function used, the pre-activation  $s_i$  is, then, mapped to  $a_i$ :

$$a_i = f(s_i). \quad (2)$$

In the next step, the activation  $a_i$  of the neuron serves as input to the next layer, and the procedure is repeated until the end of the output layer of the network is reached [11].

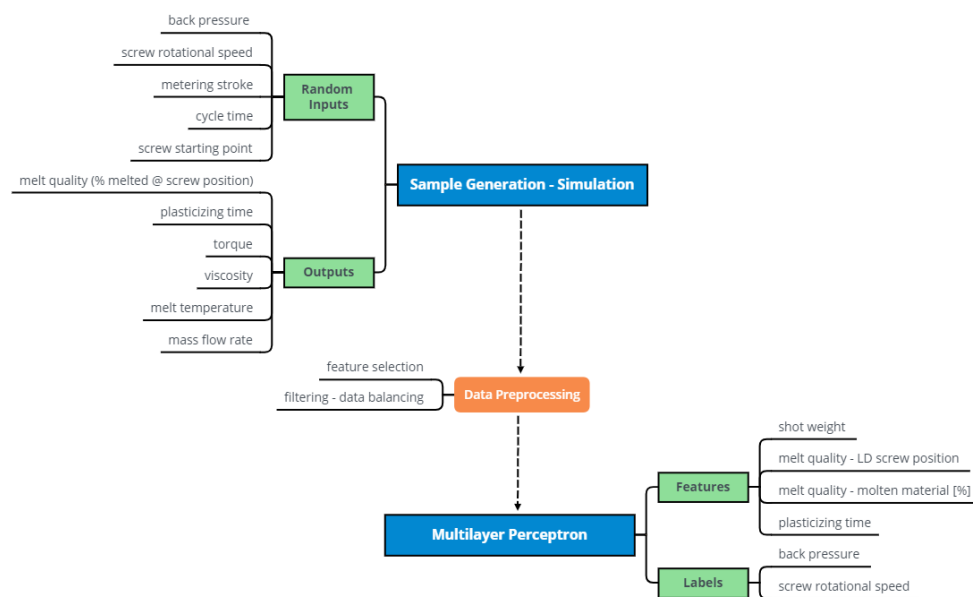
The network is trained in the backward pass, where all weights and biases are updated. This is normally done via gradient-descent methods after computing the error (i.e., loss) in the output layer between the prediction (forward pass) and real label. The error is backpropagated from the last layer through the hidden layer and finally to the input layer [12].

### 3. Methods

We describe the workflow for constructing a regression model that can predict basic machine settings—that is, the back pressure and screw rotational speed—for an injection molding plasticizing process. All distributions and parameter values shown in this section are based on the material “PP-HE125MO” and a three-zone screw with an LD ratio of 20 and a diameter of 30 mm.

#### 3.1. Data Generation and Preprocessing

Figure 3 presents a flowchart of the neural network construction. The first branch at the top left illustrates the input parameters for the simulation and the outputs that are generated. The groundwork for the multilayer perceptron model was laid by simulating 2000 data points with the S3 Software.



**Figure 3.** Flowchart—The construction of a neural network model (multilayer perceptron).

The design points were chosen by keeping all simulation-relevant input parameters (e.g., grid points and time steps) constant while varying the process parameters shown in Table 1 between the minimum and maximum values. The short S3 simulation times made finding a more efficient way of building the data set (e.g., using the design of experiment method) unnecessary. The amount of simulation data points can be decreased significantly with adequate domain knowledge, since non-feasible input values would either not converge in the simulation or would be filtered by preprocessing of the model, which is described below.

Further important process parameters include the feed-trough and cylinder temperatures, which were—for simplification—considered to be constant at 60 and 240 °C, respectively.

**Table 1.** Limits of the input parameters for the simulation. Within these limits, the data set was drawn randomly.

	Back Pressure	Metering Stroke	Screw Rotational Speed	Cycle Time
Min	25 bar	0.8 D	0.2 $\frac{\text{m}}{\text{s}}$	10 s
Max	225 bar	4 D	1 $\frac{\text{m}}{\text{s}}$	60 s

The main challenge in the prediction of the back pressure and screw rotational speed is that these parameters are used as an input to the simulations. It is important to understand that the outputs of the simulation cannot be used directly to predict these parameters for basic machine settings. Hence, a model that only reproduces the simulation is unhelpful. Therefore, at this point, the following questions must be answered:

- Which features (inputs) can be selected from the data in order to predict the desired labels?
- How can the model fulfill the requirement of good melt quality for the predictions?

A crucial feature is the shot weight, which can be derived from the mass flow rate and the plasticizing time. In our approach, the melt quality is measured by the percentage of molten material along the screw length. For example, the screw position (in length-to-diameter ratio; LD; melt quality—feature 1) at which 99% of the material is molten (melt quality—feature 2) can be determined and used as input to the model in the form of two features. The fourth feature for predicting the back pressure and screw rotational speed is the corresponding plasticizing time, which is directly given by the simulation output. Hence, the input of the model is defined by the following features:

- shot weight;
- melt quality—LD screw position;
- melt quality—molten material [%]; and
- plasticizing time.

We found that the simulation input parameters cycle time and screw starting point had a negligible impact on the model performance and, therefore, need not be considered. Information about the metering stroke is included in the shot weight. The distributions of all parameters of the raw data set are shown in Figure 4. Since the simulation input values were drawn randomly (see Table 1), the distributions are well balanced within their limits. However, the distributions of the simulation outputs—melt quality (melt value and LD) and plasticizing time—are highly unbalanced.

The simulation output information about melt quality is given by a large array that describes the melt percentage along the screw length. The important samples in our data set are those with good melt quality. For each sample, the LD screw position at which 99% of the material is molten was, therefore, determined and extracted into the data set. However, numerous data points remained that did not fulfill this requirement. Apparently, the screw positions of all these samples are at the very end of the screw (LD 20.5), which can be seen in the top right distribution in Figure 4.

The requirement of 99% molten material makes the distribution curve of the melt value relatively unbalanced. All samples with a melt value greater than 0.01 (<99%) correspond to the screw position LD 20.5.

To ensure that the model is trained only by samples that guarantee good melt quality, problematic data points were discarded. Given the distributions of the raw data set, this was easily achieved by discarding all samples with a screw position equal to 20.5 LD.

Due to the requirement to predict only operating points with good melt quality, the model was not trained with “bad” samples. This filtering process reduced the data from 2000 to 915 samples. The corresponding distributions (Figure 5) show that the data set was much more balanced, which was also beneficial for training the multilayer perceptron.



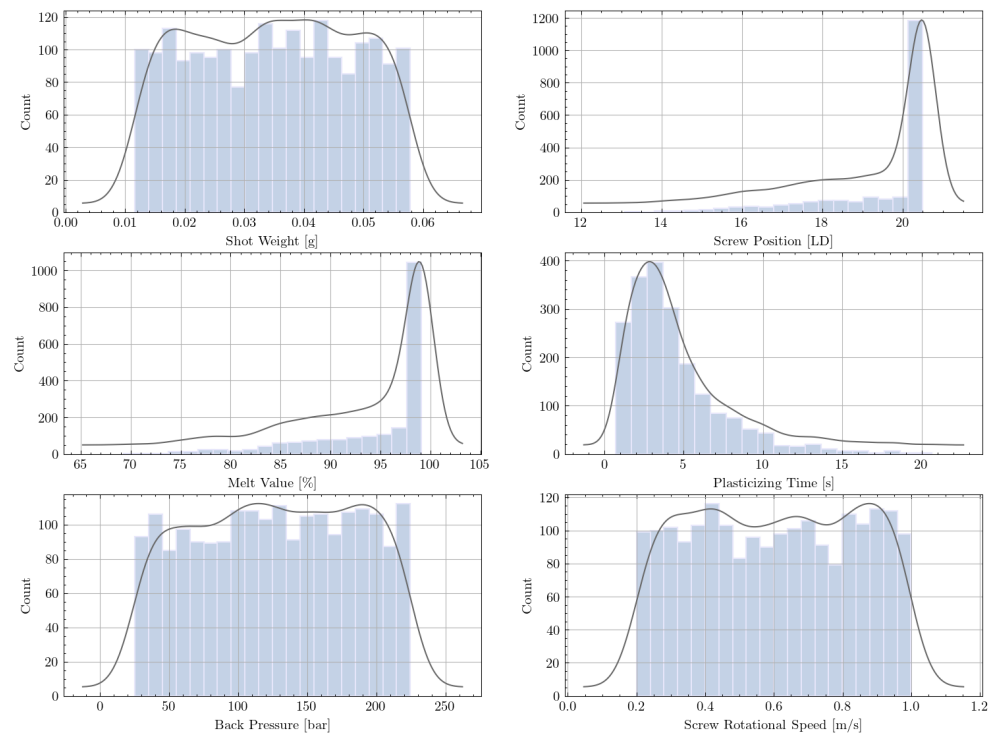


Figure 4. Distribution of the features and labels for the raw data set (2000 samples).

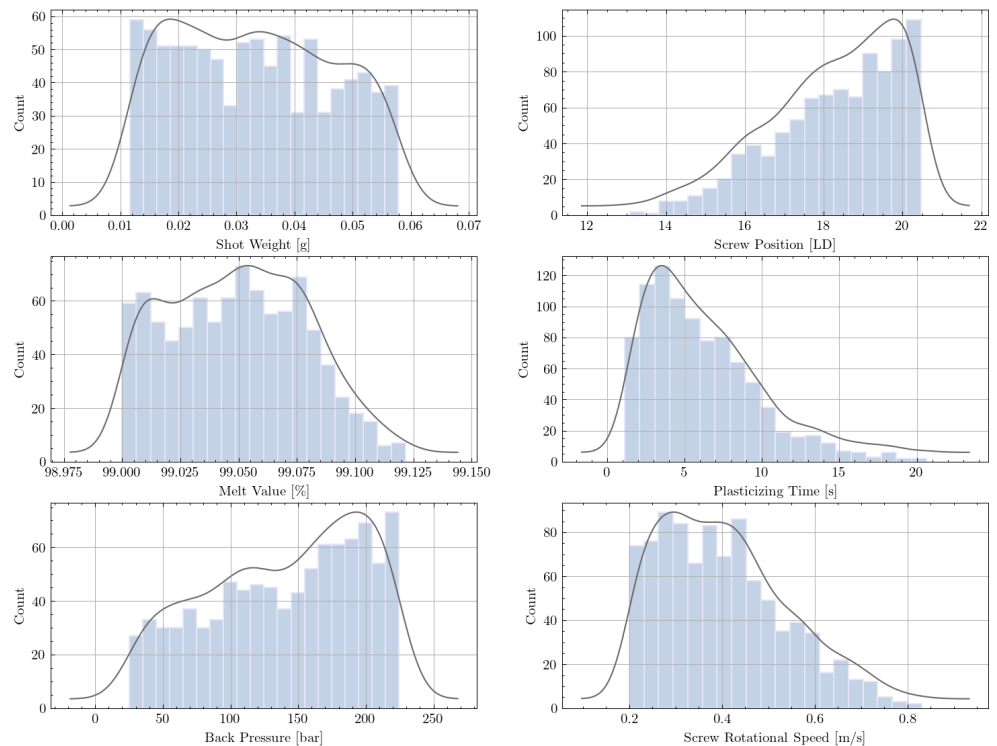


Figure 5. Distribution of the features and labels for the filtered data set (915 samples).

### 3.2. Model Construction

Numerous supervised machine learning methods are available for building a model that can handle data sets with complex non-linearities. We trained models using prevalent machine learning algorithms. We compared the following methods:

- multilayer perceptron,
- Gaussian process regression,

- support vector regression,
- polynomial regression,
- random forest, and
- gradient boosting.

Since the multilayer perceptron outperformed all other methods (see Section 4—“Results”), we explain the model construction for this method only. The neural network was implemented with Python’s [13] open-source library Pytorch [14], using the following architecture and hyperparameters:

- Training set: 549 samples
- Validation set: 183 samples
- Test set: 183 samples
- Layer structure: 4 → 50 → 50 → 30 → 2
- Activation function: Tanh (for all layers)
- Optimizer: Pytorch Adam
- Loss function: Pytorch MSE
- Learning rate epoch 0–600:  $10^{-3}$
- Learning rate epoch 600–1200:  $10^{-4}$
- Learning rate epoch 1200–1500:  $10^{-5}$
- Weight decay:  $10^{-4}$
- Batch size: 32
- Epochs: 1500.

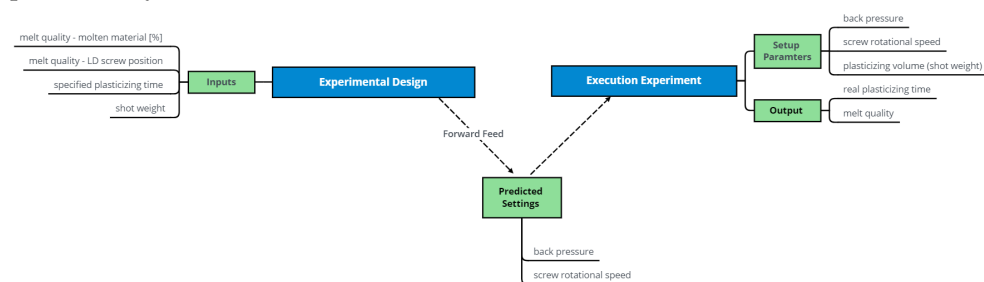
This specific setting was found with help of a hyperparameter study. Fewer epochs would also have resulted in a good model; however, the small data set (compared to image data sets) allowed fast training. Overfitting was only detected with a much larger number of trainable parameters.

### 3.3. Experimental Evaluation of the Model

Validating the model performance with results from a real injection molding machine required experiments to be developed. Two basic parameter settings (the screw rotational speed and back pressure) were predicted by the neural network model with the following ranges of feature values:

- melt value: 99% molten for each data point;
- screw Position (LD): 16, 18, 20;
- shot weight (kg): 0.02, 0.035, 0.05; and
- plasticizing time (s): 1–15.

The workflow is described in Figure 6. Since the multilayer perceptron model cannot outperform the simulation it is built on, its predictions must be validated with data points produced by a real machine.



**Figure 6.** Flowchart—Experimental evaluation of the model.

For every combination of LD and shot weight, 40 samples with increasing plasticizing times were created, which resulted in a data frame of  $3 \times 3 \times 40 = 360$  samples. All 360 samples served as input to the model, which predicted the corresponding parameter settings in the forward feed. Since the simulations were limited to the ranges 25–225 bar

for the back pressure and 0.2–1 m/s for the screw rotational speed, the predictions of the 360 samples had to be filtered to discard all non-feasible data points.

Table 2 lists the parameters of the experiments, where the shot weight and melt value were 0.035 kg and 99% for all samples.

**Table 2.** Experimental configurations for 0.035 kg shot weight and 99% melt value. The first entry describes that, for a back pressure of 148.7 bar and a screw rotational speed of 0.24 m/s, 99% of 35 g of material is predicted to be melted at screw position LD 16 within a plasticizing time of 9.62 s.

Screw Position [LD]	Plasticizing Time [s]	Back Pressure [bar]	Screw Rotational Speed [ $\frac{m}{s}$ ]
16	9.62	148.7	0.24
16	11.05	90.9	0.20
16	12.13	38.7	0.16
18	6.03	163.2	0.38
18	7.10	84.9	0.30
18	7.82	37.1	0.25
20	3.87	180.4	0.60
20	4.59	102.2	0.45
20	5.31	38.1	0.36

#### 4. Results

To identify the most suitable modeling approach for our purpose, we compared various supervised learning methods in terms of their performance. Table 3 shows the overall absolute mean errors in percentages and the corresponding standard deviations for the two labels back pressure and screw rotational speed for both the training and the test sets. The algorithms are listed in order of decreasing performance and for the sake of completeness, all hyperparameters of the corresponding best model are provided in the supplementary material. A low mean error on the training set and a much higher error on the test set indicates overfitting.

This means that the model can reproduce already seen data (i.e., training data) very well, while its prediction of unseen data (i.e., test data) is poorer. This was especially the case for Gaussian process regression and for polynomial regression. Decision-tree methods—random forest and gradient boosting—were unsuitable for this data set when the settings from the hyperparameter search were used. Overall, the multilayer perceptron outperformed all other methods on the given data set, as it exhibited a markedly lower generalization error on the test set.

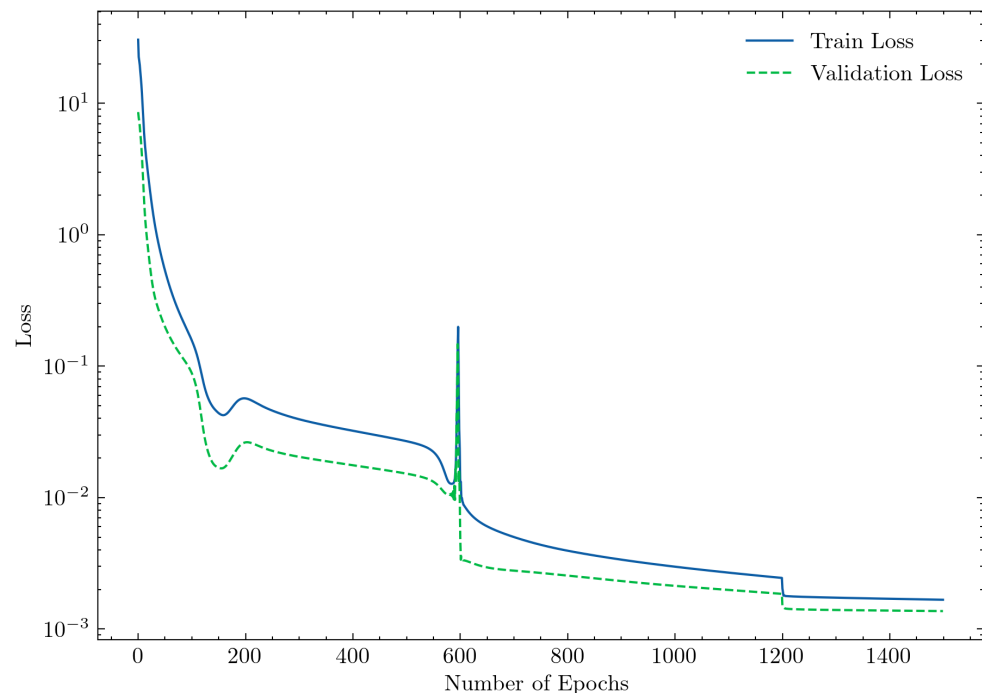
**Table 3.** Comparison of relevant supervised machine learning methods. The absolute prediction errors of the labels back pressure and screw rotational speed are listed for the training and test sets.

Method	Mean Error [%]		Std Error [%]	
	Train	Test	Train	Test
Multilayer Perceptron	0.21	0.27	0.26	0.37
Gaussian Process Regression	0.08	1.16	0.18	2.25
Polynomial Regression	0.34	1.27	0.55	4.98
Support Vector Regression	2.57	2.87	2.64	3.81
Random Forest	8.39	21.42	14.40	37.18
Gradient Boosting	18.44	24.34	31.44	43.54

##### 4.1. Results—Multilayer Perceptron Model

With increasing complexity, neural networks tend to overfit to training data. The hyperparameters (e.g., learning rate) must, therefore, be tuned such that the generalization risk error (i.e., the error on the test set) is kept low. Figure 7 plots the losses of the training and validation sets. Both losses decreased steadily until reaching a low plateau, which indicates a generalized model. The loss was calculated in a loop over all epochs for the corresponding data sets and was aggregated over the batch sizes.

Therefore, with the same batch size, but varying lengths of the training and validation set, the resulting loss for the validation set could be lower than for the training set. At epoch 600, the learning rate decreased from  $10^{-3}$  to  $10^{-4}$  and, at epoch 1200, to  $10^{-5}$ . Decreasing the learning rate is a commonly used approach because it allows greater weight changes in the beginning of the training phase and smaller changes at the end [15].



**Figure 7.** Losses on the training and validation data sets in the training phase.

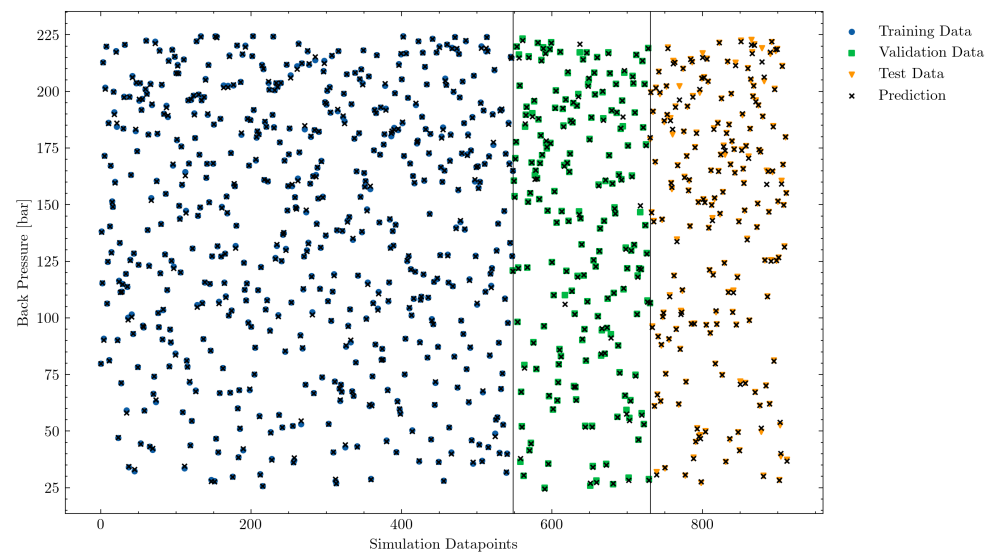
Table 4 lists the model performances for the training and test sets for the two labels back pressure and screw rotational speed. Regression models are usually evaluated by the mean squared error. For better interpretation, we chose the root-mean-squared error as a metric. As expected from the loss curves, the errors of the labels were very low for both data sets. This indicates good generalization and shows that the model predicted all simulation data points almost perfectly within the chosen limits.

**Table 4.** Performance of the neural network model.

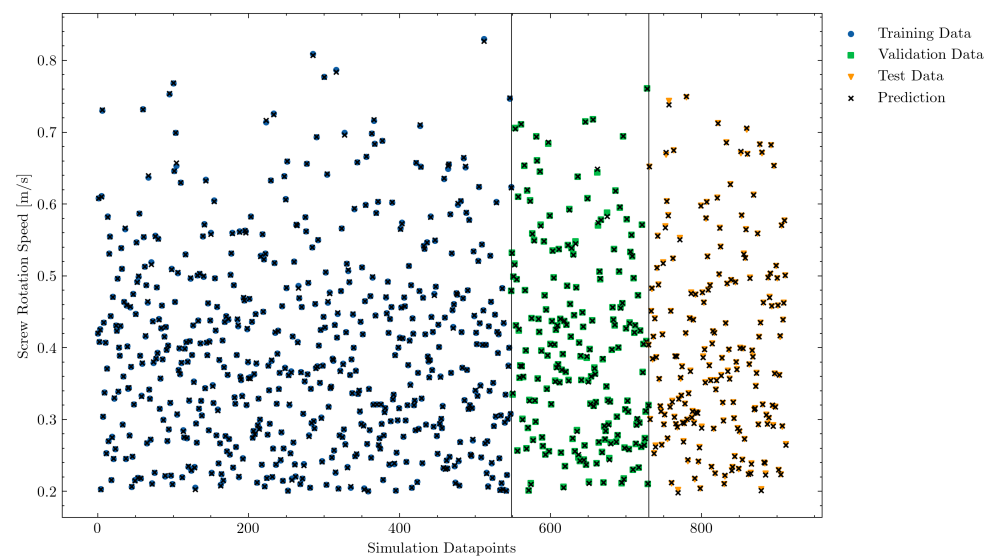
Label	RMSE Train	RMSE Test
Back Pressure [bar]	0.41	0.61
Screw Rotational Speed [m/s]	0.0008	0.001

Figures 8 and 9 visualize the values of the input parameters back pressure and screw rotational speed for all data points. During the training phase, the model learned only from the blue samples, and, for the hyperparameter search, the green unseen validation data points were taken. During the evaluation phase, the generalization error was determined with the unseen data points of the test set. As explained in the Methods section, all samples achieved good melt quality at screw positions between LD 16 and LD 20.

The multilayer perceptron model predictions, illustrated by a black cross in Figures 8 and 9, provide further evidence of the good generalization of the model to unseen data (validation and test sets). Note that the training set predictions were very accurate, while the validation and test set predictions were slightly poorer for some specific samples. However, the deviations of the predictions of unseen samples were sufficiently small to ensure a well-generalized model for both labels.



**Figure 8.** Accuracy of the back pressure predictions on the training (samples from which the model is trained), validation (unseen samples for hyperparameter tuning during training), and test (evaluation on unseen samples after training) data sets.

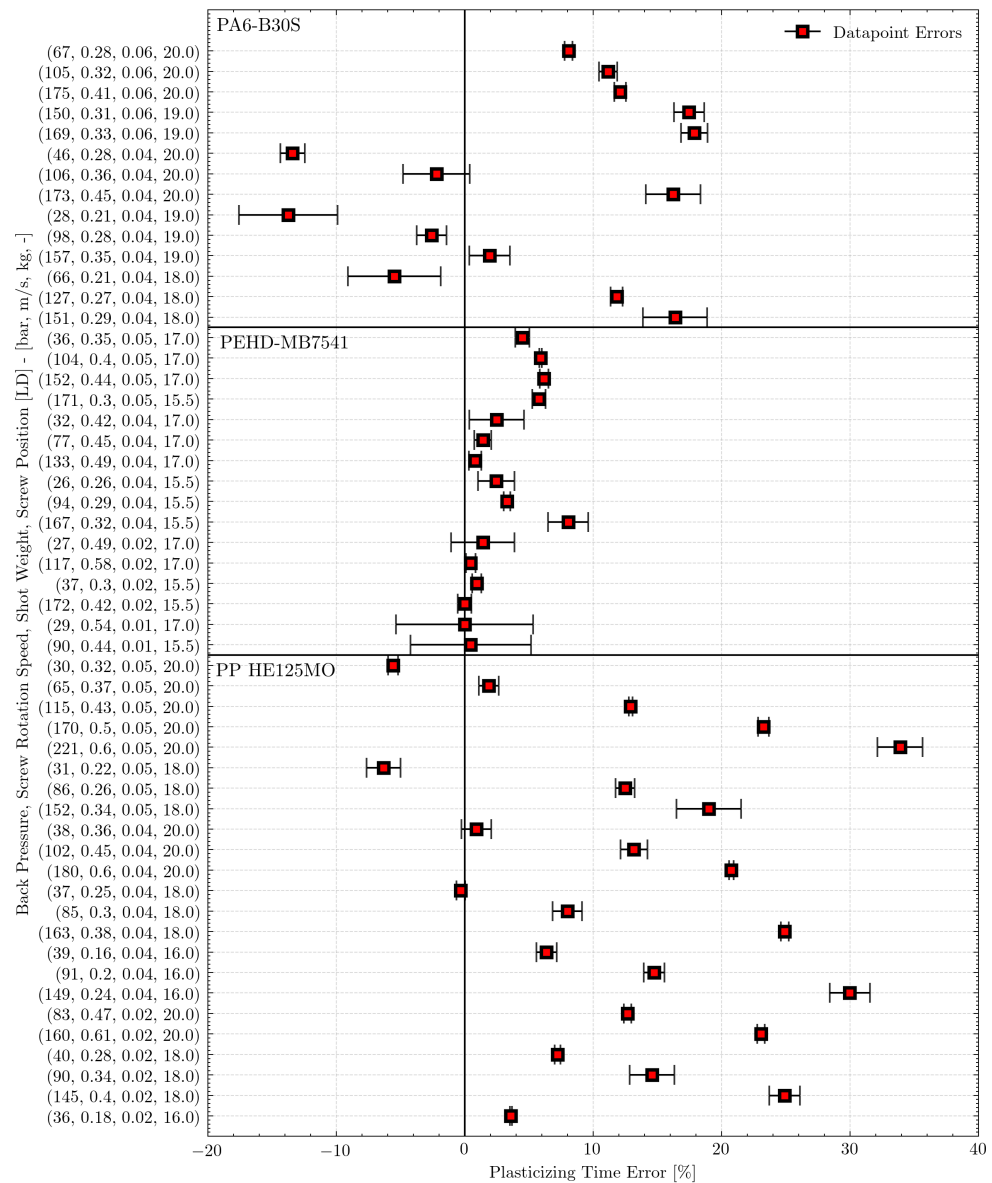


**Figure 9.** Accuracy of the screw rotational speed predictions on the training (samples from which the model is trained), validation (unseen samples for hyperparameter tuning during training), and test (evaluation on unseen samples after training) data sets.

#### 4.2. Results—Model vs. Experiment

We established that the simulation can be accurately described by the neural network model. However, our main objective was the prediction of settings for the back pressure and screw rotational speed given the boundary conditions of a specified melt quality and plasticizing time at a selected screw position.

Figure 10 plots the errors in plasticizing time—given as the mean and standard deviation for each sample—for three experimental runs performed respectively with the materials PP-HE125MO, PEHD-MB7541, and PA6-B30S. The materials were fully characterized at our institute in regard to all relevant rheologic and thermodynamic material parameters that were required for the simulations. We, therefore, assume that differences between the model and experiment were not caused by inadequate material models. The plasticizing error is illustrated by the mean and standard deviation of three measurements for each sample.



**Figure 10.** Mean error between the real and desired plasticizing times based on the predicted basic parameter settings obtained for three materials. Each scattered sample shows the mean and the standard deviation of three experiments per operating point. The mean absolute errors were 2.8%, 10.8%, and 14.5% for PEHD-MB7541, PA6-B30S, and PP-HE125MO, respectively. The ordinate shows the machine setting arrays for all experiments. An array contains the back pressures and screw rotational speeds predicted by the neural network model for specified shot weights and plasticizing times. The screw position where the material is 99% melted is described by the LD value. For example, the sample at the bottom (PP-HE125MO with the array (36, 0.18, 0.02, and 16)) shows a mean error of about 3% between the real and desired plasticizing times. The input information that the shot weight of 20 g is 99% melted at screw position LD 16 was fed into the neural network model, which predicted 36 bar back pressure and a 0.18 m/s screw rotational speed.

The experimental results (see Table 5) show that the predictions of the basic parameter settings were good for the PEHD-MB751 material, with an average absolute error of 2.8%, an absolute standard deviation of 2%, and a maximum error of 8%. For this material, our approach produced suitable machine settings. For PA6-B30S, the absolute mean error was 10.8% with a standard deviation of 6% and a maximum error of 18%. For PP-HE125MO, the prediction performance was poorer, with an absolute mean error of 14.5%, a standard deviation of 10%, and a maximum error of 34%.

**Table 5.** Absolute errors between the real and desired plasticizing times for the predicted parameter settings. The mean and standard deviation were calculated based on all samples per material. Each maximum error was based on only one data point and gives further insights into the differences among the observations of each material.

	PP-HE125MO	PEHD-MB7541	PA6-B30S
Mean	14.4%	2.8%	10.8%
Std	10%	2%	6%
Max	34%	8%	18%

Note that the errors, illustrated in Figure 10, are due mainly to the simulation not yet being able to consider machine behavior, such as material feeding and conveying of solid material. It appears that machine behavior plays a decisive role in the prediction of PP-HE125MO, since we observed considerably greater errors between the simulated and real torques.

#### 4.3. Conclusions and Outlook

We presented a workflow for constructing a simulation-data-based multilayer perceptron model that is able to predict settings for the plasticizing parameters back pressure and screw rotational speed to result in operating points with good melt quality (fully melted material). We demonstrated that, after feature extraction and further preprocessing of the data set, the input variables—screw position where 99% of the material is molten, plasticizing time, and shot weight—were sufficient to provide a reliable, generalized model. The filtered data set comprising 915 simulation data points was split into training, validation, and test sets. The overall performance of the simulation model (digital twin) was assessed by calculating the root-mean-squared error and was visualized in plots. The small error on the test set indicates a low generalization error and, therefore, good performance on unseen data.

For further evaluation of our approach, we conducted experiments with three different materials at the predicted operating points and determined the difference between the real and desired plasticizing times. The melt quality was estimated visually and was acceptable in all cases. The average absolute errors between the real and desired plasticizing times were 2.8%, 10.8%, and 14.5% for PEHD-MB7541, PA6-B30S, and PP-HE125MO, respectively. These errors can be attributed to differences between simulation and reality that arise mainly from machine behavior and the material used. For PEHD, the prediction agreed well with the experimental result; however, for PP, the errors were larger because of machine behavior (increased back pressure). The overall accuracy, however, was high enough to obtain a suitable starting point for optimizing the machine settings.

In the future, given the continuous improvements in simulation accuracy, data-based machine learning models will provide even better assistance to operators in choosing suitable basic machine settings. The errors caused by machine behavior could be minimized by building a second model that includes experimental samples or by updating the existing model by means of transfer learning methods [4,6]. Incorporating cylinder temperatures into the predictions will require more complex models, which is another possible avenue for future research.

**Supplementary Materials:** The following are available online at <https://www.mdpi.com/article/10.3390/polym13162652/s1>.

**Author Contributions:** M.S. and D.A.; Conceptualization, M.S. and D.A.; Data curation, M.S. and D.A.; Formal analysis, G.S.; Funding acquisition, M.S. and D.A.; Investigation, M.S.; Methodology, M.S. and D.A.; Software, G.S.; Supervision, M.S.; Visualization, M.S. and D.A.; Writing—original draft. All authors have read and agreed to the published version of the manuscript.

**Funding:** This research received no external funding.

**Institutional Review Board Statement:** Not applicable.

**Informed Consent Statement:** Not applicable.

**Data Availability Statement:** The data presented in this study are available on request from the corresponding author.

**Acknowledgments:** Open Access Funding by the University of Linz.

**Conflicts of Interest:** The authors declare no conflict of interest.

## References

1. Fernandes, C.; Pontes, A.J.; Viana, J.C.; Nóbrega, J.M.; Gaspar-Cunha, A. Modeling of Plasticating Injection Molding—Experimental Assessment. *Int. Polym. Process.* **2014**, *29*, 558–569. [[CrossRef](#)]
2. Subramanian, M.N. *The Basics of Troubleshooting in Plastics Processing*; Wiley: Hoboken, NJ, USA, 2011; ISBN 978-0-470-62606-1.
3. Singh, M.; Fuenmayor, E.; Hinchy, E.P.; Qiao, Y.; Murray, N.; Devine, D. Digital Twin: Origin to Future. *ASI* **2021**, *4*, 36. [[CrossRef](#)]
4. Hopmann, C.H.; Theunissen, M.; Heinisch, J. *Von der Simulation in die Maschine—Objektivierte Prozesseinrichtung durch Maschinelles Lernen*; VDI Wissensforum GmbH (Hrsg.); Spritzgießen: Baden-Baden, Germany, 2018; pp. 29–42. [[CrossRef](#)]
5. Lee, C.; Na, J.; Park, K.; Yu, H.; Kim, J.; Choi, K.; Park, D.; Park, S.; Rho, J.; Lee, S. Development of Artificial Neural Network System to Recommend Process Conditions of Injection Molding for Various Geometries. *Adv. Intell. Syst.* **2020**, *2*, 2000037. [[CrossRef](#)]
6. Tercan, H.; Guajardo, A.; Heinisch, J.; Thiele, T.; Hopmann, C.; Meisen, T. Transfer-Learning: Bridging the Gap between Real and Simulation Data for Machine Learning in Injection Molding. *Procedia CIRP* **2018**, *72*, 185–190. [[CrossRef](#)]
7. Limper, A. *Verfahrenstechnik der Thermoplastextrusion*; Carl Hanser Verlag: Munich, Germany, 2012; ISBN 978-3-446-41744-1.
8. Altmann, D. Advanced Process Simulation for Single-Screw Plasticizing Units in Injection Molding. Ph.D. Thesis, Johannes Kepler University, Linz, Austria, 2019.
9. Janssens, J. *Data Science at the Command Line: Facing the Future with Time-Tested Tools*; O'Reilly and Associates: Sebastopol, CA, USA, 2014; ISBN 978-1-491-94785-2.
10. Marius, P.; Balas, V.E.; Perescu-Popescu, L.; Mastorakis, N.E. Multilayer perceptron and neural networks. *WSEAS Trans. Circuits Syst.* **2009**, *8*, 579–588.
11. Bishop, C.M. *Neural Networks for Pattern Recognition*; Oxford University Press: New York, NY, USA, 1995; ISBN 978-0-19-853864-6.
12. Rumelhart, D.; Hinton, G.; Williams, R. Learning representations by back-propagating errors. *Nature* **1986**, *323*, 533–536. [[CrossRef](#)]
13. Van Rossum, G.; Drake, F.L., Jr. *Python Reference Manual*; CreateSpace: Scotts Valley, CA, USA, 2009; ISBN 978-1-4414-1269-0.
14. Paszke, A.; Gross, S.; Massa, F.; Lerer, A.; Bradbury, J.; Chanan, G.; Killeen, T.; Lin, Z.; Gimelshein, N.; Antiga, L.; et al. PyTorch: An Imperative Style, High-Performance Deep Learning Library. *Adv. Neural Inf. Process. Syst.* **2019**, *32*, 8024–8035. Available online: <http://papers.neurips.cc/paper/9015-pytorch-an-imperative-style-high-performance-deep-learning-library.pdf> (accessed on 28 April 2021).
15. Wu, Y.; Liu, L.; Bae, J.; Chow, K.H.; Iyengar, A.; Pu, C.; Wei, W.; Yu, L.; Zhang, Q. Demystifying Learning Rate Policies for High Accuracy Training of Deep Neural Networks. *arXiv* **2019**, arXiv:1908.06477.





## Article

# Numerical Study of the Effect of Thixotropy on Extrudate Swell

Michelle Spanjaards<sup>1,2</sup>, Gerrit Peters<sup>1</sup>, Martien Hulsen<sup>1</sup> and Patrick Anderson<sup>1,\*</sup>

<sup>1</sup> Department of Mechanical Engineering, Eindhoven University of Technology, P.O. Box 513, 5600 MB Eindhoven, The Netherlands; m.m.a.spanjaards@tue.nl (M.S.); g.w.m.peters@tue.nl (G.P.); m.a.hulsen@tue.nl (M.H.)

<sup>2</sup> VMI Holland B.V., Gelriaweg 16, P.O. Box 161, 8161 RK Epe, The Netherlands

\* Correspondence: P.D.Anderson@tue.nl

**Abstract:** The extrusion of highly filled elastomers is widely used in the automotive industry. In this paper, we numerically study the effect of thixotropy on 2D planar extrudate swell for constant and fluctuating flow rates, as well as the effect of thixotropy on the swell behavior of a 3D rectangular extrudate for a constant flowrate. To this end, we used the Finite Element Method. The state of the network structure in the material is described using a kinetic equation for a structure parameter. Rate and stress-controlled models for this kinetic equation are compared. The effect of thixotropy on extrudate swell is studied by varying the damage and recovery parameters in these models. It was found that thixotropy in general decreases extrudate swell. The stress-controlled approach always predicts a larger swell ratio compared to the rate-controlled approach for the Weissenberg numbers studied in this work. When the damage parameter in the models is increased, a less viscous fluid layer appears near the die wall, which decreases the swell ratio to a value lower than the Newtonian swell ratio. Upon further increasing the damage parameter, the high viscosity core layer becomes very small, leading to an increase in the swell ratio compared to smaller damage parameters, approaching the Newtonian value. The existence of a low-viscosity outer layer and a high-viscosity core in the die have a pronounced effect on the swell ratio for thixotropic fluids.

**Keywords:** viscoelasticity; thixotropy; extrudate swell; FEM

**Citation:** Spanjaards, M.; Peters, G.; Hulsen, M.; Anderson, P. Numerical Study of the Effect of Thixotropy on Extrudate Swell. *Polymers* **2021**, *13*, 4383. <https://doi.org/10.3390/polym13244383>

Academic Editors: Salah Aldin Faroughi, Luís L. Ferrás, Alexandre M. Afonso and Célio Bruno Pinto Fernandes

Received: 25 November 2021  
Accepted: 8 December 2021  
Published: 14 December 2021

**Publisher's Note:** MDPI stays neutral with regard to jurisdictional claims in published maps and institutional affiliations.



**Copyright:** © 2021 by the authors. Licensee MDPI, Basel, Switzerland. This article is an open access article distributed under the terms and conditions of the Creative Commons Attribution (CC BY) license (<https://creativecommons.org/licenses/by/4.0/>).

## 1. Introduction

In the automotive industry, rectangular rubber strips are extruded that are used to make the carcass of car tires. The dimensions and quality of the rubber extrusion products highly depend on the rheological properties of the rubber compound [1]. These compounds are complex materials in the sense that they contain many additives such as plasticizers, curing agents and about 30% by weight of reinforcing fillers to enhance the mechanical properties of the final product [2].

The addition of fillers increases the viscosity of the compound due to the existence of filler–filler and polymer–filler interactions and is essential to the successful use of rubber in the extrusion process [3,4]. When using carbon black fillers, the primary filler particles form aggregates, and the size and shape of these aggregates are deformation-independent. These aggregates, however, can cluster together to form agglomerates, which can form a filler–filler network that is held together by weak van der Waals-type forces. Because of the fragility of the bonds between the agglomerates, they can break under stress, but when the stress is removed, these bonds will reform again [5]. This leads to a reversible decrease in the viscosity, or so-called thixotropic behavior. For rubber compounds, this is also known as the Payne effect [6].

The Payne effect has also been attributed to several other mechanisms, such as the agglomeration/deagglomeration of filler aggregates, breakup/reformation of the filler–filler and polymer–filler network [7,8], chain desorption from the fillers [9], yielding of the glassy layer between the fillers [10] and disentanglement of the absorbed chains [11]. The

paper by Rueda et al. reviews the current knowledge about the rheology and applications of highly filled polymers [12].

Dangtungee et al. [13,14] experimentally studied the extrudate swell of polypropylene filled with different weight percentages of  $\text{CaCO}_3$  and  $\text{TiO}_2$  nano-particles. They found that swell was reduced by increasing particle concentration. This was explained by the limited mobility of the polymers due to the fillers, hindering the elastic recovery at the die exit. For an LDPE filled with different weight percentages of salt of different sizes, it was also found that the rigid particles lead to a decreased mobility of the polymer chains. No effect of the particle size was found [15].

In highly-filled rubber compounds, a decrease in extrudate swell can be observed with increasing filler content [16–18]. This reduction also occurs if the reinforcing character of the carbon-black is increased or the particle size is decreased and was attributed to a higher volume fraction of “occluded rubber”. Here, the fillers reduce the mobility of the polymer chains, prohibiting the elastic recoil of the polymer chains. For highly reinforcing carbon-blacks, extrudate swell is restrained by a more complex mechanism due to the complex compound morphology.

Since thixotropy has a pronounced effect on the viscosity of the material, bands of different viscosities can coexist in the die during the extrusion process. Due to the high shear rate at the die wall, a low viscous layer will be present there. The inelastic theory of extrudate swell presented by Tanner [19] showed that a less viscous outer layer results in a decreasing swell ratio that can even go below one. This was also found by Mitsoulis [20] in extrudate swell studies for double-layer flows.

The aim of this work is to qualitatively study the effect of thixotropy on the extrudate swell behavior of viscoelastic materials using the Finite Element Method. This is a relevant problem since the extrusion of filled rubber compounds is widely used in the automotive industry and the thixotropic behavior due to the incorporation of these fillers has a pronounced effect on the shape of the final extrusion product. Therefore, we assume that the undamaged material resembles a highly filled polymer filled with agglomerates of an elastic filler–filler/filler–polymer network. The weak physical bonds linking adjacent filler agglomerates can break up when the material is deformed, leading to a material with the properties of a highly filled polymer with less structure compared to the undamaged material. The disappearance of this structure effectively reduces the elasticity in the material. This thixotropic effect due to the added fillers is modeled using a structure parameter that indicates the degree of local structure in the material. The evolution of this structure parameter is modeled using a rate and stress-controlled kinetic equation. The difference between both approaches is discussed. In many industrial processes, the flow rate is not constant but fluctuates in time. Therefore, the effect of structure damage and recovery on extrudate swell is studied for a constant and fluctuating flow rate.

The paper is structured as follows: first, the problem definition and a description of the modeling is given in Section 2. This is followed by a detailed explanation of the numerical method used in this work in Section 3. A convergence study and the results for the constant flow rate and fluctuating flow rate are presented in Section 4. Here, the difference in the results for a stress and a rate-controlled kinetic equation for the structure parameter are discussed, as well as the influence of different damage and recovery parameters on the swell ratio of the extrudate.

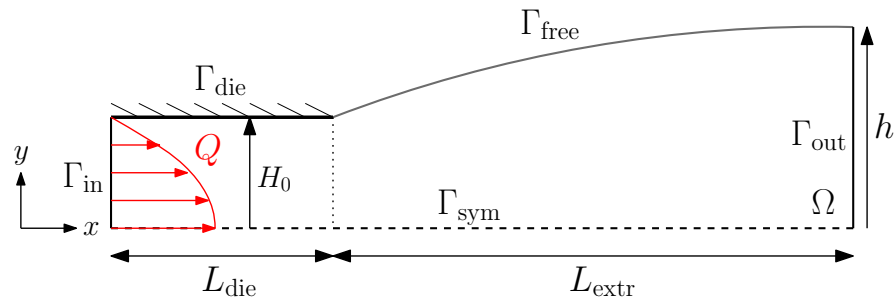
## 2. Problem Description

Two problems are treated in this paper: a 2D planar swell problem and the swell of a 3D rectangular extrudate, both for a thixotropic fluid.

### 2.1. 2D Planar Problem

For the 2D planar problem, a schematic representation of the fluid domain  $\Omega$  is shown in Figure 1. In the first part of the domain, the fluid is contained in a planar die with

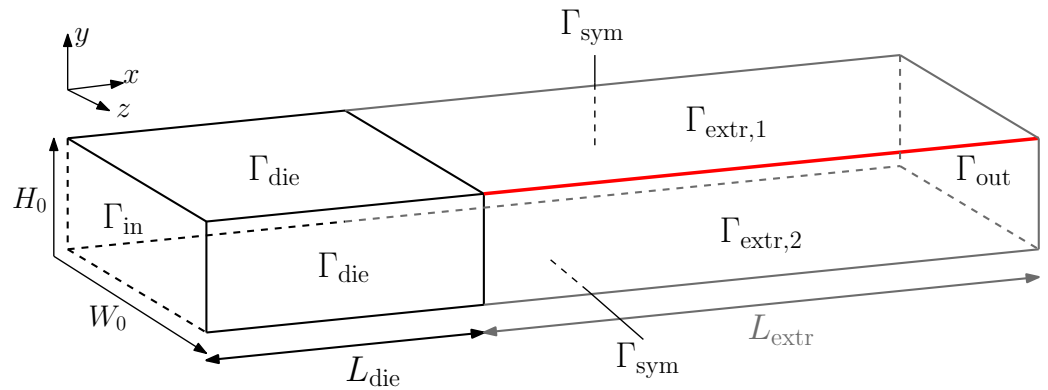
half-height  $H_0$  and length  $L_{die} = 2H_0$ . At the inlet of the die, a flow rate  $Q$  is applied with a fully developed flow profile. The extrudate has length  $L_{extr} = 5H_0$ .



**Figure 1.** Schematic representation of the 2D planar extrudate swell problem. The free surface of the extrudate is indicated in gray.

### 2.2. Three-Dimensional Problem

For the 3D rectangular extrudate, a schematic representation of the fluid domain  $\Omega$  is shown in Figure 2.



**Figure 2.** Schematic representation of the 3D problem of an extrudate emerging from a rectangular die. The corner line used in the corner-line method is depicted in red.

The first part of the domain is the fluid contained in a rectangular die of height  $H_0$  and width  $W_0$ . A constant flow rate  $Q$  is applied at the inlet  $\Gamma_{in}$  of the die. After length  $L_{die} = 2H_0$ , the fluid exits the die. The extrudate is modeled for a length  $L_{extr} = 5H_0$  after the die exit. The corner line of the extrudate, used in the corner-line method as presented by Spanjaards et al. [21], is indicated in red. Only a quarter of the domain is modeled to save computational costs. The rectangular die has an aspect ratio of 2:1 with  $W_0 = 2H_0$ .

### 2.3. Balance Equations

It is assumed that the fluid is incompressible, inertia can be neglected and that there are no external body forces acting on the fluid. This leaves the following equations for the mass and momentum balance in the fluid domain  $\Omega$ :

$$-\nabla \cdot \sigma = 0 \quad \text{in } \Omega, \tag{1}$$

$$\nabla \cdot \mathbf{u} = 0 \quad \text{in } \Omega, \tag{2}$$

where  $\mathbf{u}$  is the fluid velocity and  $\sigma$  is the Cauchy stress tensor:

$$\sigma = -p\mathbf{I} + 2\eta_s\mathbf{D} + \tau. \tag{3}$$

Here,  $p$  is the pressure,  $\mathbf{I}$  the unit tensor and  $2\eta_s\mathbf{D}$  is the Newtonian (or viscous) stress tensor with solvent viscosity  $\eta_s$  and rate-of-deformation tensor  $\mathbf{D} = (\nabla\mathbf{u} + \nabla\mathbf{u}^T)/2$ . The viscoelastic stress tensor is represented by  $\tau$ .

### 2.4. Constitutive Equations

The viscoelastic stress tensor is expressed in terms of the conformation tensors  $c_k$ :

$$\boldsymbol{\tau} = \sum_{k=1}^m G_k(c_k - \mathbf{I}), \tag{4}$$

where  $m$  is the number of modes and  $G_k$  is the polymer modulus of mode  $k$ .

The evolution of the conformation tensors  $c_k$  is given by

$$\frac{Dc_k}{Dt} - (\nabla \mathbf{u})^T \cdot c_k - c_k \cdot \nabla \mathbf{u} + f(c_k) = \mathbf{0}, \tag{5}$$

where  $D()/Dt = \partial()/\partial t + \mathbf{u} \cdot \nabla()$  denotes the material derivative, and  $f(c_k)$  depends on the constitutive model used. In this paper, the Giesekus model is used [22]:

$$f(c_k) = \frac{1}{\lambda_k} [c_k - \mathbf{I} + \alpha_k(c_k - \mathbf{I})^2], \tag{6}$$

where  $\alpha_k$  is the mobility parameter of mode  $k$  that influences shear-thinning. Other constitutive equations can be used due to the generality of our method.

### 2.5. Thixotropy Model

In thixotropic materials, it is known that the added fillers can form two types of networks: filler–filler networks and polymer–filler networks. These networks improve the strength of the material. These networks are held together by weak physical bonds. When the material is deformed, these bonds can break, but after flow cessation, these bonds can reform again. To model this thixotropic behavior, a structure parameter  $\zeta$  is defined which indicates the degree of structure in the material, as discussed in Spanjaards et al. [23]. If  $\zeta = 1$ , the material is undamaged and the filler–filler/polymer–filler networks are intact. For  $\zeta = \zeta_{\text{inf}}$ , no network structures are left:

$$\zeta = \begin{cases} 1, & \text{Undamaged; structures intact} \\ \zeta_{\text{inf}}, & \text{Maximum damage.} \end{cases}$$

For the minimum value for  $\zeta_{\text{inf}} = 0$ , no structure is left. Inspired by the Leonov modeling [24], the effect of structure damage is modeled by adjusting the relaxation times of the undamaged spectrum  $\lambda_{0,k}$  ( $\zeta = 1$ ) with the current structure parameter:

$$\lambda_k = \zeta \lambda_{0,k}. \tag{7}$$

The polymer modulus  $G_k$  is assumed to be independent of the structure change in the material. Notice that, using this approach, the polymer viscosity  $\eta_{p,k}(\zeta)$  and the relaxation time  $\lambda_k(\zeta)$  of mode  $k$  depend on the structure according to  $\eta_{p,k}(\zeta) = G_k \lambda_k(\zeta)$ . The ratio between the solvent viscosity and the zero-shear viscosity for the undamaged material is defined as  $\beta_0 = \eta_s / \eta_0$ . Here,  $\eta_0 = \eta_s + \eta_{p0}$  is the zero-shear viscosity, with  $\eta_{p0} = \sum_{k=1}^m \eta_{p0,k}$  being the total polymer viscosity of the undamaged material.

The evolution of the structure parameter can be described with a rate or stress-controlled kinetic equation. The rate-controlled equation is as follows [24]:

$$\frac{D\zeta}{Dt} = \frac{1 - \zeta}{\lambda_\theta} - E\gamma^*(\zeta - \zeta_{\text{inf}}), \tag{8}$$

where  $\lambda_\theta$  is a characteristic time scale for the recovery of the material structure,  $E = \sqrt{2\text{tr}\mathbf{D}^2}$  is a measure of the deformation rate based on the rate of deformation tensor  $\mathbf{D}$ , corresponding to the shear rate in shear flows. Furthermore,  $\gamma^*$  is a dimensionless fitting parameter that

indicates how much of the applied deformation leads to the damage of the structure. We modified Equation (8) to obtain the following stress-controlled equation:

$$\frac{D\xi}{Dt} = \frac{1 - \xi}{\lambda_\theta} - \frac{\tau_c(\boldsymbol{\tau})}{\eta_{p0}} \tau^* (\xi - \xi_{inf}), \tag{9}$$

where  $\tau_c(\boldsymbol{\tau})$  is a characteristic stress in the material that is a function of the viscoelastic stress tensor, and  $\tau^*$  is a dimensionless fitting parameter that describes how much of the present stress contributes to the damage of the elastic network. Here, the equivalent von Mises shear stress is used as characteristic stress  $\tau_c(\boldsymbol{\tau})$  [25]:

$$\tau_c(\boldsymbol{\tau}) = \sqrt{\frac{1}{2} \hat{\boldsymbol{\tau}} : \hat{\boldsymbol{\tau}}}, \tag{10}$$

with  $\hat{\boldsymbol{\tau}} = \boldsymbol{\tau} - \frac{1}{3}(\text{tr } \boldsymbol{\tau})\mathbf{I}$ , the deviatoric part of the total viscoelastic stress tensor.

### 2.6. Arbitrary Lagrangian–Eulerian Formulation

For both the 2D planar and 3D swell problem, a body-fitted approach is used to take into account the movement of the free surfaces. To this end, the domain is described with a mesh that is moving in time in such a way that it follows the movement of the free surfaces, but not necessarily the movement of the fluid. Therefore, the governing equations are rewritten in the Arbitrary Lagrangian–Eulerian (ALE) formulation [26]. The convective terms in equations that contain material derivatives have to be corrected for the mesh movement:

$$\frac{D(\cdot)}{Dt} = \frac{\partial(\cdot)}{\partial t} \Big|_{x_g} + (\mathbf{u} - \mathbf{u}_m) \cdot \nabla(\cdot). \tag{11}$$

where  $\partial(\cdot)/\partial t|_{x_g}$  denotes the time derivative at a fixed grid point  $x_g$  and  $\mathbf{u}_m$  is the mesh velocity.

### 2.7. Free Surface Description

#### 2.7.1. Two-Dimensional Planar Problem

For the 2D planar problem, the evolution of the free surface is described using a 1D height function [27]:

$$\frac{\partial h}{\partial t} + u_x \frac{\partial h}{\partial x} = u_y, \tag{12}$$

where  $h$  is the height of the free surface in every node on  $\Gamma_{\text{free}}$  and the subscript  $y$  indicates the swell direction of the free surface.

#### 2.7.2. Three-Dimensional Problem

For the 3D problem, the corner-line method as described in [21] is used to obtain the positions of the free surfaces. Here, the corner lines of the extrudate are described as material lines. The following kinematic equation is solved to obtain the  $y$  and  $z$ -positions of these lines:

$$\frac{\partial \mathbf{d}}{\partial t} + u_x \frac{\partial \mathbf{d}}{\partial x} = \mathbf{u}_{2D}, \tag{13}$$

where  $\mathbf{d}$  is the position vector containing the positions  $f$  in  $y$  and  $z$ -directions  $\mathbf{d} = (f_y, f_z)$ , and  $\mathbf{u}_{2D}$  is the velocity vector containing the velocities in  $y$  and  $z$ -directions  $\mathbf{u}_{2D} = (u_y, u_z)$ .

The free surfaces, connected by a corner line, are described using 2D height functions [27]. The domain of the height function is not constant in time but changes due to the movement of the corner lines. This change has to be taken into account, and this is done using the ALE method. This leads to the following equation to obtain the heights  $h$  of the free surfaces:

$$\frac{\partial h}{\partial t} \Big|_{x_g} + u_x \frac{\partial h}{\partial x} + (u_z - u_{m,z}) \frac{\partial h}{\partial z} = u_y, \tag{14}$$

where  $\partial(\cdot)/\partial t|_{x_g}$  denotes the time derivative in a fixed grid point of the 2D grid of the expanding domain, the subscript  $z$  indicates the direction of the expanding 2D  $(x,z)$  domain, and  $u_{m,z}$  is the corresponding mesh velocity. The subscript  $y$  indicates the swell direction of the upper free surface (see Figure 2). For the free surfaces at the sides of the die,  $y$  and  $z$  in Equation (14) are interchanged due to the rotation of the surface with respect to the upper free surfaces.

### 2.8. Boundary- and Initial Conditions

Schematic representations of the 2D and 3D domains are shown in Figure 1 and in Figure 2, respectively. Fully developed inflow conditions are prescribed at the inlet boundary  $\Gamma_{in}$  by first solving a subproblem of a periodic channel. A flow rate  $Q$  is enforced to this channel as a constraint using a Lagrange multiplier. The periodic velocity, structure parameter and conformation tensor solution of this channel are prescribed as an essential boundary condition to the inlet boundary ( $\Gamma_{in}$ ) of the problem. Note, that the periodic solution is a function of time  $t$ . At the walls of the die ( $\Gamma_{die}$ ), a no-slip boundary condition is applied, whereas the tractions are zero at the free surfaces ( $\Gamma_{free}$ ). At the outlet ( $\Gamma_{out}$ ), a free outflow is described, which means that there is no velocity in  $y$  and  $z$ -directions and the traction in  $x$ -direction is zero. The boundary conditions are given by

$$\begin{aligned}
 \mathbf{u}_{in} &= \mathbf{u}_{chan} && \text{on } \Gamma_{in}, \\
 \mathbf{c}_{k,in} &= \mathbf{c}_{k,chan} && \text{on } \Gamma_{in}, \\
 \zeta_{in} &= \zeta_{chan} && \text{on } \Gamma_{in}, \\
 \mathbf{u} &= \mathbf{0} && \text{on } \Gamma_{die}, \\
 u_y &= 0 && \text{on } \Gamma_{out}, \\
 t_x &= 0 && \text{on } \Gamma_{out}, \\
 \mathbf{t} &= \mathbf{0} && \text{on } \Gamma_{free},
 \end{aligned} \tag{15}$$

where  $\mathbf{u}_{chan}$ ,  $\zeta_{chan}$  and  $\mathbf{c}_{k,chan}$  are obtained from the separate periodic channel problem. The traction vector on the surface with an outwardly directed normal  $\mathbf{n}$  is denoted by  $\mathbf{t} = \boldsymbol{\sigma} \cdot \mathbf{n}$ . An essential boundary condition on the height function of every free surface is applied such that the free surface stays attached to the die.

The initial conditions for the height functions are given by

$$\begin{aligned}
 \mathbf{d}(t = 0) &= \mathbf{d}_0, \\
 h(t = 0) &= H_0,
 \end{aligned} \tag{16}$$

where  $\mathbf{d}_0$  and  $H_0$  are equivalent to the coordinates of the corner points of the die and the height of the die, respectively. The initial condition for the conformation tensor  $\mathbf{c}_k$  in Equation (5) is given by

$$\mathbf{c}_k(t = 0) = \mathbf{I}, \tag{17}$$

The fluid is initially assumed to be undamaged, which leads to the following initial condition for the structure parameter  $\zeta$ :

$$\zeta(t = 0) = 1 \tag{18}$$

The initial conditions presented in Equations (17) and (18) are applied to both the periodic inlet channel and  $\Omega$ .

### 3. Numerical Method

The finite element method is used to solve the governing equations. The log-conformation representation [28], SUPG [29] and DEVSS-G [30] are used for stability in solving the constitutive equation. SUPG is also used for stability in the height function equations of the free surfaces and the corner lines.

### 3.1. Weak Formulations

The weak formulation of the balance equations can be derived by multiplying the equations with test functions and integrating over the domain using partial integration and the Gauss theorem.

The weak form of the mass and momentum balance and the constitutive equation can now be formulated as follows: find  $\mathbf{u}$ ,  $p$ ,  $\mathbf{G}$  and  $\mathbf{s}_k$  such that

$$((\nabla v)^T, \nu(\nabla \mathbf{u} - \mathbf{G}^T)) + (D_v, 2\eta_s \mathbf{D} + \boldsymbol{\tau}) - (\nabla \cdot v, p) = 0, \tag{19}$$

$$(q, \nabla \cdot \mathbf{u}) = 0, \tag{20}$$

$$(\mathbf{H}, -\nabla \mathbf{u} + \mathbf{G}^T) = 0, \tag{21}$$

$$\left( \zeta + \tau_1(\mathbf{u} - \mathbf{u}_m) \cdot \nabla \zeta, \frac{\partial \mathbf{s}_k}{\partial t} \Big|_{x_g} + (\mathbf{u} - \mathbf{u}_m) \cdot \nabla \mathbf{s}_k - \mathbf{g}(\mathbf{G}, \mathbf{s}_k) \right) = 0, \tag{22}$$

for all admissible test functions  $v, q, \mathbf{H}, \zeta$ . Furthermore,  $D_v = (\nabla v + (\nabla v)^T)/2$ ,  $(\cdot, \cdot)$  denotes the inner product on domain  $\Omega$ , and  $\nu$  and  $\tau_1$  are parameters due to DEVSS-G and SUPG stabilization, respectively. Furthermore,  $\mathbf{s}_k = \log c_k$ . More information on log-conformation stabilization and the function  $\mathbf{g}$  can be found in [28], whereas more information on the DEVSS-G method and the projected velocity gradient  $\mathbf{G}$  can be found in [30].

The weak form of the evolution equations for the rate and stress-controlled structure parameter can be formulated as follows: find  $\zeta$  such that

$$\left( \chi + \tau_2 \mathbf{u} \cdot \nabla \chi, \frac{\partial \zeta}{\partial t} \Big|_{x_g} + (\mathbf{u} - \mathbf{u}_m) \cdot \nabla \zeta - \frac{1 - \zeta}{\lambda_\theta} + f(\zeta - \zeta_{\text{inf}}) \right) = 0 \tag{23}$$

for admissible test functions  $\chi$ . Here,  $f = E\gamma^*$  for the rate-controlled model,  $f = (\tau_c \tau^*)/\eta_{p0}$  for the stress-controlled model, and  $\tau_2$  is again a parameter due to SUPG stabilization. For the 2D problem, the weak formulation for the height function is the same as formulated by Choi and Hulsen [31], whereas for the 3D problem, the weak formulations of the height functions of the corner lines and the free surfaces can be found in [21].

### 3.2. Spatial Discretization

For the 2D planar isoparametric problem, triangular  $P_2P_1$  (Taylor–Hood) elements are used for the velocity and pressure. For the conformation, triangular  $P_1$  elements are used. For the 1D height function, quadratic line elements are used, whereas for the kinetic equations of the structure parameter, triangular  $P_1$  elements are used. A structured mesh is generated using Gmsh [32]. For the 3D isoparametric problem, tetrahedral  $P_2P_1$  (Taylor–Hood) elements are used for the velocity and pressure, whereas for the conformation, tetrahedral  $P_1$  elements are used. For the 1D height functions of the corner lines, quadratic line elements are used, whereas for the 2D height functions of the free surfaces, quadratic triangular elements are used. For the kinetic equations of the structure parameter, tetrahedral  $P_1$  elements are used. Equations (22) and (23) are solved using SUPG for stability. The SUPG parameters are obtained as follows:

$$\tau = \beta_{\text{SUPG}} \frac{h_{\text{elem}}}{2|\mathbf{u}|}. \tag{24}$$

where  $\beta_{\text{SUPG}} = 1$ ,  $\tau$  is calculated in every integration point and  $h_{\text{elem}}$  is the element size and is defined using the method of Hughes et al. [33]. SUPG stabilization is also used for the height function of the free surface. More information on the SUPG parameter for the weak form of the height function for the 2D planar problem can be found in [31], whereas for the 3D problem, this can be found in [21].



### 3.3. Time Discretization

A predictor–corrector scheme is used to obtain the positions of the free surface. To start, a Newtonian time step is performed with an initially homogeneous undamaged structure parameter field  $\zeta = 1$  to obtain the initial velocities and pressures. The numerical procedure of every time step is now as follows:

**Step 1** Predict and update the position of the free surface,  $x_{\text{free}}$ , in the bulk mesh. For the first time step, the prediction of the position equals the initial position:  $x_{\text{free,pred}} = x_{\text{free},0}$ . For subsequent time steps, a second-order prediction of the free surface position is used:

$$x_{\text{free,pred}} = 2x_{\text{free}}^n - x_{\text{free}}^{n-1}. \quad (25)$$

**Step 2** Construct the ALE mesh. This is done by solving a Laplace equation to obtain the mesh displacement, as explained in [21]. The new coordinates of the nodes are calculated using this obtained mesh displacement.

**Step 3** The mesh velocities can now be obtained by numerically differentiating the mesh displacement. In the first time step, the mesh velocities are zero, since the height function is equal to the initial height  $H_0$ . For subsequent time steps, a second-order backward differencing scheme is used, using the updated mesh nodes:

$$u_m^{n+1} = \frac{\frac{3}{2}x_m^{n+1} - 2x_m^n + \frac{1}{2}x_m^{n-1}}{\Delta t}, \quad (26)$$

where  $\Delta t$  is the time step used.

**Step 4** A prediction is done for the velocity and the conformation fields. In the first time step, a first-order prediction is used:  $\hat{u} = u^n$ ,  $\hat{c} = c^n$ . For subsequent time steps, a second-order prediction of the velocity and conformation field is used:

$$\hat{u} = 2u^n - u^{n-1}, \quad (27)$$

$$\hat{c} = 2c^n - c^{n-1}. \quad (28)$$

The velocity prediction is used to calculate  $E^{n+1}$  in the rate-controlled kinetic equation for  $\zeta$ , whereas the conformation prediction is used to calculate the von Mises equivalent shear stress  $\tau_c(\hat{\tau})$ , as given by Equation (10), in the stress-controlled equation for  $\zeta$ . Equation (23) can now be solved to obtain the structure parameter  $\zeta^{n+1}$  in every node of the mesh. For the first time step, first-order time integration is used:

$$\left. \frac{\partial \zeta}{\partial t} \right|_{x_g} = \frac{\zeta^{n+1} - \zeta^n}{\Delta t}, \quad (29)$$

whereas for subsequent time steps, second-order time integration is used:

$$\left. \frac{\partial \zeta}{\partial t} \right|_{x_g} = \frac{\frac{3}{2}\zeta^{n+1} - 2\zeta^n + \frac{1}{2}\zeta^{n-1}}{\Delta t}. \quad (30)$$

The relaxation times are now updated using  $\zeta^{n+1}$ .

**Step 5** Using the method of D'Avino and Hulsen [34] for decoupling the momentum balance from the constitutive equation, the velocities  $u^{n+1}$  and pressures  $p^{n+1}$  are computed. Using this implicit stress formulation, the balance equations are solved using a prediction for the viscoelastic stress tensor to find  $u_{n+1}$  and  $p_{n+1}$  at every time step.

**Step 6** After solving for the new velocities and pressures, the actual conformation tensor  $c^{n+1}$  is found using a second-order, semi-implicit extrapolated backward differencing scheme with conformation prediction for Equation (22).

**Step 7** Update the position of the free surface by solving the evolution equation of the height function (12). For the first time step, first-order time integration is used, whereas for subsequent time steps, second-order time integration is used, as explained in [31].

For the 3D problem, the time integration scheme as presented in [21] is used. The structure parameter  $\zeta$  is calculated in the same way as presented in the time integration scheme in this section.

#### 4. Results

First, the results for mesh and time convergence are shown, followed by results for the extrudate swell of thixotropic fluids. The relevant parameters used throughout this work are given in Table 1. From now on, we refer to  $\gamma^*$  and  $\tau^*$  as the “damage parameters”.

**Table 1.** Material parameters used in this study. Additionally, the parameters  $\beta = 0.1$  and  $\zeta_{\text{inf}} = 0.1$  are used throughout this paper.

Mode	$\lambda_{0,k}/\lambda_{\text{avg}}$	$G_{0,k}\lambda_{\text{avg}}/\eta_{p0}$	$\alpha$
1	10	0.0048	0.3
2	1	0.48	0.3
3	0.1	4.8	0.3

where  $\lambda_{\text{avg}} = (\sum_{k=1}^m G_{0,k}\lambda_{0,k}^2) / (\sum_{k=1}^m \eta_{p0,k})$  is the viscosity averaged relaxation time of the undamaged material, with  $m$  the number of modes. The Weissenberg number of the problem is defined as follows:

$$\text{Wi} = \frac{U_{\text{avg}}\lambda_{\text{avg}}}{H_0} \quad (31)$$

This spectrum is chosen because it represents an elastic material with strong shear-thinning behavior, as is characteristic for rubber compounds [35].

##### 4.1. Convergence

To verify if the rate and stress-controlled thixotropy models are correctly implemented, a convergence study is performed. A convergence study of the 2D and 3D swell code was performed by Spanjaards et al. in [21,36]. Therefore, we now focus on the implementation of the thixotropy models. In this convergence study, the thixotropy model is decoupled from the flow, which means that the relaxation times are not adjusted with the structure parameter  $\zeta$ . A channel flow with length  $L = 100H_0$  of a single-mode Upper Convected Maxwell (UCM) fluid (with relaxation time  $\lambda_0$  and  $\eta_s = 0$ ) is modeled. A flow rate  $Q$  is applied at the channel inlet, and the analytical solution of a fully developed flow is prescribed to the velocity and the viscoelastic stress tensor. The Weissenberg number of the problem equals  $\text{Wi} = 1$ . For a fully developed channel flow of an UCM fluid, the velocity, shear rate and viscoelastic stresses can be found to be

$$u_x(y) = \frac{3Q}{2H_0} \left(1 - \frac{y^2}{H_0^2}\right) \quad (32)$$

$$\dot{\gamma} = \frac{3Q}{H_0^3} y, \quad (33)$$

$$\sigma_{xx} = 2\eta_0\dot{\gamma}^2, \quad \sigma_{yy} = 0, \quad \sigma_{xy} = \eta_0\dot{\gamma}, \quad (34)$$

where  $H_0$  is the half height of the channel,  $\eta_0$  is the zero-shear viscosity of the fluid,  $Q$  is the flow rate applied at the inlet of the channel, and  $y$  is the  $y$ -coordinate of the height of the channel. Analytical solutions of Equations (8) and (9) can be defined as follows:

$$\zeta_{\text{an}} = A e^{-(\frac{1}{\lambda_\theta} + f)t} + \zeta_{\text{eq}}, \quad (35)$$

with

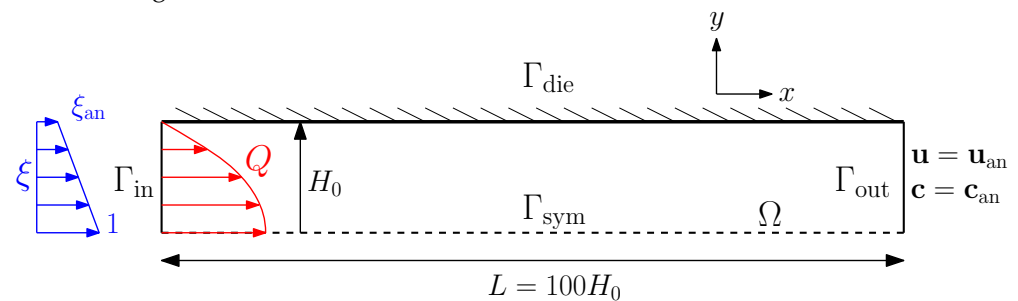
$$A = 1 - \frac{1 + f\lambda_\theta \zeta_{\text{inf}}}{1 + f\lambda_\theta} \tag{36}$$

where  $f$  and  $\zeta_{\text{eq}}$  can be expressed as follows for the rate and stress-controlled equation, respectively:

$$f = \dot{\gamma}\gamma^* \text{ (rate)}, \quad f = \frac{\tau_c(\boldsymbol{\tau})}{\eta_0} \tau^* \text{ (stress)}, \tag{37}$$

$$\zeta_{\text{eq}} = \frac{1 + f\lambda_\theta \zeta_{\text{inf}}}{1 + f\lambda_\theta} \tag{38}$$

To avoid a singular point at the die wall, a linear profile for the structure parameter  $\zeta$  is applied as an essential boundary condition at the inlet. At the die wall, the analytical solution for  $\zeta$  is prescribed while linearly decreasing to zero with the  $y$ -coordinate at the symmetry axis of the channel. A schematic representation of the 2D channel problem is shown in Figure 3.



**Figure 3.** Schematic representation of the 2D channel problem used in the convergence study.

#### 4.1.1. Mesh Convergence

The solution of  $\zeta_{\text{an}}$  for meshes with different element sizes is compared to the computed  $\zeta$  at the outlet of the channel  $\Gamma_{\text{out}}$  for the rate and stress-controlled implementation. More information on the meshes used can be found in Table 2. Here,  $h_{\text{elem}}$  is the element size over the height with respect to the channel height  $H_0$ . The relative error at a time  $t = 10\lambda_0$  is defined as

$$\epsilon(y) = \frac{\left( \int_{\Gamma_{\text{out}}} (\zeta - \zeta_{\text{an}})^2 \right)^{1/2}}{\left( \int_{\Gamma_{\text{out}}} \zeta_{\text{an}}^2 \right)^{1/2}} \Bigg|_{t=10\lambda_0}, \tag{39}$$

where  $\zeta$  is the structure parameter on the outlet of the channel,  $\zeta_{\text{an}}$  is the analytical solution,  $\epsilon(y)$  is the relative error in  $\zeta$  for different heights  $y$  on the outlet, and  $\Gamma_\epsilon$  is  $\Gamma_{\text{out}}$ .

**Table 2.** Meshes used in the mesh convergence study on a 2D channel flow problem.

Mesh	# Nodes	$h_{\text{elem}}/H_0$
M1	7209	0.25
M2	27217	0.125
M3	105633	0.0625
M4	416065	0.03125

The result is shown in Figure 4. For both methods, convergence with order two is obtained, which was expected based on the order of interpolation of the elements.

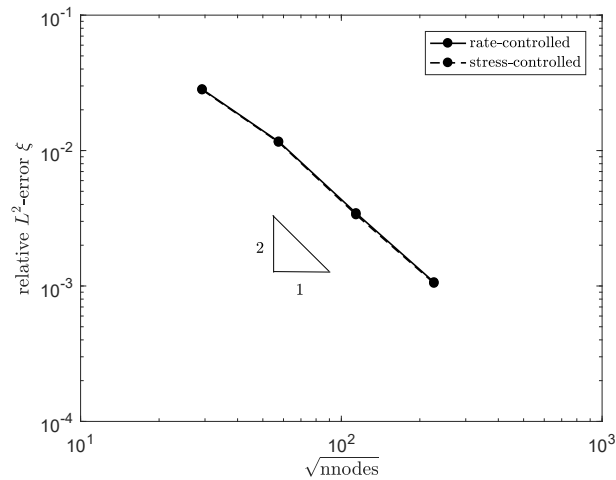


Figure 4. Relative error in  $\zeta$  at the outlet of the channel for 2D meshes with different element sizes.

Figure 5 shows a 2D planar swell mesh that is one uniform refinement step coarser compared to the mesh used throughout the remainder of this paper. The coarsest element size at the symmetry axis of the mesh used in this paper is  $h_{\text{sym}} = 0.05H_0$ . The mesh is progressively refined with a factor of 5 towards the die wall  $h_{\text{wall}} = 0.01H_0$ , and with a factor of 10 towards the die exit  $h_{\text{die-exit}} = 0.005H_0$ .

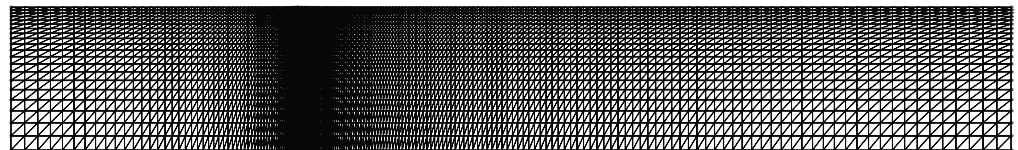


Figure 5. Two-dimensional planar swell mesh one uniform refinement step coarser compared to the mesh used throughout the remainder of this paper.

The 3D problem is much more computationally demanding than the 2D planar problem. Therefore, a coarser mesh is used. The 3D mesh is shown in Figure 6. Here, the coarsest element size is  $h_{\text{sym}} = 0.2H_0$ . The mesh is refined with a factor 5 at the die exit. Since this mesh is much coarser than the 2D planar mesh, the 3D results will only be used to get a qualitative idea of the influence of thixotropy on the final extrudate shape. More information about the 2D and 3D swell mesh used in this paper can be found in Table 3.

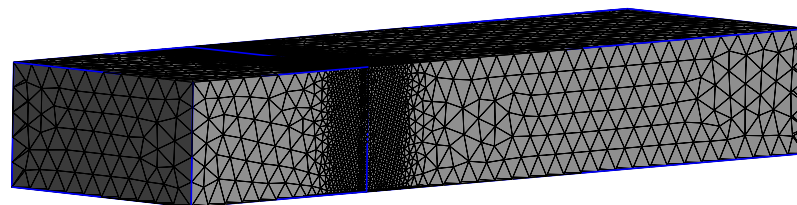


Figure 6. Three-dimensional mesh used in this study. Refinement factor at the die exit is 5.

Table 3. Two and three-dimensional meshes for the swell problems in this paper.

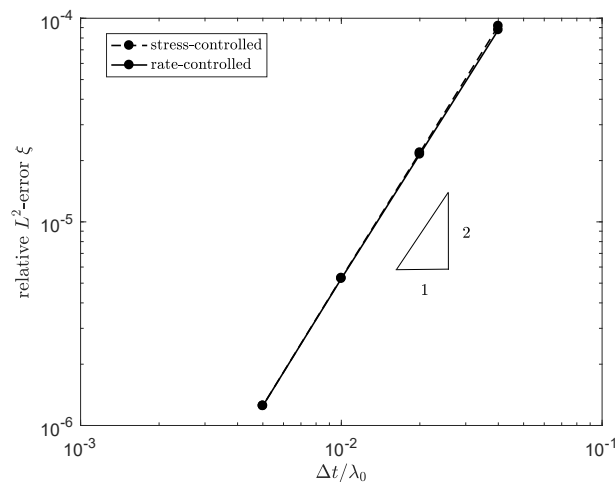
Mesh	# Nodes	# Elements	$h_{\text{sym}}/H_0$	$h_{\text{wall}}/H_0$	$h_{\text{die-exit}}/H_0$
2D	58401	28800	0.05	0.01	0.005
3D	50467	32444	0.2	0.2	0.04

#### 4.1.2. Time Convergence

Time convergence is tested on Mesh M4. The solution for different time step sizes is compared to a reference solution for a reference time step that is two times smaller compared to the smallest time step tested. The relative error at time  $t = \lambda_0$  is calculated as follows:

$$\epsilon(y) = \frac{\left( \int_{\Gamma_{\text{out}}} (\zeta - \zeta_{\text{ref}})^2 \right)^{1/2}}{\left( \int_{\Gamma_{\text{out}}} \zeta_{\text{ref}}^2 \right)^{1/2}} \Bigg|_{t=\lambda_0}, \quad (40)$$

where  $\zeta_{\text{ref}}$  is the solution for the reference time step. The result is shown in Figure 7. For both methods, convergence with order two is obtained, with was expected based on the order of the time integration.



**Figure 7.** Relative error in  $\zeta$  at the outlet of the channel at time  $t = \lambda_0$ , for different time step sizes  $\Delta t$  for the rate and stress-controlled approach.

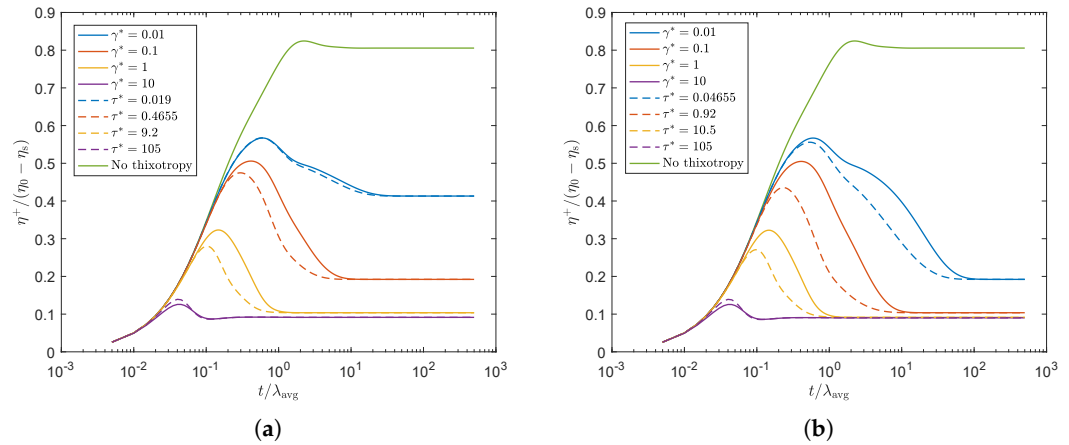
Throughout this paper, a time step size of  $\Delta t = 1.25 \cdot 10^{-3} \lambda_{\text{avg}}$  is used.

#### 4.2. Constant Flow Rate

At first, a constant flow rate is applied to the inlet of the die. The influence of the model parameters in the rate and stress-controlled equations for the structure parameter ( $\lambda_\theta$ ,  $\gamma^*$ ,  $\tau^*$ ) is studied in this section, as well as the difference between the rate and stress-controlled approach.

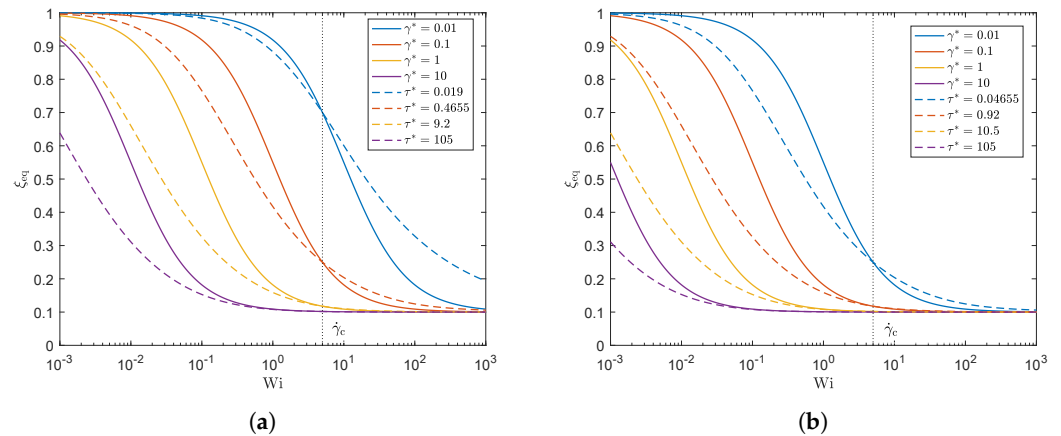
##### 4.2.1. Rheology

In order to study the differences between the rate and stress-controlled approach, the rheology of both methods has to be matched. To this end, we chose to match the equilibrium value for the structure parameter  $\zeta_{\text{eq}}$  in steady shear (see Equation (38)) for both methods at a characteristic shear rate  $\dot{\gamma}_c = U_{\text{avg}}/H_0$ . This characteristic shear rate is used in the simulations throughout this paper when the two models are compared and corresponds to a Weissenberg number of  $Wi = 5$ . The transient polymer viscosity for two different recovery time scales  $\lambda_\theta$  and different damage model parameters  $\gamma^*$  and  $\tau^*$  is shown in Figure 8. This figure shows that the steady state viscosity is indeed the same for the rate and stress-controlled approach for the characteristic shear rate, but the transient behaviors are not.



**Figure 8.** Transient polymer viscosity for  $\dot{\gamma}_c$ , where  $\gamma^*$  and  $\tau^*$  are chosen such that  $\zeta_{eq}$  is matched for the rate and stress-controlled approach to obtain the same steady-state rheology for both models. **(a)**  $\lambda_\theta = 10\lambda_{avg}$ . **(b)**  $\lambda_\theta = 100\lambda_{avg}$ .

The stress-controlled approach predicts a smaller overshoot compared to the rate-controlled approach for all damage parameters except the highest, for which a slightly higher overshoot is predicted by the stress-controlled approach. Figure 9 shows the equilibrium value of  $\zeta$  in steady state for different Weissenberg numbers for both approaches. The vertical black dotted line indicates the Weissenberg number corresponding to the characteristic shear rate for which both models match. This figure shows that  $\zeta_{eq}$  is indeed matched for the characteristic shear rate. It is however clear that for  $\dot{\gamma} < \dot{\gamma}_c$ , the stress-controlled approach predicts a smaller value for  $\zeta_{eq}$  (indicating more structural damage), whereas for  $\dot{\gamma} > \dot{\gamma}_c$ , the stress-controlled approach predicts a larger value for  $\zeta_{eq}$  (less structural damage) compared to the rate-controlled approach.



**Figure 9.** Equilibrium structure parameter  $\zeta_{eq}$  as a function of Weissenberg number. Here,  $\gamma^*$  and  $\tau^*$  are chosen such that  $\zeta_{eq}$  is matched for the rate and stress-controlled approach at a characteristic shear rate  $\dot{\gamma}_c$ . **(a)**  $\lambda_\theta = 10\lambda_{avg}$ . **(b)**  $\lambda_\theta = 100\lambda_{avg}$ .

The damage parameters used in this paper to compare the stress and rate-controlled approach are given in Table 4.

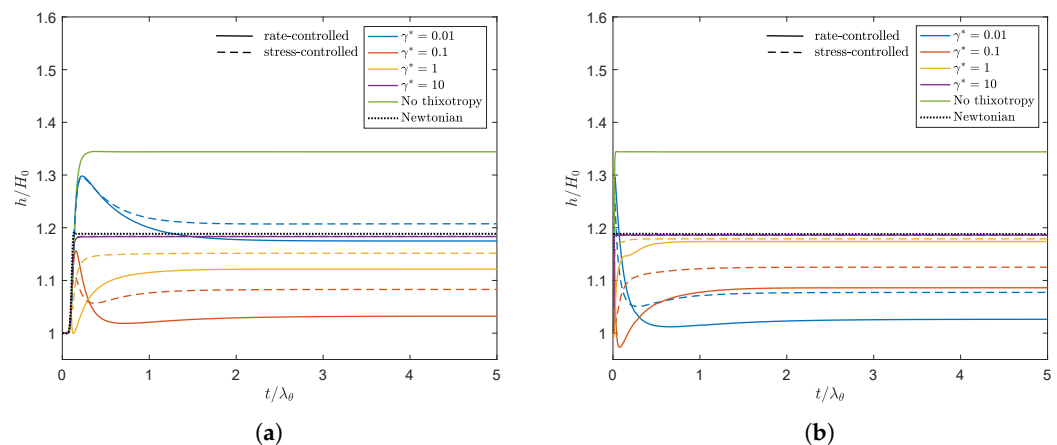
**Table 4.** Damage parameters used to match the rheology of the rate-controlled approach ( $\gamma^*$ ) and the stress-controlled approach ( $\tau^*$ ) at the characteristic shear rate  $\dot{\gamma}_c$  for two different recovery time scales.

$\lambda_\theta = 10\lambda_{\text{avg}}$		$\lambda_\theta = 100\lambda_{\text{avg}}$	
$\gamma^*$	$\tau^*$	$\gamma^*$	$\tau^*$
0.01	0.019	0.01	0.04655
0.1	0.4655	0.1	0.92
1	9.2	1	10.5
10	105	10	105

#### 4.2.2. Influence Model and Model Parameters on Swell Behavior

In this section, we study the influence of different recovery time scales  $\lambda_\theta$  and damage parameters  $\gamma^*$ ,  $\tau^*$ , on the 2D planar swell behavior of thixotropic fluids. A constant flow rate  $Q$  is applied at the inlet such that  $Wi = 5$ . The differences between the rate and stress-controlled approaches are presented. Results are compared for two Weissenberg numbers ( $Wi = 1$ ,  $Wi = 5$ ) for the rate-controlled approach with  $\lambda_\theta = 10\lambda_{\text{avg}}$  and different damage parameters  $\gamma^*$  to study the effect of elasticity.

Figure 10 shows the swell ratio of the point of the free surface on  $\Gamma_{\text{out}}$  in time for different model parameters and both the rate and stress-controlled models for  $Wi = 5$ . The swell ratio for the viscoelastic fluid without thixotropy is also added, as well as the Newtonian swell ratio.



**Figure 10.** Swell ratio as a function of dimensionless time of the point of the free surface on  $\Gamma_{\text{out}}$  for different values of  $\gamma^*$  for the rate-controlled approach and the corresponding value of  $\tau^*$  for the stress-controlled approach. (a)  $\lambda_\theta = 10\lambda_{\text{avg}}$  and (b)  $\lambda_\theta = 100\lambda_{\text{avg}}$ . Solid lines are the rate-controlled model predictions, dashed lines are the corresponding stress-controlled model predictions. The black dashed line indicates the Newtonian swell ratio. (a)  $\lambda_\theta = 10\lambda_{\text{avg}}$ . (b)  $\lambda_\theta = 100\lambda_{\text{avg}}$ .

From this figure, the following trends can be observed:

- **Observation 1:** A larger damage parameter does not necessarily lead to a smaller swell ratio. Upon increasing the damage parameter, the results first show a swell ratio smaller than the swell ratio of a Newtonian fluid. Further increasing the damage parameter leads to a swell ratio approaching the value of a Newtonian fluid.
- **Observation 2:** The stress-controlled approach always results in a larger steady state swell ratio compared to the rate-controlled approach.
- **Observation 3:** For large values of the damage parameter ( $\gamma^*$  and  $\tau^*$ ), the swell ratio is higher when  $\lambda_\theta$  is larger, whereas for small values of the damage parameter, the opposite effect is observed.

- **Observation 4:** For  $\gamma^* = 0.01\text{--}0.1$ , the swell ratio of the outer point of the free surface shows a maximum. For  $\gamma^* = 1$ , a maximum and a minimum in the swell ratio are observed.
- **Observation 5:** Thixotropy seems to always decrease the swell ratio compared to the case without thixotropy. This agrees with our expectations, since thixotropy decreases the elasticity in the material by decreasing the relaxation times. The swell ratio for the largest damage parameter tested approaches the swell ratio for a Newtonian fluid.

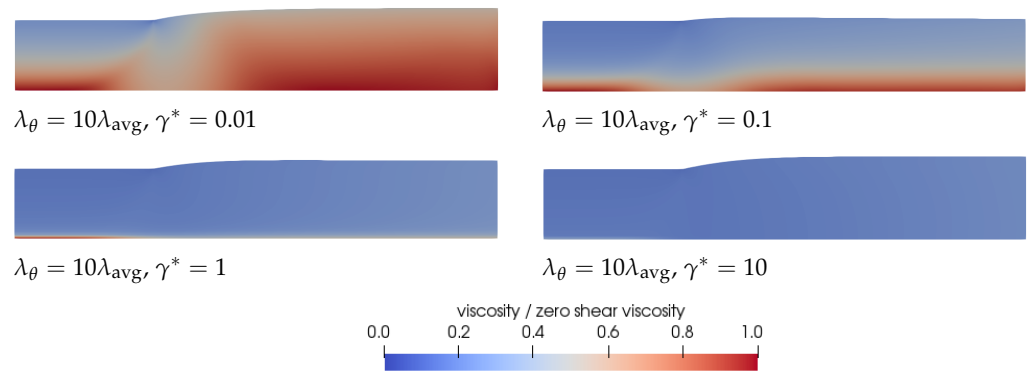
We will first focus on **Observation 1**. A smaller  $\gamma^*$  leads to less damage and therefore to larger relaxation times and more elasticity in the material compared to a larger  $\gamma^*$ . Therefore, initially, a decrease in swell ratio is observed upon increasing the damage parameter. However, when we continue to increase  $\gamma^*$ , the steady state swell ratio starts to increase again. Since the relaxation times are adjusted with the local structure parameter  $\zeta$  (See Equation (7)) but the moduli are kept constant, the viscosity  $\eta_p = \sum_{k=1}^m G_k(\zeta\lambda_{0,k})$  also changes locally with  $\zeta$ . The total shear viscosity  $\eta = \eta_s + \eta_p$  divided by the zero-shear viscosity in the whole domain is shown in Figure 11 for  $\lambda_\theta = 10\lambda_{\text{avg}}$  for the rate-controlled approach. This figure shows that upon increasing  $\gamma^*$ , first a low viscosity layer appears at the die wall. Upon further increasing the damage parameter, the viscosity difference in the die becomes smaller because the thickness of this low viscosity layer increases. The region with the highest viscosity is always in the middle of the die (at the symmetry line in Figure 11). The ratio of the total viscosity and the zero-shear viscosity is plotted over the height of the inlet of the die in Figure 12a. This figure shows that for small values of the damage parameter, there is a region of low viscosity fluid at to the die wall, but there is also a high viscosity region near the symmetry axis. Upon increasing the damage parameter, the thickness of this high viscosity core decreases until eventually there is only a small region of high viscosity fluid left near the symmetry axis of the die, approaching the result for a purely Newtonian fluid with a constant viscosity. The corresponding dimensionless velocity magnitude for the rate-controlled approach plotted over the die height at the inlet is shown in Figure 12b. This figure shows that the velocity profile is initially flattened with increasing  $\gamma^*$ , decreasing the swell ratio because the flow starts to look more like a plug flow. Upon further increasing  $\gamma^*$ , the thickness of the low viscosity layer increases, and the velocity profile becomes more parabolic again, leading to an increased swell ratio.

According to the inelastic swell theory presented by Tanner [19], a less viscous outer layer results in a decreasing swell ratio when the core region is large. This is also what is initially observed in Figure 10. However, **Observation 1** shows that when the high viscosity core becomes very small, the swell ratio starts to increase again and approaches the Newtonian swell ratio.

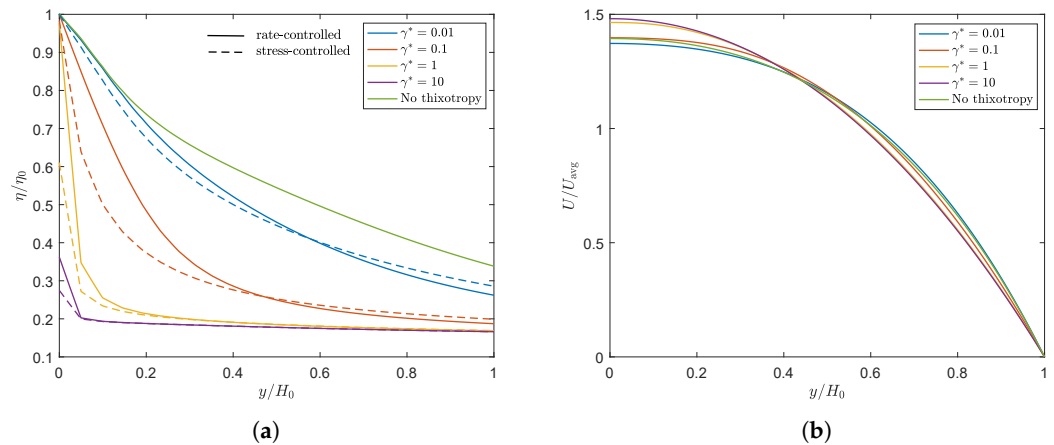
To explain **Observation 2**, we plotted the damage terms  $(E\gamma^*, \tau_c\tau^*/\eta_{p0})$  as a function of the Weissenberg number in steady shear for both approaches in Figure 13 (left). This figure shows that, due to the dependency of  $\tau_c$  on the local structure in the material, the damage term in the stress-controlled approach is not linearly dependent on the Weissenberg number, whereas this is the case for the rate-controlled approach. Figure 9 shows that this difference leads to a smaller structure parameter for small Weissenberg numbers but a higher structure parameter for high Weissenberg numbers for the stress-controlled approach. This is also shown in Figure 13 (right), where the contour lines for the structure parameter  $\zeta$  are plotted for both approaches ( $\lambda_\theta = 10\lambda_{\text{avg}}, \gamma^* = 1$ ). Unless indicated otherwise, all contour plots presented in this paper are made with equidistant contour lines with an interval of 0.01. The stress-controlled approach predicts a smaller undamaged core compared to the rate-controlled approach. Figure 12 shows that for small values of the damage parameter, the viscosity close to the die wall is higher for the stress-controlled approach compared to the rate-controlled approach but smaller close to the symmetry axis. This leads to a flatter velocity profile for the rate-controlled approach and therefore to a larger swell ratio for the stress-controlled approach. For larger damage parameters, however, the high viscosity core even seems to be smaller for the stress-controlled approach compared to the rate-controlled approach. This leads to a larger maximum velocity and a



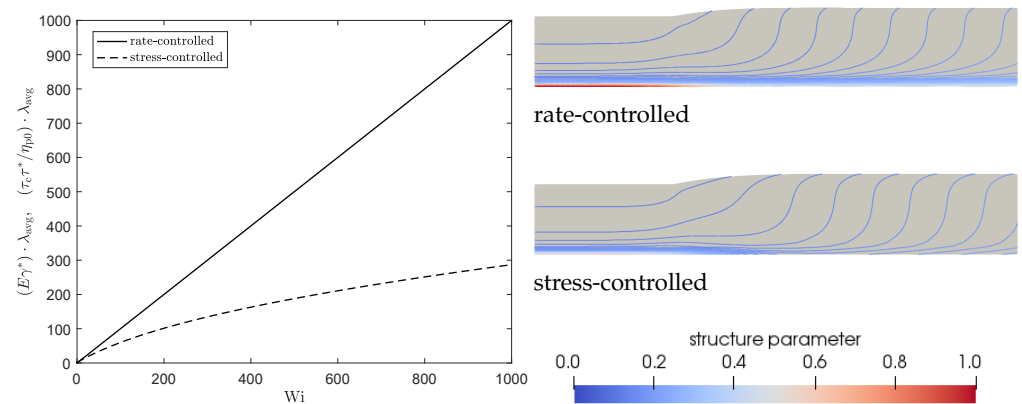
more parabolic velocity profile in the die. This also causes the stress-controlled approach to predict a larger swell ratio.



**Figure 11.** Total shear viscosity divided by the zero-shear viscosity predicted by the rate-controlled approach for  $\lambda_\theta = 10\lambda_{avg}$  and different damage parameters  $\gamma^*$ .

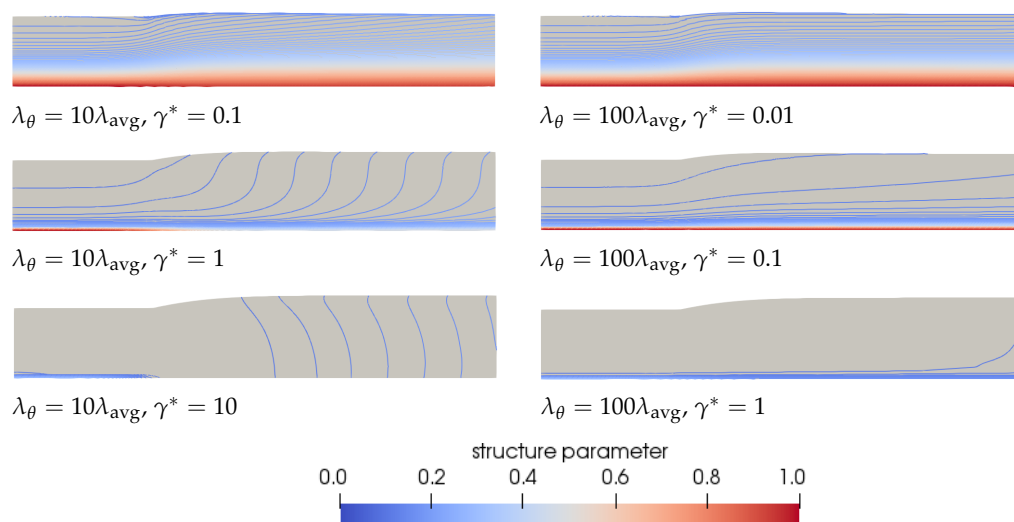


**Figure 12.** Ratio of the total viscosity and the zero-shear viscosity over the die height at  $\Gamma_{in}$  for  $\lambda_\theta = 10\lambda_{avg}$  and different damage parameters for the rate and stress-controlled approaches (a). Dimensionless velocity magnitude over the die height at  $\Gamma_{in}$  for  $\lambda_\theta = 10\lambda_{avg}$  and different damage parameters for the rate-controlled approach (b). (a)  $\lambda_\theta = 10\lambda_{avg}$ . (b)  $\lambda_\theta = 10\lambda_{avg}$ .



**Figure 13.** Damage terms of the rate and stress-controlled approaches as a function of Weissenberg number in steady shear (left). Contour plots of the structure parameter  $\zeta$  for  $\lambda_\theta = 10\lambda_{avg}$  and  $\gamma^* = 1$  for the rate-controlled approach and the corresponding values for the stress controlled approach (right). Unless indicated otherwise, all contour plots presented in this paper are made with equidistant contour lines with an interval of 0.01.

To explain **Observation 3**, we refer to Equation (38). This equation shows that the same equilibrium value of the structure parameter is found if the damage parameter times the recovery time scale is equal. This means that  $\gamma^* = 0.1$ ,  $\lambda_\theta = 10\lambda_{\text{avg}}$  gives the same equilibrium structure as  $\gamma^* = 0.01$ ,  $\lambda_\theta = 100\lambda_{\text{avg}}$ . Figure 10 also shows that the swell ratio for the values that give the same  $\zeta_{\text{eq}}$  are close but not equal. This can be explained by the different transient behavior for different recovery time scales  $\lambda_\theta$ . Figure 14 shows the contour plots for the structure parameter for  $\lambda_\theta = 10\lambda_{\text{avg}}$  (left) and  $\lambda_\theta = 100\lambda_{\text{avg}}$  (right) for different  $\gamma^*\lambda_\theta$  combinations that give the same  $\zeta_{\text{eq}}$ .



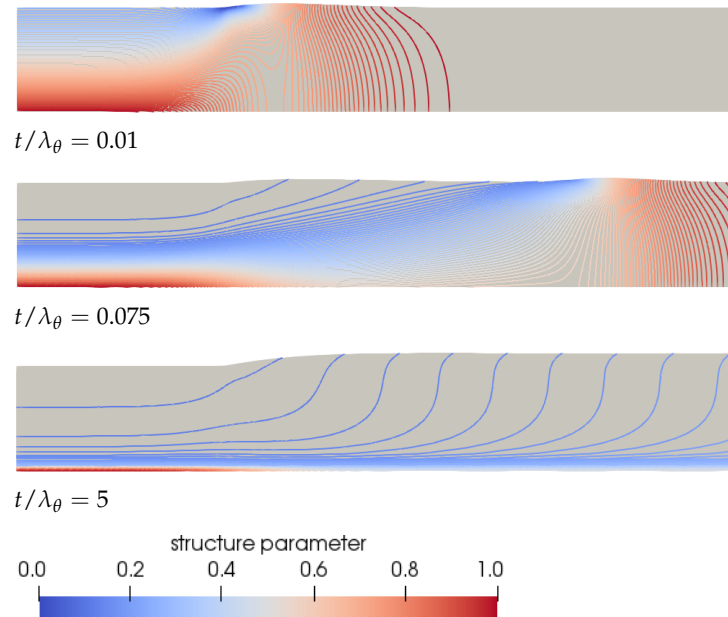
**Figure 14.** Contour plots of the structure parameter  $\zeta$  predicted by the rate-controlled approach for  $\lambda_\theta = 10\lambda_{\text{avg}}$  (**left**) and  $\lambda_\theta = 100\lambda_{\text{avg}}$  (**right**) for different damage parameter and recovery time scale combinations that give the same  $\zeta_{\text{eq}}$ .

From this figure, we can conclude that for large damage parameters, there is a large area in the die where the material has structure parameter  $\zeta = \zeta_{\text{inf}}$ . This also shows that the layers of fluid with a certain structure parameter  $\zeta$  extend over a greater length close to the free surface (contour lines are more horizontal) when  $\lambda_\theta$  is larger. This can be attributed to the difference in transient behavior, because the time for the fluid to recover is longer. In the extrudate, the shear rates and the stresses are low, and therefore the structure can recover here. This will take longer when  $\lambda_\theta$  is larger, meaning that the viscosity in the low viscosity layer away from the symmetry line will be lower for a longer time when  $\lambda_\theta = 100\lambda_{\text{avg}}$ . This leads to a larger velocity in the  $x$ -direction in the extrudate compared to  $\lambda_\theta = 10\lambda_{\text{avg}}$  but a lower velocity in the  $y$ -direction. This leads to more extended layers of fluid with a certain structure parameter  $\zeta$ .

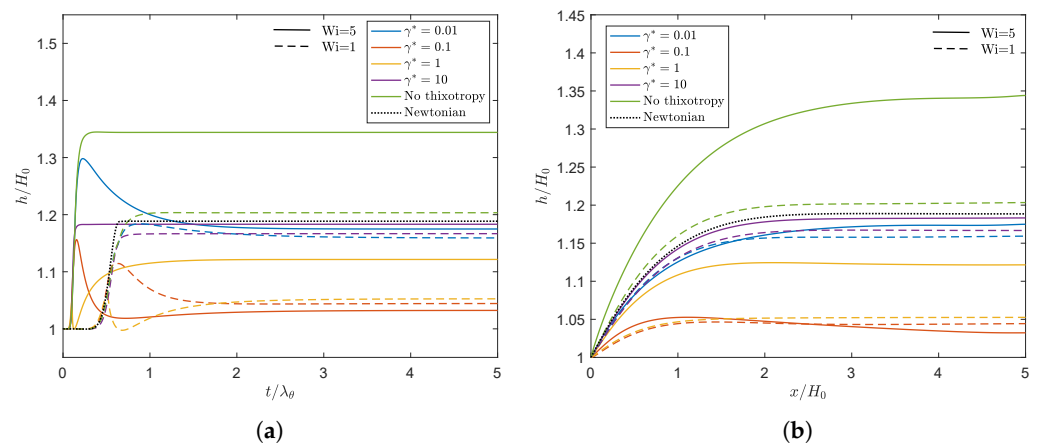
To explain **Observation 4**, we have to look at the transient behavior of the structure in the material. Initially, the fluid is undamaged ( $\zeta = 1$ ). Due to flow, a small layer of damaged fluid starts to grow near the die wall. At this point, the fluid is still elastic and will start to swell once it leaves the die, leading to the maximum in the swell ratio. While the damaged layer of fluid starts to grow, a low viscosity and more viscous layer appears near the die wall, leading to a decrease in the swell ratio. After a certain amount of time, this layer spans almost the whole height of the die, leading to a small high viscosity core layer, and the swell ratio starts to increase again, leading to the minimum for  $\gamma^* = 1$ . This is schematically shown in Figure 15 for  $\lambda_\theta = 10\lambda_{\text{avg}}$ ,  $\gamma^* = 1$ . This figure also shows the convection of the maximum and minimum swell height of the free surface.

To show the influence of the Weissenberg number, simulations are also performed for  $Wi = 1$ . Figure 16a shows the swell ratio in time for  $\lambda_\theta = 10\lambda_{\text{avg}}$  and different damage parameters for the rate-controlled equation. The result shows the same qualitative trend as Figure 10 for increasing  $\gamma^*$ . The overall swell ratio is higher for a higher Weissenberg number due to the larger effect of elasticity in the material. For both values of  $Wi$ , it is

observed that upon increasing the damage parameter, first, a swell ratio smaller than the Newtonian value is obtained. Upon further increasing  $\gamma^*$ , the swell ratio approaches the Newtonian value.  $\gamma^* = 0.1$  is the only damage parameter for which a lower final swell ratio is predicted for  $Wi = 5$  compared to  $Wi = 1$ . Figure 16b shows that the final swell ratio for this damage parameter close to the die exit ( $x/H_0 = 0$ ) is higher for  $Wi = 5$  compared to  $Wi = 1$ , whereas near  $\Gamma_{out}$  ( $x/H_0 = 5$ ), the opposite is observed. Therefore, we suspect that there is a complex interplay between higher swell due to a higher Weissenberg number and a decrease in swell due to larger damage at higher  $Wi$  for  $\gamma^* = 0.1$  in the extrudate. More research is needed to fully understand this phenomenon.



**Figure 15.** Contour plots of the structure parameter  $\zeta$  predicted by the rate-controlled approach for  $\lambda_\theta = 10\lambda_{avg}$  and  $\gamma^* = 1$  for different instances in time.

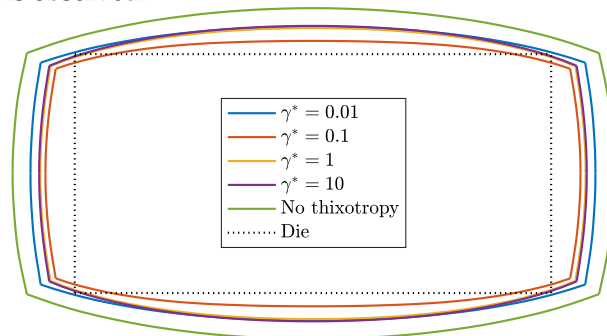


**Figure 16.** Swell ratio as a function of dimensionless time for the point of the free surface on  $\Gamma_{out}$  (a) and final swell ratio of the free surface as a function of the  $x$ -coordinate along the free surface (b). Here,  $x/H_0 = 0$  corresponds to the  $x$ -coordinate at the die exit. Results are obtained for different values of  $\gamma^*$  for the rate-controlled approach using two different Weissenberg numbers. Solid lines indicate the results for  $Wi = 5$ , whereas dashed lines indicate the results for  $Wi = 1$ .

#### 4.2.3. Three-Dimensional Extrudate Swell

Three-dimensional simulations of a viscoelastic fluid emerging from a rectangular die with an aspect ratio of 2:1 are performed to show the effect of a changing structure in the

material in three-dimensional extrudates. The rate-controlled approach is used to model the time-dependent evolution of the structure in the material. Figure 17 shows the contour of the extrudate shape in steady state for  $\lambda_\theta = 10\lambda_{\text{avg}}$ , different damage parameters and  $Wi = 5$ . Here, a similar effect of thixotropy on extrudate swell as for the 2D planar problem is observed.



**Figure 17.** Contour of a 3D extrudate of a thixotropic viscoelastic fluid. Evolution of the structure in the material is modeled using the rate-controlled approach with  $\lambda_\theta = 10\lambda_{\text{avg}}$  and different damage parameters for  $Wi = 5$ .

Initially, the swell decreases when thixotropy is introduced. For increasing  $\gamma^*$ , however, the swell ratio starts to increase again. This effect is more pronounced for the height of the extrudate than the width of the extrudate. This can be attributed to the higher shear rate in the height direction compared to the width direction. The swell ratios for a thixotropic fluid are always smaller compared to the viscoelastic fluid without thixotropy.

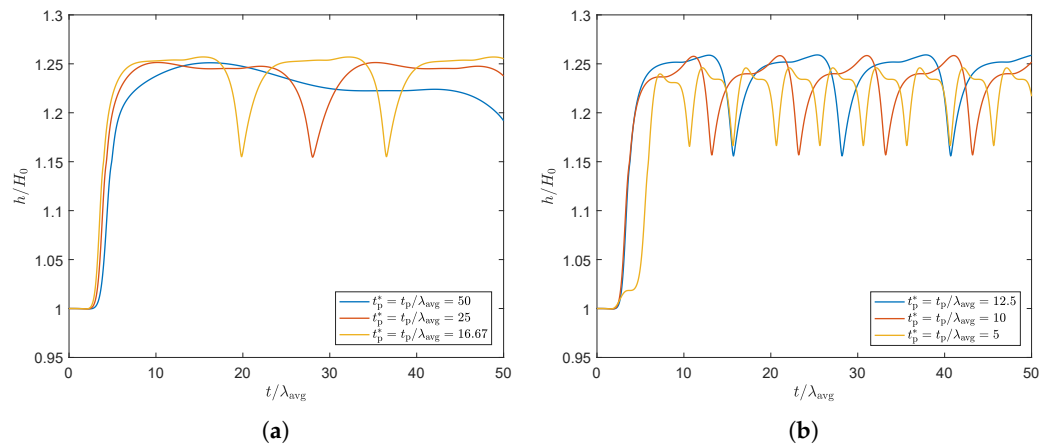
#### 4.3. Fluctuating Flow Rate

All previous results are obtained by applying a constant flow rate  $Q$  at the die inlet. However, in many industrial processes, the flow rate is not constant but fluctuates in time. In this section, the effect of a fluctuating flow rate on the structure in the material and the swell ratio of the 2D planar extrudate is studied using the rate-controlled model for the kinetic equation of the structure parameter  $\zeta$ . A sinusoidal flow rate is applied to the inlet, with different periods  $2\pi/t_p$ , where  $t_p$  is the time it takes for the sine function to complete one period:

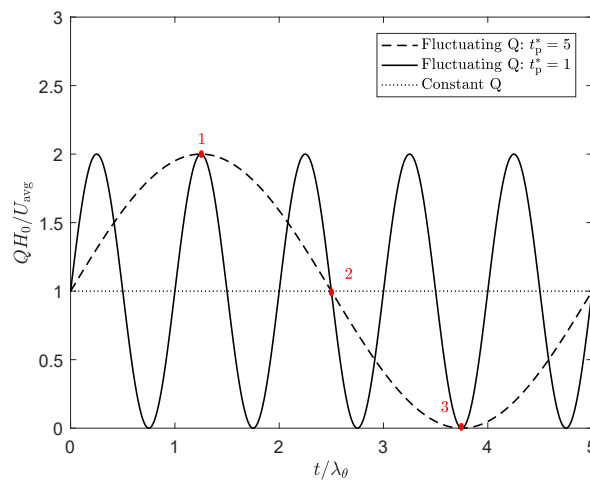
$$Q = \sin\left(2\pi\frac{t}{t_p}\right) + U_{\text{avg}}H_0. \quad (41)$$

First, the effect of a fluctuating flow rate is studied for the non-thixotropic fluid and an average Weissenberg number of  $Wi = 1$ . Here, flow rates are applied with different dimensionless times for the period of a sine  $t_p^* = t_p/\lambda_{\text{avg}}$ . The swell ratio of the outer point on the free surface at  $\Gamma_{\text{out}}$  is shown as a function of dimensionless time in Figure 18. This figure shows that, although the flow rate is sinusoidal, the corresponding periodicity in the swell ratio is presented by a higher-order sine function, where two frequencies are visible. An explanation for this is as follows: for high flow rates, more fluid is flowing through the die at a certain time interval compared to lower flow rates. Therefore, it takes longer for the effect of the decrease in flow rate to be noticed at the end of the extrudate compared to the effect of the increase in flow rate, and the effect of two different time scales is observed.

The frequencies chosen to study the influence of thixotropy on extrudate swell for a fluctuating flow rate correspond to the following dimensionless times for one period of the sine:  $t_p^* = t_p/\lambda_\theta = 1$ ,  $t_p^* = t_p/\lambda_\theta = 5$ , as shown in Figure 19. Results are obtained for  $\lambda_\theta = 10\lambda_{\text{avg}}$ , different damage parameters and an average Weissenberg number of  $Wi = 1$ .

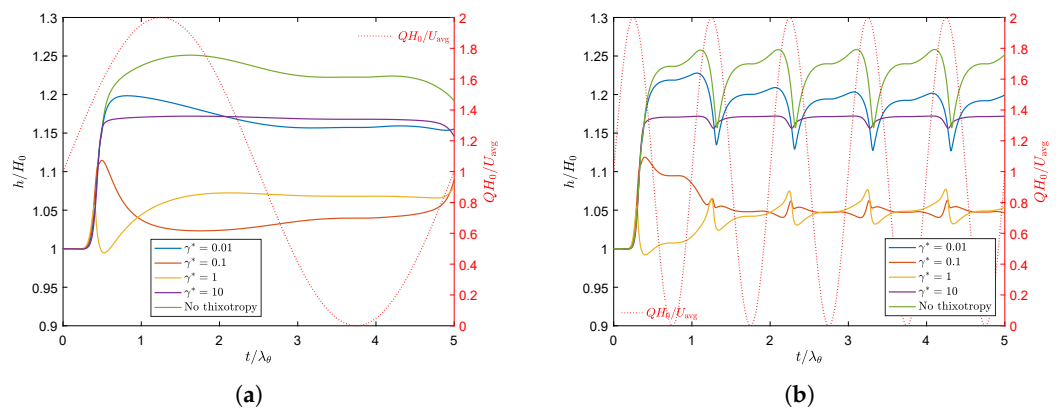


**Figure 18.** Swell ratio as a function of dimensionless time for the point of the free surface on  $\Gamma_{out}$ , for a sinusoidal flow rate with dimensionless frequency  $f^* = 1/t_p^*$ , with  $t_p^* = t_p/\lambda_{avg}$ .



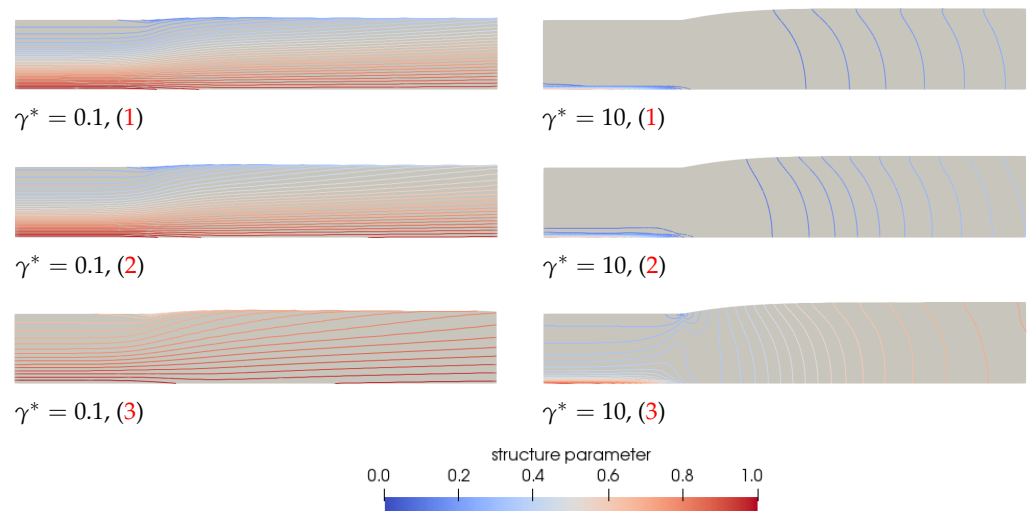
**Figure 19.** Sinusoidal flow rate with dimensionless period  $t_p^* = t_p/\lambda_\theta = 1$  (solid line), and  $t_p^* = t_p/\lambda_\theta = 5$  (dashed line) and the constant flow rate applied in previous results (dotted line).

Figure 20 shows the swell ratio of the point of the free surface on  $\Gamma_{out}$  as a function of dimensionless time for a fluctuating flow rate with both dimensionless periods  $t_p^*$ . The swell ratio is plotted for different values of  $\gamma^*$ .



**Figure 20.** Swell ratio as a function of dimensionless time for the point of the free surface on  $\Gamma_{out}$ , for different values of  $\gamma^*$  and a sinusoidal flow rate with dimensionless frequency  $f^* = 1/t_p^*$ , with  $t_p^* = t_p/\lambda_\theta = 5$  (a), and  $t_p^* = t_p/\lambda_\theta = 1$  (b). The red dotted line represents the applied flow rate.

This figure shows that for a fluctuating flow rate, the fluctuation is also visible in the swell ratio of the end point of the free surface. For small values of  $\gamma^*$  and non-thixotropic materials, the swell ratio increases with  $Q$ , due to an increase in the Weissenberg number, and decreases when the flow rate decreases. Since the material starts to swell more when the flow rate increases, and it takes time for this material to reach the end of the extrudate, there is a delay between the maximum in the flow rate and the corresponding maximum in the swell ratio for small values of  $\gamma^*$  and the non-thixotropic fluid. For the high frequency case, the fluctuations in the swell ratio are much more pronounced compared to the small frequency case. The fluctuations seem to weaken when the damage parameter increases. It can also be observed that, for the high frequency case, the maxima for  $\gamma^* = 1$  and  $\gamma^* = 10$  occur at the same dimensionless time as the minima for  $\gamma^* = 0.01$  and the non-thixotropic fluid. For higher values of  $\gamma^*$ , the structure parameter will be smaller when  $Q$  is large due to an increasing shear rate, meaning that the structure in the material is more damaged and the fluid becomes less elastic. This decreases the swell ratio. When  $Q$  decreases again, the structure in the material increases, hence increasing the elasticity and thus the swell ratio. The complex coupling of the competing effect of decreasing  $Wi$  due to damaging the structure at high flow rates, while simultaneously increasing the shear rate at higher flow rates and therefore increasing  $Wi$ , leads to the complex transient behavior for a fluctuating flow rate. To show the change in structure in the material, the contour of the structure parameter  $\zeta$  is shown in Figure 21 for  $\gamma^* = 0.1$  and  $\gamma^* = 10$  at a time interval where the flow rate is at its maximum (1), the flow rate equals the constant applied flow rate (2) and where the flow rate is at its minimum (3), as indicated in Figure 19. Figure 21 clearly shows the change in structure at the different moments in time, due to the fluctuating flow rate. When the flow rate is at its maximum (1), there is a large area of damaged material (small structure parameter  $\zeta$ ) in areas where the shear rate is high. This is much more severe when the damage parameter is large. When the flow rate decreases again, the material has time to recover, and the structure parameter will increase again.



**Figure 21.** Contour plots of the structure parameter  $\zeta$  predicted by the rate-controlled approach for  $\lambda_\theta = 10\lambda_{\text{avg}}$  and  $\gamma^* = 0.1$  (left) and  $\gamma^* = 10$  (right) for different instances in time as indicated by the red numbers in Figure 19 for a fluctuating flowrate  $Q$ . The contour plots in this figure are made with equidistant contour lines with an interval of 0.025 for clarity.

## 5. Conclusions

In this paper, we studied the effect of thixotropy on extrudate swell. To this end, we used a rate and stress-controlled equation for a structure parameter that indicates the degree of structure in the material. The relaxation times are adjusted with this structure parameter, which effectively means that the fluid becomes less elastic when the structure is damaged.

Rate and stress-controlled approaches are compared by matching the damage parameters in the evolution equation for the structure parameter in such a way that the steady state structure parameter and the steady state viscosity are matched at a characteristic shear rate. Furthermore, the effects of the recovery time scale and the damage parameter in the kinetic equation for the structure parameter are studied. It was found that thixotropy in general decreases the swell ratio. When the damage parameter in the models is increased, an outer layer with lower viscosity appears near the die wall, which decreases the swell ratio to a value below the Newtonian swell ratio. Upon further increasing the damage parameter, the high viscosity core becomes very small, leading to an increase in the swell ratio approaching the Newtonian value. Furthermore, it was found that the stress-controlled approach always predicts a larger swell ratio compared to the rate-controlled approach for the Weissenberg number range studied in this paper.

Results for varying the recovery time scale of the structure in the material show that even though the damage and recovery parameters predict the same equilibrium value for  $\xi$ , a different transient behavior of the structure is observed. This leads to different, but comparable, swell ratios for the same equilibrium structure parameter.

The effect of thixotropy on the swell ratio is studied for two different Weissenberg numbers ( $Wi = 1$ ,  $Wi = 5$ ). Results show an overall higher swell ratio for the higher Weissenberg number. However, a complex interplay between higher swell due to a higher Weissenberg number and a decrease in swell due to larger damage at higher  $Wi$  is observed for small damage parameters. This interplay is an interesting topic for future research.

A proof of concept of the thixotropy model is given in 3D by performing simulations for  $Wi = 5$  using the rate-controlled approach and different damage parameters. Contours of the final extrudate shape show a similar effect of thixotropy on extrudate swell compared to the 2D planar problem.

Finally, the effect of a fluctuating flow rate is studied for the rate-controlled approach. To this end, a sinusoidal flow rate is applied with different frequencies. Results show that the fluctuation in the swell ratio decreases with increasing damage parameter. There also seems to be a complex coupling between the decrease of  $Wi$  when the structure is damaged at high flow rates and the increase in  $Wi$  due to an increasing shear rate at increasing flow rates. This leads to complex transient behavior.

In conclusion, this paper shows that thixotropy in general decreases extrudate swell, but complex transient behavior occurs when the fluid is thixotropic. Results show that the emergence of fluid layers with different viscosities in the die due to thixotropy highly influences the swell ratio.

**Author Contributions:** This research was part of the Ph.D. work of M.S. under the guidance and supervision of her supervisors G.P., M.H. and P.A. All authors have read and agreed to the published version of the manuscript.

**Funding:** The results of this study have been obtained through the FLEX-Pro project, which was in part funded by the European Funding for Regional Development (EFRO). The research is performed in collaboration with VMI Holland B.V.

**Institutional Review Board Statement:** Not applicable.

**Informed Consent Statement:** Not applicable.

**Conflicts of Interest:** The authors declare no conflict of interest.

## References

1. Stieger, S.; Mitsoulis, E.; Walluch, M.; Ebner, C.; Kerschbaumer, R.C.; Haselmann, M.; Mostafaiyan, M.; Kämpfe, M.; Kühnert, I.; Wießner, S.; et al. On the Influence of Viscoelastic Modeling in Fluid Flow Simulations of Gum Acrylonitrile Butadiene Rubber. *Polymers* **2021**, *13*, 2323. [[CrossRef](#)]
2. Sattayanurak, S.; Sahakaro, K.; Kaewsakul, W.; Dierkes, W.K.; Reuvekamp, L.A.E.M.; Blume, A.; Noordermeer, J.W.M. Synergistic effect by high specific surface area carbon black as secondary filler in silica reinforced natural rubber tire tread compounds. *Polym. Test.* **2020**, *81*, 106–173. [[CrossRef](#)]

3. Robertson, C.; Hardman, N.J. Nature of carbon black reinforcement of rubber: Perspective on the original polymer nanocomposite. *Polymers* **2021**, *13*, 538. [[CrossRef](#)]
4. Kumar, V.; Alam, M.N.; Manikkavel, A.; Song, M.; Lee, D.J.; Park, S.S. Silicone Rubber Composites Reinforced by Carbon Nanofillers and Their Hybrids for Various Applications: A Review. *Polymers* **2021**, *13*, 2322. [[CrossRef](#)]
5. Rogers, B. *Rubber Compounding, Chemistry and Applications*; Taylor & Francis Group, LLC: Boca Raton, FL, USA, 2016.
6. Payne, A.R. The dynamic properties of carbon black-loaded natural rubber vulcanizates. Part I. *J. Appl. Polym. Sci.* **1962**, *6*, 57–63. [[CrossRef](#)]
7. Shi, X.; Sun, S.; Zhao, A.; Zhang, H.; Zuo, M.; Song, Y.; Zheng, Q. Influence of carbon black on the Payne effect of filled natural rubber compounds. *Compos. Sci. Technol.* **2021**, *203*, 108586. [[CrossRef](#)]
8. Zhao, A.; Shi, X.; Zhang, H.; Song, Y.; Zheng, Q. Insights into the Payne Effect of Carbon Black Filled Styrene-butadiene Rubber Compounds. *Chin. J. Polym. Sci.* **2021**, *39*, 81–90. [[CrossRef](#)]
9. Sternstein, S.S.; Zhu, A.J. Reinforcement mechanism of nanofilled polymer melts as elucidated by nonlinear viscoelastic behavior. *Macromolecules* **2002**, *19*, 7262–7273. [[CrossRef](#)]
10. Montes, H.; Lequeux, F.; Berriot, J. Influence of the Glass Transition Temperature Gradient on the Nonlinear Viscoelastic Behavior in Reinforced Elastomers. *Macromolecules* **2003**, *36*, 8107–8118. [[CrossRef](#)]
11. Sarvestani, A.S. On the Emergence of the Payne Effect in Polymer Melts Reinforced with Nanoparticles. *Macromol. Theory Simul.* **2016**, *25*, 312–321. [[CrossRef](#)]
12. Ruede, M.M.; Auscher, M.C.; Fulchiron, R.; Périé, T.; Martin, G.; Sonntag, P.; Cassagnau, P. Rheology and applications of highly filled polymers: A review of current understanding. *Prog. Polym. Sci.* **2017**, *66*, 22–53. [[CrossRef](#)]
13. Dangtungee, R.; Yun, J.; Supaphol, P. Melt rheology and extrudate swell of calcium carbonate nanoparticle-filled isotactic polypropylene. *Polym. Test.* **2005**, *24*, 2–11. [[CrossRef](#)]
14. Dangtungee, R.; Supaphol, P. Melt rheology and extrudate swell of titanium (IV) oxide nanoparticle-filled isotactic polypropylene: Effects of content and surface characteristics. *Polym. Test.* **2008**, *27*, 951–956. [[CrossRef](#)]
15. Dangtungee, R.; Supaphol, P. Melt rheology and extrudate swell of sodium chloride-filled low-density polyethylene: Effects of content and size of salt particles. *Polym. Test.* **2010**, *29*, 188–195. [[CrossRef](#)]
16. Freakley, P.K.; Sirisinha, C. The influence of state-of-mix on the extrudate swell of a carbon black-filled styrene-butadiene rubber compound. *J. Appl. Polym. Sci.* **1997**, *65*, 305–315. [[CrossRef](#)]
17. Kim, J.; Han, M.; Go, J.; Seungkeun, O. Die extrusion behavior of carbon black-filled block copolymer thermoplastic elastomers. *J. Appl. Polym. Sci.* **1993**, *49*, 1777–1789. [[CrossRef](#)]
18. Leblanc, J.L. Rubber-filler interactions and rheological properties in filled rubber compounds. *Prog. Polym. Sci.* **2002**, *27*, 627–687. [[CrossRef](#)]
19. Tanner, R.I. A new inelastic theory of extrudate swell. *J. Non-Newton. Fluid Mech.* **1980**, *6*, 289–302. [[CrossRef](#)]
20. Mistoulis, E. Extrudate swell in double-layer flows. *J. Rheol.* **1986**, *30*, S23. [[CrossRef](#)]
21. Spanjaards, M.M.A.; Hulsen, M.A.; Anderson, P.D. Transient 3D finite element method for predicting extrudate swell of domains containing sharp edges. *J. Non-Newton. Fluid Mech.* **2019**, *270*, 79–95. [[CrossRef](#)]
22. Giesekus, H. A simple constitutive equation for polymer fluids based on the concept of deformation-dependent tensorial mobility. *J. Non-Newton. Fluid Mech.* **1982**, *11*, 69–109. [[CrossRef](#)]
23. Spanjaards, M.M.A.; Peters, G.W.M.; Hulsen, M.A.; Anderson, P.D. Towards the development of a strategy to characterize and model the rheological behavior of filled uncured compounds. *Polymers* **2021**, *13*, 4068. [[CrossRef](#)]
24. Joshi, P.G.; Leonov, A.I. Modeling of steady and time-dependent responses in filled, uncured, and crosslinked rubbers. *Rheol. Acta* **2001**, *40*, 350–365. [[CrossRef](#)]
25. Saramito, P.; Wachs, A. Progress in numerical simulation of yield stress fluid flows. *Rheol. Acta* **2017**, *56*, 211–230. s00397-016-0985-9. [[CrossRef](#)]
26. Hu, H.H.; Patankar, N.A.; Zhu, M.Y. Direct numerical simulations of fluid-solid systems using the Arbitrary Lagrangian-Eulerian technique. *J. Comput. Phys.* **2001**, *169*, 427–462. [[CrossRef](#)]
27. Keunings, R. An algorithm for the simulation of transient viscoelastic flows with free surfaces. *J. Comput. Phys.* **1986**, *62*, 199–220. [[CrossRef](#)]
28. Hulsen, M.A.; Fattal, R.; Kupferman, R. Flow of viscoelastic fluids past a cylinder at high Weissenberg number: Stabilized simulations using matrix logarithms. *J. Non-Newton. Fluid Mech.* **2005**, *127*, 27–39. [[CrossRef](#)]
29. Brooks, A.N.; Hughes, T.J.R. Streamline upwind/Petrov-Galerkin formulations for convection dominated flows with particular emphasis on the incompressible Navier-Stokes equations. *Comput. Methods Appl. Mech. Eng.* **1982**, *32*, 199–259. [[CrossRef](#)]
30. Bogaerds, A.C.B.; Hulsen, M.A.; Peters, G.W.M.; Baaijens, F.P.T. Stability analysis of injection molding flows. *J. Rheol.* **2004**, *48*, 765–785. [[CrossRef](#)]
31. Choi, Y.J.; Hulsen, M.A. Simulation of extrudate swell using an extended finite element method. *Korea-Aust. Rheol. J.* **2011**, *23*, 147–154. [[CrossRef](#)]
32. Geuzaine, C.; Remacle, J.F. Gmsh: A 3-D finite element mesh generator with built-in pre- and post-processing facilities. *Int. J. Numer. Methods Eng.* **2009**, *79*, 1309–1331. [[CrossRef](#)]
33. Hughes, T.; Mallet, M.; Akira, M. A new finite element formulation for computational fluid dynamics: II. Beyond SUPG. *Comput. Methods Appl. Mech. Eng.* **1986**, *54*, 341–355. [[CrossRef](#)]



34. D'Avino, G.; Hulsen, M.A. Decoupled second-order transient schemes for the flow of viscoelastic fluids without a viscous solvent contribution. *J. Non-Newton. Fluid Mech.* **2010**, *165*, 1602–1612. [[CrossRef](#)]
35. Isayev, A.I. *11- Injection Molding of Rubbers*; Pergamon: Amsterdam, The Netherlands, 1989; pp. 355–378.
36. Spanjaards, M.M.A.; Hulsen, M.A.; Anderson, P.D. Computational analysis of the extrudate shape of three-dimensional viscoelastic, non-isothermal extrusion flows. *J. Non-Newton. Fluid Mech.* **2020**, *282*, 104310. [[CrossRef](#)]

## Article

# Towards the Development of a Strategy to Characterize and Model the Rheological Behavior of Filled, Uncured Rubber Compounds

M. M. A. Spanjaards<sup>1,2</sup>, G. W. M. Peters<sup>1</sup>, M. A. Hulsen<sup>1</sup> and P. D. Anderson<sup>1,\*</sup>

<sup>1</sup> Department of Mechanical Engineering, Eindhoven University of Technology, P.O. Box 513, 5600 MB Eindhoven, The Netherlands; m.m.a.spanjaards@tue.nl (M.M.A.S.); g.w.m.peters@tue.nl (G.W.M.P.); m.a.hulsen@tue.nl (M.A.H.)

<sup>2</sup> VMI Holland B.V., Gelriaweg 16, 8161 RK Epe, The Netherlands

\* Correspondence: P.D.Anderson@tue.nl

**Abstract:** In this paper, an experimental strategy is presented to characterize the rheological behavior of filled, uncured rubber compounds. Oscillatory shear experiments on a regular plate-plate rheometer are combined with a phenomenological thixotropy model to obtain model parameters that can be used to describe the steady shear behavior. We compare rate- and stress-controlled kinetic equations for a structure parameter that determines the deformation history-dependent spectrum and, thus, the dynamic thixotropic behavior of the material. We keep the models as simple as possible and the characterization straightforward to maximize applicability. The model can be implemented in a finite element framework as a tool to simulate realistic rubber processing. This will be the topic of another work, currently under preparation. In shaping processes, such as rubber- and polymer extrusion, with realistic processing conditions, the range of shear rates is far outside the range obtained during rheological characterization. Based on some motivated choices, we will present an approach to extend this range.

**Citation:** Spanjaards, M.M.A.; Peters, G.W.M.; Hulsen, M.A.; Anderson, P.D. Towards the Development of a Strategy to Characterize and Model the Rheological Behavior of Filled, Uncured Rubber Compounds. *Polymers* **2021**, *13*, 4068. <https://doi.org/10.3390/polym13234068>

Academic Editor: Klaus Werner Stöckelhuber

Received: 19 October 2021

Accepted: 18 November 2021

Published: 23 November 2021

**Publisher's Note:** MDPI stays neutral with regard to jurisdictional claims in published maps and institutional affiliations.



**Copyright:** © 2021 by the authors. Licensee MDPI, Basel, Switzerland. This article is an open access article distributed under the terms and conditions of the Creative Commons Attribution (CC BY) license (<https://creativecommons.org/licenses/by/4.0/>).

**Keywords:** fillers; rubber compounds; viscoelasticity; thixotropy; structure

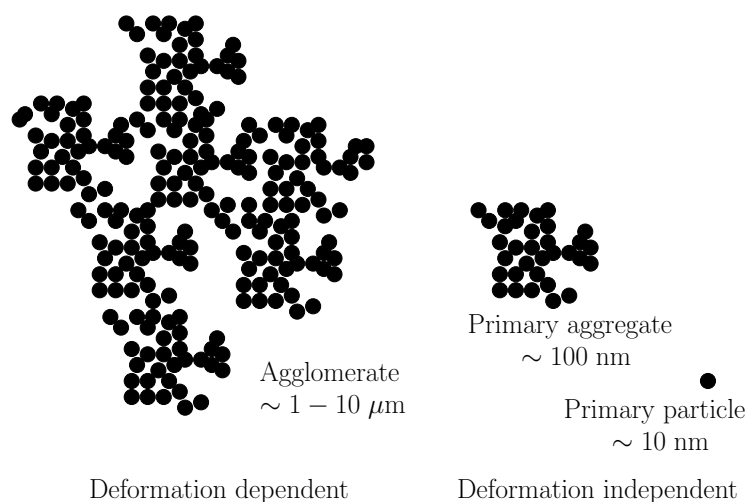
## 1. Introduction

Rubber extrusion is widely used in the automotive industry to produce, for example, rectangular rubber strips, which can be stripwinded into the carcass of a car tire, and weather strips that seal a car door and prevent rainwater and dust from coming in. Rubber-like materials are typically viscoelastic and show nonlinear and time-dependent rheological behavior under stress. The dimensions and quality of the rubber extrusion products highly depend on the rheological properties of the compound. Rubber compounds are complex materials in the sense that they contain many additives, such as plasticizers, curing agents, and they contain about 30% by weight of reinforcing fillers [1].

Carbon black and silica are the two most popular types of fillers in the automotive industry to improve the mechanical behavior of rubber products. They are both active fillers, which means they interact with the polymer matrix. The reinforcing effect of the fillers is therefore based on polymer–filler, as well as filler–filler interactions. Since carbon-black suspensions are used in numerous industrial applications, ranging from tire rubbers to ink and electrochemical energy storage devices [2–4], they are considered as highly relevant thixotropic colloidal suspensions. Therefore, this paper will focus on carbon-black reinforced rubber compounds.

The dispersion of the fillers in the polymer matrix is critical; the better the dispersion, the better the performance properties of the compound [5,6]. Furthermore, the addition of carbon-black increases the viscosity which leads to a change in the flow characteristics of the compound. The primary carbon-black particles form aggregates and the size and shape of these aggregates are deformation-independent. These aggregates can cluster together to form agglomerates, which can form a network that is held together by weak

van der Waals-type forces. These networks are very sensitive to even small changes in strain and continue to separate as the strain increases [7]. These different types of carbon-black structures are schematically depicted in Figure 1. The fragile bonds between the agglomerates can break under stress but will reform again once the stress is removed. This leads to a reversible decrease in the viscosity. This thixotropic behavior is also known as the Payne effect, and makes rheological characterization of the compounds challenging [8]. When shear is applied to carbon-black suspensions, shear-thinning behavior is observed which is consistent with structural break-down of these agglomerates [9–11].



**Figure 1.** Schematic representation of carbon-black aggregates and the flocculation into agglomerates.

The Payne effect has been attributed to several mechanisms, such as the agglomeration/de-agglomeration of filler aggregates, breakup/reformation of the filler–filler and polymer–filler network [12,13], chain desorption from the fillers [14], yielding of the glassy layer between the fillers [15] and disentanglement of the absorbed chains [16].

Considerable research has been performed to characterize the dynamic mechanical properties of filled rubber compounds [17–24]. Addition of fillers leads to two contributions to the dynamic modulus of the material; a strain-dependent contribution and a strain-independent one. The modulus decreases with increasing strain due to a partial reversible breakdown of the filler–filler network, whereas filler–rubber interactions contribute to the strain-independent part [25]. The reversible networks created by the filler particles also result in additional elastic behavior of the compound.

The concept of thixotropy was introduced by Péterfi [26]. Since then, the modeling of thixotropy has been studied extensively and is considered as one of the most challenging problems in colloid rheology. The underlying changes in microstructure are often complex and still poorly understood. In the review of Larson and Wei [27], a summary is given of the most used models to describe thixotropic behavior. In their review, they restrict the term thixotropy to nearly inelastic behavior so that it cannot be confused with non-linear viscoelasticity. Mewis and Wagner described a definition of thixotropy that is based on viscosity [9]. This definition implies a time-dependent decrease of viscosity induced by flow that is reversible when the flow is decreased or arrested.

Most simplistic thixotropy models are based on a kinetic equation that describes the evolution of a structure parameter to express the state of the structure in the material. A distinction is made between rate- and stress-controlled models. The basic form of a rate-controlled kinetic equation for a structure parameter was initially proposed by Goodeve and Whitfield [28]. Here, the structure parameter is controlled by the shear rate and used to adjust the viscosity of the material. De Souza Mendes and Thompson [29] find it more reasonable that structure evolution is controlled by the stress, since stress is needed to break bonds in the microstructure.

Another continuum approach to describe highly filled polymer liquids was described by Leonov [30]. This constitutive model also uses a kinetic approach for structure breakdown and reformation. The rheological behavior is assumed to be dominated by filler–filler interaction. Simhambhatla and Leonov [31] extended this model to describe the rheological behavior of filled polymers with dominant filler–matrix interaction. They make use of a rate-controlled kinetic equation for a structure parameter and divide the stress into a contribution of the ‘free chains’ and one for the ‘trapped chains’. This model was validated with various rheological experiments by Joshi and Leonov [32].

Many phenomenological models that are based on the evolution of a structure parameter describe experimental data well. However, they provide no clear information about the microstructure of the material. Population Balance Models (PBMs) take into account the flow-induced changes of the microstructure and describe how these changes influence the bulk rheology of the material. In the last years, there has been a growing interest in developing thixotropic constitutive models from PBMs [33,34].

Recent work of Narayan and Palade compared a natural configuration approach and a structural parameter approach to model the thixotropic behavior in filled elastomers [35]. Although both approaches capture the rheological behavior reasonably well, they found there were still some aspects of the Payne effect that were inadequately described. Rendek and Lion [36] performed experiments to study the influence of strain-induced transient behavior of the Payne effect for filler-reinforced elastomers and also proposed a constitutive model. This model was later extended to investigate the influence of strain-amplitude and temperature [37]. Modeling the effects of strain-amplitude and frequency on the thixotropic behavior of carbon-black reinforced elastomers was done amongst others in [38,39].

In this paper, we will propose a straightforward experimental strategy to characterize the thixotropic behavior of reinforced rubber compounds. To this end, oscillatory measurements on a standard plate-plate rheometer are performed. Inspired by the Leonov modeling, the thixotropic behavior is modeled with a kinetic evolution equation for a structure parameter. Model predictions obtained with a rate- and stress-controlled kinetic equation are compared in order to investigate the typical features of these two approaches. The focus of this work is on this comparison and not the best quantitative description of experimental results, i.e., the modeling is more qualitative. The oscillatory shear measurements provide model parameters that can be used to predict steady shear results. What distinguishes our approach from previous work is the relatively straightforward coupling between the nonlinear viscoelastic behavior described by the constitutive model and the thixotropic behavior described by the structure parameter. To be able to predict properties of extrusion products of rubber compounds, numerical simulations can be a powerful tool [40–43]. For these simulations, the material behavior, including the rheological behavior, needs to be described. Although the presented model is a first-order model, only able to qualitatively predict the thixotropic behavior, the straightforward coupling between the nonlinear viscoelastic and thixotropic behavior maximizes its applicability and can help to give insight in the behavior under realistic processing conditions.

The paper is build up as follows: first the material and experimental strategy are introduced in Section 2. Section 3 introduces the rate- and stress-controlled thixotropic model. It is explained how the model parameters in both approaches are obtained. The results of the model predictions using both the rate- and stress-controlled equation are presented in Section 4, for oscillatory- and steady-shear. Finally, the results of both approaches are discussed in Section 5.

## 2. Materials and Methods

### 2.1. Materials

#### 2.1.1. Filled, Uncured Rubber Compound

Oscillatory-shear experiments are performed on a carbon-black filled styrene butadiene uncured rubber compound provided by Evonik Industries. The ingredients of the rubber compound are shown in Table 1 in parts per hundred rubber (phr).

**Table 1.** Ingredients of the rubber compound in phr.

	Ingredient	[phr]
Stage 1	BUNA VSL 4526-2	96.25
	CB1220	30
	N339	72
	ZnO RS	2.00
	Stearic acid	1.00
	Vivatec 500	8.75
	Vulkanox HS/LG	1.50
	Vulkanox 4020/LG	2.00
	Protektor G 3108	2.00
Stage 2	Vulkacit CZ/EG C	1.60
	Sulfur	1.40

### 2.1.2. Sample Preparation

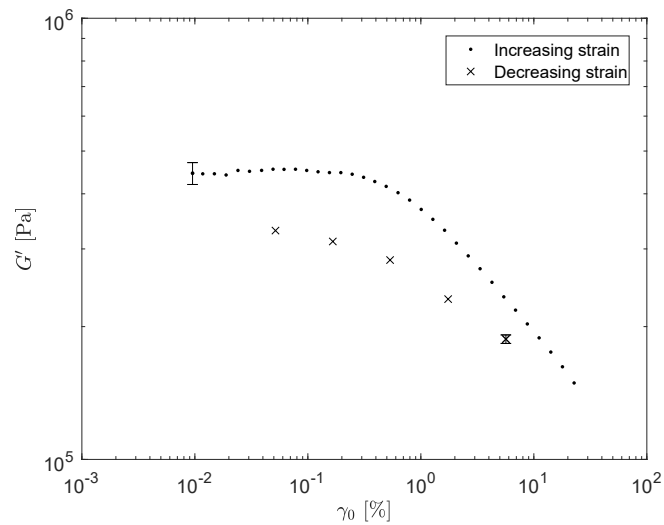
Plates are molded from the rubber compound by compressing the rubber with a hot press of Fontijne Holland (Type: TP 400) for three minutes, while keeping a constant normal force of 100 kN applied to the rubber at 100 °C. This is followed by compressing the rubber for three minutes at the same constant normal force at  $T = 25$  °C. Teflon sheets are used to prevent the rubber from adhering to the press plates. Circular samples with a diameter of 25 mm and a thickness of 2 mm are obtained by die-cutting them from the pressed plates. To reduce the torque needed to perform oscillatory-shear measurements at large strain amplitudes, also circular samples with a diameter of 8 mm and a thickness of 2 mm are used.

## 2.2. Methods

Rheological measurements on rubber compounds, i.e., thixotropic materials, are limited in terms of frequency in case of dynamic measurements, shear rate and temperature range. The latter due crosslinking at higher temperatures. Moreover, the performance and interpretation of dynamic measurements are more complicated for compounds than for regular polymers because of thixotropic behavior; properties can change during the measurements. The thixotropic behavior is caused by filler particles that create a reversible network, resulting in additional elastic behavior. This network can be (partly) destroyed by flow gradients and recovers after the flow has stopped. When the filler-network is completely destroyed one should observe the rheological characteristics of a filled polymer that is still a highly nonlinear viscoelastic material, i.e., very high zero-shear rate viscosity, clear shear thinning, normal stresses, glassy behavior at high frequencies. In this paper, we apply dynamic oscillatory shear measurements to characterize this behavior.

### 2.2.1. Dynamic Oscillatory Shear Measurements

We will first focus on the results of dynamic measurements, i.e., oscillatory shear experiments, performed with a strain-controlled rheometer (TA-instruments, RDAIII), using a plate-plate geometry, from which a limited rheological spectrum is obtained. To determine the strain amplitude range for which the filler networks remain undamaged, a strain sweep is performed where the storage modulus  $G'$  is measured with increasing strain amplitude ( $T = 75$  °C). To show that the decrease in  $G'$  is not caused by nonlinear viscoelasticity only, the measurement is immediately followed by a strain sweep with decreasing strain amplitude. The result is shown in Figure 2. This figure shows the effect of thixotropy, since the curve measured with decreasing strain amplitude shows lower values for  $G'$  as the curve measured with increasing strain amplitude. The measurements in this figure are repeated three times to show reproducibility.



**Figure 2.** Strain sweep measurements of  $G'$  for increasing strain (black dots), followed by strain sweep measurements for decreasing strain (black crosses).

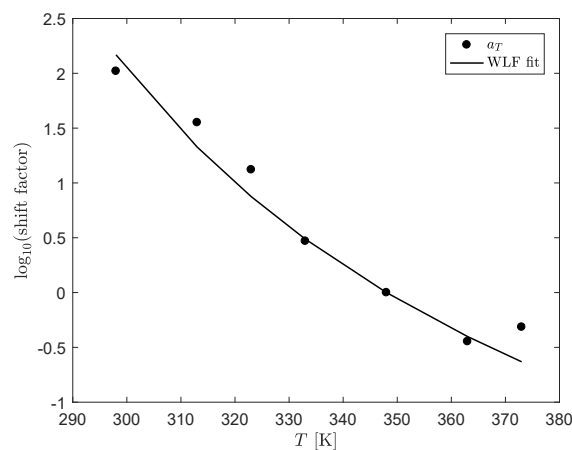
To study the effect of deformation on the material properties of the compound, a relaxation spectrum of the undamaged material is needed to use as starting point. To this end, frequency sweeps are performed with a low strain amplitude of  $\gamma_0 = 0.1\%$  at different temperatures. Time Temperature Superposition (TTS) is used to construct mastercurves for the storage- and loss-moduli ( $G'$  and  $G''$ ), and the phase-angle  $\delta$ , respectively. The horizontal shift-factors used in the TTS are shown in Figure 3. A vertical shift was not required. The WLF equation is used to fit the horizontal shift-factors  $a_T$  [44]:

$$\log_{10}(a_T) = \frac{-C_1(T - T_{\text{ref}})}{C_2 + (T - T_{\text{ref}})}, \quad (1)$$

where  $C_1$  and  $C_2$  are empirical constants obtained via a least-squares fit and their values can be found in Table 2 and  $T_{\text{ref}} = 75^\circ\text{C}$  is the reference temperature of the mastercurves.

**Table 2.** WLF parameters.

$C_1$ [-]	$C_2$ [K]
4.54	154.64



**Figure 3.** Horizontal  $a_T$  shift-factors used in the time temperature superposition to construct mastercurves of  $G'$ ,  $G''$  and  $\delta$  and the obtained WLF-fit to the horizontal shift factors  $a_T$ .

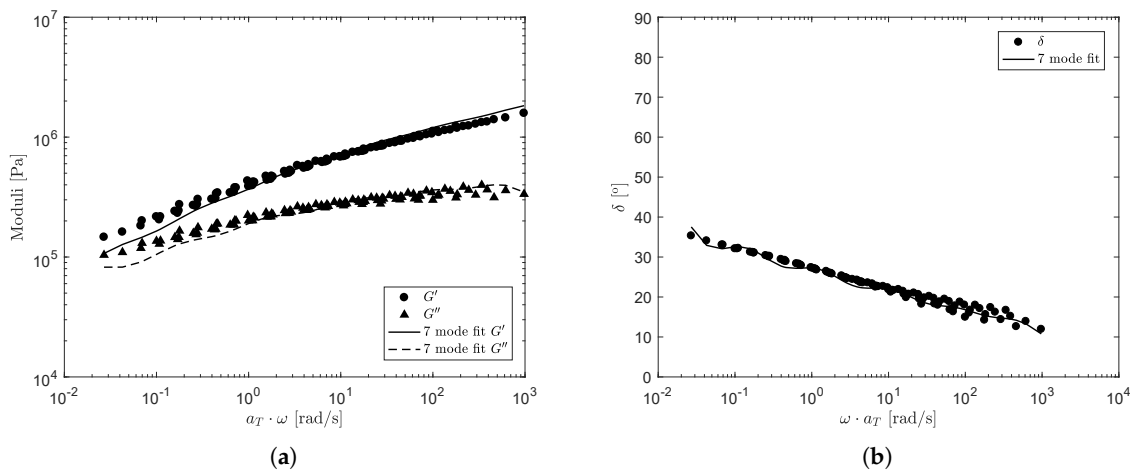
The constructed mastercurves for the storage- and loss-moduli and the phase-angle are shown in Figure 4. For the compound used in this paper, 7-modes seemed to be sufficient to obtain a good fit. For other compounds, the number of modes can be different. The relaxation spectrum for the undamaged material is obtained by performing a 7-mode least-squares fit on the mastercurves of  $G'$  and  $G''$  and  $\delta$ , using the Maxwell model [45]:

$$G'(\omega) = \sum_{k=1}^m \frac{G_k \lambda_k^2 \omega^2}{1 + (\lambda_k \omega)^2}, \quad G''(\omega) = \sum_{k=1}^m \frac{G_k \lambda_k \omega}{1 + (\lambda_k \omega)^2}, \quad \delta(\omega) = \arctan(G''(\omega)/G'(\omega)), \quad (2)$$

where  $m$  is the number of modes. The resulting fit is also shown in Figure 4. The values for the relaxation times  $\lambda_{0,k}$  and moduli  $G_{0,k}$  are shown in Table 3. Here, the subscript  $()_0$  indicates the spectrum used to characterize the undamaged material.

**Table 3.** Relaxation spectrum of a 7-mode Maxwell fit of  $G'$  and  $G''$  of the undamaged material.

Mode	$G_{0,k}$ [Pa]	$\lambda_{0,k}$ [s]
1	$1.25 \times 10^5$	75.93
2	$1.45 \times 10^5$	6.16
3	$2.27 \times 10^5$	0.91
4	$3.16 \times 10^5$	0.14
5	$4.05 \times 10^5$	0.022
6	$5.30 \times 10^5$	0.0032
7	$6.80 \times 10^5$	0.0003



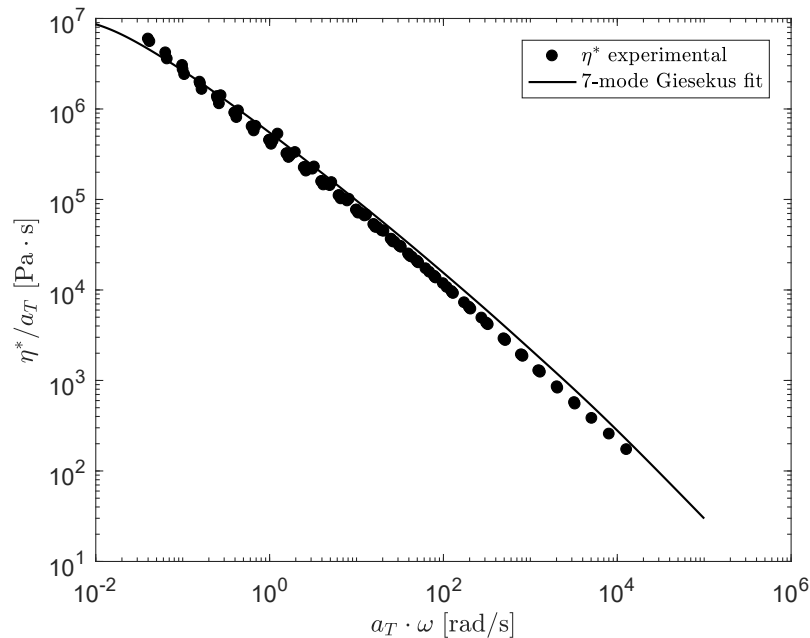
**Figure 4.** Mastercurves of the storage- and loss modulus measured with a strain amplitude of  $\gamma_0 = 0.1\%$  at  $T = 75^\circ\text{C}$  (a) and the corresponding mastercurve of the phase-angle  $\delta$  (b). Solid and dashed lines correspond to the 7-mode Maxwell fit of Table 3 to the data. The kinks in the fit of  $\delta$  can be attributed to the contribution of the different modes, i.e., it is not a continuous spectrum. A smoother curve can be obtained by adding more modes in the suitable frequency range ( $\lambda = 1/\omega$ ). However, this makes the modeling also more computationally expensive.

To predict nonlinear viscoelastic behavior of the compounds, a Giesekus model is used to calculate the viscoelastic stress [46]:

$$\lambda_k \left( \frac{D\tau_k}{Dt} - L \cdot \tau_k - \tau_k \cdot L^T \right) + \tau_k + \frac{\lambda_k \alpha_k}{\eta} \tau_k^2 = 2\eta_k D, \quad \tau = \sum_{k=1}^m \tau_k \quad (3)$$

where  $D()/Dt$  denotes the material derivative,  $\tau$  is the total viscoelastic stress tensor,  $L$  is the velocity gradient,  $D = (\nabla u + \nabla u^T)/2$  is the rate-of-deformation tensor,  $\eta_k = G_k \lambda_k$  is the shear viscosity of mode  $k$  and  $\alpha_k$  is the mobility parameter of mode  $k$  that influences shear-thinning. Note that it is not possible to perform steady shear measurements on

the compounds without measuring the effect of thixotropy. To get an estimate of the mobility parameter  $\alpha_k$  of the Giesekus model for every mode  $k$ , the model is fitted to the experimental data of the complex viscosity for the undamaged material. The result is shown in Figure 5. The nonlinear parameters obtained are given in Table 4.



**Figure 5.** Fit of the Giesekus model to experimental data of the complex viscosity measured with oscillatory shear experiments.

**Table 4.** Nonlinear parameter  $\alpha_k$  used in the Giesekus model for nonlinear viscoelastic stress calculations.

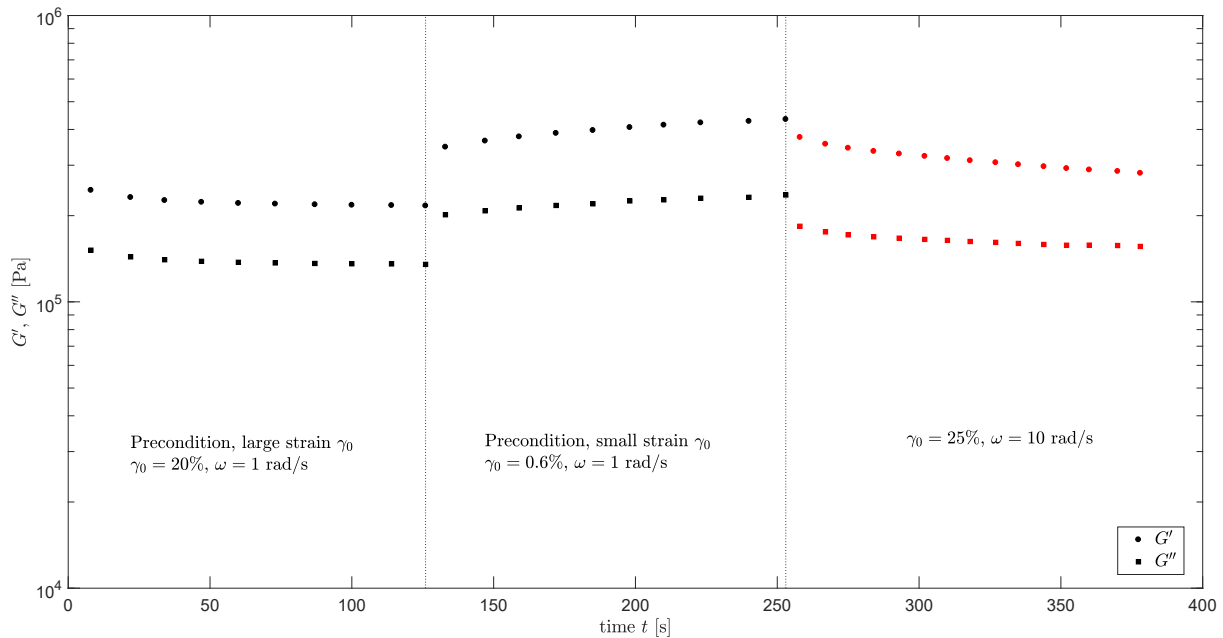
Mode	$\alpha_k$ [-]
1	0.4
2	0.4
3	0.4
4	0.4
5	0.4
6	0.4
7	0.25

Next, mastercurves are constructed for different degrees of structural damage. A horizontal shift between mastercurves of the moduli of different degrees of structural damage could be observed for a large frequency range. Together with the assumption that structural damage leads to a ‘reduced’ time scale due to destruction of the elastic network in the material, this led to the choice to focus on the mastercurves of the phase-angle  $\delta$  in this work. To erase any structural memory and make sure the starting properties of every sample are approximately the same, a pre-shear is applied. The measuring protocol of every point on the mastercurves with different degrees of structural damage in the material is shown in Figure 6 and is defined as follows:

1. For every sample, first a pre-shear (indicated in black) is applied by performing oscillatory shear measurements of  $t = 120$  s,  $\omega = 1$  rad/s and a strain amplitude of  $\gamma_0 = 20\%$  during which the structure will break down;
2. This is followed by a pre-shear during which the structure can (partially) recover again, by performing oscillatory shear measurements of  $t = 120$  s,  $\omega = 1$  rad/s and a strain amplitude of  $\gamma_0 = 0.6\%$ ;

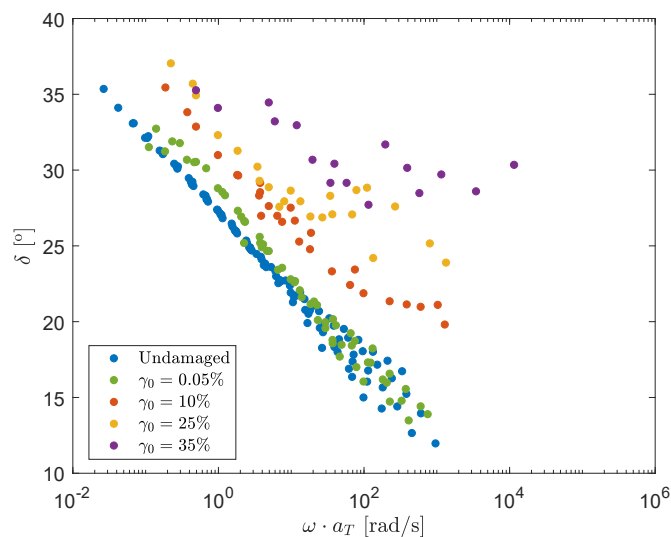


3. These pre-shear measurements are followed by an oscillatory shear measurement of again  $t = 120$  s, but for different frequencies  $\omega$  and strain amplitudes  $\gamma_0$  (indicated in red);
4. The storage and loss moduli at time  $t = 350$  s are used to calculate the phase-angle  $\delta$  and this gives one single point on the mastercurve with strain amplitude  $\gamma_0$ .



**Figure 6.** Measuring protocol to construct mastercurves of  $\delta$  for different degrees of structural damage.

The result for the mastercurves with different strain amplitudes, and therefore different degrees of structural damage, are shown in Figure 7. Here, every point is a separate experiment performed using the protocol as shown in Figure 6. It is important to note that the mastercurve for  $\gamma_0 = 0.05\%$  is used to characterize the *recovery* behavior of the material. For this curve, only a pre-shear of  $t = 120$  s,  $\omega = 1$  rad/s and a strain amplitude of  $\gamma_0 = 20\%$  is applied, meaning that step 2 in the measuring protocol is skipped. This is followed by an oscillatory shear measurement of again  $t = 120$  s, but for different frequencies  $\omega$  and a strain amplitude of  $\gamma_0 = 0.05\%$  during which the material can recover.



**Figure 7.** Mastercurves ( $T = 75$  °C) of the phase-angle  $\delta$  for different degrees of structural damage by applying different strain amplitudes  $\gamma_0$ .

### 2.2.2. Steady Shear Measurements

Steady shear measurements are provided by VMI Holland B.V. and measurements were performed on an in-house made device. The compound is extruded in a closed, pressurized chamber containing a double-cone plate geometry. The pressure-method [47] is used to determine the shear viscosity  $\eta$  and the first normal stress difference coefficient  $\Psi_1$  from the measurements. Measurements are performed for a temperature range  $T = 70\text{--}90\text{ }^\circ\text{C}$  to construct mastercurves for  $T = 75\text{ }^\circ\text{C}$ . Results are presented in Section 4.3.

## 3. Thixotropy Model

In this section, the assumptions and observations that lead to the model approach are presented. This is followed by the mathematical description of the rate- and stress-controlled thixotropy model used throughout this paper.

### 3.1. Model Definition

From Figure 7, the following assumptions/observations can be made:

- It is assumed that structural damage leads to a ‘reduced’ time scale due to destruction of the elastic network. Combined with the observation that structural damage causes the phase-angle  $\delta$  to shift horizontally for a large range of frequencies, this leads to the assumption that the influence of structural damage on the phase-angle can be described with a horizontal shift factor  $a_\zeta$  for increasing the strain amplitude  $\gamma_0$ .
- For higher angular frequencies  $\omega$ , there is an upswing in the phase-angle and the effect of damage can no longer be described by a pure horizontal shift.
- This upswing is more pronounced for higher levels of structural damage and starts at lower frequencies.

The undamaged mastercurve of  $\delta$  shows a linear dependency on  $\log_{10} \omega$ . Therefore, a linear line can be fitted through this mastercurve. For small  $\omega$ , a horizontal shift factor  $a_\zeta$  is applied to this linear fit, to obtain linear lines that fit the mastercurves for the different strain amplitudes  $\gamma_0$ . This is schematically depicted in Figure 8. This horizontal shift plays a crucial role in the model definition in this paper and the shift-factors  $a_\zeta$  for the different strain amplitudes can be found in Table 5.

**Table 5.** Horizontal shift  $a_\zeta$  for the different strain amplitudes in Figure 7.

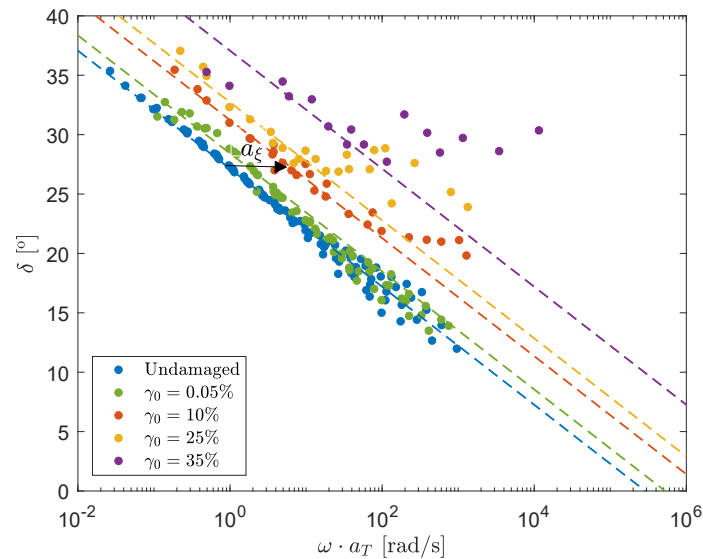
$\gamma_0$ [%]	$a_\zeta$ [-]	$1/a_\zeta$ [-]
0.05	1.81	0.55
10	6.67	0.15
25	13.33	0.075
35	100	0.01

Using a horizontal shift  $a_\zeta$  on the mastercurves of the phase-angle suggests that the effect of damage of the filler networks can be modeled by adjusting the relaxation times of the undamaged material. To show that this hypothesis is valid, the horizontal shift between the linear fits through the mastercurves are obtained and the relaxation times are adjusted accordingly:

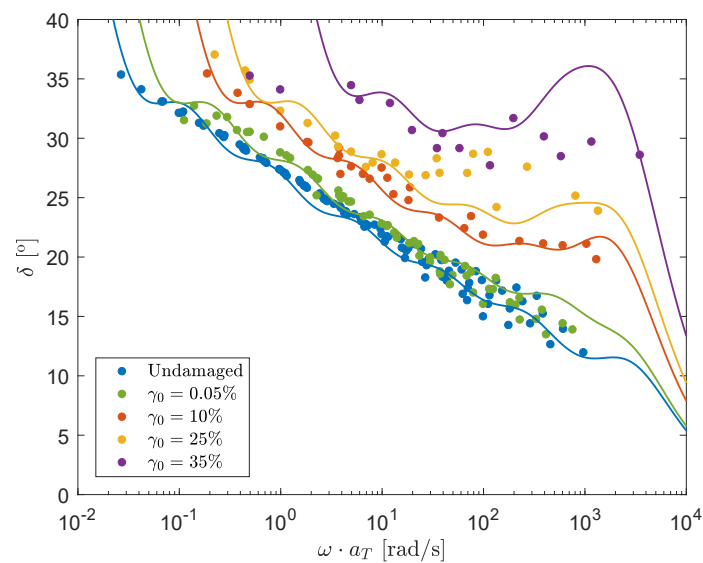
$$\lambda_k = \lambda_{0,k} \cdot \frac{1}{a_\zeta}. \quad (4)$$

For high frequencies, an upswing in the phase-angle is observed that becomes more pronounced for higher strain amplitudes. Structural damage is assumed to be dominant for the modes with the largest relaxation times, i.e., the relaxation times that are thought to be mostly related to the elastic filler network. Therefore, it is assumed that small relaxation times (corresponding to high frequencies) do not contribute to the elastic network. Following this reasoning, the horizontal shift of these modes should be limited. The measured upswing at high frequencies can now be used to determine this limited horizontal shift. Numerical experiments showed that the factor  $1/a_\zeta$  in Equation (4) for the two modes

with the smallest relaxation times should be limited to describe the measured upswing at high frequencies. It was found that the experimental data were described best when the smallest relaxation time was not adjusted ( $1/a_{\xi} = 1$ ) and, for mode six,  $1/a_{\xi}$  was limited to  $\min(1/a_{\xi}) = 0.1$ . The result is shown in Figure 9.



**Figure 8.** Mastercurves of different degrees of structural damage show a horizontal shift  $a_{\xi}$  with respect to the undamaged mastercurve.



**Figure 9.** Results for the mastercurves of the phase-angle by adjusting the undamaged relaxation times with the horizontal shift-factors  $a_{\xi}$ .

Even though upswings in  $\delta$  have been measured in the past for elastic materials [48] and the upswing in the experimental data is captured well by limiting the damage of the smallest relaxation times, it has to be noted that the experimental results obtained at high frequencies are prone to experimental errors. Therefore, the measurements at high  $\omega$  have to be considered less accurate than the measurements at small  $\omega$ .

### Extended Spectrum

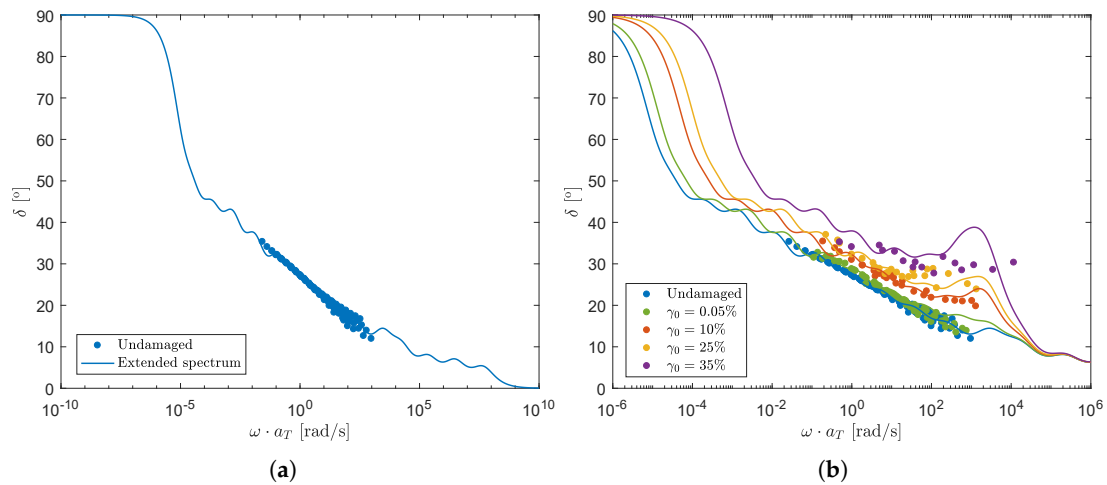
So far, we have focused on the results of dynamic measurements, i.e., oscillatory shear experiments, from which a limited (7-mode) rheological spectrum is obtained. Based on a combination of arguments and some observations, this spectrum can be extended such that the shear rate range becomes applicable to realistic processing conditions.

For a compound with network structures that are finite, i.e., without a network structure that spans the whole sample, the phase-angle has limits: ( $\delta(\omega \rightarrow 0) = 90^\circ$ ), ( $\delta(\omega \rightarrow \infty) = 0^\circ$ ). The relaxation spectrum can now be extended to lower and higher frequencies than the measurement range, such that the slope of the undamaged mastercurve is preserved over a large range, keeping the phase-angle limits in mind. The result is shown in Figure 10a. Notice that with this choice the material shows a Newtonian plateau for (very) small  $\omega$ . When an ‘infinite network’ would exist in the sample, the phase-angle would show a limiting phase-angle close to zero for small  $\omega$ , indicating that the material has a yield-stress. When choosing the right parameters, one can also model this behavior. However, we do not consider this possibility of yielding, since we have no experimental evidence for such behavior for the compound considered. The relaxation times  $\lambda_{0,k}$  and moduli  $G_{0,k}$  of the extended spectrum are given in Table 6.

**Table 6.** Extended 15-mode relaxation spectrum for the undamaged material.

Mode	$G_{0,k}$ [Pa]	$\lambda_{0,k}$ [s]
1	$0.02 \times 10^5$	$1 \times 10^5$
2	$0.04 \times 10^5$	$2 \times 10^4$
3	$0.1 \times 10^5$	$3 \times 10^3$
4	$0.3 \times 10^5$	$4 \times 10^2$
5	$0.7 \times 10^5$	50.00
6	$1.3 \times 10^5$	5.80
7	$2.1 \times 10^5$	0.91
8	$3.0 \times 10^5$	0.14
9	$4.0 \times 10^5$	0.022
10	$5.0 \times 10^5$	0.0032
11	$6.80 \times 10^5$	0.0003
12	$7.00 \times 10^5$	$50 \times 10^{-6}$
13	$7.00 \times 10^5$	$40 \times 10^{-7}$
14	$8.00 \times 10^5$	$30 \times 10^{-8}$
15	$8.00 \times 10^5$	$20 \times 10^{-9}$

Following the same reasoning as for the 7-mode spectrum, the horizontal shift for modes with small relaxation times, corresponding to high frequencies, is again limited. Using numerical experiments, the maximum adjustment factor for mode 10 was found to be  $\min(1/a_\zeta) = 0.1$ . Modes 11–15 were not adjusted ( $1/a_\zeta = 1$ ). The extended spectrum can now be used to fit the experimental mastercurves for the different degrees of structural damage. The result is shown in Figure 10b. Both the horizontal shift and the upswing are captured quite well. For practical reasons, we will not take into account the plateau limits in the phase-angle for the model predictions. Therefore, the 7-mode spectrum will be used in the remainder of this paper.



**Figure 10.** Phase-angle of the undamaged material as a function of frequency fitted with a 15-mode extended relaxation spectrum (a) and phase-angle as a function of frequency for different degrees of structural damage fitted with a 15-mode extended relaxation spectrum (b).

### 3.2. Mathematical Description

Results in the previous section show that adjusting the relaxation times of the undamaged spectrum with the horizontal shift  $a_{\zeta}$  between the different mastercurves of the phase-angle  $\delta$  leads to a successful prediction of the measured behavior. Therefore, a structure parameter  $\zeta$  is defined based on this horizontal shift-factor  $a_{\zeta}$  as  $\zeta = 1/a_{\zeta}$ . If  $\zeta = 1$ , then the material is undamaged and the filler networks are intact, whereas  $\zeta = \zeta_{\text{inf}}$  indicates a completely damaged material where no network structures due to the fillers are left:

$$\zeta = \begin{cases} 1, & \text{Undamaged; structures intact} \\ \zeta_{\text{inf}}, & \text{Maximum damage,} \end{cases}$$

here, the minimum value for  $\zeta_{\text{inf}}$  that can be used is  $\zeta_{\text{inf}} = 0$ . The value for  $\zeta_{\text{inf}}$  is related to the limited horizontal shift for small relaxation times introduced in the previous section to capture the upswing in  $\delta$  for high frequencies. This means that for the 7-mode spectrum  $\zeta_{\text{inf}}$  can be defined as follows:

$$\zeta_{\text{inf}} = [0, 0, 0, 0, 0, 0.1, 1]. \tag{5}$$

To model the thixotropic behavior, we compare a rate- and stress-controlled phenomenological structure parameter  $\zeta$  to adjust the relaxation times of the undamaged spectrum, to obtain the relaxation spectrum of the damaged material. First, the mathematical description of both models is given, followed by the approach to obtain the different model parameters. The following kinetic equations are based on the work of Leonov et al. [30–32].

#### 3.2.1. Rate-Controlled Model

$$\frac{D\zeta}{Dt} = \frac{1 - \zeta}{\lambda_{\theta}} - E\gamma^*(\zeta - \zeta_{\text{inf}}), \tag{6}$$

where  $D()/Dt = \partial()/\partial t + \mathbf{u} \cdot \nabla()$  is the material derivative,  $\lambda_{\theta}$  is a characteristic time scale for the recovery of the material structure,  $E = \sqrt{2\text{tr}\mathbf{D}^2}$  is a measure of the deformation rate based on the rate of deformation tensor  $\mathbf{D}$ , corresponding to an effective shear rate in shear flows. Furthermore,  $\gamma^*$  is a fitting parameter that indicates how much of the applied deformation leads to damage of the structure in the material and  $\zeta_{\text{inf}}$  is a fitting parameter that limits the degree of damage that can be done to the material. This parameter is introduced, since the rheological characteristics of an unfilled polymer that is still a highly nonlinear

viscoelastic material should be observed when the filler-network is completely destroyed.

For the oscillatory shear measurements,  $E$  is defined as follows:

$$E(t) = |\gamma_0 \omega \cos(\omega t)|, \quad (7)$$

which can be simplified to:

$$\langle E \rangle = \frac{2\gamma_0 \omega}{\pi}, \quad (8)$$

to take  $E$  as the average over the period of oscillation [32].

### 3.2.2. Stress-Controlled Model

$$\frac{D\zeta}{Dt} = \frac{1 - \zeta}{\lambda_\theta} - \frac{\tau_c(\zeta)}{\eta_0} \tau^* (\zeta - \zeta_{\text{inf}}), \quad (9)$$

where  $\tau_c(\tau)$  is a characteristic stress in the material that is a function of the viscoelastic stress tensor  $\tau$ ,  $\eta_0$  is the zero shear viscosity of the undamaged material and  $\tau^*$  is a fitting parameter that describes how much of the present stress contributes to damage of the elastic network. Here, the equivalent von Mises shear stress is used as characteristic stress  $\tau_c$  [49]:

$$\tau_c = \sqrt{\frac{1}{2} \hat{\tau} : \hat{\tau}}, \quad (10)$$

with  $\hat{\tau} = \tau - \frac{1}{3}(\text{tr } \tau)\mathbf{I}$ , the deviatoric part of the total viscoelastic stress tensor.

Since  $\zeta$  is related to the horizontal shift between the mastercurves of  $\delta$ , the relaxation times of the undamaged material  $\lambda_{0,k}$  are now adjusted using the structure parameter  $\zeta$  to obtain the relaxation times  $\lambda_k$  of the damaged material:

$$\lambda_k = \lambda_{0,k} \cdot \zeta, \quad (11)$$

where  $\lambda_{0,k}$  are the initial relaxation times obtained from fitting the mastercurves of the undamaged material of Figure 4. Here, in contrast to the Leonov model, the coupling between the nonlinear viscoelastic behavior described by the constitutive equation and the structure parameter is very straightforward through the relaxation times.

### 3.3. Model Parameters

We use one single structure parameter for all seven modes in the relaxation spectrum shown in Table 3 and therefore assume that  $\zeta$  describes the overall structure in the material. The structure parameter for the different mastercurves in Figure 7 is obtained from the horizontal shift of the linear fits for the different strain amplitudes  $\zeta = 1/a_\zeta$  (see Table 5). This structure parameter is plotted as a function of the applied strain amplitude in Figure 11. Note that  $\zeta$  for  $\gamma_0 = 0.05\%$  is smaller than one, because this point indicates the horizontal shift of the recovery curve after the applied pre-shear of step 1 in the measuring protocol. Since this is the only 'recovery' curve, this point is indicated with a star. Since the horizontal shift is the same for a wide range of frequencies, the model parameters should be chosen such that the structure parameter  $\zeta$  is approximately the same as this horizontal shift for different frequencies. Using the deformation history as shown in Figure 6, the evolution of the structure parameter  $\zeta$  can be calculated using an explicit Euler method. It was found that for the rate-controlled model, the effect of  $\omega$  was too pronounced if  $E$  was calculated using Equation (7). It can be argued that for high frequencies, a high strain-amplitude leads to a lower degree of damage than for low frequencies, because the structure acts more like

an elastic solid at high  $\omega$ . In order to capture this behavior, the effective shear rate  $E$  is given a power law-like dependence on the frequency  $\omega$ :

$$\langle E \rangle = \frac{2\gamma_0\omega^p}{(\omega^*)^{p-1}\pi}. \tag{12}$$

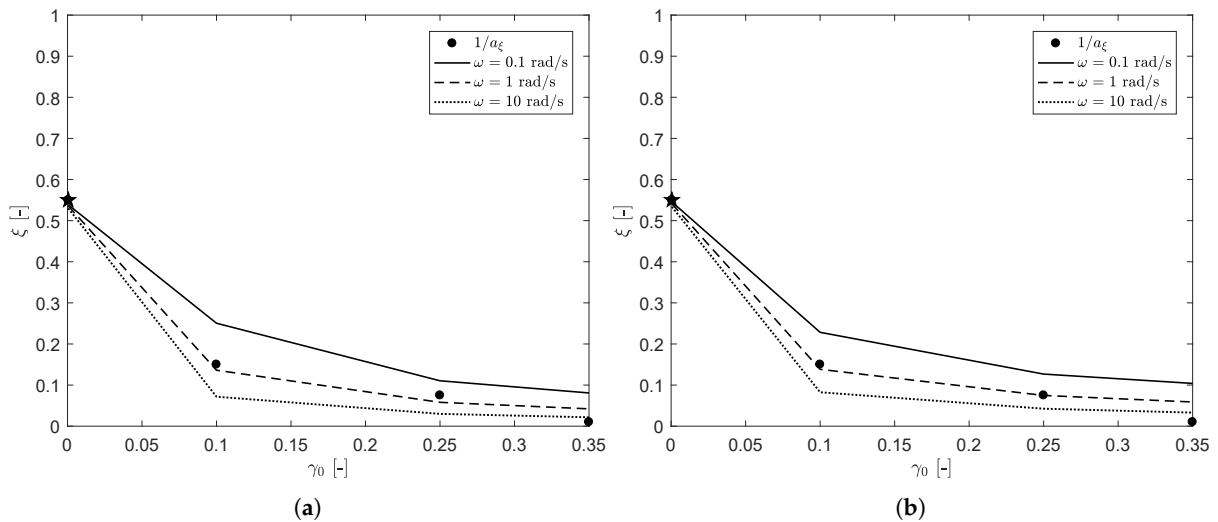
To avoid problems with the unit of  $\gamma^*$ , a characteristic  $\omega^*$  is introduced. Here,  $\omega^* = 1$  rad/s since the horizontal shift  $a_{\zeta}$  is based on the shift at this frequency.

For the stress-controlled method, the characteristic stress is calculated as  $\tau_c(\tau) = |G^*|\gamma_0$ , where  $G^*$  is the complex modulus  $G^* = \sqrt{(G'^2 + G''^2)}$  calculated with the damaged spectrum, obtained from the previous time step. It is important to note that this stress only equals the von Mises shear stress if linear rheological behavior is assumed. Results of fitting the structure parameter as a function of strain amplitude for frequencies in the range  $\omega = [0.1, 1, 10]$  rad/s for the two different models are shown in Figure 11. Here, it is tried to get the difference in the structure parameters for the different frequencies as small as possible, to obtain the same horizontal shift for a wide frequency range, while still using realistic values for the fitting parameters.

The obtained fitting parameters for both models are given in Table 7.

**Table 7.** Fit parameters used to fit  $\zeta$  as a function of the strain amplitude  $\gamma_0$ .

$\lambda_\theta$ [s]	$\gamma^*$ [-]	$p$ [-]	$\tau^*$ [-]
170	0.6	0.3	17.6



**Figure 11.** Structure parameter  $\zeta$  obtained from the horizontal shift  $a_{\zeta}$  between the mastercurves of the phase-angle with different strain amplitudes fitted by the rate-controlled model (a) and the stress-controlled model (b) for different frequencies  $\omega$ . The horizontal shift of the recovery curve  $\gamma_0 = 0.05\%$  is indicated with a star.

The values for  $\zeta_{inf}$  were obtained in Section 3.1 from capturing the upswing while adjusting the relaxation times with the horizontal shift factor  $\lambda_0 = \lambda \cdot 1/a_{\zeta}$ .

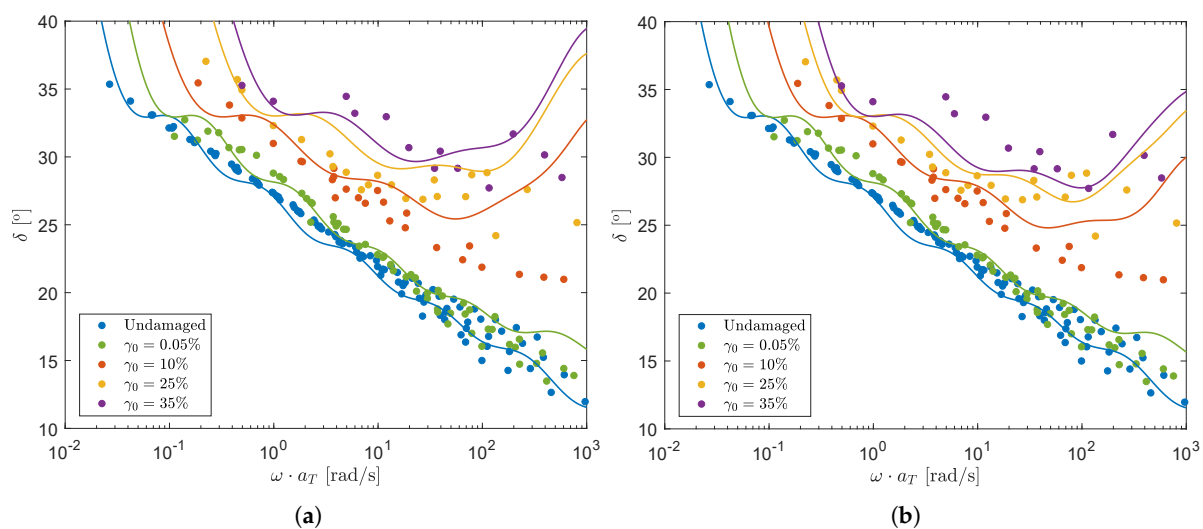
#### 4. Results

This section will show results of model predictions in oscillatory shear and steady shear for the rate- and stress-controlled model. First, dynamic oscillatory model predictions of the mastercurves of the phase angle are shown for both methods. This is followed by dynamic model predictions of oscillatory shear measurements of the damage recovery behavior for a fixed frequency of  $\omega = 1$  rad/s and different strain amplitudes. Here, a distinction is made between predictions with a homogeneous flow assumption and more

realistic non-homogeneous flow conditions where nonlinear viscoelasticity is taken into account. Finally, model predictions are shown for steady shear data for both approaches.

#### 4.1. Mastercurve Model Predictions in Oscillatory Shear

The 7-mode spectrum is used to calculate the model predictions in oscillatory shear. The structure parameter  $\zeta$  is calculated for every point on the mastercurves of Figure 7, using an Explicit Euler method and taking the applied pre-shear into account. For the rate-controlled method,  $E$  is calculated using the power law-like dependence on  $\omega$  as described in Equation (12). For the stress-controlled method, the characteristic stress is again calculated as  $\tau_c(\boldsymbol{\tau}) = |G^*|\gamma_0$ , where  $G^*$  is the complex modulus  $G^* = \sqrt{(G'^2 + G''^2)}$  calculated with the damaged spectrum, obtained from the previous time step and, thus, linear rheological behavior is assumed. The results for the rate- and stress-controlled method are shown in Figure 12.



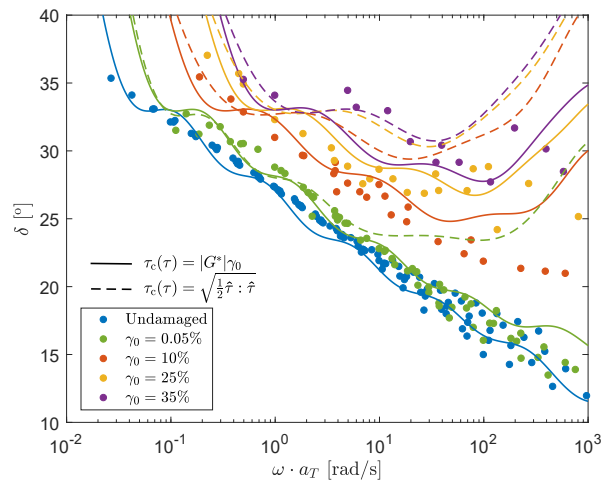
**Figure 12.** Model predictions of oscillatory shear measurements for the rate-controlled model, using a power law-like dependence on the frequency (a) and for the stress-controlled model assuming linear rheological behavior (b).

Results show that both models give a qualitative prediction of the measured mastercurves.

The approximation of the characteristic stress  $\tau_c(\boldsymbol{\tau}) = |G^*|\gamma_0$  can only be used for small Weissenberg numbers. For large strain amplitudes and frequencies, normal stresses will start to play a role such that  $|G^*|\gamma_0 < \sqrt{\frac{1}{2} \hat{\boldsymbol{\tau}} : \hat{\boldsymbol{\tau}}}$ . Figure 13 shows a comparison between the model predictions using  $\tau_c(\boldsymbol{\tau}) = |G^*|\gamma_0$  and the von Mises shear stress calculated using a Giesekus model.

This figure shows that for high strain amplitudes, but especially for high frequencies, assuming linear viscoelastic behavior is no longer allowed since model predictions using the von Mises shear stress are highly different from model predictions using  $\tau_c(\boldsymbol{\tau}) = |G^*|\gamma_0$ . The von Mises stress is much higher than the shear stress for high frequencies, because normal stresses can no longer be neglected. Results show that, similar to the rate-controlled model, the frequency dependence is over-predicted compared to the experimental data. At these high frequencies, the measurements are also prone to experimental errors. The oscillatory shear measurements are therefore mainly used to obtain model parameters to do qualitative predictions for small  $\omega$  and in steady shear. It should also be noted that in the fitting procedure linear viscoelastic behavior is assumed:  $\tau_c(\boldsymbol{\tau}) = |G^*|\gamma_0$ . A more consistent fitting procedure, using the von Mises shear stress, might give better results for the oscillatory shear behavior. However, with the current model, this will most likely lead to an over-prediction of the rheological properties in steady shear.





**Figure 13.** Model predictions of oscillatory shear measurements for the stress-controlled model, using  $\tau_c(\tau) = |G^*|\gamma_0$  (solid lines) and  $\tau_c = \sqrt{\frac{1}{2} \dot{\tau} : \dot{\tau}}$  (dashed lines).

#### 4.2. Damage Recovery Behavior Model Prediction in Oscillatory Shear

The 7-mode relaxation spectrum in combination with the rate- and stress-controlled thixotropic models is used to model the dynamic behavior of the compound. The fitting parameters as found in Table 7 are used. Here, a distinction is made between a homogeneous flow assumption and a more realistic non-homogeneous flow as present in a plate-plate rheometer.

##### 4.2.1. Homogeneous Flow Assumption

Oscillatory shear measurements are performed for different strain amplitudes and  $\omega = 1$  rad/s to find the damage–recovery behavior of the compound. A frequency of  $\omega = 1$  rad/s is chosen to avoid experimental problems at high shear rates and problems with nonlinear rheological behavior. These measurements are again repeated three times to test the reproducibility. The evolution of the structure parameter  $\zeta$  is again modeled using an explicit Euler scheme to solve Equations (6) and (9), using  $E$  as defined by Equation (12) for the rate-controlled method, and the stress  $\tau_c(\tau) = |G^*|\gamma_0$  calculated with  $\zeta$  from the previous time step for the stress-controlled method. The flow is assumed to be homogeneous (no radial dependence) and nonlinear viscoelasticity is neglected. The undamaged relaxation times as listed in Table 3 are adjusted using Equation (11), and the storage and loss moduli are calculated using Equation (2). The experimental results and the model prediction for the storage- and loss moduli are shown in Figure 14 for both methods. This figure shows that the damage–recovery behavior of the compound is captured quite well for both approaches.

##### 4.2.2. Non-Homogeneous Flow

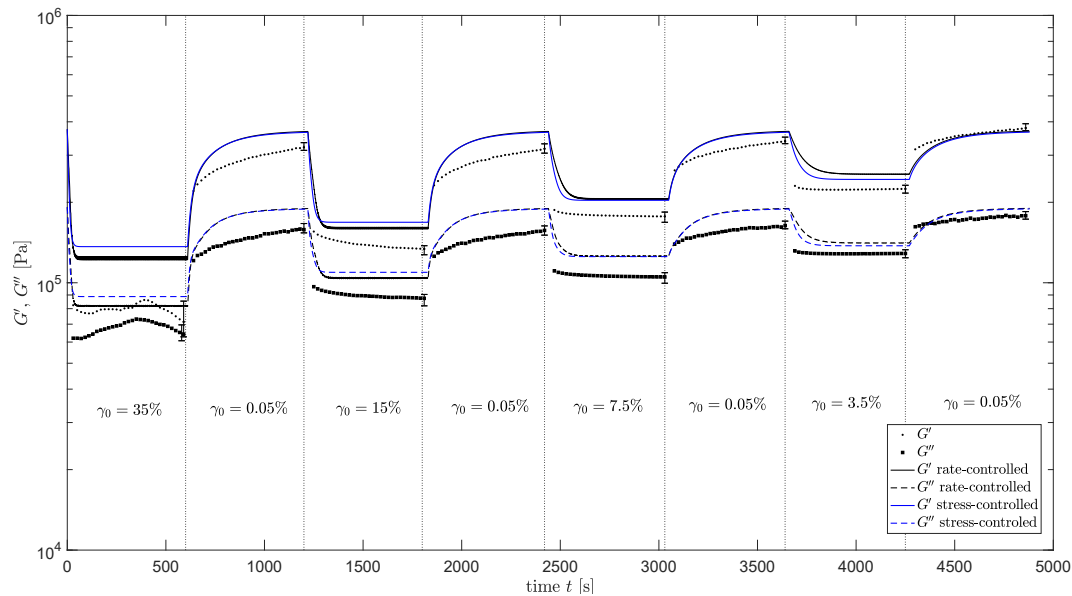
In the previous section, the assumption of homogeneous flow was used. However, in reality, the flow in a plate-plate rheometer is non-homogeneous and, thus, the shear rate is linearly dependent on the radius  $r$  in the sample. This means the structure parameter  $\zeta$  and the material properties will also be  $r$ -dependent. Therefore, full computations are performed where a sinusoidal strain is applied that depends on the radial position  $r$  in the sample:

$$\gamma(r, t) = \frac{r}{R_{\text{plate}}} \cdot \gamma_0 \sin(\omega t), \tag{13}$$

$$E(r, t) = \frac{r}{R_{\text{plate}}} \cdot \gamma_0 \omega \cos(\omega t), \tag{14}$$

where  $r$  is the radial position in the sample and  $R_{\text{plate}}$  is the radius of the plate of the rheometer. Nonlinear viscoelastic behavior is taken into account by using a Giesekus model to calculate the viscoelastic stresses. An Explicit Euler scheme is used to calculate the viscoelastic stress from Equation (3) as a function of time and radius. From this stress, the torque can be calculated [50]:

$$M = 2\pi \int_0^R r\tau_{\theta z}(r)rdr. \quad (15)$$



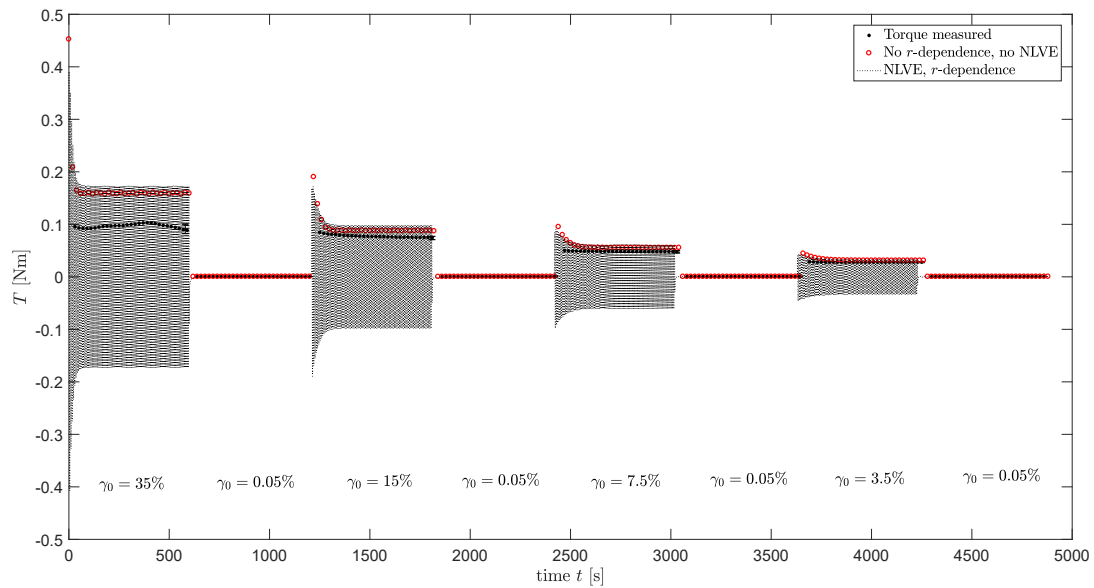
**Figure 14.** Dynamic experimental measurements of the damage–recovery behavior ( $\omega = 1$  rad/s) of the compound (dots) and model predictions using a homogeneous flow assumption and the 7-mode relaxation spectrum (solid lines) for the rate-controlled method (black) and the stress-controlled method (blue).

The rheometer software determines the stress  $\tau_{\theta z}$  from this torque with the following equation:

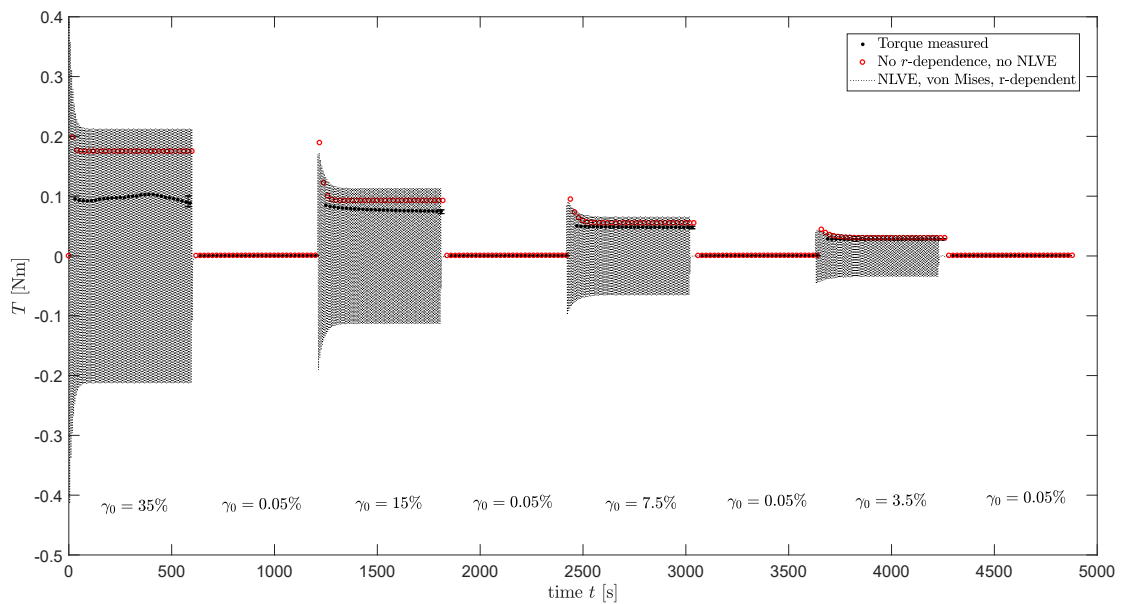
$$\tau_{\theta z} = \frac{2M}{\pi R^3}. \quad (16)$$

For viscoelastic fluids, this equation is a linear approximation. From this stress,  $G'$  and  $G''$  can be calculated. The viscoelastic stress is calculated using the Giesekus model with  $\alpha_k$  parameters as can be found in Table 4.

The evolution of the structure parameter is also calculated using an explicit Euler method, taking the radial dependence of the applied strain into account. The relaxation times are adjusted using the calculated structure parameter and used in the calculations of the viscoelastic stress tensor. For the stress-controlled method,  $\zeta$  is calculated using the von Mises shear stress as characteristic stress  $\tau_c$ . To this end, the von Mises stress calculated from  $\tau$  in the previous time step is used. The torque measured during the oscillatory shear measurements of the damage–recovery behavior of Figure 14 is now calculated using Equation (15). Using this method, both the non-homogeneous flow and nonlinear viscoelasticity are taken into account. The result is shown in Figure 15 for the rate-controlled method and, in Figure 16, for the stress-controlled method. These figures show that for  $\omega = 1$  rad/s and the strain amplitudes applied in the oscillatory shear experiments, neglecting nonlinear viscoelastic behavior and radial dependence of the strain still gives qualitative results.



**Figure 15.** Dynamic experimental measurements of the torque during the damage–recovery behavior measurements of the compound (dots), model predictions using a homogeneous flow assumption and the 7-mode relaxation spectrum (blue dots) and model predictions taking  $r$ -dependence and Nonlinear Viscoelastic (NLVE) behavior into account (dotted line) for the rate-controlled model.



**Figure 16.** Dynamic experimental measurements of the torque during the damage–recovery behavior measurements of the compound (dots), model predictions using a homogeneous flow assumption and the 7-mode relaxation spectrum (blue dots) and model predictions taking  $r$ -dependence and nonlinear viscoelastic behavior into account (dotted line) for the stress-controlled model.

### 4.3. Model Prediction in Steady Shear

Finally, model predictions using the rate- and stress-controlled method in steady shear are presented. To this end, an equilibrium value of the structure parameter is used to calculate the viscosity  $\eta$  and the first normal stress difference coefficient  $\Psi_1$  for different shear rates. The equilibrium value of the structure parameter  $\zeta_{eq}$  can be calculated by

setting the time derivative in Equations (6) and (9) equal to zero. This gives the following expression for  $\zeta_{eq}$ , for the rate- and stress-controlled method, respectively:

$$\zeta_{eq} = \frac{1 + E\gamma^* \zeta_{inf} \lambda_\theta}{1 + E\gamma^* \lambda_\theta}, \tag{17}$$

$$\zeta_{eq} = \frac{1 + \frac{\tau_c(\tau_{eq})}{\eta_0} \tau^* \zeta_{inf} \lambda_\theta}{1 + \frac{\tau_c(\tau_{eq})}{\eta_0} \tau^* \lambda_\theta}. \tag{18}$$

For the stress-controlled equation, the von Mises stress  $\tau_c(\tau)$  is calculated using a Giesekus model. Here, Newton–Raphson iteration is used to obtain the steady state viscoelastic stress tensor for a specific shear rate. Picard iteration is performed to obtain  $\tau_c(\tau_{eq})$ . By calculating the equilibrium value of the structure parameter for different shear rates, the 7-mode relaxation spectrum of the undamaged material is adjusted and the viscosity  $\eta$  and  $\Psi_1$  can be calculated using the analytical solutions of the Giesekus model:

$$\eta(\dot{\gamma}) = \sum_{k=1}^m \frac{\eta_k(1 - f_k)^2}{1 + (1 - 2\alpha_k)f_k}, \tag{19}$$

$$\Psi_1(\dot{\gamma}) = \sum_{k=1}^m \frac{2\eta_k \lambda_k f_k (1 - \alpha_k f_k)}{\alpha_k (1 - f_k) (\lambda_k \dot{\gamma})^2}, \tag{20}$$

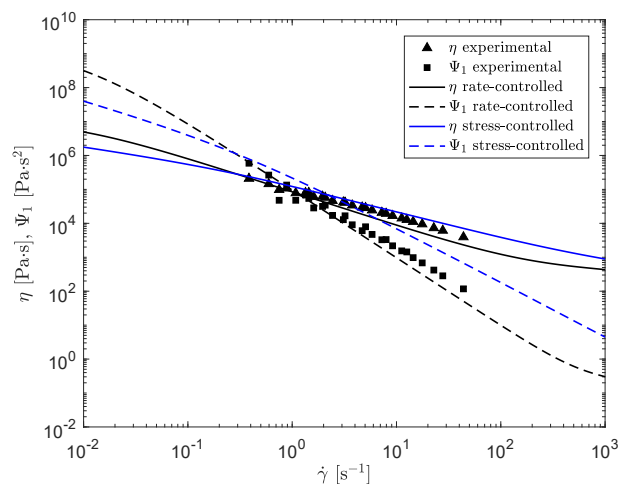
where  $f_k$  is expressed as follows:

$$f_k = \frac{1 - \chi_k}{1 + (1 - 2\alpha_k)\chi_k}, \tag{21}$$

with,

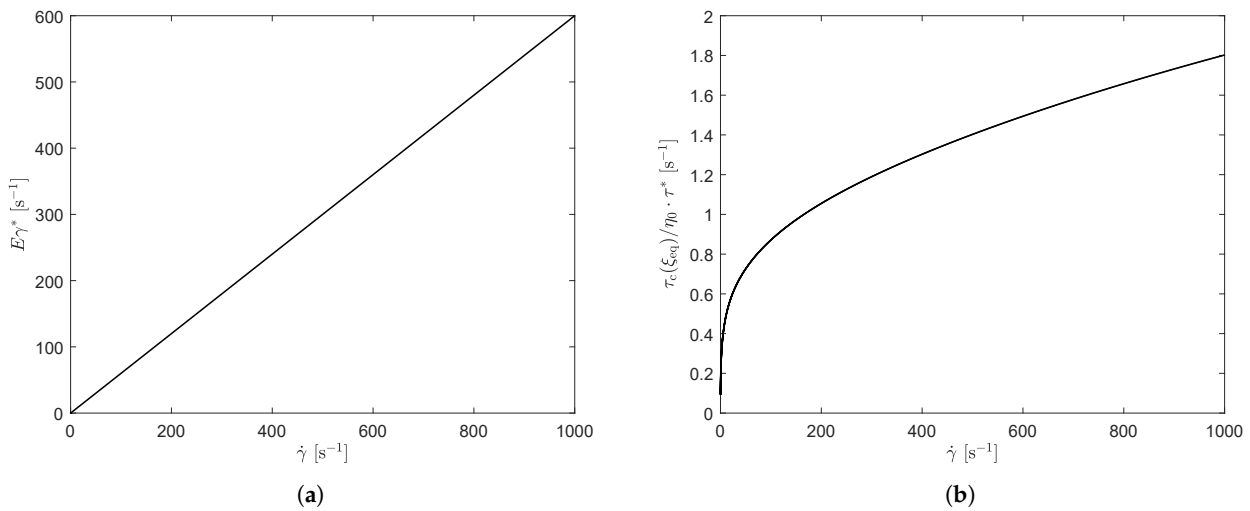
$$\chi_k = \left( \frac{[1 + 16\alpha_k(1 - \alpha_k)(\lambda_k \dot{\gamma})^2]^{1/2} - 1}{8\alpha_k(1 - \alpha_k)(\lambda_k \dot{\gamma})^2} \right)^{1/2}. \tag{22}$$

The result is shown in Figure 17. Here, the black lines indicate the result for the rate-controlled model, whereas the blue lines present the result for the stress-controlled model.



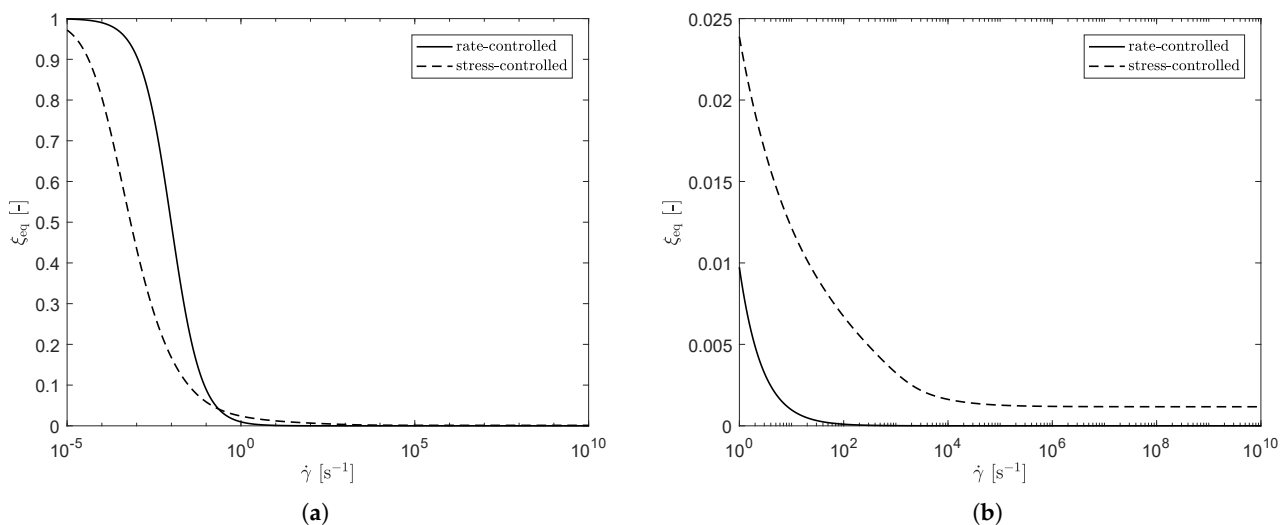
**Figure 17.** Steady shear predictions of the viscosity  $\eta$  and first normal stress difference coefficient  $\Psi_1$  for the rate-controlled (black) and stress-controlled (blue) method and experimental data provided by VMI Holland B.V. (triangles and squares).

This figure shows that both, the viscosity and the first normal stress difference coefficient are predicted to be lower for small shear rates and higher for large shear rates for the stress-controlled model compared to the rate-controlled model. Both models capture the experimental trends reasonably well, but the prediction of  $\Psi_1$  is too high for larger shear rates, for the stress-controlled approach. Figure 18 shows the damage terms of both approaches as a function of shear rate. This figure shows that for the rate-controlled model, the damage term is linearly dependent on shear rate, whereas for the stress-controlled model, this dependency is no longer linear.



**Figure 18.** Model predictions of the damage term  $E\gamma^*$  as a function of shear rate for the rate-controlled model (a) and  $\tau_c(\tau_{eq})/\eta_0 \cdot \tau^*$  for the stress-controlled model (b).

Figure 19a shows  $\zeta_{eq}$  as a function of shear rate for both approaches. This figure shows a clear difference between the rate- and stress-controlled approach, leading to the differences in steady-shear predictions. Figure 19b shows a zoomed-in version of (a). Here, it is observed that for the stress-controlled approach,  $\zeta_{eq}$  reaches a plateau at  $\zeta_{eq} \neq 0$  for high shear rates, whereas it goes to zero for the rate-controlled approach. This means that the stress-controlled approach always predicts a higher level of structure present in the material at high shear rates, compared to the rate-controlled approach, leading to larger relaxation times and, therefore, a higher viscosity and first normal stress difference coefficient.



**Figure 19.** Model predictions of  $\zeta_{eq}$  as a function of shear rate for both approaches (a) and a zoom-in at high shear rates (b).

Figure 20 shows the shear stress  $\tau$  as a function of  $\zeta_{eq}$  for both approaches. Compared to the rate-controlled approach, the stress for the stress-controlled approach is always lower, except for very low  $\zeta_{eq}$ , where the plateau in  $\zeta_{eq}$  is reached.

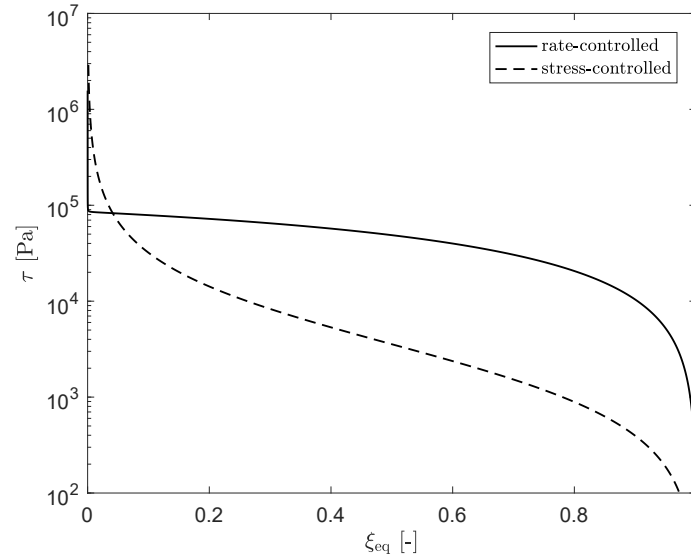


Figure 20. Shear-stress  $\tau$  as a function of  $\zeta_{eq}$  for the rate- and stress-controlled approach.

### Transient Shear Rheology

The transient viscosity can also be calculated for both models and different shear rates. The result is shown in Figure 21.

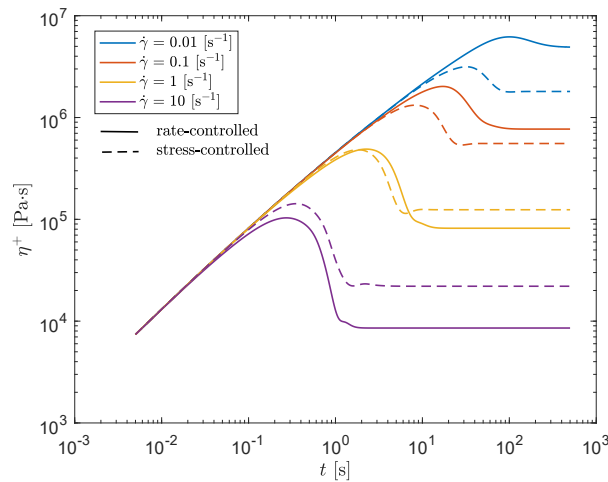


Figure 21. Transient viscosity as a function of time for different shear rates for the rate-controlled (solid lines) and stress-controlled model (dashed lines).

This figure also shows the effect of the damage-dependent characteristic stress in the stress-controlled approach. For smaller shear rates, the stress-controlled method predicts a smaller viscosity compared to the rate-controlled method. This agrees with the smaller equilibrium structure parameter for small shear rates, as was shown in Figure 20. The viscosity also reaches its equilibrium value faster for the stress-controlled method at small shear rates. For high shear rates, however, an opposite effect is observed. This is most likely caused by the damage-dependent characteristic stress in the evolution equation for the structure parameter. At large shear rates, the degree of damage is more severe, which reduces  $\zeta$  and thus the relaxation times. This reduces the characteristic stress in the material, which in turn reduces  $\zeta$ .

## 5. Discussion and Conclusions

In this paper, we presented an experimental strategy to characterize the rheological behavior of filled, uncured rubber compounds. It is tried to keep the approach as simple as possible to maximize applicability and keep the characterization straightforward. To this end, oscillatory shear experiments on a regular plate-plate rheometer were performed.

Measurements were performed for different strain amplitudes, to create mastercurves of the phase-angle for different degrees of structural damage in the material. It was found that the network destruction causes a horizontal shift  $a_{\zeta}$  in the mastercurves of  $\delta$ . This shift is approximately the same for a large range of frequencies and used to construct a structure parameter  $\zeta = 1/a_{\zeta}$ . This structure parameter is used to define the evolution of the degree of structural damage in the material and to adjust the relaxation times of the undamaged material  $\lambda_0$  accordingly.

A rate- and stress-controlled kinetic equation for the evolution of the structure parameter is compared to qualitatively describe the thixotropic behavior in the material. The evolution of the structure parameter can be modeled in time, using an explicit Euler method. The model parameters are obtained by a least-square fitting approach based on the oscillatory shear measurements. Results show that the frequency dependence is not captured well by neither the rate- nor the stress-controlled model without additional model modifications. At these high frequencies, the oscillatory shear measurements are also prone to experimental errors. It therefore has to be concluded that, although the oscillatory shear measurements are used to obtain the model parameters for the kinetic structure parameter equations, we run into limitations of both, the measurements and the models, when normal stresses become significantly large.

The experimental damage–recovery behavior measured in oscillatory shear can be described reasonably well with both approaches for  $\omega = 1$  rad/s. For the strain amplitudes used in the oscillatory shear measurements in this work and  $\omega = 1$  rad/s, it is shown that it is allowed to neglect nonlinear viscoelasticity, and non-homogeneous flow in the plate-plate rheometer to model the damage–recovery experiments. However, this can be taken into account when larger strain amplitudes or frequencies are desired.

The model parameters obtained from the oscillatory shear measurements are used to perform steady shear model predictions. The results show that, using the model parameters obtained from the oscillatory measurements, the measured trends are qualitatively captured by both models. It was found that the stress-controlled approach under-predicts the degree of damage for large deformations. Perhaps, the approach to obtain the model parameters can be adjusted to obtain a better fit in steady shear for the stress-controlled model. More research is needed to find a more suitable approach.

Rubber compounds are complex materials containing many additives. To unravel the thixotropic behavior and do quantitative predictions, a more detailed model should be developed and the influence of these additives needs to be studied systematically. The frequency and temperature dependency of the filler-filler or filler-polymer networks has to be studied in future work. We believe that the thixotropy model and experimental strategy presented in this paper can be a starting point for characterizing the thixotropic behavior of such compounds. The trends measured in steady shear, using model parameters obtained from oscillatory shear measurements, are captured reasonably well for both models. As such, a qualitative prediction of the rheological behavior under relevant processing conditions can be done. However, more research is needed to systematically obtain the fitting parameters and give more quantitative results in both oscillatory and steady shear.

**Author Contributions:** Methodology, G.W.M.P., M.A.H. and P.D.A., supervision, P.D.A., writing—original draft preparation, M.M.A.S., writing—review and editing, G.W.M.P. and M.A.H. All authors have read and agreed to the published version of the manuscript.

**Funding:** The results of this study have been obtained through the FLEX-Pro project, which was in part funded by the European Funding for Regional Development (EFRO). The research is performed in collaboration with VMI Holland B.V.

**Institutional Review Board Statement:** Not applicable.

**Informed Consent Statement:** Not applicable.

**Data Availability Statement:** The data that support the findings of this study are available from the corresponding author upon reasonable request.

**Conflicts of Interest:** The authors declare no conflict of interest.

## References

- Sattayanurak, S.; Sahakaro, K.; Kaewsakul, W.; Dierkes, W.K.; Reuvekamp, L.A.E.M.; Blume, A.; Noordermeer, J.W.M. Synergistic effect by high specific surface area carbon black as secondary filler in silica reinforced natural rubber tire tread compounds. *Polym. Test.* **2020**, *81*, 106–173. [\[CrossRef\]](#)
- Spinelli, H.J. Polymeric Dispersants in Ink Jet Technology. *Adv. Mater.* **1998**, *10*, 1215–1218. [\[CrossRef\]](#)
- Donnet, J.B. Nano and microcomposites of polymers elastomers and their reinforcement. *Compos. Sci. Technol.* **2003**, *63*, 1085–1088. [\[CrossRef\]](#)
- Duduta, M.; Ho, B.; Wood, V.C.; Limthongkul, P.; Brunini, V.E.; Carter, W.C.; Chiang, Y. Semi-Solid Lithium Rechargeable Flow Battery. *Adv. Energy Mater.* **2011**, *1*, 511–516. [\[CrossRef\]](#)
- Hess, W.M. Characterization of dispersions. *Rubber Chem. Technol.* **1991**, *64*, 386–449. [\[CrossRef\]](#)
- Coran, A.Y.; Donnet, J.B. The dispersion of carbon black in rubber Part I. Rapid Method for Assessing Quality of Dispersion. *Rubber Chem. Technol.* **1992**, *65*, 973–997. [\[CrossRef\]](#)
- Rogers, B. *Rubber Compounding, Chemistry and Applications*; Taylor & Francis Group, LLC: West Chester, PA, USA, 2016.
- Payne, A.R. The dynamic properties of carbon black-loaded natural rubber vulcanizates. Part I. *J. Appl. Polym. Sci.* **1962**, *6*, 57–63. [\[CrossRef\]](#)
- Mewis, J.; Wagner, N.J. Thixotropy. *Adv. Colloid Interface Sci.* **2009**, *147–148*, 214–227. [\[CrossRef\]](#)
- Armstrong, M.J.; Beris, A.N.; Rogers, S.A.; Wagner, N.J. Dynamic shear rheology and structure kinetics modeling of a thixotropic carbon black suspension. *Rheol. Acta* **2017**, *56*, 811–824. [\[CrossRef\]](#)
- Hipp, J.B.; Richards, J.J.; Wagner, N.J. Structure-property relationships of sheared carbon black suspensions determined by simultaneous rheological and neutron scattering measurements. *J. Rheol.* **2019**, *63*, 423–438. [\[CrossRef\]](#)
- Shi, X.; Sun, S.; Zhao, A.; Zhang, H.; Zuo, M.; Song, Y.; Zheng, Q. Influence of carbon black on the Payne effect of filled natural rubber compounds. *Compos. Sci. Technol.* **2021**, *203*, 108586. [\[CrossRef\]](#)
- Zhao, A.; Shi, X.; Zhang, H.; Song, Y.; Zheng, Q. Insights into the Payne Effect of Carbon Black Filled Styrene-butadiene Rubber Compounds. *Chin. J. Polym. Sci.* **2021**, *39*, 81–90. [\[CrossRef\]](#)
- Sternstein, S.S.; Zhu, A.J. Reinforcement mechanism of nanofilled polymer melts as elucidated by nonlinear viscoelastic behavior. *Macromolecules* **2002**, *19*, 7262–7273. [\[CrossRef\]](#)
- Montes, H.; Lequeux, F.; Berriot, J. Influence of the Glass Transition Temperature Gradient on the Nonlinear Viscoelastic Behavior in Reinforced Elastomers. *Macromolecules* **2003**, *36*, 8107–8118. [\[CrossRef\]](#)
- Sarvestani, A.S. On the Emergence of the Payne Effect in Polymer Melts Reinforced with Nanoparticles. *Macromol. Theory Simul.* **2016**, *25*, 312–321. [\[CrossRef\]](#)
- Medalia, A.I. Effect of carbon black on dynamic properties of rubber vulcanizates. *Rubber Chem. Technol.* **1978**, *51*, 437–523. [\[CrossRef\]](#)
- Donnet, J.B.; Chand Bansal, R.; Wang, M.-J. *Carbon Black Science and Technology*; Marcel Dekker: New York, NY, USA, 1993; pp. 377–387.
- Payne, A.R.; Whitaker, R.E. Low strain dynamic properties of filled rubbers. *Rubber Chem. Technol.* **1971**, *44*, 440–478. [\[CrossRef\]](#)
- Leblanc, J.L. Rubber-filler interactions and rheological properties in filled rubber compounds. *Prog. Polym. Sci.* **2002**, *27*, 627–687. [\[CrossRef\]](#)
- Fröhlich, J.; Niedermeier, W.; Luginsland, H.D. The effect of filler–filler and filler–elastomer interaction on rubber reinforcement. *Compos. Part Appl. Sci. Manuf.* **2005**, *36*, 449–460. [\[CrossRef\]](#)
- Robertson, C.G.; Hardman, N.J. Nature of carbon black reinforcement of rubber: Perspective on the original polymer nanocomposite. *Polymers* **2021**, *13*, 538. [\[CrossRef\]](#)
- Plagge, J.; Lang, A. Filler-polymer interaction investigated using graphitized carbon blacks: Another attempt to explain reinforcement. *Polymer* **2021**, *218*, 123513. [\[CrossRef\]](#)
- Nagaraja, S.M.; Henning, S.; Ilisch, S.; Beiner, M. Common Origin of Filler Network Related Contributions to Reinforcement and Dissipation in Rubber Composites. *Polymers* **2021**, *13*, 2534. [\[CrossRef\]](#)
- Sarkawi, S.; Dierkes, W.K.; Noordermeer, J.W.M. Filler-to-filler and filler-to-rubber interactions in silica-reinforced natural rubber as visualized by TEM network visualization. In Proceedings of the 11th Kautschuk Herbst Kolloquium, Hannover, Germany, 26–28 November 2014; pp. 1–10.
- Péterfi, T. Die Abhebung der Befruchtungsmembran bei Seeigeleiern. *Wilhelm Roux' Archiv für Entwicklungsmechanik der Organismen* **1927**, *112*, 680–695. [\[CrossRef\]](#)
- Larson, R.G.; Wei, Y. A review of thixotropy and its rheological modeling. *J. Rheol.* **2019**, *63*, 477–501. [\[CrossRef\]](#)
- Goodeve, C.; Whitfield, G. The measurement of thixotropy in absolute units. *Trans. Faraday Soc.* **1938**, *34*, 511–520. [\[CrossRef\]](#)



29. de Souza Mendes, P.R.; Thompson, R.L. A critical overview of elasto-viscoplastic thixotropic modeling. *J. Non-Newton. Fluid Mech.* **2012**, *187–188*, 8–15. [[CrossRef](#)]
30. Leonov, A.I. On the rheology of filled polymers. *J. Rheol.* **1990**, *34*, 1039–1068. [[CrossRef](#)]
31. Simhambhatla, M.; Leonov, A.I. On the rheological modeling of filled polymers with particle matrix interaction. *Rheol. Acta* **1995**, *34*, 329–338. [[CrossRef](#)]
32. Joshi, P.G.; Leonov, A.I. Modeling of steady and time-dependent responses in filled, uncured, and crosslinked rubbers. *Rheol. Acta* **2001**, *40*, 350–365. [[CrossRef](#)]
33. Azikri de Deus, H.P.; Dupim, G.S.P.M. On behaviour of the thixotropic fluids. *Phys. Lett.* **2013**, *377*, 478–485. [[CrossRef](#)]
34. Mwasame, P.M.; Beris, A.N.; Diemer, R.B.; Wagner, N.J. A constitutive equation for thixotropic suspensions with yield stress by coarse graining a population balance model. *AIChE J.* **2017**, *63*, 517–531. [[CrossRef](#)]
35. Narayan, S.P.A.; Palade, L.I. Comparison of a natural configuration approach and a structural parameter approach to model the Payne effect. *Acta Mech.* **2020**, *231*, 4781–4802. [[CrossRef](#)]
36. Rendek, M.; Lion, A. Strain induced transient effects of filler reinforced elastomers with respect to the Payne-Effect: Experiments and constitutive modeling. *J. Appl. Math. Mech.* **2010**, *90*, 436–458. [[CrossRef](#)]
37. Rendek, M.; Lion, A. Amplitude- and temperature effects of filler-reinforced rubber: Experiments and Modelling. *Proc. Appl. Math. Mech.* **2016**, *6*, 15155–15166. [[CrossRef](#)]
38. Höfer, P.; Lion, A. Modelling of frequency- and amplitude-dependent material properties of filler-reinforced rubber. *J. Mech. Phys. Solids* **2009**, *57*, 500–520. [[CrossRef](#)]
39. Österlöf, R.; Wentzel, H.; Kari, L.; Diercks, N.; Wollscheid, D. Constitutive modelling of the amplitude and frequency dependency of filled elastomers utilizing a modified Boundary Surface Model. *Int. J. Solids Struct.* **2014**, *51*, 3431–3438. [[CrossRef](#)]
40. Stieger, S.; Mitsoulis, E.; Walluch, M.; Ebner, C.; Kerschbaumer, R.C.; Haselmann, M.; Mostafaiyan, M.; Kämpfe, M.; Kühnert, I.; Wießner, S.; et al. On the Influence of Viscoelastic Modeling in Fluid Flow Simulations of Gum Acrylonitrile Butadiene Rubber. *Polymers* **2021**, *13*, 2323. [[CrossRef](#)]
41. Spanjaards, M.M.A.; Hulsen, M.A.; Anderson, P.D. Transient 3D finite element method for predicting extrudate swell of domains containing sharp edges. *J. Non-Newton. Fluid Mech.* **2019**, *270*, 79–95. [[CrossRef](#)]
42. Spanjaards, M.M.A.; Hulsen, M.A.; Anderson, P.D. Computational analysis of the extrudate shape of three-dimensional viscoelastic, non-isothermal extrusion flows. *J. Non-Newton. Fluid Mech.* **2020**, *282*, 104310. [[CrossRef](#)]
43. Spanjaards, M.M.A.; Hulsen, M.A.; Anderson, P.D. Die shape optimization for extrudate swell using feedback control. *J. Non-Newton. Fluid Mech.* **2021**, *293*, 104552. [[CrossRef](#)]
44. Williams, M.L.; Landel, R.F.; Ferry, J.D. The temperature dependence of relaxation mechanisms in amorphous polymers and other glass-forming liquids. *J. Am. Chem. Soc.* **1955**, *77*, 3701–3707. [[CrossRef](#)]
45. Morrison, F.A. *Understanding Rheology*; Oxford University Press: Oxford, UK, 2001.
46. Giesekus, H. A simple constitutive equation for polymer fluids based on the concept of deformation-dependent tensorial mobility. *J. Non-Newton. Fluid Mech.* **1982**, *11*, 69–109. [[CrossRef](#)]
47. Alcoutlabi, M.; Baek, S.G.; Magda, J.J.; Xiangfhu, S.; Hutcheson, S.A.; McKenna, G.B. A comparison of three different methods for measuring both normal stress differences of viscoelastic liquids in torsional rheometers. *Rheol. Acta* **2009**, *48*, 191–200. [[CrossRef](#)]
48. Ferry, J.D. *Properties of Polymers*; Wiley: Hoboken, NJ, USA, 1980.
49. Saramito, P.; Wachs, A. Progress in numerical simulation of yield stress fluid flows. *Rheol. Acta* **2017**, *56*, 211–230. [[CrossRef](#)]
50. Macosko, C.W. *Rheology, Principles, Measurements, and Applications*; Wiley: Hoboken, NJ, USA, 1994.

## Article

# A Slow-Release Fertilizer of Urea Prepared via Melt Blending with Degradable Poly(lactic acid): Formulation and Release Mechanisms

Mujtahid Kaavessina \*, Sperisa Distantina and Esa Nur Shohih

Chemical Engineering, Universitas Sebelas Maret, Surakarta 57126, Indonesia;  
sperisa\_distantina@staff.uns.ac.id (S.D.); esanurshohih@gmail.com (E.N.S.)

\* Correspondence: mkaavessina@staff.uns.ac.id

**Abstract:** In this research, a low molecular weight poly(lactic acid) (or PLA) synthesized from direct polycondensation was melt compounded with urea to formulate slow-release fertilizer (SRF). We studied the influence of the molecular weight ( $M_w$ ) of PLA as a matrix and the urea composition of SRF towards release kinetics in water at 30 °C. The physical appearance of solid samples, the change in urea concentration, and acidity (pH) of water were monitored periodically during the release test. Three studied empirical models exhibited that diffusion within the matrix dominated the urea release process, especially when the release level was less than 60%. Thus, a lower  $M_w$  of PLA and a higher urea content of SRF showed a faster release rate. For the entire length of the release experiment, a combination of diffusion and degradation mechanisms exhibited the best agreement with the experimental data. The hydrolytic degradation of PLA may begin after 96 h of immersion (around 60% release level), followed by the appearance of some micro-holes and cracks on the surface of the SRF samples. Generally, this research revealed the good release performance of urea without residues that damage the soil structure and nutrient balance.

**Keywords:** poly(lactic acid); urea; melt blending; slow-release fertilizer

**Citation:** Kaavessina, M.; Distantina, S.; Shohih, E.N. A Slow-Release Fertilizer of Urea Prepared via Melt Blending with Degradable Poly(lactic acid): Formulation and Release Mechanisms. *Polymers* **2021**, *13*, 1856. <https://doi.org/10.3390/polym13111856>

Academic Editors: Célio Bruno Pinto Fernandes, Salah Aldin Faroughi, Luís L. Ferrás and Alexandre M. Afonso

Received: 20 April 2021

Accepted: 29 May 2021

Published: 3 June 2021

**Publisher's Note:** MDPI stays neutral with regard to jurisdictional claims in published maps and institutional affiliations.



**Copyright:** © 2021 by the authors. Licensee MDPI, Basel, Switzerland. This article is an open access article distributed under the terms and conditions of the Creative Commons Attribution (CC BY) license (<https://creativecommons.org/licenses/by/4.0/>).

## 1. Introduction

The global consumption of agricultural products has steadily increased proportionally with world population growth. Rice, maize, and wheat are the most important cereals worldwide in terms of production. Nowadays, agricultural intensification is the main alternative that encourages farmers to increase agricultural production with limited agricultural land. Exploiting natural resources, such as soil, water, space, or energy, is necessary for every stage of large-scale agriculture. Many reports have described the depletion of organic matter, chemical contamination of soil, decreased soil fertility, and water spring deterioration related to agricultural products [1–3]. The main challenge has become to increase the quantity and quality of crops product via sustainable agriculture.

Fertilization is an effort to restore soil fertility that plays an important role in crop production. Thus, it contributes primarily and directly to the production costs. Pypers et al. reported that the key to successful plant fertilization is the appropriate dosage and timing of fertilization [4]. Improper fertilization techniques, inappropriate fertilization times, and both excessive and insufficient fertilizer doses contribute to detrimental effects on the environment. Indeed, this condition affects the quality and quantity of agricultural products.

Urea is very widely used in agriculture, known as nitrogen fertilizer, because of its high nitrogen content (46%). Nitrogen is a necessary nutrient for plant growth, and it is the most crucial factor commonly considered to be yield-limiting. The conversion mechanism of how urea becomes nitrogen absorbable by plants in the form of ammonium ( $\text{NH}_4^+$ ) and nitrate ( $\text{NO}_3^-$ ) is known well [5,6]. The urease enzyme in moist soil will encourage the nitrogen in urea to be converted into ammonium ( $\text{NH}_4^+$ ) via hydrolysis. In

the nitrification process, ammonium is converted into nitrite ( $\text{NO}_2^-$ ) and then to nitrate ( $\text{NO}_3^-$ ) by oxidation [5]. However, many factors can easily eliminate both substances ( $\text{NH}_4^+$  and  $\text{NO}_3^-$ ) from soils, such as drainage; denitrification of nitrate-producing nitrous oxide gas ( $\text{N}_2\text{O}$ ), nitric oxide gas (NO), or nitrogen gas ( $\text{N}_2$ ); nitrogen volatilization; and surface run-off [7]. Thus, it has been estimated that only 30–50% of the nitrogen in urea can be absorbed by plants [8,9].

Many efforts have been studied and applied to reduce the loss of nitrogen and to conserve and protect our environment, such as (i) fertilization management: integrated and site-specific management, and balanced fertilization; (ii) chemical additives such as nitrification inhibitors; and (iii) modification of fertilizer properties: controlled/slow-release fertilizer (CRF or SRF) [10,11]. In the last decade, CRF/SRF has become an exciting topic for researchers in academia and industry.

SRF is the type of fertilizer that releases nutrient elements slowly and regularly, approaching the absorption patterns of plants. The nutrient elements contained in the fertilizers do not get carried away by the water. The synthesis of SRF combines fertilizer (such as urea) and other materials with water retention properties. Recently, three methods were developed to produce SRF, i.e., (i) chemically combined fertilizers, (ii) coated fertilizers, and (iii) physically blended fertilizers [8,9,12].

In SRF formulation, commercial or developed SRFs mostly utilize materials such as urea–formaldehyde (UF), sulfur, zeolite or modified zeolite, bentonite, polyolefin, polyvinylidene chloride, polystyrene, etc. These materials are used alone or in combination with others as coatings, matrices, carriers, or grafted materials in SRFs [12–16], which do not easily degrade properly in the soil. These accumulated residues of SRFs allow damage to the soil structure and nutrient balance in the soil. Therefore, the research focus trend has been switched to exploiting safer and environmentally friendly materials that can also control the release rate of SRF.

This problem inspired the idea of utilizing low molecular weight poly(lactic acid) as a fertilizer carrier matrix. As known, poly(lactic acid) is not polluting to the environment after it has naturally degraded in a humid environment or a solution. It could decompose into natural products/biomass and gasses that are not harmful/toxic to the crop plants [17,18]. Thus, there is no residual accumulation in the use of this material in SRF formulations.

In our previous work, the degradation rate of poly(lactic acid) or PLA was affected by other polymers or substances in blends or its molecular weight [19,20]. Based on the results, we studied the possibility of developing fertilizer by utilizing low molecular weight PLA as a substitute for the existing matrices of SRF. The objectives of this research were: (i) to formulate slow-release fertilizer (SRF) of urea by exploiting the potential properties of low molecular weight ( $M_w$ ) PLA as a matrix, and (ii) to study the urea release mechanisms of SRF through three mathematical model approaches.

We blended micro-size urea into the melt of low molecular weight PLA obtained through direct polycondensation of lactic acid to achieve the objectives. Different loadings of urea in matrix and molecular weights of PLA were analyzed regarding their release behavior. The presence of urea in the SRF was detected by Fourier transform infra-red (FTIR). The release of urea in the SRF was studied through a static release experiment designed mainly according to the other research methods [8,9]. The concentration of urea in the solution was recorded, as well as its acidity (pH). Before and after the release test, a morphological analysis of the samples was conducted by scanning electron microscopy (SEM).

## 2. Materials and Methods

The lactic acid in a 88–90% aqueous solution was produced by Scharlau (Barcelona, Spain) with a density of 1.20 ( $20^\circ/4^\circ$ ). Stannous (II) chloride dihydrate (98%), urea powder, and chloroform were ordered from Sigma-Aldrich (Jakarta, Indonesia). Methanol was produced by Avonchem (Macclesfield, UK). All chemicals were used as received without any additional purification.

Direct polycondensation of lactic acid was carried out without any solvents in the 500 mL flat-bottom 3-necked flasks completed by a Dean–Stark trap. Nitrogen flowed into this flask through a capillary inlet. The reaction condition was controlled at 138 °C and stirred at 150 rpm using a magnetic heat stirrer, RCT Basic IKAMAG® safety control. Stannous (II) chloride as the catalyst was added at about 0.1 wt%.

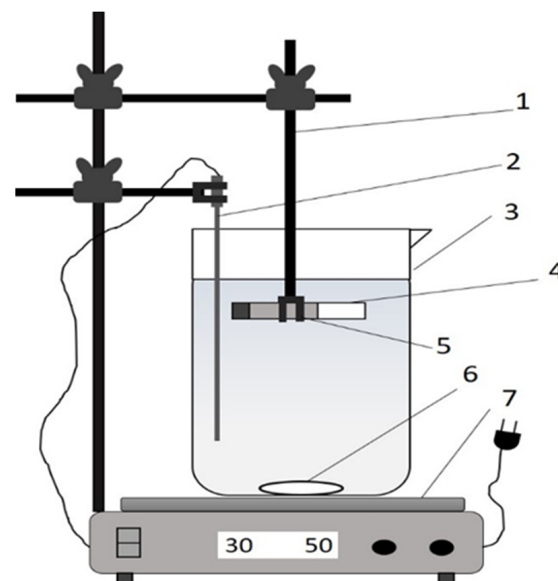
Micro-sized urea was blended in a micro-compounder at 50 rpm and 110 °C for 1 min. The granulation process was carried out by dripping the molten SRF on a tray. The nomenclature of samples prepared and analyzed in this investigation is shown in Table 1.

**Table 1.** Nomenclature of samples.

Sample	Polymerization Time, h	Average $M_w$ of PLA, Da	Urea Content in 3 g of SRF, g
Neat PLA	16	6015.2	0
SRF101	16	6015.2	0.01
SRF201	24	10,264.7	0.01
SRF301	32	13,564.2	0.01
SRF203	24	10,264.7	0.03
SRF205	24	10,264.7	0.05

The average molecular weight of synthesized PLA was determined at 30 °C by a Waters Alliance GPCV 2000 system. Tetrahydrofuran (THF) as the mobile phase was set at a flow rate of 1 mL/min. The presence of urea in formed SRF was detected using a Perkin-Elmer 630 IR spectrophotometer (FTIR) within the IR spectrum range of 4000–400  $\text{cm}^{-1}$ .

A static release experiment was performed at room temperature (around 30 °C). Figure 1 depicts the experimental apparatus for determining the static release of urea in water, emulating previous research [8,9]. A small magnetic stirrer bar (3 mm diameter and 6 mm long) was used to stir the samples at 50 rpm. SRF samples (3 g) were put into a tube, 25 mm long and 5 mm in diameter, with one end closed. The tube containing the SRF was placed horizontally in a glass beaker (150 mL) filled with 100 mL of water. Periodically, the urea concentration and the acidity (pH) of water were recorded. Urea was detected using a Genesis 20 Visible spectrophotometer (Thermo Scientific, Waltham, MA, USA) operating at a wavelength of 440 nm assisted by Ehrlich reagent. The urea concentration was calculated using a standard curve that correlated the urea concentration and absorbency value on the spectrophotometer reading. The degraded solids of SRFs were observed regarding their morphology via scanning electron microscopy (SEM), JEOL JSM-6360A (Tokyo, Japan), at 15 kV.



**Figure 1.** Scheme of the static release apparatus: 1 Tripod and clamp, 2 thermocouple (PT1000), 3 glass beaker, 4 sample tube, 5 SRF sample, 6 magnetic stirrer bar, and 7 magnetic heat stirrer.

Three mathematical models were applied to analyze the release mechanism by fitting the curve of the fractional release, i.e., (i) the Korsmeyer–Peppas model, (ii) the diffusion–relaxation model, and (iii) the diffusion–degradation model. OriginPro software 2016 assisted in plotting the nonlinear fit of the three models to determine the parameter constants.

The first model only considers the diffusion that occurred during urea release, as presented below [21,22]:

$$\frac{M_t}{M_\infty} = k t^n \quad (1)$$

where  $M_t$  is the amount of urea released at time  $t$  (g),  $M_\infty$  is the amount of urea released over an infinite time or the total amount of urea when it is all released from the SRF sample (g), and  $t$  is the time of urea release (m). The  $k$  value is the kinetic constant, combining the characteristics of the urea–SRF system, and  $n$  is the release exponent, representing a transport mechanism, whereas  $M_t/M_\infty$  refers to the fraction of urea released in water at time  $t$ . In the diffusion–relaxation model, 2 constants refer to the diffusion and the relaxation, as formulated below [8,23,24]:

$$\frac{M_t}{M_\infty} = k_1 t^m + k_2 t^{2m} \quad (2)$$

where  $k_1$  and  $k_2$  are associated with diffusion and relaxation, respectively. The  $m$  value is determined to be 0.43, based on the geometric shape of SRF representing the diffusion exponent [23]. For the diffusion–degradation model, there is 1 constant related to diffusion and 3 constants related to degradation, as defined below:

$$\frac{M_t}{M_\infty} = at^{0.5} + bt + ct^2 + dt^3 \quad (3)$$

where  $a$  is associated with diffusion and the 3 constants ( $b$ ,  $c$  and  $d$ ) are associated with degradation.

### 3. Results and Discussion

Lactic acid was polymerized solely without any solvents through direct polycondensation. Stannous chloride dihydrate ( $\text{SnCl}_2 \cdot 2\text{H}_2\text{O}$ ) was added as the catalyst and the temperature was set at 138 °C during polymerization. As seen in Table 1, the average molecular weight of poly(lactic acid) obtained varied in accordance with the polymerization time. The polycondensation time of lactic acid varied at 16, 24, and 32 h and resulted in an average molecular weight of 6015.2 Da, 10,264.7 Da, and 13,564.2 Da, respectively. Further, this obtained poly(lactic acid) was blended with micro-sized urea to make slow-release fertilizer (SRF), as summarized in Table 1.

#### 3.1. Molecular Structure of Slow-Release Fertilizer (SRF)

The SRF's structure was investigated using an infra-red (IR) spectrophotometer to verify urea and PLA's successful blending through melt blending. Figure 2 shows the IR spectra of some samples. The neat PLA sample (Figure 2A) was also scanned to determine urea's presence in slow-release fertilizer. Five dominant peaks show the functional group of poly(lactic acid). The wavenumber around 870  $\text{cm}^{-1}$  shows the peak representing the bond of  $-\text{C}-\text{C}-$ . This peak also indicates the semi-crystalline phase of the obtained PLA. The methyl groups  $-\text{CH}-$  or  $-\text{CH}_3$  appear at the wavenumber around 2944  $\text{cm}^{-1}$  and 1382  $\text{cm}^{-1}$  with different vibration modes. Garlotta [25] explained that stretching and bending modes are represented by the peaks at 2944  $\text{cm}^{-1}$  and 1382  $\text{cm}^{-1}$ , respectively. The peaks at the wavenumbers around 1740  $\text{cm}^{-1}$ , 1093  $\text{cm}^{-1}$  and 1182  $\text{cm}^{-1}$  represent the carboxyl group's presence, i.e.,  $\text{C}=\text{O}$  and  $\text{C}-\text{O}$  with the same vibration mode (stretching).

Only three peaks appear on the IR spectra of the SRF samples, i.e., around 3472  $\text{cm}^{-1}$ , 1585  $\text{cm}^{-1}$ , and 1560  $\text{cm}^{-1}$  (Figure 2B, C and D). These peaks represent the groups of  $\text{N}-\text{H}$  stretching,  $\text{N}-\text{H}$  deformation, and  $\text{C}-\text{N}$  stretching, respectively [26]. Based on this analysis, the urea in slow-release fertilizer can be detected and proven qualitatively.

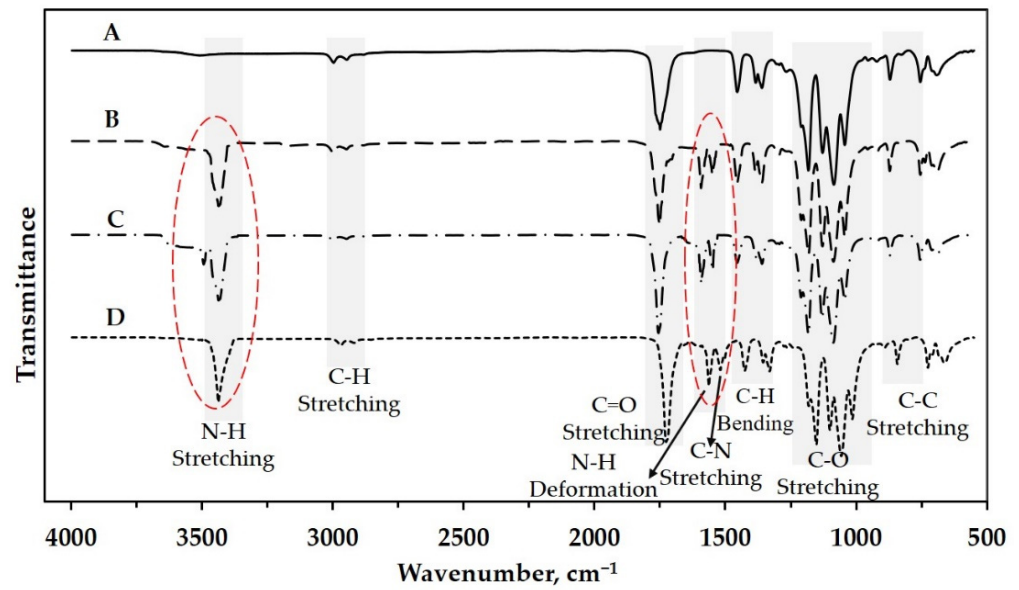


Figure 2. IR spectra of (A) neat PLA and some slow-release fertilizer: (B) SRF101, (C) SRF201, and (D) SRF301.

### 3.2. Urea Release Behavior

Further, all samples were then tested in the static release apparatus (Figure 1) to study their urea release behavior in water. This test provides two data simultaneously relating to the change in the urea concentration and the acidity (pH) of water. Table S1 (in the Supplementary Materials) tabulates data on the urea concentration in water during the release test. These data were then processed to calculate the accumulated fraction of urea released in water during the immersion, as depicted in Figure 3. The release fraction presents information on the amount of urea released at time *t* compared with the total urea in the SRF sample. As observed during the release test, there is no visible swelling of SRF.

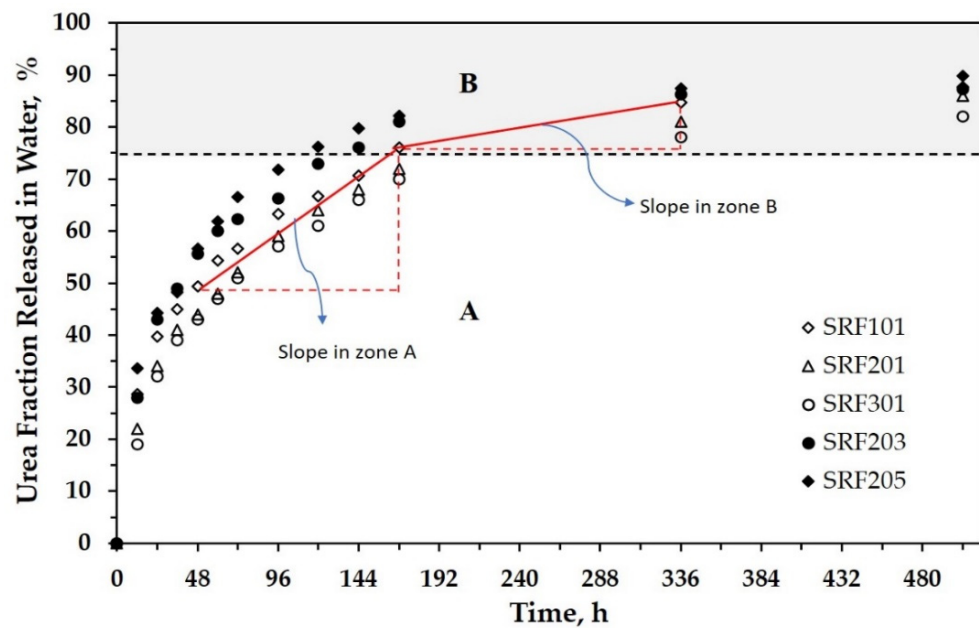


Figure 3. Fractional release of urea as a function of time for all SRF samples.

Figure 3 can be divided virtually into two zones (A and B). As seen, urea’s release appears to find the release equilibrium at around 75%. For all samples, the slope of urea release in Zone A is sharper than that in Zone B. This shows that urea was released rapidly in the first stage (Zone A), then the release rate tended to be slow in Zone B. For example,

the fraction of released urea in Zone A for SRF101 changed by about 25% within 120 h (in the range of 48–168 h). In Zone B, it required a time of around 168 h (in the range of 168–336 h) to achieve an additional urea release of 12.5%. The increasing concentration of urea in SRF urged the urea release to be faster. After immersion for 96 h, the percentage of urea release reached about 59%, 66%, and 72% for urea concentrations of 1% (SRF201), 3% (SRF203), and 5% (SRF205), respectively. This phenomenon proves that urea, with its hygroscopic property, still existed and affected the release process.

The other phenomenon that can be highlighted is the molecular weight ( $M_w$ ) of poly(lactic acid) itself. This parameter describes the length of PLA chains, which have different properties. Utilizing the higher  $M_w$  of poly(lactic acid) tended to inhibit the urea release. After immersion for 96 h, the percentage of urea release was monitored at 63%, 59%, and 57% when the  $M_w$  of PLA was 6015.2 Da (SRF101), 10,264.7 Da (SRF201), and 13,564.2 Da (SRF301), respectively. This showed that the permeability of PLA decreased with increasing molecular weight so that the contact of water and urea in the PLA matrix was increasingly inhibited. Further explanations are discussed in the modeling section.

The utilization of the low molecular weight poly(lactic acid) as a matrix of SRF aimed to exploit its degradable property. Qi et al. reported a review of the biochemical processes of PLA degradation. They concluded that those processes mainly included chemical hydrolysis and biodegradation in the natural soil microcosm [17]. The presence of ester bonds in PLA can be broken with the chemical hydrolysis that may occur during the PLA's immersion. Carboxylic acid and alcohol arise as a result of breaking the ester bonds. Indeed, the existence of carboxylic acid influences the acidity of the solution. Instead, the urea initially tends to be alkaline when it dissolves in water [27]. Thus, the monitored pH values of solutions describe the result of combining properties between carboxylic acid and urea dissolved in water. The changes in the solution acidity are tabulated periodically in Table 2.

**Table 2.** Changes in acidity (pH) during the urea release test.

Time, h	Acidity (pH) of Solution					
	Neat PLA	SRF101	SRF201	SRF301	SRF203	SRF205
0	6.80 ± 0.01	6.80 ± 0.01	6.80 ± 0.01	6.80 ± 0.01	6.80 ± 0.01	6.80 ± 0.01
12	6.79 ± 0.02	7.27 ± 0.05	6.95 ± 0.08	6.97 ± 0.05	7.19 ± 0.05	7.26 ± 0.06
24	6.78 ± 0.02	7.39 ± 0.05	7.08 ± 0.03	7.06 ± 0.05	7.33 ± 0.06	7.43 ± 0.04
32	6.76 ± 0.02	7.52 ± 0.06	7.15 ± 0.03	7.16 ± 0.06	7.41 ± 0.06	7.59 ± 0.03
48	6.75 ± 0.01	7.55 ± 0.03	7.20 ± 0.03	7.23 ± 0.07	7.54 ± 0.05	7.70 ± 0.03
60	6.74 ± 0.01	7.38 ± 0.03	7.29 ± 0.08	7.33 ± 0.05	7.67 ± 0.04	7.81 ± 0.03
72	6.72 ± 0.01	7.22 ± 0.05	7.35 ± 0.08	7.34 ± 0.03	7.71 ± 0.06	7.63 ± 0.05
96	6.69 ± 0.02	7.19 ± 0.04	7.33 ± 0.07	7.29 ± 0.04	7.57 ± 0.06	7.58 ± 0.05
120	6.62 ± 0.04	7.16 ± 0.03	7.25 ± 0.07	7.20 ± 0.06	7.51 ± 0.08	7.52 ± 0.03
144	6.50 ± 0.04	7.08 ± 0.05	7.16 ± 0.05	7.15 ± 0.08	7.50 ± 0.06	7.48 ± 0.04
168	6.45 ± 0.03	7.01 ± 0.03	7.10 ± 0.06	7.13 ± 0.05	7.44 ± 0.05	7.43 ± 0.02
336	6.34 ± 0.04	6.96 ± 0.05	7.04 ± 0.05	7.06 ± 0.04	7.38 ± 0.03	7.37 ± 0.03
504	6.20 ± 0.03	6.92 ± 0.04	6.99 ± 0.03	7.01 ± 0.09	7.31 ± 0.06	7.33 ± 0.06

In Table 2, for neat PLA, the acidity (pH) tends to be constant or decrease slightly in the time range between 0 and 96 h, then becomes relatively more apparent with increasing time above 96 h. This means that the hydrolytic degradation may begin after 96 h, which is indicated by the release of acid resulting from scission of the PLA chain. All samples of SRF showed the same tendency. The pH increased gradually and was followed by a decrease during the range of immersion time. This exciting phenomenon could be explained by the urea release causing the increasing pH of the solution, then the acid from PLA degradation decreasing the pH solution. This statement will be analyzed using the mathematical models, as discussed in this article.

By using pH values, the initial degradation time can be observed at different times. The degradation time of SRF101, SRF201 and SRF301 was initiated around 60, 72 and 72 h,

respectively. This means that increasing the molecular weight of PLA caused a shift to the longer initial degradation time. This statement is confirmed by the morphological sample after immersion at a specific time.

### 3.3. Modeling of Urea Release Behavior

Some researchers have reported several mathematical models associated with the release mechanisms of an active substance from a matrix. These models were developed via different approaches, considering (i) only the diffusion and (ii) the combination of diffusion and other factors such as relaxation and erosion/degradation [22,23,28]. In this article, three mathematical models were used to analyze the release mechanism by fitting the curve of the fractional release, i.e., the Korsmeyer–Peppas model, the diffusion–relaxation model, and the diffusion–degradation model. We examined and verified the fit of the curves of the experimental data with these developed models. The proper model will be applied to describe the release mechanism and explain the studied variables, i.e., the molecular weight of poly(lactic acid) and the urea concentration in SRF.

The Korsmeyer–Peppas model is a simple exponential expression to analyze the controlled release behavior of an active substance from its matrices. Table 3 recapitulates the data from fitting the curve of the fractional release of urea using the Korsmeyer–Peppas model. This model elaborates the values of  $n$  depending on the geometric shape of the sample. For the spherical form,  $n < 0.43$  corresponds to Fickian diffusion, while  $0.43 < n < 0.85$  represents anomalous transport (non-Fickian diffusion) [21]. It can be seen that all samples of SRF exhibit Fickian diffusion. This table also presents  $R^2$ , which shows how close the data are to the fitted regression line. Based on the  $R^2$  values, all the samples' release curves have good enough agreement with this model.

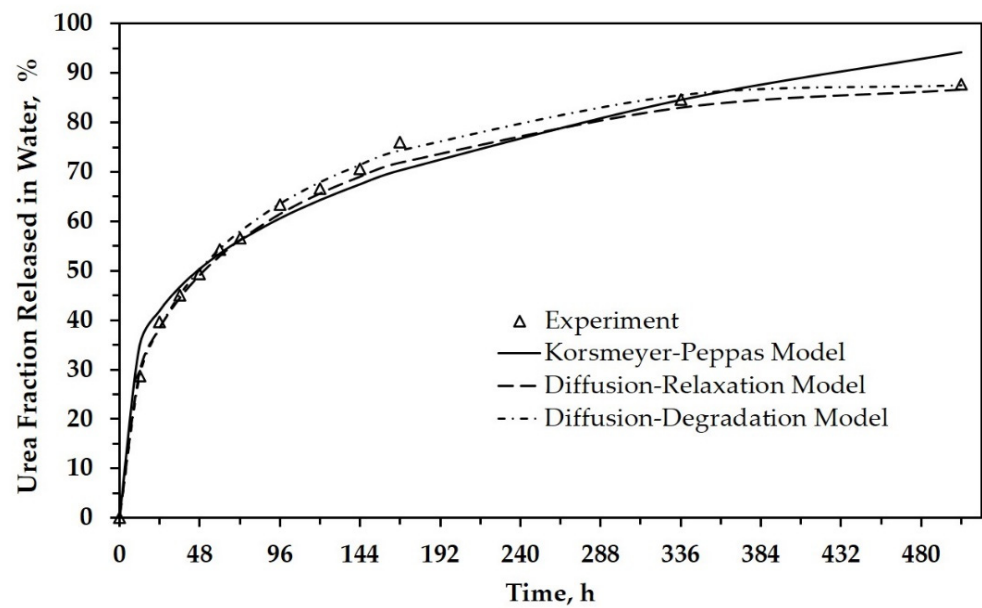
**Table 3.** Diffusion parameters from the Korsmeyer–Peppas model.

Sample	Diffusion/Korsmeyer–Peppas Model			
	$k$	$n$	$R^2$	Type of Diffusion
Neat PLA	-	-	-	-
SRF101	$0.1796 \pm 0.0157$	$0.2663 \pm 0.0173$	0.9789	Fickian
SRF201	$0.1406 \pm 0.0155$	$0.3028 \pm 0.0216$	0.9721	Fickian
SRF301	$0.1343 \pm 0.0173$	$0.3043 \pm 0.0251$	0.9629	Fickian
SRF203	$0.2142 \pm 0.0262$	$0.2417 \pm 0.0244$	0.9553	Fickian
SRF205	$0.2334 \pm 0.0274$	$0.2315 \pm 0.0235$	0.9524	Fickian

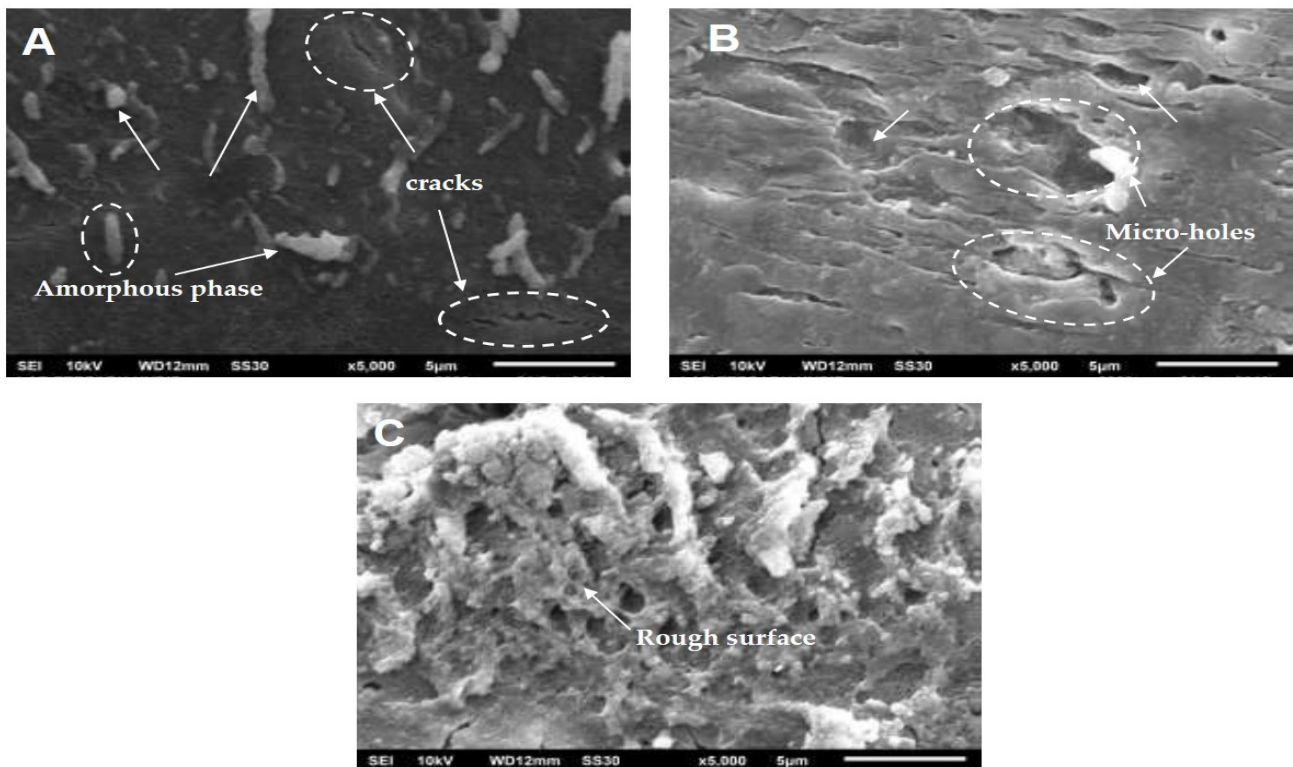
Peppas et al. already explained that this equation is accurate for the first 60% of a release fraction curve [21]. This explanation agrees with our results, as shown in Figure 4 and Figure S1 (in the Supplementary Materials), which depicts the urea fraction released versus time. For more than 60%, the difference in the data between the experimental results and the model calculation is relatively large. It indicates that diffusion transport dominates in the first 60% of release for all SRF samples. Referred to as the Fickian diffusional release, this mass transfer occurs by the usual molecular diffusion of urea due to the gradient of chemical potential.

The first model describes only the initial kinetic behavior (the release level is less than 60%). We have already analyzed the matrix's morphology solely during the immersion to explain the release behavior over the entire range of immersion time (0–504 h). Figure 5 shows the SEM images of neat PLA before (Figure 5A) and after immersion in water for 168 h (Figure 5B) and 504 h (Figure 5C). The SEM image in Figure 5A shows a difference in polymer density, indicating the crystalline and amorphous phases in solid poly(lactic acid). The presence of the amorphous phase looks whiter in color and has cracks (shown by arrows). SEM images of PLA after the degradation test in water show significant changes, as seen in Figure 5B,C. The PLA surface became rough and developed numerous micro-holes along the length of the degradation time.





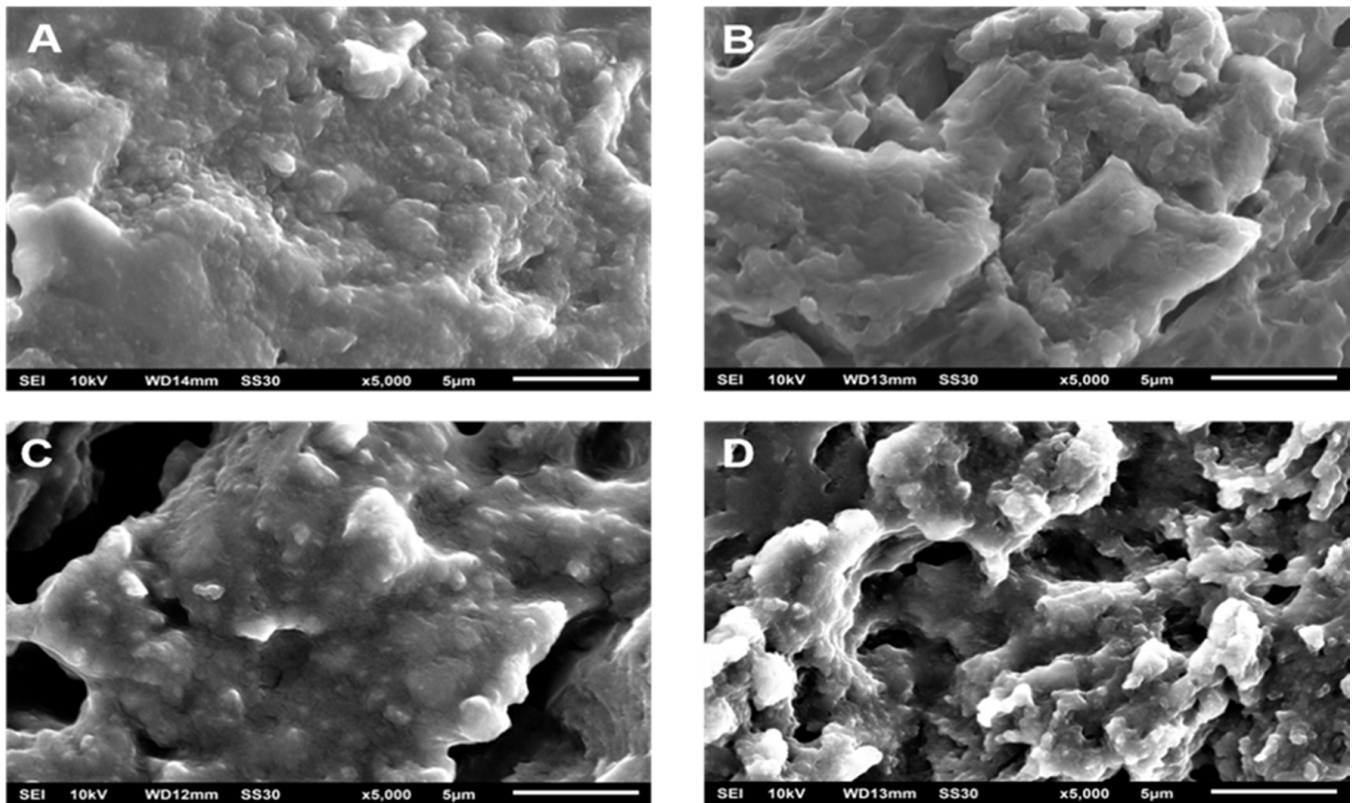
**Figure 4.** The urea fraction released in water as a function of time for SRF101, based on experimental and calculation data.



**Figure 5.** SEM images of neat PLA with different immersion times: 0 h (A), 168 h (B) and 504 h (C).

In a previous study, some researchers reported that water diffusion into the amorphous phase initiates the PLA's hydrolytic degradation in aqueous or humid environments. This process involves the scission of PLA chains that are dominant in ester bonds concentrated in this phase to generate a lower  $M_w$  PLA or monomer (lactic acid). Thus, the degradation occurs preferentially in the amorphous phase and then continues to the crystalline phase [29–31]. The rough surface and numerous micro-holes could be ascribed to PLA chain scission and removal in both phases.

In the above explanation, PLA as a matrix is degraded during the hydrolytic degradation test after a certain period. This phenomenon is strongly suspected of affecting urea's release from the matrix, especially after immersion above 96 h when the solution's pH tends to decrease more significantly (see Table 2 for neat PLA). Figure 4 shows that the release level of urea is about 60% after immersion for 96 h. When correlated with the Korsmeyer–Peppas model, several other factors influenced release after 96 h. Thus, we carried out a morphological analysis of SRF samples after immersion for a specific time (Figure 6). This analysis is expected to support a mathematical model that depicts the urea's release throughout the range of time studied.



**Figure 6.** Morphological changes of SRF201 during immersion at different times: 0 h (A), 96 h (B), 168 h (C), 504 h (D).

Figure 6A shows the SRF201's morphology before the process of urea release. The distribution of micro-sized urea is evenly distributed in the PLA matrix with little aggregation being formed. This indicates that the stirring process can disperse the urea. After immersion for 96 h (see Figure 6B), several holes appeared to be forming, showing a degradation of the polymer matrix. The holes became enlarged and the degradation effect became more visible with increasing immersion times of 168 h (Figure 6C) and 504 h (Figure 6D). The existence of these holes may be caused by (i) the initial degradation of PLA in the amorphous area or (ii) the release of urea aggregate (if any) in the SRF samples.

Figure 6 shows that the morphological changes in SRF became more significant above 96 h, but the released urea fraction tended to be less (see Figure 3). This phenomenon illustrates the possibility of different urea release mechanisms before PLA degradation and when the PLA degradation occurred.

As mentioned above, we also examined and verified the curve fit of the experimental data with two models, i.e., the diffusion–relaxation model and the diffusion–degradation model. Both models are used to further describe the release behavior over the entire period of the release time.

Figure 4 depicts the urea release as a function of time for SRF101 based on experimental data and the calculation data. It can be seen that the empirical model also has better

agreement with experimental release data when relaxation or degradation are considered as parameters in the model. All constants related to both the relaxation and degradation parameters are analyzed and tabulated in Tables 4 and 5. Both tables also tabulate the calculated data's R-squared ( $R^2$ ), known as the coefficient of determination.

**Table 4.** Diffusion and relaxation parameters from the diffusion–relaxation model.

Sample	Diffusion–Relaxation Model		
	$k_1$	$k_2$	$R^2$
Neat PLA	-	-	-
SRF101	$0.1119 \pm 1.98 \times 10^{-3}$	$-0.0036 \pm 1.84 \times 10^{-4}$	0.9949
SRF201	$0.1015 \pm 2.56 \times 10^{-3}$	$-0.0028 \pm 2.39 \times 10^{-4}$	0.9916
SRF301	$0.0981 \pm 3.16 \times 10^{-3}$	$-0.0028 \pm 2.95 \times 10^{-4}$	0.9865
SRF203	$0.1284 \pm 2.27 \times 10^{-3}$	$-0.0047 \pm 2.11 \times 10^{-4}$	0.9972
SRF205	$0.1352 \pm 1.95 \times 10^{-3}$	$-0.0051 \pm 1.81 \times 10^{-4}$	0.9969

**Table 5.** Diffusion and degradation parameters from the diffusion–degradation model.

Sample	Diffusion–Degradation Model				$R^2$
	$a$	$b$	$c$	$d$	
Neat PLA	-	-	-	-	-
SRF101	$0.0932 \pm 2.67 \times 10^{-3}$	$-3.11 \times 10^{-3} \pm 3.86 \times 10^{-4}$	$2.32 \times 10^{-6} \pm 1.26 \times 10^{-7}$	$-1.80 \times 10^{-9} \pm 1.51 \times 10^{-7}$	0.9987
SRF201	$0.0705 \pm 2.84 \times 10^{-3}$	$-7.54 \times 10^{-4} \pm 4.12 \times 10^{-5}$	$-3.33 \times 10^{-6} \pm 1.35 \times 10^{-7}$	$3.92 \times 10^{-9} \pm 1.61 \times 10^{-10}$	0.9985
SRF301	$0.0656 \pm 5.77 \times 10^{-3}$	$-6.83 \times 10^{-5} \pm 8.36 \times 10^{-5}$	$-5.80 \times 10^{-6} \pm 2.74 \times 10^{-7}$	$6.91 \times 10^{-9} \pm 2.74 \times 10^{-10}$	0.9936
SRF203	$0.0986 \pm 4.19 \times 10^{-3}$	$-2.91 \times 10^{-3} \pm 6.07 \times 10^{-4}$	$-6.21 \times 10^{-8} \pm 1.99 \times 10^{-9}$	$1.10 \times 10^{-9} \pm 2.37 \times 10^{-10}$	0.9972
SRF205	$0.1028 \pm 3.10 \times 10^{-3}$	$-2.92 \times 10^{-3} \pm 4.48 \times 10^{-4}$	$-1.23 \times 10^{-6} \pm 1.47 \times 10^{-7}$	$2.92 \times 10^{-9} \pm 1.75 \times 10^{-10}$	0.9984

Table 4 presents the obtained parameters from the data analysis using the diffusion–relaxation model. It can be seen that there is a large gap between the  $k_1$  and  $k_2$  constants. Besides that, the  $k_1$  value is always higher than  $k_2$ . This fact indicates that the diffusion of urea from the PLA matrix dominates its release. The relaxation term only has a minimal effect on diffusion. The negative sign in the  $k_2$  value indicates a correction for the dominance of diffusion in the model. The  $R^2$  value of this model shows a better-fitting curve compared with the Korsmeyer–Peppas model.

The  $k_1$  value tends to decrease proportionally to the increase in the PLA's molecular weight (see SRF101, SRF201, and SRF301). This result verifies the previous statement quantitatively, namely that utilizing the higher  $M_w$  poly(lactic acid) tended to inhibit the urea release. The  $k_1$  value decreased from about 0.1119 to 0.1015, and 0.0981, when the PLA's molecular weight increased from 6015.2 to 10,264.7, and 13,564.2 Da, respectively.

The  $k_1$  value also describes urea concentration's effect on its release (see SRF201, SRF203, and SRF205). Quantitatively, the  $k_1$  value increased from about 0.1015 to 0.1284 and 0.1352 when urea concentration was increased from 0.01 to 0.03 and 0.05 g/3 g of SRF. Again, this result confirms our previous statement that urea's hygroscopic property in the matrix is still in existence and affects its release during immersion.

Table 5 presents the constants obtained from the data analysis using the diffusion–degradation model. This model has better accuracy than the previous two models as shown by the  $R^2$  value (closer to 1). In the data analysis, the constant of  $a$ , which indicates the diffusion factor, has a much greater value than the other three constants ( $b$ ,  $c$ , and  $d$ ). Again, the obtained data show that diffusion was a dominant factor during urea release. Even though the constant values of  $b$ ,  $c$ , and  $d$  are very small, they illustrate that other factors influenced the urea release, especially at the release level above 60% (see Figure 4). Because these three factors are related to degradation, it can be highlighted that poly(lactic acid) degradation also influences urea release. The effects of degradation may not be as significant as those caused by diffusion. It might be that PLA begins to degrade after 96 h of immersion, as previously described. Moreover, most of the urea in the PLA matrix had been released in the solution.

### 3.4. Urea Release Duration

Table 6 tabulates some materials explored to examine the influence on the urea release rate. These materials were utilized as encapsulating matrices, coating materials, blending materials, etc. It can be seen that different combinations of these materials gave many possibilities for the formulation of slow-release fertilizers. The addition of modifiers that act as binders, fillers, or emulsifiers had different effects on the urea release performance, depending on the property of the modifier itself or the interaction between the modifier and the primary material in the SRF. For example, the hydrophilicity of the modifier in bentonite-based SRF, hydroxypropyl methyl-cellulose (HPMC), was more hydrophilic and induced a faster urea release than that of starch [9]. A different result was reported by Pereira et al. [6], namely that the hydrophilicity causes a good interaction between polyacrylamide hydrogels and bentonite, resulting in a slower release of urea compared with polycaprolactone.

The addition of emulsifiers, such as span-80, increased the dispersity of the sealant in sulfur-based SRF. Yu and Li reported that brittle paraffin's coating efficiency as a hydrophobic sealant was improved due to the span-80 enhancing its adhesion [15]. Both synthetic and natural polymers were also explored as coating materials or matrices. The formulation of the hydrophilicity and hydrophobicity of the polymers and modifiers significantly influenced the release pattern [16,32–36].

Table 6 provides an overview of several successful attempts to slow urea's release with varying release durations. The utilization of inorganic materials and synthetic polymers in SRF raises problems on the other side. Fertilization with sulfur-coated urea (SCU) has the potential to improve soil acidity. However, polymer and minerals in SRF will leave the residue, contributing to other forms of pollution, and they are difficult to degrade properly in the soil [12]. In this study, the release duration of the obtained SRFs was about 168 h to achieve 75% urea release when tested in water. This result is comparable with the other results, as shown in Table 6. This SRF utilized the low molecular weight poly(lactic acid) without any other additives or modifiers. Thus, this fertilizer is promising because it does not leave residues that damage the soil structure and the nutrient balance in the soil. PLA can be naturally degraded into substances that are not toxic and harmful to plants [17,18].

**Table 6.** The urea release duration of slow-release fertilizer (SRF) conducted in this work and some other reports.

Material + Modifier (Additive)	Preparation Method	Release Test	* Release Duration	Ref.
<u>Mineral</u>				
Natural bentonite + binder: corn starch or hydroxypropyl methyl-cellulose	Melt blending	Higuchi procedure in water at 30 °C	118 h or 48 h	[9]
Montmorillonite clay (bentonite) + hydrophobic/hydrophilic polymer: polycaprolactone or polyacrylamide hydrogel	Melt blending	Immersed in an aqueous medium at room temperature	30 h or 60 h	[6]
<u>Sulphur-based</u>				
Phosphogypsum + paraffin wax + span-80 (as emulsifier)	Coating	Static release test in water at 25 °C	240 h	[15]
<u>Synthetic polymer</u>				
Polyurethane + mesoporous silica	Coating	Immersed in deionized water at 25 °C	10–50 d	[33]
Polystyrene + wax	Coating	Immersed in deionized water at 25 °C	42 d	[34]
Polystyrene + polyurethane			70 d	
<u>Degradable synthetic polymer</u>				
Polyesters: poly(hexamethylene succinate)/PHS	Melt blending	Immersed in deionized water at 25 °C	400 h	[24]
Polyvinyl alcohol + biochar	Melt blending	Buried in soil column experiment at 25 °C	25 d	[16]
<u>Natural polymer</u>				
Starch + glycerol	Coating	Buried in compost soil at 25 °C	15–30 d	[32]
Alginate + K-carrageenan/celite superabsorbent	Coating	Buried in soil at 25 °C	6 d	[35]
Chitosan salicylaldehyde	Solvent casting	Immersed in distilled water at 25 °C	200 h	[36]
Poly(lactic acid) with a low molecular weight	Melt blending	Static release test in water at 30 °C	168 h	This study

\* Time required to achieve 75% release.

#### 4. Conclusions

Slow-release fertilizer (SRF) with urea was successfully synthesized through melt blending between low molecular weight poly(lactic acid) and urea. Through the FTIR spectra and SEM images, we can confirm the presence of urea and its distribution in the SRF. To investigate the urea release mechanism of SRFs in water, we obtained the fractional release data of urea from static release experiments and we evaluated these data by fitting the curve of the fractional release through three mathematical models. It was found that a higher urea concentration in the SRF exhibited a faster release of urea. The hygroscopic property of urea could still exist and influence the release process. Utilizing the higher molecular weight poly(lactic acid) had a slower urea release due to the decreasing permeability of PLA. The low permeability inhibited the contact between water and urea in the PLA matrix. The diffusion–degradation model showed the best match between all samples' release behavior and the mathematical approaches compared with the other two models. However, the three studied models showed the same tendency that diffusion within the matrix dominated the urea release process, especially when the release level was less than 60%. The erosion (in this case, as hydrolytic degradation) of the PLA matrix may begin after 120 h of immersion. This immersion time indicates that the urea release level was around 60%. Thus, above this level, the degradation factor began to appear and, in the model, it had the best match with the experimental data. This SRF is promising because it does not leave residues that damage the soil structure and the nutrient balance in the soil.

**Supplementary Materials:** The following are available online at <https://www.mdpi.com/article/10.3390/polym13111856/s1>. Table S1: Urea concentration in water during the urea release test. Figure S1: The urea fraction released in water as a function of time based on the experimental and calculated data: (a) SRF201, (b) SRF301, (c) SRF203, and (d) SRF205.

**Author Contributions:** Conceptualization, all authors; methodology, M.K. and S.D.; validation, M.K. and E.N.S.; investigation, E.N.S.; writing—original draft preparation, E.N.S.; writing—review and editing, M.K. and S.D.; visualization, M.K. and S.D.; supervision, M.K. All authors have read and agreed to the published version of the manuscript.

**Funding:** This research was funded by the Ministry of Research Technology and Higher Education (PTUPT research scheme) in 2018, grant number 089/SP2H/LT/DRPM/2018. The APC was funded by the Institute of Research and Community Service, Universitas Sebelas Maret, Indonesia.

**Institutional Review Board Statement:** Not Applicable.

**Informed Consent Statement:** Not Applicable.

**Data Availability Statement:** Data are contained within the article.

**Conflicts of Interest:** The authors declare no conflict of interest. The funders had no role in the design of the study; in the collection, analyses, or interpretation of data; in the writing of the manuscript; or in the decision to publish the results.

#### References

1. Forleo, M.B.; Palmieri, N.; Suardi, A.; Coaloa, D.; Pari, L. The eco-efficiency of rapeseed and sunflower cultivation in Italy. Joining environmental and economic assessment. *J. Clean. Prod.* **2018**, *172*, 3138–3153. [[CrossRef](#)]
2. Dwivedi, S.L.; Lammerts van Bueren, E.T.; Ceccarelli, S.; Grando, S.; Upadhyaya, H.D.; Ortiz, R. Diversifying food systems in the pursuit of sustainable food production and healthy diets. *Trends Plant Sci.* **2017**, *22*, 842–856. [[CrossRef](#)]
3. Miao, Y.; Stewart, B.A.; Zhang, F. Long-term experiments for sustainable nutrient management in China. A review. *Agron. Sustain. Dev.* **2011**, *31*, 397–414. [[CrossRef](#)]
4. Pypers, P.; Sanginga, J.-M.; Kasereka, B.; Walangululu, M.; Vanlauwe, B. Increased productivity through integrated soil fertility management in cassava–legume intercropping systems in the highlands of sud-kivu, dr congo. *Field Crop. Res.* **2011**, *120*, 76–85. [[CrossRef](#)]
5. Chien, S.H.; Teixeira, L.A.; Cantarella, H.; Rehm, G.W.; Grant, C.A.; Gearhart, M.M. Agronomic effectiveness of granular nitrogen/phosphorus fertilizers containing elemental sulfur with and without ammonium sulfate: A review. *Agron. J.* **2016**, *108*, 1203–1213. [[CrossRef](#)]

6. Pereira, E.I.; da Cruz, C.C.T.; Solomon, A.; Le, A.; Cavigelli, M.A.; Ribeiro, C. Novel slow-release nanocomposite nitrogen fertilizers: The impact of polymers on nanocomposite properties and function. *Ind. Eng. Chem. Res.* **2015**, *54*, 3717–3725. [[CrossRef](#)]
7. Dubey, A.; Mailapalli, D.R. Development of control release urea fertilizer model for water and nitrogen movement in flooded rice. *Paddy Water Environ.* **2018**, *16*, 1–13. [[CrossRef](#)]
8. Xiaoyu, N.; Yuejin, W.; Zhengyan, W.; Lin, W.; Guannan, Q.; Lixiang, Y. A novel slow-release urea fertiliser: Physical and chemical analysis of its structure and study of its release mechanism. *Biosyst. Eng.* **2013**, *115*, 274–282. [[CrossRef](#)]
9. Hermida, L.; Agustian, J. Slow release urea fertilizer synthesized through recrystallization of urea incorporating natural bentonite using various binders. *Environ. Technol. Innov.* **2019**, *13*, 113–121. [[CrossRef](#)]
10. Spiertz, J.H.J. Nitrogen, sustainable agriculture and food security. A review. *Agron. Sustain. Dev.* **2010**, *30*, 43–55. [[CrossRef](#)]
11. Jat, R.A.; Wani, S.P.; Sahrawat, K.L.; Singh, P.; Dhaka, S.R.; Dhaka, B.L. Recent approaches in nitrogen management for sustainable agricultural production and eco-safety. *Arch. Agron. Soil Sci.* **2012**, *58*, 1033–1060. [[CrossRef](#)]
12. Lawrence, D.; Wong, S.K.; Low, D.Y.S.; Goh, B.H.; Goh, J.K.; Ruktanonchai, U.R.; Soottitantawat, A.; Lee, L.H.; Tang, S.Y. Controlled release fertilizers: A review on coating materials and mechanism of release. *Plants* **2021**, *10*, 238. [[CrossRef](#)] [[PubMed](#)]
13. Latifah, O.; Ahmed, O.H.; Majid, N.M.A. Enhancing nitrogen availability from urea using clinoptilolite zeolite. *Geoderma* **2017**, *306*, 152–159. [[CrossRef](#)]
14. Lateef, A.; Nazir, R.; Jamil, N.; Alam, S.; Shah, R.; Khan, M.N.; Saleem, M. Synthesis and characterization of zeolite based nano-composite: An environment friendly slow release fertilizer. *Microporous Mesoporous Mater.* **2016**, *232*, 174–183. [[CrossRef](#)]
15. Yu, X.; Li, B. Release mechanism of a novel slow-release nitrogen fertilizer. *Particuology* **2019**, *45*, 124–130. [[CrossRef](#)]
16. Chen, S.; Yang, M.; Ba, C.; Yu, S.; Jiang, Y.; Zou, H.; Zhang, Y. Preparation and characterization of slow-release fertilizer encapsulated by biochar-based waterborne copolymers. *Sci. Total Environ.* **2018**, *615*, 431–437. [[CrossRef](#)]
17. Qi, X.; Ren, Y.; Wang, X. New advances in the biodegradation of poly(lactic acid). *Int. Biodeterior. Biodegrad.* **2017**, *117*, 215–223. [[CrossRef](#)]
18. Valentina, I.; Haroutioun, A.; Fabrice, L.; Vincent, V.; Roberto, P. Poly(lactic acid)-based nanobiocomposites with modulated degradation rates. *Materials* **2018**, *11*, 1943. [[CrossRef](#)]
19. Kaavessina, M.; Distantina, S.; Chafidz, A.; Fadilah; Al-Zahrani, S. The influences of elastomer toward degradability of poly(lactic acid). *Aip Conf. Proc.* **2016**, *1710*, 030031.
20. Kaavessina, M.; Chafidz, A.; Distantina, S.; Al-Zahrani, S.M. Characterization of poly(lactic acid) synthesized via direct polycondensation with different treatments of  $\text{SnCl}_2$  as a catalyst. *Arpn J. Eng. Appl. Sci.* **2016**, *11*, 9992–9998.
21. Ritger, P.L.; Peppas, N.A. A simple equation for description of solute release ii. Fickian and anomalous release from swellable devices. *J. Control. Release* **1987**, *5*, 37–42. [[CrossRef](#)]
22. Dash, S.; Murthy, P.N.; Nath, L.; Chowdhury, P. Kinetic modeling on drug release from controlled drug delivery systems. *Acta Pol. Pharm.* **2010**, *67*, 217–223.
23. Peppas, N.A.; Sahlin, J.J. A simple equation for the description of solute release. Iii. Coupling of diffusion and relaxation. *Int. J. Pharm.* **1989**, *57*, 169–172. [[CrossRef](#)]
24. Bi, S.; Barinelli, V.; Sobkowicz, M.J. Degradable controlled release fertilizer composite prepared via extrusion: Fabrication, characterization, and release mechanisms. *Polymers* **2020**, *12*, 301. [[CrossRef](#)]
25. Garlotta, D. A literature review of poly(lactic acid). *J. Polym. Environ.* **2001**, *9*, 63–84. [[CrossRef](#)]
26. Manivannan, M.; Rajendran, S. Investigation of inhibitive action of urea- $\text{Zn}^{2+}$  system in the corrosion control of carbon steel in sea water. *Int. J. Eng. Sci. Technol.* **2011**, *3*, 8048–8060.
27. Bull, H.B.; Breese, K.; Ferguson, G.L.; Swenson, C.A. The pH of urea solutions. *Arch. Biochem. Biophys.* **1964**, *104*, 297–304. [[CrossRef](#)]
28. Upadrashta, S.; Katikaneni, P.; Hileman, G.; Keshary, P. Direct compression controlled release tablets using ethylcellulose matrices. *Drug Dev. Ind. Pharm.* **2008**, *19*, 449–460. [[CrossRef](#)]
29. Kaavessina, M.; Chafidz, A.; Ali, I.; Al-Zahrani, S.M. Characterization of poly(lactic acid)/hydroxyapatite prepared by a solvent-blending technique: Viscoelasticity and in vitro hydrolytic degradation. *J. Elastomers Plast.* **2014**, *47*, 753–768. [[CrossRef](#)]
30. Elsayy, M.; Kim, K.-H.; Park, J.-W.; Deep, A. Hydrolytic degradation of polylactic acid (PLA) and its composites. *Renew. Sustain. Energy Rev.* **2017**, *79*, 1346–1352. [[CrossRef](#)]
31. Ndazi, B.S.; Karlsson, S. Characterization of hydrolytic degradation of polylactic acid/rice hulls composites in water at different temperatures. *Express Polym. Lett.* **2011**, *5*, 119–131. [[CrossRef](#)]
32. Versino, F.; Urriza, M.; García, M.A. Eco-compatible cassava starch films for fertilizer controlled-release. *Int. J. Biol. Macromol.* **2019**, *134*, 302–307. [[CrossRef](#)]
33. Li, L.; Sun, Y.; Cao, B.; Song, H.; Xiao, Q.; Yi, W. Preparation and performance of polyurethane/mesoporous silica composites for coated urea. *Mater. Des.* **2016**, *99*, 21–25. [[CrossRef](#)]
34. Yang, Y.-c.; Zhang, M.; Li, Y.; Fan, X.-h.; Geng, Y.-q. Improving the quality of polymer-coated urea with recycled plastic, proper additives, and large tablets. *J. Agric. Food Chem.* **2012**, *60*, 11229–11237. [[CrossRef](#)]

35. Wang, Y.; Liu, M.; Ni, B.; Xie, L. K-carrageenan–sodium alginate beads and superabsorbent coated nitrogen fertilizer with slow-release, water-retention, and anticompaction properties. *Ind. Eng. Chem. Res.* **2012**, *51*, 1413–1422. [[CrossRef](#)]
36. Iftime, M.M.; Ailiesei, G.L.; Ungureanu, E.; Marin, L. Designing chitosan based eco-friendly multifunctional soil conditioner systems with urea controlled release and water retention. *Carbohydr. Polym.* **2019**, *223*, 115040. [[CrossRef](#)]

## Article

# On the Response of a Herschel–Bulkley Fluid Due to a Moving Plate

N'dri Arthur Konan <sup>1,2</sup>, Eilis Rosenbaum <sup>1</sup> and Mehrdad Massoudi <sup>1,\*</sup>

<sup>1</sup> U.S. Department of Energy, National Energy Technology Laboratory (NETL), 626 Cochran Mill Road, Pittsburgh, PA 15236, USA

<sup>2</sup> NETL Support Contractor, 3610 Collins Ferry Road, Morgantown, WV 26507, USA

\* Correspondence: mehrdad.massoudi@netl.doe.gov

**Abstract:** In this paper, we study the boundary-layer flow of a Herschel–Bulkley fluid due to a moving plate; this problem has been experimentally investigated by others, where the fluid was assumed to be Carbopol, which has similar properties to cement. The computational fluid dynamics finite volume method from the open-source toolbox/library OpenFOAM is used on structured quad grids to solve the mass and the linear momentum conservation equations using the solver “overInterDyMFoam” customized with non-Newtonian viscosity libraries. The governing equations are solved numerically by using regularization methods in the context of the overset meshing technique. The results indicate that there is a good comparison between the experimental data and the simulations. The boundary layer thicknesses are predicted within the uncertainties of the measurements. The simulations indicate strong sensitivities to the rheological properties of the fluid.

**Keywords:** boundary layer; Herschel–Bulkley fluid; yield stress; Carbopol; cement

**Citation:** Konan, N.A.; Rosenbaum, E.; Massoudi, M. On the Response of a Herschel–Bulkley Fluid Due to a Moving Plate. *Polymers* **2022**, *14*, 3890. <https://doi.org/10.3390/polym14183890>

Academic Editor: Francesco Paolo La Mantia

Received: 5 August 2022

Accepted: 10 September 2022

Published: 17 September 2022

**Publisher’s Note:** MDPI stays neutral with regard to jurisdictional claims in published maps and institutional affiliations.



**Copyright:** © 2022 by the authors. Licensee MDPI, Basel, Switzerland. This article is an open access article distributed under the terms and conditions of the Creative Commons Attribution (CC BY) license (<https://creativecommons.org/licenses/by/4.0/>).

## 1. Introduction

Constitutive modeling of complex fluids [1], sometimes referred to as non-linear fluids or non-Newtonian fluids, has received much attention in the literature [2–4]. Most of the naturally occurring and synthetic fluids are non-linear fluids, for example, polymer melts, suspensions, blood, slurries, drilling fluids, mud, etc., [5–7]. There are many empirical or semi-empirical constitutive equations that have been suggested for these fluids. Many non-linear constitutive relations have also been derived based on the techniques of continuum mechanics [8–11]. The non-linearities oftentimes appear due to higher gradient terms or time derivatives.

Cement and concrete are among two of the most interesting complex materials. In fact, at least since the publication of a paper by Rivlin & Ericksen [12], who discussed fluids of complexity  $n$  (see also Truesdell & Noll [13]), to the recently published book [14], the term ‘complex fluid’ refers, in general, to fluid-like materials whose response, namely the stress tensor, is ‘non-linear’ in some fashion. This non-linearity can manifest itself in a variety of forms such as memory effects, yield stress, creep or relaxation, normal-stress differences, etc., [15,16]. Cement has many applications, and it has been used in the oil and gas industries, where a cement slurry is pumped in the annulus space between the well casing and the geological formations surrounding the wellbore. This is carried out primarily to isolate the wellbore to keep fluids from migrating to other layers of the formation and secondly to prevent the corrosion and the eventual damage to the casing for the life of the well [17,18]. In time, the cement begins to harden. If the fluids from the surrounding formations penetrate the well, then disasters, both financial and operational, can occur, causing a shutdown and replacement of the cement. This unwanted phenomenon is known as ‘gas migration’ (see, e.g., [19]). In their powder forms, cement and concrete behave as bulk solids (granular materials); when mixed with water, initially they act as flowing suspensions (slurry) [20,21]; with chemical reactions and hydration occurring



inside the suspension, the cement becomes a paste-like material (viscoelastic or viscoplastic) exhibiting yield stress and thixotropy [22,23]; and eventually, when it has hardened, the cement behaves as a poro-elastic material. Thus, cement can behave and can respond differently depending on the application and the conditions. When measuring its viscosity or its yield stress, cement generally behaves like a viscoplastic material.

In polymers, we can see a similar diversity. Agassant et al. [24] (p. xix) indicate that, in general, in polymer processing applications, one can distinguish three different stages: (1) the plastification (molten) stage where the polymer goes from a solid-like material, for example, powders or granular, to a fluid-like material, followed by (2) the molten polymer (see also [25]) being pushed or forced into molds or dies, and finally, (3) the stage where a final shape is given to the material, usually carried out via cooling. An excellent and early reference where the fundamentals of the modeling of these various stages in polymer processing are considered is the book by Middleman [26]. The Herschel–Bulkley (H-B) fluid model has been used in a variety of applications. Some recent applications are mentioned here. Ziaee et al. [27] studied colloidal-gas-aphron (CGA)-based fluids in drilling applications by modeling the fluid as a H–B fluid. In their study of solid-free polymer drilling fluid (SFPDF) with natural gas hydrates (NGH), Wang et al. [28], used the Herschel–Bulkley model. A new promising area for the application and use of polymeric gels seems to be in CO<sub>2</sub> underground storage where supercritical gas tends to leak through microcracks in wellbores (see [29]), where in some cases cement slurries, used in oilfields, are too viscous and are not able to penetrate the cracks. Chauhan et al. [30] looked at the characteristics of gum karaya suspensions as a fracturing fluid and developed an empirical Herschel–Bulkley model capable of predicting the temperature and concentration sensitivity of the apparent viscosity. Zheng et al. [31] looked at the effects of temperature and the rheological impact of a commonly used drilling fluid polymer-treating agent used in the petroleum industries; they mention that the dispersion was reasonably described by a Herschel–Bulkley model. Millian et al. [32] studied the rheological behavior of gel polymer electrolytes (GPE) used as a suspending fluid in a zinc-slurry-air RFB by fitting their experimental data to the Herschel–Bulkley model.

In his pioneering work on flow of yield stress fluids, Oldroyd [33] proposed a plastic boundary-layer theory, defined as a region of sufficiently slow plastic flow characterized by a large Oldroyd (Od or Bingham) number and evolving in the limit of small Reynolds numbers. Oldroyd further argued that the thickness of such a plastic boundary layer is of the order of  $Od^{-1/2}d$  (where  $d$  is a characteristic length). The proposed theory relied upon a certain number of assumptions, especially at the boundary between the elastic and the plastic states of the material, in addition to the assumption of a constant positive sign of the velocity gradient inside the boundary layer. When such a slow steady plastic flow develops near infinite or semi-finite thin plates, Oldroyd discussed a case of constant thickness, as well as a case of a variable layer with a thickness ranging from zero at the leading edge to a finite value far away from the edge. He also derived expressions for both the velocity and the pressure distributions inside the boundary layer, which depend on the Oldroyd number.

Piau [34] discussed Oldroyd's theory by pointing out certain inconsistencies buried in the approach; he mentioned five points. Essentially, these points can be summarized as the Dirichlet and the Neumann velocity boundary condition issues at the outer limit of the boundary layer where the transition occurs from a flowing material (a fluid) to an elastic material and at the wall. In addition, Piau pointed out that the assumptions on the pressure gradient and the symmetry conditions were not satisfied. Balmforth et al. [35] also claim that "Oldroyd's analysis runs into difficulties when the boundary layer buffers a wall, being unable to satisfy all the boundary conditions and the continuity equation". Piau revisited the theory and, in contrast to Oldroyd's approach, the Bingham stress of the material's plastic behavior was supplemented with the Hooke model for the linear elastic behavior that prevails in the outer unyielded regions. Piau [34] further identified and derived constant and variable lens-shaped boundary layer thicknesses and velocity

distributions; he looked at the lower and the upper bound solutions consistent with the outer elastic region. The (viscous) drag forces acting on the plate in the context of these solutions, as derived by Piau, increase linearly with the yield stress and exhibits a relatively weak dependence on the Oldroyd (or the Bingham) number, which was assumed to be ‘large’ while the dependence of the drag forces was proportional to  $Od^{-1/2}$ .

Piau & Debiane [36] extended this work to shear-thinning fluids in the context of a Herschel–Bulkley fluid with no-slip conditions at the walls. They showed that the boundary thickness along with the velocity distribution, as well as the (viscous) drag force acting on the plate, are explicitly functions of the power-law exponent. For instance, in the framework of the constant thickness model of the boundary layer, the slope of the velocity distribution is found to be determined by the power-law exponent. For the case of slip at the walls, Piau & Debiane [36] introduced a dimensionless number (ratio of the yield stress to the consistency index and the fluid velocity), which is a measure of the slip at the wall. In the context of the constant-boundary-thickness model, they found that slip at the wall reduces the viscous drag, while the fluid velocity inside the boundary layer increases with decreasing slip. Ahonguio et al. [37] experimentally investigated the influence of slip at the wall in the limit of non-inertial flow with relatively large Oldroyd numbers (varying from 16 to 40). These authors found that the slip velocity decreases with the Oldroyd number. The consequences are (i) a thinner boundary layer and (ii) a reduction in the drag, which is consistent with the slip at the wall described by Piau and Debiane [36], although the definition of the boundary layer thickness in Ahonguio et al. [37] is different from that used by Piau & Debiane. In another work, Ahonguio et al. [38] showed that their laboratory measurements of the drag coefficient for a Carbopol gel flowing past a thin fixed plate compared well with the Piau & Debiane model.

Balmforth et al. [39] revisited the derivation of Oldroyd’s theory by numerically studying flow past a thin plate. These authors also investigated a jet-like intrusion; these two examples, referred to as Oldroyd’s canonical problems, were meant to illustrate their approach. Most importantly, Balmforth et al. discussed that the magnitude of the small parameter ( $\epsilon$ ), associated with the re-scaling of the flow in the normal direction that sets both the thickness of the boundary layer and the angular velocity of the rotating plug, must be  $Bi^{-1/2}$  ( $Bi$  being the Bingham number) in order to match the pressure within the viscoplastic boundary layer. These authors claim that there is “a missing ingredient in Piau’s boundary-layer scaling argument”.

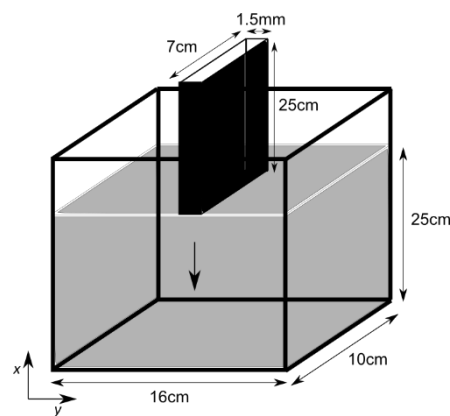
In the context of a boundary layer developing away from rigid boundaries (referred to “remote boundary layers” by Oldroyd [33]), Chevalier et al. [40] discussed experiments of slow injections of a yield stress fluid into a stagnant fluid (the same fluid), by means of an extrusion syringe. They observed that the injected fluid penetrates as a solid-like block over the whole injection surface, while the large surrounding material remains at rest. Their study shows the existence of a thin boundary through which the motion of the injected material occurs. They also reported a decrease in that boundary layer with an increasing of the Bingham number. Chevalier et al. also looked at the data from Boujlel et al. [1] where a plate was slowly immersed into a bath of Carbopol gel at rest. As the fluid was stressed beyond the yield point, a thin layer around the plate developed. Boujlel et al. showed the measurements of the boundary layer size for various immersion velocities as well as the distribution of the velocity within the yielded region.

The response of a yield-stress fluid, for example, a Herschel–Bulkley fluid [41], due to the motion of a plate can provide useful information about the resistance (drag) to flow and how the plate can move in the yielded regions as opposed to the viscous regions of the flow. In a sense, this flow arrangement can be thought of as an idealization of the slow movement of a vane in a viscometer while measuring the yield stress of cement or a yield stress fluid [42]. Carbopol is a fluid which has been studied extensively and has similar properties to cement. In this paper, we present numerical solutions to the boundary-layer flow of a Herschel–Bulkley fluid showing a solid-like behavior away from the boundaries, which were reported by Boujlel et al. [1]. In Section 2, we provide a description of the

problem while briefly mentioning the experimental investigation of Boujlel et al. [1], which is relevant to our work. This is followed by an overview of the mathematical model (in Sections 3 and 4) used to describe the fluid and the flow conditions. The numerical method is presented in Section 5, and the results which are obtained using regularization approach in the context of the overset meshing technique are compared and discussed against the measurements of Boujlel et al. [1]. Finally, some conclusions and interesting points for future work are provided.

## 2. Problem Statement

The experiments of Boujlel et al. [1] of a plate slowly being immersed in a yield stress fluid are numerically investigated here. The yield stress fluid, which is at rest in a parallelepiped-shaped container 10 cm wide, 25 cm high and 16 cm deep, is a solution of Carbopol in water with a concentration of 0.5%. The fluid is assumed to behave as a Herschel–Bulkley fluid, and its rheological properties are obtained from fitting of the rheometrical flow curves: the yield stress ( $\tau_0$ ), the consistency ( $k$ ), and the power-law exponent ( $n$ ) are approximated as 59.5 Pa, 23.6 Pa.s<sup>n</sup>, and 0.38, respectively, for shear rates ranging between 10<sup>-2</sup> s<sup>-1</sup> and 10<sup>2</sup> s<sup>-1</sup>. The plate is 25 cm long ( $l$ ), 7 cm wide ( $w$ ) with a thickness ( $d$ ) 1.5 mm. The flow domain along with the immersed plate are sketched in Figure 1.



**Figure 1.** Sketch of the plate being immersed into the Carbopol fluid.

The flow conditions simulated in this work are summarized in Table 1. A total of three cases with different plate immersion velocity ( $U_p$ ) are considered. As shown in Table 1, the flow conditions correspond to very small Reynolds numbers, usually associated with the Stokes regime ( $Re \ll 1$ ). In the limit of such (creeping) flow conditions where the inertial effects are negligible, the flow depends on the Bingham number, which for these experimental conditions, indicates yield stress effects which dominate the viscous ones (by about 2 to 3 times). While the limit of small Reynolds numbers is attained, one may notice that the Bingham numbers are not as large as they are prescribed in the theories (see [33,34,36,39]). The Reynolds ( $Re$ ) and the Bingham ( $Bi$ ) numbers are defined below as (see the dimensionless form of the equation):

$$Re = \rho U_p^2 / k (U_p / d)^n \quad (1)$$

$$Bi = \tau_0 / k (U_p / d)^n \quad (2)$$

where  $\tau_0$  is the yield stress,  $k$  the consistency,  $n$  the power-law exponent,  $\rho$  the density of the fluid,  $U_p$  is a reference velocity, and  $d$  is a reference length. In their experiments, Boujlel et al. defined an observation window (of 5 cm × 6.5 cm) 5 cm below the Carbopol bath surface, where successive pictures were taken once the leading edge of the plate appeared in the window until it was immersed to a depth of 20 cm. The average velocity profile of the Carbopol as well as the boundary layer thickness discussed in the result

sections below are extracted from these measurements at 15 cm above the leading edge of the plate. The boundary layer thickness is estimated as the flow region extent delineated in its upper bound by the constant fluid velocity.

**Table 1.** Flow conditions and the associated dimensionless numbers.

Case	$U_p$ [m/s]	Re [-]	Bi [-]
1	1	$5.2 \times 10^{-5}$	2.93
2	3	$3.1 \times 10^{-4}$	1.93
3	5	$7.0 \times 10^{-4}$	1.59

As mentioned in the introduction, Piau & Debiante [36] showed that the boundary layer thickness ( $\delta$ ) can, in the context of the Herschel–Bulkley fluid, be approximated by a function which depends on the Oldroyd (or the Bingham) number:

$$\delta \cong d Bi^{-1/(1+n)} \quad (3)$$

### 3. Governing Equations

In this problem, we do not consider thermo-chemical or electromagnetic effects. Therefore, the governing equations of motion for a single component fluid include the conservation equations for mass, linear momentum, and angular momentum (see, e.g., [43]).

#### 3.1. Conservation of Mass

$$\frac{\partial \rho}{\partial t} + \text{div}(\rho \mathbf{v}) = 0, \quad (4)$$

where  $\partial/\partial t$  is the partial derivative with respect to time,  $\text{div}$  is the divergence operator,  $\mathbf{v}$  is the velocity vector, and  $\rho$  is the density of the fluid. If the fluid is assumed to be incompressible, then it can only undergo isochoric (i.e., volume preserving) motions, so:

$$\text{div} \mathbf{v} = 0 \quad (5)$$

#### 3.2. Conservation of Linear Momentum

$$\rho \frac{d\mathbf{v}}{dt} = \text{div} \mathbf{T} + \rho \mathbf{b}, \quad (6)$$

where  $d/dt$  is the total time derivative given by  $d(\cdot)/dt = \partial(\cdot)/\partial t + [\text{grad}(\cdot)]\mathbf{v}$  and  $\text{grad}$  is the gradient operator,  $\mathbf{b}$  is the body force vector, and  $\mathbf{T}$  is the Cauchy stress tensor.

#### 3.3. Conservation of Angular Momentum

The conservation of the angular momentum indicates that the stress tensor is symmetric when there are no couple stresses, that is:

$$\mathbf{T} = \mathbf{T}^T \quad (7)$$

Looking at the above equations, we can see that before we can solve any problems, we need a constitutive relation for  $\mathbf{T}$ . In the next section, we provide a brief discussion of the stress tensor  $\mathbf{T}$  used in this paper.

These conservation equations are supplemented with boundary and initial conditions, both at the walls and at the free-surface boundaries. The no-slip BC is prescribed at the plate and the walls such that:

$$\mathbf{v} = \mathbf{U}_p, \text{ at the plate boundaries} \quad (8)$$

$$\mathbf{v} = \mathbf{0}, \text{ at the container's walls} \quad (9)$$

where  $U_p$  is the plate immersion velocity. The Neumann zero gradient condition is imposed at the free surface for the velocity vector. For the initial conditions, since the fluid is initially at rest, we use:

$$\mathbf{v}(\mathbf{x}, 0) = \mathbf{0} \tag{10}$$

#### 4. Constitutive Relation for the Stress Tensor

For many complex fluids, yield stress is an important rheological parameter [44–47]. In the oil and gas industries, predicting the yield stress for cement slurries is also important [48]. Here, a cement slurry is pumped in the well and then it begins to hydrate quickly and develop strength [49]. The difficulties related to yield stress measurements have been discussed, for example in [50–53]. Coussot [53] and Coussot et al. [54] reviewed different methods for measuring the yield stress for thixotropic non-Newtonian fluids. Experimental measurements for the yield stress are usually conducted either by direct rheometric techniques or indirect techniques. For a detailed discussion related to cement applications, see the report by Tao et al. [55]. One of the disadvantages of the direct techniques is the wall-slip effects, which cause under-estimation of the yield stress [56,57]. One of the most widely used techniques to measure the yield stress is the vane method since there is no wall slip during the shearing process within the material [56,58–60]. Using the vane method [58,61], we can measure the peak torque–time response by rotating the vane immersed in the fluid. As mentioned in the Introduction section, the motion of a vane in the paste/suspension is of interest to us here.

In general, it can be assumed that the (Cauchy) stress tensor  $T$  for yield stress fluids, such as cement, can be defined as

$$T = T_y + T_v \tag{11}$$

where  $T_y$  is the yield stress tensor and  $T_v$  is the viscous stress tensor. In general, for cement, the yield stress can be a function of many parameters, such as the volume fraction,  $w/c$ , etc.

$$T_y = T_y\left(\phi, \frac{w}{c}, \dots\right) \tag{12}$$

where  $\phi$  is the volume fraction, and  $w/c$  is the water-to-cement ratio. In a recent review article, Tao et al. [62], proposed a very general constitutive relationship for  $T_v$ :

$$T_v = -pI + \mu_0 \left(1 - \frac{\phi}{\phi_m}\right)^{-\beta} (1 + \lambda^n) \left[1 + \alpha \text{tr}A_1^2\right]^m A_1 + \alpha_1 A_2 + \alpha_2 A_1^2 \tag{13}$$

$$\frac{d\lambda}{dt} = \frac{1}{t_0} - \kappa\lambda\dot{\gamma} \tag{14}$$

where the kinematical tensors  $A_1$  and  $A_2$  are defined as:

$$A_1 = \text{grad}\mathbf{v} + (\text{grad}\mathbf{v})^T \tag{15}$$

$$A_2 = \frac{dA_1}{dt} + A_1(\text{grad}\mathbf{v}) + (\text{grad}\mathbf{v})^T A_1 \tag{16}$$

where  $p$  is the pressure,  $\lambda(t)$  is the structural parameter describing the degree of flocculation or aggregation. They used Krieger’s idea [63] for the volume fraction dependence of the viscosity, where  $\mu_0$  is the (reference) coefficient of viscosity,  $\text{tr}$  is the trace operator, and  $m$  is the power law exponent, a measure of non-linearity of the fluid related to the shear-thinning effects (when  $m < 0$ ) or shear-thickening effects (when  $m > 0$ ). This model potentially is capable of exhibiting normal stress effects through the terms  $\alpha_1$  and  $\alpha_2$ , thixotropy effects because of the presence of the structural parameter  $\lambda$ , shear-rate-dependent effects of the viscosity through the two parameters  $\alpha$  and  $m$  (showing shear-thinning or shear-thickening effects), and the concentration dependency of viscosity through the two parameters  $\phi_m$  and  $\beta$ . A simplified version Equation (13) was used in our earlier study [62].

For the yield stress part, historically, Oldroyd [33] derived a proper (frame invariant) 3D form for the Bingham fluid [64] by assuming that the material behaves as a linear elastic solid below the yield stress; he used the von Mises criterion for the yield surface. Thus:

$$T = \left[ \eta_p + \frac{\tau_y}{\sqrt{\frac{1}{2}\Pi_{A_1}}} \right] A_1 \text{ when } \left[ \frac{1}{2}T : T \right] \geq \tau_y^2 \tag{17}$$

$$T = GE \text{ when } \left[ \frac{1}{2}T : T \right] < \tau_y^2 \tag{18}$$

where  $G$  is the shear modulus, indicating that below the yield stress, the material behaves as a linear elastic solid, obeying the Hooke’s Law, and where  $E$  is the strain tensor and the second invariant of the tensor  $A_1$  is:

$$\Pi_{A_1} \equiv A_1 : A_1 \tag{19}$$

As Denn [65] indicates, if the material is assumed to be inelastic prior to yielding, then  $G \rightarrow \infty$ , and Equation (18) is replaced by:

$$A_1 = \mathbf{0} \text{ when } \left[ \frac{1}{2}T : T \right] < \tau_y^2 \tag{20}$$

Macosko [66] (p. 96) mentions that for many fluids with a yield stress, there is a lower *Newtonian* regime rather than a *Hookean* one, and thus one can use a two-viscosity (bi-viscous) model, such as:

$$T = \eta_p A_1 \text{ for } \Pi_{A_1}^{1/2} \leq \dot{\gamma}_c \tag{21}$$

$$T = 2 \left[ \frac{\tau_y}{|\Pi_{A_1}|^{1/2}} + K|\Pi_{A_1}|^{\frac{n-1}{2}} \right] A_1 \text{ for } \Pi_{A_1}^{1/2} > \dot{\gamma}_c \tag{22}$$

where  $\dot{\gamma}_c$  is the critical shear rate. In this paper, we use the Herschel–Bulkley model, and thixotropy is not considered. Thus, the stress in the fluid is given by:

$$T = -pI + \tau \tag{23}$$

where  $p$  is the pressure (the mean value of the stress tensor),  $I$  is the identity tensor, and  $\tau$  is the stress tensor:

$$\tau = \left[ k|\Pi_{A_1}|^{\frac{n-1}{2}} + \frac{\tau_0}{|\Pi_{A_1}|^{1/2}} \right] A_1 \text{ for } \Pi_{A_1}^{1/2} > \tau_0 \tag{24}$$

$$A_1 = \mathbf{0} \text{ for } \Pi_{A_1}^{1/2} \leq \tau_0 \tag{25}$$

in which  $\tau_0$  is the yield stress,  $k$  is the consistency index, and  $n$  is the power-law exponent, which measures of non-linearity of the fluid and is related to the shear-thinning effects (when  $n < 1$ ) or shear-thickening effects (when  $n > 1$ ).  $\Pi_{\tau}$  and  $\Pi_{A_1}$  are the second invariants of the stress tensor and of the kinematical tensor  $A_1$ . In Equation (24), the total contribution in the brackets, which defines the viscosity of the fluid, is the sum of the shear (viscous) ( $\mu_v = k|\Pi_{A_1}|^{(n-1)/2}$ ) and the apparent ( $\mu_{app} = \tau_0/|\Pi_{A_1}|^{1/2}$ ) viscosities.

In this paper, we ignore the micro-structure of the cement, i.e., the size and the shape of the particles, and the impact of the porosity and how the volume fraction affects the motion of the fluid. Thus, we represent the cement suspension as a viscoplastic fluid modeled as a Herschel–Bulkley fluid, given by Equations (23)–(25).

### 5. Numerical Approach

The computational fluid dynamics finite volume method from the open-source toolbox/library, OpenFOAM [67], is used on structured quad grids to solve the mass and the linear momentum conservation equations, using the solver “overInterDyMFoam” customized with non-Newtonian viscosity libraries. In our numerical scheme, we use the regularization methods. Indeed, to avoid the numerical implementation challenges associated with the discontinuity (singularity) in the stress tensor field between the unyielded and the yielded regions, the regularization method is used where the stress tensor  $\tau$  is replaced with an  $\epsilon$ -dependent small parameter such that:

$$\tau_\epsilon = \eta_\epsilon \left( |\Pi_{2D}|^{1/2} \right) \mathbf{A}_1 \tag{26}$$

where the  $\epsilon$ -dependent viscosity  $\eta_\epsilon$  is approximated in this work according to Papanastasiou [68] by:

$$\eta_\epsilon \left( |\Pi_{A_1}|^{1/2} \right) = k |\Pi_{A_1}|^{(n-1)/2} + \frac{\tau_0}{|\Pi_{A_1}|^{1/2}} \left[ 1 - \exp \left( - \frac{|\Pi_{A_1}|^{1/2}}{\epsilon} \right) \right] \tag{27}$$

Two other commonly used regularization methods are also employed to study the sensitivity of the solution to such viscosity approximations; these two methods are the “simple” algebraic procedure (see e.g., [69]) and the approximation suggested by Bercovier & Engelman [70], given below, respectively:

$$\eta_\epsilon \left( |\Pi_{A_1}|^{1/2} \right) = k |\Pi_{A_1}|^{(n-1)/2} + \frac{\tau_0}{\epsilon + |\Pi_{A_1}|^{1/2}} \tag{28}$$

$$\eta_\epsilon \left( |\Pi_{A_1}|^{1/2} \right) = k |\Pi_{A_1}|^{(n-1)/2} + \frac{\tau_0}{[\epsilon^2 + |\Pi_{A_1}|]^{1/2}} \tag{29}$$

A detailed examination of the convergence challenges and issues associated with the regularized solutions are discussed, for example, in Frigaard & Nouar [71] and Saramito & Wachs [72].

Substituting Equations (23)–(25) in Equation (6), we have the basic equations, which need to be solved numerically:

$$\text{div } \mathbf{v} = 0 \tag{30}$$

$$\rho \left( \frac{\partial \mathbf{v}}{\partial t} + [\text{grad } \mathbf{v}] \mathbf{v} \right) = -\text{grad } p + \text{div} \left( \eta_\epsilon \left( |\Pi_{2D}|^{1/2} \right) \mathbf{A}_1 \right) + \rho \mathbf{g} \tag{31}$$

And the boundary conditions are,

- at the moving plate:

$$\mathbf{v} = \mathbf{U}_p, \tag{32}$$

$$\mathbf{n} \cdot \text{grad } p = -\rho \mathbf{n} \cdot [\mathbf{v} \cdot \text{grad } \mathbf{v}] \tag{33}$$

- at the container’s walls:

$$\mathbf{v} = \mathbf{0} \tag{34}$$

$$\mathbf{n} \cdot \text{grad } p = 0 \tag{35}$$

and the initial conditions are:

$$\mathbf{v}(\mathbf{x}, 0) = \mathbf{0}, \tag{36}$$

$$p(\mathbf{x}, 0) = 0 \tag{37}$$

The dimensionless forms of the equations are presented in Appendix A.

The grid of the computational domain is generated relying upon the overset mesh technique, which in this work consists of a uniform grid (in each direction) of the background mesh of the entire flow domain, supplemented by a fine grid around the downward moving plate. With this fine (or overset) mesh, the grid in the normal direction to the plate is clustered using nonuniform spacings according to a geometric series with a rational stretching factor; this would better capture the gradients as the plate moves through the fluid. Figure 2 shows the background mesh, as well as the overset mesh which covers a region that extends over 3 cm at either side of the plate. Shown in Table 2 is the summary of the overset grid densities used to study the sensitivity of the solution to the mesh refinement.

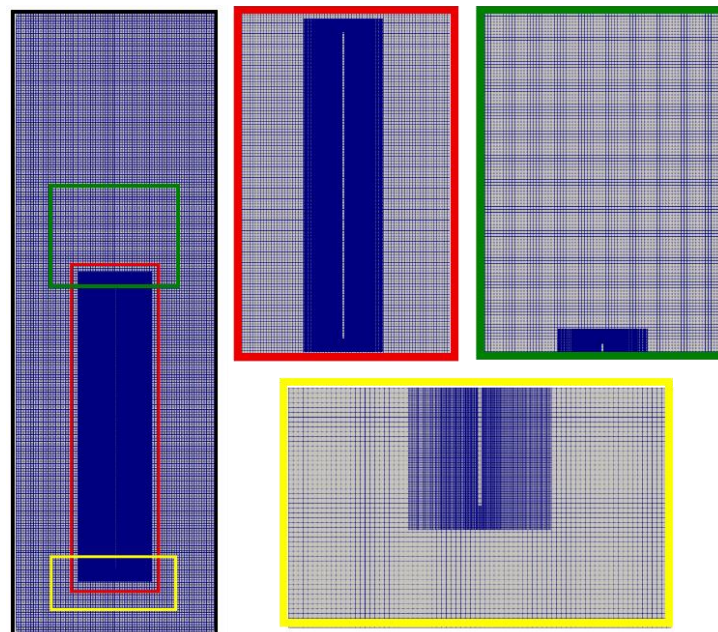


Figure 2. Overset grid of the flow domain.

Table 2. Summary of the mesh densities.

Mesh Details		Coarse	Medium	Finer
Wall-normal [mm]	$\Delta y_{\min}$	0.2	0.15	0.1
	$\Delta y_{\max}$	0.4	0.3	0.2
Streamwise, $\Delta x$ [mm]		1.25	1	0.8
Mesh size		60,404	89,940	138,824

The convective term in the momentum equations is discretized using the second order “linear” scheme. Spatial gradients are also discretized using the second order “linear” scheme (central differences with linear interpolation). The simulations are performed while discretizing the unsteady terms with a backward Eulerian scheme. The coupling between the background and the overset grids at these mesh boundaries is accomplished for the resolved fields ( $\mathbf{v}$ ,  $p$ ) through a cell-volume-weighted interpolation scheme.

In the next section we discuss the results of our numerical simulations.

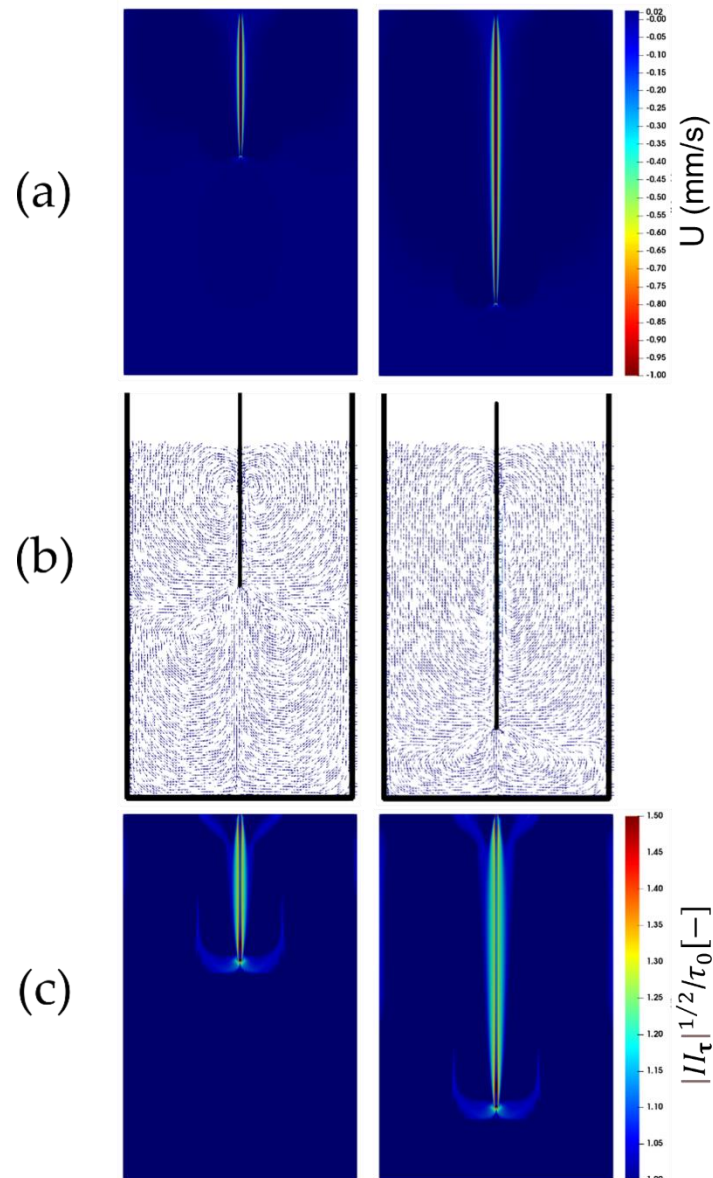
## 6. Results

### 6.1. Flow Visualization

Figures 3a, 4a and 5a show the contour plots of the instantaneous (vertical) velocity of the fluid as the plate is being immersed. As seen, the fluid mainly moves within a narrow area around the plate. There are two recirculation zones below the plate’s leading edge, and the upward displacements at either side of the plate are readily apparent beyond this



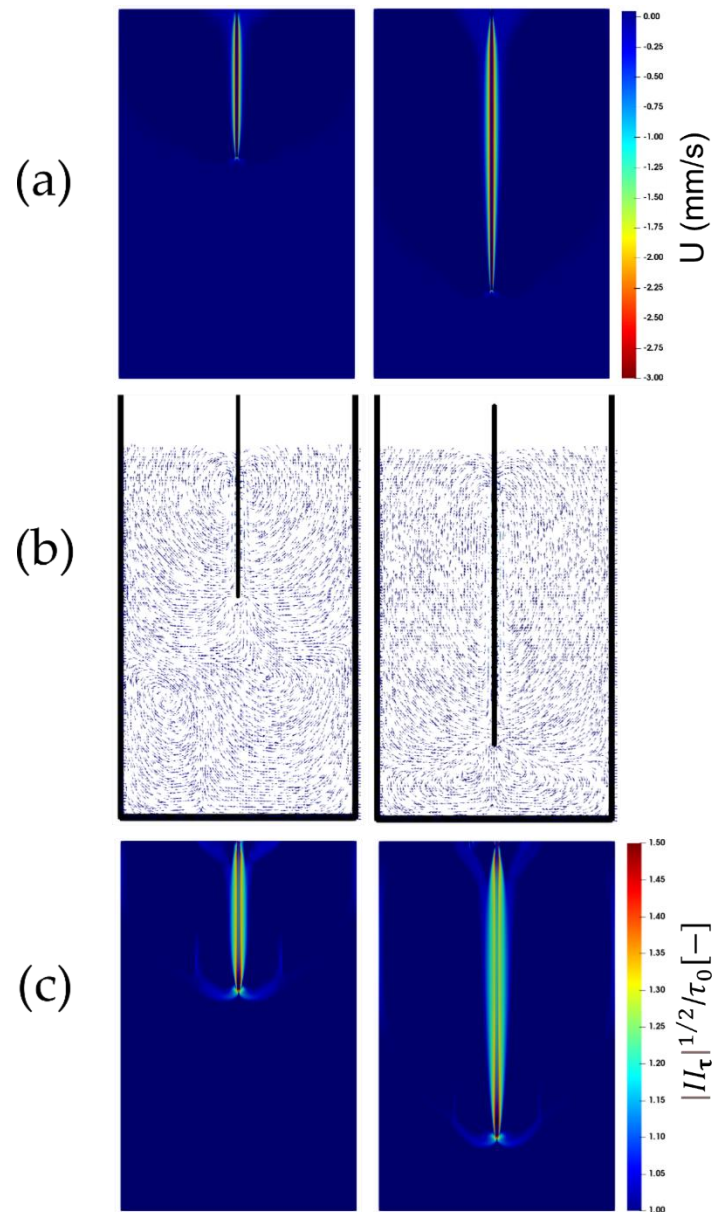
narrow area in the vicinity of the plate, where the fluid is dragged down by the plate (see Figures 3b, 4b and 5b). This flow pattern, which is consistent with the experimental observations, remains unchanged with an increase in the immersion velocity.



**Figure 3.** Snapshots of the flow for the plate immersion velocity of 1 mm/s. Parcels on the left-hand side show the immersion after 10 cm, while those on the right-hand side show the immersion after 20 cm. The top contour plots are (a) the fluid velocity, and (c) the bottom contours are the square root of the second invariant of the viscous stress tensor compared to the yield stress  $\tau_0$ . The middle vector (b) fields show the velocity vectors within the domain.

The square root of the second invariant of the viscous tensor (i.e.,  $|\text{II}_\tau|^{1/2}$ ) plotted in Figures 3c, 4c and 5c, is compared against the yield stress  $\tau_0$ . It appears that the larger values of the second invariants of the viscous stress tensor are localized just around the plate. The fluid region, which is identified as the region where the second invariant exceeds the yield stress  $\tau_0$ , following the von Mises yield criterion, exhibits an anchor-like shape around the plate. This indicates that, in addition to the material, which behaves as a fluid within a small envelope surrounding the plate, there exists also a fluid-like region attached to the leading edge of the plate which extends at either side of the leading edge of the

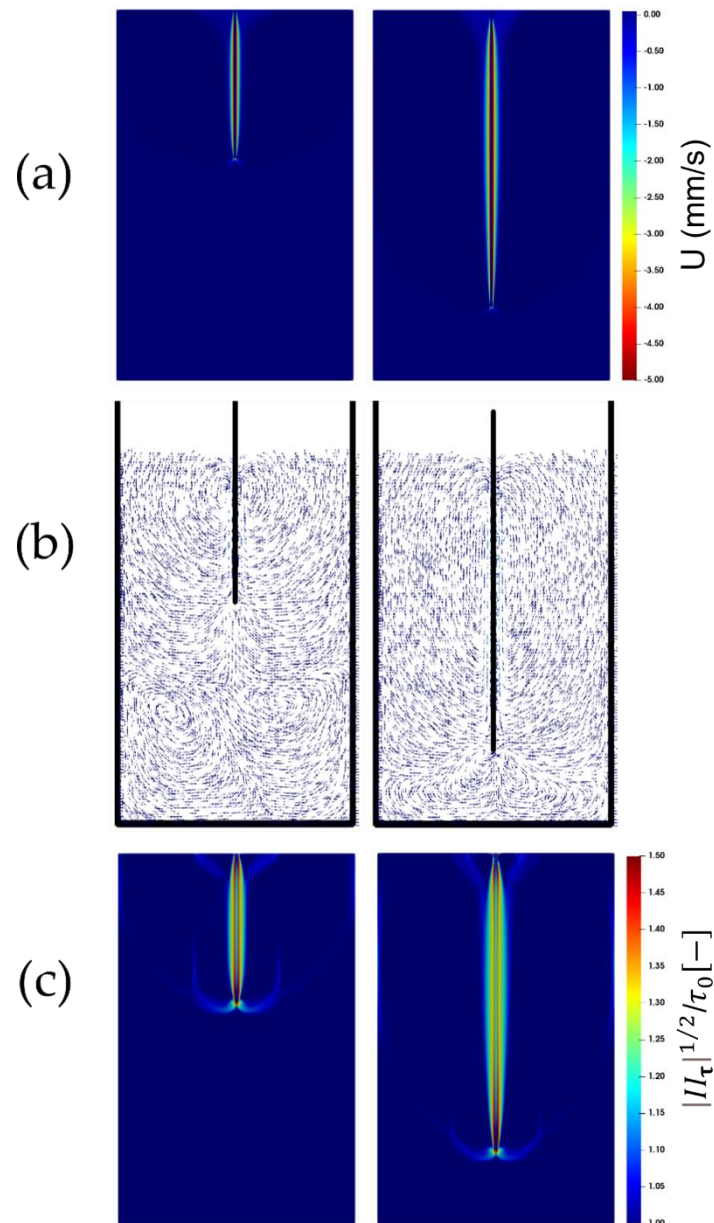
plate. This could have originated from the material deformation caused and sustained by the continuous penetration of the leading edge of the plate. Boujlel et al. [1] reported that although some material was liquefied just below the leading edge of the plate, most of the material was liquefied around the leading edge. Furthermore, two narrow fluid regions also appear at the walls of the container.



**Figure 4.** Snapshots of the flow for the plate immersion velocity of 3 mm/s. The top contour plots are (a) the fluid velocity, and (c) the bottom contours are the square root of the second invariant of the viscous stress tensor compared to the yield stress  $\tau_0$ . The middle vector (b) fields show the velocity vectors within the domain.

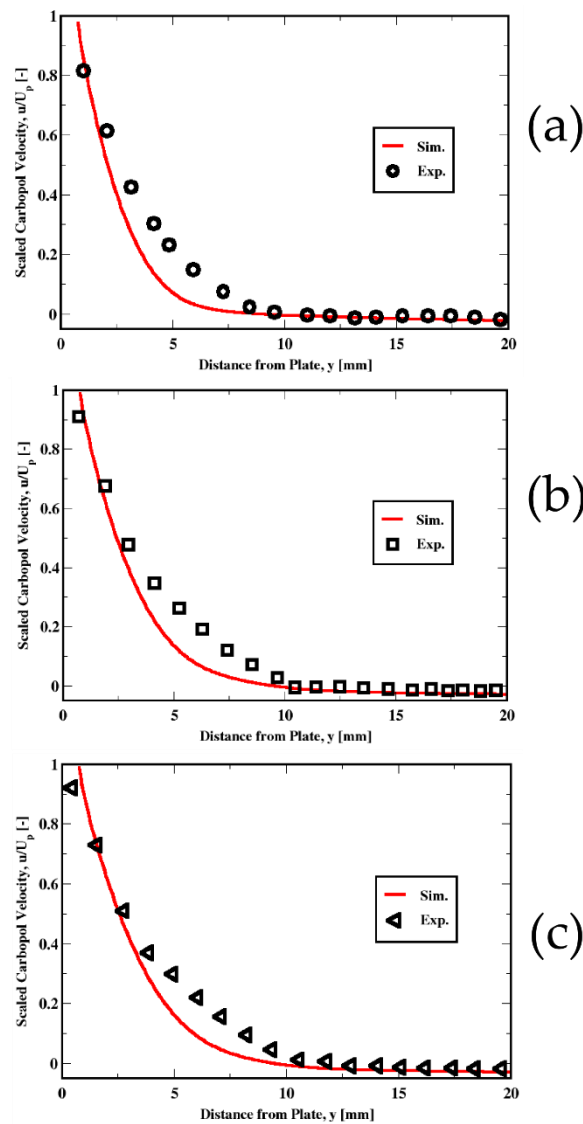
Figure 6a–c compares the numerical predictions of the fluid velocity for the three different immersion velocities of the plate. These comparisons show that, away from the plate, within the previously identified solid-like region, the upward velocities of the fluid are accurately captured. Near the plate, where the Carbopol behaves like a liquid, the predictions are satisfactory as well. However, a slight mismatch of the profiles against the measurements occurs as the solid-like behavior region is approached. The reason is unclear. However, we can speculate that the solid–fluid transition, where both the solid and the

liquid regimes could potentially co-exist, may have not been adequately captured in the simulations. Putz & Burghlea [73] reported from their experimental observations that such a transition is characterized by a competition between destruction and reformation of the gel.

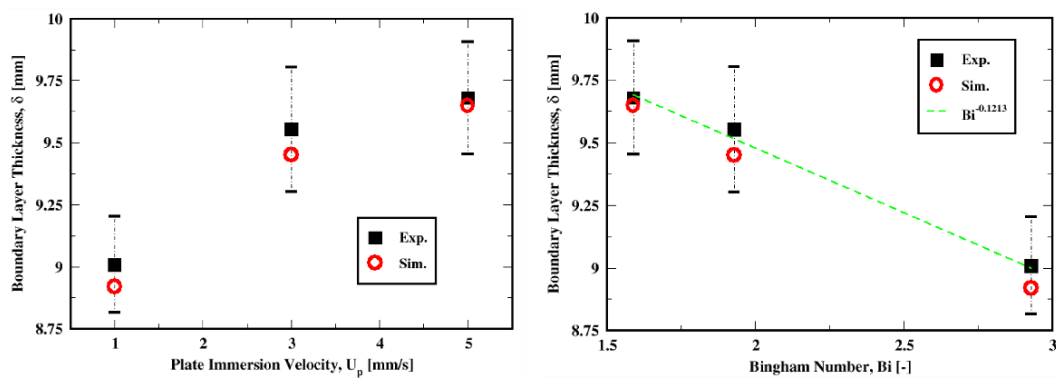


**Figure 5.** Snapshots of the flow for the plate immersion velocity of 5 mm/s. The top contour plots are (a) the fluid velocity, and (c) the bottom contours are the square root of the second invariant of the viscous stress tensor compared to the yield stress  $\tau_0$ . The middle vector (b) fields show the velocity vectors within the domain.

The boundary-layer thickness, measured as the extent of the yielded region adjacent to the plate, is plotted for the three velocities in Figure 7. The plot shows that the variation in the yielded region with the increase in the plate velocity is adequately predicted both in trend and quantitatively; the maximum relative error over these three conditions is only about 1.07%. The predictions are indeed within the uncertainties of the experimental data as shown by the error bars.



**Figure 6.** Distribution of the velocity of the Carbopol fluid. Plots from top (a), middle (b), and bottom (c) refer to the immersion velocities of 1 mm/s, 3 mm/s, and 5 mm/s, respectively.



**Figure 7.** Thickness of the boundary layer with respect to the immersion velocity of the plate (left) and the Bingham number (right).

We can see from Figure 7 that an increase in the Bingham number results in a decrease in the boundary layer thickness. This suggests that for creeping flows, where the yield stress dominates over the viscous stress, the boundary layer developing around the moving

plate will exhibit a negative correlation dependence on the Bingham number. This is consistent with the boundary layer theory proposed by Piau & Debiante [36], which is an improvement and extension to the Herschel–Bulkley model of Oldroyd’s theory [33]. Indeed, Piau & Debiante showed that the boundary layer thickness scales as  $Bi^{-1/(1+n)}$ , which with the current rheological properties results in  $Bi^{-0.7246}$  (given that  $n = 0.38$ ). However, the experimental data (or at least the subset investigated in this work), indicate that the thickness scaled as  $Bi^{-0.1213}$ .

6.2. Mesh and Regularization Sensitivities

The sensitivity of the solution to the mesh and the regularization method are examined below for the plate velocity of 1 mm/s. The sensitivity to the mesh resolution is performed using Papanastasiou’s approximation (with  $\epsilon = 10^{-5}$ ). The mesh densities along with the resolutions are summarized in Table 2. Figure 8 compares the velocity profiles for the three grids against the measurements. It is apparent that the medium-grid solution does quite well with the fine-grid prediction, while the coarse-grid one slightly deviates from those two solutions. Furthermore, it can be seen from the fine-grid solution that the slight mismatch remains despite the refinement, especially in the vicinity of the plate. As summarized in Table 3, the predicted boundary layer thickness with respect to different grids are within the measurement uncertainties. The prediction with the medium grid compares well with the fine grid predictions and the slight mismatch in the velocity profile marginally reflects grid resolution issues.

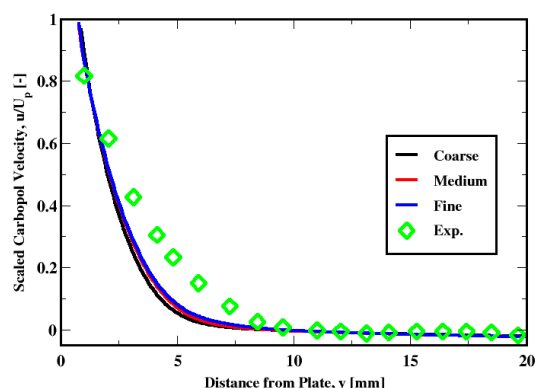


Figure 8. Sensitivity of the velocity distribution to the mesh refinement.

Table 3. Summary of the boundary layer thickness sensitivities to the mesh refinement and the regularization model.

Experiments [mm]	Mesh Sensitivity [mm]			Regularization Sensitivity [mm]		
	Coarse	Medium	Fine	Simple	Bercovier–Engelman	Papanastasiou
9.01 ± 0.20	8.64	8.92	9.33	12.67	9.21	8.92

The influence of the regularization method is shown in Figure 9. This plot shows that there is little difference between the Bercovier–Engelman and the Papanastasiou methods. The boundary layer thickness prediction compared in Table 3 shows that the difference is very small. As for the “simple” regularization approach, the velocity profile seems to be less accurately predicted; the same observation holds for the thickness of the boundary layer (see Table 3).

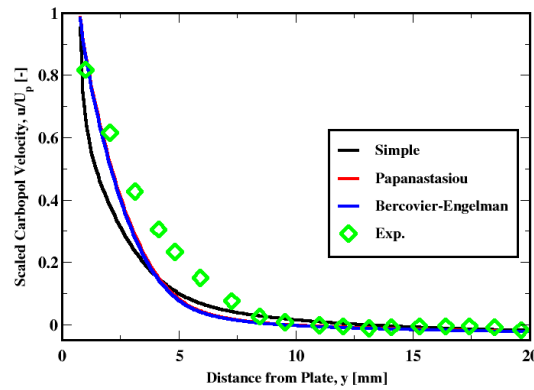


Figure 9. Sensitivity of the velocity distribution to the regularization model.

6.3. Results for Different Fluid Properties

Here, we look at the difference between the numerical predictions of the velocity inside the boundary layer obtained by prescribing the thickness of the boundary layer ( $\delta$ ), and the velocity distribution measured by Boujlel et al. (2012). This velocity distribution is a function of the boundary layer thickness ( $\delta$ ) (see [1,36]):

$$u = U_p \left[ 1 - \left( 1 - \frac{y}{\delta} \right)^{1+1/n} \right], \quad 0 < y < \delta \tag{38}$$

where  $U_p$  is the plate velocity and  $n$  is the power-law exponent of the Herschel–Bulkley fluid model.

In Figure 10, we plot the velocity distribution using the measured thickness of  $\delta = 9.01$  mm and  $\delta = 14.4$  mm proposed by Boujlel et al. The plot prediction using the measured thickness exhibits a less satisfactory agreement contrary to the larger boundary layer thickness for which a very good agreement is found. Since the only difference is due to a different value of the boundary layer thickness, which depends on the Bingham number, we think it would be interesting to look at different values for the properties of the fluid and see the impact on the results.

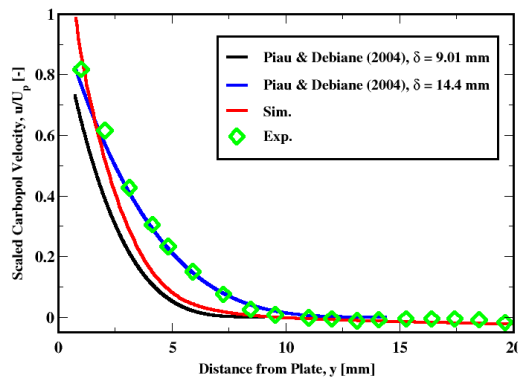


Figure 10. Predictions of the velocity distribution using Piau and Debiane (2004) model for a prescribed boundary layer thickness.

Although Boujlel et al. [1] carefully prepared and performed the measurements, they did not mention uncertainties in their measurements. Piau [74] argued from an extensive literature review that often the rheometry of Carbopol aqueous gels is not without measurement difficulties.

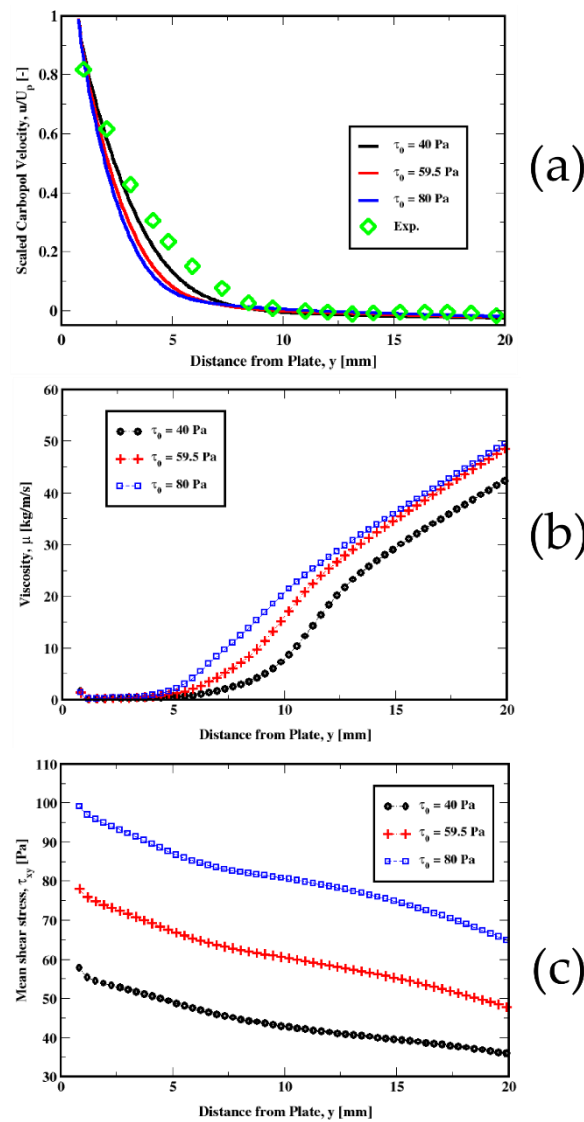
We now look at the boundary-layer flow for different properties of a yield-stress fluid modeled as a Herschel–Bulkley fluid. The results for the velocity profiles show a systematic slight mismatch of the predictions against the measurements in the yielded region behaving

as a solid-like material. Table 4 lists the different rheological properties which we use in our simulations.

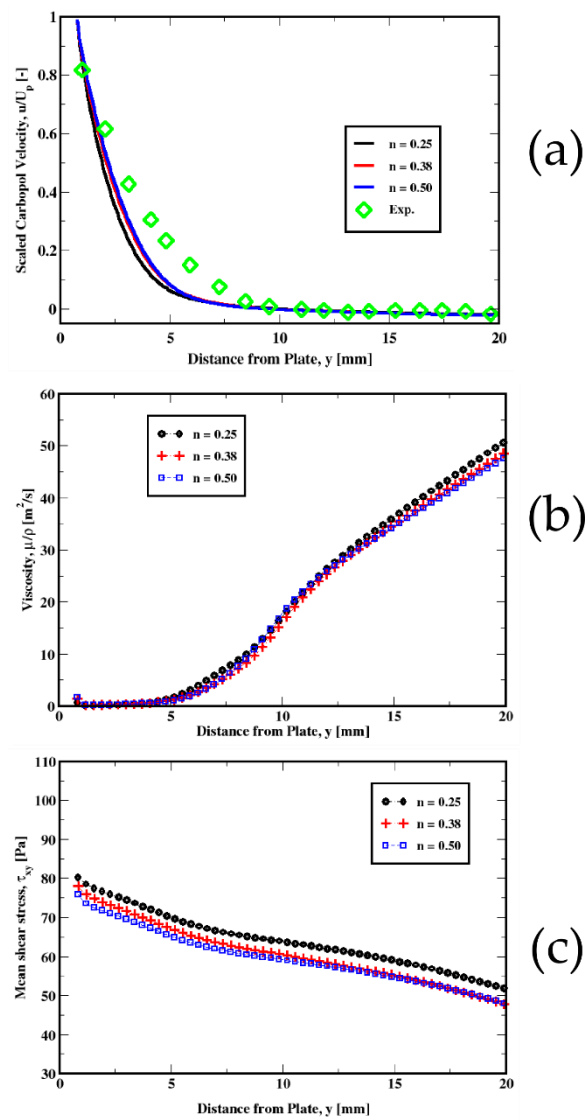
**Table 4.** Different rheological properties. (\*) Bi is calculated for the plate immersion velocity of 1 mm/s. (-) refers to the same rheological property as the “Baseline” measured property.

	$\tau_0$ [Pa]	$k$	$n$	(*) Bi [-]
Baseline	59.5	23.6	0.38	2.94
Yield stress	40.0	-	-	1.98
	80.0	-	-	3.95
Consistency	-	14.0	-	4.96
	-	34.0	-	2.04
Power-law exponent	-	-	0.25	2.79
	-	-	0.50	3.09

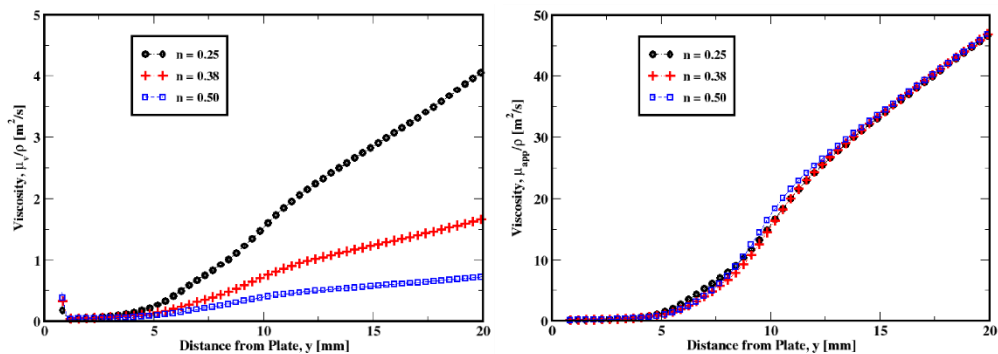
In Figures 11–14, we plot the variations in the mean velocity ( $U$ ), the kinematic viscosity ( $\mu/\rho$ ), and the mean shear stress ( $\tau_{xy}$ ) for different material properties.



**Figure 11.** Influence of the yield stress on the distribution of the velocity (top plot) (a) for the plate immersion velocity of 1 mm/s. The middle (b) and the bottom (c) plots represent the variations in the kinematic viscosity and the mean shear stress, respectively.

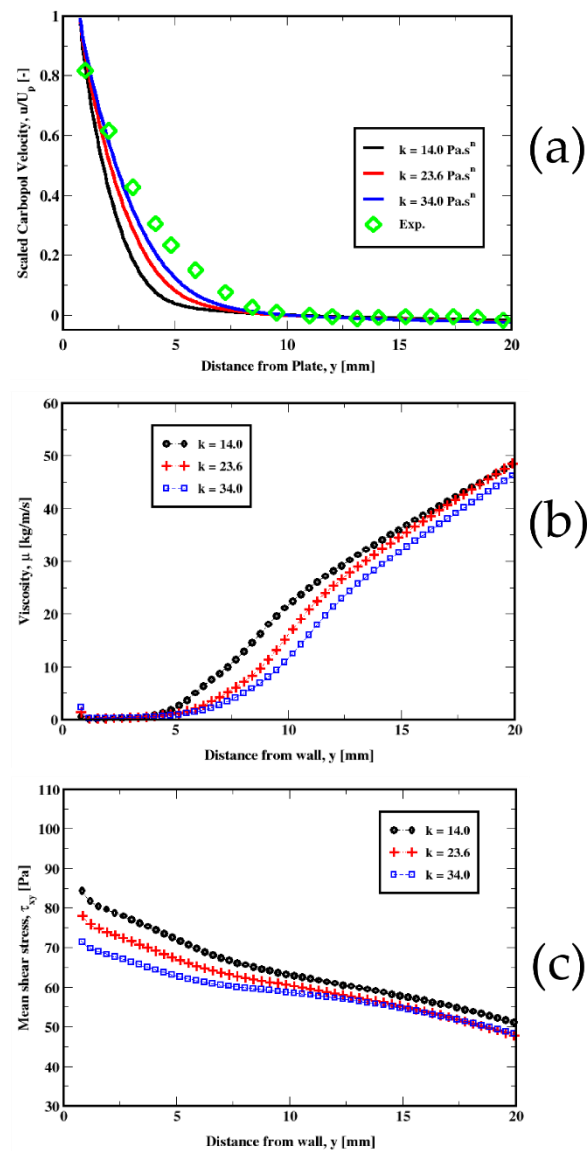


**Figure 12.** Influence of the power-law exponent on the distribution of the velocity of the fluid (a) (top plot) for the plate immersion velocity of 1 mm/s. The middle (b) and the bottom (c) plots represent the variation in the kinematic viscosity and the mean shear stress, respectively.



**Figure 13.** Influence of the power-law exponent on the viscous (left plot) and the apparent (right plot) viscosities for the plate immersion velocity of 1 mm/s.





**Figure 14.** Influence of the consistency index on the distribution of the velocity of the Carbopol fluid (top plot) (a) for the plate immersion velocity of 1 mm/s. The middle (b) and the bottom (c) plots represent the variation in the kinematic viscosity and the mean shear stress, respectively.

Figure 11a compares the velocity predictions for different values of the yield stress. For smaller values of the yield stress, we see a better agreement with the experimental data. We also notice similar behavior for the viscosity and the mean shear stress shown in Figure 11b,c. The tendency of the fluid to resist shearing motion as conveyed by the viscosity, clearly increases with the yield stress as shown in Figure 11b. This plot further exhibits a steeper increase in the viscosity within the transition region between the fluid-like and the solid-like behaviors. Figure 11c also shows how the mean shear stress changes with the tangential shearing forces between the fluid and the plate, from near the plate to the far-field regions. These clearly indicate an increase in the friction at the plate with the yield stress, which result in slower velocities.

For different values of the power-law exponent ( $n$ ), we could see similar tendencies (see Figure 12). However, the variations are not that accentuated as is the case for the yield stress discussed above. Only slight increases are apparent in both the viscosity and the mean shear stress (see Figure 12b,c), which result in a slight change in the velocity, especially for  $n = 0.25$ , where the mean shear stress is relatively higher compared to  $n = 0.38$  and  $n = 0.50$ . The viscous and the apparent viscosities plotted in Figure 13 show that

the apparent viscosity is one order of magnitude larger than the regular (shear) viscosity for each of the power-law exponents used in this study. Therefore, even though some shear-thinning effects takes place, the yield stress effects appear to be dominant. Piau & Debiante [36] and later Boujlel et al. [1] showed that the slope is determined by the power law exponent. In other words, the shear-thinning effects strongly influence the velocity field in the boundary layer.

The velocity distribution in the vicinity of the plate plotted in Figure 14, shows that an increase in the consistency index results in a steeper profile, thus reducing the discrepancy. Typically, the change in the consistency index appears to show a similar change in the viscosity and the mean shear stress. This is illustrated by an increase in the viscosity and in the mean shear stress, especially in the wall region (see Figure 14b,c), causing a flatter profile as a result of the increased friction at the wall.

## 7. Conclusions

The boundary layer experiments of Boujlel et al. [1], where a plate is slowly immersed into a Carbopol yield-stress fluid, are numerically investigated. The fluid is modeled as a Herschel–Bulkley fluid. The numerical approach uses the Papanastasiou regularization of the apparent viscosity associated with the Herschel–Bulkley constitutive model in the context of the overset meshing technique. The physics of the flow appears to be adequately captured for the three flow conditions investigated in this work. It is seen that the boundary layer develops in the vicinity of the plate as the leading edge steadily advances into the fluid. The velocity distribution seems to be in good agreement with the measurements. Specifically, the upward velocity distributions of the unyielded material are reasonably captured. However, a slight mismatch is noticeable within the yielded region near the solid-plug flow. It is shown that the transition between the fluid-like and the solid-like states, is very sensitive to the rheological properties of the fluid. Subsequent simulations show a strong dependence of the mean shear stress on these rheological properties that could cause different values for the friction at the wall. This behavior is consistent with the existing theories [36]. In our numerical investigations, we assume a no-slip condition at the walls. The influence of the slip at the walls (see [36,38]) is left for future work.

**Author Contributions:** All authors jointly conceived the idea to conduct this study. M.M. conducted some of the theoretical work and N.A.K. conducted some of the theoretical work, the literature review, and all the computational work. M.M. and E.R. contributed to the formal analysis, methodology, and interpretation of the results. All authors have read and agreed to the published version of the manuscript.

**Funding:** This research received no external funding.

**Acknowledgments:** This work was performed in support of the U.S. Department of Energy’s Fossil Energy and Carbon Management’s Environmentally Prudent Stewardship and executed through the National Energy Technology Laboratory (NETL) Research & Innovation Center’s Remediation and Reuse of Onshore Resources.

**Conflicts of Interest:** The authors declare no conflict of interest.

**Disclaimer:** This project was funded by the United States Department of Energy, National Energy Technology Laboratory, in part, through a site support contract. Neither the United States Government nor any agency thereof, nor any of their employees, nor the support contractor, nor any of their employees, makes any warranty, express or implied, or assumes any legal liability or responsibility for the accuracy, completeness, or usefulness of any information, apparatus, product, or process disclosed, or represents that its use would not infringe privately owned rights. Reference herein to any specific commercial product, process, or service by trade name, trademark, manufacturer, or otherwise does not necessarily constitute or imply its endorsement, recommendation, or favoring by the United States Government or any agency thereof. The views and opinions of authors expressed herein do not necessarily state or reflect those of the United States Government or any agency thereof.

## Appendix A

In this Appendix, we present the dimensionless form of the governing equations. Assuming a reference length scale  $d$  and a reference velocity  $U_p$ , we can define dimensionless length, time, velocity, and pressure as:

$$\mathbf{x}^* = \mathbf{x}/d, \quad t^* = \eta_0 t / \rho d^2, \quad \mathbf{v}^* = \mathbf{v}/U_p, \quad p^* = pd/\eta_0 U_p \quad (\text{A1})$$

where  $\eta_0 = k(U_p/d)^{n-1}$  is a characteristic viscosity associated with Herschel–Bulkley fluids. Thus, the dimensionless mass and momentum equations can be written as:

$$\text{div}^* \mathbf{v}^* = 0 \quad (\text{A2})$$

$$\frac{\partial \mathbf{v}^*}{\partial t^*} + Re [\text{grad}^* \mathbf{v}^*] \mathbf{v}^* = -\text{grad}^* p^* + \text{div}[(1 + Bi)A_1^*] + b^* \quad (\text{A3})$$

where  $b^* = (\rho e^2 / \eta_0 U_p) b$  is the dimensionless body force and  $Re$  and  $Bi$  are the Reynolds and Bingham numbers, respectively. In the limit of  $Re \rightarrow 0$ , the inertia does not contribute to the flow dynamics.

## References

- Boujlel, J.; Maillard, M.; Lindner, A.; Ovarlez, G.; Chateau, X.; Coussot, P. Boundary layer in pastes—Displacement of a long object through a yield stress fluid. *J. Rheol.* **2012**, *56*, 1083. [\[CrossRef\]](#)
- Schowalter, E.R. *Mechanics of Non-Newtonian Fluids*; Pergamon Press: New York, NY, USA, 1978.
- Oldroyd, J.G. An approach to non-Newtonian fluid mechanics. *J. Non-Newton. Fluid Mech.* **1984**, *14*, 9–46. [\[CrossRef\]](#)
- Larson, R.G. *The Structure and Rheology of Complex Fluids*; Oxford University Press: New York, NY, USA, 1999.
- Li, M.-G.; Feng, F.; Wu, W.-T.; Massoudi, M. Numerical Simulations of the Flow of a Dense Suspension Exhibiting Yield-Stress and Shear-Thinning Effects. *Energies* **2020**, *13*, 6635. [\[CrossRef\]](#)
- Fernandes, C.; Fakhari, A.; Tukovic, Ž. Non-Isothermal Free-Surface Viscous Flow of Polymer Melts in Pipe Extrusion Using an Open-Source Interface Tracking Finite Volume Method. *Polymers* **2021**, *13*, 4454. [\[CrossRef\]](#)
- Wong, L.S. Durability Performance of Geopolymer Concrete: A Review. *Polymers* **2022**, *14*, 868. [\[CrossRef\]](#) [\[PubMed\]](#)
- Batra, R.C. *Elements of Continuum Mechanics*; American Institute of Aeronautics and Astronautics (AIAA) Inc.: Reston, VA, USA, 2006.
- Haupt, P. *Continuum Mechanics and Theory of Materials*, 2nd ed.; Springer: Berlin/Heidelberg, Germany, 2002.
- Liu, I.S. *Continuum Mechanics*; Springer-Verlag: Berlin/Heidelberg, Germany, 2002.
- Massoudi, M.; Vaidya, A. On some generalizations of the second grade fluid model. *Nonlinear Anal. Part II Real World Appl.* **2008**, *9*, 1169–1183. [\[CrossRef\]](#)
- Rivlin, R.S.; Ericksen, J.L. Stress deformation relations for isotropic materials. *J. Rat. Mech. Anal.* **1955**, *4*, 323–425. [\[CrossRef\]](#)
- Truesdell, C.; Noll, W. *The Non-Linear Field Theories of Mechanics*; Springer: New York, NY, USA, 1992.
- Deshpande, A.P.; Krishnan, J.M.; Sunil, P.B. *Rheology of Complex Fluids*, 1st ed.; Springer: Berlin/Heidelberg, Germany, 2010; ISBN 978-1-4419-6493-9.
- Denn, M.M.; Bonn, D. Issues in the flow of yield-stress liquids. *Rheol. Acta* **2011**, *50*, 307–315. [\[CrossRef\]](#)
- Beris, A.N.; Tsamopoulos, J.A.; Armstrong, R.C.; Brown, R.A. Creeping motion of a sphere through a Bingham plastic. *J. Fluid Mech.* **1985**, *158*, 219–244. [\[CrossRef\]](#)
- Lootens, D.; Hébraud, P.; Lécolier, E.; Van Damme, H. Gelation, Shear-Thinning and Shear-Thickening in Cement Slurries. *Oil Gas Sci. Technol.* **2004**, *59*, 31–40. [\[CrossRef\]](#)
- Banfill, P.F. The rheology of fresh cement and concrete—a review. In Proceedings of the 11th International Cement Chemistry Congress, Durban, South Africa, 11–16 May 2003; Volume 1, pp. 50–62.
- Tao, C.; Rosenbaum, E.; Kutchko, B.G.; Massoudi, M. A Brief Review of Gas Migration in Oilwell Cement Slurries. *Energies* **2021**, *14*, 2369. [\[CrossRef\]](#)
- Carreau, P.J.; De Kee, D.; Chhabra, R.J. *Rheology of Polymeric Systems*; Hanser/Gardner Publications: Cincinnati, OH, USA, 1997.
- Tao, C.; Kutchko, B.G.; Rosenbaum, E.; Wu, W.-T.; Massoudi, M. Steady Flow of a Cement Slurry. *Energies* **2019**, *12*, 2604. [\[CrossRef\]](#)
- Mewis, J.; Spaul, A.J.B. Rheology of Concentrated Dispersions. *Adv. Colloid Interface Sci.* **1976**, *6*, 173–200. [\[CrossRef\]](#)
- Mewis, J.; Wagner, N.J. *Colloidal Suspension Rheology*; Cambridge University Press: Cambridge, UK, 2012.
- Agassant, J.F.; Avenas, P.; Carreau, P.J.; Vergnes, B.; Vincent, M. *Polymer Processing: Principles and Modeling*; Carl Hanser Verlag GmbH Co KG.: Munich, Germany, 2017.
- Denn, M.M. Simulation of polymer melt processing. *AIChE J.* **2009**, *55*, 1641–1647. [\[CrossRef\]](#)
- Middleman, S. *Fundamentals of Polymer Processing*; McGraw-Hill: New York, NY, USA, 1977.

27. Ziaee, H.; Arabloo, M.; Ghazanfari, M.H.; Rashtchian, D. Herschel–Bulkley rheological parameters of lightweight colloidal gas aphron (CGA) based fluids. *Chem. Eng. Res. Des.* **2015**, *93*, 21–29. [[CrossRef](#)]
28. Wang, S.; Yuan, C.; Zhang, C.; Chen, L.; Liu, J. Rheological properties with temperature response characteristics and a mechanism of solid-free polymer drilling fluid at low temperatures. *Appl. Sci.* **2016**, *7*, 18. [[CrossRef](#)]
29. Shafiei, M.; Bryant, S.; Balhoff, M.; Huh, C.; Bonnecaze, R.T. Hydrogel formulation for sealing cracked wellbores for CO<sub>2</sub> storage. *Appl. Rheol.* **2017**, *27*, 27–34.
30. Chauhan, G.; Verma, A.; Das, A.; Ojha, K. Rheological studies and optimization of Herschel–Bulkley flow parameters of viscous karaya polymer suspensions using GA and PSO algorithms. *Rheol. Acta* **2018**, *57*, 267–285. [[CrossRef](#)]
31. Zheng, W.; Wu, X.; Huang, Y. Impact of polymer addition, electrolyte, clay and antioxidant on rheological properties of polymer fluid at high temperature and high pressure. *J. Pet. Explor. Prod. Technol.* **2020**, *10*, 663–671. [[CrossRef](#)]
32. Milián, D.; Roux, D.C.; Caton, F.; El Kissi, N. Rheological behavior of gel polymer electrolytes: Yield stress and viscoelasticity. *Rheol. Acta* **2022**, *61*, 401–413. [[CrossRef](#)]
33. Oldroyd, J.G. Two-dimensional plastic flow of a Bingham solid. A plastic boundary-layer theory for slow motion. *Proc. Camb. Philos. Society. Math. Phys. Sci.* **1947**, *43*, 383–395. [[CrossRef](#)]
34. Piau, J.-M. Viscoplastic boundary layer. *J. Non-Newton. Fluid Mech.* **2002**, *102*, 193–218. [[CrossRef](#)]
35. Balmforth, N.J.; Craster, R.V.; Hewitt, D.R. Building on Oldroyd’s viscoplastic legacy: Perspectives and new developments. *J. Non-Newton. Fluid Mech.* **2021**, *294*, 104580. [[CrossRef](#)]
36. Piau, J.-M.; Debiane, K. The adhesive or slippery flat plate viscoplastic boundary layer for a shear-thinning power-law viscosity. *J. Non-Newton. Fluid Mech.* **2004**, *117*, 97–107. [[CrossRef](#)]
37. Ahonguio, F.; Jossic, L.; Magnin, A. Influence of slip on the flow of a yield stress fluid around a flat plate. *AIChE J.* **2016**, *62*, 1356–1363. [[CrossRef](#)]
38. Ahonguio, F.; Jossic, L.; Magnin, A.; Dufour, F. Flow of an elasto-viscoplastic fluid around a flat plate: Experimental and numerical data. *J. Non-Newton. Fluid Mech.* **2016**, *238*, 131–139. [[CrossRef](#)]
39. Balmforth, N.J.; Craster, R.V.; Hewitt, D.R.; Hormozi, S.; Maleki, A. Viscoplastic boundary layers. *J. Fluid Mech.* **2017**, *813*, 929–954. [[CrossRef](#)]
40. Chevalier, T.; Rodts, S.; Chateau, X.; Boujlel, J.; Maillard, M.; Coussot, P. Boundary layer (shear-band) in frustrated viscoplastic flows. *EPL* **2013**, *102*, 48002. [[CrossRef](#)]
41. Herschel, W.H.; Bulkley, R. Measurement of Consistency as Applied to Rubber-Benzene Solutions. *Am. Soc. Test Proc.* **1926**, *26*, 621–633.
42. Headrick, E.D.; Spaulding, R.; Rosenbaum, E.; Kutchko, B.; Massoudi, M. *The Effects of Conditioning and Additives on the Viscosity Measurement of Cement Slurries*; NETL Technical Report Series; U.S. Department of Energy: Washington, DC, USA, 2022; submitted.
43. Slattery, J.C. *Advanced Transport Phenomena*; Cambridge University Press: Cambridge, UK, 1999.
44. Barnes, H.A. The yield stress—A review or ‘ $\pi\alpha\nu\tau\alpha$   $\rho\epsilon\iota$ ’—Everything flows? *J. Non-Newton. Fluid Mech.* **1999**, *81*, 133–178. [[CrossRef](#)]
45. Barnes, H.A. The ‘yield stress myth?’ paper—21 years on. *Appl. Rheol.* **2007**, *17*, 43110-1–43110-5. [[CrossRef](#)]
46. Barnes, H.A.; Walters, K. The yield stress myth? *Rheol. Acta* **1985**, *24*, 323–326. [[CrossRef](#)]
47. Assaad, J.J.; Harb, J.; Maalouf, Y. Measurement of Yield Stress of Cement Pastes Using the Direct Shear Test. *J. Non-Newton. Fluid Mech.* **2014**, *214*, 18–27. [[CrossRef](#)]
48. Assaad, J.J.; Harb, J.; Maalouf, Y. Effect of Vane Configuration on Yield Stress Measurements of Cement Pastes. *J. Non-Newton. Fluid Mech.* **2016**, *230*, 31–42. [[CrossRef](#)]
49. Watts, B.; Tao, C.; Ferraro, C.; Masters, F. Proficiency analysis of VCCTL results for heat of hydration and mortar cube strength. *Constr. Build. Mater.* **2018**, *161*, 606–617. [[CrossRef](#)]
50. Moller, P.; Fall, A.; Chikkadi, V.; Derks, D.; Bonn, D. An Attempt to Categorize Yield Stress Fluid Behaviour. *Philos. Trans. R. Soc. A Math. Phys. Eng. Sci.* **2009**, *367*, 5139–5155. [[CrossRef](#)] [[PubMed](#)]
51. Dinkgreve, M.; Paredes, J.; Denn, M.M.; Bonn, D. On Different Ways of Measuring ‘the’ Yield Stress. *J. Non-Newton. Fluid Mech.* **2016**, *238*, 233–241. [[CrossRef](#)]
52. Nguyen, Q.D.; Boger, D.V. Measuring the Flow Properties of Yield Stress Fluids. *Annu. Rev. Fluid Mech.* **1992**, *24*, 47–88. [[CrossRef](#)]
53. Coussot, P. Yield Stress Fluid Flows: A Review of Experimental Data. *J. Non-Newton. Fluid Mech.* **2014**, *211*, 31–49. [[CrossRef](#)]
54. Coussot, P.; Nguyen, Q.D.; Huynh, H.T.; Bonn, D. Viscosity Bifurcation in Thixotropic, Yielding Fluids. *J. Rheol.* **2002**, *46*, 573–589. [[CrossRef](#)]
55. Tao, C.; Rosenbaum, E.; Kutchko, B.; Massoudi, M. *The Importance of Vane Configuration on Yield Stress Measurements of Cement Slurry*; DOE/NETL-2020/2116; NETL Technical Report Series; U.S. Department of Energy, National Energy Technology Laboratory: Morgantown, WV, USA, 2020; p. 24. [[CrossRef](#)]
56. Saak, A.W.; Jennings, H.M.; Shah, S.P. The Influence of Wall Slip on Yield Stress and Viscoelastic Measurements of Cement Paste. *Cem. Concr. Res.* **2001**, *31*, 205–212. [[CrossRef](#)]
57. Barnes, H.A. A Review of the Slip (Wall Depletion) of Polymer Solutions, Emulsions and Particle Suspensions in Viscometers: Its Cause, Character, and Cure. *J. Non-Newton. Fluid Mech.* **1995**, *56*, 221–251. [[CrossRef](#)]
58. Nguyen, Q.D.; Boger, D.V. Direct Yield Stress Measurement with the Vane Method. *J. Rheol.* **1985**, *29*, 335–347.
59. Liddel, P.V.; Boger, D.V. Yield Stress Measurements with the Vane. *J. Non-Newton. Fluid Mech.* **1996**, *63*, 235–261. [[CrossRef](#)]

60. Banfill, P.F.G.; Saunders, D.C. On the Viscometric Examination of Cement Pastes. *Cem. Concr. Res.* **1981**, *11*, 363–370. [[CrossRef](#)]
61. Nguyen, Q.D.; Boger, D.V. Yield Stress Measurement for Concentrated Suspensions. *J. Rheol.* **1983**, *27*, 321–349. [[CrossRef](#)]
62. Tao, C.; Kutchko, B.G.; Rosenbaum, E.; Massoudi, M. A Review of Rheological Modeling of Cement Slurry in Oil Well Applications. *Energies* **2020**, *13*, 570. [[CrossRef](#)]
63. Krieger, I.M.; Dougherty, T.J. A mechanism for non-Newtonian flow in suspensions of rigid spheres. *Trans. Soc. Rheol.* **1959**, *3*, 137–152. [[CrossRef](#)]
64. Bingham, E.C. *Fluidity and Plasticity*; McGraw Hill: New York, NY, USA, 1922.
65. Denn, M.M. *Polymer Melt Processing: Foundations in Fluid Mechanics and Heat Transfer*; Cambridge University Press: Cambridge, UK, 2008; ISBN 1-316-58314-7.
66. Macosko, C.W. *Rheology: Principles, Measurements, and Applications*; Wiley: Hoboken, NJ, USA, 1994.
67. OpenFOAM v2012. Available online: <http://www.openfoam.org> (accessed on 3 August 2022).
68. Papanastasiou, T.C. Flows of materials with yield. *J. Rheol.* **1987**, *31*, 385–404. [[CrossRef](#)]
69. Allouche, M.; Frigaard, I.A.; Sona, G. Static wall layers in the displacement of two viscoplastic fluids in a plane channel. *J. Fluid Mech.* **2000**, *424*, 243–277. [[CrossRef](#)]
70. Bercovier, M.; Engelman, M. A finite-element method for incompressible non-Newtonian flows. *J. Comput. Phys.* **1980**, *36*, 313–326. [[CrossRef](#)]
71. Frigaard, I.A.; Nouar, C. On the usage of viscosity regularisation methods for visco-plastic fluid flow computation. *J. Non-Newtonian Fluid Mech.* **2005**, *127*, 1–26. [[CrossRef](#)]
72. Saramito, P.; Wachs, A. Progress in numerical simulation of yield stress fluid flows. *Rheol. Acta* **2017**, *56*, 211–230. [[CrossRef](#)]
73. Putz, A.M.V.; Burghelea, T.I. The solid–fluid transition in a yield stress shear thinning physical gel. *Rheol. Acta* **2009**, *48*, 673–689. [[CrossRef](#)]
74. Piau, J.-M. Carbopol gels: Elastoviscoplastic and slippery glasses made of individual swollen sponges meso- and macroscopic properties, constitutive equations and scaling laws. *J. Non-Newton. Fluid Mech.* **2007**, *144*, 1–29. [[CrossRef](#)]

## Article

# Numerical Simulation and Experimental Validation of Hybrid Injection Molded Short and Continuous Fiber-Reinforced Thermoplastic Composites

Patrick Hirsch \*, Marianne John, Daniel Leipold, André Henkel, Sylvia Gipser, Ralf Schlimper and Matthias Zscheuye

Fraunhofer Institute for Microstructure of Materials and Systems IMWS, 06120 Halle (Saale), Germany; marianne.john@imws.fraunhofer.de (M.J.); daniel.leipold@imws.fraunhofer.de (D.L.); andre.henkel@imws.fraunhofer.de (A.H.); sylvia.gipser@imws.fraunhofer.de (S.G.); ralf.schlimper@imws.fraunhofer.de (R.S.); matthias.zscheuye@imws.fraunhofer.de (M.Z.)

\* Correspondence: patrick.hirsch@imws.fraunhofer.de; Tel.: +49-345-5589-264

**Citation:** Hirsch, P.; John, M.; Leipold, D.; Henkel, A.; Gipser, S.; Schlimper, R.; Zscheuye, M. Numerical Simulation and Experimental Validation of Hybrid Injection Molded Short and Continuous Fiber-Reinforced Thermoplastic Composites. *Polymers* **2021**, *13*, 3846. <https://doi.org/10.3390/polym13213846>

Academic Editors: Célio Bruno Pinto Fernandes, Salah Aldin Faroughi, Luís L. Ferrás and Alexandre M. Afonso

Received: 17 September 2021

Accepted: 2 November 2021

Published: 7 November 2021

**Publisher's Note:** MDPI stays neutral with regard to jurisdictional claims in published maps and institutional affiliations.



**Copyright:** © 2021 by the authors. Licensee MDPI, Basel, Switzerland. This article is an open access article distributed under the terms and conditions of the Creative Commons Attribution (CC BY) license (<https://creativecommons.org/licenses/by/4.0/>).

**Abstract:** In-situ thermoforming and overmolding of continuous fiber-reinforced thermoplastic composites by hybrid injection molding enables the mass production of thermoplastic lightweight structures with a complex geometry. In this study, the anisotropic mechanical behavior of such hybrid injection molded short and continuous fiber-reinforced thermoplastics and the numerical simulation of the resulting mechanical properties under flexural loading were investigated. For this, the influence of the volume flow rate between 25 and 100 cm<sup>3</sup>/s during injection molding of a PP/GF30 short fiber-reinforced overmolding material was studied and showed a strong effect on the fiber orientation but not on the fiber length, as investigated by computer tomography and fiber length analysis. Thus, the resulting anisotropies of the stiffness and strength as well as the strain hardening investigated by tensile testing were considered when the mechanical behavior of a hybrid test structure of short and continuous fiber-reinforced thermoplastic composites was predicted by numerical simulations. For this, a PP/GF60 and PP/GF30 hybrid injection molded test structure was investigated by a numerical workflow with implemented injection molding simulation data. In result, the prediction of the mechanical behavior of the hybrid test structure under flexural loading by numerical simulation was significantly improved, leading to a reduction of the deviation of the numerically predicted and experimentally measured flexural strength from 21% to 9% in comparison to the isotropic material model without the implementation of the injection molding data.

**Keywords:** numerical simulation; hybrid injection molding; continuous fiber-reinforced thermoplastics

## 1. Introduction

The use of thermoplastic fiber-reinforced composites as high-performance materials for lightweight structures has been going on for several decades. Continuous fiber-reinforced thermoplastics (TPC) processed by pultrusion unidirectional fiber-reinforced tapes are regarded as the material class with the highest lightweight potential in many applications combining high mechanical properties and economical manufacturing processes [1]. Furthermore, TPCs enable a load adapted structural design by orientation of the fiber direction to the load path of the part application [2]. The specific design of such TPCs is based on the constitutive equation theory of laminates [3–5]. In doing so, numerical simulations with adjusted material models do allow the prediction of the rate dependent non-linear mechanical behavior of complex shaped parts made out of TPCs [6]. Recent technology developments made in-situ thermoformed and overmolded laminate structures of TPCs available by hybrid injection molding, which enables the mass production of thermoplastic lightweight structures with a complex geometry and a high degree of functional integration [7]. The process flow of this technology is comparable to the already implemented

process flow of continuous fiber-reinforced thermoplastics consisting of textile fiber components and consist of the heating, hot handling and thermoforming of the TPC with subsequent overmolding in the same mold [8,9]. Typical applications of such thermoplastic lightweight structures are automotive parts with large-scale production [10]. However, the implementation of this approach for reliable lightweight structures is strongly dependent on the ability to precisely predict the mechanical behavior of the processed parts in the application, which is usually carried out by reverse engineering and numerical simulation techniques [11,12]. In doing so, structural analysis of hybrid injection molded parts must include the anisotropic mechanical behavior of the TPC as well as of the long or short fiber-reinforced overmolding material. Since the local fiber orientation of the TPC laminate is adjusted and therefore known, the major focus to improve the prediction accuracy of the structural properties has to be on the correct consideration of the microstructure of the overmolding material and its anisotropic behavior. In here, the local fiber orientation is strongly dependent on the part geometry, raw material constitutions and processing conditions but can be numerically simulated and implemented in the structural analysis by a multi-scale methodology [13,14]. However, deviations between the predicted mechanical behavior by the numerical simulations and the experimental results, especially for complex part geometries, are still a problem and can be attributed to imprecise mapping of the local fiber orientation of the overmolding material from the injection molding simulation to the structural analysis [14]. Additionally, the non-isothermal formation of the boundary between the TPC and the overmolding material, e.g., by simulation of the molecular dynamics at the interface, has to be considered in hybrid processes to reduce the error between the simulation and the real structural behavior [15,16].

Thus, a more advanced workflow by connection of the injection molding simulation, the material modelling and the structural analysis of the processed part has to be implemented for precise prediction of the mechanical behavior of hybrid injection molded short and continuous fiber-reinforced thermoplastic composite parts. However, the implementation of the local fiber orientations of the overmolding material from the injection molding simulation in the structural analysis is actually not a fully automated process, e.g., impaired by different mesh types. In result, underprediction or overprediction of the local stiffness and strength of the overmolding material depending upon the fiber orientation and direction of loading does occur. In this study, the numerical simulation of a hybrid injection molded continuous fiber-reinforced thermoplastic composite test structure was carried out by a new numerical workflow. This new workflow allows the automated implementation of the local fiber orientation from injection molding simulations to structural analysis by finite element modelling and therefore a more precise consideration of the local anisotropic mechanical behavior of the overmolding material including its hardening behavior. Validation of the predicted mechanical behavior of processed hybrid test structures under flexural loading was carried out by experimental analysis. Additionally, comparison of isotropic and anisotropic structural simulations was carried out to investigate prediction accuracy of the new workflow especially at higher deformations in the flexural tests.

## 2. Materials and Methods

### 2.1. Materials

#### 2.1.1. Continuous Fiber-Reinforced Thermoplastic Composites

TPC laminates made of unidirectional glass fiber-reinforced polypropylene tapes (PP/GF60-UD, Plytron GN 638T, Elekon, Luzern, Switzerland) were used for the experimental investigations. Important properties of the used tapes are shown in Table 1. The manufactured laminates consisted of 8 layers with a symmetrical and balanced  $0^\circ/90^\circ$ -lay-up ( $0^\circ, 90^\circ, 90^\circ, 0^\circ, 0^\circ, 90^\circ, 90^\circ, 0^\circ$ ). In result, TPC laminates with total dimensions of  $396 \text{ mm} \times 120 \text{ mm} \times 2 \text{ mm}$  were used as laminate inserts for the hybrid injection molding process.

**Table 1.** Properties of the PP/GF60-UD unidirectional glass fiber-reinforced polypropylene tapes used for manufacturing of TPC laminates as provided by the supplier.

Property	Unit	Value
Glass fiber mass content	wt%	60
(Ply) thickness	mm	0.25
Density	g/cm <sup>3</sup>	1.5
Tensile modulus E11	GPa	28
Tensile modulus E22	GPa	3.2
Tensile strength	MPa	720
Flexural modulus	GPa	21
Flexural strength	MPa	436

### 2.1.2. Short Fiber-Reinforced Thermoplastic Composites

Overmolding of the TPC laminates was carried out with a short glass fiber-reinforced polypropylene compound (PP/GF30, Hostacom G3 N01 L, Lyondell Basell, Rotterdam, Netherlands) to investigate the resulting mechanical properties of the hybrid injection molded test structures. The compound was used in pellet form with a fiber mass content of 30 wt% and was dried before injection molding at 80 °C for 4 h. Important properties of the overmolding material are shown in Table 2.

**Table 2.** Properties of the PP/GF30 short fiber-reinforced thermoplastic composite used for overmolding of TPCs as provided by the supplier.

Property	Unit	Value
Glass fiber mass content	wt%	30
Glass fiber length	mm	0.5
Density	g/cm <sup>3</sup>	1.14
Tensile modulus	GPa	6.5
Tensile strength	MPa	90
Flexural modulus	GPa	5.5
Flexural strength	MPa	120

## 2.2. Experimental Work

### 2.2.1. Production of Test Structures

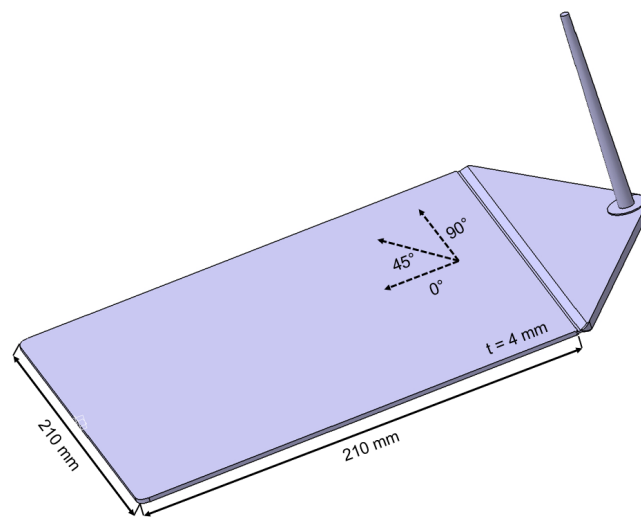
#### Injection Molding of Short Fiber-Reinforced Thermoplastic Composites

An industrial injection molding machine with a maximum clamping force of 200 t (KM200-1000C2, KraussMaffei, Munich, Germany) was used for the experimental processing tests and its influence to the anisotropic mechanical properties of the short glass fiber-reinforced thermoplastic (see Table 3). Thus, test plates with the dimensions of 210 mm × 210 mm × 4 mm were produced from the PP/GF30 compound with a melt temperature of 230 °C and a mold temperature of 40 °C. To investigate the influence of the flow profiles and the corresponding shear stresses on the resulting mechanical properties, the experiments were carried out by varying the volume flow rate between 25, 50 and 100 cm<sup>3</sup>/s. The subsequent analysis of the samples was carried out by means of fiber length and fiber orientation analysis as well as tensile testing of standard test specimens machined out in 0°, 45° and 90° related to the flow direction, as shown in Figure 1. In result, nine different sets of test specimens were analyzed regarding their mechanical properties. Labeling of those sets can be found in Table 3. Additionally, test structures with the geometry shown in Figure 2 were made of the hybrid injection molded thermoplastic composites for comparative experimental and numerical investigations.

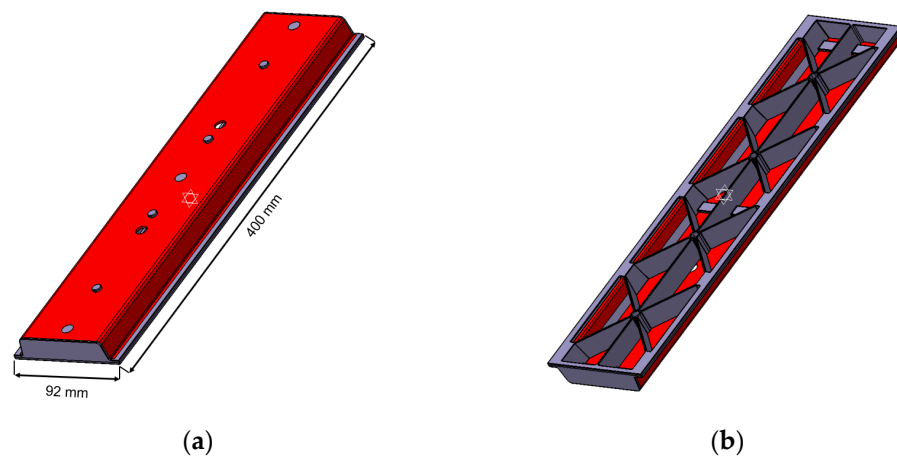


**Table 3.** Labeling of the analyzed test specimen of the PP/GF30 short fiber-reinforced thermoplastic composites and the corresponding volume flow rate and orientation related to flow direction due to injection molding and sample preparation from test plates, respectively.

Denomination	Volume Flow Rate [cm <sup>3</sup> /s]	Orientation Related to Flow Direction [°]
PP/GF30-100-0	100	0
PP/GF30-100-45	100	45
PP/GF30-100-90	100	90
PP/GF30-50-0	50	0
PP/GF30-50-45	50	45
PP/GF30-50-90	50	90
PP/GF30-25-0	25	0
PP/GF30-25-45	25	45
PP/GF30-25-90	25	90



**Figure 1.** Geometry of the injection molded test plates made of PP/GF30 short fiber-reinforced thermoplastic composite.



**Figure 2.** Geometry of the hybrid injection molded thermoplastic composite bending test structure with the PP/GF60 continuous fiber-reinforced thermoplastic composite in red and the PP/GF30 short fiber-reinforced thermoplastic composite in grey: (a) top and (b) bottom.

**Hybrid Injection Molding of Short and Continuous Fiber-Reinforced Thermoplastic Composites**

For the production of the hybrid injection molded short and continuous fiber-reinforced thermoplastic structures an industrial injection molding machine with a maximum clamping force of 200 t (KM200-1000C2, KraussMaffei, Munich, Germany) was used, additionally

equipped with an infrared heating station and automation robot-gripper system. The whole process had a cycle time of 120 s and consisted of the infrared heating of the TPC laminates to a temperature of 215 °C, the hot handling of the heated laminates and fixation in the mold by the robot and the subsequent thermoforming as well as overmolding with the short fiber-reinforced thermoplastic composite material (using melt temperature of 210 °C and a mold temperature of 45 °C). The volume flow rate during the injection step was set to 50 cm<sup>3</sup>/s and the central injection point of the complex hybrid structure was used to avoid any weld lines in the overmolded short fiber-reinforced composite material. A schematic depiction of the geometry of the produced hybrid structures is shown in Figure 3.



**Figure 3.** Experimental equipment used for fiber length analysis of the PP/GF30 short fiber-reinforced thermoplastic composite: (a) electric furnace and (b) photo scanner.

### 2.2.2. Morphological Analysis

#### Fiber Length Analysis of Short Fiber-Reinforced Thermoplastic Composites

The fiber length analysis of the test specimens was performed in two steps. First, the test specimens were pyrolyzed at 600 °C for 3 h in an electric furnace (LT 5/12, Nabatherm, Lilienthal, Germany) to separate the fibers from the matrix. Subsequently, the fibers were suspended in a water solution and then scanned with a photo scanner (Perfection V800 Dual Lens, Epson, Suwa, Nagano, Japan) to determine their fiber length distribution. The scanned images were analyzed using FIVER software to acquire the number of fibers and the length distribution for each sample.

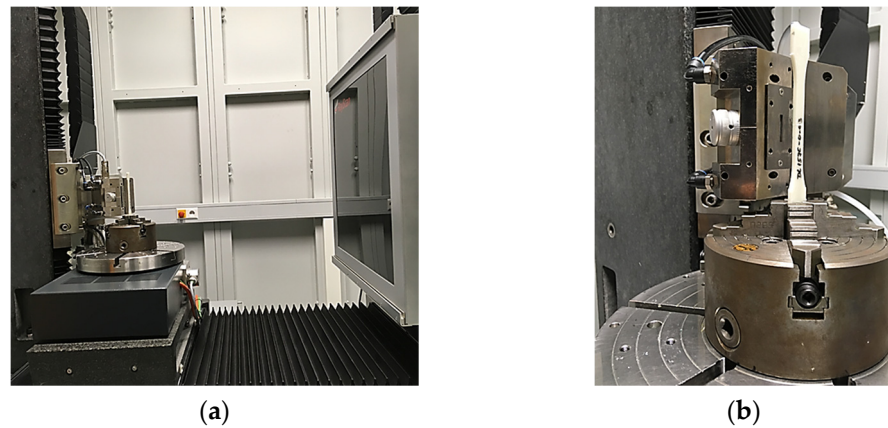
#### Fiber Orientation Analysis of Short Fiber-Reinforced Thermoplastic Composites

The fiber orientation analysis of the test specimens was carried out by computed tomography (CT). For this, each test specimen was clamped on the turntable of the CT system (RayScan 200E, RayScan Technologies GmbH, Meersburg, Germany) and X-ray projections were taken during a full circulation of 360°, using 600 projections per second with a voltage of 70 kV and a current of 130 µA (see Figure 4). The resulting 3D image data set was analyzed using VGStudio analysis software (VGStudio MAX 2.2, Volume Graphics GmbH, Heidelberg, Germany).

### 2.2.3. Mechanical Testing

#### Tensile Test of Short Fiber-Reinforced Thermoplastic Composites

Investigation of the anisotropic mechanical properties of the injection molded test plates of the PP/GF30 compound was carried out by tensile tests on machined out 1A test specimens according to ISO 527 at 24.5 °C with a universal test machine (Z050, Zwick Roell, Ulm, Germany) as shown in Figure 5. The measurement of the tensile modulus was carried out at 1 mm/min test speed, while the tensile strength was tested at 10 mm/min. The test specimens were machined out from the injection molded test plates in 0°, 45° and 90° related to the flow direction.



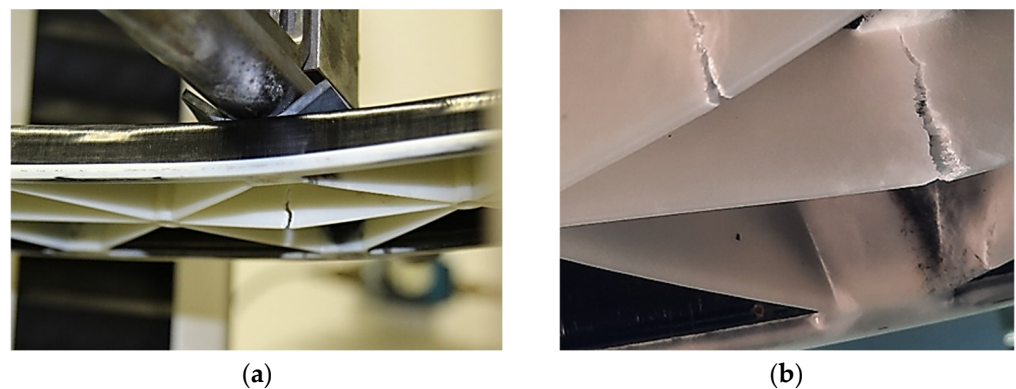
**Figure 4.** Experimental set up used for fiber orientation analysis of the PP/GF30 short fiber-reinforced thermoplastic composite: (a) computed tomography system and (b) test specimen clamped on turntable.



**Figure 5.** Tensile test according to ISO 527 on machined out standard test specimens of the PP/GF30 injection molded short fiber-reinforced thermoplastic composite.

#### Flexural Test of Hybrid Injection Molded Thermoplastic Composites

Three-point flexural tests of the hybrid injection molded thermoplastic composites were performed according to DIN EN ISO 14125, recommended for bending of continuous fiber-reinforced plastics, at 22.8 °C (room temperature, RT) with a universal testing machine (Z050, Zwick Roell, Ulm, Germany). A support spacing of 360 mm was used for the tests, while the supports had a diameter of 30 mm. The continuous deformation speed of the tests was set to 2 mm/min and the test was carried out until failure of the structure occurred. As can be seen in Figure 6, the failure was located in the rip area consisting of short fiber-reinforced thermoplastic composite overmolding material. The force of the machine was recorded as well as the displacement by extensometer under the middle of the specimen (center deflection).



**Figure 6.** Three-point flexural test of the PP/GF60 and PP/GF30 hybrid injection molded thermo-plastic composite test structure: (a) test set-up and (b) failure of ribs as a result of the bending load.

### 2.3. Numerical Simulations

#### 2.3.1. Theoretical Background

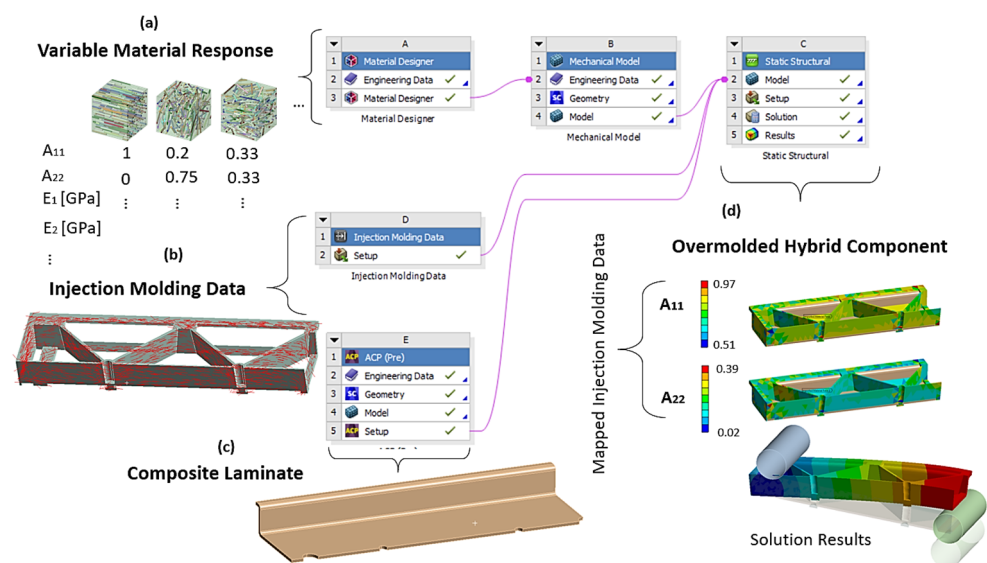
Describing the correct mechanical behavior of hybrid thermoplastic composites through finite element modeling simulations has been traditionally a challenge because of the complex anisotropic, inhomogeneous and multiscale nature of these materials. Hybrid TPCs combine unidirectional or woven fabrics made of continuous fibers and thermoplastic matrix (stacked, heated and compressed before to laminates) with a short fiber reinforced thermoplastic material via injection molding (overmolding). The resulting TPC hybrid component is a continuous structure that has the complex and three-dimensional shape of an injection molded part and the structural backbone of a continuous composite laminate.

The most common approach in finite element simulations of composite materials is based on macroscale phenomenological modelling, where layered shells, layered-solids, stacked solid elements and stacked or layered continuum shells are used to represent the laminate. The specific material properties of each laminate typically are obtained through experimental investigations and the application of the classical laminate theory [17]. However, such a phenomenological modelling technique has a limited applicability only to continuous fiber-reinforced composites with anisotropic but local nearly homogenous properties. Thus, multiscale techniques are required to capture the complex microstructures in hybrid injection molded short and continuous fiber-reinforced thermoplastic composites [18,19]. Nevertheless, multiscale techniques have traditionally encountered a limited adoption in modeling of the mechanical behavior of composites because of the large requirements in terms of computing capacity for such simulations. Thus, a variety of acceleration techniques have been developed over the years to solve the computing capacity issues related to the solution of finite element static problems involving two-scale homogenization approaches (FE2 analyses) [20], among them reduced order models [21,22], the (non-uniform) transformation field analysis [23], response surface models [24,25] and machine learning approaches such as neural networks [26,27]. However, while these homogenization techniques can be used to describe the material behavior dependent on the specific local microstructure, further modeling and numerical challenges arise after the onset of failure (e.g., cracking, fiber bridging, and delamination mechanisms) occurring in the composite component at higher deformations [28–30]. Capturing the details of such nonlinear post failure behavior is still the subject of different research investigations and is neglected in this work.

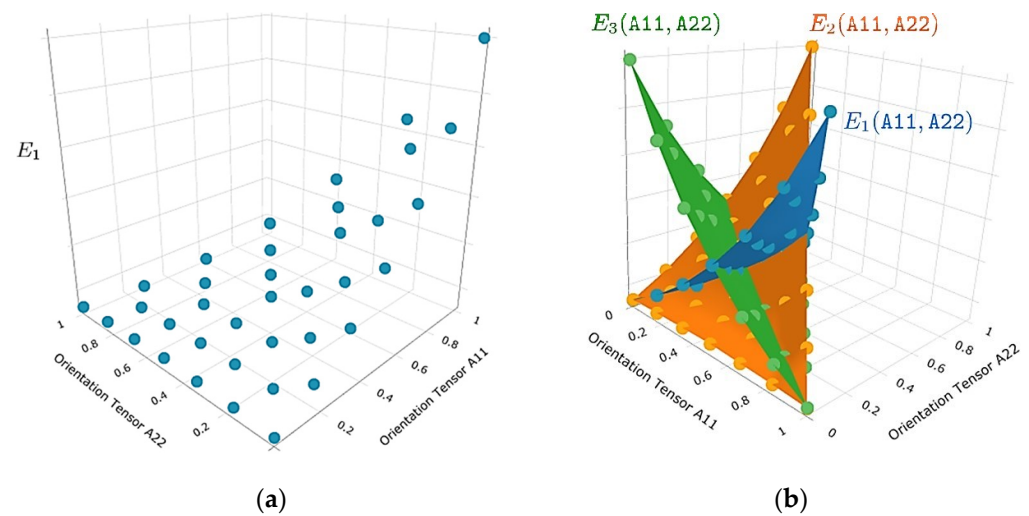
#### 2.3.2. Overview of the Workflow

The numerical workflow of the used multiscale approach for hybrid composites is shown in Figure 7. The relevant elastic properties and the mechanical behavior of continuous fiber-reinforced laminates were determined experimentally. The tool Material Designer (MD) in ANSYS Workbench (ANSYS 2021R1, Ansys Inc., Canonsburg, PA, USA) was used uniquely for capturing the material response of the short fiber-reinforced overmolding

material of the hybrid composite component. Within MD, for a number of sample orientations, an effective elastic-plastic model was derived by a mean-field homogenization method based on the Mori-Tanaka formulation [31]. Considering symmetry arguments, the fiber orientation tensor was reduced to a triangle in the 2-dimensional space given by the eigenvalues of the orientation tensor, as shown in Figure 8. Then, linear interpolation on the fiber orientation triangle was used to compute the elastic-plastic properties for each imported fiber orientation state (elastic moduli and Hill’s yield strengths of the plastic response for the material directions in tensorial listing). In the analysis carried on for this work, the combination of the Mori-Tanaka method with orientations averaging based on the closure approximation by Cintra and Tucker [32] were used for the derivation of elastic properties. For calculation of the plastic response, an orientation-dependent anisotropic Hill yield criterion was combined with an isotropic hardening model following the empirical exponential model suggested by Voce and anisotropic yield surface [33,34]. The needed stress-strain values were derived from uniaxial tension experiments with two types of test specimens: in flow direction and also perpendicular to the flow direction from the injection molded plates of the short fiber-reinforced composite material used for overmolding. The fiber orientation field of these test specimens were obtained numerically by injection molding simulations. In result, two test curves consisting of the uniaxial true stress versus true plastic strain, from tensile specimens cut out flow direction ( $0^\circ$ ) and perpendicular to it ( $90^\circ$ ), were obtained and subsequently fitted to determine the non-linear isotropic hardening model parameters of the short fiber-reinforced composite material. This variable material response as a function of the fiber orientations was then combined with the imported local fiber orientation in each element from the injection molding simulation and transferred to the mechanical solver.



**Figure 7.** Workflow of the multiscale model in ANSYS Mechanical using the Material Designer (MD): (a) creation of the material response as a function of the microstructure by an interpolation grid with attached elastic and plastic parameters, (b) import of injection molding data, i.e., the second order orientations tensors from the injection molding software, (c) modeling of the ply-based continuous fiber-reinforced TPC laminate and (d) mapping of the injection molding data to the short fiber-reinforced parts and bonding to the continuous fiber-reinforced laminate.



**Figure 8.** Visualization of the properties of generated variable material response with respect to the axes of principal orientations: (a) interpolation grid for  $E_1$  and (b) interpolation grids and interpolation surfaces for  $E_1$ ,  $E_2$  and  $E_3$  as functions of principal orientations  $A_{11}$  and  $A_{22}$ . The user is given the possibility to generate analogous plots for the other 6 homogenized elastic parameters of the orthotropic behavior in the coordinate system defined by the principal axes of 2nd order orientation tensors.

### 2.3.3. Numerical Simulation of Injection Molding

The numerical simulations for the injection molding of the test plates with the PP/GF30 compound as well as the hybrid injection molding parts in combination with TPC laminate inserts were carried out using Moldex3D software (Moldex3D 2021R1OR, CoreTech System Co., Ltd., Zhubei, Taiwan). Here, based on the gate and cooling system as well as the mold cavity geometry, a model with a volume mesh was built up. The simulation parameters were derived from the processing parameters of the real injection molding processes. The thermodynamic and rheological material parameters of the examined PP/GF30 short fiber-reinforced thermoplastic composite were taken from the Moldex3D database.

The simulations of the injection molding process with a flow speed of  $50 \text{ cm}^3/\text{s}$  were evaluated with regard to the resulting fiber orientation and length depending on the simulation parameters. The fiber orientation corresponds to the distribution of the fiber orientation vector of the plastic melt at the end of the packing step and can be seen in Figure 9 for the hybrid injection molded structure. In here, a value of 0.33 means that the orientation of the fibers is random and a value of 1 means that the fibers are 100% oriented in the flow direction. The obtained data of the hybrid injection molding simulation was imported into ANSYS Workbench (ANSYS 2021R1, Ansys Inc., Canonsburg, PA, USA) for structural analysis. Additionally, experimental validation of the simulated local fiber length and orientation for the test plates was carried out.

### 2.3.4. Numerical Simulation of Flexural Test

The numerical simulation of the flexural test of the hybrid injection molded thermoplastic composite beam was carried out within ANSYS workbench 2021R1 (ANSYS 2021R1, Ansys Inc., Canonsburg, PA, USA) as a static structural simulation. The part geometry and mesh were implemented as described in the workflow of Figure 7. A proper mesh was generated by using volume elements of an edge length of 2 mm. Elements with a linear regression function were used and the mesh size and elements were checked by convergence study. In general, two types of homogenizations for material are possible, a finite element representative elementary volume model or using a mean field Mori-Tanaka analytical model [31]. In this study the analytical model was used. Therefore, the engineering data of the reinforcing fibers and of the matrix polymer was added separately in the

material designer. Here, the different material properties of the polymer matrix and the reinforcing fibers were defined by directly specifying orthotropic elastic material values for both phases. A fiber volume fraction of 13.5% and an aspect ratio of 23.5 were defined for the short fiber-reinforced overmolding material. In the next step, the master curves of the tensile tests of the short fiber-reinforced thermoplastic composites were added to the material designer to define their nonlinear isotropic hardening behavior by curve fitting according to the Hill plasticity model (see Figure 10). Therefore, the experimental data of true stress and plastic strain were implemented. The final material parameters used for the material model definition are shown in Table 4.

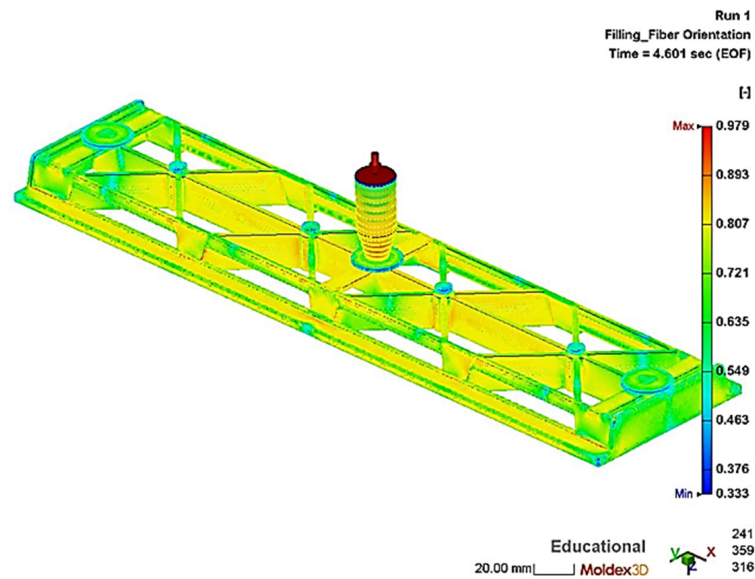


Figure 9. Simulated fiber orientation of the PP/GF30 short fiber-reinforced thermoplastic composite overmolding material in the hybrid test structure.

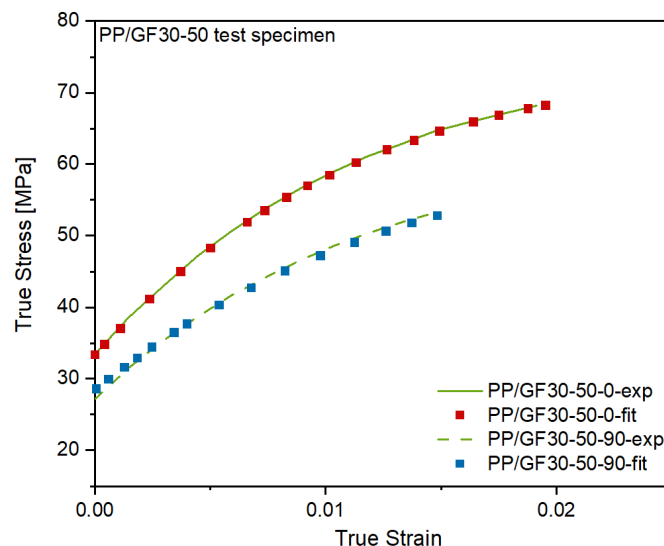
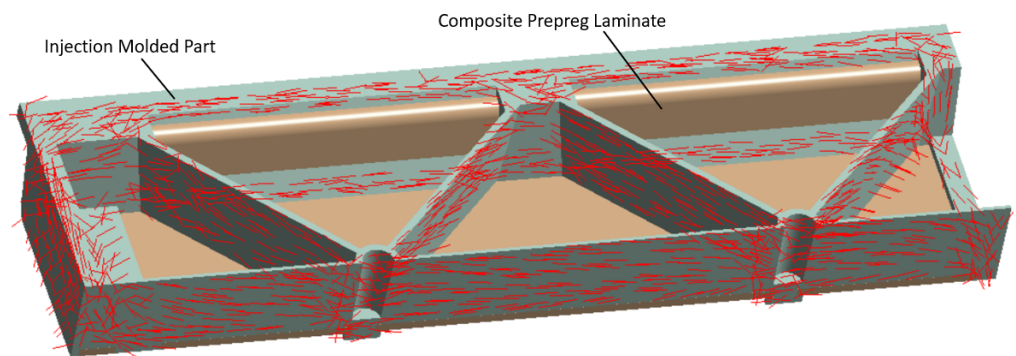


Figure 10. Experimental and fitted stress-strain-curves of the PP/GF30 short fiber-reinforced thermoplastic composite in flow direction and perpendicular to it.

**Table 4.** Numerical simulation input parameters of the PP/GF30 short fiber-reinforced thermoplastic composite.

Property	Unit	Value	Origin
Tensile modulus of matrix (PP)	GPa	1.4	supplier
Tensile modulus of reinforcing fiber (GF)	GPa	73	supplier
Fiber volume content	%	13.5	pyrolysis
Fiber aspect ratio	-	23.5	fiber length analysis
Fiber orientation component A11	-	0.61	CT analysis
Fiber orientation component A22	-	0.27	CT analysis
Yield strength $\sigma_0$	MPa	20.9	ANSYS
Hardening law parameter $R_0$	-	313.4	ANSYS
Hardening law parameter $R_{\infty}$	-	22.6	ANSYS
Hardening law parameter b	-	245.2	ANSYS

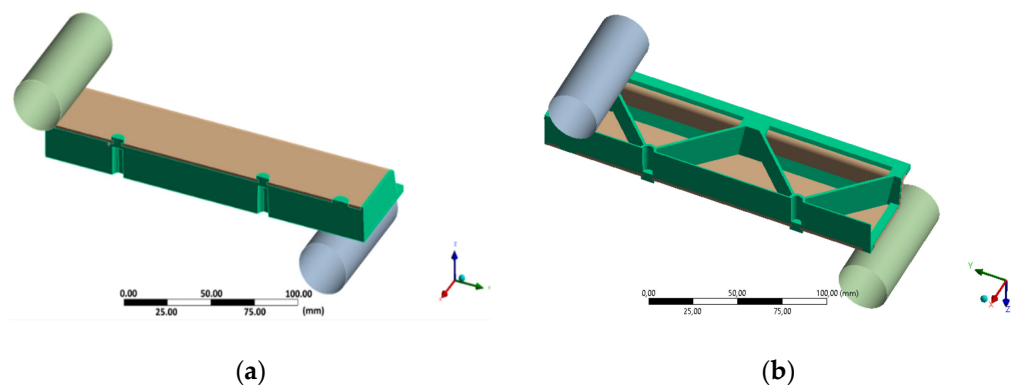
After this step, the material designer was connected to the engineering data of the static structural analysis. In this work, the following two types of data during the mapping process onto the mesh of the short fiber reinforced plastic part were considered: the principal fiber directions from the injection molding simulations as shown in Figure 11 and the two largest eigenvalues of the fiber orientation tensor. Additionally, local variation of the nominal fiber volume fraction and the presence of residual stresses can be considered but were neglected here. The short fiber-reinforced thermoplastic composite part was then combined with the continuous fiber-reinforced laminate using contact elements to simulate a perfect bonding interface. A quarter model of the hybrid composite test structure in a three-point flexural test configuration is shown in Figure 12. In here, the injection molded short fiber-reinforced thermoplastic area is shown in green and the continuous fiber-reinforced thermoplastic in brown. The following displacements constraints were applied to the FE model: the support is imposed with no displacement as well as no rotations and the punch with a 25 mm ramped displacement in y direction.



**Figure 11.** Main fiber directions of the PP/GF30 short fiber-reinforced thermoplastic composite mapped to the meshed geometry of the test bending structure using the orientation tensor output from the injection molding simulation. The injection molded part is directly bonded to the continuous fiber-reinforced laminate using contact elements.

Since the described structural model is based on an implicit calculation and it is limited for a quasi-static load case situation. The prediction of the mechanical behavior of the test structures is therefore only as good as the material model is precise and valid. Deviations between the experiment and the simulation of the test structures mainly arise because the data for the material model has been determined on standard tensile test specimens and it is assumed that these properties and hardening behavior is also found in the real test structure.





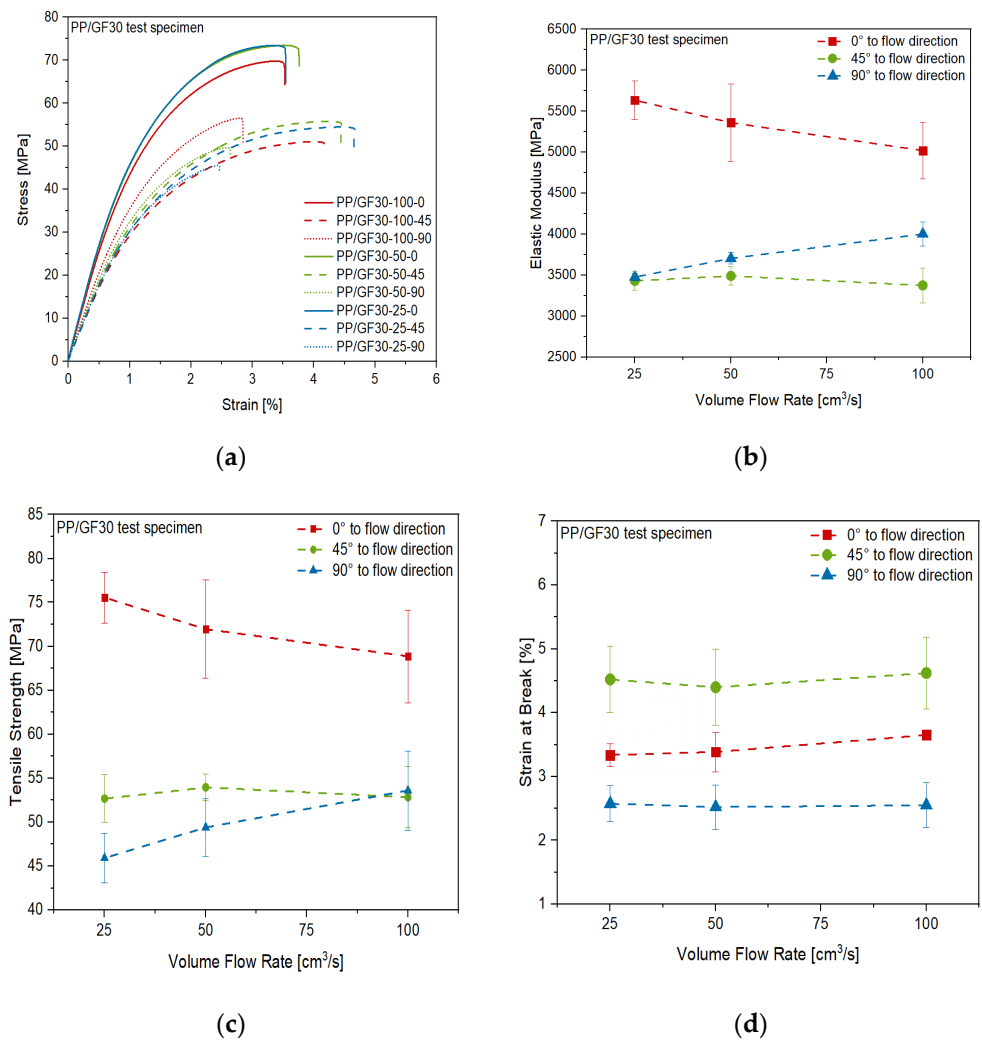
**Figure 12.** Quarter model of the three-point flexural test of the hybrid injection molded thermoplastic composite test structure. The injection molded PP/GF30 short fiber-reinforced thermoplastic composite is shown in green and the PP/GF60 continuous fiber-reinforced thermoplastic composite in brown: (a) top view and (b) bottom view.

### 3. Results and Discussion

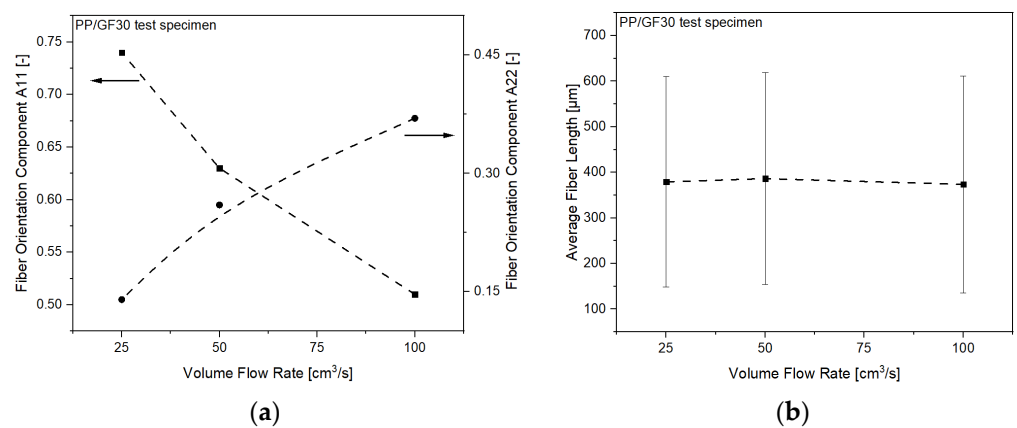
#### 3.1. Anisotropy of Injection Molded Short Fiber-Reinforced Thermoplastic Composites

The results of the tensile tests of the PP/GF30 short fiber-reinforced thermoplastic composite material are shown in Figure 13. Anisotropic and inhomogeneous behavior of the material was found, depending on the volume flow rate and direction during the injection molding process of the test plates. This can be seen in the stress-strain-curves of the test specimen cut out in the different directions (Figure 13a). The highest stiffness and strength were measured in flow direction, while these properties are decreasing with volume flow rate, which can be seen in Figures 13b,c. It is also shown that the opposite trend was found perpendicular to the flow direction, while no significant influence of the flow rate on the stiffness and strength in  $45^\circ$  to the flow direction was found. However, in this direction the highest strain at break was measured, without any significant influence of the flow rate, as shown in Figure 13d. These trends correlate to the flow rate dependent short fiber orientation mechanisms during injection molding as published by Bay and Tucker III [35,36]. As reported by Oumer and Mamat [37], at low flow rates the short fibers are more oriented in the flow direction and therefore the stiffness and strength of the composite are higher in this direction. Given the results shown in Figure 13, the same mechanism has to be stated for the PP/GF30 short fiber-reinforced composite material used in this study.

To validate this effect, CT measurements of the fiber orientation in the processed PP/GF30 short fiber-reinforced thermoplastic composite test samples have been analyzed. The measured fiber orientation components A11 and A22 of the composites are shown in Figure 14a. It can be seen that the A11 orientation component is decreasing with increasing flow rate, while the opposite trend is shown for the A22 component. This clearly indicates the flow rate dependent fiber orientation and resulting anisotropic mechanical behavior. As reported by Huang and Lai [38], this can be attributed to a flow-fiber coupling effect, diminishing the flow direction orientation tensor component A11 and simultaneously enhancing the cross-flow orientation tensor component A22. However, no influence of the flow rate on the average fiber length was found, as shown in Figure 14b. Numerical simulation of such fiber orientation mechanisms has been studied and significant theoretical orientation models have been developed, including RSC (Reduced Strain Closure), ARD (Anisotropic Rotary Diffusion), and iARD-RPR (improved ARD and Retarding Principal Rate) [39–41]. They have been widely applied in commercial injection molding simulation software such as Moldex3D or Moldflow, with good agreement between the predictions and the experimental data obtained.



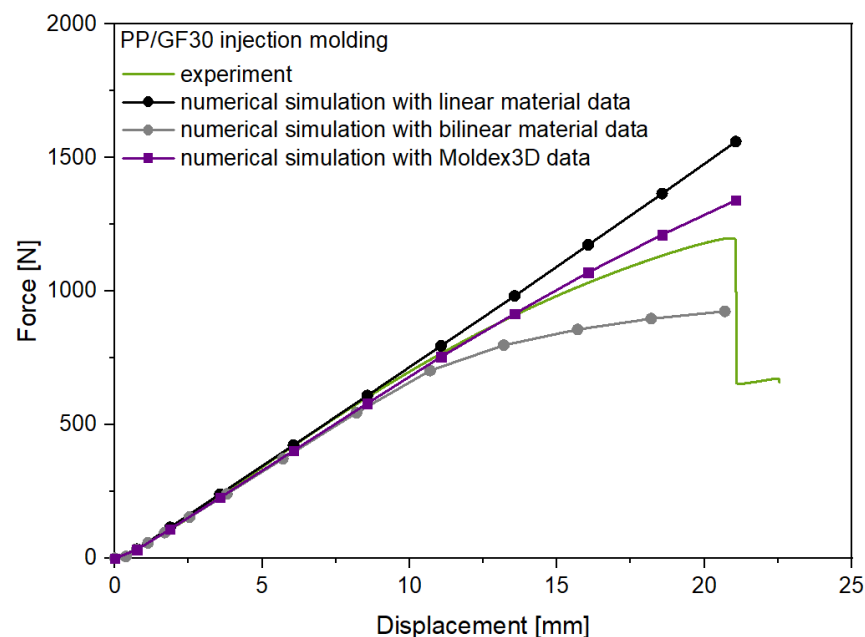
**Figure 13.** Anisotropic mechanical properties of the PP/GF30 short fiber-reinforced thermoplastic composite as a function of volume flow rate during injection molding: (a) stress-strain diagram from tensile test, (b) elastic modulus, (c) tensile strength and (d) strain at break.



**Figure 14.** Morphological properties of the PP/GF30 short fiber-reinforced thermoplastic composite as a function of volume flow rate: (a) fiber orientation components A11 and A22 as experimentally measured by CT and (b) average fiber length as experimentally measured by fiber length analysis.

### 3.2. Numerical Simulation and Experimental Validation of Injection Molding of Short Fiber-Reinforced Thermoplastic Composites

The experimental and numerical results for the flexural test of the PP/GF30 short fiber-reinforced thermoplastic composite test structure are shown in Figure 15. As can be seen, the experimental force-displacement curve is showing nonlinear behavior after a displacement of 10 mm. These experimental results are compared to the three different structural analysis carried out with linear, bilinear and injection molding simulation data (Moldex3D) to investigate the effect of the precise consideration of the anisotropic mechanical behavior. For the structural analysis with the linear and bilinear material approach no fiber orientation information were added from the injection molding simulation.



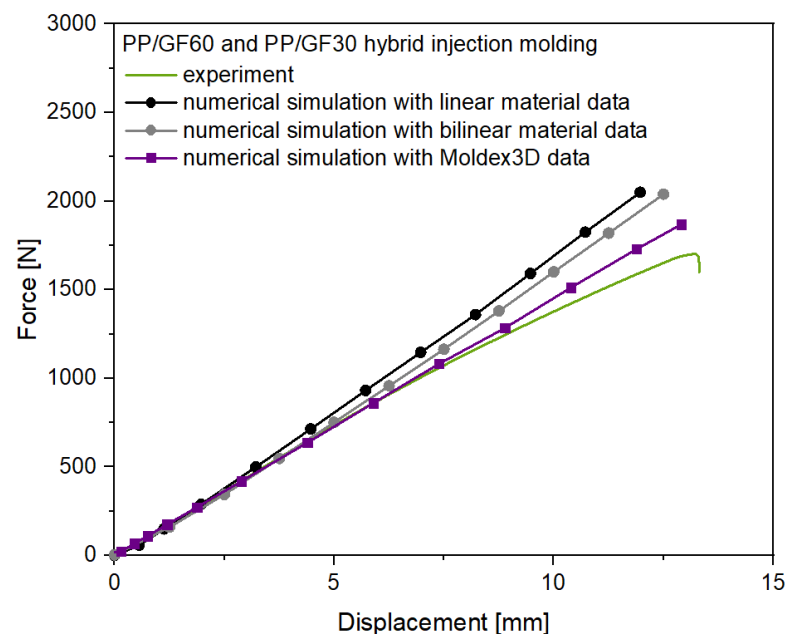
**Figure 15.** Experimental and numerical results for the flexural test of the PP/GF30 short fiber-reinforced thermoplastic composites test structure.

In result, for all three material models the initial stiffness of the injection molded short fiber-reinforced composite test structure was predicted well. However, the nonlinear displacement behavior was not predicted correctly by the approaches with the linear and bilinear material models, leading to an overprediction of the flexural strength by the linear model with a deviation of 31% and an underprediction with a deviation of 21% by the bilinear model. In contrast, the simulated force-displacement curve considering the input data from the injection molding simulation fits the experimental data significant more precisely but also not completely until failure at 21 mm displacement, leading to an overprediction of the flexural strength with a deviation of 13%. However, these findings demonstrate the importance of consideration of the process dependent anisotropic and local inhomogeneous mechanical behavior of short fiber-reinforced thermoplastic composites in the structural analysis of injection molded parts. This has also been reported for other short fiber-reinforced thermoplastic composite materials using specific anisotropic simulation methodologies. Gruber and Wartzack [42] could improve the precision of the absolute displacement prediction of short fiber-reinforced composite structures under flexural loading by usage of an integrative simulation approach similar to the numerical workflow in this study. Ogierman and Kokot [43] showed in a comparative analysis of a short fiber-reinforced composite with different fiber orientations that simplification of the material model of injection-molded parts and considering it as isotropic corresponding to the random orientation of the fibers or orthotropic corresponding to unidirectional orientation can lead to unacceptable errors in determining the natural frequencies, displacement and

stresses. This was also reported by Vlach and Stekly [44], who showed that the prediction deviation of the longitudinal modulus and modal frequencies in complex shaped injection molded parts made of short fiber-reinforced composites can be significantly reduced by consideration of the anisotropic material behavior.

### 3.3. Numerical Simulation and Experimental Validation of Flexural Test of Hybrid Injection Molded Thermoplastic Composites

The experimental and numerical results for the flexural test of the hybrid PP/GF60 continuous TPC and PP/GF30 short fiber-reinforced thermoplastic composite test structure are shown in Figure 16. In comparison to the short fiber-reinforced test structure without the continuous fiber-reinforced laminate the stiffness of the hybrid structure prevents a stronger nonlinear behavior and shows only little yielding effects, leading to an experimental curve nearly linear until failure. Additionally, the flexural strength of the hybrid test structure was increased in comparison to the short fiber-reinforced thermoplastic composites test structure. However, to investigate the influence of the anisotropic mechanical behavior of the short fiber-reinforced overmolding material, again three different numerical simulation were made. The approaches with a linear and additionally with a bilinear material model and with no information on fiber orientation from the injection molding simulation did not predict the deformation behavior of the hybrid test structure correctly, showing significant deviations after 5 mm displacement. Both approaches lead to an overprediction of the flexural strength by 21% and 20%, respectively. This can be explained with the dominant stiffness of the PP/GF60 laminate in the test structure. Implementation of the local fiber orientations from the injection molding simulation and using a variable short fiber-reinforced composite material model did significantly improve the accuracy of the simulation with a resulting overprediction of the flexural strength 9%. However, when the hardening behavior of the short fiber-reinforced composite material is considered the simulated force-displacement curve fits the experimental data but also not completely until failure at 13 mm displacement.



**Figure 16.** Experimental and numerical results for the flexural test of the PP/GF60 and PP/GF30 hybrid injection molded thermoplastic composite test structure.

These findings show that the anisotropic and local inhomogeneous mechanical behavior of the short fiber-reinforced thermoplastic overmolding material in hybrid structures with continuous fiber-reinforced composites must be considered to predict the mechanical behavior, especially at higher flexural stresses. Comparable findings have been reported

by Ding et al. [45], where the overprediction of the flexural strength was attributed to the brittleness of the composite structure, leading to penetration of the material by the load head during the test, and the delamination failure at the interfaces of the TPC material. Both effects have to be considered for the experimental results of the flexural test with the hybrid test structure in this study as well, similarly leading to an overprediction of the flexural strength by the numerical simulations. However, in comparison to the findings of Zschehyge et al. [46], who focused on the damage modeling of the TPC part of a comparable hybrid structure and considered isotropic material modeling of the overmolding part, the numerical simulation of the flexural behavior in this study are more precise. Additionally, the deviations of the simulation to the experimental results at higher displacements can be addressed to the fact that the hardening curves of the PP/GF30 short fiber-reinforced composite overmolding material were determined with the results of the tensile tests of the injection molded test plates. Here, especially the different cooling rates during processing can lead to a different crystallinity and hardening behavior in comparison to the test structure of the flexural tests [47].

#### 4. Conclusions

Short fiber-reinforced thermoplastic composites processed by injection molding show anisotropic mechanical behavior, which is dependent on the local fiber orientation resulting from part design and process parameters. As shown in this study for PP/GF30 test plates, the volume flow rate during injection molding has a significant influence on the fiber orientation of such short fiber-reinforced composites with a higher orientation in flow direction and at lower volume flow rates. This results in higher stiffness and strength values in the flow direction at lower volume flow rates, causing a process dependent anisotropic mechanical behavior. Consideration of this anisotropic and local inhomogeneous mechanical behavior is important for the precise prediction of the deformation and failure behavior of injection molded parts by numerical simulations. This is shown for the deformation behavior of a PP/GF30 short fiber-reinforced test structure under flexural load with a new numerical workflow implementing the local fiber orientation as provided by injection molding simulation. In result, the deviation of the numerically predicted and experimentally measured flexural strength could be reduced from 31% to 13%. Thus, it has also been shown for a PP/GF60 and PP/GF30 hybrid injection molded thermoplastic composite test structure that consideration of the anisotropic and local inhomogeneous mechanical behavior of the overmolding material is as well crucial for prediction of the deformation behavior of such hybrid short and continuous fiber-reinforced thermoplastic composites under flexural load. The deviation of the numerically predicted and experimentally measured flexural strength could be reduced from 21% to 9% in this case. Although the continuous fiber-reinforced composites dominate the mechanical behavior of the hybrid structure at low displacement, the critical failure is prone to be initiated by crack propagation in the short fiber-reinforced overmolding material due to the higher flexural stresses at higher displacements and lower strength of this material.

**Author Contributions:** Conceptualization, P.H. and M.J.; methodology, P.H. and M.J.; software, M.J. and D.L.; validation, A.H. and S.G.; formal analysis, P.H.; investigation, P.H.; data curation, P.H.; writing—original draft preparation, P.H. and M.J.; writing—review and editing, R.S. and M.Z.; visualization, P.H.; supervision, P.H.; project administration, P.H.; funding acquisition, P.H. All authors have read and agreed to the published version of the manuscript.

**Funding:** This research was funded by Investitionsbank Sachsen-Anhalt, grant number 1704/00007.

**Data Availability Statement:** All data included in this study are available upon request by contact with the corresponding author.

**Conflicts of Interest:** The authors declare no conflict of interest.

## References

1. Minchenkov, K.; Vedemikov, A.; Safonov, A.; Akhatov, I. Thermoplastic pultrusion: A review. *Polymers* **2021**, *13*, 180. [[CrossRef](#)]
2. Burkhart, A.; Cramer, D. Continuous fibre-reinforced thermoplastic tailored blanks. *JEC Compos. Mag.* **2006**, *43/22*, 41–43.
3. Cao, Z.; Guo, D.; Fu, H.; Han, Z. Mechanical simulation of thermoplastic composite fiber variable-angle laminates. *Materials* **2020**, *13*, 3374. [[CrossRef](#)]
4. Carrera, E. Theories and finite elements for multi-layered anisotropic, composites plates and shells. *Arch. Comput. Methods Eng.* **2002**, *9*, 87–140. [[CrossRef](#)]
5. Tabiei, A.; Zhang, W. Composite laminate delamination, simulation and experiment: A review of recent development. *Appl. Mech. Rev.* **2018**, *70*, 030801. [[CrossRef](#)]
6. Zschoyge, M.; Gude, M.; Boehm, R.; Hufenbach, W. Strain rate dependent deformation and damage behaviour of textile-reinforced thermoplastic composites. In Proceedings of the 17th European Conference on Composite Materials, Munich, Germany, 26–30 June 2016.
7. Kropka, M.; Muehlbacher, M.; Neumeier, T.; Altstaedt, V. From UD-tape to Final Part—A Comprehensive Approach Towards Thermoplastic Composites. *Procedia CIRP* **2017**, *66*, 96–100. [[CrossRef](#)]
8. Bonefeld, D.; Obermann, C. Spriform: A hybrid technique for serial production of 3d parts of continuous fiber reinforced thermoplastics. In Proceedings of the ECCM15-15TH European Conference on Composite Materials, Venice, Italy, 24–28 June 2012.
9. Cherouat, A.; Borouchaki, H. Present state of the art of composite fabric forming: Geometrical and mechanical approaches. *Materials* **2009**, *2*, 1835–1857. [[CrossRef](#)]
10. Kroll, L.; Meyer, M.; Nendel, W.; Schormair, M. Highly rigid assembled composite structures with continuous fiber-reinforced thermoplastics for automotive applications. *Procedia Manuf.* **2019**, *33*, 224–231. [[CrossRef](#)]
11. Bussetta, P.; Correia, N. Numerical forming of continuous fibre reinforced composite material: A review. *Compos. Part A Appl. Sci. Manuf.* **2018**, *113*, 12–31. [[CrossRef](#)]
12. Müzel, S.D.; Bonhin, E.P.; Guimaraes, N.M.; Guidi, E.S. Application of the finite element method in the analysis of composite materials: A review. *Polymers* **2020**, *12*, 818. [[CrossRef](#)]
13. Adam, L.; Assaker, R. Integrated nonlinear multi-scale Material Modelling of Fiber Reinforced Plastics with DIGIMAT: Application to Short and Continuous Fiber Composite. In Proceedings of the 11th World Congress on Computational Mechanics, Barcelona, Spain, 20–25 July 2014.
14. Reclusado, C.A.T.; Nagasawa, S. Modeling of fiber-reinforced plastics taking into account the manufacturing process. In Proceedings of the ECCOMAS Congress, Crete Island, Greece, 5–10 June 2016.
15. Chen, L.; Deng, T.; Zhuo, H.; Huang, Z.; Peng, X.; Zhuo, H. A numerical simulation method for the one-step compression-stamping process of continuous fiber reinforced thermoplastic composites. *Polymers* **2021**, *13*, 3237. [[CrossRef](#)] [[PubMed](#)]
16. Jiang, B.; Zhang, M.; Fu, L.; Zhuo, M.; Zhai, Z. Molecular dynamics simulation on the interfacial behavior of over-molded hybrid fiber reinforced thermoplastic composites. *Polymers* **2020**, *12*, 1270. [[CrossRef](#)]
17. Matter, M.; Gmür, T.; Cugnoni, J.; Schorderet, A. Numerical-experimental identification of the elastic and damping properties in composite plates. *Compos. Struct.* **2009**, *90*, 180–187. [[CrossRef](#)]
18. Mortazavian, S.; Fatemi, A. Fatigue behavior and modelling of short fiber reinforced polymer composites: A literature review. *Int. J. Fatigue* **2015**, *70*, 297–321. [[CrossRef](#)]
19. Antin, K.-N.; Laukkanen, A.; Andersson, T.; Smyl, D.; Vilaca, P. A multiscale modelling approach for estimating the effect of defects in unidirectional carbon fiber reinforced polymer composites. *Materials* **2019**, *12*, 1885. [[CrossRef](#)] [[PubMed](#)]
20. Andrä, H.; Kabel, M.; Staub, S.; Krizikalla, F.; Schulz, V. Numerische Homogenisierung für viskoelastische Faserverbundwerkstoffe. *NAFEMS Online-Mag.* **2012**, *21*, 70–83.
21. Yvonnet, J.; He, Q.C. The reduced model multiscale method (R3M) for the non-linear homogenization of hyperelastic media at finite strains. *J. Comput. Phys.* **2007**, *223*, 341–368. [[CrossRef](#)]
22. Bhattarjee, S.; Matous, K. A nonlinear manifold-based reduced order model for multiscale analysis of heterogeneous hyperelastic materials. *J. Comput. Phys.* **2016**, *313*, 635–653. [[CrossRef](#)]
23. Fritzen, F.; Leuschner, M. Reduced basis hybrid computational homogenization based on a mixed incremental formulation. *Comput. Methods Appl. Mech. Eng.* **2013**, *260*, 143–154. [[CrossRef](#)]
24. Temizer, I.; Wriggers, P. An adaptive method for homogenization in orthotropic nonlinear elasticity. *Comput. Methods Appl. Mech. Eng.* **2007**, *35–36*, 3409–3423. [[CrossRef](#)]
25. Köbler, J.; Schneider, M.; Ospald, F.; Andrä, H.; Müller, R. Fiber orientation interpolation for the multiscale analysis of short fiber reinforced composite parts. *Comput. Mech.* **2018**, *61*, 729–750. [[CrossRef](#)]
26. Furukawa, T.; Yagawa, G. Implicit constitutive modelling for viscoplasticity using neural networks. *Int. J. Numer. Methods Eng.* **1998**, *43*, 195–219. [[CrossRef](#)]
27. Hürkamp, A.; Gellrich, S.; Ossowski, T.; Beuscher, J.; Thiede, S.; Herrmann, C.; Dröder, K. Combining simulation and machine learning as digital twin for the manufacturing of overmolded thermoplastic composites. *J. Manuf. Mater. Process.* **2020**, *4*, 92. [[CrossRef](#)]
28. Mortazavian, S.; Fatemi, A. Effects of fiber orientation and anisotropy on tensile strength and elastic modulus of short fiber reinforced polymer composites. *Compos. Part B Eng.* **2015**, *72*, 116–129. [[CrossRef](#)]

29. Hartley, W.D.; McCann, J.; Davis, S.; Hocker, T.; Bobba, S.; Verghese, N.; Bajaj, D.; Yu, H.Z.; Dillard, D.A. Fracture characterization of overmold composite adhesion. *J. Thermoplast. Compos. Mater.* **2020**, *33*, 1–21. [[CrossRef](#)]
30. Russo, A.; Zarelli, M.; Sellitto, A.; Riccio, A. Fiber bridging induced toughening effects on the delamination behavior of composite stiffened panels under bending loading: A numerical/experimental study. *Materials* **2019**, *12*, 2407. [[CrossRef](#)]
31. Lee, D. Local anisotropy analysis based on the Mori-Tanaka model for multiphase composites with fiber length and orientation distributions. *Compos. Part B Eng.* **2018**, *148*, 227–234. [[CrossRef](#)]
32. Cintra, J.S.; Tucker, C.L. Orthotropic closure approximations for flow-induced fiber orientation. *J. Rheol.* **1995**, *39*, 1095–1122. [[CrossRef](#)]
33. Aretz, H. A simple isotropic-distortional hardening model and its application on elastic-plastic analysis of localized necking in orthotropic sheet metals. *Int. J. Plast.* **2008**, *24*, 1457–1480. [[CrossRef](#)]
34. Borges, M.F.; Antunes, F.V.; Prates, P.A.; Branco, R. A numerical study of the effect of isotropic hardening parameters on mode I fatigue crack growth. *Metals* **2020**, *10*, 177. [[CrossRef](#)]
35. Bay, R.S.; Tucker, C.L., III. Fiber orientation in simple injection moldings. Part I: Theory and numerical methods. *Polym. Compos.* **1992**, *13*, 317–331. [[CrossRef](#)]
36. Bay, R.S.; Tucker, C.L., III. Fiber orientation in simple injection moldings. Part II: Experimental Results. *Polym. Compos.* **1992**, *13*, 332–341. [[CrossRef](#)]
37. Oumer, A.N.; Mamat, O. A review of effects of molding methods, mold thickness and other processing parameters on fiber orientation in polymer composites. *Asian J. Sci. Res.* **2013**, *6*, 401–410. [[CrossRef](#)]
38. Huang, C.-T.; Lai, C.-H. Investigation on the coupling effects between flow and fibers on Fiber-Reinforced Plastic (FRP) injection parts. *Polymers* **2020**, *12*, 2274. [[CrossRef](#)] [[PubMed](#)]
39. Foss, P.H.; Tseng, H.-C.; Snawerdt, J.; Chang, Y.-J.; Yang, W.-H.; Hsu, C.-H. Prediction of fiber orientation distribution in injection molded parts using Moldex3D simulation. *Polym. Compos.* **2014**, *35*, 671–680. [[CrossRef](#)]
40. Tseng, H.-C.; Chang, R.-Y.; Hsu, C.-H. The use of shear-rate-dependent parameters to improve fiber orientation predictions for injection molded fiber composites. *Compos. Part A Appl. Sci. Manuf.* **2018**, *104*, 81–88. [[CrossRef](#)]
41. Kugler, S.K.; Dey, A.P.; Saad, S.; Cruz, C.; Kech, A.; Osswald, T. A flow-dependent fiber orientation model. *J. Compos. Sci.* **2020**, *4*, 96. [[CrossRef](#)]
42. Gruber, G.; Wartzack, S. Three-point bending analyses of short fiber reinforced thermoplastics: A comparison between simulation and test results. *SAS Technol. J.* **2013**, *12*, 1–8.
43. Ogierman, W.; Kokot, G. A study on fiber orientation influence on the mechanical response of a short fiber composite structure. *Acta Mech.* **2016**, *227*, 173–183. [[CrossRef](#)]
44. Vlach, J.; Steklý, J. Multiscale modeling of short fibre reinforced composites and it's relationship to modal analysis of machinery parts. *Int. Sci. J. Machines. Technol. Mater.* **2019**, *5*, 241–244.
45. Ding, G.; Zhang, Y.; Zhu, Y. Experimental and numerical investigation of the flexural behavior of CFRP box girders. *Adv. Compos. Lett.* **2019**, *28*, 1–13. [[CrossRef](#)]
46. Zscheyge, M.; Böhm, R.; Hornig, A.; Gerritzen, J.; Gude, M. Rate dependent non-linear mechanical behaviour of continuous fibre-reinforced thermoplastic composites—Experimental characterisation and viscoelastic-plastic damage modelling. *Mater. Des.* **2020**, *193*, 108827. [[CrossRef](#)]
47. Rizvi, S.J.A. Effect of injection molding parameters on crystallinity and mechanical properties of isotactic polypropylene. *Int. J. Plast. Technol.* **2017**, *21*, 404–426. [[CrossRef](#)]

Article

# Direct Synthesis of Gold Nanoparticles in Polymer Matrix

Quang Truong Pham, Gia Long Ngo, Xuan An Nguyen, Chi Thanh Nguyen, Isabelle Ledoux-Rak and Ngoc Diep Lai \*

LuMin, ENS Paris-Saclay, CentraleSupélec, CNRS, Université Paris-Saclay, 91190 Gif-sur-Yvette, France

\* Correspondence: ngoc-diep.lai@ens-paris-saclay.fr

**Abstract:** We report an original method for directly fabricating gold nanoparticles (Au NPs) in a polymer matrix using a thermal treatment technique and theoretically and experimentally investigate their plasmonic properties. The polymeric-metallic nanocomposite samples were first prepared by simply mixing SU-8 resist and Au salt with different concentrations. The Au NPs growth was triggered inside the polymer through a thermal process on a hot plate and in air environment. The Au NPs creation was confirmed by the color of the nanocomposite thin films and by absorption spectra measurements. The Au NPs sizes and distributions were confirmed by transmission electron microscope measurements. It was found that the concentrations of Au salt and the annealing temperatures and durations are all crucial for tuning the Au NPs sizes and distributions, and, thus, their optical properties. We also propose a simulation model for calculations of Au NPs plasmonic properties inside a polymer medium. We realized that Au NPs having large sizes (50 to 100 nm) play an important role in absorption spectra measurements, as compared to the contribution of small NPs (<20 nm), even if the relative amount of big Au NPs is small. This simple, low-cost, and highly reproducible technique allows us to obtain plasmonic NPs within polymer thin films on a large scale, which can be potentially applied to many fields.

**Keywords:** Au nanoparticles; plasmonics; polymer matrix; nanocomposite; thermal annealing

**Citation:** Pham, Q.T.; Ngo, G.L.; Nguyen, X.A.; Nguyen, C.T.; Ledoux-Rak, I.; Lai, N.D. Direct Synthesis of Gold Nanoparticles in Polymer Matrix. *Polymers* **2023**, *15*, 16. <https://doi.org/10.3390/polym15010016>

Academic Editors: Célio Bruno Pinto Fernandes, Salah Aldin Faroughi, Luís L. Ferrás and Alexandre M. Afonso

Received: 29 November 2022

Revised: 12 December 2022

Accepted: 16 December 2022

Published: 20 December 2022



**Copyright:** © 2022 by the authors. Licensee MDPI, Basel, Switzerland. This article is an open access article distributed under the terms and conditions of the Creative Commons Attribution (CC BY) license (<https://creativecommons.org/licenses/by/4.0/>).

## 1. Introduction

Metallic nanoparticles (NPs) are widely used in diverse applications, thanks to their surface plasmon resonance (SPR), i.e., the collective oscillation of free electrons in resonance with the incident light, for example, in photocatalysis [1,2], sensing [3–5], optical data storage [6–8], or medicine [9,10]. Many applications require the incorporation of these plasmonic NPs into different materials, especially polymers, to form the so-called plasmonic nanocomposites [11–15].

To fabricate the metal NPs inside a polymer medium, the common synthesis approach is to insert the presynthesized NPs, by using different techniques [16,17], into polymer aqueous solution. It was shown that, in this case, NPs usually aggregate and the metallic NPs lose their SPR properties. For this reason, stabilizing agents are required to obtain homogeneously dispersed NPs [18]. However, achieving a homogeneous spatial distribution at large scales inside the polymer matrix is still challenging [19]. Such disadvantages may directly affect the optical properties of the system [20], notably by inducing a large broadening of the plasmon resonance peak. To solve this problem, direct synthesis methods of NPs inside polymer matrix have been proposed. Different methods are investigated, such as chemical methods [21,22], and physical methods such as thermal treatment [13,14,23] and ultraviolet (UV) illumination [12,24]. The direct synthesis method thus allows to separate the polymer-shaping process from the control of NPs dispersion inside the medium [19].

Among different polymers, SU-8 resist is a favourable polymer because it is a low-cost material and is commonly applied in various fields, such as photonic devices [25,26] and microfluidics [27,28], thanks to its excellent mechanical properties [29], chemical stability [30], good biocompatibility [31], and functionalizability [32]. In addition according



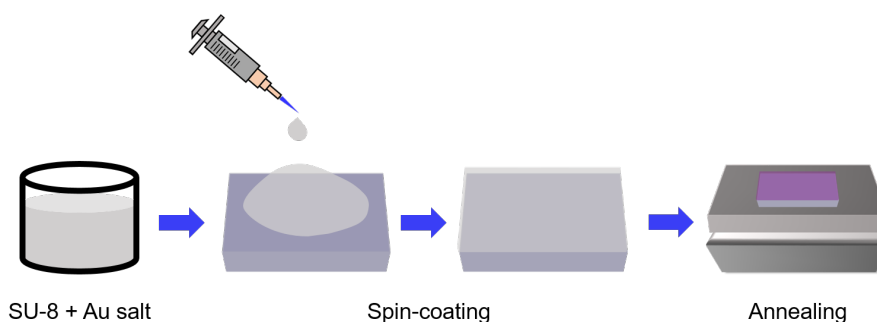
to previous work, SU-8 has great potential in photoreduction due to the generation of high chemical functionality and free radicals during the photochemical process [12]. There are several works regarding the fabrication of gold (Au) NPs inside SU-8 resist, mainly based on the photoreduction effect. For example, Shukla et al. presented a method for fabricating Au nanostructures within a polymeric matrix using the two-photon lithography technique [33]. In such a system, there is a simultaneous reduction of Au precursor and a polymerization of SU-8 resist, resulting in Au NP-doped polymeric lines. Chen et al. reported a method for directly synthesizing an Au NPs monolayer on the surface of SU-8 under a UV exposure [12]. Despite all these publications, the formation of Au NPs inside SU-8 resist by light or by thermal effect has not been fully investigated yet.

In the present work, we report a simple, low-cost, fast, reproducible, and efficient method to directly fabricate Au NPs inside SU-8 based on thermal effects without any intervention of light. In contrast to other chemical and photoreduction methods, only SU-8 and Au salt ( $\text{HAuCl}_4 \cdot 3\text{H}_2\text{O}$ ) are needed in this approach; no additional functionalization process and reducing agents are required. We investigated in detail the influence of Au salt concentrations, annealing temperatures, and annealing times on the formation of NPs. Moreover, to better understand the characteristics of Au NPs inside a polymer medium, a simulation model was also proposed, allowing to investigate their optical properties and to compare with experimental results.

## 2. Materials and Methods

Gold(III) chloride trihydrate ( $\geq 99.9\%$  trace metals basis)/Au salt with the chemical formula  $\text{HAuCl}_4 \cdot 3\text{H}_2\text{O}$  was purchased from Sigma-Aldrich. SU-8 2000.5 (epoxy-based negative photoresist) was purchased from MicroChem Corporation.

Au NPs were fabricated inside a polymer film deposited on a glass substrate following the process shown in Figure 1. The general procedure follows three steps, all of them in air environment conditions: (i) Au salt was mixed with SU-8 2000.5 at different weight ratios (wt.%) by stirring for 20 minutes for complete dissolution. (ii) The nanocomposite metal/resist solution was then deposited on a glass substrate by spin-coating at 500 rpm for 5 s and then at 2000 rpm for 30 s. (iii) After that, thermal annealing treatment was carried out at different temperatures, between room temperature and  $240\text{ }^\circ\text{C}$  (accuracy  $\pm 1\text{ }^\circ\text{C}$ ), using a standard hot plate.



**Figure 1.** Fabrication procedure of Au NPs in polymer film by a solvent-evaporation-assisted thermal annealing technique.

The nanocomposite film thickness was measured using a profilometer in a clean room, and ranged from 500 to 1000 nm. The plasmonic color can be observed by eye and by using a standard camera combined with an optical microscope. The plasmonic properties of the Au NPs in SU-8 resist were characterized by an ultraviolet–visible (UV–Vis) spectrometer. To evaluate Au NPs sizes, shapes, and distributions, the nanocomposite was dropped on a carbon-coated Cu grid and examined by a transmission electron microscope (TEM).

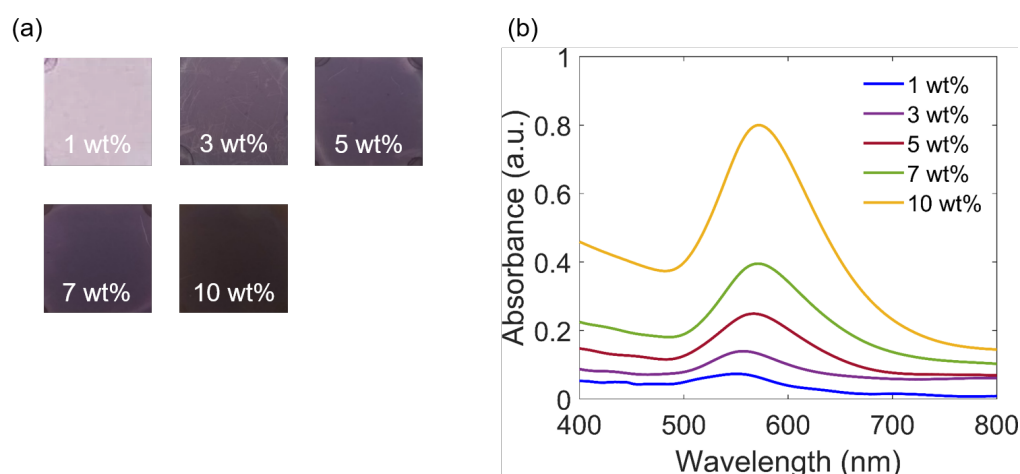
### 3. Experimental Results and Discussions

#### 3.1. Mechanism

Generally, the process to form Au NPs needs to be implemented through complete reduction of Au precursor to induce nucleation and then particles. For example, Au NPs synthesis in SU-8 was previously carried out under light illumination, where SU-8 acts as a photoreduction agent and its polymerization effect induces the formation of nucleations and NPs [12,33]. In the case described here, there is no obvious reducing agent present (SU-8 exists but without light). We observed that the solvent of SU-8 resist plays an important role in the formation of Au NPs. Indeed, we tested different kinds of SU-8 resists, such as SU-8 2000.5 (more solvent) and SU-8 2002 and 2005 (less solvent), but only SU-8 2000.5 allows us to obtain Au NPs. The reason is that the solvent concentration of SU-8 2000.5 is higher than that of SU-8 2002 and 2005, and enough to assist the movement of the Au salt. Thus, the mechanism of the formation of Au NPs in SU-8 can be explained as follows. First, it was suggested that the thermal effect decomposes the Au salt to form  $\text{Au}^{\circ}$  [34]. During the annealing process, the solvent evaporates, pushing  $\text{Au}^{\circ}$  to form crystalline seeds and, consequently, Au NPs. We therefore refer to this fabrication method as a solvent-evaporation-assisted thermal annealing technique.

#### 3.2. Dependence on Concentrations

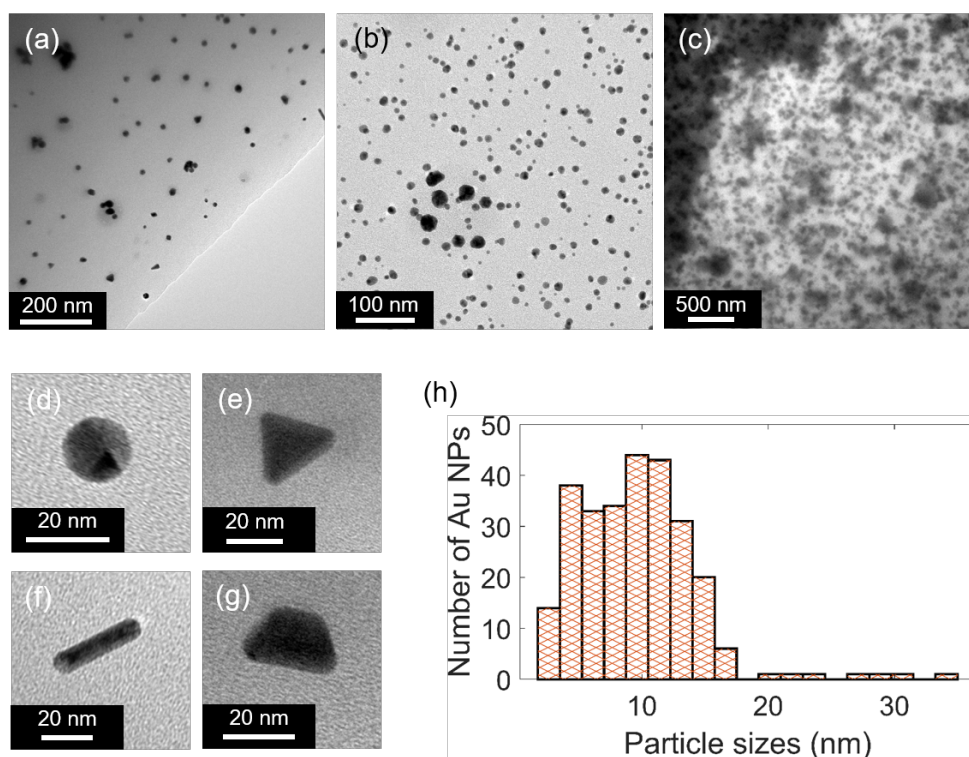
The influence of the different concentrations of Au salt on the formation of Au NPs is shown in Figure 2. Five nanocomposite samples of SU-8 2000.5 mixed with various concentrations of the Au salt, from 1 wt.% to 10 wt.%, were annealed at 95 °C for 5 min in the dark. The formation of Au NPs is confirmed by different measurements: by observing the color change of the sample (Figure 2a), by recording absorption spectra (Figure 2b), and by TEM images (Figure 3). The color becomes darker for higher concentrations because more NPs are formed. The higher concentration also leads to an increase in the absorbance, which is illustrated in Figure 2b. Furthermore, the absorption peaks displayed both a redshift, from around 550 nm for 1 wt.% to about 570 nm for 10 wt.%, and a broadening of the peak width. This physical phenomenon is due to the contribution of Au NPs with bigger sizes, which will be explained more clearly in the simulation part. In addition, the peak width broadening with higher concentration was also suggested by the previous works [16,35] due to more polydispersed Au NPs.



**Figure 2.** The formation of Au NPs depends on the concentrations of Au salt: (a) Direct smartphone pictures of the nanocomposite samples, obtained by SU-8 mixed with different concentrations of Au salt after annealing at 95 °C in 5 min. (b) The corresponding absorption spectra indicating the plasmonic effects of Au NPs inside SU-8 thin film.

Figure 3 shows TEM images and the size distribution of generated Au NPs after thermal treatments. It is found that the increase in the concentration of Au salt leads to

the generation of more Au NPs (Figure 3a–c). Indeed, for low concentrations of Au salts (1 wt.% and 3 wt.%), the NPs are well separated and easily distinguished. However, for high Au salt concentrations, such as 7 wt.%, Au NPs become too dense. We also found that different shapes of Au NPs are observed, such as nanospheres, nanoprisms, nanorods, and nanotrapezoids (Figure 3d–g), as compared to the dominant spherical shape on a large scale. The domination of spherical or near-spherical particles could be explained by the lowest energy needed for the nanosphere formation, which is thermodynamically preferred [36,37]. For nonspherical shape or anisotropic growth, the formation probability is much lower because it requires more energy to fight against thermodynamics [37]. To more easily control the particular shape of Au NPs, surfactants and shape-directing reagents could be added to selectively choose the specific facets to grow, resulting in desired particle shapes [36,38]. In actuality, special shapes such as Au nanorods exhibit two absorption peaks: one is related to electron oscillation along the transverse direction, and the other is related to electron oscillation along the longitudinal direction [39]. However, in Figure 2, only one resonant peak is observed because the contribution of these special shape NPs is very small compared to the contribution of spherical-like shape NPs. In addition, we can see in Figure 3h that most Au NPs are quite small, with diameters around 10 nm, indicating that in the actual conditions, this method creates mainly small NPs. This can bring some advantages because the smaller the size of Au NPs, the higher the ratio between surface area and volume, resulting in more catalytic activity, which can be used for biosensor technology [40–42]. However, it is important to note that for all samples obtained with different Au salt concentrations, we found that some bigger Au NPs are also formed even in very small quantities, and are surrounded by mostly small NPs (see the center of Figure 3b).

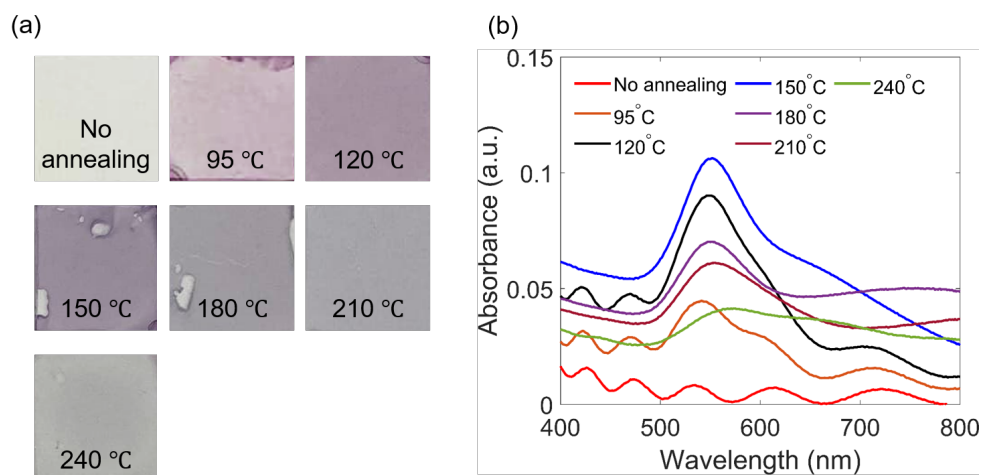


**Figure 3.** TEM images of the samples with different concentrations of Au salt: (a) 1 wt.%, (b) 3 wt.%, and (c) 7 wt.% after annealing at 95 °C in 5 min. (d–g) The special shapes of generated Au NPs after thermal treatment. (h) The size distribution of Au NPs for 3 wt.% Au salt.

### 3.3. Dependence on Annealing Temperatures

The effect of annealing temperature on the formation of Au NPs was also investigated. Several nanocomposite samples of SU-8 2000.5 mixed with 1 wt.% Au salt were prepared and annealed on a hot plate at different temperatures for the same annealing duration

of 5 min. As can be seen from Figure 4a, the increase in annealing temperatures leads to the modification of color shades of the metallic/polymeric samples: changing from colorless to purple after heating, becoming darker when increasing the temperature until 150 °C, and then becoming faded. UV-Vis absorption spectra were recorded and are shown in Figure 4b. Again, for the sample without thermal treatment, no absorption peak is observed. When the annealing temperature is increased, Au NPs are formed, as indicated by the resonant plasmonic peaks at around 550 nm. When the annealing temperature is varied, the SPR amplitudes and positions vary accordingly. This can be explained by the fact that the increase of the annealing temperature leads to an increase of the SU-8 solvent evaporation rate, which affects the formation of Au NPs. In general, SPR peaks have a tendency to shift toward longer wavelengths, and their widths broaden when the annealing temperature increases. In fact, the acceleration of the solvent evaporation process helps the formation of Au NPs with bigger sizes, thus explaining the redshift and broadening peak width effects, respectively. However, when heating the nanocomposite samples at higher temperatures, from 180 °C to 240 °C, as seen in Figure 4a, Au NPs cannot be formed and the plasmonic effect is not clearly visible, because at this high temperature, the SU-8 solvent evaporates too fast and Au salt/nucleations do not have enough time to form Au NPs. Furthermore, at high temperatures, the polymerization of SU-8 resist can occur via an effect called thermal polymerization, resulting in a more rigid polymer matrix, which also prevents the formation of Au NPs. It should be noted that the thermal annealing process is also applied to samples prepared several days earlier, but neither the color of the sample nor the absorption peaks can be observed. This is because after waiting for a few days, the SU-8 solvent has already evaporated from the spin-coated samples. This again confirms our proposed mechanism that the solvent of the SU-8 resist plays an important role in the generation of Au NPs. In addition, heat treatment is important, because without it, no color is observed, meaning that no Au NPs were formed for the samples stored in a dark box and at room temperature for a few days. For these samples, the solvent was slowly and totally evaporated.

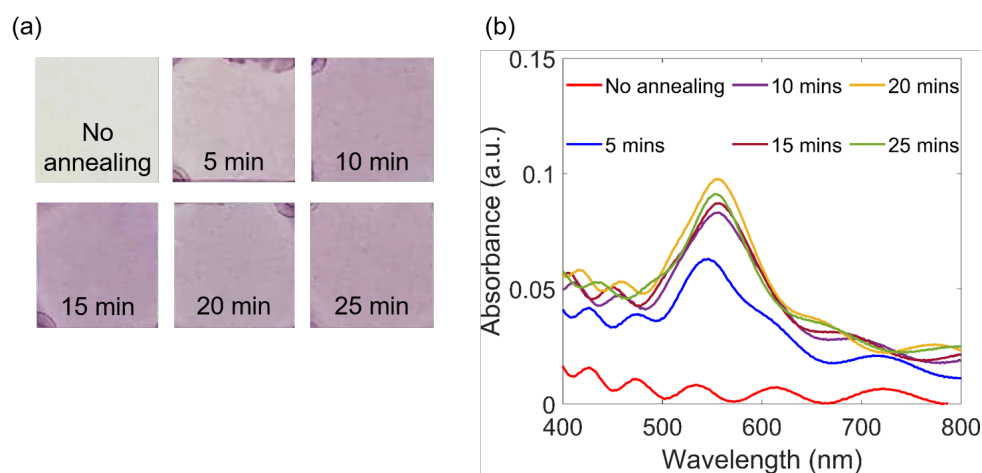


**Figure 4.** The temperature dependence on the formation of Au NPs: (a) Direct smartphone pictures of the nanocomposite samples of SU-8 mixed with 1 wt.% Au salt, obtained by thermal treatment at different temperatures. (b) The corresponding SPR spectra.

### 3.4. Dependence on Annealing Duration

Another factor that contributes to the change of Au NPs optical properties is annealing duration. Several samples of SU-8 2000.5 mixed with 1 wt.% Au salt were prepared and then placed on a hot plate preliminary heated to a stable temperature (95 °C). Individual samples were taken out after a chosen annealing duration. Figure 5a shows sample colors after experiencing different annealing times. The purple color illustrates the formation of Au NPs, which was also proved by SPR peaks, as shown in Figure 5b. When the annealing

time increases, the peaks have a tendency to move to longer wavelengths. This is because a longer annealing time leads to a higher probability of forming bigger Au NPs. The result does not change much when the annealing duration is longer than 25 min, since the formation of Au NPs is achieved. At longer annealing times, a possible effect is thermal polymerization of SU-8 resist, as mentioned above, which may induce a solid polymer matrix and a slight change of its refractive index, resulting in a small change of Au NPs SPR peak.



**Figure 5.** Formation of Au NPs depends on different annealing times: (a) Direct smartphone pictures of the nanocomposite samples of SU-8 mixed with 1 wt.% Au salt, obtained by annealing method at 95 °C for different durations. (b) The corresponding SPR spectra.

#### 4. Numerical Investigation of Au NPs inside a Polymer Medium

Thus far, we experimentally characterized the formation and optical properties of Au NPs within SU-8 resist. Since Au NPs show highly dispersed size distributions, to better understand the contribution of size effect to the resonance peaks of the nanocomposite samples, theoretical or numerical studies are needed. Indeed, there are many studies on the influence of a single metal NP size on the plasmonic effect based on Mie theory [43–46]. However, when considering the case of multiple Au NPs with different sizes being placed together inside a polymeric medium, there is no work that comprehensively explains the role of the NPs size in the characteristics of the resonance peaks. Here, we performed numerical simulations using a commercial three-dimensional finite-difference time-domain (FDTD) solver (Ansys Lumerical software) to study the optical properties of Au NPs in a polymeric medium. The FDTD method is recognized as a powerful numerical method to simulate the optical effect of metal NPs or nanostructures [47–51].

##### 4.1. Simulation Model

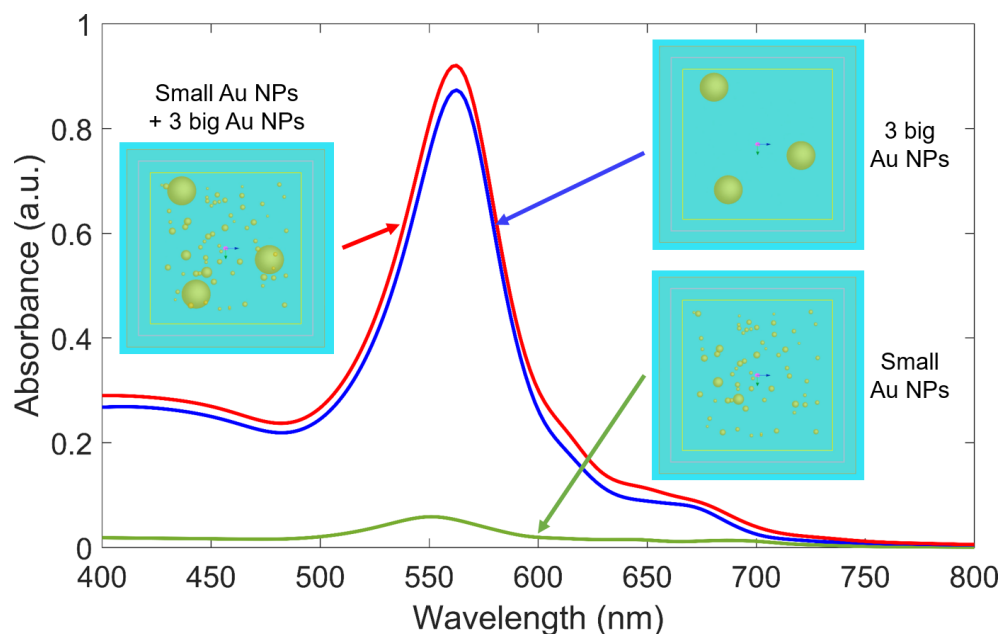
First, TEM images were processed by a MATLAB image processing algorithm to extract the size distribution of Au NPs. Then, spherical Au particles with the same number and size distribution were generated inside the FDTD simulation region using a random number seeding function with a normal distribution. As mentioned, the dominant shape of NPs is sphere-like; therefore, we chose the shape of NPs as a sphere for simplicity without affecting the physical meaning. We note that these spherical Au NPs were randomly distributed on a 500 nm thick layer of SU-8 film on top of a glass substrate to be consistent with the experiment. We assume that the refractive indices of SU-8 and glass are 1.58 and 1.48, respectively, in visible range. The dielectric constant for Au was taken from the experimental data of [52]. The exciting light source is a total-field scattered-field (TFSF) source with a wavelength range between 400 nm and 800 nm to match the operating bandwidth of the UV-Vis spectrometer. An override mesh region was added to the whole TFSF source region with a mesh size of 0.5 nm to ensure the convergence of the simulation

results. The boundary conditions are perfectly matched layers, which allows outgoing waves from the inside of a computational region to be strongly absorbed without being reflected back. The absorbance was calculated from an analysis group, which is located inside the TFSF source but outside the Au NPs.

#### 4.2. Simulation Results

##### 4.2.1. Effect of Particle Size Distribution

The experimental results show that Au NPs have polydisperse size distribution, with most of the small NPs under 20 nm in diameter and a small fraction of bigger NPs with sizes ranging from 20 to 100 nm, depending on the sample and the TEM image acquisition location. Since the size distribution of Au NPs is clearly divided into two regions, to evaluate the size effect, we simulate three separate cases, as follows. In the first case, only Au NPs with sizes smaller than 20 nm are considered. In the second case, we consider only three Au NPs with a size of 50 nm, representing big particles. In the third case, a combination of the two previous cases is investigated. Results are shown in Figure 6. As can be clearly seen, for the first case, when the simulation region only contains small Au NPs, the absorbance value is very low compared to the absorbance value of the second case, where three big Au NPs are simulated. As a result, for the third case, the absorption spectrum is almost identical to the second case and is mainly made of three big Au NPs contributions. It is also worth noting that the peak experiences a redshift when adding three big Au NPs into the first case, which shows that both the amplitude and the position of the resonance peaks are determined mainly by big Au NPs. This is understandable since a particle with a diameter of 50 nm has a scattering cross-section as well as a volume many times larger than for a particle with a size of 10 nm. This is also indicated in Mie theory when the absorption coefficient and peak position depend strongly on the radius of spherical Au NPs [53].

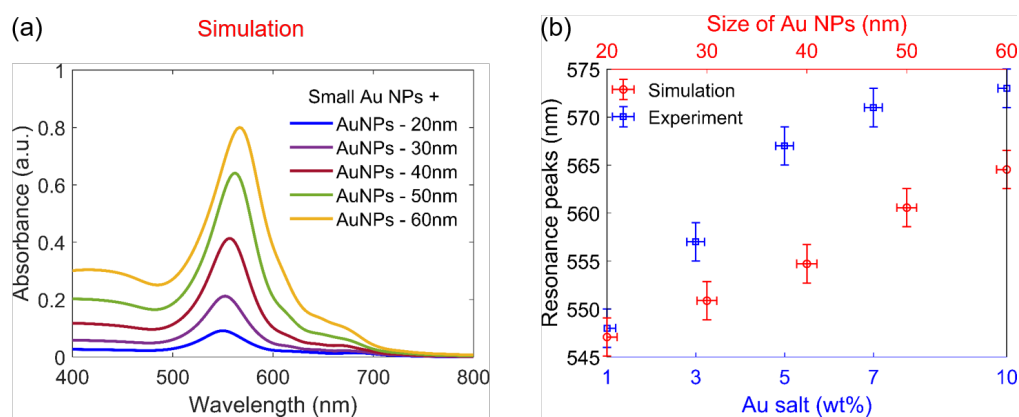


**Figure 6.** Absorption spectra of Au NPs in three cases: (i) only small Au NPs with the size of around 10 nm, (ii) only 3 big Au NPs with the size of 50 nm, and (iii) the combination between many numbers of small Au NPs and 3 big Au NPs. The three insets show the top view of the corresponding three simulation models using FDTD. The refractive indices of surrounding medium (SU-8) and glass substrate are 1.58 and 1.48, respectively.

##### 4.2.2. Effect of Particle Size and Comparison with Experimental Results

In the previous section, the big Au NPs are demonstrated as the main contributors to the amplitude and position of the absorption peaks. We also conducted simulations for cases

with varying sizes of big NPs and compared them with the experiment to try to explain the primary mechanism that affects the absorption peaks. Figure 7a shows the simulated absorption spectra of five simulation regions, which contain both small (10 nm) Au NPs and three big Au NPs having the size from 20 nm to 60 nm. As can be clearly seen, when the size of big Au NPs increases, the resonance peak experiences redshift, increased amplitude value, and widening. When comparing them to the experiment results in Figure 2b, the absorption spectra follow the same trend when increasing Au salt concentration. This trend is also demonstrated by comparing the position of the resonance peaks between simulation and experiment, as shown in Figure 7b. This implies that, in practice, when increasing the concentration of Au salt, Au NPs are generated with a bigger size even though the number of particles smaller than 20 nm still dominates. In actuality, due to technical limitations, we can only observe Au NPs in some regions on a carbon-coated Cu grid by using TEM where the thickness of the film is very thin ( $\approx 500$  nm). Therefore, simulation results are needed to gain a better understanding of the nanocomposite samples. We note that the experimental spectral peaks are always wider than the simulated ones. This is because when using the UV-Vis spectrometer, the illuminated region on the sample is very large ( $\approx$ mm). We therefore measured signals from several big particles (main contributors) of different sizes, leading to a widening of the absorption spectrum peak, while for simulations, only three big Au NPs were considered.



**Figure 7.** Absorption spectra of Au NPs: (a) Theoretical calculation of the regions containing Au NPs with different sizes from 20 nm to 60 nm surrounded by many small (10 nm) Au NPs. (b) Comparison of resonance peak positions between simulation and experiment. The error bars indicated for each point are as follows:  $\pm 1$  nm for Au NPs size;  $\pm 0.2$  wt.% for Au salt concentration; and  $\pm 2$  nm for SPR peak position.

## 5. Conclusions

In this study, a simple, low-cost, and fast method of thermal annealing for directly fabricating Au NPs inside a polymer matrix was demonstrated. Firstly, we heated the nanocomposite sample of an SU-8 resist mixed with Au salt in suitable conditions to grow Au NPs. The formation of Au NPs was explained by the thermal decomposition and solvent evaporation at suitable annealing temperatures and duration. Excellent Au NPs in SU-8 resist were obtained by optimum conditions: (i) concentrations of Au salt of 1–3 wt.%; (ii) annealing temperatures of 90–100 °C; and (iii) annealing duration of 1–5 min. The optical properties of Au NPs were characterized by different methods, such as optical and electronic microscopes and UV-Vis spectrometers. Secondly, the FDTD simulation model was first developed to investigate the optical properties of Au NPs inside polymer medium. Thanks to the simulation results, the size of Au NPs was recognized as an important contributor to the resonance peaks when considering many Au NPs with different sizes distributed in the space. Different applications of this Au NPs/SU-8 nanocomposite could be exploited, such as for data storage, plasmonic/photonic devices, and surface-enhanced Raman scattering (SERS) spectroscopy. This approach suggests that this thermal effect

could be used by other setups, such as laser systems to directly fabricate metallic NPs within the polymer with potential applications to plasmonic and metamaterial structures.

**Author Contributions:** Q.T.P. performed the setting experiments and analyzed the data. G.L.N. performed simulations. X.A.N. prepared the samples. C.T.N., I.L.-R. and N.D.L. reviewed and edited the manuscript. N.D.L. supervised the project. All authors have read and agreed to the published version of the manuscript.

**Funding:** This research received no external funding

**Institutional Review Board Statement:** Not applicable.

**Conflicts of Interest:** The authors declare no conflict of interest.

### Abbreviations

The following abbreviations are used in this manuscript:

Au NPs	Gold nanoparticles
TEM	Transmission electron microscope
SPR	Surface plasmon resonance
UV-vis	Ultraviolet–visible
FDTD	Finite-difference time domain

### References

- Cheng, H.; Fuku, K.; Kuwahara, Y.; Mori, K.; Yamashita, H. Harnessing single-active plasmonic nanostructures for enhanced photocatalysis under visible light. *J. Mater. Chem. A* **2015**, *3*, 5244–5258. [[CrossRef](#)]
- Ma, X.C.; Dai, Y.; Yu, L.; Huang, B.-B. Energy transfer in plasmonic photocatalytic composites. *Light Sci. Appl.* **2016**, *5*, e16017. [[CrossRef](#)] [[PubMed](#)]
- Lee, S.Y.; Jeon, H.C.; Yang, S.-M. Unconventional methods for fabricating nanostructures toward high-fidelity sensors. *J. Mater. Chem.* **2012**, *13*, 5900–5913. [[CrossRef](#)]
- Zhang, Q.; Chen, C.; Wan, G.; Lei, M.; Chi, M.; Wang, S.; Min, D. Solar light induced synthesis of silver nanoparticles by using lignin as a reductant, and their application to ultrasensitive spectrophotometric determination of mercury (II). *Microchim. Acta* **2019**, *186*, 1–10. [[CrossRef](#)] [[PubMed](#)]
- Zhang, Q.; Xie, G.; Xu, M.; Su, Y.; Tai, H.; Du, H.; Jiang, Y. Visible light-assisted room temperature gas sensing with ZnO-Ag heterostructure nanoparticles. *Sens. Actuators B Chem.* **2018**, *259*, 269–281. [[CrossRef](#)]
- Gu, M.; Zhang, Q.; Lamon, S. Nanomaterials for optical data storage. *Nat. Rev. Mater.* **2016**, *1*, 1–14. [[CrossRef](#)]
- Ditlbacher, H.; Krenn, J.R.; Lamprecht, B.; Leitner, A.; Aussenegg, F.R. Spectrally coded optical data storage by metal nanoparticles. *Opt. Lett.* **2000**, *25*, 563–565. [[CrossRef](#)]
- Mansuripur, M.; Zakharian, A.R.; Lesuffleur, A.; Oh, S.-H.; Jones, R.J.; Lindquist, N.C.; Im, H.; Kobaykov, A.; Moloney, J.V. Optics Express. *Plasmon. Nano-Struct. Opt. Data Storage* **2009**, *10*, 14001–14014.
- Salata, O.V. Applications of nanoparticles in biology and medicine. *J. Nanobiotechnol.* **2004**, *2*, 1–6. [[CrossRef](#)]
- Zhang, L.; Gu, F.X.; Chan, J.M.; Wang, A.Z.; Langer, R.S.; Farokhzad, O.C. Nanoparticles in medicine: Therapeutic applications and developments. *Clin. Pharmacol. Ther.* **2008**, *83*, 761–769. [[CrossRef](#)]
- Horiuchi, S.; Nakao, Y. Polymer/metal nanocomposites: Assembly of metal nanoparticles in polymer films and their applications. *Curr. Nanosci.* **2007**, *3*, 206–214. [[CrossRef](#)]
- Chen, Y.-J.; Chang, W.-H.; Li, C.-Y.; Chiu, Y.-C.; Huang, C.-C.; Lin, C.-H. Direct synthesis of monolayer gold nanoparticles on epoxy based photoresist by photoreduction and application to surface-enhanced Raman sensing. *Mater. Des.* **2021**, *197*, 109211. [[CrossRef](#)]
- Porel, S.; Venkatram, N.; Narayana Rao, D.; Radhakrishnan, T.P. In situ synthesis of metal nanoparticles in polymer matrix and their optical limiting applications. *J. Nanosci. Nanotechnol.* **2007**, *7*, 1887–1892. [[CrossRef](#)] [[PubMed](#)]
- Saikia, R.; Gogoi, P.; Barua, P.K.; Datta, P. Spectroscopic studies on Ag/PVA nanocomposite thin films prepared by thermal annealing process. *Int. J. Nanosci.* **2011**, *10*, 427–432. [[CrossRef](#)]
- Kunwar, P.; Hassinen, J.; Bautista, G.; Ras, R.H.A.; Toivonen, J. Sub-micron scale patterning of fluorescent silver nanoclusters using low-power laser. *Sci. Rep.* **2016**, *6*, 1–6. [[CrossRef](#)]
- Dong, J.; Carpinone, P.L.; Pyrgiotakis, G.; Demokritou, P.; Moudgil, B.M. Synthesis of precision gold nanoparticles using Turkevich method. *KONA Powder Part. J.* **2020**, *37*, 224–232. [[CrossRef](#)]
- De Souza, C.D.; Nogueira, B.R.; Rostelato, M.E.C.M. Review of the methodologies used in the synthesis gold nanoparticles by chemical reduction. *J. Alloys Compd.* **2019**, *798*, 714–740. [[CrossRef](#)]
- Kraynov, A.; Müller, T.E. Concepts for the stabilization of metal nanoparticles in ionic liquids. *Appl. Ion. Liq. Sci. Technol.* **2011**, *9*, 235–260.



19. Nadal, E.; Barros, N.; Peres, L.; Goetz, V.; Respaud, M.; Soulantica, K.; Kachachi, H. In situ synthesis of gold nanoparticles in polymer films under concentrated sunlight: Control of nanoparticle size and shape with solar flux. *React. Chem. Eng.* **2020**, *10*, 330–341. [[CrossRef](#)]
20. Ghosh, S.K.; Pal, T. Interparticle coupling effect on the surface plasmon resonance of gold nanoparticles: From theory to applications. *Chem. Rev.* **2007**, *107*, 4797–4862. [[CrossRef](#)]
21. Sohn, B.-H.; Seo, B.-W.; Yoo, S.-I. Changes of the lamellar period by nanoparticles in the nanoreactor scheme of thin films of symmetric diblock copolymers. *J. Mater. Chem.* **2002**, *6*, 1730–1734. [[CrossRef](#)]
22. Rifai, S.; Breen, C.A.; Solis, D.J.; Swager, T.M. Facile in situ silver nanoparticle formation in insulating porous polymer matrices. *Chem. Mater.* **2006**, *18*, 21–25. [[CrossRef](#)]
23. Porel, S.; Singh, S.; Radhakrishnan, T.P. Polygonal gold nanoplates in a polymer matrix. *Chem. Commun.* **2005**, 2387–2389. [[CrossRef](#)]
24. Alexandrov, A.; Smirnova, L.; Yakimovich, N.; Sapogova, N.; Soustov, L.; Kirsanov, A.; Bityurin, N. UV-initiated growth of gold nanoparticles in PMMA matrix. *Appl. Surf. Sci.* **2005**, *248*, 181–184. [[CrossRef](#)]
25. Bêche, B. Integrated photonics devices on SU8 organic materials. *Int. J. Phys. Sci.* **2010**, *5*, 612–618.
26. Williams, H.E.; Freppon, D.J.; Kuebler, S.M.; Rumpf, R.C.; Melino, M.A. Fabrication of three-dimensional micro-phonic structures on the tip of optical fibers using SU-8. *Opt. Express* **2011**, *19*, 22910–22922. [[CrossRef](#)]
27. Tavakoli, H.; Zhou, W.; Ma, L.; Perez, S.; Ibarra, A.; Xu, F.; Zhan, S.; Li, X.J. Recent advances in microfluidic platforms for single-cell analysis in cancer biology, diagnosis and therapy. *TRAC Trends Anal. Chem.* **2019**, *117*, 13–26. [[CrossRef](#)]
28. Sathyanarayanan, G.; Haapala, M.; Sikanen, T. Interfacing digital microfluidics with ambient mass spectrometry using SU-8 as dielectric layer. *Micromachines* **2018**, *9*, 649. [[CrossRef](#)]
29. Feng, R.; Farris, R.J. Influence of processing conditions on the thermal and mechanical properties of SU8 negative photoresist coatings. *J. Micromech. Microeng.* **2002**, *13*, 80. [[CrossRef](#)]
30. Lee, K.Y.; LaBianca, N.; Rishton, S.A.; Zolgharnain, S.; Gelorme, J.D.; Shaw, J.; Chang, T.H.-P. Micromachining applications of a high resolution ultrathick photoresist. *J. Vac. Sci. Technol. B Microelectron. Nanometer Struct. Process. Meas. Phenom.* **1995**, *13*, 3012–3016. [[CrossRef](#)]
31. Chen, Z.; Lee, J.-B. Biocompatibility of su-8 and its biomedical device applications. *Micromachines* **2021**, *12*, 794. [[CrossRef](#)] [[PubMed](#)]
32. Xue, P.; Bao, J.; Chuah, Y.J.; Menon, N.V.; Zhang, Y.; Kang, Y. Protein covalently conjugated SU-8 surface for the enhancement of mesenchymal stem cell adhesion and proliferation. *Langmuir* **2014**, *30*, 3110–3117. [[CrossRef](#)] [[PubMed](#)]
33. Shukla, S.; Vidal, X.; Furlani, E.P.; Swihart, M.T.; Kim, K.-T.; Yoon, Y.-K.; Urbas, A.; Prasad, P.N. Subwavelength direct laser patterning of conductive gold nanostructures by simultaneous photopolymerization and photoreduction. *ACS Nano* **2008**, *5*, 1947–1957. [[CrossRef](#)] [[PubMed](#)]
34. Zhang, J.; Gao, Y.; Alvarez-Puebla, R.A.; Buriak, J.M.; Fenniri, H. Synthesis and SERS properties of nanocrystalline gold octahedra generated from thermal decomposition of HAuCl<sub>4</sub> in block copolymers. *Adv. Mater.* **2006**, *18*, 3233–3237. [[CrossRef](#)]
35. Zabetakis, K.; Ghann, W.E.; Kumar, S.; Daniel, M.-C. Effect of high gold salt concentrations on the size and polydispersity of gold nanoparticles prepared by an extended Turkevich–Frens method. *Gold Bull.* **2012**, *45*, 203–211. [[CrossRef](#)]
36. Sajanlal, P.R.; Sreeprasad, T.S.; Samal, A.K.; Pradeep, T. Anisotropic nanomaterials: Structure, growth, assembly, and functions. *Nano Rev.* **2011**, *2*, 5883. [[CrossRef](#)]
37. Leontidis, E.; Kleitou, K.; Kyprianidou-Leodidou, T.; Bekiari, V.; Lianos, P. Gold colloids from cationic surfactant solutions. 1. Mechanisms that control particle morphology. *Langmuir* **2002**, *18*, 3659–3668. [[CrossRef](#)]
38. Niu, W.; Zhang, L.; Xu, G. Seed-mediated growth of noble metal nanocrystals: Crystal growth and shape control. *Nanoscale* **2013**, *5*, 3172–3181. [[CrossRef](#)]
39. Chen, H.; Kou, X.; Yang, Z.; Ni, W.; Wang, J. Shape- and size-dependent refractive index sensitivity of gold nanoparticles. *Langmuir* **2008**, *24*, 5233–5237. [[CrossRef](#)]
40. Yazdian-Robati, R.; Hedayati, N.; Dehghani, S.; Ramezani, M.; Alibolandi, M.; Saeedi, M.; Abnous, K.; Taghdisi, S.M. Application of the catalytic activity of gold nanoparticles for development of optical aptasensors. *Anal. Biochem.* **2021**, *629*, 114307. [[CrossRef](#)]
41. Chen, J.; Lu, Y.; Yan, F.; Wu, Y.; Huang, D.; Weng, Z. A fluorescent biosensor based on catalytic activity of platinum nanoparticles for freshness evaluation of aquatic products. *Food Chem.* **2020**, *310*, 125922. [[CrossRef](#)] [[PubMed](#)]
42. Charbgoon, F.; Ramezani, M.; Darroudi, M. Bio-sensing applications of cerium oxide nanoparticles: Advantages and disadvantages. *Biosens. Bioelectron.* **2017**, *96*, 33–43. [[CrossRef](#)] [[PubMed](#)]
43. Liang, C.-C.; Liao, M.-Y.; Chen, W.-Y.; Cheng, T.-C.; Chang, W.-H.; Lin, C.-H. Plasmonic metallic nanostructures by direct nanoimprinting of gold nanoparticles. *Opt. Express* **2011**, *19*, 4768–4776. [[CrossRef](#)] [[PubMed](#)]
44. Jain, P.K.; Lee, K.S.; El-Sayed, I.H.; El-Sayed, M.A. Calculated absorption and scattering properties of gold nanoparticles of different size, shape, and composition: Applications in biological imaging and biomedicine. *J. Phys. Chem. B* **2006**, *110*, 7238–7248. [[CrossRef](#)] [[PubMed](#)]
45. Fu, Q.; Sun, W. Mie theory for light scattering by a spherical particle in an absorbing medium. *Appl. Opt.* **2001**, *40*, 1354–1361. [[CrossRef](#)]
46. Marhaba, S. Effect of size, shape and environment on the optical response of metallic nanoparticles. In *Noble and Precious Metals-Properties, Nanoscale Effects and Applications*; IntechOpen: London, UK, 2017.

47. Tong, Q.C.; Mao, F.; Luong, M.H.; Do, M.T.; Ghasemi, R.; Tien, T.Q.; Nguyen, T.D.; Lai, N.D. Arbitrary Form Plasmonic Structures: Optical Realization, Numerical Analysis and Demonstration Applications. In *Plasmonics*; IntechOpen: London, UK, 2018.
48. Cheng, L.; Zhu, G.; Liu, G.; Zhu, L. FDTD simulation of the optical properties for gold nanoparticles. *Mater. Res. Express* **2020**, *7*, 125009. [[CrossRef](#)]
49. Mao, F.; Ngo, G.L.; Nguyen, C.T.; Ledoux-Rak, I.; Lai, N.D. Direct fabrication and characterization of gold nanohole arrays. *Opt. Express* **2021**, *29*, 29841–29856. [[CrossRef](#)]
50. Buil, S.; Laverdant, J.; Berini, B.; Maso, P.; Hermier, J.-P.; Quélin, X. FDTD simulations of localization and enhancements on fractal plasmonics nanostructures. *Opt. Express* **2012**, *20*, 11968–11975. [[CrossRef](#)]
51. Gomez-Cruz, J.; Bdour, Y.; Stamplecoskie, K.; Escobedo, C. FDTD Analysis of Hotspot-Enabling Hybrid Nanohole-Nanoparticle Structures for SERS Detection. *Biosensors* **2022**, *12*, 128. [[CrossRef](#)]
52. Haynes, W.M.; Lide, D.R.; Bruno, T.J. *CRC Handbook of Chemistry and Physics*; CRC Press: Boca Raton, FL, USA, 2016.
53. Hulst, H.C.; van de Hulst, H.C. *Light Scattering by Small Particles*; Courier Corporation: Chelmsford, MA, USA, 1981.

**Disclaimer/Publisher’s Note:** The statements, opinions and data contained in all publications are solely those of the individual author(s) and contributor(s) and not of MDPI and/or the editor(s). MDPI and/or the editor(s) disclaim responsibility for any injury to people or property resulting from any ideas, methods, instructions or products referred to in the content.



## Article

# Radiation Shielding of Fiber Reinforced Polymer Composites Incorporating Lead Nanoparticles—An Empirical Approach

Rabie A. Abu Saleem <sup>1,\*</sup>, Nisrin Abdelal <sup>2</sup>, Ahmad Alsabbagh <sup>1</sup>, Maram Al-Jarrah <sup>1</sup> and Fatima Al-Jawarneh <sup>1</sup>

<sup>1</sup> Nuclear Engineering Department, Jordan University of Science and Technology, P.O. Box 3030, Irbid 22110, Jordan; Ahalsabbagh@just.edu.jo (A.A.); maramahmad072@gmail.com (M.A.-J.); Fatima.jawa97@gmail.com (F.A.-J.)

<sup>2</sup> Mechanical Engineering Department, Jordan University of Science and Technology, P.O. Box 3030, Irbid 22110, Jordan; nrabdelal@just.edu.jo

\* Correspondence: raabusaleem@just.edu.jo

**Abstract:** In the present work, an empirical approach based on a computational analysis is performed to study the shielding properties of epoxy/carbon fiber composites and epoxy/glass fiber composites incorporating lead nanoparticle (PbNPs) additives in the epoxy matrix. For this analysis, an MCNP5 model is developed for calculating the mass attenuation coefficients of the two fiber reinforced polymer (FRP) composites incorporating lead nanoparticles of different weight fractions. The model is verified and validated for different materials and different particle additives. Empirical correlations of the mass attenuation coefficient as a function of PbNPs weight fraction are developed and statistically analyzed. The results show that the mass attenuation coefficient increases as the weight fraction of lead nanoparticles increases up to a certain threshold (~15 wt%) beyond which the enhancement in the mass attenuation coefficient becomes negligible. Furthermore, statistical parameters of the developed correlations indicate that the correlations can accurately capture the behavior portrayed by the simulation data with acceptable root mean square error (RMSE) values.

**Keywords:** fiber reinforced polymer composites; lead nanoparticles; shielding; attenuation coefficient; empirical derivation

**Citation:** A. Abu Saleem, R.; Abdelal, N.; Alsabbagh, A.; Al-Jarrah, M.; Al-Jawarneh, F. Radiation Shielding of Fiber Reinforced Polymer Composites Incorporating Lead Nanoparticles—An Empirical Approach. *Polymers* **2021**, *13*, 3699. <https://doi.org/10.3390/polym13213699>

Academic Editors: Salah Aldin Faroughi, Luis L. Ferrás, Alexandre M. Afonso and Célio Bruno Pinto Fernandes

Received: 14 September 2021  
Accepted: 21 October 2021  
Published: 27 October 2021

**Publisher's Note:** MDPI stays neutral with regard to jurisdictional claims in published maps and institutional affiliations.



**Copyright:** © 2021 by the authors. Licensee MDPI, Basel, Switzerland. This article is an open access article distributed under the terms and conditions of the Creative Commons Attribution (CC BY) license (<https://creativecommons.org/licenses/by/4.0/>).

## 1. Introduction

The utilization of radiation has been steadily growing over the last decades in a variety of fields including medical, industrial and agricultural fields. Despite the immense benefits of radiation, it has the potential to pose a significant safety hazard for human health and the environment. There are three fundamental concepts pursued for better protection against radiation; decreasing the exposure time as much as possible, increasing the distance between the radiation source and the entity of interest and using a shielding material to physically separate the entity of interest from radiation. These three concepts are implemented as much as practically possible to reduce the total absorbed dose due to radiation exposure. This is referred to as the ALARA (as low as reasonably achievable) principle [1].

The performance of a material as a radiation shield is usually assessed by its capacity to halt the penetration of the incident radiation through different interaction mechanisms. Gamma radiation, characterized by high penetration power, interacts with matter by three different processes, namely, photoelectric absorption, Compton scattering and pair production. The probability of each interaction to occur depends on the energy of the incident gamma radiation and the composition of the shielding material. Photoelectric absorption is the predominant process for gamma radiations with low energies interacting with materials of high atomic number. For gamma radiations with high energies, pair production becomes the predominant process. The bulk behavior of gamma interaction with the shield material is characterized by the linear attenuation coefficient ( $\mu$ ) which depends on both

the energy of the incident radiation and the characteristics of the material. A desirable shielding material is capable of attenuating gamma radiation with minimal alteration to its mechanical, thermal and electrical properties as well as its chemical and physical stability. All in all, several factors should be taken into account when a radiation shield is designed, this includes the type of radiation and its energy level, radiation intensity, material cost and the diversity of material properties including weight, toxicity and environmental compatibility [1–3]. Concrete, lead and bismuth are among the commonly used material for shielding against gamma radiation.

Research studies on developed materials for radiation shielding applications have been boosted due to their imperative role in the advanced technologies that use ionizing radiation such as radiology, nuclear medicine, advanced material characterization and controlled modification of the properties of many materials. This diverse range of functions needs advanced materials to be used for manufacturing protective structures to protect humans and the environment from the harmful effects of ionizing radiation. Alshahrani et al. investigated the radiation shielding properties of newly developed high Fe content amorphous alloys. They reported the shielding capacity per unit thickness of the investigated alloys within the photon energy spectrum considered [4]. From a different perspective, Tishkevich et al. studied designing shielding materials to protect the critical elements and blocks of the electronic products and semi-conductor units that work in elevated radiation environments. They particularly studied the structure and attenuation coefficients of the WCu composite material when used in electron and proton radiation environments, and they showed that the use of WCu composite materials offers a very attractive alternative to lead (Pb), in terms of protection against ionizing radiation, as an environmentally friendly material and from the point of view of mass-dimensional parameters [5]. Kara et al. evaluated the shielding properties of fabricated dolomite doped glasses for gamma-rays. They showed that dolomite additive improves the gamma protecting capacity of lithium borate glasses. As a result, it was concluded that a glass sample with the highest dolomite additive content exhibits better efficiency in terms of radiation shielding [6]. Researchers have also investigated enhancing the shielding properties for materials with well-known superior shielding properties, such as concrete. Aygün et al. investigated new chromium ore based heavy concrete containing different types of minerals. They showed that concretes with additives and aggregates have better, gamma-ray and neutron, shielding features in comparison with standard concrete and some heavy types of concrete [7].

Composite materials are widely used in aircraft applications due to their competing superior properties in terms of weight, cost, dimensional stability, and dielectric strength [8–11]. For aircraft applications, the shielding properties of a material become a key factor due to the elevated level of cosmic radiation with increased altitude. For aviation applications, the cosmic radiation interacts with the earth's atmosphere and produces secondary particles including protons, neutrons, electrons, positrons, and photons [12]. There have been several studies that focus on the effective dose received by the aircrews during their flights. One study was based on Monte Carlo simulations using FLUKA code performed to study the ability of the aircraft structure to shield against galactic cosmic rays [13].

Recent research studies explored a variety of composite materials as potential shielding materials, this includes epoxy/Pb<sub>3</sub>O<sub>4</sub> composites [14], tungsten/epoxy composites [15], Gd<sub>2</sub>O<sub>3</sub>/epoxy composites [16], nano concrete composites [2,17], and composites of silicon resin with additives [3]. In general, there are two major phases constituting a composite material, a continuous phase characterized by low stiffness and a weak structure called the matrix phase and a stiffer and stronger phase called the reinforcement phase that can be continuous or discontinuous. Fiber reinforced polymer (FRP) composites constitute a family of materials that has been extensively studied for a variety of applications [18,19]. When these composites are used for radiation shielding, the alteration in their mechanical and structural properties becomes a key factor in determining their suitability. For FRP

composites, the polymer component is more amenable to changes in its mechanical and structural properties [20,21]. Epoxy, characterized by good durability against gamma and neutron radiation compared to other polymers, has been widely studied as a matrix phase for FRP composites utilized in the field of radiation and nuclear applications [22,23]. Little research has been conducted to study the shielding properties of FRP composites with lead nanoparticle additives.

In a previous study, mass attenuation coefficients of silicon resin loaded with PbO, Bi<sub>2</sub>O<sub>3</sub>, and WO<sub>3</sub> micro- and nanoparticles were calculated [3]. In that study, results for mass attenuation coefficients ( $\mu_m$ ) from a Monte Carlo Simulation were validated against data from the National Institute of Standards and Technology (NIST). The results showed that mass attenuation coefficients for composites with nanoparticles filler were better than that of composites with microparticles. This was attributed to the fact that smaller particle size leads to more uniform distribution in the matrix and an increased surface to mass ratio. Furthermore, the results showed that the attenuation power of the composite increases as the weight percentage of the filler increases. Tekin et al. studied the influence of micro- and nanoparticle size for WO<sub>3</sub> and Bi<sub>2</sub>O<sub>3</sub> particle types on shielding properties of hematite-serpentine concrete (HSC) using MCNPX code [24]. The model was validated by comparing results for mass attenuation coefficients of HSC from the MCNPX model with those obtained from XCOM at different energies, and a good agreement between the two sets of results was observed. The result showed that mass attenuation coefficients of nanoparticles/HSC composites were better than those of microparticles/HSC composites. Moreover, mass attenuation results for Bi<sub>2</sub>O<sub>3</sub>/HSC composites were better than those of WO<sub>3</sub>/HSC composites. This is due to the fact that the density and the atomic number for bismuth (Bi) are higher than those for tungsten (W). Tekin et al. studied the effect of nano/micro-sized WO<sub>3</sub> particles on mass attenuation coefficient for concrete using MCNPX code, the model was validated by calculating the mass attenuation coefficient for concrete using MCNPX model and comparing the result with the one from XCOM at different energies and he found a good agreement between the results. The results showed that the mass attenuation coefficient for nanoparticles was better than that for microparticles and the mass attenuation coefficient decreased as the energy of the radiation source increased [25]. In a separate study, Tekin et al. developed an MCNPX model to study the mass attenuation coefficient of lead doped with nano-sized barite (BaSO<sub>4</sub>) [26]. Results from the MCNPX model were benchmarked against standard XCOM data at different radiation energies. The results of MCNPX simulations showed that the mass attenuation coefficient of lead was improved upon the addition of nano-sized barite, furthermore, the mass attenuation coefficient decreased as the energy of the incident gamma radiation was increased.

In another study, Kazemi et al. developed an MCNPX model to study the shielding properties for novel polyvinyl alcohol (PVA)/WO<sub>3</sub> composite using micro- and nanosized WO<sub>3</sub> particles [27]. The model was validated by comparing mass attenuation coefficients of aluminum from the National Institute of Standards and Technology (NIST) tables to those calculated by the MCNPX model at 0.662 MeV incident radiation energy. It was found that composites with WO<sub>3</sub> nanoparticles exhibit mass attenuation coefficients higher than those of composites with WO<sub>3</sub> microparticles. Finally, a summary of research results related to the shielding properties of composite materials is presented in Table 1.

In this study, an empirical approach is followed to derive mathematical correlations for the shielding properties of composite materials based on computational analysis. The analysis is performed to shed the light on the shielding properties of epoxy/carbon-fiber composites and epoxy/glass-fiber composites incorporating lead nanoparticles (PbNPs) taking into account the effect of varying the content of lead nanoparticles on the investigated properties. Fiber reinforced polymer (FRP) composites are chosen for this study because they are considered a promising candidate for structural applications due to their superior relevant properties such as lightweight, high specific strength, sound insulation, durability and corrosion resistance [8,9]. Furthermore, epoxy is considered as the matrix phase

for this study because its excellent mechanical and chemical properties, good adhesive strength and dimensional stability make it a promising candidate for applications featuring severe radiation environments [15]. Moreover, superior properties of both carbon fiber and glass fiber, considered in this study, led to their wide utilization as reinforcement phases in composite materials. Such properties include high tensile strength, high modulus, high chemical resistance, and temperature resistance [8,28,29]. Finally, the high surface to volume ratio of nanoparticles leads to improving their mechanical and shielding properties, justifying the consideration of lead nanoparticles, a well-known gamma shielding material, for this research study [19].

**Table 1.** Shielding properties for different composite materials.

Shielding Material	Density (g/cm <sup>3</sup> )	Linear Attenuation Coefficient (cm <sup>-1</sup> )	Mass Attenuation Coefficient (cm <sup>2</sup> /g)	References
Lead	11.34	1.133	0.0999	[29]
Ordinary concrete	2.203	0.144	0.0654	[8]
Steel	8.020	0.433	0.0540	[8]
Epoxy/20 wt% PbO	-	0.091	-	
HD-PE/10 wt% PbO	1.051	0.105	0.0999	[30]
HD-PE/50 wt% PbO	1.652	0.189	0.1144	
Polyester/5 wt% PbO	1.2325	0.0997	0.0809	
Polyester/10 wt% PbO	1.2891	0.114	0.0842	
Polyester/20 wt% PbO	1.4285	0.1264	0.0884	[31]
Polyester/30 wt% PbO	1.6042	0.1422	0.0887	
Polyester/40 wt% PbO	1.855	0.1735	0.0935	
Polyester/50 wt% PbO	2.1721	0.206	0.0948	
Epoxy/50 wt% PbO	2.0034	0.17796	0.0888	[32]
Epoxy/70 wt% PbO	2.987	0.2723	0.0912	
Rubber/5 wt% Pb	-	0.00165	-	
Rubber/20 wt% Pb	-	0.00221	-	[33]
Rubber/50 wt% Pb	-	0.00298	-	
Rubber/75 wt% Pb	-	0.00478	-	
Epoxy/10 wt% PbO	1.26	0.1097	0.0871	
Epoxy/30 wt% PbO	1.53	0.1414	0.0924	[34]
Epoxy/50 wt% PbO	2.05	0.2005	0.0978	
Epoxy/70 wt% PbO	2.93	0.3091	0.1055	

#### Monte Carlo N-Particle (MCNP5) Code

Monte Carlo simulations using the Monte Carlo N-Particle (MCNP5) code were considered as a source of data to derive mathematical correlations describing the shielding properties of composite materials with different fiber content and different weight fractions of lead nanoparticles.

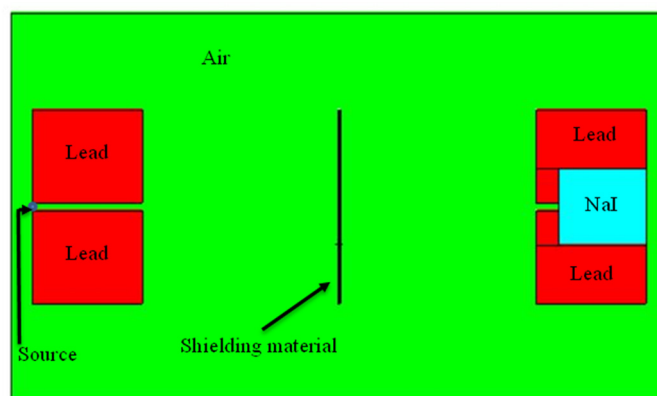
Monte Carlo codes have been used extensively in studying the shielding properties of different composites incorporating nano-sized materials [27,35–39]. MCNP5 has been extensively used in the field of nuclear applications and radiology, more specifically radiation shielding and detection [1,40]. The code is generally used to solve the transport equations of photons, neutrons, and electrons, based on Monte Carlo methods where a particle is tracked until it is either absorbed or escaped the physical domain of interest. Every possible interaction of the particle is accounted for by assigning probability values (interaction cross-sections) and the overall behavior of the particles is recorded in an average sense. In other words, the expectation (mean) of the probability distribution function describing the behavior is calculated. Simulations with MCNP5 require preparation of an input file that contains a description of the problem including material compositions, geometry specifications, location and characteristics of the particles. Moreover, the type of output data required from such simulations is also specified in the input file (called tallies) and it is delivered to the user in a text output file. The input file of an MCNP5 simulation contains three main sections, namely, the cell cards section, where the shape and material content of the physical space of interest is defined, the surface cards section,

where the surfaces used for the geometry definition of all cells are specified and the data card section, where all other aspects of the simulation are specified including the simulation mode, material isotopic content and type of output data required from the simulation (tallies). Each section is a collective of several text lines called cards. For more details on calculations theory and input file specifications the reader is advised to review MCNP5 manuals [40,41].

## 2. Methodology

In the present study, MCNP5 (version 5), is used in the photon transport mode (P-mode) to track the photon population of gamma radiation, in the form of collimated monoenergetic beams, inside the shielding material. Results from these simulations are used to determine linear attenuation coefficients of composite samples of different fiber contents and different weight fractions of lead nanoparticles.

A point isotropic source was defined using the source definition card (SDEF) with a source energy of 0.662 MeV corresponding to  $^{137}\text{Cs}$  source. The source is located at the center of the detection area emitting photons in a direction perpendicular to the composite sheet. Two sets of lead collimators were used, a source collimator consisting of two cuboids at the upper and lower sides of the source and a detector collimator located at the detector opposite to the source. Between the two sets of collimators, a shielding sheet of composite material is located with accurately specified dimensions. A cell flux tally (F4) is defined in the data cards section of the MCNP5 input file to estimate the total number of photons per unit area entering the cell that represents the NaI detector. Figure 1 shows a schematic of the physical domain defined for the MCNP5 simulation.



**Figure 1.** Schematic of the shielding test setup in the MCNP5 model.

Cross-sectional data used in the simulation were obtained from the Evaluated Nuclear Data Files (ENDF/B-VI) library. For all simulations, the history cutoff card (NPS) was defined with a total of  $10^6$  histories to be run in the problem and a relative statistical error set to less than 0.1%. Time, energy and particle weight cutoffs were all set to default values. Simulation real run time ranged between 1–3 h depending on the weight fraction of lead nanoparticles used. Simulations were performed using a machine with core i5-8250U CPU and 1.8 GHz speed. Upon completion of all simulations, a MATLAB script was developed to extract the desired data from the output files, process it and perform calculations for the determination of the shielding properties of the simulated material. Furthermore, statistical information was obtained from the output files to assess the precision of the results. All statistical parameters were satisfactory with relative error values less than 0.00035 and variance of the variance values less than  $6.5 \times 10^{-6}$ , for all simulations.

The first step of this computational analysis was to validate the MCNP5 model for shielding materials of known properties. Mass attenuation coefficients of lead and aluminum with different radiation energies were considered. Results of the mass attenuation coefficient ( $\mu_m$ ) from the MCNP5 model were compared to those obtained from the photon cross-sections database (XCOM) provided by the National Institute of Standards and



Technology (NIST). MCNP5 results were also compared to calculation results based on the theoretical formulations presented in reference [42]. The formulations presented in this reference were in accordance with data obtained from the National Nuclear Data Center in Brookhaven National Laboratory. Moreover, the MCNP5 model was verified by comparing results of mass attenuation coefficients for silicon-resin/37.5 wt%WO<sub>3</sub>, silicon-resin/37.5 wt%PbO, and silicon-resin/37.5 wt%Bi<sub>2</sub>O<sub>3</sub> composites to those reported by literature [3].

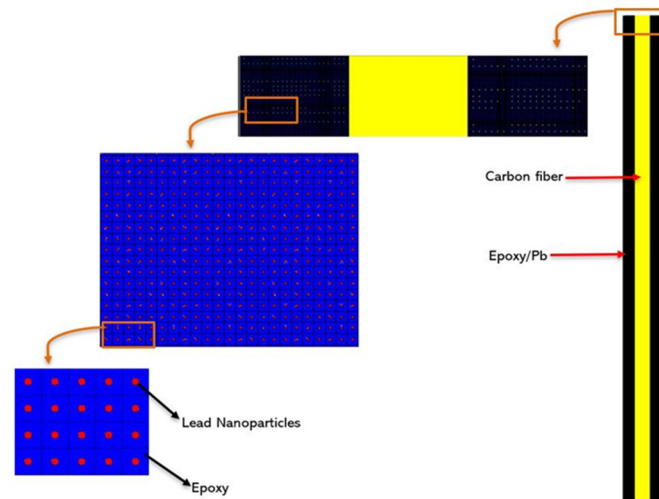
Finally, an MCNP5 model was developed to calculate linear attenuation coefficients of epoxy/fiber composites with different weight fractions of lead nanoparticles. Simulations were performed for a point isotropic source with a collimated and monoenergetic beam of 0.662 MeV energy. The composite material was modeled by a sheet of three alternating layers, two layers of epoxy-PbNPs mixture and one layer of fiber (carbon fiber or glass fiber). The simulated sheets mimic composite samples that are prepared by the well-known vacuum bagging process for fabricating fiber reinforced polymer (FRP) composites [43]. To achieve a 50:50 weight balance between fiber and epoxy, dimensions and compositions of the alternating layers were chosen such that the total mass of the two epoxy-PbNPs layers is similar to that of the fiber layer. Lead nanoparticles were uniformly distributed within the epoxy matrix using LATTICE and UNIVERSE features provided by MCNP5. The mixture was modeled by a lattice of epoxy cuboids each with a lead nanoparticle sphere of 80 nm diameter located at the center. Cuboid dimensions were changed for each weight fraction of lead nanoparticles to satisfy the aforementioned mass balance condition. Dimensions of the lattice cell for different weight fractions of lead nanoparticles along with corresponding material densities are reported in Table 2.

**Table 2.** Lattice dimensions and composite densities used in MCNP5 model.

Lead Nanoparticles Weight Fraction %	Length of Lattice Cube Side $\times 10^{-5}$ cm	Density of the Composite Material $\text{g/cm}^3$	
		With Carbon Fiber	With Glass Fiber
0	-	1.336	1.540
1	6.496	1.343	1.549
2	5.1401	1.351	1.559
2.5	4.7644	1.354	1.564
3	4.4765	1.358	1.569
4	4.0546	1.366	1.580
5	3.7521	1.373	1.590
6	3.5197	1.381	1.600
7	3.3328	1.389	1.611
7.5	3.2518	1.393	1.616
8	3.1774	1.397	1.622
9	3.0451	1.405	1.633
10	2.93	1.413	1.644
12.5	2.6976	1.434	1.672
15	2.5168	1.455	1.701
17.5	2.3698	1.477	1.731
20	2.2462	1.500	1.762
22.5	2.1397	1.524	1.795
25	2.0461	1.548	1.829
27.5	1.9627	1.573	1.864
30	1.8873	1.599	1.900
32.5	1.81814	1.625	1.938
35	1.755	1.653	1.977
37.5	1.6960	1.681	2.018
40	1.6408	1.711	2.061
42.5	1.5888	1.742	2.105
45	1.5395	1.773	2.152
47.5	1.4926	1.806	2.200
50	1.4477	1.840	2.251

A cross-sectional view of the composite sheet as modeled in MCNP5 is shown in Figure 2. The dimensions of the fiber sheet are set to 0.045 cm  $\times$  5 cm  $\times$  5 cm. For

epoxy/PbNps sheets, the width and the height are set to  $5\text{ cm} \times 5\text{ cm}$  and the thickness was varied based on the weight fraction of lead nanoparticles. As for material densities, values of  $1.7\text{ g/cm}^3$ ,  $2.565\text{ g/cm}^3$ ,  $1.1\text{ g/cm}^3$  and  $11.35\text{ g/cm}^3$  were assigned for carbon fiber, glass fiber type E epoxy and lead nanoparticles, respectively. Detailed elemental composition of both, epoxy and glass fiber as defined in the MCNP5 model are provided in Tables 3 and 4, respectively.



**Figure 2.** MCNP5 Cross-sectional screenshot for PbNPs blended into epoxy/Fiber composite.

**Table 3.** Elemental composition for epoxy (density is  $1.1\text{ g/cm}^3$ ).

Element	Weight Percentage
Carbon	0.6421
Hydrogen	0.0669
Oxygen	0.2309
Chloride	0.0601

**Table 4.** Elemental composition for E-glass fiber (density is  $2.565\text{ g/cm}^3$ ).

Element	Weight Percentage
Boron	0.022803
Oxygen	0.471950
Fluorine	0.004895
Sodium	0.007262
Magnesium	0.014759
Aluminum	0.072536
Silicon	0.247102
Potassium	0.008127
Calcium	0.143428
Titanium	0.004400
Iron	0.002739

### 3. Results and Discussion

In this section, two sets of results are presented. Validation and verification results are presented in Section 3.1 and results on the effect of varying the weight fraction of PbNPs on the mass attenuation coefficient are presented in Section 3.2 in the form of empirically derived correlations for attenuation coefficients and mass attenuation coefficients.

#### 3.1. Validation and Verification Results

Mass attenuation coefficients for lead and aluminum for photon energies of 0.511, 0.662, 1, 1.17, 1.25, 1.33, 1.5, 2, 3, and 4 MeV were calculated using MCNP5 and com-

pared to XCOM results provided by NIST and theoretical values based on the radiation shielding textbook [42]. Results of this validation for lead and aluminum are shown in Figures 3 and 4, respectively. It can be seen that there is a good agreement between the three sets of results, XCOM, MCNP5 and theoretical results. This close agreement between the different sets of results was considered as a validation for the MCNP5 model for further simulation. Moreover, it can be seen from the figures that the mass attenuation coefficient tends to decrease with increasing the radiation energy, the decrease seems to be steeper for lead.

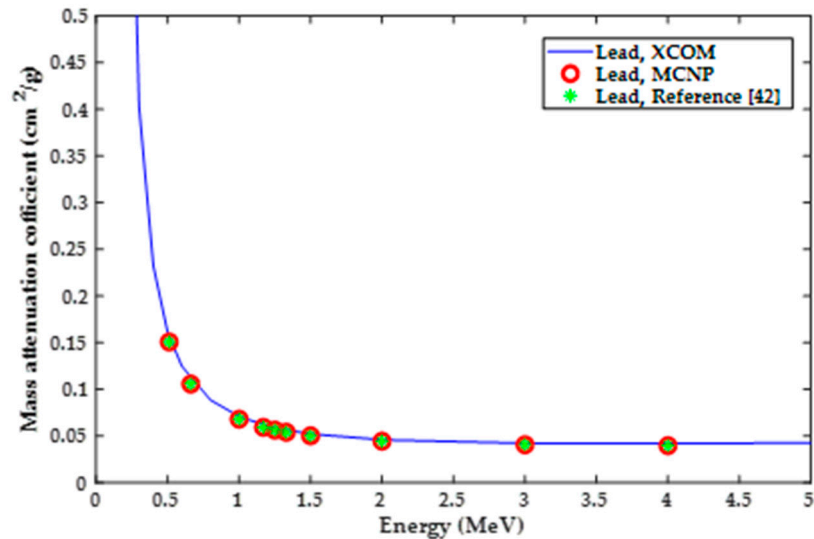


Figure 3. Validation results based on of lead mass attenuation coefficient.

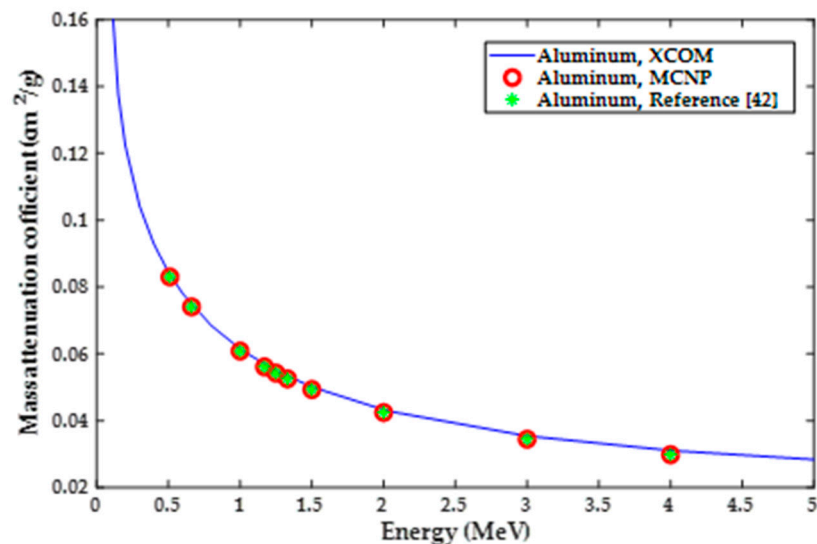
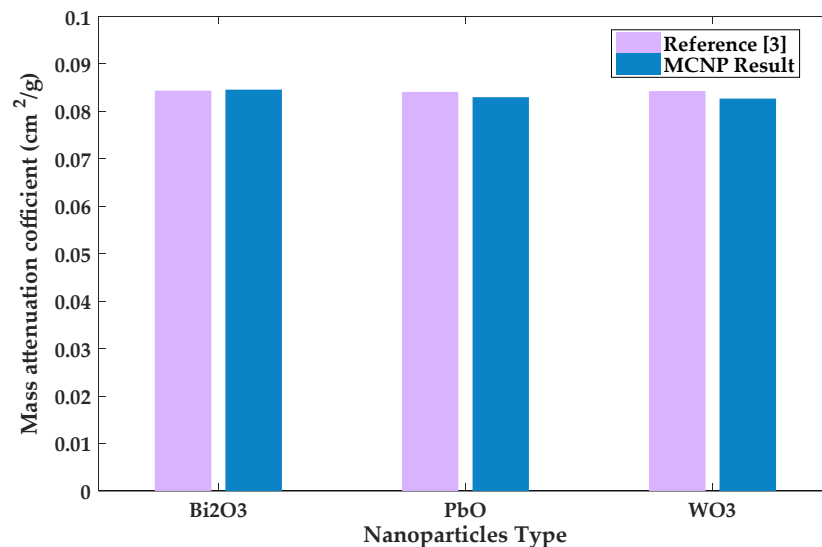


Figure 4. Validation results based on aluminum mass attenuation coefficient.

Additionally, verification of the MCNP5 model was done by comparing results from the model to those obtained in literature for composites with three different additives. By developing a new MCNP5 model containing three composite materials (silicon-resin/ $\text{WO}_3$ , silicon-resin/ $\text{PbO}$  and silicon-resin/ $\text{Bi}_2\text{O}_3$ ), the mass attenuation coefficient for each composite material was calculated for a photon energy of 0.6638 MeV and the concentration of nanoparticles equal to 37.5 wt%. Comparison between results of this analysis and Verdipoor's results [3] are shown in Figure 5. The results from Verdipoor's study entailed mass attenuation coefficients of 0.0843, 0.0841, and 0.0844  $\text{cm}^2/\text{g}$ , for silicon-resin/ $\text{WO}_3$ ,

silicon-resin/PbO and silicon-resin/Bi<sub>2</sub>O<sub>3</sub> composites, respectively. It can be seen that there is a good agreement between both sets of results with a maximum deviation of 1.9%.



**Figure 5.** Verification results based on mass attenuation coefficients of silicon resin composites.

### 3.2. Empirically Derived Correlations for the Shielding Properties of Composite Materials

MCNP5 simulations were performed to study the effect of the weight fraction of lead nanoparticles on the mass attenuation coefficient of composite materials. Results for epoxy/carbon fiber composites and epoxy/glass fiber composites are reported in Table 5. The calculated values of linear and mass attenuation coefficients for composites with weight fractions ranging from 0 wt% to 50 wt% at 0.662 MeV source energy are tabulated for increments of 2.5 wt%. Furthermore, the Mean Free Path (*MFP*), defined as the average distance between two successive photon interactions, was calculated using the following equation:

$$MFP = \frac{1}{\mu} \quad (1)$$

Additionally, material thickness for which the intensity of the incident radiation is decreased by half, called the half-value layer (*HVL*), was calculated using the following equation:

$$HVL = \frac{\ln(2)}{\mu} \quad (2)$$

In the two equations above,  $\mu$  is the linear attenuation coefficient of the material. For the two shielding properties, *MFP* and *HVL*, smaller values indicate higher rates of interaction, consequently, better shielding capabilities of the material.

Linear attenuation coefficients of glass fiber composites were found to be greater than those of carbon fiber composites, consequently, glass fiber composites exhibit smaller values for both *MFP* and *HVL*. This result is expected because the density of glass fiber is greater than the density of carbon fiber. This advantage in terms of density leads to an increased rate of interaction inside the material matrix, consequently, larger values of mass attenuation coefficients.

As shown in Figure 6, results show that mass attenuation coefficients for both, carbon fiber composites and glass fiber composites increased as the lead weight fraction was increased up to a certain limit. Beyond that point (~15 wt%), the increment in mass attenuation coefficient becomes small even when the weight fraction of lead nanoparticles continued to increase (see Figure 6). Due to the negligible change in the mass attenuation coefficients of the two composites beyond this threshold value, a weight fraction of 15 wt% PbNPs is considered the optimal value for improved shielding properties of the two

composites. By comparing the shielding properties of the two composites without PbNPs and those with 15 wt% of PbNPs, it can be concluded that the addition of lead nanoparticles leads to a reduction of ~64% in the mass required to shield against gamma radiation.

**Table 5.** Computational results of linear and mass attenuation coefficients for composite materials.

Percentage of PbNPs wt%	Carbon Fiber				Glass Fiber			
	$\mu_m$ (cm <sup>2</sup> /g)	$\mu$ (cm <sup>-1</sup> )	HVL (cm)	MFP (cm)	$\mu_m$ (cm <sup>2</sup> /g)	$\mu$ (cm <sup>-1</sup> )	HVL (cm)	MFP (cm)
0	0.0775	0.1035	6.697	9.662	0.0778	0.1198	5.786	8.347
1	0.1373	0.1844	3.759	5.423	0.1415	0.2193	3.161	4.56
2	0.1536	0.2075	3.34	4.819	0.1545	0.2410	2.876	4.149
2.5	0.1635	0.2214	3.131	4.517	0.1650	0.2581	2.686	3.874
3	0.1640	0.2228	3.111	4.488	0.1667	0.2616	2.65	3.823
4	0.1747	0.2386	2.905	4.191	0.1761	0.2782	2.492	3.595
5	0.1799	0.2470	2.806	4.049	0.1810	0.2878	2.408	3.475
6	0.1869	0.2582	2.685	3.873	0.1851	0.2963	2.339	3.375
7	0.1906	0.2648	2.618	3.776	0.1920	0.3092	2.242	3.234
7.5	0.1942	0.2705	2.562	3.697	0.1913	0.3093	2.241	3.233
8	0.1937	0.2707	2.561	3.694	0.1963	0.3183	2.178	3.142
9	0.2007	0.2819	2.459	3.547	0.1973	0.3221	2.152	3.105
10	0.2011	0.2842	2.439	3.519	0.1986	0.3265	2.123	3.063
12.5	0.2073	0.2972	2.332	3.365	0.2091	0.3496	1.983	2.86
15	0.2151	0.3131	2.214	3.194	0.2144	0.3646	1.901	2.743
17.5	0.2155	0.3184	2.177	3.141	0.2188	0.3787	1.83	2.641
20	0.2241	0.3362	2.062	2.974	0.2201	0.3879	1.787	2.578
22.5	0.2240	0.3414	2.03	2.929	0.2206	0.3960	1.75	2.525
25	0.2237	0.3463	2.002	2.888	0.2218	0.4055	1.709	2.466
27.5	0.2217	0.3486	1.988	2.869	0.2240	0.4174	1.661	2.396
30	0.2269	0.3627	1.911	2.757	0.2233	0.4243	1.634	2.357
32.5	0.2254	0.3663	1.892	2.73	0.2226	0.4313	1.607	2.319
35	0.2249	0.3717	1.865	2.69	0.2239	0.4428	1.565	2.258
37.5	0.2242	0.3770	1.839	2.653	0.2229	0.4498	1.541	2.223
40	0.2218	0.3794	1.827	2.636	0.2216	0.4567	1.518	2.19
42.5	0.2219	0.3864	1.794	2.588	0.2189	0.4608	1.504	2.17
45	0.2223	0.3942	1.758	2.537	0.2195	0.4722	1.468	2.118
47.5	0.2168	0.3915	1.77	2.554	0.2131	0.4689	1.478	2.133
50	0.2145	0.3947	1.756	2.534	0.2152	0.4845	1.431	2.064

Furthermore, a comparison between the shielding properties of the two composites (with 15 wt% of PbNPs) to those of pure lead is presented in Table 6. It can be seen from Table 6 that the linear attenuation coefficient corresponding to the two composites is ~30–35% of that achieved by pure lead. Nevertheless, both composites show better behavior than pure lead in terms of the mass attenuation coefficient. Based on the data presented in Table 6, it can be concluded that the mass of either composite (with 15 wt% of PbNPs) required to shield against a given level of radiation is ~43% of the lead mass required to shield against the same level of radiation. The reduction in the mass required for shielding against radiation opens doors for a variety of applications where light weights and high strength are desired whereas high levels of radiation are encountered, examples of such applications include aviation and medical applications.

Curve fitting, based on a two-term exponential function, was performed in an attempt to find a mathematical correlation that correlates the mass attenuation coefficient to the weight fraction of lead nanoparticles. Fitting correlations for carbon fiber composites and glass fiber composites are expressed by Equations (3) and (4), respectively.

$$\mu_{m(CF)}(x) = 0.2132e^{0.09857x} - 0.1187e^{-27.22x} \quad (3)$$

$$\mu_{m(GF)}(x) = 0.2106e^{0.1114x} - 0.1154e^{-29.31x} \quad (4)$$

In these equations,  $x$  is a number between 0 and 1 expressing the weight fraction of lead nanoparticles,  $\mu_{m(CF)}$  is the mass attenuation coefficient for epoxy/carbon fiber composite  $\text{cm}^2/\text{g}$  and  $\mu_{m(GF)}$  is the mass attenuation coefficient for epoxy/glass fiber composite  $\text{cm}^2/\text{g}$ .

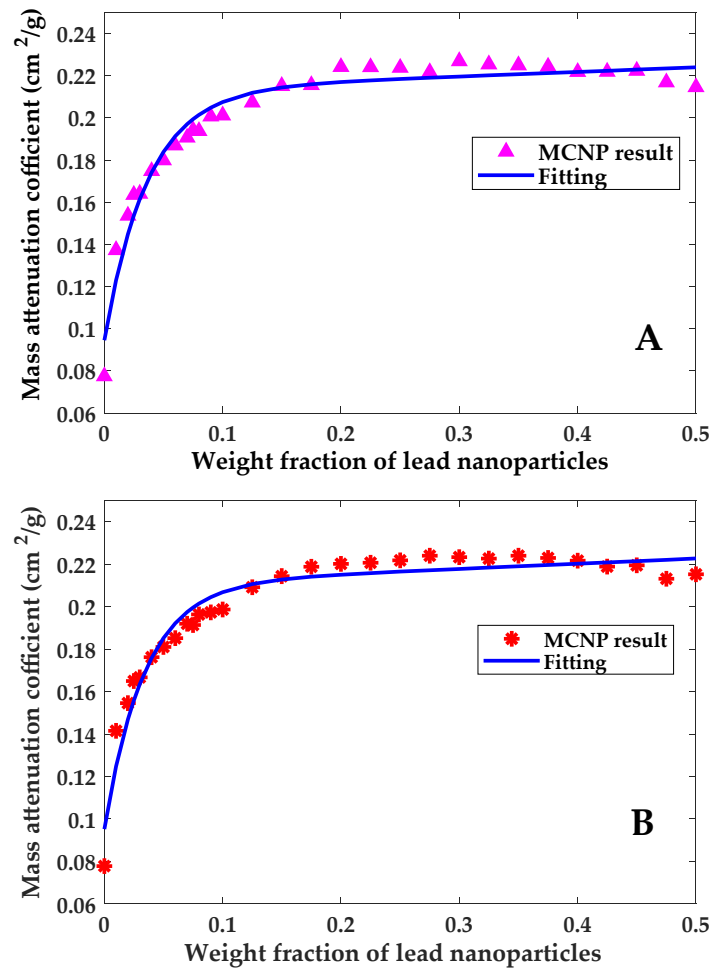


Figure 6. Computational results of  $\mu_m$  for (A) epoxy/CF-PbNPs (B) epoxy/GF-PbNPs.

Table 6. Comparison of composites with 15 wt% of PbNPs to pure lead.

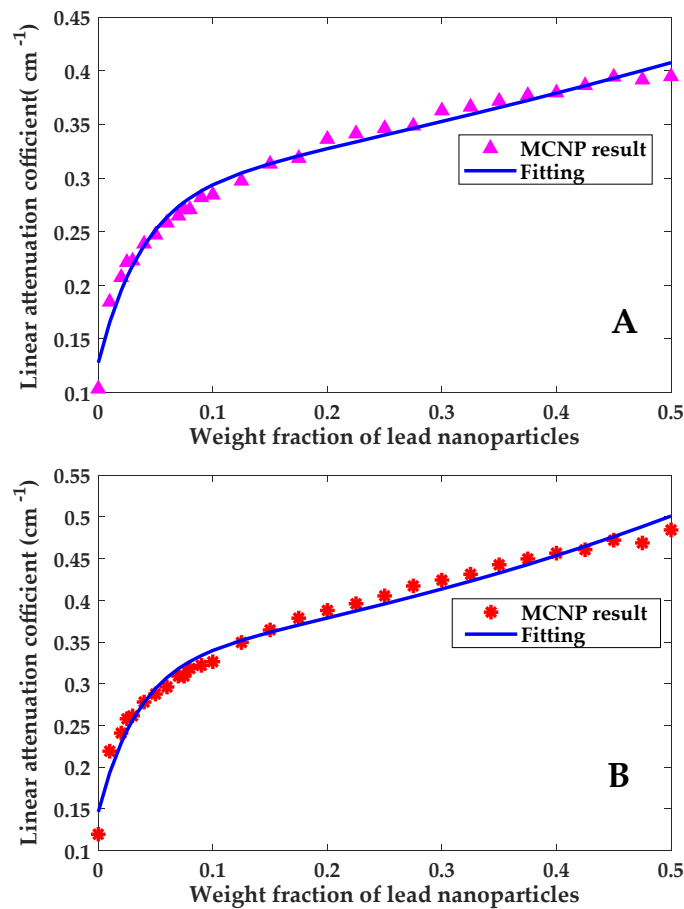
Material	Density (g/cm <sup>3</sup> )	$\mu_m$ (cm <sup>2</sup> /g)	$\mu$ (cm <sup>-1</sup> )	HVL (cm)	MFP (cm)
Pure lead	11.29	0.0917	1.0404	0.666	0.961
CF-composite	1.455	0.2151	0.3131	2.214	3.194
GF-composite	1.701	0.2144	0.3646	1.901	2.743

The value of lead weight fraction beyond which the change in mass attenuation coefficient becomes negligible is around 15 wt%. At this weight fraction, the mass attenuation coefficient is calculated at 0.2144  $\text{cm}^2/\text{g}$  and 0.2127  $\text{cm}^2/\text{g}$  for carbon fiber composites and glass fiber composites, respectively.

Moreover, curve fitting was performed for the linear attenuation coefficient data presented in Table 5. Both the simulation data and the fitting curve are shown in Figure 7. Fitting correlations for carbon fiber composites and glass fiber composites are expressed by Equations (5) and (6), respectively.

$$\mu_{CF}(x) = 0.2841e^{0.7217x} - 0.1563e^{-25.89x} \tag{5}$$

$$\mu_{GF}(x) = 0.3218e^{0.8572x} - 0.1737e^{-28.22x} \quad (6)$$



**Figure 7.** Computational results of  $\mu$  for (A) epoxy/CF-PbNPs, (B) epoxy/GF-PbNPs.

In these equations,  $x$  is a number between 0 and 1 expressing the weight fraction of lead nanoparticles,  $\mu_{CF}$  is the linear attenuation coefficient for epoxy/carbon fiber composite ( $\text{cm}^{-1}$ ) and  $\mu_{GF}$  is the linear attenuation coefficient for epoxy/glass fiber composite ( $\text{cm}^{-1}$ ).

To get an indication of the appropriateness of both correlations to capture the simulation data, statistical parameters for curve fitting were calculated and reported in Table 7. Statistical parameters in Table 7 give an indication that the correlations from curve fitting can accurately capture the behavior portrayed by the simulation data with acceptable root mean square error (RMSE) values.

**Table 7.** Statistical parameters for curve fitting.

Statistical Parameters	Carbon Fiber Composite		Glass Fiber Composite	
	$\mu_m$ ( $\text{cm}^2/\text{g}$ )	$\mu$ ( $\text{cm}^{-1}$ )	$\mu_m$ ( $\text{cm}^2/\text{g}$ )	$\mu$ ( $\text{cm}^{-1}$ )
Sum of squares for error (SSE)	0.001288	0.002421	0.001428	0.003477
R-square	0.96	0.9841	0.9527	0.9848
Adj R-square	0.9552	0.9821	0.947	0.9829
RMSE	0.007179	0.009841	0.007559	0.01179

#### 4. Conclusions

A computational model based on Monte Carlo simulations was developed using MCNP5 to derive empirical correlations for the shielding properties of epoxy/fiber composites with different weight fractions of lead nanoparticles. After verifying and validating the model, it was implemented for fiber reinforced polymer composites incorporating lead

nanoparticles and using two types of fiber, namely, carbon fiber and glass fiber. The results show that increasing the weight fraction of lead nanoparticles leads to increased values of mass attenuation coefficient. Nevertheless, there was a threshold value for PbNPs weight fraction beyond which the improvement in the mass attenuation coefficient becomes negligible. The threshold value of PbNP weight fraction was close to 15 wt%, for this weight fraction, the corresponding values for the mass attenuation coefficient were calculated at 0.2144 cm<sup>2</sup>/g for carbon fiber composites and 0.2127 cm<sup>2</sup>/g for glass fiber composites. Furthermore, the addition of lead nanoparticles led to a reduction in the *HVL* and *MFP* values, leading to decreased values for the material mass required to shield against gamma radiation. It was found that the addition of 15 wt% of PbNPs leads to a mass reduction of ~64% for the same level of shielding. Furthermore, the simulated composite samples with 15 wt% of lead nanoparticles showed better values for the mass attenuation coefficient compared to pure lead.

It can be concluded that the addition of lead nanoparticles to fiber reinforced composite materials is recommended for several applications, such as aviation applications, where high levels of radiation are expected, and light weights are required. Extensions to the work presented herein include, but are not limited to, experimental studies of the mechanical and shielding properties of composites incorporating different content of lead nanoparticles and comparing the results to the computational results of this study. Moreover, further simulation studies may be carried out for composites with different fiber content and different photon energies, shielding against other types of radiation, such as neutron and electron beam radiations, can also be investigated. Finally, other additives, such as tungsten and bismuth, can also be studied for their potential improvement on the shielding properties of fiber reinforced composite materials.

**Author Contributions:** Conceptualization, R.A.A.S., A.A. and M.A.-J.; methodology, R.A.A.S., M.A.-J. and F.A.-J.; software, M.A.-J. and F.A.-J.; validation, R.A.A.S., M.A.-J. and F.A.-J.; formal analysis, All authors; investigation, M.A.-J. and F.A.-J.; resources, R.A.A.S., A.A. and N.A.; data curation, R.A.A.S., M.A.-J. and F.A.-J.; writing—original draft preparation, R.A.A.S.; writing—review and editing, N.A., A.A., M.A.-J. and F.A.-J.; visualization, R.A.A.S. and M.A.-J.; supervision, R.A.A.S., N.A. and A.A.; project administration, R.A.A.S., N.A. and A.A.; funding acquisition, R.A.A.S., A.A. and N.A. All authors have read and agreed to the published version of the manuscript.

**Funding:** This research was funded by King Abdullah II Fund for Development (KAFFD), grant number 2019-16.

**Acknowledgments:** Gratitude is duly expressed to the King Abdullah II Fund for Development (KAFFD) for offering the financial support necessary to complete this work and the King Abdullah II Design and Development Bureau (KADDB) for their valuable supervision and guidance. This work would have not been possible without their support and assistance.

**Conflicts of Interest:** The authors declare no conflict of interest.

## References

1. ElSawy, A. Performance of Nanoparticle Materials on Radiation Shielding Properties Using Mont Carlo Method. *Int. J. Eng. Sci.* **2017**, *6*, 74–82.
2. Hassan, H.E.; Badran, H.M.; Aydarous, A.; Sharshar, T. Studying the effect of nano lead compounds additives on the concrete shielding properties for  $\gamma$ -rays. *Nucl. Instrum. Methods Phys. Res. Sect. B Beam Interact. Mater. At.* **2015**, *360*, 81–89. [[CrossRef](#)]
3. Verdipoor, K.; Alemi, A.; Mesbahi, A. Photon mass attenuation coefficients of a silicon resin loaded with WO<sub>3</sub>, PbO, and Bi<sub>2</sub>O<sub>3</sub> Micro and Nano-particles for radiation shielding. *Radiat. Phys. Chem.* **2018**, *147*, 85–90. [[CrossRef](#)]
4. Alshahrani, B.; Olarinoye, I.O.; Mutuwong, C.; Sriwunkum, C.; Yakout, H.A.; Tekin, H.O.; Al-Buriahi, M.S. Amorphous alloys with high Fe content for radiation shielding applications. *Radiat. Phys. Chem.* **2021**, *183*, 109386. [[CrossRef](#)]
5. Tishkevich, D.I.; Grabchikov, S.S.; Lastovskii, S.B.; Trukhanov, S.V.; Vasin, D.S.; Zubar, T.I.; Kozlovskiy, A.L.; Zdorovets, M.V.; Sivakov, V.A.; Muradyan, T.R.; et al. Function composites materials for shielding applications: Correlation between phase separation and attenuation properties. *J. Alloys Compd.* **2019**, *771*, 238–245. [[CrossRef](#)]
6. Kara, U.; Issa, S.A.M.; Yorgun, N.Y.; Kilicoglu, O.; Rashad, M.; Abuzaid, M.M.; Kavaz, E.; Tekin, H.O. Optical, structural and gamma ray shielding properties of dolomite doped lithium borate glasses for radiation shielding applications. *J. Non. Cryst. Solids* **2020**, *539*, 120049. [[CrossRef](#)]



7. Aygün, B.; Şakar, E.; Agar, O.; Sayyed, M.I.; Karabulut, A.; Singh, V.P. Development of new heavy concretes containing chrome-ore for nuclear radiation shielding applications. *Prog. Nucl. Energy* **2021**, *133*, 103645. [[CrossRef](#)]
8. Bhagwat, P.; Ramachandran, M.; Raichurkar, P. Mechanical Properties of Hybrid Glass/Carbon Fiber Reinforced Epoxy Composites. *Mater. Today Proc.* **2017**, *4*, 7375–7380. [[CrossRef](#)]
9. Jagannatha, T.; Harish, G. Mechanical Properties of Carbon/Glass Fiber Reinforced Epoxy Hybrid Polymer Composites. *Int. J. Mech. Eng. Robot. Res.* **2015**, *4*, 131–137.
10. Özdemir, T.; Güngör, A.; Akbay, I.K.; Uzun, H.; Babuccuoglu, Y. Nano lead oxide and epdm composite for development of polymer based radiation shielding material: Gamma irradiation and attenuation tests. *Radiat. Phys. Chem.* **2018**, *144*, 248–255. [[CrossRef](#)]
11. Shajari, S.; Arjmand, M.; Pawar, S.; Sundararaj, U.; Sudak, L.J. Synergistic effect of hybrid stainless steel fiber and carbon nanotube on mechanical properties and electromagnetic interference shielding of polypropylene nanocomposites. *Compos. Part B Eng.* **2019**, *165*, 662–670. [[CrossRef](#)]
12. O'Brien, K.; Friedberg, W. Atmospheric cosmic rays at aircraft altitudes. *Environ. Int.* **1994**, *20*, 645–663. [[CrossRef](#)]
13. Ferrari, A.; Pelliccioni, M.; Villari, R. A mathematical model of aircraft for evaluating the effects of shielding structure on aircrew exposure. *Radiat. Prot. Dosim.* **2005**, *116*, 331–335. [[CrossRef](#)] [[PubMed](#)]
14. Eid, G.A.; Kany, A.I.; El-Toony, M.M.; Madbouly, A.M.; Bashter, I.I.; Gaber, F.A. Application of Epoxy/Pb<sub>3</sub>O<sub>4</sub> Composite for Gamma Ray Shielding. *Arab J. Nucl. Sci. Appl.* **2013**, *46*, 226–233.
15. Chang, L.; Zhang, Y.; Liu, Y.; Fang, J.; Luan, W.; Yang, X.; Zhang, W. Preparation and characterization of tungsten/epoxy composites for  $\gamma$ -rays radiation shielding. *Nucl. Instrum. Methods Phys. Res. Sect. B Beam Interact. Mater. At.* **2015**, *356–357*, 88–93. [[CrossRef](#)]
16. Li, R.; Gu, Y.; Wang, Y.; Yang, Z.; Li, M.; Zhang, Z. Effect of particle size on gamma radiation shielding property of gadolinium oxide dispersed epoxy resin matrix composite. *Mater. Res. Express* **2017**, *4*, 35035. [[CrossRef](#)]
17. Rajavikraman, R.S.; Nitin, P.N. Novel Method for Radiation Shielding Using Nano-Concrete Composite. *Int. J. Mater. Sci. Eng.* **2013**, 20–23. [[CrossRef](#)]
18. Elanchezian, C.; Ramnath, B.V.; Hemalatha, J. Mechanical Behaviour of Glass and Carbon Fibre Reinforced Composites at Varying Strain Rates and Temperatures. *Procedia Mater. Sci.* **2014**, *6*, 1405–1418. [[CrossRef](#)]
19. Vázquez-Moreno, J.; Sánchez-Hidalgo, R.; Sanz-Horcajo, E.; Viña, J.; Verdejo, R.; López-Manchado, M. Preparation and Mechanical Properties of Graphene/Carbon Fiber-Reinforced Hierarchical Polymer Composites. *J. Compos. Sci.* **2019**, *3*, 30. [[CrossRef](#)]
20. Hoffman, E.N.; Skidmore, T.E. Radiation effects on epoxy/carbon-fiber composite. *J. Nucl. Mater.* **2009**, *392*, 371–378. [[CrossRef](#)]
21. Alsabbagh, A.; Abu Saleem, R.; Almasri, R.; Aljarrah, S.; Awad, S. Effects of gamma irradiation on 3D-printed polylactic acid (PLA) and high-density polyethylene (HDPE). *Polym. Bull.* **2020**, *70*, 1–15. [[CrossRef](#)]
22. Okuno, K. Neutron shielding material based on colemanite and epoxy resin. *Radiat. Prot. Dosim.* **2005**, *115*, 258–261. [[CrossRef](#)]
23. Kara, H.; Karabul, Y.; Kılıç, M.; İçelli, O.; Güven Özdemir, Z. Volcanic Rock Reinforced Epoxy Composites for Gamma Ray Shielding. *Eur. J. Sci. Technol.* **2019**, 552–560. [[CrossRef](#)]
24. Tekin, H.O.; Sayyed, M.I.; Issa, S.A.M. Gamma radiation shielding properties of the hematite-serpentine concrete blended with WO<sub>3</sub> and Bi<sub>2</sub>O<sub>3</sub> micro and nano particles using MCNPX code. *Radiat. Phys. Chem.* **2018**, *150*, 95–100. [[CrossRef](#)]
25. Tekin, H.O.; Singh, V.P.; Manıcı, T. Effects of micro-sized and nano-sized WO<sub>3</sub> on mass attenuation coefficients of concrete by using MCNPX code. *Appl. Radiat. Isot.* **2017**, *121*, 122–125. [[CrossRef](#)]
26. Tekin, H.O.; Singh, V.P.; Kara, Ü.; Manıcı, T.; Altınsoy, E.E. Investigation of Nanoparticle Effect on Radiation Shielding Property Using Monte Carlo Method. *Celal Bayar Üniversitesi Fen Bilim. Derg.* **2016**, *12*, 12. [[CrossRef](#)]
27. Kazemi, F.; Malekie, S.; Hosseini, M.A. A monte carlo study on the shielding properties of a novel polyvinyl alcohol (PVA)/WO<sub>3</sub> composite, against gamma rays, using the MCNPX code. *J. Biomed. Phys. Eng.* **2019**, *9*, 465–472. [[CrossRef](#)] [[PubMed](#)]
28. Cho, J.; Chen, J.Y.; Daniel, I.M. Mechanical enhancement of carbon fiber/epoxy composites by graphite nanoplatelet reinforcement. *Scr. Mater.* **2007**, *56*, 685–688. [[CrossRef](#)]
29. Belgin, E.E.; Aycik, G.A. Preparation and radiation attenuation performances of metal oxide filled polyethylene based composites for ionizing electromagnetic radiation shielding applications. *J. Radioanal. Nucl. Chem.* **2015**, *306*, 107–117. [[CrossRef](#)]
30. Mahmoud, M.E.; El-Khatib, A.M.; Badawi, M.S.; Rashad, A.R.; El-Sharkawy, R.M.; Thabet, A.A. Recycled high-density polyethylene plastics added with lead oxide nanoparticles as sustainable radiation shielding materials. *J. Clean. Prod.* **2018**, *176*, 276–287. [[CrossRef](#)]
31. Harish, V.; Nagaiah, N.; Kumar, H.G.H. Lead oxides filled isophthalic resin polymer composites for gamma radiation shielding applications. *Indian J. Pure Appl. Phys.* **2012**, *50*, 847–850.
32. Husain, H.S.; Rasheed Naji, N.A.; Mahmood, B.M. Investigation of Gamma Ray Shielding by Polymer Composites. *IOP Conf. Ser. Mater. Sci. Eng.* **2018**, *454*, 12131. [[CrossRef](#)]
33. Mheemeed, A.K.; Hasan, H.I.; Al-Jomaily, F.M. Gamma-ray absorption using rubber—lead mixtures as radiation protection shields. *J. Radioanal. Nucl. Chem.* **2011**, *291*, 653–659. [[CrossRef](#)]
34. Azman, N.Z.N.; Siddiqui, S.A.; Hart, R.; Low, I.M. Microstructural design of lead oxide-epoxy composites for radiation shielding purposes. *J. Appl. Polym. Sci.* **2012**, *128*, 3213–3219. [[CrossRef](#)]
35. Issa, S.A.M.; Tekin, H.O.; Erguzel, T.T.; Susoy, G. The effective contribution of PbO on nuclear shielding properties of xPbO-(100 - x)P<sub>2</sub>O<sub>5</sub> glass system: A broad range investigation. *Appl. Phys. A Mater. Sci. Process.* **2019**, *125*, 640. [[CrossRef](#)]

36. Issa, S.A.; Zakaly, H.M.H.; Pyshkina, M.; Mostafa, M.Y.A.; Rashad, M.; Soliman, T.S. Structure, optical, and radiation shielding properties of PVA–BaTiO<sub>3</sub> nanocomposite films: An experimental investigation. *Radiat. Phys. Chem.* **2021**, *180*, 109281. [[CrossRef](#)]
37. Henaish, A.M.A.; Mostafa, M.; Salem, B.I.; Zakaly, H.M.H.; Issa, S.A.M.; Weinstein, I.A.; Hemeda, O.M. Spectral, electrical, magnetic and radiation shielding studies of Mg-doped Ni–Cu–Zn nanoferrites. *J. Mater. Sci. Mater. Electron.* **2020**, *31*, 20210–20222. [[CrossRef](#)]
38. Zhang, P.; Jia, C.; Li, J.; Wang, W. Shielding composites for neutron and gamma-radiation with Gd<sub>2</sub>O<sub>3</sub>@W core-shell structured particles. *Mater. Lett.* **2020**, *276*, 128082. [[CrossRef](#)]
39. Diago, J.R. Simulation of Detector Calibration Using MCNP. 2005. Available online: <http://www.upv.es/cherne/activities/CHERNE-sem-MC.pdf> (accessed on 21 October 2021).
40. X-5 Monte Carlo Team. *MCNP—A General Monte Carlo N-Particle Transport Code, Version 5 Volume II: User's Guide*; Los Alamos National Laboratory: Los Alamos, NM, USA, 2008.
41. X-5 Monte Carlo Team. *MCNP—A General Monte Carlo N-Particle Transport Code, Version 5, Volume I: Overview and Theory*; Los Alamos National Laboratory: Los Alamos, NM, USA, 2003.
42. Shultis, J.K.; Faw, R.E. Radiation Shielding. In *Nuclear Energy*; Springer: New York, NY, USA, 2012; pp. 389–425. [[CrossRef](#)]
43. Abdurrohman, K.; Satrio, T.; Muzayadah, N.L. A comparison process between hand lay-up, vacuum infusion and vacuum bagging method toward e-glass EW 185/lycal composites. *J. Phys. Conf. Ser.* **2018**, *1130*, 012018. [[CrossRef](#)]



## Article

# A Meta-Model to Predict the Drag Coefficient of a Particle Translating in Viscoelastic Fluids: A Machine Learning Approach

Salah A. Faroughi <sup>1,\*</sup>, Ana I. Roriz <sup>2</sup> and Célio Fernandes <sup>1,2</sup>

<sup>1</sup> Geo-Intelligence Laboratory, Ingram School of Engineering, Texas State University, San Marcos, TX 78666, USA

<sup>2</sup> Department of Polymer Engineering, Institute for Polymers and Composites (IPC), Campus of Azurém, Engineering School of the University of Minho, 4800-058 Guimarães, Portugal; b12374@dep.uminho.pt (A.I.R.); cbpf@dep.uminho.pt (C.F.)

\* Correspondence: salah.faroughi@txstate.edu

**Abstract:** This study presents a framework based on Machine Learning (ML) models to predict the drag coefficient of a spherical particle translating in viscoelastic fluids. For the purpose of training and testing the ML models, two datasets were generated using direct numerical simulations (DNSs) for the viscoelastic unbounded flow of Oldroyd-B (*OB-set* containing 12,120 data points) and Giesekus (*GI-set* containing 4950 data points) fluids past a spherical particle. The kinematic input features were selected to be Reynolds number,  $0 < Re \leq 50$ , Weissenberg number,  $0 \leq Wi \leq 10$ , polymeric retardation ratio,  $0 < \zeta < 1$ , and shear thinning mobility parameter,  $0 < \alpha < 1$ . The ML models, specifically Random Forest (RF), Deep Neural Network (DNN) and Extreme Gradient Boosting (XGBoost), were all trained, validated, and tested, and their best architecture was obtained using a 10-Fold cross-validation method. All the ML models presented remarkable accuracy on these datasets; however the XGBoost model resulted in the highest  $R^2$  and the lowest root mean square error (RMSE) and mean absolute percentage error (MAPE) measures. Additionally, a blind dataset was generated using DNSs, where the input feature coverage was outside the scope of the training set or interpolated within the training sets. The ML models were tested against this blind dataset, to further assess their generalization capability. The DNN model achieved the highest  $R^2$  and the lowest RMSE and MAPE measures when inferred on this blind dataset. Finally, we developed a meta-model using stacking technique to ensemble RF, XGBoost and DNN models and output a prediction based on the individual learner's predictions and a DNN meta-regressor. The meta-model consistently outperformed the individual models on all datasets.

**Keywords:** machine learning; deep learning; stacked learning; viscoelastic flows; Oldroyd-B fluid; Giesekus fluid; sphere drag coefficient

**Citation:** Faroughi, S.A.; Roriz, A.I.; Fernandes, C. A Meta-Model to Predict the Drag Coefficient of a Particle Translating in Viscoelastic Fluids: A Machine Learning Approach. *Polymers* **2022**, *14*, 430. <https://doi.org/10.3390/polym14030430>

Academic Editor: Mirta I. Aranguren

Received: 22 December 2021

Accepted: 18 January 2022

Published: 21 January 2022

**Publisher's Note:** MDPI stays neutral with regard to jurisdictional claims in published maps and institutional affiliations.



**Copyright:** © 2022 by the authors. Licensee MDPI, Basel, Switzerland. This article is an open access article distributed under the terms and conditions of the Creative Commons Attribution (CC BY) license (<https://creativecommons.org/licenses/by/4.0/>).

## 1. Introduction

The flow of particle-laden complex fluids has been the centerpiece of many well-documented experimental, theoretical, and numerical approaches [1–4]. These fluids are non-Newtonian in character showing shear thinning, shear thickening, viscoplastic, time-dependent and viscoelastic behaviors under different flow conditions. Resolving the dynamics of particles within these fluids is extremely challenging both experimentally and computationally, especially when the matrix fluid is viscoelastic, e.g., a polymer solution or polymer melt [4–7].

Characterizing the dynamics of particles in complex fluids under different flow and/or environmental conditions requires comprehensive experimentation and simulation tools to resolve the nonlinear interplay of multiple physical variables, flow parameters and many-body interactions [8]. This is computationally expensive even when using high performance computing resources with robust parallelized algorithms [4]. In recent decades, many physics-based numerical models have been proposed to model complex fluids, see

the review by Maxey [9]. These approaches are limited to specific conditions and cannot be practically applied to large-scale engineering applications where hundreds or millions of particles are suspended, e.g., blood and other biological fluids, hydraulic fracturing, cementing, etc. [10,11]. In addition to the computing power, the insufficiency of comprehensive physics-based constitutive models to describe a broad range of complexities involved with such fluids, their use in realistic conditions encounter severe uncertainties or limitations. Therefore, the wealth of existing domain knowledge and scientific capabilities in this field need to be complemented with evolving technologies such as Machine Learning (ML) and Deep Learning (DL) to accelerate fundamental and applied research and close knowledge and computational gaps. For example, for a time intensive conventional computational model, both inner-loop (i.e., forward simulations) and the outer-loop (optimization and data assimilation) can be improved using the adaptivity and acceleration of ML- or DL-based models [12,13].

One main challenge for the application of ML and DL in the field of complex fluids is the lack of datasets. This challenge can be resolved by an in-line integration of traditional (e.g., CFD) and DL-based modeling, so-called a physics-informed DL, physics-guided DL, or digital-twin technique [14]. The ML or DL algorithms can be trained and integrated with traditional physics-based forward modeling to predict the flow dynamics under different conditions at a reduced computational cost. The latter is done by learning the solutions for ordinary and partial differential equations governing the system [13] or learning the closure laws for the pertinent physics, e.g., lift and drag forces, turbulence models, etc.

Such integration can be explored for the Eulerian-Lagrangian multi-phase model [6,15], as one of the main computational methods to resolve the flow of complex fluids. The ML/DL integration can drastically increase the robustness of this numerical algorithm that integrates the presence of multiple non-Brownian particles as the discrete material phase embedded in a viscoelastic fluid treated as a continuum phase. In particular, the momentum-exchange model, including drag, lift, hindrance, and retardation closure laws to couple the constituents [6,16,17], can be replaced with ML or DL models. In this approach, the fundamental goal is to provide reasonably accurate data-driven predictions that substitute expensive computational steps. These data-driven models learn the multitude of coupling within the complex fluids at the particle-level and enable accurate simulations of complex fluids at larger length and time scales.

In the present contribution, we propose to take the first step and complement the Eulerian-Lagrangian multi-phase approach with a data-driven drag model for the translation of a spherical particle in constant viscosity and shear thinning matrix-based viscoelastic fluids. In a constant viscosity elastic fluid, the drag coefficient decreases at low levels of elasticity, and increases at high elasticity due to the large elastic stresses developing on the surface and on the wake of the particles [1,18–20]. When the shear thinning effect is added, the drag coefficient decreases as elasticity increases. Recently, Faroughi et al. [6] developed a closure drag model for a single spherical particle translating through constant viscosity elastic fluids described by the Oldroyd-B constitutive equation. However, due to strong interaction of elasticity (e.g., high Weissenberg number) and kinematic parameters (shear thinning and thickening), a general solution for this problem that can integrate all dimensions of the data and perform well over a wide range of parameters, is still missing and cannot be formed using traditional approaches.

Accordingly, the present contribution is undertaken to achieve two goals. First, we generate and condition comprehensive datasets capturing the dynamics of a spherical particle translating through constant viscosity and shear thinning viscoelastic fluids. This is done using direct numerical simulations (DNSs) following the work of Faroughi et al. [6]. The data are processed and labeled for a set of operational conditions to be consumed by supervised ML and DL methodologies. Second, we develop data-driven drag models by examining several ML-based regression methods trained, validated and tested on the generated datasets. The performance, accuracy and productivity of different models are thoroughly evaluated based on common statistical measures.

The paper is organized in the following manner: in Section 2 we present the governing equations describing the transient, incompressible and isothermal laminar flows of viscoelastic matrix-based fluids. We also present the physical system and computational domain used to generate the training datasets. In Section 3, the ML-based regression algorithms employed to predict the viscoelastic drag coefficient are described. Next, in Section 4, we present the complexity of the training datasets in detail and compare the performance of each ML model employed to learn the characteristics of these datasets. A meta-model, based on different ML models, is then trained to fully describe the datasets. Finally, in Section 5, we summarize the main conclusions of this work.

## 2. Underlying Physics

The conservation equations governing transient, incompressible and isothermal laminar flow of viscoelastic fluids are the continuity, momentum balance and constitutive equations. The continuity and momentum balance equations read as follows,

$$\nabla \cdot (\rho \mathbf{u}) = 0 \quad (1)$$

$$\frac{\partial(\rho \mathbf{u})}{\partial t} + \nabla \cdot (\rho \mathbf{u} \mathbf{u}) + \nabla \cdot (p \mathbf{I}) - \nabla \cdot \boldsymbol{\tau} = 0 \quad (2)$$

where  $\rho$  is the fluid density,  $\mathbf{u}$  is the velocity vector,  $t$  is the time,  $p$  is the pressure,  $\mathbf{I}$  is the identity tensor and  $\boldsymbol{\tau}$  is the total extra-stress tensor, which is split into solvent ( $\boldsymbol{\tau}_S$ ) and polymeric ( $\boldsymbol{\tau}_P$ ) contributions, such that  $\boldsymbol{\tau} = \boldsymbol{\tau}_S + \boldsymbol{\tau}_P$ . These stress terms are obtained by the following constitutive equations,

$$\boldsymbol{\tau}_S = \eta_S (\nabla \mathbf{u} + \nabla \mathbf{u}^T) \quad (3)$$

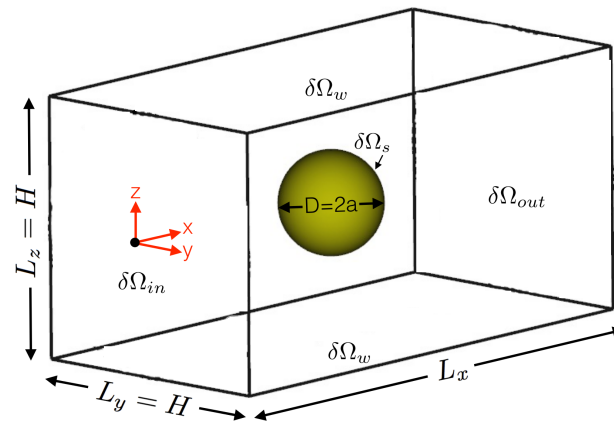
$$\lambda \overset{\nabla}{\boldsymbol{\tau}}_P + \boldsymbol{\tau}_P + \frac{\alpha \lambda}{\eta_P} \boldsymbol{\tau}_P \cdot \boldsymbol{\tau}_P = \eta_P (\nabla \mathbf{u} + \nabla \mathbf{u}^T) \quad (4)$$

where  $\eta_S$  and  $\eta_P$  are the solvent and polymeric viscosities, respectively,  $\lambda$  is the fluid relaxation time,  $\alpha$  is the mobility parameter and  $\overset{\nabla}{\boldsymbol{\tau}}_P$  indicates the upper-convective time derivative of the polymeric extra-stress tensor defined as,

$$\overset{\nabla}{\boldsymbol{\tau}}_P \equiv \frac{\partial \boldsymbol{\tau}_P}{\partial t} + \mathbf{u} \cdot \nabla \boldsymbol{\tau}_P - \boldsymbol{\tau}_P \cdot \nabla \mathbf{u} - \nabla \mathbf{u}^T \cdot \boldsymbol{\tau}_P \quad (5)$$

Equation (4) is known as the Giesekus viscoelastic constitutive model [21]. For the particular case where the mobility parameter is zero,  $\alpha = 0$ , Equation (4) reduces to the well-known quasi-linear elastic dumbbell fluid, the Oldroyd-B fluid. When written in the continuum formulation, viscoelastic fluid flows are well known to introduce numerical convergence difficulties at high Weissenberg numbers. This is mainly related to the lack of sufficient resolution of the discretization methods to resolve the exponential growth of stresses near critical points as the Weissenberg number is incremented. To prevent this issue in the calculation of the polymeric extra-stress tensor components, we follow the log-conformation approach [22,23] implemented in the OpenFOAM [24] computational library.

We use the above governing equations to perform an extensive set of DNSs and calculate the drag coefficient for a spherical particle translating in viscoelastic fluids. Figure 1 schematically illustrates the computational domain used in this study to simulate the unbounded viscoelastic flow around a sphere [6]. The domain size in flow direction,  $L_x$ , is considered larger than other dimensions to allow enough space for the polymer chains to be relaxed. Our numerical model and solver were comprehensively tested against this computational challenge (see, e.g., Fernandes et al. [25] and Faroughi et al. [6] for the case of an Oldroyd-B fluid flow around a sphere). All the numerical simulations were performed in parallel using several High-Performance Computing facilities (see Acknowledgments section). On a system with a 2.30 GHz AMD EPYC 7742 64-Core processor, the computational time for a single run was  $12 \pm 1$  h.



**Figure 1.** Schematic illustration of the computational domain (square duct) used to simulate the viscoelastic fluid flow past a sphere.

For the present problem, we define the Reynolds and Weissenberg dimensionless numbers as follows,

$$Re = \frac{2a\rho U}{\eta_0} \tag{6}$$

$$Wi = \frac{\lambda U}{a} \tag{7}$$

where  $U$  is the inlet average fluid velocity and  $a$  is the sphere radius ( $D = 2a$  is the sphere diameter). Additionally, the other dimensionless numbers considered in this work are the shear thinning mobility parameter  $\alpha$ , and the polymeric viscosity ratio  $\zeta$ . The latter is also known as the characteristic retardation ratio defined as,

$$\zeta = \frac{\eta_P}{\eta_S + \eta_P} = \frac{\eta_P}{\eta_0} \tag{8}$$

where  $\eta_0$  is the total fluid viscosity in the limit of vanishing shear rate and  $\eta_S$  and  $\eta_P$  are the solvent and polymeric contributions to the fluid viscosity, respectively.

Here, we carry out the calculations for the viscoelastic drag coefficient,  $C_D$ , using the surface integration of the total stress,  $\boldsymbol{\tau} = \boldsymbol{\tau}_P + \boldsymbol{\tau}_S$ , and pressure field,  $p$ , on the surface of the sphere as,

$$C_D = \frac{2}{\rho U^2 A} \int_{\delta\Omega_s} (\boldsymbol{\tau}_P + \boldsymbol{\tau}_S - p\mathbf{I}) \cdot \mathbf{n} \cdot \mathbf{x} dS \tag{9}$$

where  $A$  is the cross-sectional area of the sphere,  $\mathbf{n}$  is the unit normal vector to the sphere surface,  $S$ , and  $\mathbf{x}$  is the unit vector parallel to the flow direction. The results computed for the viscoelastic drag coefficient using Equation (9) are normalized by,

$$\chi = \frac{C_D}{C_D(Wi = 0)} \tag{10}$$

where  $\chi$  is the viscoelastic drag coefficient correction factor [6].

### 3. Machine Learning Regression Algorithms

To relate the input features (i.e., a set of explanatory variables,  $Re$ ,  $Wi$ ,  $\zeta$  and  $\alpha$ ) to the output features (i.e., the response variable,  $\chi$ ), different ML-based regression algorithms are employed in this work. These algorithms enable us to model multidimensional datasets which cannot be described using traditional techniques [6]. In the most basic form, the linear regression model explains a dependent variable  $y$  via a linear combination of the independent features,  $x_i$  ( $i = 1, \dots, n$ ),

$$y = \beta_0 + \beta_1 x_1 + \dots + \beta_n x_n + \varepsilon \tag{11}$$

where  $\varepsilon$  is an additive error and  $\beta_j$  ( $j = 0, \dots, n$ ) are the coefficients of the features. Despite its simplicity, this model is widely used as a baseline and a tool to analytically study the independent variables and understand the significance of the input features. To achieve more accurate estimates and prevent the overfitting issue, we consider more sophisticated regression models such as ensemble decision tree algorithms (Random Forest and Extreme Gradient Boosting) and a Deep Neural Network (DNN). These methods possess their own challenges and should be applied with special care in scenarios where the training data are sparse [26].

The Random Forest (RF) is an ensemble learning technique that alleviates the overfitting issue and offers excellent performance within the scope of the training data [27]. In this approach, multiple decision trees are constructed at training time and the mean of the individual predictions is reported as the output of the ensemble method. At each candidate splitting within each tree model, a randomly selected subset of feature space is used. This trick has proven to be very effective and the resulting models are usually robust to the overfitting problem [28]. The RF models have emerged as a versatile and highly accurate regression methodology requiring little tuning while providing interpretable outputs. In summary, the RF algorithm includes (i) randomly select  $n$  subsamples, (ii) train the regression tree for each sample, and finally (iii) average all prediction results from all trees. This algorithm has 16 main hyperparameters as listed in Table 1, and the most important ones to tune are the `n_estimators` that represents the total number of trees in the forest, and `Max_feature` that represents the number of features to consider when looking for the best split. The selection of the feature for node splitting from a random set of features decreases the correlation between different trees and, thus, the average prediction of multiple regression trees is expected to have lower variance than individual regression trees [28].

The Extreme Gradient Boosting (XGBoost) algorithm proposed by Chen and Guestrin [29] is an improved algorithm of gradient boosting to recognize complex, nonlinear patterns inside datasets. One of the differences between XGBoost and RF models is related to the way the trees are built. In RF, trees are built independent of each other, but, in XGBoost, a new tree is added to complement the already built ones [30]. A prediction value ( $y_i^*$ ) from an ensemble model can be represented as,

$$y_i^* = h(x_i) = \sum_{k=1}^K f_k(x_i), \quad i = 1, \dots, N \quad (12)$$

where  $f_k$  is a regression tree, and  $f_k(x_i)$  represents the score given by the  $k$ -th tree to the  $i$ -th observation in data. The goal in XGBoost is to minimize the regularized objective function expressed as [30],

$$L = \sum_{i=1}^N \Lambda(y_i, y_i^*) + \sum_{k=1}^K \Omega(f_k) \quad (13)$$

in order to choose functions  $f_k$ . Here,  $N$  is the number of observation (e.g., rows of data),  $\Lambda$  is the loss function which measures the accuracy and performance of the model in terms of its relationship between input ( $x_i$ ) and output ( $y_i$ ) features, and the penalty term  $\Omega$  is included to prevent too large complexity of the model, being defined as [30]

$$\Omega(f_k) = \gamma T + \frac{1}{2} \beta \|\omega\|^2 \quad (14)$$

where  $\gamma$  and  $\beta$  are parameters controlling penalty for the number of leaves,  $T$ , and magnitude of leaf weights,  $\omega$ , respectively. This penalty term makes XGBoost unique compared to general tree boosting methods. It has two main goals; (i) to prevent overfitting, and (ii) to simplify the end model produced by this algorithm. In addition to this regularized loss function, XGBoost is reinforced with two additional features that further prevent overfitting. First, the weights of each new tree can be scaled down reducing an impact of a single tree



on the final score, which provides more room for next trees to improve the model [30]. The second feature is a column sampling working in a similar way as RF where each tree is built using only a column-wise sample from the training dataset [31]. The XGBoost algorithm has 24 main hyperparameters as listed in Table 1, divided in three categories: (a) general parameters as a guide to the overall functioning, (b) booster parameters as a guide to the individual booster at each step, and (c) learning task parameters as a guide to the optimization performance.

**Table 1.** Tunable hyperparameters in different machine learning regression models applied in this study.

Model	Hyperparameters	Total Number
Random Forest	Bootstrap, criterion, max_depth, max_features, max_leaf_nodes, min_impurity_decrease, min_impurity_split, min_samples_leaf, min_samples_split, min_weight_fraction_leaf, n_estimators, n_jobs, oob_score, random_state, verbose, warm_start	16
XGBoost	base_score, booster, colsample_bylevel, colsample_bynode, colsample_bytree, gamma, importance_type, learning_rate, max_delta_step, max_depth, min_child_weight, missing, n_estimators, n_jobs, nthread, objective, random_state, reg_alpha, reg_lambda, scale_pos_weight, seed, silent, subsample, verbosity	24
DNN	activation, alpha, batch_size, beta_1, beta_2, early_stopping, epsilon, hidden_layer_sizes, learning_rate, learning_rate_init, max_iter, momentum, n_iter_no_change, nesterovs_momentum, power_t, random_state, shuffle, solver, tol, validation_fraction, verbose, warm_start	21

The Deep Neural Network (DNN) algorithms are one of the most commonly applied regression algorithms for stationary datasets [32]. The popular implementation is the multilayer perceptron (MLP), in which the architecture is optimized by iterating on various numbers of hidden neurons and layers that would lead to the best model with the highest accuracy on a dataset [33]. In MLP algorithm, the model is expressed as [34],

$$y = h \left( \varphi_0 + \sum_{j=1}^N \varphi_j g \left( \sum_{i=1}^M \theta_i x_i \right) \right) \quad (15)$$

where  $N$  and  $M$  represent the number of neurons in the hidden and input layers, respectively,  $g$  and  $h$  denote the transfer functions for the input layer and hidden layer, and the vector matrices of  $\theta$  and  $\varphi$  represent the weight values for neurons in the input and hidden layers, respectively. A cost function is defined to measure the accuracy and performance of the model in terms of its relationship between input and output features. The objective in MLP is to minimize the cost function defined as [35],

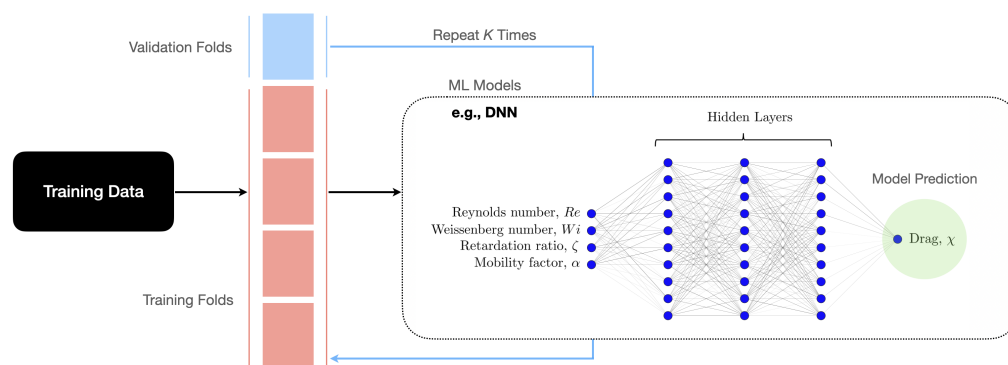
$$\text{Arg min} : \frac{1}{2n} \sum_{i=1}^n (h(x_i) - y_i)^2 \quad (16)$$

where  $n$  is the number of samples and  $h(x_i)$  represents the model prediction. The batch gradient descent technique and stochastic gradient descent are the well-known optimization algorithms used to minimize the cost function [26]. These algorithms find the direction (gradient) necessary to minimize the cost function and often they are known as a hill-climbing approach [36]. It is important to note that a DNN model might have the highest

accuracy in the training set obtained from multiple attempts, but it is prone to memorize the trend, noise, and detail in training set instead of intuitively understanding the trend in the dataset. Therefore, it loses the prediction capability. In order to avoid this, one may set a stoppage criteria for learning where the model tests its predictive capability on a validation set and stops training when validation accuracy departs from training accuracy. The DNN algorithm in total has 21 main hyperparameters as listed in Table 1, and the most important ones are hidden\_layer\_sizes and learning\_rate [37].

#### 4. Results and Discussion

This section reports the processes taken to generate training datasets and develop ML models that predict the drag coefficient correction of a spherical particle translating in viscoelastic fluids described by the Oldroyd-B (constant viscosity fluids) and Giesekus (shear thinning fluids) constitutive equations. Figure 2 shows a summary of the inputs and output data considered in the development of the ML models described in Section 3. The input features are Reynolds number, Weissenberg number, retardation ratio, and mobility parameter, and the output variable is the drag coefficient normalized by the Newtonian value, i.e.,  $\chi$  as defined in Section 2. Figure 2 shows a schematic architecture for the DNN model.



**Figure 2.** A summary of the training approach, input and output features to develop ML-based regression models (e.g., it is shown for a DNN model).

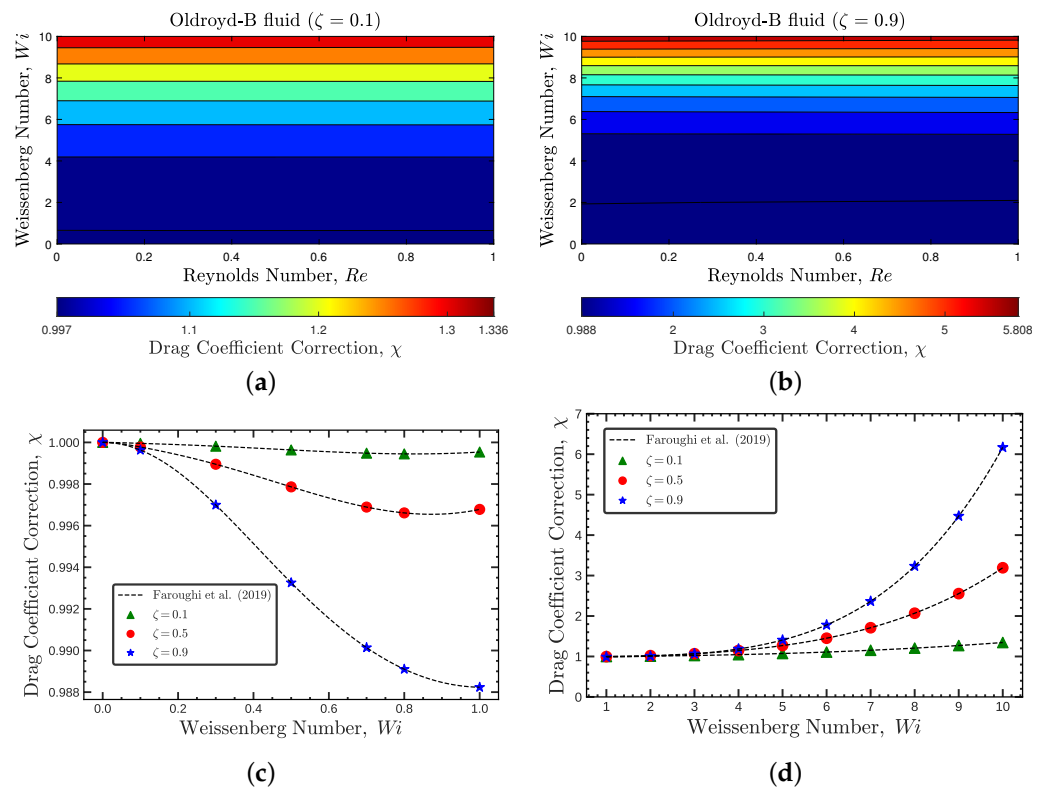
##### 4.1. Data Collection and Analysis for Oldroyd-B Fluids

For constant viscosity viscoelastic fluids [38], the relaxation time,  $\lambda$ , and retardation ratio,  $\zeta$ , are the two important characteristics that define the viscoelastic behaviors. These fluids are generally modeled using the Oldroyd-B constitutive equation [39], and best represent very dilute polymer solutions at low Weissenberg number. Direct numerical simulations (DNSs), following the methodology implemented by Faroughi et al. [6] on the physical system elaborated in Section 2, were employed to generate the training dataset for the viscoelastic drag coefficient correction of a sphere translating in Oldroyd-B fluids ( $\alpha = 0$ ). For that purpose, the range of the input features varied within  $0 < Re \leq 50$ ,  $0 \leq Wi \leq 10$ , and  $0 < \zeta < 1$ , which resulted in a total of 12,120 input values (hereafter we call this dataset *OB-set*). In addition to this dataset, we also generated a blind dataset, from a total of 60 DNSs, with an input feature coverage outside the scope or interpolated within the scope of *OB-set*. The blind dataset did not enter in the initial training, validation and testing phases and is used to scope the inference of the ML models beyond the limits of the training set, i.e., test the ML models' generalization as described in Section 4.4.

Figures 3 and 4 show the flow characteristics associated with the *OB-set*. In Figure 3a,b, the contours of the viscoelastic drag coefficient correction,  $\chi$ , are presented for Reynolds numbers  $0 < Re \leq 1$  and Weissenberg numbers  $0 \leq Wi \leq 10$  at two polymeric retardation ratios  $\zeta = 0.1$  and  $0.9$ , respectively. The viscoelastic drag coefficient correction follows the same behavior for both  $\zeta = 0.1$  and  $0.9$  across all considered  $Wi$  and  $Re$  numbers. As shown in Figure 3c,d, the viscoelastic drag coefficient correction slightly decreases at

low  $Wi$  number, hits a minimum and then sharply increases with  $Wi$  number. The drag enhancement is more significant at higher  $\zeta$  values (star blue symbols).

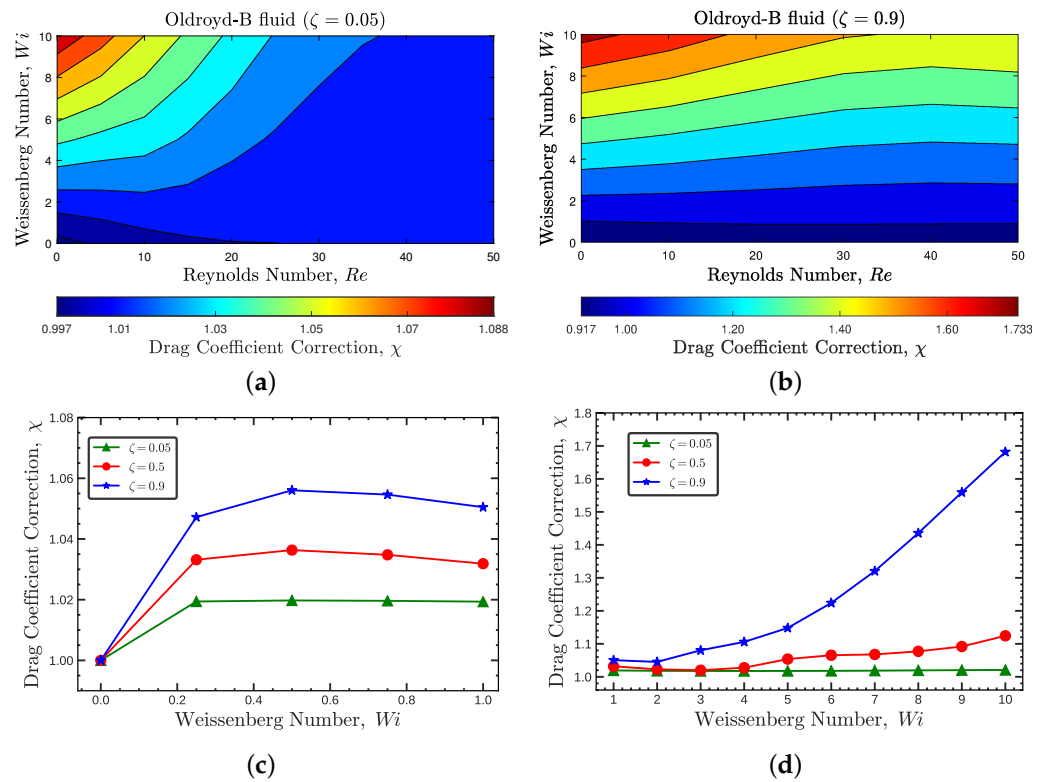
In Figure 4a,b, the contours of the viscoelastic drag coefficient correction,  $\chi$ , are presented for Weissenberg numbers  $0 \leq Wi \leq 10$  and Reynolds numbers  $Re \leq 50$  at two polymeric retardation ratios  $\zeta = 0.05$  and  $0.9$ , respectively. For both cases, the viscoelastic drag coefficient correction decreases with the increase of inertia and increases with  $Wi$ , being more noticeable for higher  $\zeta$ . Figure 4c,d, show the behavior of  $\chi$  at a fixed Reynolds number,  $Re = 50$ . The viscoelastic drag coefficient correction increases up to  $Wi < 0.2$ , then stays more or less constant up to  $Wi \approx 2$ , and then increases with  $Wi$  number, being this behavior more abrupt at higher retardation ratios.



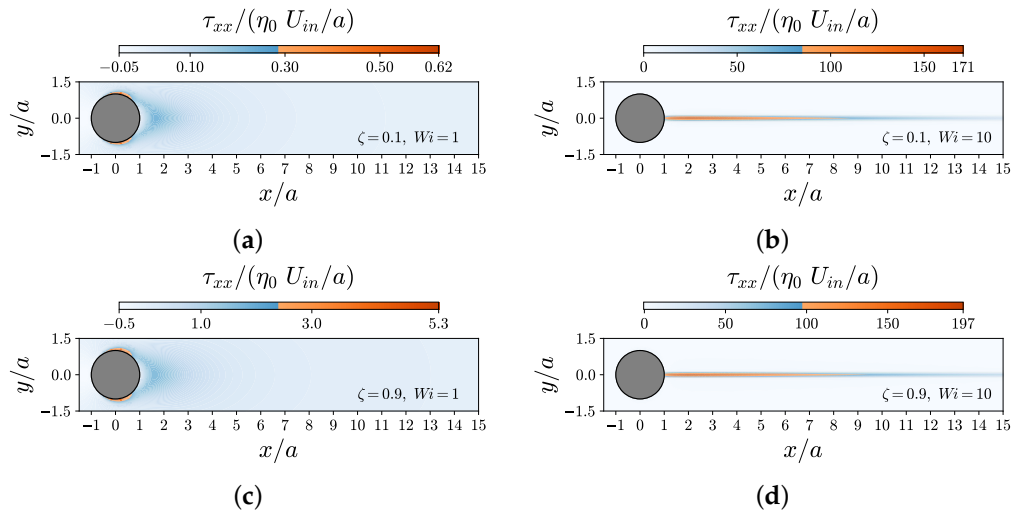
**Figure 3.** Contours of the viscoelastic drag coefficient correction,  $\chi$ , for the Oldroyd-B fluid at  $0 < Re \leq 1, 0 \leq Wi \leq 10$  and (a)  $\zeta = 0.1$  and (b)  $\zeta = 0.9$ . Panels (c,d) show the variation of  $\chi$  with Weissenberg numbers for different values of  $\zeta$  at  $Re = 1$ .

Figure 5 shows the contours of the normal component of the dimensionless polymeric stress,  $\tau_{xx}$ , for different values of  $Wi$  and  $\zeta$  at  $Re = 1$ . The left column in Figure 5 shows the  $\tau_{xx}$  contours at  $Wi = 1$ , and the right column shows the same but at  $Wi = 10$ . As expected, one observes that the magnitude of  $\tau_{xx}$  increases as  $\zeta$  increases. In addition, the location at which the maximum value of  $\tau_{xx}$  occurs shifts from the top/bottom flow separation points to the wake of the particle as  $Wi$  increases. At  $Wi = 10$ , for both  $\zeta$  values, a long wake was also observed in the downstream region of the flow, where extensional flow dominates due to the significant effects of the flow elasticity.

Due to the similarity observed in the behavior of  $\chi$  under different flow conditions ( $Re, Wi$  and  $\zeta$ ), the *OB-set* is an ideal dataset to be used in developing the building blocks for the ML-based models predicting the viscoelastic drag coefficient correction. However, the *OB-set* does not represent a large body of fluids that are encountered in nature or industrial applications. This issue is rectified in the next section using the shear thinning Giesekus constitutive equation [21] to augment the data.



**Figure 4.** Contours of the viscoelastic drag coefficient correction,  $\chi$ , for the Oldroyd-B fluid at  $0 < Re \leq 50, 0 \leq Wi \leq 10$  and (a)  $\zeta = 0.05$  and (b)  $\zeta = 0.9$ . Panels (c,d) show the variation of  $\chi$  with Weissenberg numbers for different values of  $\zeta$  at  $Re = 50$ .



**Figure 5.** Contours of the dimensionless normal component of the polymeric extra-stress tensor  $\tau_{xx}$  for the Oldroyd-B fluid at  $Re = 1$  for different values of  $\zeta$  and  $Wi$ : (a)  $\zeta = 0.1$  and  $Wi = 1$ , (b)  $\zeta = 0.1$  and  $Wi = 10$ , (c)  $\zeta = 0.9$  and  $Wi = 1$ , and (d)  $\zeta = 0.9$  and  $Wi = 10$ .

4.2. Data Collection and Analysis for Giesekus Fluids

Most of the viscoelastic fluids show mid to strong shear thinning features. Shear thinning behavior leads to more complex and nonlinear dependencies at non-vanishing Weissenberg numbers, at which shear thinning effects become more pronounced. This behavior (neglected in the previous section) dramatically changes the behavior of the viscoelastic drag coefficient correction,  $\chi$ . Therefore, the inference of the models trained based on the *OB-set* will certainly fail for shear thinning fluids. Hence, the *OB-set* must be augmented with data representing shear thinning fluids, or ML models developed based

on the *OB-set* must be further trained to also account for shear thinning effects. Several viscoelastic constitutive models have been developed over the past few decades to model shear thinning fluids [40]. The Giesekus fluid is the one generally used to best represent the polymer molecules contribution to the momentum exchange in dilute to semi-dilute polymer solutions [41]. This model is based on a concept of configuration-dependent molecular mobility, and thus, the viscoelastic component of the polymeric stress tensor is represented by  $\lambda$  and  $\zeta$  as well as the mobility parameter,  $\alpha$ . The mobility parameter varies between zero and unity (practically 0.5 is the upper limit [41]) and accounts for the shear thinning behavior of the viscoelastic fluids.

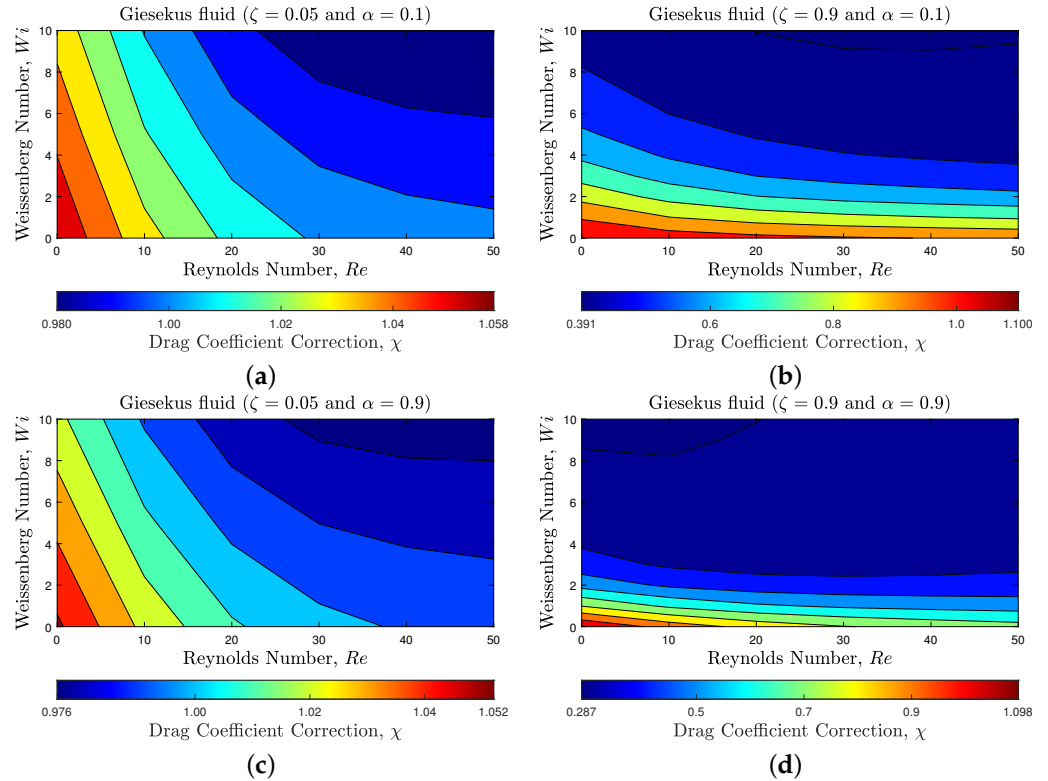
We again used DNSs to generate the training dataset for the viscoelastic drag coefficient correction of a sphere translating in Giesekus fluids. A total of 4950 numerical simulations for the unbounded flow of the shear thinning viscoelastic Giesekus fluid past a sphere (using the physical system described in Section 2) were performed. Hereafter, we call this dataset *GI-set*. Simulations were conducted under a wide range of numbers for the input features, specifically  $0 < Re \leq 50$ ,  $0 \leq Wi \leq 10$ ,  $0 < \zeta < 1$ , and  $0 < \alpha < 1$ . The end goal is to use *GI-set* to augment the *OB-set* and develop a ML-based meta-model that can be used by the scientific community to obtain a prediction of the dimensionless viscoelastic drag coefficient correction of a sphere translating in both Oldroyd-B and Giesekus fluids. We also generated a blind dataset using DNSs with flow features ( $Re$ ,  $Wi$ ,  $\zeta$  and  $\alpha$ ) outside the ranges provided in the generation of *GI-set*. This dataset, consisting of 64 data points, is used to scope the accuracy of the ML models when inferred outside the limits of the training dataset, see Section 4.4.

Figures 6 and 7 present the flow characteristics associated with *GI-set*. Figure 6 shows the contours of the viscoelastic drag coefficient correction,  $\chi$ , for  $0 < Re \leq 50$  and  $0 \leq Wi \leq 10$  at polymeric retardation ratios  $\zeta = 0.05$  and  $0.9$ , and mobility parameters  $\alpha = 0.1$  and  $0.9$ . As shown in Figure 6, increasing inertia (i.e.,  $Re$  number) leads to a reduction in the viscoelastic drag coefficient correction, similar to the behavior observed for the Oldroyd-B fluid. However, interestingly, increasing the elasticity of the flow (increasing the  $Wi$  number) results in a sharp reduction of the viscoelastic drag coefficient correction. The reduction is more pronounced at higher retardation ratio results. This behavior is totally different than what was observed for constant viscosity fluids, where the viscoelastic drag coefficient correction increases with  $Wi$ . Additionally, when the mobility parameter is increased (i.e., stronger shear thinning effect), it promotes the drag reduction even further as shown in Figure 6d.

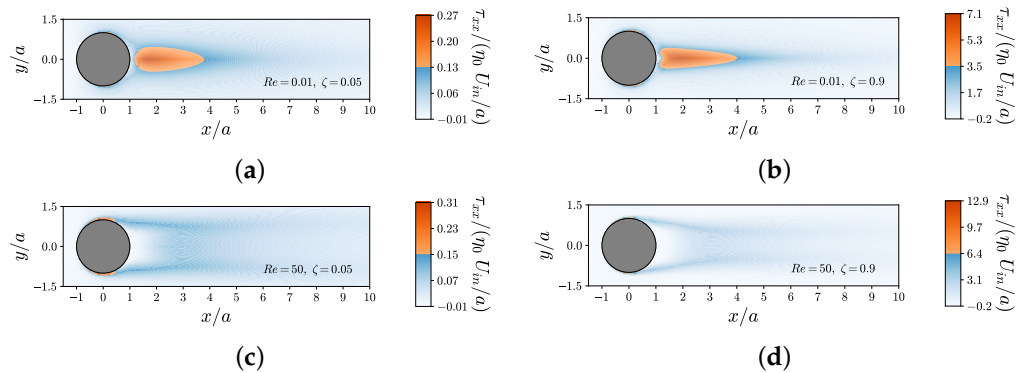
To better illustrate the complexity of the flow and the effects of all flow features ( $Re$ ,  $Wi$ ,  $\zeta$  and  $\alpha$ ), we compare the contours of the normal component of the dimensionless polymeric stress,  $\tau_{xx}$ , in Figure 7. These comparisons are shown for different values of  $Re$  (top line  $Re = 0.01$  and bottom line  $Re = 50$ ) and  $\zeta$  (left column  $\zeta = 0.05$  and right column  $\zeta = 0.9$ ) at fixed  $Wi = 5$  and  $\alpha = 0.1$ . One observes that the magnitude of  $\tau_{xx}$  increases as  $Re$  number increases. In addition, the change in the flow structure (i.e., flow separation and formation of symmetric eddies) due to  $Re$  number shifts around the location where the maximum of  $\tau_{xx}$  occurs. Figure 7 also shows that an increase in the retardation ratio  $\zeta$  promotes an elongated wake in the downstream of the flow. In Figure 8, we show the contours of  $\tau_{xx}$  for the shear thinning Giesekus viscoelastic fluid for two different values of the mobility parameter,  $\alpha = 0.1$  and  $0.5$ , at fixed  $Re = 1$ ,  $Wi = 2$  and  $\zeta = 0.5$ . As expected and illustrated in Figure 8, increasing the mobility parameter decreases the stress overshoot on the surface as well as in the wake of the sphere, which in turn drastically hinders the enhancement of the viscoelastic drag coefficient correction due to elasticity (a behavior that was observed for Oldroyd-B fluids).

Figures 3–8 collectively show the presence of a complex, multidimensional dynamics associated with a single spherical particle flowing through a viscoelastic fluid. All flow features ( $Re$ ,  $Wi$ ,  $\zeta$  and  $\alpha$ ) strongly affect the flow fields and hence the viscoelastic drag coefficient correction ( $\chi$ ). These effects can be hardly decoupled to derive an analytical/empirical or semi-empirical expression for the viscoelastic drag coefficient correction

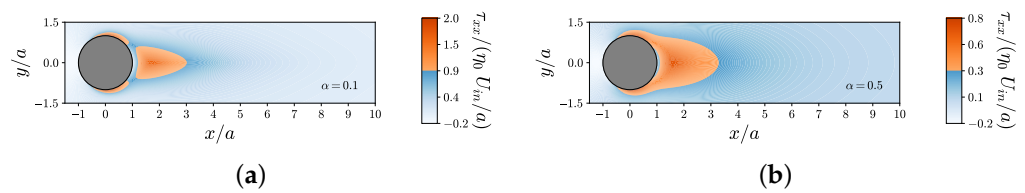
prediction. A machine learning model, however, can be developed to learn these hidden features, in addition to features that are obvious to us in the data, to predict the viscoelastic drag coefficient of a spherical particle translating in an unbounded Oldroyd-B and Giesekus viscoelastic fluids.



**Figure 6.** Contours of the viscoelastic drag coefficient correction,  $\chi$ , for the shear thinning Giesekus viscoelastic fluid for  $0 < Re \leq 50$ ,  $0 \leq Wi \leq 10$  and different values of  $\alpha$  and  $\zeta$ : (a)  $\zeta = 0.05$  and  $\alpha = 0.1$ , (b)  $\zeta = 0.9$  and  $\alpha = 0.1$ , (c)  $\zeta = 0.05$  and  $\alpha = 0.9$ , and (d)  $\zeta = 0.9$  and  $\alpha = 0.9$ .



**Figure 7.** Contours of the dimensionless normal component of the polymeric extra-stress tensor  $\tau_{xx}$  for the shear thinning Giesekus viscoelastic fluid at fixed  $Wi = 5$ ,  $\alpha = 0.1$  and different values of  $Re$  and  $\zeta$ : (a)  $Re = 0.01$  and  $\zeta = 0.05$ , (b)  $Re = 0.01$  and  $\zeta = 0.9$ , (c)  $Re = 50$  and  $\zeta = 0.05$ , and (d)  $Re = 50$  and  $\zeta = 0.9$ .



**Figure 8.** Contours of the dimensionless normal component of the polymeric extra-stress tensor  $\tau_{xx}$  for the shear thinning Giesekus viscoelastic fluid at fixed  $Re = 1$ ,  $Wi = 2$ ,  $\zeta = 0.5$  and different values of mobility parameter: (a)  $\alpha = 0.1$  and (b)  $\alpha = 0.5$ .

#### 4.3. ML Models Development

In this section, we leverage the *OB-set* and *GI-set* to train, validate and test the ML models discussed in Section 3. Based on these datasets, the design space for the input variables is defined as  $0 < Re \leq 50$ ,  $0 \leq Wi \leq 10$ ,  $0 < \zeta < 1$  and  $0 < \alpha < 1$ . First, a normalization stage is followed to restrict the input value range, which transforms the original input feature  $x$  to  $\tilde{x} = (x - x_{min}) / (x_{max} - x_{min})$ . This is a common practice which speeds up learning and leads to faster convergence, especially for the DNN model. Next, we split each dataset to a training set (consisted of 80% of the data) and a test set (consisted of 20% of the data) that are bundled randomly. One of the primary objectives in this section is to improve the performance score, based on data patterns and observed evidence. To achieve this objective, the ML model architecture needs to be optimized by tuning a specific set of hyperparameters defined for each model (see Table 1 for a complete list of hyperparameters of the ML models considered in this study).

##### 4.3.1. Hyperparameter Tuning

Hyperparameter tuning relies more on experimental results than theory, and thus the best method to determine the optimal settings is to try many different combinations and evaluate the performance of each model. However, evaluating each model only on the training set can lead to overfitting (i.e., a model scores very well on the training set but performs poorly on the test set or blind dataset). Routinely, a subset of data from the training set, known as validation set, is reserved for this purpose. We adopt the K-Fold cross-validation (K-Fold CV) technique [42,43] to conduct hyperparameter tuning. In K-Fold CV technique, the training set is further split into K number of subsets, called folds, as schematically shown in Figure 2. The ML model is then iteratively fitted K times; each time, the training is done on K-1 of the folds and evaluation is done on the Kth fold (the validation set). At the very end of training, we average the performance on each of the folds to come up with final validation metrics for the model. The trained models each defined with specific hyperparameters are compared against each other, and the best one that offer the highest accuracy metrics is selected. In this study, unless otherwise stated, we apply 10-Fold CV, i.e., to assess a different set of hyperparameters, we split our training dataset into 10 folds and train and evaluate each model with selected hyperparameters 10 times. If we select X sets of hyperparameters using 10-Fold CV technique, which represents 10X training loops on the entire training dataset (e.g.,  $X = 24$  for XGBoost ML model). This process is thus computationally tedious. To facilitate that, K-Fold technique is coupled with RandomSearchCV algorithm to optimize selected hyperparameters [44]. This coupled approach tries random combinations within a range of values given for each parameter, with a defined number of iterations of random searches. The training time, using a workstation with 48 CPU cores and a NVIDIA RTX A8000 GPU, was on average  $7 \pm 0.5$  h and  $320 \pm 8$  h, respectively, for each iteration and all iterations required to perform hyperparameter tuning for a model.

To train and compare the performance of the ML models, the accuracy is evaluated based on three common statistical measures,  $R^2$ , RMSE, and MAPE. The latter, MAPE, represents the mean-absolute-value of the ratio of estimation errors to actual values. A lower MAPE value indicates that the predicted value is closer to the ground truth. The RMSE represents the root-mean-square error, which is also used to measure the differences between

actual and predicted values by a model. The  $R^2$  coefficient represents the fitness performance, i.e., higher values of  $R^2$ , with a max value of 1, are preferred. The mathematical expressions for  $R^2$ , RMSE and MAPE are as follows [45,46],

$$R^2 = 1 - \frac{\sum_{i=1}^n (y_i - y_i^*)^2}{\sum_{i=1}^n (y_i - \bar{y}_i)^2} \quad (17)$$

$$\text{RMSE} = \sqrt{\frac{1}{n} \sum_{i=1}^n (y_i - y_i^*)^2}$$

$$\text{MAPE} = \frac{1}{n} \sum_{i=1}^n \left| \frac{y_i - y_i^*}{y_i} \right| \times 100\%$$

where  $n$  is the total number of observations,  $y_i$  is the actual value,  $y_i^*$  is the predicted value and  $\bar{y}_i$  is the average of the actual values.

#### 4.3.2. Training and Testing

We first train, validate and test three different ML-based regression models to predict the drag coefficient correction of a single spherical particle translating through a viscoelastic fluid described by the Oldroyd-B constitutive equation (using the *OB-set*). We used 10-Fold CV approach in conjunction with RandomSearchCV algorithm for hyperparameters tuning, and employed the statistical measures given in Equation (17) to analyze the accuracy of the regression models. Table 2 reports the best set of hyperparameters (i.e., best architecture) obtained for each ML model. Notice that only hyperparameters that have been tuned are reported. These architectures, tuned by cross-validation technique on the *OB-set*, offer the best statistical measures for the predictions as reported in Table 3. The accuracy between real and predicted values is remarkable for all ML models as represented by the large  $R^2$  values in Table 3. For the *OB-set*, XGBoost is the model that presents the best  $R^2$  with the lowest values of RMSE and MAPE.

**Table 2.** Optimized hyperparameters for different ML-based regression models trained, validated and tested on the *OB-set*.

Model	Hyperparameter Value
Random Forest	bootstrap = True, criterion = mse, max_depth = 110, max_features = auto, min_samples_leaf = 3, min_samples_split = 5, n_estimators = 800
XGBoost	colsample_bynode = 0.8, colsample_bytree = 0.8, learning_rate = 0.1, max_depth = 15, n_estimators = 300, objective = reg:gamma, reg_alpha = 1.2, reg_lambda = 1.3, subsample = 0.7
DNN	activation = relu, alpha = 0.0001, hidden_layer_sizes = (40, 20, 10), learning_rate = adaptive, max_iter = 8000, momentum = 0.9, n_iter_no_change = 10, solver = adam, tol = 0.0001

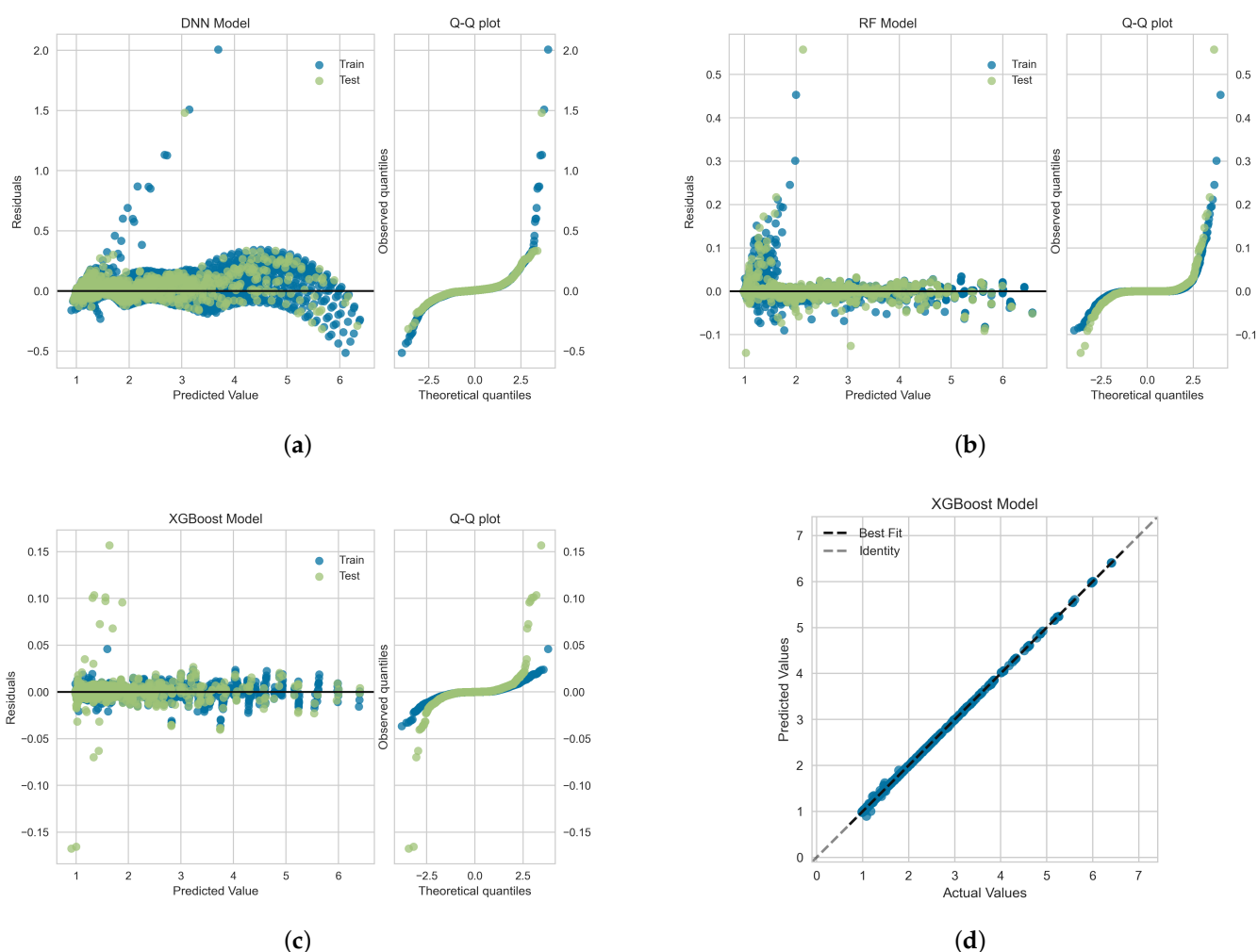
**Table 3.** Optimal statistical measures for different ML-based regression models trained, validated and tested on the *OB-set*.

	RF	XGBoost	DNN
$R^2$	0.9991	<b>0.9995</b>	0.9989
RMSE	0.0228	<b>0.0134</b>	0.0451
MAPE	0.0048	<b>0.0012</b>	0.0145

The residuals (or the prediction errors) and quantile-quantile (Q-Q) plots for the ML-based regression models trained, validated and tested on the *OB-set* are shown in Figure 9.



The residuals are computed as the difference between the actual value (in the test set) and the values predicted by the optimized ML models. Figure 9 shows that the data points are mainly scattered around the horizontal axis and the calculated error is mainly distributed around zero. Figure 9 also shows Q-Q plots for each model in which the probability distributions for errors are compared for both train and test sets by plotting their quantiles against theoretical quantiles [47]. The theoretical quantiles on the  $x$ -axis represents normal distribution as the base distribution. This plot readily depicts whether or not the residuals (errors) are normally distributed. If points are close to the normal line,  $y = x$ , then residuals are assumed to be normally distributed. It can be seen that, for all models, most of the errors lies on  $y = 0$  line and data follow a heavy tail distribution [47]. Figure 9d illustrates the comparison between the actual and predicted values of the viscoelastic drag coefficient correction,  $\chi$ , on the  $OB$ -set for the XGBoost model. As shown the best fit line coincides with the identity line, which corroborates the high  $R^2$  value presented in Table 3.



**Figure 9.** Residuals and quantile-quantile (Q-Q) plots obtained for the ML algorithms trained, validated and tested on the  $OB$ -set: (a) Neural Network, (b) Random Forrest, and (c) XGBoost models. Panel (d) shows the prediction error plot for XGBoost that yields the highest  $R^2$  as reported in Table 3.

The ML models trained on the  $OB$ -set fail, as expected, when inferred against a dataset generated for shear thinning fluids (e.g., even at  $\alpha = 0.1$ , which is just slightly outside the scope of the  $OB$ -set where  $\alpha$  is set to zero). To accurately predict the drag coefficient correction of a spherical particle translating through a more realistic viscoelastic fluid, the trained models require further augmentation. For that purpose, three different

approaches can be explored: (i) start training, validation and testing from scratch using a combination of the datasets developed for Oldroyd-B and Giesekus fluids (augmented *OB-set* and *GI-set*), (ii) use transfer learning technique [48] where models with knowledge gained on the *OB-set* are further reinforced using *GI-set*, or (iii) infuse physics in the models' architecture using the constitutive fluid models as loss or activation function broadening the range over which the ML models are valid [49]. The latter approach is outside the scope of the current study and will be explored elsewhere. The accuracy obtained for the model derived by the second approach (i.e., transfer learning) was found to be significantly lower than the first approach when tested on the blind datasets. This is mainly due to the difficulty associated with transfer learning in decision tree ML models (Random Forest in particular where there is a limited capacity to accommodate local changes [50]). Thus, we adopted the first approach to develop ML-based models that satisfies both Oldroyd-B and Giesekus fluids. This approach is also challenging because datasets are not balanced. The weight of the *OB-set* (bigger dataset with 12,120 data points) is a lot larger than the *GI-set* (smaller dataset with 4950 data points), and consequently ML models will be more biased towards the *OB-set* (e.g., undermines the effects of  $\alpha$  on the models' predictability). To resolve this issue, we used synthetic minority over-sampling technique [51], SMOTE, which blends under-sampling of the majority set (*OB-set*) with a special form of over-sampling of the minority set (*GI-set*). In SMOTE, we synthesized elements for the minority set, based on the data that already exist. It works randomly by picking a point from the minority set and computing the k-nearest neighbors for this point. The synthetic points for minority set (*GI-set*) are placed between the chosen point and its neighbors. This process continues until we reach balanced states for both datasets, hereafter we call this dataset *SMOTE-set* containing 21,750 data points.

Again, we used 10-Fold CV approach in conjunction with the RandomSearchCV algorithm for the hyperparameters tuning of the ML models trained, validated and tested on *SMOTE-set*. Table 4 reports the best set of hyperparameters (i.e., best architecture) obtained for each one of the ML model employed in this work. These architectures offer the best statistical measures ( $R^2$ , RMSE and MAPE) for the ML-based regression models as reported in Table 5. The accuracy obtained for all ML models is acceptable as represented by the large  $R^2$  and low RMSE values. For the *SMOTE-set*, again, the XGBoost model possesses the highest  $R^2$ , and the lowest values of RMSE and MAPE. This result is in agreement with the literature [44,52–54] and shows that the decision-tree models perform better than neural network models to learn hidden features on relatively midsize datasets. However, performing well on the test set still does not guarantee the accuracy of decision-tree-based regression models when inferred on blind datasets generated outside the scope of training set or interpolated within the training sets (see Section 4.4).

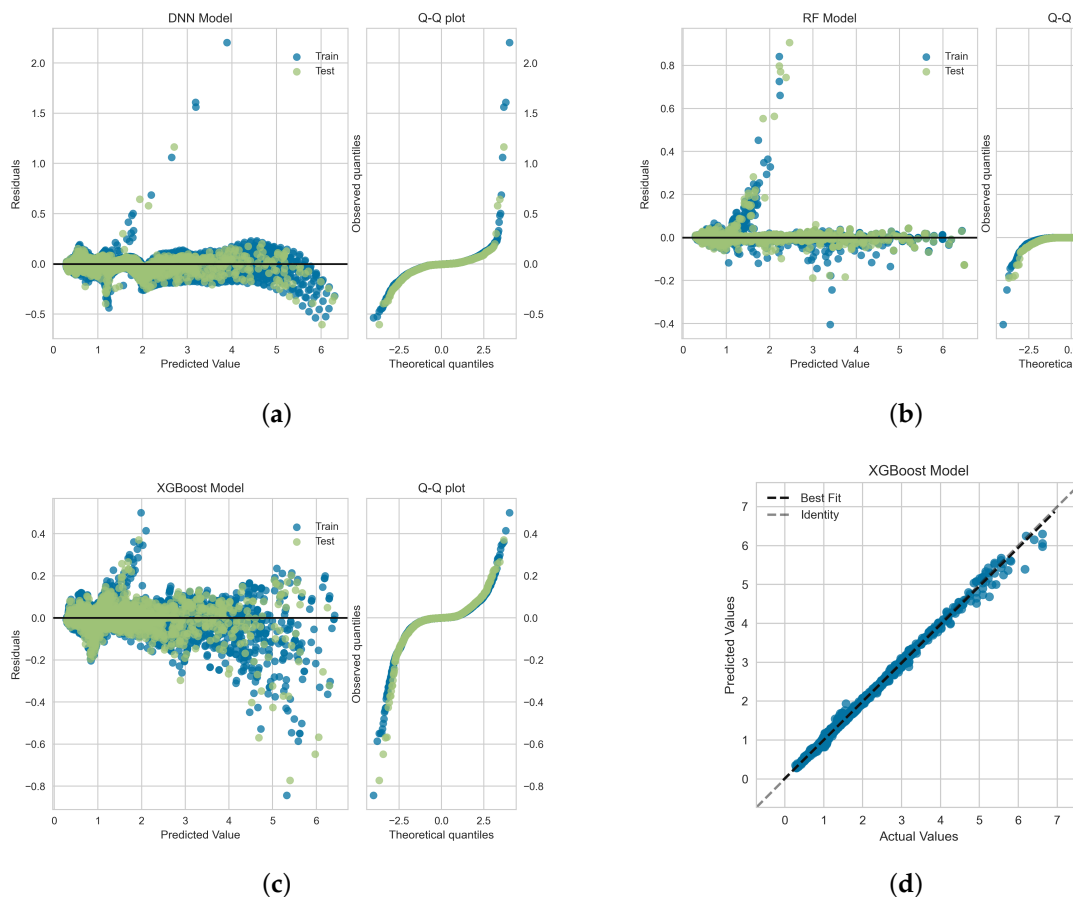
**Table 4.** Optimized hyperparameters for the different ML-based regression models trained, validated and tested on *SMOTE-set*.

Model	Hyperparameter Value
Random Forest	bootstrap = True, criterion = mse, max_depth = 45, max_features = auto, min_samples_leaf = 3, min_samples_split = 5, n_estimators = 950
XGBoost	colsample_bynode = 1, colsample_bytree = 0.8, learning_rate = 0.2, max_depth = 5, n_estimators = 400, objective = reg:gamma, reg_alpha = 1.2, reg_lambda = 1.3, subsample = 0.7
DNN	activation = relu, alpha = 0.0001, hidden_layer_sizes = (120, 50, 20, 3), learning_rate = adaptive, max_iter = 10,000, momentum = 0.95, n_iter_no_change = 15, solver = adam, tol = 0.0001

**Table 5.** Optimal statistical measures for different ML-based regression models trained, validated and tested on *SMOTE-set*.

	RF	XGBoost	DNN
$R^2$	0.9965	<b>0.9967</b>	0.9945
RMSE	0.0388	<b>0.0378</b>	0.0463
MAPE	0.0131	<b>0.0127</b>	0.0216

In Figure 10, we show the residuals and Q-Q plots for the ML models trained, validated and tested on *SMOTE-set*. The residuals are computed as the difference between the actual value (in the test set) and the values predicted by the optimized ML models. Figure 10 again shows that the data points are mainly scattered around the horizontal axis and the calculated error is mainly distributed around zero. The Q-Q plots for Random Forest and DNN models again depict that most of the errors lies on  $y = 0$  line, within the standard deviation range, and data follow a heavy tail distributions [47]. For the XGBoost model, the residuals are closer to the normal line,  $y = x$ , and thus, they follow a distribution closer to normal distribution. Figure 9d illustrates the comparison between the actual and predicted values of the viscoelastic drag coefficient correction,  $\chi$ , for the *SMOTE-set* using the XGBoost model. This comparison corroborates the high  $R^2$  values presented in Table 5 and the fact that the residual plot for XGBoost model is symmetric around  $y = 0$  as shown in Figure 9c.

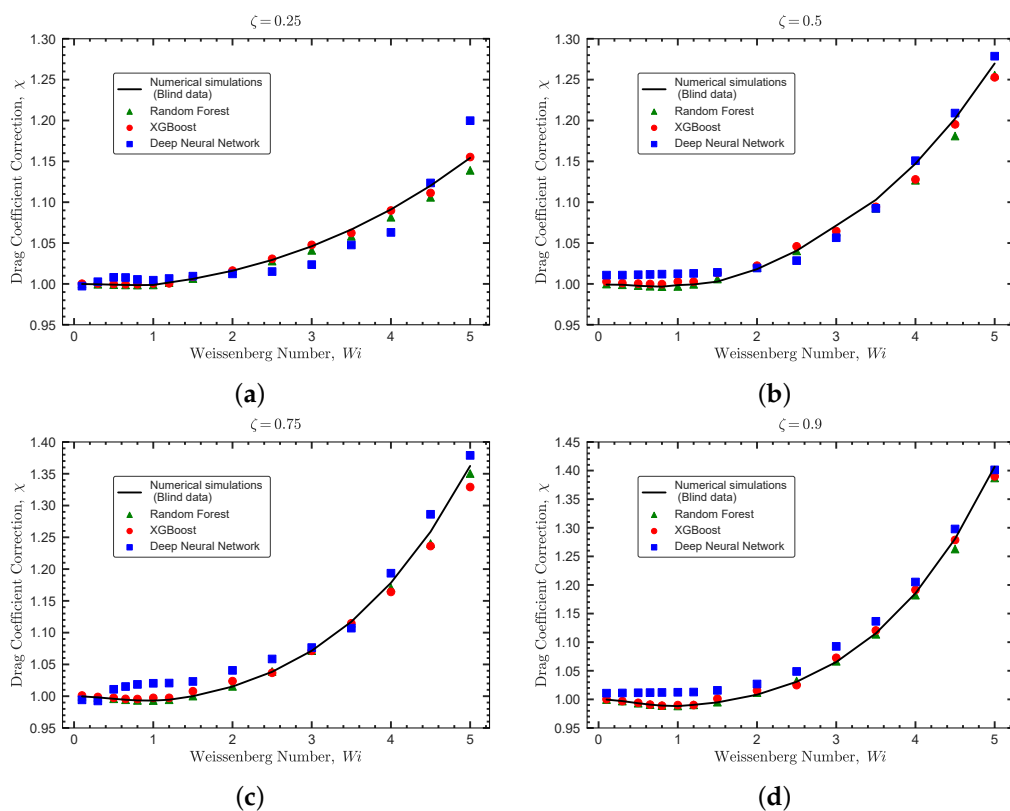


**Figure 10.** Residuals and quantile-quantile (Q-Q) plots obtained for the ML algorithms trained, validated and tested on *SMOTE-set*: (a) Neural Network, (b) Random Forrest, and (c) XGBoost models. Panel (d) shows the prediction error plot for XGBoost that yields the highest  $R^2$  as reported in Table 5.

#### 4.4. Models Performance on Blind Datasets

To further evaluate the performance of the ML models trained on *SMOTE-set* in Section 4.3, we test them against blind datasets. We designed the blind datasets to have an input feature coverage outside the scope of training set or interpolated within the training sets. The blind datasets are generated using DNSs on the physical system described in Section 2 following the work of Faroughi et al. [6] for both Oldroyd-B and Giesekus fluids.

The blind dataset for the Oldroyd-B fluid is constructed with a total of 60 DNS runs using  $\zeta = \{0.25, 0.5, 0.75, 0.9\}$ ,  $Wi = \{0.1, 0.3, 0.5, 0.65, 0.8, 1, 1.2, 1.5, 2, 2.5, 3, 3.5, 4, 4.5, 5\}$  at a constant  $Re = 1$ . Figure 11 shows the comparisons between the real values for the viscoelastic drag coefficient correction (obtained by DNSs and represented with a solid line) and the values predicted by the ML models (represented by symbols). The ML models used in this comparison are those trained, validated and tested based on the *OB-set*. As depicted in Figure 11, all models perform very well to predict the blind dataset. The statistical measures for ML models to predict this blind dataset are reported in Table 6. The XGBoost model performs superior than other models and its predictions are in a very good agreement with the numerical results.



**Figure 11.** Validation of the ML models against the blind dataset generated for the Oldroyd-B fluid. The comparisons are between the DNSs (solid lines showing the real values for the viscoelastic drag coefficient correction) and the predicted values by the ML models. The comparisons are shown at  $Re = 1$  for different values of  $\zeta$ : (a)  $\zeta = 0.25$ , (b)  $\zeta = 0.5$ , (c)  $\zeta = 0.75$  and (d)  $\zeta = 0.9$ . The predictions obtained with the Deep Neural Network, Random Forest and XGBoost models are represented by square, triangle and circle symbols, respectively.

**Table 6.** Statistical measures for different ML-based regression models tested against the blind dataset provided for Oldroyd-B fluids.

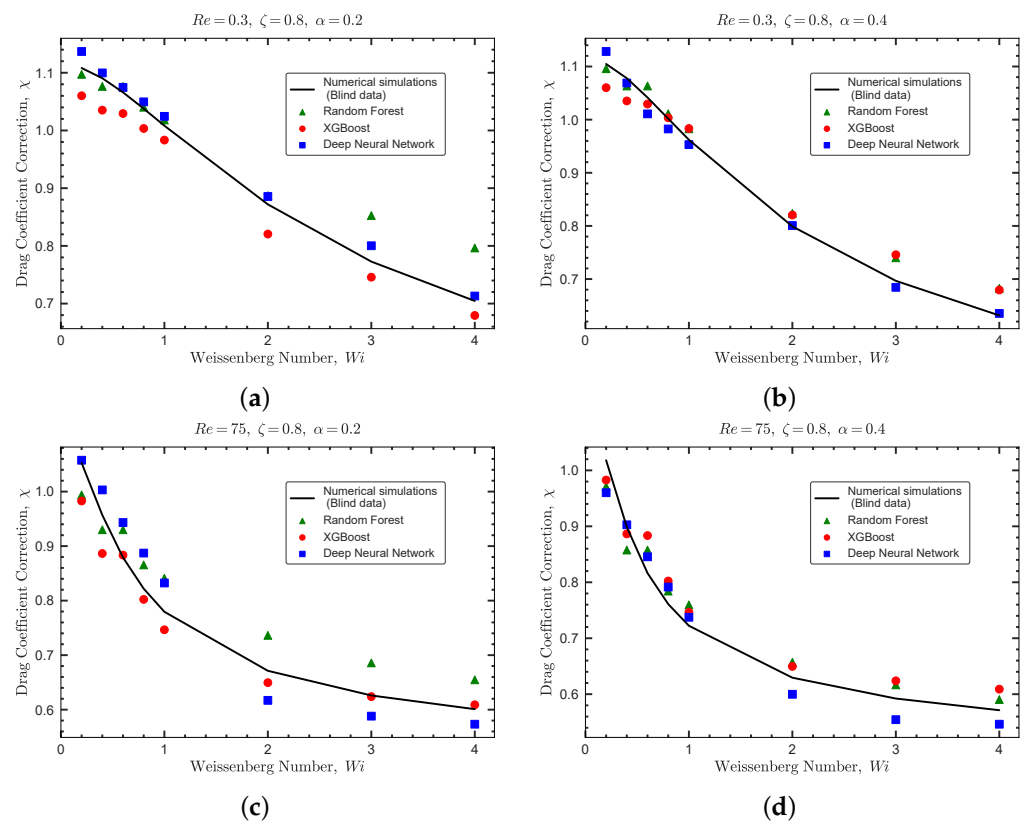
	RF	XGBoost	DNN
$R^2$	0.9926	<b>0.9931</b>	0.9621
RMSE	0.0085	<b>0.0074</b>	0.0173
MAPE	0.051	<b>0.0042</b>	0.0139

The blind dataset for Giesekus fluids is constructed with a total of 64 DNS runs using  $Re = \{0.3, 75\}$ ,  $\zeta = \{0.15, 0.8\}$ ,  $\alpha = \{0.2, 0.4\}$ , and  $Wi = \{0.2, 0.4, 0.6, 0.8, 1, 2, 3, 4\}$ . Figure 12 shows the comparisons for two sample sets between the real values of the viscoelastic drag coefficient correction obtained by DNS (solid lines) and the predicted values by the ML models (symbols). The ML models used in this comparison are trained, validated and tested based on *SMOTE-set*. The statistical measures to predict this blind dataset are reported in Table 7. A sharp reduction in prediction performance is noticed for all models. This is due to two reasons: (i) the presence of values of  $Re$  which are out of the limits of the *SMOTE-set*, and (ii) the sparsity of data points in the combined dataset, i.e., *OB-set* and *GI-set*. Even using the SMOTE technique to balance the data sets (enforce the effect of high  $Re$  numbers and  $\alpha$ ), the ML models trained on *SMOTE-set* show a relatively poorer performance in predicting the blind dataset compared to the same models trained and tested on the *OB-set* (see Figure 11 and Table 6).

As shown in Figure 12, the DNN model performs slightly better than the decision tree models for both  $Re$  and  $\alpha$  values. In general, ensemble decision tree models (e.g., XGBoost) are easy to train and prevent overfitting to a great extent [44,52,55]; however, they do not perform well in predicting sparse datasets where interpolation between input features is required. On the other hand, deep neural networks models are hard to train, but offer a better performance when inferred outside the scope of the training dataset or when interpolation between input features is needed [55,56]. Therefore, the DNN model provides a better potential for the generality of the model. In addition, for a ML model to be fully predictive under any new or unseen conditions (e.g., flow features), physics must complement the model. This can only be achieved using deep learning models, known as physics-based neural networks [57] or physics-guided neural networks [58] that mimic an infinitely deep model. Incorporating physics in DNN is essential in the field of particle-laden fluid flow, because it is not a data-oriented domain (i.e., large datasets can be hardly found). Developing true physics-based neural network is outside the scope of the current work, and it will be presented elsewhere. Here, to resolve this issue and provide a meta-model for the viscoelastic drag coefficient correction that can be coupled with Eulerian-Lagrangian algorithms [4], we use stacking technique [59]. This technique leverages the superiority of all developed ML models (i.e., the fact that each model performs better in a different section of the data), and is a very powerful method to increase the generality of the model in predicting unseen data.

**Table 7.** Statistical measures for ML-based models tested against the blind dataset provided for Oldroyd-B and Giesekus fluids.

	RF	XGBoost	DNN
$R^2$	0.8664	0.8566	<b>0.9013</b>
RMSE	0.0495	0.0516	<b>0.0428</b>
MAPE	0.0326	0.0341	<b>0.0305</b>

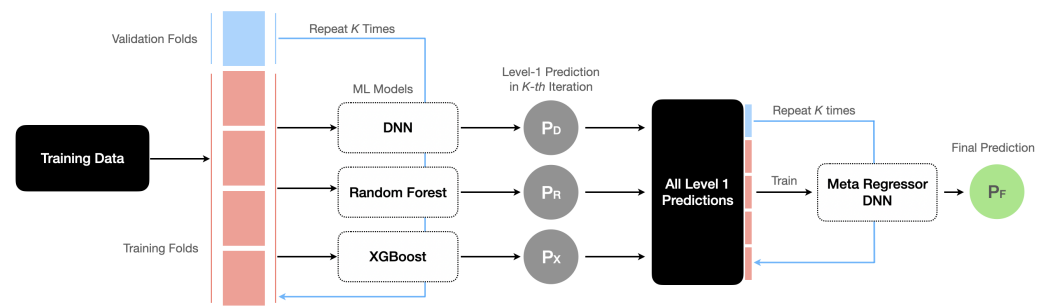


**Figure 12.** Validation of the ML models against blind datasets generated for Giesekus fluids. The comparisons are between the DNSs (solid lines showing the real values for the viscoelastic drag coefficient correction) and the predicted values by the ML models. The comparisons are shown at  $\zeta = 0.8$  for different values of  $Re$  and  $\alpha$ : (a)  $Re = 0.3$  and  $\alpha = 0.2$ , (b)  $Re = 0.3$  and  $\alpha = 0.4$ , (c)  $Re = 75$  and  $\alpha = 0.2$ , and (d)  $Re = 75$  and  $\alpha = 0.4$ . The predictions obtained with the Deep Neural Network, Random Forest and XGBoost models are represented by square, triangle and circle symbols, respectively.

#### 4.5. Model Ensembling

In this section, we leverage stacking which is an ensemble learning technique to combine multiple ML-based regression models via a meta-regressor. The objective is to develop a meta-model with high accuracy when predicting the drag coefficient for a particle translating in viscoelastic fluids. In previous sections, we showed that different ML models perform better on different sections of the data when inferred against blind datasets. For example, the XGBoost performs better on the Oldroyd-B blind dataset (see Table 6), and the DNN model performs better on the Giesekus blind dataset (see Table 7). The hypothesis here is to leverage the superiority of all developed ML models (i.e., decision tree models to prevent overfitting and DNN model to learn complicated features in a sparse dataset) and increase the generality of the model in predicting unseen data.

A schematic architecture for the stack model is shown in Figure 13. We first use the ML models trained on *SMOTE-set* (with their best architectures found in the previous section) to provide the level-1 predictions. These predictions are then provided as input features to the second-level regressor, which is a DNN meta-regressor. The hyperparameters for DNN meta-regressor are also tuned again using the 10-Fold CV approach in conjunction with the RandomSearchCV algorithm, similar to other models. The stack model is trained, validated and tested on *SMOTE-set*. The optimized architecture obtained for the DNN meta-regressor is reported in Table 8. This meta-model developed using stacking generalizes better and provides more accurate predictions on unseen data when compared to the performance of the individual models. One example comparison is reported in Table 9. As reported, the  $R^2$  value for the meta-model increased to 0.9472 from 0.9013, which was previously obtained for the DNN model, as the best model in Section 4.4 to predict the blind datasets.



**Figure 13.** A schematic architecture for the meta-model to predict the viscoelastic drag coefficient using the stacking technique ensembling three optimized ML models and a meta-regressor.

**Table 8.** Optimized hyperparameters for the DNN meta-regressor trained, validated and tested on *SMOTE-set*.

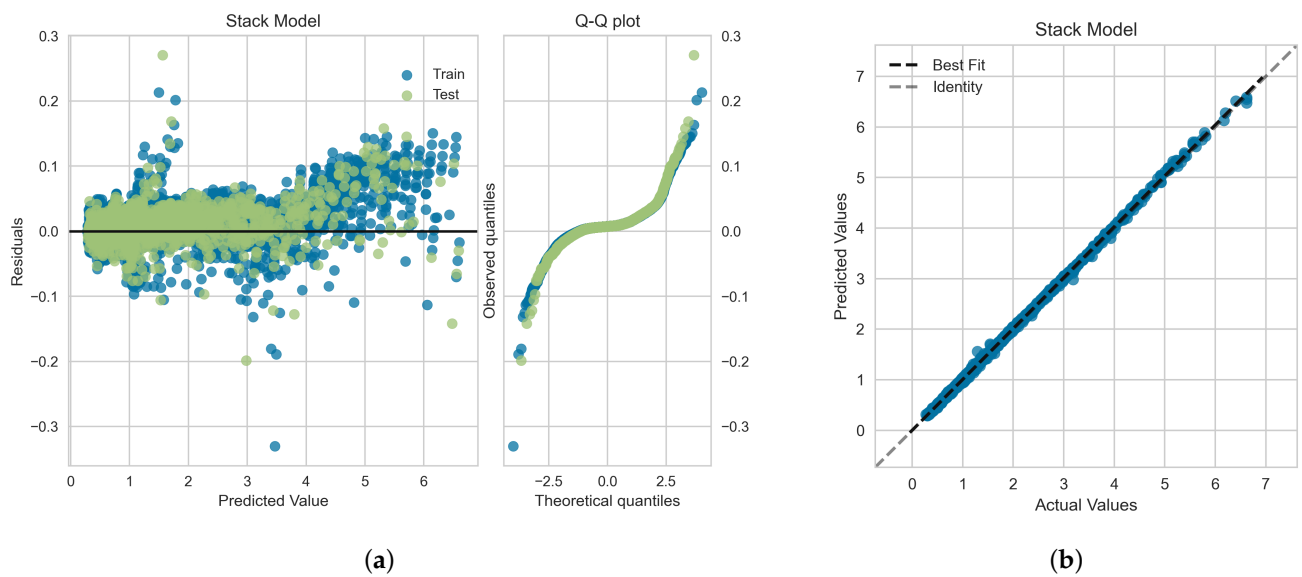
Model	Hyperparameter Value
DNN Meta-Regressor	activation = relu, alpha = 0.0001, hidden_layer_sizes = (20, 40, 10), learning_rate = adaptive, max_iter = 10,000, momentum = 0.95, n_iter_no_change = 15, solver = adam, tol = 0.0001

**Table 9.** Comparison of the statistical measures for the performance of the meta-model and DNN model against the *SMOTE-set* and blind datasets.

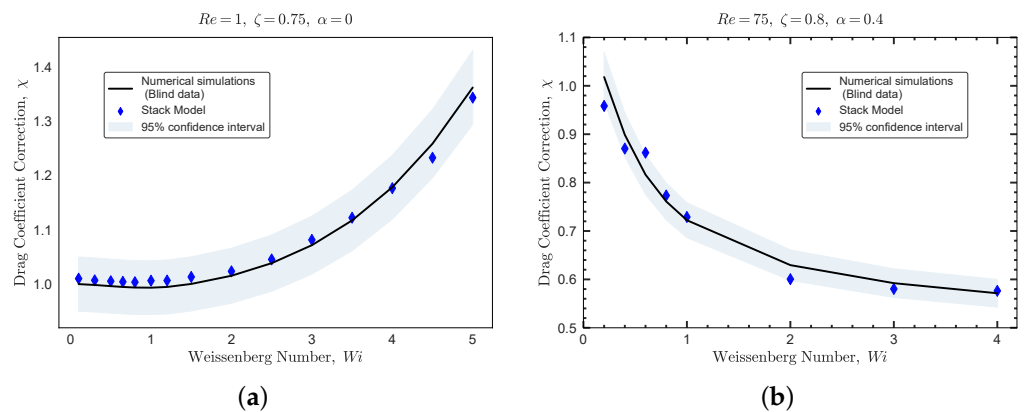
	Meta-Model		DNN Model	
	SMOTE-Set	Blind Set	SMOTE-Set	Blind Set
$R^2$	0.9993	0.9472	0.9945	0.9013
RMSE	0.0178	0.0313	0.0463	0.0428
MAPE	0.0103	0.0209	0.0216	0.0305

In Figure 14, we show the residuals and Q-Q plots for the meta-model trained, validated and tested on *SMOTE-set*. Figure 14a shows that the data points are mainly scattered around the horizontal axis and the calculated error is mainly distributed around zero. The Q-Q plot for meta-model depicts that most of the errors lies closer to  $y = x$  line within the standard deviation range, and thus the data follow a distribution closer to normal distribution [47]. Figure 14b illustrates the comparison between the actual and predicted values of the viscoelastic drag coefficient correction using the meta-model. The very good agreement between the meta-model predictions and the actual values corroborates the high  $R^2$  values presented in Table 9 and the fact that the residual plot for meta-model is relatively symmetric around  $y = 0$  as shown in Figure 14a.

Figure 15 shows the performance of the meta-model against the blind datasets generated for Oldroyd-B and Giesekus viscoelastic fluids. The blind datasets are shown using solid lines for the flow of an Oldroyd-B fluid past a sphere at  $Re = 1$ ,  $\zeta = 0.75$  and  $\alpha = 0$ , and for the flow of a Giesekus fluid past a sphere at  $Re = 75$ ,  $\zeta = 0.8$  and  $\alpha = 0.4$ . The predictions obtained with the meta-model are represented by diamond symbols in Figure 15a,b. A 95% confidence interval region for the meta-model predictions is also illustrated. These comparisons and the statistical measures reported in Table 9 collectively show that the meta-model consistently outperforms the individual decision tree ML models as well as the DNN model on all unseen datasets.



**Figure 14.** (a) Residuals and quantile-quantile (Q-Q) plots and (b) prediction error plot obtained for the meta-model shown in Figure 13 and trained, validated and tested on *SMOTE-set*. The statistical measures are reported in Table 9.



**Figure 15.** Performance of the meta-model (stack model) against the blind datasets generated for Oldroyd-B and Giesekus fluids. The blind datasets are shown using solid lines for the flow of an Oldroyd-B fluid past a sphere at (a)  $Re = 1$ ,  $\zeta = 0.75$  and  $\alpha = 0$ ; and for the flow of a Giesekus fluid past a sphere at (b)  $Re = 75$ ,  $\zeta = 0.8$  and  $\alpha = 0.4$ . The predictions obtained with the meta-model are represented by diamond symbols. A 95% confidence interval region for the predictions is also shown.

This meta-model alongside the training datasets (*OB-set* and *GI-set*) are packaged and published with this paper, as supplementary materials. The viscoelastic fluid dynamics community can leverage this meta-model in their simulations and/or leverage the data to train new data-driven models.

## 5. Conclusions

This study presents a framework to predict the drag coefficient of a spherical particle translating in viscoelastic fluids. To this end, continuum simulations and Machine Learning (ML) models were employed to generate a data-driven meta-model. We first generated two datasets using direct numerical simulations; the *OB-set* (the dataset for the Oldroyd-B fluid) and the *GI-set* (the dataset for the Giesekus fluid) that include a total of 12,120 and 4950 data points, respectively. The kinematic input features were selected to be Reynolds number,  $0 < Re \leq 50$ , Weissenberg number,  $0 \leq Wi \leq 10$ , polymeric retardation ratio,



$0 < \zeta < 1$ , and shear thinning mobility parameter,  $0 < \alpha < 1$ . Three ML regression models, Random Forest (RF), Deep Neural Network (DNN) and Extreme Gradient Boosting (XGBoost), were employed to predict the drag coefficient enhancement or reduction due to the fluids' elasticity and shear thinning effects. The ML models were all trained, validated, and tested on the *OB-set* and *SMOTE-set* (a balanced dataset combining the *OB-set* and *GI-set*), and their best architecture (i.e., tuned hyperparameters) were obtained using a 10-Fold cross-validation method. All the ML models presented remarkable accuracy when trained and inferred on these datasets; however the XGBoost model resulted in the highest  $R^2$  and lowest RMSE and MAPE measures.

The trained ML models were also tested against a blind dataset where the input features coverage was outside the scope of the training set or interpolated within the training sets. A total of 124 data points were generated using DNSs for both Oldroyd-B and Giesekus fluids. The predictions obtained with the DNN model achieved the highest  $R^2$  and lowest RMSE and MAPE measures when inferred on the blind test dataset. To leverage the power of all models (decision tree models to prevent overfitting and DNN model to learn complicated features), we developed a meta-model using stacking technique. The meta-model ensembles RF, XGBoost, and DNN models and outputs a prediction based on the individual learner's predictions and a DNN meta-regressor. The meta-learner model consistently outperformed the individual decision tree and DNN models on all datasets.

**Supplementary Materials:** The following supporting information can be downloaded at: <https://www.mdpi.com/article/10.3390/polym14030430/s1>.

**Author Contributions:** Conceptualization, S.A.F. and C.F.; Formal analysis, S.A.F. and C.F.; Investigation, S.A.F., A.I.R. and C.F.; Methodology, S.A.F. and C.F.; Resources, S.A.F. and C.F.; Software, S.A.F. and C.F.; Supervision, S.A.F. and C.F.; Validation, S.A.F., A.I.R. and C.F.; Writing—original draft, S.A.F., A.I.R. and C.F.; Writing—review & editing, S.A.F. and C.F. All authors have read and agreed to the published version of the manuscript.

**Funding:** This research was funded by FEDER funds through the COMPETE 2020 Programme and National Funds through FCT (Portuguese Foundation for Science and Technology) under the projects UID-B/05256/2020, UID-P/05256/2020 and MIT-EXPL/TDI/0038/2019—APROVA—Deep learning for particle-laden viscoelastic flow modelling (POCI-01-0145-FEDER-016665) under MIT Portugal program.

**Institutional Review Board Statement:** Not applicable.

**Informed Consent Statement:** Not applicable.

**Data Availability Statement:** Not applicable.

**Acknowledgments:** The authors would like to acknowledge the University of Minho cluster under the project NORTE-07-0162-FEDER-000086 (URL: <http://search6.di.uminho.pt>), the Minho Advanced Computing Center (MACC) (URL: <https://macc.fcn.pt>) under the project CPCA\_A2\_6052\_2020, the Consorzio Interuniversitario dell'Italia Nord Est per il Calcolo Automatico (CINECA) under the Project HPC-EUROPA3 (INFRAIA-2016-1-730897) with the support of the EC Research Innovation Action under the H2020 Programme, and PRACE—Partnership for Advanced Computing in Europe under the project icei-prace-2020-0009, for providing HPC resources that have contributed to the research results reported within this paper. The authors thank Professor Gareth Huw McKinley from the Hatsopoulos Microfluids Laboratory, Department of Mechanical Engineering at the Massachusetts Institute of Technology for insightful comments regarding this work.

**Conflicts of Interest:** The authors declare no conflict of interest.

## References

1. Chhabra, R.P. *Bubbles, Drops, and Particles in Non-Newtonian Fluids*; CRC Press: Boca Raton, FL, USA, 2007; ISBN 978-0-4290-7480-6. [[CrossRef](#)]
2. Deshpande, A.P.; Krishnan, J.M.; Kumar, S. *Rheology of Complex Fluids*; Springer: New York, NY, USA, 2010; ISBN 978-1-4419-6493-9. [[CrossRef](#)]

3. Barbati, A.C.; Desroches, J.; Robisson, A.; McKinley, G.H. Complex fluids and hydraulic fracturing. *Annu. Rev. Chem. Biomol. Eng.* **2016**, *7*, 415–453. [CrossRef]
4. Fernandes, C.; Faroughi, S.A.; Carneiro, O.S.; Nóbrega, J.M.; McKinley, G.H. Fully-resolved simulations of particle-laden viscoelastic fluids using an immersed boundary method. *J. Non-Newton. Fluid Mech.* **2019**, *266*, 80–94. [CrossRef]
5. Faroughi, S.; Huber, C. A generalized equation for rheology of emulsions and suspensions of deformable particles subjected to simple shear at low Reynolds number. *Rheol. Acta* **2014**, *54*, 85–108. [CrossRef]
6. Faroughi, S.A.; Fernandes, C.; Nóbrega, J.M.; McKinley, G.H. A closure model for the drag coefficient of a sphere translating in a viscoelastic fluid. *J. Non-Newton. Fluid Mech.* **2020**, *277*, 104218. [CrossRef]
7. Fernandes, C.; Faroughi, S.A.; Ribeiro, R.; Roriz, A.I.; McKinley, G.H. Finite volume simulations of particle-laden viscoelastic fluid flows: Application to hydraulic fracture processes. *Eng. Comput.* **2021**. [CrossRef]
8. Faroughi, S.A.; Huber, C. Crowding-based rheological model for suspensions of rigid bimodal-sized particles with interfering size ratios. *Phys. Rev. E* **2014**, *90*, 052303. [CrossRef]
9. Maxey, M. Simulation methods for particulate flows and concentrated suspensions. *Annu. Rev. Fluid Mech.* **2017**, *49*, 171–193. [CrossRef]
10. Faroughi, S.A.; Huber, C. A self-similar behavior for the relative viscosity of concentrated suspensions of rigid spheroids. *Rheol. Acta* **2017**, *56*, 35–49. [CrossRef]
11. Faroughi, S.A.; Pruvot, A.J.-C.; McAndrew, J. The rheological behavior of energized fluids and foams with application to hydraulic fracturing. *J. Pet. Sci. Eng.* **2018**, *163*, 243–263. [CrossRef]
12. Kutz, J.N. Deep learning in fluid dynamics. *J. Fluid Mech.* **2017**, *814*, 1–4. [CrossRef]
13. Brunton, S.L.; Noack, B.R.; Koumoutsakos, P. Machine learning for fluid mechanics. *Annu. Rev. Fluid Mech.* **2020**, *52*, 477–508. [CrossRef]
14. Molinaro, R.; Singh, J.-S.; Catsoulis, S.; Narayanan, C.; Lakehal, D. Embedding data analytics and CFD into the digital twin concept. *Comput. Fluids* **2021**, *214*, 104759. [CrossRef]
15. Fernandes, C.; Semyonov, D.; Ferrás, L.L.; Nóbrega, J.M. Validation of the CFD-DPM solver DPMFoam in OpenFOAM through analytical, numerical and experimental comparisons. *Granul. Matter* **2018**, *20*, 64. [CrossRef]
16. Kelbaliyev, G.I. Drag coefficients of variously shaped solid particles, drops, and bubbles. *Theor. Found. Chem. Eng.* **2011**, *45*, 248–266. [CrossRef]
17. Faroughi, S.A.; Huber, C. Unifying the relative hindered velocity in suspensions and emulsions of nondeformable particles. *Geophys. Res. Lett.* **2015**, *42*, 53–59. [CrossRef]
18. Gheissary, G.; van den Brule, B.H.A.A. Unexpected phenomena observed in particle settling in non-Newtonian media. *J. Non-Newton. Fluid Mech.* **1996**, *67*, 1–18. [CrossRef]
19. Chilcott, M.D.; Rallison, J.M. Creeping flow of dilute polymer solutions past cylinders and spheres. *J. Non-Newton. Fluid Mech.* **1988**, *29*, 381–432. [CrossRef]
20. McKinley, G.H. Steady and transient motion of spherical particles in viscoelastic liquids. In *Transport Processes in Bubble, Drops, and Particles*; Chhabra, R., Kee, D.D., Eds.; Taylor & Francis: New York, NY, USA, 2002; pp. 338–375. ISBN 978-1-5603-2906-0.
21. Giesekus, H. A simple constitutive equation for polymer fluids based on the concept of deformation-dependent tensorial mobility. *J. Non-Newton. Fluid Mech.* **1982**, *11*, 69–109. [CrossRef]
22. Habla, F.; Tan, M.W.; Hablberger, J.; Hinrichsen, O. Numerical simulation of the viscoelastic flow in a three-dimensional lid-driven cavity using the log-conformation reformulation in OpenFOAM. *J. Non-Newton. Fluid Mech.* **2014**, *212*, 47–62. [CrossRef]
23. Pimenta, F.; Alves, M.A. Stabilization of an open-source finite volume solver for viscoelastic fluid flows. *J. Non-Newton. Fluid Mech.* **2017**, *239*, 85–104. [CrossRef]
24. OpenFOAM. The Open Source CFD Toolbox. 2004. Available online: <https://www.openfoam.com/> (accessed on 5 December 2021).
25. Fernandes, C.; Araujo, M.S.B.; Ferrás, L.L.; Nóbrega, J.M. Improved both sides diffusion (iBSD): A new and straightforward stabilization approach for viscoelastic fluid flows. *J. Non-Newton. Fluid Mech.* **2017**, *249*, 63–78. [CrossRef]
26. Goodfellow, I.; Bengio, Y.; Courville, A. *Deep Learning*; MIT Press: Cambridge, MA, USA, 2016.
27. Liaw, A.; Wiener, M. Classification and regression by randomForest. *R News* **2002**, *2*, 18–22.
28. Smith, P.F.; Ganesh, S.; Liu, P. A comparison of random forest regression and multiple linear regression for prediction in neuroscience. *J. Neurosci. Methods* **2013**, *220*, 85–91. [CrossRef]
29. Chen, T.; Guestrin, C. XGBoost: A scalable tree boosting system. In Proceedings of the 22nd ACM SIGKDD International Conference on Knowledge Discovery and Data Mining, San Francisco, CA, USA, 13–17 August 2016; pp. 785–794. [CrossRef]
30. Luckner, M.; Topolski, B.; Mazurek, M. Application of XGBoost algorithm in fingerprinting localisation task. In *Computer Information Systems and Industrial Management*; Saeed, K., Homenda, W., Chaki, R., Eds.; Springer: Cham, Switzerland, 2017; pp. 661–671. ISBN 978-3-319-59105-6. [CrossRef]
31. Brownlee, J. *XGBoost with Python: Gradient Boosted Trees with XGBoost and Scikit-Learn*; Machine Learning Mastery. 2016. Available online: [https://books.google.pt/books?id=HgmqDwAAQBAJ&printsec=copyright&redir\\_esc=y#v=onepage&q&f=false](https://books.google.pt/books?id=HgmqDwAAQBAJ&printsec=copyright&redir_esc=y#v=onepage&q&f=false) (accessed on 5 January 2022).
32. Specht, D.F. A general regression neural network. *IEEE Trans. Neural Netw.* **1991**, *2*, 568–576. [CrossRef] [PubMed]

33. Mahmudul, M.; Mia, A.; Biswas, S.K.; Urmi, M.C.; Siddique, A. An algorithm for training multilayer perceptron (MLP) for image reconstruction using neural network without overfitting. *Int. J. Sci. Technol. Res.* **2015**, *4*, 271–275.
34. Jiang, H.; Zou, Y.; Zhang, S.; Tang, J.; Wang, Y. Short-term speed prediction using remote microwave sensor data: Machine learning versus statistical model. *Math. Probl. Eng.* **2016**. [[CrossRef](#)]
35. Palyam, R.K. Deep feature interpolation for image content changes. In Proceedings of the IEEE Conference on Computer Vision and Pattern Recognition (CVPR), Honolulu, HI, USA, 22–25 July 2017; pp. 6090–6099. [[CrossRef](#)]
36. Trillos, N.G.; Morales, F.; Morales, J. Traditional and accelerated gradient descent for neural architecture search. In *Geometric Science of Information*; Nielsen, F., Barbaresco, F., Eds.; Springer International Publishing: Cham, Switzerland, 2021; pp. 507–514. ISBN 978-3-030-80209-7.
37. Asiltürk, I.; Çunkaş, M. Modeling and prediction of surface roughness in turning operations using artificial neural network and multiple regression method. *Expert Syst. Appl.* **2011**, *38*, 5826–5832. [[CrossRef](#)]
38. James, D.F. Boger fluids. *Annu. Rev. Fluid Mech.* **2009**, *41*, 129–142. [[CrossRef](#)]
39. Oldroyd, J.G. On the formulation of rheological equations of state. *Proc. R. Soc. Lond. Ser. Math. Phys. Eng. Sci.* **1950**, *200*, 523–541. [[CrossRef](#)]
40. Joseph, D.D. *Fluid Dynamics of Viscoelastic Liquids*; Springer: Berlin/Heidelberg, Germany, 1990; ISBN 978-1-4612-8785-8.
41. Cherizol, R.; Sain, M.; Tjong, J. Review of non-Newtonian mathematical models for rheological characteristics of viscoelastic composites. *Green Sustain. Chem.* **2015**, *5*, 6–14. [[CrossRef](#)]
42. Anguita, D.; Ghelardoni, L.; Ghio, A.; Oneto, L.; Ridella, S. The ‘K’ in K-fold cross validation. In Proceedings of the 20th European Symposium on Artificial Neural Networks, Computational Intelligence and Machine Learning (ESANN), Bruges, Belgium, 25–27 April 2012; pp. 441–446.
43. Jung, Y.; Hu, J. A K-fold averaging cross-validation procedure. *J. Nonparametr. Stat.* **2015**, *27*, 167–179. [[CrossRef](#)] [[PubMed](#)]
44. Memon, N.; Patel, S.B.; Patel, D.P. Comparative analysis of artificial neural network and XGBoost algorithm for PolSAR image classification. In *International Conference on Pattern Recognition and Machine Intelligence*; Springer International Publishing: Cham, Switzerland, 2019; pp. 452–460. ISBN 978-3-030-34868-7.
45. Coleman, C.D.; Swanson, D.A. On MAPE-R as a measure of cross-sectional estimation and forecast accuracy. *J. Econ. Soc. Meas.* **2007**, *32*, 219–233. [[CrossRef](#)]
46. Zeraatpisheh, M.; Ayoubi, S.; Jafari, A.; Tajik, S.; Finke, P. Digital mapping of soil properties using multiple machine learning in a semi-arid region, central Iran. *Geoderma* **2019**, *338*, 445–452. [[CrossRef](#)]
47. Guha, P.; Chakraborty, B. On a multivariate generalization of quantile-quantile plot. In *International Conference on Robust Statistics*; 2009; p. 62, ISBN 978-88-903330-0-2. Available online: [https://www.researchgate.net/profile/Tadeusz-Bednarski/publication/220363666\\_Frechet\\_Differentiability\\_in\\_Statistical\\_Inference\\_for\\_Time\\_Series/links/552502a80cf2caf11bfcf362/Frechet-Differentiability-in-Statistical-Inference-for-Time-Series.pdf#page=84](https://www.researchgate.net/profile/Tadeusz-Bednarski/publication/220363666_Frechet_Differentiability_in_Statistical_Inference_for_Time_Series/links/552502a80cf2caf11bfcf362/Frechet-Differentiability-in-Statistical-Inference-for-Time-Series.pdf#page=84) (accessed on 5 January 2022).
48. Yang, Q.; Zhang, Y.; Dai, W.; Pan, S.J. *Transfer Learning*; Cambridge University Press: Cambridge, UK, 2020; ISBN 978-1107016903.
49. Thuerey, N.; Holl, P.; Mueller, M.; Schnell, P.; Trost, F.; Um, K. Physics-Based Deep Learning. 2021. Available online: <https://physicsbaseddeeplearning.org> (accessed on 5 December 2021).
50. Segev, N.; Harel, M.; Mannor, S.; Crammer, K.; El-Yaniv, R. Learn on source, refine on target: A model transfer learning framework with random forests. *IEEE Trans. Pattern Anal. Mach. Intell.* **2016**, *39*, 1811–1824. [[CrossRef](#)]
51. Chawla, N.V.; Bowyer, K.W.; Hall, L.O.; Kegelmeyer, W.P. SMOTE: Synthetic minority over-sampling technique. *J. Artif. Intell. Res.* **2002**, *16*, 321–357. [[CrossRef](#)]
52. Fauzan, M.A.; Murfi, H. The accuracy of XGBoost for insurance claim prediction. *Int. J. Adv. Soft Comput. Its Appl.* **2018**, *10*, 159–171.
53. Giannakas, F.; Troussas, C.; Krouska, A.; Sgouro-poulou, C.; Voyiatzis, I. XGBoost and deep neural network comparison: The case of teams’ performance. In *International Conference on Intelligent Tutoring Systems*; Springer: Cham, Switzerland, 2021; pp. 343–349. ISBN 978-3-030-80420-6. [[CrossRef](#)]
54. Shehadeh, A.; Alshboul, O.; Mamlook, R.E.A.; Hamedat, O. Machine learning models for predicting the residual value of heavy construction equipment: An evaluation of modified decision tree, LightGBM, and XGBoost regression. *Autom. Constr.* **2021**, *129*, 103827. [[CrossRef](#)]
55. Ahmad, M.; Hippolyte, J.-L.; Mourshed, M.; Rezgui, Y. Random forests and artificial neural network for predicting daylight illuminance and energy consumption. In Proceedings of the 15th International Building Performance Simulation Association Conference, San Francisco, CA, USA, 7–9 August 2017; pp. 1949–1955. [[CrossRef](#)]
56. Kim, J.Y.; Cho, B.H.; Im, S.M.; Jeon, M.J.; Kim, I.Y.; Kim, S.I. Comparative study on artificial neural network with multiple regressions for continuous estimation of blood pressure. In *Conference Proceedings IEEE Engineering in Medicine and Biology Society*; IEEE: Piscataway, NJ, USA, 2005; pp. 6942–6945. [[CrossRef](#)]
57. Willard, J.; Jia, X.; Xu, S.; Steinbach, M.; Kumar, V. Integrating physics-based modeling with machine learning: A survey. *arXiv* **2020**, arXiv:2003.04919.
58. Lu, L.; Pestourie, R.; Yao, W.; Wang, Z.; Verdugo, F.; Johnson, S.G. Physics-informed neural networks with hard constraints for inverse design. *Soc. Ind. Appl. Math. J. Sci. Comput.* **2021**, *43*, B1105–B1132. [[CrossRef](#)]
59. Sill, J.; Takács, G.; Mackey, L.; Lin, D. Feature-weighted linear stacking. *arXiv* **2009**, arXiv:0911.0460.

## Article

# Microfluidic Rheometry and Particle Settling: Characterizing the Effect of Polymer Solution Elasticity

Salah A. Faroughi <sup>1,\*</sup> and Francesco Del Giudice <sup>2</sup>

<sup>1</sup> Geo-Intelligence Laboratory, Ingram School of Engineering, Texas State University, San Marcos, TX 78666, USA

<sup>2</sup> Department of Chemical Engineering, Faculty of Science and Engineering, School of Engineering and Applied Sciences, Swansea University Bay Campus, Fabian Way, Swansea SA1 8EN, UK; francesco.delgiudice@swansea.ac.uk

\* Correspondence: salah.faroughi@txstate.edu

**Abstract:** The efficient transport of solid particles using polymeric fluids is an important step in many industrial operations. Different viscoelastic fluids have been designed for this purpose, however, the effects of elasticity have not been fully integrated in examining the particle-carrying capacity of the fluids. In this work, two elastic fluid formulations were employed to experimentally clarify the effect of elasticity on the particle drag coefficient as a proxy model for measuring carrying capacity. Fluids were designed to have a constant shear viscosity within a specific range of shear rates,  $\dot{\gamma} < 50$  (1/s), while possessing distinct (longest) relaxation times to investigate the influence of elasticity. It is shown that for dilute polymeric solutions, microfluidic rheometry must be practiced to obtain a reliable relaxation time (as one of the measures of viscoelasticity), which is on the order of milliseconds. A calibrated experimental setup, furnished with two advanced particle velocity measurement techniques and spheres with different characteristics, was used to quantify the effect of elasticity on the drag coefficient. These experiments led to a unique dataset in moderate levels of Weissenberg numbers,  $0 < Wi < 8.5$ . The data showed that there is a subtle reduction in the drag coefficient at low levels of elasticity ( $Wi < 1$ ), and a considerable enhancement at high levels of elasticity ( $Wi > 1$ ). The experimental results were then compared with direct numerical simulation predictions yielding  $R^2 = 0.982$ . These evaluations endorse the numerically quantified behaviors for the drag coefficient to be used to compare the particle-carrying capacity of different polymeric fluids under different flow conditions.

**Keywords:** viscoelasticity; particle settling; dilute polymeric solutions; Oldroyd-B model; microfluidic rheometry; drag coefficient; hydraulic fracturing

**Citation:** Faroughi, S.A.; Del Giudice, F. Microfluidic Rheometry and Particle Settling: Characterizing the Effect of Polymer Solution Elasticity. *Polymers* **2022**, *14*, 657. <https://doi.org/10.3390/polym14040657>

Academic Editor: Alexander Malkin

Received: 8 January 2022

Accepted: 4 February 2022

Published: 9 February 2022

**Publisher's Note:** MDPI stays neutral with regard to jurisdictional claims in published maps and institutional affiliations.



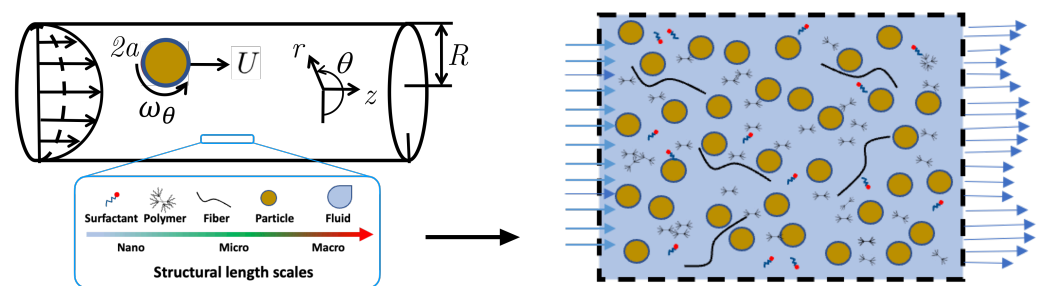
**Copyright:** © 2022 by the authors. Licensee MDPI, Basel, Switzerland. This article is an open access article distributed under the terms and conditions of the Creative Commons Attribution (CC BY) license (<https://creativecommons.org/licenses/by/4.0/>).

## 1. Introduction

The dynamics of solid particles flowing through polymeric fluids is strongly affected by viscoelasticity of the fluid [1,2]. Elasticity of the fluid, in addition to viscosity, is an integral element to consider when designing efficient solid particle transport in many advanced manufacturing and industrial operations, such as processing of highly-filled viscoelastic polymer melts and elastomers [3,4], processing of semi-solid conductive flow battery slurries [5], cement slurries flow [6], and biological applications like the flow-induced migration of circulating cancer cells in biopolymeric media such as blood [7]. Hydraulic fracturing operations in tight oil and gas fields [8] is another important application of particle-laden polymeric fluids. As shown in Figure 1, in hydraulic fracturing hundreds of millions of sand particles (also known as proppant) are co-injected alongside fracturing fluids (e.g., dilute polymeric and surfactant solutions with/out fibers) to preserve the conductivity of the induced fracture networks after the pressure release [9,10].

Due to the lack of physics and theoretical models, or computational power, state-of-the-art fracturing simulators ignore the relevance of the flow properties (i.e., elastic

response under an external flow) of polymeric fluids [2,11–13]. Some attempts have been made in this direction for particle-free polymer solutions, however, not in the context of hydraulic fracturing, and for very basic geometrical shapes of the channel [14,15]. Fluid elasticity specifically alters the sedimentation and rotation rate of a particle, which in turn causes different cross-stream flow-induced migration behaviors, affecting the overall particle transport efficiency [15–18]. There is still a need to fully understand how to tune the properties of polymeric fluids to efficiently transport particles. To fill this gap, not only are the effect of particle shapes and types considered [19,20], but also different carrying polymeric fluids are being formulated [8,21]. For these fluids, considering the importance of polymer type, structure, solubility, and charge, the most common variables to design new solutions are the average polymer molecular weight,  $M_w$ , and the polymer concentration,  $c$  [22,23]. Dilute polymeric solutions, in this work, refer to a solution with  $0.01 \leq c/c^* \leq 1$ , where  $c^*$  is the overlap concentration [22,24].



**Figure 1.** Schematic of sand particles transport in hydraulic fracturing operation where hundreds of millions of sand particles are co-injected alongside fracturing fluids (e.g., dilute polymeric and surfactant solutions with/out fibers) to preserve the conductivity of the induced fracture networks after the pressure release.

Despite the complexity of such systems, the particle-carrying capacity of a fluid is estimated by mapping the translation of a single sphere in inertia-less steady-state conditions [25,26]. In hydraulic fracturing, the importance of this measuring criterion has been originated by the low shear rate conditions experienced by particles within the fractures after the pressure release. This test has been bench-marked since Sir George Stokes calculated, for the first time, the drag force on a single sphere translating through an unbounded Newtonian fluid. The model introduced by Stokes, however, only accounted for the shear viscosity of the fluid, and required other correction factors to be suitable under different flow conditions or fluid types. In a series of works [17,27,28], Gomma et al. showed that the effective shear viscosity is not the only factor to design efficient particle transport, and the fluid elasticity, quantified via the shear modulus, also plays a significant role. Several researchers [1,23,29–32] conducted comprehensive experimental and numerical investigations to determine the effect of fluid elasticity on the terminal velocity of a single sphere settling in a non-Newtonian elastic fluid in order to quantify the drag coefficient. These studies, even though they, in some cases, provided contradictory conclusions [11,33], generally showed that the fluid elasticity hinders the particles' motion, and the effect is more pronounced at a high level of elasticity [2,23].

In many practical cases, because of the strong interactions between elasticity and viscosity of the polymeric fluids, the hindrance due to elasticity was intermingled with the inherent shear-thinning properties, i.e., the fact that the viscosity of the polymeric fluid surrounding the falling sphere decreases during the sphere motion [11]. Blyton et al. [11] formulated different fluids to study the effect of fluid elasticity and shear-thinning individually, at a very high levels of flow elasticity. They concluded that the terminal velocity of a spherical particle in fluids possessing similar shear viscosity profiles decreases significantly with increasing the elasticity. Faroughi et al. [2] conducted direct numerical simulations to construct a correction model for the drag force on a particle translating in dilute polymer solutions with low to moderate levels of elasticity in negligible inertia conditions. This

approximate model accounted for the effect of elasticity considering the viscoelastic fluids with constant viscosity, e.g., Boger fluids [34]. This model predicts that the drag coefficient of a particle slightly decreases at low levels of elasticity, but substantially increases at high level of elasticity. The latter is due to the large elastic stresses developing on the surface as well as in the wake of the particle [2]. This approximate drag model thus explained some of the contradictory conclusions generated in previous studies. However, this numerically-driven model itself has not been verified experimentally yet due to the lack of data at moderate level of elasticity, i.e., dilute polymeric solutions.

The current study is undertaken to fulfill two main goals: (i) outline an appropriate scheme to infer the particle-carrying capacity of polymeric fluids, and (ii) generate unique static settling, or drag coefficient, data in moderate levels of elasticity. To this end, first, the theoretical background is briefly reviewed for the particle dynamics and rheology measurements (e.g., conventional and microfluidic rheometry) to accurately determine the parameters required to infer the drag coefficient. Then, two fluid formulations are designed with distinct longest relaxation times to carry out the inertia-less particle settling tests at low to moderate level of elasticity. Next, the experimental setup and velocity measurement procedures are elaborated, and the experimental results are presented and weighted against the approximate drag model developed by Faroughi et al. [2]. Finally, the main conclusions of the work are summarized.

## 2. Theoretical Background

### 2.1. Dimensionless Parameters

The interplay among different mechanisms controlling particle transport can be studied by decoupling different relevant forces acting on particles. The most important ones induced by the viscoelastic fluids are the drag, inertial, and transversal forces for which the theoretical developments are very limited [2]. Dimensionless numbers can be employed here to examine the particle transport behavior highlighting the importance of relevant forces. The viscoelasticity of polymeric fluids can be quantified using Weissenberg number,  $Wi$ , defined as,

$$Wi \equiv \lambda \dot{\gamma} = \frac{\lambda U}{a}, \quad (1)$$

for a spherical particle with radius  $a$  settling through the fluid. Here,  $\lambda$  is the longest relaxation time, and  $\dot{\gamma}$  represents a characteristic shear rate defined based on the terminal settling velocity,  $U$ , of the particle. For a Newtonian fluid, the Weissenberg number is  $Wi = 0$  corresponding to zero elasticity. A higher Weissenberg number,  $Wi > 0$ , represents a more pronounced elasticity in the fluid.

The presence of coiled or stretched polymers also impacts the effective shear viscosity of the polymeric fluid through hydrodynamic and physical interactions similar to the presence of a cloud of solid particles [35,36]. This effect can be parameterized using,

$$\zeta = \frac{\eta_P}{\eta_S + \eta_P} = \frac{\eta_P}{\eta_0}, \quad (2)$$

where  $\zeta$  represents the retardation ratio,  $\eta_P$  is the polymer contribution to the shear viscosity,  $\eta_S$  is the solvent contribution to the shear viscosity, and  $\eta_0 = \eta_P + \eta_S$  is the total shear viscosity in the limit of vanishing shear rate. For constant-viscosity viscoelastic fluids, e.g., Boger fluids [34], the relaxation time and retardation ratio,  $\lambda$  and  $\zeta$  repetitively, are the two important characteristics that define viscoelastic behaviors. These fluids are generally modeled using the Oldroyd-B constitutive equation [37] that best represents the polymer contribution to the momentum exchange in very dilute polymer solutions at low Weissenberg number. However, many realistic suspending fluids show mid to strong shear-thinning features, leading to more complex and nonlinear dependencies at nonvanishing Weissenberg numbers at which shear-thinning effects become even more pronounced [38]. Several viscoelastic constitutive models have been developed over the past few decades to

model such fluids [39–41]. Among all, the Giesekus model [42] is generally used to best represent the polymer contribution to the momentum exchange in dilute to semidilute polymer solutions. The Giesekus model is developed based on configuration-dependent molecular mobility. Therefore, the viscoelastic component of the polymeric stress tensor is represented by  $\lambda$  and  $\zeta$  as well as the mobility factor,  $\alpha$ , which theoretically varies between zero and unity (practically between zero and 0.5 [12]) and accounts for the shear-thinning behavior of the polymeric fluids.

Another important dimensionless number is the Reynolds number representing the ratio between inertial and viscous forces, which is defined as,

$$Re = \frac{\rho_f U a}{\eta_0}, \quad (3)$$

where  $\rho_f$  is the density of the fluid. Particles experience different flow regimes, i.e., turbulent to creeping flow regimes categorized by  $Re$  number, in different operations. The particle static settling experiment, as a method to differentiate the carrying capacity of fluids, has generally been studied at low Reynolds numbers,  $Re \ll 1$ , corresponding to the creeping flow regime [17,23].

## 2.2. Drag Coefficient for Viscoelastic Fluids

For a single particle settling in a viscoelastic fluid, one may carry out the drag coefficient on the surface of the particle using a surface integration of the total stress comprising the polymeric and solvent stress contributions,  $\boldsymbol{\tau}_p + \boldsymbol{\tau}_s$ , and the pressure field,  $p$ ,

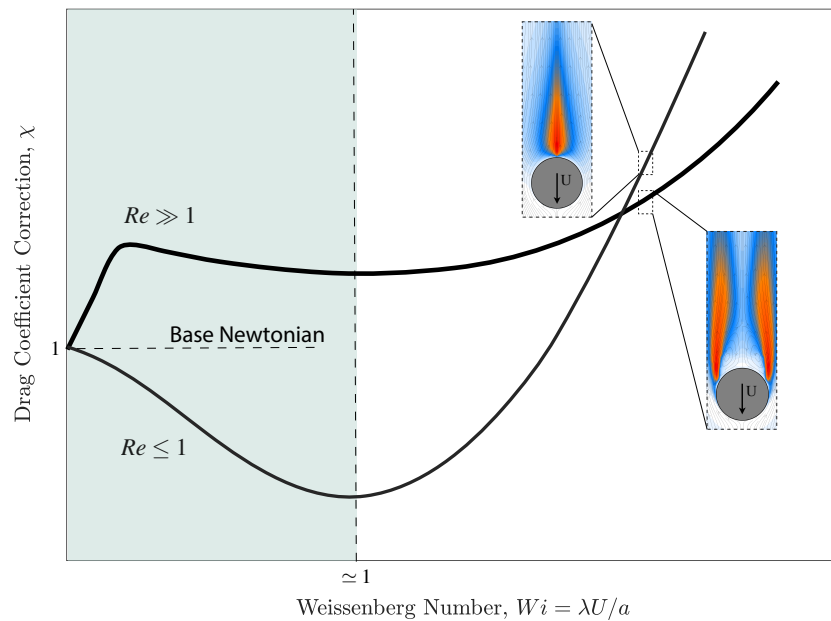
$$C_D = \frac{2}{\rho_f U^2 A} \int_{\delta\Omega_s} (\boldsymbol{\tau}_p + \boldsymbol{\tau}_s - p\mathbf{I}) \cdot \mathbf{n} \cdot \mathbf{x} \, dS. \quad (4)$$

In experimental studies, the drag coefficient can be calculated using the terminal velocity,  $U$ , measured for a sphere settling under the action of gravity,  $g$ , through a fluid. A relationship between the drag coefficient and terminal velocity can be deduced using the drag and gravitational force balance, leading to,

$$C_D = \frac{8ga}{3U^2} \left( \frac{\rho_p - \rho_f}{\rho_f} \right), \quad (5)$$

where  $\rho_p$  and  $\rho_f$  are the density of the particle and fluid, respectively. Equations (4) and (5) at  $Re \ll 1$  and zero elasticity,  $Wi = 0$ , reduces to the base visco-inelastic (or Newtonian) value for the drag coefficient, namely  $C_D = 24/Re$  [43]. At higher elasticity, the drag coefficient may increase or decrease depending on the flow conditions. Faroughi et al. [2] showed that at high Reynolds number,  $Re \gg 1$ ,  $C_D$  in a viscoelastic is always bigger than the base Newtonian value, as shown in Figure 2. At  $Re \leq 1$ , the drag coefficient of the particle first decreases (by a small amount) at low Weissenberg numbers, then bounces back at a critical Weissenberg number, and finally increases drastically due to large elastic stresses developing on the surface and in the wake of the particle. This phenomenon schematically shown in Figure 2 is also well reported in the literature [1,33]. The insets in Figure 2 show the profile of the polymeric axial stress developed in the wake of the particle at different Reynolds numbers. As depicted, at low  $Re$ , the polymer chains are stretched in the wake of particle with a maximum value close to the rear stagnation point where strong extensional flow is dominant. At high  $Re$ , due to the strong inertial effects, the axisymmetric flow past the particle shifts to a symmetry-breaking steady flow with a helical wake structure. The formation of symmetric eddies in the wake of particle relaxes the polymer chains on the center-line, and pushes the stress overshoot (maximum stretch) close to the flow separation points. The nonlinear inertial effects causing the formation of a steady axisymmetric toroidal eddy in the wake of the sphere greatly reduces the effect of elasticity on the drag coefficient. As illustrated in Figure 2, at high Weissenberg numbers,

the monotonic enhancement of the drag coefficient arising from viscoelasticity is more pronounced for low  $Re$  flows. This is an important observation, as the elasticity effects at low  $Re$  regimes are more applicable to many industry operations (e.g., the proppant placement in the fracture networks [2,17]).



**Figure 2.** Schematic profiles of the drag correction coefficient vs. Weissenberg number for a particle translating through an unbounded viscoelastic fluid at different Reynolds numbers. The insets show the profile of the polymeric axial stress developed in the wake of the particle, i.e., the extent over which polymer chains are stretched due to the strong extensional flow (red and white colors show the maximum and minimum stresses, respectively).

Due to strong interactions of the fluid viscoelasticity and the complex kinematics of the mixed shearing and extensional flow around the particles, an exact solution to Equation (4) that performs well over a wide range of viscoelastic parameters is missing. Faroughi et al. [2] tackled this problem to a great extent using direct numerical simulation to parameterize the canonical behavior of the drag coefficient considering the strong interaction of viscoelasticity and kinematic parameters. They used Oldroyd-B model to parameterize the contribution of the polymer microstructural changes at a particle level to the momentum exchange between the mixture constituents of a dilute polymer solution. The Oldroyd-B model simply represents an elastic fluid with a constant viscosity, and hence elastic effects can be studied alone. This constitutive model is a good approximate model for Boger fluids made of a sufficiently viscous solvent, in which stresses due to the elasticity are quantifiable [34]. The Oldroyd-B model, however, may not be marginally accurate, especially in extreme extensional flow where the fictitious entropic spring allows for infinite stretching, i.e., infinite stress [1]. Faroughi et al. [2] observed a self-similarity of the evolution in the drag coefficient in the inertia-less flow regime,  $Re \leq 1$ , and fitted the numerical simulations in this regime to develop an explicit model for the drag coefficient correction. The model by Faroughi et al. [2] at  $Wi \leq 1$  reduces to

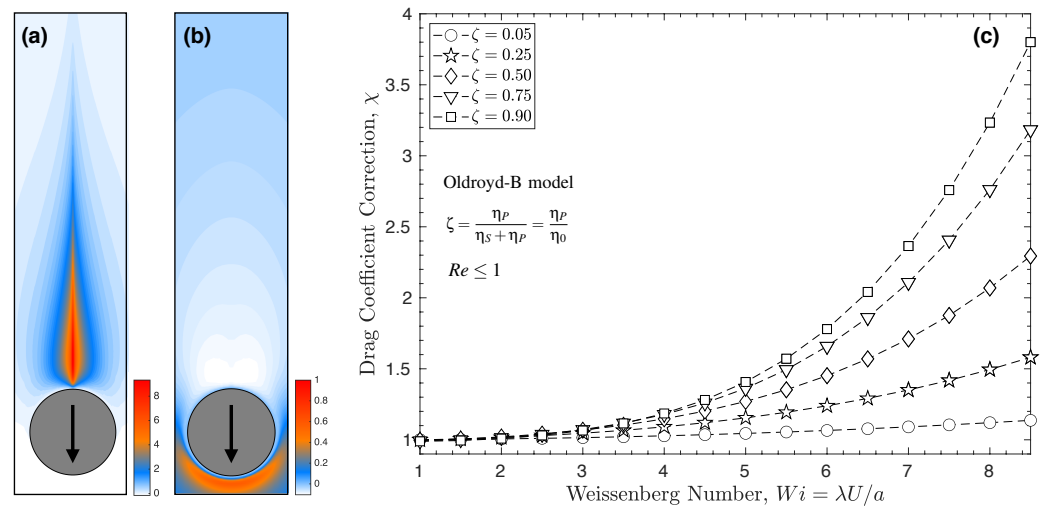
$$\chi = \frac{C_D}{(24/Re)} = 1 + \frac{1}{Wi^4 + (6.288 - 6.111\zeta)Wi^2 + 0.0534} \left( \begin{aligned} &((0.06665\zeta - 0.06392\zeta^2)Wi^6 + \\ &(-0.09422\zeta + 0.07025\zeta^2)Wi^4 + \\ &(-0.00443\zeta + 0.00248\zeta^2)Wi^2 \end{aligned} \right), \tag{6}$$

and at  $Wi \gg 1$  reduces to



$$\chi = \frac{C_D}{(24/Re)} = 1 + \frac{1}{Wi^4 + (0.5014\zeta - 0.02511\zeta^2)Wi^2} \left( (0.0005713\zeta^2)Wi^8 + (0.0006 + 0.02517\zeta - 0.02148\zeta^2)Wi^6 + (-0.02511\zeta + 0.0009496\zeta^2)Wi^4 \right), \tag{7}$$

for the drag coefficient correction,  $\chi$ , which is predicted within 95% accuracy for  $Wi < 5$  and  $0 < \zeta < 1$ , see Figure 3. At low elasticity regime,  $Wi \leq 1$ , Equation (6) predicts very small reductions in drag for which  $\chi \approx 1$  is a safe assumption for practical applications. However, at high elasticity  $Wi > 1$ , as shown in Figure 3c plotting Equation (7), the drag can be drastically enhanced and must be taken into consideration when comparing the carrying capacity of different fluids.



**Figure 3.** The effect of elasticity on the drag coefficient of a particle settling through a viscoelastic fluid. Panel (a,b) shows the contours of dimensionless polymeric stress components,  $\tau_{P_{rr}}$  and  $\tau_{P_{\phi\phi}}$  developed in the wake and front of the particle, respectively, at  $Re = 0.1$ ,  $Wi = 2$ , and  $\zeta = 0.5$  [20]. These stress components both increase with  $Wi$  and hinder the particle settling velocity, i.e., increase the drag coefficient of the particle. Contours are shown in the spherical polar coordinate frame,  $\{r, \theta, \phi\}$ , on the  $r - \theta$  plane where  $0 \leq \theta \leq 2\pi$ . The polymeric stress components are normalized by  $\eta_0 U/a$ . Panel (c) illustrates the relationship between the drag correction coefficient and Weissenberg number obtained from Equation (7) for an inertia-less spherical particle translating through an unbounded Oldroyd-B fluid with different polymeric retardation ratios.

### 2.3. Rheological Properties

To determine the drag coefficient using Equations (6) and (7), one needs to glean the retardation ratio and relaxation time, among other rheological parameters, for dilute polymer solutions. The change in the zero-shear viscosity due to the presence of polymers of different types is relatively straightforward to measure using a conventional bulk rheometry [44–46] or using microfluidic viscometers [47,48]. Knowing the shear viscosity of the Newtonian solvent,  $\eta_s$ , one may characterize the Newtonian plateau region at lower shear rates, i.e., where the viscosity is independent of the shear rate, using a stress controlled shear rheometer, see for example Rubinstein and Colby [22], Kulicke and Clasen [49]. This method simply provides the zero-shear viscosity of the solution,  $\eta_0$ , using which the polymer contribution to the zero-shear viscosity,  $\eta_p = \eta_0 - \eta_s$ , and the fluid’s retardation ratio,  $\zeta$ , can be determined using Equation (2).

The determination of the relaxation time,  $\lambda$ , is not as simple as retardation ratio. Polymer solutions are usually best described using a spectrum of relaxation times accounting

for relaxation processes occurring within the chain itself, as well as within the network of chains. For the shear flows of dilute polymer solutions, the determination of relaxation times poses several challenges. In these cases, the weak viscoelasticity signals can hardly be captured using conventional methods [50]. For an ideal dilute polymeric solution, the chain–chain interactions are absent, and the viscoelasticity of the fluid reduces to the viscoelasticity of isolated chains that still possess multiple relaxation processes related to the chain itself and the sub-chains on the backbone [22]. The relaxation process for the chain is slower than that of the sub-chains [50]. This suggests that the viscoelasticity of a dilute polymer solution, comprised of polymers with monodisperse molecular weight distribution, can be quantified by the longest relaxation time within the spectrum. The longest relaxation time is the time required for an isolated chain to relax from a stretched configuration to a random coil configuration [22,51]. Other modes with relaxation time smaller than the longest relaxation time do not appreciably contribute to the stress as they are not excited by the flow. The longest relaxation time strongly depends on both molecular weight and concentration of the polymer. Note that for low concentration and low molecular weight, measurements have to be performed at higher frequencies as the dominant dynamics gravitate to occur on shorter timescales [47]. Sometimes these frequencies are out of reach using conventional bulk rheometry due to the detection limit of the instrumentation caused by the onset of the inertial effects [47,52–54]. For example, the longest relaxation time is on the order of milliseconds and below for low-viscous water-based viscoelastic fluids [50,55]. In these scenarios, microfluidics has proven to be a promising tool to capture the correct modes of the dilute polymeric solutions [48].

### 3. Materials and Methods

#### 3.1. Fluids and Preparation

Two different elastic fluids were used to investigate the influence of elasticity on the drag coefficient for slow flow around a sphere. The first fluid was composed of 0.1 wt.% polyacrylamide (5–6 MDa) dissolved in a solvent made of 90 wt.% glycerol and 10 wt.% DI water (this fluid is tagged as PAM/GLY for the rest of this paper). Polyacrylamide is known to adopt a relatively extended conformation in low salinity, and a random coil conformation in solutions containing high concentrations of ions. Deionized water is then used as a solvent to remove the reduction in extensibility of this polyacrylamide-based Boger fluid prepared for different measurements. The second fluid was composed of dissolving 16 wt.% high molecular weight polystyrene (20 MDa) in a solvent made of 70 wt.% low molecular weight polystyrene (500 Da) and 30 wt.% tricresyl phosphate (this fluid is tagged as PS/TCP for the rest of this paper). The mixture of tricresyl phosphate with low molecular weight polystyrene is known to be a good solvent for high molecular weight polystyrene, and results in a high extensibility for the solution [56,57]. For both fluids, conventional rheology experiments were conducted with several measurement geometries (cone-and-plate, parallel plate, concentric cylinder) to increase the range of shear rates. Each measurement is also repeated three times to ensure the integrity of the data. The rheology of the solutions was monitored as a function of time to be completely homogeneous (experimental error < 2%) before measuring the final properties under the conditions of controlled room temperature at the same temperature as the falling sphere experiments (i.e.,  $T = 20\text{ }^{\circ}\text{C}$ ). For these solutions,  $\eta_0$  and  $\zeta$  are obtained using viscometric properties; the shear viscosity was measured as a function of shear rate fitted by the Carreau model [58,59]. The longest relaxation time was measured using the normal stress difference [60,61] and  $\mu$ -rheometer [50] methods for PS/TCP and PAM/GLY, respectively.

#### 3.2. Particle Settling Experiments

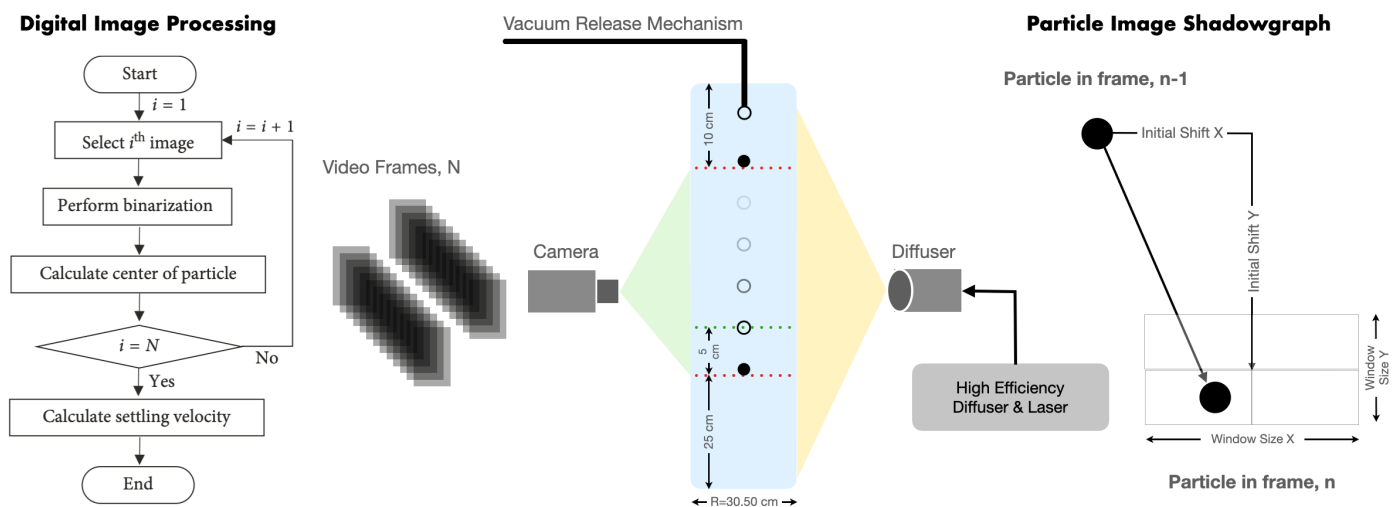
To probe a broad range of Weissenberg numbers, different Boger fluids possessing different relaxation times are needed. Due to the difficulty to formulate Boger fluids (i.e., polymer solutions with constant viscosity), various sizes and types of spherical particles were used with  $D = 2a = \{0.5 - 12\}$  mm and densities  $\rho = \{1300 - 7800\}$  kg/m<sup>3</sup>. All these

particles are commercially available with a high precision, i.e., with diameter tolerance smaller than 25  $\mu\text{m}$ , at Cospheric LLC, Santa Barbara, CA, USA. Using this set of spheres falling through the formulated solutions, it was possible to keep the nominal shear rates, accounting for wall decelerating effect, smaller than  $\dot{\gamma} < 50 \text{ s}^{-1}$ , and explore the effect of Reynolds number and Weissenberg number on drag coefficient for a desired range of  $Re < 1$  and  $0 < Wi < 8.5$ , respectively.

The transient motion of a sphere along the center line of a glass cylindrical tube (with internal radius of  $R = 15.25 \text{ cm}$ ) is captured and measured using two techniques, (i) digital image processing (DIP) following Kim et al. [62], and (ii) particle image shadowgraph (PIS) following Arnipally et al. [23] to measure independent estimates of the steady-state terminal velocity of the particle settling through the Boger fluids. The DIP and PIS procedures to calculate the settling velocity are summarized in Figure 4. In DIP, binarization is used to differentiate target (particle) and background (viscoelastic fluid). After binarization, the particle region is converted to a set of white pixels, and the centroid of white pixels is marked to determine the position of the particle in each image. The displacement of the centroid, i.e., the difference of the position of the particle, in two consecutive images with a known time interval leads to the settling velocity. The PIS technique works based on the fundamental principle that shadow forms as light travels through different mediums of different refractive indices. The position of the particle in each image is determined depending on the shadow intensity. The settling velocity is then calculated using particle displacement in two consecutive images with known time interval as shown in Figure 4. Refer to Kim et al. [62] and Arnipally et al. [23] for measurement calibration and details about the required devices in these setups. The accuracy of both measurements are mostly limited to the spatial and temporal resolution of the image acquisition device and the light source to record the Lagrangian displacement of the falling sphere. It is important to note that releasing the sphere below the free surface right on the cylinder's center line greatly affects the velocity data and particle trajectory. Therefore, the setup requires a reliable particle release mechanism on top of the cylinder. In this work, a firm vacuum mechanism was attached to a tube holding the particle at its end at around three particle diameter below the free surface. The reliability of measuring techniques and the accuracy of the data obtained are constantly checked against a Newtonian fluid. In our setup configuration, the confinement ratio is defined as the ratio of particle radius to cylinder radius varies in the range of  $a/R = \{0.0016 - 0.0384\}$  for which the Faxen correction factor [2],

$$f_w\left(\frac{a}{R}\right) = \left(1 - 2.10444\left(\frac{a}{R}\right) + 2.08877\left(\frac{a}{R}\right)^3 - 0.94813\left(\frac{a}{R}\right)^5 - 1.372\left(\frac{a}{R}\right)^6 + 3.87\left(\frac{a}{R}\right)^8 - 4.19\left(\frac{a}{R}\right)^{10} + \dots\right)^{-1}, \quad (8)$$

approaches unity. Therefore, the effect of cylinder walls on the drag coefficient could be safely neglected. This assumption is in accordance with Arigo et al. [63] and provides us with the ability to directly compare the experimental results with Equation (7) developed for unbounded domain. Several calculations were also made using the theoretical analysis for the terminal velocity of the largest particles in the lowest viscosity fluid to obtain the right measurement window for the experiments assuring particle reaches its terminal velocity. Images were taken inside a window located 25 cm above the bottom of the cylindrical and 10 cm below the fluid free surface. A distance of 50 mm above the bottom line was found to satisfy all configurations reaching the steady-state velocity. Each velocity measurement is repeated five times, assuring the statistical accuracy and repeatability of the acquired data. In each velocity measurement, after cross-checking PIS and DIP methods, an average value of the velocities by these two methods was used in drag coefficient calculation. A relatively long time-interval (30 min) between measurements was considered to allow these elastic Boger fluids to fully relax to their stress-free state before running the next experiments [23].



**Figure 4.** A schematic representation of the experimental setup and procedures to measure the settling velocity and drag coefficient of spherical particles translating through viscoelastic fluids.

### 3.3. Rheological Measurements

Both polymer solutions and their respective Newtonian solvents are characterized by a steady-shear flow procedure using a stress controlled shear rheometer (DHR-3 by TA Instrument using cone-and-plate, parallel plate, concentric cylinder geometries). All rheological measurements were performed at carefully controlled room temperature,  $T = 20\text{ }^{\circ}\text{C}$ .

The longest relaxation time for the PAM/GLYC system could not be measured using conventional rheometry due to technical limitations of the instruments. Instead, the  $\mu$ -rheometer method, i.e., a microfluidic rheometer, was used for the measurements of the longest relaxation time [50,54]. The working principle of the  $\mu$ -rheometer is based on the transverse migration of solid particles occurring when the suspending viscoelastic fluid flows under an inertia-less Poiseuille flow through a confined straight microchannel. In this method, the fraction of particles aligned on the center-line, i.e.,  $f_1$  moving through the band number 1 as shown in Figure 5a, which is measured experimentally using optical microscopy at a distance, namely  $L$ , from the inlet position. This step is performed by dividing the cross-section of the microchannel arbitrarily into six bands for which the average velocities and cross-sectional area are calculated, see Del Giudice et al. [54] for more details. Knowing the expected velocities for particles in each band calculated from the fluid velocity, one can apply a particle tracking method to calculate the normalized fraction of particles in the first band using,

$$f_1 = \frac{N_1/A_1V_1}{\sum N_k/A_kV_k}, \quad (9)$$

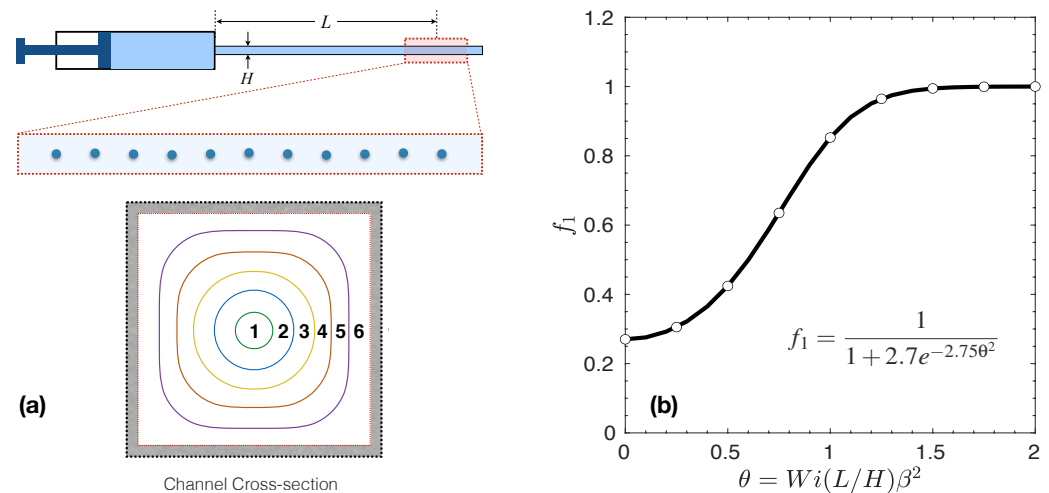
where  $N_k$  represents the number of particles flowing in the band  $k$ , and  $V_k$  and  $A_k$ , respectively, show the average velocity and the cross-sectional area of the fluid enclosed in the  $k$ th band. For a given set of geometrical parameters (e.g., the channel cross-section diameter,  $H$ , and the confinement ratio defined as  $\beta = D_p/H$  where  $D_p$  is the diameter of the suspended particles), once  $f_1$  is measured, the  $\theta$  value can be calculated using the master curve shown in Figure 5b. The  $\theta$  value can be then translated to the longest relaxation time of the solution knowing  $\theta = Wi(L/H)\beta^2$  [54].

It is important to note that the master curve plotted in Figure 5a does not need calibration for different geometrical setups and is universal for any viscoelastic fluids as long as the Weissenberg number of the flow is kept below  $Wi < 0.5$  (within the rheometry

experiments), and the confinement ratio is equal or smaller than 0.1, together corresponding to  $\theta \leq 1.4$ . For a cylindrical microchannel with diameter  $H$ , the following equation,

$$\lambda = \frac{\pi}{4} \frac{1}{\beta^2} \frac{H^4}{LQ} \sqrt{\frac{1}{2.75} \ln\left(\frac{2.7f_1}{1-f_1}\right)}, \quad (10)$$

can be deduced for the longest relaxation time of dilute polymer solutions using the aforementioned procedures to evaluate  $f_1$ . Here, the characteristic shear rate in  $Wi$  number is replaced by  $\dot{\gamma} = 4Q/\pi H^3$  in which  $Q$  represents the imposed volumetric flow rate. Here, specifically, polystyrene particles having a 10  $\mu\text{m}$  diameter (Polysciences Inc) were added to the PAM/GLY solutions at a mass concentration  $\phi = 0.01$  wt%. Flowing particles were observed using an inverted microscope (Zeiss Axiovert), while videos were recorded with a high-speed camera (Photron Mini UX50). The flow rate was controlled using a pressure pump (Dolomite Microfluidics). The resulting videos were analysed using a particle tracking software subroutine in IDL [64].



**Figure 5.** Schematic representation of a microfluidic-based device to measure the longest relaxation time of ultra-dilute and dilute polymer solutions. Panel (a) shows the  $\mu$ -rheometer device that operates based on the transverse migration of solid particles in viscoelastic fluid flowing through a confined straight microchannel [54]. The bands marked on the cross-section of the channel is used to count particles trapped in those regions as they traveled a length of  $L$ , especially the fraction of particles aligned on the central band,  $f_1$ . Panel (b) shows the master curve for  $f_1$  that can be directly used to approximate the longest relaxation time of ultra-dilute polymer solutions. This master curve does not need calibration for different geometrical setups and is universal for any viscoelastic fluids as long as  $Wi < 0.5$  within the rheometry experiments, and the confinement ratio between the suspended particle diameter,  $D_p$ , and channel cross-section diameter (or depth),  $H$ , is  $D_p/H \leq 0.1$ .

## 4. Results and Discussion

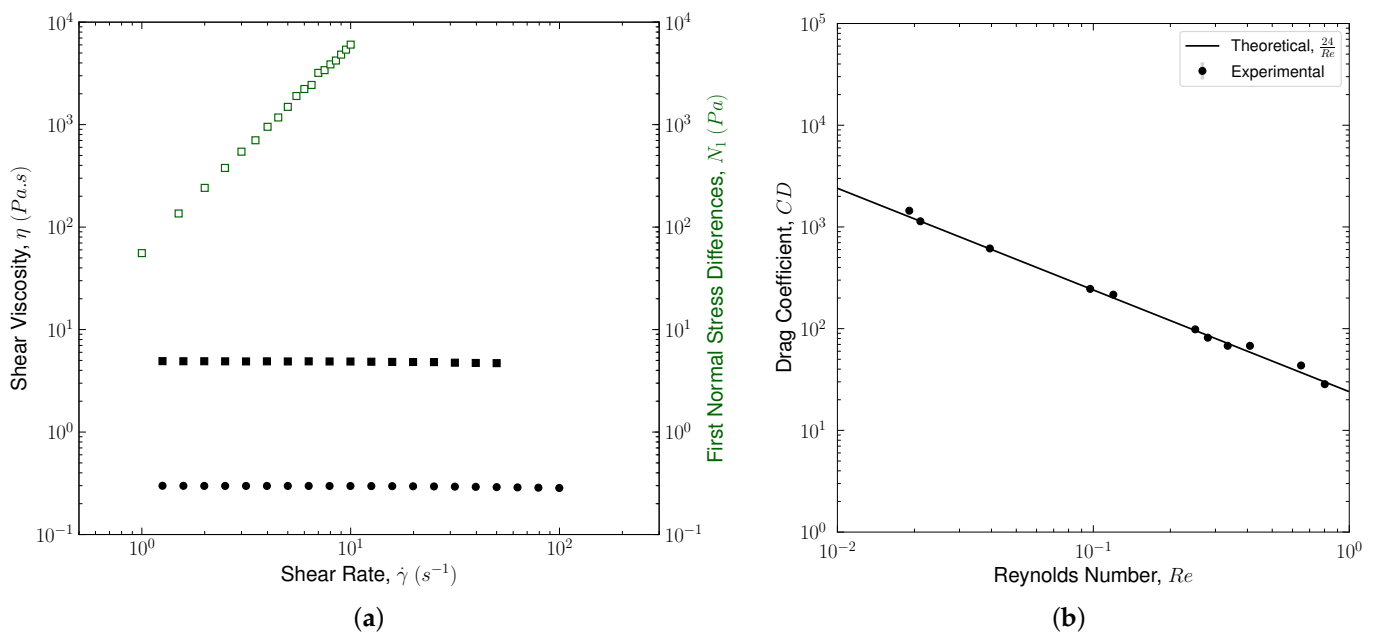
### 4.1. Fluids Rheology

Results of the bulk shear rheology measurements are shown in Figure 6a. For the PS/TCP solution, the fluid was designed to stay within the semi-dilute regime,  $c > c^*$ . Here,  $c^*$  is the overlap concentration defined as [22],

$$c^* = \frac{M_w}{\frac{4}{3}\pi N_A R_g^3} \simeq \frac{0.77}{[\eta]}, \quad (11)$$

where  $N_A$  is Avogadro's constant,  $R_g$  is the radius of gyration, and  $[\eta]$  denotes the intrinsic viscosity that depends on the molar mass of the chain, the degree of polymer chain branching, as well as the type of solvent in which the polymer is dissolved [22]. The overlap

concentration is used to distinguish the onset of semi-dilute and eventually entangled regimes. At  $c > c^*$ , the polymer solution viscoelasticity is not only related to the individual chain contributions, but to the developed network of coils that dramatically changes the solution behavior under different flow conditions [49,65]. The shear viscosity and first normal stress difference,  $N_1$ , are reported in Figure 6a for the PS/TCP solution. For the PAM/GLY solution, the fluid was designed to stay within the dilute regime,  $c < c^*$ . In this regime, the individual polymer chains are far placed and rare hydrodynamic, steric, or frictional interactions present [24]. Therefore, the viscoelasticity of the solution is mostly associated with the viscoelasticity of individual polymer coils summed linearly. For the PAM/GLY solution, only the shear viscosity as a function of the shear rate is reported. Due to the detection limit of the rheometer in this regime, a reliable measurement for  $N_1$  was not produced.



**Figure 6.** Panel (a) shows the results of the shear viscosity (filled circles for PAM/GLY fluid and filled squares for PS/TCP fluid) and the first normal stress difference  $N_1$  (empty squares for PS/TCP fluid) as a function of shear rate. Panel (b) shows the comparison between theory and experimental results obtained for the drag coefficient of a spherical particle translating through a Newtonian fluid at  $Re \leq 1$ . The solvent for the PS/TCP fluid is used as the test Newtonian fluid possessing  $\eta_s = 2.17$  (Pa.s). The errorbars account for the dispersion around the average value of the drag coefficient measured experimentally. The mean value of the relative standard deviation for all measurements, conducted at  $T = 20$  °C and repeated five times, was less than 0.10%.

Both polymer solutions maintain a constant viscosity, as one of the most important characteristics of the Boger fluid, within the full range of shear rates present in the settling experiments at  $\dot{\gamma} < 50$  (1/s). The zero-shear viscosity,  $\eta_0$ , and the polymer contribution to the solution viscosity,  $\eta_p$ , are determined by fitting the Carreau model [40],

$$\eta = \eta_\infty + (\eta_0 - \eta_\infty) \left( 1 + (\lambda \dot{\gamma})^2 \right)^{\frac{n-1}{2}}, \tag{12}$$

to the viscosity data shown in Figure 6a. In Equation (12),  $\eta_\infty$  is the plateau viscosity at infinite shear rate, and  $n$  is the flow index accounting for the shear-thinning of the solution. For Boger fluids, the flow index should approach unity,  $n \rightarrow 1$ . The  $\lambda$ , here, has a unit of time and generally corresponds to the inverse of the shear rate at which the turnover occurs between the Newtonian plateau and the shear-thinning region [66]. From the best fit, at  $c > c^*$ ,  $\lambda$  in Equation (12) can be used as an estimate of the longest relaxation time.

This conclusion is based on the fact that the polymer chains are not in a random coiled configuration anymore and start to stretch at the onset of shear-thinning features. The best fit of Equation (12) to the PS/TCP viscosity data shown in Figure 6a leads to  $\eta_0 = 4.32$  (Pa.s) and  $\eta_p = 2.15$  (Pa.s) with  $R^2 = 0.987$ . The best fit to PAM/GLY viscosity data shown in Figure 6a leads to  $\eta_0 = 0.31$  (Pa.s) and  $\eta_p = 0.22$  (Pa.s) with  $R^2 = 0.992$ .

For the PS/TCP solution, the longest relaxation time is determined using the first normal stress difference,  $N_1$ . This is a well-practiced approach to determine an approximate value for the longest relaxation time of polymer solutions at  $c > c^*$  [67]. This is because, under shear flow, the polymers dissolved in the base fluid tend to align with the flow streamlines, while they inherently tend to come back to their undisturbed conformation. These chain-level interactions lead to an extra tension in the direction of the flow attributed to the fluid elasticity. Normal stresses are zero for Newtonian fluids, i.e.,  $N_1 = 0$ . Normal stresses thus could be used as a measure to obtain the level of elasticity, and hence, the relaxation time for polymeric (viscoelastic) fluids. All nonlinear constitutive models of viscoelastic fluids provide an expression to predict normal stress differences [60]. For a Boger fluid represented by Oldroyd-B model under a steady shear flow,  $N_1$  can be determined as,

$$N_1 = 2\eta_0\lambda\zeta\dot{\gamma}^2, \quad (13)$$

which is linear in both  $\lambda$  and  $\zeta$  [60,68]. At a known value of  $\zeta = \eta_p/\eta_0$ , fitting Equation (13) to the measured  $N_1$  data (see Figure 6) leads to the longest relaxation time of the polymer solution. The best fit of Equation (13) to the  $N_1$  data reported for PS/TCP solution leads to  $\lambda = 2.463$  (s) with  $R^2 = 0.996$ .

For the dilute PAM/GLY solution where  $c < c^*$ , the characterization of elasticity effects and relaxation times is beyond the range measurable in the conventional geometries used in most of the shear and extensional rheometers [50]. Therefore, the  $N_1$  method hardly provides reliable estimation for  $\lambda$  as it is difficult to ensure the integrity of the experimental data [68–70]. In these cases, a very rough method to provide an approximate value for the longest relaxation time is to use the Zimm theory [22]. This theory assumes the longest relaxation time is independent of the polymer concentration in a very dilute polymer solutions. However, this assumption is not valid under all flow conditions. For example, under strong extensional flow such as flow past a particle, polymer coils become substantially stretched resulting in an increased volume of interaction, which causes the overlap to happen at polymer concentration much below the  $c^*$ . Clasen et al. [24] concluded that the longest relaxation time depends on the polymer concentration even at  $c/c^* < 1$ , but this dependency truly vanishes at  $c/c^* < 0.01$ , known as ultra-dilute polymer solutions, regardless of how much polymer chains are deformed beyond their equilibrium state. For  $0.01 \leq c/c^* \leq 1$ , the longest relaxation time is shown to exhibit a power-law scaling with the reduced concentration,  $c/c^*$ , where the magnitude of the exponent depends on the thermodynamic quality of the solvent [24]. Several methods have been proposed to glean the longest relaxation time for this region [55], from which those based on microfluidics are shown to outperform the others to estimate the relaxation time of viscoelastic fluids, down to milliseconds [53,54]. As described in Section 3.3, the newest microfluidics method is the  $\mu$ -rheometer [50]. This method is utilized to obtain the longest relaxation time for the dilute PAM/GLY solution in this work. The  $\mu$ -rheometer approach predicted  $\lambda = 0.023$  s for this solution, which is smaller by two orders of magnitude than the value predicted for the PS/TCP solution.

These PAM/GLY and PS/TCP fluid choices provide the possibility to experimentally explore the effect of viscoelasticity on the drag coefficient of a sphere settling in both weakly elastic fluid flows,  $Wi \leq 1$ , and highly elastic fluid flows,  $Wi > 1$ . Table 1 summarizes the rheological results for both PAM/GLY and PS/TCP solutions.

**Table 1.** Fluid rheological characteristics. For the PS/TCP solution, the longest relaxation time is determined by fitting the Oldroyd-B model expressed by Equation (13) to the data measured for  $N_1$  shown in Figure 6a. For the PAM/GLY solution, the longest relaxation time is determined using the  $\mu$ -rheometer approach. The zero-shear viscosity,  $\eta_0$ , and the solvent and polymer contributions to the viscosity,  $\eta_S$  and  $\eta_P$ , are determined by fitting Equation (12) to the viscosity data shown in Figure 6a.

Boger Fluids	$\rho_f$ (kg/m <sup>3</sup> )	$\eta_0$ (Pa.s)	$\eta_S$ (Pa.s)	$\eta_P$ (Pa.s)	$\zeta$ (-)	$\lambda$ (s)
PAM/GLY	1242.1	0.31	0.09	0.22	0.709	0.023
PS/TCP	1162.8	4.32	2.17	2.15	0.497	2.463

#### 4.2. Drag Measurements

Conducting the particle settling experiments using viscoelastic fluids is challenging. For example, at a low Weissenberg number, the changes in the drag coefficient may well be within the experimental error. At a high Weissenberg number, the polymer chains may not relax to their stress-free condition if experiments are not well-spaced temporally. Therefore, to generate statistically significant data, a highly calibrated setup for velocity measurement (as shown in Figure 4) is needed in addition to a multitude of measurement repetitions. In this work, all the settling experiments are conducted at a constant room temperature,  $T = 20$  °C, unless otherwise stated. The experimental setup and velocity measurement procedures (DIP and PIS) are constantly calibrated by comparing the drag coefficient of spheres with different densities in an asymptotically unbounded Newtonian fluid at  $Re \leq 1$ . For this purpose, spherical particles with different characteristics (i.e., types, diameters, and densities) were used as summarized in Table 2. The solvent for the PS/TCP fluid (i.e., 70 wt.% low molecular weight polystyrene and 30 wt.% tricresyl phosphate) was also used as the test Newtonian fluid possessing  $\eta_s = 2.17$ . The terminal velocity,  $U$ , measured for a sphere settling under the action of gravity in this Newtonian fluid was measured using DIP and PIS methods, converted to the drag coefficient using Equation (5) and finally compared with  $C_D = 24/Re$ . For each particle, the velocity (and hence the drag coefficient) measurement is repeated five times. A sample result for this calibration process is shown in Figure 6b, where a good agreement between the experimental data and the universal drag coefficient is observed at a different Reynolds number ( $Re < 1$ ). The errorbars in Figure 6b account for the dispersion around the average value of the drag coefficient measured experimentally. The mean value of the relative standard deviation for all measurements, conducted at  $T = 20$  °C and repeated five times, was less than 0.10%. This small deviation is greatly attributed to the small temperature tolerance, and possibly the particle release mechanism.

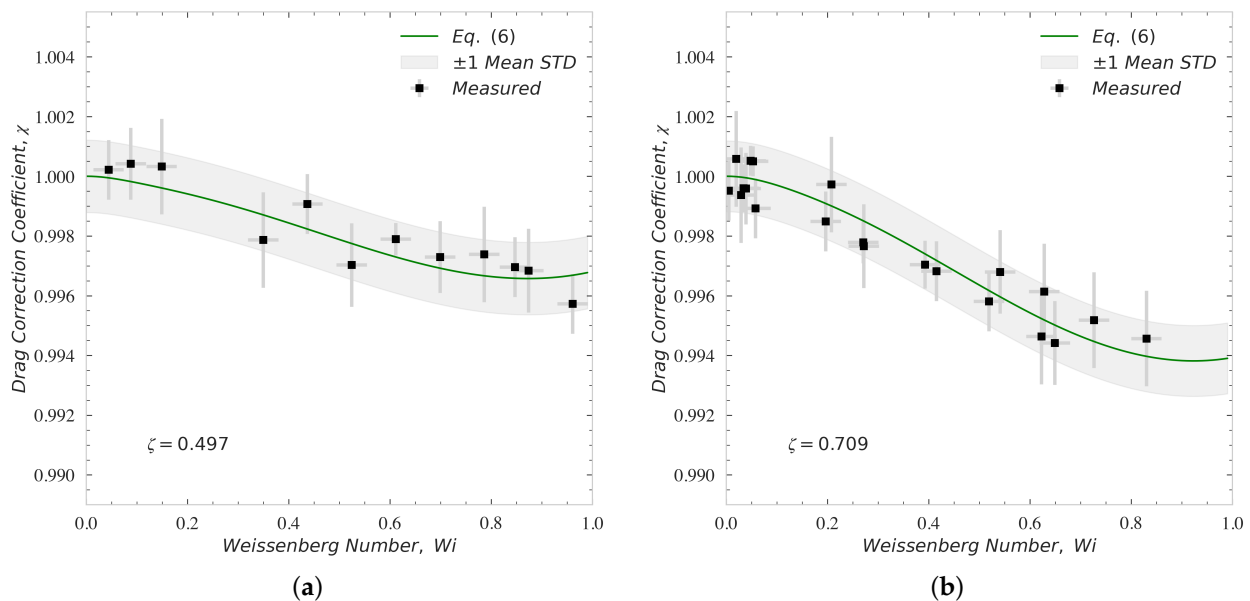
**Table 2.** Spherical particle characteristics used in settling measurements.

Material	Density (kg/m <sup>3</sup> )	Diameter (mm)	$\dot{\gamma}$ (1/s)	$Re$	$Wi$
Cellulose Acetate	1300	1.0–12.0	<4.0	<1.0	<1.0
White Polymer	1800	5.0–6.0	<13	<1.0	<2.5
Soda Lime Glass	2500	1.0–8.0	<45	<1.1	<8.5
Yttria Zirconia	6000	0.5–1.6	<29	<0.2	<5.2
Stainless Steel	7800	0.5–1.2	<30	<0.1	<5.5

In viscoelastic fluids, as discussed in Section 2, the drag coefficient not only changes with  $Re$ , but also varies as a function of the Weissenberg number and retardation ratio, i.e.,  $C_D = f(Re, Wi, \zeta)$ . The effect of  $Wi$  and  $\zeta$  on the drag coefficient of a spherical particle at  $Re < 1$  was experimentally studied using the calibrated experimental setup and measurement procedures. Here, to quantify the effect of Weissenberg number, spherical particles with different characteristics were used to achieve  $0 < Wi < 8.5$ . These particles were carefully selected to produce (i) a shear rate below than 50 (1/s) to stay in the constant-viscosity flow regime, and (ii) a Reynolds number below than unity ( $Re < 1$ ) for both



PAM/GLY and PS/TCP solutions. The characteristics of the particles, and the associated ranges of  $Wi$ ,  $Re$ , and  $\dot{\gamma}$  obtained for each family of particles, are reported in Table 2.

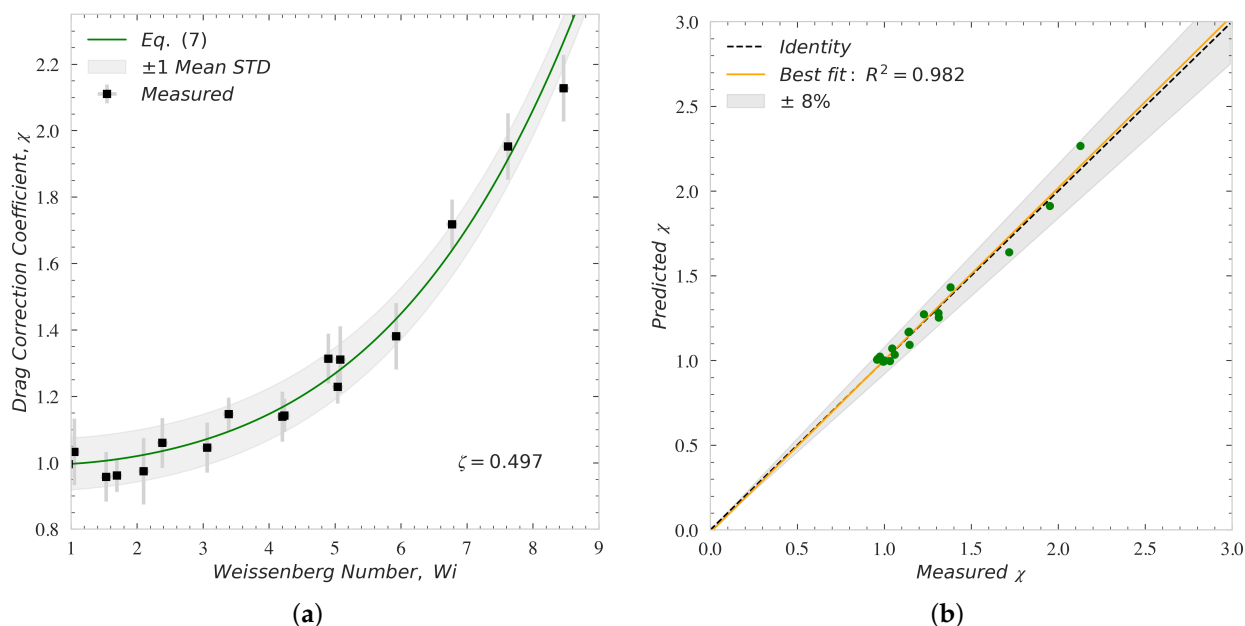


**Figure 7.** The comparison between measured and theoretical drag correction coefficient for particles settling through an asymptotically unbounded viscoelastic fluid at  $Re < 1$  and  $Wi < 1$ . Panel (a) shows the comparison for PS/TCP solution, and Panel (b) shows the comparison for PAM/GLY solution. The errorbars account for the dispersion around the average value of the drag coefficient and  $Wi$  measured experimentally (5 measurements were carried out for each  $Wi$  value to assure the repeatability). The shaded area highlights a region constructed using the theoretical values of  $\chi$  (Equation (6))  $\pm \sigma$ , where  $\sigma$  denotes the mean standard deviation for all measurements conducted for each solution.

Figure 7 shows the comparison between the measured and theoretical drag correction coefficient,  $\chi$ , for particles settling through an asymptotically unbounded fluid at low Reynolds numbers,  $Re < 1$ , and low Weissenberg number,  $Wi < 1$ . The theoretical drag correction coefficients are calculated from Equation (6). This comparison is shown for the PS/TCP solution with  $\zeta = 0.497$  in Figure 7a, and for the PAM/GLY solution with  $\zeta = 0.709$  in Figure 7b. As expected from the literature [1,2,33] and Equation (6), using a carefully measured relaxation times and other rheological properties, the calibrated velocity measurement procedures captured a slight reduction in drag coefficient for both values of  $\zeta$  at  $Wi < 1$  and  $Re < 1$ . In these measurements, again, each settling test is repeated five times assuring the statistical accuracy and repeatability of the acquired data. The vertical errorbars account for the dispersion around the average value of the drag coefficient correction measured experimentally at each  $Wi$ . The horizontal errorbars account for the dispersion around the average value of Weissenberg number attributed to the tolerance of sphere diameters and shear rate measurement. The shaded area highlights a region constructed using the theoretical values of  $\chi$  (Equation (6)) extended by  $\pm 1 \sigma$ , where  $\sigma$  denotes the mean standard deviation for all measurements conducted at  $Wi < 1$ . The mean value of the relative standard deviation is 0.11% for the PS/TCP solution and 0.12% for the PAM/GLY solution. Figure 7 shows that increasing the polymer viscosity, i.e., the retardation ratio, results in a more pronounced reduction of the drag coefficient at  $Wi < 1$ .

At higher Weissenberg numbers, no data was produced for the PAM/GLY solution due to its very low relaxation time and the limitation on the particle size satisfying  $\dot{\gamma} < 50$  (1/s) and  $Re < 1$ . However, for the PS/TCP solution that possess a high zero-shear viscosity and a large relaxation time, a broad range for  $Wi$  was achieved using the particles listed in Table 2 while satisfying all other kinematic constraints. Figure 8a shows the comparison

between the measured and theoretical drag correction coefficient,  $\chi$ , for particles settling through an asymptotically unbounded PS/TCP solution at  $Re < 1$  and  $Wi > 1$ . As expected from the literature [2,23] and Equation (7), the drag coefficient for a spherical particle increases, i.e.,  $\chi > 1$ . The experimental results follow Equation (7) very well at  $Re < 1$ . The vertical and horizontal errorbars account for the dispersion around the average value of the measured drag coefficient correction and  $Wi$ , respectively. The horizontal errorbars are smaller than the symbols and thus are masked in Figure 8a. The shaded area highlights a region constructed using the theoretical values of  $\chi$  (Equation (7)) extended by  $\pm 1\sigma$ , where  $\sigma$  denotes the mean standard deviation for all measurements conducted. The mean value of the relative standard deviation is 5.97% for all measurements conducted in the PS/TCP solution at  $Wi > 1$ . The mean value of the relative standard deviation in this case is one order of magnitude larger than its counterpart obtained for Newtonian and slightly elastic fluids ( $Wi < 1$ ). The increase in the relative standard deviation measured at high Weissenberg numbers might be attributed to (i) higher elasticity effects pushing the particle off the flow centerline where it starts to rotate, (ii) repetitive experiments causing large and continual disturbance of the polymer chains located on the flow centerline. Figure 8b illustrates the comparison between measured drag coefficient correction and predicted drag coefficient corrections calculated using Equations (6) and (7). The best fit to the data yields  $R^2 = 0.982$ . The shaded area highlights the bounds encompassing all the data by extending the identity line,  $x = y$ , by  $\pm 8\%$ .



**Figure 8.** Panel (a) shows the comparison between measured and calculated drag correction coefficient for particles settling through an asymptotically unbounded PS/TCP solution at  $Re < 1$  and  $Wi > 1$ . The errorbars account for the dispersion around the average value of the drag coefficient and  $Wi$  measured experimentally (5 measurements were carried out for each  $Wi$  value to assure the repeatability). The shaded area highlights the region where the theoretical values are extended by  $\pm\sigma$ . Here,  $\sigma$  denotes the mean standard deviation for the measurements. Panel (b) shows the comparison between measured drag coefficient correction and predicted drag coefficient corrections of particles calculated using Equations (6) and (7). The shaded area in panel (b) highlights the bounds encompassing all the data by extending the identity line,  $x = y$ , by  $\pm 8\%$ .

The experimental data plotted in Figures 7 and 8 are unique and were not reported previously in the literature. These data were captured using carefully designed elastic fluids and velocity measurement procedures. These datasets show the presence of an initial reduction (i.e., second order decrease in  $Wi \leq 1$ ), as well as a large enhancement (i.e.,

higher order increase in  $Wi > 1$ ) in the viscoelastic drag coefficient due to elasticity. These data also confirm that the approximate model, Equations (6) and (7), developed based on direct numerical simulation of Oldroyd-B fluids past a sphere, can confidently predict the effect of elasticity on the viscoelastic drag coefficient at  $0 < Wi < 8.5$ . This moderate range of Weissenberg number is typically experienced by particles in dilute polymeric fracturing fluids, with  $\lambda \approx O(100 \text{ ms})$ , flowing through the fracture networks with  $\dot{\gamma} \approx O(100 \text{ 1/s})$ ; see, for example, Malhotra and Sharma [71] and Hu et al. [72]. Therefore, this numerically-driven model can be used to rapidly compare the particle-carrying capacity of different polymeric fluids.

When polymeric solutions are strongly shear-thinning, the effect of elasticity on the drag coefficient reduction or enhancement can be masked [12,23]. Shear-thinning behavior leads to more complex and nonlinear dependencies at non-vanishing Weissenberg numbers. Very recently, Faroughi et al. [13] numerically studied the coupled effects of elasticity, shear-thinning, and inertia on the viscoelastic drag coefficient correction. When considering a strong shear-thinning behavior, they showed that increasing inertia (i.e.,  $Re$  number) and elasticity (increasing the  $Wi$  number) of the flow lead to a strong reduction in the viscoelastic drag coefficient correction. These effects not only mask the enhancement due to elasticity (e.g., the one observed in Figure 8 for a Boger fluid), but also decrease it sharply to a value lower than unity ( $\chi < 1$ ). The shear-thinning effects on the particle transport, however, have not been comprehensively quantified, and require further investigations.

## 5. Conclusions

In this work, we performed an experimental campaign using different polymer solutions and rheological techniques to validate a theoretical model introduced previously [2] to describe particle settling in viscoelastic liquids with negligible shear-thinning. With this aim, we employed two Boger fluid formulations with distinct longest relaxation time values, and spherical particles with different characteristics were used to quantify the effect of Weissenberg number (i.e., elasticity) on the drag coefficient in  $0 < Wi < 8.5$  at  $Re < 1$ . The drag coefficient decreases with  $Wi$  at a low level of elasticity ( $Wi < 1$ ), and increases with  $Wi$  at a high level of elasticity ( $Wi > 1$ ). The comparison between the measured and calculated drag coefficient data collectively yields  $R^2 = 0.982$ , endorsing the accuracy of the approximate model for the range studied here. Our experimental results also show a self-similarity in the evolution of the drag coefficient with elasticity in the inertia-less flow regime. Future work should focus on the combined effect of fluid shear-thinning, elasticity, and inertia on the particle settling behavior, a problem that is not still fully understood and quantified.

**Author Contributions:** S.A.F. designed the research, performed the settling experiments and analyzed the data. F.D.G. carried out the microfluidic measurements. S.A.F. and F.D.G. wrote the manuscript and approved the final submission. All authors have read and agreed to the published version of the manuscript.

**Funding:** F.D.G. acknowledges support from EPSRC New Investigator Award (grant ref. no. EP/S036490/1).

**Institutional Review Board Statement:** Not applicable.

**Informed Consent Statement:** Not applicable.

**Data Availability Statement:** Data can be found at <https://gilab.wp.txstate.edu/research/> (accessed on 4 February 2022).

**Conflicts of Interest:** The authors declare that they have no known competing financial interests or personal relationships that could have appeared to influence the work reported in this paper.

## References

- McKinley, G.H. Steady and transient motion of spherical particles in viscoelastic liquids. In *Transport Processes in Bubbles, Drops and Particles*; Chhabra, R., De Kee, D., Eds.; Taylor and Francis: Abingdon, UK, 2001; pp. 338–375.
- Faroughi, S.; Fernandes, C.; Nóbrega, J.M.; McKinley, G. A closure model for the drag coefficient of a sphere translating in a viscoelastic fluid. *J. Non-Newton. Fluid Mech.* **2020**, *277*, 104218. [[CrossRef](#)]
- Liff, S.M.; Kumar, N.; McKinley, G.H. High-performance elastomeric nanocomposites via solvent-exchange processing. *Nat. Mater.* **2007**, *6*, 76–83. [[CrossRef](#)] [[PubMed](#)]
- Tang, D.; Marchesini, F.H.; Cardon, L.; D'hooge, D.R. State of the-Art for Extrudate Swell of Molten Polymers: From Fundamental Understanding at Molecular Scale toward Optimal Die Design at Final Product Scale. *Macromol. Mater. Eng.* **2020**, *305*, 2000340. [[CrossRef](#)]
- Olsen, T.; Helal, A.; McKinley, G.H.; Kamrin, K. Coupled dynamics of flow, microstructure, and conductivity in sheared suspensions. *Soft Matter* **2016**, *12*, 7688–7697. [[CrossRef](#)]
- Tao, C.; Kutchko, B.G.; Rosenbaum, E.; Wu, W.T.; Massoudi, M. Steady flow of a cement slurry. *Energies* **2019**, *12*, 2604. [[CrossRef](#)]
- Lim, E.J.; Ober, T.J.; Edd, J.F.; Desai, S.P.; Neal, D.; Bong, K.W.; Doyle, P.S.; McKinley, G.H.; Toner, M. Inertio-elastic focusing of bioparticles in microchannels at high throughput. *Nat. Commun.* **2014**, *5*, 1–9. [[CrossRef](#)]
- Barbati, A.C.; Desroches, J.; Robisson, A.; McKinley, G.H. Complex fluids and hydraulic fracturing. *Annu. Rev. Chem. Biomol. Eng.* **2016**, *7*, 415–453. [[CrossRef](#)]
- Almubarak, T.; Ng, J.H.; Sokhanvarian, K.; Khaldi, M.; Nasr-El-Din, H.A. Development of a Mixed Polymer Hydraulic Fracturing Fluid for High Temperature Applications. In Proceedings of the Unconventional Resources Technology Conference, Houston, TX, USA, 23–25 July 2018; pp. 4145–4162.
- Yang, B.; Zhao, J.; Mao, J.; Tan, H.; Zhang, Y.; Song, Z. Review of Friction Reducers used in Slickwater Fracturing Fluids for Shale Gas Reservoirs. *J. Nat. Gas Sci. Eng.* **2018**, *62*, 302–313. [[CrossRef](#)]
- Blyton, C.A.; Gala, D.P.; Sharma, M.M. A comprehensive study of proppant transport in a hydraulic fracture. In Proceedings of the SPE Annual Technical Conference and Exhibition, Houston, TX, USA, 28–30 September 2015.
- Fernandes, C.; Faroughi, S.; Carneiro, O.; Nóbrega, J.M.; McKinley, G. Fully-resolved simulations of particle-laden viscoelastic fluids using an immersed boundary method. *J. Non-Newton. Fluid Mech.* **2019**, *266*, 80–94. [[CrossRef](#)]
- Faroughi, S.A.; Roriz, A.I.; Fernandes, C. A Meta-Model to Predict the Drag Coefficient of a Particle Translating in Viscoelastic Fluids: A Machine Learning Approach. *Polymers* **2022**, *14*, 430. [[CrossRef](#)]
- Tang, D.; Marchesini, F.H.; Cardon, L.; D'hooge, D.R. Three-dimensional flow simulations for polymer extrudate swell out of slit dies from low to high aspect ratios. *Phys. Fluids* **2019**, *31*, 093103. [[CrossRef](#)]
- Spanjaards, M.; Jaensson, N.O.; Hulsen, M.A.; Anderson, P.D. A numerical study of particle migration and sedimentation in viscoelastic couette flow. *Fluids* **2019**, *4*, 25. [[CrossRef](#)]
- Wang, P.; Yu, Z.; Lin, J. Numerical simulations of particle migration in rectangular channel flow of Giesekus viscoelastic fluids. *J. Non-Newton. Fluid Mech.* **2018**, *262*, 142–148. [[CrossRef](#)]
- Gomaa, A.; Gupta, D.; Carman, P. Viscoelastic behavior and proppant transport properties of a new high-temperature viscoelastic surfactant-based fracturing fluid. In Proceedings of the SPE International Symposium on Oilfield Chemistry, Houston, TX, USA, 28–30 September 2015.
- Yu, Z.; Wang, P.; Lin, J.; Hu, H.H. Equilibrium positions of the elasto-inertial particle migration in rectangular channel flow of Oldroyd-B viscoelastic fluids. *J. Fluid Mech.* **2019**, *868*, 316–340. [[CrossRef](#)]
- Liang, F.; Sayed, M.; Al-Muntasheri, G.A.; Chang, F.F.; Li, L. A comprehensive review on proppant technologies. *Petroleum* **2016**, *2*, 26–39. [[CrossRef](#)]
- Faroughi, S.A.; Pruvot, A.J.C.J.; McAndrew, J. The rheological behavior of energized fluids and foams with application to hydraulic fracturing. *J. Pet. Sci. Eng.* **2018**, *163*, 243–263. [[CrossRef](#)]
- Al-Muntasheri, G.A. A critical review of hydraulic-fracturing fluids for moderate-to ultralow-permeability formations over the last decade. *SPE Prod. Oper.* **2014**, *29*, 243–260. [[CrossRef](#)]
- Rubinstein, M.; Colby, R.H. *Polymer Physics*; Oxford University Press: New York, NY, USA, 2003; Volume 23.
- Arnipally, S.K.; Kuru, E. Settling velocity of particles in viscoelastic fluids: a comparison of the shear-viscosity and elasticity effects. *SPE J.* **2018**, *23*, 1689–1705. [[CrossRef](#)]
- Clasen, C.; Plog, J.; Kulicke, W.M.; Owens, M.; Macosko, C.; Scriven, L.; Verani, M.; McKinley, G.H. How dilute are dilute solutions in extensional flows? *J. Rheol.* **2006**, *50*, 849–881. [[CrossRef](#)]
- Elgaddafi, R.; Ahmed, R.; Growcock, F. Settling behavior of particles in fiber-containing Herschel Bulkley fluid. *Powder Technol.* **2016**, *301*, 782–793. [[CrossRef](#)]
- Geri, M.B.; Imqam, A.; Bogdan, A.; Shen, L. Investigate The Rheological Behavior of High Viscosity Friction Reducer Fracture Fluid and Its Impact on Proppant Static Settling Velocity. In Proceedings of the SPE Oklahoma City Oil and Gas Symposium, Oklahoma City, OK, USA, 9–10 April 2019.
- Gomaa, A.; Gupta, D.; Carman, P. Viscoelastic behavior and proppant transport properties of a new associative polymer-based fracturing fluid. In Proceedings of the SPE International Symposium and Exhibition on Formation Damage Control, Lafayette, LA, USA, 26–28 February 2014.

28. Gomaa, A.M.; Gupta, D.; Carman, P.S. Proppant transport? viscosity is not all it's cracked up to be. In Proceedings of the SPE Hydraulic Fracturing Technology Conference, The Woodlands, TX, USA, 3–5 February 2015.
29. Acharya, A.R. Particle transport in viscous and viscoelastic fracturing fluids. *SPE Prod. Eng.* **1986**, *1*, 104–110. [[CrossRef](#)]
30. Van den Brule, B.; Gheissary, G. Effects of fluid elasticity on the static and dynamic settling of a spherical particle. *J. Non-Newton. Fluid Mech.* **1993**, *49*, 123–132. [[CrossRef](#)]
31. Gheissary, G.; Van den Brule, B. Unexpected phenomena observed in particle settling in non-Newtonian media. *J. Non-Newton. Fluid Mech.* **1996**, *67*, 1–18. [[CrossRef](#)]
32. Chilcott, M.; Rallison, J.M. Creeping flow of dilute polymer solutions past cylinders and spheres. *J. Non-Newton. Fluid Mech.* **1988**, *29*, 381–432. [[CrossRef](#)]
33. Chhabra, R.P. *Bubbles, Drops, and Particles in Non-Newtonian Fluids*; CRC Press: Boca Raton, FL, USA, 2006.
34. James, D.F. Boger fluids. *Annu. Rev. Fluid Mech.* **2009**, *41*, 129–142. [[CrossRef](#)]
35. Faroughi, S.A.; Huber, C. A generalized equation for rheology of emulsions and suspensions of deformable particles subjected to simple shear at low Reynolds number. *Rheol. Acta* **2015**, *54*, 85–108. [[CrossRef](#)]
36. Faroughi, S.A.; Huber, C. A self-similar behavior for the relative viscosity of concentrated suspensions of rigid spheroids. *Rheol. Acta* **2017**, *56*, 35–49. [[CrossRef](#)]
37. Oldroyd, J.G. On the formulation of rheological equations of state. *Proc. R. Soc. Lond. A* **1950**, *200*, 523–541. [[CrossRef](#)]
38. Del Giudice, F.; Sathish, S.; D'Avino, G.; Shen, A.Q. "From the edge to the center": Viscoelastic migration of particles and cells in a strongly shear-thinning liquid flowing in a microchannel. *Anal. Chem.* **2017**, *89*, 13146–13159. [[CrossRef](#)]
39. Denn, M.M. Issues in viscoelastic fluid mechanics. *Annu. Rev. Fluid Mech.* **1990**, *22*, 13–32. [[CrossRef](#)]
40. Macosko, C.W.; Larson, R.G. *Rheology: Principles, Measurements, and Applications*; VCH Publishers Inc.: New York, NY, USA, 1994.
41. Joseph, D.D. *Fluid Dynamics of Viscoelastic Liquids*; Springer Science & Business Media: Berlin/Heidelberg, Germany, 2013.
42. Cherizol, R.; Sain, M.; Tjong, J. Review of Non-Newtonian Mathematical Models for Rheological Characteristics of Viscoelastic Composites. *Green Sustain. Chem.* **2015**, *5*, 6. [[CrossRef](#)]
43. Kelbaliyev, G. Drag coefficients of variously shaped solid particles, drops, and bubbles. *Theor. Found. Chem. Eng.* **2011**, *45*, 248–266. [[CrossRef](#)]
44. Tanner, R.I. *Engineering Rheology*; OUP Oxford: Oxford, UK, 2000.
45. Pipe, C.J.; Majmudar, T.S.; McKinley, G.H. High shear rate viscometry. *Rheol. Acta* **2008**, *47*, 621–642. [[CrossRef](#)]
46. Malkin, A.Y.; Isayev, A.I. *Rheology: Concepts, Methods, and Applications*; Elsevier: Amsterdam, The Netherlands, 2017.
47. Gupta, S.; Wang, W.S.; Vanapalli, S.A. Microfluidic viscometers for shear rheology of complex fluids and biofluids. *Biomicrofluidics* **2016**, *10*, 043402. [[CrossRef](#)]
48. Del Giudice, F. A Review of Microfluidic Devices for Rheological Characterisation. *Micromachines* **2022**, *13*, 167. [[CrossRef](#)]
49. Kulicke, W.M.; Clasen, C. *Viscosimetry of Polymers and Polyelectrolytes*; Springer Science & Business Media: Berlin/Heidelberg, Germany, 2004.
50. Del Giudice, F.; Haward, S.J.; Shen, A.Q. Relaxation Time of Dilute Polymer Solutions: A Microfluidic Approach. *J. Rheol.* **2017**, *61*, 327–337. [[CrossRef](#)]
51. Adam, M.; Delsanti, M. Viscosity and longest relaxation time of semi-dilute polymer solutions. I. Good solvent. *J. Phys.* **1983**, *44*, 1185–1193. [[CrossRef](#)]
52. Zilz, J.; Schäfer, C.; Wagner, C.; Poole, R.J.; Alves, M.A.; Lindner, A. Serpentine channels: Micro-rheometers for fluid relaxation times. *Lab Chip* **2014**, *14*, 351–358. [[CrossRef](#)] [[PubMed](#)]
53. Haward, S. Microfluidic extensional rheometry using stagnation point flow. *Biomicrofluidics* **2016**, *10*, 043401. [[CrossRef](#)] [[PubMed](#)]
54. Del Giudice, F.; D'vino, G.; Greco, F.; De Santo, I.; Netti, P.A.; Maffettone, P.L. Rheometry-on-a-chip: Measuring the relaxation time of a viscoelastic liquid through particle migration in microchannel flows. *Lab Chip* **2015**, *15*, 783–792. [[CrossRef](#)] [[PubMed](#)]
55. Dinic, J.; Zhang, Y.; Jimenez, L.N.; Sharma, V. Extensional relaxation times of dilute, aqueous polymer solutions. *ACS Macro Lett.* **2015**, *4*, 804–808. [[CrossRef](#)]
56. Solomon, M.; Muller, S. Flow past a sphere in polystyrene-based Boger fluids: The effect on the drag coefficient of finite extensibility, solvent quality and polymer molecular weight. *J. Non-Newton. Fluid Mech.* **1996**, *62*, 81–94. [[CrossRef](#)]
57. Solomon, M.; Muller, S. Study of mixed solvent quality in a polystyrene–dioctyl phthalate–polystyrene system. *J. Polym. Sci. Part B Polym. Phys.* **1996**, *34*, 181–192. [[CrossRef](#)]
58. Morrison, F.A. *Understanding Rheology*; Oxford University Press: New York, NY, USA, 2001; Volume 1.
59. Shaw, M.T. *Introduction to Polymer Rheology*; John Wiley & Sons: Hoboken, NJ, USA, 2012.
60. Morozov, A.; Spagnolie, S.E. Introduction to complex fluids. In *Complex Fluids in Biological Systems*; Springer: Berlin/Heidelberg, Germany, 2015; pp. 3–52.
61. Phan-Thien, N.; Mai-Duy, N. *Understanding Viscoelasticity: An Introduction to Rheology*; Springer: Berlin/Heidelberg, Germany, 2013.
62. Kim, D.; Son, Y.; Park, J. Prediction of settling velocity of nonspherical soil particles using digital image processing. *Adv. Civ. Eng.* **2018**, *2018*, 4647675. [[CrossRef](#)]
63. Arigo, M.; Rajagopalan, D.; Shapley, N.; McKinley, G.H. The sedimentation of a sphere through an elastic fluid. Part 1. Steady motion. *J. Non-Newton. Fluid Mech.* **1995**, *60*, 225–257. [[CrossRef](#)]

64. Crocker, J.C.; Grier, D.G. Methods of digital video microscopy for colloidal studies. *J. Colloid Interface Sci.* **1996**, *179*, 298–310. [[CrossRef](#)]
65. Graessley, W.W. Polymer chain dimensions and the dependence of viscoelastic properties on concentration, molecular weight and solvent power. *Polymer* **1980**, *21*, 258–262. [[CrossRef](#)]
66. Chun, M.S.; Ko, M.J. Rheological correlations of relaxation time for finite concentrated semiflexible polyelectrolytes in solvents. *J. Korean Phys. Soc.* **2012**, *61*, 1108–1113. [[CrossRef](#)]
67. Krishnan, J.M.; Deshpande, A.P.; Kumar, P.S. *Rheology of Complex Fluids*; Springer: Berlin/Heidelberg, Germany, 2010.
68. Zell, A.; Gier, S.; Rafai, S.; Wagner, C. Is there a relation between the relaxation time measured in CaBER experiments and the first normal stress coefficient? *J. Non-Newton. Fluid Mech.* **2010**, *165*, 1265–1274. [[CrossRef](#)]
69. Jensen, E.A.; Christiansen, J.D. Measurements of first and second normal stress differences in a polymer melt. *J. Non-Newton. Fluid Mech.* **2008**, *148*, 41–46. [[CrossRef](#)]
70. Saengow, C.; Giacomin, A.J. Normal stress differences from Oldroyd 8-constant framework: Exact analytical solution for large-amplitude oscillatory shear flow. *Phys. Fluids* **2017**, *29*, 121601. [[CrossRef](#)]
71. Malhotra, S.; Sharma, M.M. Settling of spherical particles in unbounded and confined surfactant-based shear thinning viscoelastic fluids: An experimental study. *Chem. Eng. Sci.* **2012**, *84*, 646–655. [[CrossRef](#)]
72. Hu, Y.T.; Chung, H.; Jason, M. What is more important for proppant transport, viscosity or elasticity? In Proceedings of the SPE Hydraulic Fracturing Technology Conference, The Woodlands, TX, USA, 3–5 February 2015.



## Article

# Viscoelastic Property of an LDPE Melt in Triangular- and Trapezoidal-Loop Shear Experiment

Shuxin Huang <sup>1,2</sup>

<sup>1</sup> Department of Engineering Mechanics, Shanghai Jiao Tong University, Shanghai 200240, China; huangshuxin@sjtu.edu.cn

<sup>2</sup> Key Laboratory of Hydrodynamics of the Ministry of Education, Shanghai Jiao Tong University, Shanghai 200240, China

**Abstract:** The time-dependent viscoelastic behaviors of a low-density polyethylene melt (LDPE) in a triangular- and trapezoidal-loop shear experiment reported previously are described here by an integral-type Rivlin–Sawyers (RS) constitutive equation. The linear viscoelasticity of the melt was obtained through a dynamic frequency sweep experiment at a small strain and fitted by a relaxation spectrum. The nonlinear viscoelasticity was characterized by viscosity. All the experimental viscoelastic behaviors of the melt can be divided into two types in terms of the predictions of the RS model: (1) predictable time-dependent viscoelastic behaviors at low shear rates or during short-term shear, and (2) unpredictable shear weakening behavior occurring at the high shear rate of  $3\text{--}5\text{ s}^{-1}$  during long-term shear with the characteristic time interval of about  $40\text{--}100\text{ s}$ . The influence of experimental error caused possibly by inhomogeneous samples on the viscoelasticity of the melt was analyzed, and the large relative error in the experiment is about  $10\text{--}30\%$ .

**Keywords:** LDPE; triangular-loop shear; trapezoidal-loop shear; time-dependent viscoelastic property; Rivlin–Sawyers equation

**Citation:** Huang, S. Viscoelastic Property of an LDPE Melt in Triangular- and Trapezoidal-Loop Shear Experiment. *Polymers* **2021**, *13*, 3997. <https://doi.org/10.3390/polym13223997>

Academic Editor: Célio Bruno Pinto Fernandes

Received: 15 October 2021

Accepted: 8 November 2021

Published: 19 November 2021

**Publisher's Note:** MDPI stays neutral with regard to jurisdictional claims in published maps and institutional affiliations.



**Copyright:** © 2021 by the author. Licensee MDPI, Basel, Switzerland. This article is an open access article distributed under the terms and conditions of the Creative Commons Attribution (CC BY) license (<https://creativecommons.org/licenses/by/4.0/>).

## 1. Introduction

There are many flow phenomena in the plastic and rubber industry [1], e.g., profile extrusion, film casting, and molding, and the shear viscosity of polymer melts is a fundamental parameter governing these flows since shear viscosity is related to the flow loss or pressure drop in flows. Shear viscosity includes steady and time-dependent for polymer melt, and both are the manifestation of the viscoelastic property of melt. This study aims to extensively understand the transient shear viscoelastic property of a polymer melt, although other viscoelasticity, such as extensional, is also of importance in practice.

The shear viscoelastic properties of variety of commercial or industry-grade polymer melts have been published, e.g., low-density polyethylene (LDPE) [2–8], linear low-density polyethylene (LLDPE) [9,10], high-density polyethylene (HDPE) [4,5,10–12], polypropylene (PP) [13–15], polystyrene (PS) [4,16], and polyamide 6 (PA6) [17]. Five types of shear viscoelastic properties are usually included in these publications, which are: (1) linear viscoelastic property, i.e., frequency sweep at small strain, (2) steady shear viscosity, (3) steady first normal stress difference ( $N_1$ ), (4) shear stress growth in step rate experiment, and (5)  $N_1$  growth in step rate experiment. Sometimes, the second steady normal stress difference of polymer melt is reported [7,10], but far less than others because of the difficulty in experimental technique. The published works above—and other similar and unlisted studies not discussed here—raise the understanding of the viscoelastic properties of industrial polymer melts. The applications of the reported experimental viscoelastic properties of polymer melt that are seen in publications are mainly based on two aspects. One aspect is to examine the theoretical model of viscoelastic property of polymer melt [3,5–11,13,15–22], and the other is to simulate the flow in polymer processing numerically according to the published viscoelastic experimental data [23–28].



Constitutive equations are useful in the numerical simulation of polymer processing since constitutive equations provide the stress used in the momentum equation. The accuracy of the theoretical simulation depends on the constitutive equation [25,26]. A large number of constitutive equations have been proposed, and 13 were listed in a recent review [28] on the use of constitutive equations in extrusion cast film processing, in which most are typical and often used in both polymer processing and viscoelastic characterization of the polymer melt, and some can be seen in the references above [3,7–11,13,15,17,19–21]. The choice of the constitutive equation in applications depends on the researcher because the researcher usually uses the model that can be used. Due to three factors, i.e., the deficiencies of constitutive equations, the complicated viscoelastic property of polymer melts, and various complex flows in polymer processing, we must modify, remedy, or research the equations in studies [5,6,9,19]. A valid, simple, and accurate constitutive equation is preferred in theoretical simulation in the polymer processing industry.

In 2004, the authors of [29] reported three shear triangular-loop experiments and shear stress growth in a step rate experiment of an LDPE melt at 150 °C, and a modified Huang model [30] was employed to characterize the time-dependent viscoelasticity of the melt. In the following theoretical works [31–34], some constitutive equations were adopted, modified, or proposed to describe this group of experimental data and to evaluate the capability of these equations. An evident phenomenon is that some equations [31,33] are unable to provide a reasonable explanation for the decreasing stress at a high shear rate during long-term shear. In order to know more about the phenomenon of the LDPE melt, another 16 groups of loop experiments [35] were conducted using both triangular- and trapezoidal-loop shear modes, and five types of flow behaviors were specified according to the forms of the stress–shear rate curves in triangular-loop experiments. Type I flow is a strong shear strengthening behavior and the maximum stress occurs in the ramping-down region of shear rate; Type II is a weak shear strengthening behavior—the maximum stress appears at the maximum shear rate and the stress in the ramping-down region is higher than that in the up region; Type III is that the stress in the down region is almost superposed upon that in the up region at the beginning of ramping-down region; Type IV is that the stress-down curve is lower than the stress-up, and two curves have a cross point, where the shear rate is usually higher than  $1 \text{ s}^{-1}$  for the melt; Type V is an apparent shear-weakening behavior, not only the stress-down curve is lower than the stress-up, but the shear rate of the cross point is usually lower than  $1 \text{ s}^{-1}$ .

The difference between the step rate experiment and the triangular- or trapezoidal-loop experiment is in the number of variables. Step rate only has a time variable, and loop has two variables of time and shear rate. Therefore, the flow in a loop is slightly complicated. The advantage of the loop experiment is that the unsteady onset in the step rate experiment can be reduced or controlled by the ramping-up process of the shear rate. Greener and Connelly [36] (1986) reported three typical stress–shear rate curves in triangular-loop experiments for a polyacrylamide solution, which did not contain Type I and V flows in [35]. In earlier experimental work of [29], both Type II and III flows were not included. Therefore, the experimental viscoelastic data in [35] can be used to further examine the capability of the constitutive equation, and then promote the understanding of the various time-dependent viscoelastic behaviors of the melt.

The remainder of the paper is organized as follows. Section 2 provides the theoretical analysis of the loop experiment by the Rivlin–Sawyers model [37,38] and the characterization of the viscoelastic properties of the LDPE melt at 150 °C. Section 3 presents the predicted transient viscoelasticities of the melt and the discussions on the shear weakening behavior. Section 4 presents the conclusions of the study.

## 2. Materials and Methods

### 2.1. LDPE

The industry-grade LDPE resin (PE-FSB-23D022/Q200, SINOPEC Shanghai Petrochemical Company Ltd., Shanghai, China) was used in the experiment. The basic char-

acteristics of the plastic are given in Table 1. The mass-average molar mass  $M_w$ , the number-average molar mass  $M_n$ , and  $M_w/M_n$  were determined by gel permeation chromatography (GPC).

**Table 1.** Basic characteristics of the sample.

Material	MFI (g/10 min, 190 °C)	Density (g/cm <sup>3</sup> )	$M_w$ (g/mol)	$M_n$ (g/mol)	$M_w/M_n$
LDPE-Q200	2	0.922	94,003	9719	9.672

## 2.2. Setup

The Advance Rheometric Expansion System (ARES, Rheometric Scientific Inc., New Castle, IN, USA) with stainless-steel parallel plates was used to measure the viscoelastic property of the LDPE melt at 150 °C. The diameter of the plate is 25 mm, and the gap size between the parallel plates is about 1.84 mm. The present experimental data only includes the dynamic sweep at small and large strain, and most of the experimental results, i.e., triangular- and trapezoidal-loop data, have been published in [35].

## 2.3. Rivlin–Sawyers (RS) Model

The RS model [37,38] is a type of integral model, and a factorized RS model [38] is simplified here and written as:

$$\sigma = \int_{-\infty}^t m(t-t') \cdot \phi_1(I_1, I_2) \cdot [\delta - C_t^{-1}(t')] dt', \quad (1)$$

where  $\sigma$  is the extra stress tensor at the present time  $t$ ,  $m(t-t')$  is the time-dependent memory function,  $t'$  is the past time,  $\phi_1(I_1, I_2)$  is a strain-dependent function,  $I_1$  and  $I_2$  are the first invariants of  $C_t^{-1}$  and  $C_t$ , respectively,  $C_t$  is the Cauchy strain tensor,  $C_t^{-1}$  is the Finger strain tensor, and  $\delta$  is the unit tensor. The memory function is given as:

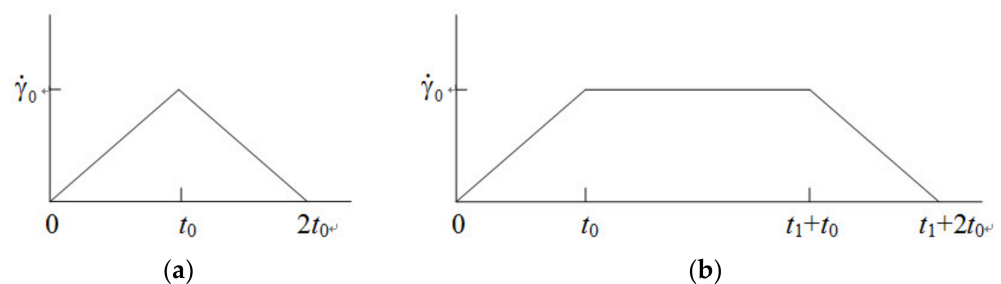
$$m = \sum_i \frac{g_i}{\lambda_i} \cdot e^{-\frac{t-t'}{\lambda_i}}, \quad (2)$$

where  $\lambda_i$  and  $g_i$  are the relaxation times and the relaxation modulus coefficients, respectively. The  $\phi_1$ -function is an exponential model, which is written as follows in shear flow [39]:

$$\phi_1(I_1, I_2) = e^{-k\gamma}, \quad (3)$$

where  $k$  is a parameter and  $\gamma$  is shear strain. The parameter  $k$  is obtained by fitting to the experiment in shear flow [31].

The schematic diagrams of loop experiments are shown in Figure 1, where  $\dot{\gamma}_0$  is the imposed maximum shear rate,  $t_0$  is a characteristic time interval of the loop in the ramping-up or -down region of shear rate, and  $t_1$  is a time interval with the constant maximum shear rate. The theoretical analysis of the triangular-loop experiment based on the RS model is given in [31], and therefore, the equations of trapezoidal-loop are presented here.



**Figure 1.** Schematic diagrams of loop experiments, (a) triangular-loop, and (b) trapezoidal-loop.

### 2.4. Shear Strain and Stress in Trapezoidal-Loop

The shear rate in the trapezoidal-loop experiment is,

$$\dot{\gamma} = a_0 t, \quad \text{for} \quad 0 \leq t \leq t_0, \quad (4a)$$

$$\dot{\gamma} = \dot{\gamma}_0, \quad \text{for} \quad t_0 \leq t \leq t_1 + t_0, \quad (4b)$$

$$\dot{\gamma} = a_0(t_1 + 2t_0 - t), \quad \text{for} \quad t_1 + t_0 \leq t \leq t_1 + 2t_0, \quad (4c)$$

where  $a_0 = \dot{\gamma}_0/t_0$ , is the change rate of shear rate in the ramping-up or -down region.

In the ramping-up region ( $0 \leq t \leq t_0$ ), the strain history of the trapezoidal loop is,

$$\gamma(t, t') = \frac{1}{2} a_0 (s^2 - 2ts), \quad \text{for} \quad t - t' \leq t, \quad (5a)$$

$$\gamma(t, t') = -\frac{1}{2} a_0 t^2, \quad \text{for} \quad t - t' > t, \quad (5b)$$

where  $s = t - t'$ , is the elapsed time. Equation (5) is the same as that of the triangular loop in [31]. In the steady shear region with the maximum shear rate ( $t_0 \leq t \leq t_1 + t_0$ ), the shear strain history is,

$$\gamma(t, t') = -s \dot{\gamma}_0, \quad \text{for} \quad t - t' \leq t - t_0, \quad (6a)$$

$$\gamma(t, t') = \frac{1}{2} a_0 (t_0^2 - 2t_0 t + t^2 - 2ts + s^2), \quad \text{for} \quad t - t_0 < t - t' \leq t, \quad (6b)$$

$$\gamma(t, t') = \frac{1}{2} a_0 (t_0^2 - 2t t_0), \quad \text{for} \quad t - t' > t, \quad (6c)$$

In the down region ( $t_1 + t_0 \leq t \leq t_1 + 2t_0$ ), the strain history is

$$\gamma(t, t') = \frac{1}{2} a_0 s (2t - 4t_0 - s - 2t_1), \quad \text{for} \quad t - t' \leq t - t_1 - t_0, \quad (7a)$$

$$\gamma(t, t') = \frac{1}{2} a_0 (t_0^2 + t_1^2 + t^2 + 2t_0 t_1 - 2t_1 t - 2t_0 t - 2t_0 s), \quad \text{for} \quad t - t_1 - t_0 \leq t - t' < t - t_0, \quad (7b)$$

$$\gamma(t, t') = \frac{1}{2} a_0 (2t_0^2 + t_1^2 + 2t^2 + s^2 + 2t_0 t_1 - 2t_1 t - 4t_0 t - 2ts), \quad \text{for} \quad t - t_0 \leq t - t' \leq t, \quad (7c)$$

$$\gamma(t, t') = \frac{1}{2} a_0 (2t_0^2 + t_1^2 + t^2 + 2t_0 t_1 - 2t_1 t - 4t_0 t), \quad \text{for} \quad t - t' > t. \quad (7d)$$

The shear stress in the trapezoidal loop can be calculated using the RS model in terms of the flow history above, which is written as

$$\tau = \frac{1}{2} a_0 \sum_i \frac{g_i}{\lambda_i} \int_0^t e^{-\frac{s}{\lambda_i}} \cdot e^{-\frac{1}{2} k a_0 (2ts - s^2)} \cdot (2ts - s^2) ds + \frac{1}{2} a_0 t^2 \cdot e^{-\frac{1}{2} k a_0 t^2} \cdot \sum_i g_i e^{-\frac{t}{\lambda_i}}, \quad \text{for} \quad 0 \leq t \leq t_0, \quad (8a)$$

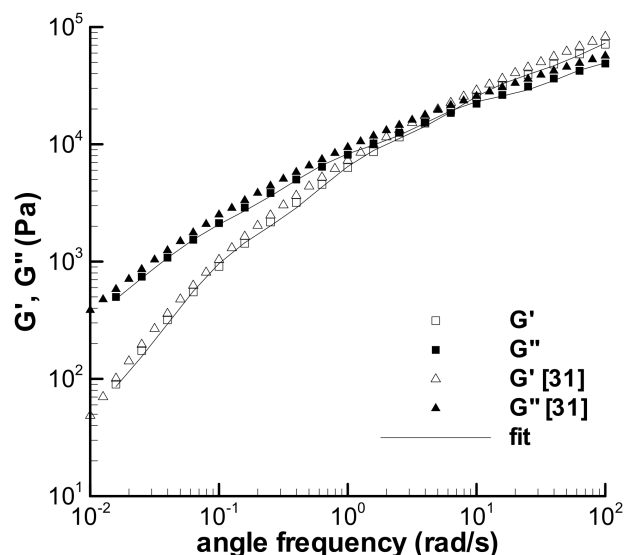
$$\tau = \sum_i \frac{g_i}{\lambda_i} \int_0^{t-t_0} e^{-\frac{s}{\lambda_i}} \cdot e^{-k \cdot s \dot{\gamma}_0} \cdot s \dot{\gamma}_0 ds + \frac{1}{2} a_0 \sum_i \frac{g_i}{\lambda_i} \int_{t-t_0}^t e^{-\frac{s}{\lambda_i}} \cdot e^{-k \cdot \frac{1}{2} a_0 (-t_0^2 + 2t_0 t - t^2 + 2ts - s^2)} \cdot (-t_0^2 + 2t_0 t - t^2 + 2ts - s^2) ds + \frac{1}{2} a_0 (-t_0^2 + 2t t_0) \cdot e^{-k \cdot \frac{1}{2} a_0 (-t_0^2 + 2t t_0)} \cdot \sum_i g_i e^{-\frac{t}{\lambda_i}}, \quad \text{for} \quad t_0 \leq t \leq t_1 + t_0, \quad (8b)$$

$$\tau = \frac{1}{2} a_0 \sum_i \frac{g_i}{\lambda_i} \int_0^{t-t_0} e^{-\frac{s}{\lambda_i}} \cdot e^{-k \cdot \frac{1}{2} a_0 (-2t + 4t_0 + s + 2t_1)} \cdot s (-2t + 4t_0 + s + 2t_1) ds + \frac{1}{2} a_0 \sum_i \frac{g_i}{\lambda_i} \int_{t-t_0}^t e^{-\frac{s}{\lambda_i}} \cdot e^{-k \cdot \frac{1}{2} a_0 (-t_0^2 - t_1^2 - t^2 - 2t_0 t_1 + 2t_1 t + 2t_0 t + 2t_0 s)} \cdot (-t_0^2 - t_1^2 - t^2 - 2t_0 t_1 + 2t_1 t + 2t_0 t + 2t_0 s) ds + \frac{1}{2} a_0 \sum_i \frac{g_i}{\lambda_i} \int_{t-t_0}^t e^{-\frac{s}{\lambda_i}} \cdot e^{-k \cdot \frac{1}{2} a_0 (-2t_0^2 - t_1^2 - 2t^2 - s^2 - 2t_0 t_1 + 2t_1 t + 4t_0 t + 2ts)} \cdot (-2t_0^2 - t_1^2 - 2t^2 - s^2 - 2t_0 t_1 + 2t_1 t + 4t_0 t + 2ts) ds + \frac{1}{2} a_0 (-2t_0^2 - t_1^2 - t^2 - 2t_0 t_1 + 2t_1 t + 4t_0 t) \cdot e^{-k \cdot \frac{1}{2} a_0 (-2t_0^2 - t_1^2 - t^2 - 2t_0 t_1 + 2t_1 t + 4t_0 t)} \cdot \sum_i g_i e^{-\frac{t}{\lambda_i}} \quad \text{for} \quad t_1 + t_0 \leq t \leq t_1 + 2t_0. \quad (8c)$$

Equation (8a) is also the same as that of the triangular loop in [31]. Equations (8a)–(8c) can be deduced further to obtain an analytical solution. However, it is more convenient to solve Equation (8) numerically, i.e., using the Legendre–Gauss integration method. Therefore, the numerical method was adopted here.

### 2.5. Viscoelastic Characterization of the LDPE Melt

As mentioned above in Section 1, a small amount of the time-dependent viscoelasticity of the LDPE melt at 150 °C has been studied in earlier works [29,31]. The difference between the experimental data in [29,31] and those in [35] should be caused by samples, and two batches of the sample sheets molded are used in two experiments. For example, Figure 2 shows the present storage modulus ( $G'$ ) and loss modulus ( $G''$ ) obtained in the dynamic frequency sweep experiment at the small strain of 0.05, accompanied by the reported  $G'$  and  $G''$  of the melt [31], and the deviation between two groups of the experimental data could be caused by the samples. Moreover, the experimental data obtained by the samples—cut from one sheet or from one batch of the sheets—also contain errors, which can be seen in the following analysis, making it difficult to analyze the time-dependent viscoelastic behaviors of the LDPE melt.



**Figure 2.** Dynamic frequency sweep experiments of the LDPE (Q200) melt at 150 °C ( $\gamma = 5\%$ ) and its characterization.

The characterization of the viscoelastic property of the LDPE melt includes two parts. One is to obtain the relaxation spectrum  $\lambda_i$  and  $g_i$  in Equation (2) by fitting the frequency sweep data of the melt in Figure 2, and the other is to obtain the parameter  $k$  in Equation (3) by fitting the viscosities in Figure 3.

The calculated  $G'$  and  $G''$  in Figure 2 describe the present linear viscoelastic property of the melt, which can be used to analyze the loop experiments in [35] because the sample of the  $G'$  and  $G''$  experiment is derived from the same batch of samples used in the loop experiments. The relaxation spectrum fitted is listed in Table 2, together with the previous spectrum [31], and both spectra are different.

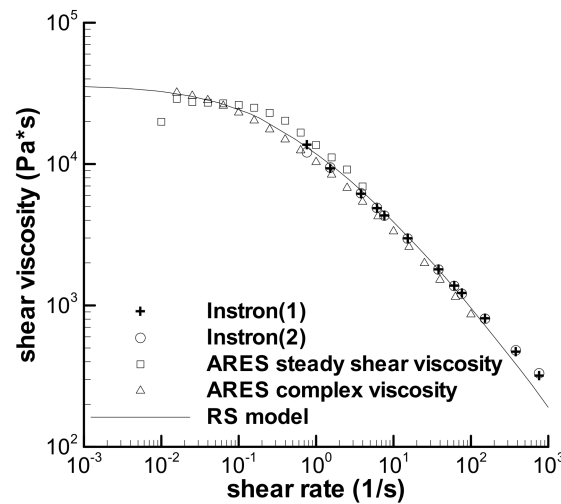


Figure 3. Shear viscosities of the LDPE (Q200) melt at 150 °C and fitting by the RS model.

Table 2. Relaxation spectra of the LDPE(Q200) melt at 150 °C.

i	$\lambda_i$ (s)	Present Work	Ref. [31]
		$g_i$ (Pa)	$g_i$ (Pa)
1	$10^{-4}$	$2.236 \times 10^5$	$1.420 \times 10^6$
2	$10^{-3}$	$1.177 \times 10^5$	0
3	$10^{-2}$	$6.524 \times 10^4$	$7.941 \times 10^4$
4	$10^{-1}$	$2.862 \times 10^4$	$3.288 \times 10^4$
5	$10^0$	$9.025 \times 10^3$	$1.051 \times 10^4$
6	$10^1$	$1.620 \times 10^3$	$1.991 \times 10^3$
7	$10^2$	$6.000 \times 10^1$	$3.000 \times 10^1$
8	$10^3$	$1.000 \times 10^0$	$1.000 \times 10^0$

Due to the change of linear viscoelasticity, the magnitude of complex viscosity ( $\eta^*$ ) obtained here is different from that reported [31], which is shown in Figure 3 and denoted by “ARES complex viscosity”. Four groups of the experimental viscosity curves are included in Figure 3, where “Instron(1)”, “Instron(2)”, and “ARES steady shear viscosity” are three groups of the viscosity curves cited from [31], and “ARES complex viscosity” is a set of new data. Thus, the parameter  $k$  was fitted to the experimental viscosities in Figure 3 and the value of  $k$  obtained is 0.192. The previous  $k$  is 0.235 [31]. It is worth noting that many shear-viscosity measurement experiments, not less than 40 groups, have been conducted at different times by an INSTRON-4467 capillary rheometer using a die with the length-to-diameter ratio of 40, and these viscosity curves agree quite well with each other. Therefore, three groups of the viscosity curves reported previously [31] were still used in the present work. The shear-thinning viscosity of the LDPE melt can be described by the RS model, except for some deviation at a shear rate higher than  $200 \text{ s}^{-1}$ .

The influence of experimental errors caused by sample deviation or other unknown factors is usually mixed with the effect of experimental conditions, such as  $\dot{\gamma}_0$ , and it is difficult to observe the experimental errors directly among the experimental results. We can discern an error now by assuming a homogeneous effect of the error on an experiment, e.g., a minute defect in a sample could lower the experimental data conducted with the sample, and then, a changing spectrum approach can be adopted here to understand the influence of the error. The homogeneity hypothesis can be seen from the approximate parallel characteristic between the present and the previous  $G'$  and  $G''$  data [31] in Figure 2, thus, the changing spectrum approach can be obtained by modifying the relaxation modulus

coefficient with a constant parameter, which can shift the present  $G'$  and  $G''$  approximately to the previous curves. The changing spectrum approach is written as,

$$\lambda'_i = \lambda_i, g'_i = f \cdot g_i \quad (9)$$

where  $f$  is the constant.  $\lambda_i$  and  $g_i$  in Equation (2) will be replaced with  $\lambda'_i$  and  $g'_i$  as  $f$  is used. The homogeneous parameter  $f$  is obtained by fit.

The possible experimental error above is regarded as a sample error in the present work. The deviation between the loop experiments in [35] and those in [29] could be attributed to different batches of the sample sheets, and the deviation only between the loop experiments in [35] could be caused by the inhomogeneous samples—though the samples were cut from a batch of the sheets. The present characterization of the viscoelastic property of the LDPE melt will be used primarily to analyze the experimental errors of the samples in [35] since the same sample batch was adopted in two experiments. The changing spectrum approach employed is similar to that in [40–42], and the  $f$ -parameter in [40–42] is a variable.

### 3. Results and Discussion

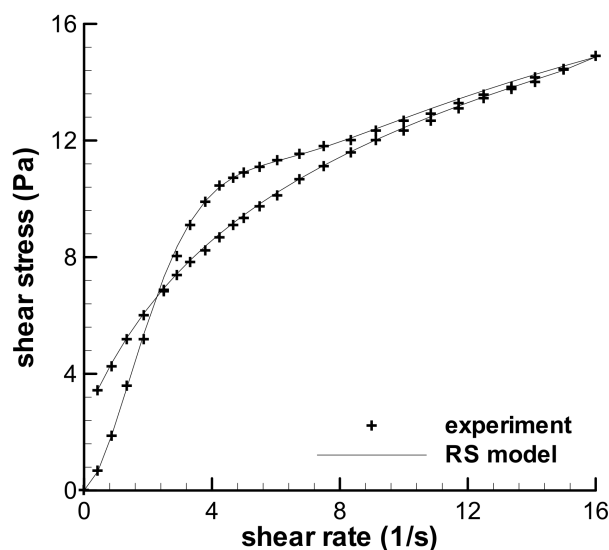
#### 3.1. Validation of the RS Model

In the previous work on the predictions of three triangular-loop experiments [31], Type I flow can be predicted well, however, both Type IV and V cannot. The deviation between the calculation and experiment on Type IV flow is slight. One of the typical results of triangular-loop experiments given by Greener and Connolly [36] in 1986 is also a Type IV flow, which was employed here to testify the validation of the theoretical equation of triangular loop. The maximum shear rate of the Type IV flow—according to Greener and Connolly [36]—is  $16 \text{ s}^{-1}$  and the time interval  $t_0$  is 10 s. The relaxation spectrum of the polyacrylamide solution given by Greener and Connolly is reproduced in Table 3, and the value of the  $k$ -parameter in the RS model is 0.25, which was obtained by fitting the stress growth tests [36].

**Table 3.** Relaxation spectrum of the polyacrylamide solution given by Greener and Connolly [36].

$i$	$\lambda_i$ (s)	$g_i$ (Pa)
1	0.0001	25.4
2	0.001	84.5
3	0.01	7.9
4	0.032	7.552
5	0.1	4.8
6	0.32	3.68
7	1	2.06
8	3.2	1.0752
9	10	0.41
10	32	0.1376
11	100	0.0076

Figure 4 shows the calculated result and the experimental data of the triangular loop experiment of the polyacrylamide solution, and the calculation agrees well with the experiment. This indicates that Type IV flow can be predicted by the RS model and the theoretical analysis on the loop experiment is reliable.



**Figure 4.** The prediction of the triangular-loop experiment with the maximum shear rate of  $16 \text{ s}^{-1}$  and the  $t_0$  of 10 s, and the experimental data given by Greener and Connelly [36].

### 3.2. Predictions of the Triangular-Loops

#### 3.2.1. Short-Term Shear with $t_0 = 0.1 \text{ s}$

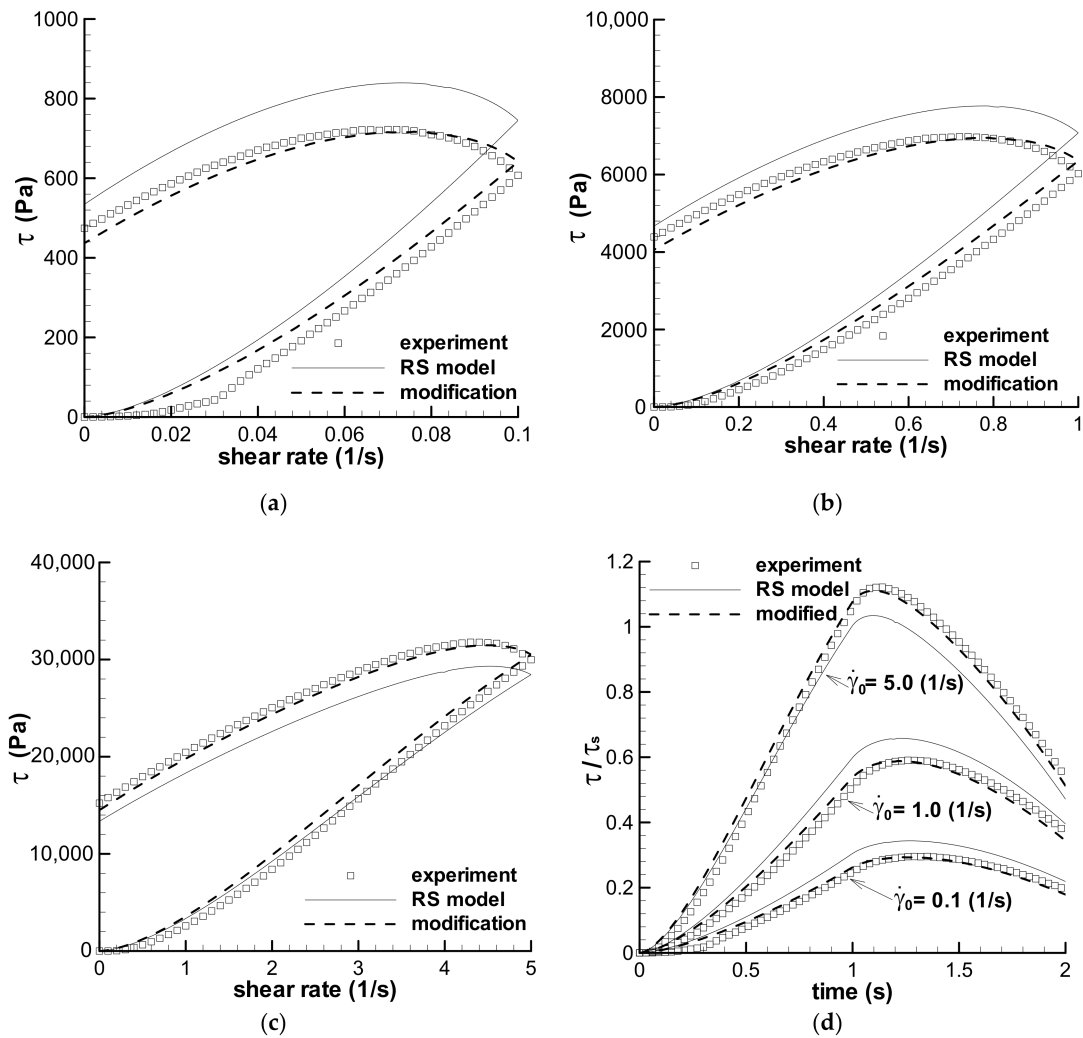
Figure 5 shows the predictions of the triangular-loop experiments with the same  $t_0$  of 1.0 s for the LDPE(Q200) melt at  $150 \text{ }^\circ\text{C}$ , in which Figure 5a–c shows the stress–shear rate curves, and Figure 5d shows the stress–time curves obtained with three maximum shear rates— $0.1 \text{ s}^{-1}$ ,  $1 \text{ s}^{-1}$ , and  $5 \text{ s}^{-1}$ . Evident deviations exist between the calculations of the RS model and the experiments in Figure 5, however, we can still observe three similarities from the calculations and experiments. The first is that both the calculated and the experimental forms of three triangular loops are similar; the second is that three groups of calculations and the corresponding experiments have similar shear–strain strengthening phenomenon, i.e., the maximum stress occurs at a lower shear rate in the ramping-down region, and not at the maximum shear rate; the third is that the ratios of the maximum shear stress ( $\tau_{\text{max}}$ ) over the stress at the maximum shear rate ( $\tau_{t_0}$ ) in three triangular loops with  $t_0 = 1 \text{ s}$  show a similar decreasing trend with increasing shear rate for both the calculated and the experimental data, which are shown in Figure 6.

As stated in Section 2.5, deviations between the calculations and experiments in Figure 5 are regarded as resulting from inhomogeneous samples. Thus, the changing spectrum approach was employed to study the influence of sample deviation, and the calculations with parameter  $f$  are also shown in Figure 5. We can see that the effect of  $f$  is significant. The homogeneity hypothesis of the errors should be true, and the changing spectrum method is available to reduce the errors between experiments. The fitted values of  $f$  are given in Table 4.

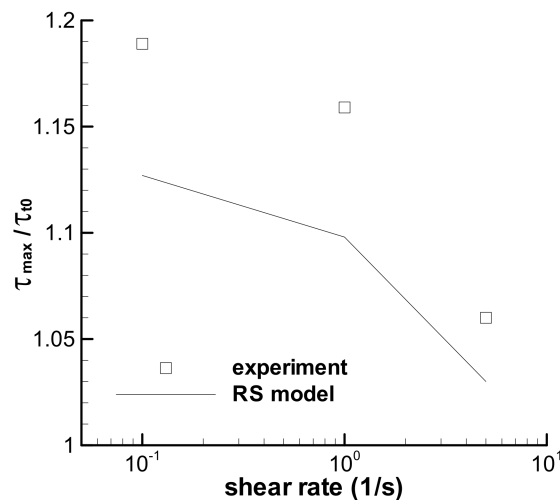
**Table 4.** Parameter  $f$  used in Equation (9) for discerning the obvious experimental errors.

Experiments	$f$
Triangular loop ( $\dot{\gamma}_0 = 0.1 \text{ s}^{-1}$ , $t_0 = 1 \text{ s}$ ) [35]	0.758
Triangular loop ( $\dot{\gamma}_0 = 1 \text{ s}^{-1}$ , $t_0 = 1 \text{ s}$ ) [35]	0.819
Triangular loop ( $\dot{\gamma}_0 = 5 \text{ s}^{-1}$ , $t_0 = 1 \text{ s}$ ) [35]	1.145
Triangular loop ( $\dot{\gamma}_0 = 1 \text{ s}^{-1}$ , $t_0 = 10 \text{ s}$ ) [35]	1.114
Triangular loop ( $\dot{\gamma}_0 = 0.1 \text{ s}^{-1}$ , $t_0 = 100 \text{ s}$ ) [35]	1.102
Trapezoidal loop ( $\dot{\gamma}_0 = 0.1 \text{ s}^{-1}$ , $t_0 = 1 \text{ s}$ , $t_1 = 200 \text{ s}$ ) [35]	0.875
Trapezoidal loop ( $\dot{\gamma}_0 = 0.1 \text{ s}^{-1}$ , $t_0 = 100 \text{ s}$ , $t_1 = 200 \text{ s}$ ) [35]	0.899
Frequency sweep in SAOS [31] <sup>1</sup>	1.314

<sup>1</sup> SAOS denotes small amplitude oscillation shear.



**Figure 5.** Predictions of the triangular-loop experiments with the same characteristic time  $t_0$  of 1.0 s. The stress–shear rate curves with the maximum shear rates of  $0.1 \text{ s}^{-1}$  (a),  $1 \text{ s}^{-1}$  (b), and  $5 \text{ s}^{-1}$  (c) are given. (d) Shows the stress–time curves. Symbols are experiments, solid lines are the calculations by the RS model, and dashed lines are the calculations by the modified spectrum with  $f$  in Table 4.  $\tau_s$  is the steady shear stress calculated by the RS model at the maximum shear rate.



**Figure 6.** Ratios of the maximum shear stress over the stress at  $t_0 = 1 \text{ s}$  for three triangular loops with  $t_0 = 1 \text{ s}$ . Symbol is the experimental data [35], and line is the calculation.



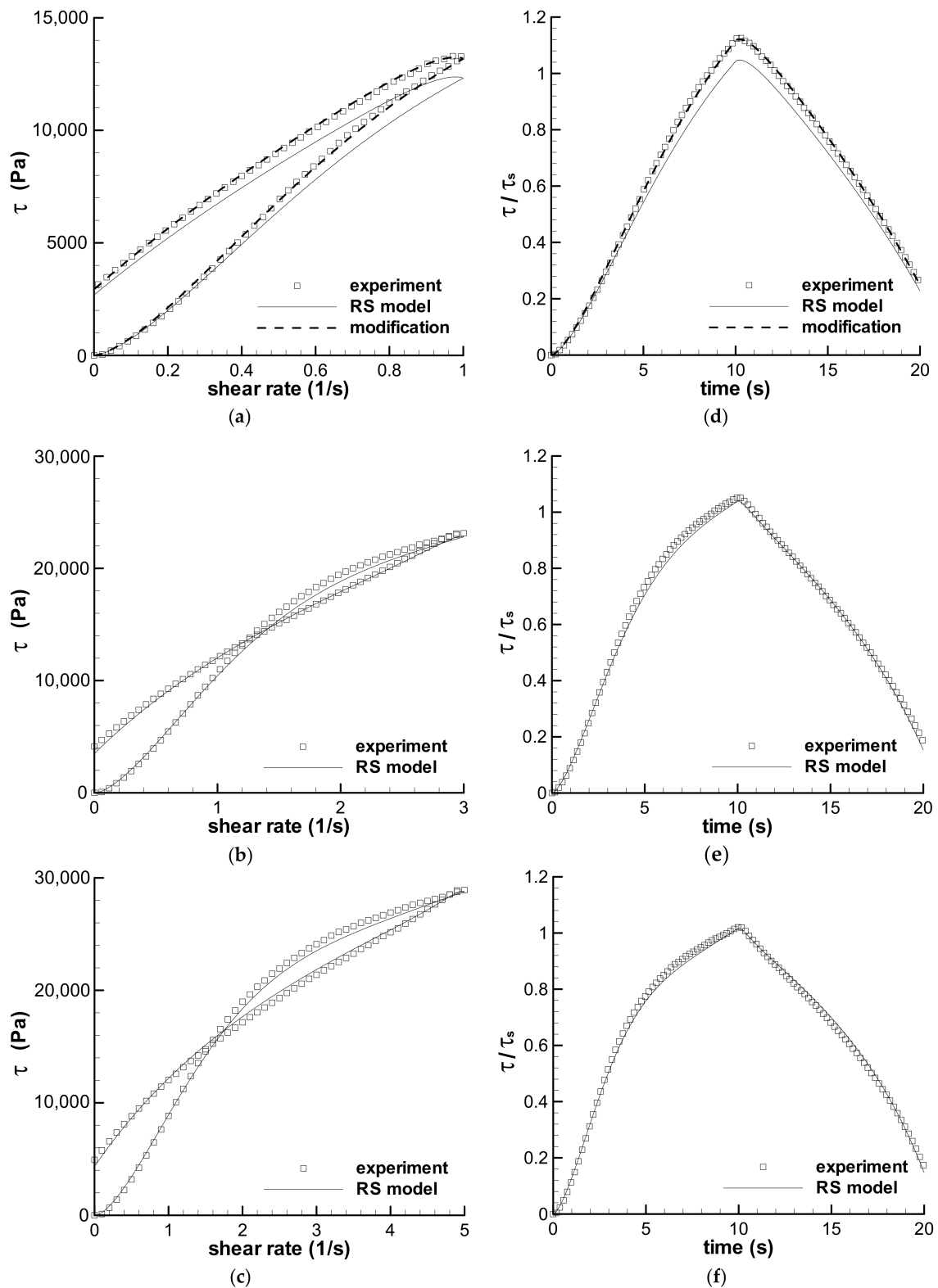
According to the stress–shear rate curves in Figure 5, we can see the qualitative contributions of both shear strain and shear rate on the viscoelastic stress. The stress still increases as the shear rate decreases at the beginning of the ramping-down region of shear rate, and the maximum shear stress is not at the maximum shear rate, which indicates the obvious contribution of shear strain on the stress due to the increase in strain. As the shear rate decreases further, the stress decreases with the decreasing shear rate, although shear strain is still increasing. This shows the effect of the shear rate. At the end of the loop, the shear rate is zero and the strain effect is shown again due to the existence of residual stress. Therefore, the LDPE melt is a viscoelastic material because the stress in the triangular loop is controlled simultaneously by both shear strain and shear rate.

Stress growth at a low shear rate in Figure 5 is known here as shear strain strengthening behavior, which is Type I flow and denoted by  $\tau_{\max}/\tau_{t_0}$  in Figure 6. All three triangular loops show shear strain strengthening behavior under short-term shear, although the maximum shear rate changes from low to high values, and the RS model can describe the phenomenon by excluding the possible experimental errors. Figure 6 also shows that the shear strain strengthening at a low shear rate is more obvious than that at a high shear rate, which can be related to the relative growth of strain, i.e., the ratio of the strain at the maximum stress over the strain at  $t_0$ . The ratios of strain growth at the maximum shear rates of 0.1, 1.0, and 5.0 s<sup>−1</sup> are 1.51, 1.47, and 1.24, respectively, for three triangular loop experiments, and 1.47, 1.39, and 1.19, respectively, for the calculations of the RS model. Both the ratios of strain growth are the decreasing functions of shear rate. The larger the ratio of strain growth is, the higher the shear strain strengthening during short-term shear.

The normalized maximum stresses at the low maximum shear rates, e.g., 0.1 s<sup>−1</sup> and 1.0 s<sup>−1</sup>, are much lower than 1.0 in Figure 5d, because the shear flows, at low shear rates, do not approach the steady status during short-term shear. This phenomenon can be used to explain the low viscosity at the shear rate of 0.01 s<sup>−1</sup> in Figure 3, which was obtained by steady shear mode in the ARES rheometer. The low viscosity at 0.01 s<sup>−1</sup> in Figure 3 could contain error caused by short-term shear.

### 3.2.2. Medium-Term Shear with $t_0 = 10$ s

The predictions of the triangular loop experiments with the same  $t_0$  of 10 s are shown in Figure 7, where both the stress–rate curves and the stress–time curves are given simultaneously. Figure 7a shows Type II flow, and Figure 7b,c shows Type IV flow. Two calculations with the maximum shear rates of 3 s<sup>−1</sup> and 5 s<sup>−1</sup> are in good agreement with the experimental results, but that with the maximum shear rate of 1 s<sup>−1</sup> indicates some deviation with the experiment. The influence of inhomogeneous samples could be the reason for the deviation, and therefore, the  $f$ -parameter was employed to modify the calculation, which shows perfect agreement with the experiment in Figure 7a,d. The fitted  $f$  for the experiment is listed in Table 4. The time-dependent viscoelastic behaviors of the LDPE melt in the triangular-loop experiments with medium loop time  $t_0$  can be illustrated by the RS model. Moreover, the stress–time curves in Figure 7d–f indicates that the stress at the maximum shear rate has been up to the steady shear status during the ramping-up process of 10 s.



**Figure 7.** Predictions of the triangular-loop experiments with the same characteristic time  $t_0$  of 10 s. The stress–shear rate curves with the maximum shear rates of  $1 \text{ s}^{-1}$  (a),  $3 \text{ s}^{-1}$  (b), and  $5 \text{ s}^{-1}$  (c) are given. The stress–time curves with maximum shear rates of  $1 \text{ s}^{-1}$  (d),  $3 \text{ s}^{-1}$  (e), and  $5 \text{ s}^{-1}$  (f) are also shown. Symbols are experiments, solid lines are the calculations by the RS model, and dashed lines in (a,d) are the calculations by the modified spectrum with  $f$  in Table 4.  $\tau_s$  is the steady shear stress calculated by the RS model at the maximum shear rate.

### 3.2.3. Long-Term Shear with $t_0 = 40$ s and 100 s

The triangular loop experiments with the longest loop-time  $t_0$  of 100 s were predicted by the RS model and are shown in Figure 8. The obvious shear strain strengthening, i.e., the maximum shear stress occurs at a low shear rate, disappears in all the experiments and calculations, however, slight strain strengthening in the ramping-down region of shear rate also appears in the experiment with a maximum shear rate of  $0.1 \text{ s}^{-1}$  in Figure 8a. The original prediction of the RS model with the spectrum in Table 2 shows deviation from the experiment with a maximum shear rate of  $0.1 \text{ s}^{-1}$  in Figure 8a, but the modification with parameter  $f$  shows excellent agreement with the experiment. The  $f$ -parameter is also listed in Table 4. Figure 8a shows Type II flow, Figure 8b shows Type III flow, and Figure 8c,d show Type V flow. Thus, the predictions in Figure 8 can be divided into two groups. One group is that the calculations of the RS model agree with the experiments with the maximum shear rates of  $0.1 \text{ s}^{-1}$  and  $1.0 \text{ s}^{-1}$ , i.e., Type II and III flows. The other group is that the calculated stress–shear rate curves do not agree with the experiments with the maximum shear rates of  $3 \text{ s}^{-1}$  and  $5 \text{ s}^{-1}$ , i.e., Type V flows in Figure 8c,d.

**Table 5.** Relaxation spectrum of the LDPE melt obtained after long-term dynamic shear sweep (300 s) at large strain (300%) at  $150 \text{ }^\circ\text{C}$ .

$i$	$\lambda_i$ (s)	$g_i$ (Pa)
1	$10^{-4}$	$2.207 \times 10^5$
2	$5 \times 10^{-3}$	$5.173 \times 10^4$
3	$5 \times 10^{-2}$	$1.409 \times 10^4$
4	$10^{-1}$	$6.016 \times 10^3$
5	$10^0$	$5.802 \times 10^3$
6	$1.3 \times 10^1$	$8.030 \times 10^2$
7	$10^2$	$4.700 \times 10^1$
8	$10^3$	$3.000 \times 10^0$

The calculations by the RS model in Figure 8c,d are in good agreement with the experiments at a shear rate lower than about  $2 \text{ s}^{-1}$  in the ramping-up region of shear rate, and at the following shear rate, the prediction is always larger than the experiment except that at the end of the loop. A feature of the calculated stress–shear rate curves in Figure 8c,d is that the calculated stress curves in the ramping-up region almost overlap those calculated in the ramping-down region at a shear rate higher than that of the cross point of two calculated stress curves. However, the experimental stress curves in Figure 8c,d form an obvious loop at the shear rate higher than that of the cross point of two experimental stress curves, and the experimental stress curves in the ramping-down region are always lower than those in the ramping-up region at the shear rate higher than the cross point. The obvious loop phenomenon in the experiment, in the present paper, is known as shear weakening behavior. A similar loop phenomenon can also be observed in another triangular loop experiment with the maximum shear rate of  $5 \text{ s}^{-1}$  and a time interval  $t_0$  of 40 s (as shown in Figure 9). The shear weakening behavior cannot be seen in the three stress–shear rate curves of the triangular-loop experiments of Greener and Connolly [36]. Moreover, the RS model cannot describe the shear weakening behavior, i.e., Type V flow, which is influenced by both high shear rate and long-term shear.

Five types of the viscoelastic behaviors specified in the triangular-loop experiments of the LDPE melt [35] can be divided into two types in terms of the calculations by the RS model. One type shows the time-dependent viscoelastic behavior that can be described by the RS model, although some errors appear in the experimental work. Original Type I–IV behaviors [35] belong to the predictable type. The other shows shear-weakening viscoelastic property, i.e., Type V flow, which cannot be described by the RS model.

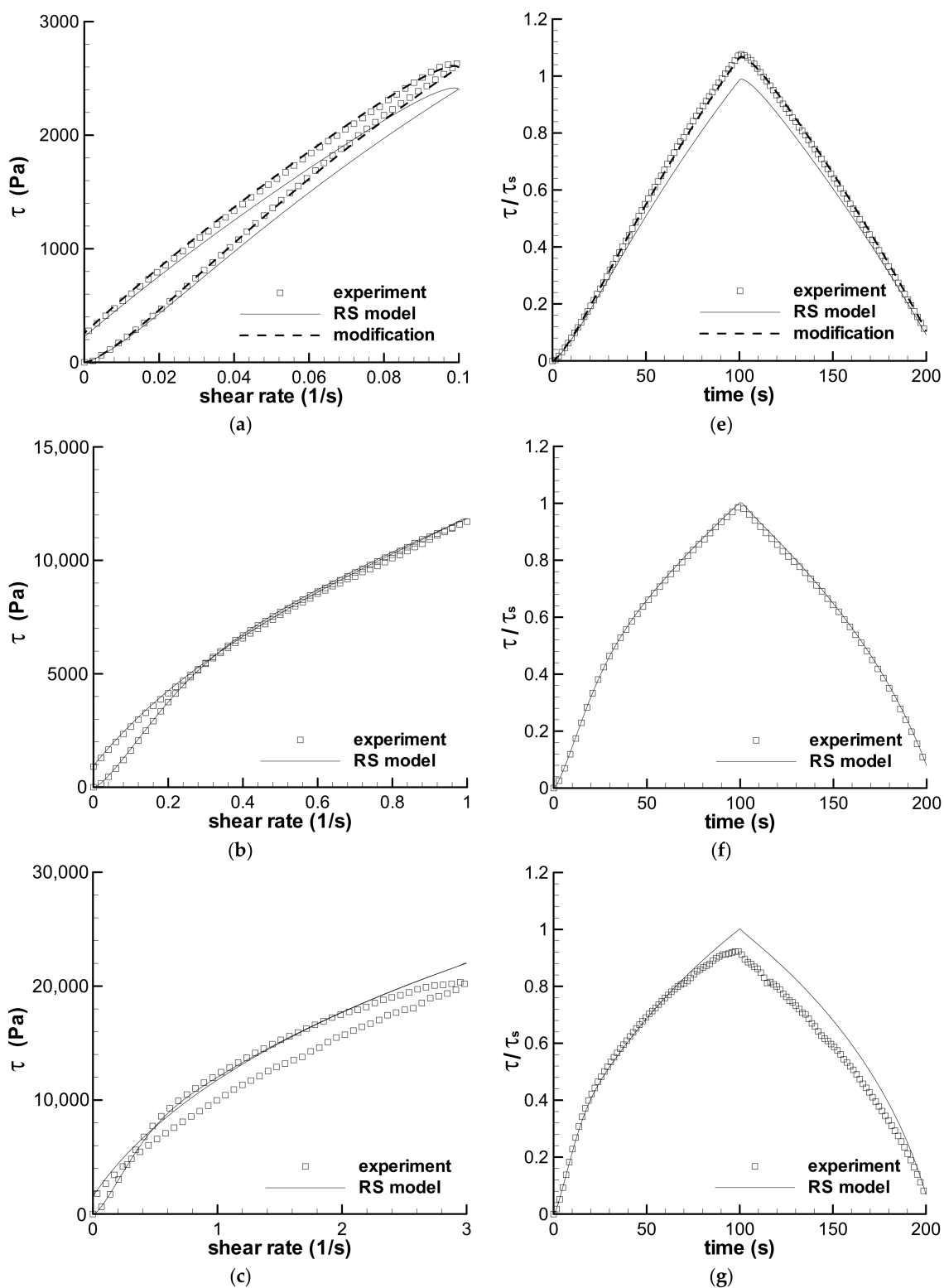
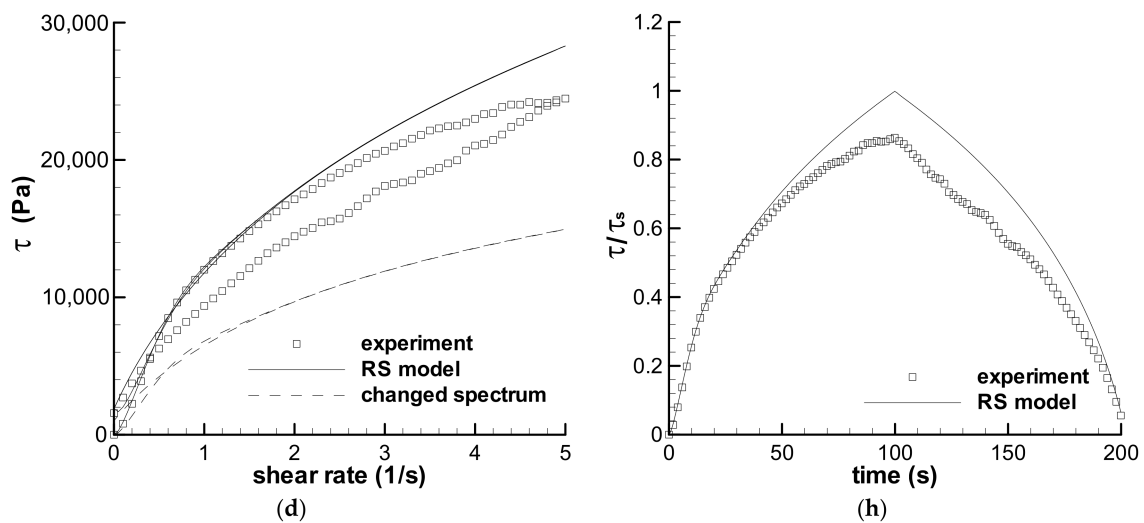
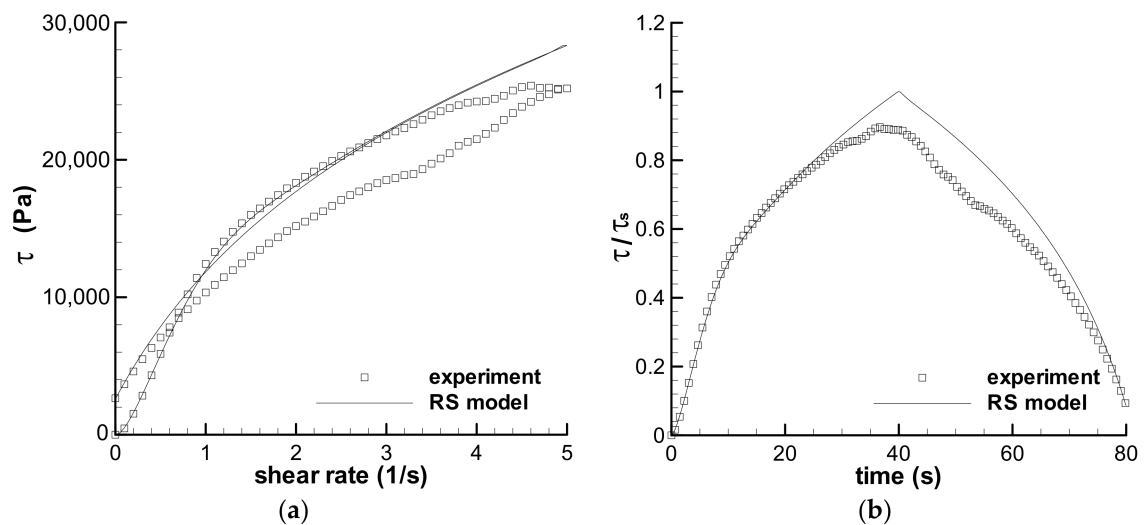


Figure 8. Cont.



**Figure 8.** Predictions of the triangular-loop experiments with the same characteristic time  $t_0$  of 100 s. The stress–shear rate curves with maximum shear rates of 0.1 s<sup>-1</sup> (a), 1 s<sup>-1</sup> (b), 3 s<sup>-1</sup> (c), and 5 s<sup>-1</sup> (d) are given. The stress–time curves with the maximum shear rates of 0.1 s<sup>-1</sup> (e), 1 s<sup>-1</sup> (f), 3 s<sup>-1</sup> (g), and 5 s<sup>-1</sup> (h) are also shown. Symbols are experiments, solid lines are the calculations by the RS model, bold dashed lines in (a,e) are the calculations by the modified spectrum with  $f$  in Table 4, dashed line in (d) is calculated using a changed spectrum in Table 5, and  $\tau_s$  is the steady shear stress calculated by the RS model at the maximum shear rate.



**Figure 9.** Prediction of the triangular-loop experiment with the characteristic time  $t_0$  of 40 s. The stress–shear rate curve with maximum shear rates of 5 s<sup>-1</sup> is given in (a), and the corresponding stress–time curve is in (b). Symbol is experiment, line is the calculation by the RS model, and  $\tau_s$  is the steady shear stress calculated by the RS model at the maximum shear rate.

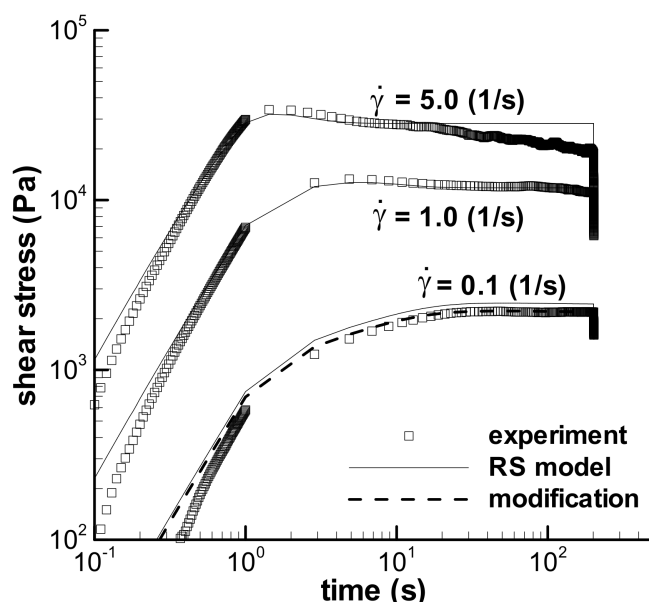
It is unclear whether the shear weakening viscoelastic property is an intrinsic viscoelastic property of the melt, however, it is worth affirming that part of the viscoelastic data in Type V flow is reasonable according to the comparison of the experiments to the calculations in Figures 8c,d and 9. Therefore, there are two problems with the shear weakening behavior. One is that if the shear weakening is caused by experimental error, the influence of the error should be discerned for obtaining reliable data. The other is that if the shear weakening is a property of the melt, the RS theoretical model is incapable of characterizing the property and should be improved.

### 3.3. Predictions of the Trapezoidal-Loops

Two groups of trapezoidal-loop experiments were also conducted in [35] to understand the time-dependent viscoelastic property of the LDPE melt at 150 °C. As illustrated in Figure 1,  $t_0$  is 1 s in one group, and 100 s in the other. The parameter  $t_1$  is always 200 s for two groups.

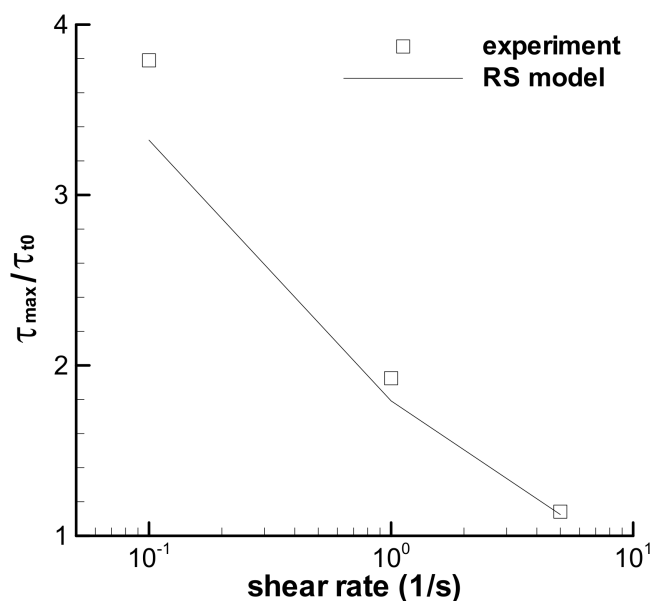
#### 3.3.1. Short-Term Startup Shear with $t_0 = 1$ s

Figure 10 shows the predictions of the trapezoidal-loop experiments with maximum shear rates of  $0.1 \text{ s}^{-1}$ ,  $1.0 \text{ s}^{-1}$ , and  $5.0 \text{ s}^{-1}$  and with  $t_0 = 1$  s and  $t_1 = 200$  s. The prediction of the experiment with  $0.1 \text{ s}^{-1}$  was modified by  $f$  in Table 4 due to the possible deviation of samples, which is presented in Figure 10 and is in agreement with the experiment. The prediction at the maximum shear rate of  $1 \text{ s}^{-1}$  also agrees with the experiment. However, the prediction at the maximum shear rate of  $5 \text{ s}^{-1}$  is in agreement with the experiment only in the time range lower than about 10 s. After 10 s, the calculation approaches constantly, and the experiment drops gradually during long-term shear. The shear weakening behavior appears in the trapezoidal loop experiment with the maximum shear rate of  $5 \text{ s}^{-1}$ , which still cannot be described by the RS model.



**Figure 10.** Predictions of the trapezoidal-loop experiments with the maximum shear rates of  $0.1 \text{ s}^{-1}$ ,  $1 \text{ s}^{-1}$  and  $5 \text{ s}^{-1}$ ,  $t_0 = 1$  s and  $t_1 = 200$  s. Solid line is the calculation by the RS model, and dashed line is the modification with  $f = 0.875$  in Table 4.

Shear-strain strengthening behavior occurs again in the trapezoidal loop experiments, which behaves as the growth of stress in the constant shear-rate region from the time at  $t_0$  to that at the maximum shear stress in Figure 10. The RS model can describe the strengthening. The ratio of the maximum shear stress  $\tau_{\max}$  in the constant shear-rate region over the shear stress at  $t_0$  is employed to quantify the shear strengthening, and the calculated ratios are shown in Figure 11, together with the experimental results [35]. Both groups' ratios are the decreasing function of the shear rate. Large ratios at low shear rates indicate an obvious contribution of growth of strain on the stress, and elasticity is apparent at a low shear rate for the melt. Moreover, the  $\tau_{\max}/\tau_{t_0}$  in Figure 11 is much larger than that in Figure 6 at the corresponding shear rate, which indicates the significant effect of the shear rate.



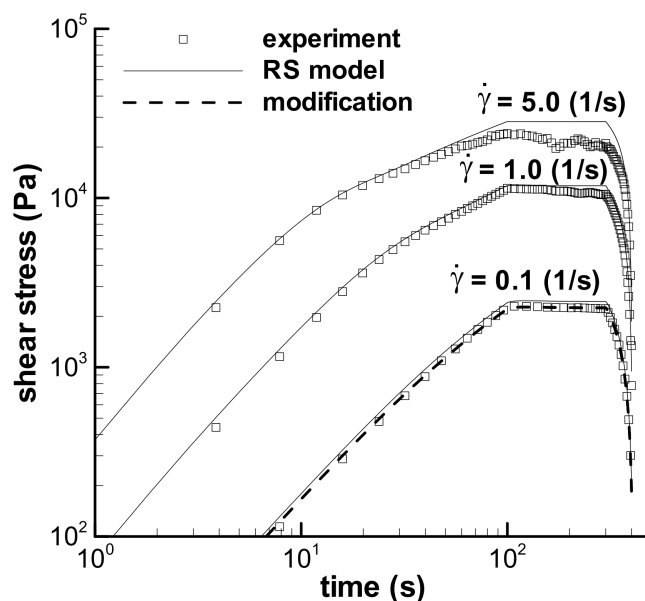
**Figure 11.** Ratios of the maximum shear stress over the stress at  $t_0 = 1$  s for three trapezoidal loops with  $t_0 = 1$  s. Symbol is the experimental data [35], and line is the calculation. The subscript  $t_0$  denotes the beginning time of the constant shear-rate region, i.e.,  $t_0$ .

Stress overshoot is usually described in the step rate experiment by the ratio of the maximum shear stress over the steady shear stress during long-term shearing, i.e.,  $\tau_{\max} / \tau_s$  [43,44]. The  $\tau_{\max} / \tau_s$ , i.e., the intensity of overshoot, calculated by the RS model for melt in the trapezoidal loop experiments with  $t_0 = 1$  s, is an increasing function of the shear rate, the same trend as the reported overshoots [43,44]. However, the experimental stress at the maximum shear rate of  $5 \text{ s}^{-1}$  gradually drops with time, and the experimental overshoot intensity contains part of the shear-weakening effect if we use the stress at a time of 201 s as the steady shear stress to describe the overshoot. Thus, it is challenging to describe the real stress overshoot for the shear-weakening viscoelastic flow at a high shear rate.

### 3.3.2. Long-Term Startup Shear with $t_0 = 100$ s

The predictions of the trapezoidal-loop experiments with maximum shear rates of  $0.1 \text{ s}^{-1}$ ,  $1 \text{ s}^{-1}$ , and  $5 \text{ s}^{-1}$ ,  $t_0 = 100$  s and  $t_1 = 200$  s are shown in Figure 12, where the modified calculation of the experiment with  $0.1 \text{ s}^{-1}$  is also given simultaneously. It is obvious that all three trapezoidal-loop experiments and calculations do not exhibit strain strengthening behavior due to the large  $t_0$ . Moreover, both a slight and a severe shear-weakening behavior occur at maximum shear rates of  $1 \text{ s}^{-1}$  and  $5 \text{ s}^{-1}$ , respectively, during long-term shear. The calculations of the RS model reaffirm the shear-weakening phenomenon of the melt.

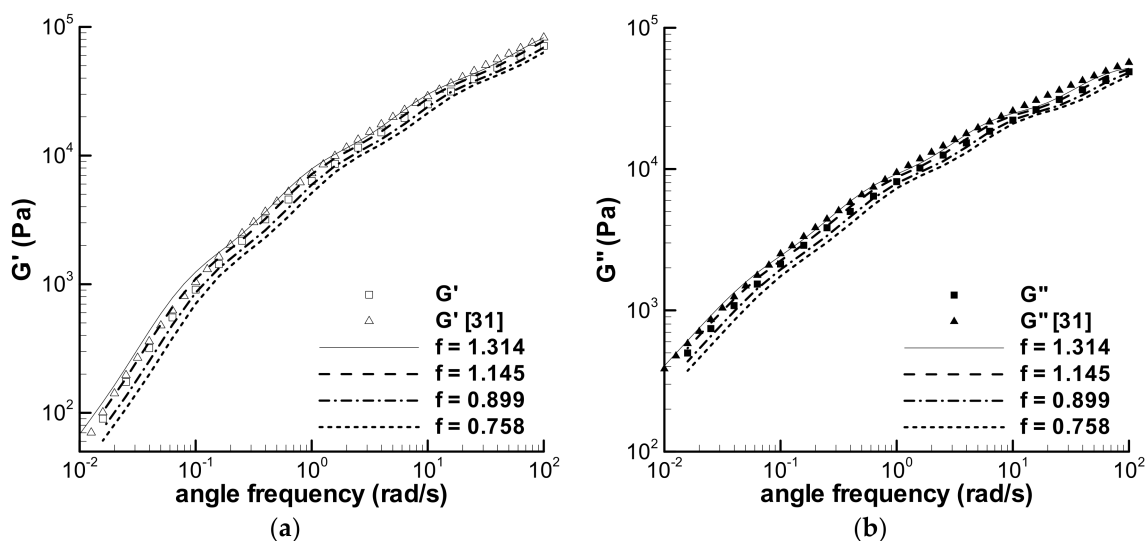
According to the experimental and calculated loops, both shear strain strengthening and stress overshoot are time-dependent viscoelastic behaviors. Shear strain strengthening may not be evidently affected by the shear-weakening behavior of viscoelastic fluid due to short-term startup shear, which could be more suitable for illuminating the elastic behavior of fluid; moreover, stress overshoot could contain some shear-weakening effect due to long-term shear sometimes at a shear rate, which complicates stress overshoot.



**Figure 12.** Predictions of the trapezoidal-loop experiments with the maximum shear rates of  $0.1 \text{ s}^{-1}$ ,  $1 \text{ s}^{-1}$  and  $5 \text{ s}^{-1}$ ,  $t_0 = 100 \text{ s}$  and  $t_1 = 200 \text{ s}$ . Solid line is the calculation by the RS model, and dashed line is the modification with  $f = 0.899$  in Table 4.

### 3.4. $f$ Effect

In Sections 3.2 and 3.3, the influences of possible sample deviations were analyzed using the changing spectrum method, and the modified calculations with  $f$  in Table 4 by the RS model are in good agreement with the loop experiments. The effects of four  $f$ -parameters on the original relaxation spectrum in Table 2 are shown in Figure 13, accompanied by the present experimental  $G'$  and  $G''$  in Figure 2 and the previous [31]. The calculations of four changed spectra show an approximate parallel property to the original spectrum. The modified  $G'$  and  $G''$  for the previous frequency sweep experiment with  $f = 1.314$  are acceptable although there are some deviations. It is unclear whether the difference between the present  $G'$  and  $G''$  and the previous is caused by the sample, nonetheless, the changing spectrum method is effective.



**Figure 13.** Calculated frequency sweep in small amplitude oscillatory shear mode using some spectra with  $f$  in Table 4, the present  $G'$  and  $G''$  experimental data (square symbol) and the reported  $G'$  and  $G''$  [31] (triangle symbol). (a)  $G'$ , and (b)  $G''$ .

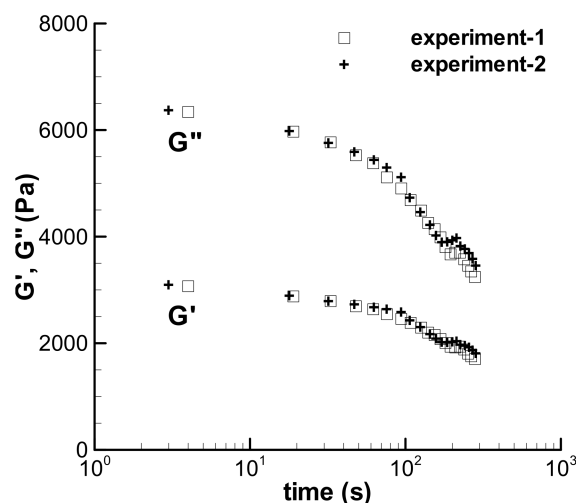


Eight groups of experiments have been modified with  $f$  in Table 4, in which the largest  $f$  is 1.314 for discerning the difference between two frequency sweep experiments. Another  $f$  varies from 0.758 to 1.145. Therefore, the relative error between the present frequency sweep experiment and the other experiments is about 10–30%, and the definition of relative error is  $|f - 1| / 1 \times 100$ . If the error is regarded as sample deviation, the error includes not only the deviation between different batches of the molded sheets but one batch.

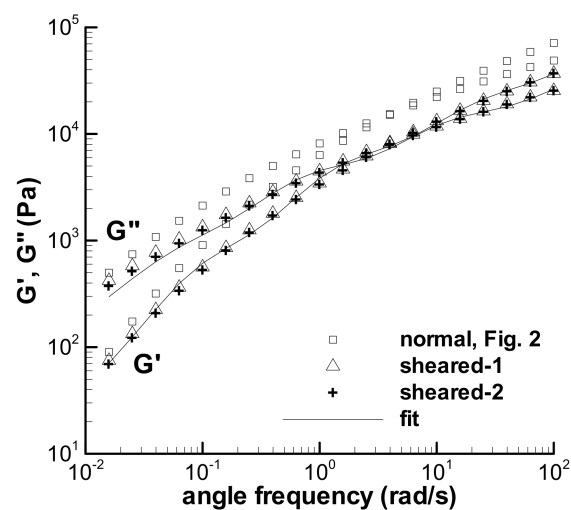
### 3.5. Discussion on the Shear Weakening Behavior

It can be assumed that the shear weakening phenomenon of a viscoelastic fluid is the result of a temporal, irreversible change of the structure in the fluid, which can lead to changes in the viscoelastic property during the shearing process. Then, shear weakening behavior cannot be described by the constitutive equation without considering the structure effect on the change in viscoelasticity. In order to understand the structure effect of long-time shearing on the change in linear viscoelasticity, a composite experiment including both the trapezoidal-loop and the dynamic frequency sweep should be conducted. For example, we first conduct the trapezoidal loop experiment with a maximum shear rate of  $5 \text{ s}^{-1}$ ,  $t_0 = 100 \text{ s}$ , and  $t_1 = 200 \text{ s}$ , then, simultaneously, we carry out the dynamic frequency sweep at a small strain of 5%. However, the composite cannot be carried out, since the ARES rheometer has a limitation in which the dynamic test must be conducted before the transient or the steady shear test. The startup position of dynamic sweep is fixed for the ARES rheometer, and the position at the end of the loop experiment is unlike that required in the dynamic sweep. No alternative method was found to solve the position problem and the scheme was abandoned.

Another approach to qualitatively research the influence of nonlinear large strain shear on the change of linear viscoelasticity for the LDPE(Q200) melt at  $150 \text{ }^\circ\text{C}$  was then adopted, i.e., both the nonlinear and linear shear experiments are accomplished in dynamic mode. A time sweep of 300 s at the large strain of 300% with an angle frequency of  $1 \text{ rad/s}$  was carried out first, and then, the frequency sweep in small amplitude oscillation shear at a 5% strain was immediately conducted. The experimental  $G'$  and  $G''$  data in two-time sweep experiments at the large strain of 300% are shown in Figure 14, which decrease with time due to the nonlinear shear effect. The  $G'$  and  $G''$  in two small-amplitude oscillation shear experiments obtained upon the cessation of the time sweep of 300 s at the large strain in Figure 15 are reduced by comparing with the normal  $G'$  and  $G''$ . The decrease in  $G'$  and  $G''$  in Figures 14 and 15 could be the manifestation of shear weakening phenomenon. The linear viscoelasticity of the melt could be changed by the shear weakening effect in shearing.



**Figure 14.** Dynamic time sweeps at large strain,  $\gamma = 300\%$ , in dynamic shear mode for the LDPE melt at  $150 \text{ }^\circ\text{C}$  ( $\omega = 1 \text{ rad/s}$ ).



**Figure 15.** Dynamic frequency sweep experiments at  $\gamma = 5\%$  for the LDPE melt at  $150\text{ }^{\circ}\text{C}$ , which are obtained after the time sweeps at the large strain in Figure 14, and the fit on the frequency sweep experiments.

To understand the qualitative influence of the altered linear viscoelasticity on the calculation of the loop experiment, a new relaxation spectrum of the LDPE melt was fitted to the  $G'$  and  $G''$  obtained using the shear weakening process in Figure 14 and given in Table 5; the calculated linear viscoelastic property with the new spectrum is shown in Figure 15. Assuming that the nonlinear characteristic of the LDPE melt is not influenced by the shear weakening behavior, the triangular loop experiment with the maximum shear rate of  $5\text{ s}^{-1}$  and  $t_0$  of  $100\text{ s}$  was calculated again with the spectrum in Table 5 and shown in Figure 8d by a dashed line. The new spectrum evidently reduces the calculated stress of the triangular loop, indicating the qualitative effect of the change of linear viscoelasticity on the description of the shear weakening behavior of the viscoelastic fluid.

The linear viscoelasticity or the relaxation spectrum is unchanged in the characterization of the viscoelastic property of a fluid using the RS model. Thus, the RS model is unsuitable for describing the shear weakening flow behavior of viscoelastic fluid caused possibly by the change of microstructure under large-strain shear. Some structuralized viscoelastic theories [40,42,45,46] may be available in characterizing the shear weakening behavior of the viscoelastic fluid. It is worth noting that the shear weakening in the triangular loop experiment with the maximum shear rate of  $5\text{ s}^{-1}$  and  $t_0$  of  $100\text{ s}$  in Figure 8d was enveloped by the calculations with both the original spectrum in Table 2 and the new spectrum in Table 5, which indicates that the structure-dependent spectrum approach [40] may be valid in describing the shear weakening behavior.

One crucial issue is whether the shear weakening behavior of the LDPE melt is the manifestation of experimental errors, e.g., edge fracture and loss of material from the gap. Some authors [16,22,47] have emphasized the effect of edge fracture on the shear weakening in the step rate experiment. However, shear weakening may be induced by other factors, such as the shear-structure effect stated above. Previously, shear modification or shear refinement of polythene [48] was reported from an industry viewpoint, and shear modification refers to the reduction in viscoelasticity in shearing, similar to the shear weakening behavior. Rudin [49] (1983) published a review on shear modification, and the authors in [50,51] introduced the possible mechanisms of shear modification. Therefore, the edge fracture effect is still an issue for shear weakening behavior.

#### 4. Conclusions

Five types of viscoelastic behaviors specified in the triangular-loop experiments of the LDPE (Q200) melt reported previously [35] were predicted in this study using the Rivlin–Sawyers (RS) model. The viscoelastic properties of the melt were characterized

using both the frequency sweep in the small-amplitude oscillation shear experiment and the steady shear viscosities. Type I–IV viscoelastic behaviors can be predicted by the RS model, although some errors appear in the experimental work. Type V flow cannot be predicted, which shows shear-weakening behavior. Most of the calculations agree with the experiments, indicating that both the previous experiments and present theoretical analyses are reasonable.

The trapezoidal-loop experiments of the melt in [35] were also predicted. The shear strain strengthening behavior occurring during the short-term startup shear process in the trapezoidal-loop experiment can be described well by the RS model, which is caused by both the growth of strain and shear rate effect and is similar to that in the triangular-loop experiment. The shear-weakening behavior in the trapezoidal-loop experiment also cannot be described by the model.

Differences between some of the calculations and experiments could be caused by sample deviation, which can be discerned through the changing spectrum approach. The modified calculations with the changing spectrum approach show agreement with the experiments. The large relative error in the experiment is about 10–30%.

The shear weakening behavior of the melt is an issue that can be studied further from two perspectives. One is to study the influence of edge fracture, and the other is to study the effect of changed linear viscoelastic property induced by shear, which could lead to a reasonable description of the shear weakening behavior by theoretical model if the structure effect is real.

**Funding:** This research was partly funded by the National Natural Science Foundation of China, grant number 10402024.

**Institutional Review Board Statement:** Not applicable.

**Informed Consent Statement:** Not applicable.

**Data Availability Statement:** The data that supports the findings of this study are available within the article.

**Conflicts of Interest:** The author declares no conflict of interest.

## References

- Han, C.D. *Rheology in Polymer Processing*; Academic Press: New York, NY, USA, 1976.
- Meissner, J. Modifications of the weissenberg rheogoniometer for measurement of transient rheological properties of molten polyethylene under shear. comparison with tensile data. *J. Appl. Polym. Sci.* **1972**, *16*, 2677–2899. [[CrossRef](#)]
- Laun, H.M. Description of the non-linear shear behaviour of a low density polyethylene melt by means of an experimentally determined strain dependent memory function. *Rheol. Acta* **1978**, *17*, 1–15. [[CrossRef](#)]
- Laun, H.M. Prediction of elastic strains of polymer melts in shear and elongation. *J. Rheol.* **1986**, *30*, 459–501. [[CrossRef](#)]
- Wagner, M.H.; Rubio, P.; Bastian, H. The molecular stress function model for polydisperse polymer melts with dissipative convective constraint release. *J. Rheol.* **2001**, *45*, 1387–1412. [[CrossRef](#)]
- Bastian, H. Non-Linear Viscoelasticity of Linear and Long-Chain Branched Polymer Melts in Shear and Extensional Flows. Ph.D. Thesis, University of Stuttgart, Stuttgart, Germany, 2001.
- Pivokonsky, R.; Zatloukal, M.; Filip, P. On the predictive/fitting capabilities of the advanced differential constitutive equations for branched LDPE melts. *J. Non-Newton. Fluid Mech.* **2006**, *135*, 58–67. [[CrossRef](#)]
- Li, B.; Yu, W.; Cao, X.; Chen, Q. Horizontal extensional rheometry (HER) for low viscosity polymer melts. *J. Rheol.* **2020**, *64*, 177–190. [[CrossRef](#)]
- Zatloukal, M. Differential viscoelastic constitutive equations for polymer melts in steady shear and elongational flows. *J. Non-Newton. Fluid Mech.* **2003**, *113*, 209–227. [[CrossRef](#)]
- Pivokonsky, R.; Zatloukal, M.; Filip, P. On the predictive/fitting capabilities of the advanced differential constitutive equations for linear polyethylene melts. *J. Non-Newton. Fluid Mech.* **2008**, *150*, 56–64. [[CrossRef](#)]
- Konagantia, V.K.; Ansaria, M.; Mitsoulis, E.; Hatzikiriakos, S.G. Extrudate swell of a high-density polyethylene melt: II. Modeling using integral and differential constitutive equations. *J. Non-Newton. Fluid Mech.* **2015**, *225*, 94–105. [[CrossRef](#)]
- Morelly, S.L.; Alvarez, N.J. Characterizing long-chain branching in commercial HDPE samples via linear viscoelasticity and extensional rheology. *Rheol. Acta* **2020**, *59*, 797–807. [[CrossRef](#)]
- Pivokonsky, R.; Zatloukal, M.; Filip, P.; Tzoganakis, C. Rheological characterization and modeling of linear and branched metallocene polypropylenes prepared by reactive processing. *J. Non-Newton. Fluid Mech.* **2009**, *156*, 1–6. [[CrossRef](#)]

14. Zhang, X.; Li, H.; Chen, W.; Feng, L. Rheological properties and morphological evolutions of polypropylene/ethylene-butene copolymer blends. *Polym. Eng. Sci.* **2012**, *52*, 1740–1748. [[CrossRef](#)]
15. Drabek, J.; Zatloukal, M. Evaluation of thermally induced degradation of branched polypropylene by using rheology and different constitutive equations. *Polymers* **2016**, *8*, 317. [[CrossRef](#)]
16. Costanzo, S.; Huang, Q.; Ianniruberto, G.; Marrucci, G.; Hassager, O.; Vlassopoulos, D. Shear and extensional rheology of polystyrene melts and solutions with the same number of entanglements. *Macromolecules* **2016**, *49*, 3925–3935. [[CrossRef](#)]
17. Laun, H.M.; Schmidt, G. Rheotens tests and viscoelastic simulations related to high-speed spinning of Polyamide 6. *J. Non-Newton. Fluid Mech.* **2015**, *222*, 45–55. [[CrossRef](#)]
18. Rolon-Garrido, V.H.; Pivokonsky, R.; Filip, P.; Zatloukal, M.; Wagner, M.H. Rheological characterization and constitutive modeling of two LDPE melts. *AIP Conf. Proc.* **2009**, *1152*, 32–43.
19. Pivokonsky, R.; Filip, P. Predictive/fitting capabilities of differential constitutive models for polymer melts—reduction of nonlinear parameters in the eXtended Pom-Pom model. *Colloid. Polym. Sci.* **2014**, *292*, 2753–2763. [[CrossRef](#)]
20. Pladis, P.; Meimaroglou, D.; Kiparissides, C. Prediction of the viscoelastic behavior of low-density polyethylene produced in high-pressure tubular reactors. *Macromol. React. Eng.* **2015**, *9*, 271–284. [[CrossRef](#)]
21. Yang, J.; Fan, L.; Dai, Y. Modified single-mode Leonov rheological equations for polymer melts and solutions. *J. Macromol. Sci. Part B-Phys.* **2015**, *54*, 424–432. [[CrossRef](#)]
22. Poh, L.; Li, B.; Yu, W.; Narimissa, E.; Wagner, M.H. Modeling of nonlinear extensional and shear rheology of low-viscosity polymer melts. *Polym. Eng. Sci.* **2021**, *61*, 1077–1086. [[CrossRef](#)]
23. Luo, X.L.; Tanner, R.I. Finite element simulation of long and short circular die extrusion experiments using integral models. *Int. J. Numer. Meth. Eng.* **1988**, *25*, 9–22. [[CrossRef](#)]
24. Goublomme, A.; Draily, B.; Crochet, M.J. Numerical prediction of extrudate swell of a high-density polyethylene. *J. Non-Newton. Fluid Mech.* **1992**, *44*, 171–195. [[CrossRef](#)]
25. Groublomme, A.; Crochet, M.J. Numerical prediction of extrudate swell of a high-density polyethylene: Further results. *J. Non-Newton. Fluid Mech.* **1993**, *47*, 281–287. [[CrossRef](#)]
26. Huang, S.X.; Lu, C.J. Stress relaxation characteristic and extrudate swell of the IUPAC-LDPE melt. *J. Non-Newton. Fluid Mech.* **2006**, *136*, 147–156. [[CrossRef](#)]
27. Cao, W.; Shen, Y.; Wang, P.; Yang, H.; Zhao, S.; Shen, C. Viscoelastic modeling and simulation for polymer melt flow in injection/compression molding. *J. Non-Newton. Fluid Mech.* **2019**, *274*, 104186. [[CrossRef](#)]
28. Barborik, T.; Zatloukal, M. Steady-state modeling of extrusion cast film process, neck-in phenomenon, and related experimental research: A review. *Phys. Fluids* **2020**, *32*, 061302. [[CrossRef](#)]
29. Huang, S.; Lu, C. The non-linear and time-dependent rheological characteristic for a LDPE melt and its description. *Acta Polym. Sin.* **2004**, *3*, 339–344. (In Chinese)
30. Fang, B.; Jiang, T. A novel constitutive equation for viscoelastic-thixotropic fluids and its application in the characterization of blood hysteresis loop. *Chin. J. Chem. Eng.* **1998**, *6*, 264–270.
31. Huang, S.; Lu, C. The descriptions of viscoelastic for a LDPE melt by using Wagner equation and the predictions on its non-linear and time-dependent characteristic. *Acta Polym. Sin.* **2004**, *6*, 818–825. (In Chinese)
32. Huang, S.; Lu, C. The characterization on the time-dependent nonlinear viscoelastic of a LDPE melt by using a simple thixotropy model. *Acta Mech. Sin.* **2005**, *21*, 330–335. [[CrossRef](#)]
33. Huang, S.; Lu, C.; Fan, Y. The time-dependent viscoelastic of an LDPE melt. *Acta Mech. Sin.* **2006**, *22*, 199–206. [[CrossRef](#)]
34. Huang, S.; Lu, C. Characterizations on the thixotropy-loop tests using UCM model with a rate-type kinetic equation. *Chin. J. Polym. Sci.* **2006**, *24*, 609–617. [[CrossRef](#)]
35. Huang, S.; Lu, C. The thixotropy-loop behaviors of an LDPE melt: Experiment and simple analysis. *J. Hydrodyn.* **2006**, *18*, 666–675. [[CrossRef](#)]
36. Greener, J.; Connelly, R.W. The response of viscoelastic liquids to complex strain histories: The thixotropic loop. *J. Rheol.* **1986**, *30*, 285–300. [[CrossRef](#)]
37. Rivlin, R.S.; Sawyers, K.N. Nonlinear continuum mechanics of viscoelastic fluids. *Annu. Rev. Fluid Mech.* **1971**, *3*, 117–146. [[CrossRef](#)]
38. Bird, R.B.; Armstrong, R.C.; Hassager, O. *Dynamics of Polymeric Fluids, Volume 1. Fluid Mechanics*, 2nd ed.; Wiley: New York, NY, USA, 1987.
39. Meister, B.J. An integral constitutive equation based on molecular network theory. *Trans. Soc. Rheol.* **1971**, *15*, 63–89. [[CrossRef](#)]
40. Huang, S. Viscoelastic characterization and prediction of a wormlike micellar solution. *Acta Mech. Sin.* **2021**. [[CrossRef](#)]
41. Huang, S. Viscoelastic characterization of the mucus from the skin of loach. *Korea-Aust. Rheol. J.* **2021**, *33*, 1–9. [[CrossRef](#)]
42. Huang, S. Structural viscoelasticity of a water-soluble polysaccharide extract. *Int. J. Biol. Macromol.* **2018**, *120*, 1601–1609. [[CrossRef](#)]
43. Kalyon, D.M.; Gevgilili, H. Wall slip and extrudate distortion of three polymer melts. *J. Rheol.* **2003**, *47*, 683–699. [[CrossRef](#)]
44. Osaki, K.; Inoue, T.; Isomura, T. Stress overshoot of polymer solutions at high rates of shear. *J. Polym. Sci. Part B-Polym. Phys.* **2000**, *38*, 2043–2050. [[CrossRef](#)]
45. Yziquel, F.; Carreau, P.J.; Moan, M.; Tanguy, P.A. Rheological modeling of concentrated colloidal suspensions. *J. Non-Newton. Fluid Mech.* **1999**, *86*, 133–155. [[CrossRef](#)]

46. Acierno, D.; La Mantia, F.P.; Marrucci, G.; Titomanlio, G. A nonlinear viscoelastic model with structure-dependent relaxation times: I. basic formulation. *J. Non-Newton. Fluid Mech.* **1976**, *1*, 125–145. [[CrossRef](#)]
47. Santangelo, P.G.; Roland, C.M. Interrupted shear flow of unentangled polystyrene melts. *J. Rheol.* **2001**, *45*, 583–594. [[CrossRef](#)]
48. Hanson, D.E. Shear modification of polythene. *Polym. Eng. Sci.* **1969**, *9*, 405–413. [[CrossRef](#)]
49. Rudin, A.; Schreiber, H.P. Shear modification of polymers. *Polym. Eng. Sci.* **1983**, *23*, 422–430. [[CrossRef](#)]
50. Leblans, P.J.R.; Bastiaansen, C. Shear modification of low-density polyethylene: Its origin and its effect on the basic rheological functions of the melt. *Macromolecules* **1989**, *22*, 3312–3317. [[CrossRef](#)]
51. Van Prooyen, M.; Bremner, T.; Rudin, A. Mechanism of shear modification of low density polyethylene. *Polym. Eng. Sci.* **1994**, *34*, 570–579. [[CrossRef](#)]

## Article

# The Feasibility of an Internal Gas-Assisted Heating Method for Improving the Melt Filling Ability of Polyamide 6 Thermoplastic Composites in a Thin Wall Injection Molding Process

Thanh Trung Do, Tran Minh The Uyen and Pham Son Minh \*

HCMC University of Technology and Education, Ho Chi Minh City 71307, Vietnam; trungdt@hcmute.edu.vn (T.T.D.); uyentmt@hcmute.edu.vn (T.M.T.U.)

\* Correspondence: minhps@hcmute.edu.vn; Tel.: +84-938-226-313

**Abstract:** In thin wall injection molding, the filling of plastic material into the cavity will be restricted by the frozen layer due to the quick cooling of the hot melt when it contacts with the lower temperature surface of the cavity. This problem is heightened in composite material, which has a higher viscosity than pure plastic. In this paper, to reduce the frozen layer as well as improve the filling ability of polyamide 6 reinforced with 30 wt.% glass fiber (PA6/GF30%) in the thin wall injection molding process, a preheating step with the internal gas heating method was applied to heat the cavity surface to a high temperature, and then, the filling step was commenced. In this study, the filling ability of PA6/GF30% was studied with a melt flow thickness varying from 0.1 to 0.5 mm. To improve the filling ability, the mold temperature control technique was applied. In this study, an internal gas-assisted mold temperature control (In-GMTC) using different levels of mold insert thickness and gas temperatures to achieve rapid mold surface temperature control was established. The heating process was observed using an infrared camera and estimated by the temperature distribution and the heating rate. Then, the In-GMTC was employed to produce a thin product by an injection molding process with the In-GMTC system. The simulation results show that with a gas temperature of 300 °C, the cavity surface could be heated under a heating rate that varied from 23.5 to 24.5 °C/s in the first 2 s. Then, the heating rate decreased. After the heating process was completed, the cavity temperature was varied from 83.8 to about 164.5 °C. In-GMTC was also used for the injection molding process with a part thickness that varied from 0.1 to 0.5 mm. The results show that with In-GMTC, the filling ability of composite material clearly increased from 2.8 to 18.6 mm with a flow thickness of 0.1 mm.

**Citation:** Do, T.T.; Uyen, T.M.T.; Minh, P.S. The Feasibility of an Internal Gas-Assisted Heating Method for Improving the Melt Filling Ability of Polyamide 6 Thermoplastic Composites in a Thin Wall Injection Molding Process. *Polymers* **2021**, *13*, 1004. <https://doi.org/10.3390/polym13071004>

Academic Editor: Célio Bruno Pinto Fernandes

Received: 6 March 2021

Accepted: 22 March 2021

Published: 24 March 2021

**Publisher's Note:** MDPI stays neutral with regard to jurisdictional claims in published maps and institutional affiliations.



**Copyright:** © 2021 by the authors. Licensee MDPI, Basel, Switzerland. This article is an open access article distributed under the terms and conditions of the Creative Commons Attribution (CC BY) license (<https://creativecommons.org/licenses/by/4.0/>).

**Keywords:** injection molding; thermoplastic composites; mold heating; mold temperature control; melt filling; thin wall injection molding

## 1. Introduction

In injection molding, the selection of an appropriate cavity surface temperature is a key point in plastic processing, especially with thin products or molding processes with low viscosity materials, such as composites [1–3]. With a hot mold surface, the part quality will be improved, although the cycle time will be longer. A lower temperature of the cavity surface will decrease the cooling time, but could lead to an increased number of faults in the product [4–7]. Therefore, recent research has focused on achieving molding with a high cavity temperature and a cycle time that is as short as possible. In the field of injection molding, thin wall injection molding is used to produce a variety of polymer equipment because of the product price and capability for high-volume production. Most applications of thin wall injection molding are in the field of optical products (such as CDs and DVDs) and micro channel devices. In the field of optics production, the injection

molding method also has advantages in the production of waveguides, optical gratings, and optical switches [8–10], as well as many products involving micro channel devices, such as capillary analysis systems, micro pumps, and lab-on-a-chip applications [11,12].

In the filling step of the injection molding process, to improve material flow, a high cavity temperature is an important requirement to satisfy the filling of thin wall locations. A high cavity temperature also supports a lower filling pressure. However, if the molding process operates with a high mold temperature, the warpage and shrinkage of parts will occur. In addition, the molding cycle time will be increased for the part that reaches the ejection temperature. To achieve a molding process with a high cavity surface and reduce the frozen layer, many methods of mold temperature control have been investigated in recent years [8]. The initial method used to obtain a high mold temperature was to increase the temperature of cooling water as high as 90 or 100 °C [12–14]. When targeting temperatures are higher than 100 °C, heaters are inserted into the mold plate. The thermal energy of the heater thus forms the local heating source of the mold plate [15]. After that, the high temperature from water steam [16] is sometimes used to maintain the temperature of the cavity surface at a high value. However, this method requires that the equipment be operated at high pressure; therefore, the cost of safety equipment is a disadvantage of this method. Further, flexible heating equipment has been suggested and used for auxiliary heating. However, the experimental results show that the method can only increase the cavity temperature by several tens of degrees centigrade.

Instead of heating the entire mold cavity volume, in recent years, many researchers have suggested the use of the mold surface heating method for molding with high cavity temperatures, such as in induction heating [17–20], high-frequency proximity heating [21,22], and gas-assisted mold temperature control (GMTC) [23–30]. The first two methods support a fast heating rate with a fairly good prediction ability. However, induction heating is applied only for steel molds with a high permeability. On the other hand, besides the advance in fast heating, the induction heating method could easily cause the mold plate to overheat, particularly at the edges. On the contrary, with gas heating, the heating rate is not as high as that of the induction heating, but it can be used for almost the entire mold material. In addition, due to the heat convection between the hot gas and the cavity surface, which has a lower temperature, the gas heating has the ability to prevent the mold from overheating.

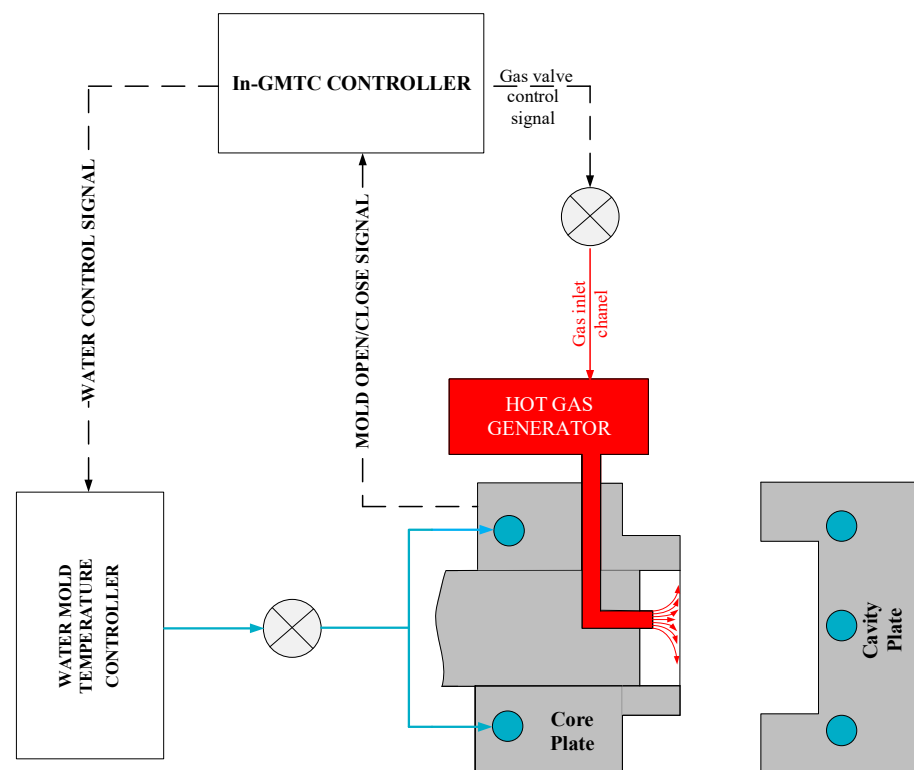
In previous research, the gas heating structure was assembled into the mold to improve the heating efficiency, including the heating rate and temperature distribution [20–23]. In this design, the hot gas flows and directly exchanges thermal energy to the mold surface. The conduction heating process increases the cavity temperature. Tests of this approach have shown positive results. However, the loss of thermal energy when the air transfers from the heating source to the heating surface is still too great with this approach. This issue is due to the fact that the heating source is separated from the mold or because the heating surface is too far from the heating source. So, to minimize this limitation, the external gas-assisted mold temperature control (Ex-GMTC) method was investigated [24–26]. In this molding process, the mold structure is almost the same as the traditional structure. The heating equipment is moved to the heating surface with a robot arm. This method has some advantages as the heating rate and temperature distribution of the cavity surface can be controlled. However, the disadvantage of Ex-GMTC is the cost of additional equipment; furthermore, moving the hot gas generator is not very safe.

Therefore, based on the disadvantages shown in our previous research, in this study, an internal gas-assisted mold temperature control (In-GMTC) approach was used with different levels of insert thickness ( $t$ ) and gas temperatures to achieve rapid mold surface temperature control for high-aspect-ratio thin wall injection molding. A set of systematic experiments was conducted to correlate the effect of heating conditions, including heating efficiency and temperature distribution uniformity. The feasibility of using internal air-assisted heating for mold surface temperature control during the injection process to

improve the melt flow length was evaluated by applying this system to a real molding process with part thicknesses varying from 0.1 to 0.5 mm.

## 2. Simulation and Experimental Method

Internal gas-assisted mold temperature control (In-GMTC) is a new technique in the field of cavity surface heating that can not only provide heating but also facilitate cooling. In general, the goals of mold temperature control are to increase the temperature of the mold surface to the target temperature before filling with the melt and cooling the melt to the ejection temperature. In this research, the internal GMTC (In-GMTC) system consisted of a hot-gas generator system (including an air compressor with an air pressure of 7 bars, an air drier, a gas valve, and a high-efficiency gas heater) and water mold temperature controller, as shown in Figure 1.

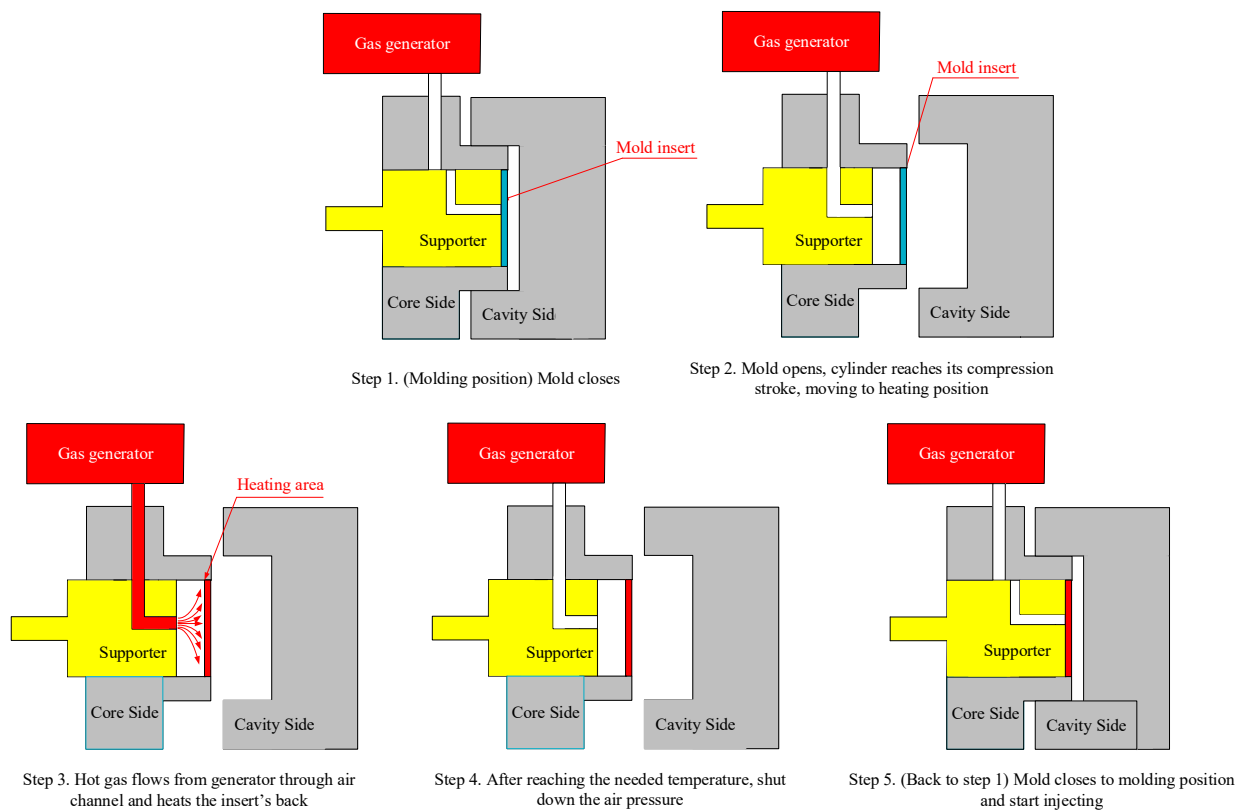


**Figure 1.** The internal gas-assisted mold temperature control (In-GMTC) system.

In line with our previous research into the GMTC [22,23], the hot gas generator consisted of an air compressor, an air dryer, a gas valve for volumetric flow control and a high-efficiency gas heater. In this research, the function of the high-power hot gas generator system was to support a heat source, providing a flow of hot air up to 400 °C with an inlet gas pressure of up to 7 bars. In this research, the hot gas generator was hung on the mold so that, in each cycle, the heating process could be started without the support of other equipment such as in the external gas-assisted mold temperature control (Ex-GMTC). Another advantage of this method is that the distance between the hot gas generator and the heating surface was reduced, meaning that the wasted energy was reduced. For the coolant system, a mold temperature controller was used to provide the water at a defined temperature to cool the mold after the filling process and to warm the mold to the initial temperature at the beginning of the experiment. In this research, the initial mold temperature was set at 40 °C. To both control and observe the temperature at the cavity surface, five temperature sensors were used to obtain the real-time mold temperature and to provide feedback to the In-GMTC controller.



In this research, hot gas was used as a heating source to increase the cavity surface temperature of the injection mold. For the heating operation, first, by opening the mold, two mold plates moved from the closing position to the opening position (Figure 2—Step 1 and Step 2). In Step 2, the supporter moved backward to create a gap between the supporter block and the mold insert. This gap allowed the hot gas to flow and make contact with the mold insert. Second, the hot gas drier was moved to the heating position, as shown in Figure 2—Step 3. Then, the air was heated as it flowed through the gas drier and the outside of the gas drier transferred the hot air, which contacted directly with the cavity surface. This hot gas heated the cavity surface to the target temperature (Figure 2—Step 3). Third, when the mold reached the required temperature, the air supply was turned off (Figure 2—Step 4). Then, the mold was completely closed in preparation for the filling process of the melt (Figure 2—step 5). In Step 5, the supporter block moved toward and contacted with the mold insert so that the mold insert did not become deformed when it stopped due to the filling pressure from the hot melt.



**Figure 2.** Mold position in the heating stage of the In-GMTC process.

Figure 3 shows the position of the In-GMTC and the mold plate in the injection molding. The gas drier, with a size of 240 mm × 100 mm × 80 mm, is shown in Figure 4. The gas channel was cut inside the gas drier with a width of 5 mm and depth of 10 mm. In this research, the mold cavity was filled by an insert with a size of 77 mm × 77.4 mm. The inserts and the locations of temperature measurement are shown in Figure 5. To observe the heating effect of In-GMTC on the stamp temperature, five temperature measurement points were used. One was located at the top point, which was close to the outlet of the gas drier. The other four were located as shown in Figure 5. In this paper, the influence of stamp thickness on the heating process was observed. To study the temperature distribution of the heating area, a simulation model was built as in the experiment. Because the stamp was inserted into the mold, there was a small air gap between the stamp and the mold; thus, within a short time, this air gap acted as an insulation layer. Therefore, according to previous research [21,22], the simulation model included only two volumes: the stamp

volume and the air volume. The geometric view and the meshing model of the system are shown in Figure 6 and Table 1. In this model, the hot gas temperature was varied from 200 to 400 °C under a pressure of 7 bar. The direction of this hot gas flow was set perpendicular to the heating surface. In the simulation, the initial gas volume was set at 40 °C with a pressure of 1 atm. The outlet of the hot gas was set as the opening area, with an air temperature of 40 °C and a pressure of 1 atm. In addition, the initial temperature of the P20 steel insert was set at 40 °C. In order to improve the simulation precision, a hex-dominant element was used to mesh the insert part. To improve the simulation accuracy, a small element size was applied at location S1. In addition, the inflation meshing method was applied with 10 layers at the contact surfaces. In the simulation, the heat transfer mode around all external surfaces of the mold plate was set to free convection to the air, with an ambient temperature of 40 °C and a heat transfer coefficient of 10 W/m<sup>2</sup> K. The heating process was simulated using ANSYS software (ANSYS, Inc., Ho Chi Minh City, Vietnam) with the same experimental parameters.

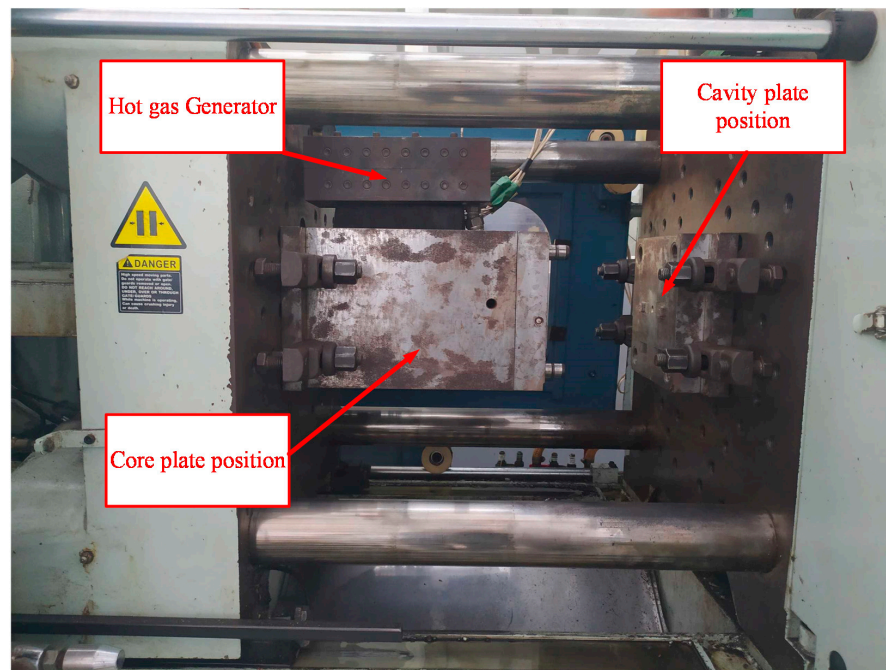


Figure 3. The experimental setup for In-GMTC.

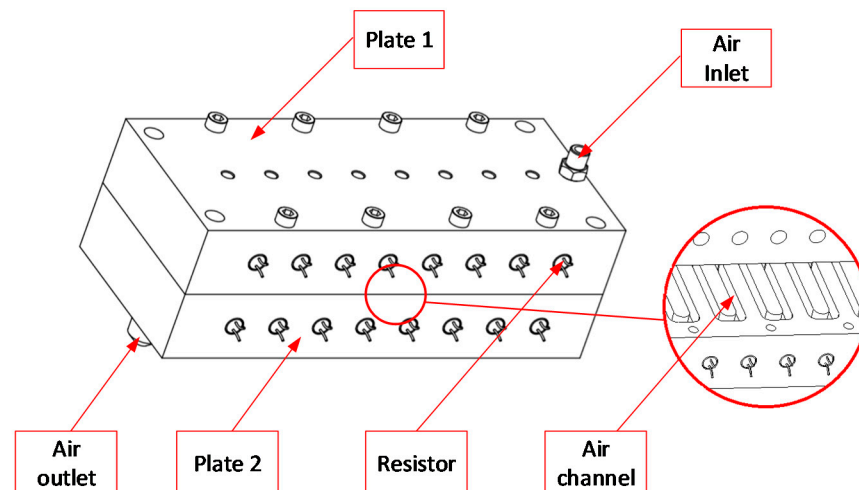


Figure 4. The hot gas generator.

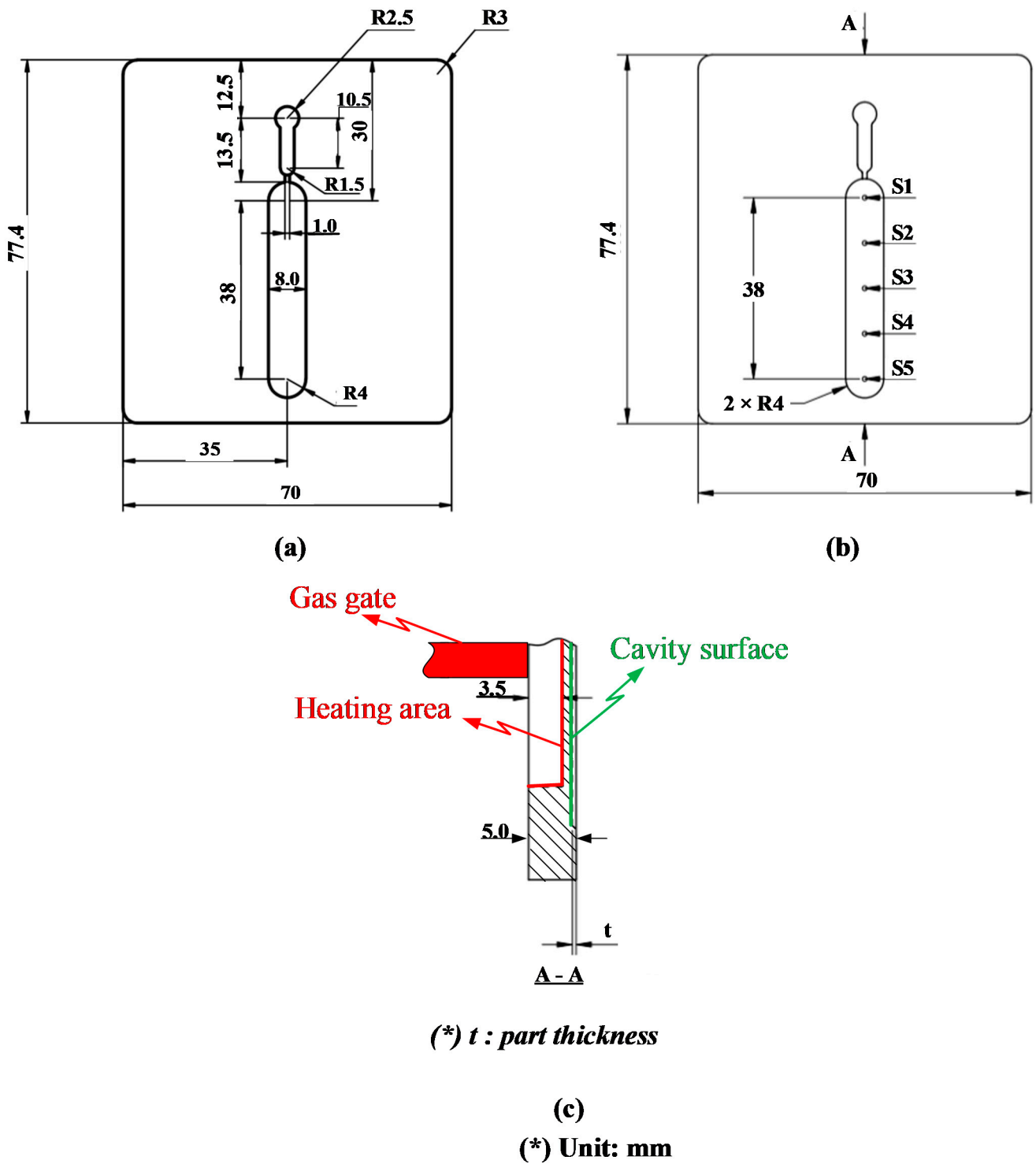


Figure 5. Insert dimension (a) with the sensor locations S1 to S5 (b) and the heating surface of the insert (c).

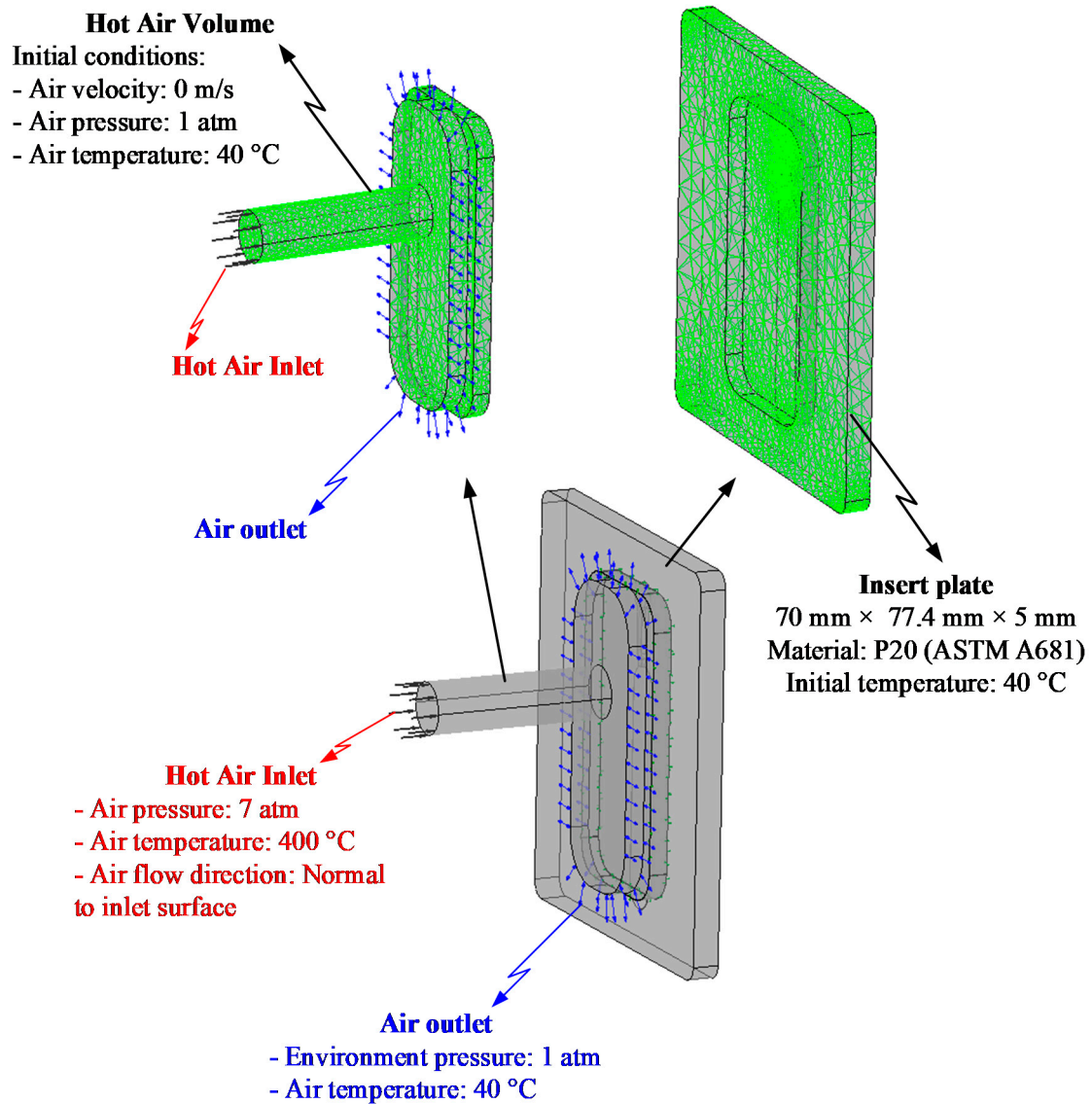


Figure 6. Boundary conditions and the meshing model at the insert area.

Table 1. Material properties (for simulation).

Material	Properties	Unit	Value
Air	Molecular mass	kg/kmol	28.96
	Density	kg/m <sup>3</sup>	1.185
	Specific heat capacity	J/kg K	1004.4
	Dynamic viscosity	kg/ms	$1.831 \times 10^{-5}$
	Thermal conductivity	W/mK	0.0261
Steel	Molecular mass	kg/kmol	55.85
	Density	kg/m <sup>3</sup>	7854
	Specific heat capacity	J/kg K	434
	Thermal conductivity	W/mK	60.5

To observe the influence of In-GMTC on the melt flow length, the real molding process was performed with the cavity insert as in Figure 5. This insert was added into the cavity plate as shown in Figure 7. This cavity had a size of 46 mm × 8 mm. The insert was manufactured for the experiment with melt flow thicknesses of 0.1, 0.2, 0.3, 0.4, and 0.5 mm. With the common injection molding process, this range of thicknesses represents a kind

of thin wall injection molding, which easily results in the short shot problem when the injection pressure is low; however, with an overly high injection pressure, the flash problem easily arises. Thus, with the ability of mold temperature control, the In-GMTC was applied for this molding process to observe the improvement in product quality when the injection molding process was operated with a moderate injection pressure. In this paper, polyamide 6 reinforced with 30 wt.% of glass fiber (PA6/GF30% from Lanxess AG, Cologne, Germany) was used for the molding process, and the molding parameter was maintained for all testing cases, as shown in Table 2. The SW-120B (Shine Well Machinery Co., Ltd., Taichung City, Taiwan) molding machine was used in the experiment.

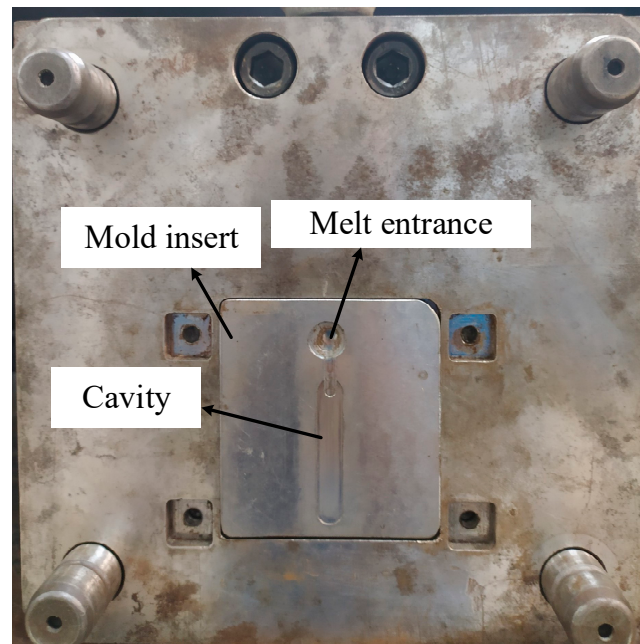


Figure 7. The mold for the melt flow length testing with the gate heating area.

Table 2. The molding parameters for the product of the front cover plate.

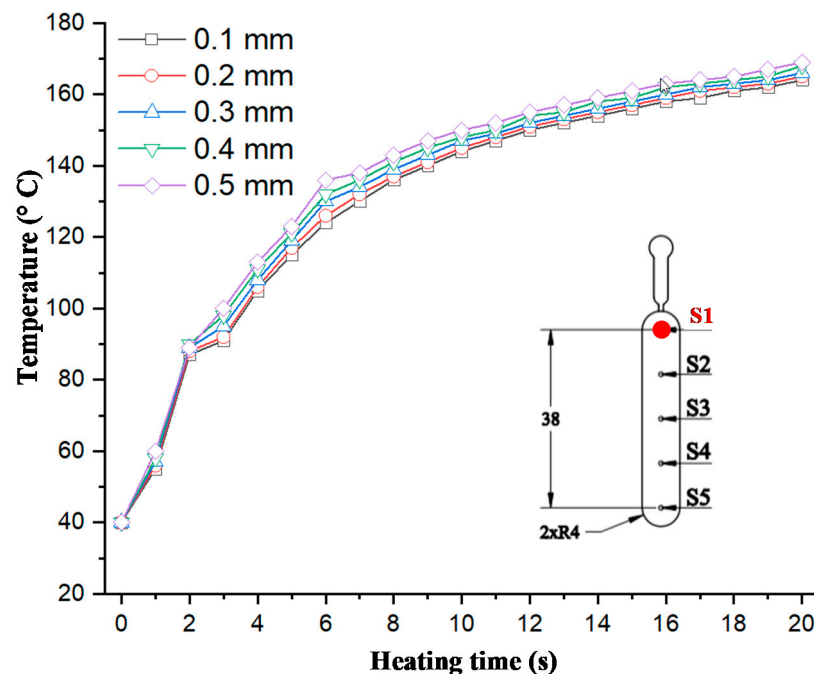
Molding Parameter	Unit	Value
Injection speed	cm <sup>3</sup> /s	23
Injection pressure	atm	35
Injection time	s	1.5
Packing time	s	2
Packing pressure	atm	35
Cooling time	s	15
Mold temperature	°C	50
Melt temperature	°C	265
Pre-heating time by In-GMTC	s	20

### 3. Results and Discussions

#### 3.1. Effect of Part Thickness on the Mold Temperature Control

In injection molding, the part geometry is an important element that not only impacts on the part formation but also the molding parameters. With a thin product, there are many methods for improving the melt filling by molding at high temperature, such as induction heating and heater heating. Of these methods, gas-assisted mold temperature control has shown many positive results [20–23]. With gas-assisted mold temperature control, the structure of the stamp insert is often used to increase the heating efficiency. Based on the results of these research works, the stamp thickness is one of the most important parameters of mold design and is impacted by the part thickness. Therefore, in this paper,

to estimate the heating ability of In-GMTC, an insert with a size of 77.4 mm × 77 mm was inserted into the cavity plate, and the heating process was achieved with a hot gas temperature of 300 °C; the gap between the gas gate and the heating surface was 3.5 mm (Figure 5c). By simulation with the model, as shown in Figure 6, the results of the variation in the mold temperature (at sensor S1—Figure 5) versus time for a heating time of 20 s are described as shown in Figure 8. For an initial mold temperature of 40 °C, it can be seen that the In-GMTC heated the plate to above 170.4 °C. This shows that the In-GMTC can support a heating rate of 6.5 °C/s. With the change in part thickness from 0.1 to 5.0 mm, the temperature at sensor S1 varied from 164.3 to 170.4 °C. This temperature range was higher than the glass transition temperature of almost all common plastic material. In former papers on gas-assisted mold temperature control [20–22], when the GMTC was applied for a heating area of 58 mm × 30 mm, a gas flow rate of 500 L/min and a gas temperature of 300 °C, the maximum heating rate was only about 2.2 °C/s [25]. This means that the In-GMTC, with the system design and heating process shown in Figure 2, has a great advantage in terms of the heating efficiency of the mold surface.



**Figure 8.** Temperature comparison at the center of the heating area (Point S1) in simulations with different product thicknesses.

To observe the influence of part thickness on the heating step, five stamp thicknesses were used for the experiment. Figure 8 shows that with thicknesses of 0.1, 0.2, 0.3, 0.4, and 0.5 mm, the temperature at sensor S1 varied from 164.3 to 170.4 °C; this means that the heating rate increased from 6.2 to 6.5 °C/s. The increase in heating rate when the part thickness increased can be explained by the thermal energy needed to heat the stamp volume. Because the stamp and the mold plate were separated by an isolation layer, with the same heating source, the heating result mainly depended on the stamp volume. So, with a thinner stamp, more thermal energy is needed to increase the stamp temperature. Based on the design shown in Figure 5c, because the stamp thickness and gap between the gas gate to the heating surface were 5 and 3.5 mm, respectively, with a thicker part, the less material there was at the cavity; therefore, a better heating rate was achieved with a thicker product. However, the difference in the heating rate when the part thickness changed from 0.1 to 0.5 mm was small. Therefore, in thin wall injection molding, this property is an advantage of this heating method, which could support mold temperature control with a thin wall part and a thickness that could be varied to lower than 0.5 mm.

The temperature curves in Figure 8 show that the heating rate was extremely high in the first 2 s, with the heating rate varying between 23.5 and 24.5 °C/s. This heating rate is higher than those of many heating methods reported in recent years [19–25]. After the first 2 s, the heating rate decreased. Although the temperature of the heating surface was not the same as the cavity surface (which was measured) as in Figure 5c, the temperature change was almost the same as those shown in other research on gas-assisted mold temperature control, which can be explained by the absorption of thermal energy and heat transfer. In this research, the heating surface absorbed the thermal energy, and the thickness at sensor S1 was thin, meaning that this thermal energy was held within a small material volume, resulting in a rapid temperature increase at sensor S1. This phenomenon was clearly apparent in the first 2 s. However, the higher temperature meant that the thermal energy at the thin cavity location transferred to another area with a lower temperature. So, this phenomenon lowered the heating rate at the cavity surface. In addition, with a heating time of 20 s, the temperature curves did not show the same limitation as in other studies [24,25]. Therefore, the temperature at the cavity surface still increased with a longer heating time or a high-powered heating source. However, as mentioned above, the temperature at 20 s was high enough to facilitate the melt flowing, and so based on this simulation, the heating time of 20 s was used for the following cases.

In our former study, when the internal GMTC was used for mold surface heating, there was a temperature difference between the inlet and outlet area [20–22]. Therefore, in this research, to evaluate the uniformity of the heating process under various stamp thicknesses, the temperature distribution at the cavity surface of the stamp, as shown in Figure 5a, was measured and compared using a simulation and experiments. Figure 9 shows the simulation result regarding the temperature distribution of the cavity. The temperatures of five sensors were measured at the end of the heating step and are compared in Figure 10. These results show that the highest temperature was located at the top of the stamp (sensor S1), which was closest to the hot gas gate, and the temperature was lower at the bottom of the stamp. This kind of distribution was better than that of previous research on the internal GMTC, which often found unbalanced temperatures between the two sides of the cavity area [20,22]. In addition, compared with the induction heating method [14,16,17], the In-GMTC method solved the problem regarding the low temperature at the center of the heating area and would therefore be better for application in real molding products. This result also shows that the temperature differences between the five sensor locations were 81.3, 81.1, 80.5, 79.1, and 78.2 °C with product thicknesses of 0.1, 0.2, 0.3, 0.4, and 0.5 mm, respectively. These results also prove that, with a heating time of 20 s, for all types of stamp thickness, the temperature of the cavity varied from over 83.8 to approximately 164.5 °C and the higher temperature was close to the melt entrance, which could lead to a greater reduction in the frozen layer. Thus, the pressure drop of the hot melt was limited and the melt could flow faster. This means that this temperature distribution was suitable for use in the injection molding process. In addition, these results also show that the lowest temperature could almost satisfy the mold temperature of common plastic materials and the highest temperature was not so high that degradation of plastic materials would occur.

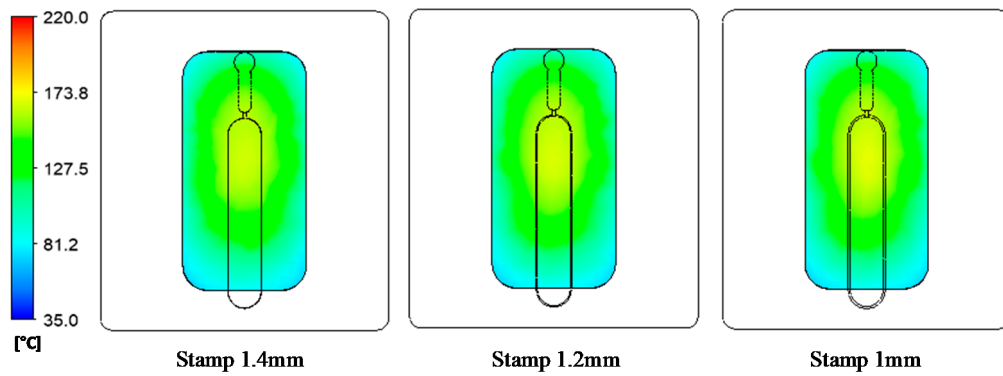


Figure 9. Temperature distribution of the molding area with an initial temperature of 40 °C, a gas temperature of 300 °C, an inlet gas pressure of 7 bars, and a heating time of 20 s.

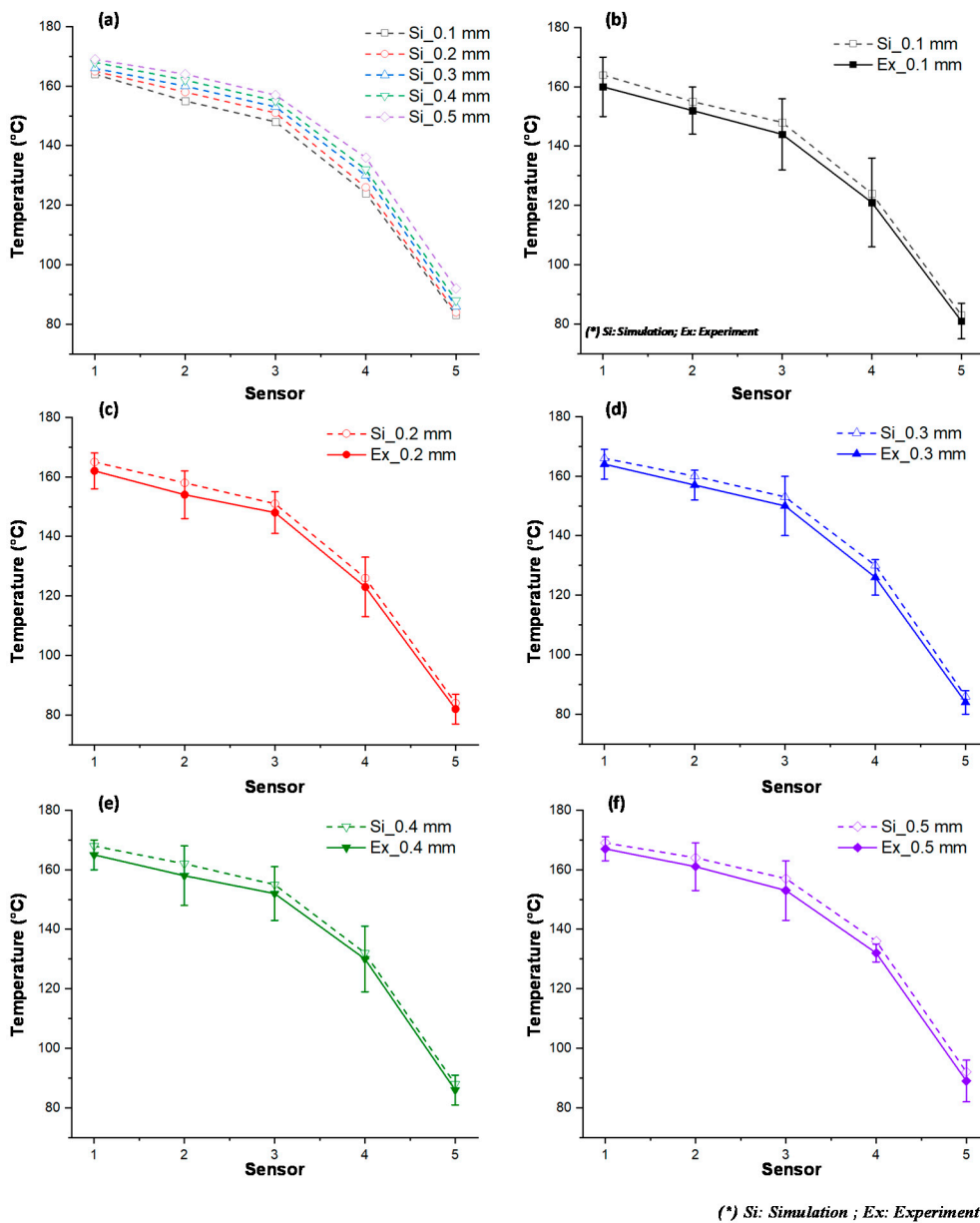


Figure 10. Temperature along the center line in simulations with different product thicknesses.



To verify the accuracy of the simulation result, the experiment achieved the same boundary condition as that in the simulation. The experiment was performed 10 times for each case; after that, the average value was represented for each case. Then, the temperature at the sensors was measured and compared with the simulation result, as shown in Figure 10. The comparison shows that the temperature difference between the simulation and experiment was lower than 10 °C. This difference is due to the measurement delay of the sensor, especially as, in this state, the thermal energy transferred quickly from the higher temperature area to the lower temperature area. However, in general, this result shows that the results of the simulation and the experiment have a good agreement.

### 3.2. Effect of the Inlet Temperature on the Heating Process

In the GMTC method, the gas temperature is an important element, which can be represented by the heating source. In the application of GMTC, a higher gas temperature causes the heating rate to increase. However, the amount of wasted energy will also increase. Therefore, in this study, this was investigated with the model shown in Figures 5 and 6 with gas temperatures of 200, 300, and 400 °C, a product thickness of 0.5 mm corresponding to the stamp thickness of 1 mm and a heating time of 20 s.

Figures 11 and 12 show the temperature distribution under different air temperatures with a stamp thickness of 1 mm. This result shows that with the higher inlet temperature, the heating process became more effective, resulting in a higher temperature at the center of the plate, as well as the temperature difference on the plate increasing. In detail, based on the simulation result, the temperature differences along the center line of the stamp were 54.2, 79.1, and 85 °C, with inlet temperatures of 200, 300, and 400 °C, respectively. In this paper, a comparison was performed between three different inlet temperatures, as shown in Figure 13a. To verify the accuracy of the simulation result, the experiment was performed with the same gas gap. The temperature at five sensors was collected and compared, as shown in Figure 13b–d, and the temperature distribution is shown in Figure 12. The comparison shows that the simulation and the experiment have a good agreement. In other research on the GMTC [20–25], the heating process was influenced by another wild source; however, with the In-GMTC, the heating process was achieved in the private volume, meaning that the simulation and the experimental result exhibited good agreement. Therefore, this heating method could be easier to predict by simulation than the external GMTC. Figure 13b–d shows that the mean temperature in the experiment was slightly lower than the simulation result. This was due to the fact that the simulation results show the temperature at the end of heating step exactly; however, in the experiment, there was a delay time associated with the thermal camera obtaining the thermal picture, and in this delay time, the thermal energy at the higher temperature area was transferred to the lower temperature area, resulting in a lower temperature being obtained by the thermal camera.

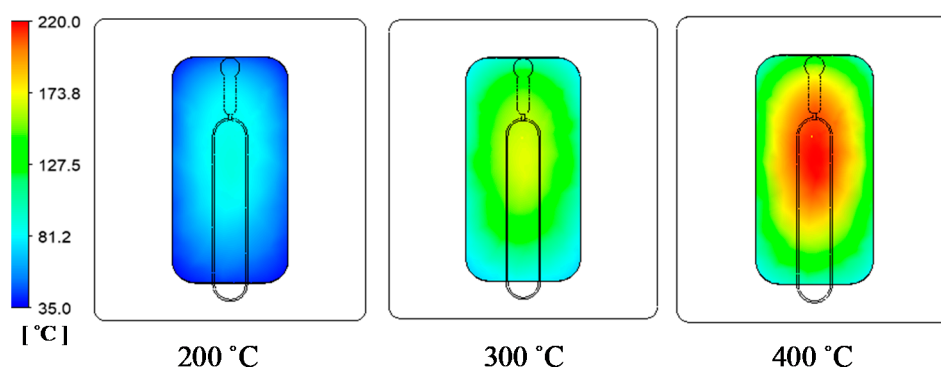


Figure 11. Temperature distribution of the stamp under different air inlet temperatures with a heating time of 20 s.

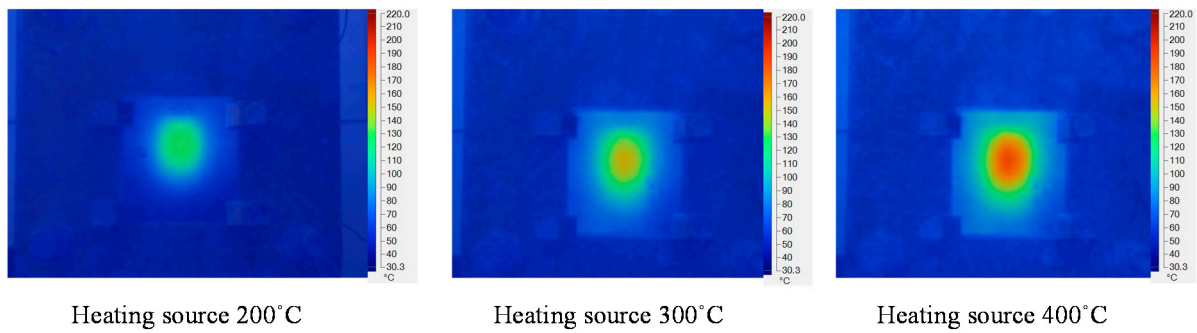
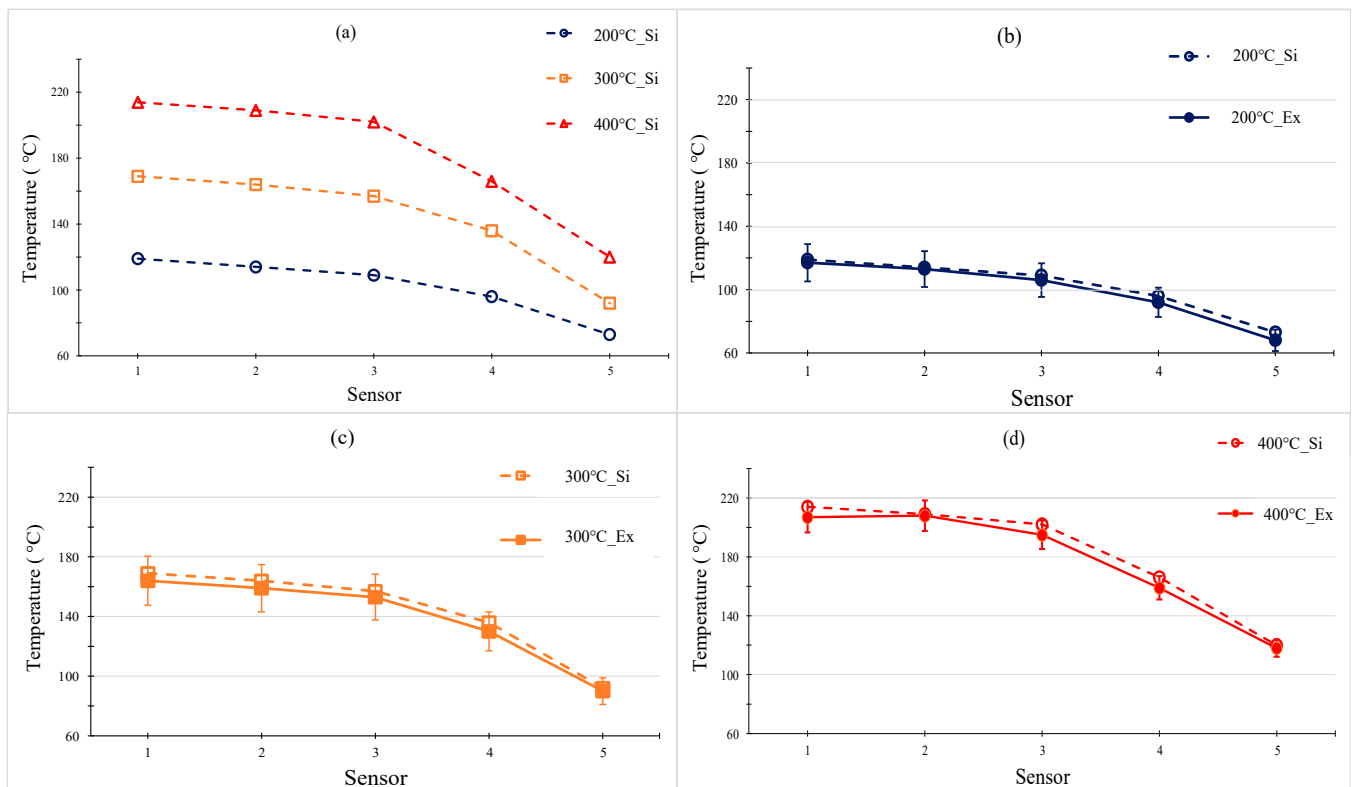


Figure 12. Temperature distribution of the cavity plate after 20 s of heating under different hot gas temperatures.



(\*) Si: Simulation ; Ex: Experiment

Figure 13. The comparison of temperatures along the center line by simulation (a) with different inlet temperatures with a heating time of 20 s and stamp thickness of 0.5 mm under gas temperature of 200 °C (b); 300 °C (c) and 400 °C (d).

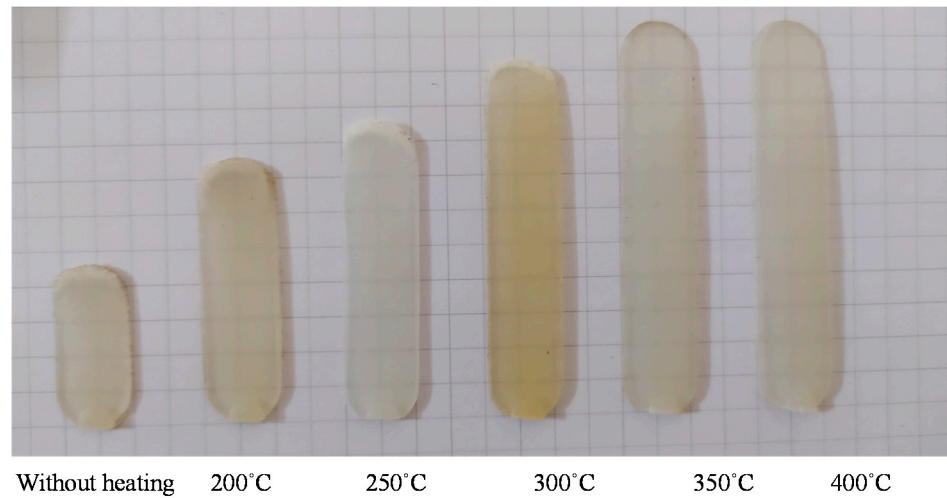
### 3.3. Improve the Melt Flow Length of the Polyamide 6 Thermoplastic Composites by Internal Gas Heating for the Gate Temperature Control

To verify the efficiency of In-GMTC for use in the mold temperature control, the mold of melt flow length testing was used for experiment. The dimension of cavity is shown in Figure 5a. The melt flow thickness varied from 0.1 to 0.5 mm. The injection molding experiment was carried out with PA6/GF30% plastic and the molding parameters are shown in Table 3. For the common injection molding cycle, the mold temperature should be set in the range of 20–80 °C; however, with the thin wall product as in this case, to fill the cavity, the mold temperature must be set as high as the system can tolerate. This set up allows for easy flow due to the reduction in the freeze layer of the melt flow [3]. However, when the mold temperature is high, energy is inevitably wasted, and other problems occur such as warpage or flashing. To avoid these problems, local mold temperature control is presented in this paper. Instead of maintaining the entirety of the mold plate at the high

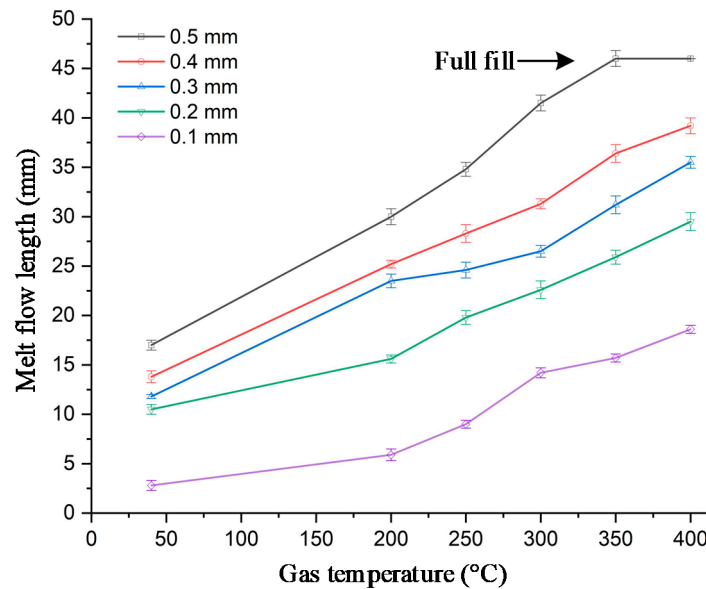
temperature, local mold temperature control was achieved for the cavity area by applying local air pre-heating at the beginning of the molding cycle. The high temperature at the gate area reduced the pressure drop of the melt flow when it passed the area [10]. Figure 7 shows the cavity plate with an insert, which included the cavity area and the gate area. In the same manner as the above structure, the gate area was re-designed with a steel insert to improve the heating efficiency. This insert had a dimension of 77 mm × 77.4 mm × 5 mm. To observe the influence of gas temperature on the heating process, gas with temperatures of 200, 250, 300, 350, and 400 °C were used with a heating time of 20 s. To verify the heating efficiency as well as the ability to perform local heating, an infrared camera was used to obtain the temperature distribution at the end of the heating step. After that, the real molding cycle was achieved with the parameters shown in Table 3. For each gas temperature, the molding cycle was operated for 20 cycles to stabilize all of the systems; then, the product of the next 10 cycles was collected to compare the melt flow lengths. Figure 14 shows the temperature distribution and the melt flow pattern with different gas temperatures. The gate temperature and melt flow length were measured. They are shown in Table 3. The temperature distribution shows that the high temperature was focused only at the gate area, which was heated by the hot gas for 20 s. Therefore, the mold plate was maintained at the low temperature in all molding cycles, which reduced the warpage and flashing, as well as the amount of energy wasted when compared with the common case. In the case without heating, the melt flow pattern shows that the melt length was 17 mm when the gate temperature was only about 50 °C. With the In-GMTC, when the gas temperature increased from 200 to 400 °C, the gate temperature varied from 50 to 216 °C with a heating time of 20 s. In other research, when the mold temperature was higher than the glass transition temperature, the melt flowed easily [16–22]. Thus, in this paper, Figure 14 shows that when the gas temperature was higher than 350 °C, the cavity was completely filled. In addition, these results for a 0.5 mm part thickness also prove that the In-GMTC leads to a large improvement in the melt flow length for the thin wall injection molding product—an increased melt flow length from 36.9% to 100% (fully filled) was observed when the mold plate was maintained at approximately a common temperature. The filling ability of PA6/GF30% for other part thicknesses was compared, as shown in Figure 15. In general, these results show that the In-GMTC method has a positive influence on the flow ability of PA6/30%GF, which was verified with flow with part thicknesses of 0.1–0.5 mm.

**Table 3.** The experimental results of an internal gas-assisted mold temperature control (In-GMTC) for the melt flow length of polyamide 6 reinforced with 30 wt.% glass fiber (PA6/GF30%).

Heating Results.	Part Thickness	Hot Gas Temperature (°C)					
		Without Heating	200	250	300	350	400
Melt flow length (mm) (percent filling)	0.5 mm	17 (36.9%)	30 (65.2%)	34.8 (75.6%)	41.5 (90.2%)	46 (100%)	46 (100%)
	0.4 mm	13.8 (30.0%)	25.2 (54.8%)	28.3 (61.5%)	31.3 (68.0%)	36.4 (79.1%)	39.2 (85.2%)
	0.3 mm	11.8 (25.7%)	23.5 (51.1%)	24.6 (53.5%)	26.5 (57.6%)	31.2 (67.8%)	35.5 (77.2%)
	0.2 mm	10.5 (22.8%)	15.6 (33.9%)	19.8 (43.0%)	22.6 (49.1%)	25.9 (56.3%)	29.5 (64.1%)
	0.1 mm	2.8 (6.1%)	5.9 (12.8%)	9.0 (19.6%)	14.2 (30.9%)	15.7 (34.1%)	18.6 (40.4%)



**Figure 14.** The melt flow length of a 0.5 mm part thickness with and without In-GMTC under different hot gas temperatures.



**Figure 15.** The melt flow length and gate temperature under different gas temperatures for In-GMTC.

#### 4. Conclusions

In this study, an internal gas-assisted mold temperature control (In-GMTC) under different flow thicknesses ( $t$ ) (0.5, 1.0, 1.5, and 2.0 mm) and a gas temperature that varied from 200 to 400 °C was applied to achieve rapid mold surface temperature control. Then, the In-GMTC was applied to verify the melt flow length of PA6/GF30% material in the thin wall injection molding cycle. Based on the results, the following conclusions were obtained:

- The influence of the insert thickness on the heating process was unclear. For a small heating area, a thinner stamp provided a higher heating rate. The heating rate was about 6.5 °C/s over 20 s. However, for the first 2 s, an extremely high heating rate was observed—24.5 °C/s.
- In combination with the insert thickness, the gas temperature is an important parameter, as it has a large impact on the heating rate, as well as the temperature difference at the cavity surface. The temperature differences along the center line of the stamp were 54.2, 79.1, and 85 °C with inlet temperatures of 200, 300, and 400 °C, respectively.

- The results for the temperature distribution show that the highest temperature was located at the top of stamp (sensor S1), which was closest to the hot gas gate, and the temperature was lower at the bottom of the stamp. This kind of distribution is more favorable than those of previous research on the internal GMTC, which often obtained unbalanced temperatures between two sides of the cavity area.
- Using the ANSYS software with the CFX module, the heating process by In-GMTC could be predicted with good accuracy. The comparison between the simulation and experiment proved that because the heating method in this paper was used in the private volume, the simulation and the experimental results show good agreement.
- The application of In-GMTC for the real molding cycle shows that the melt flow length was clearly improved when the In-GMTC was used at the back of the mold insert, which increased the melt flow length from 36.9% to 100% (fully filled) when the mold plate was maintained at approximately a common temperature. The filling ability of PA6/GF30% with other part thicknesses was explored, and the results show that the In-GMTC method has a positive influence on the flow ability of PA6/GF30%, which was verified for part thicknesses of 0.1–0.5 mm.

**Author Contributions:** Conceptualization, T.T.D. and P.S.M.; funding acquisition, T.T.D. and P.S.M.; investigation, P.S.M. and T.M.T.U.; project administration, T.T.D. and P.S.M.; supervision, T.T.D., and P.S.M.; visualization, T.T.D., P.S.M., and T.M.T.U.; writing—original draft, P.S.M. and T.M.T.U.; writing—review and editing, T.T.D. and P.S.M. All authors have read and agreed to the published version of the manuscript.

**Funding:** This research was funded by the Ministry of Education and Training, project Grant No. B2020-SPK-01, and hosted by Ho Chi Minh City University of Technology and Education, Vietnam.

**Institutional Review Board Statement:** Not applicable.

**Informed Consent Statement:** Not applicable.

**Data Availability Statement:** The data used to support the findings of this study are available from the corresponding author upon request.

**Acknowledgments:** The authors thank Bui Duc Duan, Nguyen Hoai Nam, Hoang Thien Bao, Tran Van Duy, Vo Son Lam, Hoang Le Minh Quan, and Nguyen Huynh Nam Huy for their assistance with and discussions surrounding the experiment and simulation.

**Conflicts of Interest:** The authors declare no conflict of interest.

## References

1. Sykutera, D.; Czyżewski, P.; Szewczykowski, P. The Microcellular Structure of Injection Molded Thick-Walled Parts as Observed by In-Line Monitoring. *Materials* **2020**, *13*, 5464. [[CrossRef](#)] [[PubMed](#)]
2. Sobolčiak, P.; Abdulgader, A.; Mrlik, M.; Popelka, A.; Abdala, A.A.; Aboukhlewa, A.; Karkri, M.; Kiepfner, H.; Bart, H.-J.; Krupa, I. Thermally Conductive Polyethylene/Expanded Graphite Composites as Heat Transfer Surface: Mechanical, Thermo-Physical and Surface Behavior. *Polymers* **2020**, *12*, 2863. [[CrossRef](#)] [[PubMed](#)]
3. Weng, C.; Li, J.; Lai, J.; Liu, J.; Wang, H. Investigation of Interface Thermal Resistance between Polymer and Mold Insert in Micro-Injection Molding by Non-Equilibrium Molecular Dynamics. *Polymers* **2020**, *12*, 2409. [[CrossRef](#)]
4. González-Balderas, R.M.; Felix, M.; Bengoechea, C.; Guerrero, A.; Orta Ledesma, M.T. Influence of Mold Temperature on the Properties of Wastewater-Grown Microalgae-Based Plastics Processed by Injection Molding. *Algal Res.* **2020**, *51*, 102055. [[CrossRef](#)]
5. Sánchez, R.; Martínez, A.; Mercado, D.; Carbonel, A.; Aisa, J. Rapid Heating Injection Moulding: An Experimental Surface Temperature Study. *Polym. Test.* **2021**, *93*, 106928. [[CrossRef](#)]
6. Ronkay, F.; Molnar, B.; Dogossy, G. The Effect of Mold Temperature on Chemical Foaming of Injection Molded Recycled Polyethylene-Terephthalate. *Thermochim. Acta* **2017**, *651*, 65–72. [[CrossRef](#)]
7. Li, K.; Yan, S.-L.; Pan, W.-F.; Zhao, G. Optimization of Fiber-Orientation Distribution in Fiber-Reinforced Composite Injection Molding by Taguchi, Back Propagation Neural Network, and Genetic Algorithm–Particle Swarm Optimization. *Adv. Mech. Eng.* **2017**, *9*. [[CrossRef](#)]
8. Zhang, H.; Zhang, N. Polymer Micro Injection Molding. *Ref. Modul. Mater. Sci. Mater. Eng.* **2021**. [[CrossRef](#)]
9. Wu, C.-H.; Chen, W.-S. Injection Molding and Injection Compression Molding of Three-Beam Grating of DVD Pickup Lens. *Sens. Actuators A Phys.* **2006**, *125*, 367–375. [[CrossRef](#)]

10. Li, K.; Huang, X.; Chen, Q.; Xu, G.; Xie, Z.; Wan, Y.; Gong, F. Flexible Fabrication of Optical Glass Micro-Lens Array by Using Contactless Hot Embossing Process. *J. Manuf. Process.* **2020**, *57*, 469–476. [[CrossRef](#)]
11. Lee, J.H.; Park, S.H.; Kim, S.H.; Ito, H. Replication and Surface Properties of Micro Injection Molded PLA/MWCNT Nanocomposites. *Polym. Test.* **2020**, *83*, 106321. [[CrossRef](#)]
12. Murata, Y.; Kanno, R. Effects of Heating and Cooling of Injection Mold Cavity Surface and Melt Flow Control on Properties of Carbon Fiber Reinforced Semi-Aromatic Polyamide Molded Products. *Polymers* **2021**, *13*, 587. [[CrossRef](#)] [[PubMed](#)]
13. Vázquez, M.; Paull, B. Review on Recent and Advanced Applications of Monoliths and Related Porous Polymer Gels in Micro-Fluidic Devices. *Anal. Chim. Acta* **2010**, *668*, 100–113. [[CrossRef](#)] [[PubMed](#)]
14. Venkatesh, G.; Ravi Kumar, Y.; Raghavendra, G. Comparison of Straight Line to Conformal Cooling Channel in Injection Molding. *Mater. Today Proc.* **2017**, *4*, 1167–1173. [[CrossRef](#)]
15. Lucchetta, G.; Fiorotto, M.; Bariani, P.F. Influence of Rapid Mold Temperature Variation on Surface Topography Replication and Appearance of Injection-Molded Parts. *CIRP Ann.* **2012**, *61*, 539–542. [[CrossRef](#)]
16. Guilong, W.; Guoqun, Z.; Huiping, L.; Yanjin, G. Analysis of Thermal Cycling Efficiency and Optimal Design of Heating/Cooling Systems for Rapid Heat Cycle Injection Molding Process. *Mater. Des.* **2010**, *31*, 3426–3441. [[CrossRef](#)]
17. Huang, M.-S.; Huang, Y.-L. Effect of Multi-Layered Induction Coils on Efficiency and Uniformity of Surface Heating. *Int. J. Heat Mass Transf.* **2010**, *53*, 2414–2423. [[CrossRef](#)]
18. Mrozek, K.; Muszyński, P.; Poszwa, P. Application of Magnetic Concentrator for Improvement in Rapid Temperature Cycling Technology. *Polymers* **2020**, *13*, 91. [[CrossRef](#)]
19. Chen, S.-C.; Jong, W.-R.; Chang, Y.-J.; Chang, J.-A.; Cin, J.-C. Rapid Mold Temperature Variation for Assisting the Micro Injection of High Aspect Ratio Micro-Feature Parts Using Induction Heating Technology. *J. Micromech. Microeng.* **2006**, *16*, 1783–1791. [[CrossRef](#)]
20. Sung, Y.-T.; Hwang, S.-J.; Lee, H.-H.; Huang, D.-Y. Study on Induction Heating Coil for Uniform Mold Cavity Surface Heating. *Adv. Mech. Eng.* **2014**, *6*, 349078. [[CrossRef](#)]
21. Yao, D.; Kimerling, T.E.; Kim, B. High-Frequency Proximity Heating for Injection Molding Applications. *Polym. Eng. Sci.* **2006**, *46*, 938–945. [[CrossRef](#)]
22. Kim, B.H.; Yao, D. Method for Rapid Mold Heating and Cooling. US Patent 684645, 25 January 2005.
23. Chen, S.-C.; Chien, R.-D.; Lin, S.-H.; Lin, M.-C.; Chang, J.-A. Feasibility Evaluation of Gas-Assisted Heating for Mold Surface Temperature Control during Injection Molding Process. *Int. Commun. Heat Mass Transf.* **2009**, *36*, 806–812. [[CrossRef](#)]
24. Chang, J.A. Investigation on the Establishment and Analyses of Rapid Mold Surface Temperature Control Using Gas-Assisted Heating. Ph.D. Thesis, Chung Yuan Christian University, Chung Yuan, Taiwan, 2008.
25. Chen, S.-C.; Lin, C.-Y.; Chang, J.-A.; Minh, P.S. Gas-Assisted Heating Technology for High Aspect Ratio Microstructure Injection Molding. *Adv. Mech. Eng.* **2013**, *5*, 282906. [[CrossRef](#)]
26. Chen, S.-C.; Chang, Y.-J.; Chang, J.-A.; Peng, H.-S.; Wang, Y.-C. Dynamic Mold Temperature Control Using Gas-Assisted Heating and Its Effect on the Molding Replication Qualities of Micro Channels. In Proceedings of the ASME 2008 International Manufacturing Science and Engineering Conference, Evanston, IL, USA, 7–10 October 2008; Volume 2. [[CrossRef](#)]
27. Minh, P.S.; Do, T.T.; Uyen, T.M.T. The Feasibility of External Gas-Assisted Mold-Temperature Control for Thin-Wall Injection Molding. *Adv. Mech. Eng.* **2018**, *10*, 168781401880610. [[CrossRef](#)]
28. The Nhan, P.; Do, T.T.; Anh Son, T.; Son Minh, P. Study on External Gas-Assisted Mold Temperature Control for Improving the Melt Flow Length of Thin Rib Products in the Injection Molding Process. *Adv. Polym. Technol.* **2019**, *2019*, 1–17. [[CrossRef](#)]
29. The Uyen, T.M.; Truong Giang, N.; Do, T.T.; Anh Son, T.; Son Minh, P. External Gas-Assisted Mold Temperature Control Improves Weld Line Quality in the Injection Molding Process. *Materials* **2020**, *13*, 2855. [[CrossRef](#)]
30. Giang, N.T.; Minh, P.S.; Son, T.A.; Uyen, T.M.T.; Nguyen, T.-H.; Dang, H.-S. Study on External Gas-Assisted Mold Temperature Control with the Assistance of a Flow Focusing Device in the Injection Molding Process. *Materials* **2021**, *14*, 965. [[CrossRef](#)] [[PubMed](#)]



Article

# Flows of Linear Polymer Solutions and Other Suspensions of Rod-like Particles: Anisotropic Micropolar-Fluid Theory Approach

Vladimir Shelukhin <sup>1,2</sup><sup>1</sup> Lavrentyev Institute of Hydrodynamics, 630090 Novosibirsk, Russia; shelukhin@list.ru<sup>2</sup> Mathematical Department, Novosibirsk State University, 630090 Novosibirsk, Russia

**Abstract:** We formulate equations governing flows of suspensions of rod-like particles. Such suspensions include linear polymer solutions, FD-virus, and worm-like micelles. To take into account the particles that form and their rotation, we treat the suspension as a Cosserat continuum and apply the theory of micropolar fluids. Anisotropy of suspensions is determined through the inclusion of the microinertia tensor in the rheological constitutive equations. We check that the model is consistent with the basic principles of thermodynamics. In addition to anisotropy, the theory also captures gradient banding instability, coexistence of isotropic and nematic phases, sustained temporal oscillations of macroscopic viscosity, shear thinning and hysteresis. For the flow between two planes, we also establish that the total flow rate depends not only on the pressure gradient, but on the history of its variation as well.

**Keywords:** suspension; rodlike particles; rheology; micropolar fluids; anisotropy; hysteresis

**Citation:** Shelukhin, V. Flows of Linear Polymer Solutions and Other Suspensions of Rod-like Particles: Anisotropic Micropolar-Fluid Theory Approach. *Polymers* **2021**, *13*, 3679. <https://doi.org/10.3390/polym13213679>

Academic Editors: Célio Bruno Pinto Fernandes, Salah Aldin Faroughi, Luís L. Ferrás and Alexandre M. Afonso

Received: 14 September 2021

Accepted: 16 October 2021

Published: 25 October 2021

**Publisher's Note:** MDPI stays neutral with regard to jurisdictional claims in published maps and institutional affiliations.



**Copyright:** © 2021 by the author. Licensee MDPI, Basel, Switzerland. This article is an open access article distributed under the terms and conditions of the Creative Commons Attribution (CC BY) license (<https://creativecommons.org/licenses/by/4.0/>).

## 1. Introduction

There is a class of complex fluids which can be considered as suspensions of rod-like particles. Examples include linear polymer solutions, worm-like micelles, FD-virus, liquid crystals, etc. Such a class enjoys interesting properties like anisotropy [1], gradient and vorticity banding [2–4], shear banding instabilities [5], transition between isotropic and nematic phases [6], and cluster formation [7,8].

Here, we formulate a new mathematical model which is good for concentrated suspensions and show that it predicts anisotropy and some other properties of suspensions of rod-like particles. To this end, we study Poiseuille-like shear flows. The practice of pumping oil in pipelines shows that the total oil flux can depend not only on the pressure gradient, but on the history of pumping as well [9]. We establish that the developed model captures such an effect and show its relationship with the hysteresis phenomenon.

Studies of rodlike particles flow in fluids go back to Jeffrey's work on interactions of a floating isolated ellipsoid with unbounded linear shear fluid flow [10]. It turns out that such a particle periodically rotates in Jeffrey's orbits, which depend on the geometry of the particle and its initial orientation. Jeffrey's approach was developed further in a number of kinematic models [11,12], which include equations both for particle mass centre and for the direction vector with the help of a third rank shape tensor. Available experiments [13,14] confirmed applicability of the generalized Jeffery equations. Such an approach formed basis for extensions accounting for rod–rod interactions [15,16] and for the prediction fibre alignment distributions in moulded parts [17]. Equations proposed in [18] also allow for governing particles motion in a simplified situation where the rod orientation is restricted to the plane spanned by the direction of shear and the direction of gravity.

In a number of studies, the search for the rheology of suspensions of rodlike particles is reduced to establishing the relationship between stress and rate of strain in shear flows. In [19], starting from experiments with FD-viruses, it was studied how viscosity depends



on concentration, shear rate and ionic strength. An expression for viscosity was derived in [20] with the use of friction coefficients parallel and perpendicular to the rod axis. We refer the reader to detailed description of viscosity representation formulas to [1,19,21]; the viscosity dependence on shear rate is also discussed there.

Our approach is different. We use methods of mechanics of continua by applying conservation laws only and not involving the concept of particle direction. To take into account particle rotation and form, we apply the theory of micropolar fluids, which allows for particle microinertia [22]. According to this theory, which is a part of rational mechanics, any infinitesimal volume contains sufficiently many particles. This is why such an approach is applicable for suspensions with a high concentration of particles. As is proved within the micropolar fluid theory in [23], it is due to particle rotation that the Segre–Silberberg effect occurs. Such an effect is known as a tubular pinch phenomenon, stating that particles tend to migrate towards a concentric annular region for the laminar flow of neutrally buoyant dilute suspension of rigid spheres through a circular tube [24]. There is one more effect caused by particle rotation and rotational diffusion. This is the separation of particles when flowing between two concentric rotating cylinders [25].

The micropolar fluid theory allows for intrinsic rotations and micro-inertia thanks to the concept of the Cosserat continuum where each material point is treated as a rigid body [26]. We formulate anisotropic constitutive law by including the micro-inertia tensor into stress/rate of strain relationships. Such an idea of anisotropy was first formulated in [27]. In a great number of papers, rotation of the particles is neglected and the anisotropy is taken into account by using the differences of normal stresses [28].

In the micro-polar fluid theory allowing for internal spins, stress tensor loses symmetry, couple stress appears, and the angular momentum equation should be included into conservation laws. Formulation of rheological constitutive laws in the present paper involves introduction of new viscosities both relative to the Cauchy stress tensor and to the couple stress tensor. Skew-symmetric and anisotropic viscosities are introduced in addition to the common shear viscosity, which we call here symmetric viscosity. While there are experiments [29] and theories [25] to determine the skew-symmetric viscosity, the question of measuring the anisotropic viscosity remains open. We cannot quantitatively confirm our equations by three-dimensional experiments, since the calculations were carried out on the basis of one-dimensional flows. However, we prove that it is precisely due to the anisotropic viscosity that these equations capture such effects as hysteresis, shear gradient banding instability and phase transition.

The flow of short polymer chains in the channels can be regarded as an example of the applicability of the method outlined in this work. The flow of such polymers between graphite surfaces is studied in [30] by the molecular dynamic simulation technique. It is established there that the polymer chains exhibit preferential alignment of oligomers parallel to the surfaces with increasing shear rate. Though in the present paper it is assumed that rods lie in the plane orthogonal to the bounding planes, we predict like in [30] that the apparent viscosity shows an oscillatory behaviour and its variation versus the shear rate corresponds to the shear thinning phenomenon. We perform calculations of the simple flow depending on one variable only; nevertheless, we capture appearance and instability of the nematic phase. More complicated phase transition was addressed in [31] for colloidal suspensions in water; the nucleation of a kagom lattice from solution was detected.

The goal of Section 2 is to remind foundations of the micropolar fluid theory and formulate conservation and constitutive laws obeying the basic principles of thermodynamics. In Section 3, we derive equations for one-dimensional Poiseuille-like shear flows. Finally, in Section 4, we perform calculations explaining different phenomena. In addition to anisotropy, the calculations predict gradient banding instability, phase transition between isotropic and nematic phases, sustained temporal oscillations of macroscopic viscosity, shear thinning and hysteresis. For the flow between two planes, we also establish that the total flow rate depends not only on the pressure gradient, but on the history of its variation as well.

## 2. Anisotropic Micropolar Fluids

We remind basic notions of the micro-polar fluid theory. Given a material point labelled by the Lagrangian coordinate-vector  $\xi$ , the position vector  $\mathbf{x}(t, \xi)$  at the time instant  $t$  in the three dimensional Euclidean space jointly with orthogonal director-vectors  $\mathbf{d}_i(t, \xi), i = 1, 2, 3$ , are assigned to such a point to treat it as a rigid body. Orientation of  $\mathbf{d}_i$  is controlled by an orthogonal tensor  $Q(t, \xi)$ :

$$\mathbf{d}_i(t, \xi) = Q(t, \xi)\mathbf{d}_i(0, \xi), \quad Q^*Q = QQ^* = I.$$

Here,  $I$  is the identity matrix with the elements  $\delta_j^i$ ,  $Q^*$  is the adjoint matrix,  $(Q^*)_{ij} = Q_{ji}$ . The skew-symmetric tensor  $\Omega(t, \mathbf{x}) = Q_t Q^*$  defines the particle's rotation with the angular velocity

$$\boldsymbol{\omega}(t, \mathbf{x}) = \mathbf{e}_i \times (\Omega \mathbf{e}_i) / 2 = \boldsymbol{\epsilon} : \Omega / 2, \quad (\Omega \mathbf{a})_i = \Omega_{ij} a_j \forall \mathbf{a} \in \mathbb{R}^3,$$

where  $\{\mathbf{e}_i\}_1^3$  is an orthonormal basis in  $\mathbb{R}^3$  and  $\boldsymbol{\epsilon}$  is the Levi-Civita third order tensor,

$$\boldsymbol{\epsilon}(\mathbf{a}, \mathbf{b}, \mathbf{c}) = \mathbf{a} \cdot (\mathbf{b} \times \mathbf{c}), \quad \mathbf{e}_i \times \mathbf{e}_j = \epsilon_{sij} \mathbf{e}_s, \quad \epsilon_{sij} = \boldsymbol{\epsilon}(\mathbf{e}_s, \mathbf{e}_i, \mathbf{e}_j), \quad (\boldsymbol{\epsilon} : \Omega)_i = \epsilon_{ijk} \Omega_{jk}.$$

Given the velocity field  $\mathbf{v}(t, \mathbf{x}) = \mathbf{x}_t(t, \xi)$ , we introduce the rate of strain tensors [22].

$$B = \nabla \mathbf{v} - \Omega, \quad A = \nabla \boldsymbol{\omega},$$

where  $(\nabla \mathbf{v})_{ij} = \partial v_i / \partial x_j$ . Observe that both  $B$  and  $A$  are objective relative to the change of frame of references.

Let  $\rho, \mathbf{s}, T$  and  $N$  stand for the mass density, the specific internal spin, the Cauchy stress tensor and the angular moment tensor, respectively. We introduce the material derivative  $\dot{\rho}$  (or  $d\rho/dt$ ) related to the velocity field  $\mathbf{v}$  as follows

$$\dot{\rho} = \frac{\partial \rho}{\partial t} + v_i \frac{\partial \rho}{\partial x_i} \quad \text{or} \quad \dot{\rho} = \frac{\partial \rho}{\partial t} + (\mathbf{v} \cdot \nabla) \rho. \tag{1}$$

Conservation laws of mass, momentum and angular momentum are given by the equations

$$\dot{\rho} + \rho \operatorname{div} \mathbf{v} = 0, \tag{2}$$

$$\rho \dot{\mathbf{v}} = \operatorname{div} T + \rho \mathbf{f}, \tag{3}$$

$$\rho \dot{\mathbf{s}} = \operatorname{div} N - \boldsymbol{\epsilon} : T + \rho \mathbf{l}, \tag{4}$$

where  $\mathbf{f}$  is the mass force density,  $\mathbf{l}$  is the mechanical couple density, and

$$(\operatorname{div} T)_i = \partial T_{ij} / \partial x_j.$$

Observe that the stress tensor  $T$  is not symmetric. Given an orthonormal basis  $\{\mathbf{e}_i\}_1^3$ , the vector

$$\mathbf{t} = \mathbf{e}_i \times (T \cdot \mathbf{e}_i) = \boldsymbol{\epsilon} : T$$

does not depend on the choice of the basis and it is a stress symmetry defect measure in the sense that the equality  $\mathbf{t} = 0$  implies  $T^* = T$  and vice versa. By the definition of  $\mathbf{t}$ , we have the formula

$$\mathbf{t} \cdot \boldsymbol{\omega} = T : \Omega. \tag{5}$$

The internal specific spin is defined by the formula  $\mathbf{s} = J\boldsymbol{\omega}$ , where the symmetric inertia tensor  $J[\text{cm}^2]$  obeys the identity [22]

$$\dot{J} - \Omega J + J \Omega = 0. \tag{6}$$

Before proceeding to constitutive laws, we address the thermodynamics issue. Given a specific internal energy  $e$ , the total energy  $E = \mathbf{e} + \mathbf{v} \cdot \mathbf{v}/2 + \mathbf{s} \cdot \boldsymbol{\omega}/2$  satisfies the equation [32]

$$\rho \dot{E} = \text{div} (T^* \mathbf{v} + N^* \boldsymbol{\omega} - \mathbf{q}) + \rho \mathbf{f} \cdot \mathbf{v} + \rho \mathbf{l} \cdot \boldsymbol{\omega}, \tag{7}$$

where  $\mathbf{q}$  is the heat flux obeying the Fourier law  $\mathbf{q} = -\kappa \nabla \theta$ , with  $\kappa$  standing for the heat conductivity. Generally, internal energy  $e$  depends on  $\rho, \eta$  and  $J, e = e(\rho, \eta, J)$ , where  $\eta$  is the specific entropy. It is common knowledge that absolute temperature and pressure are defined by the derivatives  $\theta = \partial e / \partial \eta, p = \rho^2 \partial e / \partial \rho$  respectively [33]. We calculate that

$$\dot{\mathbf{e}} = \mathbf{e}_\rho \dot{\rho} + \mathbf{e}_\eta \dot{\eta} + \nabla_j \mathbf{e} : \dot{J}, \quad \text{where} \quad \nabla_j \mathbf{e} : \dot{J} = \left( \dot{J}_{ij} \frac{\partial}{\partial J_{ij}} \right) \mathbf{e}.$$

From the rheological point of view, the internal energy  $e(\rho, \eta, J)$  should be an isotropic function of  $J$ . Hence,  $\nabla_j \mathbf{e}$  is also an isotropic function of  $J$ ; it implies that [34]

$$\nabla_j \mathbf{e} = \alpha_0 \mathbf{I} + \alpha_1 J + \alpha_2 J^2, \tag{8}$$

where the scalar functions  $\alpha_i$  depend on invariants of  $J$ . Now, it follows from (6) and (8) that  $\nabla_j \mathbf{e} : \dot{J} = 0$ .

We use Equation (6) to calculate that

$$\frac{d}{dt} (\mathbf{s} \cdot \boldsymbol{\omega}) = \dot{\mathbf{s}} \cdot \boldsymbol{\omega} + \mathbf{s} \cdot \dot{\boldsymbol{\omega}} = 2\dot{\mathbf{s}} \cdot \boldsymbol{\omega}.$$

Hence,

$$\rho \dot{E} = \frac{p}{\rho} \dot{\rho} + \rho \theta \dot{\eta} + \rho \dot{\mathbf{v}} \cdot \mathbf{v} + \rho \dot{\mathbf{s}} \cdot \boldsymbol{\omega} = -p \text{div} \mathbf{v} + \rho \dot{\mathbf{v}} \cdot \mathbf{v} + \rho \dot{\mathbf{s}} \cdot \boldsymbol{\omega}. \tag{9}$$

Multiplying Equations (3) and (4) by  $\mathbf{v}$  and  $\boldsymbol{\omega}$ , respectively, we arrive at the energetic equality

$$\rho \mathbf{v} \cdot \dot{\mathbf{v}} + \rho \boldsymbol{\omega} \cdot \dot{\mathbf{s}} = \text{div} (T^* \mathbf{v} + N^* \boldsymbol{\omega}) - T : B - N : A + \rho \mathbf{f} \cdot \mathbf{v} + \rho \mathbf{l} \cdot \boldsymbol{\omega} \tag{10}$$

With  $S$  standing for the viscous part of the stress tensor  $T$ , we write the representation formula  $T = -p\mathbf{I} + S$ . Hence,  $T : B = -p \text{div} \mathbf{v} + S : B$ , where  $T : B = T_{ij} B_{ij}$ . Now, it follows from (7), (9) and (10) that the entropy equation

$$\rho \dot{\eta} + \text{div} \left( \frac{\mathbf{q}}{\theta} \right) = \frac{R}{\theta}, \tag{11}$$

holds, with the function

$$R = S : B + N : A + \frac{\kappa |\nabla \theta|^2}{\theta}$$

standing for the entropy production. The second law of the thermodynamics  $R \geq 0$  can be formulated as

$$S : B + N : A \geq 0. \tag{12}$$

In what follows, we use the notations

$$B_s = \frac{B + B^*}{2}, \quad B_a = \frac{B - B^*}{2}$$

for the symmetric and skew-symmetric parts of  $B$ . We formulate anisotropic constitutive laws as follows:

$$S = 2\mu_s B_s + 2\mu_a B_a + 2\mu_{an} \sigma^2 J B, \quad N = \frac{2\nu}{\sigma^2} A + 2\nu_{an} A J, \tag{13}$$

where  $\mu_s, \mu_a, \mu_{an}, \nu, \nu_{an}$  [g/(cm · s)] are the viscosities and  $\sigma$  [cm<sup>-1</sup>] is the specific particles surface area. The first rheological equation in (13) suggests that the contributions of the symmetric part  $B_s$  and skew-symmetric part  $B_a$  of the rate of strain tensor  $B$  into local stress state are different. The fact that both  $S$  and  $N$  depend on  $J$  implies anisotropy. Such an approach was first formulated in [22]. Observe that the objectivity of the  $S$  and  $N$  results form the objectivity of  $B$ ,  $A$  and  $J$  [22].

Due to the symmetry of  $J$ , one can verify that

$$JB : B = \sum_1^3 \lambda_j |B^* \mathbf{e}_j|^2,$$

where  $\mathbf{e}_j$  and  $\lambda_j$  are the eigenvectors and the eigenvalues of  $J$ . Observe that  $\lambda_j \geq 0$  provided each suspension particle enjoys an axis of rotational symmetry. For such suspensions, we find that

$$S : B = 2\mu_s B_s : B_s + 2\mu_a B_a : B_a + 2\mu_{an} \sigma^2 \sum_1^3 \lambda_j |B^* \mathbf{e}_j|^2 \geq 0.$$

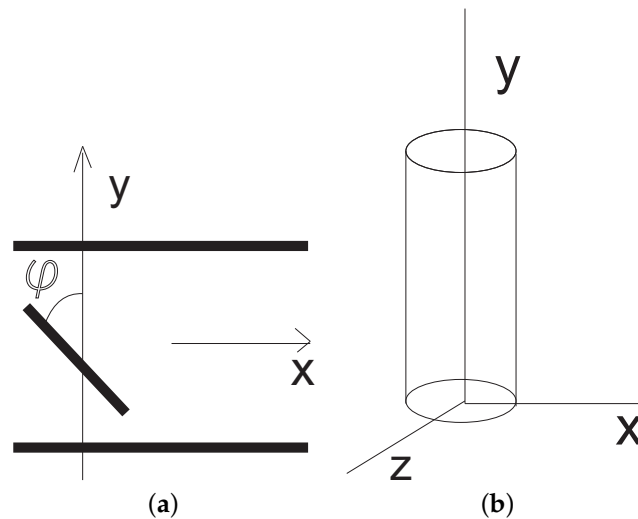
Similarly, one can verify that

$$AJ : J = \sum \lambda_j |A \mathbf{e}_j|^2.$$

Thus, the constitutive laws (13) satisfy the thermodynamic restriction (12), provided the suspension particles are axially symmetric.

### 3. Poiseuille Flows

We consider one-dimensional flows along the horizontal  $x$ -axis in the vertical layer  $|y| < H$  between two parallel planes under the prescribed pressure gradient  $\nabla p = (p_x, 0, 0)$ ,  $p_x(t) < 0$ , Figure 1a. In this case,  $v_2 = v_3 = 0$ ,  $v_1 = v(y, t)$ . We assume that the suspension particles are the rods of the same size; they lie in the plane  $z = 0$  and rotate around the  $z$ -axis. Hence,  $\omega = (0, 0, \omega)$ .



**Figure 1.** (a) Schema of particle's position in one-dimensional flows. (b) The cylinder approximation of the rod-like particle.

Let us describe the micro-inertia tensor  $J$ . First, we consider a cylinder  $V_0$  stretched along the  $y$ -axis with the height  $h$  and the radius  $r$ , Figure 1b. By definition, the inertia tensor  $J(V_0)$  of  $V_0$  is given by the formula

$$J(V_0) = \int_{V_0} |\zeta|^2 \cdot I - \zeta \otimes \zeta d\zeta \quad \text{or} \quad J_{ij}(V_0) = \int_{V_0} |\zeta_k|^2 \delta_{ij} - \zeta_i \zeta_j d\zeta,$$

where  $I$  is the identity matrix and  $\mathbf{a} \otimes \mathbf{b}$  stands for the tensor product of two vectors  $\mathbf{a}$  and  $\mathbf{b}$ ,  $(\mathbf{a} \otimes \mathbf{b})_{ij} = a_i b_j$ . Calculations reveal that

$$J(V_0) = \begin{pmatrix} r^2/4 + h^2/3 & 0 & 0 \\ 0 & r^2/2 & 0 \\ 0 & 0 & r^2/4 + h^2/3 \end{pmatrix}.$$

In the limit as  $r \rightarrow 0$ , we obtain the inertia tensor of the rod particle stretched along the  $y$ -axis:

$$J^0 = \lim_{r \rightarrow 0} J(V_0) = j_0 \begin{pmatrix} 1 & 0 & 0 \\ 0 & 0 & 0 \\ 0 & 0 & 1 \end{pmatrix}, \quad j_0 = h^2/3.$$

Let  $J(V)$  be the inertia tensor of the cylinder  $V$ , which is produced by rotation of  $V_0$  around the  $z$ -axis by the angle  $\varphi$  counted from the axis  $y$  counter-clockwise, see Figure 1a. By definition of the spin  $\mathbf{s}$ , we find that

$$\mathbf{s} = J(V) \cdot \boldsymbol{\omega} = \int_V \mathbf{x} \times (\boldsymbol{\omega} \times \mathbf{x}) \, dx = Q_\varphi J^0 Q_\varphi^* \cdot \boldsymbol{\omega},$$

where  $Q_\varphi$  is the orthogonal matrix such that

$$\Omega = \dot{Q}_\varphi Q_\varphi^*, \quad \Omega \cdot \mathbf{h} = \boldsymbol{\omega} \times \mathbf{h} \forall \mathbf{h}, \quad (Q^*)_{ij} = Q_{ji}, \tag{14}$$

$$Q_\varphi = \begin{pmatrix} \cos \varphi & -\sin \varphi & 0 \\ \sin \varphi & \cos \varphi & 0 \\ 0 & 0 & 1 \end{pmatrix}, \quad \Omega = \begin{pmatrix} 0 & -\omega & 0 \\ \omega & 0 & 0 \\ 0 & 0 & 0 \end{pmatrix}, \tag{15}$$

with “dot” standing for the material derivative (1) related to the velocity vector  $\mathbf{v}$ . Thus,  $J(V) = Q_\varphi J(V_0) Q_\varphi^*$ . In the limit as  $r \rightarrow 0$ , we obtain the inertia tensor  $J(\varphi)$  of the rod particle with the position angle  $\varphi$ :

$$J(\varphi) = Q_\varphi J^0 Q_\varphi^* = j_0 \begin{pmatrix} \cos^2 \varphi & \sin \varphi \cos \varphi & 0 \\ \sin \varphi \cos \varphi & \sin^2 \varphi & 0 \\ 0 & 0 & 1 \end{pmatrix}, \quad \frac{\partial \varphi}{\partial t} = \varphi_t = \omega. \tag{16}$$

Given an initial distribution of particle’s angles  $\varphi_0(y)$ , we denote the initial micro-inertia tensor by  $J_0(y) = J(\varphi_0(y))$ :

$$J|_{t=0} = J_0. \tag{17}$$

For the described one-dimensional flows, the material derivative  $\dot{J}$  reduces to the time derivative  $J_t$ . With the use of Equation (15), (6) can be written as follows:

$$\frac{\partial}{\partial t} J_{11} = -2\omega J_{12}, \quad \frac{\partial}{\partial t} J_{12} = \omega(J_{11} - J_{22}), \quad \frac{\partial}{\partial t} J_{22} = 2\omega J_{12}, \tag{18}$$

and  $J_{ij} = 0$  otherwise. Observe that

$$\frac{\partial J_{ij}}{\partial t} = \frac{\partial J_{ij}}{\partial \varphi} \frac{\partial \varphi}{\partial t} = J'_{ij} \omega, \quad J'_{ij} = \frac{\partial J_{ij}}{\partial \varphi}.$$

Hence, the system (18) is equivalent to

$$J'_{11} = -2J_{12}, \quad J'_{12} = J_{11} - J_{22}, \quad J'_{22} = 2J_{12}, \quad J_{ij}|_{\varphi=\varphi_0} = J_0. \tag{19}$$

One can verify that the matrix  $J$  in (16) solves the system (19).

We calculate the rate of strain tensors and find that

$$\begin{aligned}
 B &= \begin{pmatrix} 0 & v_y + \omega & 0 \\ -\omega & 0 & 0 \\ 0 & 0 & 0 \end{pmatrix}, \quad B^* = \begin{pmatrix} 0 & -\omega & 0 \\ v_y + \omega & 0 & 0 \\ 0 & 0 & 0 \end{pmatrix}, \quad (20) \\
 B_s &= \begin{pmatrix} 0 & v_y/2 & 0 \\ v_y/2 & 0 & 0 \\ 0 & 0 & 0 \end{pmatrix}, \quad B_a = \begin{pmatrix} 0 & v_y/2 + \omega & 0 \\ -v_y/2 - \omega & 0 & 0 \\ 0 & 0 & 0 \end{pmatrix}, \\
 j_0^{-1}JB &= \begin{pmatrix} -\omega \cos \varphi \sin \varphi & \cos^2 \varphi (v_y + \omega) & 0 \\ -\omega \sin^2 \varphi & \cos \varphi \sin \varphi (v_y + \omega) & 0 \\ 0 & 0 & 0 \end{pmatrix}, \\
 A &= \begin{pmatrix} 0 & 0 & 0 \\ 0 & 0 & 0 \\ 0 & \omega_y & 0 \end{pmatrix}, \quad j_0^{-1}AJ = \begin{pmatrix} 0 & 0 & 0 \\ 0 & 0 & 0 \\ \omega_y \cos \varphi \sin \varphi & \omega_y \sin^2 \varphi & 0 \end{pmatrix}, \quad (21)
 \end{aligned}$$

Let us denote

$$\varepsilon_1 = \frac{\mu_a}{\mu_s}, \quad \varepsilon_{20} = \frac{\mu_{an}j_0\sigma^2}{\mu_s}, \quad \varepsilon_{30} = \frac{\nu_{an}j_0\sigma^2}{\nu}, \quad B^0 = B_s + \varepsilon_1 B_a + \varepsilon_{20}JB.$$

Calculations reveal that matrix  $B^0$  is equal to

$$\begin{pmatrix} -\varepsilon_{20}\omega \cos \varphi \sin \varphi & \frac{v_y(1+\varepsilon_1+2\varepsilon_{20}\cos^2 \varphi)}{2} + \omega(\varepsilon_1 + \varepsilon_{20}\cos^2 \varphi) & 0 \\ \frac{v_y(1-\varepsilon_1)}{2} - \omega(\varepsilon_1 + \varepsilon_{20}\sin^2 \varphi) & \varepsilon_{20}\cos \varphi \sin \varphi (v_y + \omega) & 0 \\ 0 & 0 & 0 \end{pmatrix}.$$

We consider incompressible fluids with the assumption  $\rho = \text{const}$ . For one-dimensional flows, the incompressibility condition  $\text{div } \mathbf{v} = 0$  is satisfied automatically. Other conservation laws (3) and (4) become

$$\varphi_t = \omega, \quad \rho v_t = -p_x + \frac{\partial S_{12}}{\partial y}, \quad \rho j_0 \omega_t = \frac{\partial N_{32}}{\partial y} + S_{21} - S_{12}. \quad (22)$$

For one-dimensional flows, the constitutive laws (13) reduce to

$$S_{ij} = 2\mu_s B_{ij}^0, \quad N_{32} = 2\frac{\nu}{\sigma^2} A_{32} + 2\nu_{an}(AJ)_{32}. \quad (23)$$

Observe that

$$S_{21} - S_{12} = 2\mu_s(B_{21}^0 - B_{12}^0), \quad B_{21}^0 - B_{12}^0 = -v_y(\varepsilon_1 + \varepsilon_{20}\cos^2 \varphi) - \omega(2\varepsilon_1 + \varepsilon_{20}).$$

We formulate boundary conditions at  $|y| = H$  as follows:

$$\mathbf{v} = 0, \quad \boldsymbol{\omega} = \frac{\alpha}{2} \nabla \times \mathbf{v}, \quad 0 \leq \alpha \leq 1. \quad (24)$$

The first condition in (24) states that velocity obeys the no-slip condition. The second condition in (24) has the meaning that the micro-rotation  $\boldsymbol{\omega}$  depends linearly on the macro-rotation  $\nabla \times \mathbf{v}/2$  [25].

Let  $V$  and  $T$  stand for the velocity and time reference values. We denote  $\Omega = V/H$  and choose  $T = 1/\Omega$ . We introduce dimensionless variables as follows:

$$S' = \frac{1}{2\mu_s\Omega} S, \quad N' = \frac{H\sigma^2}{2\nu\Omega} N, \quad B'^0 = \frac{B^0}{\Omega}, \quad Re = \frac{H^2\rho\Omega}{\mu_s},$$

$$y' = \frac{y}{H}, v' = \frac{v}{V}, t' = \frac{t}{T}, \omega' = \frac{\omega}{\Omega}, \Pi = \frac{|p_x|H^2}{2V\mu_s}, \gamma = \frac{v}{H^2\mu_s\sigma^2}.$$

In new variables, Equation (22) become

$$\varphi_{t'} = \omega', \quad \frac{Re}{2}v'_{t'} = \Pi + \frac{\partial S'_{12}}{\partial y'}, \quad \frac{Rej_0}{2H^2}\omega'_{t'} = \gamma \frac{\partial N'_{32}}{\partial y'} + S'_{21} - S'_{12}. \tag{25}$$

In what follows, we consider quasi-steady slow flows. Neglecting terms with small Reynolds numbers in (25), we arrive at the equations

$$\varphi_{t'} = \omega', \quad 0 = \Pi + \frac{\partial S'_{12}}{\partial y'}, \tag{26}$$

$$0 = \gamma \frac{\partial}{\partial y'} \left[ \omega'_{y'}(1 + \varepsilon_{30} \sin^2 \varphi) \right] - [v'_{y'}(\varepsilon_1 + \varepsilon_{20} \cos^2 \varphi) + \omega'(2\varepsilon_1 + \varepsilon_{20})], \tag{27}$$

where

$$S'_{12} = \frac{v'_{y'}(1 + \varepsilon_1 + 2\varepsilon_{20} \cos^2 \varphi)}{2} + \omega'(\varepsilon_1 + \varepsilon_{20} \cos^2 \varphi).$$

Because of the symmetry conditions

$$v'(-y', t') = v'(y', t'), \quad \omega'(-y', t') = -\omega'(y', t'), \quad \varphi(-y', t') = \varphi(y', t')$$

we consider flows only in the upper half-layer  $0 < y' < 1$ . In such a case the initial and boundary conditions take the form

$$\varphi|_{t'=0} = \varphi_0(y'), v'(1) = 0, v'_{y'}(0) = 0, \omega'(1) = -0.5\alpha v'_{y'}(1), \omega'(0) = 0. \tag{28}$$

To perform numerical solution, one should fix the dimensionless parameters  $\Pi, \varepsilon_1, \varepsilon_{20}, \varepsilon_{30}, \gamma, \alpha$ .

#### 4. Results of Calculations

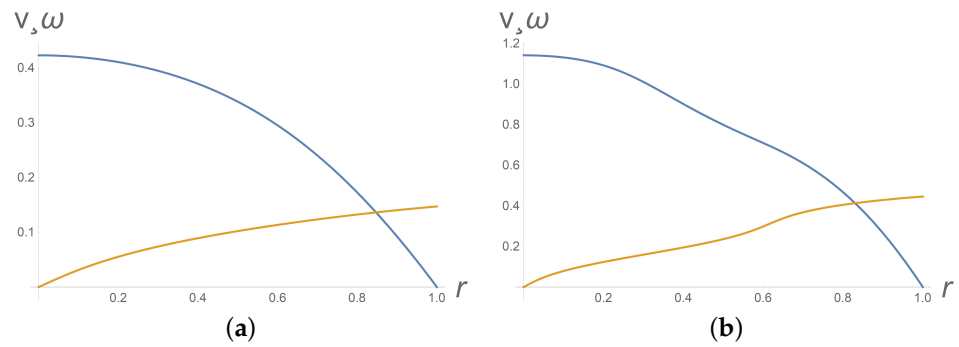
Here, we address the system (26)–(28) by applying the Wolfram Mathematica solver.

It is well known in many complex fluids that a shear banding effect occurs when applied shear stress is above some critical value [4,35,36]. Such a phenomenon is characterized by coexisting bands of different shear rates and /or viscosities. Depending on the directional alignment of the banded structure, there are two types of shear banding for suspensions of rod-like particles: gradient banding and vorticity banding [2–4]. In the case of gradient banding, the flow separates into bands of different shear rates along the gradient direction. With reference to the coordinate system of Figure 1a,  $x$  is the flow direction along the velocity vector  $\mathbf{v} = (v, 0, 0)$ ,  $y$  is the gradient direction along which the flow has non-zero derivative  $\partial v / \partial y$ . The  $z$ -axis is the vorticity direction along the non-zero macro-vorticity vector  $\nabla \times \mathbf{v}$ .

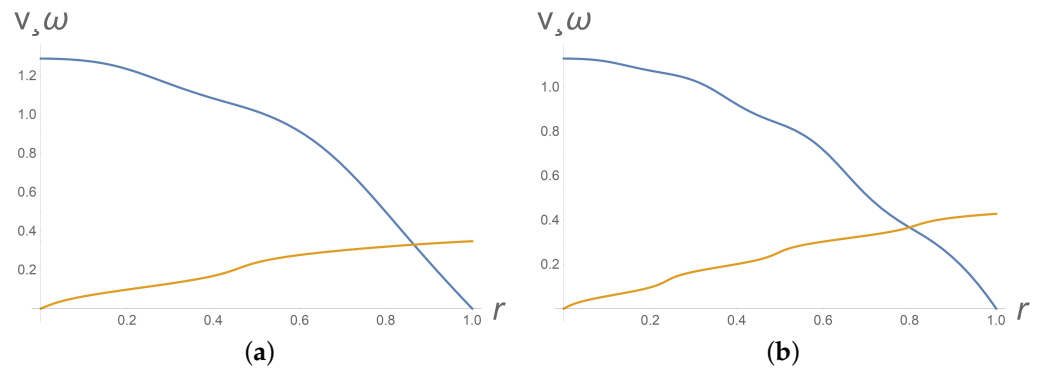
The system (26)–(28) cannot be applied for description of the vorticity banding since the corresponding one-dimensional flow does not depend on the  $z$ -variable. However, calculations reveal that the system (26)–(28) can really capture the gradient banding. Figure 2 depicts appearance of gradient banding when shear stress increases; calculations are performed at  $t = 10$  for

$$\varepsilon_1 = 1, \quad \varepsilon_{20} = 2, \quad \varepsilon_{30} = 2, \quad \gamma = 1.3, \quad \alpha = 0.3, \quad \varphi_0 = 0. \tag{29}$$

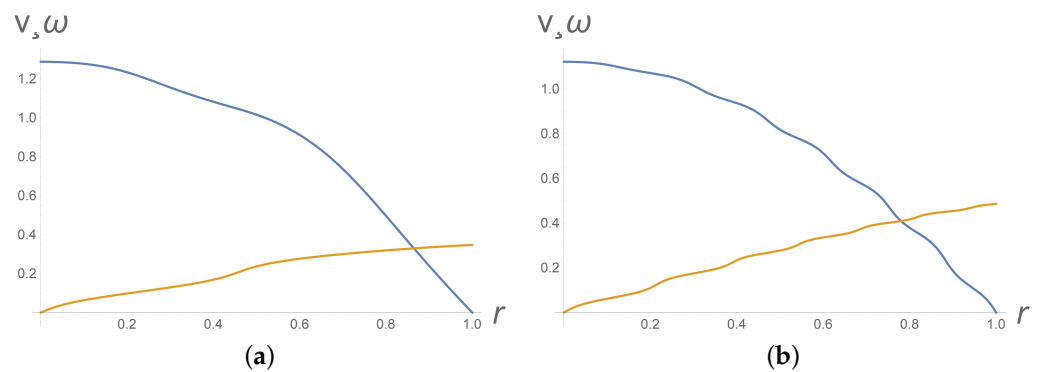
Intervals where  $\varphi(y) = \text{const}$  or  $\omega(y) = \text{const}$  correspond to the nematic phase. The profiles of the intrinsic angular velocity  $\omega$  at Figures 2b and 3 imply appearance and instability of the nematic phase. Figure 4b depicts the phase transition from the isotropic phase to the nematic phase.



**Figure 2.** From top to bottom, profiles of the dimensionless velocity  $v(y)$  and dimensionless micro-spin  $\omega(y)$  on the upper half-layer  $0 < y < 1$  at dimensionless time  $t = 10$  for dimensionless pressure gradient (a)  $\Pi = 0.85$  and (b)  $\Pi = 2.85$ . Gradient banding development is observed at high pressure gradients (b).



**Figure 3.** Gradient banding instability with respect to time. From top to bottom, dimensionless velocity  $v(y)$  and dimensionless micro-spin  $\omega(y)$  profiles at  $\Pi = 2.85$  for different dimensionless times  $t = 15$  (a) and  $t = 25$  (b). Values of other parameters are as in the data list (29).



**Figure 4.** Gradient banding instability with respect to initial particles orientation. From top to bottom, profiles of dimensionless velocity  $v(y)$  and dimensionless micro-spin  $\omega(y)$  at  $\Pi = 2.85$  and at  $t = 15$  for initial  $\varphi_0(y) = 0$  (a) and  $\varphi_0(y) = 4y + 9y^2$  (b). Values of other parameters are as in the data list (29).

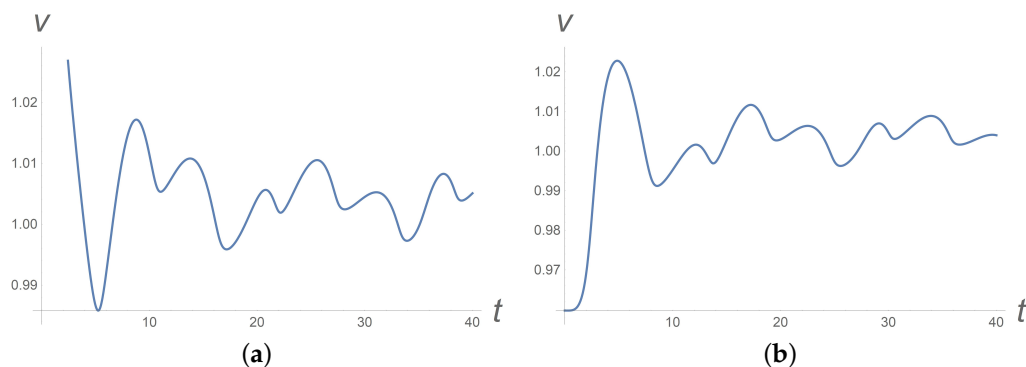
Figure 3 shows gradient banding instability with respect to time. A treatment of time dependent phenomena for worm-like micelles can be found in [5].

It turns out that the gradient banding is also unstable with respect to initial particles orientation. When passing from spatially homogeneous initial orientation of particles  $\varphi_0(y) = 0$  to a spatially heterogeneous orientation (like  $\varphi_0(y) = 4y + 9y^2$ ), the gradient banding effect becomes more pronounced, see Figure 4.

Many shear banding systems display oscillations or irregular fluctuations. Example systems include worm-like micelles [37]. Within the developed anisotropic model, one



can observe a chaotic behaviour of the shear velocity even at a constant applied pressure gradient, see Figure 5. Basically, it is due to anisotropic viscosities in the rheological constitutive laws (13).



**Figure 5.** Time variation of the velocity in the middle of the channel at a constant pressure gradient in dimensionless variables (a) for homogeneous transversal initial particles orientation and (b) for non-homogeneous initial particles orientation along the channel.

Next, we consider questions motivated by oil transportation through pipelines. To optimize pumping, additives are used that change the microstructure of oil. As a result, it is discovered that friction factor can depend not only on oil discharge, but on its prehistory as well [38]. It turns out that the smallest friction losses are achieved by decreasing rather than increasing the flow rate to a predetermined level [9]. Let us show that the developed mathematical model in Section 1 captures such an effect.

First, we establish that the system (26)–(28) does not provide one-to-one correspondence between the pressure gradient  $\Pi$  and the total fluid flux  $Q = 2 \int_0^1 v dy$ . Given a time-dependent pressure gradient  $\Pi(t)$ , one can calculate the corresponding total flux  $Q(t)$ . Let us consider the parametric line

$$\Pi = \Pi_0(1 + \sin \pi t), \quad Q = Q(t), \quad 0 < t < 1, \tag{30}$$

which corresponds to the curve  $\widehat{O, P, L}$  on the  $(\Pi, Q)$ -plane, Figure 6. The lower part  $\widehat{O, A, P}$  of this curve corresponds to the time interval  $0 < t < 1/2$ . Along this part, both  $Q$  and  $\Pi$  grow,  $\Pi_0 < \Pi < 2\Pi_0$ . The top part  $\widehat{P, B, L}$  of the curve corresponds to the time interval  $1/2 < t < 1$ . Along this part, both  $Q$  and  $\Pi$  decrease.

For typical viscous fluids like a power law fluid, there is a one-to-one correspondence between  $\Pi$  and  $Q$ ; as a consequence, the lines  $\widehat{O, P, L}$  and  $\widehat{P, B, L}$  coincide. It is not the case for the anisotropic fluid considered here. Given  $\Pi_*$  satisfying the inequalities  $\Pi_0 < \Pi_* < 2\Pi_0$ , how can one determine a corresponding flux  $Q$ ? It follows from Figure 6 that there are two values  $Q_A$  and  $Q_B$  corresponding to  $\Pi_*$ . Indeed, let us consider the intersection of the vertical line  $\Pi = \Pi_*$  with the curve  $\widehat{O, P, L}$ . On this way we arrive at the points  $A$  and  $B$ :

$$A = (\Pi_*, Q_A), \quad B = (\Pi_*, Q_B).$$

Clearly, there are  $t_A$  and  $t_B$  such that

$$0 < t_A < 1/2 < t_B < 1, \quad \Pi(t_A) = \Pi(t_B) = \Pi_*, \quad Q_A < Q_B, \quad Q_i = Q(t_i),$$

with  $i = A, B$ .

Let us choose the points  $C = (\Pi_C, Q_C)$  and  $D = (\Pi_D, Q_D)$  in such a way that

$$\Pi_C < \Pi_* < \Pi_D.$$

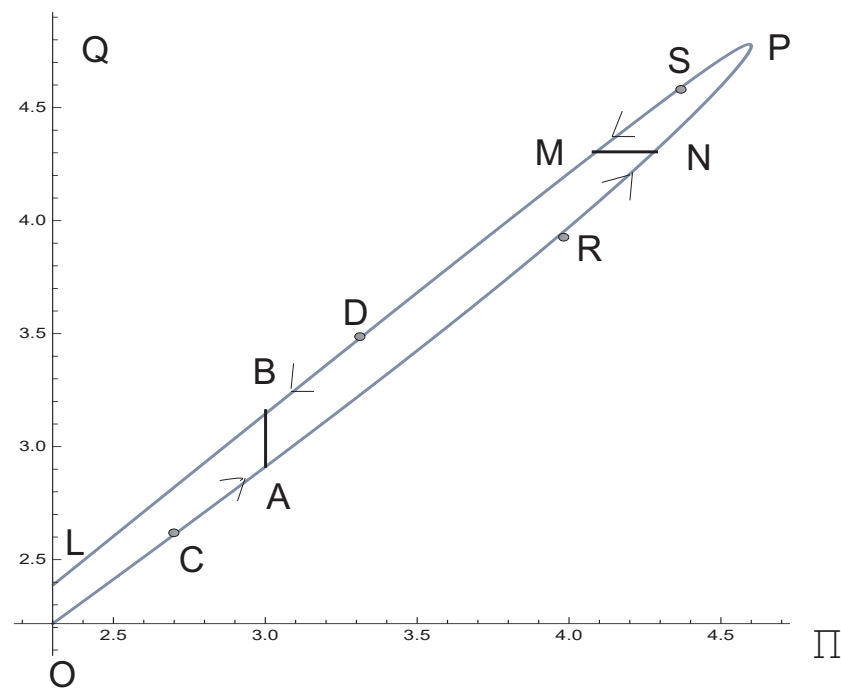
When the value of  $\Pi$  goes from the low value  $\Pi_C$  to  $\Pi_*$ , the value of  $Q$  changes from  $Q_C$  to

$$Q_A = \lim_{\Pi \nearrow \Pi_*} Q(\Pi).$$

When the value of  $\Pi$  goes from the upper value  $\Pi_D$  to  $\Pi_*$ , the value of  $Q$  changes from  $Q_D$  to

$$Q_B = \lim_{\Pi \searrow \Pi_*} Q(\Pi).$$

Thus, total flux depends not only on pressure gradient, but on the evolution history of pressure gradient as well.



**Figure 6.** On the  $(\Pi, Q)$ -plane, the hysteresis loop corresponding to process (30) for rather small  $\epsilon_{20}, \epsilon_{30}$ , with  $\Pi_0 = 2.3$ .

Similarly, we consider determination of  $\Pi$  starting from values of  $Q$ . Again, one should know a prehistory of  $Q$ . Indeed, let us consider a total flux  $Q_*$ , which is between  $Q|_{t=0}$  and  $Q|_{t=1/2}$ . Let us consider the intersection of the horizontal line  $Q = Q_*$  with the hysteresis loop  $\widehat{O, P, L}$ . In this way, we arrive at the points  $N$  and  $M$ :

$$N = (\Pi_N, Q_*), \quad M = (\Pi_M, Q_*).$$

Clearly, there are  $t_N$  and  $t_M$  such that

$$0 < t_N < 1/2 < t_M < 1, \quad Q(t_N) = Q(t_M) = Q_*, \quad \Pi_M < \Pi_N, \quad \Pi_i = \Pi(t_i),$$

with  $i = N, M$ . Let us choose points  $R = (\Pi_R, Q_R)$  and  $S = (\Pi_S, Q_S)$  in such a way that  $Q_R < Q_* < Q_S$ .

If  $Q$  goes from the lower value  $Q_R$  to  $Q_*$  then  $\Pi$  changes from  $\Pi_R$  to

$$\Pi_N = \lim_{Q \nearrow Q_*} \Pi(Q).$$

If  $Q$  goes from the upper value  $Q_S$  to  $Q_*$  then  $\Pi$  changes from  $\Pi_S$  to

$$\Pi_M = \lim_{Q \searrow Q_*} \Pi(Q).$$

Thus, pressure gradient depends not only on total flux, but on the prehistory evolution of total flux as well.

As far as the oil pipelines are concerned, the designed oil flux can be obtained in two ways: by switching from a fast or slow flux. By the developed anisotropic model, the pressure drop to ensure the designed oil flux is less in the first case.

Now, we consider friction losses which play an important role in oil pumping through pipelines. Returning to dimension variables, we remind that the mean velocity  $U$  and the friction factor  $\lambda$  are defined as follows:

$$U = \frac{1}{2H} \int_{-H}^H v(y) dy, \quad |p_x| = \frac{\lambda}{2H} \frac{\rho U^2}{2}.$$

In dimensionless variables, we have

$$U' = \int_0^1 v'(y) dy = \frac{Q}{2}, \quad \Lambda \equiv \frac{Re \cdot \lambda}{8} = \frac{\Pi}{U'^2},$$

where  $\Lambda$  is the reduced friction factor.

To analyse flows on the plane  $(U', \Lambda)$ , we omit the prime indexes. Calculations reveal that, starting from the pressure gradient law

$$\Pi(t) = \Pi_0(1 + \sin \pi t),$$

the curve

$$U = U(t), \quad \Lambda(t) = \frac{\Pi(t)}{U^2(t)}, \quad 0 < t < 1,$$

becomes as is shown in Figure 7. The top part of this curve corresponds to the time interval  $0 < t < 1/2$ . Along this part, both  $U$  and  $\Pi$  grow,  $\Pi_0 < \Pi < 2\Pi_0$ , whereas  $\Lambda$  decreases. The lower part of the curve corresponds to the time interval  $1/2 < t < 1$ . Along this part, both  $U$  and  $\Pi$  decrease, whereas  $\Lambda$  grows. How can one calculate the friction factor  $\Lambda$  corresponding to a designed mean velocity  $U^*$ ? The answer depends on the history; one can attain  $U_*$  by increasing  $U$  or by decreasing  $U$ . Given  $U_*$  lying between  $U_{min} = U|_{t=0}$  and  $U_{max} = U|_{t=1/2}$ , we choose  $t_1$  and  $t_2$  in such a way that

$$0 < t_1 < 1/2 < t_2 < 1, \quad U(t_1) = U(t_2) = U_*.$$

With  $\Lambda_i$  standing for  $\Lambda(t_i)$ , one can conclude from Figure 7 that  $\Lambda_1 > \Lambda_2$  despite the fact that both  $\Lambda_1$  and  $\Lambda_2$  correspond to the same  $U_*$ . Thus,

$$\Lambda_1 = \lim_{U \nearrow U_*} \Lambda(U) = \Lambda|_{U_*-} > \Lambda|_{U_*+} = \lim_{U \searrow U_*} \Lambda(U) = \Lambda_2.$$

Returning to the issue of oil transportation, one can attain the productive regime in two ways by switching from a faster or from a slower flux. After switching to a productive regime, the developed friction loss is less in the first case. Such a conclusion agrees with known in situ data [9].

Consider the stress response to a change in velocity gradient. It follows from the dimensional steady-state Equation (22) that the shear stress  $S_{12}$  is given by the formula

$$S_{12} = p_x y, \quad \tilde{\tau} \equiv -S_{12}|_{y=H} = -p_x H,$$

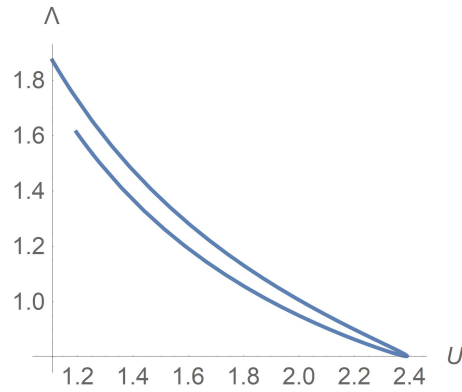
where  $\tilde{\tau}$  is the stress at the upper plane  $y = H$ . Let us calculate the curve  $\tilde{\tau} = \tilde{\tau}(\dot{\gamma}_1)$  where  $\dot{\gamma}_1 = -v'_y|_{y=H}$ . Observe that  $\dot{\gamma}_1$  does not stay for the the shear rate in the micropolar fluid theory. We pass to the dimensionless variables

$$\tau = \frac{\tilde{\tau}}{2\mu_s \Omega} = \Pi, \quad \dot{\gamma} = -v'_y|_{y'=1}, \quad \dot{\gamma}_1 = \Omega \dot{\gamma}.$$

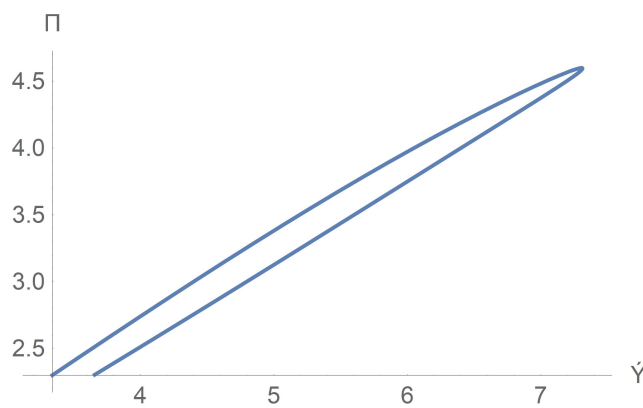
Performing calculation of the parametric curve

$$\Pi = \Pi_0(1 + \sin \pi t), \quad \dot{\gamma} = \dot{\gamma}(t), \quad 0 < t < 1, \tag{31}$$

we arrive at the hysteresis loop  $\tau = \tau(\dot{\gamma})$ , which is shown in Figure 8. Thus, there is no one-to-one correspondence between velocity gradient and shear stress in shear flows. Such an effect has been seen in worm-like micelle solutions [39].

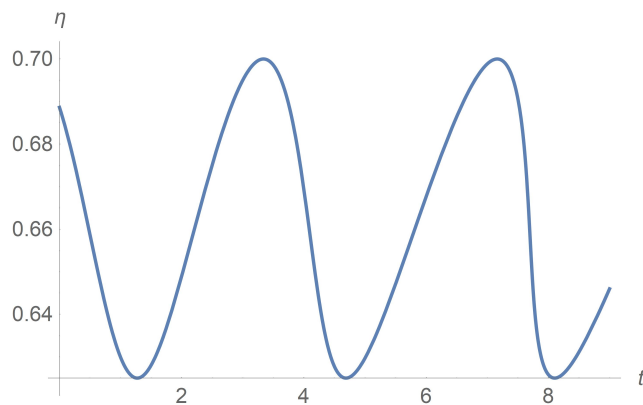


**Figure 7.** Hysteresis loop on the  $(U, \Lambda)$  plane, where  $U$  is the mean velocity and  $\Lambda$  is the friction factor. The data are the same as in Figure 2.



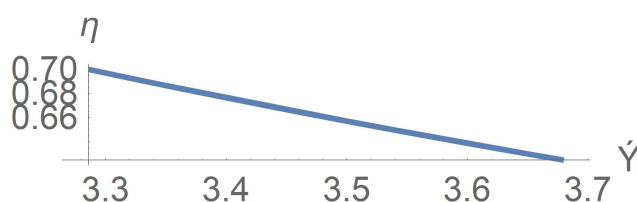
**Figure 8.** Hysteresis of the rheological stress–strain curve  $\Pi = \Pi(\dot{\gamma})$ .

Let us introduce the apparent viscosity  $\eta_a = \bar{\tau}/\dot{\gamma}_1$ . Figure 9 depicts how its dimensionless replica  $\eta = \tau/\dot{\gamma}$  varies with time for the case  $\Pi = \text{const}$ . Sustained temporal oscillations of macroscopic viscosity are observed in [40] for the rod-like suspension.



**Figure 9.** Apparent viscosity versus time. The case  $\Pi = \Pi_0 = \text{const}$ .

As far as the function  $\eta = \eta(\dot{\gamma})$  is concerned, the shear thinning nature of suspensions of rod-like particles is clearly depicted on Figure 10 in agreement with observations in [1].



**Figure 10.** Apparent viscosity  $\eta$  versus velocity gradient  $\dot{\gamma}$  for the case  $\Pi = \Pi_0 = \text{const}$ .

## 5. Discussion

We address rheology of suspensions of rodlike particles. To take into account both particle–fluid and particle–particle interactions, we treat the suspension as a Cosserat continuum and apply the micropolar fluid theory approach. Assuming that local stress depends on the rods directions, we include the micro-inertia tensor into constitutive laws as an independent variable jointly with the rate of strain tensors. The micropolar fluid theory allows for particle’s rotation obeying the angular momentum conservation law. The Cauchy stress tensor loses symmetry and the couple stress tensor is of importance. This is why one should formulate two stress-rate of strain rheological equations for the stress tensor and the couple stress tensor. Unlike a Newtonian fluid, a micropolar fluid is characterized by two rates of strain tensors, through which the linear velocity gradient and the angular velocity gradient are expressed. The impact of variation of rate of strains and the micro-inertia onto the local stress state in the rheological equations is manifested through the viscosities. This is why, in addition to the usual shear viscosity, we also introduce skew-symmetric and anisotropic viscosities. The derived governing equations are proved to be consistent with basic principles of thermodynamics. By performing calculations of simple one-dimensional pressure driven flows between two parallel planes, we establish that the skew-symmetric and the anisotropic viscosities underlie a number of important properties, which include gradient banding instability, coexistence of isotropic and nematic phases, sustained temporal oscillations of macroscopic viscosity, shear thinning and hysteresis. Keeping in mind data for oil transport in pipelines, we also establish that the total flow rate depends not only on the pressure gradient, but on the history of its variation as well.

**Funding:** The research in Section 2 on rheology of anisotropic micropolar fluids is funded by the Government of the Russian Federation (Grant No. 14.W03.31.0002). The theoretical research and computations in Sections 3–5 concerning flows between two planes are funded by Russian Science Foundation (Grant No. 20-19-00058; Funder ID: 10.13039/501100006769).

**Institutional Review Board Statement:** Not applicable.

**Informed Consent Statement:** Not applicable.

**Data Availability Statement:** Not applicable.

**Conflicts of Interest:** The authors declare no conflict of interest.

## References

1. Ganani, E.; Powell, R.L. Suspensions of rodlike particles: Literature review and data correlations. *J. Compos. Mater.* **1985**, *19*, 194–215. [[CrossRef](#)]
2. Dhont, J.K.G.; Kang, K.; Lettinga, M.P.; Briels, W.J. Shear-banding instabilities. *Korea-Aust. Rheol. J.* **2010**, *22*, 291–308.
3. Kang, K.; Lettinga, M.P.; Dogic, Z.; Dhont, J.K.G. Vorticity banding of rodlike virus suspensions. *Phys. Rev. E* **2006**, *74*, 026307. [[CrossRef](#)] [[PubMed](#)]
4. Olmsted, P.D. Perspective on shear banding in complex fluids. *Rheol. Acta* **2008**, *47*, 283–300. [[CrossRef](#)]
5. Fielding, S.M.; Olmsted, P.D. Spatio-temporal oscillations and rheo-chaos in a simple model of shear banding. *Phys. Rev. Lett.* **2004**, *92*, 084502. [[CrossRef](#)]
6. Lettinga, M.P.; Dhont, J.K.G. Non-equilibrium phase behaviour of rod-like viruses flow. *J. Phys. Condens. Matter* **2004**, *16*, S3929–S3939. [[CrossRef](#)]

7. Koch, D.L.; Shaqfeh, E.S.G. The instability of a dispersion of sedimenting spheroids. *J. Fluid Mech.* **1989**, *209*, 521–542. [[CrossRef](#)]
8. Butler, J.; Shaqfeh, E.S.G. Dynamic simulations of the inhomogeneous sedimentation of rigid fibres. *J. Fluid Mech.* **2002**, *468*, 205–237. [[CrossRef](#)]
9. Kutukov, S.E.; Gol'yanov, A.I.; Chetvertkova, O.V. Fluid dynamics of crude oil flow: The longer-term study of pressure losses in oil pipelines. *Neft. Khozyaystvo (Oil Ind.)* **2019**, *8*, 136–140. (In Russian) [[CrossRef](#)]
10. Jeffery, G.B. The motion of ellipsoidal particles immersed in a viscous fluid. *Proc. R. Soc. Lond.* **1922**, *102*, 161–179.
11. Bretherton, F.P. The motion of rigid particles in a shear flow at low Reynolds number. *J. Fluid Mech.* **1962**, *14*, 284–304. [[CrossRef](#)]
12. Giesekus, H. Strömungen mit Konstanten Geschwindigkeitsgradienten und die Bewegung von darin suspendierten Teilchen. *Rheol. Acta* **1962**, *2*, 101–112. [[CrossRef](#)]
13. Goldsmith, H.L.; Mason, S.G. The microrheology of dispersions. In *Rheology*; Eirich F.R., Ed.; Academic Press: New York, NY, USA, 1967; Volume 4.
14. Taylor, G.I. The motion of ellipsoidal particles in a viscous fluid. *Proc. R. Soc.* **1923**, *103*, 58–61.
15. Folgar, F.; Tucker, C.L. Orientation behaviour of fibres in concentrated solutions. *J. Reinf. Plast. Compos.* **1984**, *3*, 98–119. [[CrossRef](#)]
16. Monjezi, S.; Jones, J.D.; Nelson, A.K.; Park, J. The Effect of Weak Confinement on the Orientation of Nanorods under Shear Flows. *Nanomaterials* **2018**, *8*, 130. [[CrossRef](#)]
17. Jackson, W.C.; Folgar, F.; Tucker, C.L. Prediction and control of fibre orientation in molded parts. In *Polymer Blends and Composites in Multi Phase Systems*; Han, C.D., Ed.; ACS: Washington, DC, USA, 1984; Volume 206, pp. 279–299.
18. Helzel, C.; Tzavaras, A.E. Comparison of macroscopic models describing the collective response of sedimenting rod-like particles in shear flows. *Phys. Nonlinear Phenom.* **2016**, *337*, 18–29. [[CrossRef](#)]
19. Graf, C.; Kramer, H.; Deggelmann, M.; Hagenbüchle, M.; Johner, C.; Martin, C.; Weber, R. Rheological properties of suspensions of interacting rodlike FD-virus particles. *J. Chem. Phys.* **1993**, *98*, 4920. [[CrossRef](#)]
20. Altenberger, A.R.; Dahler, J.S. Macromolecules on the kinetic theory and rheology of a solution of rigid-rodlike macromolecules. *Macromolecules* **1985**, *18*, 1700–1710. [[CrossRef](#)]
21. Powell, R.L. Rheology of suspensions of rodlike particles. *J. Stat. Phys.* **1991**, *62*, 1073–1094. [[CrossRef](#)]
22. Eringen, A.C. *Microcontinuum Field Theories: I. Foundations and Solids*; Springer: New York, NY, USA, 1999.
23. Shelukhin, V.V.; Neverov, V.V. Thermodynamics of micropolar Bingham fluids. *J. Non-Newton. Fluid Mech.* **2016**, *236*, 83–90. [[CrossRef](#)]
24. Segré, G.; Silberberg, A. Radial Poiseuille flow of suspensions. *Nature* **1961**, *189*, 209–210. [[CrossRef](#)]
25. Shelukhin, V.V. Rotational particle separation in solutions: Micropolar fluid theory approach. *Polymers* **2021**, *13*, 1072. [[CrossRef](#)]
26. Cosserat, E.; Cosserat, F. *Théorie des Corps Déformables*; Herman: Paris, France, 1909.
27. Eringen, A.C. Theory of anisotropic micropolar fluids. *Int. J. Eng. Sci.* **1980**, *18*, 5–17. [[CrossRef](#)]
28. Ovarlez, G.; Mahaut, F.; Deboeuf, S.; Lenoir, N.; Hormozi, S.; Chateau, X. Flows of suspensions of particles in yield stress fluids. *J. Rheol.* **2015**, *59*, 1449. [[CrossRef](#)]
29. Migun, N.P.; Prokhorenko, P.P. *Fluid Dynamics and Heat Transfer of Gradient Flows of Microstructural Fluids*; Nauka Tekhnika: Minsk, Belarusia, 1984. (In Russian)
30. Eslami, H.; Müller-Plathe, F. Viscosity of nanoconfined polyamide-6,6 oligomers: Atomistic reverse nonequilibrium molecular dynamics simulation. *J. Phys. Chem. B* **2010**, *114*, 387–395. [[CrossRef](#)]
31. Eslami, H.; Gharibi, A.; Müller-Plathe, F. Mechanisms of nucleation and solid-solid-phase transitions in triblock Janus assemblies. *J. Chem. Theory Comput.* **2021**, *17*, 1742–1754. [[CrossRef](#)]
32. Shelukhin, V.V.; Růžička, M. On Cosserat-Bingham Fluids. *Z. Angew. Math. Mech.* **2013**, *93*, 57–72. [[CrossRef](#)]
33. Landau, L.D.; Lifshits, E.M. *Fluid Mechanics, Course of Theoretical Physics*, 2nd ed.; Pergamon Press: Oxford, UK, 1987.
34. Truesdell, C.; Noll, W. *The Non-Linear Field Theories of Mechanics, Handbuch der Physik*; Springer: New York, NY, USA, 1965; Volume III, Part 3.
35. Fielding, S.M. Complex dynamics of shear banded flows. *Soft Matt.* **2007**, *3*, 1262. [[CrossRef](#)]
36. Hoffman, R.L. Discontinuous and dilatant viscosity behaviour in concentrated suspensions. I. Observation of a flow instability. *Trans. Soc. Rheol.* **1972**, *16*, 155. [[CrossRef](#)]
37. Bandyopadhyay, R.; Basappa, G.; Sood, A.K. Observation of chaotic dynamics in dilute sheared aqueous solutions of CTAT. *Phys. Rev. Lett.* **2000**, *84*, 2022–2025. [[CrossRef](#)]
38. Kutukov, S.E.; Golyanov, A.I.; Chetvertkova, O.V. The establishment of pipeline hydraulics: Retrospective of researches of hydraulic losses in pipes. *Neft. Khozyaystvo (Oil Ind.)* **2019**, *7*, 128–133. (In Russian) [[CrossRef](#)]
39. Hu, Y.T.; Boltenhagen, P.P.; Pine, D.J. Shear thickening in low-concentration solutions of wormlike micelles. I Direct visualization of transient behavior and phase transitions. *J. Rheol.* **1998**, *42*, 1185–1208. [[CrossRef](#)]
40. Ivanov, Y.; Van de Ven, T.G.M.; Mason, S.G. Damped oscillations in the viscosity of suspensions of rigid rods: I. Monomodal suspensions. *J. Rheol.* **1982**, *26*, 213. [[CrossRef](#)]



Review

# Recent Advances in Elongational Flow Dominated Polymer Processing Technologies

Zhongke Yuan, Xiaochuan Chen and Dingshan Yu \*

Key Laboratory for Polymeric Composite and Functional Materials of Ministry of Education and Key Laboratory of High-Performance Polymer-based Composites of Guangdong Province, School of Chemistry, Sun Yat-Sen University, Guangzhou 510275, China; yuankzh3@mail.sysu.edu.cn (Z.Y.); chenxch29@mail2.sysu.edu.cn (X.C.)

\* Correspondence: yudings@mail.sysu.edu.cn; Tel.: +86-21-84111395

**Abstract:** The continuous development of plasticizing conveying methods and devices has been carried out to meet the needs of the polymer processing industry. As compared to the conventional shear-flow-dominated plasticizing and conveying techniques, a new method for processing polymers based on elongational flow was proposed. This new method and the related devices such as vane extruders, eccentric rotor extruders and so on, exhibited multiple advantages including shorter processing time, higher mixing effectiveness, improved product performance and better adaptability to various material systems. The development of new techniques in the field of polymer material processing has opened up a broad space for the development of new plastic products, improved product performance and reduced processing costs. In this review, recent advances concerning the processing techniques based on elongational flow are summarized, and the broad applications in polymer processing as well as some future opportunities and challenges in this vibrant area are elucidated in detail.

**Citation:** Yuan, Z.; Chen, X.; Yu, D. Recent Advances in Elongational Flow Dominated Polymer Processing Technologies. *Polymers* **2021**, *13*, 1792. <https://doi.org/10.3390/polym13111792>

**Keywords:** polymer processing; elongational flow; vane extruder; eccentric rotor extruder; numerical simulation

Academic Editors: Célio Bruno Pinto Fernandes, Salah Aldin Faroughi, Luís L. Ferrás and Alexandre M. Afonso

Received: 11 May 2021  
Accepted: 25 May 2021  
Published: 29 May 2021

**Publisher's Note:** MDPI stays neutral with regard to jurisdictional claims in published maps and institutional affiliations.



**Copyright:** © 2021 by the authors. Licensee MDPI, Basel, Switzerland. This article is an open access article distributed under the terms and conditions of the Creative Commons Attribution (CC BY) license (<https://creativecommons.org/licenses/by/4.0/>).

## 1. Introduction

During the past few decades, the advancements in plasticizing and conveying methods and the related devices for polymers and polymer composites have been widely demonstrated to provide substantial property enhancements [1–5]. To date, the most commonly applied polymer plasticizing and conveying systems are based on screws, such as single-screw extruders (SSE), twin-screw extruders (TSE), and so on.

In general, all of these processes involve the following functional zones: (a) a solid conveying section, (b) a melting and melt conveying section, and (c) a metering section [1,2]. In the solids conveying zone of the extruder, the solid feeds are compacted within the screw channel by the rotation of the screw to form a solid plug. The conveying mechanism is based on shear flow where the solid materials are transported by frictional drag, which is dependent on the intrinsic material properties (e.g., heat conductivity) and on the friction between the materials and the screw/barrel [2,6]. Thus, a long thermo-mechanical history is needed for solid conveying completion, which entails long processing time and high energy consumption.

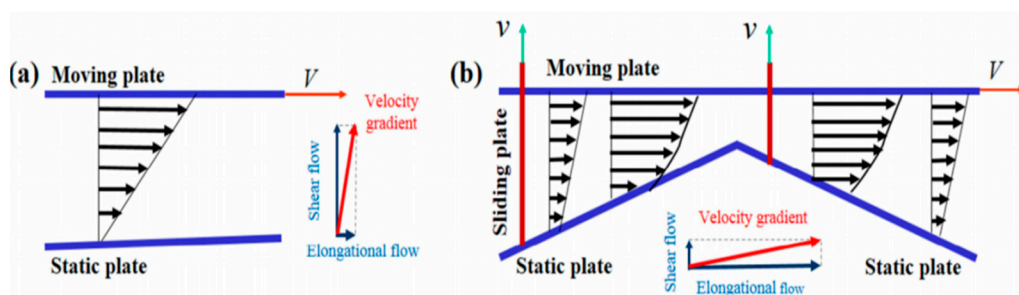
Shear flows have been proven to be less energy-efficient towards both dispersive and distributive mixing when compared to elongational flows [6–9]. Much effort has been devoted to developing plasticizing and conveying devices that impart elongation-dominated flows, such as the introduction of extensional mixing elements (EME) into the conventional single-screw [10,11] and twin-screw extruders [12,13]. The novel non-screw devices known as vane extruders (VE) are comprised of several vane plasticizing and conveying units [14], and the later-developed eccentric rotor extruders (ERE) are dominated by a continuous elongational flow field [15,16].



In this review, we provide a brief review covering the latest advancements in plasticizing and conveying methods and the related devices based on elongation-dominated flows as well as their applications in polymer processing including single polymer/polymer blends, polymer–inorganic composites, and fiber-reinforced polymer composites. Furthermore, we also highlight some typical examples of practical applications in processing special polymer composites. Lastly, we elucidate some challenges and potential solutions in this vibrant field. We expect that this review and upcoming efforts in this field will provide useful guidelines for developing highly efficient processing of polymer materials based on elongational flows.

## 2. Plasticizing and Conveying Devices, Mechanism, and Simulations

The plasticizing and conveying process of polymers and their composites, can generally be divided into shear-flow-dominated flow fields and elongational-flow-dominated flow fields. In order to further elaborate the differences between shear-flow-dominated flow field and elongational-flow-dominated flow field, simplified two-plate and three-plate models are presented in the schematic diagrams shown in Figure 1.



**Figure 1.** Schematic diagrams of (a) shear flow field and (b) elongational flow field. Reproduced under the CC BY-NC-ND license from [17].

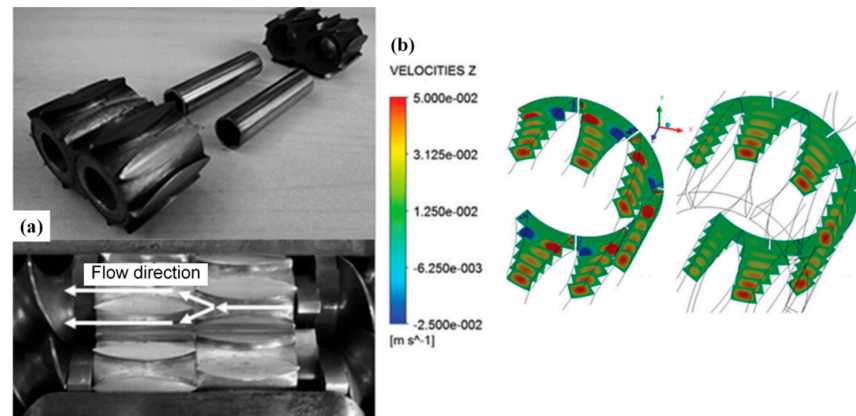
Figure 1a exhibits a simplified two-plate model for conventional screw-based plasticizing and conveying devices dominated by a shear flow field, in which the screw and the barrel are simplified as two parallel plates (a moving plate for screws and a static plate for the barrel) and the relative movement of the two plates was simplified as the flow field pattern. Enforced by the drag effect of the moving plate, the materials mainly underwent the process of shear deformation. The major component of the velocity gradient, which occupies the dominant position, is the shear flow. Figure 1b shows the simplified 3-plate model for the elongational flow dominated process. In the plasticizing and conveying process, the volume of materials undergoes repeated (or periodic) change owing to the synchronized movement of the moving plate and the sliding plate, endowing a dominant elongational flow. Although the specific structure of the devices differs, researchers have successfully incorporated the elongational flow elements by setting single or multiple convergence-divergence channels in the systems [6,10–16].

This section will present recent simulations and theoretical advancements regarding various means to incorporate elongational flow in the plasticizing and conveying process.

### 2.1. The Extensional Mixing Element in Conventional Screw Extruders

As for the introduction of the extensional mixing element (EME) into the conventional SSE and TSE systems, Carson et al. [18] designed the flow channels of the EME in a conventional TSE system, as shown in Figure 2a, to incorporate a specific extension flow on a material through the concentric converging-diverging channels. Simulations of the EME using ANSYS-Polyflow demonstrated that the outlet flow of each diverging channel from the EME unit possessed a linear increase in velocity with much stronger stress components in the flow direction than the shear components (Figure 2b), showing the desired elongational characteristics. Pandey et al. [6] extended the EME concept to SSE systems to fully

exploit the good conveying property and enhance the poor mixing capability of SSE. A similar flow domain is established upon finite-element (FE) modeling optimization where biaxial EME showed higher elongation ratio, which was also experimentally validated in various polymer composite systems.

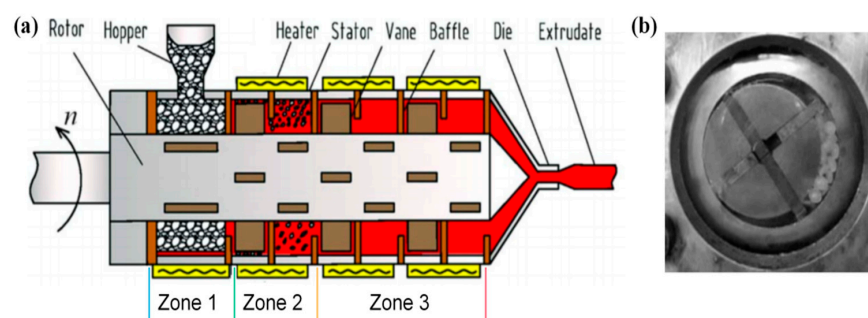


**Figure 2.** (a) Structure of the extensional mixing element (EME) and flow direction in two EMEs in series. (b) Velocity profiles for two EME in series. Reproduced with permission from [18]. Copyright 2015, John Wiley and Sons.

### 2.2. The Vane Extruders

The basic structures of VEs, which were invented by Qu [19], as shown in Figure 3, include several plasticizing and conveying zones comprised of a cylinder-shaped hollow barrel as the stator, a columned eccentric rotor, and multiple vanes installed on the rotor. When the rotor starts rotating, the space between the vanes and the stator is restricted, subsequently the periodical volume increase and decrease forces the materials through a compaction-mill-discharge process with a short thermo-mechanical history.

Qu and co-workers [20] established a mathematical model regarding the power consumption and pressure building in the solid compaction zone (zone 1 in Figure 3) based on the stress distribution. They found that with increased eccentricity of the vane, the pressure of the compressed solid increased, resulting in an increased total power consumption. According to their study, the major power dissipation is heat transfer and its solid compressing and heating efficiency is better than that of a conventional screw extruder with the same setting parameters. The solid conveying in the solid compaction zone (zone 1) [21] and solid conveying zone (zone 2) [14], as shown in Figure 3, were also theoretically studied and experimentally validated. It was found that the transferred power, despite the general power dissipation in the system (dynamic friction, pressure increase etc.), increases exponentially via the positive conveying, while a steady increase is observed in the static friction dragging.



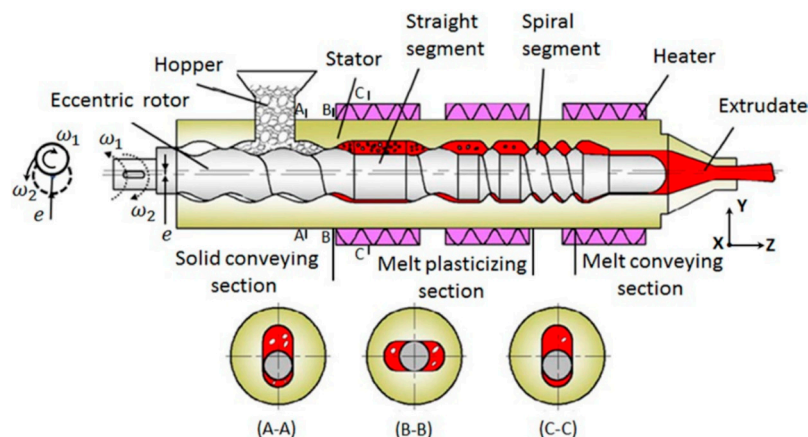
**Figure 3.** (a) Structure of a vane extruder (VE) with different working sections. (b) Photograph of the solid compaction zone. Reproduced with permission from [21]. Copyright 2014, John Wiley and Sons.

Apart from pressure establishment and solid conveying, researchers also studied other characteristics of the VE using modeling and simulations. Xie et al. [22] investigated the energy consumption and mixing characteristics in the melt conveying zone (zone 3 in Figure 3) using computational fluid dynamics, by varying the vane arrangements including four uniformly/non-uniformly distributed vanes, and six uniformly distributed vanes, and tuning the eccentricity of the rotor. It was found that the mixing performance of the VE is proportional to the degree of eccentricity and best performance was exhibited with the four uniformly distributed vanes setting.

Huang et al. [23] derived the velocity distribution and the mixing characteristics of the solid conveying zone (zone 2 in Figure 3) and examined the velocity profiles of the materials between each vane. It was revealed that the increasing power-law index led to a decreased dimensionless velocity profile which resulted in more efficient material dispersion and uniformity compared to traditional shear-dominated extrusion.

### 2.3. The Eccentric Rotor Extruders

Qu and co-workers [24] also developed an elongational-flow-dominated method and devices based on volume pulsed deformation, namely the eccentric rotor extruder (ERE), the basic structure of which is schematically illustrated in Figure 4. The rotation of the spiral-shaped eccentric rotor forced the materials in the space between rotor and stator through multiple converging-diverging zones periodically along both axial and radial directions, hence endowing a plasticizing and conveying process with volume pulsed deformation.



**Figure 4.** Structure of the eccentric rotor extruder (ERE) with different rotating states. Reproduced with permission from [25]. Copyright 2018, John Wiley and Sons.

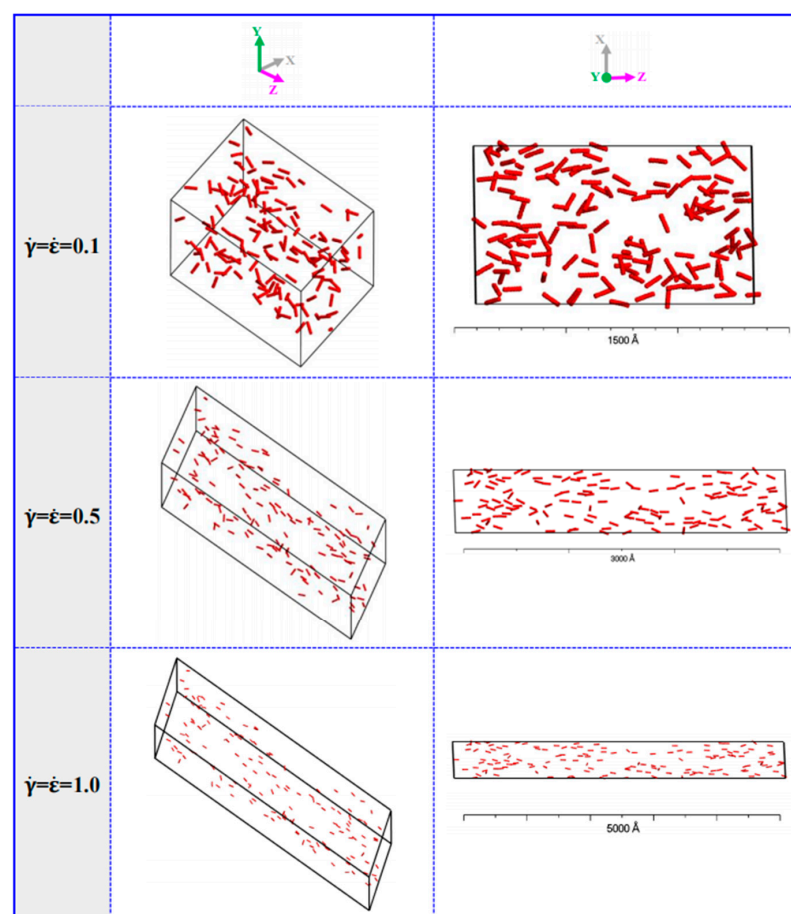
Wen et al. [25] analyzed the flow field in the melt conveying section based on fluid dynamics simulations. Varying technological parameters in the melt conveying section such as rotor speed, radius, and eccentricity in the numerical simulation model, the energy consumption and output efficiency of the ERE were studied. Verified by the demonstration experiment, the simulation analysis revealed that the power of the rotor varied in the same trend with the rotation angle and the production efficiency based on the output efficiency and power consumption is more closely related to the eccentricity of the rotor rather than the rotating speed.

Fan et al. [26] applied particle tracking in the numerical simulation of dispersive and distributive mixing characteristics for the ERE and established a visualization of the mixing process. In the aspect of parameter optimization, a rotation speed of 45 r/min enabled the best mixing performance while increases in the radius and eccentricity of the ERE could also result in improved mixing performance.

While Ultra-high molecular weight polyethylene (UHMWPE) has the same basic molecular structure as that of ordinary polyethylene, its ultra-long molecular chain and

exceptionally high entanglement density drastically enhance the interaction between molecules, resulting in its unique properties such as high wear resistance, low friction coefficient, high toughness, and biological inertia. Our group studied UHMWPE and its composites under the elongational flow induced by the ERE, using FE simulations [27], dissipative particle dynamics (DPD) simulations [28–30], and experimental validations [31].

We applied the FE simulations in a carbon nanotubes (CNTs)/UHMWPE composite to investigate the effect of various elongational–shear coupled flow field on the deformation and stress response [27]. It was found that both pure elongational flow and shear flow would significantly increase the risk of structural damage. And by tuning the elongational/shear loading ratio (force loading only), a maximum Mises stress in the axial direction and the maximal shear stress were found at 0.45 m and 0.61 m respectively within the pressure ranges of 24–10 MPa and 0.9–0.3 MPa, below the yield strength of the CNT/UHMWPE composite (~29.8 MPa). We further put the microscale structure and interfacial performances of the CNT/UHMWPE system into consideration and employed the DPD simulations to investigate the dispersion and orientation evolution of the CNTs in UHMWPE matrix under various elongational–shear coupled rates [28]. We found that increased elongational/shear loading ratio would result in improved orientation of the CNTs and a more ordered morphology of the composite (as shown in Figure 5). Moreover, this improvement is less dependent on the concentration of CNTs as the mean square displacement of the CNTs in the matrix exhibited slight changes with increased concentrations of CNTs from 3 to 10%.



**Figure 5.** The structure of carbon nanotubes/ultra-high molecular weight polyethylene (CNTs/UHMWPE) composites at 10% CNTs under different extensional–shear coupled rates. The red beads represent CNTs. Reproduced under the Creative Common CC BY license from [28].

We also adopted the Souza-Martins method in DPD simulations in search for the predicted flow behaviors of UHMWPE/polyamide 6 (UHMWPE/PA6) blends [29]. By varying the parameters such as mass fractions of UHMWPE/PA6 and elongational/shear coupled rate, it was found that the distribution features of the composite had a minor dependence on the flow variations and mass fractions of the component, yet the orientation behaviors were shifted from micelle-like structure to chain-like structures. The DPD simulations performed in the UHMWPE/polypropylene (UHMWPE/PP) composite [30] showed that the chain conformations differed according to different flow types. Random coils of the polymer chains became collapsed configurations and perpendicular to the flow direction under shear-dominated flows. But by imparting the elongation-dominated coupled flow, the polymer chains appear to be parallel to the flow direction and formed a uniform PP layer.

These findings in theoretical simulations could be of general importance for better in-depth understanding of the mechanism of system evolution and correlations between setting parameters and the properties of the products, and more importantly, can be utilized for device-design optimizations and processing-parameter configurations.

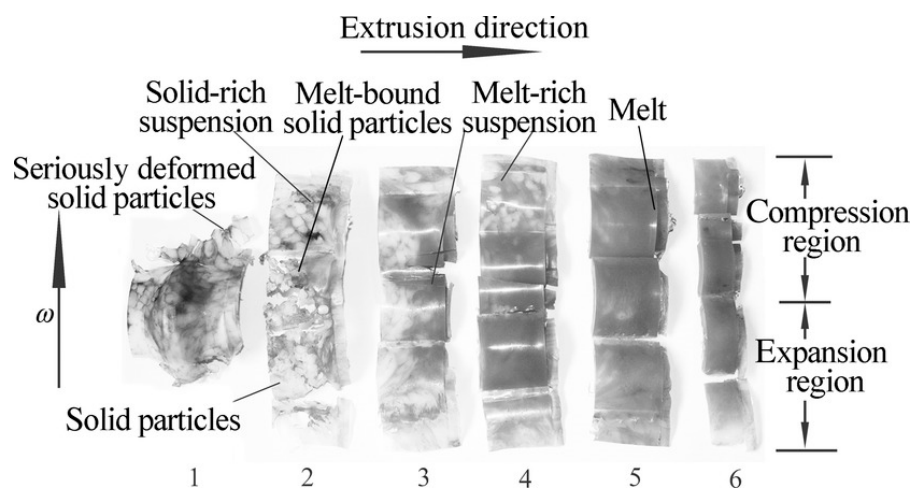
### 3. Applications of Elongational Flow Dominated Plasticizing and Convey Devices

As mentioned in the above section, the elongation-dominated flow has been proved effective to improve the production efficiency of the plasticizing and conveying process and to enhance the products properties of polymers and their composites. Concurrently, much effort has been devoted into the applications of the elongational flow dominated plasticizing and conveying in plural polymer-based systems. The following section describes studies of single polymer/polymer composites, polymer-inorganic composites, and fiber-reinforced polymer composites processed by elongational flow dominated devices. Applications of such devices in processing UHMWPE and its composites is highlighted and discussed.

#### 3.1. Single Polymer/Polymer Composites

Free volume between the polymer chains allows a limited mobility of polymer chains under shear flow field or extensional deformation force. Significant improvement in the orientations and crystalline properties of the polymers and the dispersive/distributive uniformity of the polymer blends after the plasticizing and conveying processes, would result in better overall performances of the products.

Qu et al. [32] studied the melting behavior of high-density polyethylene (HDPE) under controlled variations of eccentricity and rotating speed. By studying the carcass of HDPE removed from different zones in the VE, it was observed that the HDPE pellets underwent different melting mechanisms in different zones of the VE, as demonstrated in Figure 6. In the first few vane units, the HDPE feed was compacted and conveyed under the positive deformation force instead of the friction-induced dragging force in the screw extruders and heated via friction energy dissipation and plastic energy dissipation. With ongoing conveying process, plastic energy dissipation and viscous energy dissipation took place as heat sources, resulting in a deformation mixing-melting with significantly improved processing efficiency. The total length of 6 vane units to reach melt-completion could be as short as 140 mm. Yin et al. [33] also used HDPE to study the impact of the rotation speed and die pressure on the output of VEs, as compared to that of a conventional SSEs. The output of the VE exhibited a linear positive correlation to the rotation speed and independence from the die pressure.



**Figure 6.** Photographs of high-density polyethylene (HDPE) removed from six VE units. Reproduced with permission for [32]. Copyright 2013, John Wiley and Sons.

Liu et al. [34] used low density polyethylene (LDPE) to disclose the melting mechanism in elongational flow induced by vane extruders. The melting of LDPE with varied operation parameters (temperature of the heat unit and rotation speed) was examined dynamically by cooling and disassembling the VE units. Unlike the screw-based extruders, after the melt film is formed between the compacted LDPE pellets and the stator in VE, the melts were removed constantly and migrated through voids of LDPE pellets, thus accelerating the heat transfer and dramatically shortening the melting process.

Recently, Wu et al. [35] investigated the melting and crystalline behaviors of recycled poly(ethylene terephthalate) (PET) and comparative analysis was made between ERE and conventional TSE. The molar mass of TSE-processed PET samples decreased significantly more than that of ERE-processed samples, due to longer residence time and much stronger shear component in the flow field, and the lamellar thickness of the primary crystallization for ERE-processed PET samples is higher than that for virgin PET samples. As a result, the tensile strength of ERE-processed samples (63.8–66.8 MPa) was slightly improved compared to virgin PET (59.3 MPa), and almost twice that of TSE-processed PET (25.8–31.2 MPa).

The research mentioned above demonstrated the superiority of the elongational flow dominated plasticizing and convey devices over conventional screw-based extruders, in both product performance enhancement and processing efficiency for single polymer.

Polymer blends, the mixtures of different polymers with various properties, is a very effective way to tailor the properties and performances of the polymeric materials. Apart from the intrinsic properties of the selected polymer pairs, the performance of the polymer blends is also determined by the final microstructures [36,37]. However, most of the polymer pairs were immiscible and would lead to unsatisfactory phase transformation such as co-continuous structure. It is well known that the processing methods and the related devices have significant influence on the phase transformation of the processed materials and play important roles in the manipulation the microstructures of final products [35,38,39]. Wu et al. [40] extruded immiscible linear low-density polyethylene (LLDPE)/polystyrene (PS) blends using the VE. By analyzing the phase transformation in the recovery mode, a 325.861% genuine elongational ratio was found, and the morphology development during recovery further indicated that the imposition of the elongational flow field successfully improved the distribution uniformity of the dispersive phase.

He et al. [41] prepared the LLDPE/PET blends using both TSE and ERE and compared the mechanical properties and morphology of different samples. It was revealed that the application of the continuous elongational flow results in better distribution of PET in LLDPE matrix with a certain compatibilizer, exhibiting 226% and 394% improvements in impact strength and elongation at break, respectively. More recently, they successfully improved the properties of metallocene polyethylene (m-PE)/PET blends using ERE [42].

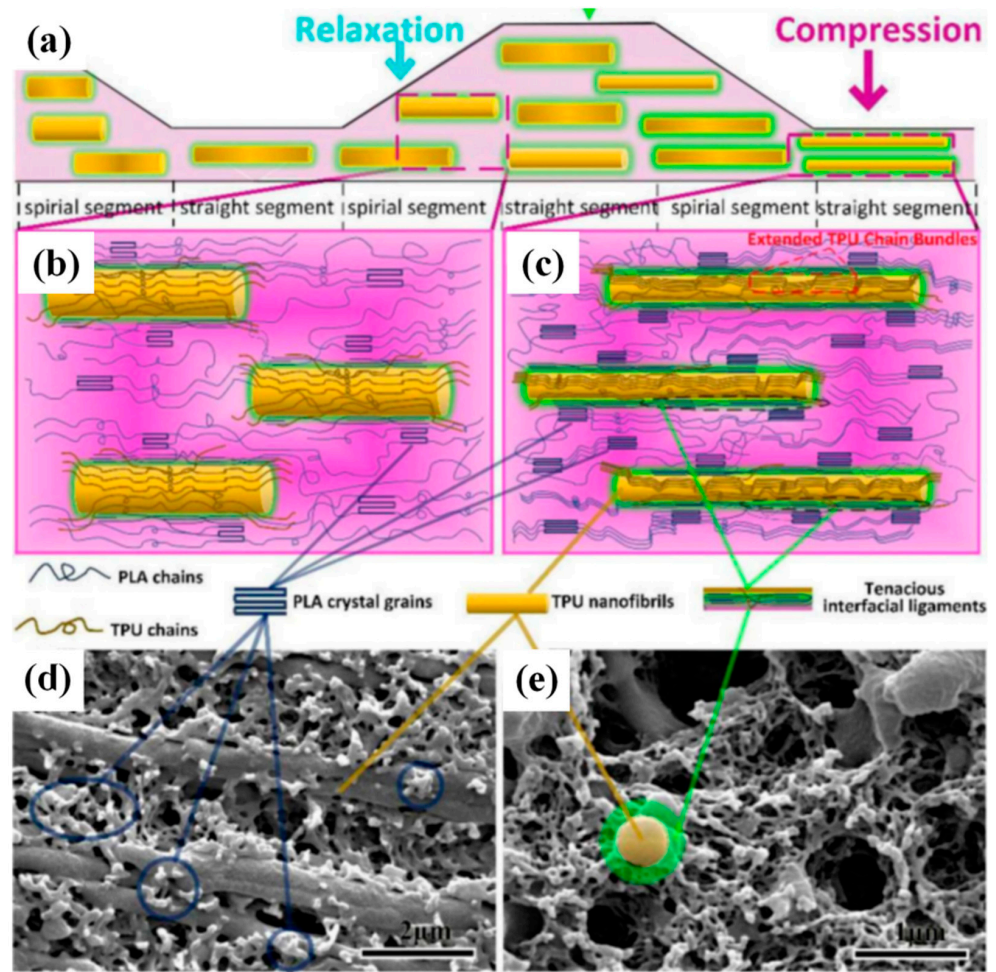
Improvements in both particle/particle size distribution of PET in m-PE matrix were found as compared with the shear flow dominated process in TSE. This research should enlighten new ways of PET modification and applications for recycled PET.

Poly-L-lactic acid (PLA) as a biodegradable and biocompatible polymer, has attracted intensive attentions of researchers. Simple and effective methods to improve the crystallization of the PLA matrix for further mechanical-strength enhancements were proposed [43–46].

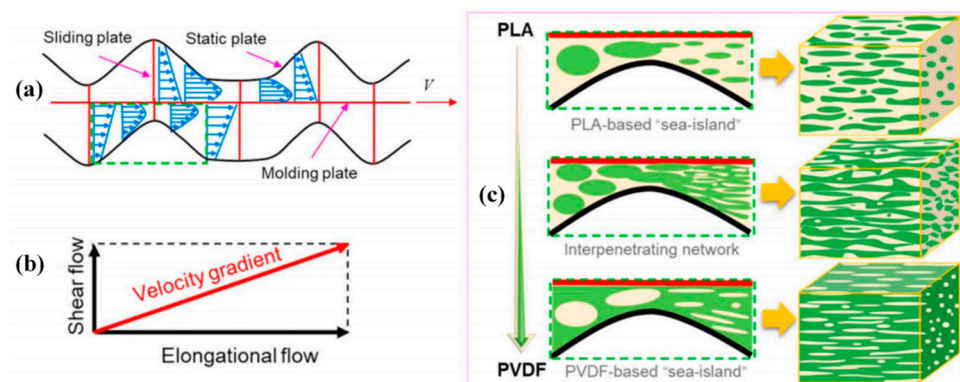
Elastomeric ethylene-butyl acrylate-glycidyl methacrylate terpolymer (EBA-GMA) was blended with PLA under elongational flow by Fang et al. [43]. The epoxy groups in EBA-GMA are reactive with the end-OH in PLA during the melt blending process and the cross-linking PLA/EBA-GMA interface thus formed contributed to the impact strength enhancement. Meanwhile, the elongational flow field induced the formation of more stable crystal of PLA. Owing to the synergy of the aforementioned mechanisms, the impact strength of the PLA/EBA-GMA blends showed a drastic improvement from  $\sim 2.58 \text{ kJ m}^{-2}$  to  $\sim 55 \text{ kJ m}^{-2}$ . He et al. studied the reinforcement of PLA from ERE-processed in-situ formed oriented thermoplastic poly(ether)urethane (TPU) nanofibers [44]. As demonstrated in Figure 7, the extended TPU chain bundles in the converging channel worked as nucleating sites, enabling significant improvement in the crystallization of the PLA and the PLA-TPU interfacial adhesion. With an optimized TPU content of 25 wt%, an impact strength of  $73.5 \text{ kJ m}^{-2}$  was achieved. Further study demonstrated that the interfacial relaxation through the plastic deformation of PLA/TPU matrix endowed a better absorption and dissipation of fracture energy after an annealing process [45]. Thus, reaching a balanced toughness of  $90.3 \text{ kJ m}^{-2}$  and a stiffness of  $\sim 2.15 \text{ GPa}$ . Zhang et al. [46] prepared the composite of polycaprolactone (PCL) and PLA using ERE. Under the elongational flow, PLA/PCL composite showed explicit in-situ fiberization and improved compatibility of both components. Optimized composites with a PLA content of 80% reached the highest elongation at break of 476.7%, while the thermal stability was increased by  $5.4 \text{ }^\circ\text{C}$  compared to the neat PLA.

The improved compatibility between PLA and in-situ fiberized components due to both the increased contacted area [47,48] and the on-fiber nucleating effect [44,45]. And the synergetic enhancement induced by the elongational flow dominated plasticizing and conveying process might be further expanded in other polymer composites.

Most recently, on the basis of ERE, the novel twin-eccentric rotor extruder (TERE) was developed [49], and Zhang et al. [50] used TERE to study the mechanism of orientation and dispersion evolution in polyvinylidene fluoride (PVDF) and PLA blends. The melt formed certain “sea-island” regions and an interpenetrating network under repeated breakup and coalescence as demonstrated in Figure 8, and the effective dielectric properties of PLA/PVDF were achieved by varying PVDF ratio.



**Figure 7.** (a) Schematic of the formation process of thermoplastic poly(ether)urethane (TPU) nanofibers in ERE. The formation of poly-L-lactic acid (PLA) crystal grains in (b) relaxation and (c) compression channel. The SEM images of (d) etched and (e) ultrasonic cleaned fractures. Reproduced with permission from [44]. Copyright 2019, Elsevier.



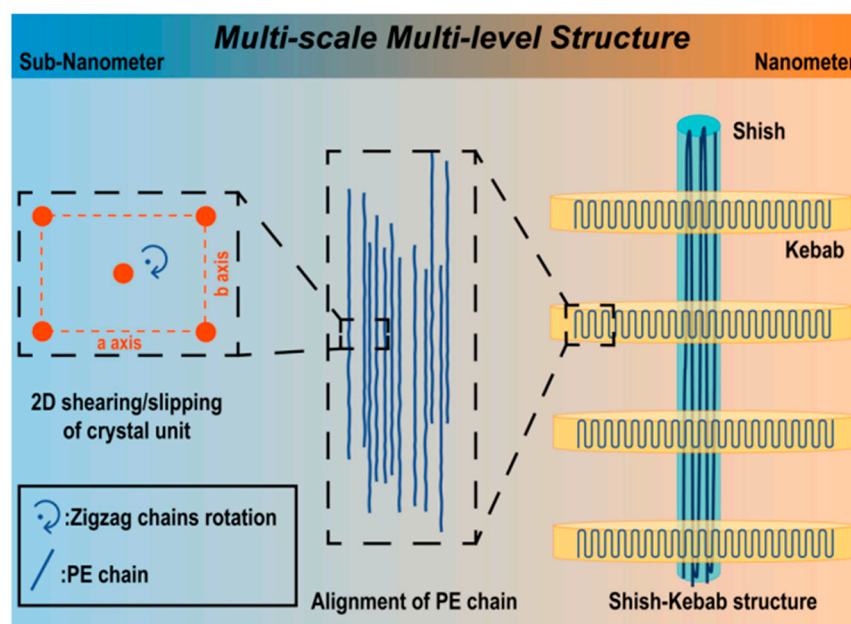
**Figure 8.** The schematic illustration of (a) simplified flow field in twin-eccentric rotor extruder (TERE), (b) velocity gradient, and (c) morphology evolution of PLA/PVDF composites. Reproduced with permission from [50]. Copyright 2021, Elsevier.

As mentioned, UHMWPE exhibited extremely high melt viscosity and near-zero melt mobility in the plasticizing and conveying process, putting the conventional shear-flow-dominated processing techniques in a dilemma. Researchers [31,51,52] explored



the applications of elongational-flow-dominated plasticizing and conveying devices in UHMWPE processing and significant advancements were made.

Zhang et al. [51] for the first time successfully plasticized and extruded the UHMWPE without additives using the ERE. They found that the elongational volume deformation enforced a continuous change of the volume of UHMWPE, leading to a better exposure of the unmelted “core” to the heat source, and dramatically enhancing the heating and mass transfer efficiency. Our group [31] performed further comparative analysis of UHMWPE processed under elongational flow and shear flow. We found that the rotation of UHMWPE nascent powder was restrained under the intensive extensional volume deformation, which led to the increased entanglement in the final defect-free products. The shorter residence time of UHMWPE in the extruder also enabled a well preserved molecular weight of the UHMWPE extrudant compared to the UHMWPE nascent powders. Recently, Huang et al. [52] prepared the PE/UHMWPE composite using ERE with a view towards high-voltage applications. The study showed that the PE/UHMWPE formed a shish-kebab multilevel structure, as schematically illustrated in Figure 9, and more intensive elongational flow would lead to more aligned polymer chains in this structure. Compared with conventional cross-linked PE, the PE/UHMWPE showed a higher dielectric constant and a higher dielectric breakdown voltage.



**Figure 9.** Schematic illustration of PE/UHMWPE prepared under elongational flow. Reproduced with permission from [52]. Copyright 2020, American Chemical Society.

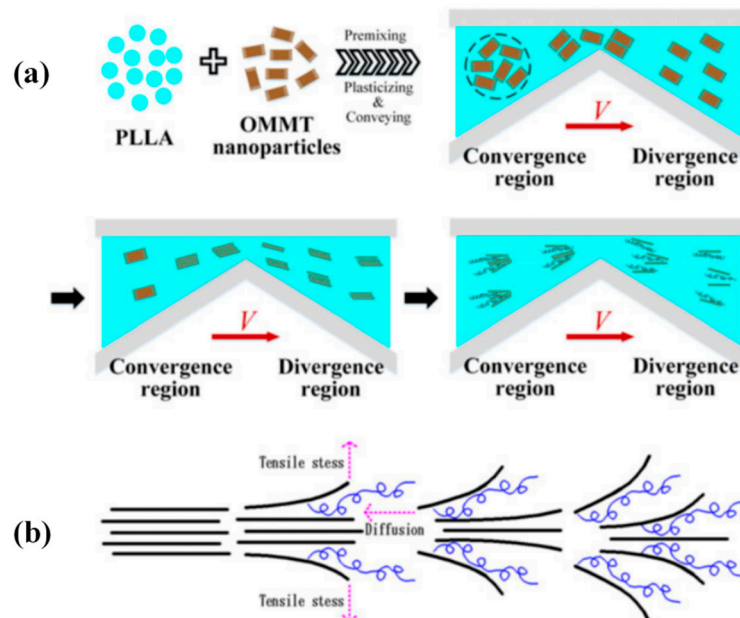
Based on the studies mentioned above, it is evident that elongational flow dominated processing techniques could not only improve the production efficiency but also bring enhanced properties and expanded applications of polymer/polymer composites.

### 3.2. Polymer-Inorganic Composites

In recent decades, polymer-inorganic nanocomposite materials have been widely reported with substantial enhancements in both chemical and mechanical properties. However, aggregation of nanoparticles has been one of the major issues that hinders exploiting the full potential of polymer-inorganic nanocomposites. To date, researchers have applied elongational volume deformation enforced by the elongational flow dominated plasticizing and conveying devices in plural polymer-inorganic composites with various nanofillers, such as montmorillonite (MMT) [53,54], organically modified montmorillonite (OMMT) [16,55–57], titanium dioxide (TiO<sub>2</sub>) [54,58], calcium salt [59,60], and carbon nan-

otubes (CNT) [54,61], realizing high dispersion effectiveness or even in-situ exfoliation of reaggregated nanofillers.

Wu et al. [53] prepared the PP/PS/MMT blends using ERE. With the addition of MMT nanofillers, the size of the PS dispersive phase was reduced, and compatibility of PP/PS improved. The synergy of extensional deformation and interfacial interaction enabled the MMT nanoparticles to exfoliate during processing. They further studied the in-situ exfoliation phenomenon in the poly-L-lactide (PLLA)/OMMT composite [16]. As demonstrated in Figure 10a, after premixing, the aggregated OMMT nanoparticles were first dispersed by repeated converging-diverging channels in ERE, then a double-side exfoliation of the OMMT nanoparticles took place under the perpendicular tensile stress and diffusion of PLLA chains, as shown in Figure 10b. This double-side exfoliation mechanism has also proven to be more effective than conventional layer-by-layer exfoliation mechanism in shear flow dominated processing devices in other polymer/OMMT composites. In ERE processed PLA/PBS/OMMT composites, Tan et al. [55] described the mechanism of the intercalation and exfoliation under elongation flow more intuitively with a simplified model, proving that this elongational flow induced dispersion and exfoliation mechanism could be applied in processing ternary polymer-inorganic composites. More research regarding the poly-L-lactide/poly ethylene glycol)/organomodified montmorillonite nanocomposites (PLLA/PEG/OMMT) were carried out by Wu et al. [15,56]. It was revealed that the increase in interlayer spacing of OMMT nanofiller under elongational flow significantly increased the nucleation density and nucleation rate in the composites, providing improved thermal stability. Zhang et al. [57] prepared the PP/OMMT composites using both ERE and TSE, and the comparative investigation showed that even at a high OMMT loading, nano-tactoids of clay were formed instead of intensive reaggregation proving that the double-sided exfoliation process induced by elongation flow is more effective.



**Figure 10.** The Schematic illustration of (a) dispersion and exfoliation process of organically modified montmorillonite (OMMT) particles, and (b) double-side exfoliation mechanism. Reproduced with permission from [16]. Copyright 2017, John Wiley and Sons.

It is widely recognized that nanofiller could accelerate the crystallization of polymers during processing, due to increased nucleating sites. Zhang et al. [58] studied PLA/TiO<sub>2</sub> composites under elongational flow induced by VE. They found that instead of the rotation of aggregated particles in steady shear flow, the nanoparticles were separated and dispersed under repeated volume deformation through the converging channels in VE, leading to improved thermal stability, increased toughness and UV resistance. Jia et al. [59] compared

the VE-extruded and SSE-extruded LDPE/nanoprecipitated calcium carbonate (NPCC) composites. VE-extruded samples presented better dispersion and distribution of nano- $\text{CaCO}_3$  particles, leading to a 30% increase in elongation at break (from 810% to 840%) compared to SSE-extruded counterparts. Chen et al. [60] prepared a ternary blend of PLA/PBS and calcium sulfate whiskers (PLA/PBS/CSW) using VE. The well-distributed CSW improved the poor compatibility of PLA and PBS, and the finely dispersed and distributed PLA droplets in the PBS matrix induced by the elongational flow in VE resulted in improvements in the thermal resistance for PBS.

Owing to the high aspect ratio and low compatibility with polymer blends, CNTs and multiwalled carbon nanotubes (MWCNTs) were easily aggregated during the processing in polymer blends, hindering the property improvement of such composites. Meng et al. [61] prepared the polypropylene/poly(ethylene-co-octene)/MWCNT composites (PP/POE/MWCNT) utilizing the ERE-induced elongational flow. The well-dispersed MWCNTs in the polymer matrix promoted significant improvements in heterogeneous nucleation, resulting in better tensile strength, flexibility and thermal stability of the ERE-extruded samples as compared to TSE-extruded samples.

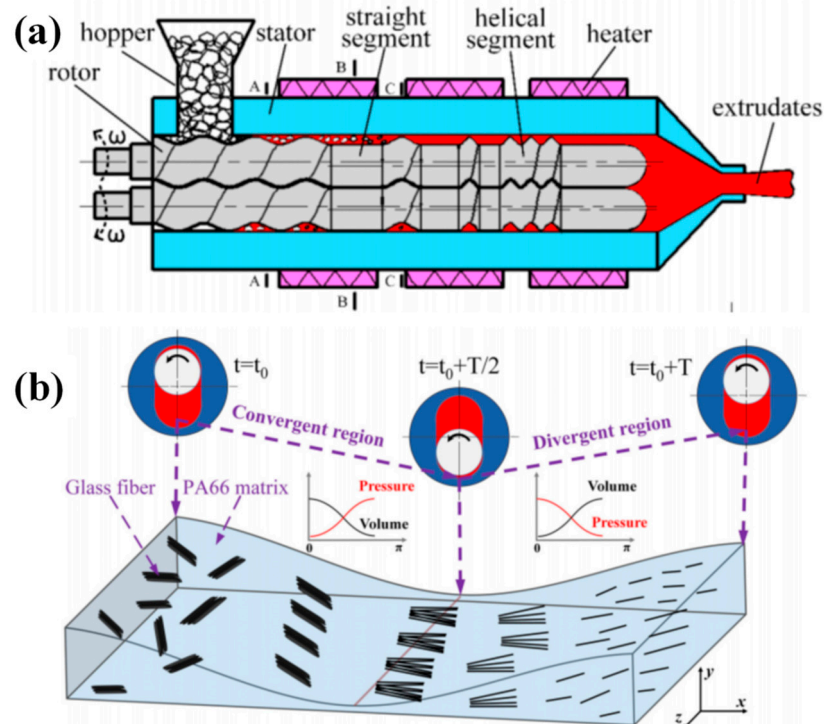
Lin et al. [62] prepared the UHMWPE/OMMT composites using ERE and investigated the thermal-mechanical properties. In contrast to other polymer/OMMT composites, most of the nanoplates were well exfoliated and intercalated in the UHMWPE matrix under ERE-induced elongational flow, even at a high OMMT content. This might be due to the ultra-long chains and ultra-high entanglement density of UHMWPE, which increased the mean spacing distance, as simulated in previous theoretical work [27]. With a 1 wt% OMMT addition, the UHMWPE/OMMT composites exhibited an increase in impact strength from  $127.3 \text{ kJ m}^{-2}$  to  $155.2 \text{ kJ m}^{-2}$  as compared to neat UHMWPE.

As proven by the aforementioned studies in this section, the elongational flow dominated processing techniques could improve the dispersion and distribution of nanofillers as well as the crystallization and consequent performances of the targeted polymer/polymer blends in the polymer-inorganic composites.

### 3.3. Fiber-Reinforced Polymer Composites

Fiber-reinforced polymer composites possess many advantages such as light weight, recyclability and corrosion resistance [63,64]. However, the conventional shear flow dominated extrusion devices face some troubling issues, such as the attrition of fibers caused by the friction with the heated barrel, the poor orientation and distribution of fibers in the shear flow field, and limited fiber-polymer compatibility. In the search of solutions to these problems, researchers employed the elongational dominated flow in fiber-reinforced polymer composites processing.

Wu et al. [65] fabricated the sisal fiber (SF)/PP composites under elongational flow field induced by VE. It was found that the simple addition of maleic anhydride-grafted polypropylene as a compatilizer would result in good performance of the SF/PP composites without the need for complex fiber treatment as in conventional extrusion methods [64,66]. Most recently, Wu et al. [17] and Guo et al. [67] investigated the glass fiber (GF) reinforced PA6 and PA66 composites using a novel TERE, as shown in Figure 11a. They found that the shear flow field formed in the conventional plastic molding devices such as SSE and TSE, can break up the agglomerates by applying excessive shearing intensity, but the subsequent low retention of the average fiber length, would lead to performance degradation. In contrast, under elongational flow field, induced by TERE, the fibers were well-dispersed and evenly distributed in polymer matrix, as demonstrated in Figure 11b. The average fiber lengths in TERE-extruded GF/PA6 and GF/PA66 composites were 2.7 and 3.2 times that of TSE-extruded samples. The increased fiber length retention resulted in substantial increase in impact strength, flexural strength, and tensile strength as well.



**Figure 11.** Schematic illustration of (a) overall structure of TERE. Reproduced under the CC BY-NC-ND license from [17]. and (b) the dispersion mechanism of glass fiber (GF) in the PA66 matrix. Reproduced with permission from [67]. Copyright 2020, John Wiley and Sons.

These studies demonstrated the distinct advantages of elongational flow dominated processing over conventional shear flow dominated techniques in providing good dispersion and length retention of fibers in fiber-reinforced polymer composites. It is expected to be a simple and feasible way to process expanded fiber-reinforced polymer composites such as carbon fibers, modification-free natural fiber composites and so on.

#### 4. Conclusions and Prospects

For over half a century, researchers have realized the superiority of elongational flow field in polymer plasticizing and conveying process over shear flow field. Limited by the device design, the shear flow dominated plasticizing and conveying methods and related devices were still the dominant processing techniques for polymer and polymer composites. With the emerging theoretical studies and equipment designs in elongational flow dominated plasticizing and conveying technologies, as we summarized and discussed in this review, many of the critical issues in conventional screw-based extrusion devices such as long thermal-mechanical history, high energy consumption, and dependence on material properties have been solved with the application of EME replacements, vane extruders and eccentric rotor extruders. These methods and related devices also showed great potential to solve more specific problems like the dispersion and distribution of the polymer components, reaggregation of nanofiller and retention of fiber length.

Despite the great advancements that have been made in this vibrant field, numerous issues of the currently reported methods and devices still remain to be solved. First, as in EME-modified screw-extruders, repeated insertion of the EME would lead to severe pressure loss, thus the elongational flow dominated sections can't totally replace the screw-based sections. Second, as in the vane extruder, the stiffness of the vanes becomes the limiting factor in applications in extreme conditions, and dead ends in the flow channel, though much smaller than TSE, still need structural optimization. Third, as for the eccentric rotor extruder, with increasing eccentricity and rotation speed, the power consumption also increased. The search for the balance between power consumption, throughput of the prod-

ucts, and products' overall performance is still to be resolved. Last, future developments in the visualization of the plasticizing/conveying process and in-situ characterization techniques would help us further understand the intrinsic mechanisms and offer more efficient optimization of the processes. We believe that with these issues solved and upcoming developments in this field, the elongational flow dominated processing technologies will contribute more to the sustainable development of polymer processing industries.

**Author Contributions:** Conceptualization, Z.Y. and D.Y.; writing—original draft preparation, Z.Y. and X.C.; writing—review and editing, Z.Y. and D.Y.; funding acquisition, Z.Y. and D.Y. All authors have read and agreed to the published version of the manuscript.

**Funding:** This research was funded by National Key R&D Program of China, grant number 2016YFB0302301; the National Natural Science Foundation of China, grant number 52003303; China Postdoctoral Science Foundation, grant number 2020M672932.

**Institutional Review Board Statement:** Not applicable.

**Informed Consent Statement:** Not applicable.

**Data Availability Statement:** The data presented in this study are available on request from the corresponding author.

**Acknowledgments:** We would thank Changlin Cao for the helpful discussion.

**Conflicts of Interest:** The authors declare no conflict of interest.

## References

- Müller, K.; Bugnicourt, E.; Latorre, M.; Jorda, M.; Sanz, Y.E.; Lagaron, J.M.; Miesbauer, O.; Bianchin, A.; Hankin, S.; Bölz, U.; et al. Review on the Processing and Properties of Polymer Nanocomposites and Nanocoatings and Their Applications in the Packaging, Automotive and Solar Energy Fields. *Nanomaterials* **2017**, *7*, 74. [[CrossRef](#)] [[PubMed](#)]
- Vlachopoulos, J.; Strutt, D. Polymer processing. *Mater. Sci. Technol.* **2003**, *19*, 1161–1169. [[CrossRef](#)]
- Fu, S.-Y.; Sun, Z.; Huang, P.; Li, Y.-Q.; Hu, N. Some basic aspects of polymer nanocomposites: A critical review. *Nano Mater. Sci.* **2019**, *1*, 2–30. [[CrossRef](#)]
- Thakur, V.K.; Kessler, M.R. Self-healing polymer nanocomposite materials: A review. *Polymer* **2015**, *69*, 369–383. [[CrossRef](#)]
- Kargazadeh, H.; Mariano, M.; Huang, J.; Lin, N.; Ahmad, I.; Dufresne, A.; Thomas, S. Recent developments on nanocellulose reinforced polymer nanocomposites: A review. *Polymer* **2017**, *132*, 368–393. [[CrossRef](#)]
- Pandey, V.; Maia, J.M. Extension-dominated improved dispersive mixing in single-screw extrusion. Part 1: Computational and experimental validation. *J. Appl. Polym. Sci.* **2020**, *138*, 49716. [[CrossRef](#)]
- Rauwendaal, C.; Osswald, T.; Gramann, P.; Davis, B. Design of Dispersive Mixing Devices. *Int. Polym. Process.* **1999**, *14*, 28–34. [[CrossRef](#)]
- Elemans, P.H.M.; Van Wunnik, J.M. The effect of feeding mode on dispersive mixing efficiency in single-screw extrusion. *Polym. Eng. Sci.* **2001**, *41*, 1099–1106. [[CrossRef](#)]
- Miroshnikov, Y.P.; Egorov, A.K.; Egorova, M.V. Measuring of coalescence in polymer melt blends flowing through converging channels. *J. Appl. Polym. Sci.* **2011**, *120*, 2724–2733. [[CrossRef](#)]
- Pandey, V.; Chen, H.; Ma, J.; Maia, J.M. Extension-dominated improved dispersive mixing in single-screw extrusion. Part 2: Comparative analysis with twin-screw extruder. *J. Appl. Polym. Sci.* **2021**, *138*, 49765. [[CrossRef](#)]
- Chen, H.; Maia, J.M. Improving dispersive mixing in compatibilized polystyrene/polyamide-6 blends via extension-dominated reactive single-screw extrusion. *J. Polym. Eng.* **2021**, *41*, 397–403. [[CrossRef](#)]
- Chen, H.; Pandey, V.; Carson, S.; Maia, J.M. Enhanced Dispersive Mixing in Twin-Screw Extrusion via Extension-Dominated Static Mixing Elements of Varying Contraction Ratios. *Int. Polym. Process.* **2020**, *35*, 37–49. [[CrossRef](#)]
- Chen, H.; Guo, M.; Schiraldi, D.; Maia, J.M. Morphology optimization of poly(ethylene terephthalate)/polyamide blends compatibilized via extension-dominated twin-screw extrusion. *J. Polym. Eng.* **2021**, *41*, 218–225. [[CrossRef](#)]
- Qu, J.-P.; Zhang, G.-Z.; Chen, H.-Z.; Yin, X.-C.; He, H.-Z. Solid conveying in vane extruder for polymer processing: Effects on pressure establishment. *Polym. Eng. Sci.* **2012**, *52*, 2147–2156. [[CrossRef](#)]
- Wu, T.; Yuan, D.; Qu, J.P. Preparation of poly(L-lactide)/poly(ethylene glycol)/organo-modified montmorillonite nanocomposites via melt intercalation under continuous elongation flow. *J. Polym. Eng.* **2018**, *38*, 449–460. [[CrossRef](#)]
- Wu, T.; Tong, Y.; Qiu, F.; Yuan, D.; Zhang, G.; Qu, J. Morphology, rheology property, and crystallization behavior of PLLA/OMMT nanocomposites prepared by an innovative eccentric rotor extruder. *Polym. Adv. Technol.* **2017**, *29*, 41–51. [[CrossRef](#)]
- Wu, T.; Huang, Z.-X.; Wang, D.-Z.; Qu, J.-P. Effect of continuous elongational flow on structure and properties of short glass fiber reinforced polyamide 6 composites. *Adv. Ind. Eng. Polym. Res.* **2019**, *2*, 93–101. [[CrossRef](#)]

18. Carson, S.O.; Covas, J.A.; Maia, J.M. A New Extensional Mixing Element for Improved Dispersive Mixing in Twin-Screw Extrusion, Part 1: Design and Computational Validation. *Adv. Polym. Technol.* **2015**, *36*, 455–465. [[CrossRef](#)]
19. Qu, J.P. Method and a Device for Plasticizing and Transporting Polymer Material Based on Elongation Rheology. US 2010/0135102A1, 6 August 2009.
20. Qu, J.-P.; Zhao, X.-Q.; Li, J.-B.; Cai, S.-Q. Power consumption in the compacting process of polymer particulate solids in a vane extruder. *J. Appl. Polym. Sci.* **2012**, *127*, 3923–3932. [[CrossRef](#)]
21. Li, J.-B.; Qu, J.-P.; Xu, Y.-S.; Zhang, G.-Z.; Zhai, S.-F.; Zhao, Y.-Q.; Yin, X.-C. Solids conveying in the solids compaction zone of vane extruder. *Polym. Eng. Sci.* **2014**, *55*, 719–728. [[CrossRef](#)]
22. Xie, H.-L.; Wen, J.-S.; Fan, D.-J.; Lei, S.-K.; Jiang, S.-C.; Zhou, X.-L. Numerical Simulation of Mixing Characteristics and Energy Consumption in Vane Extruders with Different Structure Parameters. *J. Macromol. Sci. Part. B* **2017**, *48*, 395–408. [[CrossRef](#)]
23. Huang, Z.; Luo, P.; Tong, J.; Su, F. Velocity Distribution of Extensional Flow Fields in an Eccentric Cylinder of an Extensional Extruder. *J. Macromol. Sci. Part. B* **2018**, *57*, 732–745. [[CrossRef](#)]
24. Qu, J.; Zhang, G.; Yin, X. Volume Pulsed Deformation Plastic and Conveying Method and Device by Eccentric Rotor. US 2019/10307950B2, 4 June 2019.
25. Wen, J.-S.; Yang, M.-K.; Fan, D.-J. Numerical simulation of energy consumption in the melt conveying section of eccentric rotor extruders. *Adv. Polym. Technol.* **2018**, *37*, 3335–3347. [[CrossRef](#)]
26. Fan, D.-J.; Yang, M.-K.; Wen, J.-S. Numerical Simulation of Mixing Characteristics in the Eccentric Rotor Extruder with Different Process Conditions and Structural Parameters. *Adv. Polym. Technol.* **2019**, 8132308. [[CrossRef](#)]
27. Wang, J.; Cao, C.; Yu, D.; Chen, X. Deformation and Stress Response of Carbon Nanotubes/UHMWPE Composites under Extensional-Shear Coupling Flow. *Appl. Compos. Mater.* **2017**, *25*, 35–43. [[CrossRef](#)]
28. Wang, J.; Cao, C.; Chen, X.; Ren, S.; Chen, Y.; Yu, D.; Chen, X. Orientation and Dispersion Evolution of Carbon Nanotubes in Ultra High Molecular Weight Polyethylene Composites under Extensional-Shear Coupled Flow: A Dissipative Particle Dynamics Study. *Polymers* **2019**, *11*, 154. [[CrossRef](#)] [[PubMed](#)]
29. Wang, J.X.; Li, P.; Cao, C.L.; Ren, S.J.; Yu, D.S. A Dissipative Particle Dynamics Study of Flow Behaviors in Ultra High Molecular Weight Polyethylene/Polyamide 6 Blends Based on Souza-Martins Method. *Polymers* **2019**, *11*, 1275. [[CrossRef](#)]
30. Wang, J.; Chen, X.; Cao, C.; Yu, D. Chain conformation and dynamics in ultrahigh molecular weight polyethylene melts undergoing extensional–shear coupled flow: Insight from dissipative particle dynamics simulation. *Polym. Int.* **2020**, *69*, 1213–1219. [[CrossRef](#)]
31. Cao, C.; Chen, X.; Wang, J.; Lin, Y.; Guo, Y.; Qian, Q.; Chen, Q.; Feng, Y.; Yu, D.; Chen, X. Structure and properties of ultrahigh molecular weight polyethylene processed under a consecutive elongational flow. *J. Polym. Res.* **2017**, *25*, 16. [[CrossRef](#)]
32. Qu, J.; Zhang, N.; Yu, X.; Zhang, G.; Liu, S.; Tan, B.; Liu, L. Experimental Investigation of Polymer Pellets Melting Mechanisms in Vane Extruders. *Adv. Polym. Technol.* **2013**, *32*, 21336. [[CrossRef](#)]
33. Yin, X.; Li, S.; He, G.; Zhang, G.; Qu, J. Experimental Study of the Extrusion Characteristic of a Vane Extruder Based on Extensional Flow. *Adv. Polym. Technol.* **2016**, *35*, 21545.
34. Liu, H.; Luo, Y.; Zhang, G.; Chen, J.; Yang, Z.; Qu, J. Modeling of Pressure-Induced Melt Removal Melting in Vane Extruder for Polymer Processing. *Adv. Polym. Technol.* **2014**, *33*, 21452. [[CrossRef](#)]
35. Wu, H.; Lv, S.; He, Y.; Qu, J.-P. The study of the thermomechanical degradation and mechanical properties of PET recycled by industrial-scale elongational processing. *Polym. Test.* **2019**, *77*, 105882. [[CrossRef](#)]
36. Poyekar, A.V.; Bhattacharyya, A.R.; Panwar, A.S.; Simon, G.; Sutar, D.S. Influence of Noncovalent Modification on Dispersion State of Multiwalled Carbon Nanotubes in Melt-Mixed Immiscible Polymer Blends. *ACS Appl. Mater. Interfaces* **2014**, *6*, 11054–11067. [[CrossRef](#)]
37. Dimzoski, B.; Fortelný, I.; Šlouf, M.; Sikora, A.; Micháľková, D. Morphology evolution during cooling of quiescent immiscible polymer blends: Matrix crystallization effect on the dispersed phase coalescence. *Polym. Bull.* **2013**, *70*, 263–275. [[CrossRef](#)]
38. Rosales, C.; Bernal, C.; Pettarin, V. Effect of blend composition and related morphology on the quasi-static fracture performance of LLDPE/PP blends. *Polym. Test.* **2020**, *90*, 106598. [[CrossRef](#)]
39. Salehiyan, R.; Ray, S.S.; Ojijo, V. Processing-driven morphology development and crystallization behavior of immiscible polylactide/poly(vinylidene fluoride) blends. *Macromol. Mater. Eng.* **2018**, *303*, 1800349. [[CrossRef](#)]
40. Wu, Z.; Wang, Q.; Zhao, Y.; Fan, Q.; Yang, H.; Qu, J. Elongational effect on immiscible polymer blends via novel vane plasticating extruder. *Mechanics* **2017**, *23*, 900–907.
41. He, H.Z.; Xue, F.; Jia, P.F.; He, G.J.; Huang, Z.X.; Liu, S.M.; Xue, B. Linear low-density polyethylene/poly(ethylene terephthalate) blends compatibilization prepared by an eccentric rotor extruder: A morphology, mechanical, thermal, and rheological study. *J. Appl. Polym. Sci.* **2018**, *135*, 46489. [[CrossRef](#)]
42. He, H.-Z.; Xue, F.; Xue, B.; Liu, S.-M.; Huang, Z.-X.; Zhang, H. Improved Properties of Metallocene Polyethylene/Poly(ethylene terephthalate) Blends Processed by an Innovative Eccentric Rotor Extruder. *Polymers* **2020**, *12*, 585. [[CrossRef](#)]
43. Fang, C.; Lu, X.; Qu, J. Preparation and properties of biodegradable poly(lactic acid)/ethylene butyl acrylate glycidyl methacrylate blends via novel vane extruder. *Plast. Rubber Compos.* **2019**, *48*, 364–373. [[CrossRef](#)]
44. He, Y.; Yang, Z.-T.; Qu, J.-P. Super-toughened poly(lactic acid)/thermoplastic poly(ether)urethane nanofiber composites with in-situ formation of aligned nanofibers prepared by an innovative eccentric rotor extruder. *Compos. Sci. Technol.* **2019**, *169*, 135–141. [[CrossRef](#)]

45. He, Y.; Xu, W.-H.; Zhang, H.; Qu, J.-P. Constructing Bone-Mimicking High-Performance Structured Poly(lactic acid) by an Elongational Flow Field and Facile Annealing Process. *ACS Appl. Mater. Interfaces* **2020**, *12*, 13411–13420. [[CrossRef](#)] [[PubMed](#)]
46. Yang, Z.-T.; Yang, J.-X.; Fan, J.-H.; Feng, Y.-H.; Huang, Z.-X. Preparation of super-toughened Poly(L-lactide) composites under elongational flow: A strategy for balancing stiffness and ductility. *Compos. Sci. Technol.* **2021**, *208*, 108758. [[CrossRef](#)]
47. Bai, H.; Huang, C.; Xiu, H.; Zhang, Q.; Deng, H.; Wang, K.; Chen, F.; Fu, Q. Significantly improving oxygen barrier properties of polylactide via constructing parallelaligned shish-kebab-like crystals with well-interlocked boundaries. *Biomacromolecules* **2014**, *15*, 1507–1514. [[CrossRef](#)]
48. Liu, T.; Lian, X.; Li, L.; Peng, X.; Kuang, T. Facile fabrication of fully biodegradable and biorenewable poly (lactic acid)/poly (butylene adipate-co-terephthalate) insitu nanofibrillar composites with high strength, good toughness and excellent heat resistance. *Polym. Degrad. Stabil.* **2020**, *171*, 109044. [[CrossRef](#)]
49. Qu, J.; Yang, Z.; Feng, Y.; Yin, X. Biaxial or Tri-Axial Eccentric Rotor Volume Pulsed Deformation Plasticizing Method and Device. US 2018/0200937A1, 16 September 2017.
50. Zhang, H.; Wei, X.; Qu, J. Microstructure evolution and mechanism of PLA/PVDF hybrid dielectrics fabricated under elongational flow. *Polymer* **2021**, *224*, 123719. [[CrossRef](#)]
51. Zhang, H.C. Study on the Melt Extrusion Process of UHMWPE and Its Morphology and Properties under Elongational Flow. Ph.D. Thesis, South China University of Technology, Guangzhou, China, 2016.
52. Huang, Z.-X.; Zhao, M.-L.; Qu, J.-P. Polyethylene-Based Single Polymer Composites Prepared under Elongational Flow for High-Voltage Applications. *Ind. Eng. Chem. Res.* **2020**, *59*, 18607–18615. [[CrossRef](#)]
53. Wu, T.; Yuan, D.; Qiu, F.; Chen, R.; Zhang, G.; Qu, J. Polypropylene/polystyrene/clay blends prepared by an innovative eccentric rotor extruder based on continuous elongational flow: Analysis of morphology, rheology property, and crystallization behavior. *Polym. Test.* **2017**, *63*, 73–83. [[CrossRef](#)]
54. Zhang, X.-Q.; Tan, Y.-B.; Chen, R.-Y.; Zhang, G.-Z.; Qu, J.-P. Dimensional impact of nanofillers on the micromorphology and rheology of PP/PS composites under continuous elongation flow. *Polym. Adv. Technol.* **2018**, *29*, 2952–2962. [[CrossRef](#)]
55. Tan, L.; He, Y.; Qu, J. Structure and properties of Polylactide/Poly(butylene succinate)/Organically Modified Montmorillonite nanocomposites with high-efficiency intercalation and exfoliation effect manufactured via volume pulsating elongation flow. *Polymer* **2019**, *180*, 121656. [[CrossRef](#)]
56. Wu, T.; He, Y.; Qu, J. Effect of continuous elongational flow on structure and properties of poly(L-lactic acid)/poly(ethylene glycol) blend and its organo-modified montmorillonite nanocomposites. *Polym. Compos.* **2019**, *40*, E617–E628. [[CrossRef](#)]
57. Zhang, G.; Wu, T.; Lin, W.; Tan, Y.; Chen, R.; Huang, Z.; Yin, X.; Qu, J. Preparation of polymer/clay nanocomposites via melt intercalation under continuous elongation flow. *Compos. Sci. Technol.* **2017**, *145*, 157–164. [[CrossRef](#)]
58. Zhang, H.; Huang, J.; Yang, L.; Chen, R.; Zou, W.; Lin, X.; Qu, J. Preparation, characterization and properties of PLA/TiO<sub>2</sub> nanocomposites based on a novel vane extruder. *RSC Adv.* **2015**, *5*, 4639–4647. [[CrossRef](#)]
59. Jia, S.; Qu, J.; Zhai, S.; Huang, Z.; Wu, C.; Chen, R.; Feng, Y. Effects of dynamic elongational flow on the dispersion and mechanical properties of low-density polyethylene/nanoprecipitated calcium carbonate composites. *Polym. Compos.* **2013**, *35*, 884–891. [[CrossRef](#)]
60. Chen, R.; Zou, W.; Wu, C.; Jia, S.; Huang, Z.; Zhang, G.; Yang, Z.; Qu, J. Poly(lactic acid)/poly(butylene succinate)/calcium sulfate whiskers biodegradable blends prepared by vane extruder: Analysis of mechanical properties, morphology, and crystallization behavior. *Polym. Test.* **2014**, *34*, 1–9. [[CrossRef](#)]
61. Meng, C.; Qu, J.-P. Structure-property relationships in polypropylene/poly(ethylene-co-octene)/multiwalled carbon nanotube nanocomposites prepared via a novel eccentric rotor extruder. *J. Polym. Eng.* **2018**, *38*, 427–435. [[CrossRef](#)]
62. Lin, W.; Hou, A.; Feng, Y.-H.; Yang, Z.-T.; Qu, J.-P. UHMWPE/organoclay nanocomposites fabricated by melt intercalation under continuous elongational flow: Dispersion, thermal behaviors and mechanical properties. *Polym. Eng. Sci.* **2018**, *59*, 547–554. [[CrossRef](#)]
63. Mars, J.; Chebbi, E.; Wali, M.; Dammak, F. Numerical and experimental investigations of low velocity impact on glass fiber-reinforced polyamide. *Compos. Part B-Eng.* **2018**, *146*, 116–123. [[CrossRef](#)]
64. Faruk, O.; Bledzki, A.K.; Fink, H.-P.; Sain, M. Biocomposites reinforced with natural fibers: 2000–2010. *Prog. Polym. Sci.* **2012**, *37*, 1552–1596. [[CrossRef](#)]
65. Wu, C.; Jia, S.; Chen, R.; Huang, Z.; Zhai, S.; Feng, Y.; Yang, Z.; Qu, J. Composites of sisal fiber/polypropylene based on novel vane extruder: Effect of interface and damage on mechanical properties. *J. Reinf. Plast. Compos.* **2013**, *32*, 1907–1915. [[CrossRef](#)]
66. Adeniyi, A.G.; Onifade, D.V.; Ighalo, J.O.; Adeoye, A.S. A review of coir fiber reinforced polymer composites. *Compos. Part. B Eng.* **2019**, *176*, 107305. [[CrossRef](#)]
67. Guo, K.; Wang, D.; Zhang, G.; Song, J.; Wu, T.; Qu, J. Effect of series explosion effects on the fiber length, fiber dispersion and structure properties in glass fiber reinforced polyamide 66. *Polym. Adv. Technol.* **2021**, *32*, 505–513. [[CrossRef](#)]

## Article

# Influence of the Alkali Treatment of Flax and Hemp Fibers on the Properties of PHBV Based Biocomposites

Wiesław Frącz \*, Grzegorz Janowski and Łukasz Bąk

Department of Materials Forming and Processing, Rzeszow University of Technology, 35-959 Rzeszow, Poland; gjan@prz.edu.pl (G.J.); lbak@prz.edu.pl (Ł.B.)

\* Correspondence: wf@prz.edu.pl; Tel.: +48-17-8651-714

**Abstract:** This study assessed the impact of alkali treatment of hemp and flax fibers on mechanical properties (determined by means of the uniaxial tensile test, impact tensile strength test and hardness test), processing properties (the course of the extrusion and injection process) and usable properties (shrinkage of molded pieces, degree of water absorption) of biocomposites on the base of poly (3-hydroxybutyric-co-3-hydroxyvaleric acid) (PHBV) biopolymer. For this purpose, 1 mm of length flax and hemp fibers was surface-modified by means of aqueous solution of NaOH (sodium hydroxide) with concentrations of 2%, 5% and 10%. The composites were made using the extrusion technology. The test specimens were produced by injection molding technology. In total, eight types of biocomposites with modified and non-modified fibers were produced, and each biocomposite contained the same filler content (15 wt.%). Their properties were compared in some cases with pure PHBV polymer. In the case of biocomposites filled with hemp fibers, it was noted that an increase of the alkalizing solution concentration improved most of the tested properties of the obtained biocomposites. On the other hand, in the case of flax fibers, there was a significant decrease in most of the mechanical properties tested for the composite containing fibers etched by 10% NaOH solution. The obtained results were verified by examining fibers and the destroyed specimens with a scanning electron microscope (SEM) and an optical microscope, which confirmed, especially, the significant geometry changes of the flax fibers etched by 10% NaOH solution. This procedure also resulted in a significant change of processing properties—a composite of this fiber type required about 20 °C lower temperature during the extrusion and injection molding process in order to obtain the right product. These results lead to the important conclusion that for each filler of the plant-origin and polymer matrix, the fiber alkalization method should be selected individually in order to improve the specific properties of biocomposites.

**Citation:** Frącz, W.; Janowski, G.; Bąk, Ł. Influence of the Alkali Treatment of Flax and Hemp Fibers on the Properties of PHBV Based Biocomposites. *Polymers* **2021**, *13*, 1965. <https://doi.org/10.3390/polym13121965>

Academic Editors: Célio Bruno Pinto Fernandes, Salah Aldin Faroughi, Luís L. Ferrás and Alexandre M. Afonso

Received: 26 April 2021

Accepted: 10 June 2021

Published: 14 June 2021

**Keywords:** poly (3-hydroxybutyric-co-3-hydroxyvaleric acid) (PHBV); flax; hemp; short fibers; injection molding; extrusion; properties

**Publisher's Note:** MDPI stays neutral with regard to jurisdictional claims in published maps and institutional affiliations.



**Copyright:** © 2021 by the authors. Licensee MDPI, Basel, Switzerland. This article is an open access article distributed under the terms and conditions of the Creative Commons Attribution (CC BY) license (<https://creativecommons.org/licenses/by/4.0/>).

## 1. Introduction

The main components of plant-origin fibers are cellulose, hemicellulose and lignin. Cellulose is synthesized in plants, trees and grasses and even in some varieties of algae, fungi and bacteria. The most common and abundantly available cellulose is contained in cotton (about 90% cellulose content) [1,2]. The proportion of cellulose in plants may vary depending on the species and age of the plant. Cellulose is a hydrophilic biopolymer consisting of a linear chain of glucose molecules linked by  $\beta$ -1,4-glycosidic bonds that contain hydroxyl groups. These groups form intermolecular and intramolecular hydrogen bonds with the macromolecule itself as well as with other cellulose macromolecules or polar molecules. Fibers of plant origin are hydrophilic. Although the chemical structure of cellulose from different natural fibers is the same, the degree of polymerization is different. The mechanical properties of the fibers largely depend on the degree of polymerization of the cellulose. In plants, cellulose has two different unit cells: I and II. In an alkaline



environment, cellulose I is converted to II. Form II is more thermodynamically stable, which provides higher thermal resistance and strength [2]. Hemicellulose is a heterogeneous biopolymer of a group of polysaccharides and their derivatives, linked by  $\beta$ -glycosidic bonds to form branched chains. In contrast to alkaline-soluble cellulose, hemicellulose is less resistant to dilute acids [3]. Lignin fills the spaces between the polysaccharide fibers, binding them together. The presence of these component fibers causes a stiffening of the cell walls to protect against chemical and physical damage. Lignin is a polymer with monomers derived from phenolic alcohols. The presence of this compound in the fibers reduces the penetration of water into the cells and stiffens the material [4]. It should be noted that individual components of plant-origin fibers degrade in various temperature ranges. Above 200 °C, hemicellulose degrades, and above 300 °C, cellulose degrades. Lignin is the most thermally resistant—it degrades above 350 °C. Obviously, the mechanical properties of the fibers decrease with the degradation of successive compounds that build plant fiber [5].

Hydroxyl groups (OH) in cellulose, hemicellulose and lignin build a large number of hydrogen bonds inside the macromolecule and between macromolecules in the cell wall of plant-origin fibers. The action of water on the plant fibers causes these bonds to break. The hydroxyl groups then form new hydrogen bonds with the water molecules that promote the swelling of the fiber. The swelling of the cell wall generates very strong forces. The theoretical value of the pressure may be about 165 MPa [6], but the real swelling pressure is half of the calculated value [7,8]. Cellulose fibers interact with water not only on the surface but also in the entire volume. The structure of cellulosic materials consists of crystalline and amorphous regions. Amorphous areas easily absorb chemical compounds such as dyes and resins, and the presence of crystalline areas makes chemical penetration difficult [9].

The possibility of water absorption by cellulose fibers depends on the following aspects, among others [1,2]:

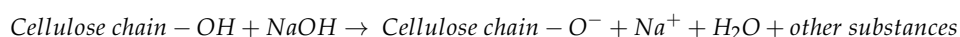
- Purity of cellulose: Raw cellulosic material, such as unwashed sisal fibers, absorbs at least twice as much water as washed fibers due to a 24% pectin content.
- Degree of crystallinity: All the OH groups in the amorphous phase are accessible to water, while only a small amount of water interacts with the surface OH groups of the crystalline phase.

The main disadvantage of cellulose fibers is their highly polar nature, which makes them incompatible with non-polar polymers. The poor resistance to water absorption makes the use of natural fibers less attractive for applications involving external factors such as rain, snow and hail [10].

The polymers have different affinity for the fiber due to the difference in their chemical structure [11–14]. Effective filling of composites with plant fibers depends on moisture content, fiber–matrix interfacial adhesion, cellulose content and the degree of crystallinity. In order to increase the possibility of adhesion of the fibers to the polymer matrix, reduce water absorption, increase the proportion of cellulose in the fiber and increase the degree of crystallinity, different methods of fiber surface modification are used.

Cellulose fibers can be physically modified, e.g., by calendaring, stretching, thermal treatment, plasma treatment and corona discharge. In turn, chemical methods of modification of fibers include silanization, alkalization, acetylation, graft copolymerization and modification with enzymes [15,16]. One of the most popular methods of chemically modifying the surface of fibers is alkalization, often referred to as mercerization. This method is based on the action of a sodium hydroxide solution (at the appropriate concentration) on the plant fiber.

The reaction of sodium hydroxide with cellulose is shown by the equation below:



Hydroxyl groups, which are polar in nature, are blocked by the action of sodium, and water is released as a byproduct of the reaction. Moreover, the abovementioned chemical treatment removes lignin, pectin, waxy substances and natural oils covering the outer

surface of the fiber cell wall. This can increase the proportion of cellulose in the fiber and the roughness of the cell wall surface. Additionally, alkalization enables the conversion of type I cellulose to type II, which increases the thermodynamic resistance and strength properties of cellulose and consequently of the entire plant fiber [16–19]. It is worth noting that alkalization also shortens the cellulose chains [19].

The effect of surface modification, and in particular the alkalization of hemp and flax fibers, has been the subject of many studies [20–27]. Ouajai and Shanks [20] found that pectin and hemicellulose were removed during the alkalization from hemp fibers. Mwaikambo et al. [21] conducted FTIR studies to confirm that hemicellulose was removed by treatment with a base solution of cellulose fibers, including hemp fibers. In [22], the mercerization of hemp fiber increased the tensile strength and bending strength of PP–hemp fiber composites, which indicates an improvement in interfacial bonding after alkaline treatment. The highest values of tensile and bending strength of PP composites reinforced with hemp fibers were obtained with a 4% sodium base solution treatment. Meanwhile, the tensile and bending strength of the composite filled with fibers treated with 6% NaOH solution was lower than in the case of composites etched with 2% and 4% NaOH solutions. The results of the work by Hu et al. [23] also indicate that the tensile strength and flexural strength values are higher when the hemp fibers are alkalized. The authors also noted that the alkaline treatment of the fibers effectively removed non-cellulose fractions, which resulted in a 25.9% reduction in fiber weight and had a positive effect on the mechanical properties by improving the fiber–matrix bonds. The surface morphology of the fiber was significantly changed after the treatment by removing the non-cellulose layer on the fiber, resulting in a higher surface roughness. In the work of Pickering [24], the alkalization of hemp fibers improved their adhesion to polymer matrices. This was due to a change in the fiber surface properties, removal of non-crystalline components such as hemicellulose, lignin and pectin [25] and removal of waxes and fatty acids that may adversely affect interfacial bonds. Van de Weyenberg and co-authors [26] investigated the influence of some methods of physical modification of flax fibers on the properties of composites (fiber volume content was 40%) with a polyethylene matrix. Li and co-authors [27] investigated the properties of polyethylene–flax fiber biocomposites. The composites contained 10 wt.% fiber contents and were processed by extrusion and injection molding. Five surface modification methods were used: mercerization, silanization, potassium permanganate, acrylic acid and soda chlorite treatment to improve the bond between the fibers and the matrix. It was noticed that the tensile strength of the biocomposite increased after the flax fibers were alkalized.

An important problem is the constantly increasing amount of plastic waste in Europe and all over the world. It should be mentioned that these materials are mostly of petrochemical origin [28], are not biodegradable and are recycled with varying degrees of success. Poly (3-hydroxybutyric-co-3-hydroxyvaleric acid) (PHBV) belonging to the group of polyhydroxyalkanoates (PHAs) is a polymer of natural origin that is fully biodegradable. Due to its high production costs, it is rarely used as an injection molded material and therefore has little commercialization potential. One of the methods of reducing production costs and improving the properties of the abovementioned biopolymer is the use of plant-origin fibers as a filler in the PHBV matrix.

Quite a large number of studies conducted on PHBV composites with a matrix of plant fibers concern the possibility of processing mainly by compression molding of thin layers or films [29–32]. Some results have been obtained with composites manufactured on a very small scale [33]. Both compression molding of thin composite sheets and processing on mini extruders and mini injection molding machines are limited processes due to the fact that they are difficult to relate to actual processing conditions. Composites with a PHBV matrix filled with fibers of plant origin such as coconut [34–38], bamboo [39–46], abaca [47,48], pineapple [32,49] and sisal [50–52] have been the subject of research.

There is a noticeable amount of information on the possibility of processing and assessing the properties of PHBV composites with cellulose fibrous fillers such as flax,

hemp and wood fiber—i.e., the most popular and available fibers in European countries. In this regard, for example, in the work of Keller [53], a PHBV composite was produced—hemp fiber by means of a co-rotating twin-screw extruder. Fibers with a length ranging from 5 to 25 mm were tested. PHBV with the trade name Biopol D400 GN was used as the polymer matrix. Due to the instability of filler introduction, manual dispensing of entangled fibers not only resulted in non-uniform granules but also caused fiber stagnation in the area of the die inlet, especially at higher fiber contents. In order to ensure stable work, an attempt was made, *inter alia*, to spinning to obtain a greater degree of homogenization, and the configuration of the screw zones was optimized to minimize damage to the fibers during the mixing process. Shortening of the fibers and loss of rectilinear geometry were noticed during the process. A composite with a volume fraction of fibers equal to 32% was obtained. The produced granulate was injected into the mold with the geometry of the samples intended for the uniaxial tensile test. The study also found that using hemp fibers in the PHBV matrix did not improve the tensile strength, while it was found that the maximum elongation was reduced compared to pure PHBV.

The work of Barkoul and co-authors [54] focused on the assessment of the properties of PHBV–flax fiber composites with variable flax fiber content. The tests were performed for samples produced by injection molding and compression molding. The polymer matrix was PHB with the trade name Biopol. Poly (3-hydroxyvaleric acid) was added to the PHB in an amount of 8 and 12% by weight. The length of the linen fibers used was approximately 10 mm, and the fibers arranged in the form of a mat 25 mm. The volume fraction of fibers in the polymer matrix was changed and amounted to: 0%, 20%, 30% and 40%. The mat saturated with biopolymer was pressed. The polymer matrix and the fibers were mixed using a rotary rheometer to prepare the injection molding granulate. The mixture was then granulated and injected into a mold. The mechanical properties of the obtained composites with the mass fraction of filler from 10% to 30% were compared. Similar values of Young's modulus were noted for samples produced by the two methods. Slightly higher values of the elasticity modulus were obtained for injection molded samples (approximately 6 GPa at 30% by volume of the filler). In the case of the tensile strength and the maximum elongation of the samples, similar results were obtained for both methods. In the case of the Izod impact toughness test, significantly higher impact toughness values were obtained for pressed samples.

On the other hand, when analyzing the studies on the possibility of using short hemp, flax fibers in the PHBV matrix, little information was noticed regarding the production, processing and evaluation of the properties of this type of composites. The fibers used in the abovementioned works were usually characterized by quite a long length, with a very large statistical dispersion. This could be the reason for determining random properties of the obtained composites. In addition, fibers that were too long in relation to the diameter of the extruder screw and injection molding machine underwent mechanical degradation, as a result of which the said fiber length spread could be even greater. Moreover, there is no information on the modification of the surface of the fibers in order to improve the adhesion of the fiber to the matrix. The large and variable ratio of the fiber size to the size of the pure PHBV granulate also resulted in a very low degree of homogenization of the composites. Therefore, it was important to consider the possibility of using short fibers in the PHBV matrix, e.g., with a length of 1 mm and a very small length spread, and the matrix in the form of a powder. This would probably make it possible to obtain composites with a higher degree of homogenization. It should be mentioned that some of the works did not use conventional devices for the preparation of pellets, i.e., an extruder; hence, the observations and obtained results regarding the obtaining of composite pellets may not reflect possible phenomena and problems on an industrial scale. Based on the literature review on the composition and surface modification of plant fibers, it was noticed that the use of an appropriate method of fiber etching affects the properties of the obtained biocomposites. Therefore, research was undertaken on the influence of the surface treatment of flax and hemp fibers on the properties of the obtained PHBV matrix biocomposites.

## 2. Materials and Methods

### 2.1. Materials

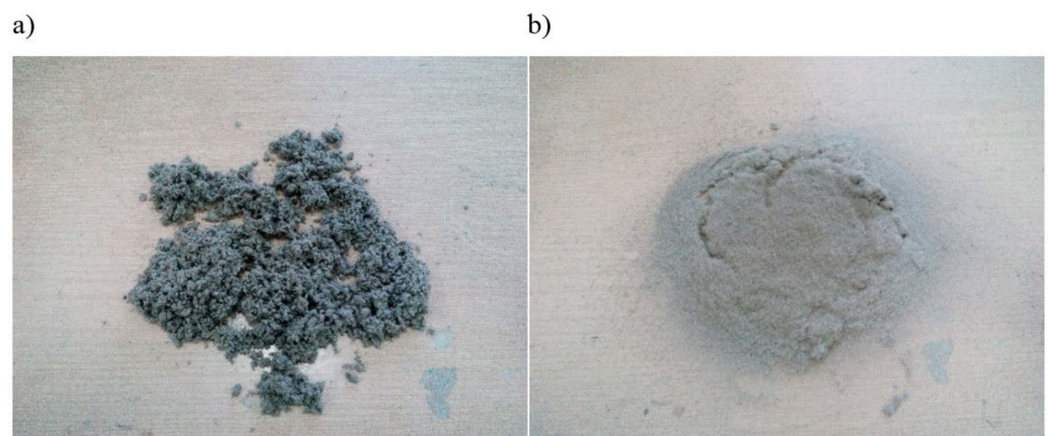
The PHBV powder Enmat Y1000 trade name of Helian Polymers (Belfeld, The Netherlands) trade name was used as the polymer matrix. The molar proportion of HV in the biopolymer was 8%, the density of the biopolymer  $1250 \text{ kg/m}^3$  and the softening point ranged from 165 to 175 °C.

Hemp and flax fibers (delivered by EKOTEX company (Kowalowice, Poland)) with a length of approximately 1 mm and an average length-to-diameter ratio (L/d) of approximately 10 were used as the filler in the polymer matrix.

The produced biocomposites contained flax or hemp fibers with a 15% mass fraction. For the surface modification of the fibers, an aqueous sodium hydroxide solution with concentrations of 2%, 5% and 10% was used.

### 2.2. Sample Preparation

The surface of the fibers was modified with sodium hydroxide solution for various concentrations, i.e., 2%, 5% and 10% NaOH. The selection of the percentage concentration was established based on the literature [55–60]. Mercerization was carried out for 1 h in a rotor device, whereby the fibers were constantly mixed with the solution. During the alkalization, the temperature of the mixture increased. Then, the fibers were washed with water until they were neutral, filtered off with a centrifuge and dried at 90 °C. As a result of the surface modification carried out, the fibers tended to form larger clusters (Figure 1a), which is an undesirable effect that could negatively affect the proper homogenization of the fiber-PHBV mixture. All clusters of fibers were screened on a sieve (the mesh size was 1.5 mm), thanks to which a more uniform distribution of filler size used in the PHBV was obtained (Figure 1b).



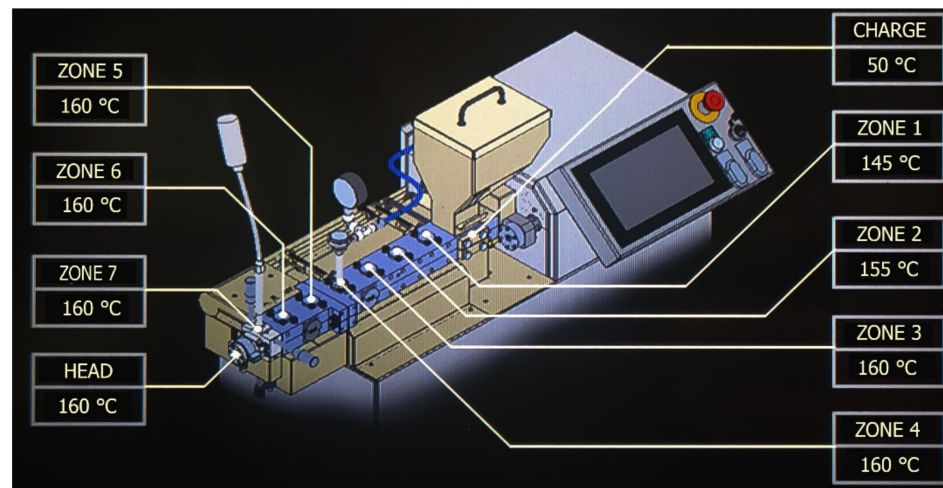
**Figure 1.** Hemp fibers alkalinized with 10% NaOH solution: (a) before sieving, (b) after sieving.

Eight types of PHBV matrix biocomposites with the following markings were produced in the extrusion process:

- K0—containing hemp fibers not surface-modified;
- K2—containing hemp fibers surface-modified with 2% NaOH solution;
- K5—containing hemp fibers surface-modified with 5% NaOH solution;
- K10—containing hemp fibers surface-modified with 10% NaOH solution;
- L0—containing flax fibers not surface-modified;
- L2—containing flax fibers surface-modified with 2% NaOH solution;
- L5—containing flax fibers surface-modified with 5% NaOH solution;
- L10—containing flax fibers surface-modified with 10% NaOH solution.

The biocomposites were extruded using a ZAMAK REA-2P12A twin-screw extruder produced by ZAMAK Mercator company (Skawina, Poland) at constant temperature values on individual heating zones of the extruder in the range from 145 (zone 1) to 160 °C

(head) (Figure 2). The list of set temperatures is presented in Table 1. Only in the case of biocomposite with flax fibers alkalinized with 10% NaOH solution was it required to lower the temperatures by approximately 20 °C in all heating zones due to the very low viscosity of the extrudate obtained. At given default temperatures (such as during extrusion of other biocomposites), the extrudate was characterized by a very low viscosity, from which it was difficult to obtain extrudates of the correct length. Moreover, the extrusion process of this composite was unstable—jumps of the pressure value at the extruder head by approximately 30% were noticed.



**Figure 2.** Areas on the individual heating zones of the twin screw extruder for K0 biocomposite extrusion.

**Table 1.** The temperatures set on the individual heating zones of the twin screw extruder.

Type of Biocomposite	Head	Zones 3–7	Zone 2	Zone 1	Charge
K0, K2, K5, K10, L0, L2, L5	160 °C	160 °C	155 °C	145 °C	50 °C
L10	140 °C	140 °C	135 °C	125 °C	50 °C

Extrusion of all biocomposites was carried out with constant screw rotational speed of 50 rpm. Extrusion was carried out using an extrudate granulating station equipped with a cooling bath and a granulator. It should be noted that both the polymer matrix and the plant fibers were earlier dried for 3 h at a temperature of 90 °C before the extrusion process. The obtained granules were used for the production of specimens for testing mechanical properties by means of injection molding technology.

A DrBoy 55E injection molding machine, produced by BOY Machines Inc. (Exton, PA, USA) equipped with a Priamus system for monitoring and controlling the injection molding process was used for the manufacturing process of the samples.

An injection mold with inserts intended for uniaxial tensile testing (in accordance with PN-EN ISO 527-1) [61] was used in the tests. The “dog-bone” geometry samples for all types of biocomposites and biopolymers were manufactured with the adjustable parameters listed in Table 2. Only in the case of the biocomposite with flax fibers alkalinized with 10% NaOH solution were the lower temperatures by approximately 20 °C in all heating zones of the injection molding machine required. At the set default temperatures, the injected material was characterized by a very low viscosity, which made it difficult to obtain a workpiece with the correct shape.

**Table 2.** The processing parameters of samples for uniaxial tensile testing.

Parameter	K0, K2, K5, K10, L0, L2, L5	L10
Mold temperature (°C)	60	60
Melt temperature (°C)	167	147
Cooling time (s)	25	25
Packing time (s)	25	25
Packing pressure (MPa)	30	30
Flow rate (cm <sup>3</sup> /s)	35	35
Mold temperature (°C)	60	60

### 2.3. Methods

The Zwick Z030 testing machine was used to determine the strength properties of the obtained composites. The uniaxial tensile test was carried out in accordance with the EN ISO 527-1 standard for specimens with “dog-bone” geometry. Each series of specimens consisted of seven pieces for subsequent statistical analysis. On the basis of the obtained test results, the following were analyzed: Young’s modulus (E), tensile strength ( $\sigma_M$ ) and elongation at break ( $\epsilon_M$ ). The results were statistically processed, where the arithmetic mean (AM), standard deviation (SD) and the coefficient of variation (CV) were determined. The Brinell method was used in accordance with PN-EN ISO 2039-1 [62] in two areas of samples intended for the uniaxial tensile test, i.e., in the measuring zone for the uniaxial tensile test (zone A) and in the gripping part (zone B). For this purpose, a Zwick 3106 hardness tester was used. Each series of samples consisted of seven pieces for subsequent statistical analysis.

Tests of biocomposite samples in the impact tensile test were carried out too. The impact tensile strength was determined in accordance with the EN ISO 8256 [63] standard. A CEAST 9050 pendulum hammer produced by Instron Inc. Europe (Buckinghamshire, UK) was used for this purpose. Sample geometry was modified according to the standard. The notch was milled for entire sample packages. Each series of samples consisted of seven pieces for subsequent statistical analysis.

The degree of water absorption of the produced samples was tested based on the EN ISO 62 [64] standard. The molding shrinkage of the “dog-bone” geometry was tested on the basis of the EN ISO 294-4 [65] standard.

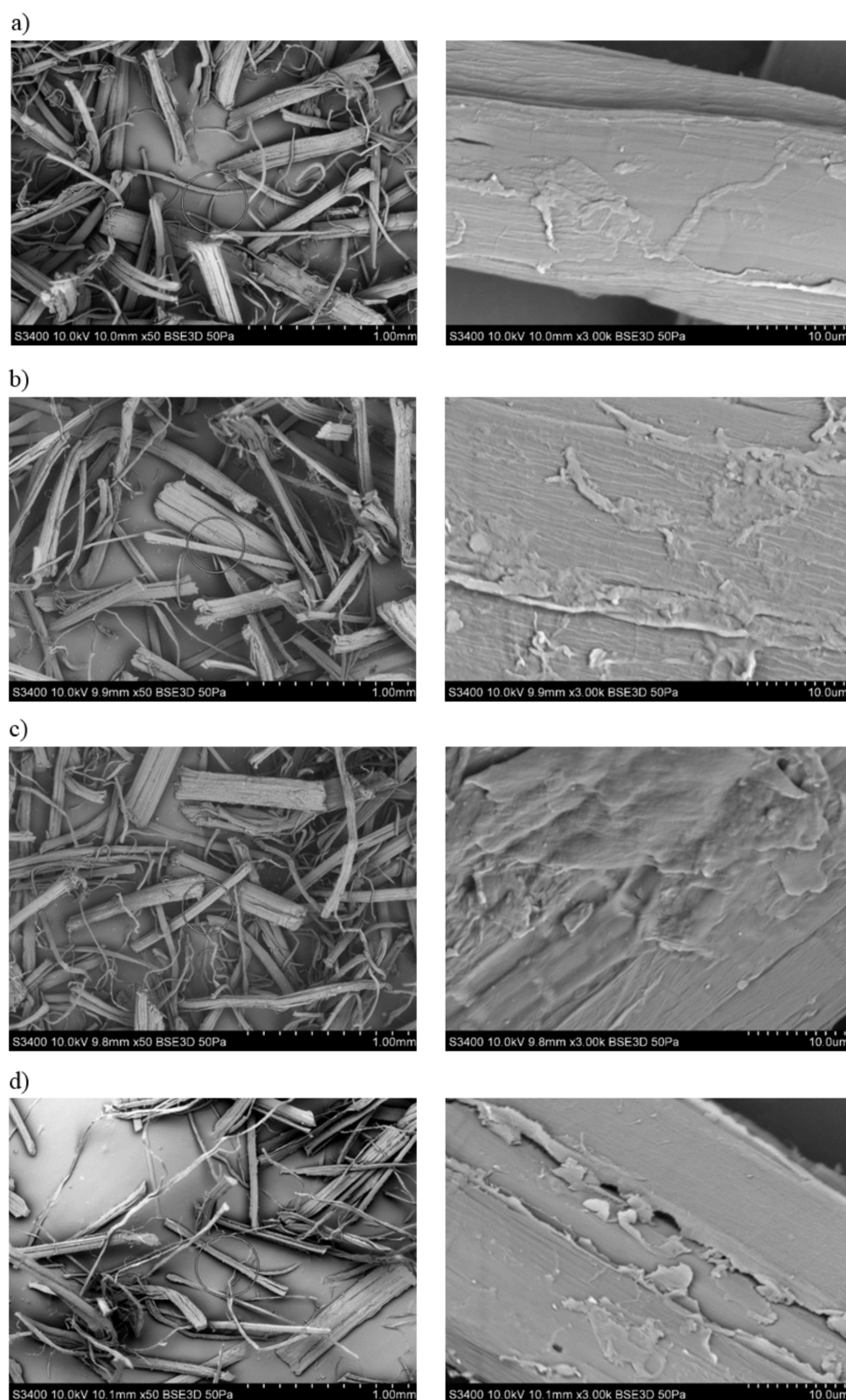
The study of sample topography was carried out using a HITACHI S-3400 scanning electron microscope (SEM) produced by Hitachi Inc. (Tokyo, Japan). In order to visually assess the surface and geometry of the fibers and composites, a Nikon MM 800 workshop microscope produced by Nikon Inc. (Tokyo, Japan), a Nikon LV-100D optical microscope and a Alicona Infinite Focus 3D microscope produced by Alicona Imaging GmbH, (Raaba/Graz, Austria) were used.

## 3. Results

### 3.1. Assessment of the Surface Microstructure of Composites

In order to assess the degree of etching of plant fibers, a scanning electron microscopy study was carried out using a HITACHI S-3400 scanning electron microscope (SEM).

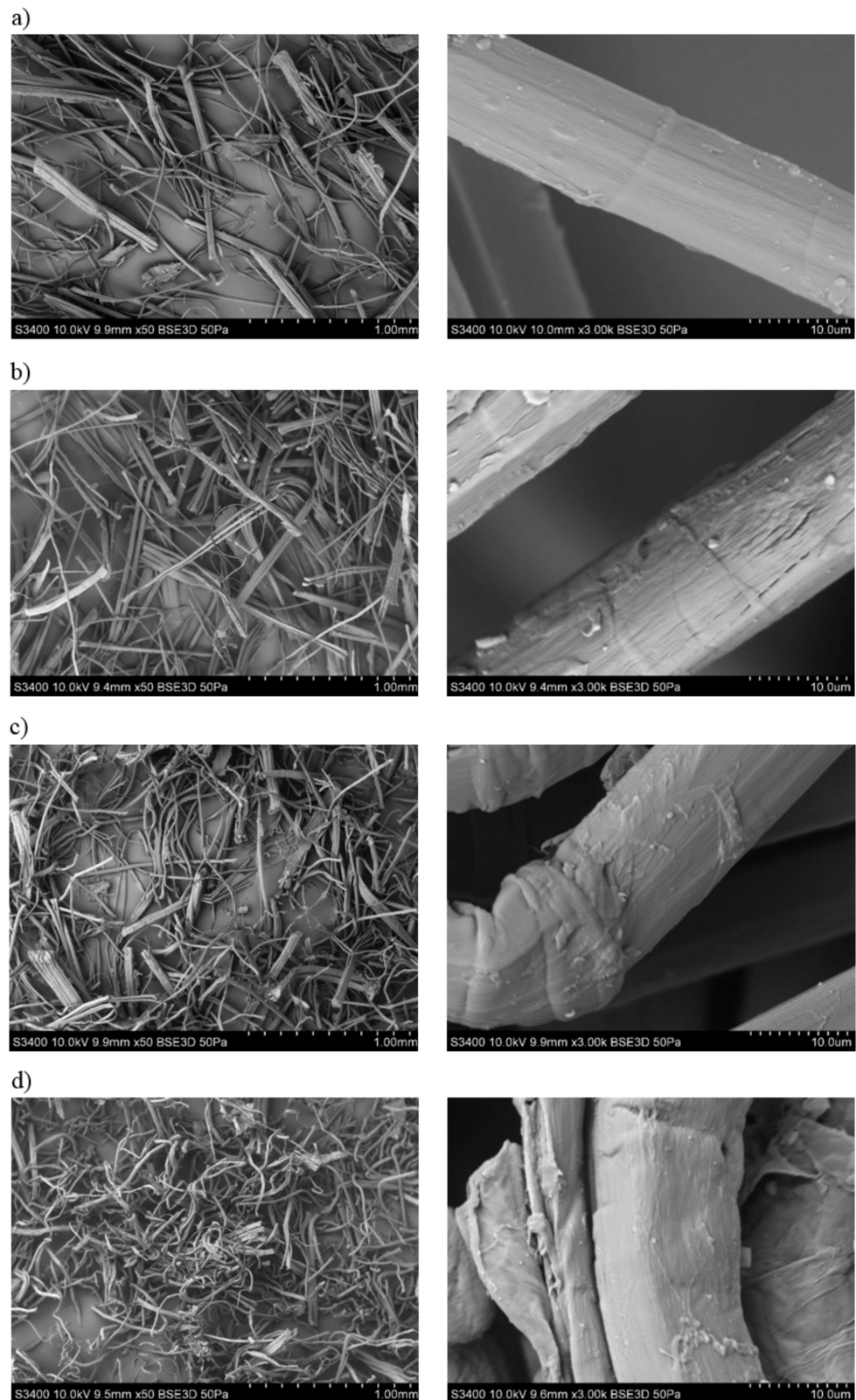
By analyzing the SEM photographs (Figure 3) of hemp fibers subjected to alkalization, it can be observed that the surface of the fibers is more developed than before the modification. Moreover, the fibers subjected to the mercerization process are characterized by a slightly smaller diameter, while maintaining a rectilinear geometry.



**Figure 3.** SEM photographs of hemp fibers: (a) unmodified, (b) exposed to 2% NAOH solution, (c) exposed to 5% NAOH solution, (d) exposed to 10% NAOH solution.

By analyzing the SEM images of flax fibers (Figure 4), an increase in the degree of surface development after treatment with NaOH solution can be observed. When treating the fibers with a 5% solution and especially with 10%, the fibers lose their rectilinear

geometry; they are twisted and form groups of interconnected “bundles”. For all images of flax fibers after chemical modification, the diameter of the fibers is smaller.

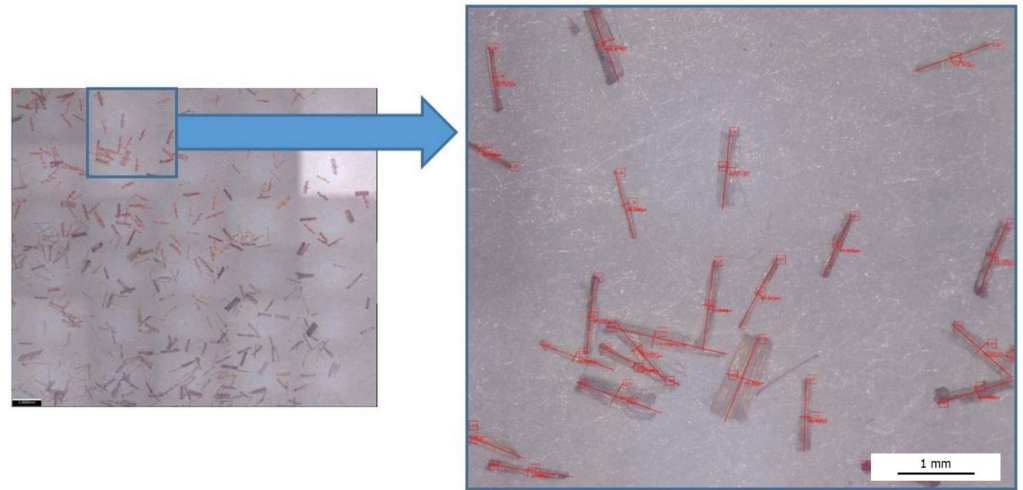


**Figure 4.** SEM photographs of flax fibers: (a) unmodified, (b) alkalinized by 2% NaOH solution, (c) alkalinized by 5% NaOH solution, (d) alkalinized by 10% NaOH solution.



### 3.2. The Fibers Shape Assessment of Factor Using Microscopic Examination

An analysis of the length and diameter of the fibers before and after surface modification was performed. For this purpose, photos of fibers were taken (Figure 5) using the Alicona Infinite Focus microscope. Then, after taking the photographs, about 100 fibers from each set were measured, where the length ( $L$ ) and diameter ( $d$ ) of each fiber were determined. The results were statistically analyzed (Table 3). The standard deviation ( $SD$ ) (in relation to length— $SD_L$ , diameter— $SD_d$ ) and the coefficient of variation ( $CV$ ) (in relation to length— $CV_L$ , diameter— $CV_d$ ) were determined.



**Figure 5.** Example photograph of cellulose fibers for which the length and diameter were measured.

**Table 3.** Average value of hemp and flax fiber length and diameter as well as the shape factor in statistical analysis.

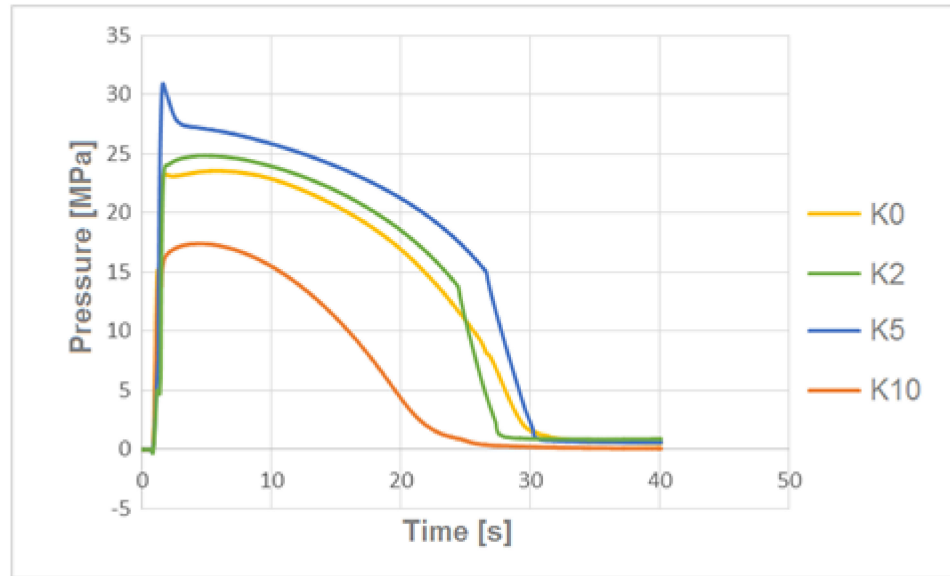
Type of Biocomposite	L (mm)	$SD_L$	$CV_L$	d (mm)	$SD_d$	$CV_d$	L/d
L0	1.002	0.114	11.38	0.095	0.058	61.05	10.55
L2	0.994	0.113	11.37	0.090	0.055	61.11	11.04
L5	1.001	0.118	11.79	0.065	0.038	58.46	15.40
L10	0.998	0.121	12.12	0.047	0.029	61.70	21.23
K0	0.987	0.112	11.35	0.138	0.051	36.96	7.15
K2	1.003	0.102	10.17	0.134	0.050	37.31	7.49
K5	0.997	0.099	9.93	0.121	0.038	31.40	8.24
K10	0.991	0.095	9.59	0.113	0.042	37.17	8.77

When analyzing the results (Table 3) concerning the measurement of the length and diameter of the fibers, it should be noted that the diameter of flax fibers after modification using 10% NaOH solution was reduced by approximately 51%, which resulted in an increase in the shape factor to a value of approximately 21. On the other hand, the hemp fibers alkalinized by 10% NaOH solution were characterized by a reduced diameter of approximately 18%, which resulted in the obtained shape factor of approximately 9. In the case of fiber length measurement, the degree of surface modification did not change the length value.

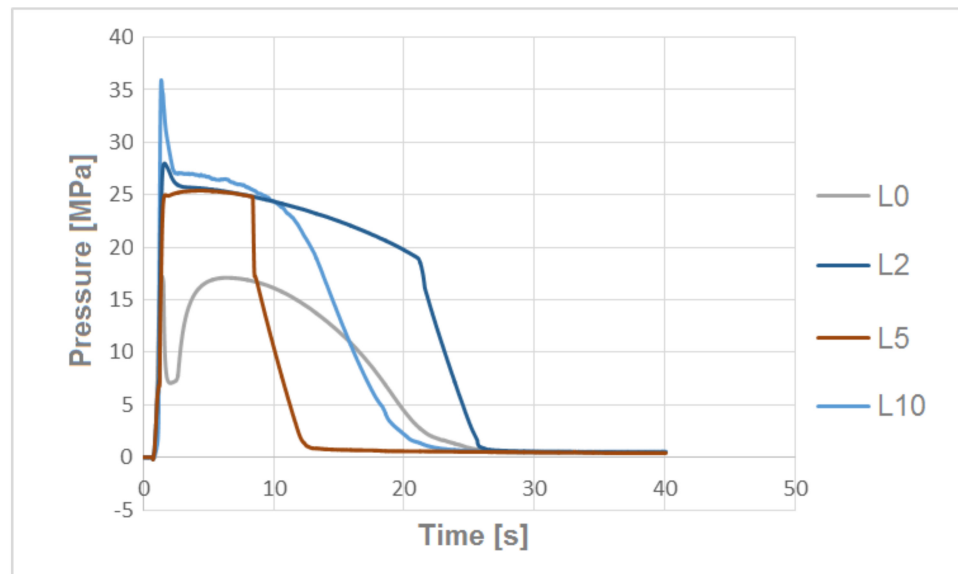
### 3.3. The Pressure Change Profile Analysis in the Mold Cavity

By analyzing the pressure profiles in the mold cavity for biocomposites filled with hemp fibers alkalinized with various concentrations of NaOH solution (Figure 6), lower

pressures in the mold cavity were obtained for the composite with fibers modified with 10% NaOH solution. In the case of pressure profiles for biocomposites filled with flax fibers (Figure 7), there was a problem with obtaining the correct switching point during injection—this is evidenced by undesirable temporary pressure increase. Additionally, as the degree of flax fiber modification increased, higher pressure values were observed for the corresponding biocomposites.



**Figure 6.** The pressure profiles in the mold cavity for composites filled with unmodified hemp fibers and modified with alkalized 2%, 5% and 10% NaOH solution.

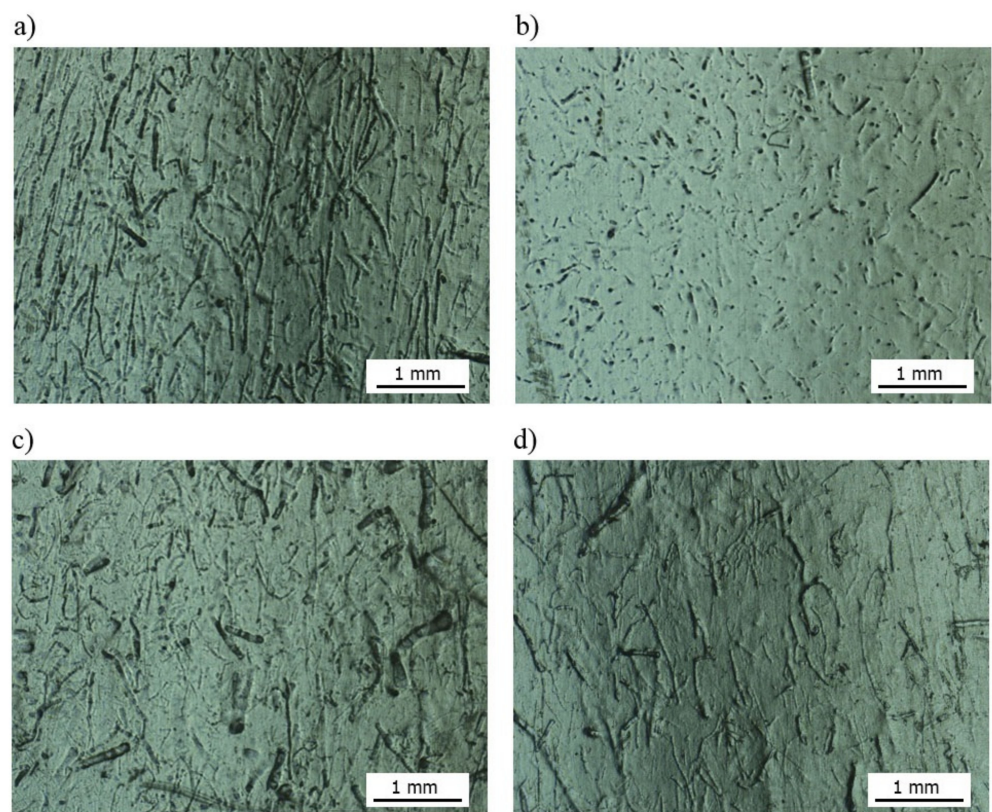


**Figure 7.** The pressure profiles in the mold cavity for composites filled with unmodified flax fibers and modified with alkalized 2%, 5% and 10% NaOH solution.

The obtained samples were intended for testing the mechanical properties and quality of the molded piece.

### 3.4. The Surface Quality Assessment of the Molded Piece Using Optical Microscopy

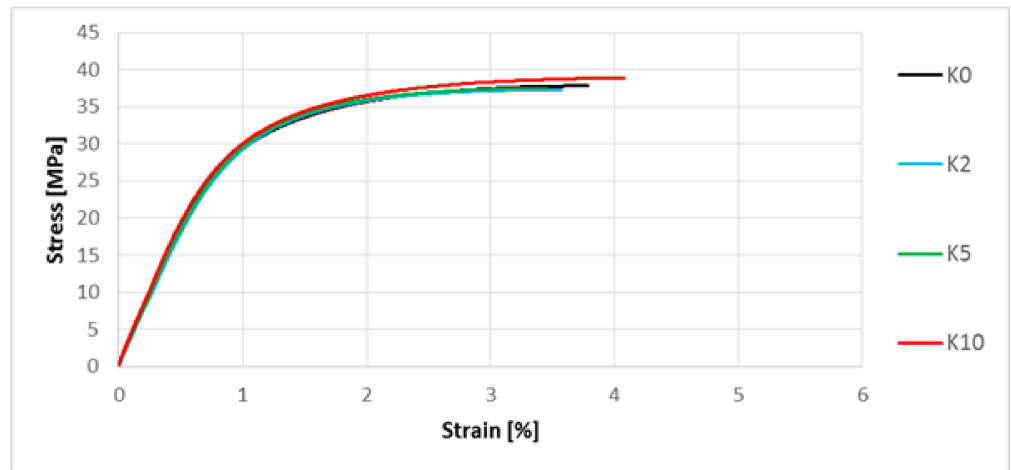
Additional tests were carried out by means of an optical microscope to assess the quality of the sample surfaces of “dog-bone” shape (in the measuring zone) made of biocomposites filled with unmodified fibers and alkalized with 10% sodium hydroxide solution. It was observed (Figure 8) that the flax fibers after surface modification are barely visible in the polymer matrix, in contrast to unmodified flax fibers. This may indicate that the flax fibers modified with 10% NaOH solution are excessively etched, i.e., they degrade and therefore do not fulfill the proper filler function. In the case of hemp fibers modified with 10% NaOH solution, it was noticed that the degree of fiber dispersion is more favorable than that for a biocomposite with unmodified fiber—the fibers have a smaller diameter, are more regularly distributed in the polymer matrix and a greater unidirectional tendency is noticeable.



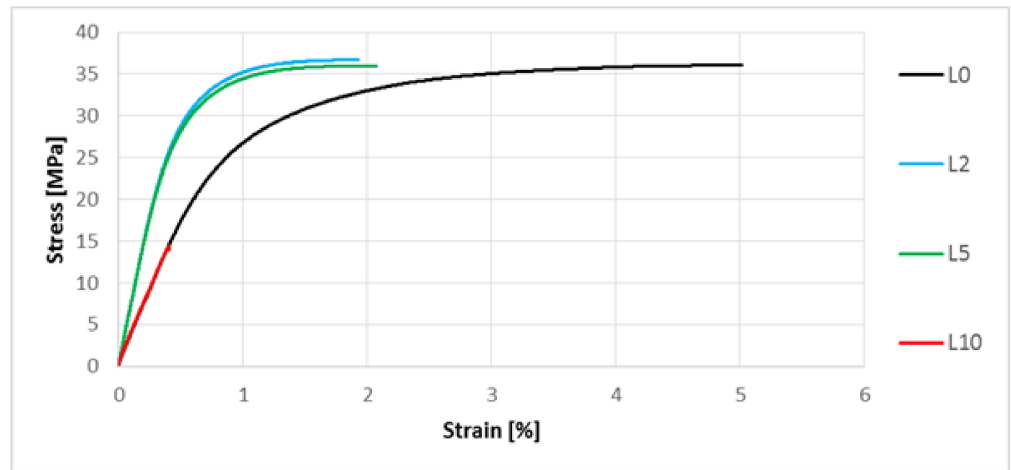
**Figure 8.** Areas of molded piece surface (50× magnification) for biocomposites: (a) L0, (b) L10, (c) K0, (d) K10.

### 3.5. Determination of Mechanical Properties by Means of the Uniaxial Tensile Test

A uniaxial tensile test was performed. The representative stress–strain characteristics are shown in Figures 9 and 10.



**Figure 9.** Stress–strain characteristics for composites with unmodified hemp fibers and those modified by 2%, 5% and 10% NaOH solution.



**Figure 10.** Stress–strain characteristics for composites with unmodified and modified flax fibers exposed to 2%, 5% and 10% NaOH solution.

Analyzing the results (Table 4), it was noticed that the alkalization on hemp fibers used as a filler in biocomposites had a positive effect on the increase of Young’s modulus in relation to the biocomposite with unmodified hemp fibers (increase by approximately 5% for the composite marked K10), as well as tensile strength (increase by approximately 1.5% for the composite marked K10). In the case of elongation at break, no direct relationship was found regarding the effect of examined solution concentration. In the case of biocomposites with fibers modified by 2% and 5% NaOH solution, there was a decrease in the elongation value, while for the biocomposite with fibers modified by 10% NaOH solution, the elongation value slightly increased compared to the biocomposite in which hemp fibers were not alkalinized.

**Table 4.** Results from the uniaxial tensile test for biocomposites with unmodified hemp fibers and fibers exposed to 2%, 5% and 10% NaOH solution.

Type of Biocomposite	Statistics	E (MPa)	$\sigma_M$ (MPa)	$\epsilon_M$ (%)
K0	AM	3815.78	37.58	3.83
	SD	24.00	0.23	0.06
	CV	0.63	0.62	1.66
K2	AM	3855.64	37.17	3.57
	SD	45.64	0.84	0.07
	CV	1.18	2.25	2.02
K5	AM	3885.91	37.65	3.73
	SD	47.73	0.52	0.08
	CV	1.23	1.42	2.32
K10	AM	3992.55	38.11	4.05
	SD	43.10	1.08	0.14
	CV	1.12	2.84	3.45

Analyzing the results (Table 5) of the static tensile test for composites containing flax fibers alkalinized by 2% NaOH solution, an increase of the Young's modulus (by approximately 10%) and tensile strength (by approximately 2%) was noted, as well as a of elongation at break (by approximately 17%) in relation to the biocomposite with unmodified flax fibers. In the case of a further increase in the concentration of the NaOH solution used on flax fibers, the mechanical properties of the biocomposites deteriorate, but they significantly decrease for the biocomposite with flax fibers modified with 10% NaOH solution. There was a decrease of elongation at break by about 91% and in tensile strength by about 58% compared to the composite with unmodified flax fibers.

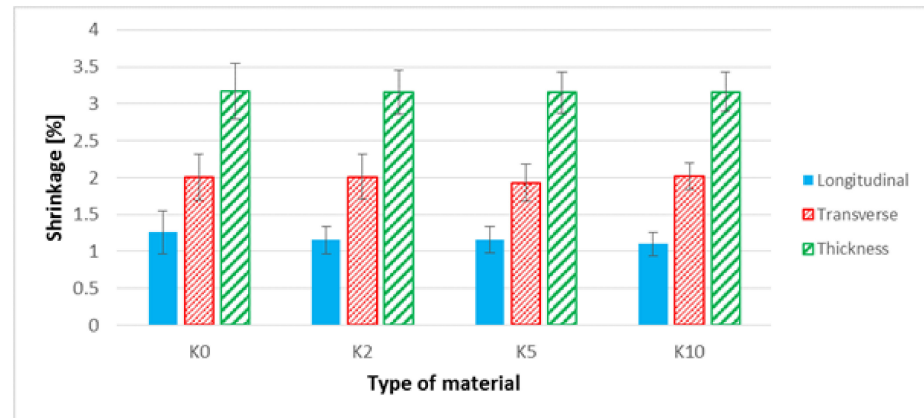
**Table 5.** Results from the uniaxial tensile test for biocomposites with unmodified flax fibers and exposed to: 2%, 5% and 10% NaOH solution.

Type of Material	Statistics	E (MPa)	$\sigma_M$ (MPa)	$\epsilon_M$ (%)
L0	AM	3495.11	36.29	5.07
	SD	41.71	0.53	0.25
	CV	1.19	1.45	4.90
L2	AM	3860.63	36.94	4.21
	SD	45.22	0.34	0.12
	CV	1.17	0.98	3.38
L5	AM	3762.51	35.78	4.00
	SD	55.10	0.82	0.07
	CV	1.46	2.28	1.81
L10	AM	3352.45	15.35	0.46
	SD	143.21	1.29	0.07
	CV	4.27	8.42	16.09

### 3.6. The Shrinkage Biocomposites Assessment

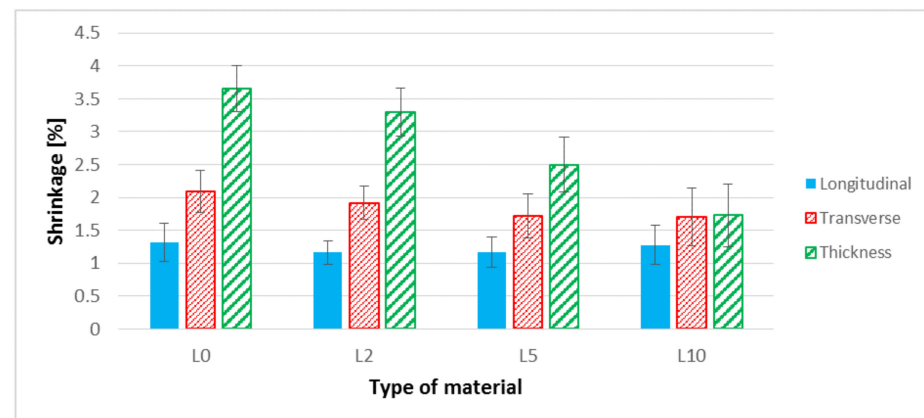
Analyzing the results concerning the shrinkage of the samples (Figure 11), in the case of the hemp fiber modification by a 10% NaOH solution, the value of the longitudinal shrinkage of the biocomposite was reduced by approximately 13% compared to the samples made of the biocomposite filled with unmodified hemp fibers, but observed changes were

lower than the error bar. Moreover, in the case of longitudinal contraction, a smaller scatter of the results for biocomposites with modified fibers was noted. In the case of transverse contraction of biocomposites filled with hemp fibers, no significant changes were observed after the fibers were alkalinized by sodium hydroxide.



**Figure 11.** Linear shrinkage of samples: longitudinal, transverse and in thickness, for biocomposites filled with hemp fibers before and after surface modification.

Analyzing the results of the shrinkage (Figure 12) for samples made of biocomposites filled with flax fibers, a decrease in longitudinal shrinkage by approximately 12% for samples made of L2 and L5 biocomposites can be observed. In the case of transverse shrinkage and in thickness of the molded part, a significant decrease in the values for the L10 biocomposite was found. In the case of transverse shrinkage, this decrease was approximately 19% and for thickness shrinkage approximately 53% in relation to the biocomposite filled with unmodified flax fibers.



**Figure 12.** Linear shrinkage of samples: longitudinal, transverse and in thickness for biocomposites filled with flax fibers before and after surface modification.

### 3.7. The Brinell Hardness Test

When interpreting the results of the hardness of biocomposites in area A (Figures 13 and 14), an approximate 5% increase in the hardness value for the K10 biocomposite as compared to the K0 biocomposite can be observed. Also noticeable is an approximate 16% increase in the hardness value for L10 biocomposites in relation to the biocomposite filled with unmodified flax fibers. The highest hardness values in area A of all biocomposites discussed in the previous section was noted for the L10 biocomposite. When analyzing area B (Figures 13 and 14), a slight decrease in the hardness value for biocomposites filled with modified hemp fibers can be noted.

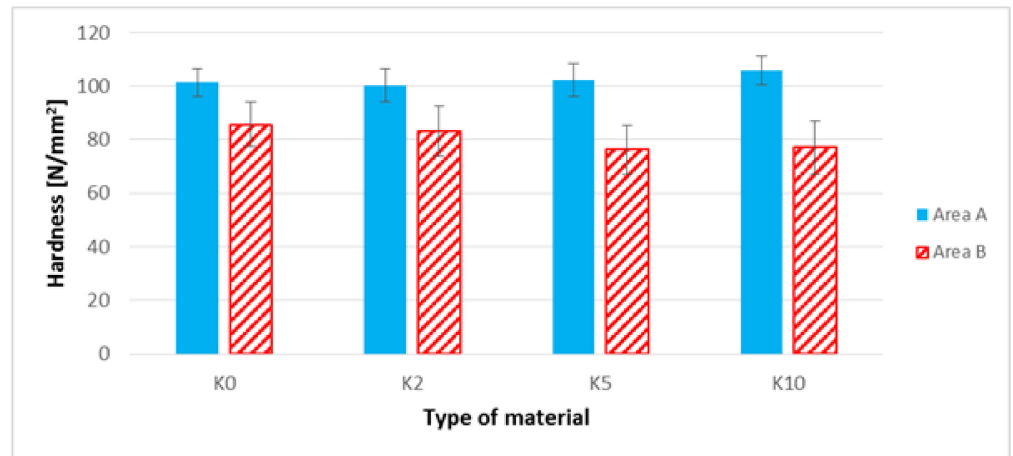


Figure 13. Hardness of composites filled with hemp fibers before and after surface modification in areas A and B of the sample.

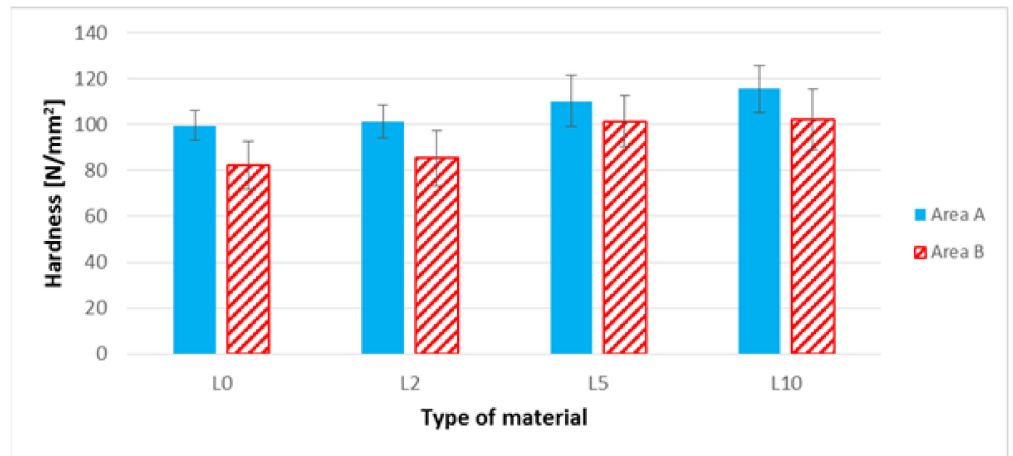


Figure 14. Hardness of composites filled with flax fibers before and after surface modification in areas A and B of the sample.

In the case of biocomposites with flax fibers, an increase in the hardness of samples in area B was observed for biocomposites with modified flax fibers, modified with NaOH solution at a concentration of 5% and 10%. This increase was approximately 24% in relation to the biocomposite filled with unmodified flax fibers.

### 3.8. Impact Tensile Strength Test

When analyzing the results of the impact tensile strength (Figure 15), in the case of PHBV-hemp fiber biocomposites, an increase in the value of this parameter by approximately 12% (for K10) was noted in relation to the biocomposite with unmodified hemp fibers. On the other hand, in the group of biocomposites filled with flax fibers, a gradual decrease in impact tensile strength is visible along with the degree of etching of the fibers—a decrease in impact tensile strength can be noticed by a maximum of approximately 62% (for L10) compared to the biocomposite filled with unmodified flax fibers.

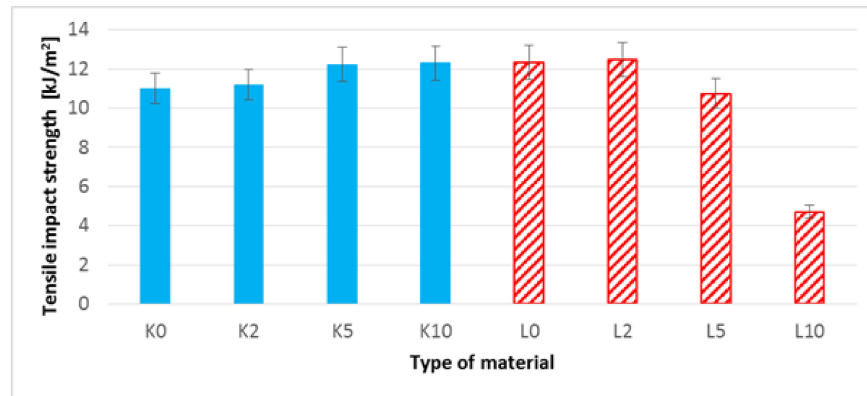


Figure 15. Impact tensile strength of biocomposites filled with hemp and flax fibers before and after surface modification.

### 3.9. The Water Absorption Assessment

The water absorption was assessed. In the case of biocomposites filled with hemp fibers (Figure 16), a decrease in the degree of water absorption was observed with an increase in the concentration of the alkalized solution used for alkalizing the fibers used in biocomposites. For the biocomposite filled with hemp fibers etched with 10% NaOH solution, an approximate 16% decrease in water absorption was noted (on the last day of the test). In the case of biocomposites filled with flax fibers (Figure 17), an increase in water absorption is visible for biocomposites with modified fibers (5% and 10% NaOH solution)—an approximate 133% maximum increase in water absorption was observed on the last day of the test (for L10) in relation to the biocomposite filled with unmodified fibers.

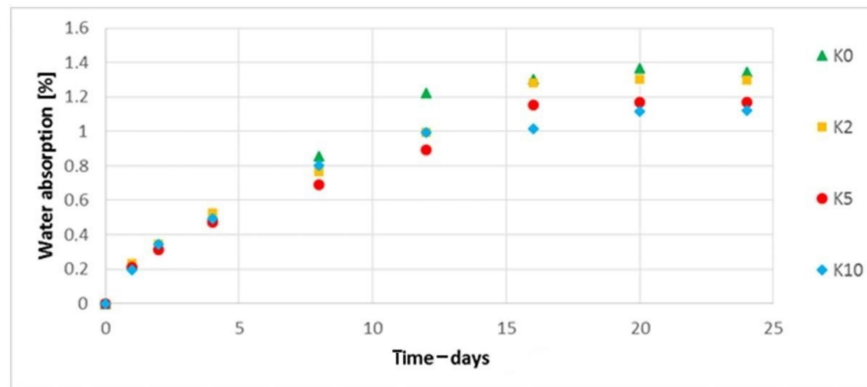


Figure 16. Water absorption of composites filled with unmodified and modified hemp fibers.

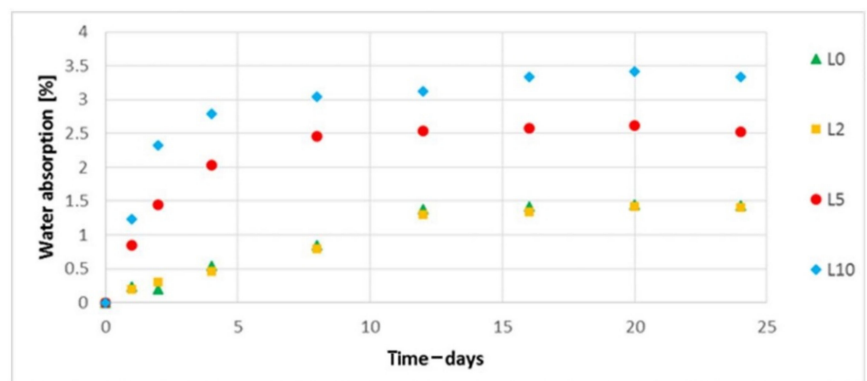
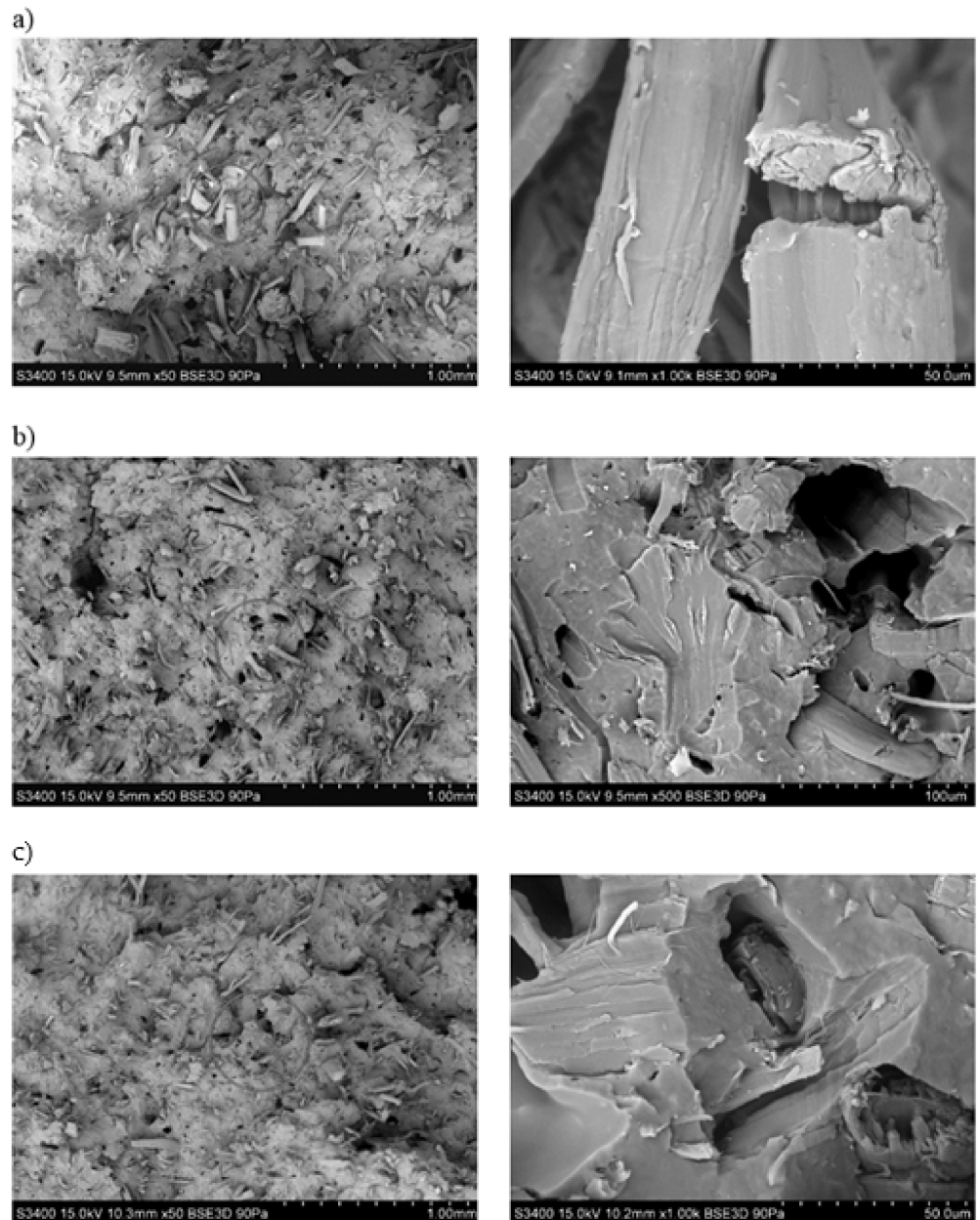


Figure 17. Water absorption of composites filled with unmodified and modified flax fibers.

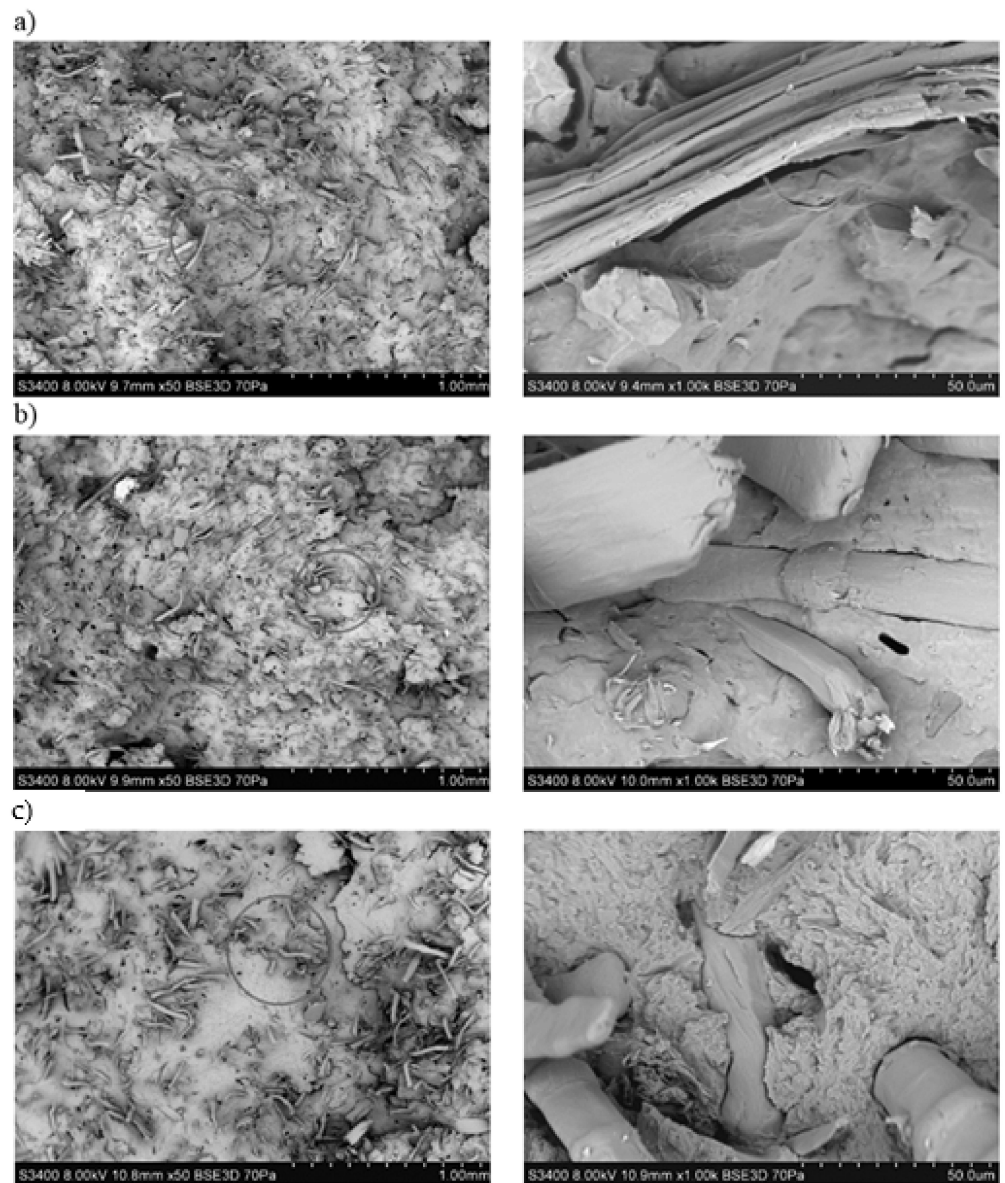


### 3.10. Assessment of the Composite Surface Microstructure

Analyzing the chosen SEM photos (Figure 18), which represent the fracture surface of specimens, it can be noticed that the hemp fibers after alkalization embedded in the polymer matrix have a reduced diameter. Moreover, no significant differences were observed in the microstructure of the biocomposites. In the case of biocomposites with flax fibers (Figure 19), as the alkalizing degree of fibers in the polymer matrix increases, the fibers become increasingly twisted and unevenly distributed in the matrix.



**Figure 18.** SEM photographs of fracture surface of biocomposite samples filled with hemp fibers: (a) unmodified, (b) alkalized with 2% NaOH solution, (c) alkalized with 10% NaOH solution.



**Figure 19.** SEM photographs of fracture surface of biocomposite samples filled with flax fibers: (a) unmodified, (b) alkalized with 2% NaOH solution, (c) alkalized with 10% NaOH solution.

#### 4. Discussion

The results presented in the paper cover four basic aspects: the structure of fibers and composites and the processing, mechanical and functional properties of biocomposites. Two types of fibers were alkalized with three NaOH solutions of different percentages. In the current known studies, the authors used different concentrations of the alkalizing solution for different types of fibers—there are no specific recommendations on what concentrations should be used to optimally improve the properties of the fibers. The percentages of NaOH solutions used in the study were determined based on the literature review. It should be emphasized, however, that in some studies 20% NaOH solutions were used, and the presented research focuses mainly on the topic of using a new, more widely unknown polymer matrix.

At the stage of producing biocomposites by extrusion, significant differences in the processing properties of the produced composites filled with various flax fibers were found. In the case of composites with fibers alkalized with 10% NaOH solution, it was noticed, by the same processing parameters, that the obtained biocomposite had a very

low, unstable viscosity, making it impossible to use (with these technological parameters) this processing method. Reducing the processing temperature by 20 °C could stabilize the process and produce the correct extrudate. A similar phenomenon was also observed in the case of injection of test samples. In this case, the processing temperature was reduced by 20 °C (Table 2). The measured value of pressure in the mold cavity (Figure 7) for the L10 biocomposite was almost twice (pressure of 36 MPa) that of the composite with non-alkalized fibers (pressure of 17 MPa), which proves a significant increase in biocomposite viscosity (Figure 7).

In the case of composites with hemp fibers, pressure changes in the mold cavity followed a different trend (Figure 6)—for the composite, the fibers of which were etched with 10% NaOH solution, lower pressures in the cavity were recorded. This behavior may be due to the geometry of the fibers.

It was found that flax fibers significantly increased the aspect ratio  $L/d$  after being made alkaline with 10% NaOH solution. A particularly high value of  $L/d = 21.23$  (Table 3) was observed for these fibers. The fibers were not shortened, and their diameter decreased by almost half, which may indicate a large delamination of the fibers in their structure. Moreover, when analyzing SEM pictures of flax fibers (Figure 4), not only was delamination visible but also a reduction in rectilinear geometry. Fibers became twisted (often even tangled), which proves a reduction in fiber stiffness.

In the case of the PHBV–flax fiber composite, the reduction of the  $L/d$  ratio for the fibers after etching with 10% NaOH solution (L10 composite) did not improve the mechanical properties of the composite. There was a decrease in the tensile strength (from 36.29 to 15.35 MPa), modulus of elasticity (from 3495.11 to 3352.45 MPa) and impact tensile strength (from 12.32 to 4.71 kJ/m<sup>2</sup>) compared to the composite, the fibers of which were not alkalized (L0). It was also found that the tensile strength deteriorated for composite L10 (15.45 MPa) as compared to pure PHBV (35.48 MPa) [66]. In addition, the observed change in the geometry of the fiber causes a decrease in the viscosity of the composite during extrusion and injection molding; hence, it was required to lower processing temperatures in both processes. These processing aspects are confirmed in the photographs of molded pieces made on the outer layer (Figure 8). Fibers of high stiffness, i.e., non-etched ones, constitute inclusions that act as an obstacle to the flow of the polymer matrix; hence, they are clearly visible on the outer layer of the molded pieces.

In the case of flax fibers etched with 10% NaOH solution, they are barely visible on the outer layer of the molded piece—as twisted bundles of low stiffness—preventing the flowing stream of polymer matrix; hence, they are immersed in the flowing core and slightly visible on the outer layer. In the case of composites with hemp fibers—both in the extrusion and injection molding processes—no significant differences were found, which is confirmed by the almost unchanged geometry of the fibers; despite being alkalized with 10% NaOH solution, they are still straight and stiff with slightly increased  $L/d$  aspect ratio (from 7.15 to 8.77), which indicates an almost slight reduction in the fiber diameter.

The next stage of the research focused on the assessment of selected mechanical properties. In the case of uniaxial tensile test results (Figure 9, Table 4) for composites with hemp fibers, a slight improvement in Young's modulus and tensile strength were noted. This is most likely due to an increase in the  $L/d$  ratio and increased adhesion of the fibers to the polymer matrix. In the case of flax fibers, another relationship was noted—the L10 composite was characterized by the lowest values of Young's modulus and tensile strength (Table 5, Figure 10), and the digested fibers, in the form of bundles of reduced stiffness, no longer fulfilled the function of a filler in the form of short fibers, ultimately not improving the mechanical properties in the direction of force. In the case of hardness, for composites with hemp fibers (Figure 13), a difference in hardness was noted in the tested measurement zones; in the grip part of the tested molded part, the hardness was lower than in the measuring part of the sample. This difference is due to the fact that during the filling of the mold cavity in the injection process, a change in the geometry of the mold cavity in the nip part results in the disorientation of the fibers, i.e., their more chaotic arrangement.

On the other hand, in the measuring part of the dog-bone sample, the stream of polymer with the fiber flows for a longer time in the channel with a constant cross-section, which results in unidirectional arrangement of the fibers of this part of the mold cavity. As can be seen, the increase in the hardness of the composite is slight after the surface modification of the hemp fibers. In the case of composites with flax fibers (Figure 14), a completely different trend was noted—the fibers no longer function as a typical fibrous filler, and their chaotic arrangement as coiled bundles of low stiffness does not result in the formation of resistance during the polymer flow, which in turn translates into deep fibers sinking into the internal layers of the tested specimen. This is confirmed by very small differences in hardness in the measurement zones of specimens. On the other hand, when analyzing the hardness results in terms of fiber alkalization, an upward trend was noted with increasing concentration of the alkalizing solution. Flax fibers, increasingly digested, twisted and less stiff, settle in the core of the molded part, and due to the lowering of the viscosity of the flowing plastic stream, the mold cavity is “more tightly packed”, which translates into an increase in the density of the entire material. This also translates into an improvement in thickness shrinkage. Impact tensile strength results for hemp fiber composites show the classic trend of improved adhesion of the fibers to the matrix and increased L/d ratio.

When analyzing the performance parameters of the obtained composites, it is necessary to mention the changes in shape and dimensions. In the case of shrinkage of the molded piece, a slight (within the measuring error) reduction of the longitudinal shrinkage was observed. This is probably due to a slight increase of the fiber aspect ratio. In turn, in the case of flax fibers, the previously described trend can be seen with increasing NaOH concentration. The straightness and stiffness of the fibers decrease, which reduces their role as a fibrous filler, which does not change the longitudinal shrinkage. On the other hand, a significant reduction in thickness shrinkage is the result of major “packing” the mold cavity with a composite of lower viscosity. Such “packing” of the cavity is the cause of increased water absorption in the case of the composite with fibers etched with 10% NaOH solution. Taking into account the SEM photographs of the molded piece (Figure 8b), the fibers are less deposited on the outer layer; hence, the tendency to absorb water should be lower. On the other hand, in the case of composites with hemp fibers, the water absorption decreases with the increase of NaOH concentration; fibers have a more developed surface, increasing the adhesion of the fibers to the matrix.

The research carried out in this work is therefore a novelty in the context of production, processing and also in the evaluation of the properties of the obtained composites in terms of processing, usability and evaluation of mechanical properties. Moreover, the paper shows the methods of preparing flax and hemp fibers in terms of the desired properties of the products.

## 5. Conclusions

The obtained test results indicate that the effect of the alkalizing solution concentration should be selected individually for a specific type of natural fiber and polymer matrix.

The alkali treatment of cellulose fibers causes significant changes of the fiber diameters; it is especially visible for flax fibers, where the diameter reduction was over 50% compared to unmodified fibers (L0 composite) to fibers modified by 10% of NaOH solution (L10 composite).

Slight improvement of Young's modulus, tensile strength and hardness of composites with hemp fibers alkalized by NaOH solutions was found, and the best results were observed for biocomposites filled with hemp fibers modified with 10% NaOH solution. In addition, in terms of processing (for the same processing parameters), lower (by about 47%) cavity pressures were reported for the same biocomposite with fibers alkalized by means of 10% NaOH solution.

When the concentration of the alkalizing solution for flax fibers increases, no analogous relationship can be seen. It can be noticed that the fibers are quite sensitive to the action of sodium hydroxide; after treating the fibers with a 2% NaOH solution, most of the

discussed properties (Young's modulus, tensile strength, shrinkage of samples) of the biocomposite slightly improved. On the other hand, after using higher concentrations of NaOH solutions, most of the properties of biocomposites filled with flax fibers deteriorated. This is especially visible for samples filled with flax fibers alkalinized with 10% NaOH solution, where the mechanical properties of the biocomposite designated by the uniaxial tensile test deteriorated significantly as well as in the impact tensile strength test, and the degree of water absorption increased. Processing (extrusion and injection molding) of a biocomposite, the flax fibers of which were alkalinized with 10% NaOH solution, was unstable—higher pressure values with greater fluctuations were achieved. In the SEM tests it was found that the flax fibers alone and embedded in the matrix after the surface modification with 10% NaOH solution twist and form larger groups. This may indicate the fiber diameter reduction and loss of properties as a fibrous filler.

The research presented in the paper shows that the use of a 10% NaOH solution on hemp fibers improves the properties of the biocomposite in most of the analyzed areas. When using flax fibers, it is difficult to indicate the correct concentration of the alkalinizing solution. To improve the Young's modulus and tensile strength, 2% NaOH should be used. On the other hand, when using 10% NaOH, shrinkages of the molded piece (L10) decreased (reduced by approximate maximum values of longitudinal 9%, transverse 21%, thickness 61%) and hardness increased significantly (by an approximate maximum of 24%) compared to unmodified fibers (for L0 composite). The results obtained for the L10 composite are puzzling; hence, there is a great need to understand the causes of this phenomenon. For this purpose, it is planned to perform, inter alia, DSC and TGA tests as well as to determine the composite processing window and to explain phenomena described in this article.

Moreover, the results presented in the article constitute the basis for further research directions aimed at examining other methods of surface modification of fibers used as a filler in the PHBV matrix.

**Author Contributions:** Conceptualization, W.F., G.J.; methodology, W.F., G.J.; software, Ł.B., G.J.; validation, W.F.; formal analysis, G.J., W.F.; investigation, Ł.B., G.J.; resources, G.J., Ł.B.; data curation, G.J.; writing—original draft preparation, G.J., W.F.; writing—review and editing, W.F., G.J.; visualization, G.J.; supervision, W.F.; funding acquisition, W.F. All authors have read and agreed to the published version of the manuscript.

**Funding:** This research received no external funding.

**Institutional Review Board Statement:** Not applicable.

**Informed Consent Statement:** Not applicable.

**Data Availability Statement:** The data presented in this study are available on request from the corresponding author.

**Conflicts of Interest:** The authors declare no conflict of interest.

## References

1. Kalia, S.; Kaith, B.S.; Kaur, I. *Cellulose Fibers: Bio- and Nano-Polymer Composites: Green Chemistry and Technology*; Springer Science & Business Media: Berlin/Heidelberg, Germany, 2011.
2. Kim, J.K.; Pal, K. *Recent Advances in The Processing of Wood-Plastic Composites*; Springer Science & Business Media: Berlin/Heidelberg, Germany, 2010.
3. Klyosov, A.A. *Wood-Plastic*; John Wiley & Sons: Hoboken, NJ, USA, 2007.
4. Rouchi, A.M. Lignin and Lignin Biosynthesis. *Chem. Eng. News* **2000**, *78*, 29–32. [[CrossRef](#)]
5. Väisänen, T.; Haapala, A.; Lappalainen, R.; Tomppo, L. Utilization of agricultural and forest industry waste and residues in natural fiber-polymer composites: A review. *Waste Manag.* **2016**, *54*, 62–73. [[CrossRef](#)] [[PubMed](#)]
6. Stamman, A.J. *Wood and Cellulose Science*; Ronald Press: New York, NY, USA, 1964.
7. Tarkow, H.; Turner, H.D. The swelling pressure of wood. *For. Prod. J.* **1958**, *8*, 193–197.
8. Kondo, T. Hydrogen bonds in regioselectively substituted cellulose derivatives. *J. Polym. Sci. Part B Polym. Phys.* **1994**, *32*, 1229–1236. [[CrossRef](#)]
9. Hearle, J.W.; Morton, W.E. *Physical Properties of Textile Fibres*; Woodhead Publishing: Manchester, UK, 2008.

10. Smole, M.S.; Hribernik, S.; Kurečić, M.; Krajnc, A.U.; Kreže, T.; Kleinschek, K.S. *Surface Properties of Non-Conventional Cellulose Fibres*; Springer International Publishing: Cham, Switzerland, 2019.
11. Nair, K.M.; Diwan, S.M.; Thomas, S. Tensile properties of short sisal fiber reinforced polystyrene composites. *J. Appl. Polym. Sci.* **1996**, *60*, 1483–1497. [[CrossRef](#)]
12. George, J.; Bhagawan, S.S.; Prabhakaran, N.; Thomas, S. Short pineapple-leaf-fiber- reinforced low-density polyethylene composites. *J. Appl. Polym. Sci.* **1995**, *57*, 843–854. [[CrossRef](#)]
13. Joseph, K.; Varghese, S.; Kalaprasad, G.; Thomas, S.; Prasannakumari, L.; Koshy, P.; Pavithran, C. Influence of interfacial adhesion on the mechanical properties and fracture behaviour of short sisal fibre reinforced polymer composites. *Eur. Polym. J.* **1996**, *32*, 1243–1250. [[CrossRef](#)]
14. Joseph, P.V.; Mathew, G.; Joseph, K.; Thomas, S.; Pradeep, P. Mechanical properties of short sisal fiber-reinforced polypropylene composites: Comparison of experimental data with theoretical predictions. *J. Appl. Polym. Sci.* **2003**, *88*, 602–611. [[CrossRef](#)]
15. Faruk, O.; Bledzki, A.K.; Fink, H.P.; Sain, M. Biocomposites reinforced with natural fibers: 2000–2010. *Prog. Polym. Sci.* **2012**, *37*, 1552–1596. [[CrossRef](#)]
16. Pach, J.; Kaczmar, J.W. Wpływ chemicznej modyfikacji włókien konopnych na wybrane właściwości mechaniczne kompozytów na osnowie polipropylenowej. *Polimery* **2011**, *56*, 385–389. [[CrossRef](#)]
17. Nevell, T.P.; Zeronian, S.H. *Cellulose Chemistry and Its Applications*; Halsted Press: New York, NY, USA, 1985.
18. Happey, F. *Applied Fibre Science*; Academic Press: London, UK, 1979.
19. Nguyen, T.; Zavarin, E.; Barrall, E.M. Thermal Analysis of lignocellulosic materials: Part I. Unmodified materials. *J. Macromol. Sci. Rev. Macromol. Chem.* **1981**, *20*, 1–65. [[CrossRef](#)]
20. Ouajai, S.; Shanks, R.A. Composition, structure and thermal degradation of hemp cellulose after chemical treatments. *Polym. Degrad. Stab.* **2005**, *89*, 327–335. [[CrossRef](#)]
21. Mwaikambo, L.Y.; Ansell, M.P. Chemical modification of hemp, sisal, jute, and kapok fibers by alkalization. *J. Appl. Polym. Sci.* **2002**, *84*, 2222–2234. [[CrossRef](#)]
22. Suardana, N.P.G.; Piao, Y.; Lim, J.K. Mechanical properties of hemp fibers and hemp/pp composites: Effects of chemical surface treatment. *Mater. Phys. Mech.* **2011**, *11*, 1–8.
23. Hu, R.; Lim, J.K. Fabrication and mechanical properties of completely biodegradable hemp fiber reinforced polylactic acid composites. *J. Compos. Mater.* **2007**, *41*, 1655–1669. [[CrossRef](#)]
24. Pickering, K.L.; Sawpan, M.A.; Jayaraman, J.; Fernyhough, A. Influence of loading rate, alkali fibre treatment and crystallinity on fracture toughness of random short hemp fibre reinforced poly lactide biocomposites. *Compos. Part A Appl. Sci. Manuf.* **2011**, *42*, 1148–1156. [[CrossRef](#)]
25. Zafeiropoulos, N.E.; Williams, D.R.; Baillie, C.A.; Matthews, F.L. Engineering and characterisation of the interface in flax fibre/polypropylene composite materials. Part I. Development and investigation of surface treatments. *Compos. Part A Appl. Sci. Manuf.* **2002**, *33*, 1083–1093. [[CrossRef](#)]
26. Van de Weyenberg, I.; Ivens, J.; De Coster, A.; Kino, B.; Baetens, E.; Verpoest, I. Influence of processing and chemical treatment of flax fibres on their composites. *Compos. Sci. Technol.* **2003**, *63*, 1241–1246. [[CrossRef](#)]
27. Li, X.; Panigrahi, S.; Tabil, L.G. A study on flax fiber-reinforced polyethylene biocomposites. *Appl. Eng. Agric.* **2009**, *25*, 525–531. [[CrossRef](#)]
28. Sikora, J.; Gajdoš, I.; Puzska, A. Polyethylene-Matrix Composites with Halloysite Nanotubes with Enhanced Physical/Thermal Properties. *Polymers* **2019**, *11*, 787. [[CrossRef](#)]
29. Zini, E.; Focarete, M.L.; Noda, I.; Scandola, M. Bio-composite of bacterial poly (3-hydroxybutyrate-co-3-hydroxyhexanoate) reinforced with vegetable fibers. *Compos. Sci. Technol.* **2007**, *67*, 2085–2094. [[CrossRef](#)]
30. Avella, M.; La Rota, G.; Martuscelli, E.; Raimo, M.; Sadocco, P.; Elegir, G.; Riva, R. Poly (3-hydroxybutyrate-co-3-hydroxyvalerate) and wheat straw fibre composites: Thermal, mechanical properties and biodegradation behaviour. *J. Mater. Sci.* **2000**, *35*, 829–836. [[CrossRef](#)]
31. Roy, I.; Visakh, P.M. *Polyhydroxyalkanoate (PHA) Based Blends, Composites and Nano-Composites*; Royal Society of Chemistry: Cambridge, UK, 2014.
32. Luo, S.; Netravali, A.N. Interfacial and mechanical properties of environment-friendly “green” composites made from pineapple fibers and poly (hydroxybutyrate-co-valerate) resin. *J. Mater. Sci.* **1999**, *34*, 3709–3719. [[CrossRef](#)]
33. Bhardwaj, R.; Mohanty, A.K.; Drzal, L.T.; Pourboghrat, F.; Misra, M. Renewable resource-based green composites from recycled cellulose fiber and poly (3-hydroxybutyrate-co-3-hydroxyvalerate) bioplastic. *Biomacromolecules* **2006**, *7*, 2044–2051. [[CrossRef](#)]
34. Torres-Giner, S.; Hilliou, L.; Melendez-Rodriguez, B.; Figueroa-Lopez, K.J.; Madalena, L.; Cabedo, D.; Covas, J.A.; Vicente, A.A.; Lagaron, J.M. Melt processability, characterization, and antibacterial activity of compression-molded green composite sheets made of poly (3-hydroxybutyrate-co-3-hydroxyvalerate) reinforced with coconut fibers impregnated with oregano essential oil. *Food Packag. Shelf Life* **2018**, *17*, 39–49. [[CrossRef](#)]
35. Hosokawa, M.N.; Darros, A.B.; Moris, V.A.D.S.; Paiva, J.M.F.D. Polyhydroxybutyrate Composites with Random Mats of Sisal and Coconut Fibers. *Mater. Res.* **2017**, *20*, 279–290. [[CrossRef](#)]
36. Javadi, A.; Srithep, Y.; Pilla, S.; Lee, J.; Gong, S.; Turng, L.S. Processing and characterization of solid and microcellular PHBV/coir fiber composites. *Mater. Sci. Eng. C* **2010**, *30*, 749–757. [[CrossRef](#)]

37. Macedo, J.D.S.; Costa, M.F.; Tavares, M.I.; Thiré, R.M. Preparation and characterization of composites based on polyhydroxybutyrate and waste powder from coconut fibers processing. *Polym. Eng. Sci.* **2010**, *50*, 1466–1475. [[CrossRef](#)]
38. Corradini, E.; Ferreira, F.C.; Agnelli, J.A.; Marconcini, J.M.; Mattoso, L.H.; Rosa, M.F. Water uptake, water solubility, mechanical and morphological properties of corn gluten meal and poly (hydroxybutyrate-co-hydroxyvalerate) composites reinforced with green coconut fibers. *Polímeros* **2013**, *23*, 807–813. [[CrossRef](#)]
39. Qian, S.; Dai, X.; Qi, Y.; Ren, H. Preparation and characterization of polyhydroxybutyrate-bamboo lignophenol biocomposite films. *BioResources* **2015**, *10*, 3169–3180. [[CrossRef](#)]
40. Liu, D.; Song, J.; Anderson, D.P.; Chang, P.R.; Hua, Y. Bamboo fiber and its reinforced composites: Structure and properties. *Cellulose* **2012**, *19*, 1449–1480. [[CrossRef](#)]
41. Krishnaprasad, R.; Veena, N.R.; Maria, H.J.; Rajan, R.; Skrifvars, M.; Joseph, K. Mechanical and thermal properties of bamboo microfibril reinforced polyhydroxybutyrate biocomposites. *J. Polym. Environ.* **2009**, *17*, 109–114. [[CrossRef](#)]
42. Rajan, K.P.; Veena, N.R.; Maria, H.J.; Rajan, R.; Skrifvars, M.; Joseph, K. Extraction of bamboo microfibrils and development of biocomposites based on polyhydroxybutyrate and bamboo microfibrils. *J. Compos. Mater.* **2011**, *45*, 1325–1329. [[CrossRef](#)]
43. Liu, L.; Qin, L.; Ming, Z.; Peng, C.; Zhi-hui, W.; Qun, G. Effect of Bamboo Flour Size on Properties of Bamboo/PHBV Bio-Composites. *J. Zhejiang For. Sci. Technol.* **2011**, *4*, 1–3.
44. Jiang, L.; Chen, F.; Qian, J.; Huang, J.; Wolcott, M.; Liu, L.; Zhang, J. Reinforcing and toughening effects of bamboo pulp fiber on poly (3-hydroxybutyrate-co-3-hydroxyvalerate) fiber composites. *Ind. Eng. Chem. Res.* **2009**, *49*, 572–577. [[CrossRef](#)]
45. Jiang, L.; Huang, J.; Qian, J.; Chen, F.; Zhang, J.; Wolcott, M.P.; Zhu, Y. Study of poly (3-hydroxybutyrate-co-3-hydroxyvalerate) (PHBV)/bamboo pulp fiber composites: Effects of nucleation agent and compatibilizer. *J. Polym. Environ.* **2008**, *16*, 83–93. [[CrossRef](#)]
46. Yu, Z. Study on Mechanical Properties of The Bamboo Fiber/PHBV Composites. *J. Text. Res.* **2004**, *6*, 1–14.
47. Shibata, M.; Takachiyo, K.I.; Ozawa, K.; Yosomiya, R.; Takeishi, H. Biodegradable polyester composites reinforced with short abaca fiber. *J. Appl. Polym. Sci.* **2002**, *85*, 129–138. [[CrossRef](#)]
48. Teramoto, N.; Urata, K.; Ozawa, K.; Shibata, M. Biodegradation of aliphatic polyester composites reinforced by abaca fiber. *Polym. Degrad. Stab.* **2004**, *86*, 401–409. [[CrossRef](#)]
49. Luo, S.; Netravali, A.N. Mechanical and thermal properties of environment-friendly “green” composites made from pineapple leaf fibers and poly (hydroxybutyrate-co-valerate) resin. *Polym. Compos.* **1999**, *20*, 367–378. [[CrossRef](#)]
50. Dingtungee, R.; Tengsuthiwat, J.; Boonyasopon, P.; Siengchin, S. Sisal natural fiber/clay-reinforced poly (hydroxybutyrate-co-hydroxyvalerate) hybrid composites. *J. Thermoplast. Compos. Mater.* **2015**, *28*, 879–895. [[CrossRef](#)]
51. Badia, J.D.; Kittikorn, T.; Strömberg, E.; Santonja-Blasco, L.; Martínez-Felipe, A.; Ribes-Greus, A.; Karlsson, S. Water absorption and hydrothermal performance of PHBV/sisal biocomposites. *Polym. Degrad. Stab.* **2014**, *108*, 166–174. [[CrossRef](#)]
52. Tengsuthiwat, J.; Boonyasopon, P.; Dingtungee, R.; Siengchin, S. Characterization of poly (hydroxybutyrate-co-hydroxyvalerate)/Sisal Fiber/Clay bio-composites Prepared by Casting Technique. *Period. Polytech. Eng. Mech. Eng.* **2016**, *60*, 103–112. [[CrossRef](#)]
53. Keller, A. Compounding and mechanical properties of biodegradable hemp fibre composites. *Compos. Sci. Technol.* **2003**, *63*, 1307–1316. [[CrossRef](#)]
54. Barkoula, N.M.; Garkhail, S.K.; Peijs, T. Biodegradable composites based on flax/polyhydroxybutyrate and its copolymer with hydroxyvalerate. *Ind. Crops Prod.* **2010**, *31*, 34–42. [[CrossRef](#)]
55. Lu, N.; Oza, S.; Ferguson, I. Effect of alkali and silane treatment on the thermal stability of hemp fibers as reinforcement in composite structures. *Adv. Mater. Res.* **2012**, *415*, 666–670. [[CrossRef](#)]
56. Shahzad, A. Hemp fiber and its composites—A review. *J. Compos. Mater.* **2012**, *46*, 973–986. [[CrossRef](#)]
57. Sair, S.; Oushabi, A.; Kammouni, A.; Tanane, O.; Abboud, Y.; Hassani, F.O.; El Bouari, A. Effect of surface modification on morphological, mechanical and thermal conductivity of hemp fiber: Characterization of the interface of hemp–Polyurethane composite. *Case Stud. Therm. Eng.* **2017**, *10*, 550–559. [[CrossRef](#)]
58. Gassan, J.; Mildner, I.; Bledzki, A.K. Influence of fiber structure modification on the mechanical properties of flax fiber-epoxy composites. *Mech. Compos. Mater.* **1999**, *35*, 435–440. [[CrossRef](#)]
59. Aly, M.; Hashmi, M.S.J.; Olabi, A.G.; Benyounis, K.Y.; Messeiry, M.; Hussain, A.I.; Abadir, E.F. Optimization of alkaline treatment conditions of flax fiber using Box–Behnken method. *J. Nat. Fibers* **2012**, *9*, 256–276. [[CrossRef](#)]
60. Gopalakrishnan, P.; Saiah, R.; Gattin, R.; Saiter, J.M. Effect of mercerization of flax fibers on wheat flour/flax fiber biocomposite with respect to thermal and tensile properties. *Compos. Interfaces* **2008**, *15*, 759–770. [[CrossRef](#)]
61. ISO 527-1, *Plastics—Determination of tensile properties. In Part 1: General principles*; ISO Copyright Office: Geneva, Switzerland, 2012.
62. ISO 2039-1, *Plastics—Determination of hardness. In Part 1: Ball indentation method*; ISO Copyright Office: Geneva, Switzerland, 2001.
63. *ISO 8256, Plastics—Determination of Tensile-Impact Strength*; ISO Copyright Office: Geneva, Switzerland, 2004.
64. *ISO 62, Plastics—Determination of Water Absorption*; ISO Copyright Office: Geneva, Switzerland, 2008.

65. ISO 294-4, Plastics—Injection moulding of test specimens of thermoplastic materials. In *Part 4: Determination of Moulding Shrinkage*; ISO Copyright Office: Geneva, Switzerland, 2001.
66. Czerniecka-Kubicka, A.; Janowski, G.; Pyda, M.; Frącz, W. Biocomposites based on the poly (3-hydroxybutyrate-co-3-hydroxyvalerate) matrix with the hemp fibers: Thermal and mechanical properties. *J. Therm. Anal. Calorim.* **2021**, *112*, 1–13.





## Article

# Non-Isothermal Crystallization Kinetics of Poly(ethylene glycol) and Poly(ethylene glycol)-B-Poly( $\epsilon$ -caprolactone) by Flash DSC Analysis

Xiaodong Li \*, Meishuai Zou \*, Lisha Lei and Longhao Xi

Beijing Institute of Technology, School of Materials Science and Engineering, Beijing 100081, China; 3220201147@bit.edu.cn (L.L.); 1120180368@bit.edu.cn (L.X.)

\* Correspondence: bitlxd@bit.edu.cn (X.L.); zoums@bit.edu.cn (M.Z.); Tel.: +86-10-6891-3908 (M.Z.)

**Abstract:** The non-isothermal crystallization behaviors of poly(ethylene glycol) (PEG) and poly(ethylene glycol)-b-poly( $\epsilon$ -caprolactone) (PEG-PCL) were investigated through a commercially available chip-calorimeter Flash DSC2+. The non-isothermal crystallization data under different cooling rates were analyzed by the Ozawa model, modified Avrami model, and Mo model. The results of the non-isothermal crystallization showed that the PCL block crystallized first, followed by the crystallization of the PEG block when the cooling rate was 50–200 K/s. However, only the PEG block can crystallize when the cooling rate is 300–600 K/s. The crystallization of PEG-PCL is completely inhibited when the cooling rate is 1000 K/s. The modified Avrami and Ozawa models were found to describe the non-isothermal crystallization processes well. The growth methods of PEG and PEG-PCL are both three-dimensional spherulitic growth. The Mo model shows that the crystallization rate of PEG is greater than that of PEG-PCL.

**Keywords:** PEG-PCL; non-isothermal crystallization; flash differential scanning calorimeter

**Citation:** Li, X.; Zou, M.; Lei, L.; Xi, L. Non-Isothermal Crystallization Kinetics of Poly(ethylene glycol) and Poly(ethylene glycol)-B-Poly( $\epsilon$ -caprolactone) by Flash DSC Analysis. *Polymers* **2021**, *13*, 3713. <https://doi.org/10.3390/polym13213713>

Academic Editors: Célio Bruno Pinto Fernandes, Salah Aldin Faroughi, Luís L. Ferrás and Alexandre M. Afonso

Received: 29 September 2021  
Accepted: 21 October 2021  
Published: 27 October 2021

**Publisher's Note:** MDPI stays neutral with regard to jurisdictional claims in published maps and institutional affiliations.



**Copyright:** © 2021 by the authors. Licensee MDPI, Basel, Switzerland. This article is an open access article distributed under the terms and conditions of the Creative Commons Attribution (CC BY) license (<https://creativecommons.org/licenses/by/4.0/>).

## 1. Introduction

Differential scanning calorimetry (DSC) is commonly used to study the crystallization behavior of polymers [1–5]. However, the actual processing technology of polymer materials, including injection molding, blown film, and spinning, the actual cooling rate is far greater than the maximum cooling rate that can be achieved by conventional DSC. Therefore, it is difficult to use DSC to simulate the crystallization environment of polymers in the actual processing. In order to solve the above problems, people have turned to the development of a new type of calorimeter with miniaturization, high sensitivity, and high temperature resolution, and with ultra-fast temperature rise and fall rates. In 2010, METTLER TOLEDO used the ceramic substrate chip sensor MultiSTAR USF1 (XI-400) to manufacture the first commercial power-compensated fast scanning chip calorimeter Flash DSC 1 [6–8]. Fast-scan chip-calorimetry (FDSC) has been developed in recent years. At present, the heating rate of flash DSC2+ can reach 3,000,000 K/s, and the cooling rate can reach 2,400,000 K/s. The ultra-fast heating and cooling rate of FDSC is mainly due to the chip sensor used in the instrument [9]. The chip sensor consists of two independent calorimeters, corresponding to the sample and reference sample areas. The calorimeter has a double-layer film structure, which is a silicon nitride film and a silicon oxide film dielectric layer. The total thickness of the double-layer film is about 2 p.m. The center of the calorimeter film is the temperature control area with a diameter of about 0.5 mm. With the help of a microscope, the experimenter can place a sample of tens of microns into the central area of the calorimeter to obtain uniform temperature control.

The biggest advantage of FDSC lies in its ultra-high cooling rate, which is controllable in the preparation of specific structures and specific thermal history materials. In addition, its ultra-fast heating rate can greatly inhibit the structural rearrangement during the

heating process. This phenomenon shows its unique advantages in the crystallization research of many polymer materials. For example, Cavallo uses FDSC to compare the isothermal crystallization kinetics of isotactic polypropylene, propylene/butene copolymer, and propylene/hexene copolymer in the range of 0–90 °C [10]. Chen et al. studied the change in the crystal morphology of polyvinylidene fluoride-chlorotrifluoroethylene [P(VDF-CTFE)] by adding a nucleating agent via FDSC [11].

Currently, efforts are focused on understanding the non-isothermal crystallization behavior of polymers, because polymer processing is usually carried out under non-isothermal conditions. Different methods have been developed to evaluate non-isothermal crystallization based on DSC experimental data, such as Ozawa model, Avrami model, Mo model, etc., [12–14]. Some of these methods can be better explained in the DSC experimental data obtained at a lower cooling rate [15–18]. However, it is a mystery whether it can be better explained when it is applied to the FDSC experimental data of the ultra-fast cooling rate.

Poly(ethylene glycol)-*b*-poly( $\epsilon$ -caprolactone) (PEG-PCL) has good biocompatibility, biodegradability, and is easy to synthesize. These properties make it have great potential in drug delivery systems [19–23]. Many properties of this type of block copolymers, such as drug permeability, degradation performance and mechanical properties, are significantly affected by their crystalline behavior and aggregate structure [24–29]. Therefore, the study of their crystallization behaviors has important theoretical and practical significance. Bogdanov et al. characterized the thermal properties of three PCL-*b*-PEG copolymers [30]. It was concluded that the PCL blocks crystallize first, which determines the total copolymer structure and leads to imperfect crystallization of the PEG blocks. Shiomi et al. observed the morphology of spherulites of PCL-PEG-PCL triblock copolymers with different block lengths [31].

In this report, we selected the homopolymer PEG and block copolymer PEG-PCL to study their non-isothermal crystallization behavior under a high cooling rate measured by FDSC. The Ozawa model, Avrami model, and Mo model are used to evaluate the non-isothermal crystallization behavior of PEG and PEG-PCL at high cooling rates, and compare the results with the non-isothermal crystallization results by DSC.

## 2. Materials and Methods

### 2.1. Materials

The PEG ( $M_w = 5000$ ), PCL ( $M_w = 5000$ ), and PEG-PCL (50%/50%mol,  $M_w = 10,000$ ) used in this experiment were purchased from Guangzhou TanSh technology Co., Ltd (Guangzhou, China).

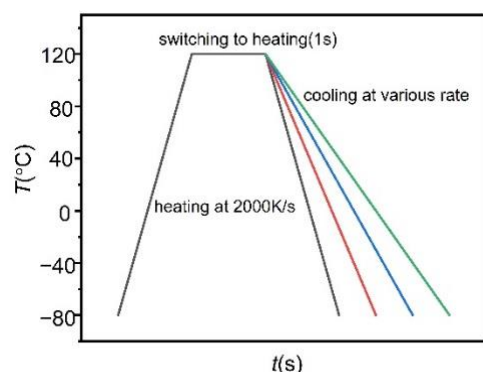
### 2.2. Test Instrument

The flash differential scanning calorimeter used was Flash DSC2+ (manufactured by Mettler-Toledo Company). At the beginning of all experiments, each sensor was adjusted and calibrated. All the detections were conducted under a nitrogen atmosphere with a constant flow rate of 80 mL/min.

The bulk samples were cut into small pieces (about 10–100 ng) and then were transferred to the sensor center within an area of (0.2–0.5) mm<sup>2</sup> under the microscope. In order to maintain good contact between the sample and the sensor, a pre-melting procedure was adopted, with repeated heating and cooling procedures; the heating and cooling rates of pre-melting were both 10 K/s.

### 2.3. Non-Isothermal Crystallization Process

The non-isothermal crystallization was performed as follows: the samples were heated up to 120 °C higher than the melting point of the samples at a heating rate of 2000 K/s, this temperature was maintained for 1 s to obtain the equilibrium of the melt. Then the samples were cooled to –80 °C at different cooling rates, which is lower than its glass transition temperature. The temperature program is shown in Figure 1.

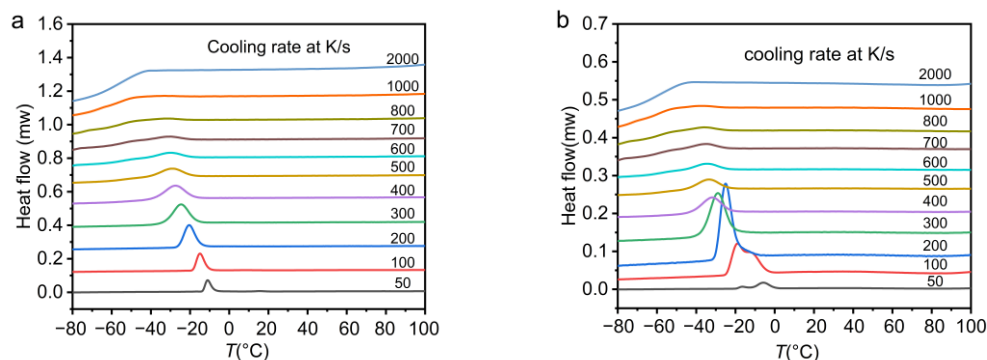


**Figure 1.** Temperature-time profiles of fast-scan measurements for the samples prepared at different cooling rates for crystallization.

### 3. Results and Discussion

#### 3.1. Crystallization of Samples under Various Cooling Rates

Figure 2 plots the cooling curves of PEG and PEG-PCL under various cooling rates measured by FDSC. In Figure 2a, an obvious crystallization peak can be observed when the cooling rate is low. The crystallization exothermic peak of PEG becomes broad and weak when the cooling rate reaches 800 K/s. PEG is completely inhibited from crystallization when the cooling rate exceeds 1000 K/s. In Figure 2b, double crystallization peaks appear on the cooling curve of PEG-PCL when the cooling rate is 50 K/s, and 100 K/s, which shows that both the PEG block and the PCL block can crystallize when the cooling rate is low. This is similar to the results measured by Hiroki et al. using DSC; they found that PCL crystallized first, followed by the crystallization of PEG with preservation of the PCL crystal lamellar structure [29]. However, the double crystallization peak becomes a single peak when the cooling rate reaches 200 K/s. The crystallization peak of PEG-PCL disappears when the cooling rate continues to increase to 1000 K/s.



**Figure 2.** (a) PEG (b) PEG-PCL at different cooling rates of heat flow rate and temperature change cooling curve.

The relative crystallinity  $X(T)$  can be obtained from the ratio of the area of the exothermic peak of the crystallization at the temperature of the curve to the area of the entire crystallization peak when the crystallization is completed. The formula is as follows [12]:

$$X(T) = \frac{\int_{T_0}^T (dH_c/dT)dT}{\int_{T_0}^{T_\infty} (dH_c/dT)dT} \tag{1}$$

where  $T_0$  and  $T_\infty$  represent the initial temperature and final temperature of the crystallization process, respectively.

Figure 3a is the curve of relative crystallinity with temperature in the crystallization process of PEG. The relative crystallinity and the crystallization temperature are obviously

reverse S-shaped. Figure 3b is the curve of relative crystallinity with the temperature during the crystallization of PEG-PCL. The curve is not an obvious reverse s-shaped curve when the heating rate is 50 K/s. The reason is that the PEG block and PCL block of PEG-PCL crystallize at different temperatures. Therefore, the peak splitting behavior on the crystallization curve is obvious.

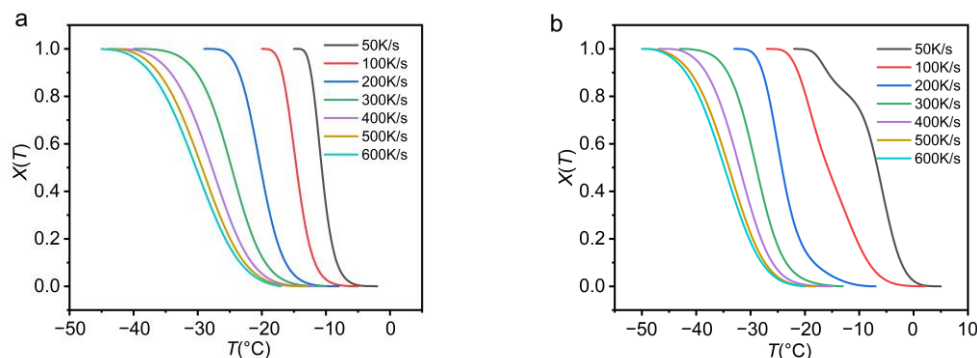


Figure 3. (a) PEG (b) PEG-PCL relative crystallinity curve with temperature.

The values of  $T_0$  (initial crystallization temperature),  $D$  (crystallization temperature range),  $t_{1/2}$  (half-time of crystallization) and  $T_{1/2}$  (half-temperature of crystallization) of PEG and PEG-PCL are listed in Table 1 when the crystallization rate is 50 K/s, 100 K/s, 200 K/s, 300 K/s, 400 K/s, 500 K/s, and 600 K/s. In the entire non-isothermal crystallization process, the crystallization time and the corresponding temperature have the following relationship [12]:

$$t = \frac{T - T_0}{\Phi} \tag{2}$$

Table 1.  $T_0$ ,  $D(K)$ ,  $t_{1/2}$ ,  $T_{1/2}$  values of PEG and PEG-PCL at different cooling rates.

Cooling Rate (K/s)	PEG				PEG-PCL			
	$T_0$ (°C)	$D$ (°C)	$t_{1/2}$ (s)	$T_{1/2}$ (°C)	$T_0$ (°C)	$D$ (°C)	$t_{1/2}$ (s)	$T_{1/2}$ (°C)
50	−2	13	0.1726	−10.63	5	27	0.2340	−6.70
100	−5	15	0.0968	−14.68	2	25	0.1777	−15.77
200	−8	21	0.0605	−20.10	−7	26	0.0866	−24.32
300	−10	30	0.0487	−24.61	−13	30	0.0535	−29.06
400	−12	32	0.0393	−27.72	−15	32	0.0429	−32.17
500	−13	31	0.0323	−29.13	−18	32	0.0315	−33.74
600	−17	28	0.0221	−30.26	−20	30	0.0248	−34.87

It is clear that as the cooling rate increases, the half crystallization time becomes shorter, which means that the crystallization rate becomes faster and faster. The half crystallization time of PEG is shorter than that of PEG-PCL, indicating that the crystallization rate of PEG is faster than that of PEG-PCL. At a cooling rate of 50–200 K/s, the crystallization temperature range of PEG-PCL is larger than those of the PEG polymer, which means that the presence of the PCL block makes the crystallization temperature range of PEG-PCL wide. The initial crystallization temperature of PEG-PCL is significantly higher than that of PEG. This is because the PCL block crystallizes first, and the crystallization temperature of PCL is higher than that of PEG. However, as the cooling rate continues to increase, the initial crystallization temperature of PEG-PCL becomes less than that of the PEG polymer. In order to explain this phenomenon, we used FDSC to study the crystallization behavior of PCL with a molecular weight of 5000, and we found that PCL no longer crystallizes when the cooling rate is 50 K/s. Therefore, we infer that when the cooling rate reaches 300 K/s, the crystallization of the PCL block is inhibited. After the cooling rate reaches 300 K/s, we find that the crystallization temperature range of PEG-PCL is approximately

the same as that of PEG. This also proves from the side that only the PEG block crystallizes when the cooling rate exceeds 300 K/s. When the cooling rate is too fast, the PCL block cannot crystallize and the PCL block inhibits the crystallization of the PEG block.

In general, we found that the crystallization behavior of PEG-PCL and PEG observed by FDSC is not completely consistent with the results observed through conventional DSC. For PEG, we found that when the cooling rate reaches 1000 K/s, its crystallization behavior is inhibited. For PEG-PCL, we found that when the cooling rate is 50 K/s–200 K/s, the PCL block crystallizes first and then the PEG segment crystallizes, which is consistent with the conventional DSC observation results. However, only the PEG segment crystallizes when the cooling rate reaches 300 K/s. Neither the PEG block nor the PCL block participates in the crystallization when the cooling rate reaches 1000 K/s.

### 3.2. Non-Isothermal Crystallization Kinetic Analysis

#### 3.2.1. Ozawa Equation

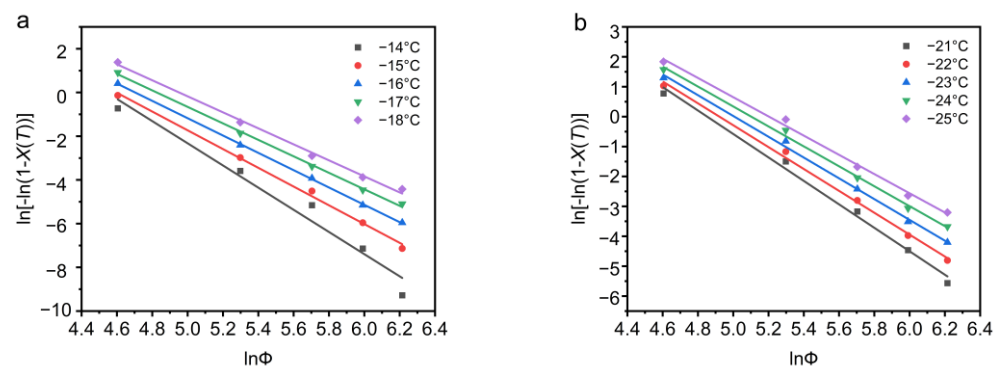
According to the Ozawa model, the crystallinity at a certain temperature has the following relationship with the heating or cooling rate  $\Phi$  [13]:

$$\ln [1 - X(T)] = -\frac{k_0(T)}{\Phi^m} \quad (3)$$

where  $k_0(T)$  is the crystallization rate constant,  $m$  is the exponent which is related to the crystal formation and nucleation mechanism where one-dimensional growth,  $m = 2$ ; two-dimensional growth,  $m = 3$ ; three-dimensional growth,  $m = 4$ , and  $X(T)$  is the relative crystallinity. It can be derived from the logarithm of both sides of the equation:

$$\ln\{-\ln[1 - X(T)]\} = \ln k_0(T) - m \ln \Phi \quad (4)$$

According to the analysis of the Ozawa model, the graph of  $\ln[-\ln(1 - X(T))]$  versus  $\ln\Phi$  should show a linear relationship, with a slope exponent of  $m$  and an intercept of  $\ln k_0(T)$ . At different temperatures  $T$ , the relationship between  $\ln[-\ln(1 - X(T))]$  and  $\ln\Phi$  analyzed by the Ozawa model is shown in Figure 4. It can be seen from Figure 4 that the Ozawa model fits the experimental data very well.



**Figure 4.** (a) PEG and (b) PEG-PCL non-isothermal crystallization process  $\ln[-\ln(1 - X(T))]$  plots  $\ln\Phi$ .

The Ozawa parameters  $m$ ,  $\ln k_0(T)$ ,  $k_0(T)$  showed in Table 2 are obtained from Figure 4. Both  $m$  and  $k_0(T)$  decrease with decreasing temperature. The average value of  $m$  of PEG is 4.15, which indicates that PEG is three-dimensional spherulitic growth. The average  $m$  of PEG-PCL is 3.52, which means that the crystallization behavior and nucleation mechanism of PEG-PCL and PEG are different. However, since the crystallization behavior of PEG-PCL is related to the cooling rate; we cannot directly judge its specific crystallization behavior through the average value.

**Table 2.** Ozawa parameters of PEG and PEG-PCL at different temperatures.

PEG			PEG-PCL		
$T/^\circ\text{C}$	$m$	$k_0(T)$	$T/^\circ\text{C}$	$m$	$k_0(T)$
−14	5.07	$13.5 \times 10^8$	−21	3.92	$1.82 \times 10^8$
−15	4.28	$3.63 \times 10^8$	−22	3.66	$0.65 \times 10^8$
−16	3.96	$1.25 \times 10^8$	−23	3.47	$0.36 \times 10^8$
−17	3.77	$0.79 \times 10^8$	−24	3.33	$0.24 \times 10^8$
−18	3.67	$0.74 \times 10^8$	−25	3.21	$0.18 \times 10^8$
	$\bar{m} = 4.15$			$\bar{m} = 3.52$	

3.2.2. Avrami Equation

According to the revised Avrami model, the relative crystallinity can be calculated by the following formula [12]:

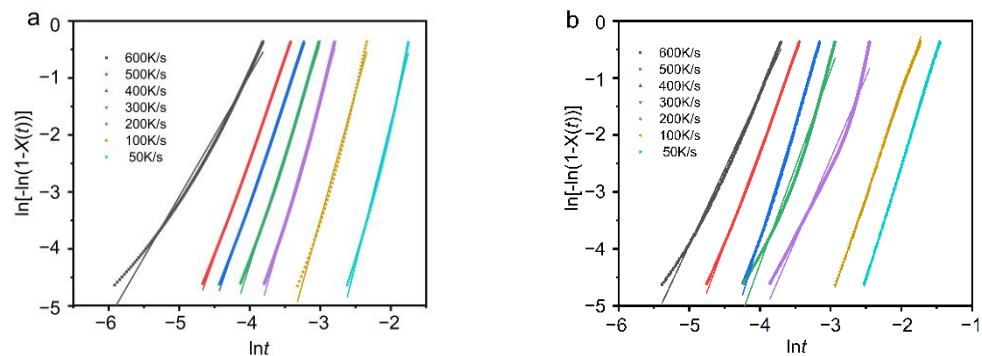
$$X(t) = 1 - \exp(-Z_t t^n) = 1 - \exp[-(K_{Avrami} t)^n] \tag{5}$$

Transform the equation and take the logarithm on both sides to obtain

$$\ln[-\ln(1 - X(t))] = n \ln t + \ln Z_t \tag{6}$$

where  $Z_t$  and  $n$  represent the kinetic rate constant and Avrami exponent, respectively. If  $\ln[-\ln(1 - X(t))]$  is plotted against  $\ln t$ , the intercept of the graph is  $Z_t$ , and the slope is  $n$ . The Avrami equation was originally used to study the phase transition of metals, and now it is also commonly used to study the isothermal crystallization kinetics of semi-crystalline polymers. The Avrami exponent can evaluate the growth dimension and nucleation mechanism of crystalline polymers.

Figure 5 presents plots of  $\ln[-\ln(1 - X(t))]$  as a function of  $\ln t$  for PEG and PEG-PCL. In Figure 5, plots of  $\ln[-\ln(1 - X(t))]$  versus  $\ln t$  showed good linearity.



**Figure 5.** (a) PEG and (b) PEG-PCL non-isothermal crystallization  $\ln[-\ln(1 - X(t))]$  plotting  $\ln t$ .

Table 3 summarizes the main kinetic parameters of PEG deduced from the Avrami analysis. It can be seen from the table that the value of the Avrami index  $n$  decreases with the increase in the cooling rate, which indicates that the crystallization dimension of PEG decreases with the increase in the crystallization rate. The average value of the Avrami exponent is 3.83, which indicates that the nucleation growth mode of PEG is mainly homogeneous nucleation spherulite growth. The data of non-isothermal crystallization of PEG observed by DSC also reported that its Avrami index is between 3.8 and 4.5 [16]. The crystallization rate constantly increases as the cooling rate increases. This is because the cooling rate increases and the crystallization becomes faster. However, when the temperature drop rate is 600 K/s, the decrease in the crystallization rate constant is due to the suppression of crystallization at a higher temperature drop rate.

**Table 3.** Avrami parameters of PEG at different cooling rates.

$\Phi$ (K/s)	$n$	$Z_t$ (s <sup>-n</sup> )	$k$ (s <sup>-1</sup> )	$1/t_{1/2}$ (s <sup>-1</sup> )	$(Z_t/\ln 2)^{1/n}$ (s <sup>-1</sup> )
50	4.95	$3.36 \times 10^3$	5.16	5.79	5.55
100	4.45	$1.99 \times 10^4$	9.25	10.33	10.04
200	4.32	$1.13 \times 10^5$	14.78	16.53	16.09
300	3.89	$7.92 \times 10^4$	32.84	20.53	19.96
400	3.61	$7.92 \times 10^4$	43.05	25.44	25.18
500	3.46	$9.20 \times 10^4$	52.92	30.96	30.24
600	2.14	$2.00 \times 10^3$	34.87	45.25	41.39

Additionally, it shows a satisfying agreement between the reciprocal crystallization half-times ( $1/t_{1/2}$ ) that were directly determined from the experimental data and those that were deduced from the Avrami parameters. This shows that the calculated parameters can describe the non-isothermal crystallization process of PEG well.

Table 4 is a summary of the parameters of PEG-PCL. Since the crystallization behavior of PEG-PCL is different at different cooling rates, the values of  $n$  calculated according to the Avrami equation are also very different. The value of  $n$  is close to 4 when the cooling rate is 50–100 K/s, indicating that the nucleation growth mode of PEG-PCL is the homogeneous nucleation of three-dimensional spherulitic growth. When the cooling rate is 200–600 K/s, the average value of the Avrami exponent of PEG-PCL is 3, indicating that the crystallization method is mainly the growth of three-dimensional spherulites with heterogeneous nucleation. The crystallization rate constantly increases with the increase in the cooling rate, which indicates that the faster the cooling rate, the faster the crystallization.

**Table 4.** Avrami parameters of PEG-PCL at different cooling rates.

$\Phi$ (K/s)	$n$	$Z_t$ (s <sup>-n</sup> )	$k$ (s <sup>-1</sup> )	$1/t_{1/2}$ (s <sup>-1</sup> )	$(Z_t/\ln 2)^{1/n}$ (s <sup>-1</sup> )
50	4.03	$2.47 \times 10^2$	3.92	4.27	4.29
100	3.62	$3.87 \times 10^2$	5.19	5.63	5.73
200	2.87	$4.83 \times 10^2$	8.61	11.55	9.78
300	3.40	$1.13 \times 10^4$	15.56	18.69	17.48
400	4.02	$2.11 \times 10^5$	21.11	23.31	23.12
500	3.31	$5.93 \times 10^4$	27.67	31.75	30.91
600	2.65	$1.13 \times 10^4$	33.84	40.32	38.86

Similarly, we compared the reciprocal crystallization half-times ( $1/t_{1/2}$ ) that were directly determined from the experimental data and those that were deduced from the Avrami parameters. It also shows good consistency, which means that the calculated parameters can describe the non-isothermal crystallization process of PEG-PCL well.

### 3.2.3. Combined Avrami Equation and Ozawa Equation

Because there are many parameters of non-isothermal crystallization, it is difficult to describe with a single method. For this reason, Mo Zhishen et al. proposed a new method to analyze the kinetic parameters of polymer crystallization, combining the Ozawa equation and the Avrami equation to obtain the following equation [14]:

$$\ln Z_t + n \ln t = \ln k_0(T) - m \ln \Phi \quad (7)$$

For a certain crystallinity, the equation can be changed to:

$$\ln \Phi = \ln F(T) - b \ln t \quad (8)$$

where the physical meaning of  $F(T)$  is the necessary cooling rate when the measured system arrives at a certain crystallinity degree at 1 min (or 1 s) crystallization time.  $b = n/m$ ,  $n$  is the Avrami exponent, and  $m$  is the Ozawa exponent. Under a certain degree of crystallinity,



plot  $\ln\Phi$  versus  $\ln t$ , the slope is  $-b$ , and the intercept is  $\ln F(T)$ . The larger the  $F(T)$ , the lower the crystallization rate of the system. Figure 6 is a plot of  $\ln\Phi$  versus  $\ln t$ . It can be seen that the linear relationship between  $\ln\Phi$  and  $\ln t$  is great in Figure 6.

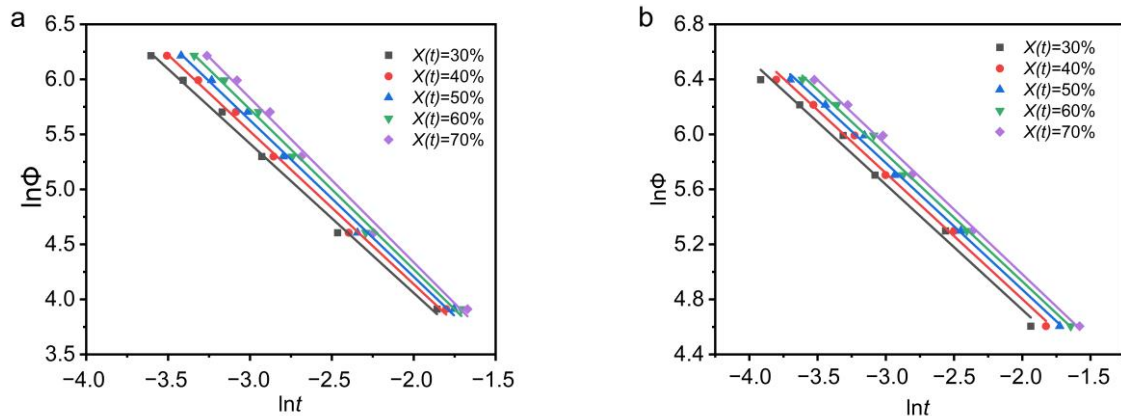


Figure 6. (a) PEG (b) PEG-PCL non-isothermal crystallization of  $\ln\Phi$  vs.  $\ln t$ .

At the same time,  $F(T)$  and  $b$  are summarized in Table 5. The  $b$  value of PEG and PEG-PCL increases with the increase in crystallinity. For PEG,  $b > 1$ , which means that the Avrami exponent of PEG is greater than the Ozawa exponent. For PEG-PCL,  $b < 1$ , which indicates that the Avrami exponent of PEG-PCL is smaller than the Ozawa exponent. For PEG, the  $F(T)$  value does not change much with the increase in crystallinity. The  $F(T)$  of PEG-PCL increases with the increase in crystallinity, which means that the crystallization rate of PEG-PCL decreases with the increase in crystallinity. Meanwhile, the  $F(T)$  of PEG is lower than that of PEG-PCL, indicating that the crystallization rate of PEG-PCL is slower than that of PEG, and this is consistent with the above results.

Table 5. Values of PEG and PEG-PCL parameters under Mo model.

$X(T)$	PEG			PEG-PCL		
	$b$	$F(T)$	$r^2$	$b$	$F(T)$	$r^2$
30%	1.36	3.8574	0.99642	0.91	18.3568	0.99171
40%	1.39	3.8962	0.99625	0.92	19.4919	0.99519
50%	1.42	3.8962	0.99566	0.92	20.6972	0.99718
60%	1.45	3.8962	0.99494	0.93	21.5419	0.99746
70%	1.49	3.8574	0.99409	0.94	22.1980	0.99704

#### 4. Conclusions

The non-isothermal crystallization behavior and isothermal crystallization behavior of PEG, and PEG-PCL were studied by FDSC. We found that both the PEG block and the PCL block of PEG-PCL can crystallize when the cooling rate is 50–100 K/s. When the cooling rate continues to increase, only the PEG block can crystallize. Neither the PEG block nor the PCL block of PEG-PCL can crystallize when the cooling rate reaches 1000 K/s. The Ozawa model and the Avrami model mainly tell us the growth dimension of crystals, while the MO model can tell us the rate of crystallization. Through the combination of the three models, we can better simulate the cooling and crystallization process in the actual machining process. The analysis of non-isothermal crystallization kinetics shows that the Ozawa, improved Avrami and Mo methods can describe the system well. The Ozawa exponent increases with increasing temperature, and the value of  $n$  is close to 4, which indicates that the crystallization process is three-dimensional growth. The Avrami exponent of PEG is 2.14 to 4.95, and its growth mode is mainly three-dimensional spherulitic growth. The Avrami exponent of PEG-PCL is close to 4 when the cooling rate is 50–100 K/s, the growth mode is mainly the three-dimensional spherulite growth with homogeneous

nucleation. When the cooling rate is 200–600 K/s, the average Avrami exponent of PEG-PCL is near 3, and its growth mode is mainly three-dimensional spherulitic growth with heterogeneous nucleation. The MO model shows that the crystallization rate of PEG is greater than that of PEG-PCL.

**Author Contributions:** Investigation, X.L. and M.Z.; data curation, L.X. and L.L.; writing—original draft preparation, L.L.; writing—review and editing, L.L. and X.L.; supervision, M.Z.; project administration, M.Z. and X.L. All authors have read and agreed to the published version of the manuscript.

**Funding:** This research received no external funding.

**Institutional Review Board Statement:** Not applicable.

**Informed Consent Statement:** Not applicable.

**Data Availability Statement:** Not applicable.

**Conflicts of Interest:** The authors declare no conflict of interest.

## References

- Liu, M.; Zhao, Q.; Wang, Y.; Zhang, C.; Mo, Z.; Cao, S. Melting behaviors, isothermal and non-isothermal crystallization kinetics of nylon 1212. *Polymer* **2003**, *44*, 2537–2545. [[CrossRef](#)]
- Liu, X.; Wu, Q. Non-isothermal crystallization behaviors of polyamide 6/clay nanocomposites. *Eur. Polym. J.* **2002**, *38*, 1383–1389. [[CrossRef](#)]
- Nojima, S.; Ono, M.; Ashida, T. Crystallization of block copolymers II. morphological study of poly(ethylene glycol)-poly( $\epsilon$ -caprolactone) block copolymers. *Polym. J.* **1992**, *24*, 1271–1280. [[CrossRef](#)]
- Gioffredi, E.; Cassulo, G.; Frache, A.; Maffettone, P.L. iPP crystallization: Micro and nano fillers effects. *AIP Conf. Proc.* **2010**, *1255*, 120–122. [[CrossRef](#)]
- Yu, S.; Li, X.; Guo, X.; Li, Z.; Zou, M. Curing and characteristics of  $N,N,N',N'$ -tetraepoxypropyl-4,4'-diaminodiphenylmethane epoxy resin-based buoyancy material. *Polymers* **2019**, *11*, 1137. [[CrossRef](#)] [[PubMed](#)]
- Iervolino, E.; Van Herwaarden, A.W.; Van Herwaarden, F.G.; Van De Kerkhof, E. Thermochemica Acta Temperature calibration and electrical characterization of the differential scanning calorimeter chip UFS1 for the Mettler-Toledo Flash DSC 1. *Thermochim. Acta* **2011**, *522*, 53–59. [[CrossRef](#)]
- Mathot, V.; Pyda, M.; Pijpers, T.; Vanden, G.; Van De Kerkhof, E.; Van Herwaarden, S.; Van Herwaarden, F.; Leenaers, A. The Flash DSC 1, a power compensation twin-type, chip-based fast scanning calorimeter (FSC): First findings on polymers. *Thermochim. Acta* **2011**, *522*, 36–45. [[CrossRef](#)]
- Van Herwaarden, S.; Iervolino, E.; Van Herwaarden, F.; Wijffels, T.; Leenaers, A. Thermochemica Acta Design, performance and analysis of thermal lag of the UFS1 twin-calorimeter chip for fast scanning calorimetry using the Mettler-Toledo Flash DSC 1. *Thermochim. Acta* **2011**, *522*, 46–52. [[CrossRef](#)]
- He, Y.; Xie, K.; Wang, Y.; Zhou, D.; Hu, W. Characterization of polymer crystallization kinetics via fast-scanning chip-calorimetry. *Wuli Huaxue Xuebao/Acta Phys. Chim. Sin.* **2020**, *36*, 1–12. [[CrossRef](#)]
- Cavallo, D.; Gardella, L.; Alfonso, G.C.; Mileva, D.; Androsch, R. Effect of comonomer partitioning on the kinetics of mesophase formation in random copolymers of propene and higher  $\alpha$ -olefins. *Polymer* **2012**, *53*, 4429–4437. [[CrossRef](#)]
- Chen, Y.; Yao, L.; Yang, C.; Zhang, L.; Zheng, P.; Liu, A.; Shen, Q.D. In-depth understanding of interfacial crystallization: Via Flash DSC and enhanced energy storage density in ferroelectric P(VDF-CTFE)/Au NRs nanocomposites for capacitor application. *Soft Matter* **2018**, *14*, 7714–7723. [[CrossRef](#)] [[PubMed](#)]
- Avrami, M. Kinetics of phase change. I: General theory. *J. Chem. Phys.* **1939**, *7*, 1103–1112. [[CrossRef](#)]
- Ozawa, T. Kinetics of non-isothermal. *Polymer* **1971**, *12*, 150–158. [[CrossRef](#)]
- Liu, T.; Mo, Z.; Wang, S.; Zhang, H. Isothermal melt and cold crystallization kinetics of poly(aryl ether ether ketone) (PEEK). *Eur. Polym. J.* **1997**, *33*, 1405–1414. [[CrossRef](#)]
- Sun, H.; Feng, J.; Wang, J.; Yu, B.; Zhang, Z.; Sun, H.; Feng, J.; Wang, J.; Yu, B.; Zhang, Z. Monte Carlo Simulation Study of Isothermal Crystallization Kinetics of Polyethylene Glycol Monte Carlo Simulation Study of Isothermal Crystallization Kinetics of Polyethylene Glycol. *Polym.-Plast. Technol. Eng.* **2011**, *50*, 1552–1556. [[CrossRef](#)]
- Wei, T.; Zheng, B.; Yi, H.; Gao, Y.; Guo, W. Thermal Analysis and Non-Isothermal Kinetics of Poly (ethylene glycol) with Different Molecular Weight. *Polym. Eng. Sci.* **2014**, *54*, 2872–2876. [[CrossRef](#)]
- Coburn, N.; Douglas, P.; Kaya, D.; Gupta, J.; McNally, T. Advanced Industrial and Engineering Polymer Research Isothermal and non-isothermal crystallization kinetics of composites of poly (propylene) and MWCNTs. *Adv. Ind. Eng. Polym. Res.* **2018**, *1*, 99–110. [[CrossRef](#)]
- Yang, Z.; Peng, H.; Wang, W.; Liu, T. Crystallization behavior of poly( $\epsilon$ -caprolactone)/layered double hydroxide nanocomposites. *J. Appl. Polym. Sci.* **2010**, *116*, 2658–2667. [[CrossRef](#)]

19. Brandt, J.V.; Piazza, R.D.; dos Santos, C.C.; Vega-Chacón, J.; Amantéa, B.E.; Pinto, G.C.; Magnani, M.; Piva, H.L.; Tedesco, A.C.; Primo, F.L.; et al. Synthesis and colloidal characterization of folic acid-modified PEG-b-PCL Micelles for methotrexate delivery. *Colloids Surf. B Biointerfaces* **2019**, *177*, 228–234. [[CrossRef](#)] [[PubMed](#)]
20. Gong, C.Y.; Shi, S.; Wang, X.H.; Wang, Y.J.; Fu, S.Z.; Dong, P.W.; Chen, L.J.; Zhao, X.; Wei, Y.Q.; Qian, Z.Y. Novel composite drug delivery system for honokiol delivery: Self-assembled poly(ethylene glycol)-poly( $\epsilon$ -caprolactone)-poly(ethylene glycol) micelles in thermosensitive poly(ethylene glycol)-poly( $\epsilon$ -caprolactone)-poly(ethylene glycol) hydrogel. *J. Phys. Chem. B* **2009**, *113*, 10183–10188. [[CrossRef](#)] [[PubMed](#)]
21. Villamil, J.C.; Parra-Giraldo, C.M.; Pérez, L.D. Enhancing the performance of PEG-b-PCL copolymers as precursors of micellar vehicles for amphotericin B through its conjugation with cholesterol. *Colloids Surf. A Physicochem. Eng. Asp.* **2019**, *572*, 79–87. [[CrossRef](#)]
22. Behl, A.; Parmar, V.S.; Malhotra, S.; Chhillar, A.K. Biodegradable diblock copolymeric PEG-PCL nanoparticles: Synthesis, characterization and applications as anticancer drug delivery agents. *Polymer* **2020**, *207*, 122901. [[CrossRef](#)]
23. Gökçe Kocabay, Ö.; İsmail, O. Preparation and optimization of biodegradable self-assembled PCL-PEG-PCL nano-sized micelles for drug delivery systems. *Int. J. Polym. Mater. Polym. Biomater.* **2021**, *70*, 328–337. [[CrossRef](#)]
24. Sun, J.; He, C.; Zhuang, X.; Jing, X.; Chen, X. The crystallization behavior of poly(ethylene glycol)-poly( $\epsilon$ -caprolactone) diblock copolymers with asymmetric block compositions. *J. Polym. Res.* **2011**, *18*, 2161–2168. [[CrossRef](#)]
25. Sun, J.; Hong, Z.; Yang, L.; Tang, Z.; Chen, X.; Jing, X. Study on crystalline morphology of poly(L-lactide)-poly(ethylene glycol) diblock copolymer. *Polymer* **2004**, *45*, 5969–5977. [[CrossRef](#)]
26. Zhu, W.; Xie, W.; Tong, X.; Shen, Z. Amphiphilic biodegradable poly(CL-b-PEG-b-CL) triblock copolymers prepared by novel rare earth complex: Synthesis and crystallization properties. *Eur. Polym. J.* **2007**, *43*, 3522–3530. [[CrossRef](#)]
27. Gong, C.Y.; Shi, S.; Dong, P.W.; Kan, B.; Gou, M.L.; Wang, X.H.; Li, X.Y.; Luo, F.; Zhao, X.; Wei, Y.Q.; et al. Synthesis and characterization of PEG-PCL-PEG thermosensitive hydrogel. *Int. J. Pharm.* **2009**, *365*, 89–99. [[CrossRef](#)] [[PubMed](#)]
28. Huang, C.L.; Jiao, L.; Zeng, J.B.; Zhang, M.; Xiao, L.P.; Yang, K.K.; Wang, Y.Z. Crystallization behavior and morphology of double crystalline poly(butylene succinate)-poly(ethylene glycol) multiblock copolymers. *Polymer* **2012**, *53*, 3780–3790. [[CrossRef](#)]
29. Takeshita, H.; Fukumoto, K.; Ohnishi, T.; Ohkubo, T.; Miya, M.; Takenaka, K.; Shiomi, T. Formation of lamellar structure by competition in crystallization of both components for crystalline e crystalline block copolymers. *Polymer* **2006**, *47*, 8210–8218. [[CrossRef](#)]
30. Bogdanov, B.; Vidts, A.; Van Den Bulcke, A.; Verbeeck, R.; Schacht, E. Synthesis and thermal properties of poly(ethylene glycol)—poly( $\epsilon$ -caprolactone) copolymers. *Polymer* **1998**, *39*, 1631–1636. [[CrossRef](#)]
31. Shiomi, T.; Imai, K.; Takenaka, K.; Takeshita, H.; Hayashi, H.; Tezuka, Y. Appearance of double spherulites like concentric circles for block-poly( $\epsilon$ -caprolactone). *Polymer* **2001**, *42*, 3233–3239. [[CrossRef](#)]

## Article

# Transfer Learning Applied to Characteristic Prediction of Injection Molded Products

Yan-Mao Huang, Wen-Ren Jong \* and Shia-Chung Chen

Department of Mechanical Engineering, Chung Yuan Cristian University, Taoyuan City 320314, Taiwan; H05850207@hotmail.com (Y.-M.H.); shiachun@cycu.edu.tw (S.-C.C.)

\* Correspondence: wenren@cycu.edu.tw

**Abstract:** This study addresses some issues regarding the problems of applying CAE to the injection molding production process where quite complex factors inhibit its effective utilization. In this study, an artificial neural network, namely a backpropagation neural network (BPNN), is utilized to render results predictions for the injection molding process. By inputting the plastic temperature, mold temperature, injection speed, holding pressure, and holding time in the molding parameters, these five results are more accurately predicted: EOF pressure, maximum cooling time, warpage along the Z-axis, shrinkage along the X-axis, and shrinkage along the Y-axis. This study first uses CAE analysis data as training data and reduces the error value to less than 5% through the Taguchi method and the random shuffle method, which we introduce herein, and then successfully transfers the network, which CAE data analysis has predicted to the actual machine for verification with the use of transfer learning. This study uses a backpropagation neural network (BPNN) to train a dedicated prediction network using different, large amounts of data for training the network, which has proved fast and can predict results accurately using our optimized model.

**Citation:** Huang, Y.-M.; Jong, W.-R.; Chen, S.-C. Transfer Learning Applied to Characteristic Prediction of Injection Molded Products. *Polymers* **2021**, *13*, 3874. <https://doi.org/10.3390/polym13223874>

**Keywords:** injection molding; CAE; machine learning; transfer learning

Academic Editors: Célio Bruno Pinto Fernandes, Salah Aldin Faroughi, Luís L. Ferrás and Alexandre M. Afonso

Received: 28 September 2021  
Accepted: 4 November 2021  
Published: 9 November 2021

**Publisher's Note:** MDPI stays neutral with regard to jurisdictional claims in published maps and institutional affiliations.



**Copyright:** © 2021 by the authors. Licensee MDPI, Basel, Switzerland. This article is an open access article distributed under the terms and conditions of the Creative Commons Attribution (CC BY) license (<https://creativecommons.org/licenses/by/4.0/>).

## 1. Introduction

In recent years, the computer, communications, and consumer electronics industries (hereafter referred to as the 3Cs) have developed vigorously, and their increasing diversity of products has led to the shortening of product life cycles. In order to reduce a costly trial-and-error process and speed up product development to match product life cycle demand, many companies have introduced computer-aided engineering (CAE) technology to their molded products' production processes in order to enhance the quality of those products, ideally avoiding defects. However, due to the physical characteristics of each injection machine being irregular, even though possible problems are eliminated at the CAE stage, there is still a necessity to rely on the experience of on-site personnel to manually adjust the parameters of said machines for the actual molding process to be carried out successfully. As such, in order to achieve the accuracy required for a product, CAE technology alone cannot currently provide sufficient assistance regarding such processes requiring a precise injection of molding to create products.

When defects do occur in products created via an injection molding process, these are not due to simple linear problems. Therefore, there is no way to use simple judgment rules to predict numerical values. In related research literature, Rosa et al. [1] mention that experimental design, i.e., design achieved using experimental techniques, is widely used to optimize injection molding parameters, thus improving product quality. However, conventional experimental design methods are usually complicated and may often fail to achieve the results expected. When the number of molding parameters increases, these methods require many trials. (It can be said that as the number of parameters to be included increases, the number of trials necessarily increases.) Therefore, the Taguchi orthogonal method is used to select experimental trial data and used to reduce the number of trials

required to obtain clear results; Marins et al. [2] propose the use of the Taguchi method and analysis of variance (ANOVA) to evaluate the impact of varied injection molding parameters regarding warpage, shrinkage, and mechanical properties of plastic parts. Marins et al. use two different plastics, one of which acrylonitrile butadiene styrene (ABS) is used in this study. Their control factors are mold temperature, holding pressure, holding time, plastic melt temperature, cooling time, mold water flow, and injection speed. The results of their experiments show that when ABS was used for trials, the controlling factors regarding shrinkage, warpage, and bending defects are holding time and holding pressure.

Hifsa et al. [3] use the Taguchi method with grey relational analysis to find the best parameter configuration for injection molding of HDPE/TiO<sub>2</sub> nanocomposites.

In another related work on machine learning, Luo et al. [4] employ an artificial neural network to resin transfer molding (RTM) using simulation analysis results as training data and flow behavior and filling time as output, combined with a genetic algorithm to optimize the prediction results. Their research results show that this method can effectively assist the engineer to determine the optimum locations of injection gates and vents for the best processing performance, i.e., short filling time and high quality (minimum defects).

However, Kenig et al. [5] mention that the mechanical properties of plastics and molding parameters are highly nonlinear. Therefore, they are difficult to predict. Kenig et al. use the design of experiment (DOE) method in combination with artificial neural networks to accurately predict the mechanical properties of the product. This method can be used to predict other molding results effectively.

Moreover, Denni [6] proposes the use of the Taguchi method, a backpropagation neural network (BPNN), and the hybrid particle swarm and genetic algorithms to find optimal parameter settings. The results of Denni's experiments show that this optimized system not only improves the quality of plastic parts but also effectively reduces process variation. Denni also mentions that a backpropagation algorithm will cause difficulty in reaching optimal solutions or overfitting due to poor initial link values or excessive training numbers. Therefore, genetic algorithms are added to alleviate this shortcoming and increase the accuracy of predictions.

Furthermore, Kwak et al. [7] propose a kind of artificial neural network architecture to solve the multivariable problem that affects the optical mold during the injection molding process using the two control factors of suppressing porosity and reducing the minimum thickness combined with an artificial neural network to make predictions, which proved that this technology can effectively improve the product quality of optical molds.

In addition, Castro et al. [8] assert that injection molding is the most important process for mass production of plastic products; however, the difficulty in optimizing the injection molding process lies in performance measurement. Therefore, CAE, statistical methods, artificial neural networks (ANN), and data envelopment analysis (DEA) are several methods to solve the problems encountered in injection molding.

In their work, Shen et al. [9] mention that injection-molded products are sensitive to the conditions of the injection process, so they use backpropagation to process the nonlinear relationship between the process parameters and product quality and combine genetic algorithms to optimize the process parameters to reduce product shrinkage. Their results show that the combination of backpropagation and genetic algorithms can be an effective tool for optimizing process parameters.

Mirigul [10] uses the Taguchi method to carry out experimental design and ANOVA to perform analysis, finding that the most important factors that affect polypropylene (PP) and polystyrene (PS) shrinkage are holding pressure and melt temperature, and through these trials, with melt temperatures, holding pressures, holding times used as input, and the shrinkage rate used as output, an artificial neural network training is conducted. Mirigul's research results show that PP shrinkage prediction error is 8.6%, and for PS, it is 0.48%, which proves that this method is an effective tool for predicting shrinkage.

Additionally, Yin et al. [11] propose a 5-input nodes, 1-output node backpropagation for neural network learning. The 5 input signals are mold temperature, melt temperature,

filling pressure, filling time, and holding time. The hidden layer contains two neural layers, each with 20 neurons, and the output signal is warpage deformation. This method successfully uses finite element analysis of data for training and the prediction error of the control systems is within 2%.

Alberto and Ramón [12] mention that the process parameters are one of the final yet important steps during production; they are used to improve product quality in final production, but the adjusted parameters might affect the quality of a product due to the instability of material and machine. Instability affects product quality. From their work, we can see that using machine learning can accurately improve stability and quickly improve product quality.

Deng and Yu [13] propose general deep learning methodologies and provide an overview of their application to various signal and information processing tasks. Per their work, there are three criteria for selecting an application area: the author's professional knowledge, the application areas that have been successfully transformed by the use of deep learning technology, and the application areas that are potentially affected by deep learning. Their monograph also introduces the principle of pretraining in unsupervised learning.

In the work of Jong et al. [14], the hyperparameters of a backpropagation neural network (BPNN) are optimized with the smaller, the better feature (STB) from the Taguchi method, and they propose a 5-input, 3-output artificial neural network architecture, where the 5 inputs are injection speed, holding time, holding pressure, mold temperature, melt stability, and the 3 outputs are end of filling (EOF) pressure, maximum cooling time, and warpage along the Z-axis. There are two hidden layers: the first layer has 7 neurons, and there are 3 neurons in the second hidden layer. The network is trained for the second time with new training data for addressing Z-axis warping, and in terms of the warping deformation value, the error is reduced from 7.26% to 3.69%.

Sinno et al. [15] propose that between classification tasks in similar fields, transfer learning, if performed successfully, would greatly improve the performance of learning by avoiding expensive data-labeling efforts.

In the research literature related to transfer learning, Dan et al. [16] use an artificial neural network that recognizes various symbols, and it is retrained with the data of capital letters. The results show that using the original network for transfer learning can accelerate the training efficiency of the neural network. Furthermore, pretrained neural networks consistently outperform randomly initialized neural networks on new tasks with few labeled data. This result is also applied to Chinese character recognition for accelerated neural networks.

Huang et al. [17] propose a sharing cross-language hidden layer concept for the learning of various languages, and this hidden layer of cross-language learning features transformations during transfer learning in which the error can be reduced to 28% at best.

Jiahuan et al. [18] introduce model-based transfer learning and data augmentation, the knowledge from other vision tasks is transferred to industrial defect inspection tasks, resulting in high accuracy with limited training samples. Experimental results on an injection molding product showed that the detection accuracy was improved to about 99% when only 200 images per category were available. In comparison, conventional CNN models and the support vector machine method could achieve an average accuracy of only about 88.70% and 86.90%, respectively.

Yannik, L. et al. [19] used induced network-based transfer learning to reduce the necessary amount of injection molding process data for the training of an artificial neural network in order to conduct a data-driven machine parameter optimization for injection molding processes. From the research results, it is found that the source model of the injection molding process of the part similar to the part of the target process achieves the best result. Transfer learning technology has the potential to significantly improve the relevance of AI methods in process optimization in the plastics processing industry.

In their work, Shin et al. [20] mention that because ImageNet collects a large number of image tags, the neural network acquires enough training data to make accuracy ever-improving. Their research results show that ImageNet network transfers to thoracic-abdominal lymph node (LN) detection and interstitial lung disease (ILD) classification problems with good accuracy, proving that neural networks can be extended to other medical applications through transfer learning.

Hasan et al. [21] mention that when the amount of training data is not sufficient when using training with random initialization, it is difficult to find an optimal solution. This research first pretrains the network with simulated and analyzed data and then performs transfer learning with actual experimental training. Their research results show that this pretrained method can make a network converge quickly and can obtain results similar to those of the control group with less training data. In related work, Hasan et al. [22] mention that machine learning has great potential in the injection molding process, and their research involves using different masses of LEGO bricks as training data and then transferring what is learned to LEGO bricks of other sizes for quality prediction. The network used in their study contains four hidden layers of neurons, the numbers of which are 45, 45, 20, and 20, respectively. Rectified linear unit (ReLU) is used as the activation function, the learning rate is 0.01, and the first two neural layers are frozen during the transfer learning process to ensure that important knowledge will not be lost during the transfer process.

From the aforementioned works, it can be found that in the application of the injection molding process, most research is used to predict product weights, and less focus is given to injection pressure, product shrinkage, warpage, or other issues. Additionally, beyond the issue of weight, another criterion for judging whether the injection molding process for any given product meets the standard is the shrinkage rate. At present, 3C products are becoming more and more complex, so the assembly accuracy of the product is demanding, making the parameters related to the shrinkage rate complicated. The injection speed of the machine, mold temperature, holding pressure, and holding time are directly related. Therefore, the on-site staff cannot quickly determine how to adjust the production process to meet the tolerance specified during the design. The transfer learning method proposed herein trains an artificial neural network with fewer actual parameters, which can be used in the future to assist mold testing staff to quickly adjust machine parameters.

## 2. Relevant Technical Research

In recent years, with the ever-increasing speed of computer operations, artificial neural networks have once again been widely discussed. With the development of TensorFlow as an open-source resource by the Google Development Team, the application of artificial neural networks has begun to develop rapidly. Artificial neural networks can be “trained” with a significant amount of data constructing a network with rapid prediction and judgment capabilities. However, not all trials can easily have a large amount of training data collected. Therefore, the concept of transfer learning is also proposed. Neural networks trained through similar trials can reduce the amount of training data and time necessary to construct new networks.

Regarding programming development, this research uses the programming language Python to interface with API via TensorFlow 2.0 (a Python-friendly open source library) to develop artificial neural networks. After the release of TensorFlow version 2.0, the high-level API highly supports Keras to reduce the difficulty of getting started and enables interdisciplinary researchers to construct neural networks and adjust network hyperparameters more conveniently.

### 2.1. Artificial Neural Networks (ANN)

Artificial neural networks are currently widely used in the field of machine learning and artificial intelligence. An artificial neural network consists of an input layer, a hidden layer, and an output layer. Each layer is composed of several neurons. This study utilizes a

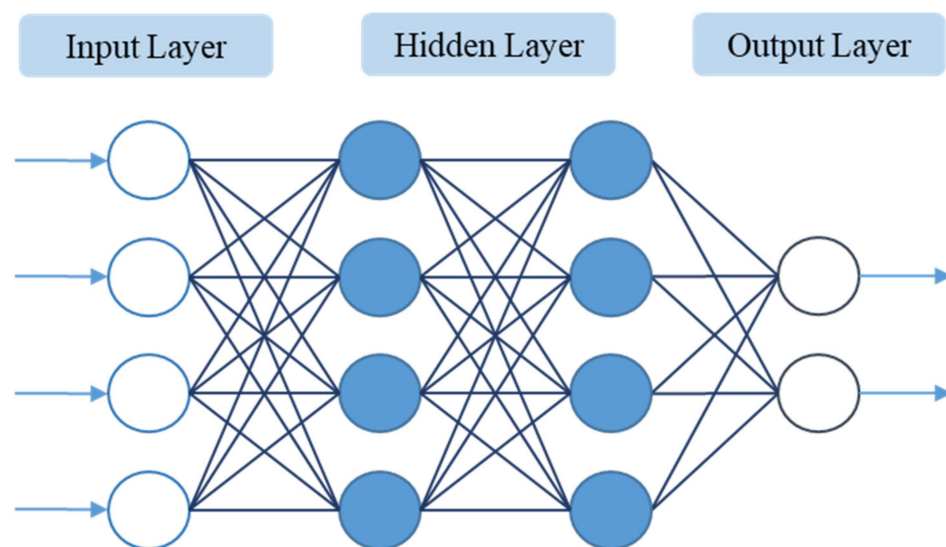
backpropagation neural network as a training method, and it adjusts the values of weight and bias between each neuron based on the results of each training trial.

### 2.1.1. Backpropagation Neural Network (BPNN)

A backpropagation neural network (BPNN) is a kind of supervised learning that uses the gradient descent method to correct the erroneous difference between the expected value and the output value. Its characteristic is that each neuron has a differentiable activation function, and the network is highly connected.

The curve of injection molding product has multiple and deformable characteristics. It is hard to use a simple principle to predict. Therefore, this research is based on BPNN to predict these irregular data.

The BPNN network structure can be divided into three layers. As shown in Figure 1, the first layer is the input layer. The input layer will receive data from the outside world. Usually, these data will be preprocessed first. After receiving the data, the input layer will transmit the data to the next layer. The number of hidden layers and the number of neurons in each layer are designed according to different modeling problems, and because each neuron is highly connected to each other, the architecture of the hidden layer will directly affect the calculation speed of each training run; the third layer is the output layer, the predicted values calculated by the hidden layer are exported to the outside world from this layer, and according to different activation functions, these will have different functions. Common ones are numerical prediction, classification, and probability, and so on.

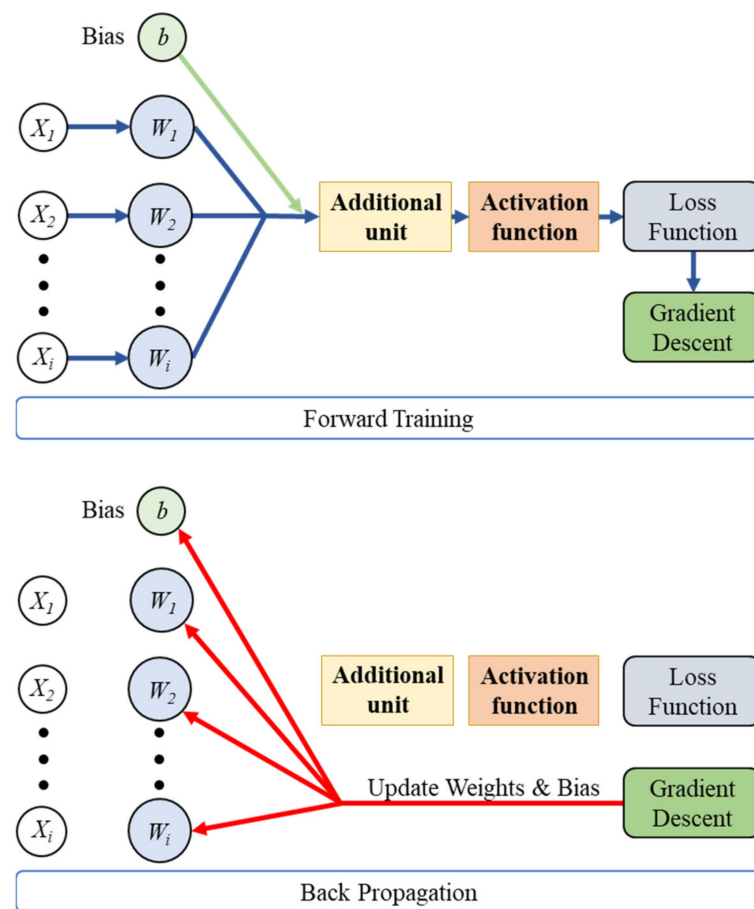


**Figure 1.** Artificial neural network architecture.

### 2.1.2. Training and Learning Process

A backpropagation neural network is trained through the use of multiple sets of data and continuously adjusts the weight value of each link until the error of the network output meets the expected range. The training process is characterized by forward flow of information in the prediction mode and backward flow of error corrections in the learning process. Usually, the initialized weight value and offset value are randomly generated, so the data need to be passed in the forward direction. The input data passed to the output layer after the weight value, offset value, addition function, and activation function of the link are calculated and predicted values can be received; the reverse signal transmission is the reverse transmission stage of the network training. The error between the network's predicted value and the target value is first calculated, and then the learning effect is controlled by the gradient descent method using the learning rate. The learning process is shown in Figure 2.





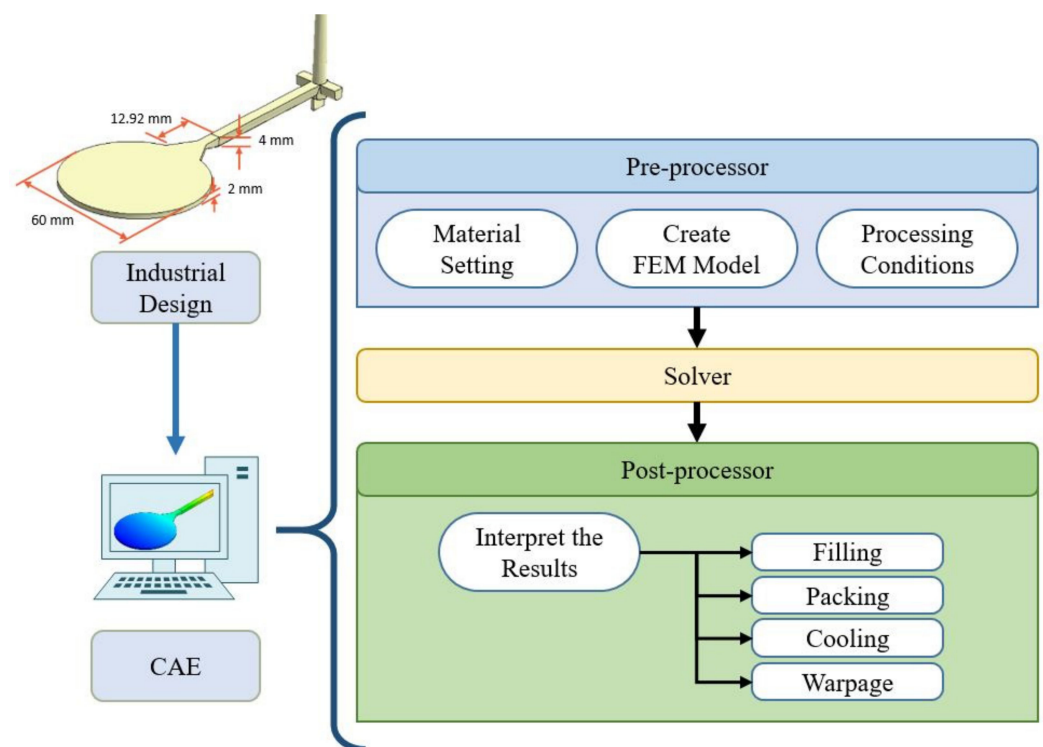
**Figure 2.** Basic architecture of a backpropagated neural network (BPNN).

## 2.2. Transfer Learning (TL)

The concept of transfer learning originated from the study of human behavior by scientists. Human beings can transfer past experience to different fields and thereby accelerate their learning in those fields new to them. In the field of machine learning, the artificial neural network algorithm was developed by simulating the operation of human nerves, and it also has the characteristics of transfer learning. When we do not have enough labeled data to train the model, we can use a similar or the same type of data to “pretrain” a model; with and on the basis of this properly trained model, a usable model can be trained by using less labeled data. Transfer learning can be divided into two types—first, the transition from virtual to actual reality, and second, among similar areas (as is explained shortly hereafter). If the acquisition of training data is overly risky, the amount of data required is too large, or it takes a lot of time and money, using a computer simulation can obtain sufficient training data in a fast, safe, and cost-effective manner. For example, if automatic driving technology were directly applied to a real road test before it is mature, it would be extremely dangerous. Therefore, the use of computer-simulated driving for a road network as pretraining and then transferring that to actual road training will greatly reduce both risks and data requirements. Another transfer method is to transfer to a similar field. For example, the module used for truck identification can be quickly applied to sedan identification, which not only reduces the training data required but also speeds up the network training. To achieve an effective transfer of learning, the data selection must be as similar as possible, and, if possible, the data should be adjusted to match the data type of the original network. Therefore, the data must be guaranteed to be normalized without too much deviation; otherwise, the content received by the network will be different from the setting.

### 2.3. Computer-Aided Engineering (CAE)

Computer-aided engineering (CAE) is the use of finite element software to establish an analysis model and perform rapid calculations on a computer for simulation. It is mainly used in various engineering fields. Using the injection molding industry as an example, engineers can perform simulation analysis via computer at an early stage of product design and then evaluate the feasibility of that product design, as shown in Figure 3. This technology can greatly shorten the development time, analyze and correct designs at the initial stage, and reduce manpower and material costs in the subsequent testing process so as to accelerate the time of product development, improve the product yield and quality, and then increase the yield.



**Figure 3.** Flowchart of CAE design analysis.

### 2.4. The “Random Shuffle” Method

In machine learning, the most important thing is the correctness and quantity of training data. Sufficient training data is one of the primary factors to ensure accuracy, but how to use such hard-earned data is another issue of importance. Although machine learning is fast and accurate, it never makes mistakes, so no matter how many calculations are processed, the same result will be obtained. When humans are learning, because of factors such as distractions and different preferences, the same information is evaluated differently, which increases the likelihood of different resultant possibilities. Therefore, when processing training data, that data can be randomly grouped, as shown in Figure 4, by splitting it into multiple sets for learning purposes, the possibility of optimization can thus be enhanced. This method, which we coin here as “random shuffle,” is similar to the concept of training on batch commonly used in machine learning. “Training on batch” describes when a training data set is divided into multiple batches in order to avoid the difficulty of convergence due to processing too much training data at a time. The greatest difference between training on batch and random shuffle is that the former uses the data in only one training run, while random shuffle utilizes incomplete data sets for each run, thus increasing the chance of mutation during all training runs. Because each training data set is incomplete, after training, you need to train it again using the complete data set. Random shuffle can be regarded as a kind of pretraining, and then the full data are used

to make final adjustments to the pretraining network, such as shown in Figure 5, where the data segmentation of random shuffle needs to be searched for using the trial-and-error method. This research has been tested at 80% of the full data segmentation with a learning rate of 0.1, which shows an improved effect. In terms of epochs, the number depends on the amount of data in the set—the more training data that are in the set, the fewer epochs will be needed.

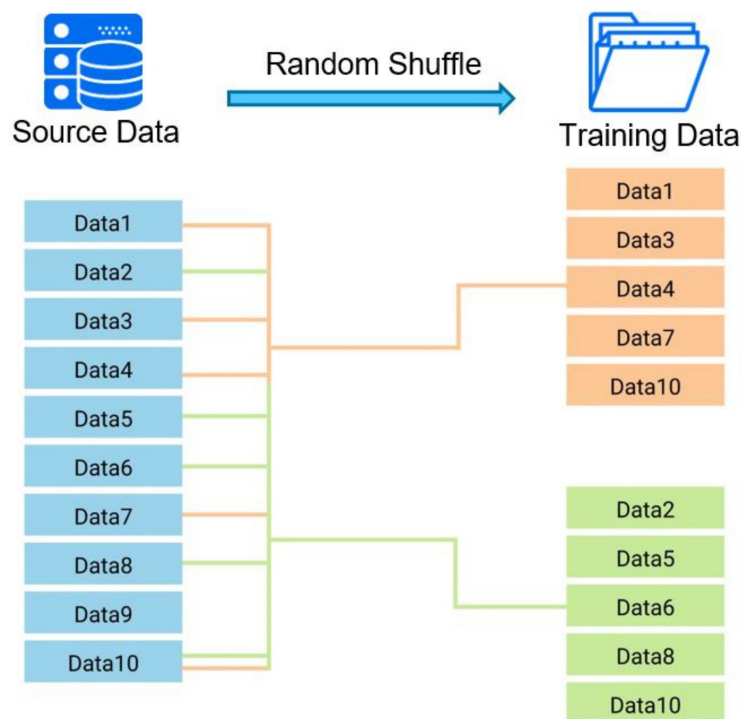


Figure 4. Schematic diagram of random shuffle.

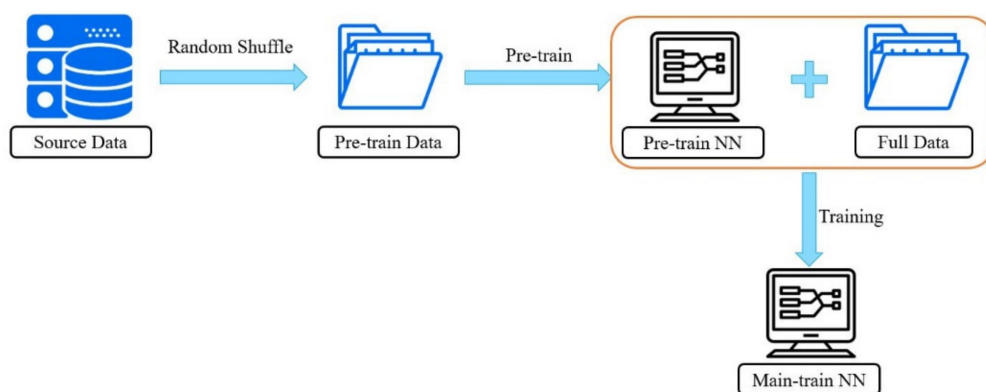


Figure 5. The random shuffle training process.

### 2.5. Data Normalization

Data normalization is used to compare data from different units. A unit of a set of data can be removed and analyzed. Taking the injection molding parameters applied to neural network training as an example, a temperature of 200 degrees for a plastic and the holding time of 5 s as the input layer, due to the high value of the plastic’s temperature, more iterations will be required in the calculations with the gradient descent (algorithm), which will cause too many iterations on the holding pressure intervals with a relatively small value that, in turn, causes overfitting. Therefore, the preprocessing of data is important for machine learning. The two most common methods in the field of machine learning are min–max normalization and Z-score standardization.

The main purpose of minimum and maximum normalization is to scale all the data to between  $[0, 1]$  and retain the distribution state of the data. The calculation method is shown in Equation (1). This method is mainly used when the difference among data sets is too great, which can accelerate the convergence of the model and avoid potential overfitting; Z-score standardization is used to convert the data and to make it conform with normal distribution, so that the average value is equal to 0 and the standard deviation is equal to 1. The calculation method is shown in (2); it is mainly used to further optimize data when the data themselves have close to a normal distribution. The data used in this study are all evenly distributed, and the numerical difference between each input is large, so the minimum and maximum normalization will be used to perform the preprocessing of the data.

$$X_{nom} = \frac{X - X_{min}}{X_{max} - X_{min}} \in [0, 1] \quad (1)$$

$$Z = \frac{X - \mu}{\sigma} \sim N(0, 1) \quad (2)$$

## 2.6. The Taguchi Method

The Taguchi method is a statistical method developed by Dr. Taguchi Genichi in the 1950s. It can improve design quality and computational cost efficiency. Through the use of an orthogonal meter, the interference of noise on the product can be reduced, the number of trials can be reduced, and the quality variation can be reduced to achieve the purpose of robust design.

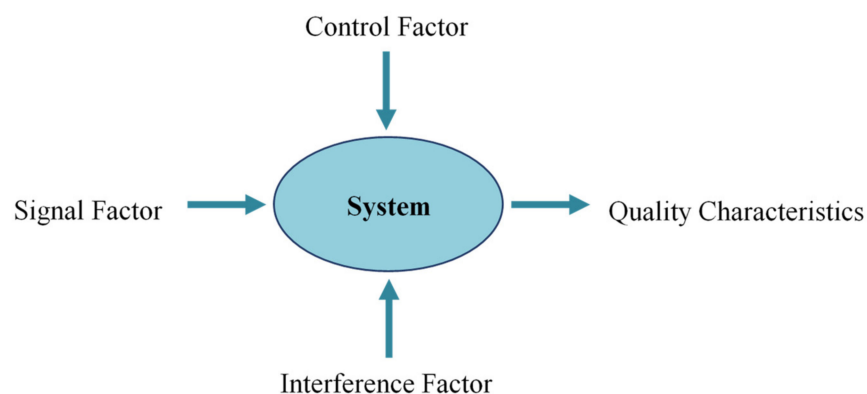
### 2.6.1. Quality Characteristics

Appropriate quality characteristics have the following two criteria: one is that real, continuous functions are required, and the other is that a monotonic function is preferred. It may likely be anticipated that “smaller” error between the inferred value and the target output value is better, so it has a quality characteristic of “the smaller, the better” (STB), and for STB, its target value of the  $S/N$  ratio should be approximating 0. The definition of the  $S/N$  ratio is shown in Equation (3).

$$S/N = -10 \log \left[ \frac{1}{n} \sum_{i=1}^n y_i^2 \right] \quad (3)$$

### 2.6.2. Definition and Selection of Experimental Factors

The factors that affect quality characteristics can be divided into three categories, namely control factors, signal factors, and interference factors (also called noise factors), as shown in Figure 6. The quality of the design will affect whether the subsequent results achieve the standard desired and will not change with excessive variation due to the interference of external factors, that is, sensitivity to the interference factor is reduced.

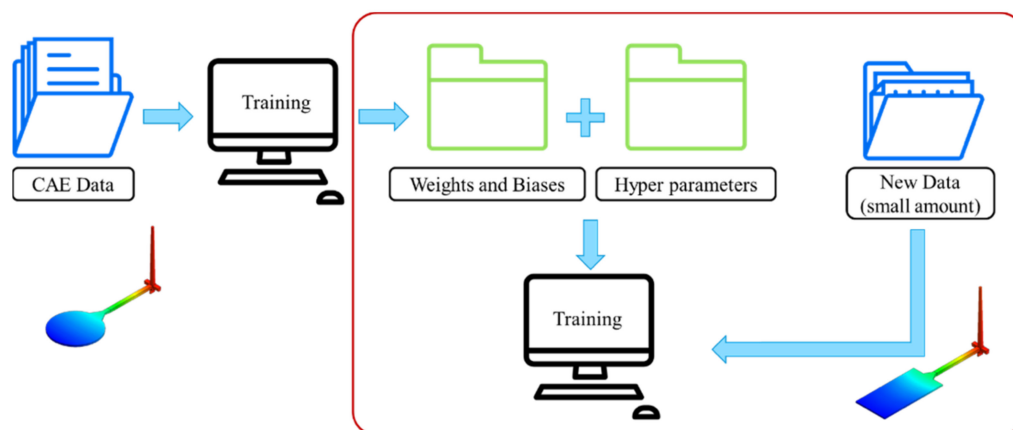


**Figure 6.** Experimental factors in Taguchi designs.

Three strategies can be used for interference factors: random experiment, internal orthogonal table, and interference experiment. If the quality characteristics are still not affected by the extreme compound interference factors, then the combination is the best stable design and can resist changes from other interference factors. To understand the Taguchi orthogonal method as mentioned prior, the main effect between the factors, that is, the degree of influence of the factor on the quality characteristics, and the fact that the average effect of each factor is the experimental combination configured in the Taguchi orthogonal table experiment, must be understood and ascertained, and then the  $S/N$  ratio of each factor calculated, and finally made a response table.

### 3. Using CAE Data to Study Transfer Learning among Different Models

Because of the fact that actual injection molding data is difficult to obtain, this study first uses CAE software to analyze a circular flat plate as the source of training data and combines our random shuffle and database normalization processes for network training and optimization; then, the trained network will be transferred and used on a similar but square plate model. Finally, the use of the CAE data of the square plate model is used to readjust the transferred weight and bias to make the entire network more suitable for the numerical prediction of the square plate, as shown in Figure 7.



**Figure 7.** Transfer learning process between different models.

#### 3.1. Network Training of the Circular Flat Model

This study uses a circular flat panel model to perform the pretraining of the backpropagation neural network (BPNN). The pretraining is divided into two parts: data collection and network parameter tuning. The pretraining is to provide a set of available initial weight and bias for the square flat panel model as a training purpose.

##### 3.1.1. Training Materials

The training data are produced by using the mold flow analysis software, Moldex3D. Each set of training data contains 5 control factors as input values and 5 analysis results as expected values of output. The input values are injection speed, holding pressure, holding time, plastic temperature, and mold temperature; the output values are gate EOF (end of Filling) pressure, maximum cooling time, the value of warpage along the Z-axis, product shrinkage along the X-axis, and product shrinkage along the Y-axis. The measurement points are shown in Figure 8.

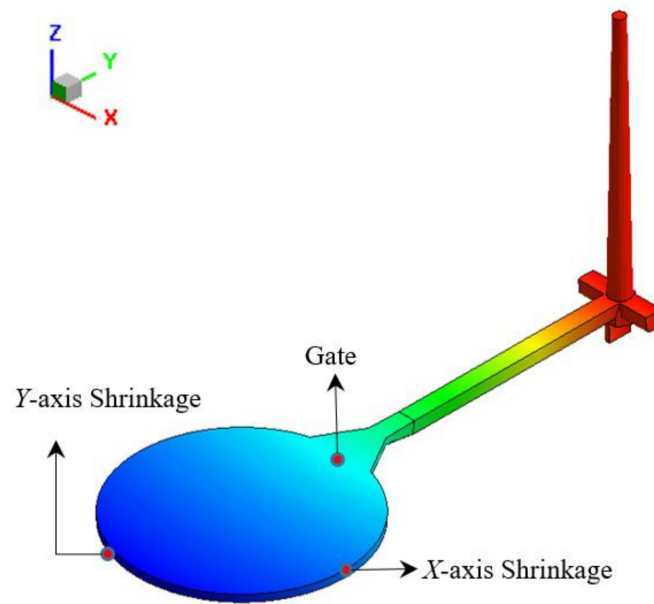


Figure 8. CAE data measurement location of the circular flat model.

In terms of the process parameters, this study takes the default setting provided by Moldex3D as a reference and then set values according to the number of levels. Among the 5 control factors, the injection speed, melt temperature, mold temperature, holding time, and holding pressure are set at 3 levels, and then using a full factorial trial, a total of 243 sets of training data will be produced. The detailed training data parameters are shown on Table 1. After the artificial neural network training is completed, it needs to be tested with data that has not been learned at all. In this study, 16 sets of parameters corresponding to the L16 orthogonal table of the Taguchi method are used as verification data. The detailed parameters are shown on Table 2.

Table 1. Training data factors and level settings (CAE-243).

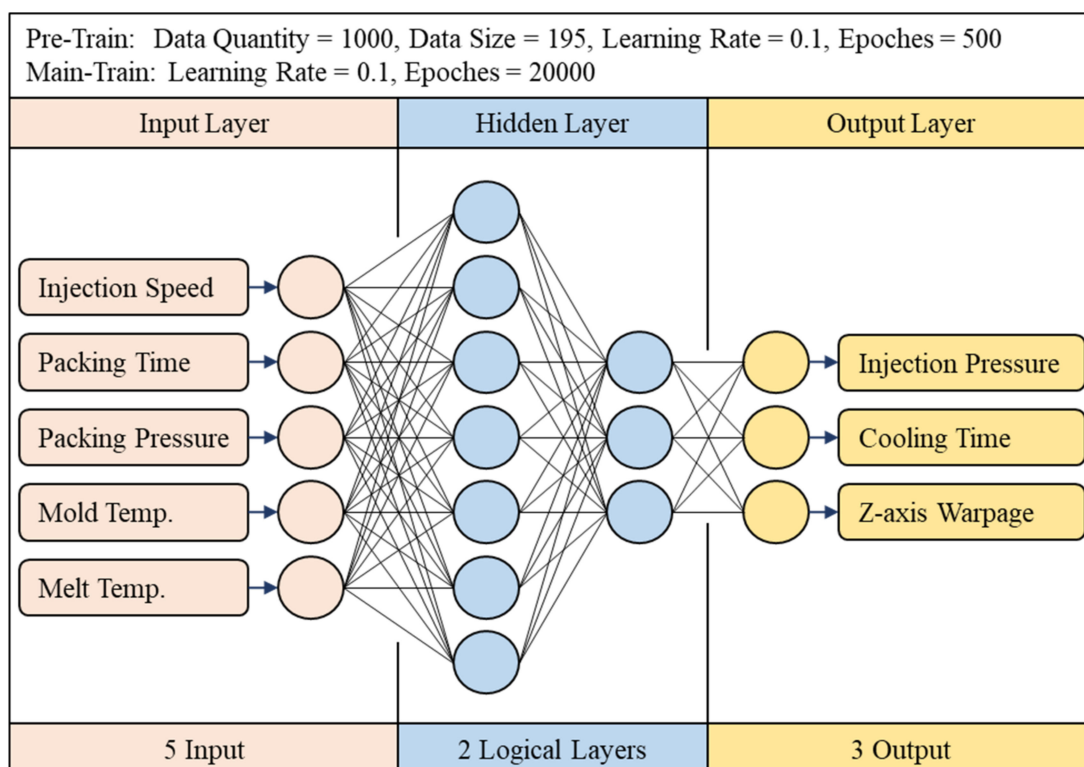
Factor	Default	Level	Level	Level
Melt Temperature (°C)	210	185	207.5	230
Packing Time (sec)	4.5	3	6	9
Packing Pressure (MPa)	135	100	130	160
Injection Speed (mm/sec)	70	50	65	80
Mold Temperature (°C)	50	40	55	70
Total Processed Data			243	

### 3.1.2. Hyperparameter Settings

In terms of artificial neural networks, this study uses the optimized network parameters proposed by Jong et al. [14]. The parameters that need to be set are the number of training times, the number of repetitions, the activation function, the learning rate, the optimization method, the initial link value, the number of hidden layers, and the number of neurons; this network architecture is shown in Figure 9. As for other settings, the number of training runs is reduced to 20,000 due to the introduction of random shuffle for pretraining, and the learning rate is 0.1. Both hidden layers use sigmoid as the activation function and use the stochastic gradient descent (SGD) for optimization, and the network hyperparameter settings are shown on Table 3.

**Table 2.** Validation data settings (CAE-243).

No.	Melt Temp. (°C)	Packing Time (sec)	Packing Pressure (MPa)	Injection Speed (mm/sec)	Mold Temp. (°C)
1	195	4	110	55	45
2	195	5	120	60	50
3	195	7	140	70	60
4	195	8	150	75	65
5	205	4	120	70	65
6	205	5	110	75	60
7	205	7	150	55	50
8	205	8	140	60	45
9	210	4	140	75	50
10	210	5	150	70	45
11	210	7	110	60	65
12	210	8	120	55	60
13	220	4	150	60	60
14	220	5	140	55	65
15	220	7	120	75	45
16	220	8	110	70	50



**Figure 9.** Optimal network architecture (CAE-243).

**Table 3.** Network hyperparameter settings (CAE-243).

Parameters	Value	Parameters	Value
Epoch	20,000	Learning Rate	0.1
Hidden Layer 1	7	Initial Weight	Random
Hidden Layer 2	3	Initial Bias	Random
Optimized Method	SGD	Activation Function	Sigmoid

As for the data input, this research uses random shuffle to randomly divide 243 process parameters into 1000 sets of training data. Each set of data contains 195 (80%) process

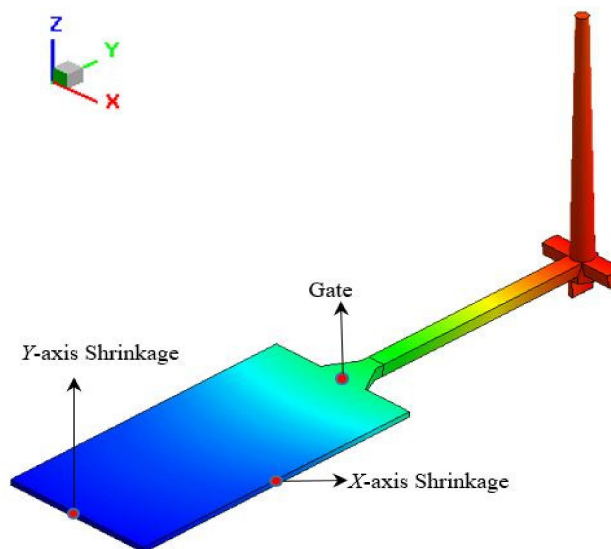
parameters. The network alternates a set for training every 500 trials during training to avoid overfitting occurring.

### 3.2. Transfer Learning of the Square Plate Model

In terms of transfer learning, the square plate and the round plate model are the same, as are the network architecture of the two, as well as the optimized weight and bias values for both, and then the training data of the square plate are used to fine-tune the network to achieve the goal of transfer learning.

#### 3.2.1. Training Materials

The training data are the same as those of the round flat model. The five analysis results are used as the expected values of output. The input values are injection speed, holding pressure, holding time, plastic temperature, and mold temperature; the output values are EOF pressure, maximum cooling time, the value of warpage along the Z-axis, the amount of product shrinkage along the X-axis, and the offset of the product along the Y-axis. The measurement point positions are shown in Figure 10.



**Figure 10.** Model measurement position for the square plate.

The purpose of transfer learning is to reduce the required training data and save calculation time. Therefore, in the training data setting for the square tablet, the L27 orthographic table of the Taguchi method is used to produce 27 sets of training data as input, as shown on Table 4. The L16 orthogonal array produces 16 sets of verification parameters to verify the network, as shown on Table 5.

#### 3.2.2. Hyperparameter Tuning

The hyperparameters used in the transfer learning of the square plate are the same as those used for the round plate. The architecture uses two hidden layers. The first layer contains seven neurons, and the second layer contains three neurons. For other settings, the learning rate is 0.1. Both hidden layers use sigmoid as the activation function. A transfer function is used to input weight and bias. The network hyperparameter settings are shown on Table 6.



Table 4. Square tablet training data (CAE-27).

No.	Melt Temp(°C)	Packing Time (sec)	Packing Pressure (MPa)	Injection Speed (mm/sec)	Mold Temp. (°C)
1	185	3	100	50	40
2	185	3	100	50	55
3	185	3	100	50	70
4	185	6	130	65	40
5	185	6	130	65	55
6	185	6	130	65	70
7	185	9	160	80	40
8	185	9	160	80	55
9	185	9	160	80	70
10	207.5	3	130	80	40
11	207.5	3	130	80	55
12	207.5	3	130	80	70
13	207.5	6	160	50	40
14	207.5	6	160	50	55
15	207.5	6	160	50	70
16	207.5	9	100	65	40
17	207.5	9	100	65	55
18	207.5	9	100	65	70
19	230	3	160	65	40
20	230	3	160	65	55
21	230	3	160	65	70
22	230	6	100	80	40
23	230	6	100	80	55
24	230	6	100	80	70
25	230	9	130	50	40
26	230	9	130	50	55
27	230	9	130	50	70

Table 5. CAE verification data for square tablet (CAE-27).

No.	Melt Temp. (°C)	Packing Time (sec)	Packing Pressure (MPa)	Injection Speed (mm/sec)	Mold Temp. (°C)
1	195	4	110	55	45
2	195	5	120	60	50
3	195	7	140	70	60
4	195	8	150	75	65
5	205	4	120	70	65
6	205	5	110	75	60
7	205	7	150	55	50
8	205	8	140	60	45
9	210	4	140	75	50
10	210	5	150	70	45
11	210	7	110	60	65
12	210	8	120	55	60
13	220	4	150	60	60
14	220	5	140	55	65
15	220	7	120	75	45
16	220	8	110	70	50

### 3.2.3. Hyperparameter Tuning

The hyperparameters used in the transfer learning of the square plate are the same as those used for the round plate. The architecture uses two hidden layers. The first layer contains seven neurons, and the second layer contains three neurons. For other settings, the learning rate is 0.1. Both hidden layers use sigmoid as the activation function. A transfer

function is used to input weight and bias. The network hyperparameter settings are shown on Table 6.

**Table 6.** Hyperparameters settings for the square plate (CAE-27).

Parameters	Value	Parameters	Value
Epoch	20,000	Learning Rate	0.1
Hidden Layer 1	7	Initial Weight	Transfer
Hidden Layer 2	3	Initial Bias	Transfer
Optimized Method	SGD	Activation Function	Sigmoid

As for the data input, this research uses random shuffle to randomly divide 27 sets of process parameters into 1000 sets of training data. Each set of data contains 22 (80%) process parameters. The network alternates a set of training for every 500 trials during training to avoid the occurrence of overfitting.

### 3.3. Comparison of Transfer Learning Results among Different Products

This study compares the training process of transfer learning with full data and random shuffle processing and discusses the results of transfer learning based on the two results of the *S* mean error and standard deviation.

#### 3.3.1. Training Results of the Round Plate Model

In this study, the prediction results of 243 groups of circular flat models analyzed via Moldex3D were used as the input value for the backpropagation neural network, and the data processing method of random shuffle was utilized to improve accuracy of prediction. With the same training data, network architecture, and hyperparameter settings, after using the data processing method of random shuffle, the average error of EOF pressure, cooling time, warpage value along the Z-axis, shrinkage along the X-axis, and shrinkage along the Y-axis all delivered different degrees of improvement, of which Z-axis warpage shows the most significant mitigation. In addition to reducing the average error, random shuffle also has different degrees of optimization vis-à-vis the standard deviation. The standard deviation regarding warpage has been reduced most obviously. Our detailed comparison results are shown on Table 7.

**Table 7.** CAE data training results for the round flat plate model (CAE-243).

Circle Plate Result (CAE-243)						
		EOF Pressure	Cooling Time	Z-Axis Warpage	X-Axis Shrinkage	Y-Axis Shrinkage
Full Data	AVG (%)	12.67	8.78	29.84	14.80	13.36
	STD	5.29	4.48	45.46	18.33	11.71
Random Shuffle	AVG (%)	11.22	8.61	19.89	12.83	10.72
	STD	5.22	4.42	26.45	13.91	7.54
Difference	AVG (%)	1.45	0.16	9.94	2.06	2.63
	STD	0.07	0.05	19.01	4.42	4.17

#### 3.3.2. Training Results for the Square Flat Model

In the case of trials on the square plate, this study only uses 27 sets of training data as the input value for the backpropagation neural network, and the process parameters are the same as those for the round plate. Our detailed training results are shown on Table 8. If 27 sets of data are used for training directly, among the five output values, only EOF pressure and cooling time are having less than 10% of predicted error. As for warpage along the Z-axis, shrinkage along the X-axis, and shrinkage along the Y-axis, their error is high, of which the 59% for the warpage along the Z-axis is the highest. After using random shuffle to reprocess the data, the error rate and standard deviation of the five output results

are all reduced, but the errors of warpage and shrinkage along the X and Y axes are still significant.

**Table 8.** Training results for the square flat model (CAE-27).

Square Plate Result (CAE-27)						
		EOF Pressure	Cooling Time	Z-Axis Warpage	X-Axis Shrinkage	Y-Axis Shrinkage
Full Data	AVG (%)	4.85	10.98	59.61	17.14	20.64
	STD	2.18	7.43	66.65	22.05	18.43
Random Shuffle	AVG (%)	3.91	10.16	56.25	15.39	18.54
	STD	1.90	6.40	60.58	18.66	17.63
Difference	AVG (%)	0.94	0.82	3.36	1.75	2.10
	STD	0.28	1.03	6.07	3.39	0.81

### 3.3.3. Transfer Learning Results for the Square Tablet Model

The round flat and square flat are both flat types of models. Therefore, this study uses the trained round flat network architecture as the network architecture for square flat training and integrates the optimized weight and bias into the network as the starting values for square tablet training. Our training results are shown on Table 9. Without preprocessing the data, using the optimized weight and bias from training for the round flat plate, the error value and standard deviation of the EOF pressure, cooling time, shrinkage along the X-axis, and shrinkage along the Y-axis are all reduced, except for the average of percentage errors for warpage along the Z-axis, which has increased from 59.61% to 79.96%; if the data are preprocessed with random shuffle, the error value and standard deviation of the five output items will decrease, among which the warpage has been mitigated most obviously, and the error value has been reduced from 79.96% dropped to 31.05%, and the standard deviation dropped from 70.34% to 17.56%.

**Table 9.** Transfer learning results for the square flat model (CAE-27).

Square Plate with Transfer Learning Result (CAE-27)						
		EOF Pressure	Cooling Time	Z-Axis Warpage	X-Axis Shrinkage	Y-Axis Shrinkage
Full Data	AVG (%)	3.44	8.69	79.96	15.02	18.15
	STD	1.83	5.36	70.34	10.85	12.18
Random Shuffle	AVG (%)	2.77	8.48	31.05	11.81	16.46
	STD	1.80	4.94	17.56	8.97	11.19
Difference	AVG (%)	0.67	0.22	48.91	3.22	1.69
	STD	0.03	0.42	52.78	1.89	0.99

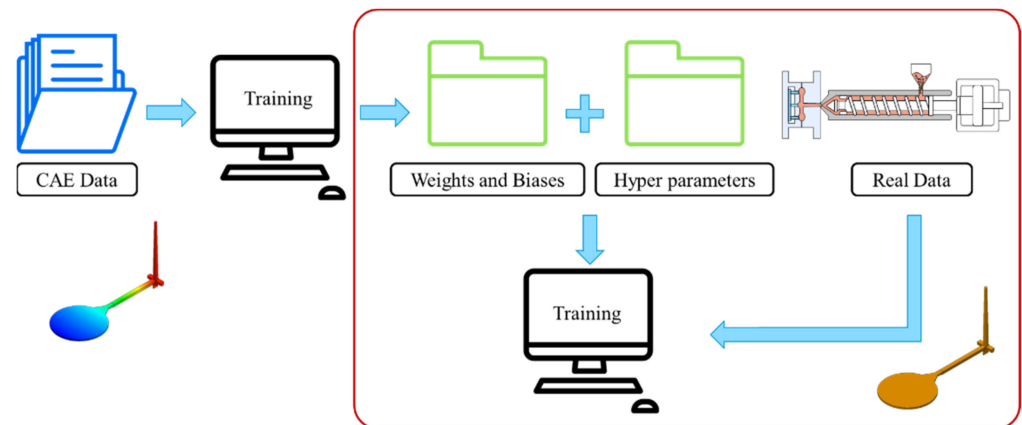
## 4. Prediction of Molding Using the Network Trained via CAE Data and Transferred for Actual Injection

In this section, the use of a larger amount of circular flat model CAE data to train a more accurate neural network is described and discussed. This network trained with CAE data is then transferred to the actual injection molding prediction, and the circular flat data obtained from actual trials are used for retraining to verify that there is feasibility of conversion between virtual and actual reality models for the injection molding process.

### 4.1. Transfer Learning between Virtual and Actual Reality

In the transfer learning process between virtual and actual reality, because the same model is used, the two sets or types of data must be as similar as possible. If the actual data and the CAE data are too divergent, prediction accuracy is seriously impacted after the final transfer. Therefore, the data collection during the running of trials is important. In

this study, with the gates, the in-mold pressure sensor was used to collect measurements of the pressure change curve. After the product was left for one day, the round plate of the amount of change in the X- and Y-axis was measured using a coordinate measuring machine; however, warpage and cooling time data are difficult to obtain, so these two results are not considered during the transfer process. The entire process is shown in Figure 11.



**Figure 11.** Flow chart of transfer learning from virtual to actual reality trials.

#### 4.2. Round Flat CAE Data Pretraining

The prediction accuracy before transfer of learning greatly affects the results after transfer. Therefore, herein, the use of more CAE data and the reoptimization by tuning the hyperparameters using the Taguchi method and the performance of pretraining before TL are detailed and discussed. All prediction errors of the training model are maintained at less than 5% of the total.

##### 4.2.1. Training Data

The training data in this section are produced by the mold flow analysis software, Moldex3D. The number of data sets has been increased from 243 sets to 1024 sets. Each set of training data contains 5 control factors as input values and 5 analysis results as expected output values. The input values are injection speed, holding pressure, holding time, plastic temperature, and mold temperature, respectively; and the output values are gate EOF pressure, maximum cooling time, warpage along Z-axis, shrinkage along the X-axis, and shrinkage along the Y-axis. The position of the measuring point is shown in Figure 12.

In terms of process parameters, for this study, the preset value provided by Moldex3D is taken as the reference, and then the value is adjusted according to the number of levels. Among the five control factors, the injection speed, melt temperature, mold temperature, holding pressure time, and holding pressure are all set at level 4, and then using the full factor method, a total of 1024 sets of training data are produced. Our detailed training data parameters are shown on Table 10. After the artificial neural network training is completed, it needs to be tested with data that have not yet been learned. In this study, 16 sets of parameters corresponding to the L16 orthogonal table of the Taguchi method are used as verification data. Our detailed parameters are shown on Table 11.

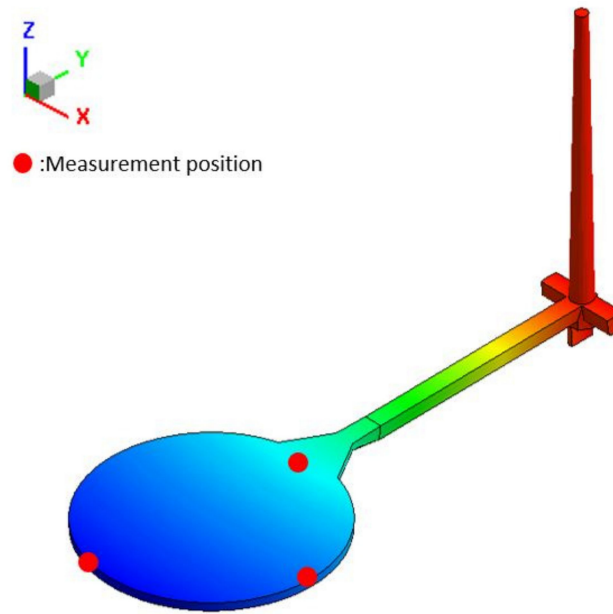


Figure 12. Measurement position of the round plate model.

Table 10. Training data for the round plate (CAE-1024).

Factor	Default	Level			
Melt Temperature (°C)	210	185	200	215	230
Packing Time (sec)	4.5	3	5	7	9
Packing Pressure (MPa)	135	100	120	140	160
Injection Speed (mm/sec)	70	50	60	70	80
Mold Temperature (°C)	50	40	50	60	70
Total Process Data	1024				

Table 11. Validation data for the round plate (CAE-1024).

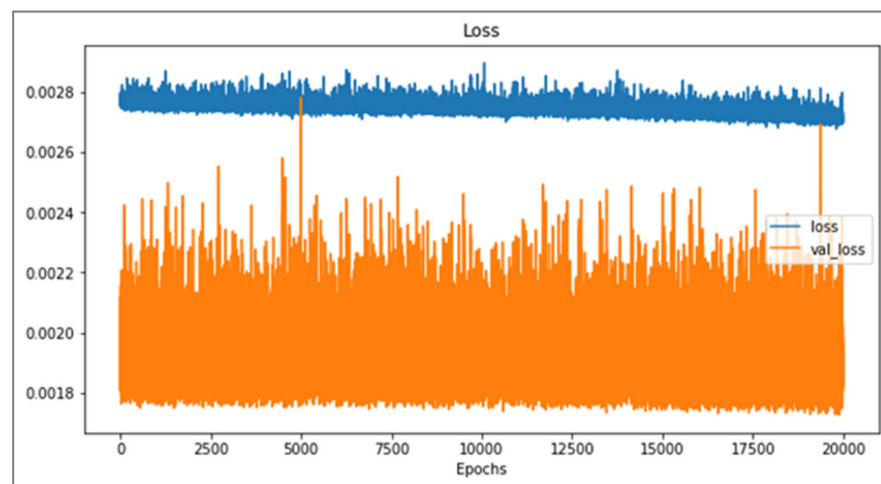
No.	Melt Temp. (°C)	Packing Time (sec)	Packing Pressure (MPa)	Injection Speed (mm/sec)	Mold Temp. (°C)
1	194	4.2	112	56	46
2	194	5.4	124	62	52
3	194	6.6	136	68	58
4	194	7.8	148	74	64
5	203	4.2	124	68	64
6	203	5.4	112	74	58
7	203	6.6	148	56	52
8	203	7.8	136	62	46
9	212	4.2	136	74	52
10	212	5.4	148	68	46
11	212	6.6	112	62	64
12	212	7.8	124	56	58
13	221	4.2	148	64	58
14	221	5.4	136	56	64
15	221	6.6	124	74	46
16	221	7.8	112	68	52

#### 4.2.2. Hyperparameter Tuning

In order to achieve better prediction accuracy, 1024 sets of data are used in this section and 1024 process parameters are randomly divided into 200 sets of training data with

random shuffle. Each set of data contains 819 (80%) processes. A set of training materials is changed every 50 runs during training to avoid overfitting.

This study uses the optimized network architecture proposed by Jong et al. [14] to train 1024 sets of CAE data and found that if the warpage along the Z-axis cannot be less than 5%, loss value cannot continue to decrease, even with the number of training runs increased; for this, the change of loss value can be observed from either the training data or verification data. If overfitting is the cause of the inability to reduce accuracy, the loss values of the two (i.e., the loss value of the training and verification set) will cross over. However, in fact, the loss values of the two, though they fluctuate significantly, remain parallel, and there is no crossover phenomenon, as shown in Figure 13. The rapid rises and falls, seen illustrated in Figure 13, represent that weight and bias are continuously being updated, but the loss value cannot be further reduced. Therefore, it can be inferred that in the optimized network architecture proposed by Jong et al. [14], the number of neurons cannot fully learn the knowledge presented by the 1024 sets of data. Therefore, in this section, discussion of use of the Taguchi method to recorrect the optimized network design and hyperparameters is present, and factor levels are shown in Table 12, while the orthogonal array is shown in Table 13.



**Figure 13.** Comparison diagram for loss value in the training set and the verification set.

**Table 12.** Artificial neural network factors and level settings.

Factor	Parameters	Level 1	Level 2	Level 3
A	Training Cycle	10,000	20,000	30,000
B	Learning Rate	0.05	0.1	0.3
C	Hidden Layer 1	7	9	11
D	Hidden Layer 2	7	9	11

#### 4.2.3. Hyperparameter Optimization

In this section, with the use of random shuffle, 200 sets of new data are made with 80% of the full data (819 sets of data) are detailed and discussed. Because each set of data is relatively large, in order to avoid overlearning the content of a single set of data, the epoch is set to 50, and the learning rate is 0.1 for pretraining, hyperparameter optimization, using Z-axis warpage as the indicator of optimization as discussed prior in Section 3, and the error percentage between the predicted value and the expected value is used as the optimization target (i.e., STB). Trials results from the Taguchi orthogonal array are shown on Table 14. The most effective result is No. 5, the warpage along Z-axis is 5.22%, and our ANOVA analysis is shown on Table 15. The optimization factors are A2, B1, C3, D1, and the corresponding hyperparameters are as follows: training times 20,000, learning rate 0.05, 11 neurons in the first layer, and 7 neurons in the second layer, and the difference between

the optimized parameters and No. 5 is only the factor B, which are the learning rates of 0.05 and 0.1, respectively.

**Table 13.** L9 orthogonal table (CAE-1024).

No	A	B	C	D	Training Cycle	Learning Rate	Hidden Layer 1	Hidden Layer 2
1	1	1	1	1	10,000	0.05	7	7
2	1	2	2	2	10,000	0.1	9	9
3	1	3	3	3	10,000	0.3	11	11
4	2	1	2	3	20,000	0.05	9	11
5	2	2	3	1	20,000	0.1	11	7
6	2	3	1	2	20,000	0.3	7	9
7	3	1	3	2	30,000	0.05	11	9
8	3	2	1	3	30,000	0.1	7	11
9	3	3	2	1	30,000	0.3	9	7

**Table 14.** Experimental results from the Taguchi orthogonal array.

No	A	B	C	D	EOF Pressure	Cooling Time	Z–Axis Warp	X–Axis Radius	Y–Axis Radius	S/N Ratio
1	1	1	1	1	5.04	3.21	7.10	2.22	1.99	−17.03
2	1	2	2	2	4.90	3.20	7.31	2.28	2.18	−17.28
3	1	3	3	3	4.97	3.55	8.10	2.28	2.22	−18.17
4	2	1	2	3	4.98	1.36	5.50	2.17	2.56	−14.81
5	2	2	3	1	5.10	1.72	5.22	2.04	2.20	−14.35
6	2	3	1	2	4.78	3.42	6.78	2.11	2.38	−16.62
7	3	1	3	2	5.04	1.32	5.85	1.98	1.96	−15.34
8	3	2	1	3	5.18	2.06	6.39	1.73	2.40	−16.11
9	3	3	2	1	4.94	1.13	6.26	2.08	2.09	−15.93

**Table 15.** ANOVA analysis (CAE-1024).

	A	B	C	D
LEVEL 1	−17.49	−15.73	−16.59	−15.77
LEVEL 2	−15.26	−15.91	−16.41	−16.41
LEVEL 3	−15.79	−16.91	−15.95	−16.36

It can be found from Figure 14 that the C and D factors representing the neural network structure in the ANOVA analysis, in the indications, are the same as the results given prior in Section 3, which is the first layer is the bigger, the better, and the second layer is the smaller, the better, and the first layer is larger than the second layer; as for the learning rate, it shows a trend that the smaller the value, the better, so this research uses this trend to adjust the optimized hyperparameters to 20,000 training times, learning rate 0.01, 13 neurons in the first layer, and 5 neurons in the second layer. Finally, this parameter with No. 5 and the optimized parameters are compared. The results are shown on Table 16. The optimized parameters have the smallest error value. The combination adjusted with optimized parameters is also better than No. 5. The network architecture is shown in Figure 15, and the hyperparameters are shown on Table 17.

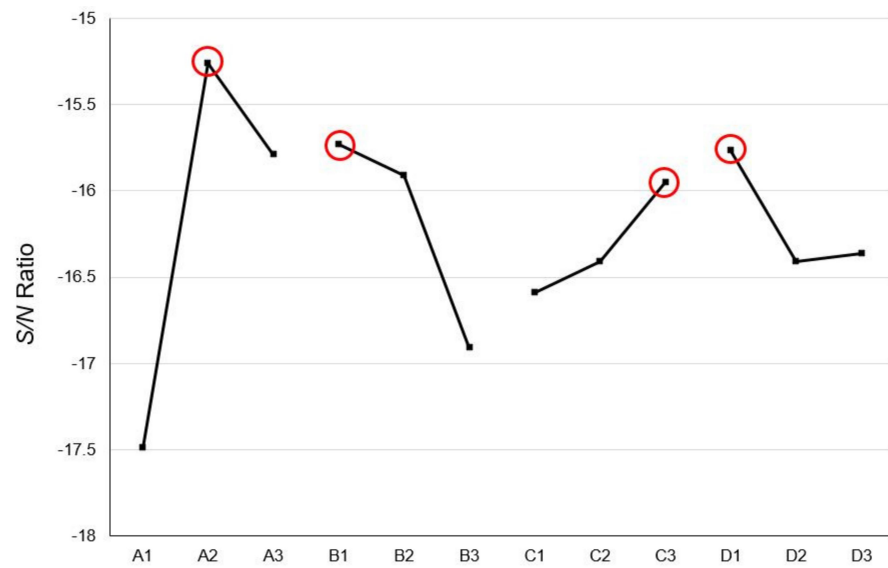


Figure 14. Response graph of S/N ratio (CAE-1024).

Table 16. Verification of optimized hyperparameters (CAE-1024).

	Training Cycle	Learning Ratio	Layer 1	Layer 2	Z-axis
No.5	20,000	0.1	11	7	5.22%
Op1.	20,000	0.05	11	7	3.61%
Op2.	20,000	0.03	13	5	4.88%

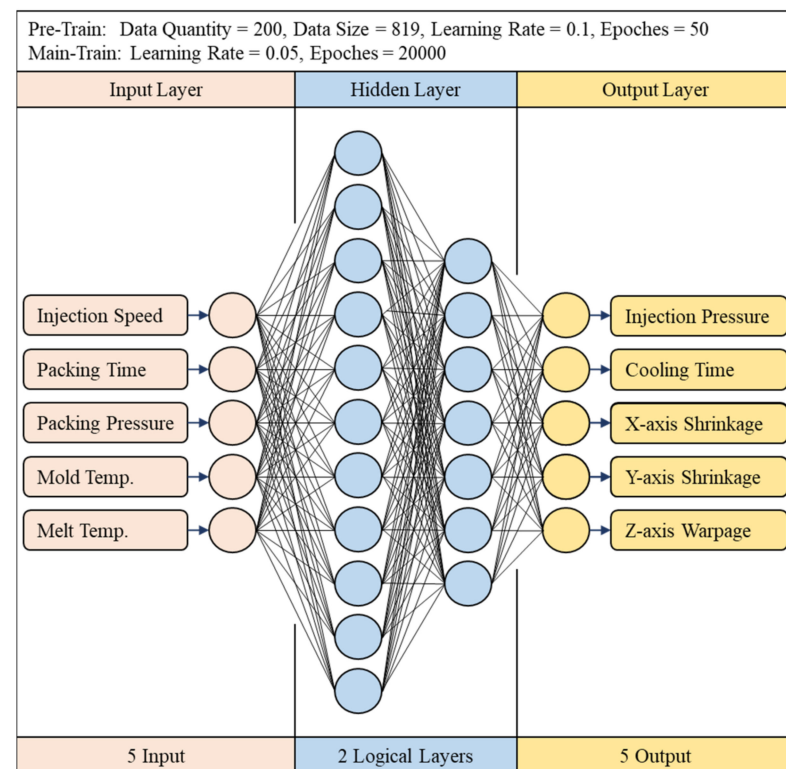


Figure 15. Optimal network architecture (CAE-1024).



**Table 17.** Optimized network hyperparameters (CAE-1024).

Parameters	Value	Parameters	Value
Epoch	20,000	Learning Rate	0.05
Hidden Layer 1	11	Initial Weight	Random
Hidden Layer 2	7	Initial Bias	Random
Optimized Method	SGD	Activation Function	Sigmoid

#### 4.3. Transfer Learning for Injection Molding

In the transfer learning between virtual and actual reality, the data collection of the actual reality trials is important. The final results will be more accurate if the CAE data are more similar. For this study, the training data and verification data are obtained by actual injection molding, and then the training data are imported to the pretrained model.

##### 4.3.1. Training Data

In terms of the training data for the injection molding process, the input values are injection speed, holding pressure, holding time, plastic temperature, and mold temperature, and the five analysis results are categorized as the expected output values, respectively. As for the output values, because it is difficult to measure the amount of warpage along the Z-axis and the maximum cooling time, so for this study, the output values of EOF pressure, shrinkage along the X-axis, and shrinkage along the Y-axis only are captured. The other two are replaced by 0 during training, so that the network can run smoothly.

The training data and verification data discussed herein are all based on the L16 OA table, each generating 16 sets of data and a total of 32 unique data sets. Due to the gap between the actual machine settings and the simulation software, the holding pressure is set at the upper limit of 140 MPa as the basis to modify the molding parameters. The relevant process parameters are shown on Tables 18 and 19.

**Table 18.** Training data for the round plate model (EXP-16).

No.	Melt Temp. (°C)	Packing Time (sec)	Packing Pressure (MPa)	Injection Speed (mm/sec)	Mold Temp. (°C)
1	185	3	100	50	40
2	185	5	113	60	50
3	185	7	126	70	60
4	185	9	139	80	70
5	200	3	113	70	70
6	200	5	100	80	60
7	200	7	139	50	50
8	200	9	126	60	40
9	215	3	126	80	50
10	215	5	139	70	40
11	215	7	100	60	70
12	215	9	113	50	60
13	230	3	139	60	60
14	230	5	126	50	70
15	230	7	113	80	40
16	230	9	100	70	50

##### 4.3.2. Hyperparameter Settings

The hyperparameters used in transfer learning are the same as those used in CAE data pretraining. In terms of the architecture, two hidden layers are used. The first layer contains 11 neurons, and the second layer contains 7 neurons. For other settings, the learning rate is 0.05. Both hidden layers use sigmoid as the activation function. Weight and bias use the transfer method. The network hyperparameter settings are shown in Table 20.

**Table 19.** Validation data for the round plate model (EXP-16).

No.	Melt Temp. (°C)	Packing Time (sec)	Packing Pressure (MPa)	Injection Speed (mm/sec)	Mold Temp. (°C)
1	194	4.2	109	56	46
2	194	5.4	118	62	52
3	194	6.6	127	68	58
4	194	7.8	136	74	64
5	203	4.2	118	68	64
6	203	5.4	109	74	58
7	203	6.6	136	56	52
8	203	7.8	127	62	46
9	212	4.2	127	74	52
10	212	5.4	136	68	46
11	212	6.6	109	62	64
12	212	7.8	118	56	58
13	221	4.2	136	62	58
14	221	5.4	127	56	64
15	221	6.6	118	74	46
16	221	7.8	109	68	52

**Table 20.** Network hyperparameter settings (EXP-16).

Parameters	Value	Parameters	Value
Epoch	20,000	Learning Rate	0.05
Hidden Layer 1	11	Initial Weight	Transfer
Hidden Layer 2	7	Initial Bias	Transfer
Optimized Method	SGD	Activation Function	Sigmoid

As for data input, this research uses random shuffle to randomly divide 16 process parameters into 1000 sets of training data. Each set of data contains 13 (80%) process parameters. The network changes one set of training data after every 500 runs during training to avoid overfitting from happening.

#### 4.4. Comparison of Simulation and Actual Transfer Learning Results, CAE Data Training Results for the Circular Flat Model

In this study, the prediction results for the 1024 sets of the circular flat model analyzed by Moldex3D were preprocessed with random shuffle data processing as the input value of the backpropagation neural network and combined with the hyperparameters generated using the Taguchi method to optimize the model. After these methods are used, the EOF pressure, cooling time, gate warpage value, shrinkage along the X-axis, and shrinkage along the Y-axis, the average error is less than 5%, and Z-axis warpage is mitigated most obviously, which is a more complicated factor. In addition to reducing the average error, random shuffle also has different degrees of optimization vis-à-vis the standard deviation. In terms of the improvement in the standard deviation, gate warpage is the most obvious. Our detailed comparison results are shown in Table 21.

##### 4.4.1. Training Results of Experimental Data of the Circular Flat Model

In the actual trials, this study only uses 16 sets of data for training and 16 sets of data for verification. The hyperparameters are the same as the CAE data for training. The detailed training results are shown in Table 22. If 16 sets of data are used for training directly, all 3 output values are not ideal. After using random shuffle to reprocess the data, the error rate of the three output results has slightly decreased, and the standard deviations have shown significant reduction.

**Table 21.** Training results for the round flat model (CAE-1024).

		Circle Plate Result (CAE-1024)				
		EOF Pressure	Cooling Time	Z-Axis Warpage	X-Axis Shrinkage	Y-Axis Shrinkage
Full Data	AVG (%)	4.01	1.84	8.50	3.48	2.73
	STD	2.61	1.35	5.21	2.78	2.23
Random Shuffle	AVG (%)	3.99	1.27	3.61	1.34	1.89
	STD	2.01	0.92	2.87	1.01	1.10
Difference	AVG (%)	0.02	0.57	4.9	2.14	0.84
	STD	0.60	0.43	2.34	1.77	1.13

**Table 22.** Training results for the round flat model (EXP-16).

		Circle Plate Result (EXP-16)				
		EOF Pressure	Cooling Time	Z-Axis Warpage	X-Axis Shrinkage	Y-Axis Shrinkage
Full Data	AVG (%)	15.03	8.31	9.26	15.03	8.31
	STD	8.58	13.34	15.73	8.58	13.34
Random Shuffle	AVG (%)	13.61	7.36	7.45	13.61	7.36
	STD	6.62	9.33	8.63	6.62	9.33
Difference	AVG (%)	1.42	0.95	1.81	1.42	0.95
	STD	4.96	4.01	7.10	4.96	4.01

#### 4.4.2. The Results of the Transfer Learning Trials Data for the Round Plate Model

In terms of data collection, the CAE and actual trials use the same model. In this study, the circular flat network structure trained with CAE data is used as the network structure for the trial data, and the optimized weight and bias are imported as training input. The training results are shown on Table 23.

**Table 23.** Results of transfer learning for the round plate model (EXP-16).

Circle Plate Result (EXP-14)		with Transfer Learning			without Transfer Learning		
		EOF Pressure	X-Axis Shrinkage	Y-Axis Shrinkage	EOF Pressure	X-Axis Shrinkage	Y-Axis Shrinkage
Full Data	AVG (%)	5.88	2.56	3.96	15.03	8.31	9.26
	STD	4.71	2.26	3.97	8.58	13.34	15.73
Random Shuffle	AVG (%)	5.56	2.35	3.91	13.61	7.36	7.45
	STD	4.20	2.19	3.42	6.62	9.33	8.63
Difference	AVG (%)	0.32	0.21	0.05	1.42	0.95	1.81
	STD	0.51	0.07	0.55	4.96	4.01	7.10

Without preprocessing the data, this study uses the optimized weight and bias of the CAE data for training, and the error values and standard deviations of the EOF pressure, shrinkage along the X-axis, and shrinkage along the Y-axis are all reduced. After the data are processed with random shuffle, the error values and standard deviation of all outputs are reduced.

## 5. Results and Discussion

Random shuffle and transfer learning for the training of neural networks have been applied for this study. It has been shown that random shuffle can effectively improve the accuracy of the network and reduce the standard deviation. Through observation of the loss value, the vibration amplitude of the loss value of the verification data decreased

significantly after using random shuffle, while transfer learning can transfer the learned knowledge to new applications. By expanding weight and bias, it can be found that the shape of weight and bias after using transfer learning is similar. Compared with the initial weight and bias group, which never used transfer learning, the difference is obvious.

### 5.1. Discussion on Random Shuffle Method's Effect

The training data has been divided into many data sets after implementing random shuffle. Therefore, the data contained in each set are incomplete and only contain partial learning content. The training process of random shuffle data can be regarded as a kind of pretraining; the fragmented data helps the weight and bias of the network to be unable to escape from the local minimum after initialization. The effect is similar to dropout. Taking the training of the 1024 sets of CAE data as an example, the loss value with and without random shuffle implemented are compared; Figure 16 shows the change in loss over 50 training runs. The loss values of the two are similar, and the loss of the verification data is volatile; Figure 17 shows the change over 100 training runs, and the amplitude of the loss value of the verification data is reduced. Figure 18 shows that change over 200 training runs. The loss value of the training data decreases faster for the sets used within the same training runs, and the loss vibration amplitude of the verification data is reduced to only half of the control group. The loss vibration amplitude of the verification data is small, meaning that the network is more stable for forecasting data.

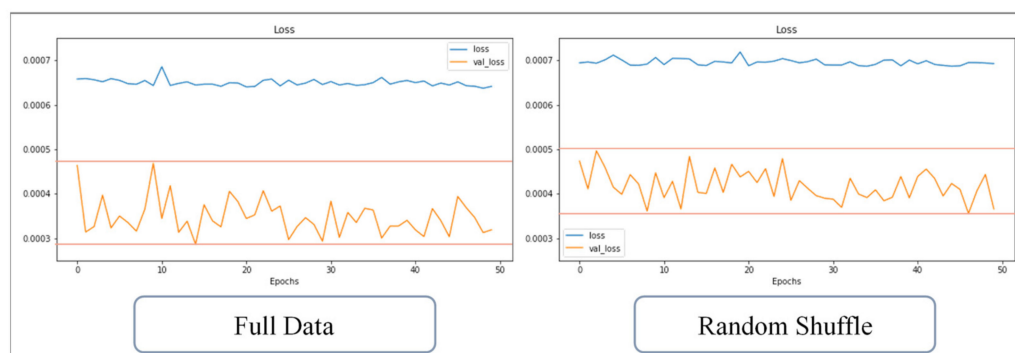


Figure 16. Change of loss value with or without random shuffle (50 runs).

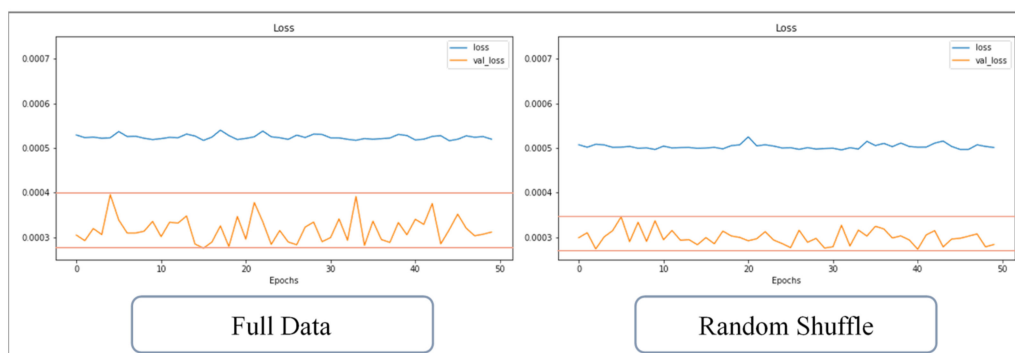


Figure 17. Change of loss value with or without random shuffle (100 runs).

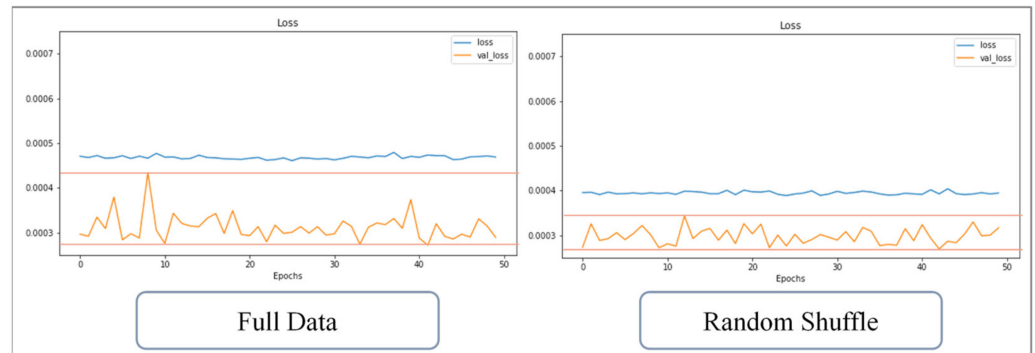


Figure 18. Change of loss value with or without random shuffle (200 runs).

5.2. Discussion on the Effect of Transfer Learning

In this section, the learning results using random shuffle for transfer learning are discussed. From Table 24, it can be seen that the error values trained directly from the square plate CAE data and the round plate trial data are not ideal; even with the data processing method of random shuffle, which can optimize standard deviation, the error value is still not ideal. Without changing any hyperparameters, the trained parameters are imported into the network before training. These results are shown in Table 25. The error values for the square and round plate trials have improved significantly. The original warpage along Z-axis of the square plate was as high as 56.25, because warpage is complicated, and the plastic flow method adopted, holding pressure, holding time, and cooling time will all affect warpage. Even experts cannot judge such trends in warpage, certainly from the 27 sets of training data, not to mention having an accurate prediction, and after importing the 243 sets for round flat data training weight and bias, the network itself already contains warpage-related trends, and then it has been fine-tuned for the square flat training data, resulting in the amount of warpage along Z-axis with a reduction of the error value of the standard deviation to 31.05%.

Table 24. Predicted results for square plate (CAE-27) and round plate (EXP-16).

Result of Square Plate (CAE-27) & Circle Plate (EXP-16)						
		EOF Pressure	Cooling Time	Z-Axis Warpage	X-Axis Shrinkage	Y-Axis Shrinkage
Square Plate	AVG (%)	3.91	10.16	56.25	15.39	18.54
	STD	1.90	6.40	60.58	18.66	17.63
Circle Plate	AVG (%)	13.61			7.36	7.45
	STD	6.62			9.33	8.63

Table 25. Transfer learning results for square plate (CAE-27) and round plate (EXP-16).

Result of Square Plate (CAE-27) & Circle Plate (EXP-16)						
		EOF Pressure	Cooling Time	Z-Axis Warpage	X-Axis Shrinkage	Y-Axis Shrinkage
Square Plate	AVG (%)	3.91	10.16	56.25	15.39	18.54
	STD	1.90	6.40	60.58	18.66	17.63
Square Plate (TL)	AVG (%)	2.77	8.48	31.05	11.81	16.46
	STD	1.80	4.94	17.56	8.97	11.19
Circle Plate	AVG (%)	13.61			7.36	7.45
	STD	6.62			9.33	8.63
Circle Plate(TL)	AVG (%)	5.56			2.35	3.91
	STD	4.20			2.19	3.42

In the actual reality trials for circular plate, after importing the optimized weight and bias from 1024 sets of circular plate data, the error value of the EOF pressure, shrinkage along the X-axis, and shrinkage along the Y-axis is reduced to less than 5%. Figure 19 shows the structure of an optimized weight and bias; Tables 26–28 show optimized weight and bias. Taking this result as an example, the weight and bias matrix between the two layers are expanded into a column and a distribution map is drawn, as shown in Figures 20–25; therein, CAE represents the original distribution before the transfer, TL represents the distribution after transfer, and EXP represents the distribution after direct training. It can be found that the weight and bias distributions of CAE and TL are almost the same, with only a numerical difference. EXP can be different in trend from the other two. Because there are only 16 sets of data for training, the distribution of weight and bias is only between [2, −2], and the other two sets are widely distributed between [6, −6].

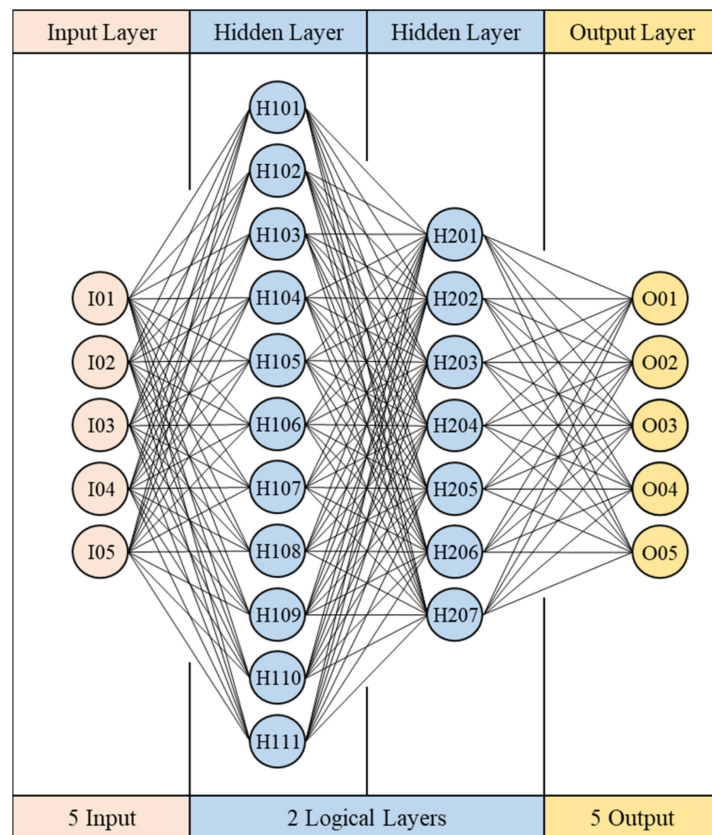


Figure 19. Optimized hyperparameters and network structure for the circular plate (CAE-1024).

Table 26. Weight and bias between the input layer and the first hidden layer (CAE-1024).

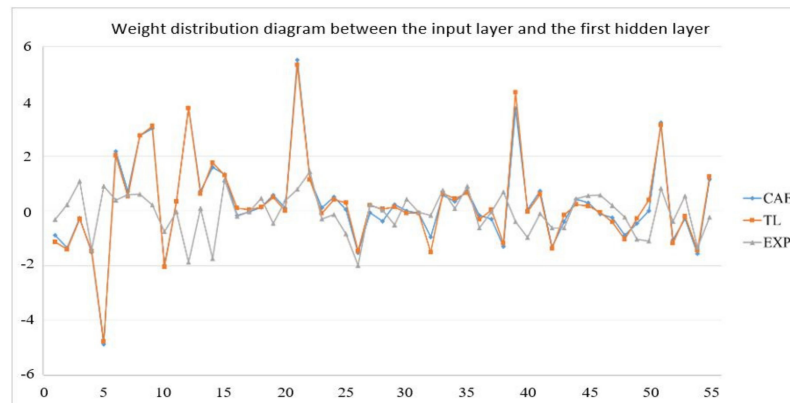
Input to Hidden Layer 1											
Weight	H101	H102	H103	H104	H105	H106	H107	H108	H109	H110	H111
I01	−1.1380	−1.3887	−0.2855	−1.4546	−4.7642	2.0215	0.5312	2.7493	3.0976	−2.0409	0.3560
I02	3.7457	0.6322	1.7630	1.2978	0.0940	0.0474	0.1391	0.4969	−0.0035	5.3307	1.1453
I03	−0.0767	0.4169	0.2950	−1.4659	0.2065	0.0649	0.1480	−0.0729	−0.0716	−1.5080	0.6472
I04	0.4478	0.6541	−0.3143	0.0424	−1.1876	4.3344	−0.0358	0.6161	−1.3805	−0.1439	0.2278
I05	0.1851	−0.0521	−0.4043	−1.0403	−0.2708	0.3893	3.1411	−1.1837	−0.1945	−1.4266	1.2472
Bias	0.4616	−0.4964	−0.3441	−0.1590	−0.4003	0.4831	−4.2604	0.7888	−0.8406	0.5141	−0.5477

**Table 27.** Weight and bias between the first and second hidden layers (CAE-1024).

Input to Hidden Layer 2							
Weight	H201	H202	H203	H204	H205	H206	H207
H101	0.4846	−0.2906	−0.4810	0.0960	4.0143	0.8524	−0.7530
H102	0.7461	0.3182	−0.0355	−0.2350	0.9976	1.7191	−0.8385
H103	−0.2167	−0.7549	0.3227	−1.3992	0.0234	0.5743	−1.3188
H104	−0.2193	1.0535	1.0047	0.3022	−1.0671	−0.8595	1.7802
H105	0.1245	0.1110	3.5158	−0.6555	0.3523	−0.1515	2.2811
H106	0.3782	−0.6278	0.1922	−0.3553	−0.9026	1.3512	1.7357
H107	−0.6336	−2.0454	−1.5661	2.2850	−1.7217	0.4527	−0.1687
H108	−0.6807	0.9787	−2.7245	−0.1729	−1.7629	0.0099	−0.0046
H109	−0.0665	−0.2635	−0.7414	−0.0496	−0.1540	−1.1532	−1.7003
H110	0.7065	0.4036	0.5818	0.4633	3.8549	−0.7217	0.6002
H111	0.2691	0.0886	−1.2342	0.6715	−0.6184	−1.4114	0.8704
Bias	0.0969	−0.4892	−0.1725	−0.2370	−1.9194	−0.2119	0.1383

**Table 28.** Weight and bias between the second hidden layer and the output layer (CAE-1024).

Hidden Layer 2 to Output					
Weight	O01	O02	O03	O04	O05
H201	0.1771	−0.9374	1.2355	1.4501	1.2729
H202	−0.8741	−1.1480	0.7641	0.0267	−0.3646
H203	1.7557	0.3356	−0.0501	1.3303	2.0018
H204	−0.6002	2.2428	1.1498	−0.0814	−0.5862
H205	0.0348	0.0010	−1.1131	−0.1650	0.2440
H206	0.7898	0.1205	−0.8733	0.8862	1.7326
H207	1.1126	0.0468	0.4803	−1.3758	−2.2127
Bias	−0.4228	0.4861	−0.2742	−0.0809	0.2185



**Figure 20.** Weight distribution diagram between the input layer and the first hidden layer.

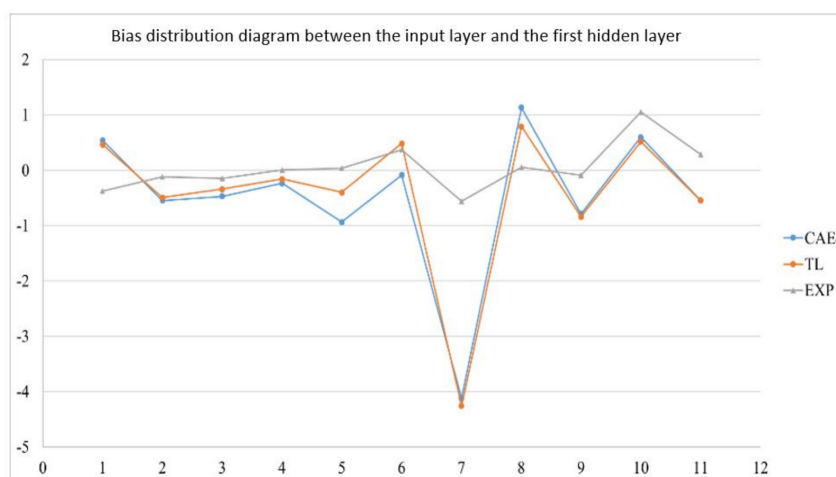


Figure 21. Bias distribution diagram between the input layer and the first hidden layer.

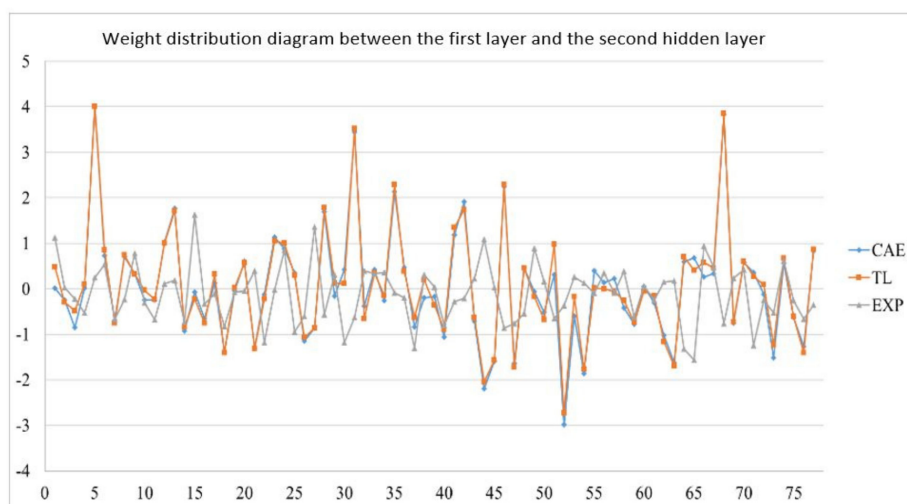


Figure 22. Weight distribution diagram between the first layer and the second hidden layer.

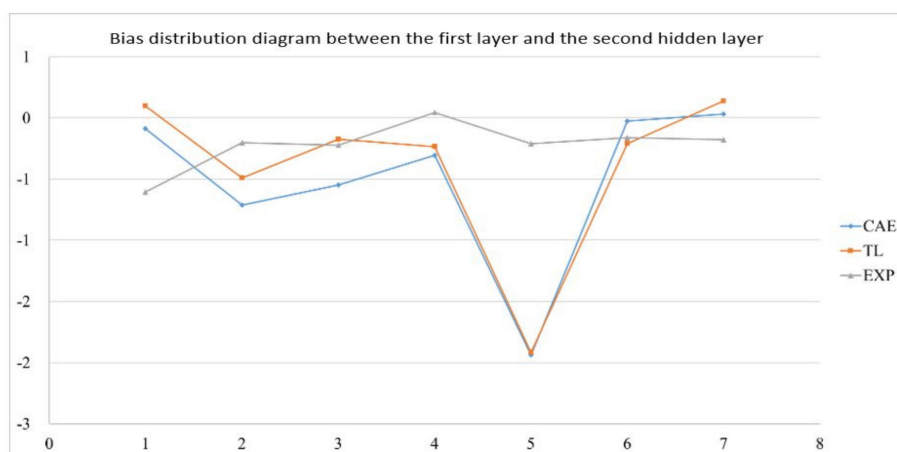


Figure 23. Bias distribution diagram between the first layer and the second hidden layer.



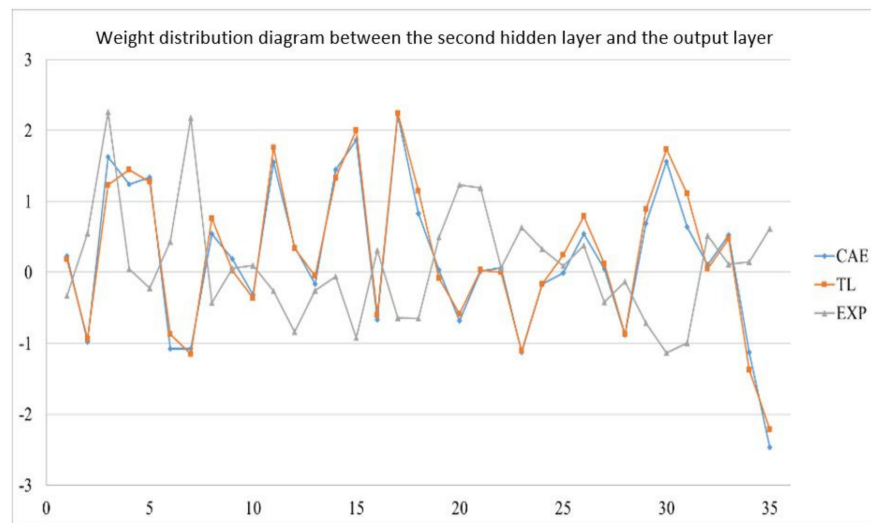


Figure 24. Weight distribution diagram between the second hidden layer and the output layer.

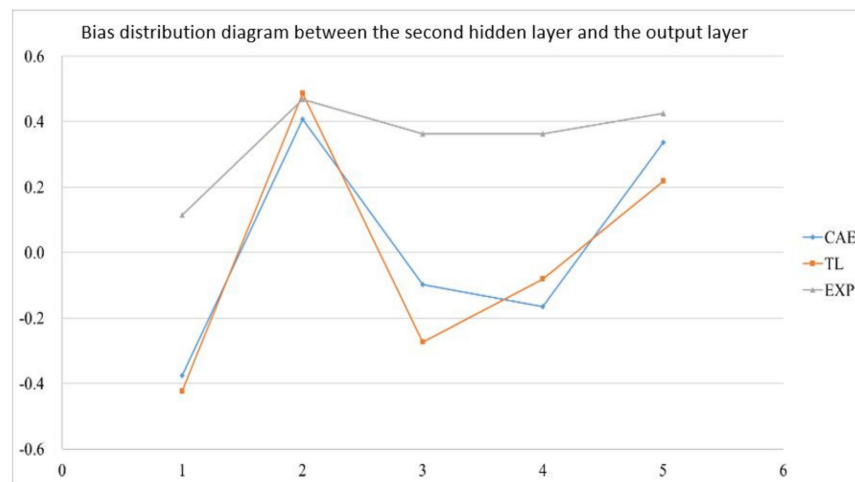


Figure 25. Bias distribution diagram between the second hidden layer and the output layer.

It can be understood from the expanded distribution graph that the distribution trend of weight and bias after the transfer has been fixed, and subsequent retraining will only change the distribution by a small margin without major changes, so there is no need for excessive training data and training runs for a usable network to be obtained quickly. Moreover, even a high number of neurons will not help a set of training data that is too small.

## 6. Conclusions

In this study, an artificial neural network has been utilized to render result predictions for the injection molding process. The CAE analysis data are used as training data and the error value is reduced to less than 5% through the Taguchi method and random shuffle method, which we have introduced herein. The performance of the network transfer to the actual machine can show that transfer learning can solve the problem of difficult data acquisition, just like Jiahuan [18] and Yannik [19]. In addition, predicting the performance of the task from the circle plate can support the argument that the transfer learning proposed by Shin [20] can maintain good performance and that its performance is better than the initial training network. In this conclusion, the applications of the neural network and transfer learning are summarized.

### 6.1. Artificial Neural Network Applications

In this study, artificial neural network training was carried out a total of four times, including via use of 243 sets of circular flat CAE data, 27 sets of square flat CAE data, 1024 sets of circular flat CAE data, and 16 sets of circular flat real data. Regarding optimization of the hyperparameters for the network, these are summarized in the following points:

1. Random shuffle can reduce the error rate and standard deviation. In this study, the data volume was 80% and the learning rate was 0.1 for random shuffle pretraining.
2. The Taguchi method can effectively optimize the hyperparameters of artificial neural networks, and after ANOVA analysis, optimal solutions can be achieved.
3. By monitoring the loss value of the training and verification data simultaneously, it can be judged whether there is overfitting. If the loss curve of the training data continues to decline while diverging ever further from the loss curve of the verification data, it may be that the training time is too long and overfitting is caused. If the two loss curves can no longer be optimized, there are two possibilities: one is that the learning rate is not suitable, which makes it impossible to get rid of the local minimum. The other is that the content of the training data is more complex, and the number of neurons is insufficient. Optimization has bottlenecks.

### 6.2. Transfer Learning Applications

This study carried out transfer learning twice, namely the transfer of CAE round plate to CAE square plate and the transfer of CAE round plate to the actual reality trial for round plate. Although both are transfer learning, the former is not using the same model. The time and space for the latter when it comes to data collection are different. Based on the results of these two transfer learning results, this study indicates the following points, summarized here:

1. Since the cost of injection data acquisition is quite high, the transfer learning can predict with less data under some specific conditions. At the same time, actual experiments can prove that transfer learning has better effects in similar work.
2. From the weight and bias distributions before and after transfer learning, it can be found that retraining will not significantly change the distribution; however, a slight change is possible. Therefore, the original network selected will determine the results of transfer learning.
3. If the set of training data is too small to contain enough effective content, the fluctuation range of weight and bias will be smaller. In this state, adding neurons will not improve the training error value.

**Author Contributions:** Conceptualization, W.-R.J.; Investigation, Y.-M.H.; Methodology, Y.-M.H.; Supervision, W.-R.J. and S.-C.C.; Validation, Y.-M.H.; Writing—original draft, Y.-M.H.; Writing—review & editing, W.-R.J. All authors have read and agreed to the published version of the manuscript.

**Funding:** This research received no external funding.

**Institutional Review Board Statement:** Not applicable.

**Informed Consent Statement:** Not applicable.

**Data Availability Statement:** Not applicable.

**Conflicts of Interest:** The authors declare no conflict of interest.

## References

1. Rosa, J.L.; Robin, A.; Silva, M.B.; Baldan, C.A.; Peres, M.P. Electrodeposition of Copper on Titanium Wires: Taguchi Experimental Design Approach. *J. Mater. Process. Technol.* **2009**, *209*, 1181–1188. [[CrossRef](#)]
2. Marins, N.H.; Mello, F.B.; Silva, R.M.; Ogliari, F. Statistical Approach to Analyze the Warp, Shrinkage and Mechanical Strength of Injection Molded Parts. *Polym. Process.* **2016**, *31*, 376–384. [[CrossRef](#)]

3. Hifsa, P.; Mohammad, S.M.; Abdel-Hamid, I.M. Optimization of Injection Molding Parameters for HDPE/TiO<sub>2</sub> Nanocomposites Fabrication with Multiple Performance Characteristics Using the Taguchi Method and Grey Relational Analysis. *Materials* **2016**, *9*, 710. [[CrossRef](#)]
4. Luo, J.; Liang, Z.; Zhang, C.; Wang, B. Optimum tooling design for resin transfer molding with virtual manufacturing and artificial intelligence. *Compos. Part A Appl. Sci. Manuf.* **2001**, *32*, 877–888. [[CrossRef](#)]
5. Kenig, S.; Ben David, A.; Omer, M.; Sadeh, A. Control of Properties in Injection Molding by Neural Networks. *Eng. Appl. Artif. Intell.* **2001**, *14*, 819–823. [[CrossRef](#)]
6. Denni, K. An Integrated Optimization System for Plastic Injection Molding Using Taguchi Method, BPNN, GA, and Hybrid PSO-GA. Ph.D. Thesis, Department of Technology Management, Chung Hua University, Hsinchu City, Taiwan, 2004.
7. Kwak, T.S.; Suzuki, T.; Bae, W.B.; Uehara, Y.; Ohmori, H. Application of Neural Network and Computer Simulation to Improve Surface Profile of Injection Molding Optic Lens. *J. Mater. Process. Technol.* **2005**, *70*, 24–31. [[CrossRef](#)]
8. Castro, C.E.; Rios, M.C.; Castro, J.M.; Lilly, B. Multiple Criteria Optimization with Variability Considerations in Injection Molding. *Polym. Eng. Sci.* **2007**, *47*, 400–409. [[CrossRef](#)]
9. Shen, C.; Wang, L.; Li, Q. Optimization of Injection Molding Process Parameters Using Combination of Artificial Neural Network and Genetic Algorithm Method. *J. Mater. Process. Technol.* **2007**, *183*, 412–418. [[CrossRef](#)]
10. Mirigul, A. Reducing Shrinkage in Injection Moldings Via the Taguchi, ANOVA and Neural Network Methods. *Mater. Des.* **2010**, *31*, 599–604. [[CrossRef](#)]
11. Yin, F.; Mao, H.; Hua, L.; Guo, W.; Shu, M. Back Propagation Neural Network Modeling for Warpage Prediction and Optimization of Plastic Products During Injection Molding. *Mater. Des.* **2011**, *32*, 1844–1850. [[CrossRef](#)]
12. Alberto, T.; Ramón, A. Machine learning algorithms for quality control in plastic molding industry. In Proceedings of the 2013 IEEE 18th Conference on Emerging Technologies & Factory Automation (ETFA), Cagliari, Italy, 10–13 September 2013. [[CrossRef](#)]
13. Deng, L.; Yu, D. *Deep Learning: Methods and Applications*; Microsoft Research; Microsoft: Redmond, WA, USA, 2014. [[CrossRef](#)]
14. Jong, W.R.; Huang, Y.M.; Lin, Y.Z.; Chen, S.C.; Chen, Y.W. Integrating Taguchi method and artificial neural network to explore machine learning of computer aided engineering. *J. Chin. Inst. Eng.* **2020**, *43*, 346–356. [[CrossRef](#)]
15. Sinno, J.P.; Qiang, Y. A Survey on Transfer Learning. *IEEE Trans. Knowl. Data Eng.* **2009**, *22*, 1345–1359. [[CrossRef](#)]
16. Dan, C.C.; Ueli, M.; Jürgen, S. Transfer learning for Latin and Chinese characters with Deep Neural Networks. In Proceedings of the 2012 International Joint Conference on Neural Networks (IJCNN), Brisbane, Australia, 10–15 June 2012. [[CrossRef](#)]
17. Huang, J.T.; Li, J.; Yu, D.; Deng, L.; Gong, Y. Cross-Language Knowledge Transfer Using Multilingual Deep Neural Network with Shared Hidden Layers. In Proceedings of the 2013 IEEE International Conference on Acoustics, Speech and Signal Processing, Vancouver, BC, Canada, 26–31 May 2013. [[CrossRef](#)]
18. Jiahuan, L.; Fei, G.; Huang, G.; Maoyuan, L.; Yun, Z.; Huamin, Z. Defect detection of injection molding products on small datasets using transfer learning. *J. Manuf. Process.* **2021**, *70*, 400–413. [[CrossRef](#)]
19. Yannik, L.; Christian, H. Induced network-based transfer learning in injection molding for process modelling and optimization with artificial neural networks. *Int. J. Adv. Manuf. Technol.* **2021**, *112*, 3501–3513. [[CrossRef](#)]
20. Shin, H.C.; Roth, H.R.; Gao, M.; Lu, L.; Xu, Z.; Nogues, I.; Yao, J.; Mollura, D.; Summer, R.M. Deep Convolutional Neural Networks for Computer-Aided Detection: CNN Architectures, Dataset Characteristics and Transfer Learning. *IEEE Trans. Med. Imaging* **2016**, *35*, 1285–1298. [[CrossRef](#)]
21. Hasan, T.; Alexandro, G.; Julian, H.; Thomas, T.; Chrisitan, H.; Tobias, M. Transfer-Learning Bridging the Gap between Real and Simulation Data for Machine Learning in Injection Molding. In Proceedings of the 51st CIRP Conference on Manufacturing Systems, Stockholm, Sweden, 16–18 May 2018; Volume 72, pp. 185–190. [[CrossRef](#)]
22. Hasan, T.; Alexandro, G.; Tobias, M. Industrial Transfer Learning: Boosting Machine Learning in Production. In Proceedings of the 2019 IEEE 17th International Conference on Industrial Informatics (INDIN), Helsinki, Finland, 22–25 July 2019. [[CrossRef](#)]

## Article

# Mold Flow Analysis of Motor Core Gluing with Viscous Flow Channels and Dipping Module

Yong-Jie Zeng <sup>1</sup>, Sheng-Jye Hwang <sup>1,\*</sup>, Yu-Da Liu <sup>2</sup> and Chien-Sheng Huang <sup>2</sup>

<sup>1</sup> Department of Mechanical Engineering, National Cheng Kung University, Tainan 701, Taiwan; tyc861220@gmail.com

<sup>2</sup> Metal Industry Research and Development Center, Kaohsiung 811, Taiwan; mouda420@gmail.com (Y.-D.L.); ccjames.huang@gmail.com (C.-S.H.)

\* Correspondence: jimpp1@mail.ncku.edu.tw; Tel.: +886-6-2757575 (ext. 62148)

**Abstract:** A motor core is formed by stacking iron sheets on top of each other. Traditionally, there are two stacking methods, riveting and welding, but these two methods will increase iron loss and reduce usage efficiency. The use of resin is the current developmental trend in the technology used to join iron sheets, which has advantages including lowering iron loss, smoothing magnetic circuits, and generating higher rigidity. The flow behavior of resin in gluing technology is very important because it affects the dipping of iron sheets and the stacking of iron sheets with resin. In this study, a set of analytical processes is proposed to predict the flow behavior of resin through the use of computer-aided engineering (CAE) tools. The research results are compared with the experimental results to verify the accuracy of the CAE tools in predicting resin flow. CAE tools can be used to predict results, modify modules for possible defects, and reduce the time and costs associated with experiments. The obtained simulation results showed that the filling trend was the same as that for the experimental results, where the error between the simulation results for the final dipping process and the target value was 0.6%. In addition, the position of air traps is also simulated in the dipping process.

**Keywords:** motor core; iron sheet; computer-aided engineering tools; gluing

**Citation:** Zeng, Y.-J.; Hwang, S.-J.; Liu, Y.-D.; Huang, C.-S. Mold Flow Analysis of Motor Core Gluing with Viscous Flow Channels and Dipping Module. *Polymers* **2021**, *13*, 2186. <https://doi.org/10.3390/polym13132186>

Academic Editors: Célio Bruno Pinto Fernandes, Salah Aldin Faroughi, Luís L. Ferrás and Alexandre M. Alonso

Received: 9 June 2021  
Accepted: 29 June 2021  
Published: 30 June 2021

**Publisher's Note:** MDPI stays neutral with regard to jurisdictional claims in published maps and institutional affiliations.



**Copyright:** © 2021 by the authors. Licensee MDPI, Basel, Switzerland. This article is an open access article distributed under the terms and conditions of the Creative Commons Attribution (CC BY) license (<https://creativecommons.org/licenses/by/4.0/>).

## 1. Introduction

In the motor core manufacturing process, one of the sources of performance degradation is the joining method used during the stacking of iron sheets. From Krings' [1] research, it can be seen that in addition to the joining method in the stacking process, the cutting method and the various combinations of iron sheets will have an impact on iron loss. Lamprecht's [2,3] research pointed out that in the iron sheet stacking process, the use of interlocking or welding methods will increase iron loss. The results were verified both experimentally and using the finite element method. Therefore, that research discusses the use of gluing technology to reduce iron loss and improve the efficiency of this process. The resin flow in gluing technology is very important. Due to the design of the viscous flow channel and the dipping module, the resin flows into an open space and forms a free surface in contact with the air, after which the iron sheet is dipped into resin. This is similar to the relationship between a stamp (iron sheet) and an ink pad (free surface). Finally, the iron sheets with resin are stacked on each other to form a motor core. In the present study, mold flow analysis software is used to predict the resin flow and analyze the iron sheet dipping process. Chang [4] established a three-dimensional numerical model to simulate the filling behavior of EMC (epoxy molding compound) in IC packaging materials. Based on the consistency between the experimental and simulation results, the accuracy of this method in the filling process of a three-dimensional model was verified. In a mold flow analysis, the free surface produced by the contact between the fluid and the air cannot be ignored. Aniszewski [5], Srinivasan [6], and Zhou [7] studied using the fluid volume

method to solve the free surface problem, and the simulations were verified to be predictive. Khalil Abdullah's [8] and Chen's [9] research pointed out the Cross Castro–Macosko model is stable and reliable on the flow rheology. Azmi's [10] and Duan's [11] research show that using the the Cross Castro–Macosko model has good results in predicting the flow behavior of thermoset materials. In Chen's [9] and Domínguez's [12] research, it can be seen that Kamal's model is a good approach to predict the change in the mechanical degree of conversion during the material curing process. Lai's [13] research shows the 3D mold flow modeling capabilities of Moldex3D, and the use of the Cross Castro–Macosko model and Kamal's model to obtain accurate results for thermoset materials.

In the present research, a discussion is made of the integration of gluing technology in the stamping process. A set of analytical methods is proposed to predict the flow behavior of resin, the results of which are used in the dipping analysis. In the case of resin flow, the fluid volume method was used to calculate the free surface that occurs when the fluid is in contact with the air.

## 2. Experiment

### 2.1. Equipment

The resin flows between the upper and lower die due to the design of the runner and the dipping module, and the iron sheet that moves with the upper die for dipping can be seen in Figure 1. In the experiment, the resin is pushed by a pump at a pressure of 0.8 MPa; the stamping equipment is set to 50 strokes per minute (50 SPM); the stamping force is 0.022 tf, and the stamping speed is 1.83 mm/s. The stamping equipment was produced by the Metal Industries Research and Development Center, Kaohsiung, Taiwan.

The runner design comprises three parts: the resin pool, the over-flow dam, and a Teflon block (see Figure 2). In addition, Figure 3 shows the design of the Teflon module. In Figure 3a, there are many holes in the top view. It is a Teflon microstructure with a 1 mm diameter and 1.5 mm spacing. Figure 3b is a bottom view of the Teflon block revealing the internal design of the Teflon block. The resin flowing into the resin pool is divided into the left and right sides. The left half has three flow channels, while the right half has one. Figure 3c shows the grooves next to the hole, which are designed to make the resin flow evenly. The purpose of this study is to explore the influence of the design of the runner and the module on the resin flow.

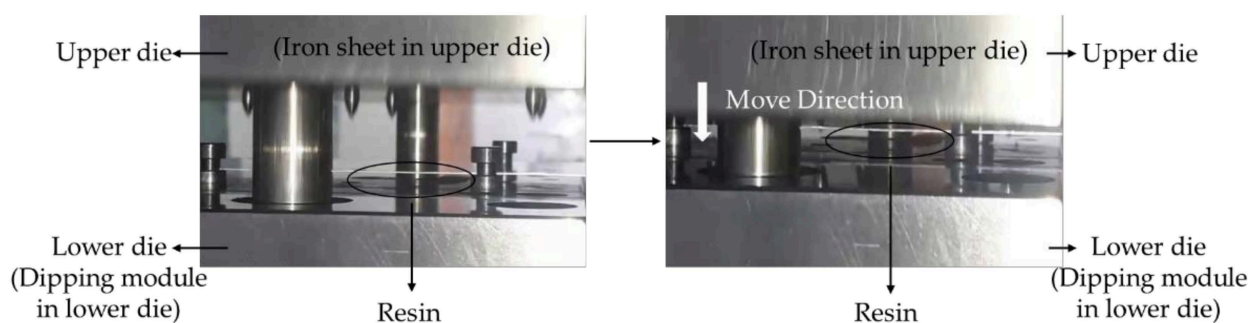


Figure 1. Motor core manufacturing process steps.

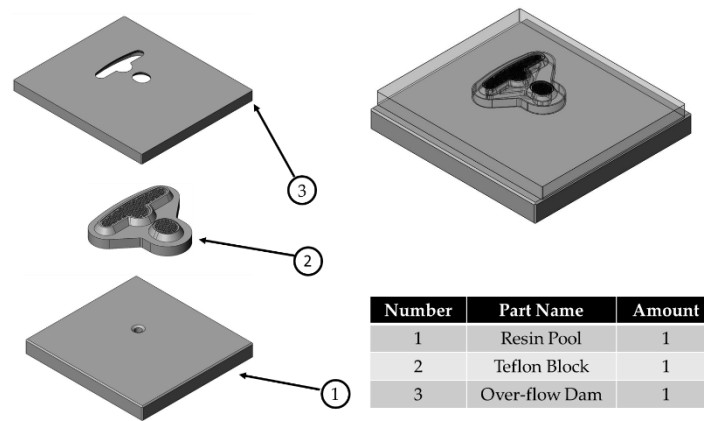


Figure 2. Runner design.

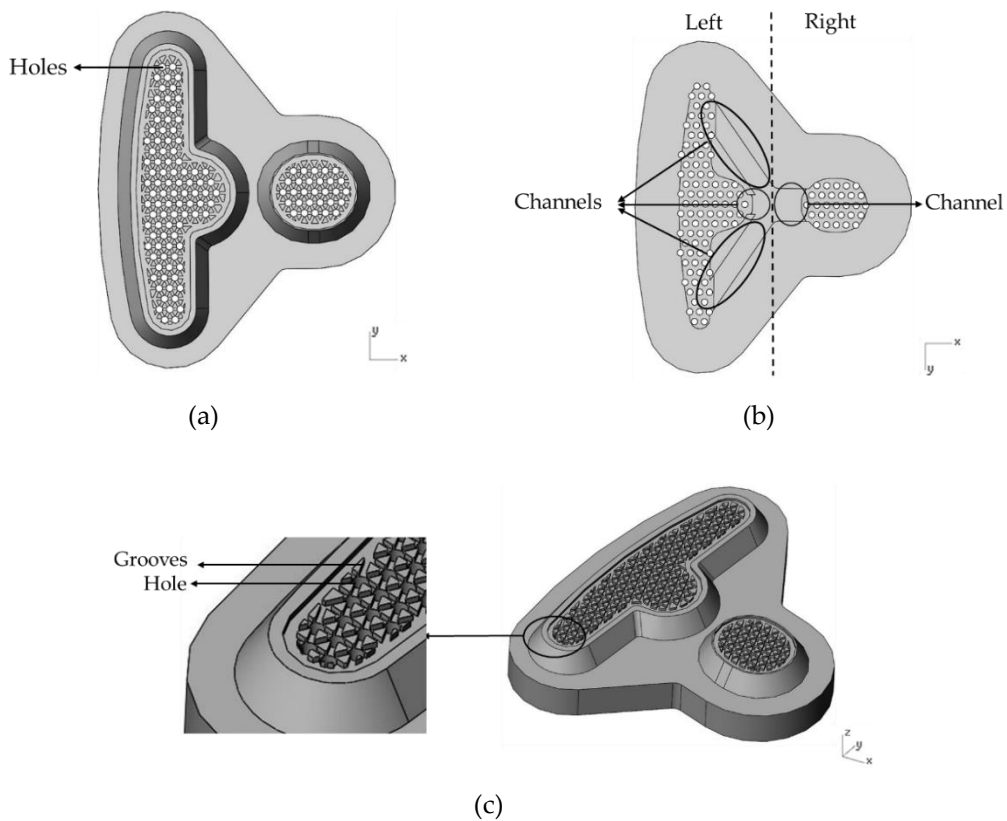
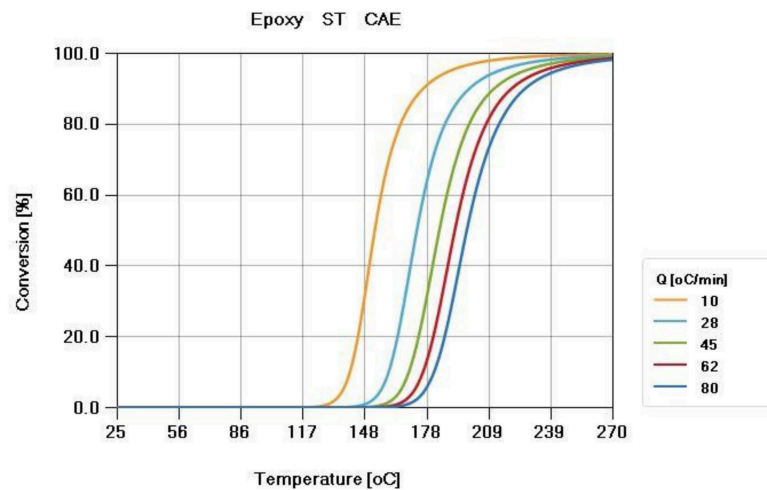


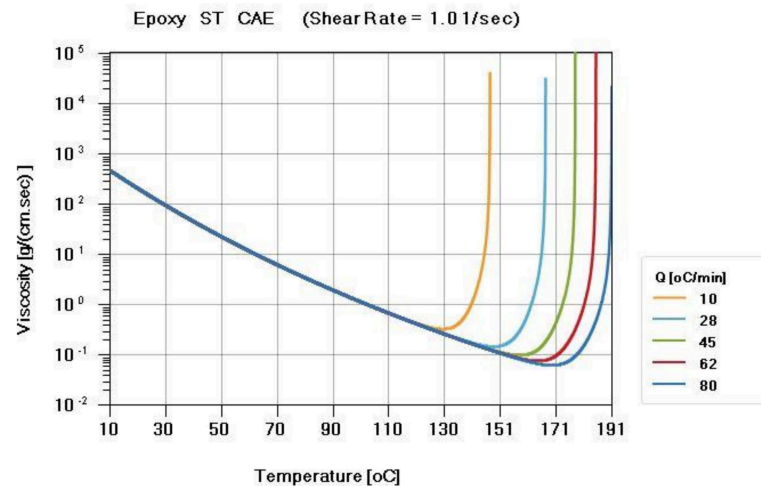
Figure 3. The design of the Teflon module. (a) Top view of the Teflon block. (b) Bottom view of the Teflon block. (c) The microstructure of the Teflon block.

### 2.2. Material

ST resin, which is a thermosetting material, was used in this study. This material was provided by the Metal Industries Research and Development Center, and the material properties were measured by CoreTech System Co., Ltd. A thermal differential scanning calorimeter (DSC) was used to measure the curing kinetics of thermosetting epoxy (Perkin Elmer DSC-8500) (Figure 4). A parallel-plate rheometer (Anton Paar MCR502) was used to measure the viscosity of the epoxy (Figure 5).



**Figure 4.** Curing kinetics curve of the ST resin. The curing kinetics is measured by a DSC with different temperature ramping rates ( $Q = 10, 28, 45, 62, 80$  °C/min).



**Figure 5.** Viscosity curve of the ST resin. The viscosity is measured by a parallel-plate rheometer at different temperatures ramping rates ( $Q = 10, 28, 45, 62, 80$  °C/min) and the viscosity changes with time.

Since the resin will solidify as the temperature rises, the curing kinetics must be considered in this study. The curing kinetics model used the Kamal’s model, while the model equation is shown in Section 3.1.

The viscosity of a thermosetting material will decrease with the increase of temperature. Because the viscosity changes with the temperature, the viscosity curve is very important in the research. The viscosity model used the Cross Castro–Macosko model, while the model equation is shown in Section 3.1.

### 3. Simulation

#### 3.1. Theoretical Background

For the flow simulations, the principle of conservation of mass, momentum, and energy was used for the governing equation.

- Continuity Equation

The mass conservation of resin during cavity filling is described by a continuity equation:

$$\frac{\partial \rho}{\partial t} + \nabla \cdot (\rho \vec{V}) = 0 \tag{1}$$

- Momentum Equation

During the resin filling process, the fluid force changes are described by the momentum equation:

$$\rho \left( \frac{\partial \vec{V}}{\partial t} + \vec{V} \cdot \nabla \vec{V} \right) = -\nabla P + \nabla \cdot \vec{\tau} + \rho \vec{g} \tag{2}$$

- Energy Equation

The energy equation is used to describe the conservation of energy in the curing process during the filling process:

$$\rho C_p \left( \frac{\partial T}{\partial t} + \vec{V} \cdot \nabla T \right) = \nabla \cdot (k \nabla T) + \eta \dot{\gamma}^2 + \frac{d\alpha}{dt} \Delta H \tag{3}$$

where  $t$  is the time;  $\rho$  is the density;  $\vec{V}$  is the velocity vector;  $P$  is the pressure;  $\vec{\tau}$  is the stress tensor;  $\vec{g}$  is the gravity;  $C_p$  is the specific heat;  $T$  is the temperature;  $\dot{\gamma}$  is the shear rate;  $\alpha$  is the degree of cure;  $\Delta H$  is the reaction heat; and  $\eta$  is the viscosity taken as the generalized Cross Castro–Macosko viscosity model [14]:

$$\eta = \frac{\eta_0 \left( \frac{\alpha_g}{\alpha_g - \alpha} \right)^{C_1 + C_2 \alpha}}{1 + \left( \frac{\eta_0 \dot{\gamma}}{\tau^*} \right)^{1 - n^*}} \tag{4}$$

$$\eta_0 = A_1 \cdot \exp \left( \frac{T_b}{T} \right) \tag{5}$$

$$T_b = \frac{E}{R} \tag{6}$$

where  $\tau^*$  is the critical shear stress;  $\dot{\gamma}$  is the shear rate;  $n^*$  is a power law index;  $T$  is the static temperature;  $\alpha$  is the degree of cure;  $\alpha_g$  is the degree of cure at gel point;  $C_1, C_2$  are the fitting constant;  $A_1$  is the exponential-fitted constant; and  $T_b$  is the reaction activation energy constant. The values of the Cross Castro–Macosko model constants Equation (4) are given in Table 1.

**Table 1.** Values of the Cross Castro–Macosko model constants. The constants were measured by a parallel-plate rheometer.

Process Parameters	Parameter Values	Unit
$\alpha_g$	0.3	-
$C_1$	5.3193	-
$C_2$	-10	-
$A_1$	$1 \times 10^{-9}$	g/(cm·s)
$T_b$	7996	K
$n^*$	0.8	-
$\tau^*$	10	dyne/cm <sup>2</sup>

$\frac{d\alpha}{dt}$  is the curing kinetics taken as Kamal’s model [15]:

$$\frac{d\alpha}{dt} = (K_a + K_b \cdot \alpha^m) \cdot (1 - \alpha)^n \tag{7}$$

$$K_a = A \cdot \exp \left( \frac{-T_a}{T} \right) \tag{8}$$

$$K_b = B \cdot \exp \left( \frac{-T_b}{T} \right) \tag{9}$$



where  $\frac{d\alpha}{dt}$  is cure reaction rate;  $\alpha$  is degree of cure;  $m, n$  are material constants;  $K_a, K_b$  are cure reaction velocity constants;  $A, B$  are cure reaction constants;  $T_a, T_b$  are activation energies. The values of Kamal's model constants Equation (7) are given in Table 2.

**Table 2.** Values of Kamal's model constants. The constants were measured by a DSC.

Process Parameters	Parameter Values	Unit
$m$	0.75648	-
$n$	2.0614	-
$A$	228.29	1/s
$B$	$2.5826 \times 10^7$	1/s
$T_a$	14,586	K
$T_b$	8619	K

- Volume of Fluid, VOF.

The free liquid surface problem is quite difficult for numerical calculations. The main reason for this issue is that the boundary of a free liquid surface is a moving boundary, and the boundary changes with time. The free liquid surface must meet the free surface kinematic boundary condition (FSKBC) and the free surface dynamic boundary condition (FSDBC) [16].

The volume of fluid (VOF) [17] is a numerical calculation method that is used to establish the interface boundary conditions for a free surface or two-fluid interfaces. The VOF method is based on defining a fractional volume function that allows a single element to be full, partially filled, or to remain empty. Through the fractional volume function, three areas can be defined in the element as follows:

$$f = \begin{cases} 0, & \text{the element is empty.} \\ 1, & \text{the element is full.} \\ 0 < f < 1, & \text{there is a fluid interface in element.} \end{cases} \quad (10)$$

The fractional volume function is governed by a transport equation:

$$\frac{\partial f}{\partial t} + \vec{V} \cdot \nabla f = 0 \quad (11)$$

The following simple serial averages are adopted in this work to approximate the density and viscosity at the interface between fluid 1 and fluid 2.

$$\rho_f = f \cdot \rho_1 + (1 - f) \cdot \rho_2 \quad (12)$$

$$\eta_f = f \cdot \eta_1 + (1 - f) \cdot \eta_2 \quad (13)$$

### 3.2. Simulation Process

This study explores the gluing technology used in the iron sheet stacking process of motor cores. The resin is transferred through resin inlet to resin pool by a pump as shown in Figures 6 and 7, so the injection molding process simulation tool, Moldex3D, is used for the filling process simulation. The resin flows through the viscous flow channels and the viscous flow channels are constituted of the resin pool and the Teflon block. When the resin flows through 122 holes in a plate, hemi-spheres of resin will be formed. An iron sheet is then dipped on the emerged resin to form a thin layer of glue to bond iron layers to make a motor core.

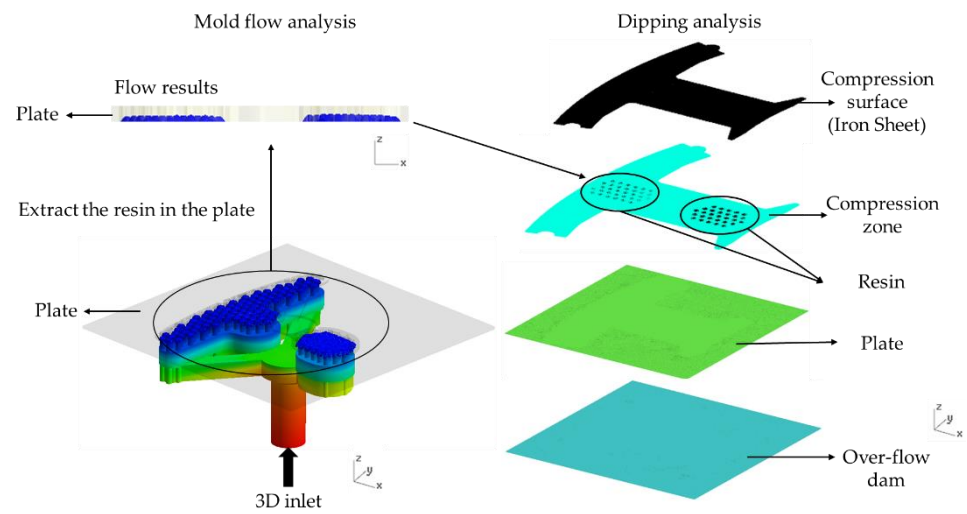


Figure 6. The simulation flow chart.

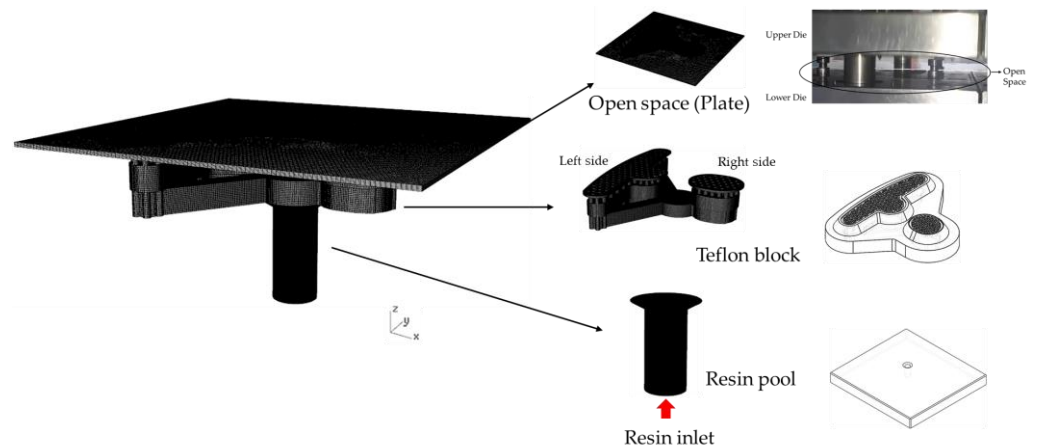


Figure 7. Mesh model used in the filling process.

During the dipping process, the iron sheet moves with the upper die. Therefore, compression molding process simulation is used to model the dipping process. The emerged hemi-sphere shaped resin in the plate is numerically extracted as the initial condition for the dipping analysis to predict whether the resin is evenly distributed on the iron sheet.

The stacking process is fully elucidated through the use of a mold flow analysis and a dipping analysis in order to establish the simulation approach used in this study.

### 3.3. Mesh Generation

For the purposes of the simulation, the process is divided into two parts, where the mesh is divided into two parts and constructed as a filling process and a dipping process. Rhinoceros 5 was the mesh modeling software used in this study.

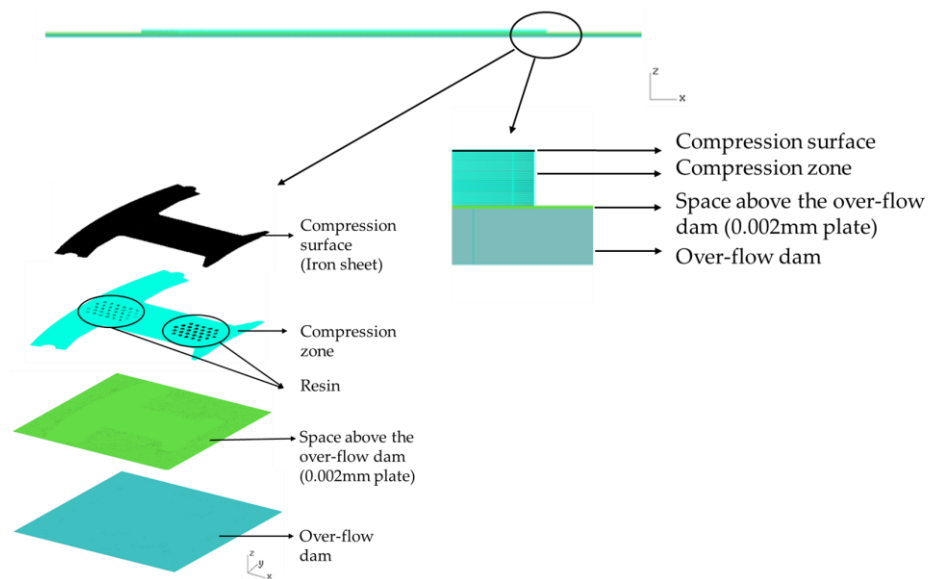
#### 3.3.1. Filling Process

A solid 3D mesh model is created through geometry, as shown in Figure 7. The resin pool and the Teflon block are constructed according to the geometry provided by the Metal Industries Research and Development Center, Kaohsiung, Taiwan. The diameter of the resin inlet is 6 mm, then the resin is divided to the left and right side by three runners (Figure 3b), and finally the resin flows out through 122 holes with 1 mm diameter. The location of the holes is shown in Figure 3a. The detail dimensions of the filling model are shown in Appendix A, Figure A1. The plate is used to simulate the open space of the resin

flow out of the system. There are 3.5 million mesh elements, for which the quality is 0.97 based on the skewness.

### 3.3.2. Dipping Process

The mesh used for the dipping process is composed of a compression surface (iron sheet), a compression zone, a space above the over-flow dam (plate), and the over-flow dam, as shown in Figure 8. The compression zone part simulates the process of gluing the iron sheet. In addition, since the resin on the iron sheet cannot exceed 0.002 mm, the resin is compressed into a space with a thickness of 0.002 mm (the space above the over-flow dam) for the simulation. There is a total of 2.5 million mesh elements, for which the quality is 0.99 based on the skewness.



**Figure 8.** Mesh model used in the dipping process.

### 3.4. Process Parameters

The stamping process is used for gluing the motor core. Due to the design of the runner and the module, the flow of the resin is very important to the overall process. Therefore, the flow is predicted through a simulation, and the experimental parameters are input into the mold flow analysis software to simulate and predict the resin flow and gluing results.

#### 3.4.1. Filling Process

In the experiment, the resin was pushed by a pump, for which the pressure was 0.8 MPa, so the injection pressure was set at 0.8 MPa. The mold temperature and the resin temperature were both set to 45 °C based on the data provided by the Metal Industry Research and Development Center, which indicates that the temperature of the resin before entering the module is about 45 °C. The mold flow analysis mold is set at 45 °C because, regardless of whether it passes through the runner in the resin pool or the runner or microstructure in the Teflon block, the resin temperature is still about 45 °C, so the resin is flowing isothermally in the glue module. In the setting of process parameters, the initial conversion rate of plastics is very important. In this study, Moldex3D mold flow analysis software was used to calculate the initial conversion rate. The resin was taken out at room temperature (25 °C) for one day, and the initial conversion rate barely changed. Therefore, the initial conversion rate was set to 0%. The process parameters can be shown in Table 3. In the experiment, the volume flow rate is 0.00053 cm<sup>3</sup>/s. The volume flow rate cannot be set in the simulation analysis, so it can only be measured based on the filling time. Since the total volume of the mesh model established in this paper was 4.16 cm<sup>3</sup>, the filling time was

set to 416 s, for which the volume flow rate was  $0.01 \text{ cm}^3/\text{s}$ . The reason why the volume flow rate of this study was set at  $0.01 \text{ cm}^3/\text{s}$  is explained in the Results and Discussion section of this paper.

**Table 3.** The parameters of the filling process.

Process Parameters	Parameter Values
Injection pressure (MPa)	0.8
Melt temperature ( $^{\circ}\text{C}$ )	45
Mold temperature ( $^{\circ}\text{C}$ )	45
Initial conversion (%)	0
Filling time (s)	416

### 3.4.2. Dipping Process

The parameters for the dipping process are shown in Table 4. The compression speed and compression force, which is the stamping speed and stamping force in the stamping process, respectively, were set based on the Metal Industries Research and Development Center guidelines. The thickness of the compression zone was 0.5 mm because the thickness of the compression zone only addressed the area where the iron sheet is prepared to glue the resin. The compression time was obtained by the compression gap divided by the compression speed. The resin and mold temperature settings were also set based on the data provided by the Metal Industries Research and Development Center. The initial conversion rate setting was calculated using Moldex3D software. From the filling process to the gluing stage, the resin in the module does not flow over 1 hour, so the conversion rate remained at 0%.

**Table 4.** The parameters of the dipping process.

Process Parameters	Parameter Values
Compression time (s)	0.273
Compression gap (mm)	0.5
Compression speed (mm/s)	1.83
Compression force (tf)	0.022
Resin temperature ( $^{\circ}\text{C}$ )	45
Mold temperature ( $^{\circ}\text{C}$ )	45
Initial conversion (%)	0

### 3.5. Mold Flow Analysis Software

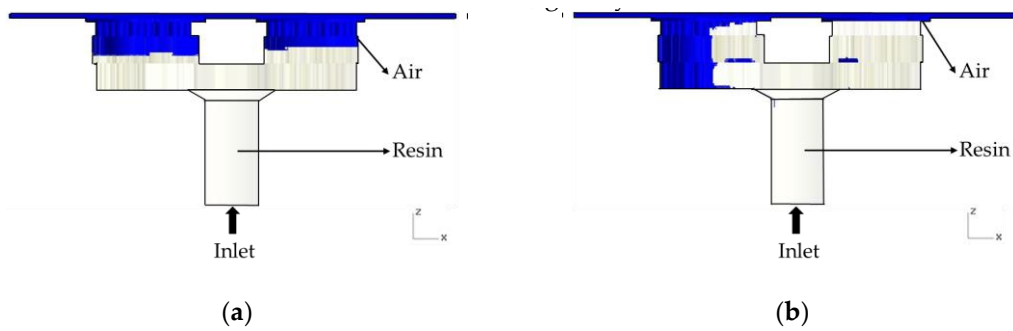
A commercially available CAE software Molde $\times$ 3D 2020 R1 special edition for free surface simulation was used for the analysis in this study. It is a CAE software used mainly for injection molding and compression molding simulations.

## 4. Results and Discussion

This section discusses the influence of gravity and the flow rate on the simulation and also discusses the resin distribution during the dipping process and the distribution of the air traps, after which a comparison of the results with the experimental results are discussed.

### 4.1. The Influence of Gravity on Simulation

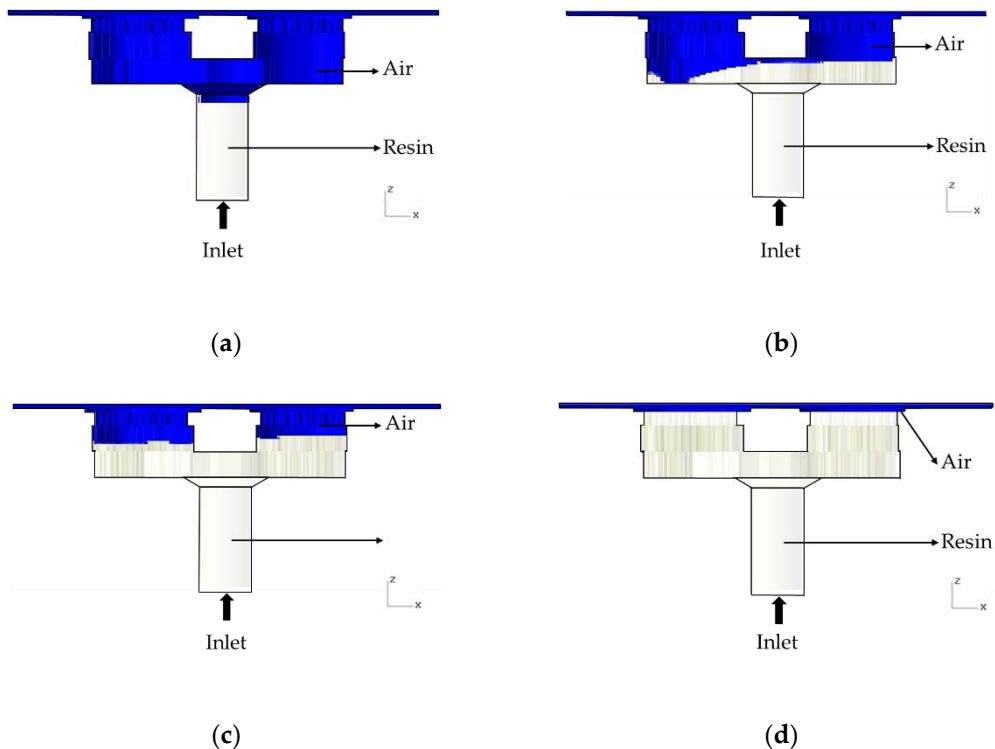
The effect of gravity in this study was very significant. Figure 9 shows the influence of gravity on the simulation. If gravity is ignored, there is a slightly unreasonable flow situation, as shown in Figure 9. When gravity is taken into account, the results are close to actual conditions. Therefore, gravity must be taken into consideration.



**Figure 9.** The effect of gravity on simulation (a) considering gravity and (b) not considering gravity.




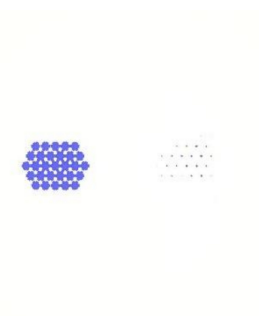

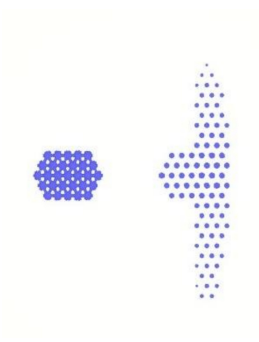

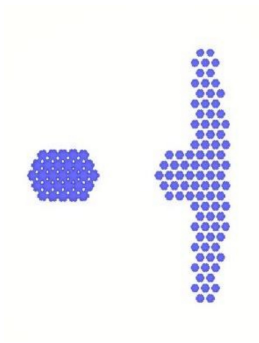
#### 4.2. The Influence of Flow Rate on Simulation

In this simulation, if the flow rate is set to be the same as the experiment in the mold flow analysis, the air resistance will be too large, which will cause the resin to fail to flow smoothly and cause the simulation to stop. Therefore, different fill times were set, which made the flow rate respectively 0.01 (see Figure 10), 0.02, 0.03, 0.04, and 0.05 cm<sup>3</sup>/s. The simulation results of the flow rate 0.02, 0.03, 0.04, 0.05 cm<sup>3</sup>/s are shown in Appendix B, Figures A2–A5. From the simulation results of different flow rates, it can be seen that the flow trend is similar at different flow rates. In this study, the flow rate closest to the experimental conditions was used for the simulation (0.01 cm<sup>3</sup>/s). Experiment and simulation results of the flow trend in the plate are shown in Table 5.



**Figure 10.** The flow rate is 0.01 cm<sup>3</sup>/s. (a) Filling 10%; (b) Filling 30%; (c) Filling 50%; (d) Filling 70%.

**Table 5.** Experiment and simulation results of flow trend in the plate. Since the filling process of the experiment is not easy to observe, there is a large gap in the total filling time. Therefore, the time difference is used to determine whether the trend is similar.

Experiment	Simulation	Experiment ( $\Delta t$ )	Simulation ( $\Delta t$ )
 40 s	 279 s	-	-
 43 s	 283 s	3 s	4 s
 45 s	 285 s	2 s	2 s
 48 s	 289 s	3 s	4 s

#### 4.3. Results for Dipping an Iron Sheet

From the results of the filling process (Table 5), it can be seen that the resin emerges first from the right side, then the middle of the left side, and finally from the two sides of

the left T-shape. There is obviously more resin on the right side than that on the left side. The emerged resin in the plate is numerically extracted, and then the resin is used as the initial condition for the dipping analysis. The simulation result of the dipping process is shown in Figure 11. The distribution of resin is uneven, which will reduce the adhesion quality of the iron sheets, and there is an over-flow on the right side, which will cause bumps when the iron chips are stacked on each other (the resin area exceeds the size of the iron sheet) (see Figure 12).

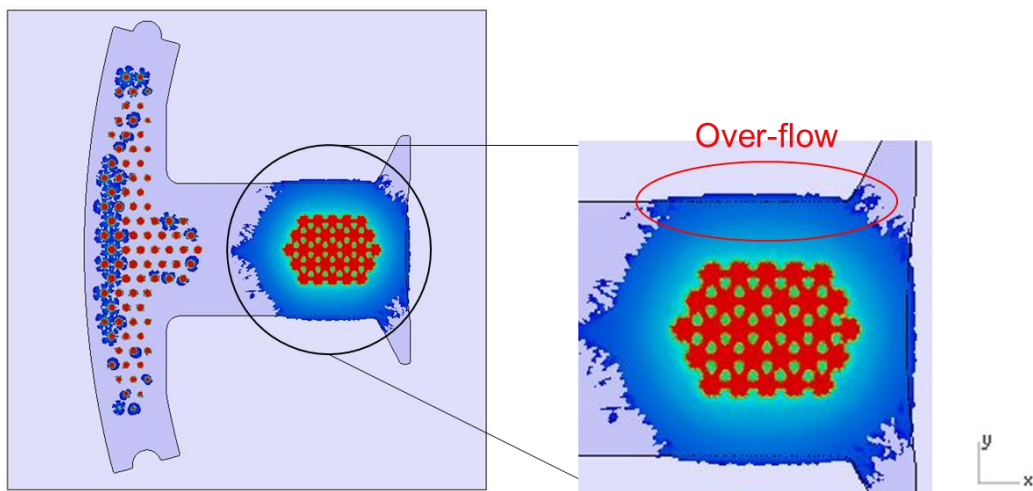


Figure 11. Top view of the dipping process results.

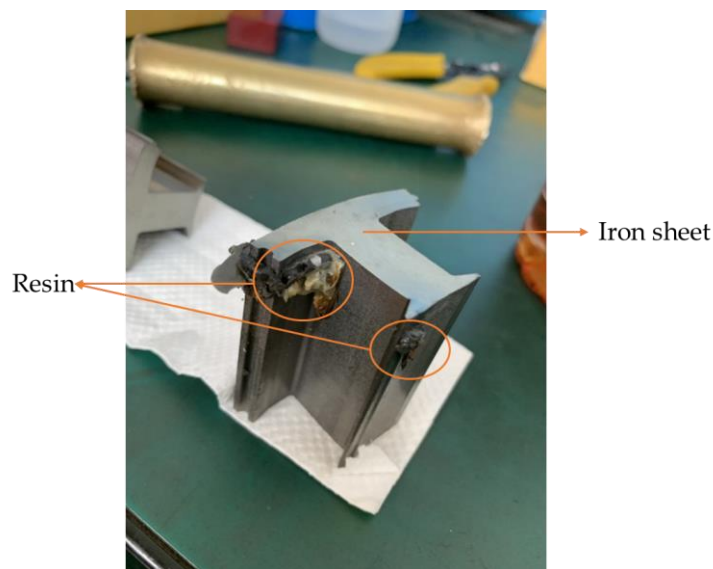


Figure 12. Schematic diagram of bumps caused by resin overflow.

#### 4.4. Air Traps Results

The simulation was very important not only in terms of predicting the flow of resin during the dipping process but also in terms of predicting the occurrence of air traps. The occurrence of air traps may reduce the adhesive area. In addition to insufficient adhesion, the subsequent heating process for the iron sheet may also produce a popcorn effect, which may decrease product quality. From Figure 13, it can be seen that most of the air traps are located on the right half. This phenomenon is due to too much resin on the right half, which causes the gas to not discharge smoothly during the dipping process.

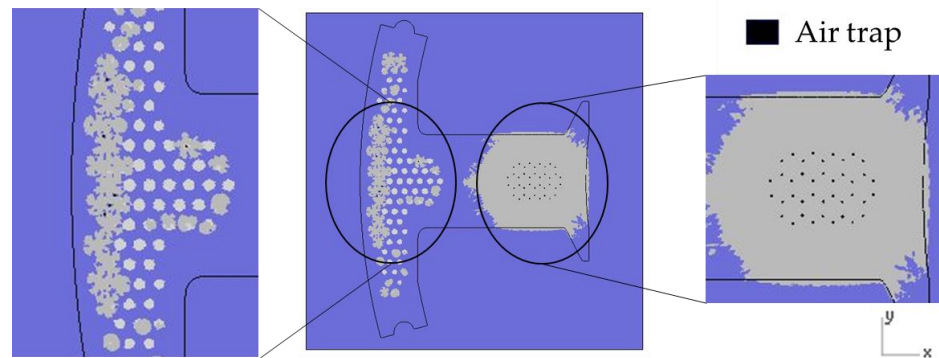


Figure 13. Position of air traps.

#### 4.5. Comparison of the Target Value and the Simulation Results

Since it is not easy to measure the resin volume in the experiment, the resin volume can be obtained by the estimated resin area ( $320.8 \text{ mm}^2$ ) times the resin thickness ( $0.002 \text{ mm}$ ) is  $0.64 \text{ cm}^3$ , which can be used as a comparison basis for simulation.

Image analysis software (ImageJ) was used to analyze the resin area associated with the dipping results, which was  $322.021 \text{ mm}^2$  (Figure 14), and the volume was  $0.644 \text{ mm}^3$ , resulting in a simulation error of 0.6%.

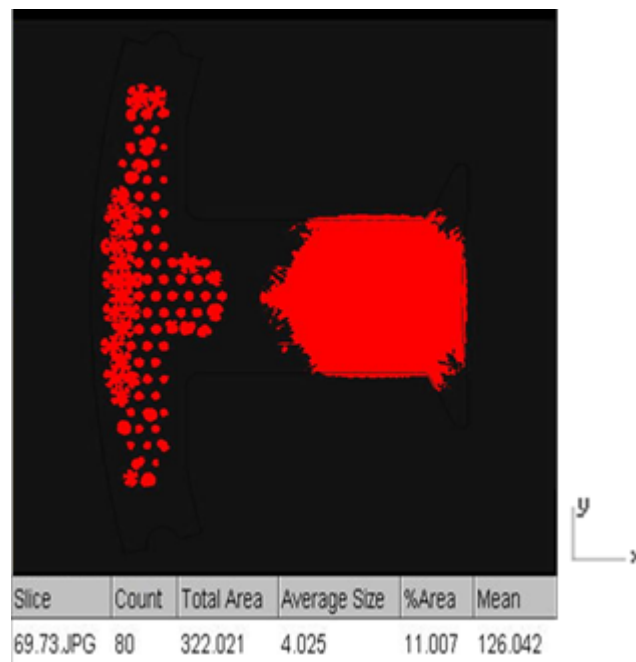


Figure 14. ImageJ measurement results.

## 5. Conclusions

This article was focused on the gluing technology used in the stamping process. The gluing method was relatively similar to other joining methods (welding, riveting), but it had advantages including lowering iron loss, smoothing the magnetic circuit, and obtaining higher overall rigidity. In this study, Moldex3D mold flow analysis software was used to predict the flow of the resin due to the design of the module and runners and the process used to stick the iron sheet during the motor core die-bonding process, in order to observe the resin flow. In this research, the flow of the plastic in the module was simulated first, and then the flow results were taken as the condition before dipping in order to predict the plastic dipping process under specific conditions.

Based on the research results, the following conclusions could be drawn:



1. The properties of the fluid in the mold flow analysis are very important. In the present research, Kamal’s reaction dynamic model and the Cross Castro–Macosko viscosity model were used to define the material parameters, so the mold flow analysis could better describe the material characteristics.
2. A mold flow analysis and a dipping analysis were used to compare the entire motor core filling and dipping process. The prediction results were very good for both the flow in the filling process and the dipping process, and it was possible to effectively predict the area where the air traps would occur when glued based on the results of the analytical software.
3. Image analysis software (ImageJ) was used to analyze the resin area in the simulation results, for which the resulting area was 322.021 mm<sup>2</sup> and the volume was 0.644 mm<sup>3</sup>. The target value of area is 320.8 mm<sup>2</sup> and the volume is 0.64 mm<sup>3</sup>. The error value for the simulation results was 0.6%, which may have been caused by extracting the resin.
4. The runner design will cause the resin to flow unevenly and there will be over-flow during the dipping process.

**Author Contributions:** Methodology, Y.-J.Z., S.-J.H., Y.-D.L., C.-S.H.; validation, S.-J.H.; formal analysis, Y.-J.Z.; writing—original draft preparation, Y.-J.Z.; writing—review and editing, Y.-J.Z. and Y.-J.Z.; supervision, S.-J.H. All authors have read and agreed to the published version of the manuscript.

**Funding:** This research received no external funding.

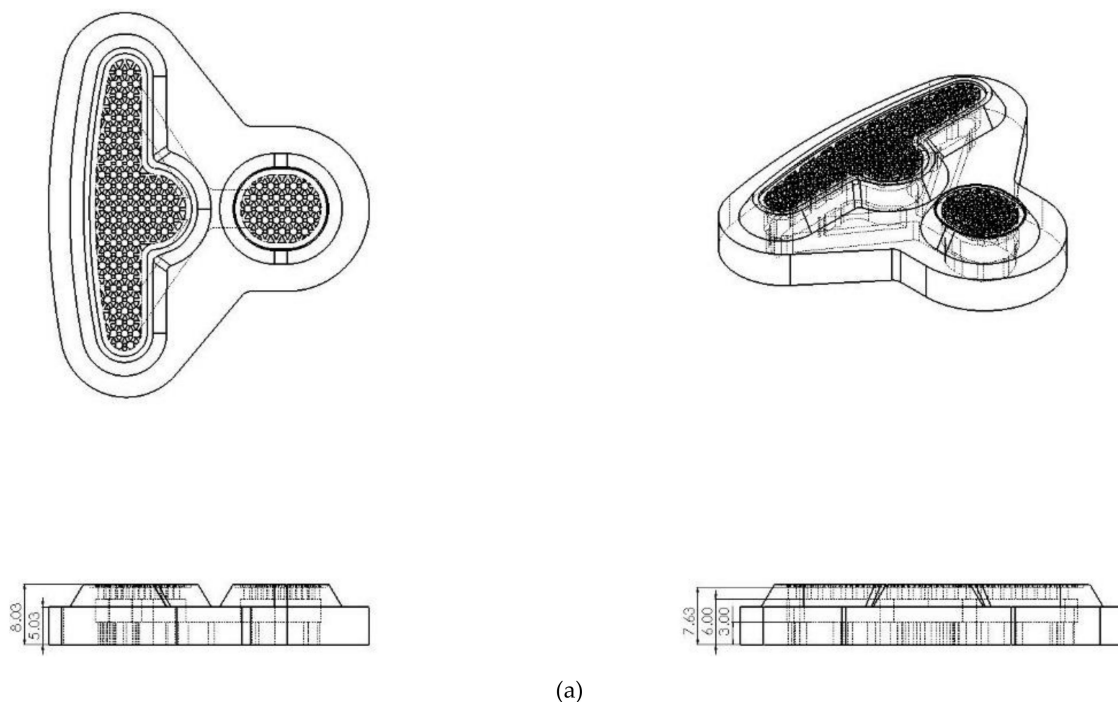
**Institutional Review Board Statement:** Not applicable.

**Informed Consent Statement:** Not applicable.

**Data Availability Statement:** The data presented in this study are available on request from the corresponding author.

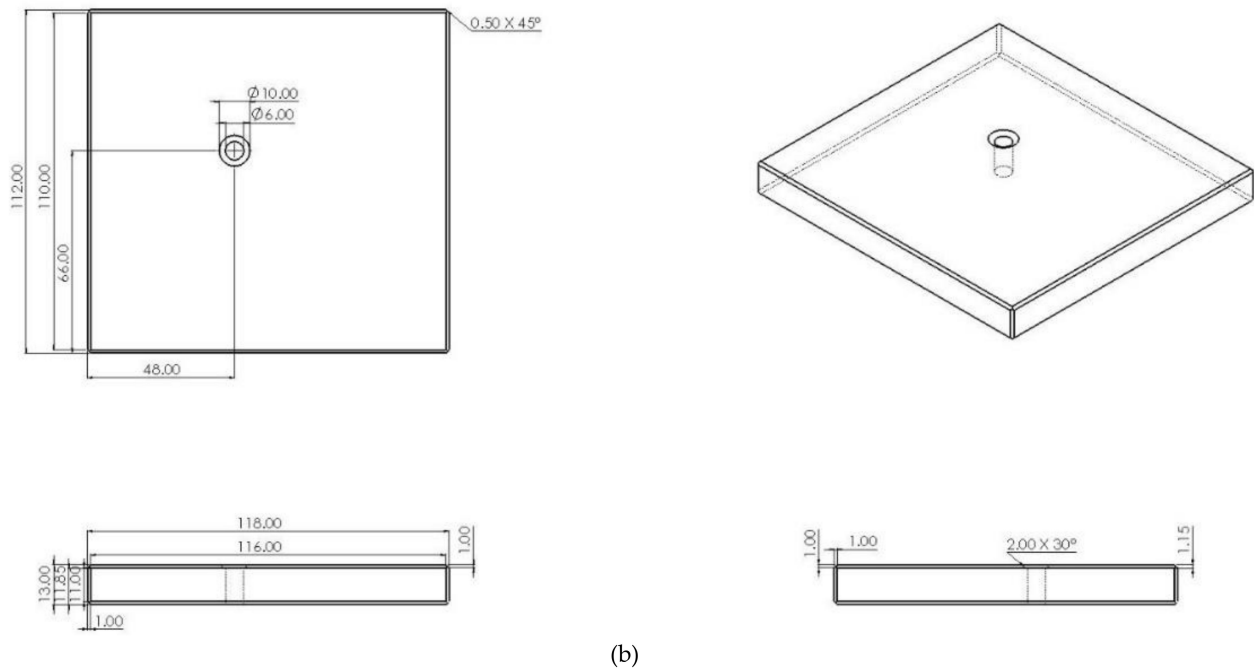
**Conflicts of Interest:** The authors declare no conflict of interest.

## Appendix A



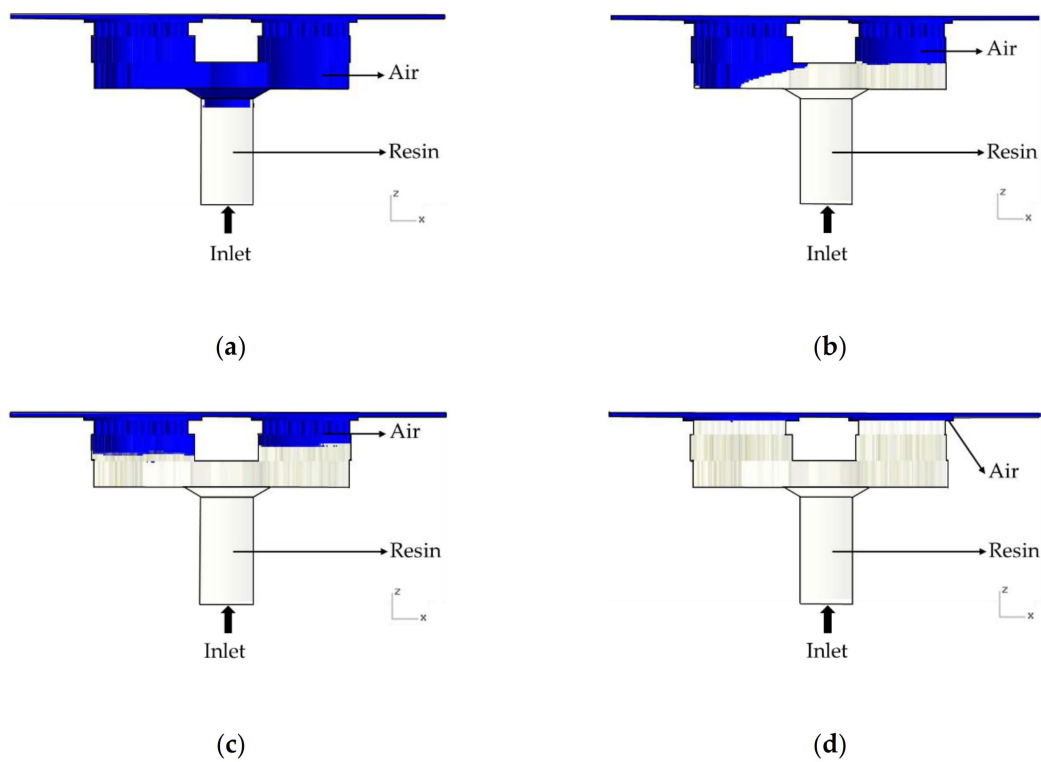
(a)

**Figure A1.** Cont.



**Figure A1.** The detail dimensions of the filling model. (Unit: mm) (a) The Teflon block; (b) The resin pool.

### Appendix B



**Figure A2.** The flow rate is  $0.02 \text{ cm}^3/\text{s}$ . (a) Filling 10%; (b) Filling 30%; (c) Filling 50%; (d) Filling 70%.

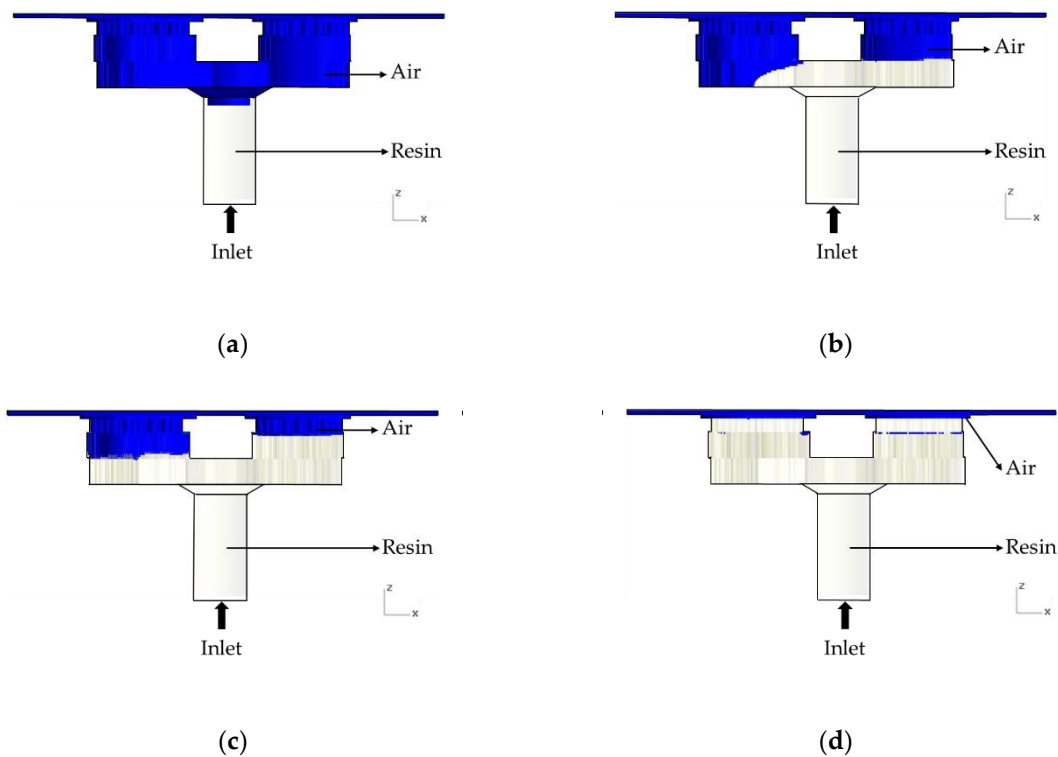


Figure A3. The flow rate is  $0.03 \text{ cm}^3/\text{s}$ . (a) Filling 10%; (b) Filling 30%; (c) Filling 50%; (d) Filling 70%.

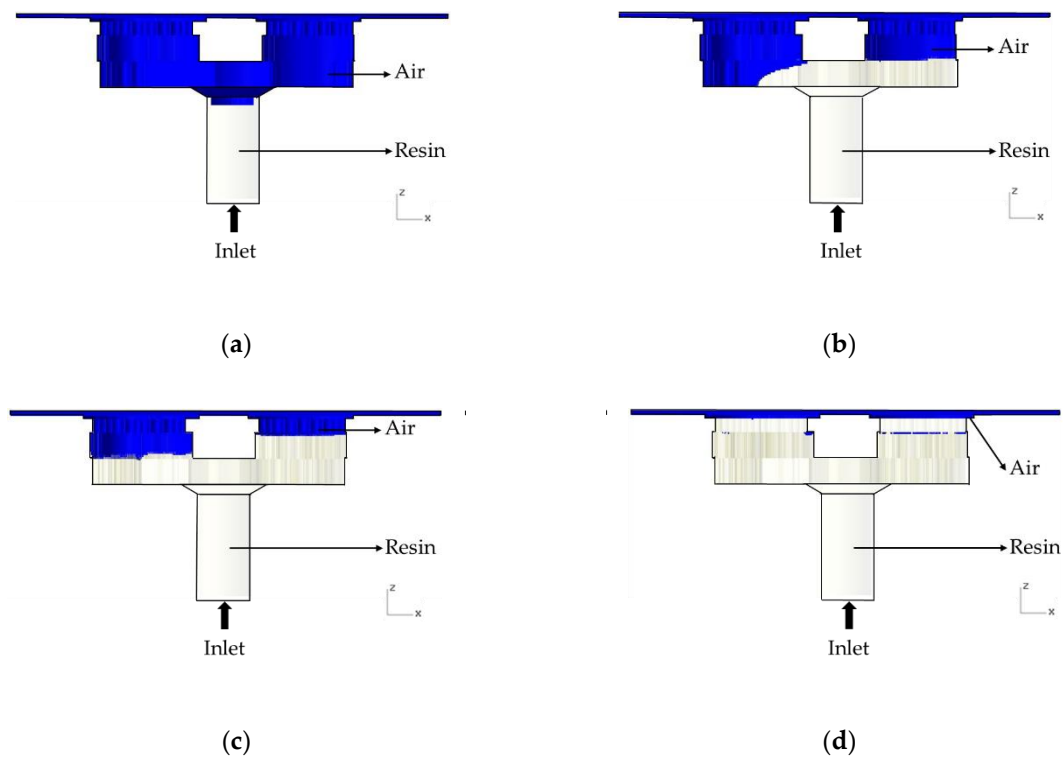
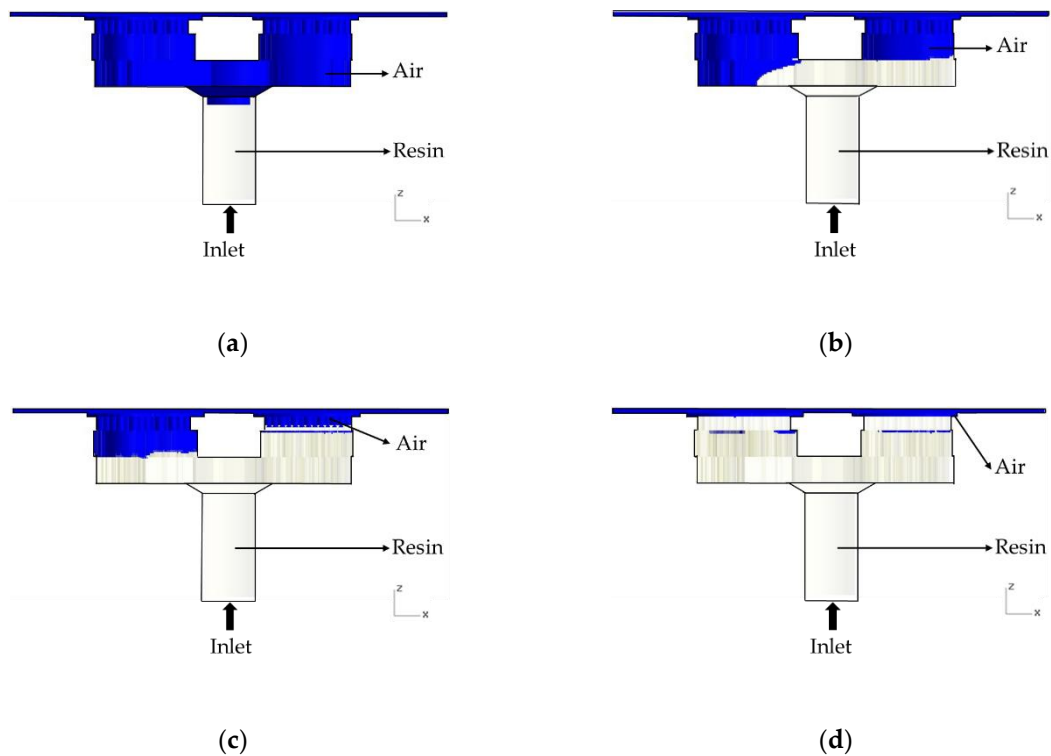


Figure A4. The flow rate is  $0.04 \text{ cm}^3/\text{s}$ . (a) Filling 10%; (b) Filling 30%; (c) Filling 50%; (d) Filling 70%.



**Figure A5.** The flow rate is  $0.05 \text{ cm}^3/\text{s}$ . (a) Filling 10%; (b) Filling 30%; (c) Filling 50%; (d) Filling 70%.

## References

1. Krings, A. Iron Losses in Electrical Machines-Influence of Material Properties. Ph.D. Thesis, Kungliga Tekniska Högskolan, Stockholm, Sverige, 2014.
2. Lamprecht, E.; Graf, R. Fundamental investigations of eddy current losses in laminated stator cores created through the impact of manufacturing processes. In Proceedings of the 2011 1st International Electric Drives Production Conference, Nuremberg, Germany, 28–29 September 2011; pp. 29–35.
3. Lamprecht, E.; Hömme, M.; Albrecht, T. Investigations of eddy current losses in laminated cores due to the impact of various stacking processes. In Proceedings of the 2012 2nd International Electric Drives Production Conference, Nuremberg, Germany, 15–18 October 2012; pp. 1–8.
4. Chang, R.-Y.; Yang, W.-H.; Hwang, S.-J.; Su, F. Three-Dimensional Modeling of Mold Filling in Microelectronics Encapsulation Process. *IEEE Trans. Compon. Packag. Technol.* **2004**, *27*, 200–209. [[CrossRef](#)]
5. Aniszewski, W.; Ménard, T.; Marek, M. Volume of Fluid (VOF) type advection methods in two-phase flow: A comparative study. *Comput. Fluids* **2014**, *97*, 52–73. [[CrossRef](#)]
6. Srinivasan, V.; Salazar, A.J.; Saito, K. Modeling the disintegration of modulated liquid jets using volume-of-fluid (VOF) methodology. *Appl. Math. Model.* **2011**, *35*, 3710–3730. [[CrossRef](#)]
7. Zhou, L.; Liu, D.-Y.; Ou, C.-Q. Simulation of Flow Transients in a Water Filling Pipe Containing Entrapped Air Pocket with VOF Model. *Eng. Appl. Comput. Fluid Mech.* **2011**, *5*, 127–140. [[CrossRef](#)]
8. Abdullah, M.K.; Abdullah, M.; Mujeebu, M.A.; Kamaruddin, S.; Ariff, Z. A Study on the Effect of Epoxy Molding Compound (EMC) Rheology during Encapsulation of Stacked-CHIP Scale Packages (S-CSP). *J. Reinf. Plast. Compos.* **2008**, *28*, 2527–2538. [[CrossRef](#)]
9. Chen, Y.-K.; Wu, G.-T.; Hwang, S.-J.; Lee, H.-H.; Hwang, D.-Y. Molded underfill for flip chip package. In Proceedings of the 2013 8th International Microsystems, Packaging, Assembly and Circuits Technology Conference (IMPACT), Taipei, Taiwan, 22–25 October 2013; pp. 310–314.
10. Azmi, M.; Abdullah, M.; Ariff, Z.; Ismail, M.; Aziz, M.A.; Abdullah, M. Flow Behavior Analysis of Emc in Molded Underfill (Muf) Encapsulation for Multi Flip-Chip Package. *J. Phys. Conf. Ser.* **2018**, *1082*, 012015. [[CrossRef](#)]
11. Duan, Y.; Wang, X.; Yang, D.; Wang, J.; Ye, W.; Wu, Y. Mold Flow Analysis of a SiP Package for Power Management. In Proceedings of the 2020 21st International Conference on Electronic Packaging Technology (ICEPT), Guangzhou, China, 12–15 August 2020; pp. 1–4.
12. Domínguez, J.; Alonso, M.; Oliet, M.; Rojo, E.; Rodríguez, F. Kinetic study of a phenolic-novolac resin curing process by rheological and DSC analysis. *Thermochim. Acta* **2010**, *498*, 39–44. [[CrossRef](#)]

13. Lai, J.-Y.; Chen, T.-Y.; Wang, M.-H.; Shih, M.-K.; Tarn, D.; Hung, C.-P. Characterization of Dual Side Molding SiP Module. In Proceedings of the 2017 IEEE 67th Electronic Components and Technology Conference (ECTC), Orlando, FL, USA, 30 May–2 June 2017; pp. 1039–1044.
14. Castro, J.M.; Macosko, C.W. Studies of mold filling and curing in the reaction injection molding process. *AIChE J.* **1982**, *28*, 250–260. [[CrossRef](#)]
15. Kamal, M.R. Thermoset characterization for moldability analysis. *Polym. Eng. Sci.* **1974**, *14*, 231–239. [[CrossRef](#)]
16. Hsiao, H.K. Nonlinear Waves Interaction with Breakwaters. Master's Thesis, National Sun Yat-sen University, Kaohsiung, Taiwan, 2004.
17. Scardovelli, R.; Zaleski, S. Direct numerical simulation of free-surface and interfacial flow. *Annu. Rev. Fluid Mech.* **1999**, *31*, 567–603. [[CrossRef](#)]

## Article

# Simulation of the Particle Transport Behaviors in Nanoporous Matter

You Wu <sup>1,2</sup>, Dandan Ju <sup>3,\*</sup>, Hao Wang <sup>3</sup>, Chengyue Sun <sup>3</sup>, Yiyong Wu <sup>1,3,\*</sup>, Zhengli Cao <sup>4</sup> and Oleg V Tolochko <sup>5</sup><sup>1</sup> School of Material Science and Engineering, Harbin Institute of Technology, Harbin 150006, China<sup>2</sup> Xi'an Aerospace Chemical Propulsion Co., Ltd., Xi'an 710000, China<sup>3</sup> Research Center of Space Physics and Science, Harbin Institute of Technology, Harbin 150006, China<sup>4</sup> Aerospace System Engineering Shanghai, Shanghai 200000, China<sup>5</sup> School of Material Science and Engineering, Peter the Great Saint Petersburg Polytechnic University, 195251 Saint Petersburg, Russia

\* Correspondence: judandan.love@163.com (D.J.); wuyiyong@hit.edu.cn (Y.W.)

**Abstract:** The transport behaviors of proton into nanoporous materials were investigated using different Monte Carlo simulation codes such as GEANT4, Deeper and SRIM. The results indicated that porous structure could enhance the proton scattering effects due to a higher specific surface area and more boundaries. The existence of voids can deepen and widen the proton distribution in the targets due to relatively lower apparent density. Thus, the incident protons would transport deeper and form a wider Bragg peak in the end of the range, as the target materials are in a higher porosity state and/or have a larger pore size. The existence of voids also causes the local inhomogeneity of proton/energy distribution in micro/nano scales. As compared, the commonly used SRIM code can only be used to estimate roughly the incident proton range in nanoporous materials, based on a homogeneous apparent density equivalence rule. Moreover, the estimated errors of the proton range tend to increase with the porosity. The Deeper code (designed for evaluation of radiation effects of nuclear materials) can be used to simulate the transport behaviors of protons or heavy ions in a real porous material with porosity smaller than 52.3% due to its modeling difficulty, while the GEANT4 code has shown advantages in that it is suitable and has been proven to simulate proton transportation in nanoporous materials with porosity in its full range of 0~100%. The GEANT4 simulation results are proved consistent with the experimental data, implying compatibility to deal with ion transportation into homogeneously nanoporous materials.

**Keywords:** Monte Carlo; nanoporous matter; proton; transport behavior; GEANT4 code

**Citation:** Wu, Y.; Ju, D.; Wang, H.; Sun, C.; Wu, Y.; Cao, Z.; Tolochko, O.V. Simulation of the Particle Transport Behaviors in Nanoporous Matter. *Polymers* **2022**, *14*, 3563. <https://doi.org/10.3390/polym14173563>

Academic Editors: Célio Bruno Pinto Fernandes, Salah Aldin Faroughi, Luís L. Ferrás and Alexandre M. Afonso

Received: 9 July 2022

Accepted: 25 August 2022

Published: 29 August 2022

**Publisher's Note:** MDPI stays neutral with regard to jurisdictional claims in published maps and institutional affiliations.



**Copyright:** © 2022 by the authors. Licensee MDPI, Basel, Switzerland. This article is an open access article distributed under the terms and conditions of the Creative Commons Attribution (CC BY) license (<https://creativecommons.org/licenses/by/4.0/>).

## 1. Introduction

With the development of nuclear energy and space exploration, materials with excellent irradiation tolerance are receiving extensive attention [1,2]. Numerous effects have been devoted to investigate the damage behaviors and mechanisms of nuclear protection materials under various irradiation resource [3–7]. For metals or inorganic crystal materials, energetic particle radiation was found to cause point defects, and the accumulation of point defects would form dislocation loops, voids, stacking fault tetrahedrons (SFTs), etc. [8]. The key to design the radiation tolerant materials is that the point defects can be partly recovered or eliminated during the radiation process [1,9]. The most popular approach is to introduce interfaces inside the materials [1,9,10], using a free surface to attract, absorb and annihilate point and line defects [7,10,11]. Chen [12] investigated the radiation response and mechanisms in a helium ion-irradiation immiscible coherent Cu/Co nanolayer and found that the interface of Cu/Co can effectively reduce the population of irradiation-induced defects.

Recently, owing to its lightweight, ultra-low metal consumption and large free surface area per unit volume [10,13], nanoporous (NP) metal shows great potential to become a new

class of radiation-resistant material. Bringa [9] reported the existence of a radiation-resistant window between the ligament size of NP foams and the irradiation dose rate. Li [10] studied the irradiation response of nanoporous Au under heavy ion beam bombardment in situ and indicated that the radiation-induced defects can be absorbed/eliminated by nanopores.

To date, the previous research has demonstrated that NP metals can be reasonably designed with strength, stability and radiation resistance [9,14], but there is still a lack of corresponding simulation calculation about the ion transport behavior in nanoporous matter (metal, inorganic and polymer). Compared to nanoporous metal and inorganic materials, nanoporous polymers exhibit excellent flexibility, thermal insulation and stability and have received extensive attentions recently [15]. Owing to their special structure (large specific surface area and high porosity) and ultra-low density, which make them an ideal material for some specific fields, such as filtration [16], catalysis and wastewater treatment field [17–19], as well as the thermal/sound insulation and aerospace activity fields [20]. The stability of a nanoporous polymer must be considered under space irradiation environments. On-orbit experiments and ground-based irradiation simulation tests are expensive and time-consuming [21], while computer simulation is a common and reliable method for evaluating the radiation effects of materials. Porosity and pore size are the main structural parameters of porous materials. However, what is not yet known is how porosity and pore size affect the transport process. In the previous research, Stopping and Range of Ions in Matter (SRIM) software [22] is always used to estimate the range of charged particles into porous matter [9]. However, SRIM can only be used to handle homogeneous or multiple-layered substances, nevertheless, it would fail in dealing with the transport behavior of ions into heterogeneous matter. It is essential to model nanoporous matter and understand the transport behavior of charged particles into nanoporous matter.

In this work, the study is divided into two sections. The first section is to simulate the transport behavior of a proton into nanoporous matter, to make clear whether the porous part takes special roles on the transport process (range, particle distribution and energy deposition). The second section is to investigate the damage behaviors of nanoporous matter (using polyimide aerogel as an example) under proton irradiation, to compare with/verify the simulation results. The obtained results for transport behaviors in porous matter would provide a path to future complex simulations calculation and irradiation-resistant nanoporous materials design.

## 2. Materials and Methods

### 2.1. Simulation Codes

The software packages of SRIM (United States) are based on Monte Carlo method [22], which is commonly used to simulate the interaction of ion beam with homogeneous or quasi-homogeneous matters (such as laminated materials).

Deeper [23] (Damage crEation and Particle transport in matter, China) is another code based on Monte Carlo method, which can only be used to handle porous materials transport process with porosity less than 52.3%.

GEANT4 [24] is a Monte Carlo application toolkit developed by CERN (European Organization for Nuclear Research, Geneva, Switzerland), which is used to simulate the physical process of particle transport in matter. In this work, Deeper and GEANT4 were used to simulate the proton into nanoporous materials.

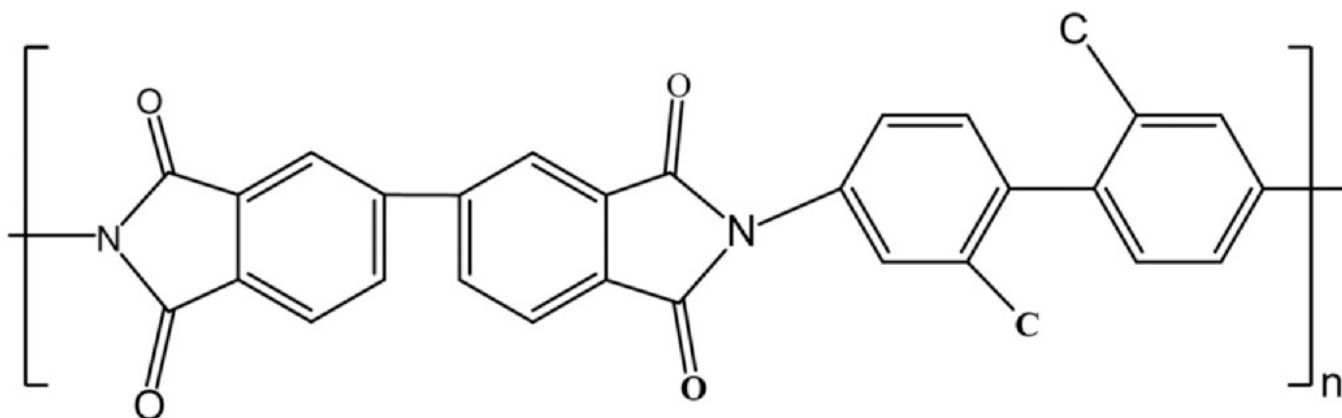
### 2.2. Proton Irradiation

The irradiation experiments were carried out using a ground simulator of space particle-radiation environments in Harbin Institute of Technology. This irradiation equipment can simulate proton, electron and ultraviolet radiation. The energy of proton and electron can be set from 30 to 200 keV, and the equipment details are described elsewhere [25]. In this work, the proton energy was set as 170 keV at a flux at  $5 \times 10^{11} \text{ cm}^{-2}\text{s}^{-1}$ . The proton fluence was set up to  $5 \times 10^{14} \text{ cm}^{-2}$  in the tests. During the irradiation, the

proton beam was incident perpendicular into the samples surface with scanning area of  $10 \times 10$  mm. The tested chamber was kept in a vacuum better than  $10^{-5}$  Pa.

### 2.3. Materials and Testing

In this work, the polyimide aerogels were obtained from Aerospace System Engineering (Shanghai, China), with specimen size  $10 \times 10 \times 5$  mm. The synthesis detail is described elsewhere [26], and the chemical structure is shown in Figure 1. The porosity of the pristine samples is 94%, and the skeleton density of polyimide is  $1.4 \text{ g}\cdot\text{cm}^{-3}$ , which is obtained using Helium pycnometer. The average pore size is measured as a diameter of 51 nm using 3H-2000PS2 nitrogen isotherm adsorption instruments, and the specific surface area is  $293 \text{ m}^2/\text{g}$  calculated by BET (Brunauer–Emmett–Teller) model. After the irradiation, the samples were notched from the non-irradiated side and fractured. The samples were coated with a platinum film for conductivity before observation, then A ZEISS field emission scanning electron microscopy from Merlin Compact was used to investigate the sample cross section. The acceleration voltage is 5 keV, and the working distance is 8 mm during tests.



**Figure 1.** The chemical structure of the repeating unit of the PI aerogel.

## 3. Results and Discussion

### 3.1. Simulation Part

#### 3.1.1. Porosity Effects

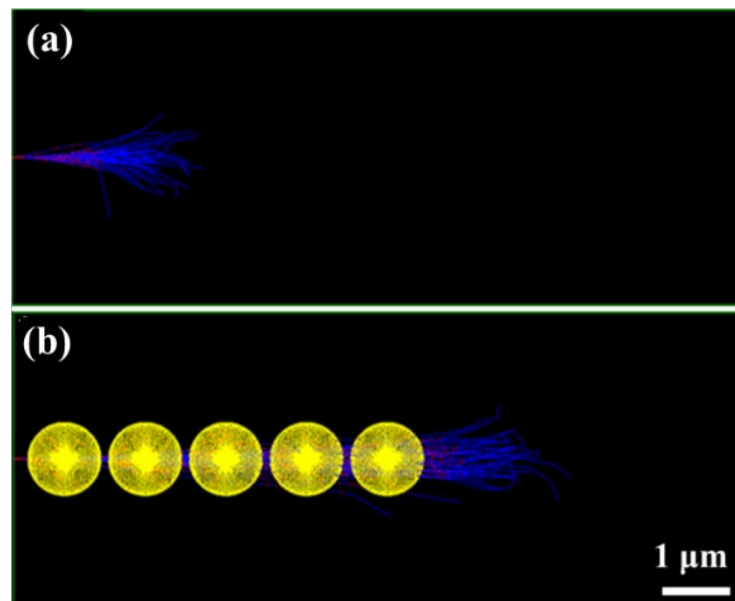
Figure 2 shows the comparison of the incident proton tracks in a solid and corresponding geometric structure with voids. It can be seen that the apparent range of the incident protons is seen much deeper and more scattered in the porous matter, implying that large number of nano-voids in the materials may exert drastic change (such as proton distribution, energy deposition, etc.) as compared with that in a normal solid matter.

In order to better understand the transport behavior of proton into nanoporous matter, a simple model was proposed for simulating the particle transport parameter in nanoporous solids, as shown in Figure 3.

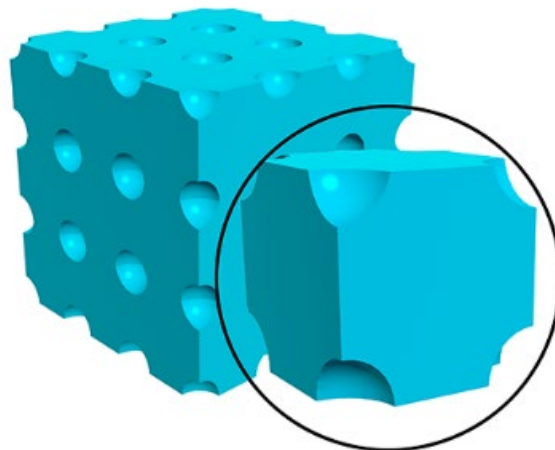
Given that the nano-porous materials are composed of spherical pores homogeneously distributed in a solid, the porous materials could be modeled as a continuous solid including periodic distributed spherical nano-holes or voids. The spacing of the adjacent voids in the coordination axes of  $X$ ,  $Y$  and  $Z$  could be defined as  $a$ ,  $b$  and  $c$ , respectively. The radius of voids is set as  $r$ . In this case, the incident particles (such as protons) should transport straightly within the voids. According to the above-defined scaling parameters, the porosity of the defined materials can be calculated using Formula (1):

$$\eta = \frac{4\pi r^3}{3abc} \quad (1)$$





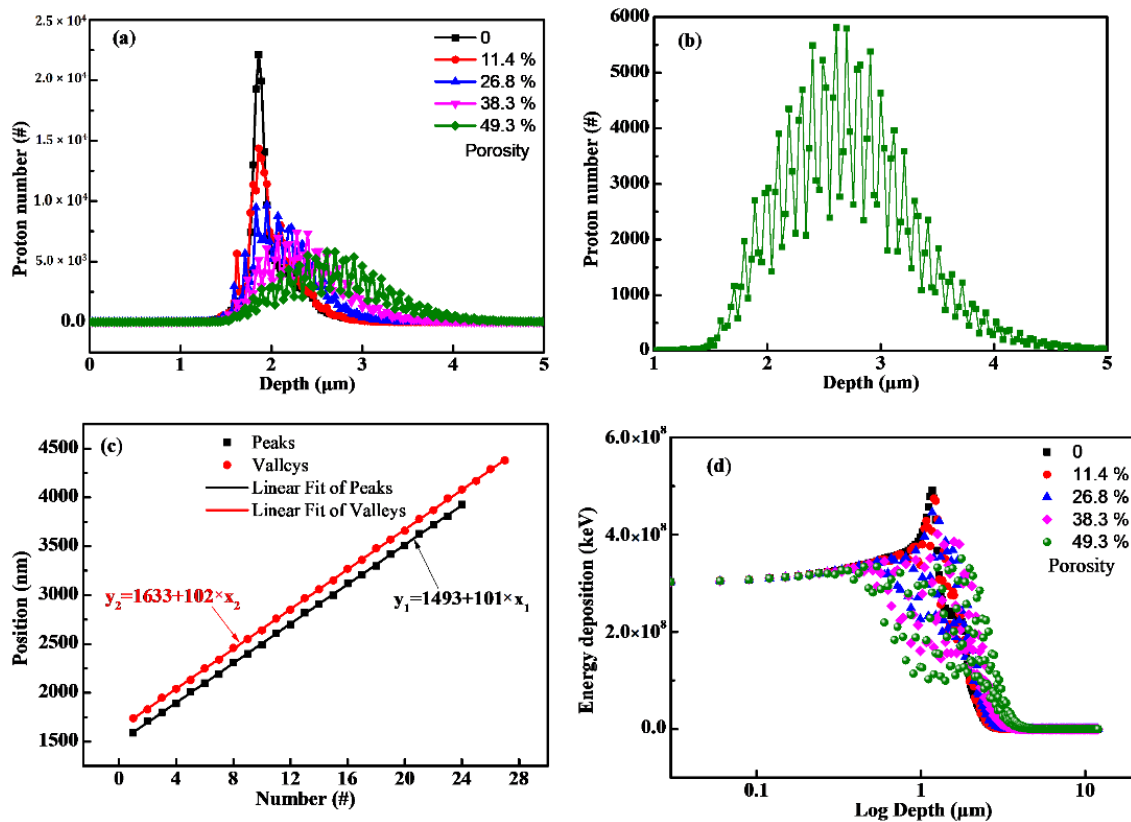
**Figure 2.** The transport behavior calculated by GEANT4: (a) Solid. (b) Geometric structure containing voids. (The black box represents the solid materials; the yellow balls represent the voids; the blue lines represent the ion tracks.).



**Figure 3.** The schematic diagram of spherical periodic porous structure.

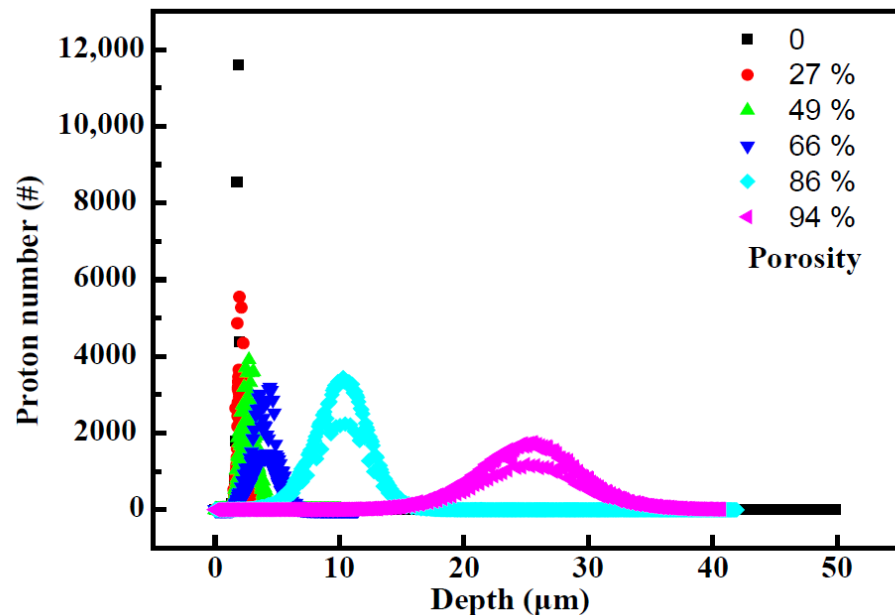
Based on the periodic nanoporous model, the transport behavior of proton into materials can be calculated using GEANT4 code. Figure 4a shows the simulated results of protons incident into different porosity materials. It can be seen that increasing the porosity, the proton range was observed increase together with a broadened Bragg peak. Moreover, one could also observe multiple subpeaks overlying on the Bragg peak. In order to analyze this phenomenon, the proton distribution curves at the porosity of 49.3% were enlarged, as shown in Figure 4b. It is worth noting that the overlying subpeaks appear periodically, and the periodic distance between adjacent sub-peaks is about 102 nm, the same as that of the adjacent voids. To better understand this phenomenon, the peak/valley positions and the corresponding numbers were counted, as shown in Figure 4c. Interestingly, there is an obvious linear relationship between the position and number of these subpeaks/valleys. The fitting slope of peaks and valleys is almost equivalent to the distance of adjacent voids (102 nm). In addition, the intercept represents the first apparent subpeak or subvalley in the distribution curves. In addition, the intercept of the peaks linear fitting equal to 14.6 times the adjacent void's distance (102 nm), while the intercept of the valleys is equal to 16 times the adjacent void's distance (102 nm). The results indicate the existence of voids would

cause the local inhomogeneity of proton distribution. More specifically, there are fewer protons deposited at the center position (namely, subvalleys position) of the spherical voids, and more protons deposited at the right of the spherical void's edge (namely, subpeaks position). Figure 4d depicts the relationship between energy deposition distribution and porosity. It shows similar characteristic to the proton distributions in the porous materials, namely energy deposition, tend to be deeper and broader in the materials when increasing the porosity. The results indicate that the existence of voids would magnify the transport process of protons and cause local inhomogeneity around the spherical voids.



**Figure 4.** (a) The relationship between proton distribution and porosity (the radius of the voids was set as 50 nm, and the distance between the adjacent voids was set as 102 nm, 111 nm, 125 nm and 166 nm, respectively); (b) a zoom view of 49.3% porosity in (a); (c) the position of peaks and valleys as a function of number; (d) the relationship between energy deposition and porosity.

However, due to the limitation of the geometric structure ( $2 \times r < a$ ), the porosity of this periodic model cannot exceed 52.3%. In this case, as the spherical pores are replaced by cubic ones, for modeling the porous materials, the porosity of the porous matter can vary from 0% to 100%. Figure 5 shows the relationship between proton distribution and porosity ranged from 0%~100%. One can see similar behaviors of proton incidents, into the materials with various porosities as the above simulated results, namely larger ranges, apparently broaden Bragg peak with overlying subpeaks and lower intensity in the end of the range.



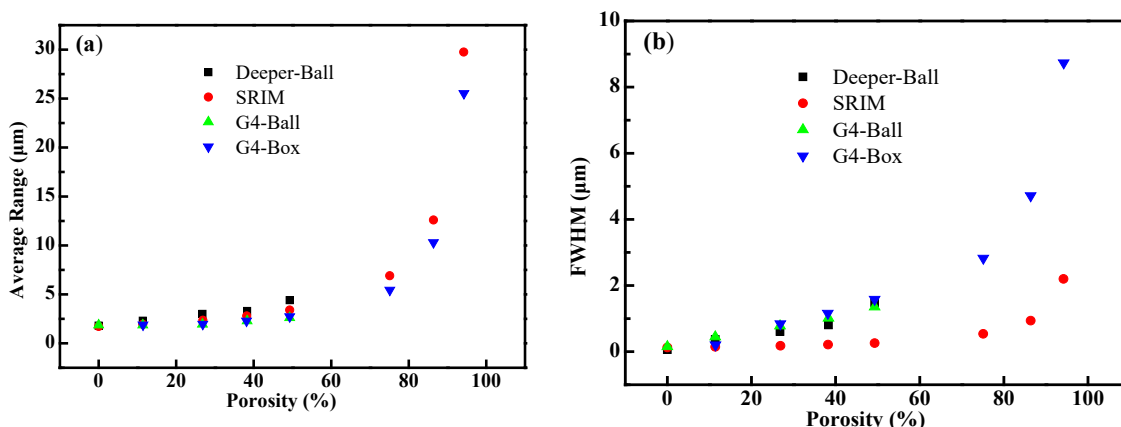
**Figure 5.** The relationship between porosity and proton distribution (the voids were set as a 100 nm cube, and the distance between the adjacent voids was set as 102 nm, 105 nm, 115 nm, 126.6 nm and 155 nm, respectively).

As comparison, the software of SRIM was also applied to evaluate the proton transport behavior in the porous materials, only if one assumes the porous materials as homogeneous, with lower density according to the porosity. Hence, the porous matter can be homogenized through Formula (2) and then the apparent density could be used for the SRIM simulation.

$$\rho = (1 - \eta) \cdot \rho_0 \quad (2)$$

where  $\rho_0$  is the density of the skeleton medium,  $\rho$  is the apparent density after homogenization and  $\eta$  is the porosity.

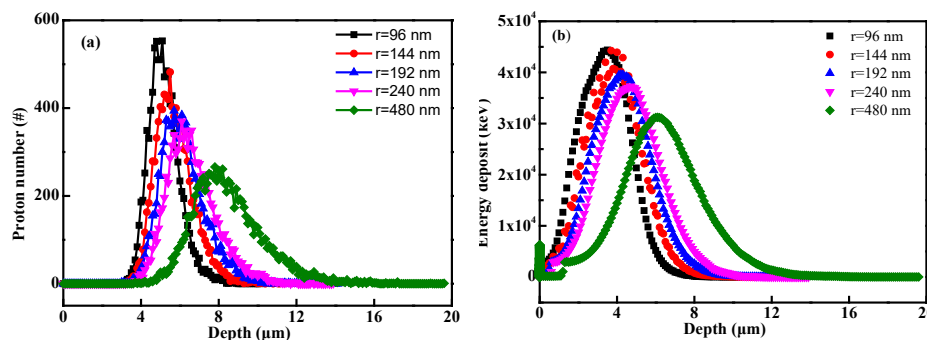
Figure 6 shows the simulation results calculated using different codes. It is understandable that for three cases simulated using GEANT4, Deeper and SRIM codes, the average proton ranges increase with the porosity in that the apparent density of the porous matter decreases accordingly (Figure 6a). However, the results of GEANT4/Deeper show some differences from those obtained using SRIM code. On one hand, the proton ranges simulated by any of the three codes (GEANT4, Deeper and SRIM) are almost the same as the porosity is smaller (Figure 6a), but when the porosity is larger than 50%, the calculated range using GEANT4 is smaller than that of SRIM. Hence, when the porosity is as large as 94%, the ranges calculated by GEANT4 and SRIM were 25.5 and 29.8  $\mu\text{m}$ , respectively. It is worth noting that this deviation becomes more pronounced as the porosity increases (Figure 6a). However, the FWHM (full width at half maxima) of the Bragg peak calculated by GEANT4 with cube voids is about 9  $\mu\text{m}$  at the porosity of 94%, while the FWHM is about 2  $\mu\text{m}$  using SRIM (Figure 6b). It can be concluded that existence of voids (GEANT4/Deeper) in solid causes more broaden distribution of incident particles than the density of the homogenized porous matter (SRIM), since that inhomogeneity in matter could enhance the scattering processes of the incident particle. When the porosity is less than 50%, SRIM [22] can be used to calculate the range of proton into porous matter, but when porosity increases, it is necessary to use GEANT4 [24] to deal with it.



**Figure 6.** The transport results calculated by different software (G4-Ball represents the GEANT4 simulation results with spherical voids, while the G4-Box represents the GEANT4 simulation results with cubic ones, and Deeper-ball represents the Deeper simulation results with spherical voids): (a) the relationship between average range and porosity; (b) the relationship between FWHM and porosity.

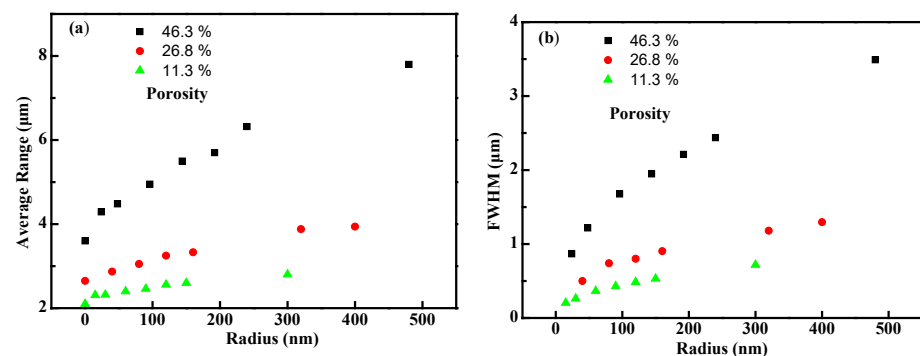
### 3.1.2. Voids Size Effect

In order to further explore the voids size effects on the transport process, the proton distribution was calculated while the porosity remains the same, and the results are shown in Figure 7. Interestingly, the distribution of protons became broader, while the range deepened, when increasing the pore radius, even though the porosity is same. Correspondingly, energy deposition in the porous matter distributes more broadly and tends to have deeper positions. The results indicated that the pore size would also magnify the transport straggling process of ion beam in matter, due to the coupling behavior between the scattering effects from the porous boundaries and the longer linear-transporting characteristic within the larger void.



**Figure 7.** (a) The relationship between proton distribution and pore size (the porosity was set as 46.3%, and the radius was set as 96, 144, 192, 240 and 480 nm, respectively); (b) the relationship between energy deposition and pore size.

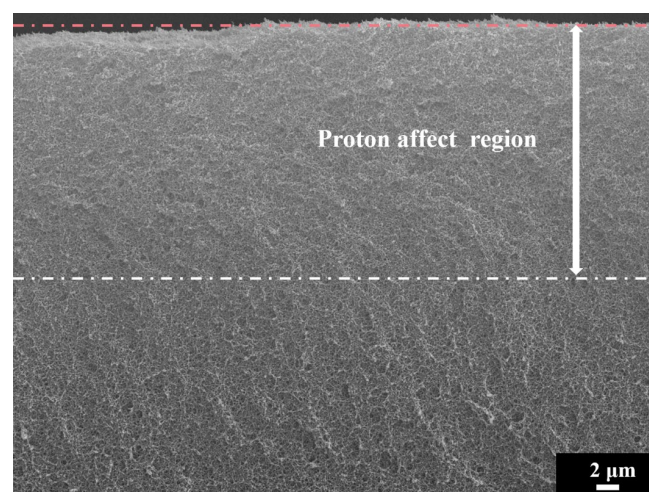
Figure 8 depicts the change rules of the proton range and the FWHM of Bragg peak as functions of the porous size. One can see that the proton range (Figure 8a) and FWHM (Figure 8b) increase with void radius without changing the porosity. On the other hand, there is an important parameter, called specific area, for a porous matter to define its performances. As we know, smaller void size means a larger specific surface area, as the matter porosity is constant [27]. Thus, the results shown in Figure 8 imply that with a constant porosity, the smaller the void size, the larger the specific surface area, and then the proton range and also the FWHM of its Bragg peak tend to be smaller. It is reasonable to say that the larger a specific surface area is, the more opportunities for the incident protons to interact with the surface/boundary and the higher the possibilities to be scattered and stopped [27], thus, a smaller proton average range and FWHM can be obtained.



**Figure 8.** (a) The relationship between proton range and radius of voids (when the porosity was kept at 46.3%, the radius was set as 24, 48, 96, 144, 192, 240 and 480 nm, respectively; when the porosity was kept at 26.8%, the radius was set as 40, 80, 120, 160, 320 and 400 nm, respectively; when the porosity was kept at 11.3%, the radius was set as 15, 30, 60, 90, 120, 150 and 300 nm, respectively); (b) the relationship between FWHM and radius of voids.

### 3.2. Experiments Part

In order to verify the simulated results, a proton irradiation experiment was carried out. Figure 9 depicts the SEM cross-section images of the polyimide aerogels (with a porosity of 98%) irradiated up to a proton fluence of  $5 \times 10^{14} \text{ cm}^{-2}$ . The cross-section image can be divided into two areas: damage area (proton effect area) and a damage-free one (out of proton range). It can be seen that the cross-section morphologies of the proton-irradiated sample show distinct features between the damaged area and damage-free area. The proton effect region is smoother and denser than the damage-free area, as reported in our previous work [28]. The average ranges calculated by GEANT4 and SRIM were 25.5 and 29.8  $\mu\text{m}$  (as shown in Figure 6), respectively. Hence, the thickness of the damaged zone is about 22.7  $\mu\text{m}$ , which is slightly smaller than the GEANT4 calculated result. This slight deviation should be attributed to the shrinkage of the aerogel during irradiation. However, there is a larger deviation to that simulated using SRIM code. It means that for a porous matter, there is some risk to evaluate the range or damaged behaviors with simulation methodology using the traditional SRIM code or density-homogenized equivalence modeling, and the higher the porosity is, the more risk for the evaluation process.



**Figure 9.** SEM cross-section images of polyimide aerogels after proton irradiations at fluences of  $5 \times 10^{14} \text{ cm}^{-2}$  (the orange dashed line is the upper edge of the sample' section, and the white dashed line is the boundary between the damaged area and damage-free area.).

#### 4. Conclusions

The transport behaviors of protons into nanoporous matter were investigated. The proton distribution moves to a deeper position and becomes wider as porosity increases, and the existence of voids causes the local inhomogeneity of proton distribution. Furthermore, the pore size affects the proton distribution, even though the porosity keeps same. The larger the void's size, the deeper the proton average range is, and the broader the FWHM of the Bragg peak. Comparing the different simulation codes, GEANT4 code could be more suitable to simulate the particle transporting processes, thus, to evaluate the inhomogeneous interaction and energy deposition behaviors, and to determine precisely the particle range.

**Author Contributions:** Conceptualization, Y.W. (You Wu) and Y.W. (Yiyong Wu); Methodology, C.S.; Software, H.W.; Validation, C.S., D.J. and Z.C.; Formal analysis, H.W. and Z.C.; Investigation, Y.W. (You Wu); Resources, O.V.T.; Data curation, D.J.; Writing—original draft preparation, Y.W. (You Wu); Writing—review and editing, Y.W. (Yiyong Wu) and D.J.; Visualization, H.W., O.V.T. and Z.C.; Supervision, Y.W. (Yiyong Wu) and D.J.; Project administration, H.W. and C.S.; Funding acquisition, Y.W. (Yiyong Wu) and D.J. All authors have read and agreed to the published version of the manuscript.

**Funding:** This research was funded by [National Natural Science Foundation of China] grant number [21975248].

**Institutional Review Board Statement:** Not applicable.

**Informed Consent Statement:** Not applicable.

**Data Availability Statement:** The data that support the findings of this study are available from the corresponding author, [Yiyong Wu and Dandan Ju], upon reasonable request.

**Acknowledgments:** This work was supported by the National Natural Science Foundation of China (No21985248), 111 Project, the Fundamental Research Funds for the Central Universities and the Open Foundation from National Key Laboratory of Materials Behavior and Evaluation Technology in Space Environments (2021XXX).

**Conflicts of Interest:** The authors declare that they have no known competing financial interests or personal relationships that could have appeared to influence the work reported in this paper.

#### References

1. Beyerlein, I.J.; Caro, A.; Demkowicz, M.J.; Mara, N.A.; Misra, A.; Uberuaga, B.P. Radiation damage tolerant nanomaterials. *Mater. Today* **2013**, *16*, 443–449. [[CrossRef](#)]
2. Li, J.; Wang, H.; Zhang, X. A Review on the Radiation Response of Nanoporous Metallic Materials. *JOM* **2018**, *70*, 2753–2764. [[CrossRef](#)]
3. Caro, M.; Mook, W.M.; Fu, E.G.; Wang, Y.Q.; Sheehan, C.; Martinez, E.; Baldwin, J.K.; Caro, A. Radiation induced effects on mechanical properties of nanoporous gold foams. *Appl. Phys. Lett.* **2014**, *104*, 233109. [[CrossRef](#)]
4. Cheng, Y.; Yao, H.; Duan, J.; Xu, L.; Zhai, P.; Lyu, S.; Chen, Y.; Maaz, K.; Mo, D.; Sun, Y.; et al. Surface Modification and Damage of MeV-Energy Heavy Ion Irradiation on Gold Nanowires. *Nanomaterials* **2017**, *7*, 108. [[CrossRef](#)]
5. Fu, E.G.; Caro, M.; Zepeda-Ruiz, L.A.; Wang, Y.Q.; Baldwin, K.; Bringa, E.; Nastasi, M.; Caro, A. Surface effects on the radiation response of nanoporous Au foams. *Appl. Phys. Lett.* **2012**, *101*, 191607. [[CrossRef](#)]
6. Li, N.; Fu, E.G.; Wang, H.; Carter, J.J.; Shao, L.; Maloy, S.A.; Misra, A.; Zhang, X. He ion irradiation damage in Fe/W nanolayer films. *J. Nucl. Mater.* **2009**, *389*, 233–238. [[CrossRef](#)]
7. Sun, C.; Bufford, D.; Chen, Y.; Kirk, M.A.; Wang, Y.Q.; Li, M.; Wang, H.; Maloy, S.A.; Zhang, X. In situ study of defect migration kinetics in nanoporous Ag with enhanced radiation tolerance. *Sci. Rep.* **2014**, *4*, 3737. [[CrossRef](#)]
8. Hu, Z.Y.; Chen, H.Q.; Zhao, Y.B.; Wang, P.P.; Yang, K.J.; Zhang, J.; Liu, Z.L.; Wang, X.J.; Fu, E.G. Abundant free surface in nanoporous copper films enhancing tolerance against helium ion irradiation. *J. Alloy. Compd.* **2020**, *843*, 155829. [[CrossRef](#)]
9. Bringa, E.M.; Monk, J.D.; Caro, A.; Misra, A.; Zepeda-Ruiz, L.; Duchaineau, M.; Abraham, F.; Nastasi, M.; Picraux, S.T.; Wang, Y.Q.; et al. Are nanoporous materials radiation resistant? *Nano Lett.* **2012**, *12*, 3351–3355. [[CrossRef](#)]
10. Li, J.; Fan, C.; Ding, J.; Xue, S.; Chen, Y.; Li, Q.; Wang, H.; Zhang, X. In situ heavy ion irradiation studies of nanopore shrinkage and enhanced radiation tolerance of nanoporous Au. *Sci. Rep.* **2017**, *7*, 39484. [[CrossRef](#)]
11. Yang, T.; Huang, X.; Wang, C.; Zhang, Y.; Xue, J.; Yan, S.; Wang, Y. Enhanced structural stability of nanoporous zirconia under irradiation of He. *J. Nucl. Mater.* **2012**, *427*, 225–232. [[CrossRef](#)]

12. Chen, Y.; Liu, Y.; Fu, E.G.; Sun, C.; Yu, K.Y.; Song, M.; Li, J.; Wang, Y.Q.; Wang, H.; Zhang, X. Unusual size-dependent strengthening mechanisms in helium ion-irradiated immiscible coherent Cu/Co nanolayers. *Acta Mater.* **2015**, *84*, 393–404. [[CrossRef](#)]
13. Li, J.; Chen, Y.; Wang, H.; Zhang, X. In situ study on enhanced heavy ion irradiation tolerance of porous Mg. *Scr. Mater.* **2018**, *144*, 13–17. [[CrossRef](#)]
14. Li, J.; Fan, C.; Li, Q.; Wang, H.; Zhang, X. In situ studies on irradiation resistance of nanoporous Au through temperature-jump tests. *Acta Mater.* **2018**, *143*, 30–42. [[CrossRef](#)]
15. Zhou, K.; Li, W.; Patel, B.B.; Tao, R.; Chang, Y.; Fan, S.; Diao, Y.; Cai, L. Three-Dimensional Printable Nanoporous Polymer Matrix Composites for Daytime Radiative Cooling. *Nano Lett.* **2021**, *21*, 1493–1499. [[CrossRef](#)]
16. Rathilal, S. Adsorption and Photocatalytic Mineralization of Bromophenol Blue Dye with TiO<sub>2</sub> Modified with Clinoptilolite/Activated Carbon. *Catalysts* **2020**, *11*, 7.
17. Sibiya, N.P.; Rathilal, S.; Tetteh, E.K. Coagulation Treatment of Wastewater: Kinetics and Natural Coagulant Evaluation. *Molecules* **2021**, *26*, 698. [[CrossRef](#)]
18. Tetteh, E.K.; Rathilal, S. Evaluation of different polymeric coagulants for the treatment of oil refinery wastewater. *Cogent. Eng.* **2020**, *7*, 1785756. [[CrossRef](#)]
19. Tetteh, E.K.; Rathilal, S. Application of organic coagulants in water and wastewater treatment. In *Organic Polymers*; IntechOpen: London, UK, 2019. [[CrossRef](#)]
20. Li, M.; Gan, F.; Dong, J.; Fang, Y.; Zhao, X.; Zhang, Q. Facile Preparation of Continuous and Porous Polyimide Aerogel Fibers for Multifunctional Applications. *ACS Appl. Mater. Interfaces* **2021**, *13*, 10416–10427. [[CrossRef](#)]
21. Yamagishi, A.; Yokobori, S.I.; Kobayashi, K.; Mita, H.; Yabuta, H.; Tabata, M.; Higashide, M.; Yano, H. Scientific Targets of Tanpopo: Astrobiology Exposure and Micrometeoroid Capture Experiments at the Japanese Experiment Module Exposed Facility of the International Space Station. *Astrobiology* **2021**, *21*, 1451–1460. [[CrossRef](#)]
22. Ziegler, J.F.; Ziegler, M.D.; Biersack, J.P. SRIM—The stopping and range of ions in matter. *Nucl. Instrum. Methods Phys. Res. Sect. B Beam Interact. Mater. At.* **2010**, *268*, 1818–1823. [[CrossRef](#)]
23. Yan, Q.; Shao, L. A Monte Carlo simulation code for calculating damage and particle transport in solids: The case for electron-bombarded solids for electron energies up to 900 MeV. *J. Nucl. Mater.* **2017**, *485*, 98–104. [[CrossRef](#)]
24. Agostinelli, S.; Allison, J.; Amako, K.; Apostolakis, J.; Araujo, H.; Arce, P.; Asai, M.; Axen, D.; Banerjee, S.; Barrand, G.; et al. GEANT4—A simulation toolkit. *Nucl. Instrum. Methods Phys. Res. Sect. A Accel. Spectrometers Detect. Assoc. Equip.* **2003**, *506*, 250–303. [[CrossRef](#)]
25. Wu, Y.; Sun, C.; Wu, Y.; Xing, Y.; Xiao, J.; Guo, B.; Wang, Y.; Sui, Y. The degradation behavior and mechanism of polytetrafluoroethylene under low energy proton irradiation. *Nucl. Instrum. Methods Phys. Res.* **2018**, *430*, 47–53. [[CrossRef](#)]
26. Fang, G.; Li, H.; Liu, J.; Ni, H.; Yang, H.; Wang, G. Intrinsically Atomic-oxygen Resistant POSS-containing Polyimide Aerogels: Synthesis and Characterization. *Chem. Lett.* **2015**, *44*, 1083–1085. [[CrossRef](#)]
27. Xie, T.; Xu, K.; Yang, B.; He, Y. Effect of pore size and porosity distribution on radiation absorption and thermal performance of porous solar energy absorber. *Sci. China Technol. Sci.* **2019**, *62*, 2213–2225. [[CrossRef](#)]
28. Wu, Y.; Ju, D.; Wang, H.; Zhao, H.; Sun, C.; Wu, Y.; Guo, B.; Wang, Y. Modification of surface structure and mechanical properties in polyimide aerogel by low-energy proton implantation. *Surf. Coat. Technol.* **2020**, *403*, 126364. [[CrossRef](#)]

Article

# Rotational Particle Separation in Solutions: Micropolar Fluid Theory Approach

Vladimir Shelukhin <sup>1,2</sup><sup>1</sup> Lavrentyev Institute of Hydrodynamics, 630090 Novosibirsk, Russia; shelukhin@list.ru<sup>2</sup> Novosibirsk State University, 630090 Novosibirsk, Russia

**Abstract:** We develop a new mathematical model for rotational sedimentation of particles for steady flows of a viscoplastic granular fluid in a concentric-cylinder Couette geometry when rotation of the Couette cell inner cylinder is prescribed. We treat the suspension as a micro-polar fluid. The model is validated by comparison with known data of measurement. Within the proposed theory, we prove that sedimentation occurs due to particles' rotation and rotational diffusion.

**Keywords:** suspensions; micro-polar fluids; yield stress

**Citation:** Shelukhin, V. Rotational Particle Separation in Solutions: Micropolar Fluid Theory Approach. *Polymers* **2021**, *13*, 1072. <https://doi.org/10.3390/polym13071072>

Academic Editor: Célio Pinto Fernandes

Received: 17 February 2021

Accepted: 24 March 2021

Published: 29 March 2021

**Publisher's Note:** MDPI stays neutral with regard to jurisdictional claims in published maps and institutional affiliations.



**Copyright:** © 2021 by the authors. Licensee MDPI, Basel, Switzerland. This article is an open access article distributed under the terms and conditions of the Creative Commons Attribution (CC BY) license (<https://creativecommons.org/licenses/by/4.0/>).

## 1. Introduction

The classical water-based drilling muds contain only water and clay and their performances are generally poor. Polymers used in drilling fluids improve stability and cutting removal. Currently, the polymer-based drilling fluids represent 15 to 18% of the total cost (about 1 million) of petroleum well drilling [1]. The reason is that such fluids appear to have load carrying capabilities, or, in other words, a yield stress, associated with the solid-like state and which primarily arises from the colloidal forces between the smallest suspended particles. Furthermore, in such systems, when the agitation is increased, a fluid-like state is recovered. Even in the fluid state, these materials usually show highly nonlinear behavior. The complex rheology related to the change of the internal state in the suspensions is still rather poorly understood.

Due to scale separation between colloidal and non-colloidal particles, polymer-based drilling muds with cuttings and other materials (concrete casting, foodstuff transport, etc.) can be considered as suspensions of noncolloidal particles embedded in a yield stress fluid. Substantial progress in the understanding of the behavior of such materials can thus be made by studying the impact of adding noncolloidal particles to a yield stress fluid of known properties [2]. Here, we develop a new mathematical model for suspensions embedded in a polymer-based fluid. To validate the approach, we consider rotation flows between two concentric cylinders when the external cylinder is fixed and the inner one rotates with a prescribed speed. The principal feature of such flows is the particles' migration toward the external boundary.

It is proved by Svedberg [3] that the particles' migration effect occurs also in pure colloidal suspensions. Moreover, sedimentation happens at high rotations. Currently, Svedberg's ultracentrifugation is known as an effective tool for studies of interaction between macromolecules of colloidal systems [4]. In this method, a highly disperse colloidal solution is enclosed in a wedge-shape cell rotating about an axis coinciding with the apex of the wedge [5]. Samples are centrifuged at speeds to produce sedimentation and shallow concentration gradients. A great progress in the study of such a flow was achieved by applying the diffusive Lamm equation based on the special empirical sedimentation coefficient [6]. Here, we restrict ourself to rotation flows of suspensions between two concentric cylinders paying attention to comparison with known laboratory experiments. We use methods of mechanics of a continuum by applying conservation laws only and



not involving the concept of sedimentation coefficient inherent in the Lamm equation. However, we also obtain the sedimentation effect.

We take into account particles rotation and rotational diffusion. To this end, we apply the theory of micropolar fluids which allows for particles rotation and microinertia. According to this theory, which is a part of rational mechanics, any infinitesimal volume contains sufficiently many particles. This is why such an approach is good for colloidal solutions. However, the micropolar fluid theory turned out to be useful in the study of suspension of noncolloidal particles and also including granular fluids. As is proved in [7], it is due to particle rotation that the Segré–Silberberg effect occurs [8]. Such an effect is known as a tubular pinch phenomenon stating that particles tend to migrate towards a concentric annular region for the laminar flow of neutrally buoyant dilute suspension of rigid spheres through a circular tube.

Important sectors handling granular fluids include civil engineering (bitumen, concrete, embankments, ballast trains, soil stability), mining (extraction, transport), the chemical industry (fuel and catalysts are often deployed in the form of grains in order to maximize the surface of exchange), the pharmaceutical industry (from the handling of powders for the manufacture of medicine to the handling of drugs themselves) and the food industry (animal food, cereals), to name but a few.

Results from laboratory experiments, numerical simulations, and theoretical approaches from other fields have enriched and renewed our understanding of granular fluids. In many rheological papers on shear flows, particle rotation is ignored. Instead, the authors apply the theory which states that microstructural non-homogeneous particles distribution is due to anisotropy. To this end, the rheological equations involve not only shear stress but normal stress differences as well [9]. The micro-polar fluid theory stands out among other approaches since it handles particle rotations and micro-inertia effects within the mechanics of continua. Such a theory finds many applications in granular flows [10], electrorheology [11,12], ferrofluids [13], visco-elastic micro-polar fluids [14], and liquid crystals [15]. Some results concern blood rheology [16–18]. Particularly, explanations were provided for phenomena including the Fåhræus–Lindqvist effect, the Fåhræus effect, and the plasma skimming effect [19–22]. Any new theory involves additional unknown rheological constants. This restricts applications and further progress. In the micro-polar theory, one such constant is a relative viscosity. What is it? First, we comment on the ordinary fluid viscosity.

In simple shear flows of typical Newtonian or non-Newtonian fluids, viscosity  $\eta_s [Pa \cdot s]$  is given by the formula  $\eta_s = \tau / \dot{\gamma}$  or

$$\tau = \eta_s \dot{\gamma}, \quad (1)$$

where  $\tau$  is the shear stress and  $\dot{\gamma}$  is the shear rate. The rates' definition will be given below.

In the micro-polar fluid theory allowing for internal spins, stress tensor loses symmetry, couple stress appears, and the angular momentum equation should be included into conservation laws. Instead of Equation (1), one writes for simple shear flows the following equation:

$$\tau = \sqrt{(\eta_s \dot{\gamma})^2 + (\eta_{sk} \dot{\gamma}_a)^2}, \quad (2)$$

where  $\dot{\gamma}_a$  is a shear rate related to particle rotation, and  $\eta_{sk}$  is an additional viscosity. In what follows, we call  $\eta_{sk}$  skew-symmetrical viscosity motivated by rheological relationships which will be discussed later.

When the volume concentration of particles  $\phi$  is equal to zero, the viscosity  $\eta_s$  of the interstitial fluid is assumed to be known. Clearly,  $\eta_s$  is the usual shear viscosity and it is well known how it can be measured. The skew-symmetric viscosity manifests itself when  $\phi > 0$ , and poor knowledge of it hampers applications of the micro-polar fluid models. The above description of possible applications supports the view that it is of importance to know how skew-symmetric viscosity depends on the particle concentration. The goal of the first sections of the present paper is to get a better insight of how  $\eta_{sk}$  depends on  $\phi$ .

In Sections 1–5, we validate some formula for the skew-symmetric viscosity and apply it in Section 6 to the problem of particles migration for the steady flows of yield stress granular fluids in a concentric-cylinder Couette geometry when rotation of the Couette cell inner cylinder is prescribed.

## 2. Micro-Polar Fluids

Here, we remind notions concerning a micropolar fluid within the theory of the Cosserat continuum. Such a fluid exhibits micro-rotational effects and micro-rotational inertia; the fluid can support couple stresses and body couples and possesses a non-symmetric stress tensor. The theory of micro-polar fluids goes back to [23–25], where gyration tensor, inertial spin, conservation of micro-inertia, and objectivity of micro-deformation rate tensors are derived and discussed. For an overview of developed theories, we refer the reader to [26,27].

In the Cosserat continuum [28], each material point is treated as a rigid body in the following sense. To such a point with the Lagrange coordinates  $(t, \boldsymbol{\zeta})$ , one can assign a position vector  $\mathbf{x}(t, \boldsymbol{\zeta})$  in the three-dimensional Euclidean space and three orthogonal directors  $\mathbf{d}_i(t, \boldsymbol{\zeta})$ ,  $i = 1, 2, 3$ . Rotation of the vectors  $\mathbf{d}_i$  is governed by a rotation orthogonal tensor  $\mathbf{Q}(t, \boldsymbol{\zeta})$ . The rotation velocity tensor

$$\boldsymbol{\Omega}(t, \mathbf{x}) = \mathbf{Q}_t \mathbf{Q}^*$$

is skew-symmetric, and it enjoys the representation formula

$$\boldsymbol{\Omega} \cdot \mathbf{h} = \boldsymbol{\omega} \times \mathbf{h} \quad \forall \quad \mathbf{h} \in \mathbb{R}^3, \quad (\boldsymbol{\Omega} \cdot \mathbf{h})_i \equiv \Omega_{ij} h_j,$$

where  $\boldsymbol{\omega}(t, \mathbf{x})$  is the micro-rotational velocity vector,

$$2\boldsymbol{\omega} = \mathbf{e}_i \times (\boldsymbol{\Omega} \cdot \mathbf{e}_i) = \boldsymbol{\epsilon} : \boldsymbol{\Omega}.$$

Here,  $\{\mathbf{e}_i\}_1^3$  is any orthogonal basis in  $\mathbb{R}^3$ , and  $\boldsymbol{\epsilon}$  is the Levi–Civita third order tensor,

$$\boldsymbol{\epsilon} \langle \mathbf{a}, \mathbf{b}, \mathbf{c} \rangle = \mathbf{a} \cdot (\mathbf{b} \times \mathbf{c}), \quad \mathbf{e}_i \times \mathbf{e}_j = \epsilon_{sij} \mathbf{e}_s, \quad \epsilon_{sij} \equiv \boldsymbol{\epsilon} \langle \mathbf{e}_s, \mathbf{e}_i, \mathbf{e}_j \rangle, \quad (\boldsymbol{\epsilon} : \boldsymbol{\Omega})_i \equiv \epsilon_{ijk} \Omega_{jk}.$$

Given a  $3 \times 3$ -matrixes  $A$  and  $B$ , we use the notation  $A^*$  for the adjoint matrix such that

$$\mathbf{a} \cdot (A \cdot \mathbf{b}) = \mathbf{b} \cdot (A^* \cdot \mathbf{a}) \quad \forall \mathbf{a}, \mathbf{b} \in \mathbb{R}^3, \quad (A^*)_{ij} = A_{ji},$$

and the scalar product  $A : B$  is defined by  $A : B = A_{ij} B_{ij}$ .

With  $\mathbf{v}(t, \mathbf{x})$  standing for the velocity of the mass center of the Cosserat material point  $(t, \boldsymbol{\zeta})$ , the micropolar fluid is characterized by two rates of strain tensors  $B$  and  $A$ :

$$B = \nabla \mathbf{v} - \boldsymbol{\Omega}, \quad A = \nabla \boldsymbol{\omega}. \tag{3}$$

Here, we use the notations  $(\nabla \mathbf{v})_{ij} = \partial v_i / \partial x_j$ ,  $(\nabla \mathbf{v})_{ij}^* = \partial v_j / \partial x_i$ . An instant stress state of such a fluid is characterized by the couple stress tensor  $\mathbf{N}(t, \mathbf{x})$  in addition to the Cauchy stress tensor  $\mathbf{T}(t, \mathbf{x})$ . Let  $S$  stand for the viscous part of the stress tensor,  $\mathbf{T} = -p \mathbf{I} + S$ . In what follows, we use the symmetric and skew-symmetric parts of a matrix  $D$ :

$$D_s = \frac{D + D^*}{2}, \quad D_a = \frac{D - D^*}{2}.$$

In the typical stress–strain relation

$$\mathbf{T} = -p \mathbf{I} + 2\eta_s \cdot (\nabla \mathbf{v})_s, \tag{4}$$

of Newtonian or non-Newtonian fluids, the scalar factor  $\eta_s$  is the viscosity,  $p$  is the pressure, with  $\mathbf{I}$  and  $\mathbf{T}$  being the identity and stress tensors. The tensor  $\mathbf{T}$  is symmetric as is well

known in the classical fluid mechanics theory, i.e.,  $T^* = T$ . Such a symmetry results from momentum and angular momentum laws. On the other hand, the angular momentum law is valid automatically if we postulate symmetry of  $T$ . This is why nobody invokes such a law in applications.

We remind readers that the constitutive laws of a simple micropolar fluid are [26]

$$T = -pI + S, \quad S = 2\eta_s B_s + 2\eta_{sk} B_a, \quad N = 2\gamma A, \tag{5}$$

where  $\eta_s, \eta_{sk}$  are the viscosities and  $\gamma$  is angular viscosity. The first rheological equation in (5) suggests that the contributions of the symmetric part  $B_s = (\nabla \mathbf{v})_s$  and skew-symmetric part  $B_a$  of the rate of strain tensor  $B$  into local stress state are different. It is proved in [25] that both the rate of strain tensors  $B$  and  $A$  are objective.

Let us introduce the relative angular velocity

$$\omega_r = \omega - \text{rot } \mathbf{v} / 2.$$

Observe that in fluid mechanics shear stress and shear rates in (1) are defined as follows:

$$\tau = \sqrt{S : S / 2}, \quad \dot{\gamma} = \sqrt{2B_s : B_s}, \quad \dot{\gamma}_a = \sqrt{2B_a : B_a} = 2|\omega_r|.$$

Due to the identity  $2(\nabla \mathbf{v})_a \cdot \mathbf{h} = \text{rot } \mathbf{v} \times \mathbf{h} \quad \forall \mathbf{h}$ , we have

$$B_a \cdot \mathbf{h} = -\omega_r \times \mathbf{h} \quad \forall \mathbf{h}.$$

Thus, the skew-symmetric viscosity characterizes how relative micro-rotations contribute into the local stress state.

Observe that in the Cosserat continua the Cauchy stress tensor is not symmetric and the vector

$$\mathbf{t} = \mathbf{e}_i \times (T \cdot \mathbf{e}_i) = \epsilon : T$$

is a stress symmetry defect measure in the sense that the equality  $\mathbf{t} = 0$  implies  $T^* = T$  and vice versa. By definition of  $\mathbf{t}$ , we have the formula

$$\mathbf{t} \cdot \omega = T : \Omega. \tag{6}$$

The momentum and the angular momentum laws are

$$\frac{\partial(\rho \mathbf{v})}{\partial t} + \text{div}(\rho \mathbf{v} \otimes \mathbf{v}) = -\nabla p + \text{div } S + \rho \mathbf{f}, \tag{7}$$

$$J \left( \frac{\partial(\rho \omega)}{\partial t} + \text{div}(\omega \otimes \rho \mathbf{v}) \right) = \text{div } N - \epsilon : S, \tag{8}$$

where  $\rho$  is the density,  $J$  is the micro-inertia scalar,  $\mathbf{f}$  is the mass force vector and

$$(\text{div } N)_i \equiv \partial N_{ij} / \partial x_j, \quad (\omega \otimes \mathbf{v})_{ij} = \omega_i v_j.$$

The density  $\rho$  satisfies the mass conservation law

$$\dot{\rho} + \rho \text{div } \mathbf{v} = 0. \tag{9}$$

### 3. Skew-Symmetrical Viscosity of Dilute Suspensions of Rigid Particles

Let us consider Couette-like steady flows of suspensions between two parallel planes in the  $x$ -direction when the upper plane  $y = h$  is fixed and the lower plane  $y = 0$  moves in the  $x$ -direction with the velocity  $V$ . The volume particle concentration  $\phi$  is assumed to be fixed.

We outline the method for determination of the skew-symmetrical viscosity  $\eta_{sk}$ . Assume that the stress applied to the moving plate can be measured. By continuity, one can

tell the fluid stress in the nearby fluid region. On the other hand, one can calculate such a fluid stress by one or another mathematical model. First, we determine the stress  $S_1^m$  at the moving plane by applying the micro-polar fluid theory. Then, we calculate the stress  $S_1^v$  at the moving plane by applying the Navier–Stokes theory. We equate the two stresses and derive the skew-symmetrical viscosity  $\eta_{sk}$  from the equality  $S_1^m = S_1^v$ .

Let us first treat the suspension as a micropolar fluid with the prescribed volume particle concentration  $\phi$ . The above assumptions upon the flows suggest that the velocity vector  $\mathbf{v}$ , the micro-rotational velocity vector  $\boldsymbol{\omega}$  and the pressure  $p$  depend on the vertical variable  $y$  only:

$$\mathbf{v} = v(y)(1, 0, 0)^T, \quad \boldsymbol{\omega} = \omega(y)(0, 0, 1)^T, \quad p = p(y), \quad 0 < y < h.$$

For such flows, the matrices  $\nabla \mathbf{v}$  and  $\Omega$  become

$$\nabla \mathbf{v} = \begin{pmatrix} 0 & v_y & 0 \\ 0 & 0 & 0 \\ 0 & 0 & 0 \end{pmatrix}, \quad \Omega = \begin{pmatrix} 0 & -\omega & 0 \\ \omega & 0 & 0 \\ 0 & 0 & 0 \end{pmatrix}, \quad \frac{\partial v}{\partial y} = v_y.$$

Hence,

$$B_s = \begin{pmatrix} 0 & v_y/2 & 0 \\ v_y/2 & 0 & 0 \\ 0 & 0 & 0 \end{pmatrix}, \quad B_a = \begin{pmatrix} 0 & v_y/2 + \omega & 0 \\ -v_y/2 - \omega & 0 & 0 \\ 0 & 0 & 0 \end{pmatrix}$$

Projections of the momentum and the angular momentum equations on the  $x$  and  $z$ -directions become

$$0 = \frac{\partial S_{12}}{\partial y}, \tag{10}$$

$$0 = \frac{\partial N_{32}}{\partial y} + S_{21} - S_{12}, \tag{11}$$

respectively, where the tensor components are given by the formulas

$$S_{21} = \mathbf{e}_y \cdot \mathbf{S} \langle \mathbf{e}_x \rangle, \quad S_{12} = \mathbf{e}_x \cdot \mathbf{S} \langle \mathbf{e}_y \rangle, \quad N_{32} = \mathbf{e}_z \cdot \mathbf{N} \langle \mathbf{e}_y \rangle.$$

Constitutive laws (5) take the form

$$S_{12} = (\eta_s + \eta_{sk}) \frac{\partial v}{\partial y} + 2\eta_{sk}\omega, \quad S_{21} = (\eta_s - \eta_{sk}) \frac{\partial v}{\partial y} - 2\eta_{sk}\omega. \tag{12}$$

We note that system (10)–(11) does not contain pressure. As is well known, it can be restored from the momentum equation projected on the  $y$ -direction.

The viscosity  $\eta_{sk}(\phi)$  vanishes when  $\phi \rightarrow 0$ . The same is true for the relative viscosity

$$\varepsilon(\phi) = \frac{\eta_{sk}(\phi)}{\eta_s},$$

which we represent via the expansion series

$$\varepsilon(\phi) = \Lambda\phi + \Lambda_2\phi^2 + \dots$$

Whereas the velocity  $\mathbf{v}$  satisfies the no-slip boundary conditions, we require that

$$\boldsymbol{\omega} = \alpha(\phi) \text{rot } \mathbf{v} / 2 \quad \text{at } y = 0 \quad \text{and } y = h, \tag{13}$$

where  $\alpha(\phi) = \alpha_0\phi$ . The latter condition implies that the micro-rotations agree with macro-rotations at the boundary [29]. For the Couette-like flows, we arrive at the following boundary-value problem in the domain  $0 < y < h$ :

$$\frac{\partial}{\partial y} \left[ (1 + \varepsilon(\phi)) \frac{\partial v}{\partial y} + 2\varepsilon(\phi)\omega \right] = 0, \tag{14}$$

$$2\gamma \frac{\partial^2 \omega}{\partial y^2} - 2\eta_s \varepsilon(\phi) \left( \frac{\partial v}{\partial y} + 2\omega \right) = 0, \tag{15}$$

$$v|_{y=0} = V, \quad v|_{y=h} = 0, \quad \omega|_{y=0,h} = -\frac{\alpha_0 \phi}{2} \frac{\partial v}{\partial y} \Big|_{y=0,h}. \tag{16}$$

We solve the boundary value problem (14)–(16) looking for  $(v, \omega)$  as the asymptotic expansion series

$$v(y, \phi) = v^0(y) + v^1(y)\phi + \dots, \quad \omega(y, \phi) = \omega^0(y) + \omega^1(y)\phi + \dots. \tag{17}$$

Setting these series in (14)–(16), one can write each equality in (14)–(16) in the form

$$\phi^0(\dots)_0 + \phi^1(\dots)_1 + \dots = 0.$$

The coefficients  $v^i$  and  $\omega^j$  are determined from the conditions  $(\dots)_k = 0$  for any  $k$ .

Particularly, if  $k = 0$ , we derive the following boundary value problems for the functions  $v^0(y), \omega^0(y)$ :

$$\frac{\partial^2 v^0}{\partial y^2} = 0, \quad v^0|_{y=0} = V, \quad v^0|_{y=h} = 0, \tag{18}$$

$$0 = \frac{\partial^2 \omega^0}{\partial y^2}, \quad \omega^0|_{y=0} = \omega^0|_{y=h} = 0. \tag{19}$$

Similarly, we find that the function  $v^1$  satisfies the boundary value problem

$$\frac{\partial}{\partial y} \left[ \frac{\partial v^1}{\partial y} + \Lambda \left( \frac{\partial v^0}{\partial y} + 2\omega^0 \right) \right] = 0, \quad v^1|_{y=0} = v^1|_{y=h} = 0. \tag{20}$$

Solving these problems, we find that

$$\omega^0 = 0, \quad v^1 = 0, \quad v^0 = V(1 - y/h).$$

Starting from the definitions (12) related to the micro-polar fluid theory, we can write the expansion series for the stress  $S_{12}(\phi)$  as follows:

$$S_{12}(\phi) = S_{12}^0 + S_{12}^1\phi + o(\phi).$$

Clearly,

$$S_{12}^0 = \eta_s \frac{\partial v^0}{\partial y}, \quad S_{12}^1 = \eta_s \frac{\partial v^1}{\partial y} + \eta_s \Lambda \left( \frac{\partial v^0}{\partial y} + 2\omega^0 \right).$$

Now, we can calculate the relative stress at the moving plane:

$$\frac{S_{12}^m(\phi)}{S_{12}^m(0)} \equiv \frac{S_{12}(\phi)}{S_{12}(0)} \Big|_{y=0} = 1 + \phi\Lambda + o(\phi). \tag{21}$$

It is assumed that both the stresses  $S_{12}^m(\phi)$  and  $S^m(0)_{12}$  are measured at the same velocity  $V$  of the moving plate.

Let us consider flows within the same Couette geometry, starting from the Navier–Stokes theory. In such a theory, the stress tensor  $S$  is symmetric. Denoting  $S = S_{12}$ , one can find the velocity  $v(y)$  by solving the boundary-value problem

$$0 = \frac{\partial S}{\partial y}, \quad S = \eta(\phi) \frac{\partial v}{\partial y}, \quad v|_{y=0} = V, \quad v|_{y=h} = 0, \tag{22}$$

where  $\eta(\phi)$  is the effective viscosity.

Let  $S_1^v$  stand for the stress  $S$  at the moving plate,  $S_1^v = S|_{y=0}$ . Given  $S_1^v$ , one can derive from (22) the following formula for the apparent viscosity  $\eta(\phi)$ :

$$\eta(\phi) = -\frac{hS_1^v}{V} \tag{23}$$

Observe that  $S_1^v$  has negative values since  $v(y)$  is a decreasing function of  $y$ . It follows from (23) that

$$\frac{\eta(\phi)}{\eta(0)} = \frac{S_1^v(\phi)}{S_1^v(0)}, \quad \eta(0) \equiv \eta_s. \tag{24}$$

It is assumed that both the stresses  $S_1^v(\phi)$  and  $S_1(0)^v$  are measured at the same velocity  $V$  of the moving plate.

For dilute suspensions, the left-hand side of (24) is given by the Einstein formula [30]

$$\frac{\eta(\phi)}{\eta_s} = 1 + E\phi + o(\phi), \quad E \simeq 2.5. \tag{25}$$

We equate the relative stresses:  $S_{12}^m(\phi)/S_{12}^m(0) = S_1^v(\phi)/S_1^v(0)$ . Now, it follows from (21), (24) and (25) that

$$1 + E\phi = 1 + \phi\Lambda + o(\phi).$$

Hence,  $\Lambda = E$ . By the above arguments, we conclude that the skew-symmetric viscosity for dilute suspensions satisfies the representation formula

$$\eta_{sk}(\phi)/\eta_s = E\phi + o(\phi), \tag{26}$$

where  $E \simeq 2.5$  is the Einstein factor.

**Remark 1.** By the same asymptotic arguments, we can conclude that for the Couette flows between two concentric cylinders formula (26) becomes

$$\eta_{sk}(\phi)/\eta_s = G \cdot E\phi + o(\phi), \tag{27}$$

where  $G$  is the geometrical factor equal to  $(R_2/R_1)^2$ , with  $R_1$  being the smaller radius.

One more conclusion from the above arguments is that there is a correlation between the Navier–Stokes theory and the micro-polar fluid theory:

$$\eta(\phi)/\eta(0) = 1 + \eta_{sk}(\phi)/\eta_s + o(\phi), \quad \eta_s = \eta(0), \tag{28}$$

where  $\eta_s, \eta_{sk}$  are the micro-polar fluid viscosities of the suspension and  $\eta(\phi)$  is the apparent viscosity of the same suspension described by the Navier–Stokes rheology. The law (28) is verified by the asymptotic series argument for dilute suspensions, with the left-hand side given by the Einstein law  $\eta(\phi) = \eta(0)(1 + E\phi) + o(\phi)$ .

On the other hand, there is an extended Krieger–Dougherty empirical closure [31]

$$\eta(\phi)/\eta(0) = (1 - \phi/\phi^*)^{-E\phi^*}, \quad E = 2.5, \tag{29}$$

for dense suspensions, where  $\phi^*$  is a maximal volume concentration. Such a closure suggests that, by setting (29) in (28), we can define the skew-symmetric viscosity  $\eta_{sk}(\phi)$  as follows:

$$(1 - \phi/\phi^*)^{-E\phi^*} = 1 + \eta_{sk}(\phi)/\eta_s. \tag{30}$$

In the next sections, we verify this empirical formula by studying flows of dense suspensions paying attention to particle rotation.

#### 4. Flows of Suspensions of Rigid Particles in the Herschel–Bulkley Fluid

By the theoretical approach of Chateau et al. [32], Ovarlez et al. [9] showed that the flows of yield stress suspensions in a concentric-cylinder Couette geometry can be modeled by a Herschel–Bulkley behavior of same index as their interstitial fluid. The theory was proved to be in an agreement with the laboratory experiments based on the magnetic resonance imaging techniques [9].

We are going to address the same experiments as in [9] to verify formula (30). First, we extend the constitutive laws (5) to allow for the yield stress rheology. According to [33], the Cosserat–Bingham fluid rheology is defined as follows:

$$S = \begin{cases} 2\eta_s B_s + 2\eta_{sk} B_a + \tau_* \frac{B_0}{|B_0|}, & \text{if } B(\mathbf{x}, t) \neq 0, \\ S_p(\mathbf{x}, t), & \text{if } B(\mathbf{x}, t) = 0, \end{cases} \quad (31)$$

$$N = \begin{cases} 2\gamma A + \tau_n \frac{A}{|A|}, & \text{if } A(\mathbf{x}, t) \neq 0, \\ N_p(\mathbf{x}, t), & \text{if } A(\mathbf{x}, t) = 0, \end{cases} \quad (32)$$

where

$$B_0 = B_s + \varepsilon B_a, \quad \varepsilon(\phi) = \frac{\eta_{sk}(\phi)}{\eta_s}$$

and  $\tau_*$  and  $\tau_n$  are yield stresses; the unknown plug tensors  $S_p$  and  $N_p$  obey the restrictions

$$|S_p| \leq \tau_*, \quad |N_p| \leq \tau_n.$$

It is proved in [34] that the formulation (31) is equivalent to the inclusion  $S \in \partial V_*(B_0)$ , where the scalar potential  $V_*(D)$  is defined for any matrix  $D \in R^{3 \times 3}$  by the formula  $V_*(D) = \eta_s |D|^2 + \tau_* |D|$ . We remind that the subdifferential formulation  $S \in \partial V_*(B_0)$  implies that

$$S : (D - B_0) \leq V_*(D) - V_*(B_0) \quad \text{for all } D \in R^{3 \times 3}.$$

Similarly, the constitutive law (32) is equivalent to the inclusion  $N \in \partial V_n(A)$  with  $V_n(D) = \gamma |D|^2 + \tau_n |D|, \forall D \in R^{3 \times 3}$ . The meaning of the plug zone  $|N(x, t)| \leq \tau_n$  is discussed in [35].

Let  $T_0$  be a characteristic time. We denote the dimensionless second invariant of the rate of strain tensor  $B_0$  by  $I: I = T_0 |B_s|$ . To transform the Cosserat–Bingham fluid constitutive laws (31) and (32) into the Cosserat–Herschel–Bulkley fluid rheological equations, we assume that

$$\eta_s = \eta_{s0} I^{n-1} \quad \text{and} \quad \frac{\eta_{sk}(\phi)}{\eta_s} = \varepsilon(\phi), \quad \text{where} \quad \varepsilon(\phi) = (1 - \phi/\phi^*)^{-E\phi^*} - 1. \quad (33)$$

Observe that the classical Herschel–Bulkley model results from the constitutive laws (31)–(33) if the particle volume concentration  $\phi$  vanishes.

We consider steady axially symmetric flows of a suspension between two coaxial cylinders centered on the  $z$ -axis. The inner cylinder of the radius  $R_1$  rotates with the angular velocity  $\Omega_0 [s^{-1}]$  and the external cylinder of the radius  $R_2$  is fixed. The volume particle concentration  $\phi$  is assumed invariable along the radial coordinate. The case of variable  $\phi$  will be addressed in Section 6.

In what follows, we use the unit vectors  $\mathbf{e}_r, \mathbf{e}_\varphi, \mathbf{e}_z$  of the cylindrical coordinate system. The assumption of axially symmetry of flows suggests that the velocity vector  $\mathbf{v}$ , the micro-rotational velocity vector  $\boldsymbol{\omega}$  and the pressure  $p$  depend on the radial variable  $r$  only:

$$\mathbf{v} = v(r)\mathbf{e}_\varphi, \quad \boldsymbol{\omega} = \omega(r)\mathbf{e}_z, \quad p = p(r), \quad \text{rot } \mathbf{v} = \left( \frac{\partial v}{\partial r} + \frac{v}{r} \right) \mathbf{e}_z, \quad \text{rot } \boldsymbol{\omega} = -\frac{\partial \omega}{\partial r} \mathbf{e}_\varphi. \quad (34)$$

For such flows, the matrices  $\nabla \mathbf{v}$  and  $\Omega$  in the cylindrical coordinate system become

$$\nabla \mathbf{v} = \begin{pmatrix} 0 & -v/r & 0 \\ \partial v & 0 & 0 \\ 0 & 0 & 0 \end{pmatrix}, \quad \Omega = \begin{pmatrix} 0 & -\omega & 0 \\ \omega & 0 & 0 \\ 0 & 0 & 0 \end{pmatrix}, \quad \nabla \omega = \begin{pmatrix} 0 & 0 & 0 \\ 0 & 0 & 0 \\ \partial \omega & 0 & 0 \end{pmatrix},$$

where we denoted  $\partial v / \partial r$  by  $\partial v$  for simplicity. Here,

$$(\nabla \mathbf{v})_{ij} = \mathbf{e}_i \cdot \mathbf{v}'(\mathbf{x}) \langle \mathbf{e}_j \rangle, \quad i = (r, \varphi, z), \quad \mathbf{v}'(\mathbf{x}) \langle \mathbf{a} \rangle = \frac{d}{d\lambda} \mathbf{v}(\mathbf{x} + \lambda \mathbf{a})|_{\lambda=0}.$$

Hence,

$$B = \begin{pmatrix} 0 & -v/r + \omega & 0 \\ \partial v - \omega & 0 & 0 \\ 0 & 0 & 0 \end{pmatrix},$$

$$B_s = \begin{pmatrix} 0 & \frac{\partial v - v/r}{2} & 0 \\ \frac{\partial v - v/r}{2} & 0 & 0 \\ 0 & 0 & 0 \end{pmatrix}, \quad B_a = \begin{pmatrix} 0 & \omega - \frac{\partial v + v/r}{2} & 0 \\ \frac{\partial v + v/r}{2} - \omega & 0 & 0 \\ 0 & 0 & 0 \end{pmatrix}$$

As for the rate of strain tensor  $A$ , we have that  $A_{zr} = \partial \omega / \partial r$  and  $A_{ij} = 0$ , otherwise. Projections of the momentum Equation (7) and the angular momentum law (8) on the vectors  $\mathbf{e}_\varphi$  and  $\mathbf{e}_z$  become

$$0 = \frac{\partial S_{\varphi r}}{\partial r} + \frac{S_{\varphi r} + S_{r\varphi}}{r}, \tag{35}$$

$$0 = \frac{\partial N_{zr}}{\partial r} + \frac{N_{zr}}{r} + S_{\varphi r} - S_{r\varphi}, \tag{36}$$

respectively, where the tensor components are given by the formulas

$$S_{\varphi r} = \mathbf{e}_\varphi \cdot S \langle \mathbf{e}_r \rangle, \quad S_{r\varphi} = \mathbf{e}_r \cdot S \langle \mathbf{e}_\varphi \rangle, \quad N_{zr} = \mathbf{e}_z \cdot N \langle \mathbf{e}_r \rangle.$$

Given a vector  $\mathbf{e}$ , we apply the notation  $(S \langle \mathbf{e} \rangle)_i = S_{ij} e_j$ . Observe that the other components of  $S$  and  $N$  are equal to zero. In what follows, we use the equation

$$\frac{\rho v^2}{r} = \frac{\partial p}{\partial r}, \tag{37}$$

resulting from projection of the momentum equation (7) onto the vector  $\mathbf{e}_r$ .

We calculate that

$$I = 2^{-1/2} T_0 \sqrt{(\partial v / \partial r - v/r)^2 + \varepsilon^2 (\partial v / \partial r + v/r - 2\omega)^2}.$$

The constitutive laws (31)–(32) become

$$S_{r\varphi} = \left( 2\eta_s + \frac{\tau_* T_0}{I} \right) \left[ \frac{1}{2} \left( \frac{\partial v}{\partial r} - \frac{v}{r} \right) - \frac{\varepsilon}{2} \left( \frac{\partial v}{\partial r} + \frac{v}{r} - 2\omega \right) \right] \quad \text{if } I \neq 0, \tag{38}$$

$$S_{\varphi r} = \left( 2\eta_s + \frac{\tau_* T_0}{I} \right) \left[ \frac{1}{2} \left( \frac{\partial v}{\partial r} - \frac{v}{r} \right) + \frac{\varepsilon}{2} \left( \frac{\partial v}{\partial r} + \frac{v}{r} - 2\omega \right) \right] \quad \text{if } I \neq 0, \tag{39}$$

$$|S_{r\varphi}|^2 + |S_{\varphi r}|^2 \leq \tau_*^2 \quad \text{if } I = 0, \tag{40}$$

$$N_{zr} = 2\gamma \frac{\partial \omega}{\partial r} + \tau_n \text{sign} \left( \frac{\partial \omega}{\partial r} \right) \quad \text{if } \frac{\partial \omega}{\partial r} \neq 0, \quad |N_{zr}| \leq \tau_n \quad \text{if } \frac{\partial \omega}{\partial r} = 0, \tag{41}$$

The boundary condition (13) for the angular velocity  $\omega$  and the no-slip condition for  $v$  become

$$\omega|_{r=R_i} = \frac{\alpha_0 \phi}{2} \left( \frac{\partial v}{\partial r} + \frac{v}{r} \right) \Big|_{R_i}, \quad v|_{r=R_1} = R_1 \Omega, \quad v|_{r=R_2} = 0. \tag{42}$$



To study numerically the boundary-value problem (33)–(42) in the annulus  $R_1 < r < R_2$ , we pass to dimensionless variables:

$$r' = \frac{r}{R_1}, \quad v' = \frac{v}{V}, \quad \omega' = \frac{\omega}{\omega_0}, \quad S'_{r\phi} = \frac{S_{r\phi}}{S_0}, \quad S'_{\phi r} = \frac{S_{\phi r}}{S_0}, \quad N'_{zr} = \frac{N_{zr}}{N_0}, \quad \gamma_1 = \frac{\gamma}{R_1^2 \eta_{s0}},$$

with

$$V = R_1 \Omega_0, \quad \omega_0 = \Omega_0, \quad T_0 = \frac{1}{\Omega_0} [\text{s}], \quad S_0 = \eta_{s0} \Omega_0, \quad \tau_{*1} = \frac{\tau_*}{\eta_{s0} \Omega_0}, \quad \tau_{n1} = \frac{\tau_n R_1}{\gamma \Omega_0}, \quad N_0 = R_1 \eta_{s0} \Omega_0.$$

Observe that the dimensionless yield stress  $\tau_{*1}$  is the inverse of the Bingham number for the Couette flows:

$$\tau_{*1} = \frac{1}{Bn}, \quad Bn = \frac{\eta_{s0} \Omega_0}{\tau_*}.$$

In new variables,

$$I = 2^{-1/2} \sqrt{(\partial'v'/\partial r' - v'/r')^2 + \varepsilon^2 (\partial'v'/\partial r' + v'/r' - 2\omega')^2}, \quad \frac{\eta_s}{\eta_{s0}} = I^{n-1}. \quad (43)$$

$$S'_{r\phi} = \left[ \frac{1}{2} \left( \frac{\partial'v'}{\partial r'} - \frac{v'}{r'} \right) - \frac{\varepsilon}{2} \left( \frac{\partial'v'}{\partial r'} + \frac{v'}{r'} - 2\omega' \right) \right] \left( 2I^{n-1} + \frac{\tau_{*1}}{I} \right) \quad \text{if } I \neq 0, \quad (44)$$

$$S'_{\phi r} = \left[ \frac{1}{2} \left( \frac{\partial'v'}{\partial r'} - \frac{v'}{r'} \right) + \frac{\varepsilon}{2} \left( \frac{\partial'v'}{\partial r'} + \frac{v'}{r'} - 2\omega' \right) \right] \left( 2I^{n-1} + \frac{\tau_{*1}}{I} \right) \quad \text{if } I \neq 0, \quad (45)$$

$$|S'_{r\phi}|^2 + |S'_{\phi r}|^2 \leq \tau_{*1}^2 \quad \text{if } I = 0, \quad (46)$$

$$N'_{zr} = \gamma_1 \left( 2 \frac{\partial'\omega'}{\partial r'} + \tau_{n1} \text{sign} \frac{\partial'\omega'}{\partial r'} \right) \quad \text{if } \frac{\partial'\omega'}{\partial r'} \neq 0, \quad |N'_{zr}| \leq \tau_{n1} \quad \text{if } \frac{\partial'\omega'}{\partial r'} = 0, \quad (47)$$

$$0 = \frac{\partial' S'_{\phi r'}}{\partial r'} + \frac{S'_{\phi r} + S'_{r\phi}}{r'}, \quad (48)$$

$$0 = \frac{\partial' N'_{zr}}{\partial r'} + \frac{N'_{zr}}{r'} + S'_{\phi r} - S'_{r\phi}, \quad (49)$$

$$\omega'|_{r'=1,a} = \frac{\alpha_0 \phi}{2} \left( \frac{\partial'v'}{\partial r'} + \frac{v'}{r'} \right) \Big|_{r'=1,a}, \quad v'|_{r'=1} = 1, \quad v'|_{r'=a} = 0. \quad (50)$$

### 5. Skew-Symmetric Viscosity versus Particles Concentration

Here, we apply the mathematical model developed in the previous section to justify formula (30) for the skew-symmetric viscosity. To perform calculations, we fix parameters of the interstitial Hershel–Bilkley fluid. Rheological constitutive law of such a fluid results from (31) by setting  $\phi = 0$ :

$$S = \begin{cases} 2\eta_s B_s + \tau_* \frac{B_s}{|B_s|}, & \text{if } B_s(\mathbf{x}, t) \neq 0, \\ S_p(\mathbf{x}, t), & \text{if } B_s(\mathbf{x}, t) = 0, \end{cases} \quad \text{where } \eta_s = \eta_{s0} (T_0 |B_s|)^{n-1}. \quad (51)$$

We denote

$$\tau_y = \sqrt{2} \tau_*, \quad \eta_{HB} = 2^{5/4} \eta_{s0} T_0^{-1/2} \quad (52)$$

and set  $n = 1/2$ ,  $R_1 = 4[\text{cm}]$ ,  $R_2 = 6[\text{cm}]$ . Then, it follows from (51) that

$$\sqrt{2S : S} = \tau_y + \eta_{HB} (\sqrt{2B_s : B_s})^{1/2}. \quad (53)$$

The concentrated emulsion obeying Equation (53) was considered in [9] with  $\tau_y = 22 [\text{Pa}]$  and  $\eta_{HB} = 5.3 [\text{Pa} \cdot \text{s}^{1/2}]$ . Given the angular velocity  $\Omega [\text{rpm}]$  of the rotating inner cylinder, we calculate that  $T_0 = 1/\Omega_0 = (60/\Omega) [\text{s}]$ . We consider the same fluid as in [9], hence one can define the consistency  $\eta_{s0}$  and the yield stress  $\tau_*$  as follows:

$$\eta_{s0} = 2^{-5/4} \eta_{HB} [\text{Pa} \cdot \text{s}^{1/2}] \left( \frac{60}{\Omega} \right)^{1/2} [\text{s}^{1/2}], \quad \tau_* = \tau_y / \sqrt{2} [\text{Pa}]. \tag{54}$$

Observe that consistency depends on  $\Omega$  because of the special choice the characteristic time  $T_0$  and the definition of the dimensionless invariant  $I$  of the rate of strain tensor  $B_s$ .

It is proved in [35] that the rotation yield stress  $\tau_n$  causes the appearance of clusters of particles, with each cluster being a plug zone which rotates as a rigid body. Conglomerates of particles were not observed in [9] for the Couette flows of suspensions between two rotating cylinders; this is why  $\tau_n$  and  $\tau_{n1}$  can be neglected. As for the dimensionless angular viscosity  $\gamma_1$  and the boundary-value dimensionless parameter  $\alpha_0$ , we variate them to fit experimental data.

Approximate solutions of the system (43)–(50) can be obtained by regularization [36]. Given a small positive  $\delta$ , we substitute the dimensionless invariant  $I$  in (44) and (45) by  $I_\delta$ , where

$$I_\delta = 2^{-1/2} \sqrt{(\partial'v'/\partial r' - v'/r')^2 + \varepsilon^2(\partial'v'/\partial r' + v'/r' - 2\omega')^2 + \delta^2},$$

with  $\delta \searrow 0$ .

First, we tune the model (43)–(50) by setting  $\phi = 0$  and addressing the pure interstitial Herschel–Bulkley fluid with  $\tau_y(0) = 22[\text{Pa}]$  and  $\eta_{HB}(0) = 5.3[\text{Pa} \cdot \text{s}^{1/2}]$  as in [9]. Equations become

$$I = 2^{-1/2} \sqrt{(\partial'v'/\partial r' - v'/r')^2}, \quad \frac{\eta_s}{\eta_{s0}} = I^{n-1}, \quad n = 1/2. \tag{55}$$

$$S'_{r\phi} = S'_{\phi r} = \frac{1}{2} \left( \frac{\partial'v'}{\partial r'} - \frac{v'}{r'} \right) \left( 2I^{n-1} + \frac{\tau_{*1}}{I} \right) \quad \text{if } I \neq 0, \tag{56}$$

$$2|S'_{r\phi}|^2 \leq \tau_{*1}^2 \quad \text{if } I = 0, \tag{57}$$

$$0 = \frac{\partial' S'_{\phi r'}}{\partial r'} + \frac{2S'_{\phi r}}{r'}, \tag{58}$$

$$v'|_{r'=1} = 1, \quad v'|_{r'=R_2/R_1} = 0. \tag{59}$$

Observe that in such a case the model (55)–(59) depends on one parameter  $\tau_{*1}(0)$  only. Given the angular velocity  $\Omega[\text{s}^{-1}]$ , we find from (52) the value of the Bingham number  $Bn(0)$  by the formula

$$Bn(0) = \frac{\eta_{HB}(0)\Omega_0^{1/2}}{2^{3/4}\tau_y(0)}. \tag{60}$$

Figures 1 and 2 depict very good agreement of calculation results for  $\phi = 0$  with experiment data [9] for different angular velocities  $\Omega_0[\text{s}^{-1}]$  but in the case of passage to the effective Bingham number  $Bn_e(0)$ :

$$Bn_e(0) = 1.5 \cdot Bn(0), \tag{61}$$

We think that such a discrepancy between the measured and effective Bingham numbers is due to the following reasons. Real 3D-flows are described by 1D-equations. The gravitation, the height of the annulus region, and the lateral boundaries effect are not taken into account. It may be that viscoelastic fluid property is also of importance, which calls for more adequate modeling.

Figure 1 corresponds to  $\Omega = 2, \Omega = 5$  and  $\Omega = 100[\text{rpm}]$ . The same agreement between calculation results and experiment data is observed for  $\Omega = 10, 20$  and  $50[\text{rpm}]$ , but we omit pictures to save the space. Figure 2a combines all velocity profiles for  $\Omega = 2, 5, 10, 20, 50$  and  $100[\text{rpm}]$ ; it fits the laboratory experiments exposed in Figure 2b. Why does the velocity profile become less steep as  $\Omega$  increases? Equations (60) and (61) answer the question. In fact, there is a motionless plug zone of the Herschel–Bulkley fluid near the exterior cylinder. Our approximate solutions based on the regularization approach do not catch the plug zone well. The bigger the plug zone, the steeper the velocity curve.

However, the dimensionless yield stress  $\tau_{*1}(0)$  stipulates the size of the plug zone and, at the same time, it varies inversely with the angular velocity  $\Omega$ .

Now, we consider suspensions assuming that they can be modeled by a Herschel–Bulkley behavior of the same index as their interstitial fluid, with their consistency and their yield stress depending on the particle volume fraction. To determine the function  $\tau_{*1}(\phi)$  in Equations (55)–(59), we apply correlations proposed in [9] for  $n = 1/2$ :

$$\frac{\eta_{HB}(\phi)}{\eta_{HB}(0)} = \left( \frac{\tau_y(\phi)}{\tau_y(0)} \right)^{3/2} \cdot (1 - \phi)^{-1/2}, \tag{62}$$

$$\frac{\tau_y(\phi)}{\tau_y(0)} = \sqrt{(1 - \phi)(1 - \phi/\phi^*)^{-2.5\phi^*}} \tag{63}$$

In our notations (see (33)), equality (63) becomes

$$\frac{\tau_y(\phi)}{\tau_y(0)} = \sqrt{(1 - \phi)(\varepsilon(\phi) - 1)}.$$

It follows from the definitions (60) and (61) that

$$\frac{\tau_{*1}(\phi)}{\tau_{*1}(0)} = \left( \frac{1 - \phi}{1 + \varepsilon(\phi)} \right)^{1/4}. \tag{64}$$

With the function  $\tau_{*1}(\phi)$  given by (64), we solve Equations (55)–(59) and find an agreement with experiment data [9]. Calculations and laboratory data depicted in Figure 3 are related to  $\phi = 0.3$  for  $\Omega = 2, 5, 10, 20, 50$  and  $100$ [rpm].

Let us return to the general system (43)–(50) which describes micropolar fluid. We fix  $\tau_{*1}$  by Equations (64), (60) and (61). To choose the dimensionless parameters  $\gamma_1$  and  $\alpha_0$ , we apply the method of least squares based on minimizing the function

$$F(\gamma_1, \alpha_0) = \sum_{i,j,k} |v'_{\gamma_1, \alpha_0}(r_i, \phi_j, \Omega_k) - v'_{data}(r_i, \phi_j, \Omega_k)|^2.$$

Here,  $v'_{data}$  is the measured velocity at different locations  $r_i$  for different volume concentrations  $\phi_j$  and different angular velocities  $\Omega_k$ ,  $v'_{\gamma_1, \alpha_0}(r, \phi, \Omega)$  is the calculated velocity, with  $\gamma_1$  and  $\alpha_0$  being prescribed. Calculations reveal that the optimal  $\gamma_1$  and  $\alpha_0$  take values  $\gamma_1^* = 10.93$  and  $\alpha_0^* = 0.79$  provided  $\tau_y(0) = 22$ [Pa] and  $\eta_{HB}(0) = 5.3$ [Pa · s<sup>1/2</sup>]. Below, we provide results of calculations with the chosen data  $\tau_{*1}$ ,  $\gamma_1^*$  and  $\alpha_0^*$ .

Figures 4 and 5a concern calculations for  $\Omega = 100$ [rpm] when  $\phi$  takes values 0, 0.1 and 0.3. Measured data in Figure 5b borrowed from [9] confirm agreement with calculations. The same is true for  $\Omega = 5$ [rpm] when  $\phi$  takes values 0, 0.1 and 0.3 as shown in Figures 6 and 7. In Figures 8 and 9,  $\phi$  is fixed equal to 0.3 with  $\Omega$  taking on the values 2, 5, 10, 20, 50, and 100[rpm]. Calculations agree with the measured data from [9].

The micro-polar fluid rheology equations (5) predict particle rotation. Figure 10 depicts profiles of the dimension angular velocity  $w(r)$  when  $\phi$  is fixed equal to 0.3 with  $\Omega$  taking on the values 2, 5, 10, 20, 50, and 100[rpm].

Although the dimensionless angular viscosity  $\gamma_1 = 2^{5/4} \gamma R_1^{-2} \eta_{HB}^{-1}(\phi) \Omega$  is determined, we can not identify the dimensional angular viscosity  $\gamma$ . Indeed, the tuning step (61) implies that we substituted  $\tau_y(0) / \eta_{HB}(0)$  by  $0.2 \cdot \tau_y(0) / \eta_{HB}(0)$ . However, in doing so, it is impossible to know individual reduced values both of  $\tau_y(0)$  and  $\eta_{HB}(0)$ . Hence, we don't know the reduced value of  $\eta_{HB}(\phi)$ .

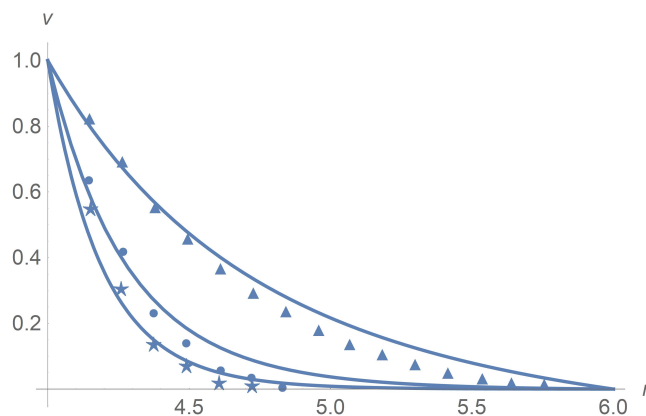
Let us comment on some discrepancy between calculations and data of measurement. One can see in Figures 4b and 7 that, with increasing the rotational velocity at a constant volume concentration  $\phi = 0.1$ , the theoretical results are shown to better agree with experiment. It is a problem of calculations. The reason is that we consider the viscoplastic fluid and the plug zone (with zero velocity and low shear stress) near the external cylinder being

larger at low rotations. The governing system of equations becomes degenerate in such a zone. Mathematical theory of degenerate systems of differential equations and corresponding numerical methods built into Wolfram Mathematica are not well developed yet. There is one more difficulty related to the Herschel–Bulkley fluid viscosity (with the power  $n = 1/2$ ) becoming infinite when the velocity gradient vanishes somewhere. To get over these difficulties, we apply the regularization technique and substitute the invariant  $I$  of the rate of strain tensor  $B_0$  in Equations (38)–(40) by its non-vanishing approximation  $I_\delta$ .

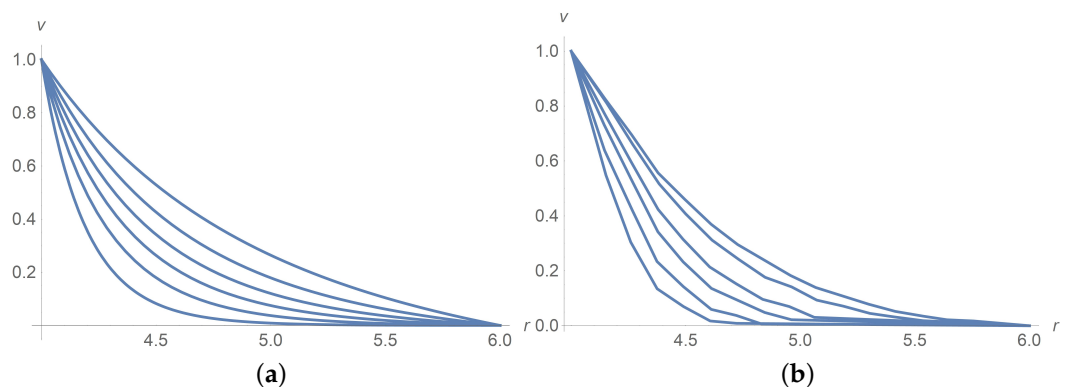
A comparison of the results in Figure 1 (upper curve), and Figure 4 at the rotational velocity  $\Omega = 100$  rpm shows that, with increasing the volume concentration, the calculated results better agree with experiments at intermediate concentrations  $\phi=0.1$ ; at lower ( $\phi = 0$ ) and at higher concentrations ( $\phi = 0.3$ ), the deviations increase. The reason is that there are no data of measurement for the dimensionless parameters  $\gamma_1$  and  $\alpha_0$ . To choose them, we apply the method of least squares based on minimizing the functional  $F(\gamma_1, \alpha_0)$ . As it happened, a discrepancy between the measured data and calculations for different concentrations and angular velocities is due to the optimal choice of these unknown parameters.

The above calculations confirm that Equation (30) for the skew-symmetric viscosity  $\eta_{sk}(\phi)$  can be of use.

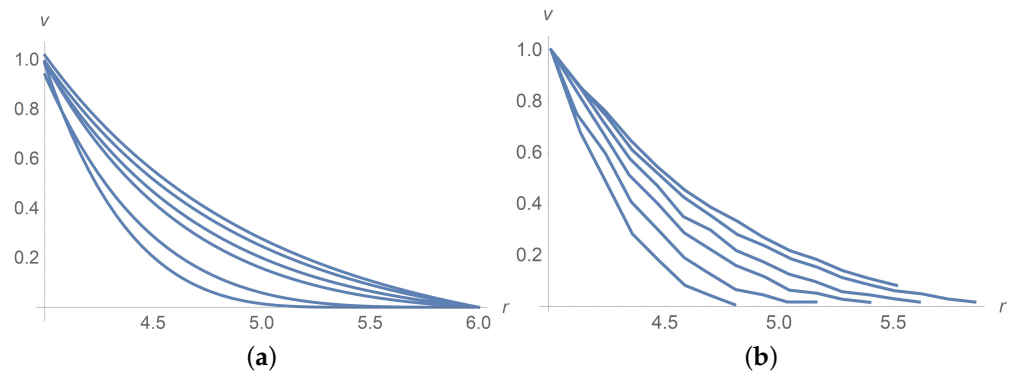
Observe that comparison with experiments for colloidal suspensions is contained in Figures 1, 2 and 5 since, in the case  $\phi = 0$ , the suspension becomes a pure colloidal fluid.



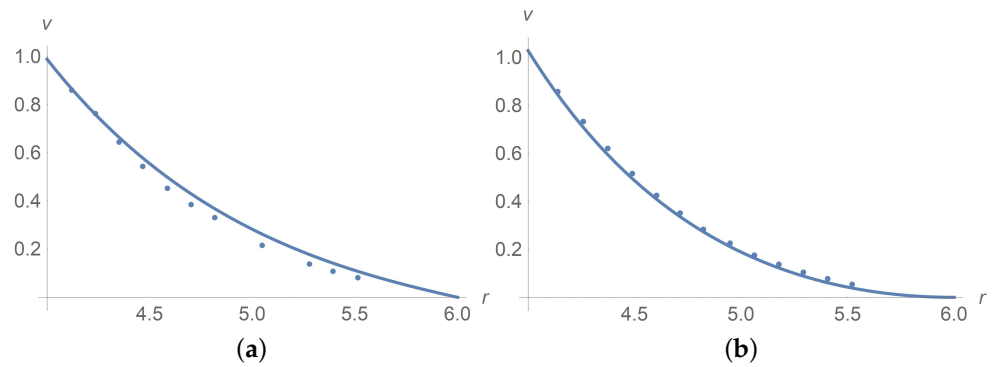
**Figure 1.** Calculated dimensionless velocity profiles (solid lines) versus the radial variable for pure interstitial Herschel–Bulkley fluid without particles,  $\phi = 0$ . The lines from the bottom upward correspond to  $\Omega = 2$ ,  $\Omega = 5$  and  $\Omega = 100$ , respectively. Stars, balls, and triangles stand for measurement data [9] in the cases  $\Omega = 2$ ,  $\Omega = 5$  and  $\Omega = 100$ , respectively.



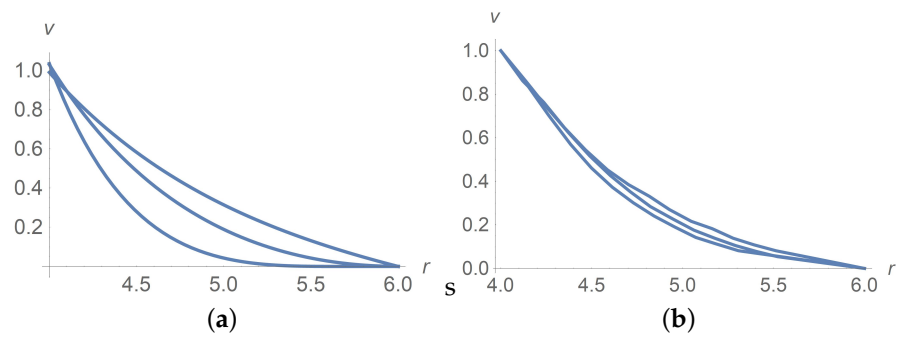
**Figure 2.** Dimensionless velocity profiles versus the radial variable in pure interstitial Herschel–Bulkley fluid without particles,  $\phi = 0$ , for  $\Omega = 2, 5, 10, 20, 50, 100$  [rpm] from the bottom upwards. (a) calculations, (b) measured data [9].



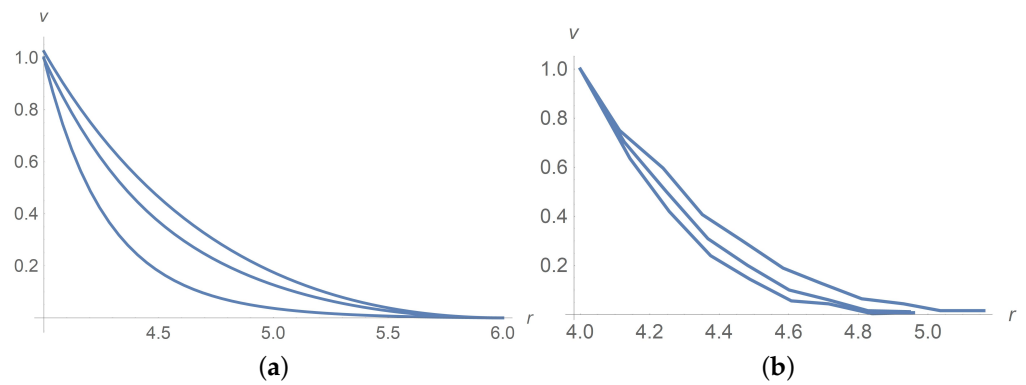
**Figure 3.** Dimensionless velocity profiles of the Herschel–Bulkley fluid with the apparent  $\eta_{HB}(\phi)$  and  $\tau_y(\phi)$  for  $\phi = 0.3$  and  $\Omega = 2, 5, 10, 20, 50, 100$ [rpm] from the bottom upwards. (a) calculations, (b) measured data [9].



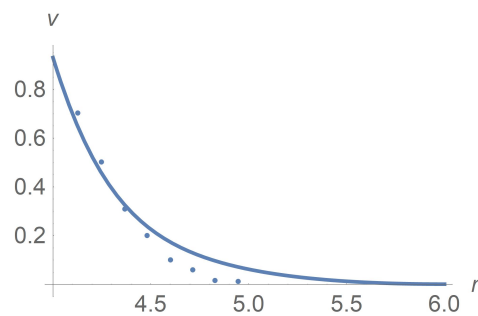
**Figure 4.** The solid line corresponds to a dimensionless velocity profile versus the radial variable for  $\Omega = 100$ [rpm]. Dots stand for experimental data [9]. (a)  $\phi = 0.3$ , (b)  $\phi = 0.1$ .



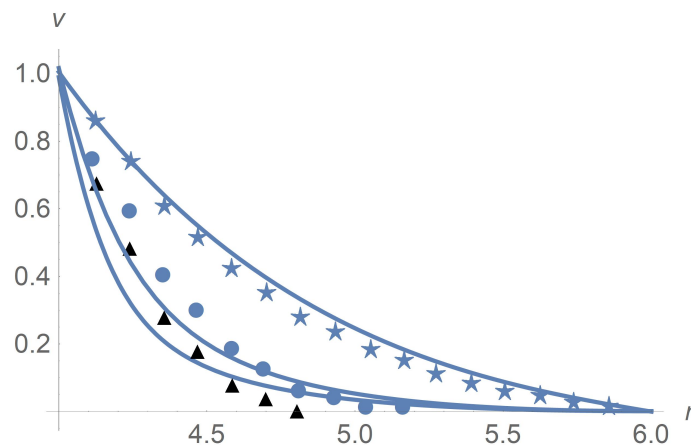
**Figure 5.** Dimensionless velocity profiles for  $\Omega = 100$ [rpm]. The curves from the bottom upwards correspond to  $\phi = 0, \phi = 0.1$  and  $\phi = 0.3$ . (a) Calculations, (b) measured data [9].



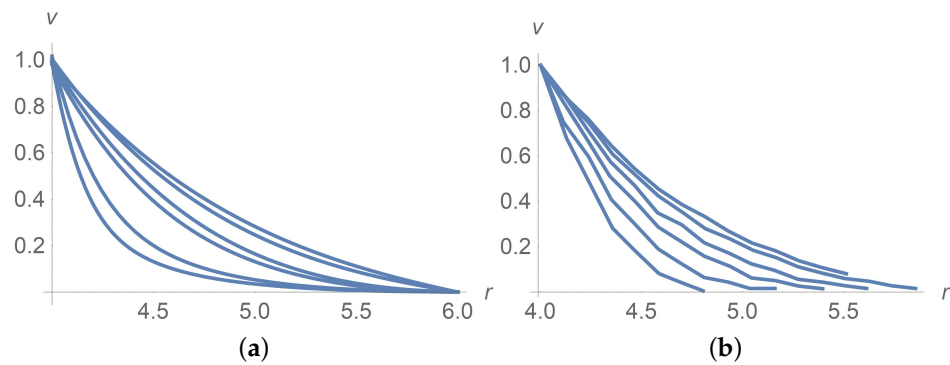
**Figure 6.** Dimensionless velocity profiles for  $\Omega = 5[\text{rpm}]$ . The curves from the bottom upwards correspond to  $\phi = 0, 0.1$  and  $0.3$ . (a) calculations, (b) measured data [9].



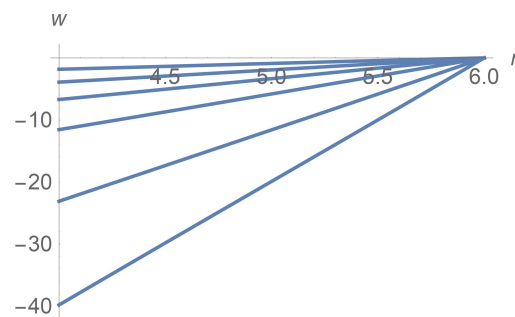
**Figure 7.** The solid line corresponds to dimensionless velocity profile versus the radial variable for  $\Omega = 5[\text{rpm}]$  and  $\phi = 0.1$ . Dots stand for experimental data [9].



**Figure 8.** Calculated dimensionless velocity profiles versus the radial variable for  $\phi = 0.3$ . The lines from bottom upward correspond to  $\Omega = 2[\text{rpm}]$ ,  $\Omega = 5[\text{rpm}]$  and  $\Omega = 50[\text{rpm}]$ , respectively. Triangles, balls and stars are the measured data from [9] corresponding to  $\Omega = 2[\text{rpm}]$ ,  $\Omega = 5[\text{rpm}]$  and  $\Omega = 50[\text{rpm}]$ , respectively.



**Figure 9.** (a) Calculated dimensionless velocity profiles for  $\phi = 0.3$ . The curves correspond to  $\Omega = 2, 5, 10, 20, 50, 100$ [rpm] from the bottom upwards. (b) Measured [9] dimensionless velocity profiles of the Herschel–Bulkley fluid with  $\phi = 0.3$  and  $\Omega$  taking values 2, 5, 10, 20, 50, 100[rpm] from the bottom upwards.



**Figure 10.** Calculated angular velocity  $w$ [rpm] profiles for  $\phi = 0.3$ . The curves correspond to  $\Omega = 2, 5, 10, 20, 50, 100$ [rpm] from the top down.

### 6. Rotational Sedimentation

Here, we consider more general mathematical model allowing for non-uniform particle distribution. We introduce the mass concentration of particles as follows:

$$c = \frac{\bar{\rho}_s \phi}{\rho}, \quad \rho = \bar{\rho}_s \phi + \bar{\rho}_f (1 - \phi), \tag{65}$$

where  $\rho$  is the total density,  $\bar{\rho}_s$  is the particle density and  $\bar{\rho}_f$  is the density of the interstitial fluid. Given  $c$ , one can restore from (65) the volume concentration and the total density by the formulas

$$\phi = \frac{\bar{\rho}_f c}{\bar{\rho}_f c + \bar{\rho}_s (1 - c)}, \quad \rho(c) = \frac{\bar{\rho}_f \bar{\rho}_s}{\bar{\rho}_f c + \bar{\rho}_s (1 - c)}. \tag{66}$$

Due to these formulas, any given function of the volume concentration like the relative viscosity  $\varepsilon(\phi)$  can be defined in terms of the mass concentration  $c$ . It is explained in [7] that  $c$  satisfies the conservation law

$$\frac{\partial(\rho c)}{\partial t} + \text{div}(\rho c \mathbf{v} + \mathbf{l}) = 0, \tag{67}$$

where  $\mathbf{l}$  is the concentration flux obeying the generalized Fick equation

$$\rho \mathbf{l} = -D \nabla c - D_p \nabla p + D_\omega \text{rot } \boldsymbol{\omega} \times \boldsymbol{\omega}_r. \tag{68}$$

The scalar parameters  $D$ [cm<sup>2</sup>/s],  $D_p$ [cm<sup>3</sup>·s/g], and  $D_\omega$  [cm<sup>2</sup>·s], stand for the diffusion, barodiffusion, and spin diffusion coefficients.

Observe that, instead of (5), the couple stress tensor  $N$  is prescribed by the rheological equation

$$N = 2\gamma A + \frac{D_\omega}{2} \epsilon : (\mathbf{1} \times \boldsymbol{\omega}_r) \tag{69}$$

to meet the entropy production law [7] where the skew-symmetric matrix  $\epsilon : \mathbf{a}$  is defined by the formula

$$(\epsilon : \mathbf{a})_{ij} = a_k \epsilon_{ikj}, \quad \mathbf{a} = a_i \mathbf{e}_i,$$

in any orthogonal basis  $\{\mathbf{e}_i\}_1^3$ . It is due to spin diffusion that the Ségre-Silberberg effect is explained within the micropolar theory [7].

Due to the identity  $\text{rot } \boldsymbol{\omega} \times \mathbf{b} = 2(\nabla \boldsymbol{\omega})_a \cdot \mathbf{b}, \forall \mathbf{b} \in R^3$ , it follows from (68) and (69) that

$$\left( \rho + \frac{D_\omega^2 |\boldsymbol{\omega}_r|^2}{4\gamma} \right) \mathbf{1} = -D \nabla c - D_p \nabla p - \frac{D_\omega}{2\gamma} N_a \cdot \boldsymbol{\omega}_r$$

in agreement with the definition of rotary diffusion [37]: “Just as the translational diffusion coefficient is calculated in terms of the drag force, so the rotary diffusion coefficient is expressed in terms of the moment of the forces on a particle executing a rotary movement.”

It follows from (9) that for steady flows the mass conservation law becomes  $\text{div } \mathbf{v} = 0$ .

With the above definitions, we arrive at the following conservation laws for steady flows:

$$\text{div}(\rho \mathbf{v} \otimes \mathbf{v}) = -\nabla p + \text{div } S + \rho \mathbf{f}, \tag{70}$$

$$J \text{div}[\boldsymbol{\omega} \otimes (\rho \mathbf{c} \mathbf{v} + \mathbf{1})] = \text{div } N - \epsilon : S, \tag{71}$$

$$\text{div}(\rho \mathbf{c} \mathbf{v} + \mathbf{1}) = 0, \tag{72}$$

with tensors  $S, N$  and the flux  $\mathbf{l}$  given by Equations (51), (69) and (68) respectively.

For the flows in a concentric-cylinder Couette geometry, we calculate that

$$\mathbf{l} = l \mathbf{e}_r, \quad \rho l = -D \frac{\partial c}{\partial r'} - D_p \frac{\partial p}{\partial r'} + \frac{D_\omega \omega_r}{2} \frac{\partial \omega}{\partial r'}.$$

Under the assumption that  $c = c(r)$ , we arrive at the formula  $\nabla c = \mathbf{e}_r \partial c / \partial r$ . Due to equation  $\text{div } \mathbf{v} = 0$ , we obtain that, for the rotation flows, the equation  $\text{div}(\rho \mathbf{c} \mathbf{v}) = 0$  holds. Now, it follows from (72) that

$$0 = \text{div } \mathbf{l} = \frac{1}{r} \frac{\partial (rl)}{\partial r} \quad \text{and} \quad rl = \text{const.}$$

At the same time, the now-flow boundary conditions  $\mathbf{l} \cdot \mathbf{n}|_{R_i} = 0$  imply that  $l = 0$  and  $\mathbf{l} = 0$ . Thus, the particles mass concentration obeys the equation  $l = 0$  or

$$\frac{\partial c}{\partial r} = -\frac{D_p}{D} \frac{\partial p}{\partial r} + \frac{D_\omega \omega_r}{2D} \frac{\partial \omega}{\partial r}.$$

Due to (37), the latter equation can be written as

$$\frac{\partial c}{\partial r} = -\frac{D_p \rho v^2}{D r} + \frac{D_\omega}{2D} \left( \omega - \frac{1}{2} \left( \frac{\partial v}{\partial r} + \frac{v}{r} \right) \right) \frac{\partial \omega}{\partial r}. \tag{73}$$

In what follows, we use the representations  $D_p = D_p^* c(1 - c), D_\omega = D_\omega^* c(1 - c)$  since both  $D_p$  and  $D_\omega$  vanish at  $c = 0$  and  $c = 1$ . Given a mean value  $c_0$  of  $c$ , we set the following condition:

$$\int_{R_1}^{R_2} r c(r) dr = \frac{c_0 (R_2^2 - R_1^2)}{2}. \tag{74}$$

As for the particle migration, there is one more approach based on the Fick law. This is known as the Lamm equation for a highly disperse colloidal solution enclosed in a wedge-



shape cell rotating at an angular velocity  $\Omega$  about an axis coinciding with the apex of the wedge [5].

Let us return to Equation (73). One more consequence of the equality  $\mathbf{l} = 0$  is that the rheological Equation (69) reduces to  $N = 2\gamma A$  in the Couette geometry.

Let us summarize the mathematical model. We look for functions  $S_{r\phi}, S_{\phi r}, N_{zr}, v, \omega, c$ , obeying the Equations (35), (36), (38)–(41) and (73), with the given function  $\varepsilon(c)$ .

We introduce dimensionless parameters

$$\rho_0 = \frac{\bar{\rho}_s}{\bar{\rho}_f}, \quad D_1 = \frac{D_p^* R_1^2 \Omega_0^2 \bar{\rho}_s}{D}, \quad D_2 = \frac{D_\omega^* \Omega_0^2}{2D}.$$

In new notations,

$$\varepsilon(c) = \left(1 - \frac{c/\phi_*}{c + \rho_0(1 - c)}\right)^{-E\phi_*} - 1.$$

Let us pass to dimensionless variables. Then, Equations (73) and (74) become

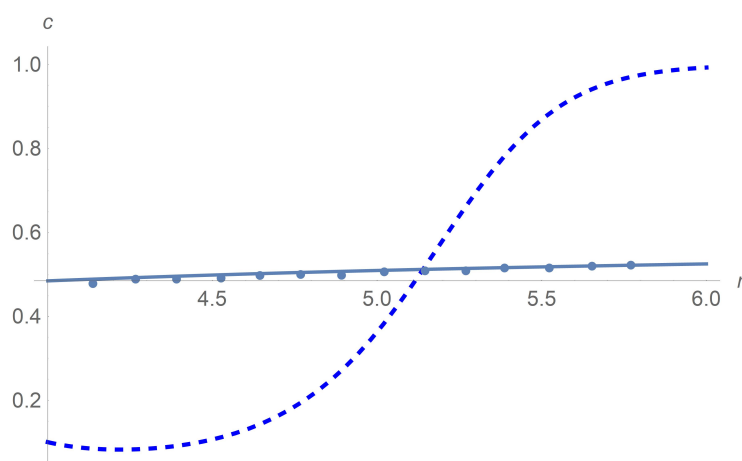
$$\frac{1}{c(1 - c)} \frac{\partial' c}{\partial r'} = -\frac{D_1 v'^2}{r'(c + \rho_0(1 - c))} + D_2 \frac{\partial' \omega'}{\partial r'} \left(\omega' - \frac{\partial' v' / \partial r' + v' / r'}{2}\right), \quad (75)$$

$$\int_1^a r' c(r') dr' = \frac{c_0(a^2 - 1)}{2}, \quad a = \frac{R_2}{R_1}. \quad (76)$$

We summarize the governing equations as follows. We look for the dimensionless functions  $v'(r')$ ,  $\omega'(r')$  and  $c(r')$  which satisfy Equations (43)–(50), (75) and (76). Observe that these equations are not decoupled since the relative viscosity  $\varepsilon(c)$  in Equations (44) and (45) depends on the particle concentration  $c$ .

Figure 11 depicts results of calculations of concentration along the radial variable. We apply the Wolfram Mathematica solver for ordinary differential equations. Agreement between calculations and experiment [9] is achieved for  $\Omega = 10^2$  rpm with the choice  $D_\omega^*/(2D) = 5 \times 10^{-5}$  [s<sup>2</sup>]. The sedimentation effect happens when we increase  $\Omega$  to  $14 \times 10^3$  [rpm]. We prove that such an effect is due to the rotational diffusion  $D_\omega$  since the particle separation does not happen when  $D_\omega = 0$ .

**Remark 2.** *It is known that, for many practical purposes, the polymers or colloidal particles can be regarded as rigid particles. Examples are triblock Janus particles which can be modeled as cross-linked polystyrene spheres whose poles are patched with sticky alkyl groups, and their middle band is covered with negative charges [38]. This is why the above results on rotational sedimentation can also be applied to polymer flows. As was proved by Svedberg, such flows are of great importance in the studies of the polymer structure. Our contribution is that we propose an alternative approach to the Lamm equation based on the empirical notion of the sedimentation coefficient [6]. The advantages are that we apply the conservation laws of continuum mechanics and take into account the shape of the particles. Moreover, we prove that the polymer sedimentation is due to its rotation. This result suggests a new direction of laboratory studies on polymer flows.*



**Figure 11.** Profiles of mass concentration  $c$ . Both the solid line that is based on calculations and dots standing for experimental data [9] correspond to  $\Omega = 10^2$  rpm. Agreement between calculations and experiment is achieved by the choice  $D_{\omega}^*/(2D) = 5 \times 10^{-5}$  [s<sup>2</sup>]. The dashed line corresponding to calculations reveals the sedimentation effect when we increase  $\Omega$  to  $14 \times 10^3$  [rpm].

## 7. Discussion

We address the rotational sedimentation of particles for steady flows of yield stress granular fluids in a concentric-cylinder Couette geometry. Apart from the Lamm equation approach, we do not use the empirical sedimentation coefficient. Instead, we apply conservation laws of the micro-polar equations which allow for particle rotation. We prove that it is due to the rotational diffusion that the particle sedimentation occurs at high angular velocity of the Couette cell inner cylinder. To validate the mathematical model, we perform a comparison with published data of measurements by choosing the relative viscosity related with the particle rotation. First, we justify analytically this choice for dilute suspensions starting from the Einstein correlation for the apparent viscosity. As for dense suspensions, we apply the Krieger–Dougherty empirical closure for the apparent viscosity. Though we performed calculations for steady flows, the developed approach allows for unsteady flows and non-spherical particles due to the micro-inertia tensor involved into the angular momentum conservation law.

**Funding:** This research was funded by RUSSIAN SCIENCE FOUNDATION Grant No. 20-19-00058.

**Data Availability Statement:** Not applicable.

**Conflicts of Interest:** The authors declare no conflict of interest.

## References

1. Khodja, M.; Canselier, J.P.; Bergaya, F.; Fourar, K.; Khodja, M.; Cohaut, N.; Benmounah, A. Shale problems and waterbased drilling fluid optimisation in the Hassi Messaoud Algerian oil field. *Appl. Clay Sci.* **2010**, *49*, 383–393. [\[CrossRef\]](#)
2. Mahaut, F.; Chateau, X.; Coussot, P.; Ovarlez, G. Yield stress and elastic modulus of suspensions of noncolloidal particles in yield stress fluids. *J. Rheol.* **2008**, *52*, 287–313. [\[CrossRef\]](#)
3. Svedberg, T.; Pedersen, K.O. *The Ultracentrifuge*; Oxford University Press: London, UK, 1940.
4. Planken, K.L.; Colfen, H. Analytical ultracentrifugation of colloids. *Nanoscale* **2010**, *2*, 1849–1869. [\[CrossRef\]](#) [\[PubMed\]](#)
5. Brautigam, C.A. Using Lamm-Equation modeling of sedimentation velocity data to determine the kinetic and thermodynamic properties of macromolecular interactions. *Methods* **2011**, *54*, 4–15. [\[CrossRef\]](#) [\[PubMed\]](#)
6. Lamm, O. Die Differentialgleichung der Ultrazentrifugierung. *Ark. Mat. Astr. Fys.* **1929**, *21 B*, 1–4.
7. Shelukhin, V.V.; Neverov, V.V. Thermodynamics of micropolar Bingham fluids. *J. Non-Newton. Fluid Mech.* **2016**, *236*, 83–90. [\[CrossRef\]](#)
8. Segré, G.; Silberberg, A. Radial Poiseuille flow of suspensions. *Nature* **1961**, *189*, 209–210. [\[CrossRef\]](#)
9. Ovarlez, G.; Mahaut, F.; Deboeuf, S.; Lenoir, N.; Hormozi, S.; Chateau, X. Flows of suspensions of particles in yield stress fluids. *J. Rheol.* **2015**, *59*, 1449. [\[CrossRef\]](#)
10. Hayakawa, H. Slow viscous flows in micropolar fluids. *Phys. Rev. E* **2000**, *61*, 5477–5492. [\[CrossRef\]](#)
11. Eckart, W.; Růžička, M. Modeling micropolar electrorheological fluids. *Int. J. Appl. Mech. Eng.* **2006**, *11*, 831–844.

12. Parthasarathy, M.; Klingenberg, D.J. Electrorheology: Mechanisms and models. *Mater. Sci. Eng. R Rep.* **1966**, *17*, 57–103. [[CrossRef](#)]
13. Rosensweig, R.E. *Ferrohydrodynamics*; Cambridge University Press: Cambridge, MA, USA, 1985.
14. Eremeyev, V.A.; Sukhov, D.A. Convective instabilities in thermo-viscoelastic micropolar fluids. *Matemáticas Enseñanza Universitaria* **2005**, *13*, 31–42.
15. Eringen, A.C. Theory of thermo-microstretch fluids and bubbly liquids. *Int. J. Eng. Sci.* **1990**, *28*, 133–143. [[CrossRef](#)]
16. Ariman, T. Microcontinuum fluid mechanics—A review. *Int. J. Eng. Sci.* **1973**, *11*, 905–930. [[CrossRef](#)]
17. Ariman, T.; Turk, M.A.; Sylvester, N.D. Application of microcontinuum fluid mechanics. *Int. J. Eng. Sci.* **1974**, *12*, 273–293. [[CrossRef](#)]
18. Turk, M.A.; Sylvester, N.D.; Ariman, T. On pulsatile blood flow. *Trans. Soc. Rheol.* **1973**, *17*, 1–21. [[CrossRef](#)]
19. Cokelet, G.R. Viscometric, in vitro and in vivo blood viscosity relationships: How are they related? (Poiseuille Award Lecture). *Biorheology* **1999**, *36*, 343–358. [[PubMed](#)]
20. Hogan, H.A.; Henriksen, M. An evaluation of a micropolar model for blood flow through an idealized stenosis. *J. Biomech.* **1989**, *22*, 211–218. [[CrossRef](#)]
21. Popel, A.S.; Johnson, P.C. Microcirculation and hemorheology. *Annu. Rev. Fluid Mech.* **2005**, *37*, 43–69. [[CrossRef](#)]
22. Pralhad, R.N.; Schultz, D.H. Modeling of arterial stenosis and its applications to blood diseases. *Math. Biosci.* **2004**, *190*, 203–220. [[CrossRef](#)] [[PubMed](#)]
23. Aero, E.L.; Bulygin, A.N.; Kuvshinski, E.V. Asymmetric hydromechanics. *Appl. Math. Mech.* **1965**, *29*, 297–308. [[CrossRef](#)]
24. Condiff, D.W.; Dahler, J.S. Fluid mechanical aspects of antisymmetric stress. *Phys. Fluids* **1964**, *7*, 842–854. [[CrossRef](#)]
25. Eringen, A.C. Theory of micropolar fluids. *J. Math. Mech.* **1966**, *16*, 1–18. [[CrossRef](#)]
26. Eringen, A.C. *Microcontinuum Field Theories I,II*; Springer: New York, NY, USA, 1999.
27. Lukaszewicz, G. *Micropolar Fluids: Theory and Applications*; Birkhäuser: Boston, MA, USA, 1999.
28. Cosserat, E.; Cosserat, F. *Theorie des Corps Deformable*; A. Hermann et Fils: Paris, France, 1909.
29. Migun, N.P.; Prokhorenko, P.P. *Fluid Dynamics and Heat Transfer of Gradient Flows of Microstructural Fluids*; Nauka Tekhnika: Minsk, Belarusia, 1984. (In Russian)
30. Einstein, A. A new determination of molecular dimensions. *Ann. Phys.* **1906**, *4*, 289–306. [[CrossRef](#)]
31. Krieger, I.M.; Dougherty, T. A mechanism for non-Newtonian flow in suspensions of rigid spheres. *Trans. Soc. Rheol.* **1959**, *3*, 137–152. [[CrossRef](#)]
32. Chateau, X.; Ovarlez, G.; Trung, K.L. Homogenization approach to the behavior of suspensions of noncolloidal particles in yield stress fluids. *J. Rheol.* **2008**, *52*, 489–506. [[CrossRef](#)]
33. Shelukhin, V.V.; Růžička, M. On Cosserat-Bingham Fluids. *Z. Angew. Math. Mech.* **2013**, *93*, 57–72. [[CrossRef](#)]
34. Basov, I.V.; Shelukhin, V.V. Nonhomogeneous incompressible Bingham viscoplastic as a limit of nonlinear fluids. *J. Non-Newton. Fluid Mech.* **2007**, *142*, 95–103. [[CrossRef](#)]
35. Shelukhin, V.V.; Neverov, V.V. Flow of micropolar and viscoplastic fluids in a Hele-Shaw cell. *J. Appl. Mech. Tech. Phys.* **2014**, *55*, 905–916. [[CrossRef](#)]
36. Shelukhin, V.V. Bingham viscoplastic as a limit of non-Newtonian fluids. *J. Math. Fluid Mech.* **2002**, *4*, 109–127. [[CrossRef](#)]
37. Landau, L.D.; Lifshitz, E.M. *Fluid Mechanics. Volume 6 of Course of Theoretical Physics*, 2nd ed.; Revised; Pergamon Press: Oxford, UK; New York, NY, USA; Beijing, China; São Paulo, Brazil; Sydney, NSW, Australia; Tokyo, Japan; Toronto, ON, Canada, 1987.
38. Eslami, H.; Khanjari, N.; Müller-Plathe, F. Self-Assembly Mechanisms of Triblock Janus Particles. *J. Chem. Theory Comput.* **2019**, *15*, 1345–1354. [[CrossRef](#)] [[PubMed](#)]

MDPI  
St. Alban-Anlage 66  
4052 Basel  
Switzerland  
Tel. +41 61 683 77 34  
Fax +41 61 302 89 18  
[www.mdpi.com](http://www.mdpi.com)

*Polymers* Editorial Office  
E-mail: [polymers@mdpi.com](mailto:polymers@mdpi.com)  
[www.mdpi.com/journal/polymers](http://www.mdpi.com/journal/polymers)





MDPI  
St. Alban-Anlage 66  
4052 Basel  
Switzerland  
Tel: +41 61 683 77 34  
[www.mdpi.com](http://www.mdpi.com)



ISBN 978-3-0365-6667-2